THE JOURNAL
OF
CHEMICAL PHYSICS

VOLUME 35, NUMBER 5 NOVEMBER, 1961

Spectrum and Magnetic Properties of Hexagonal $DyCl_3$*

H. M. CROSSWHITE AND G. H. DIEKE
Johns Hopkins University, Baltimore 18, Maryland
(Received March 20, 1961)

The absorption and fluorescence spectra of anhydrous $DyCl_3$ were investigated and the levels up to 37 000 cm^{-1} above the ground state established. Conclusive evidence is presented that the levels below 15 000 cm^{-1} belong to the ^6H and ^6F multiplets. The Zeeman effects show considerable nonlinear interactions which follow quantitatively the existing theory. The 12 low levels and their electric and magnetic field splittings are reasonably well represented by the simplified theory with L-S coupling, with the approximate crystal parameters $B_2^0 = A_2^0\langle r^2\rangle = 89.8$ cm^{-1}, $B_4^0 = -40.0$ cm^{-1}, $B_6^0 = -23.3$ cm^{-1}, $B_6^6 = 253$ cm^{-1}.

1. INTRODUCTION

THE crystal spectra of dysprosium salts have been investigated in recent years by Dieke and Singh[1] and Gramberg.[2] The former established the low lying levels from the ground state to 21 000 cm^{-1} above it through the absorption and fluorescence spectrum of $DyCl_3 \cdot 6H_2O$ while Gramberg investigated the absorption spectra of $Dy(C_2H_5SO_4)_3 \cdot 9H_2O$, $DyCl_3 \cdot 6H_2O$ and $Dy(NO_3) \cdot 6H_2O$ between 21 100 and 26 220 cm^{-1} and discussed the magnetic properties of these salts. Singh[3] investigated the absorption and fluorescence spectra of five dysprosium salts with the Zeeman effect of a number of lines. The salts are, besides those already mentioned, $Dy(BrO_3)_3 \cdot 9H_2O$ and $Dy_2(SO_4)_3 \cdot 8H_2O$. He obtained the spectrum of the chloride to 33 700 cm^{-1}.

The present paper gives a detailed analysis of the absorption and fluorescence spectrum of anhydrous $DyCl_3$ diluted by $LaCl_3$. It has been found in this laboratory that the anhydrous chlorides of the rare earths have important advantages over other known salts. These are sharp lines, greater freedom from superimposed molecular and crystal vibrations, strong fluorescence and a known simple crystal structure of high symmetry. These properties have induced us to take up the study of the spectra of the anhydrous chlorides of all rare earths, except promethium, which is now completed for most of the elements.

The first goal of the analysis of a crystal spectrum is the establishment and identification of the various electronic levels and their displacement and splitting in the electric crystal field. This was done partly for $DyCl_3 \cdot 6H_2O$ for the lower levels in the earlier paper.[1] At that time the number of levels found in this region suggested that the group of lower levels were the nine multiplet components of ^6H and ^6P. This was favored notwithstanding approximate calculations[4] which indicated that the ^6P level should be much higher and suggested that the levels observed around 10 000 cm^{-1} should be components of ^6F.

In the meantime, the reliability of the calculations has been much improved and experience with other rare earths has shown that the position of the levels is in general reproduced by the calculations to a few times 10^2 cm^{-1}. Thus it appears that Jørgensen's original suggestion that these levels are due to ^6F was correct and the results of the present paper confirm this completely. Our present results also clear up why not all the expected multiplet components were found.

Wybourne[5] has recently given a comparison of the calculated with the empirical energies in Dy^{3+}. It confirms that there can be no question about the identity of the lower group of energy levels but that above 20 000 cm^{-1} the situation is very confused. More refined calculations are necessary to clear up the situation and such calculations are now being undertaken in this laboratory

* Work carried out with support of the U. S. Atomic Energy Commission.
[1] G. H. Dieke and S. Singh, J. Opt. Soc. Am. **46,** 495 (1956).
[2] G. Gramberg, Z. Physik **159,** 125 (1960).
[3] Shobha Singh, dissertation, Johns Hopkins University, 1957 (unpublished).
[4] C. K. Jørgensen, Danske Videnskab. Selskab, Math.-fys. Medd. **29,** 11 (1955); see also Acta Chem. Scand. **11,** 981 (1957).
[5] B. G. Wybourne, dissertation, University of Canterbury, New Zealand, 1960.

Copyright © 1961 by the American Institute of Physics

TABLE I. Observed levels of $DyCl_3$.[a]

Level		2μ	E	
Z_1	$^6H_{15/2}$	3	0	z
Z_2		5	9.82	az
Z_3		3	9.97	az
Z_4		1	15.65	az
Z_5		1	40.75	
Z_6		5	80.48	
Z_7		3	121.65	
Z_8		1	140.51	
Y_1	$^6H_{13/2}$	1	3457.03	
Y_2		1	490.30	i
Y_3		3	493.13	i
Y_4		5	522.31	i
Y_5		1	546.62	i
Y_6		3	551.93	
Y_7		5	556.60	i
X_1	$^6H_{11/2}$	1	5793.28	$i\sigma$
X_2		3	801.42	π
X_3		5	842.54	σ
X_4		1	850.29	σ
X_5		3	860.69	$i\pi$
X_6		5	864.68	$i\sigma$
W_1	$^6H_{9/2}$	5	7592.16	
W_2		1	593.59	
W_3	$^6F_{11/2}$	3	598.01	$i\pi$
W_4				
W_5		3	612.9	$j\pi$
W_6			660.33	$i\sigma$
W_7			669.52	$i\sigma$
W_8		3	675.08	
W_9				
W_{10}		5	698.97	$i\sigma$
W_{11}			746.5	$j\sigma$
A_1	$^6H_{7/2}$		8937.16	$c\sigma$
A_2			944.40	$a\sigma$
A_3	$^6F_{9/2}$		952.14	$a\sigma$
A_4				
A_5		5	975.06	
A_6		1	981.14	$a\sigma$
A_7		3	999.32	$a\pi$
A_8		3	9011.78	$a\pi$
A_9			091.57	d
B_1	$^6H_{5/2}$	5	10 124.48	$a\sigma$
B_2		3	151.57	$a\pi$
B_3		1		
C_1	$^6F_{7/2}$	3	10 913.36	$a\pi z$
C_2		5	917.16	$a\sigma z$
C_3		1	922.23	$a\sigma z$
C_4		5	949.45	$a\sigma z$
D_1	$^6F_{5/2}$	1	12 315.60	$a\sigma z$
D_2		5	317.87	$a\sigma z$
D_3		3	336.08	$a\pi z$
E_1	$^6F_{3/2}$	3	13 114.47	$a\pi z$
E_2		1	116.84	$a\sigma z$
	$^6F_{1/2}$	1		
F_1		5	20 963.31	df
G			21 954.07	
H			23 302.76	
I_1		3	24 938.33	πf
I_2		1	938.68	σf
I_3		5	944.42	σ
J			25 581.08	σ
K			26 098.60	σ
L_1		1	27 260.25	σf
L_2		3	289.71	π
L_3		3	291.43	π
M			27 827.10	σ
N			28 326.17	σ
O_1		3	29 467.81	πf
O_2			481.59	σ
O_3			489.88	
P			29 866.96	σ
Q			30 583.30	σ
R			30 996.51	σ
S			31 462.30	π
T_1			32 978.10	σf
T_2			32 992.81	σ
U			33 262.40	σ
V			443.90	π
W			781.50	
X			34 600.17	
Y			35 744.48	
Z			36 279.36	

[a] All levels above F_1 were obtained from the absorption spectrum, those below as lower levels of fluorescent transitions. Exceptions are marked by notes: a—also obtained from photographic absorption spectrum, c—only obtained from photographic absorption spectrum, i—also obtained from infrared absorption, j—only obtained from infrared absorption, d—not observed in absorption from the ground state; however, absorption line from Z_2 present, f—initial state of fluorescence at 4.2°K, z—Zeeman effect analyzed, π—electric vector of ground state absorption parallel C_3 axis, σ—electric vector perpendicular C_3 axis. It should be kept in mind that the data for the states above 20 000 cm^{-1} in Table I do not come from a detailed analysis of the absorption spectrum. The study of the Zeeman effect should furnish additional data with which a more reliable determination of the μ values and other properties of these states can be made. The F state does not appear at all in absorption from the ground state though at elevated temperatures the transition from the Z_3 and Z_4 state to F_1 can be observed.

by Dr. Wybourne. Therefore, it seems wise to wait with a detailed interpretation of the levels above 20 000 cm^{-1} until these calculations are available. Gramberg, who attempted an analysis of some of these levels, came to partly inconclusive results.

We restrict ourselves, therefore, in this paper to a detailed discussion of the ^6H and ^6F levels and take up the higher ones only in so far as they are of importance as upper states of fluorescence.

2. EXPERIMENTAL PROCEDURE

The experimental procedure is that generally followed in this laboratory and has been described before. Crystals are immersed in liquid helium at temperatures from 1.7 to 4.2°K or for some results in liquid nitrogen at 77°K. The spectra are recorded with a 21-ft grating spectrograph with a 7-in. grating and a dispersion of 1.2 A/mm in the first order. In general, below 5000 A the second or third orders were used, between 5000 and 9800 A, the first order. For longer wavelengths up to 12 000 A and for survey exposures a 21-ft Wadsworth spectrograph was utilized with a first-order dispersion of 5 A/mm. The polarization is determined with a calcite rhomb. For Zeeman effects a Bitter magnet is available giving field strengths up to 40 000 gauss.

The crystals used for the earlier part of the work which contained 2% Dy in $LaCl_3$ were kindly furnished us by Dr. C. Hutchison and Dr. E. Wong of the Univer-

sity of Chicago. For the later phases we grew our own crystals according to the procedure of Hutchison and Wong[6] (5% Dy in $LaCl_3$).

For the fluorescence spectrum the crystal was, in general, illuminated by an A-H6 high-pressure mercury lamp concentrated on the crystal by a 15-in. concave mirror. The fluorescence was so bright that its spectrum could be obtained without difficulty on the large spectrograph with a dispersion of 1.2 and 0.6 A/mm. This circumstance facilitated accurate wavelength measurements and demonstrated clearly the varying widths of the individual lines. Some lines were extremely sharp (of the order 0.2 cm^{-1} width) while others were very wide and diffuse even at the lowest temperatures. This is also true for the absorption lines and is generally found in the rare earth crystal spectra.

The results reported on here have been supplemented by absorption measurements in the infrared between 1 and 3μ by F. Varsanyi which will be published in another paper.

3. ABSORPTION

The absorption spectrum at 2°K consists of groups of sharp lines which, as in other salts of the rare earths, are due to transitions from the ground state to the Stark components of the various excited states of the $4f^n$ configuration. At 4.2°K, particularly if the heat conduction is not perfect, additional lines appear which come from the higher Stark components Z_2, Z_3, Z_4 of the ground state. At 77°K additional lines appear, but all lines are more diffuse. This and the fact that many coincidences occur makes the spectrum at 77° or at higher temperatures of much less value.

We designate with A, B, C, etc., the various line groups beginning with the group near 9000 cm^{-1} in the extreme photographic infrared and proceeding to shorter wavelengths.[7] We give the same empirical designation to the excited states.

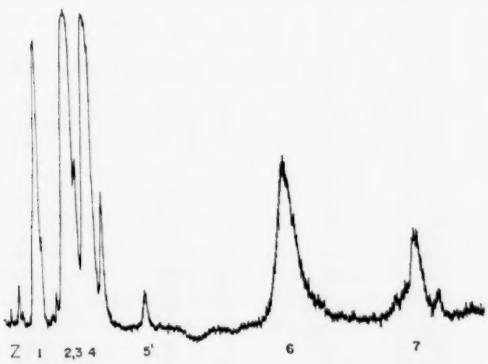

FIG. 1. The $I \rightarrow Z$ transition in fluorescence. The components of the $Z={}^6H_{15/2}$ ground state are numbered. The component 8 is too weak to show.

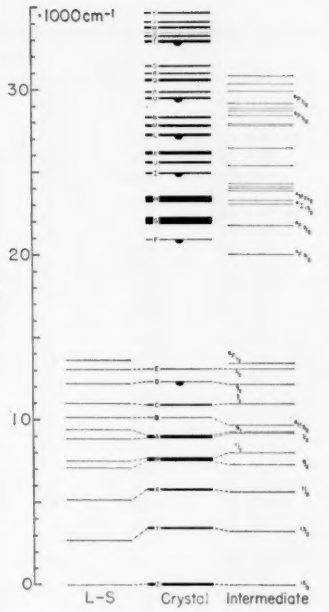

FIG. 2. Middle, observed levels of $DyCl_3$. Left, calculated in L-S coupling, right in approximate intermediate coupling.

In the photographic infrared the four groups A, C, D, and E are easily obtained and the last three named have been studied in detail in a magnetic field. Group B is very weak and needs thick crystals with a high concentration of Dy to be visible and A is a composite group.

There is no observed absorption[8] between the E group at 13 115 cm^{-1} and the F group at 20 963 cm^{-1}. From the F group there are many observed groups as far as the observations extend into the ultraviolet. The group at the shortest wavelength observed by us is near 2600 A.

The energies of the levels obtained from the measurement of the absorption and fluorescence lines are listed in Table I, but above the E level only the lowest Stark components are generally listed except where the higher components are of interest for the fluorescence. Moreover, it is not always certain whether the component listed is actually the lowest one in the group.

4. FLUORESCENCE

When a $DyCl_3$ crystal is illuminated by a high-pressure mercury A-H6 lamp, a fluorescence spectrum is observed that shows more than 400 lines from the ultraviolet to the infrared. The fluorescence spectrum changes when the exciting wavelengths are limited by

[6] C. L. Hutchison, Jr. and E. Wong, J. Chem. Phys. **29**, 754 (1958).

[7] This designation is identical with that in the former paper[1] but different from that used by Gramberg.[2] The latter's A group is our group C, and the designations are two steps different throughout.

[8] The transition to the ${}^6F_{1/2}$ level should lie in this interval but the single line in this group which would correspond to a $\Delta J=7$ transition has not been observed.

TABLE II. The fluorescence spectrum of $DyCl_3$.

ν	I	Trans		E''
26 010.86	3*b*	*O*	Y_1	3456.95
25 998.10	2*bd*	*Nd*		
945.26	3*bd*	*O*	Y_4	3522.55
916.06	1*bbd*	*O*	Y_6	3551.75
24 944.44	7	I_3	Z_1	−0.02
938.45	10*b*	*I*	Z_1	
937.04	4*bd*			
934.15	4*bd*	I_3	$Z_{2,3}$	10.27
932.33	6			
922.64	10*bb*	*I*	Z_4	15.86
921.17	10			
917.63	10*r*			
903.92	7*bbd*	I_3	Z_5	40.50
858.19	9*bb*	*I*	Z_6	80.31
847.45	4*bb*			
823.00	2*bb*	I_3	Z_7	121.42
820.28	3*bb*			
817.32	8*bb*	*I*	Z_7	121.18
810.37	5*bb*			128.13
804.04	2*bb*	I_3	Z_8	140.38
798.37	0*bb*	*I*	Z_8	140.13
705.74	9*bb*			
23 997.09	5	*T*	A_5	8981.01
839.88	4*r*			
737.94	3*r*	*L*	Y_4	3522.31
617.63	3*bd*			
302.54	8*bd*			
301.86	2*d*			
22 826.80	2	*T*	B_2	10 151.30
458.70	3*b*			
21 874.33	0	O	W_2	7593.48
869.83	5	*O*	W_3	7597.98
807.51	3*bb*	*O*	W_6	7660.30
792.34	0*bb*	*O*	W_8	7675.47
503.70	5*r*			
495.34	3*bb*			
489.92	2*b*			
487.51	10*b*	I_3	Y_1	3456.91
481.37	10*b*	*I*	Y_1	3457.13
466.61	1*b*	*L*	X_1	5793.64
458.80	9*b*	*L*	X_2	5801.45
457.84	5			
454.14	8*b*	I_3	Y_2	3490.28
451.30	3*bb*	I_3	Y_2	3493.12
448.99	3*bb*	*I*	Y_2	3489.51
445.36	10*b*	*I*	Y_3	3493.14
441.66	8*bb*			
420.19	3*bb*			
417.62	2	*L*	X_3	5842.63
416.46	8*bb*	*I*	Y_4	3522.04
415.97	9*bb*			
399.32	4*bb*	*L*	X_5	5860.93
397.81	4*bb*	I_3	Y_5	3546.61
395.83	2*bb*	*L*	X_6	5864.42
393.99	2*bb*			
391.87	7*bb*	*I*	Y_5	3546.63
386.36	6*bb*	*I*	Y_6	3552.14
385.80	6*bb*			
381.90	9*bb*	*I*	Y_7	3556.60
375.40	3*bb*			
20 968.92	2*b*			
968.30	2*b*			
963.32	0*bb*	*F*	Z_1	−0.01
955.69	9*bb*			
952.77	10*bb*	*F*	Z_3	10.54
950.79	10*bb*			
947.49	8*b*	*F*	Z_4	15.82
945.89	4*b*			
20 945.05	3*b*			
922.28	9*bb*	*F*	Z_5	41.03
918.98	3*bb*			
844.80	2*bb*			
841.02	8*bb*	*F*	Z_7	122.29
834.57	4*bb*			
822.29	5*bb*	*F*	Z_8	141.02
662.46	9	*T*	D_1	12 315.64
641.94	9	*T*	D_2	12 336.16
515.65	6	*O*	A_3	8952.16
486.84	6	*O*	A_6	8980.97
468.53	6*r*	*O*	A_7	8999.28
19 668.88	3*b*			
667.99	1*d*	*L*	W_1	7592.26
666.73	9*v*	*L*	W_2	7593.52
665.54	2*b*			
590.66	2*bd*	*L*	W_7	7669.59
585.34	2*bd*	*L*	W_8	7674.91
561:12	10*bd*	*L*	W_{10}	7669.13
145.22	6	*I*	X_1	5793.28
137.26	5	*I*	X_2	5801.24
096.06	0*b*	*I*	X_3	5842.44
088.17	2*b*	*I*	X_4	5850.33
078.97	1*d*			
078.05	5*b*	*I*	X_5	5860.45
073.55	2*bb*	*I*	X_6	5864.95
18 550.68	4	*O*	C_2	10 917.13
545.70	1*bb*	*O*	G_3	10 922.11
315.85	2*b*	*L*	A_2	8944.40
309.55	6			
308.12	10*bb*	*L*	A_3	8952.13
306.60	5			
305.51	3*b*			
297.60	4*bb*	*L*	A_4	8962.65
285.77	3*bb*			
285.16	4*bb*	*L*	A_5	8975.09
260.92	8	*L*	A_7	8999.33
260.42	7*c*			
259.42	3*c*			
248.48	7*b*	*L*	A_8	9011.77
168.57	4*bb*	*L*	A_9	9091.68
17 512.25	8			
511.80	8			
509.61	3			
509.31	4			
507.83	10			
506.16	10*b*	*F*	Y_1	3457.15
475.92	10			
472.98	10*b*	*F*	Y_2	3490.33
469.07	10*c*	*F*	Y_3	3494.24
422.32	7*b*			
421.16	3*bb*			
416.20	10*b*	*F*	Y_5	3547.11
411.40	9*bb*	*F*	Y_6	3551.91
407.54	5*bb*	*F*	Y_7	3555.77
346.44	9	*I*	W_1	7592.06
344.91	10	*I*	W_2	7593.59
340.82	10	I_1	W_3	7597.86
340.37	9*r*	I_1	W_3	7597.98
278.18	2*bb*	*I*	W_6	7660.32
269.03	3*bb*	*I*	W_7	7669.47
239.69	6*r*	*I*	W_{10}	7698.81
152.29	0	*O*	D_1	12 315.52
135.77	10*b*	*L*	B_1	10 124.48
108.68	10*b*	*L*	B_2	10 151.57
106.80	7			
16 412.69	7*r*			
411.47	3			
407.47	3*b*			

TABLE II (*continued*)

ν	I	Trans		E''
16 376.12	2			
374.56	9*r*			
372.84	8*bb*			
346.92	8	L	C_1	10 913.33
346.50	2			
344.27	3			
343.13	10*b*	L	C_2	10 917.12
341.60	2*b*			
314.31	2*b*			
312.12	10*v*			
310.14	10*bb*	L	C_4	10 950.11
307.11	7			
244.73	2			
15 986.35	10*bb*	I	A_3	8952.15
963.46	2*b*	I_2	A_6	8980.96
957.40	9*r*	I	A_6	8981.10
945.19	5*r*	I_3	A_7	8999.23
939.24	9	I	A_7	8999.26
938.85	10*b*			
932.66	3	I_3	A_8	9011.76
926.86	2*b*	I	A_8	9011.64
847.04	3*bb*	I	A_9	9091.46
173.11	4*r*			
171.66	7			
170.03	10*d*	F	X_1	5793.28
161.74	10	F	X_2	5801.57
161.26	9			
159.92	6			
120.50	2*bb*	F	X_3	5842.81
113.06	3*b*	F	X_4	5850.25
102.61	6*b*	F	X_5	5860.70
099.42	0*b*	F	X_6	5863.89
14 981.14	7*br*			
977.29	2*b*			
973.71	4*bb*			
963.46	4*b*			
944.62	1*bd*	L	D_1	12 315.63
942.41	9*bd*	L	D_2	12 317.84
941.13	2*b*			
926.06	2*bd*			
924.86	2*b*			
924.19	9*b*	L	D_3	12 336.06
147.12				
145.83	10*b*	L	E_1	13 114.42
144.82	2*d*			
144.35	3*b*			
143.29	2*b*	L	E_2	13 116.96
13 369.64	6	F	W_2	7593.67
365.09	8	F	W_3	7598.22
302.94	0*bb*	F	W_6	7660.37
271.89	3*b*			
12 315.30	0*d*	D	Z_1	0.30
307.41	3*b*	D_2	Z_3	10.46
305.47	6*b*	D	Z_2	10.13
302.14	6*b*	D_2	Z_4	15.73
299.80	1*d*	D	Z_4	15.80
299.25	3*b*			
280.09	1*bb*			
277.14	4*bb*	D_2	Z_5	40.73
234.94	3*bb*	D	Z_6	80.66
194.90	0*bb*	D	Z_7	121.70
010.95	1	F	A_3	8952.36
11 982.18	1	F	A_6	8981.13
963.56	2*r*	F	A_7	8999.75

suitable filters. This circumstance may be used to ascertain the origin of some fluorescence lines in doubtful cases.

On the whole, however, there is no difficulty in identifying a particular group of fluorescence lines as there are several excited levels from which emission takes place and the wave number differences between lines of the same final state must be equal to the wave number differences between absorption lines. Since the fluorescence spectrum could be obtained with very high dispersion, the wavelengths are sufficiently accurate not to allow any doubt about the identification. Only for the long wavelengths (>7000 A) was it necessary to rely on a smaller spectrograph (5 A/mm).

Many of the fluorescence lines are extraordinarily sharp, as sharp as the lines of the iron comparison spectrum. Others were wide and diffuse. These were invariably transitions to the higher Stark components of an electronic state, even to those of the ground state (see Fig. 1).

All states between the ground state and E have been found as the final states of fluorescence emission. It is thus possible to obtain the eight Stark components of the ground state. All the other states have been also found in absorption (A, B, C, D, E, see this paper; Y, X, W, see Varsanyi).

At low temperatures, emission is observed from the lowest Stark component of the electronic levels D, F, I, L, O, T. These are all levels which have a relatively large gap between themselves and the next lower level (see Fig. 2), a fact which favors high stability.

The data on the fluorescence spectrum are presented in Table II. The many very weak lines have been omitted unless they are classified. Such lines occurring in each spectrum are of uncertain origin and may be due to impurities. Among the identified impurities, the lines of $PrCl_3$ and $NdCl_3$ showed weakly. Whether the unclassified lines in Table II are due to unidentified impurities or to other transitions in $DyCl_3$ must be left to further work. The column E'' gives the energy of the final state obtained from the particular line.

5. THEORETICAL BACKGROUND

For the proper identification of the levels use is made of the number of Stark components occurring in each group, which is equal to $J+\frac{1}{2}$, the selection and polarization rules, the Zeeman effects, and a comparison of the empirical levels with results obtained from theoretical calculations.

The calculations carried out for Dy^{3+} in a very approximate form first by Jørgensen[4] and systematized, with the help of Racah's ideas, by Elliott, Judd, and

TABLE III. Equivalent factors in Dy^{3+} for *LS* coupling.

		$10^3\alpha$	$10^5\beta$	$10^6\gamma$
Z	$^6H_{15/2}$	−6.349	−5.920	1.035
Y	13/2	−6.838	−3.767	−1.208
X	11/2	−7.823	0.269	−6.267
W	9/2	−10.101	8.447	−23.459
A	7/2	−16.508	20.212	−152.495
B	5/2	−41.270	−250.120	0
W	$^6F_{11/2}$	4.040	−6.144	0.748
A	9/2	3.367	8.260	−8.970
C	7/2	2.116	36.342	49.333
D	5/2	−0.635	105.820	0
E	3/2	−8.889	0	0

Runciman,[9] Judd,[10] Wybourne,[5] and others, yield approximate energies and wave functions for the free-ion level. The chief approximation is that interactions of the $4f^9$ configuration with other configurations are neglected. As we are dealing with low levels, the *LS* coupling approximation is sufficiently good[11] and will be used throughout in this paper. This approximation is however entirely inadequate for the higher levels (F and higher) and therefore a detailed consideration of these will be postponed until the results of intermediate coupling calculations are available.

For C_{3h} symmetry the free ion states are modified by the following electric crystal potential:

$$V(r\theta\phi)=A_2^0r^2P_2(\zeta)+A_4^0r^4P_4(\zeta)+A_6^0r^6P_6(\zeta)+A_6^6r^6P_6^6(\zeta)e^{i6\phi}, \quad (1)$$

where $\zeta=\cos\theta$ and the A_q^s are numerical constants which are to be determined from the empirical data.

A free ion state is characterized by the quantum numbers α, L, S, J, M, where α differentiates between different states with the same $L\,S\,J\,M$. In the application of (1) we may disregard, as is commonly done, intereactions between different $\alpha\,L\,S\,J$ states and obtain the energies and wave functions outside a magnetic field from a matrix of order $J+\frac{1}{2}$ which reduces to simpler matrices each corresponding to an irreducible representation of the C_{3h} (or S_6) group. The first three terms in (1) contain only diagonal terms and leave M a good quantum number. The last term connects states differing in M by a multiple of six. This abolishes M as a good quantum number and makes it necessary to substitute the weaker crystal quantum number μ first introduced by Hellwege.[12]

The necessary matrix components can be obtained by the equivalent operator method of Stevens[13] which says that the operators V_q^s in (1) are equivalent to more familiar operators if the terms $r^qP_q^s$, are expressed in Cartesian coordinates and z^m, r^{2n}, $(x\pm iy)^p$, respectively, are replaced by the operators J_z^m, j^{2n}, $(J_x\pm iJ_y)^p$, the first two being equivalent to numerical factors M^m and $J^n(J+1)^n$. The identity is established by multiplying these operators by $A_q^s\langle r^q\rangle\sigma_q=B_q^s\sigma_q$ where σ_q is a numerical factor usually called α, β, γ for $q=2$, 4, 6, respectively. The equivalent operators and the values for α, β, γ can be obtained from data found in the literature. The latter are given in Table III for the states of interest to us. More general methods of calculating the matrix elements, valid also for intermediate coupling and when more general interactions are taken into account based on Racah's irreducible tensor operators, have been given by Judd.[10] These reduce the calculation of the matrix elements to 3-j and 6-j symbols for which convenient tables are available.

In order to carry out the numerical calculations it is necessary to know the four crystal field parameters B_q^s. These were obtained in the following way from the Stark components of the ground state.

In the absorption spectrum, the four lowest Stark components can be determined accurately, which produces three differences, insufficient for the four independent B_q^s. The fourth quantity needed can be chosen in many ways. At the time the calculations were made the higher components of the ground state were not known sufficiently well. For this reason the value of the external magnetic field which mixes the two states in equal parts with $\mu=\frac{3}{2}$, and which depends on the B_q^s, was chosen. These data determine the constants B_q^s completely, and we obtain

$$B_2^0=89.8\ \text{cm}^{-1} \qquad B_6^0=-23.3\ \text{cm}^{-1},$$
$$B_4^0=-40.0\ \text{cm}^{-1} \qquad B_6^6=253\ \text{cm}^{-1}.$$

These values of the crystal field parameters were used for all further calculations. Since the calculations are approximate, somewhat different values would have been obtained if a different set of empirical data had been used to calculate the parameters. In turn, we cannot expect exact agreement between the observed facts and the calculations based on our set of parameters. Because the neglect of intermediate spin orbit coupling is one of the most serious defects, it seems futile to strive for a better all-around agreement without taking intermediate coupling into account.

The matrices for $^6F_{3/2}$, $^6F_{5/2}$, $^6F_{7/2}$, and $^6H_{15/2}$, which must be diagonalized in order to obtain the crystal field splittings, are given in Table IV when $h=0$ is substi-

[9] J. P. Elliott, B. R. Judd, and W. A. Runciman, Proc. Roy. Soc. (London) **240**, 509 (1957).
[10] B. R. Judd, Proc. Phys. Soc. (London) **74**, 330 (1959).
[11] Wybourne has estimated that for the states under consideration departures from L, S coupling are only 4–10% (private communication).
[12] K. H. Hellwege, Ann. Physik **4**, 95 (1948).
[13] K. W. H. Stevens, Proc. Roy. Soc. (London) **A65**, 209 (1952).

tuted. They are given completely reduced for the case labeled "parallel effect."

Table V gives the Stark components for the four states in question and indicates the extent of M mixing obtained. We see that in general M is still a relatively good quantum number. Of course, for $M=\frac{1}{2}(J<\frac{11}{2})$, $M=\frac{3}{2}(J<\frac{9}{2})$, and $M=\frac{5}{2}(J<\frac{7}{2})$, M remains strictly a good quantum number in the approximation here employed.

6. ZEEMAN EFFECT

The term in the Hamiltonian that expresses interaction with the magnetic field is

$$V_h=\beta_0 g(\mathbf{J}\cdot\mathbf{H}), \tag{2}$$

where β_0 is the value of the Bohr magneton and g in our case the ordinary Landé g factor. Equation (2) can be used in this form because we may disregard true Paschen Back effects, that is, magnetic interactions

TABLE IV. Crystal field and magnetic interaction matrices for $DyCl_3$.

PARALLEL EFFECT

M	3/2	1/2
3/2	0.00+3h	
1/2		2.35+h

$^6F_{3/2}$

PERPENDICULAR EFFECT

M	3/2	1/2	-1/2	-3/2
3/2	0.00	$h\sqrt{3}$	-	-
1/2	$h\sqrt{3}$	2.35	2 h	-
-1/2	-	2 h	2.35	$h\sqrt{3}$
-3/2	-	-	$h\sqrt{3}$	0.00

PARALLEL EFFECT

M	5/2	3/2	1/2
5/2	2.28+5h		
3/2		20.49+3h	
1/2			0.00+h

$^6F_{5/2}$

PERPENDICULAR EFFECT

M	5/2	3/2	1/2	-1/2	-3/2	-5/2
5/2	2.28	$h\sqrt{5}$	-	-	-	-
3/2	$h\sqrt{5}$	20.49	$h\sqrt{8}$	-	-	-
1/2	-	$h\sqrt{8}$	0.00	3 h	-	-
-1/2	-	-	3 h	0.00	$h\sqrt{8}$	-
-3/2	-	-	-	$h\sqrt{8}$	20.49	$h\sqrt{5}$
-5/2	-	-	-	-	$h\sqrt{5}$	2.28

PARALLEL EFFECT

M	-7/2	5/2	3/2	1/2
-7/2	6.67-7h	9.23		
5/2	9.23	33.72+5h		
3/2			0.00+3h	
1/2				8.85+h

$^6F_{7/2}$

PERPENDICULAR EFFECT

M	7/2	5/2	3/2	1/2	-1/2	-3/2	-5/2	-7/2
7/2	6.67	$h\sqrt{7}$	-	-	-	-	9.23	-
5/2	$h\sqrt{7}$	33.72	$h\sqrt{12}$	-	-	-	-	9.23
3/2	-	$h\sqrt{12}$	0.00	$h\sqrt{15}$	-	-	-	-
1/2	-	-	$h\sqrt{15}$	8.85	4 h	-	-	-
-1/2	-	-	-	4 h	8.85	$h\sqrt{15}$	-	-
-3/2	-	-	-	-	$h\sqrt{15}$	0.00	$h\sqrt{12}$	-
-5/2	9.23	-	-	-	-	$h\sqrt{12}$	33.72	$h\sqrt{7}$
-7/2	-	9.23	-	-	-	-	$h\sqrt{7}$	6.67

$^6H_{15/2}$ PARALLEL EFFECT

$\mu = 1/2$

M	13/2	1/2	-11/2
13/2	36.91+13h	13.65	-
1/2	13.65	134.51+h	20.64
-11/2	-	20.64	12.86-11h

$\mu = 3/2$

M	15/2	3/2	-9/2
15/2	3.74+15h	6.66	-
3/2	6.66	105.83+3h	26.23
- 9/2	-	26.23	0.00-9h

$\mu = 5/2$

M	5/2	-7/2
5/2	60.47+5h	29.32
- 7/2	29.32	18.52-7h

TABLE IV (*continued*)

PERPENDICULAR EFFECT
$^6H_{15/2}$

μ	M	15/2	13/2	11/2	9/2	7/2	5/2	3/2	1/2	-1/2	-3/2	-5/2
3/2	15/2	3.74	$h\sqrt{15}$	-	-	-	-	6.66	-	-	-	-
1/2	13/2	$h\sqrt{15}$	36.91	$h\sqrt{28}$	-	-	-	-	13.65	-	-	-
-1/2	11/2	-	$h\sqrt{28}$	12.86	$h\sqrt{39}$	-	-	-	-	20.64	-	-
-3/2	9/2	-	-	$h\sqrt{39}$	0.00	$h\sqrt{48}$	-	-	-	-	26.23	-
-5/2	7/2	-	-	-	$h\sqrt{48}$	18.52	$h\sqrt{55}$	-	-	-	-	29.32
5/2	5/2	-	-	-	-	$h\sqrt{55}$	60.47	$h\sqrt{60}$	-	-	-	-
3/2	3/2	6.66	-	-	-	-	$h\sqrt{60}$	105.83	$h\sqrt{63}$	-	-	-
1/2	1/2	-	13.65	-	-	-	-	$h\sqrt{63}$	134.51	8 h	-	-
-1/2	-1/2	-	-	20.64	-	-	-	-	8 h	134.51	$h\sqrt{63}$	-
-3/2	-3/2	-	-	-	26.23	-	-	-	-	$h\sqrt{63}$	105.83	$h\sqrt{60}$
-5/2	-5/2	-	-	-	-	29.32	-	-	-	-	$h\sqrt{60}$	60.47

between two different free-ion states. We consider two separate cases, the parallel effect where $H=H_z$ is parallel to the crystal axis and the perpendicular effect where $H=H_x$. All other field directions can be derived from these two cases.

When the magnetic field splittings are small compared to the field free spacings of the Stark components we need only consider the diagonal elements in (2) or, in the perpendicular effect, the elements connecting the members of the degenerate pair. This leads in both cases to a linear Zeeman effect. If, however, the magnetic interaction between different Stark components cannot be disregarded, we have a crystal Paschen Back effect which leads to nonlinear and asymmetric splittings and other complications. In the parallel effect only two levels with the same quantum number μ can interact since J_z is always diagonal in M; for the perpendicular case the interacting levels differ in M by ± 1 mod 6. As pairs satisfying the latter condition are much more frequent we find nonlinear effects particularly in the perpendicular Zeeman effect.

All matrix elements of the magnetic interaction are well known as they are related directly to the components of the angular momentum. It is best to carry out the diagonalization of the matrices for the electric crystal field at the same time and the full matrices are found in Table IV with $h=\frac{1}{2}\beta_0 gH$.

These matrices were diagonalized with the help of a

TABLE V. M mixing in the $^6H_{15/2}$ state.[a]

Level	E_{calc}	μ	M	1/2	3/2	5/2	7/2	9/2	11/2	13/2	15/2
Z_1	0[b]	3/2	9/2	...	5.45	...	...	92.18	...	...	2.37
Z_2	9.83[b]	5/2	7/2	...	...	20.91	79.09	...	...	...	...
Z_3	9.97[b]	3/2	15/2	...	0.05	...	...	2.67	...	...	97.28
Z_4	15.65[b]	1/2	11/2	2.92	...	...	...	...	96.37	0.71	...
Z_5	41.72	1/2	13/2	1.30	...	...	...	...	1.10	97.60	...
Z_6	81.93	5/2	5/2	...	...	79.09	20.91	...	...	...	...
Z_7	118.74	3/2	3/2	...	94.50	...	...	5.15	...	...	0.35
Z_8	146.06	1/2	1/2	95.78	...	...	...	...	2.53	1.69	...
C_2		5/2	7/2	...	...	8.7[c]	91.3[c]	...	...	...	...
C_4		5/2	5/2	...	...	91.3[c]	8.7[c]	...	...	...	...

[a] The numbers are the squares of the amplitudes normalized to 100.
[b] These values equal the observed values.
[c] Obtained from the empirical Zeeman effect. The corresponding values calculated with the crystal parameters of the ground state are 18.0 and 82.0, respectively.

TABLE VI. Allowed transitions with polarization from the five lowest components of the ground state to the C, D, and E states.[a]

			$^6F_{3/2}$		$^6F_{5/2}$			$^6F_{7/2}$			
μ	$Z(M)$	%[b]	$E_1(3/2)$	$E_2(1/2)$	$D_1(1/2)$	$D_2(5/2)$	$D_3(3/2)$	$C_1(3/2)$	$C_2(7/2)$	$C_3(1/2)$	$C_4(5/2)$
3/2	$Z_1(9/2)$	92	π	σ	σ	σ	π	π	σ	σ	σ
5/2	$Z_2(7/2)$	79	σ	$\sigma\pi$	$\sigma\pi$	...	σ	σ	...	$\sigma\pi$	...
3/2	$Z_3(15/2)$	97	(π)	(σ)	(σ)	(σ)	(π)	(π)	σ	(σ)	σ
1/2	$Z_4(11/2)$	96	σ	...	...	$(\sigma)\pi$	σ	σ	$\sigma\pi$	...	$\sigma\pi$
1/2	$Z_5(13/2)$	98	(σ)	...	...	σ	(σ)	...	π	...	$\sigma\pi$

[a] Those not permitted by M rule but permitted by μ rule are in parentheses.
[b] Percentage of the indicated M in the state.

high-speed computer for a number of field strengths from $H=0$ to 35 100 gauss and thus the energy levels in the presence of a magnetic field obtained which formed the basis for comparison with the experimental data (see Sec. 7.2). It should be noted that in the parallel effect the value of μ is preserved, while in the perpendicular effect in general, μ loses its meaning.

7. INTERPRETATION OF THE EMPIRICAL DATA

7.1. Selection and Polarization Rules

Figure 2 shows a comparison of the observed and calculated levels, the latter with $F_2=411$ cm^{-1} and $\chi=-4.50$ chosen so as to give the best agreement for the lowest two multiplets. It is clear, as had been remarked earlier by Jørgensen[4] and Wybourne, that the levels between 10 000 and 13 100 cm^{-1} can belong only to the ^6F multiplet if we give any credence at all to the calculations.

We shall show now that all other observed properties agree with this interpretation. We shall first use the selection and polarization rules. For electric dipole radiation which seems to be predominant in $DyCl_3$ as in most other rare earth salts we have the rule: π components $\Delta\mu=\pm3$, σ components $\Delta\mu=\pm2$, ±4 for observations perpendicular to the axis. When M is a good quantum number the corresponding rule applies for M. In those cases where there is only a small degree of M mixing we expect the lines allowed by the μ rule but forbidden by the M rule to be weak.

For most observations a crystal was used which was mounted in a glass tube with a modest amount of helium, but not enough to give good heat conduction when the tube was immersed in liquid helium. Under the intense illumination the temperature was somewhat raised so that the four lowest levels Z_1, Z_2, Z_3, Z_4 of the ground state absorbed and these have the M (and μ) values $\frac{9}{2}(\frac{3}{2})$, $\frac{7}{2}(\frac{5}{2})$, $\frac{15}{2}(\frac{3}{2})$, $\frac{11}{2}(\frac{1}{2})$, while at 77°K a fifth level with $\frac{13}{2}=M(\frac{1}{2})$ also absorbs. The assignment of the M and μ values of these ground state components is best made from the Zeeman effect (see Sec. 7.2). The presence of four absorbing levels although complicating the general line pattern helps greatly in the interpretation of the upper levels. When another crystal with sufficient helium for efficient heat conduction was used, particularly when the bath temperature was lowered below 2°K, only absorption from the ground state Z_1 remained.

Table VI gives a resume of the lines to be expected in absorption from the four ground state components to all levels of $^6F_{3/2}(E)$, $^6F_{5/2}(D)$, and $^6F_{7/2}(C)$ where the components within parentheses are allowed by the μ selection rule but forbidden by the M rule in the cases where there is less than 10% M mixing. Figures 3–5 show the empirical data. The transitions shown by full lines satisfy in general both selection rules, and they are the lines actually observed. The broken lines indicate lines allowed by the μ rule but not observed or only seen in the magnetic field. Generally the lines forbidden by the M rule are absent except in the C group where both C states with $\mu=\frac{5}{2}$ behave similarly, indicating that M is not preserved, in agreement with Table V. There are, here and there, other weak lines violating the M rule indicating that M is not a perfect quantum number for the components of the ground state either. The selection and polarization rules for electric dipole radiation determine the μ and J values of the three excited states completely and there is no other possible choice compatible with the rules.

The situation for the remaining states is not quite as favorable because the empirical data are sparser. The B group near 9850 A, which must have $^6H_{5/2}$ as an upper state, is very weak. Two lines are clearly found in the absorption of a rather thick crystal and the corresponding levels B_1 and B_2 are also established from fluorescent transitions. The third component is uncertain. Fluorescence from the L level suggests that the $\mu=\frac{1}{2}$ level is at 10 153.45 but this line would be too strong for a forbidden $\frac{1}{2}\rightarrow\frac{1}{2}$ transition. Moreover, field splitting calculations put this level much higher.

All Stark components of the $Y(^6H_{13/2})$ and $X(^6H_{11/2})$ levels are well established from fluorescence transitions and largely confirmed by absorption in the infrared. In some cases where the lines are very broad the accuracy is not very good. For $^6H_{13/2}$ the spacing of the components is in good agreement with the field splitting cal-

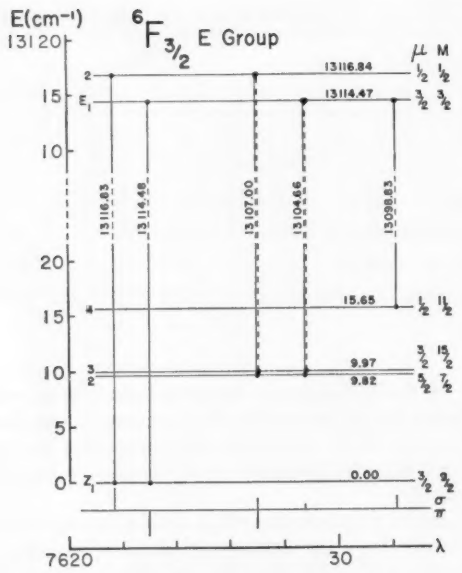

FIG. 3. Structure of the *E* group.

culations and the μ values in Table I are those of the calculated levels confirmed by the selection rules. There is much poorer agreement for $^6H_{11/2}$. The μ values are consistent with the polarization of the infrared absorption lines and the selection rules and not inconsistent with the calculated values.

The *W* and *A* groups have given considerable trouble and their structure is not yet completely clear. We believe that the *W* group accounts for $^6H_{9/2}$ and $^6F_{11/2}$ and thus should have 11 components, and that the *A* group contains $^6H_{7/2}$ and $^6F_{9/2}$ with 9 components jointly. In support of this are the following facts. The number of components in both groups is definitely more than that required if each were to contain only one free-ion state. Furthermore no other absorption or fluorescence groups can be discovered which could account for the two other states anywhere in this region. We are therefore forced to the conclusion that each of the two groups contains two free-ion states. It has not been possible, however, to find all the Stark components to be expected with this assumption, and this must be left to future work. In some cases the values of the μ numbers are fairly well established from the polarization and selection rules, in other cases there is not enough evidence for their establishment. The infrared absorption data furnished valuable clues but details will be found in another paper.[14]

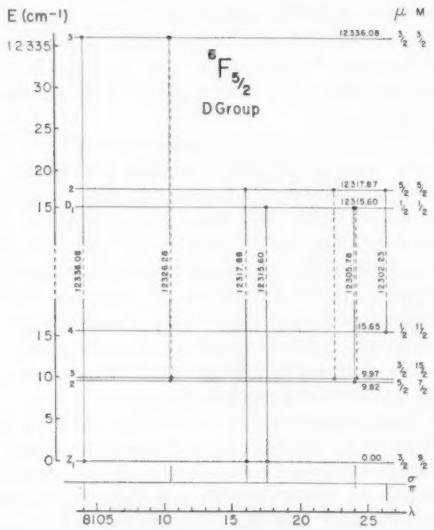

FIG. 4. Structure of the *D* group.

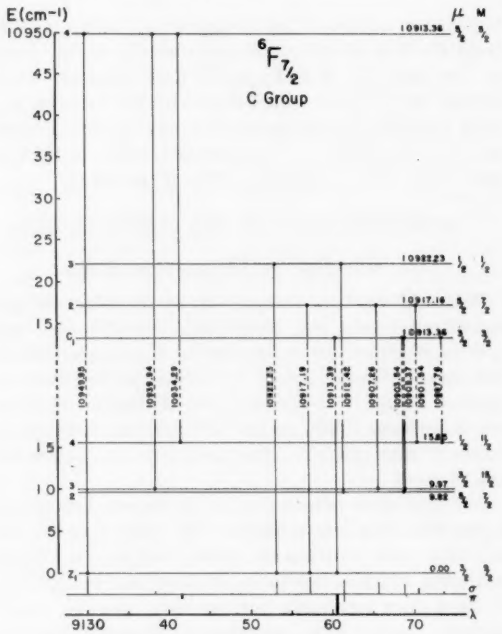

FIG. 5. Structure of the *C* group.

7.2. Zeeman Effect of the *C*, *D*, and *E* States

The selection rule and fluorescence data prove beyond any doubt that the *J* values for the *C*, *D*, and *E* states are $\frac{7}{2}$, $\frac{5}{2}$, and $\frac{3}{2}$, respectively, but cannot give a decision on whether they are ^6F or ^6P states. A clear decision between the two possibilities can be made with the help of the Zeeman effects.

In the magnetic field the patterns appear so complicated that an interpretation at one field strength seems

[14] F. Varsanyi and G. H. Dieke, J. Chem. Phys. (to be published).

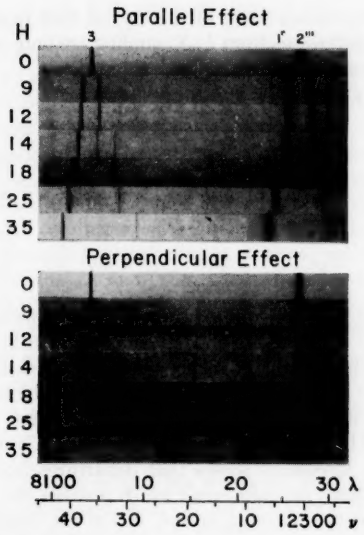

FIG. 6. Zeeman effect in the D group π polarization. Numbers on left: field strength in kilogauss.

impossible. This is particularly true at the slightly elevated temperatures where the four lowest Stark components of the ground state contribute to the absorption. For this reason photographs were obtained for a number of gradually increasing field strengths. This made it possible to follow the individual components and left no doubt as to their identification at any field strength. Figures 6 and 7 show the situation for the D group with both field directions and both polarizations.

We see particularly in Fig. 7 that the pattern at high

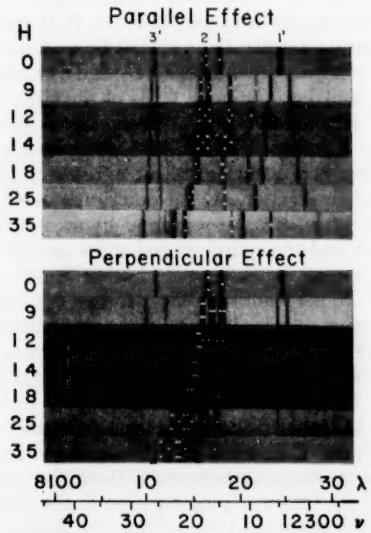

FIG. 7. Zeeman effect in the D group, σ polarization.

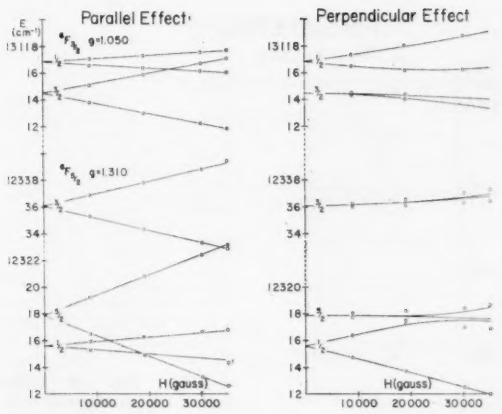

FIG. 8. Magnetic splitting of the $^6F_{5/2}$ and $^6F_{9/2}$ levels.

field strengths is so complicated that without the help of the intervening fields an interpretation would be virtually impossible. The components of the D state involved in the transitions are indicated by 1, 2, 3 and primes mean that the lines are not absorbed by the ground state but by the higher Stark components Z_2, Z_3, Z_4, respectively. Irregularities appear, e.g., in the upper part of Fig. 6 where at 14 000 gauss a third component of line 3 appears which strengthens with increase of field and is the only component left for the highest field strength. In the perpendicular effect the same line shows a very asymmetric pattern. All these irregularities are chiefly due to the final state which is evident from Figs. 11 and 12. In the perpendicular effect there are also irregularities because of the upper state (Fig. 8).

The chief reason for the complicated often asymmetric patterns with intensity anomalies are the pronounced departures from linearity and a quantitative understanding can be obtained only from a comparison with the theoretical treatment outlined in Sec. 6.

After the contributions of the ground state compo-

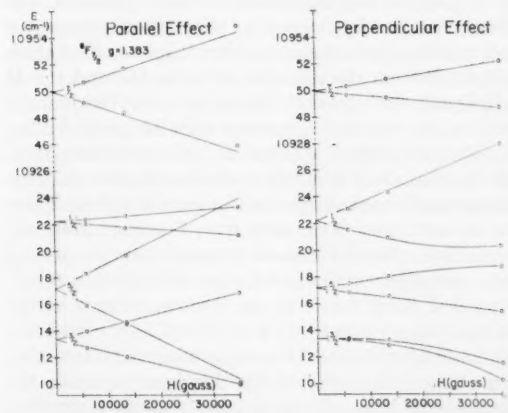

FIG. 9. Magnetic splitting of the $^6F_{7/2}$ levels.

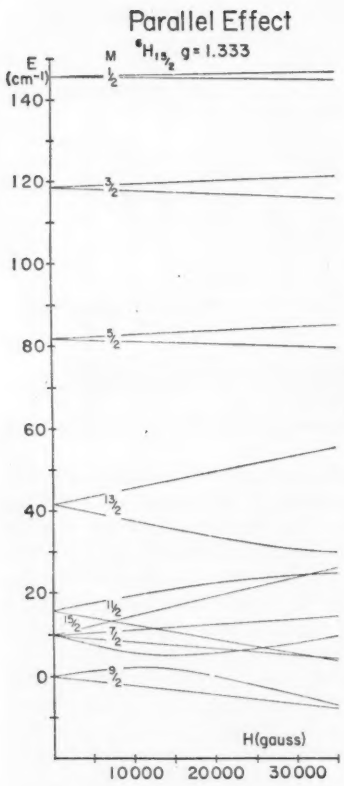

FIG. 10. Calculated magnetic splittings of $^6H_{15/2}$ levels.

nents to the observed line patterns have been eliminated (see Sec. 8), the splittings of the components of the excited states can be empirically determined. These splittings can then be compared with the patterns calculated according to the method of Sec. 6. This comparison is made in Figs. 8 and 9. The curves are the calculated energies. Since the states do not represent strictly L, S coupling, the g values were determined empirically so as to give the best agreement between calculated and observed values for the parallel effect. Furthermore, the field free energies are the empirical values and not those calculated from the matrices of Table IV, and the M mixing of C_2 and C_4 has also been determined empirically so as to give the best agreement with the parallel effect (see Table V). The circles represent the observed points. We see that there is nearly perfect agreement between theory and observations for the parallel effect. There are no noticeable departures from linearity, those observed in the line patterns all originate from the ground state components. From the statements in Sec. 6 it is clear that there should be no nonlinear effects except for the two $\mu=\frac{5}{2}$ states C_2 and C_4 and as the field free states are separated by 33 cm^{-1} the nonlinear interaction is not large. It is significant that for these two states the experimental points do not lie exactly on the theoretical curve. Except for these two levels the splittings should be entirely independent of the crystal field parameters and the deviations from L, S coupling are only reflected in the numerical g values.

These are

		g obs	g Landé	g for ^6P
E	$^6F_{3/2}$	1.050	1.067	2.400
D	$^6F_{5/2}$	1.310	1.314	1.866
C	$^6F_{7/2}$	1.383	1.397	1.714

where the values computed from the Landé formula for pure L, S coupling are also given as well as the values for ^6P with the same J. We see that the empirical values reproduce the Landé values nearly within the limits of experimental errors. The small discrepancies can be explained by departures from L, S coupling. Conversely, the good agreement shows that departures from L, S coupling must be quite small which justifies the simplified procedure outlined in Sec. 6. On the other hand there is no correspondence between the observed g values and those expected for ^6P. This completes the proof that we are dealing here with three components of the ^6F multiplet.

The patterns for the perpendicular effect were calculated with the same constants as those for the parallel effect, in particular, the same g values. We see that the agreement is not quite as good as for the parallel case although there can be no question about the general trend. The reason for the poorer showing is that in all cases shown the results depend explicitly on the crystal field parameters and the degree of M mixing. It was found later that for the perpendicular case the crystal was about 8° misaligned which contributes to the deviations, but does not account for them entirely.

The following features are observed. If M remains a good quantum number there should be no linear effect except $M=\pm\frac{1}{2}$, i.e., the states E_2, D_1, and C_3 which show all linear splittings for small fields of the right magnitude, $g(J+\frac{1}{2})$ Lorentz units. When there is mixing of $M=\frac{5}{2}$ and $\frac{7}{2}$, as for C_2 and C_4, we also expect a linear effect which here shows excellent agreement between theory and observations. In the other cases, $\mu=\frac{3}{2}$ for all J and $\mu=\frac{5}{2}$ for $J<\frac{7}{2}$, there should be no splitting for small fields and the splittings and shifts are all due to magnetic interaction with neighboring Stark components. In the perpendicular effect μ does not remain a good quantum number in such cases, which means that the μ selection and polarization rules break down, which leads to intensity anomalies which often are observed (see Figs. 6 and 7). Forbidden lines appear under the action of the field and allowed ones may become weaker and disappear altogether. These features make the analysis of the magnetic behavior without the quantitative aid of the theory so puzzling even in the simplified form. On the other hand, we see that the theory reproduces the magnetic behavior in all details.

8. THE GROUND STATE $^6H_{15/2}$

The Stark components of the ground state can be obtained through absorption at elevated temperatures or from fluorescence. The first method is restricted to the lower Stark components, because at the higher temperatures required to bring out the other components the lines are usually so broad as to make good measurements impossible. We have seen that under favorable conditions absorption from the four lowest levels showed up clearly and that it was possible to obtain detailed Zeeman effects for these levels. A fifth level at 39 cm^{-1} shows up in absorption at 77°K. The remaining ones must be obtained from fluorescence.

Good fluorescence transitions to all the components of the ground state take place from the I level and the F levels (below 24 938 and 20 963 cm^{-1}, respectively) and to a lesser extent from D (below 12 315 cm^{-1}). These establish all 8 Stark components of $^6H_{15/2}$ but there are some extra lines which are evidently caused by the interaction with crystal vibrations. This makes it difficult in some cases to decide which are the genuine Stark components. Possibly this question has no meaning, for when there is a close resonance between an electronic level and a crystal vibration, two levels may occur instead of one with no essential differences in properties. A further indication of the interaction with the crystal lattice is the broadening of the lines, especially that of the higher Stark components. This is illustrated by Fig. 1 which shows that the long wave components of the group, i.e., the transitions to the higher Stark components are much broader than the transition to the lowest components. This is often observed in the rare earth spectra both in absorption and fluorescence. Having it occur in the ground state gives perhaps the clearest clue to the significance of the broadening. As all the lines have the same upper level the broadening of the lines must be a property of the Stark components of the ground state. On the lowest electronic level are superimposed vibrations of the crystal lattice, which because they are not strictly localized to one molecular complex, are broad. One such frequency in the $LaCl_3$ lattice at about 80 cm^{-1} has been identified[15] but there must be others. Close coincidence of an electronic level with a crystal vibration will mix the two states. This broadens the electronic level and gives the superimposed crystal vibration the possibility of being absorbed directly and produce thus a supernumerary line.

The calculated parallel Zeeman effect is shown for all components in Fig. 10. There are no noticeable departures from linearity except for the two low lying $\mu=\frac{3}{2}$ levels Z_1 and Z_3 which interact strongly and, much less noticeably, for the two low $\mu=\frac{1}{2}$ levels Z_4 and Z_5. Figure 11 gives the lower part of Fig. 10 on a larger scale with

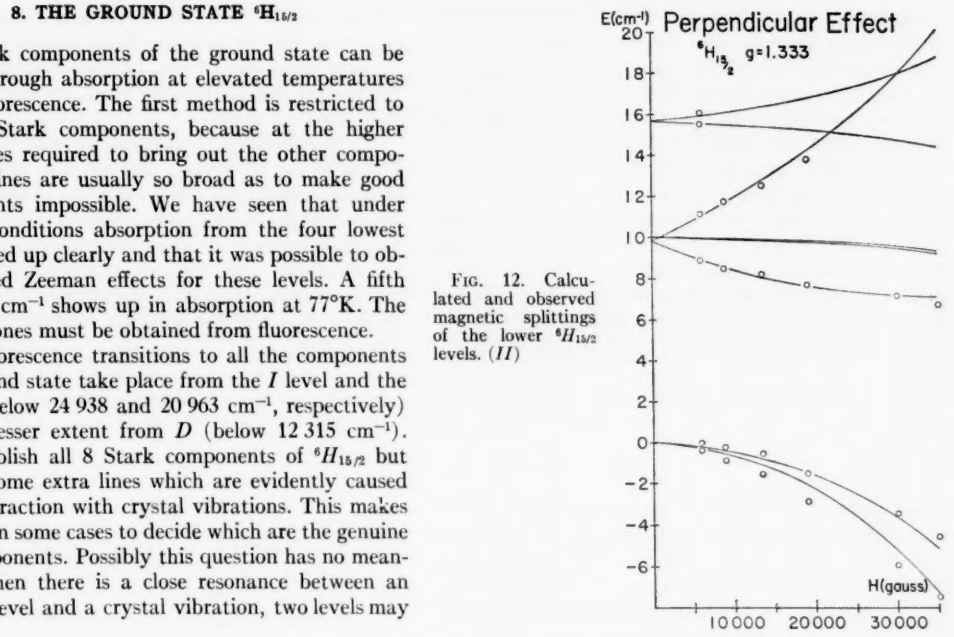

FIG. 12. Calculated and observed magnetic splittings of the lower $^6H_{15/2}$ levels. (II)

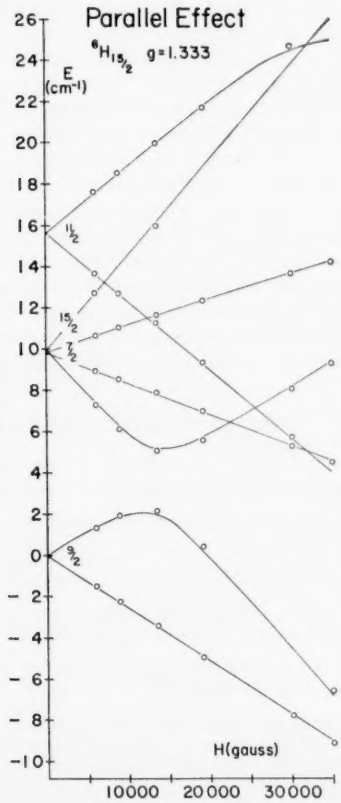

FIG. 11. Calculated and observed magnetic splitting of the lower $^6H_{15/2}$ levels. (I)

[15] F. Varsanyi and G. H. Dieke, J. Chem. Phys. **33,** 1616 (1960).

the observed points drawn in. Particularly noteworthy is the strong bend down in the upper component of Z_1 and the corresponding bend up in the lower component of Z_3. Without the interaction the two levels would intersect and the interaction results in the familiar repulsion of the two curves. As Table IV indicates, the two levels $M=\frac{9}{2}$ and $M=-\frac{15}{2}$ do not interact directly but through the level $-\frac{3}{2}$, and this interaction is the interaction through the V_6^6 term in the electric crystal field which becomes large when the magnetic field brings the two levels close together.

The same procedure used to calculate the C, D, and E perpendicular effects gives the results shown in Fig. 12. We see that the agreement between experiment and calculated effect is very satisfactory although not as perfect as for the parallel effect. This is explained by the fact that again for Fig. 12, the results do depend on the crystal field parameters which are not known with very great accuracy.

No paramagnetic resonance has been observed[5] for $DyCl_3$ evidently because the ion has no off-diagonal magnetic dipole components. Because of the strong nonlinear effects the magnetic properties cannot be given simply by quoting the splitting factors, but, as has been demonstrated, the magnetic properties can be accurately predicted from the known properties of the ${}^6H_{15/2}$ free-ion state and the observed splitting of the Stark components.

THE JOURNAL OF CHEMICAL PHYSICS VOLUME 35, NUMBER 5 NOVEMBER, 1961

Collision Mechanics in Crossed Maxwellian Molecular Beams

SHELDON DATZ
Chemistry Division, Oak Ridge National Laboratory, Oak Ridge, Tennessee*
DUDLEY R. HERSCHBACH
Department of Chemistry and Lawrence Radiation Laboratory, University of California,† Berkeley 4, California
AND
ELLISON H. TAYLOR
Chemistry Division, Oak Ridge National Laboratory, Oak Ridge, Tennessee*

(Received March 1, 1961)

A general treatment of the mechanics of collision between two Maxwellian molecular beams is described. Expressions are obtained for the distribution in collision energy, for the elastic and reactive collision rates, and for the angular distribution of the center of mass vectors for beams colliding at any angle. The treatment can accommodate any reaction cross section which can be expressed as a step function multiplied by a linear combination of powers of the relative energy.

The recoil momentum which affects the product distribution in the laboratory system is discussed, and the treatment is applied to some experimental data on the reaction of K with HBr.

INTRODUCTION

EXPERIMENTS on reaction rates are often interpreted in a collisional framework, in which the requirements for reaction of two molecules are specified in an energy-dependent cross section, and the frequency of fulfillment of the requirements is derived from Maxwell-Boltzmann statistics. For a reaction in a gas mixture, the Arrhenius equation is obtained in this way by specifying a cross section that is zero up to a critical energy and approaches a constant value above it. Recent interest in reactions between crossed molecular beams[1-5] raises the need for a comparable expression for this arrangement, as well as for an extension to include the angular distribution of products, which can be observed in these experiments. As in the case of a reacting gas mixture, the resulting equations can serve as a basis for stochastic comparison of detailed collision mechanisms with observed rates. The cross sections are in principle derivable from quantum mechanics, but for the present purpose they are treated as parameters with certain functional dependence upon collision energy.

DEVELOPMENT OF GENERAL EQUATIONS

In order to evaluate the number of collisions of a specified nature between molecules of two intersecting beams, consider elements of volume τ in each beam with τ equal to the volume of intersection of the two beams and the elements moving toward each other with relative velocity V. The number of collisions per second for a given velocity in each beam is

$$dN=\sigma(V)\,V dn_1 dn_2,$$

where dn_i/n_i is the fraction of molecules of species i in the velocity increment dv_i, and $\sigma(V)$ is the cross section, in general a function of energy. The collision rate is found by using the velocity distribution law for a volume element,

$$dn_i/n_i=4/\pi^{\frac{1}{2}}(v_i^2/\alpha_i^2)\,\exp(-v_i^2/\alpha_i^2)d(v_i/\alpha_i), \quad (1)$$

where $\alpha_i=(2RT_i/M_i)^{\frac{1}{2}}$ is the most probable velocity in the source. The result is

$$N=n_1n_2\tau A\int_0^\infty\int_0^\infty \sigma(V)\,V v_1^2 v_2^2 \times \exp[(-v_1^2/\alpha_1^2)+(-v_2^2/\alpha_2^2)]dv_1dv_2, \quad (2)$$

where $A=16/(\pi\alpha_1^3\alpha_2^3)$. The rate constant in the usual units (sec^{-1} cm^3 mole^{-1}) is

$$k=N/n_1n_2\tau. \quad (3)$$

To carry out the integration, it is convenient to change the variables to either V and ψ, the magnitude and angle of the relative velocity vector, or c and θ, those of the center-of-mass vector. The necessary transformations can be obtained from Fig. 1 by elementary kinematics.

Let the particles be numbered according to mass M_i so that $M_1<M_2$. The initial velocity vector diagram (Fig. 1) is drawn so that $\mathbf{v}_2$ is reached by a counterclockwise rotation from $\mathbf{v}_1$, and the various angles are measured from the direction of the lighter particle. The angle of intersection of the beams γ may have any

* Operated by the Union Carbide Corporation for the U. S. Atomic Energy Commission.

† Support of this work received from the Alfred P. Sloan Foundation and the U. S. Atomic Energy Commission is gratefully acknowledged.

[1] E. H. Taylor and S. Datz, J. Chem. Phys. **23,** 1711 (1955).
[2] E. F. Greene, R. W. Roberts, and J. Ross, J. Chem. Phys. **32,** 940 (1960).
[3] D. R. Herschbach, J. Chem. Phys. **33,** 1870 (1960).
[4] G. H. Kwei, J. A. Norris, and D. R. Herschbach, Bull. Am. Phys. Soc. **5,** 503 (1960).
[5] S. Datz and E. H. Taylor, "Some applications of molecular beam techniques to chemistry" in *Recent Research in Molecular Beams,* edited by I. Estermann (Academic Press Inc., New York, 1959).

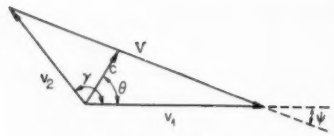

FIG. 1. Relations among initial velocity vectors.

value. The initial velocity vectors refer to an asymptotic state far from the scattering center, but for convenience are drawn as if they were just emerging from the scattering center. Thus Fig. 1 may be regarded as applying to an idealized encounter in which no interaction occurs.

From the definitions

$$V=\mathbf{v}_1-\mathbf{v}_2$$
$$M\mathbf{c}=M_1\mathbf{v}_1+M_2\mathbf{v}_2$$
$$M=M_1+M_2,$$

there follow the relations

$$V\cos\psi=v_1-v_2\cos\gamma$$
$$V\sin\psi=v_2\sin\gamma$$
$$Mc\cos\theta=M_1v_1+M_2v_2\cos\gamma$$
$$Mc\sin\theta=M_2v_2\sin\gamma. \tag{4}$$

The angles vary over the ranges

$$0<\psi<\pi-\gamma, \qquad 0<\theta<\gamma. \tag{5}$$

The necessary transformation equations are

$$v_1=V\sin(\gamma+\psi)/\sin\gamma=Mc\sin(\gamma-\theta)/M_1\sin\gamma, \tag{6}$$
$$v_2=\frac{V\sin\psi}{\sin\gamma}=\frac{Mc\sin\theta}{M_2\sin\gamma},$$
$$dv_1dv_2=(V/\sin\gamma)dVd\psi, \tag{7}$$
$$d\psi=(m^2/M_1M_2)d\theta, \tag{8}$$

and

$$(v_1^2/\alpha_1^2)+(v_2^2/\alpha_2^2)=V^2/\alpha^2. \tag{9}$$

The new functions $m=Mc/V$ and α [defined by Eq. (9)] introduced here are velocity independent, since

$$m^2\sin^2\gamma=M_1^2\sin^2(\gamma+\psi)+2M_1M_2\cos\gamma \times\sin(\gamma+\psi)\sin\psi+M_2^2\sin^2\psi,$$
$$m^{-2}\sin^2\gamma=\frac{\sin^2(\gamma-\theta)}{M_1^2}-\frac{2\cos\gamma\sin(\gamma-\theta)\sin\theta}{M_1M_2}+\frac{\sin^2\theta}{M_2^2}, \tag{10}$$

and

$$\alpha^2=\sin^2\gamma\left[\frac{\sin(\gamma+\psi)}{\alpha_1^2}+\frac{\sin^2\psi}{\alpha_2^2}\right]^{-1}$$
$$=\frac{\sin^2\gamma}{m^2}\left[\frac{\sin^2(\gamma-\theta)}{M_1^2\alpha_1^2}+\frac{\sin^2\theta}{M_2^2\alpha_2^2}\right]^{-1}. \tag{11}$$

It is interesting to note that the limiting values are constants,

$$m\to M_1 \text{ and } \alpha\to\alpha_1, \qquad \text{as } \psi\to0 \text{ and } \theta\to0,$$
$$m\to M_2 \text{ and } \alpha\to\alpha_2, \qquad \text{as } \psi\to\pi-\gamma \text{ and } \theta\to\gamma,$$

and these may therefore be considered as effective mass and velocity parameters.

Equation (3) may now be transformed by means of (6) and (7) to obtain

$$k=(A/\sin^5\gamma)\int_0^\infty\int_0^{\pi-\gamma}\sin^2(\gamma+\psi)\sin^2\psi\sigma(V)V^6 \times\exp(-V^2/\alpha^2)dVd\psi. \tag{12}$$

The integral over V may be expressed as a Laplace transform,[6]

$$G(p)=\int_0^\infty f(t)\exp(-pt)dt, \tag{13}$$

just as in the treatment of collisions in a gas mixture.[7] Here $t=V^2$, $p=1/\alpha^2$, and $f(t)=\frac{1}{2}t^{5/2}\sigma(t^{\frac{1}{2}})$.

The distribution of directions of the relative velocity vector is obtained by omitting the integration over ψ in Eq. (12);

$$P(\psi)=dk/d\psi$$
$$=\sin^2(\gamma+\psi)\sin^2\psi(A/\sin^5\gamma)G(1/\alpha^2). \tag{14}$$

This may be converted to the angular distribution of center-of-mass vectors by use of Eqs. (6) and (8);

$$P(\theta)=dk/d\theta=(dk/d\psi)(d\psi/d\theta)$$
$$=\sin^2(\gamma-\theta)\sin^2\theta(m^6/M_1^3M_2^3)(A/\sin^5\gamma)G(1/\alpha^2). \tag{15}$$

The remaining integration in Eq. (12) may be carried out over either ψ or θ, giving the rate constant

$$k=\int_0^{\pi-\gamma}P(\psi)d\psi=\int_0^\gamma P(\theta)d\theta. \tag{16}$$

The integration is tractable by analytic means for some experimentally important special cases (see below). However, a graphical integration is expedient since plots of $P(\theta)$ vs θ will usually be needed for other purposes.

The information most directly available from beam experiments is not the rate constant but the collision yield, the ratio of the reactive collision rate to the total collision rate,

$$k_r/k_t=\int_0^\gamma P_r(\theta)d\theta\Big/\int_0^\gamma P_t(\theta)d\theta. \tag{17}$$

$P_t(\theta)$ may be replaced by $P_e(\theta)$, the distribution func-

[6] See, for example, Bateman Manuscript Project, *Tables of Integral Transforms* (McGraw-Hill Book Company, Inc., New York, 1954), Vol. I, p. 127.

[7] M. A. Eliason and J. O. Hirschfelder, J. Chem. Phys. **30**, 1426 (1959).

tion for elastic scattering, because the cross section for the latter, as measured in beam experiments which can resolve very small deflections, is so large that the reactive cross section can be ignored in comparison with it.

Out of all collisions, the number of those which satisfy various presumed conditions can be found by introducing these conditions into the cross section, $\sigma(V)$, in Eq. (12). A comparison with experiment of the collision yields and angular distributions thus calculated will indicate the degree to which the assumed conditions approach reality.

CROSS SECTIONS

The cross section for elastic scattering has only a weak dependence on relative velocity and is adequately approximated by a constant value σ_e. The integration over V in Eq. (12) then yields

$$G_e(1/\alpha^2)=(15/16)\pi^{\frac{1}{2}}\alpha^7\sigma_e. \tag{18}$$

To evaluate the reactive collision rate, first consider the simple cross sections that accord with two traditional models for reaction. Model A assumes that $\sigma(V)$ is a step function with respect to relative energy and impact parameter b and is independent of orientation and internal excitation. That is,

$$\sigma(V)=0, \qquad \text{when } V<V^* \text{ or } b>b^*$$
$$\sigma(V)=\sigma_r, \qquad \text{when } V\geqslant V^* \text{ and } b\leqslant b^*, \tag{19a}$$

where σ_r is a constant, $b^*=(\sigma_r/\pi)^{\frac{1}{2}}$, and V^* is related to the activation energy E^* and reduced mass $\mu=M_1M_2/M$ by

$$E^*=\tfrac{1}{2}\mu(V^*)^2.$$

With this cross section, the integration in Eq. (12) differs from the elastic case only in that the lower limit is now V^* instead of zero.

Model B assumes further that only the component of relative velocity directed along the line of centers at impact is effective. The cross section above V^* then takes the form[7,8]

$$\sigma(V)=\sigma_r[1-(V^*/V)^2]. \tag{19b}$$

In addition to these classical models a third model (model C) will be chosen to have a cross-section function which falls off rapidly above the threshold:

$$\sigma(V)=0, \qquad V<V^*,$$
$$\sigma(V)=\sigma_r(V^*/V)^{20}, \qquad V\geqslant V^*. \tag{19c}$$

A function of this character would approximately reproduce the behavior shown by the calculations of Wall, Hiller, and Mazur[9] for the reaction $H+H_2$.

A more general form which can be readily treated consists of a step function multiplied by any linear combination of powers of the relative energy

$$\sigma(E)=0, \qquad E<E^*$$
$$=\sigma_r\sum_n c_n(E^*/E)^n, \qquad E\geqslant E^*. \tag{20}$$

The exponents n may be positive or negative integers; the constants c_n are dimensionless and can be taken as adjustable parameters. This form is perhaps general enough to represent the main feature of almost any model for reaction and includes models A, B, and C as special cases. The nonzero coefficients for these models are: for A, $c_0=1$; for B, $c_0=1$, $c_1=-1$; for C, $c_{10}=1$.

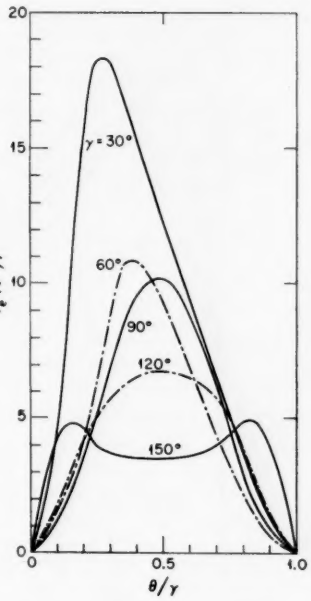

FIG. 2. Angular distribution of centroids in elastic scattering, for various angles of intersection of the beams.

ANGULAR DISTRIBUTION OF CENTROIDS

Elastic Collisions

The distribution of centroids for elastic collisions $P_e(\theta)$ is calculated from Eqs. (15) and (18). Aside from the scale factor σ_e, the distribution depends only on the beam masses, temperatures, and angle of intersection γ. In Fig. 2, distributions are plotted for several angles of intersection. The beams in this example (which corresponds to the conditions listed in Table II) have about the same average momenta. Thus the peak occurs near $\theta=45°$ for $\gamma=90°$. For an acute intersection, the distribution shifts to favor $\theta=0$, which would be the only accessible angle when $\gamma=0$ and the beams merge. On the other hand, if the beams intersect at a sufficiently obtuse angle, the distribution becomes bimodal, since in collisions between fast molecules of beam one and slow molecules of beam two, the center-of-mass vector lies nearer to beam one, and vice versa. The relative heights of the forward and

[8] R. D. Present, *Kinetic Theory of Gases* (McGraw-Hill Book Company, Inc., New York, 1958), pp. 137, 153.

[9] F. T. Wall, L. A. Hiller, Jr., and J. Mazur, J. Chem. Phys. **29**, 255 (1958).

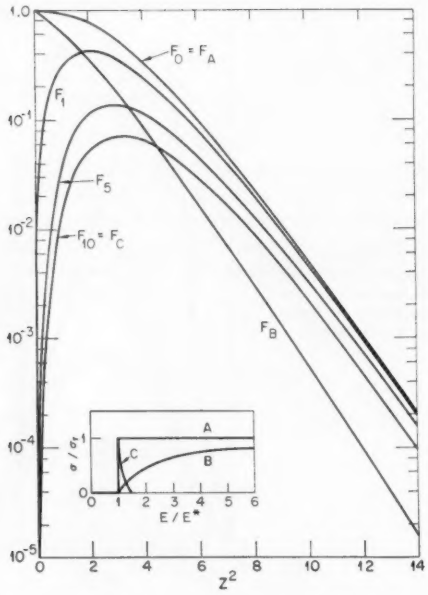

FIG. 3. Attenuation functions corresponding to various values of n in Eq. (26). The insert shows the cross section functions for the three reaction models discussed in the text.

backward peaks reflect the ratio of the average momenta of the beams.

Reactive Collisions

For any reaction cross section that can be represented by Eq. (20), $G_r(1/\alpha^2)$ can be put into the form

$$G_r(1/\alpha^2) = \sigma_r \sum_n c_n G_n(1/\alpha^2), \tag{21}$$

where

$$G_n\left(\frac{1}{\alpha^2}\right) = \int_{V^*}^{\infty} \left(\frac{V^*}{V}\right)^{2n} V^6 \exp\left(-\frac{V^2}{\alpha^2}\right) dV. \tag{22}$$

Equation (22) can be more conveniently expressed in terms of an incomplete gamma function[10]

$$G_n(1/\alpha^2) = \tfrac{1}{2}\alpha^7 z^{2n} \Gamma(-n+\tfrac{7}{2}, z^2), \tag{23}$$

where

$$\Gamma(-n+\tfrac{7}{2}, z^2) = \Gamma(a, x) = \int_x^{\infty} e^{-t} t^{a-1} dt$$

and $z = V^*/\alpha$. To make comparisons of a given experiment with the results predicted by a number of models, it is convenient to separate those terms in $P_r(\theta)$ which do not depend upon the model chosen. The result can be described as a partition of $P_r(\theta)$ into one factor identical with that for elastic scattering, in which the cross section is a constant, and another, which can be called an attenuation factor and contains those terms that depend upon the choice of model. Thus,

$$P_r(\theta) = (\sigma_r/\sigma_e) P_e(\theta) F_r(z); \tag{24}$$

$$G_r(1/\alpha^2) = (\sigma_r/\sigma_e) G_e(1/\alpha^2) F_r(z). \tag{25}$$

These attenuation factors, $F_r(z)$, hence express the premium placed upon relative energy by the reaction cross section. Because of the form of Eq. (20),

$$F_r(z) = \sum_n c_n F_n(z), \tag{26}$$

and it is necessary only to outline the calculation of the function $F_n(z)$ corresponding to a single term of Eq. (20). From Eqs. (18) and (23),

$$F_n(z) = (8/15)\pi^{-\frac{1}{2}} z^{2n} \Gamma(-n+\tfrac{7}{2}, z^2). \tag{27}$$

The integration required to evaluate the gamma function in Eq. (27) is simple for the case $n=3$ and yields

$$F_3(z) = (8z^6/15)[1-H(z)],$$

where $H(z)$ is the probability integral. The other functions are readily generated by use of a recurrence relation,

$$(n-\tfrac{5}{2}) F_{n+1}(z) + z^2 F_n(z) - (\tfrac{4}{15}) z^7 H'(z) = 0, \tag{28}$$

which is established by integrating (27) by parts. Thus for all cross sections of the form of Eq. (20), the $F_r(z)$ functions can be expressed in terms of the probability

TABLE I. Attenuation functions.[a]

z	$F_A = F_0(z)$	$F_B = F_0(z) - F_1(z)$	$(4/15) z^7 H'(z)$
0.00	1.0000-00	1.0000-00	0.0000-00
0.25	9.9999-01	9.7500-01	1.7253-05
0.50	9.9945-01	9.0023-01	1.8308-03
0.75	9.9255-01	9.7838-01	2.2886-02
1.00	9.5984-01	6.2018-01	1.1070-01
1.25	8.7320-01	4.4775-01	3.0075-01
1.50	7.2072-01	2.8882-01	5.4188-01
1.75	5.2523-01	1.6478-01	7.0740-01
2.00	3.3259-01	8.2617-02	7.0543-01
2.25	1.8160-01	3.6265-02	4.5601-01
2.50	8.5270-02	1.3911-02	3.5453-01
2.75	3.4430-02	4.6598-03	1.8595-01
3.00	1.1970-02	1.3629-03	8.1212-02
3.25	3.5895-03	3.4817-04	2.9811-02
3.50	9.3021-04	7.7733-05	9.2639-03
3.75	2.0871-04	1.5175-05	2.4512-03
4.00	4.0616-05	2.5918-06	5.5479-04
4.25	6.8660-06	3.8757-07	1.0782-04
4.50	1.0097-06	5.0770-08	1.8049-05
4.75	1.2933-07	5.8291-09	2.6092-06
5.00	1.4445-08	5.8689-10	3.2648-07

[a] For definitions, see Eqs. (27) and (29) of the text. The last two digits of each number in the table are the power of 10 to be attached (negative in all cases).

[10] Bateman Manuscript Project, *Higher Transcendental Functions* (McGraw-Hill Book Company, Inc., New York, 1953), Vol. II, p. 133.

integral and its derivative

$$H(z)=(2/\pi^{\frac{1}{2}})\int_0^z \exp(-t^2)dt,$$

$$H'(z)=(2/\pi^{\frac{1}{2}})\exp(-z^2),$$

for which extensive tables are available.[11]

The results for models A and B, for example, are found to be

$$F_A(z)=[1-H(z)]+z[1+(\tfrac{2}{3})z^2+(\tfrac{4}{15})z^4]H'(z) \quad (29a)$$

and

$$F_B(z)=[1-(\tfrac{2}{3})z^2][1-H(z)]+z[1+(\tfrac{4}{15})z^2]H'(z). \quad (29b)$$

In Fig. 3, the functions $F_n(z)$ are plotted for various values of n. Table I gives $F_A(=F_0)$ and $F_B(=F_0-F_1)$ and the function $(\tfrac{4}{15})z^7H'(z)$, so that any of the $F_n(z)$ functions may be obtained from the table by use of Eq. (28).

From Eqs. (6) and (11), it can be shown that

$$z^2=(V^*/\alpha)^2=(E^*/RT_1)(E_1/E)+(E^*/RT_2)(E_2/E), \quad (30)$$

wherein the ratios of the energy of a beam molecule to its relative energy, E_1/E and E_2/E, depend only on the masses, the intersection angle and the centroid angle, i.e.,

$$E_1/E=(m^2/\mu M_1)[\sin^2(\gamma-\theta)/\sin^2\gamma],$$

$$E_2/E=(m^2/\mu M_2)(\sin^2\theta/\sin^2\gamma). \quad (31)$$

Thus, after preparing a graph of these ratios, one may readily calculate z^2 as a function of θ for any set of values of T_1, T_2, and E^*. The variation of z^2 with θ for beams colliding at various angles is shown in Fig. 4, using as an example the experimental conditions of mass and temperature listed in Table II.[12] As seen from the limiting values,

$$z^2\rightarrow[1+(M_1/M_2)](E^*/RT_1), \quad \text{as } \theta\rightarrow 0;$$

$$z^2\rightarrow[1+(M_2/M_1)](E^*/RT_2), \quad \text{as } \theta\rightarrow\gamma, \quad (32)$$

which are the same for beams intersecting at any angle, the lowest values of z^2 occur near the beam having the higher average velocity. Since z^2 is inversely proportional to the available relative energy, the drastic changes in form of the curves for various angles of inter-

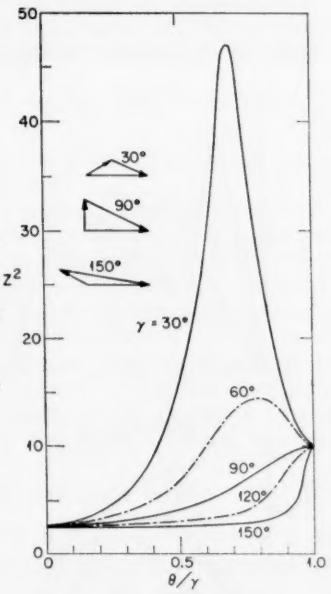

FIG. 4. Variation of the activation energy parameter z^2 with centroid angle θ for various angles of intersection of the beams.

TABLE II. Kinematics of a typical experiment: crossed beams of K(837°K) and HBr(460°K) intersecting at $\gamma=90°$.

	"Most probable" initial conditions	
	Elastic collisions	Reactive collisions[a]
v_K	5.95×10^4 cm/sec	9.14×10^4 cm/sec
v_{HBr}	3.07	3.40
c	3.12	3.75
V	6.70	9.75
θ	48.8°	37.6°
Ψ	27.3°	20.4°

Comparison of possible final states			
	$Q=-1$	$Q=0$	$Q=5$ kcal
v_{KBr}'	0.34	0.42	0.68
v_H'	28.9	35.3	57.9
x_{KBr}	11.5	9.4	5.7
x_H	0.095	0.079	0.048
Φ_{KBr}^{max}	4.8°	6.1°	10.1°
Eq. (38)% of 4π	0.16%	0.30%	0.76%

[a] The most probable reactive collision velocities are based on a collision having just enough relative energy for reaction (model A) and in which the centroid direction is that of the peak of the angular distribution. The relative energy is taken as $E=3.0$ kcal/mole, for which the most probable value of E_c is 2.2 kcal/mole.

[11] *Tables of Probability Functions* (National Bureau of Standards, Washington, D. C., 1941), Vol. I.

[12] A special case in which z^2 becomes independent of θ occurs for perpendicular collisions of beams having the same average velocity: $\alpha_1=\alpha_2$, or $T_2/T_1=M_2/M_1$. $P_r(\theta)$ in Eq. (24) then becomes simply proportional to the distribution for elastic scattering, regardless of the velocity dependence of the reaction cross section.

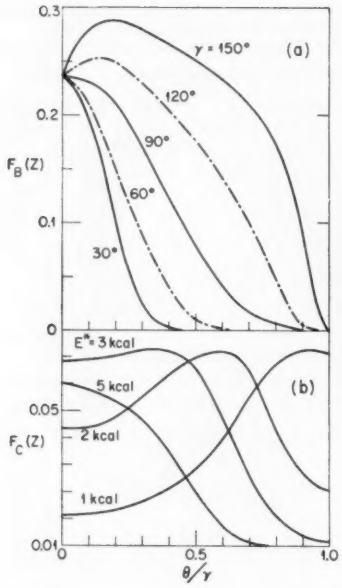

FIG. 5. Angular dependence of the attenuation factor: (a) for model B, with $E^*=3.0$ kcal/mole and various angles of intersection of the beams; (b) for model C, with $\gamma=90°$ and various values of the activation energy (kcal/mole).

section merely reflect the decrease in relative velocity accompanying the decrease in intersection angle. Changes in the value of E^* merely alter the vertical scale of the figure.

With the aid of a plot of z^2 vs θ (e.g., Fig. 4), the attenuation factor for a given cross section can be calculated as a function of θ by the use of Table I and Eqs. (24) and (28). The attenuation factor of model B is shown as a function of θ/γ in Fig. 5(a), which has been derived from Figs. 2 and 4. Results for model A are qualitatively similar. For both of these models, changing E^* merely shifts the curves about without much altering their shape. However, as seen in Fig. 3, the attenuation factor for cross sections which decrease with increasing energy above the threshold (e.g., model C) is not a monotonic function of z. Accordingly, if the range of z involved includes the hump shown in Fig. 3, the angular dependence of the attenuation factor will rapidly change character as E^* is adjusted (or as an equivalent change in beam temperatures is made). This is illustrated in Fig. 5(b). It will be noticed that for sufficiently large values of E^*, F_C has an angular dependence similar to that of F_B (because they become nearly parallel functions when z is large), so that both increase the attenuation in the direction of the faster beam. For small values of E^*, low angles are still strongly attenuated by F_B, whereas the effect is shifted to large angles by F_C.

According to Eq. (24), $P_r(\theta)$ is obtained by multiplying the attenuation factor into the distribution of centroids for elastic collisions. Figure 6 gives some typical results derived in this way from Figs. 2 and 5. The various special features discussed in connection with Figs. 2, 4, and 5 all appear superimposed in Fig. 6. In particular, the extent of the shifting and skewing of the curves in Fig. 6(a), as compared with Fig. 2, differs considerably for different angles of intersection, the attenuation being much more pronounced for acute intersections. Therefore, variation of the intersection angle would appear to be especially helpful in attempting to choose between reaction models. For example, under the conditions of Fig. 6(a), it can be shown that the ratio of the maxima in the angular distribution for the $\gamma=30°$ and the $\gamma=150°$ cases is nearly twice as large for model A as for model B.

ANGULAR DISTRIBUTION OF REACTION PRODUCTS

For the purpose of this analysis, it is convenient to divide the description of the angular distribution of products into two parts. The first is $P_r(\theta)$, the distribution of center-of-mass directions in the laboratory system, which is also the distribution of the initial directions of motion of the collision complex. The second part is the distribution of the momenta of the products relative to the coordinate system traveling with the center-of-mass (c.m. system). These can be combined to give the distribution of product in the laboratory system, but the complexity of the result poses a lengthy problem even for numerical integration. It is therefore expedient to limit the quantitative development initially to the more tractable first stage of the description, given by $P_r(\theta)$. As discussed in the foregoing, $P_r(\theta)$ is a function only of the initial kinetic energy distribution and the velocity dependence of the reaction cross section. The perturbations imposed on this distribution by the breakup of the complex can be examined

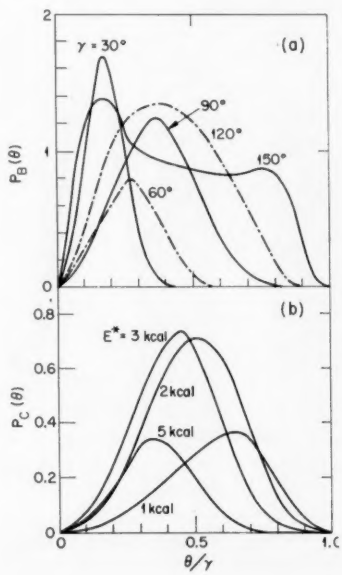

FIG. 6. Angular distribution of centroids for reactive scattering; the conditions assumed correspond to those of parts (a) and (b) of Fig. 5.

under various assumptions about the reaction mechanism, and the results compared with experiment to indicate qualitatively the range and form of the trial parameters to be used in a complete calculation of the angular distribution of products.

The magnitude of any given momentum vector in the c.m. system is a function of the initial relative energy and the energy released in the reaction. The directions of momentum vectors in the c.m. system will be anisotropic if the collision efficiency is different for different molecular orientations and if the lifetime of the complex is short compared to its rotational period. The anisotropy can be observed in the laboratory system because the experimental arrangement polarizes the direction of relative motion with respect to the direction of the center-of-mass vector.

In the dissociation of a collision complex in a reaction of the type

$$M_1+M_2\rightarrow M_3+M_4,$$

the magnitude of the velocity v_3' imparted to a product fragment in the c.m. system is calculable from energy balance,

$$v_3'=\left[\frac{2(E+Q)}{M_3[1+(M_3/M_4)]}\right]^{\frac{1}{2}}, \tag{33}$$

where E is the initial relative energy in the collision of the reactants and Q is the energy converted from internal degrees of freedom (rotational, vibrational, or electronic) to relative kinetic energy of the products. Thus Q is determined by the difference in zero-point energy of the reactants and products, $\Delta D_0°$, and the difference in internal excitation energy of the reactants, U_r, and the products U_p:

$$Q=\Delta D_0°-U_p+U_r. \tag{34}$$

Q is positive or negative, according as the collision is exothermic or endothermic.

The velocity of the product in the laboratory system, $\mathbf{v}_3$, is the vector sum of its recoil velocity, $\mathbf{v}_3'$, in the c.m. system and the velocity of the centroid in the laboratory system, $\mathbf{c}$. As the vector $\mathbf{v}_3'$ may point in any direction in the c.m. system, its possible directions generate a sphere about the tip of the center-of-mass vector, as indicated in Fig. 7. For any given recoil angle Φ_3' in the c.m. system, the possible directions of velocity vectors in the laboratory system generate a cone of half-angle Φ_3 about the original centroid direction, where

$$\tan\Phi_3=\sin\Phi_3'/(x_3+\cos\Phi_3'), \tag{35}$$

and x_3 is the ratio of the speed of the centroid in the laboratory system to that of M_3 in the c.m. system,

$$x_3=c/v_3'=\{(M_3/M_4)[E_c/(E+Q)]\}^{\frac{1}{2}}, \tag{36}$$

where $E_c=\frac{1}{2}Mc^2$, the translational energy of the center of mass. Similar equations obtain for the other product M_4.

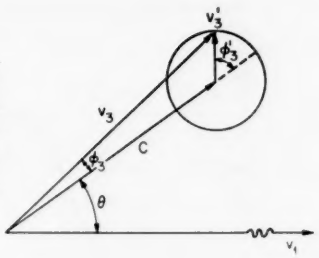

FIG. 7. Relation between the velocity vector of a product molecule M_3 as observed in the laboratory and in the center-of-mass reference system (primed).

Whenever $x_3>1$, as in Fig. 7, the laboratory distribution of the product M_3 will be confined to a forward cone about the centroid direction, regardless of the form of the distribution in the c.m. system. The maximum possible angular displacement of the product direction from the centroid direction in this case is

$$\Phi_3^{\max}=\sin^{-1}(1/x_3). \tag{37}$$

Thus, from Eqs. (34) and (36), it is seen that for given initial conditions (beam velocities and angle of intersection), the unknown parameter which determines the maximum possible broadening due to recoil is the internal excitation of the products, since in general $\Delta D_0°$ is known and U_r may be estimated from the source temperatures of the reactants.

This effect makes easiest to carry out and to interpret those reactions with values of x_3 well above unity, that reaction in which the detected product is relatively heavy and the Q value is small, such as K+HBr→H+KBr. In such cases, a considerable enhancement of intensity can be obtained, since the solid angle accessible to M_3 in the laboratory system is reduced to

$$4\pi\sin^2(\tfrac{1}{2}\Phi_3^{\max})\text{steradians} \tag{38}$$

(see Table II for examples), whereas when $x_3<1$ the product M_3 could scatter into 4π sr. For sufficiently large x_3, the recoil broadening given by Eq. (37) will be quite small (less than 3° if $x_3>20$), so that no features of the recoil scattering in the c.m. system can influence the laboratory distribution under the resolution attainable in practice. In this case the centroid distribution obtained should apply directly to the angular distribution of M_3 and the parameters in that distribution can, in principle, be evaluated.[13]

As one retreats from the limit of large x_3, the possible anisotropy in the distribution of recoil angles in the

[13] In such cases one could in principle fit the function $G(1/\alpha^2)$ in Eq. (15) to experiment and then employ an inverse Laplace transform to determine $\sigma(V)$ via Eq. (13). In practice, however, only a very crude indication of $\sigma(V)$ could be obtained without extremely accurate data. The problem is similar to that of inferring energy level spacings from measurements of thermodynamic functions as discussed by E. Blade and G. E. Kimball, J. Chem. Phys. **18**, 626 (1950); and S. H. Bauer, *ibid.* **6**, 403 (1938); **7**, 1097 (1939).

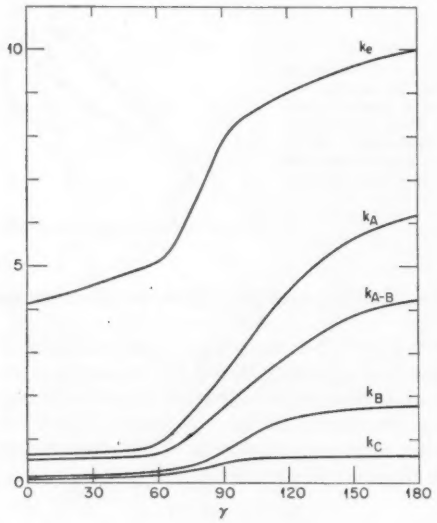

FIG. 8. Dependence of rate constants for elastic and reactive scattering ($E^*=3.0$ kcal/mole used) on the angle of intersection of the beams.

c.m. system can have a more pronounced effect on the laboratory distribution, which is thereby skewed with respect to the one expected from isotropic addition of the recoil to $P_r(\theta)$. There is, however, the further complication that the degree of anisotropy may have some velocity dependence, and this need have no simple relation to the velocity dependence of the total reaction cross section which entered into the calculation of $P_r(\theta)$.

Although it is clear that the influence of the three factors determining the contribution of recoil (interna! excitation of products, anisotropy of the angular distribution, and the velocity dependence) would be very difficult to separate by comparing the observed product distribution with $P_r(\theta)$, one may hope to find at least qualitative interpretatons which are consistent with results from different experiments and with intuition based on knowledge of molecular structure and energetics. Thus, one might expect that the degree of spreading of the observed distribution from $P_r(\theta)$ would permit a reliable estimate of the internal excitation of the products, and that the skewing of the distribution from that expected from isotropic scattering would indicate the presence of preferred molecular orientation.

RATE CONSTANT AND COLLISION YIELD

As shown in Eq. (16), the area under the curve in Figs. 2 or 6 gives the corresponding rate constant. The variation of rate constants with intersection angle is shown in Fig. 8, and it may be seen that the decrease in reaction rate accompanying a decrease in intersection angle varies considerably with the reaction model.

The calculated collision yield is the ratio of the rate constants for elastic and reactive scattering k_r/k_e. In the present treatment, this is porportional to σ_r/σ_t and otherwise depends only on E^* for a given set of experimental conditions.

Although it is clear that calculation of rate constants will, in the general case, require numerical integration, analytic integration is feasible for some special cases that will frequently occur in practice. These solutions will serve to illustrate the general features of the method and are given below.

Collisions of "Fast" and "Slow" Beams

If the most probable velocities in the colliding beams differ greatly (i.e., let $\alpha_1 \ll \alpha_2$), it will be a good approximation to set the relative velocity equal to the velocity of the faster beam, $V \simeq v_2$. This is particularly true for the higher range of velocities which is important in reactive collisions, since these velocities are on the part of the distribution curve where the intensity depends principally on the exponential. In Eq. (3), the integration over the distribution of velocities in the slower beam may then be carried out separately, so that

$$k=(4\pi^{-1})\alpha_2^{-3}\int_0^\infty v_2^3\sigma(v_2)\,\exp(-v_2^2/\alpha_2^2)dv_2. \quad (39)$$

This integral has the same form as that for a homogeneous gas. It may be written as a Laplace transform, as in Eq. (13), with

$$k=(2/\pi^{\frac{1}{2}})\alpha_2^{-3}G(p), \qquad p=1/\alpha_2^2$$
$$f(t)=t\sigma(t^{\frac{1}{2}}).$$

For a cross section of the form adopted in Eq. (20),

$$k=\sum_n c_n k_n, \quad (40)$$

the tables[10] give

$$k_n=(2/\pi^{\frac{1}{2}})\alpha_2\sigma_r z^{2n}\Gamma(2-n, z^2) \quad (41)$$

in terms of the incomplete gamma function of Eq. (27). For elastic collisions, $n=0$ and $z=0$, this yields

$$k_e=(2/\pi^{\frac{1}{2}})\alpha_2\sigma_e=\bar{v}_2\sigma_e, \quad (42)$$

where $\bar{v}_2$ is the average velocity in the source. When $n=1$, the result is also simple,

$$k_1=\bar{v}_2\sigma_r z^2\exp(-z^2). \quad (43)$$

Integration of Eq. (41) by parts gives a recurrence relation

$$(n-1)k_{n+1}+z^2k_n=z^2k_1, \quad (44)$$

from which results for any value of n are readily generated. The rate constants for models A and B have

the familiar form

$$k_A=\bar{v}_2\sigma_r(1+z^2)\exp(-z^2)$$
$$k_B=\bar{v}_2\sigma_r\exp(-z^2).$$

However, here

$$z^2=(v^*/\alpha_2)^2=(M/M_1)(E^*/RT_2). \quad (45)$$

The factor $M/M_1=M_2/\mu$ arises from the idealization that only the motion of M_2 contributes to the relative velocity. Equation (41) and derived results are only exact in the limit $\alpha_1/\alpha_2\to 0$, but remain accurate within 5% or better up to about $\alpha_1/\alpha_2\sim 0.1$, when z is greater than unity.

Perpendicular Collisions

For beams intersecting at $\gamma=90°$, Eq. (12) may be rewritten as

$$k=AD(1/\alpha_1^2)D(1/\alpha_2^2)\int_0^\infty\int_0^{\frac{1}{2}\pi}V^2\sigma(V)$$
$$\times\exp[-V^2(p+q\cos 2\psi)]dVd\psi, \quad (46)$$

where $D(x)$ is the differential operator $\partial/\partial x$. The term α^2 is replaced by its equal from Eq. (11), specialized to $\gamma=90°$, and p and q are given by

$$p=\tfrac{1}{2}[(1/\alpha_1^2)+(1/\alpha_2^2)], \qquad q=\tfrac{1}{2}[(1/\alpha_1^2)-(1/\alpha_2^2)].$$

It is convenient to number the particles so that $\alpha_1<\alpha_2$, to make q a positive quantity. Use of the identity

$$D(1/\alpha_1^2)D(1/\alpha_2^2)=\tfrac{1}{4}[D^2(p)-D^2(q)],$$

further differential operation, and integration over ψ yield[14]

$$k=\alpha_1^{-3}\alpha_2^{-3}D(-p)[D^2(p)-D^2(q)]G(p,q), \quad (47)$$

$$G(p,q)=\int_0^\infty e^{-pt}I_0(q,t)t^{-\frac{1}{2}}\sigma(t^{\frac{1}{2}})dt, \quad (48)$$

where $t=v^2$, and $I_0(q,t)$ is the modified Bessel function.

For elastic collisions, Eq. (48) can be integrated[15] in closed form, giving

$$G(p,q)=\sigma_e\pi^{\frac{1}{2}}p^{-\frac{1}{2}}{}_2F_1(\tfrac{1}{4},\tfrac{3}{4};1;\delta),$$

where ${}_2F_1(a,b;c;\delta)$ is the Gauss hypergeometric function,[16] and

$$\delta=(q/p)^2=(1-r^2)^2/(1+r^2)^2,$$

where

$$r=\alpha_1/\alpha_2.$$

The rate of elastic collisions is then given by

$$k_e=\bar{v}_2\sigma_e R_e f(\delta) \quad (49)$$

[14] Reference 10, pp. 5, 14, and 86.
[15] Reference 6, pp. 196, 370, 373 and reference 10, Vol. I, p. 135.
[16] Reference 10, Vol. I, p. 56.

TABLE III. Parameters calculated from data of reference 1 for various reaction models.

Model	Cross section above E^*	E^* kcal/mole	σ_r/σ_s (%)
A	σ_r	3.25±0.12	$1.34\times10^{-2}\pm5$
B	$\sigma_r[1-(E^*/E)]$	2.51±0.12	$2.47\times10^{-2}\pm5$
A–B	$\sigma_r(E^*/E)$	3.48±0.08	$2.01\times10^{-2}\pm5$
C	$\sigma_r(E^*/E)^{10}$	3.97±0.11	$9.14\times10^{-2}\pm5$

where

$$R_e=\pi^{\frac{1}{2}}r^4[2/(1+r^2)]^{7/2}$$

and

$$f(\delta)=\tfrac{15}{8}F+\tfrac{5}{2}(15\delta-2)F'+2\delta(21\delta-11)F''$$
$$+8\delta^2(\delta-1)F''',$$

in terms of the hypergeometric function $F={}_2F_1$ and its first three derivatives.

For inelastic collisions, analytic integration of Eq. (48) is not feasible for the types of reaction cross section included in Eq. (20). However, if α_1/α_2 is not too close to unity, a good approximation is obtained by keeping just the first term in the asymptotic expansion

$$I_0(x)\sim e^x(2\pi x)^{-\frac{1}{2}}[1+(1/8x)+\cdots].$$

With this approximation, one finds

$$k_n=\bar{v}_2\sigma_r z^{2n}[R'\Gamma(2-n,z^2)+R''\Gamma(1-n,z^2)], \quad (50)$$

where

$$R'=(1-r^2)^{-\frac{1}{2}},$$
$$R''=-\tfrac{3}{2}r^2(1-r^2)^{-5/2},$$

and $r=\alpha_1/\alpha_2$. Results for cases A and B are

$$k_A=k_0=\bar{v}_2\sigma_r\exp(-z^2)[R'(1+z^2)+R''],$$
$$k_B=k_0-k_1, \quad (51)$$

where

$$k_1=\bar{v}_2\sigma_r z^2\exp(-z^2)[R'+R''\exp(z^2)\Gamma(0,z^2)], \quad (52)$$

and

$$\Gamma(0,x)=-\operatorname{Ei}(-x)=\int_x^\infty e^{-t}t^{-1}dt$$

is the exponential integral.[17] Recurrence relations again offer a convenient means to extend the results. Using primes to distinguish the first and second terms of Eq. (50),

$$k_n=k_n'+k_n'',$$

we may write the relations as

$$(n-1)k_{n+1}'+z^2k_n'=z^2k_1'$$
$$nk_{n+1}''+z^2k_n''=z^2k_0''. \quad (53)$$

[17] E. Jahnke and F. Emde, *Tables of Functions* (Dover Publications, New York, 1945), p. 6.

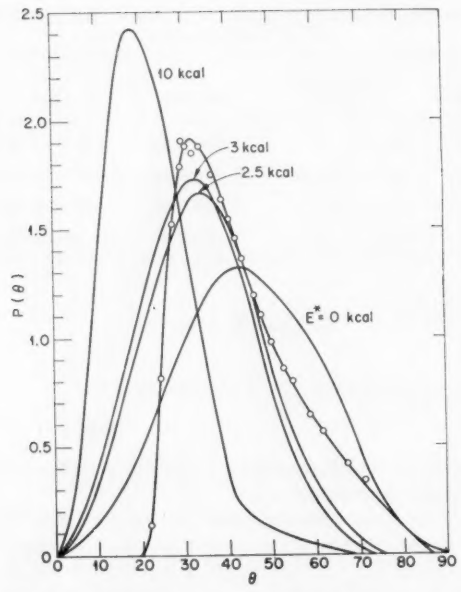

FIG. 9. Comparison of observed KBr distribution with calculated distribution of centroids for model B. The curves are normalized to unit area. Experimental conditions are as in Table II, and E^* (kcal/mole) is taken as a parameter.

The relative error due to the neglect of the second and higher terms in the asymptotic expansion will be less than

$$1/8q(v^*)^2=r^2/4z^2(1-r^2).$$

Thus Eq. (50) reduces to the proper limit, Eq. (41), as $r\rightarrow 0$, but becomes invalid in the limit $r\rightarrow 1$ and also for elastic collisions, for which $z=0$. As long as the beams have sufficiently different average velocities, however, Eq. (51) will be a suitable approximation for most chemical reaction studies; e.g., for the K+HBr reaction under the conditions of Table II, the relative error in $I_0(p, q)$ is only about 0.3% at $E^*=2.5$ kcal/mole.

If, however, the most probable velocities in the two beams are equal, $q=0$ and $I_0(0)=1$, so that Eq. (48) reduces to a standard form.[10] The results obtained are

$$k_e=\bar{v}_2\sigma_e(15\pi/16) \tag{54}$$

and

$$k_n=\bar{v}_2\sigma_r F_n(z). \tag{55}$$

Another route to Eq. (54) is the specialization of Eqs. (16) and (18). Comparing Eqs. (42) and (54), one sees that as α_1/α_2 is varied from zero to unity, the collision rate increases by a factor, $15\pi/16$, which represents the integral over the distribution of centroids. Similarly, Eq. (55) can be obtained directly from (16) and (22), since z is independent of θ when $\alpha_1=\alpha_2$ and $\gamma=90°$. Equations (49) and (50) remain accurate to about 5% even when α_1 and α_2 differ by as much as 20%.

DISCUSSION OF THE K+HBr REACTION

The application of the foregoing development will now be illustrated by a specific case, the reaction K+HBr. In the original publication on this subject,[1] the parameters of the collision theory were evaluated by comparing ratios of observed collision yields for pairs of experiments (at different reactant temperatures) with those calculated for various choices of E^*. The activation energy was then taken to be that value of E^* which gave the best agreement between the experimental and calculated ratios.[18]

The calculations in reference 1 were based on model A,[19] but it is found that any of the models in Table III give activation energies that are practically as consistent between the various experimental cases, as indicated by the quoted deviations. This occurs because E^* is large enough to make the relevant region of Fig. 3 that in which the $F_r(z)$ functions are practically parallel, so that a suitable shift of the scale of z^2 (change of E^*) makes the various attenuation factors almost the same. The present calculations indicate that the analysis would be much more sensitive to the model used if the intersection angle as well as the beam temperatures were varied, as then the attenuation factors could not be brought into such close superposition by a simple scale change. No data of this kind are yet available.

Table II summarizes the conditions for one of the experiments reported in reference 1; the calculations presented in Figs. 2–9 correspond to these conditions.

The maximum value of Q (which will give the largest possible value of $\Phi_{KBr}{}^{max}$ for given initial relative energy) occurs for reactions that leave the newly formed KBr molecule in its lowest internal state. This lies only about 4 kcal/mole below that of HBr.[20] Practically all the HBr molecules are in the ground vibrational state and most have between 0.3–1.2 kcal/mole of rotational energy, so that $Q\sim 5$ kcal/mole.

Figure 7 has been drawn for $E=3$ and $Q=5$ kcal/mole, and shows $\Phi_{KBr}{}^{max}=10.1°$ at $\theta=37.6°$; under these conditions $\Phi_{KBr}{}^{max}$ varies from 13° at $\theta=0°$ to 7° at $\theta=90°$.

The extent to which appreciable internal excitation of the KBr might be expected to shrink the recoil broadening is illustrated in Table II. For a number of highly exothermic exchange reactions with small activation energies, there is evidence that the newly formed

[18] The relation between the ratio σ_r/σ_e and the usual steric factor is discussed in reference 1. In Figs. 2, 6, and 8 we have for convenience set $\sigma_r=\sigma_e=1A^2$; multiplication of the ordinate by the proper value and the conversion factor 6.023×10^{-11} will give the rate constant in units of sec^{-1} $(moles/cc)^{-1}$.

[19] The collision energy distribution formulas used in reference 1 were incorrectly derived, but this did not lead to significant numerical errors except in the calculated centroid distributions, the discussion of which is amended here.

[20] $\Delta D_0{}^0=4.2\pm 1.1$ kcal/mole, from A. G. Gaydon, *Dissociation Energies* (Chapman and Hall, London, 1953).

bond is vibrationally highly excited.[21] Although the comparison of this nearly thermoneutral reaction with highly exothermic ones may not be entirely valid, it suggests that most of the reactive collisions in K+HBr might be expected to have Q values near zero or perhaps slightly negative. This corresponds to the formation of KBr with about 3–6 kcal/mole of vibrational and rotational energy.

In Fig. 9 the distribution of centroids calculated for model B is compared with a typical experimental curve. It is seen that the distributions calculated for $E^*=2.5$ and 3.0 kcal/mole fit reasonably well and are about as close to the KBr distribution as expected from the discussion of Q values. The sharp decline observed at 20° is not reproduced, and above 60° the calculated curve looks to be too low, but elsewhere it is notable that the experimental curve is broadened only slightly beyond the centroid distribution (especially considering that the beam widths are about 4°). Model B has been used here because it leads to the conventional form

$$k_r=\bar{v}\sigma_r \exp(-E^*/RT),$$

when applied to a homogeneous gas mixture.[7] Parameters obtained using other reaction models are given in Table III.

The usefulness of the equations developed in this paper will be fully tested only when more data under a variety of conditions become available. It may be expected that some reactions can be carried out with nearly monoenergetic beams,[2,3] but the complexity of the angular distribution is not completely removed since there remain the distributions of impact parameters and internal excitations of reactants and products. Furthermore, there will probably always be reactions for which the loss in intensity attendant with monochromatization cannot be tolerated,[22] and for which the present treatment will be necessary.

ACKNOWLEDGMENTS

The authors are most grateful to George T. Trammell for much helpful advice, to Robert E. Minturn and James L. Kinsey for assistance with the manuscript, and to F. E. Stafford and P. Toennies for their correspondence.

[21] W. D. McGrath and R. G. W. Norrish, Z. physik. Chem. (Frankfurt) **15**, 245 (1958); J. C. Polanyi, J. Chem. Phys. **31**, 1338 (1959); and F. T. Smith, *ibid.* 1352 (1959).

[22] S. Datz, *Proceedings of the Atomic and Molecular Beams Conference* (University of Denver, Denver, Colorado, 1960), p. 242.

Motion of the Ammonium Ion in Lattices of the NaCl Type*

W. VEDDER† AND D. F. HORNIG
Frick Chemical Laboratory, Princeton University, Princeton, New Jersey

(Received April 12, 1961)

The infrared spectrum of NH_4I in the NaCl-type phase gives insufficient information about the motion of the ammonium ions in that phase. Dilute solutions of NH_4^+ in NaCl-type alkali halides provide considerably more detail in the form of a fine structure in most of the absorption bands which becomes visible on sufficient cooling. This fine structure is most certainly correlated with a rotational motion of the NH_4^+ ion. However, both models suggested in the literature—free rotation and rotation of the ion about a N-H···X⁻ axis—deviate in many important respects from the experimental results.

THE ammonium halides are known to occur in four different crystalline phases. The structures of the three phases which are stable at lower temperatures and the transformations between them, in particular the role played by the NH_4^+ ion, are at present well understood. However, little is known about the structure of the phase which is stable at the highest temperatures, the NaCl-type phase. The heat capacity of this phase is lower than that of the CsCl-type phase[1–3] and this has been used as an argument in favor of essentially free rotation of the ammonium ions in the NaCl-type phase. The results of neutron diffraction, however, exclude the possibility of three dimensional free rotation. Levy and Peterson[4,5] have considered a number of models, of which only three were acceptable. In these, one, two, or three protons get as close to halide ions as possible, maintaining the nitrogen atom at its cubic site and the NH distance constant. In the model in which one proton gets as close to a halide ion as possible, they have assumed uniform rotation of the ion about this N-H···X⁻ axis. This model was originally introduced by Bauer[6] in order to explain Guillien's measurements[7] of the dielectric constant of NH_4I as a function of temperature near the λ point. Mathieu and Couture-Mathieu[8,9] have measured the depolarization of the Raman line corresponding to the twofold degenerate bending mode of the NH_4^+ ion in the NaCl-type phase and in the high temperature CsCl-type phase. They concluded from this study that in the first phase the threefold axis of the ion coincides with the fourfold axis of the crystal, whereas in the latter phase the threefold axes of ion and crystal coincide. In other words, they also support Bauer's model of uniform rotation about a N-H···X⁻ axis.

This same conclusion was obtained by Plumb and Hornig from a study of the infrared spectrum of NH_4I in its NaCl-type (room temperature) phase.[10,11] The combination of the librational mode and the threefold degenerate bending mode, which was such a clear-cut indication of libration rather than rotation in the other phases, was no longer present. Instead they found a weak and very diffuse absorption ranging from 1400 up to 2000 cm^{-1}, which was nearly temperature independent between room temperature and 78°K. From the absence of P and R maxima, the shape of the absorption band associated with the threefold degenerate bending mode and from electrostatic arguments they found support for the hypothesis of essentially free rotation about a N-H···X⁻ axis.

Studies of the proton magnetic resonance[12] of NH_4Cl have shown that the width of the resonance absorption and the change of this width on transformation from the CsCl to the NaCl phase could be explained entirely as due to interionic spin-spin coupling and the change of this quantity with change of lattice. Hence these results could yield no information about the nature of the motion in the high temperature phase except that, whatever the motion, it could not be associated with any fixed orientation or any fixed axis for times longer than 10^{-4} sec. Support for this same conclusion followed from the considerable increase in spin-lattice relaxation time for both proton and bromine nucleus with the transition from a CsCl to a NaCl-type lattice in NH_4Br. Itoh and Yamagata[13] also found a decrease of

* Based in part on a dissertation for which the experimental work was completed in 1956 at Brown University, Providence, Rhode Island, and which was written at the institute of Professor J. A. A. Ketelaar in Amsterdam and submitted to the University of Amsterdam, 1958.

† Present address: General Electric Research Laboratory, Schenectady, New York.

[1] C. C. Stephenson, L. A. Landers, and A. G. Cole, J. Chem. Phys. **20,** 1044 (1952).

[2] P. W. Bridgman, Proc. Am. Acad. Arts. Sci. **52,** 91 (1916).

[3] H. Klinkhardt, Ann. Physik **84,** 188 (1927).

[4] H. A. Levy and S. W. Peterson, J. Chem. Phys. **21,** 366 (1953).

[5] H. A. Levy and S. W. Peterson, J. Am. Chem. Soc. **75,** 1536 (1953).

[6] E. Bauer, Cahiers phys. **21,** 37 (1944).

[7] R. Guillien, Compt. rend. **208,** 1561 (1939).

[8] J. P. Mathieu and L. Couture-Mathieu, Compt. rend. **233,** 1595 (1951).

[9] L. Couture-Mathieu and J. P. Mathieu, J. chim. phys. **49,** 226 (1952).

[10] R. C. Plumb and D. F. Hornig, J. Chem. Phys. **21,** 366 (1953).

[11] R. C. Plumb and D. F. Hornig, J. Chem. Phys. **21,** 1113 (1953).

[12] H. S. Gutowski, G. E. Pake, and R. Bersohn, J. Chem. Phys. **22,** 643 (1954).

[13] J. Itoh and Y. Yamagata, J. Chem. Phys. **24,** 621 (1956).

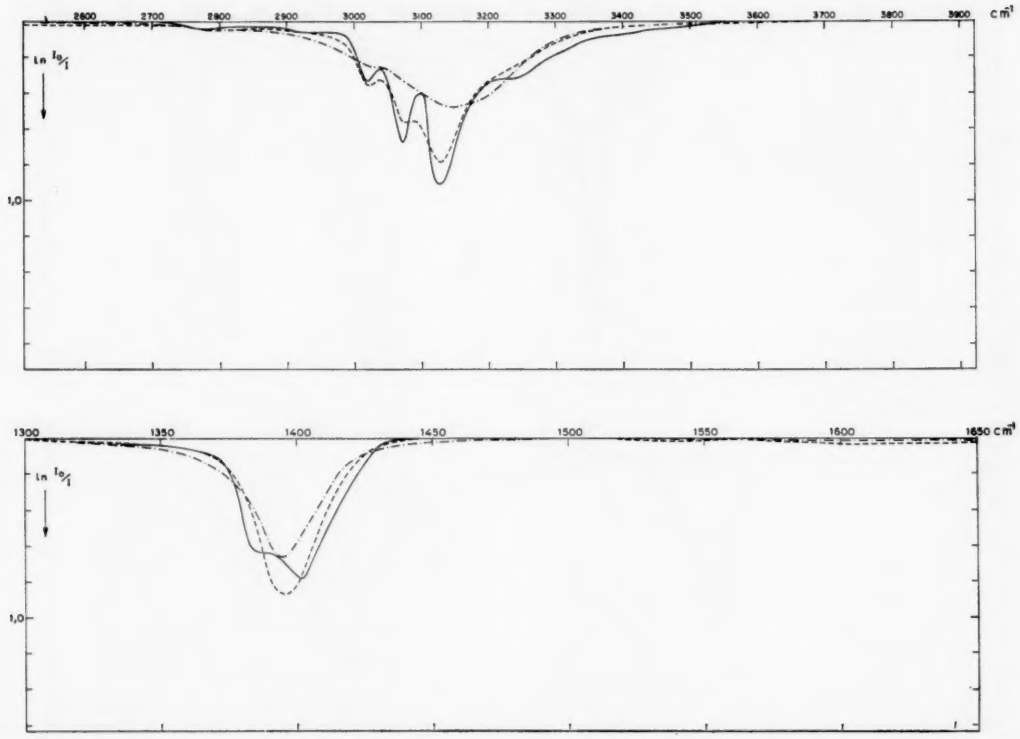

FIG. 1. The infrared spectrum of a film of NH_4I in the NaCl-type phase (thickness about 0.8μ) at room temperature -·-·-, liquid-nitrogen temperature - - - -, and liquid-helium temperature ————.

the chemical shift of the bromine resonance in the NaCl-type phase as compared to the CsCl-type phase. Since this chemical shift was shown to be associated with covalent or hydrogen bonding between the protons and the bromide ions this result indicated that the average number of protons in the vicinity of one bromide ion was less in the high temperature phase.

Summarizing this information one can say that the protons have a definite preference for being close to a halide ion, but there cannot be a fixed equilibrium orientation of the ammonium ions.

In order to throw further light on the motion of the ammonium ions, we have studied the infrared spectrum of thin films of NH_4I in the NaCl-type phase as a function of temperature down to liquid-helium temperature. We have also measured the spectrum of dilute solid solutions of NH_4^+ ions in alkali halides with the NaCl structure.

EXPERIMENTAL RESULTS

The infrared spectrometers used were a Perkin Elmer Spectrometer 12 B, converted to double beam operation,[14] and a Perkin Elmer 112G, single beam, double pass, grating instrument. During the recording of all spectra, care was taken to exclude the possibility that atmospheric H_2O or CO_2 in the light path might produce spurious absorptions.

A low-temperature cell of relatively simple design was used, differing from our ordinary low-temperature cells only in that the liquid-helium pot was surrounded by a nickel-plated copper shield which could be cooled to liquid-nitrogen temperature. A charge of about 350 cc of liquid helium held a sample at 4.2°K or very close to this for 45 min. The films were prepared by sublimation of NH_4I directly onto a polished and slightly cooled KBr window installed in the sample holder of the cell. The growth and homogeneity of the films was followed by observation of their reflection color. They showed very little scattering in the visible and near infrared and were about one micron thick. The sublimation equipment could be removed without exposing the film to the atmosphere. It was noticed that films prepared in this way at temperatures well above the transition temperature (−15°C) were often in the CsCl-type phase and if not (or not completely), always underwent the phase transition immediately upon cooling. This must have been an example of the rule (Ostwald) that unstable phases often appear first. It

[14] D. F. Hornig, G. E. Hyde, and W. A. Adcock, J. Opt. Soc. Am. **40**, 497 (1950).

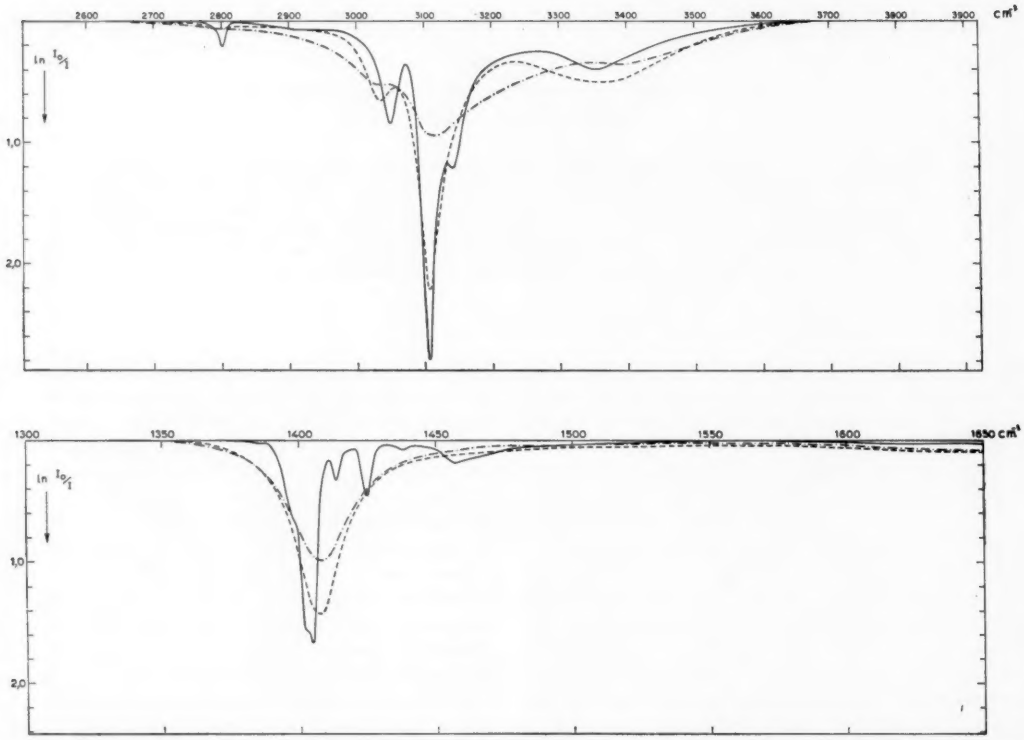

FIG. 2. The infrared spectrum of a dilute solid solution of NH_4^+ in KCl (ratio K^+ to NH_4^+ ions about 2.3×10^3) at room temperature -·-·-·-, liquid-nitrogen temperature - - - - -, and liquid-helium temperature ————.

was possible to convert a film which was in the CsCl-type phase to the NaCl-type phase in a few seconds by opening the low-temperature cell to the atmosphere. Under these circumstances, the room-temperature phase formed rapidly and it was possible to supercool a film, thus treated, reproducibly down to liquid-helium temperatures. Apparently a little water vapor catalyzes the phase transition and either this NaCl-type phase, once formed, supercools easily or the stabilizing effect of the NaCl-type structure of the KBr window plays some role.

The regions of interest in the spectrum of a film of NH_4I in the NaCl-type phase at room temperature, at 78°K and ~5°K are shown in Fig. 1.[15]

Although this region is not shown, the combination of the librational mode and the threefold degenerate bending mode, which appears at 1684 cm^{-1} in the tetragonal phase at 78°K, is absent here. In the stretching region, three components are visible, their widths decreasing as the temperature is lowered. Of these, the one at 3022 cm^{-1} is probably mainly $\nu_2+\nu_4$ in resonance with ν_3, which we assume to be represented by the doublet 3074–3128. In the bending region, a doublet seems to develop at low temperatures with components at about 1385 and 1402 cm^{-1}.

Dilute solutions of NH_4^+ ions in KCl, KBr, and KI were prepared in two ways. The first crystals formed by evaporation of a mixed solution of the ammonium halide and the alkali halide in water were first dried between filter paper, then in an oven at 120°C. They were ground to a fine powder in an agate mortar, after which the powder was again dried at 120°C. Next, pellets were pressed from the powder by the usual KBr pellet technique. In the solutions, the ratio of ammonium to alkali halide was about 1 to 10^3 by weight. Under these circumstances, pellets of about 1-mm thickness showed appropriate absorption in the regions of interest. It is known that solid solutions are formed by this procedure.[16] For the low NH_4^+ concentrations used here, the ratio of ammonium to alkali in the first crystals is smaller than the ratio in the aqueous solution by a factor varying from 10 for the chloride to three for the bromide.[17] Hence, there should have been

[15] Using the data on intensities of the NH_4^+ fundamentals in dilute solid solutions and in NH_4I obtained by C. C. Ferriso and D. F. Hornig [J. Chem. Phys. **32,** 1240 (1960)], we calculated the thickness of the film to be 0.8 μ and the ratio of K^+ to NH_4^+ ions in the dilute solutions made by method I to be 2.3×10^3.

[16] R. J. Havighurst, E. Mack, and F. C. Blake, J. Am. Chem. Soc. **47,** 29 (1925).

[17] R. Flatt and G. Burkhardt, Helv. Chim. Acta **27,** 1605 (1944).

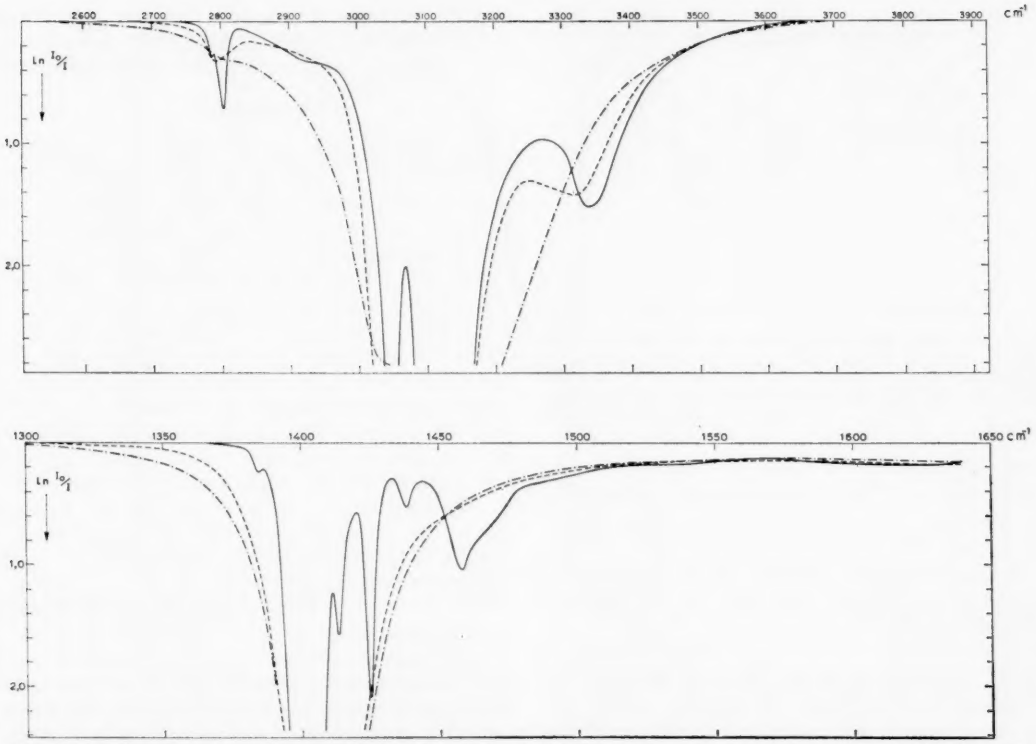

FIG. 3. The infrared spectrum of a concentrated solid solution of NH_4^+ in KCl at room temperature –·–·–·–, liquid-nitrogen temperature– – –, and liquid-helium temperature ————.

10^3 to 10^4 alkali ions to each ammonium ion in these solid solutions.[15]

We have also prepared solid solutions by diffusion of NH_4^+ into KI and KCl single crystals. Powdered ammonium halide and a polished single crystal of the alkali halide were heated together in an evacuated and sealed Vycor tube at 900–950°K for 25 to 50 hr. The tip of the tube was removed from the furnace first and excess ammonium halide allowed to crystallize at that point. After the diffusion it was found that even prolonged polishing of the window changed the intensity of the absorption bands very little. We may conclude from this that the NH_4^+ ions had penetrated well into the lattice, certainly over distances of the order of a millimeter. The scattering of the samples was reduced to negligible amounts by polishing. It is known[18] that K^+ and Cl^- diffuse readily in KCl at comparable temperatures. Since this diffusion process takes place by means of a mechanism in which vacancies in the lattice play a role, we may expect that the *ammonium ions are placed at alkali ion sites.*

We will henceforth refer to crystallization from aqueous solution as Method I, and diffusion as Method II.

Figures 2 and 3 show the spectrum of solid solutions of NH_4^+ in KCl at two different concentrations, both prepared by Method I and recorded with the prism instrument (CaF_2 prism). Figure 4 shows the bending region, recorded at liquid-helium temperature, with somewhat higher resolution and plotted on a different scale. The bending region of a solid solution of NH_4^+ in KCl prepared by Method II and recorded with the

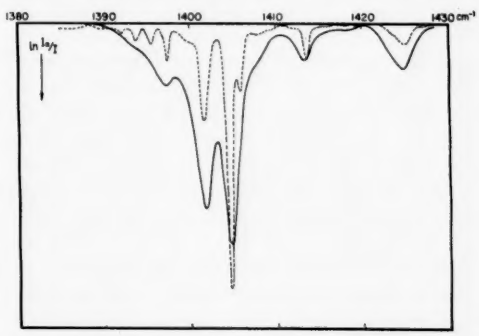

FIG. 4. Infrared spectrum in the bending region of NH_4^+ in KCl recorded with the prism instrument (resolution 5 cm^{-1}) ————, and with the grating instrument (resolution 0.7 cm^{-1}) – – –, both at liquid-helium temperature.

[18] J. F. Laurent and J. Benard, J. Phys. Chem. **Solids 3,** 7 (1957).

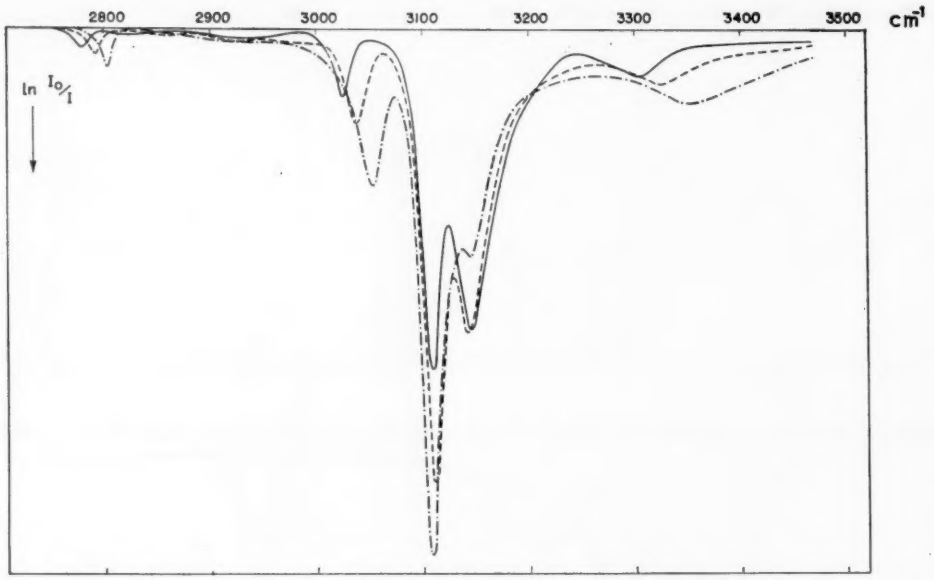

FIG. 5. Stretching regions of NH_4 in KCl -·-·-·-, KBr – – – –, and KI ———— at liquid-helium temperature and recorded with the prism instrument.

grating instrument at about 5°K is also shown in Fig. 4. Allowing for the difference in resolution (5 cm^{-1} for the prism instrument under the conditions of the spectrum in Fig. 4, 0.7 cm^{-1} for the grating instrument), it is obvious that with either method of preparation we have recorded a spectrum associated with the same species. There is no doubt that we observe fine structure in the threefold degenerate bending mode of NH_4^+ ions substituted for alkali ions in lattices of the NaCl type.

Figure 5 shows the stretching region of samples of NH_4^+ in KCl, KBr, and KI prepared by method I and recorded with the prism instrument at 5°K. The intensity scales for the individual spectra in this figure were so chosen that the absorption bands in the bending region at room temperature, plotted on these same scales, gave equal integrated band area. At about 2780–2800 cm^{-1}, one observes the first harmonic of the bending mode; between 3025 and 3055 cm^{-1} one finds $\nu_2+\nu_4$ borrowing intensity from ν_3 by Fermi resonance. ν_3 itself appears as a doublet and, by comparing Figs. 5 and 2, one sees that this doubling only becomes evident between 78 and 5°K.

We have also recorded the stretching regions of samples of NH_4^+ in KCl and KI, prepared by method II, with the grating instrument. Whereas nothing new was observed in the case of a KCl matrix, the solution of NH_4^+ in KI gave indications of further structure as can be seen from Fig. 6. Finally, Fig. 7 shows the bending region of NH_4^+ in KI (sample prepared by

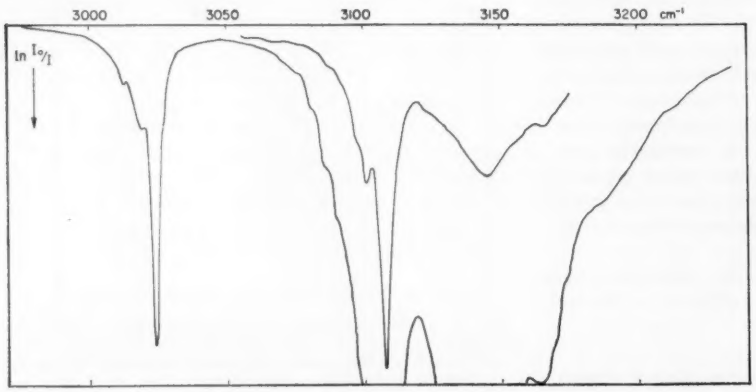

FIG. 6. Stretching region of NH_4^+ in KI (two concentrations) recorded at liquid-helium temperature with the grating instrument.

method II), recorded with the grating instrument at liquid-helium temperature. These spectra also show a considerable temperature effect (Fig. 7).

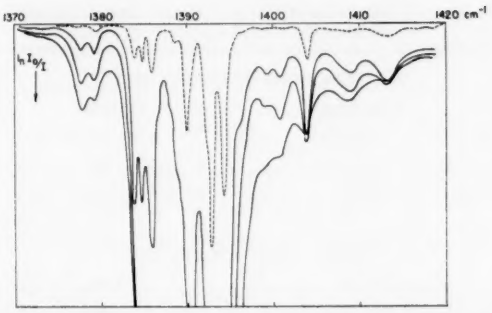

FIG. 7. Infrared spectrum in the bending region of NH_4^+ in KI, recorded with the grating instrument at liquid-helium temperature (for two concentrations: broken curve and upper solid curve) and at temperatures higher than 5°K but lower than 20°K (the two lower solid curves).

DISCUSSION

There are two aspects of these experimental results which inevitably draw attention: (a) the wealth of fine structure in the spectra of the dilute solid solutions at low temperatures (linewidths about 1 cm^{-1}); (b) in contrast, the very broad bands in the spectrum of the NH_4I films (bandwidth about 20 cm^{-1}). This difference is certainly a consequence of the coupling of the motion of neighboring ammonium ions in the pure salt. The coupling results in a dependence of the frequency of a given molecular mode on the relation between the motions of the various ammonium ions in the lattice. As a consequence, each energy level of an isolated ammonium ion must be correlated with a diffuse band in the ammonium salt. We no longer observe a line-like spectrum but a superposition of strongly broadened transitions. It is for this reason that the spectrum of the film of NH_4I is not a good starting point for a study of the motion of the ammonium ions in this phase.

In the solid solutions there are, on the average, more than 10 alkali ions between any two ammonium ions, or, put differently, the chance that two ammonium ions are neighbors is smaller than one in a hundred. Hence we may safely say that the spectra we observe in the case of the solid solutions are those of ammonium ions isolated from one another. Concerning the fine structure in the spectra of the ammonium ions in solution in KCl, KBr, and KI, two remarks can be made:

(a) The threefold degenerate bending (ν_4) and stretching (ν_3) modes of the NH_4^+ ion appear as normal, rather broad bands at room temperature and 78°K. ν_3 has the combination $\nu_2+\nu_4$ close to it and there is Fermi resonance between the upper levels of these transitions. ν_4 has a tail of weak absorption on its high-frequency side extending as far as 2000 cm^{-1}. At a temperature somewhere between 78 and 4°K (closer to the latter), the broad bands become resolved into many components. This seems a general feature; it is observed in ν_3 and ν_4 (and also in $2\nu_2+\nu_4$). There must be a multitude of closely spaced energy levels available to the ammonium ion. There is apparently also a mechanism of broadening which is very strongly temperature dependent.

(b) Although one can detect some similarities, there are many points of difference between the spectra of ammonium ions in KCl and KI in the bending region (Figs. 4 and 7). There is also pronounced difference in the stretching region (Fig. 5). Whereas, apart from the doubling already observed with the prism instrument, no further fine structure was found in the stretching region of NH_4^+ in KCl, many components were observed for NH_4^+ in KI (Fig. 6). In the bending region too it appears that the width of the lines for NH_4^+ in KI is smaller than for NH_4^+ in KCl. The obvious conclusion is that the phenomena we observe are dependent on the matrix in which the ammonium ion is located. The larger bandwidth of the fine structure components in the stretching region as compared with the bending region strongly remind one of the behavior of hydrogen bonded systems. The larger bandwidths in KCl as compared with KI are consistent with what one would expect on the basis of the fact that the crystal field is stronger in KCl than in KI.

For an isolated ammonium ion at a cubic site, it is hard to understand why the threefold degenerate modes should be split so considerably. The mode associated with the "translational" motion of the ion in its cage must be threefold degenerate, since the X, Y, and Z directions in the crystal are equivalent. Hence, the only source of multiplicity of the lower and upper state of the transition we observe can be librational or rotational levels. The temperature dependence (Fig. 7) of some of the components in the bending region in the vicinity of 5°K shows that these lines involve transitions from a number of levels very close to the ground state. Although at this stage accurate measurement of the temperature during the runs has not been possible, we estimate that the separation between the ground state and some of these levels is on the order of 5–20 cm^{-1}. These small spacings suggest a rotational rather than a librational motion of the ions.

The question is whether we are able to come to any further conclusions regarding this motion. We have already indicated a number of reasons why the motion can certainly not be considered a *free* rotation. Apart from the arguments presented above, the absence of maxima in the P and R branches at higher temperatures is a sure indication of perturbation of the motion. It is not surprising, therefore, that in a detailed analysis as well there is no agreement between the fine structure observed and that expected for a freely rotating ammonium ion. The rotation-vibration spectrum of an

TABLE I. Intensities of vibration-rotation transitions of a spherical top with $B=5.9$ cm^{-1} at 5°K.

Transition	Intensity
With nuclear spin equilibration	
1→1	0.01
0→1	0.97
1→2	0.02
Without nuclear spin equilibration	
2→1	0.03
1→0	0.06
1→1	0.19
2→2	0.04
0→1	0.31
1→2	0.31
2→3	0.06

ammonium ion, unperturbed by the crystal field, should be similar to that of CH_4 in all respects. From the accurately known NH distance (1.03 A),[12] one calculates a rotational constant $B=5.9$ cm^{-1} (compared to 5.25 cm^{-1} for CH_4[19]). In order to predict the spectrum, we must take into account Coriolis interaction in the states in which a triply degenerate mode is excited. The vibrational angular momenta are, of course, not known experimentally for the ammonium ion. Denoting the vibrational angular momenta of the threefold degenerate stretching and bending modes by ρ_3 and ρ_4, respectively, we know that in the absence of strong anharmonicity or resonances the sum $\rho_3+\rho_4$ must equal $\frac{1}{2}$. One always expects $\rho_3<\rho_4$ so we cannot be much in error if we use the values found for methane,[19] $\rho_3=0.05$ and $\rho_4=0.45$, for the ammonium ion. Since we will use only the lowest rotational levels ($J=0$, 1, and 2) in our discussion, we need not take into account a further Coriolis interaction, that between the twofold degenerate bending mode (ν_2) and ν_4.[20] This perturbation, which only becomes important for high J values, does not play a role in our qualitative arguments.

The question of whether there is nuclear spin equilibrium or not is very important. We hope to be able to come to a definite conclusion regarding this point at a later stage of this work. However, at this moment we must consider both possibilities.[21]

Excluding from consideration the nitrogen nuclear spin, there are three types of ammonium ions at room temperature, those with a total proton spin moment corresponding to $S=2$, $S=1$, or $S=0$. We will distinguish them by the symbols A, F, and E, respectively. At room temperature, the ratio of the abundance of each of these types of molecules will be given by the ratio of the number of nuclear spin functions of type A, F, or E, 5:9:2. If there is no spin equilibration, the rotational level $J=0$ in the vibrational ground state is only allowed for A-type molecules, $J=1$ only for F-type molecules, and $J=2$ for E- and F-type molecules. If there is spin equilibration, all molecules would eventually become of the A type at sufficiently low temperatures and be allowed to populate the level $J=0$.

We can now predict the spectrum one would observe at 5°K for an NH_4^+ ion if it were a freely rotating spherical top. In Table I are given the intensities for the various transitions for both cases, equilibration and no equilibration, at 5°K. Assuming a vibrational angular momentum $\zeta_3=0.05$, the spacing in the stretching region should be 11.2 cm^{-1}; whereas with $\zeta_4=0.45$, one expects a spacing of 6.5 cm^{-1} in the bending region.

The first case, a freely rotating spherical top and nuclear spin equilibration, is certainly in conflict with our findings. However, it is also impossible to obtain a fit between our spectrum and the predictions if there is no nuclear spin equilibration. We observe more lines at smaller intervals than expected on the basis of this model. There is also no explanation for the broad absorption band which appears in the case of NH_4^+ in KCl at a distance of roughly 52 cm^{-1} on the high-frequency side of the most intense component of the fine structure in the bending region (Fig. 3). For NH_4^+ in KI, apparently this same absorption band is found at a distance of 42 cm^{-1}. Also, the doubling observed in the stretching region (Fig. 5) remains unexplained unless it is the result of the effect of a Fermi resonance perturbation by $\nu_2+\nu_4$ on the rotational structure of ν_3.

We must conclude that *there is no agreement between the spectrum and the theoretical predictions for freely rotating ammonium ions.* Hence, it will be necessary to try to understand in what respects our predictions will change by increasing perturbation of the motion by the crystal field. Although it is a problem of some complexity, one could set it up quite generally, expand the potential field in which the ion moves in a suitable series, and consider the consequences of the various terms in this series. One may hope to be able to obtain from the spectrum the magnitude of the most important terms and hence a quantitative measurement of the potential field and potential barrier.

At this stage, however, we prefer to consider qualitatively a second model. We will assume that there exists an attraction between the protons and the halide ions such that once one proton gets close to a

[19] W. H. J. Childs, Proc. Roy. Soc. (London) **A153,** 555 (1936).
[20] H. A. Jahn, Proc. Roy. Soc. (London) **A168,** 495 (1938).
[21] Up to the present, proton magnetic resonance of CH_4 seems to indicate the absence of nuclear spin equilibration.[22] However, from the ultraviolet spectra of NH_2[23] and NH_3[24] radicals at low temperatures, the conclusion has been drawn that nuclear spin equilibration has taken place.
[22] K. Tomita, Phys. Rev. **89,** 429 (1953); but see H. S. Sandhu and M. Bloom, Bull. Am. Phys. Soc. **3,** 324 (1958).
[23] G. W. Robinson and M. McCarty, Jr., J. Chem. Phys. **30,** 999 (1959).
[24] K. Dressler, Ohio State Symposium Mol. Structure Spectroscopy (1960).

certain halide ion it remains there for a considerable time, during which the ion may rotate about the N-H···X$^-$ axis. Of course, we would also have to consider the librational motion of the ammonium ion about axes perpendicular to that N-H···X$^-$ axis. Restricting ourselves, however, to the limiting case, in which the frequency of this librational motion is very high, the rotational problem reduces to that of a plane rotor. The rotational energy is simply given by

$$E_{\text{rot}}=BK^2\pm 2BK\zeta$$

in the librational ground state. The last term in this expression represents the Coriolis interaction if the vibrational angular momentum ζ differs from zero.

If a certain proton is close to a halide ion and hence different from the other three, the ion loses its tetrahedral symmetry. As a consequence, there are no longer threefold degenerate modes; ν_3 as well as ν_4 split into A and E components. As a result of the attraction between proton and halide ion, we may expect the A component to be lower in frequency in the stretching region as well as in the bending region. However the A–E splitting will certainly be larger in the stretching than in the bending mode.

In the vibrational ground state, as well as for excited A modes, the vibrational angular momentum is zero. Let us call the E-mode split from the originally threefold degenerate stretching mode $\nu_3(E)$, and its vibrational angular momentum ζ_3, the E-mode split from the threefold degenerate bending mode $\nu_4(E)$ and its angular moment ζ_4, and the E mode which developed from the twofold degenerate bending mode of the tetrahedral ion, ν_2, and its angular momentum ζ_2.

Teller's rule requires $\zeta_2+\zeta_3+\zeta_4=\frac{1}{2}$ for a symmetric top with equal moments of inertia parallel and perpendicular to the top axis. Since the effect of the crystal field on equilibrium distance and force constants is small, we expect ζ_2 to be very small, ζ_3 to be about 0.1, and ζ_4 about 0.4.

By a rotation of the ion about a N-H···X$^-$ axis, only three protons change position and one can only discuss the resultant of the nuclear spin momenta of these three protons in dealing with this plane rotor model. This resultant S' may be either $\frac{3}{2}$ or $\frac{1}{2}$. Let us call ions of the type A' if $S'=\frac{3}{2}$ and of type E' if $S'=\frac{1}{2}$. For any ion the momentum of the 4th proton may be either parallel or antiparallel to S'. Hence, A'-type ions in the plane rotor problem correspond to either A- or F-type ions in our earlier notation and E'-type ions of the plane rotor problem correspond to either E or F. $K=0$ or 3 can be populated by A'-type ions only, hence by both A and F. $K=1$ or 2 can only be populated by E'-type ions, hence by both E and F.

TABLE II. Population of the lower K levels, assuming $B=5.9$ cm^{-1}, with or without nuclear spin equilibration.

Temperature	0°K		5°K		10°K	
Spin equilibration	With	Without	With	Without	With	Without
$K=0$	1.00	0.875	0.85	0.79	0.69	0.70
$K=1$	0.00	0.125	0.15	0.21	0.29	0.28
$K=2$	0.00	0.00	0.00	0.00	0.02	0.02

TABLE III. Intensities of vibration-rotation transitions for an ion rotating about a N—H···X$^-$ axis with $B=5.9$ cm^{-1}. $K=0$ is assumed to be populated by a fraction 0.8, $K=1$ by a fraction 0.2.

Transition	$K=1\to 0$	$K=\begin{matrix}0\to 0\\ 1\to 1\end{matrix}$	$K=0\to 1$	$K=1\to 2$
Intensity	0.07	0.27 0.07	0.53	0.07

That means that in this case $(5+9)/16=7/8$ of all ions may finally populate the rotational ground state. As a result, there is little difference in the population of the various K states whether there is nuclear spin equilibration or not (Table II). Assuming the $K=0$ state to be populated by a fraction 0.80, the $K=1$ state by 0.20 ($\sim$5°K), we calculate the intensities given in Table III. The spacing between $1\to 0$ and $0\to 1$, $0\to 1$, and $1\to 2$ should be identical and equal to $2B(1-\zeta)$. The $0\to 0$ and $1\to 1$ transitions are probably very close together. They are to be found between the $1\to 0$ and $0\to 1$ transition in case the A–E splitting of the threefold degenerate mode is small. However, we do not know whether this is so

Comparing the analysis of this model with the experimental results we may conclude that

(a) The A–E splitting of threefold degenerate modes offers an explanation of the doublet in the stretching region.

(b) The band at 1457 cm^{-1} in the bending region of NH_4^+ ions in KCl (and the analogous band of NH_4^+ in KI) seems too far off the band center to be explained as a result of A–E splitting. Instead, it may be correlated with the librational motion of the ion. If it corresponds to excitation of the first librational state, it would place the frequency of libration at roughly 50 cm^{-1} for NH_4^+ in KCl and 40 cm^{-1} in KI. For a librational frequency as low as 50 cm^{-1}, the amplitude $(\langle\Delta\phi^2\rangle_{\text{Av}})^{\frac{1}{2}}$ in the librational ground state would be about 20°.

(c) This model makes it possible to account for a spectrum in which most of the intensity falls within a small frequency range (<4 cm^{-1}). In fact there seems to be some similarity between the spectra in the bending region and our predictions if one assumes (1) no appreciable A–E splitting and (2) a ζ_4 of about 0.2, a rather low value. It is clear, however, that there are again many more lines than we can account for.

We are led to conclude that the model of rotation about a N-H···X$^-$ ion axis and libration about axes

perpendicular to this axis cannot account for all the details observed. Some features of the spectrum, however, seem to be in agreement with it.

CONCLUSION

The obvious conclusion is that the motion of the ammonium ion in lattices of the NaCl type is more complex than either a free rotation or a rotation about a single axis. Approaching the problem from the model of free rotation, we may ascribe the discrepancy between predicted and observed spectrum to crystal field splitting. This approach is useful as long as the splitting remains smaller than the separation between unperturbed levels of the same symmetry species. Starting from the model of rotation about a single axis, we must take into account the fact that the proton which is close to a halide ion could have been any of four, the halide ion any of six. We can then consider the model which we have discussed as describing only one of 24 identical problems. Upon lowering of the barrier separating these 24 "local" problems, mixing of the "local" wave functions will occur. This description, however, will lose significance as soon as the barrier splittings become comparable to the spacing between rotational states.

It may therefore very well be that the observed fine structure can only be interpreted after a rigorous treatment of the motion of a tetrahedral ion in an octahedral field has been completed. Such a study is already under way in this laboratory.[25]

We would not be surprised, however, to find among the wave functions describing the real motion of the ion some representing essentially one dimensional rotation about N-H$\cdots$X$^-$ halide ion axes. In fact, as soon as the ion has acquired a sizable angular momentum, this seems to be the only possible motion which avoids high barriers in the potential function. States of low angular momentum, however, and these are the ones we deal with in our low-temperature spectra, can neither be described as associated with free rotation nor with rotation about a N-H$\cdots$X$^-$ axis.

A study of the spectra of ND_4^+ ions in dilute solution in alkali halides and of the temperature dependence of the intensity of the various fine structure components may be of considerable help in the interpretation and is being undertaken.

The two factors which are of importance in determining the width of the lines in our spectra may be summarized as follows: (a) the influence of the rotational motion of surrounding NH_4^+ ions on the motion of any one ion. This accounts for the difference in appearance between the absorption bands in pure NH_4I and in the dilute solutions of NH_4^+ ions in alkali halides. The effect will persist to low temperatures, but may finally be better described as due to static orientational disorder. (b) A temperature dependent effect, undoubtedly associated with the thermal motion of the lattice surrounding the ion in the dilute solid solutions. Since, because of this, the fine structure becomes smeared out completely at temperatures not higher than about 20°K, the broadening must be associated with the excitation of low frequency, long wavelength, acoustic lattice modes. The influence of this thermal motion may be quite different for the various levels and in fact it need not surprise us that a "librational" level would be broadened to a greater extent than a "rotational" level. It also seems reasonable to expect a larger width at the same temperature for NH_4^+ in KCl than NH_4^+ in KI and a larger width in the stretching than in the bending region.

[25] H. F. King, Ph.D. thesis, Princeton (1960).

"Thermal Conductivity" and Chemical Kinetics

RICHARD S. BROKAW

Lewis Research Center, NASA, Cleveland, Ohio

(Received April 6, 1961)

A general expression is derived for the apparent "thermal conductivity" of reacting gas mixtures in which a single chemical reaction proceeds at a finite rate. In contrast to cases where reaction rates are either very high or very low, it is found that the "thermal conductivity" depends on the geometry and scale of the system—hence the quotes. This expression applies to the three geometries that can be described one-dimensionally: parallel plates, concentric cylinders, and concentric spheres. The results are limited to systems with small temperature differences, such as thermal conductivity cells, wherein reaction rate can be assumed constant. In addition to the scale and geometry, the "thermal conductivity" is determined by three types of constants having the dimensions of reciprocal length. Gas phase reaction is characterized by ϕ, which is proportional to the square root of the chemical reaction rate at equilibrium. (This is the total rate in either direction, not the net rate, which is, of course, zero.) Heterogeneous chemical reaction at the two bounding surfaces is characterized by ψ_1 and ψ_2, while χ_1 and χ_2 account for the temperature accommodation. The nature of the "thermal conductivity" is discussed for several specific systems. The expression is shown to approximate a numerical calculation of the effect of chemical reaction rate on stagnation point heat transfer. Experimental thermal conductivity data for the $N_2O_4 \rightleftarrows 2NO_2$ system are adequately described in terms of this theory. An upper limit for the rate constant for the bimolecular dissociation of N_2O_4 is estimated to be 5.3×10^9 cm^3 mole^{-1} sec^{-1} at 296°K.

INTRODUCTION

At high temperatures most gases of interest to aerodynamics and propulsion are partially dissociated and hence undergo a variety of chemical reactions. In reacting gases, heat transport may be considerably higher than in "frozen" (nonreacting) mixtures. Large amounts of heat may be carried as chemical enthalpy of molecules that diffuse because of concentration gradients; these gradients exist because the gas composition varies with temperature. For example, in a gas that absorbs heat by dissociating as the temperature is raised, heat is transferred when a molecule dissociates in the high-temperature region. In the low-temperature region the fragments recombine and release the heat absorbed at high temperature.

When chemical reaction rates are very high, chemical equilibrium can be assumed to exist locally throughout a gas mixture, and it becomes possible, by differentiating the equilibrium relationships, to relate the concentration gradients to the temperature gradient. The concentration gradients provide the driving force for the diffusional transport of chemical enthalpy. In this case, one can define an equilibrium thermal conductivity λ_e independent of apparatus geometry:

$$\lambda_e = \lambda_f + \lambda_r, \tag{1}$$

where λ_f is the thermal conductivity in the absence of chemical reactions (the "frozen" thermal conductivity) and λ_r is the augmentation due to the reactions.

The first treatment of this sort was due to Nernst,[1] who derived an essentially correct formula for the nitrogen tetroxide dissociation. (The "diffusion coefficient" used by Nernst is not the usual binary diffusion coefficient; however, Nernst was alert to this possibility.) Another example of this type of analysis is the derivation of the Eucken-type correction for the transport of internal energy in polyatomic gases. Eucken's[2] original arguments were essentially intuitive. Ubbelohde[3] took the decisive step of considering molecules with "excited" internal energy states as belonging to different chemical species; he pointed out that the flow of internal energy could be treated as energy transport due to diffusion of the "excited" molecules. This idea has been extended by Chapman and Cowling,[4] Hirschfelder,[5] and others.

Subsequently a general expression for the increase in thermal conductivity due to chemical reactions was developed[6] and later simplified.[7] This expression is applicable to mixtures involving any number of reactants, inert diluents, and chemical equilibria, provided chemical equilibrium exists locally in the temperature gradient. This general expression has been amply confirmed by calculations[8] for experimental data on the hydrogen fluoride system,[9] and also the nitrogen tetroxide system[10,11] near atmospheric pressure.

Let us now consider the reduction in heat transport caused by reduced reaction rates. Dirac[12] examined the

[1] W. Nernst, Fetschr. Ludwig Boltzmann **904** (1904).

[2] A. Eucken, Physik. Z. **14,** 324 (1913).

[3] A. R. Ubbelohde, J. Chem. Phys. **3,** 219 (1935).

[4] S. Chapman and T. G. Cowling, *The Mathematical Theory of Non-Uniform Gases* (Cambridge University Press, New York, 1952), p. 238.

[5] J. O. Hirschfelder, J. Chem. Phys. **26,** 282 (1957).

[6] J. N. Butler and R. S. Brokaw, J. Chem. Phys. **26,** 1636 (1957).

[7] R. S. Brokaw, J. Chem. Phys. **32,** 1005 (1960).

[8] R. S. Brokaw, Planetary Space Sci. **3,** 238 (1961).

[9] E. U. Franck and W. Spalthoff, Naturwissenschaften **40,** 580 (1953).

[10] K. P. Coffin and C. O'Neal, Jr., Natl. Advisory Comm. Aeronaut. Tech. Note 4209 (1958).

[11] K. P. Coffin, J. Chem. Phys. **31,** 1290 (1959).

[12] P. A. M. Dirac, Proc. Cambridge Phil. Soc. **22,** 132 (1924).

effect of chemical reaction rate on the concentration gradients near a noncatalytic wall in a dissociating gas subjected to a temperature gradient. Ubbelohde[8] calculated the effect of vibrational relaxation time on "thermal conductivity" of polyatomic molecules for parallel plates, while Schäfer, Rating, and Eucken[13] treated the corresponding problem for concentric cylinders. More recently, Meixner[14] has considered a dissociating gas between parallel plates, while Franck and Spalthoff[15] analyzed the same reaction for concentric cylinders. It should be noted that, as these relaxation effects come into play, heat transport cannot be described by a thermal conductivity which is solely a gas property. On the contrary, the "thermal conductivity" will depend on apparatus geometry and scale.

Franck and Spalthoff applied their equations to their experimental data on the thermal conductivity of dissociating bromine and fluorine. The experimental results, which fell below calculated equilibrium conductivities, were explained in terms of the theory. Similarly, Prigogine and Waelbroeck[16] have demonstrated experimentally that rotational energy transfer in hydrogen and in oxygen decreases at low pressures; these decreases are consistent with theory and known rotational relxation rates.

In this paper a general analytic expression is developed for the apparent "thermal conductivity" of reacting gas mixtures in which any single chemical reaction proceeds at a finite rate. The formulas account for heterogeneous reaction and temperature accommodation on the surfaces as well as gas phase chemical reaction. Geometries considered are: parallel plates, concentric cylinders, and concentric spheres.

Since the equilibrium reaction rate must be assumed constant to obtain analytic solutions, the results apply rigorously only to systems with small temperature differences, such as thermal conductivity cells. (It is also assumed that the gas composition deviates but slightly from equilibrium; however, this condition is less stringent and is automatically satisfied if temperature differences are small.)

The nature of the "thermal conductivity" is discussed for several specific geometries and surface activities. The principal features of the cases derived heretofore[8,13–15] are easily obtained. (There are minor differences in the formulation of boundary conditions[13,15]; in one case an incorrect diffusion equation was used.[15]) The theory is successfully applied to low-pressure conductivity data for the $N_2O_4 \rightleftarrows 2NO_2$ system.[10]

[13] K. Schafer, W. Rating, and A. Eucken, Ann. Physik **42**, 176 (1942).
[14] J. Meixner, Z. Naturforsch. **7a**, 553 (1952).
[15] E. U. Franck and W. Spalthoff, Z. Elektrochem. **58**, 374 (1954).
[16] I. Prigogine and F. Waelbroeck, *Proceedings of the Joint Conference on Thermodynamic and Transport Properties of Fluids* (The Institution of Mechanical Engineers, London, 1958), p. 128.

THEORETICAL CONSIDERATIONS

Let us consider heat conduction through a reacting gas mixture in which there is only one chemical reaction. We will treat geometries that can be described by a single coordinate r: parallel plates, concentric cylinders, and concentric spheres. The problem involves the solution of a continuity equation and a heat flux equation. There is but one continuity equation because the fluxes of the various species are related through the stoichiometry of the chemical reaction.

Let us write the chemical reaction in the balanced form[7]:

$$\sum_{i=1}^{\nu} n_i X^i = 0. \tag{2}$$

Here X^i represents the ith chemical species, and n_i is the stoichiometric coefficient for this species. The n_i are positive for reactants and negative for products (or vice versa).

The conduction or heat flux equation is

$$q = -\lambda_f r^a (dT/dr) + \sum_{i=1}^{\nu} r^a W_i H_i$$

$$\equiv -\lambda^* \left(\Delta T_w \Big/ \int_{r_1}^{r_2} r^{-a} dr \right), \tag{3}$$

where λ_f is the thermal conductivity the gas mixture would have in the absence of reaction (the "frozen" state), T is the absolute temperature, W_i is the mole flux of the ith component (moles/cm^2 sec), and H_i is the enthalpy per mole, referred to a common base. The constant a characterizes the geometry: for parallel plates, $a=0$; for concentric cylinders, $a=1$; and for concentric spheres, $a=2$. For parallel plates, q is the constant heat flux through unit area; for concentric cylinders, it is the flux through an area defined by unit height and an arc of one radian; and for concentric cylinders, it is the flux through a unit solid angle (one steradian). ΔT_w is the temperature difference between the walls.

Equation (3) serves to define an apparent "thermal conductivity" for the reacting gas λ^*. However, it will be found that λ^*, unlike the equilibrium or frozen conductivities, will depend on the geometry and scale of the system. (The "thermal conductivity" might instead be defined in terms of the gas phase temperature difference. If this is done, however, the "thermal conductivity" can exceed the equilibrium value λ_e under some circumstances.) The continuity equation simply requires that, in an incremental volume, the net rate of production of each species by chemical reaction must balance the loss by diffusion,

$$(dN_j/dt)_{\text{diff}} + (dN_j/dt)_{\text{chem}} = 0, \tag{4}$$

where N_j is the local concentration of a particular

species j in moles/cm³. Thus,

$$n_j^{-1}(dN_j/dt)_{\text{diff}} = (-1/r^a)(d/dr)r^a(W_j/n_j)$$

$$n_j^{-1}(dN_j/dt)_{\text{chem}} = \mathfrak{R}_f - \mathfrak{R}_d,$$

where $\mathfrak{R}_f$, $\mathfrak{R}_d$ are the usual expressions for the chemical rates of formation and destruction of species j in unit volume.

Thus, the continuity equation for species j becomes

$$-(1/r^a)(d/dr)r^a(W_j/n_j) + (\mathfrak{R}_f - \mathfrak{R}_d) = 0. \quad (5)$$

We will now proceed to develop explicit expressions for the diffusion and chemical kinetic terms.

The Diffusion Equation

For a mixture of ν components, the diffusion equation for species j is[17]

$$dx_j/dr = \sum_{k=1}^{\nu} \Delta_{jk}(x_j W_k - x_k W_j), \quad (6)$$

where x_j, x_k are the mole fractions of species j and k. The quantities Δ_{jk} are defined by $\Delta_{jk} \equiv RT/D_{jk}P$, where D_{jk} is the binary diffusion coefficient between species j and k, P is the pressure, and R is the gas constant in pressure-volume units. Equation (6) neglects external force fields, total-pressure gradients, and thermal diffusion.

The fluxes of the various species are related through the stoichiometry of the chemical reaction as follows:

$$W_j/n_j = W_k/n_k \quad (k = 1, 2, \cdots \nu),$$

so that the diffusion equation may be written

$$W_j/n_j = (-dx_j/dr)\left[\sum_{k=1}^{\nu} \Delta_{jk}(x_k n_j - x_j n_k)\right]^{-1}$$

$$= (-1/n_j)(D_j P/RT)(dx_j/dr). \quad (7)$$

Here we have defined the quantity

$$D_j \equiv n_j\left[\sum_{k=1}^{\nu} \frac{(x_k n_j - x_j n_k)}{D_{jk}}\right]^{-1} \quad (8)$$

as a diffusion coefficient for j in the reacting gas mixture.

The Gas Phase Chemical Kinetics

To consider the chemical kinetics, let us rewrite the chemical reaction as follows, distinguishing products and reactants:

$$\sum_{l=1}^{\mu} n_l X^l = \sum_{m=\mu+1}^{\nu} n_m X^m.$$

Thus, for $i = 1$ to μ, $n_i = n_l$; for $i = \mu+1$ to ν, $n_i = -n_m$. The n_l and n_m are chosen so as to be all positive. Let us consider the rates of formation and destruction of the particular species X^j in the l series. Then,

$$\mathfrak{R}_f - \mathfrak{R}_d = k_f \prod_{m=\mu+1}^{\nu} N_m^{n_m} - k_d \prod_{l=1}^{\mu} N_l^{n_l}, \quad (9)$$

where N_m, N_l are the concentrations of the species in moles/cm³ and k_f, k_d are the rate constants for the formation and decomposition reactions. If inerts affect the rate, they do so for both forward and backward reactions; the effect may be incorporated into the rate constants.

So far we have made no assumptions as to the extent to which the local gas composition departs from equilibrium. It is possible to substitute Eqs. (7) and (9) into Eq. (5) and thus obtain a set of continuity equations, one for each species. They are nonlinear and can only be solved numerically. In order to proceed to an analytic solution, we must now assume that the gas composition deviates only slightly from equilibrium. (Actually, this is the case for many real systems, such as thermal conductivity cells, where the variations in temperature and composition are indeed small.) We may then expand the reaction rates about the equilibrium rates, so that

$$\mathfrak{R}_f = \mathfrak{R}_{f,e} + \sum_{m=\mu+1}^{\nu} \frac{\partial \mathfrak{R}_{f,e}}{\partial N_{m,e}}(N_m - N_{m,e}) + \cdots$$

$$\cong \mathfrak{R}_{f,e}\left[1 + \sum_{m=\mu+1}^{\nu} \frac{\partial \ln \mathfrak{R}_{f,e}}{\partial N_{m,e}}(N_m - N_{m,e})\right] \quad (10)$$

with a similar expression for $\mathfrak{R}_d$. The subscripts e refer to values at chemical equilibrium. Now

$$\ln \mathfrak{R}_{f,e} = \ln k_f + \sum_{m=\mu+1}^{\nu} n_m \ln N_{m,e},$$

so that

$$\partial \ln \mathfrak{R}_{f,e}/\partial N_{m,e} = n_m/N_{m,e}$$

and

$$\mathfrak{R}_f = \mathfrak{R}_{f,e}\{1 + \sum_{m=\mu+1}^{\nu} n_m[(N_m - N_{m,e})/N_{m,e}]\},$$

with an analogous equation for $\mathfrak{R}_d$. Because the rates of the forward and back reactions at equilibrium are equal, we may designate this equilibrium rate as $\mathfrak{R}$, and

$$\mathfrak{R}_f - \mathfrak{R}_d = \mathfrak{R}\left[\sum_{m=\mu+1}^{\nu} n_m \frac{N_m - N_{m,e}}{N_{m,e}} - \sum_{l=1}^{\mu} n_l \frac{N_l - N_{l,e}}{N_{l,e}}\right]$$

$$= \mathfrak{R}\sum_{i=1}^{\nu} n_i[(x_{i,e} - x_i)/x_{i,e}]. \quad (11)$$

Actually, Eq. (11) is also valid *far* from equilibrium for systems which are first order in both directions, as well as for systems which might be termed pseudo first order. Thus, for example, a reaction of the type

$$A + B \rightleftarrows C + D$$

[17] See Eq. (8) of reference 6.

will follow Eq. (11) far from equilibrium if, say, B and D are in large excess. Important reactions such as vibrational relaxations are also pseudo first order.

We continue by expressing the various concentration deviations from equilibrium in terms of $x_{j,e}-x_j$. Since

$$x_{i,e}-x_i=(x_{j,e}-x_j)\,(dx_{i,e}/dx_{j,e}),$$

$$\mathfrak{R}_f-\mathfrak{R}_d=\mathfrak{R}(x_{j,e}-x_j)\sum_{i=1}^{\nu}(n_i/x_{i,e})\,(dx_{i,e}/dx_{j,e}).$$

An expression analogous to Eq. (7) can be written for species i; this can be combined with Eq. (7) to give an expression for $dx_{i,e}/dx_{j,e}$. Consequently,

$$\mathfrak{R}_f-\mathfrak{R}_d=\frac{(x_{j,e}-x_j)\,\mathfrak{R}}{\sum_{k=1}^{\nu}\Delta_{jk}(x_{k,e}n_j-x_{j,e}n_k)}\times\left[\sum_{i=1}^{\nu}\frac{n_i}{x_{i,e}}\sum_{k=1}^{\nu}\Delta_{ik}(x_{k,e}n_i-x_{i,e}n_k)\right]. \quad (12)$$

The term in brackets may be transformed, as indicated in footnote 10 of reference 6, and can be related to λ_r, the contribution of the reaction to the thermal conductivity when reaction rates are very high. Thus,

$$\sum_{i=1}^{\nu}\sum_{k=1}^{\nu}\Delta_{ik}(n_i/x_{i,e})\,(x_{k,e}n_i-x_{i,e}n_k)=\sum_{i=1}^{\nu-1}\sum_{k=i+1}^{\nu}\Delta_{ik}\frac{(n_ix_{k,e}-n_kx_{i,e})^2}{x_{i,e}x_{k,e}}=\lambda_r^{-1}(\Delta H^2/RT^2),$$

where ΔH is the heat of reaction. When this result is substituted into Eq. (12), we find

$$\mathfrak{R}_f-\mathfrak{R}_d=\left[(x_{j,e}-x_j)/\sum_{k=1}^{\nu}\Delta_{jk}(x_{k,e}n_j-x_{j,e}n_k)\right]\lambda_r^{-1}\frac{\Delta H^2}{RT^2}\mathfrak{R}. \quad (13)$$

Solution of the Continuity Equation

Next *assume* that temperature and composition changes are small throughout the system, so that

$$\sum_{k=1}^{\nu}\Delta_{jk}(x_kn_j-x_jn_k)\cong\text{const}\cong\sum_{k=1}^{\nu}\Delta_{jk}(x_{k,e}n_j-x_{j,e}n_k).$$

Then, when the diffusion [Eq. (7)] and simplified kinetic [Eq. (13)] equations are substituted into the continuity equation [Eq. (5)], we obtain the rather simple expression

$$(1/r^a)\,(d/dr)r^a(dx_j/dr)-\mathfrak{R}\lambda_r^{-1}(\Delta H^2/RT^2)\,(x_j-x_{j,e})=0. \quad (14)$$

Let us now define a new variable $y\equiv x_j-x_{j,e}$, where y is simply the deviation of the mole fraction of species j from the local equilibrium value. We want to relate dx_j/dr and dy/dr, which can be done by eliminating $dx_{j,e}/dr$ through the heat flux equation [Eq. (3)]. Remember, first, that

$$-\lambda_r(dT/dr)=\sum_{i=1}^{\nu}W_{i,e}H_i,$$

where the $W_{i,e}$ are the fluxes when equilibrium obtains locally through the temperature gradient. Then

$$-\lambda^*\Delta T_w\Big/r^a\int_{r_1}^{r_2}r^{-a}dr=\sum_{i=1}^{\nu}H_i[(\lambda_f/\lambda_r)W_{i,e}+W_i]=\Delta H[(\lambda_f/\lambda_r)\,(W_{j,e}/n_j)+(W_j/n_j)],$$

since $\sum n_iH_i=\Delta H$. Next, W_j and $W_{j,e}$ are eliminated through Eq. (7), and we find that

$$r^a(dx_j/dr)=r^a(\lambda_f/\lambda_e)\,(dy/dr)+(\lambda_f/\lambda_e)\,B, \quad (15)$$

where

$$B\equiv(\lambda_r/\lambda_f)\left(\lambda^*\Delta T_w\Big/\int r^{-a}dr\right)(n_j/\Delta H)\,(RT/D_jP).$$

Because we have already assumed RT/D_jP to be constant, the second term on the right-hand side is constant, and hence, upon differentiating Eq. (15),

$$(d/dr)r^a(dx_j/dr)=(\lambda_f/\lambda_e)\,(d/dr)r^a(dy/dr).$$

When we substitute this result into Eq. (14), we find that

$$(1/r^a)\,(d/dr)r^a(dy/dr)-\phi^2y=0, \quad (16)$$

where

$$\phi\equiv[(\lambda_e/\lambda_f\lambda_r)\,(\Delta H^2/RT^2)\,\mathfrak{R}]^{\frac{1}{2}}. \quad (17)$$

This parameter ϕ has the dimension of reciprocal length; it embodies the influence of the gas phase chemical kinetics on the "thermal conductivity." To proceed with the solution, we must *assume* ϕ to be constant. Since the equilibrium reaction rate $\mathfrak{R}$ usually depends on the temperature exponentially, we are limiting ourselves to systems with quite small temperature differences. In general, it is this particular assumption that will most severely limit us.

Finally, define a new dimensionless distance $z\equiv\phi r$; Eq. (16) becomes

$$(1/z^a)\,(d/dz)z^a(dy/dz)-y=0. \quad (18)$$

Equation (18) may be solved by comparing it with the generalized Bessel's equation.[18] The solution is

$$y=C_1M_p(z)+C_2M_{-p}(z), \quad (19)$$

[18] H. S. Mickley, T. K. Sherwood, and C. E. Reed, *Applied Mathematics in Chemical Engineering* (McGraw-Hill Book Company, Inc., New York, 1957), p. 174.

where

$$p=(1-a)/2 \tag{20}$$

$$\left.\begin{aligned} M_p(z) &\equiv z^p I_p(z) \\ M_{-p}(z) &\equiv z^p I_{-p}(z), \qquad p\neq 0 \\ &\equiv K_0(z), \qquad p=0 \end{aligned}\right\} \tag{21}$$

The I_p, I_{-p} are modified Bessel functions of the first kind, while the K_0 are modified Bessel functions of the second kind; C_1, C_2 are the constants of intergration, to be evaluated in the next section.

Surface Chemical Kinetics and Temperature Accommodation (Boundary Conditions)

Now let us examine the conditions at the partially catalytic walls. First we define a catalytic efficiency (a chemical accommodation coefficient) for molecules j:

$$\epsilon_j=(g_i-g_r)/(g_i-g_{r,e}).$$

Here g_i is the number of moles of species j incident upon unit surface in unit time, whereas g_r is the number reflected; $g_{r,e}$ is the number reflected if the gas composition is equilibrated.[19] The number of moles striking unit area is $\frac{1}{4}n\bar{c}_j x_j'$, where n is the number of moles per cm^3 (P/RT) and $\bar{c}_j$ is the mean molecular velocity $[(8RT/\pi M_j)^{\frac{1}{2}}]$; x_j' is the mole fraction at a short distance away from the wall (of the order of a mean free path), whence molecules striking the wall originate. Similarly,

$$g_{r,e}=\tfrac{1}{4}n\bar{c}_j x_{j,e_{\text{wall}}}.$$

At the wall at r_1, the lower value of r, the flux to the wall due to diffusion is $(-W_j)$; hence,

$$\begin{aligned} nD_j(dx_j/dr) &= g_i-g_r=\epsilon_j(g_i-g_{r,e}) \\ &= \tfrac{1}{4}n\bar{c}_j\epsilon_j(x_j'-x_{j,e_{\text{wall}}}). \end{aligned}$$

Next, consider the composition of the gas right at the wall. Half of the molecules are about to strike the wall; the mole fraction of j in this group is x_j'. The other half of the molecules have just collided with the surface; in this group the mole fraction is $\epsilon_j x_{j,e_{\text{wall}}}+(1-\epsilon_j)x_j'$. Hence,

$$x_j=\tfrac{1}{2}(2-\epsilon_j)x_j'+\tfrac{1}{2}\epsilon_j x_{j,e_{\text{wall}}}.$$

This relation may be used to eliminate x_j' from the preceding expression, and we find

$$x_j-x_{j,e_{\text{wall}}}=[(2-\epsilon_j)/2\epsilon_j](4D_j/\bar{c}_j)(dx_j/dr)_{r=r_1}. \tag{22}$$

However, the boundary condition we require is

$$y_1=x_j-x_{j,e_{\text{gas}}}=x_j-x_{j,e_{\text{wall}}}-(x_{j,e_{\text{gas}}}-x_{j,e_{\text{wall}}}). \tag{23}$$

[19] The catalytic activity of a surface for recombining atoms is frequently given in terms of γ, the fraction of the atoms striking the surface which recombine; $\epsilon=\gamma/\gamma_{\text{perfect catalyst}}$. This terminology is usually used under conditions where $\gamma_{\text{perfect catalyst}}\to 1$, so that $\gamma\to\epsilon$.

So we must investigate the quantity

$$x_{j,e_{\text{gas}}}-x_{j,e_{\text{wall}}}=(dx_{j,e}/dr)(dr/dT)(T_{\text{gas}}-T_{\text{wall}})_{r=r_1}. \tag{24}$$

Kennard[20] presents a derivation for the temperature jump $T_{\text{gas}}-T_{\text{wall}}$ for a pure gas. This derivation is easily extended to gas mixtures, with the result

$$T_{\text{gas}}-T_{\text{wall}}=[(2-\alpha)/2\alpha]\lambda_f(dT/dr)_{r=r_1}\times\Big[\sum_{k=1}^{p}\tfrac{1}{4}n\bar{c}_k x_k(C_{p_k}-\tfrac{1}{2}R)\Big]^{-1}. \tag{25}$$

Here α is the accommodation coefficient, $\bar{c}_k$ is the mean molecular velocity, and C_{p_k} is the molar heat capacity for species k. Equations (22)–(25) can be combined to give the required boundary condition:

$$y_1=(\lambda_e/\lambda_f)[(\psi_1^{-1}-\chi_1^{-1})(dx_j/dr)_{r=r_1}+\chi_1^{-1}(dy/dr)_{r=r_1}], \tag{26}$$

where

$$\psi_1\equiv(\lambda_e/\lambda_f)[2\epsilon_j/(2-\epsilon_j)]_1(\bar{c}_j/4D_j), \tag{27}$$

$$\chi_1\equiv(\lambda_e/\lambda_f)[2\alpha/(2-\alpha)]_1\frac{\sum n\bar{c}_k x_k(C_{p_k}-\frac{1}{2}R)}{4\lambda_f}. \tag{28}$$

Like ϕ, ψ_1, and χ_1 have the dimensions of reciprocal length; ψ_1 characterizes the chemistry of the surface. The ϵ_j, $\bar{c}_j$, and D_j may vary according to which particular species is considered—but ψ_1 is characteristic of the system as a whole, and not any particular species per se. The quantity χ_1 accounts for the energy transfer characteristics at the surface. By means of Eq. (15), dx_j/dr can be eliminated, with the result

$$y_1=\phi[\psi_1^{-1}+(\lambda_r/\lambda_f)\chi_1^{-1}](dy/dz)_{r=r_1}+(\psi_1^{-1}-\chi_1^{-1})(B/r_1^a). \tag{29}$$

At the other wall similar considerations apply, except that the signs of the fluxes to the wall are opposite, so that

$$-y_2=\phi[\psi_2^{-1}+(\lambda_r/\lambda_f)\chi_2^{-1}](dy/dz)_{r=r_2}+(\psi_2^{-1}-\chi_2^{-1})(B/r_2^a). \tag{30}$$

The constants ψ_2 and χ_2 are defined in the same fashion as ψ_1 and χ_1.

Equation (19) can be differentiated to yield

$$dy/dz=C_1M_{p-1}(z)+C_2M_{-p+1}(z), \tag{31}$$

where[21]

$$\left.\begin{aligned} M_{p-1}(z) &= z^p I_{p-1}(z), \\ M_{-p+1}(z) &= z^p I_{-p+1}(z), \qquad p\neq 0 \\ &= -K_1(z), \qquad p=0. \end{aligned}\right\} \tag{32}$$

[20] E. H. Kennard, *Kinetic Theory of Gases* (McGraw-Hill Book Company, Inc., New York, 1938), p. 312.

[21] Reference 18, p. 178.

Thus y_1, $(dy/dz)_1$, y_2, and $(dy/dz)_2$ can be obtained from Eqs. (19) and (31) and substituted into Eqs. (29) and (30). Equations (29) and (30) may now be solved for C_1 and C_2, with the result

$$C_1 = -Ba_1, \qquad C_2 = -Ba_{12},$$

where a_1, a_2 are constants as follows:

$$\left.\begin{aligned} a_1 &= \left\{\frac{1}{r_1^a}\left[\frac{1}{\psi_1}-\frac{1}{\chi_1}\right]\left[M_{-p}(z_2)+\phi\left(\frac{1}{\psi_2}+\frac{\lambda_r}{\lambda_f}\frac{1}{\chi_2}\right)M_{-p+1}(z_2)\right]+\frac{1}{r_2^a}\left[\frac{1}{\psi_2}-\frac{1}{\chi_2}\right]\left[M_{-p}(z_1)-\phi\left(\frac{1}{\psi_1}+\frac{\lambda_r}{\lambda_f}\frac{1}{\chi_1}\right)M_{-p+1}(z_1)\right]\right\}d^{-1}, \\ a_2 &= -\left\{\frac{1}{r_1^a}\left[\frac{1}{\psi_1}-\frac{1}{\chi_1}\right]\left[M_{p}(z_2)+\phi\left(\frac{1}{\psi_2}+\frac{\lambda_r}{\lambda_f}\frac{1}{\chi_2}\right)M_{p-1}(z_2)\right]+\frac{1}{r_2^a}\left[\frac{1}{\psi_2}-\frac{1}{\chi_2}\right]\left[M_{p}(z_1)-\phi\left(\frac{1}{\psi_1}+\frac{\lambda_r}{\lambda_f}\frac{1}{\chi_1}\right)M_{p-1}(z_1)\right]\right\}d^{-1}, \end{aligned}\right\} \tag{33}$$

and

$$\begin{aligned} d \equiv &\left[M_p(z_2)+\phi\left(\frac{1}{\psi_2}+\frac{\lambda_r}{\lambda_f}\frac{1}{\chi_2}\right)M_{p-1}(z_2)\right]\left[M_{-p}(z_1)-\phi\left(\frac{1}{\psi_1}+\frac{\lambda_r}{\lambda_f}\frac{1}{\chi_1}\right)M_{-p+1}(z_1)\right] \\ &-\left[M_p(z_1)-\phi\left(\frac{1}{\psi_1}+\frac{\lambda_r}{\lambda_f}\frac{1}{\chi_1}\right)M_{p-1}(z_1)\right]\left[M_{-p}(z_2)+\phi\left(\frac{1}{\psi_2}+\frac{\lambda_r}{\lambda_f}\frac{1}{\chi_2}\right)M_{-p+1}(z_2)\right]. \end{aligned}$$

The "Thermal Conductivity"

With the aid of Eqs. (7) and (15) the conduction equation (3) can, after some manipulation, be cast in the form

$$\lambda^*\Delta T_w \Big/ \int r^{-a}dr = \lambda_e r^a (dT/dr) + r^a(\lambda_r/\lambda_f)\left(\lambda^*\Delta T_w \Big/ \int r^{-a}dr\right)B^{-1}(dy/dr). \tag{34}$$

This expression may be multiplied by $r^{-a}dr/\Delta T_w$ and integrated, to give

$$\lambda^* = \lambda_e(\Delta T_{\text{gas}}/\Delta T_{\text{wall}}) + (\lambda_r/\lambda_f)\lambda^*\left[(y_2-y_1) \Big/ B\int r^{-a}dr\right]. \tag{35}$$

Next, we must develop an expression for

$$\Delta T_{\text{gas}}/\Delta T_{\text{wall}} = 1-\left[(T_{\text{gas}}-T_{\text{wall}})/\Delta T_{\text{wall}}\right]_{r=r_1}-\left[(T_{\text{wall}}-T_{\text{gas}})/\Delta T_{\text{wall}}\right]_{r=r_2}. \tag{36}$$

From Eq. (25) and the definition of χ_1 [Eq. (28)] we find that

$$(T_{\text{gas}}-T_{\text{wall}})_{r=r_1} = \chi_1^{-1}(\lambda_e/\lambda_f)(dT/dr)_{r=r_1}.$$

The temperature gradient at the wall can be obtained from Eq. (34), so that

$$\left[(T_{\text{gas}}-T_{\text{wall}})/\Delta T_{\text{wall}}\right]_{r=r_1} = (\lambda^*/\lambda_f)\left[(1/\chi_1 r_1^a)-(\lambda_r/\lambda_f)(\phi/\chi_1)B^{-1}(dy/dz)_1\right]\left(\int r^{-a}dr\right)^{-1}.$$

Applying similar considerations at the other wall, Eq. (36) becomes

$$\Delta T_{\text{gas}}/\Delta T_{\text{wall}} = 1-(\lambda^*/\lambda_f)\left\{(\chi_1 r_1^a)^{-1}+(\chi_2 r_2^a)^{-1}-(\lambda_r/\lambda_f)(\phi/B)\left[\chi_1^{-1}(dy/dz)_1+\chi_2^{-1}(dy/dz)_2\right]\right\}\left(\int r^{-a}dr\right)^{-1}. \tag{37}$$

When this result is substituted into Eq. (35), the "thermal conductivity" is found to be

$$\lambda^* = \frac{\lambda_e\lambda_f}{\lambda_f + F\lambda_f + G\lambda_r}, \tag{38}$$

where

$$F \equiv \left\{(\chi_1 r_1^a)^{-1}+(\chi_2 r_2^a)^{-1}+(\lambda_r/\lambda_f)\phi\left[a_1\left(\frac{M_{p-1}(z_1)}{\chi_1}+\frac{M_{p-1}(z_2)}{\chi_2}\right)+a_2\left(\frac{M_{-p+1}(z_1)}{\chi_1}+\frac{M_{-p+1}(z_2)}{\chi_2}\right)\right]\right\}\left\{\int_{r_1}^{r_2} r^{-a}dr\right\}^{-1} \tag{39}$$

and

$$G \equiv F+\left[a_1(M_p(z_2)-M_p(z_1))+a_2(M_{-p}(z_2)-M_{-p}(z_1))\right]\left[\int_{r_1}^{r_2} r^{-a}dr\right]^{-1}. \tag{40}$$

TABLE I. "Thermal conductivity" and temperature and composition profiles for parallel plates.

Case	Chemical reactivity		Temperature accommodation, χ_l	"Thermal conductivity", λ^*	Temperature profile	Composition profile
	Gas phase, φ_l	Surface, ψ_l				
1	∞	∞	∞	λ_e		
2	0	∞	∞	λ_e		
3	∞	0	∞	λ_e		
4	∞	∞	0	λ_e		
5	0	∞	0	λ_r		
6	0	0	∞	λ_f		
7	∞	0	0	0		
8	0	0	0	0		

[a_1 and a_2 are defined in Eq. (33)]. The F and G are functions of the gas phase reactivity (ϕ); the surface reactivities (ψ_1, ψ_2), the accommodation at the surfaces (χ_1, χ_2); the geometry (a, p); and the scale (r_1, r_2).

In the derivation the quantity F arises, formally, by considering the temperature jump, while G is obtained by considering the chemical reaction in the gas phase and at the surfaces. Note, nonetheless, that the two quantities are strongly coupled; if there is a temperature jump (χ_1 and/or χ_2 not very large), the chemical rates influence the magnitude of F, while the jump conditions affect G.

Examination of some specific examples suggests that F and G have the following characteristics: Both F and G are always ≥ 0. When there is negligible temperature jump at the surfaces, χ_1 and χ_2 are very large, and $F \to 0$. In this event, G lies between one and zero. For low reactivities or small scale, G approaches unity and the "thermal conductivity" given by Eq. (38) approaches the frozen value λ_f. Contrariwise, for high reactivity or large scale, G approaches zero and λ^* approaches the equilibrium value. In an analogous fashion, if ψ_1 and ψ_2 are very large, $G \to 0$, and F lies between λ_f/λ_r and zero. As a consequence the "thermal conductivity" lies between λ_r and λ_e. If both χ_1, χ_2 and ψ_1, ψ_2 are zero, F and G approach infinity, and λ^* approaches zero.

The next section deals with the nature of Eqs. (38) to (40) for some specific cases. The emphasis in this paper is on the effects of the chemical reaction; hence, temperature accommodation effects will not be considered in great detail.

APPLICATIONS TO SPECIFIC CASES

In this section the three geometries—parallel plates, concentric cylinders, and concentric spheres—will be considered in turn. The formulas for parallel plates are the most compact, so that this geometry will be considered in some detail. The discussion for cylinders will treat principally the differences between this system and parallel plates; some experimental data for nitrogen tetroxide will also be considered. Only the solution will be presented for concentric spheres.

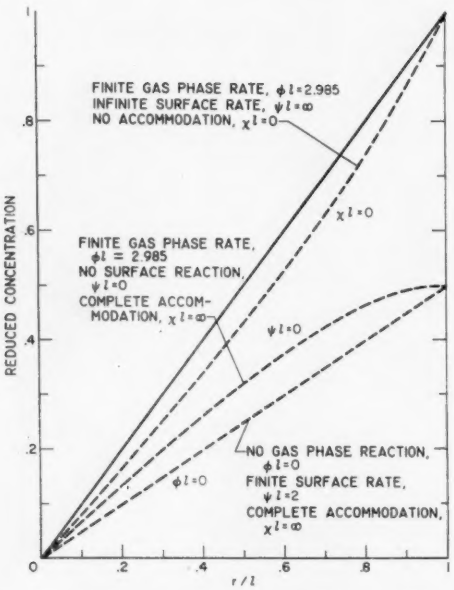
FINITE GAS PHASE RATE, $\phi l = 2.985$
INFINITE SURFACE RATE, $\psi l = \infty$
NO ACCOMMODATION, $\chi l = 0$
$\chi l = 0$
FINITE GAS PHASE RATE, $\phi l = 2.985$
NO SURFACE REACTION, $\psi l = 0$
COMPLETE ACCOMMODATION, $\chi l = \infty$
$\psi l = 0$
NO GAS PHASE REACTION, $\phi l = 0$
$\phi l = 0$
FINITE SURFACE RATE, $\psi l = 2$
COMPLETE ACCOMMODATION, $\chi l = \infty$
REDUCED CONCENTRATION
r/l
0
.2
.4
.6
.8
1

FIG. 1. Concentration profiles for parallel plates.

Parallel Plates

For this geometry $a=0$, $p=\frac{1}{2}$, and

$$\left.\begin{aligned} M_p(z) &= M_{-p+1}(z) = z^{\frac{1}{2}} I_{\frac{1}{2}}(z) = (2/\pi)^{\frac{1}{2}} \sinh z \\ M_{-p}(z) &= M_{p-1}(z) = z^{\frac{1}{2}} I_{-\frac{1}{2}}(z) = (2/\pi)^{\frac{1}{2}} \cosh z. \end{aligned}\right\} \quad (41)$$

It is convenient to choose the coordinate system so that r_1 and hence $z_1=0$ and $z_2=\phi l$, where l is the distance of separation of the plates. It is possible, of course, to substitute Eq. (41) into (39) and (40) to obtain general expressions for F and G in this geometry. The result is still cumbersome; it is more instructive to consider some specific examples.

Let us first treat a system where the gas is completely equilibrated, both temperature- and composition-wise, at one wall ($\psi_1 l$ and $\chi_1 l \to \infty$).[22] If $\psi_2=\psi$ and $\chi_2=\chi$, we find

$$F = \{(\chi l)^{-1}[1+(\psi l)^{-1}(\lambda_e/\lambda_f)(\phi l/\tanh\phi l)]\} \times \{1+[(\psi l)^{-1}+(\lambda_r/\lambda_f)(\chi l)^{-1}](\phi l/\tanh\phi l)\}^{-1} \quad (42)$$

and

$$G = \{(\psi l)^{-1}[1+(\chi l)^{-1}(\lambda_e/\lambda_f)(\phi l/\tanh\phi l]\} \times \{1+[(\psi l)^{-1}+(\lambda_r/\lambda_f)(\chi l)^{-1}](\phi l/\tanh\phi l)\}^{-1}. \quad (43)$$

It is interesting to examine the behavior of the "thermal conductivity" for this system for the limiting cases where the dimensionless parameters characterizing the gas phase reactivity ϕl, surface reactivity ψl, and temperature accommodation χl approach either infinity or zero. These cases are compared in Table I; also, the nature of the temperature and composition profiles is indicated schematically. The first four cases yield identical results: equilibrium thermal conductivity and linear profiles. In the third case the gas phase reaction equilibrates the concentration profile to the temperature profile, so that the concentration gradient exists although there is no surface reaction. Contrariwise, in the fourth example, the gas phase reaction equilibrates the temperature gradient to the concentration gradient. This illustrates the coupling effect of the gas phase reaction, which is absent in the fifth and sixth cases. The heat transport is correspondingly reduced. Finally (the last two cases), if both surface reaction and temperature accommodation are absent, there can be no heat transfer, as there is no mechanism for communicating energy from the gas phase to the surface. Similar considerations should apply to cylindrical and spherical geometries, except that the profiles for ψ or $\chi=\infty$ will be curved.

The concentration profiles can be obtained by integrating Eq. (15). For this geometry, with one wall perfectly catalytic, the result is

$$\frac{D_j P}{RT}\frac{\Delta H}{n_j}\frac{1}{\lambda_r \Delta T_w}(x_j - x_{j,1}) = \frac{\lambda^*}{\lambda_e}\left\{\frac{r}{l} - \left[\left(\frac{1}{\psi l}+\frac{1}{\chi l}\right)\frac{\sinh\phi r}{\sinh\phi l}\right] \times \left[1+\left(\frac{1}{\psi l}+\frac{\lambda_r}{\lambda_f}\frac{1}{\chi l}\right)\frac{\phi l}{\tanh\phi l}\right]^{-1}\right\}. \quad (44)$$

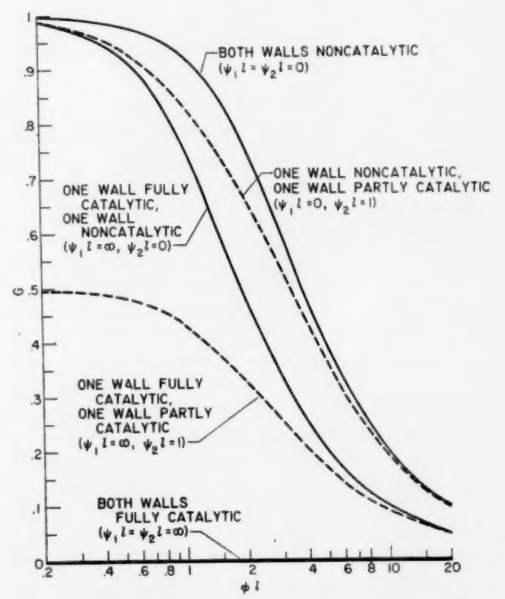

FIG. 2. G as a function of gas phase and surface reactivities (parallel plates).

[22] Actually, even when ϵ_j and α are unity, ψ and χ remain finite according to Eqs. (27) and (28). The values may be very large, however.

The quantity given by Eq. (44) is a reduced concentration; some examples are plotted in Fig. 1 for a system where $\lambda_f=\lambda_r$. The solid line indicates the equilibrium concentration profile (the first five cases in Table I). The dashed curves are for situations where λ^* lies midway between the equilibrium and frozen values. If reaction occurs only on the surface ($\phi l=0$), the profile is linear (the lowest dashed curve). When reaction occurs in the gas phase but not at the surface ($\psi l=0$), the profile is curved; since there is no surface reaction, the concentration gradient at the surface is zero. (The temperature gradient at the surface must be correspondingly steepened.) Finally, when the composition is equilibrated at the surface but there is no temperature accommodation ($\chi l=0$), reaction in the gas phase steepens the concentration gradient near the wall. (In this case the temperature gradient at the wall is zero.)

The discussion thus far has illustrated how the effects of temperature accommodation, gas phase rate, and surface rate are interrelated. The remainder of the paper will avoid further discussion of the temperature jump—χ_1 and χ_2 will be assumed infinite, which means $F=0$.

For the case of no temperature jump, Eq. (43) simplifies to

$$G=(\psi l+\phi l/\tanh\phi l)^{-1}. \tag{45}$$

On the other hand, if both the walls are equally catalytic, $\psi_1=\psi_2=\psi$, and

$$G=[(\psi l/2)+(\phi l/2)/\tanh(\phi l/2)]^{-1}. \tag{46}$$

Note that the cell with a perfectly catalytic wall is equivalent to one-half of a cell in which walls are partially catalytic. When $\psi l=0$, Eqs. (46) and (38) reduce to the expressions derived heretofore by Ubbelohde[3] and Meixner.[14]

Finally, if one wall is noncatalytic, and the other is partially catalytic, $\psi_1=0$, $\psi_2=\psi$, and

$$G=\frac{\psi l+2\phi l\tanh(\phi l/2)}{(\phi l)^2+\psi l\phi l/\tanh\phi l}. \tag{47}$$

The variation of G with gas phase reactivity ϕl for several surface activities ψl is shown in Fig. 2. When the surfaces are inactive, the highest values of gas phase reactivity are required to reduce G toward zero and cause the conductivity to approach the equilibrium value. When one wall is catalytic and the other is not, the form of the curve is the same, but a lower gas phase reaction rate is required for a given reduction in G. (These two curves are shown as solid lines in Fig. 2.) The upper dashed curve in Fig. 2 applies to a system where one wall is noncatalytic and one is partly catalytic. When the gas phase reactivity is low, reaction at this wall is important, and the curve approaches the curve for one catalytic wall. On the other hand, when ϕl is large, reaction at this wall is unimportant, and the curve approaches the curve for noncatalytic walls.

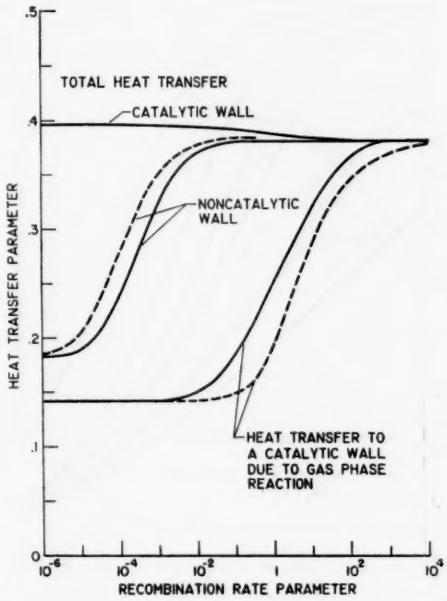

FIG. 3. Heat transfer for a boundary layer with finite recombination rates.

The lower dashed curve applies to the system where one wall equilibrates the gas while the other is partially catalytic. For the particular activity chosen ($\psi_2 l=1$), $G=\frac{1}{2}$ when $\phi l=0$. Finally, if both walls equilibrate the gas, G is zero regardless of the gas phase reactivity.

Figure 2 also shows that large changes in reaction rate are required to greatly alter G. Thus, to decrease G from 0.9 to 0.1 with noncatalytic walls, ϕl must increase by a factor of 16.7, which means that the reaction rate must change by a factor of 280.

Let us next investigate the nature of the dimensionless parameters ϕl and ψl that characterize the gas phase and surface reactions. We will consider the simplest sort of system,

$$A\underset{k_2}{\overset{k_1}{\rightleftarrows}}B.$$

For this system,

$$\lambda_r=(D_{AB}P/RT)(\Delta H^2/RT^2)x_Ax_B,$$

so that

$$\begin{aligned}(\phi l)^2&=(\lambda_e/\lambda_f)(l^2/D_{AB})(k_1/x_B)\\&=(\lambda_e/\lambda_f)(\tau_{\text{diff}}/\tau_{\text{chem}}),\end{aligned} \tag{48}$$

since l^2/D_{AB} is a diffusion time and x_B/k_1 is the relaxation time for this reaction. [Mexiner[14] first noted that the quantity $(\phi l)^2$ involved the ratio of diffusion and chemical times.] When the diffusion time is short in comparison with the chemical time, the concentration gradients are washed out by diffusion, and the frozen conductivity is obtained. On the other hand, if the

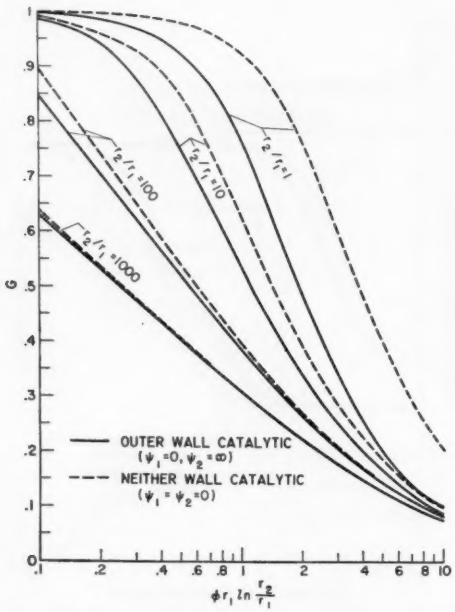

FIG. 4. G as a function of gas phase and surface reactivities for cylindrical systems of varying radius ratio.

chemical time is short, the concentration gradients are maintained and the conductivity approaches the equilibrium value. The crossover occurs when these times are of the same order of magnitude.

Even if there is no gas phase reaction ($\phi l=0$), the "thermal conductivity" will not be materially reduced unless ψl is of the order of unity. For the system in which one wall is catalytic, the conductivity will lie midway between the equilibrium and frozen values when

$$2\epsilon_A/(2-\epsilon_A)=4D_{AB}/\bar{c}_A l.$$

From simple kinetic theory, $D=\frac{1}{3}\bar{c}L$, where L is the mean free path. We may now inquire: How small must the catalytic efficiency be for the "thermal conductivity" to be materially reduced? In systems where the mean free path is small in comparison with the dimension l, the efficiency ϵ must be of the order of L/l. (Actually our treatment does not apply to systems where the mean free path is of the order of l.)

The system in which one wall is perfectly catalytic is important, since it is in some ways similar to a boundary layer in a dissociated gas flow (such as might exist in a rocket exhaust nozzle, or on the skin of a reentering vehicle). The perfectly catalytic wall corresponds to the equilibrium gas mixture at the outer edge of the boundary layer; the other wall corresponds to the cooled surface. Fay and Riddell[23] have solved the boundary-layer equations for a specific case of stagnation point heat transfer in dissociated air with a range of reaction rates for both catalytic and noncatalytic walls. Their results are shown as solid lines in Fig. 3, where a heat transfer parameter (quotient of Nusselt number and square root of Reynolds number) is plotted for various values of a recombination rate parameter. This recombination parameter is a ratio of a diffusion time to a reaction time, evaluated at stream temperature. Also shown as dashed curves are approximate values computed from Eq. (38), by associating the heat transfer parameter with λ^* and with $G=\tanh\phi l/\phi l$. When the wall is catalytic, the atom concentrations are large only in the high-temperature region. To approximate the heat transfer due to gas phase reaction, the recombination rate parameter is taken as $\tau_{\text{diff}}/\tau_{\text{chem}}=(\phi l)^2\lambda_f/\lambda_e$.

Atom recombinations differ from most other chemical rate processes in that their rates are higher at lower temperatures. When the wall is noncatalytic, the atoms tend to diffuse into and recombine in the cooler region near the wall. The approximate curve in this case has been calculated by correcting the ratio of times from stream to wall temperature.

The approximate curves for the temperature extremes are similar in shape to the exact calculations. It is to be expected that the approximations bracket the exact values, since in either case reaction must occur at average temperatures somewhat away from the temperatures at the boundaries of the system.

It seems, then, that we have a valuable tool for rapidly estimating the effects of finite reaction rate on convective heat transfer. The distance l should be associated with a boundary-layer thickness.

Concentric Cylinders

For this geometry $a=1$, $p=0$, and

$$\left.\begin{aligned} M_p(z)&=I_0(z), & M_{-p}(z)&=K_0(z)\\ M_{p-1}(z)&=I_1(z), & M_{-p+1}(z)&=-K_1(z). \end{aligned}\right\} \quad (49)$$

Concentric cylinders are important because hot-wire thermal conductivity cells are constructed in this fashion. These functions can be introduced into Eqs. (39) and (40) to obtain explicit (and cumbersome) expressions for F and G. Some values of G for cylindrical systems of various radius ratio r_1/r_2 are shown in Fig. 4. These are for systems without temperature jump ($\chi_1=\chi_2=\infty$; hence $F=0$). The solid curves are for systems in which the inner surface is noncatalytic ($\psi_1=0$), while the outer surface equilibrates the gas ($\psi_2=\infty$); the dashed curves are for systems where both surfaces are noncatalytic. The values of G are plotted against $\phi r_1 \ln(r_2/r_1)$ because, as ϕ becomes large, $G\to 1/\phi r_1 \ln(r_2/r_1)$ for the systems with the outer wall catalytic (solid curves). The curves for $r_2/r_1=1$ are simply cases of parallel plates, also shown in Fig. 2. As the radius ratio is increased, the catalytic activity of the outer surface becomes progressively less important. However, the activity of the outer surface has

[23] J. A. Fay and F. R. Riddell, J. Aeronaut. Sci. **25**, 73 (1958).

an appreciable effect on G at low reactivities even when r_2/r_1 is as large as 100. Note also that, as systems become more cylindrical, even larger changes in reaction rate (proportional to ϕ^2) are needed to appreciably alter G.

If the radius ratio is large, and the arguments z_1, z_2 are not too small, then $I_0(z_2)\gg I_0(z_1)$, $I_1(z_2)\gg I_1(z_1)$, $K_0(z_1)\gg K_0(z_2)$, and $K_1(z_1)\gg K_1(z_2)$. If it is further assumed that the outer wall is catalytic ($\psi_2=\infty$) and the temperature jump is negligible at the outer wall ($\chi_2=\infty$),

$$F=\frac{1+(\lambda_e/\lambda_f)\,(1/\psi r_1)H}{[\chi r_1\ln(r_2/r_1)]\{1+[(\psi r_1)^{-1}+(\lambda_r/\lambda_f)(\chi r_1)^{-1}]H\}},\tag{50}$$

$$G=\frac{1+(\lambda_e/\lambda_f)\,(1/\chi r_1)H}{[\psi r_1\ln(r_2/r_1)]\{1+[(\psi r_1)^{-1}+(\lambda_r/\lambda_f)(\chi r_1)^{-1}]H\}},\tag{51}$$

where $H\equiv\phi r_1K_1(\phi r_1)/K_0(\phi r_1)$. If these results are substituted into Eq. (38), an expression for the "thermal conductivity" is obtained which is very similar to the equation Franck and Spalthoff[15] derived for dissociations of the type $X_2\rightleftarrows 2X$. Franck and Spalthoff used the expression for equimolar counter diffusion rather than Eq. (7) and hence obtained a somewhat different (and incorrect) expression for ϕ for this specific type of reaction. Franck and Spalthoff formulated their boundary conditions in terms of mean free path arguments, which leads to some further minor differences (including the exact forms of χ and ψ).

Coffin and O'Neal[10] have measured the thermal conductivity of the $N_2O_4\rightleftarrows 2NO_2$ system in a hot-wire thermal conductivity apparatus ($r_2/r_1=37.1$). Their data at 296°K as a function of pressure are shown in Fig. 5. The frozen and equilibrium thermal conductivities are shown as dotted lines. The remaining curves are calculations of λ^* for various reaction rates. The theoretical curves have been adjusted to fit experiment near one atmosphere. The temperature jump has been ignored ($\chi_1=\chi_2=\infty$) and chemical reaction on the surfaces has been assumed negligible ($\psi_1=\psi_2=0$). The upper dashed curve has been calculated from the first-order dissociation rate reported by Carrington and Davidson[24]; this is an upper limit to the rate, which is attained only at very high pressures. The lower dashed curve is the second-order rate observed by Carrington and Davidson for the dissociation of N_2O_4 in nitrogen. The solid curve has been fitted to the experimental data by assuming that the second-order rate is 3.5 times faster when undiluted N_2O_4—NO_2 mixtures dissociate. Indeed, one would expect N_2O_4 and NO_2 to be more effective than N_2 as collision partners for this dissociation.

[24] T. Carrington and N. Davidson, J. Phys. Chem. 57, 418 (1953).

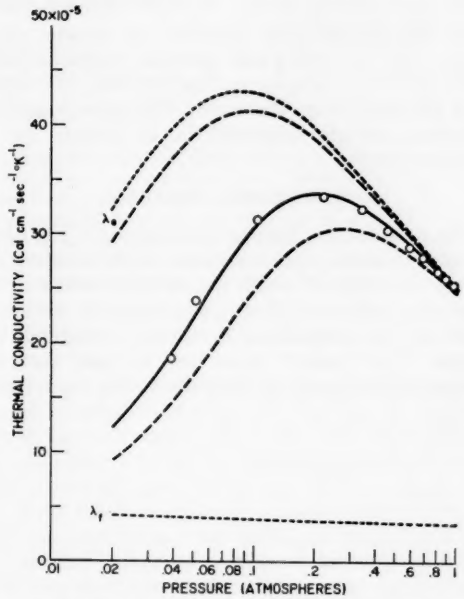

FIG. 5. "Thermal conductivity" for various reaction rates for the $N_2O_4\rightleftarrows 2NO_2$ system. $T=296$°K.

The agreement between theory and experiment shown in Fig. 5 is encouraging and suggests that this theory provides an adequate description of this phenomenon. The rate constant derived from these data is 5.3×10^9 cm^3 mole^{-1} sec^{-1}; this must be an upper limit, since if there is any surface reaction the gas phase rate must be correspondingly lower.

Concentric Spheres

For this geometry $a=2$, $p=-\frac{1}{2}$, and

$$M_p(z)=z^{-\frac{1}{2}}I_{-\frac{1}{2}}(z)=(2/\pi)^{\frac{1}{2}}\cosh z/z,$$

$$M_{-p}(z)=z^{-\frac{1}{2}}I_{\frac{1}{2}}(z)=(2/\pi)^{\frac{1}{2}}\sinh z/z,$$

$$M_{p-1}(z)=z^{-\frac{1}{2}}I_{-\frac{1}{2}}(z)=(2/\pi)^{\frac{1}{2}}[(\sinh z/z)-(\cosh z/z^2)]$$

$$M_{-p-1}(z)=z^{-\frac{1}{2}}I_{\frac{1}{2}}(z)=(2/\pi)^{\frac{1}{2}}[(\cosh z/z)-(\sinh z/z^2)].$$

If the outer wall is fully catalytic ($\psi_2=\infty$), if the temperature jump is negligible ($\chi_2=\infty$), and provided the argument z_2 is not too small, we find that

$$F=\frac{1+(\lambda_e/\lambda_f)\,(\psi r_1)^{-1}(1+\phi r_1)}{\chi r_1[1-(r_1/r_2)]\{1+[(\psi r_1)^{-1}+(\lambda_r/\lambda_f)(\chi r_1)^{-1}](1+\phi r_1)\}},\tag{52}$$

$$G=\frac{1+(\lambda_e/\lambda_f)\,(\chi r_1)^{-1}(1+\phi r_1)}{\psi r_1[1-(r_1/r_2)]\{1+[(\psi r_1)^{-1}+(\lambda_r/\lambda_f)(\chi r_1)^{-1}](1+\phi r_1)\}}.\tag{53}$$

Note the similarity of Eqs. (52) and (53) for spheres with the corresponding equations for parallel plates [Eqs. (42) and (43)] and concentric cylinders [Eqs. (50) and (51)]. If $r_1/r_2=0$, Eqs. (52) and (53) apply over the whole range of ϕ values. This corresponds to a spherical particle suspended in an infinite sea of quiescent gas.

CONCLUDING REMARKS

The equation for "thermal conductivity" [Eq. (38)] developed in this paper is a general analytic expression for gas mixtures in which one chemical reaction proceeds at a finite rate. That is, one reaction is neither so slow that the composition is constant throughout the system (the "frozen" state) nor so rapid that the composition is locally in equilibrium with the temperature. Because it is necessary to assume that the equilibrium chemical reaction rate is constant through the system, the equations apply only for small temperature differences. To consider large temperature differences one is driven to numerical techniques.[25] The geometries considered can all be described by a single distance coordinate. If other geometries are considered, partial differential equations arise, and analytic solutions will probably not be obtained.

Consequently, the author believes that solutions of this paper are the most general analytic expressions obtainable for heat conduction in a chemically reacting gas mixture with one finite reaction rate.

---

[25] D. H. Secrest and J. O. Hirschfelder, Phys. Fluids **4**, 61 (1961).

THE JOURNAL OF CHEMICAL PHYSICS VOLUME 35, NUMBER 5 NOVEMBER, 1961

Compressibility of Simple Fused Salts

FRANK H. STILLINGER, JR.

Bell Telephone Laboratories, Inc., Murray Hill, New Jersey

(Received April 13, 1961)

It is pointed out that the isothermal compressibility of monatomic molten salts should nearly equal that for a hypothetical fluid of uncharged ion cores at the same over-all particle density as the salt. The validity of this relation is equivalent to verification of conjectures concerning the number-average correlation function for ion pairs in the melt. When the ion core forces are treated as those acting between rigid spheres, it is readily possible to predict the distance of closest approach for an anion-cation pair from experimentally determined compressibilities. The corresponding distances obtained in this manner for a series of molten halides are consistent with known ion sizes, and furthermore exhibit the proper homologous series trends.

I. THEORETICAL CONSIDERATIONS

IN a recent analysis of ionic distributions in fused salts,[1] it was shown that an order-disorder treatment of these "binary mixtures" of anionic and cationic particles could formally reduce the problem of computing the canonical partition function for these substances to that for a fluid (at the same temperature and over-all number density as the salt) all of whose particles are identical. The effective potential energy acting in this equivalent fluid was found to be equal (in the case of identical ion core forces for all ion pairs) to the short-range interaction of the original ion cores, supplemented by temperature-dependent corrections arising from nonrandom mixing of ions in the melt. These latter contributions are primarily attractive, and are of considerably shorter range than the original Coulomb interactions in the salt.

Fused salts, at or not too far above their normal melting points, are typical dense liquids in the sense that the spherical constituent particles are rather closely packed together. As a consequence, there is relatively little freedom for rearrangement of the entire set of particle positions, which fact gives rise to small values of the isothermal compressibility. On the other hand, for a given set of particle positions, the Coulomb interactions between ions appear to "sort" the ions in the melt into a pseudo-crystalline array rather like the regular solid.[1] Thus, any given ion on the average is surrounded by spherical shells of electrostatic change of alternating sign, just as in the unmelted crystal, where successive shells of neighbors differ in charge sign. The effect of this sorting is, naturally, to lower the liquid's energy by a large amount, comparable in magnitude to the solid phase Madelung energy.

Although the powerful Coulomb forces produce a position discrimination between ions of different charge sign, if one were to fail to distinguish between anions and cations in a salt whose impenetrable ion cores were virtually alike (equal anion and cation size), the relatively few configurations available to these closely packed cores seems to imply that the over-all distribution of identical cores is little affected by the presence of ionic charge.[2] If this conjecture is correct, then the number-average pair correlation function, $g_m(r)$, in the dense fused salt should virtually equal that for a fluid composed of only the uncharged cores.[3] Thus, the temperature-dependent portion of the effective interaction for the "equivalent fluid" appears to have little effect on the total particle pair correlation function.

To be specific, in a salt whose various ions are present in number densities $\rho_1, \cdots, \rho_\nu$, $g_m(r)$ is related to the individual pair correlation functions $g_{\alpha\beta}^{(2)}(r)$ by

$$g_m(r)=\left[\sum_{\alpha,\beta=1}^{\nu}\rho_\alpha\rho_\beta\right]^{-1}\sum_{\alpha,\beta=1}^{\nu}\rho_\alpha\rho_\beta g_{\alpha\beta}^{(2)}(r). \tag{1}$$

Of course, the set of densities ρ_α is constrained to satisfy the electroneutrality condition:

$$\sum_{\alpha=1}^{\nu}(z_\alpha e)\rho_\alpha=0, \tag{2}$$

where the electrostatic charge on an α-type ion is some small integer z_α times the protonic charge e. It is our claim that $g_m(r)$ is almost entirely determined by the short-range ion core forces alone, at least for salts with equal ion sizes.

The strong tendency to "sort" the ions in the melt according to charge implies that the powerful Coulomb repulsion between like ions is effective in preventing close contact except between anion-cation pairs. As a result, for simple pure salts containing single anionic and cationic species, the only short-range core forces that come into play are those acting between pairs of unlike ions.[1] Therefore, the details of ion core short-range forces for pairs of like ions are irrelevant in deter-

[1] F. H. Stillinger, J. G. Kirkwood, and P. J. Wojtowicz, J. Chem. Phys. **32**, 1837 (1960).

[2] It is assumed here that sufficiently powerful external wall forces are present to maintain the over-all particle density fixed, whether or not electrostatic charges are present.

[3] For a comprehensive discussion of molecular distribution functions (specifically, the pair correlation function), see: T. L. Hill, *Statistical Mechanics* (McGraw-Hill Book Company, Inc., New York, 1956), Chap. 6.

mining the thermodynamic properties of the fused salt. In a statistical mechanical model of molten salts, therefore, it appears permissible to assume that all short-range ion core forces are the same, and equal specifically to those acting between unlike ions in the salt of interest. In this sense, it is possible to relate salts with ion radius ratios deviating somewhat from unity to a model salt with equal-sized ions.

If this second conjecture is valid, salts with unequal ion sizes also should exhibit mean pair correlation functions determined only by core interactions. In this case, however, $g_m(r)$ refers to the hypothetical nonelectrolytic fluid whose particles interact according to precisely the anion-cation short-range potential. This more general case of unequal ion size thus effectively reduces to the more convenient special case of equal sizes.

The possible use of only the anion-cation core interaction has recently been exploited by Reiss, Mayer, and Katz in the development of a corresponding-states theory of molten salts.[4] The apparent success of their treatment may be regarded as an independent confirmation of the present hypotheses about fused salt structure. Although Reiss, Mayer, and Katz find it necessary to specify a complete interaction potential for the ionic assembly, such considerations are unnecessary in the present context. In particular, there may be difficulty in defining local dielectric constants to account completely for polarization interactions in the liquid.

The replacement procedures for like ion pair core forces by those for unlike pairs is justified, unless the original radius ratio (anion to cation) is very large. In the latter case, large anions could easily be in contact with one another, and the very much smaller cations would simply occupy the interstices between the anions. Therefore, in salts such as LiI, where the ratio is about 3.5, one should anticipate deviation from the common ion size model predictions.

In the case of fluids consisting of a single type of particle, it is known that the isothermal compressibility,

$$\kappa = -1/V(\partial V/\partial p)_T \tag{3}$$

(V=volume, p=pressure, T=absolute temperature), is related to an integral of $g^{(2)}(r)$, the pair correlation function in that fluid[5]:

$$\rho kT\kappa = 1+\rho\int_0^\infty [g^{(2)}(r)-1]\cdot 4\pi r^2 dr. \tag{4}$$

ρ denotes the number density of particles in this fluid, and k is Boltzmann's constant. If our assumptions about the microscopic structure of dense fused salts are valid, then the formal equivalence of the statistical thermodynamics of the salt to that of a single component fluid implies that the salt isothermal compressibility also should be given by relation (4), but where $g^{(2)}(r)$ is to be replaced by $g_m(r)$. Furthermore, this latter mean correlation function should for all intensive purposes be equal to the pair correlation function for a fluid of uncharged ion cores, at the same temperature and over-all density as the fused salt, but with particle diameters all equal to the distance of closest approach between a pair of unlike ions.

Although, in the strict sense, ion core interactions are presumably well-defined functions for all pair separations r, the fact of very strong repulsion relative to kT even at molten salt temperatures, when r is less than the "contact" value, makes it convenient to replace the actual core potential by one appropriate to rigid spheres with some collision diameter, a. Under this circumstance, κ for the molten salt could be computed by Eq. (4) from the known correlation function for rigid spheres.[6]

Reiss, Frisch, and Lebowitz[7] have developed a statistical mechanical theory of the rigid sphere fluid which not only yields good agreement with known values of the virial coefficients for this system, but also quantitatively reproduces the Monte Carlo results for the dense fluid equation of state.[8] Their results may be displayed in the form:

$$p = \frac{6kT}{\pi a^3}\frac{y(1+y+y^2)}{(1-y)^3}.$$

$$y = \pi\rho a^3/6. \tag{5}$$

Differentiation of this equation of state with respect to V leads to:

$$\rho kT\kappa = (1-y)^4/(1+2y)^2. \tag{6}$$

If Eq. (4) is compared with this expression, it becomes clearly unnecessary to integrate the entire hard sphere pair correlation function at each density, since[9]

$$\int_0^\infty (r/a)^2[g^{(2)}(r/a)-1]d(r/a) = \frac{(y-4)(y^2+2)}{24(1+2y)^2}. \tag{7}$$

If, for a given fused salt observed at temperature T, measured values of the total ion number density and the isothermal compressibility are respectively substituted for ρ and κ in relation (6), it is subsequently possible to assign a unique value of y to this liquid. Furthermore, this deduced value of y, along with the already used value ρ of the total ion number density, allows the corresponding distance of closest anion-cation approach

[4] H. Reiss, S. W. Mayer, and J. Katz (to be published).
[5] See reference 3, p. 236.
[6] J. G. Kirkwood, E. K. Maun, and B. J. Alder, J. Chem. Phys. **18,** 1040 (1950).
[7] H. Reiss, H. L. Frisch, and J. L. Lebowitz, J. Chem. Phys. **31,** 369 (1959).
[8] W. W. Wood and J. D. Jacobsen, J. Chem. Phys. **27,** 1207 (1957).
[9] Assuming that the Reiss, Frisch, and Lebowitz equation of state (5) is substantially exact in the fluid range of densities for the rigid sphere system, Eq. (7) may be regarded as an interesting test of the accuracy of computed pair correlation functions for this system.

to be obtained from y's definition:

$$a=(6y/\pi\rho)^{\frac{1}{3}}. \tag{8}$$

If our assumptions are *not* justified, that

(a) the mean correlation function $g_m(r)$ in a dense fused salt with equal ion sizes is virtually equal to that for the fluid of uncharged cores,

(b) salts with ion size ratios differing moderately from unity are equivalent to salts with ratio unity, but the same anion-cation distance of closest approach, then the discrepancy should affect the values of a computed from Eqs. (6) and (8). It is the purpose of this article to compare values of a obtained in this manner with known crystal radii for the ions involved, with a view toward providing at least partial verification of (a) and (b).

II. NUMERICAL RESULTS AND DISCUSSION

The isothermal compressibilities for a series of molten halides are available from the sound velocity measurements of Bockris and Richards.[10] The corresponding densities for alkali halides have been measured by Yaffe and Van Artsdalen.[11] In the case of the one unsymmetrical electrolyte considered, $CdCl_2$, we have utilized the density measurements of Boardman, Dorman, and Heymann.[12]

Table I displays the anion-cation distances of closest approach computed from Eqs. (6) and (8), along with the corresponding sum of crystal radii.[13] In all cases, general agreement is observed. The computed distances deviate on the low side from the crystal values, undoubtedly because the latter correspond roughly to the minimum of the anion-cation potential curve rather than to the rapidly rising repulsive portion of this curve, which, at somewhat smaller separations, more nearly corresponds to the rigid sphere behavior postulated. This point of view is borne out by the fact that increasing temperatures yield decreased effective collision diameters; the more energetic thermally-produced collisions give rise to greater degrees of core interpenetration, since of course the ion cores are not completely rigid.

What is perhaps most significant is the fact that computed distances for each homologous series (e.g., the chlorides of lithium, sodium, potassium, and cesium) retain the correct increasing order as one travels down the periodic table. This increase follows increase of either cation or anion atomic number in a given series.

TABLE I. Values of the anion-cation collision diameter computed from the fused salt isothermal compressibilities. The corresponding sums of Pauling ionic crystal radii appear in parentheses. All distances are Angstrom units.

	T °C	600	700	800	900	1000
LiCl	(2.41)		2.31	2.26	2.20	2.14
NaCl	(2.76)			2.47	2.41	2.34
KCl	(3.14)			2.70	2.63	2.55
CsCl	(3.50)		3.01	2.93	2.84	2.74
LiBr	(2.55)	2.55	2.49	2.43	2.38	2.31
NaBr	(2.90)			2.63	2.58	2.51
KBr	(3.28)			2.85	2.78	2.70
CsBr	(3.64)		3.06	2.98	2.88	2.75
NaI	(3.11)		2.88	2.82	2.74	2.66
KI	(3.28)		3.09	3.01	2.93	2.82
$CdCl_2$	(2.78)	2.50	2.45	2.39		

In addition, the temperature variation of the effective collision diameter a appears to be slightly less for smaller ions. This is consistent with the fact that the smaller outermost (valence) orbital electrons in ions of low atomic number are held more stiffly in position than the more extended orbital electrons for large ions. Accordingly, it is harder to displace electrons in the former case in an ion pair collision, and so the smaller ions act as more nearly rigid spherical particles.

In the case of LiBr (radius ratio greater than 3), and somewhat less obviously in the case of LiCl (ratio about 3), there seems to be a tendency among the computed distances to deviate positively from the percentagewise decrease, observed in the case of the other salts, of computed a below the crystal distance. This deviation probably marks the onset of non-negligible anion-anion contacts in the melt, and therefore seems to indicate breakdown of possible application of a single-ion-size model to these melts.

In conclusion, consequently, it appears that hypotheses (a) and (b) concerning the microscopic structure of melts are consistent with the experimental compressibility data, especially in view of the several characteristics of ion core forces which, as indicated by the numerical calculations, are preserved under the scheme outlined in the preceding section.

[10] J. O'M. Bockris and N. E. Richards, Proc. Roy. Soc. (London) **241,** 44 (1957).

[11] I. S. Yaffe and E. R. Van Artsdalen, J. Phys. Chem. **60,** 1125 (1956).

[12] N. K. Boardman, F. H. Dorman, and E. Heymann, J. Phys. Chem. **53,** 375 (1949).

[13] L. Pauling, *The Nature of the Chemical Bond* (Cornell University Press, Ithaca, New York, 1960), 3rd ed., p. 514.

THE JOURNAL OF CHEMICAL PHYSICS VOLUME 35, NUMBER 5 NOVEMBER, 1961

Interfacial Solutions of the Poisson-Boltzmann Equation

FRANK H. STILLINGER, JR.

Bell Telephone Laboratories, Incorporated, Murry Hill, New Jersey

(Received April 13, 1961)

The linearized Poisson-Boltzmann equation is considered for boundary conditions corresponding to a fixed point-charge ion near the planar boundary between an electrolytic solution and a dielectric substrate. Use of the Fourier expansion for this fixed charge density allows the mean potential to be synthesized in the form of a simple quadrature. Subsequently, it is possible to compute the reversible work necessary to displace the ion atmosphere surrounding this charge into one hemisphere as the charge is brought up to the interface from the interior of the electrolyte phase. Implications for ionic adsorption processes are discussed. The result of a similar analysis for the mean potential surrounding a point dipole oriented normally to the boundary is also presented.

I

THE molecular structure at the interface between an electrolytic solution and an immersed solid body (often an electrode for an electrochemical process) is regarded, under general circumstances, as strongly controlled by several simultaneously operative factors.[1] Electrostatic charge on the solid and the consequent large interfacial electric fields can markedly orient polar solvent molecules, and thus produce local dielectric saturation. Specific chemical bonding forces give rise to a strongly bound monolayer (the inner or Helmholtz region of the electrical double layer) whose composition depends critically on the chemical differences between various ions and substrate materials. Additionally, it may be shown[2] that the finite size of ions in the electrolyte plays an important role in establishing even the qualitative character of the charge distribution in the diffuse (or Gouy) charge layer of the interfacial region.

The point of view in the present article will be to investigate a model illustrating only a single aspect of the interfacial structure problem. Specifically, we choose to analyze the form and nature of the nonspherical average potential and charge surrounding a point ion near the solution-substrate interface. In the special case that this ion resides at the boundary between the two phases, the resulting distribution of charge and the potential refer to that portion of the Gouy layer induced by a single ion adsorbed at the surface. By working entirely within the regime of the linear Poisson-Boltzmann equation, the diffuse charge distribution set up by an assembly of adsorbed ions is a linear combination of the single-ion distributions. In this manner, it is possible to avoid the commonly made assumption that the Gouy portion of the double layer is produced by a uniformly distributed surface charge. It is hoped, in later use of more realistic models of interfacial structure, in which neither the linear Poisson-Boltzmann equation is regarded as valid, nor in which solvent and substrate molecular nature are neglected, that the straightforward answers obtained here may shed some light on the qualitative nature of actual ion distributions.

The relevant solutions to the linear Poisson-Boltzmann equation are obtained as simple quadratures which, though not standard integral forms, are nevertheless amenable to ready numerical analysis in specific cases of interest. Schmutzer[3] has obtained an alternative quadrature solution to the same potential problem considered here, in terms of modified Hankel functions. There does not appear to be any simple transformation of our representation into his, but rather the two expressions are apparently independent integral representations of solution to the same boundary value problem. The last section of this paper indicates by illustration, however, that the present approach does exhibit ease of generalization to other related boundary value problems with the linear Poisson-Boltzmann equation; there, the potential and charge surrounding a normally oriented dipole in the interfacial region are likewise cast in simple quadrature form.

In addition, the present analysis leads to a computation of the reversible work necessary to force the ion atmosphere (spherically symmetric in the bulk electrolyte) of an ion to be adsorbed at the substrate-electrolyte interface, into one hemisphere. It is pointed out how this reversible work, as well as the shielded Coulomb interaction between pairs of adsorbed ions at the interface (which follows immediately from our general solutions), affect isotherms at this surface.

II

Figure 1 indicates schematically the interfacial region with which we shall be concerned. The y-z plane of a rectangular Cartesian coordinate system is the boundary between semi-infinite dielectric substrate and

[1] A comprehensive discussion of the structure and behavior of electrified interfaces may be found in *Modern Aspects of Electrochemistry*, J. O'M. Bockris, editor (Academic Press Inc., New York, 1954), Chap. 3, by R. Parsons.

[2] F. H. Stillinger and J. G. Kirkwood, J. Chem. Phys. **33**, 1282 (1960).

[3] E. Schmutzer, Z. Phys. Chem. **204**, 131 (1955).

electrolyte phases. The positive x axis, normal to this plane, is oriented into the electrolyte. D_s and D_e will denote respectively the dielectric constants of substrate ($x<0$) and electrolyte ($x>0$). A point ion with electrostatic charge Ze (Z is an integer, and e is the protonic charge) is located at x_c on the x axis in the electrolyte region. Our initial task is to compute the average charge density $\rho(\mathbf{r})$ and potential $\psi(\mathbf{r})$ at any position $\mathbf{r}$ in the vicinity of this fixed ion.

As shown in Fig. 1, it is convenient to divide space into three distinct regions: I, II, and III. The first represents the entire dielectric substrate, and since it is assumed that no electrolyte can penetrate this region, $\rho(\mathbf{r})$ must identically vanish there. Accordingly, the potential in I, which will henceforth be denoted for clarity by $\psi^{(\mathrm{I})}(\mathbf{r})$, satisfies Laplace's equation

$$\nabla^2\psi^{(\mathrm{I})}(\mathbf{r})=0 \quad (\text{region I}). \tag{1}$$

For regions II and III separated by the plane $x=x_c$, and which are characterized by potentials $\psi^{(\mathrm{II})}(\mathbf{r})$ and $\psi^{(\mathrm{III})}(\mathbf{r})$, respectively, we adopt the approach of the well-known dilute electrolyte theory of Debye and Hückel,[4] wherein these functions are supposed to satisfy the linearized Poisson-Boltzmann equation

$$\begin{aligned}\nabla^2\psi^{(\mathrm{II})}(\mathbf{r})&=\kappa^2\psi^{(\mathrm{II})}(\mathbf{r}) \qquad (0\leq x\leq x_c),\\ \nabla^2\psi^{(\mathrm{III})}(\mathbf{r})&=\kappa^2\psi^{(\mathrm{III})}(\mathbf{r}) \qquad (x_c\leq x).\end{aligned} \tag{2}$$

κ is the usual Debye parameter,

$$\kappa^2=\frac{4\pi}{D_e k_B T}\sum_{i=1}^{n} c_i(Z_i e)^2, \tag{3}$$

for an n-species electrolyte whose ions of charge $Z_i e$ have number density c_i; k_B is Boltzmann's constant, and T the absolute temperature. Consistent with, and implicit in derivation of the linear Poisson-Boltzmann equation is the simple proportionality between mean potential and charge density. Thus, for both regions II and III occupied by dilute electrolyte,

$$\rho(\mathbf{r})=-(\kappa^2 D_e/4\pi)\psi^{(\mathrm{II,III})}(\mathbf{r}) \qquad (x\geq 0). \tag{4}$$

For each position vector $\mathbf{r}$ measured from the origin of the Cartesian coordinate system,

$$\mathbf{r}=x\mathbf{u}_x+y\mathbf{u}_y+z\mathbf{u}_z,$$

($\mathbf{u}_x$, $\mathbf{u}_y$, and $\mathbf{u}_z$ are the unit vectors along the three axes), we may define an associated two-dimensional vector $\mathbf{s}$ as the projection of $\mathbf{r}$ into the y-z plane

$$\mathbf{s}=y\mathbf{u}_y+z\mathbf{u}_z. \tag{5}$$

The fixed point charge Ze in the plane $x=x_c$ is therefore equivalent to a charge density $\sigma(\mathbf{s})$ in this latter plane, which is

$$\sigma(\mathbf{s})=Ze\delta(\mathbf{s}). \tag{6}$$

$\delta(\mathbf{s})$ is the two-dimensional Dirac delta function.

[4] P. Debye and E. Hückel, Physik. Z. **24**, 185, 305 (1923).

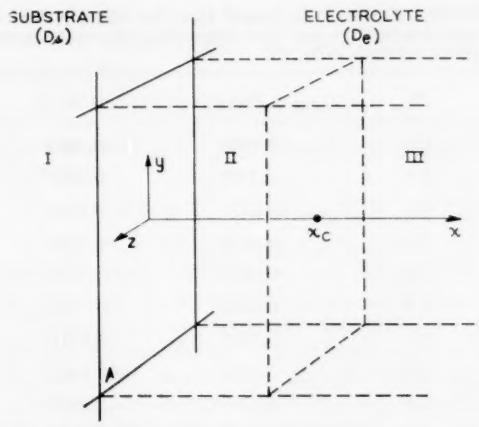

FIG. 1. The electrolyte-substrate interface ($x=0$), with a fixed point charge Ze at distance x_c from this boundary. A is the large rectangular periodicity cell (whose size is eventually allowed to become infinite), at the center of which is located the origin of the rectangular coordinate system. The dielectric constants in the substrate and electrolyte regions are, respectively, D_s and D_e.

For the purposes of later mathematical convenience, the delta function appearing in Eq. (6) is decomposed into its Fourier components. For this reason, it is desirable to introduce a large rectangular periodicity area A onto the interfacial surface which, by translation in the y and z directions, generates an infinite array of "unit cells." At distance x_c above the center of each of these cells will appear either the original point charge Ze, or one of its periodicity images. In view of the two-dimensional periodicity thus imposed on our problem, the Fourier decomposition of $\sigma(\mathbf{s})$ involves summation over a discrete set of two-dimensional vectors $\mathbf{k}$ which form the reciprocal lattice[5] to the initial unit cell subdivision of the interface

$$\sigma(\mathbf{s})=\sum_{\mathbf{k}}\sigma_k \exp(i\mathbf{k}\cdot\mathbf{s}),$$

$$\sigma_k=Ze/A. \tag{7}$$

On this account, $\sigma(\mathbf{s})$ as written here is automatically periodic with the unit cell period. Eventually, of course, we shall take the limit of infinitely large A, so as truly to isolate the original charge.

We now proceed to exploit the linearity of differential Eqs. (1) and (2). The mean potential in the interfacial region induced by a sum of several charge distributions, predicted on the basis of (1) and (2) with appropriate boundary conditions, is precisely equal to the sum of separately induced mean potentials for each charge distribution taken individually. Equation (7) has exactly this form; it analyzes a point charge on the plane $x=x_c$ into a sequence of running waves with amplitudes σ_k. Our task therefore will be

[5] L. Brillouin, *Wave Propagation in Periodic Structures* (Dover Publications, New York, 1953), Chap. VI.

TABLE I. Values of the integral $I(\alpha)$, Eq. (22), obtained by numerical integration, and the corresponding reduced atmosphere displacement work, $\alpha I(\alpha)+\frac{1}{2}$.

α	$-I(\alpha)$	$\alpha I(\alpha)+\frac{1}{2}$
0.0	0.0000	0.5000
0.1	0.2393	0.4707
0.2	0.3772	0.4246
0.3	0.4877	0.3537
0.4	0.5825	0.2670
0.5	0.6667	0.1667
0.6	0.7432	0.0541
0.7	0.8138	−0.0697
0.8	0.8796	−0.2037
0.9	0.9414	−0.3473
1.0	1.0000	−0.5000

to solve Eqs. (1) and (2) for a single unit amplitude running wave charge distribution, $\exp(i\mathbf{k}\cdot\mathbf{s})$, and subsequently to build up the solution of interest (that is, for the point charge) by summing over all wave vectors $\mathbf{k}$.[6]

When the plane $x=x_c$ bears only charge density $\exp(i\mathbf{k}\cdot\mathbf{s})$, the potentials in regions I, II, and III will be denoted by $\psi_k^{(\mathrm{I})}$, $\psi_k^{(\mathrm{II})}$, and $\psi_k^{(\mathrm{III})}$. In directions parallel to the interface, each of these three functions must exhibit the same periodicity as the inducing charge itself. Using the fact that the potential must vanish at $x=\pm\infty$, it is easy to see that the general solutions to Eqs. (1) and (2) must have the forms

$$\psi_k^{(\mathrm{I})}(\mathbf{r})=B_k^{(\mathrm{I})}\exp[i\mathbf{k}\cdot\mathbf{s}+|k|x],$$

$$\psi_k^{(\mathrm{II})}(\mathbf{r})=B_k^{(\mathrm{II},+)}\exp[i\mathbf{k}\cdot\mathbf{s}+(k^2+\kappa^2)^{\frac{1}{2}}x]+B_k^{(\mathrm{II},-)}\exp[i\mathbf{k}\cdot\mathbf{s}-(k^2+\kappa^2)^{\frac{1}{2}}x],$$

$$\psi_k^{(\mathrm{III})}(\mathbf{r})=B_k^{(\mathrm{III})}\exp[i\mathbf{k}\cdot\mathbf{s}-(k^2+\kappa^2)^{\frac{1}{2}}x]. \quad (8)$$

That these are the proper functional forms may readily be verified by insertion in the relevant differential equation.

The four multiplicative constants $B_k^{(\mathrm{I})}$, $B_k^{(\mathrm{II},+)}$, $B_k^{(\mathrm{II},-)}$, and $B_k^{(\mathrm{III})}$, must be chosen so that the functions (8) satisfy the usual electrostatic boundary conditions across the two surfaces $x=0$ and $x=x_c$. Specifically, one must demand continuity of potential at both of these planes; furthermore, the normal component of dielectric displacement must be continuous across $x=0$, but must suffer a discontinuity of $4\pi\exp(i\mathbf{k}\cdot\mathbf{s})$ in passing $x=x_c$ in the direction of the positive x axis. Application of these conditions to Eqs. (8) leads to a set of four simultaneous linear equations in the B's

$$B_k^{(\mathrm{I})}=B_k^{(\mathrm{II},+)}+B_k^{(\mathrm{II},-)},$$

$$B_k^{(\mathrm{III})}=B_k^{(\mathrm{II},+)}\exp[2(k^2+\kappa^2)^{\frac{1}{2}}x_c]+B_k^{(\mathrm{II},-)},$$

$$|\mathbf{k}|D_s B_k^{(\mathrm{I})}=(k^2+\kappa^2)^{\frac{1}{2}}D_c[B_k^{(\mathrm{II},+)}-B_k^{(\mathrm{II},-)}],$$

$$B_k^{(\mathrm{III})}=\frac{4\pi}{D_s(k^2+\kappa^2)^{\frac{1}{2}}}\exp[(k^2+\kappa^2)^{\frac{1}{2}}x_c]+B_k^{(\mathrm{II},-)}-B_k^{(\mathrm{II},+)}\exp[2(k^2+\kappa^2)^{\frac{1}{2}}x_c]. \quad (9)$$

The four Eqs. (9) may be solved to yield:

$$B_k^{(\mathrm{I})}=\frac{4\pi}{D_c(k^2+\kappa^2)^{\frac{1}{2}}+D_s|\mathbf{k}|}\exp[-(k^2+\kappa^2)^{\frac{1}{2}}x_c],$$

$$B_k^{(\mathrm{II},+)}=\frac{2\pi}{D_c(k^2+\kappa^2)^{\frac{1}{2}}}\exp[-(k^2+\kappa^2)^{\frac{1}{2}}x_c],$$

$$B_k^{(\mathrm{II},-)}=\frac{2\pi}{D_c(k^2+\kappa^2)^{\frac{1}{2}}}\left[\frac{D_c(k^2+\kappa^2)^{\frac{1}{2}}-D_s|\mathbf{k}|}{D_c(k^2+\kappa^2)^{\frac{1}{2}}+D_s|\mathbf{k}|}\right]\cdot\exp[-(k^2+\kappa^2)^{\frac{1}{2}}x_c],$$

$$B_k^{(\mathrm{III})}=\frac{2\pi}{D_c(k^2+\kappa^2)^{\frac{1}{2}}}\left\{\exp[(k^2+\kappa^2)^{\frac{1}{2}}x_c]+\frac{D_c(k^2+\kappa^2)^{\frac{1}{2}}-D_s|\mathbf{k}|}{D_c(k^2+\kappa^2)^{\frac{1}{2}}+D_s|\mathbf{k}|}\exp[-(k^2+\kappa^2)^{\frac{1}{2}}x_c]\right\}. \quad (10)$$

With these multiplicative constants now completely determined, one may proceed to synthesize the desired potential for the point charge. As already indicated, one needs only to form the linear combination

$$\psi^{(\nu)}(\mathbf{r})=\sum_{\mathbf{k}}\sigma_k\psi_k^{(\nu)}(\mathbf{r}); \qquad \nu=\mathrm{I},\ \mathrm{II},\ \mathrm{III}. \quad (11)$$

In doing so, we may simultaneously pass to the infinite A limit, so that the $\mathbf{k}$-sum in (11) may be replaced as usual by an integral over a continuous two-dimensional variable $\mathbf{k}$

$$\sum_{\mathbf{k}}\rightarrow\frac{A}{(2\pi)^2}\int d^2\mathbf{k}. \quad (12)$$

If results (10) and (8) are substituted into (11), in the integral limit (12), the potential in region I is found by straightforward manipulation to be

$$\psi^{(\mathrm{I})}(\mathbf{r})=2Ze\kappa\int_0^\infty\frac{lJ_0[(\kappa s)l]}{D_c(1+l^2)^{\frac{1}{2}}+D_s l}\cdot\exp[-(\kappa x_c)(1+l^2)^{\frac{1}{2}}+(\kappa x)l]dl, \quad s=|\mathbf{s}|, \quad \kappa l=|\mathbf{k}|, \quad (13)$$

where J_0 is the zeroth order Bessel function. In obtaining expression (13), polar coordinates in $\mathbf{k}$-space have been introduced, and the angular variable has been

[6] That the interfacial charge density is a complex number, for each $\mathbf{k}$, need cause no concern. We will be solving in effect two problems simultaneously, that for the real, and that for the imaginary part of $\exp(i\mathbf{k}\cdot\mathbf{s})$. The latter formally produces a pure imaginary potential but the set of imaginary charges and potentials disappears entirely from our final results.

eliminated by means of the identity[7]

$$2\pi J_0(\lambda)=\int_0^{2\pi} d\theta\,\exp(i\lambda\cos\theta). \tag{14}$$

In an entirely similar manner, the potential in regions II and III may be obtained. For both these regions occupied by electrolyte, one finds the single expression

$$\psi^{(\mathrm{II,III})}(\mathbf{r})=\frac{Ze\kappa}{D_e}\int_0^\infty \frac{lJ_0[(\kappa s)l]}{(1+l^2)^{\frac{1}{2}}}dl \cdot\left\{\exp[-\kappa\mid x-x_c\mid(1+l^2)^{\frac{1}{2}}]+\frac{D_e(1+l^2)^{\frac{1}{2}}-D_s l}{D_e(1+l^2)^{\frac{1}{2}}+D_s l}\cdot\exp[-\kappa(x+x_c)(1+l^2)^{\frac{1}{2}}]\right\}. \tag{15}$$

The quadratures (13) and (15) together therefore constitute the solution to the problem under consideration. Unfortunately, these integrals are not elementary standard forms, so they cannot be explicitly integrated. It is of some interest, however, to note that Eq. (15) leads to an interesting Bessel function identity in the limit x_c very large. For in this case the point charge has essentially been removed into the bulk of the electrolyte phase, and its mean potential is well known to be just the shielded Coulomb potential.[4] In this limit, therefore, we find from Eq. (15)

$$\frac{Ze}{D_e t}\exp(-\kappa t)=\frac{Ze\kappa}{D_e}\int_0^\infty \frac{lJ_0[(\kappa s)l]}{(1+l^2)^{\frac{1}{2}}}\cdot\exp[-\kappa\mid x-x_c\mid(1+l^2)^{\frac{1}{2}}]dl, \qquad l^2=s^2+(x-x_c)^2. \tag{16}$$

III

We now turn attention to the specific case $x_c=0$, corresponding to adsorption of the point ion at the solution-substrate interface. In this event, the "ion atmosphere" of the adsorbed charge is entirely confined to one hemisphere, and its charge density [through (4)] is determined by the form of $\psi^{(\mathrm{III})}(\mathbf{r})$ with x_c set equal to zero (we shall now suppress the Roman superscript)

$$\psi(\mathbf{r})=2Ze\kappa\int_0^\infty \frac{lJ_0[(\kappa s)l]}{D_e(1+l^2)^{\frac{1}{2}}+D_s l}\cdot\exp[-(\kappa x)(1+l^2)^{\frac{1}{2}}]dl \qquad (x\geq 0). \tag{17}$$

If the electrolyte were infinitely dilute ($\kappa\to 0$), the electrostatic potential would satisfy Laplace's equation in both phases. In that case, the potential in the electrolyte region would be expressible as a sum of two Coulomb potentials, one for the actual charge Ze (at x_c), and another for the apparent "image" charge $[(D_e-D_s)/(D_e+D_s)]Ze$ across the interface (at $-x_c$).[8] When the point charge is adsorbed on the substrate surface, it coalesces with its image to produce an effective charge

$$2D_eZe/(D_e+D_s).$$

As a consequence, the zero concentration limit of Eq. (17) is just

$$\psi(\mathbf{r},\ \kappa=0)=2Ze/(D_e+D_s)r. \tag{18}$$

At finite electrolyte concentration, the diffuse atmosphere of charge which forms around the adsorbed ion will tend to shield the "bare" Coulomb interaction (18). In the arbitrary concentration result (17), we may separate the contribution to $\psi(\mathbf{r})$ attributable to the adsorbed point charge alone, and the diffuse charge atmosphere. On the right side of Eq. (17), we add and subtract the two members of the identity[9]

$$\kappa\int_0^\infty J_0[(\kappa s)l]\exp[-(\kappa x)l]dl=1/r, \tag{19}$$

to obtain

$$\psi(\mathbf{r})=\frac{2Ze}{(D_e+D_s)r}+2Zek\int_0^\infty J_0[(\kappa s)l]\cdot\left\{\frac{l\exp[-(\kappa x)(1+l^2)^{\frac{1}{2}}]}{D_e(1+l^2)^{\frac{1}{2}}+D_s l}-\frac{\exp[-(\kappa x)l]}{D_e+D_s}\right\}dl. \tag{20}$$

The diffuse atmosphere contribution to $\psi(\mathbf{r})$, the integral term in Eq. (20), is in an especially suitable form for numerical analysis in specific cases of interest, on account of the rapid convergence of the integrand to zero, as l increases.

The shielding produces a finite shift in $\psi(\mathbf{r})$ at the origin (the position of the adsorbed ion). Specifically,

$$\eta=\lim_{r\to 0}\left[\psi(\mathbf{r})-\frac{2Ze}{(D_e+D_s)r}\right]=2Ze\kappa I(\alpha)/(D_e+D_s), \qquad \alpha=D_e/(D_e+D_s); \tag{21}$$

where the integral I is defined

$$I(\alpha)=-\int_0^\infty \frac{\alpha[(1+l^2)^{\frac{1}{2}}-l]}{\alpha[(1+l^2)^{\frac{1}{2}}-l]+l}dl. \tag{22}$$

The corresponding potential shift, η_0, if our point ion were located in the bulk of the electrolyte, so that it would be surrounded by a spherically symmetric atmosphere of charge, follows from the Debye-Hückel shielded potential (16)

$$\eta_0=\lim_{t\to 0}[(Ze/D_e t)\exp(-\kappa t)-(Ze/D_e t)]=-Ze\kappa/D_e. \tag{23}$$

One may regard the adsorption process for a point ion on the substrate surface as occurring by reversible

[7] E. T. Whittaker and G. N. Watson, *A Course of Modern Analysis* (Cambridge University Press, New York, 1952), p. 362.
[8] F. P. Buff and F. H. Stillinger, J. Chem. Phys. **25,** 312 (1956).
[9] G. N. Watson, *A Treatise on the Theory of Bessel Functions* (Cambridge University Press, New York, 1952), 2nd ed., p. 384.

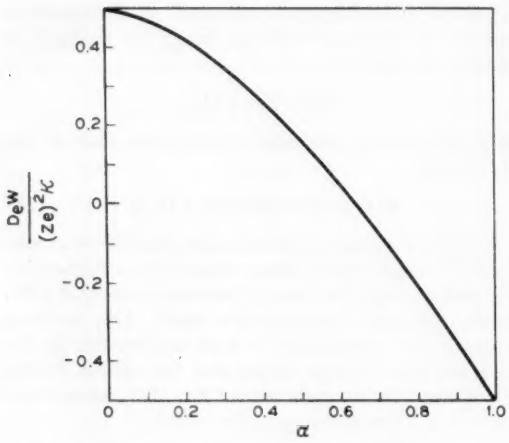

FIG. 2. Plot of the reduced atmosphere displacement work $D_eW/(Ze)^2\kappa$ vs the dielectric constant parameter α.

electrostatic discharge of the ion in the bulk electrolyte, followed by relocation of the discharged ion at the adsorption site, and finally reversible recharging of the ion to its original electrostatic charge. The excess work of adsorption W, resulting from the change in nature of the ion atmosphere shielding from bulk to interface, is just

$$W=\tfrac{1}{2}Ze(\eta-\eta_0)=[(Ze)^2\kappa/D_e][\alpha I(\alpha)+\tfrac{1}{2}]. \quad (24)$$

Equivalently, this work may be interpreted as work of displacement of the originally spherically symmetric ion atmosphere into one hemisphere. Although our expression (24) for this "atmosphere displacement work" is strictly valid only in the asymptotic limit of infinitely dilute electrolytes (on account of use of the linear Poisson-Boltzmann equation), we speculate that a qualitatively similar result will be of importance in predicting the character of ionic adsorption from moderately concentrated solutions.

Table I presents the results of numerical integration on $I(\alpha)$ over the physically meaningful range $0\leq\alpha\leq1$.[10] The corresponding reduced atmosphere displacement work, $D_eW/(Ze)^2\kappa$, is exhibited in Fig. 2. For small values of $\alpha(D_e\ll D_s)$, this work is seen to be positive, whereas when α is near 1 $(D_e\gg D_s)$ it is negative. The change of sign is found to occur at $\alpha=0.645$, or $D_e/D_s=1.815$, and at this point, no displacement work need be performed for adsorption from dilute solution. The trend of the sign of the atmosphere displacement work is easy to rationalize in terms of the relative size of the actual absorbing point ion's charge in the bulk solution, Ze, and its effective value at the surface, $2D_eZe/(D_e+D_s)$.

The qualitative effect of the displacement work W on the adsorption isotherms at the electrolyte-substrate interface is quite clear. When $W>0$, it is more difficult to adsorb ions at the surface than from infinitely dilute solution (where $W=0$), so the number of adsorbed ions is depressed. The contrary conclusion naturally holds when $W<0$. The effect of W is simply to add a concentration dependence to the adsorption energy measured at infinite dilution.

It should be stressed that the technique of this article is useful in another connection when it is undertaken explicitly to compute adsorption isotherms. The actual interface will contain a certain finite density of adsorbed ions which, by virtue of their proximity to one another, tend to interact. Accordingly, it has often been pointed out[11] that the assembly of adsorbed particles should be treated as a nonideal two-dimensional gas. The appropriate ion-ion interaction for a pair adsorbed on the surface may immediately be obtained from Eq. (17), with x set equal to zero. For this expression then provides the value of the mean potential at distance s along the surface from an adsorbed point ion of charge Ze. The pair interaction is equal to this mean potential evaluated at the appropriate pair separation, times the charge on the other ion. If both ions have charge Ze, the surface interaction [which we denote by $\varphi(s)$] is

$$\varphi(s)=Ze\psi(\mathbf{r},\,x=0)$$
$$=2(Ze)^2\kappa\int_0^\infty \frac{lJ_0[(\kappa s)l]}{D_e(1+l^2)^{\frac{1}{2}}+D_s}dl. \quad (25)$$

The properties of the adsorbed nonideal two-dimensional gas may in principle now be computed by constructing a canonical partition function using a total interaction potential which is a sum, over all pairs adsorbed on the surface, of functions φ.

Finally, we re-emphasize that the average potential in the electrolyte when many point ions have been adsorbed at the surface, is just a linear superposition of shielded potentials of form (17), centered at each of these ions. Once again, this is a consequence of the assumed linearity of the functional equations for ψ. The resulting picture of the diffuse portion of the electrical double layer near a discrete set of adsorbed ions, will be that of a rather lumpy charge distribution. The "lumpiness" is determined primarily by the value of the dimensionless ratio of the Debye length $1/\kappa$ (roughly the ion atmosphere width) to the distance between adsorbed ion nearest neighbors. Only for large values of this ratio is it proper to treat the adsorbed charge as uniformly spread over the interface in computing the Gouy layer diffuse charge distribution.

IV

The purpose of this last section is to indicate briefly the procedure analogous to that of Sec. II, in the

[10] One readily verifies the results for the exactly integrable special cases: $I(\frac{1}{2})=-\frac{2}{3}$, and $I(1)=-1$. Furthermore, for small positive α, $I(\alpha)\sim\alpha\log\alpha$.

[11] J. H. DeBoer, *The Dynamical Character of Adsorption* (Oxford University Press, New York, 1953), Chap. VII.

case that a point dipole (rather than a point charge) resides at distance x_c from the interface, with its axis normal to this interface. If the magnitude of the dipole moment (pointing toward the interior of the electrolyte) is μ, then the dipole density $\mu(\mathbf{s})$ on the plane $x=x_c$ may be Fourier analyzed into running wave contributions

$$\mu(\mathbf{s})=\mu\delta(\mathbf{s})$$
$$=\sum_{\mathbf{k}}\mu_k\exp(i\mathbf{k}\cdot\mathbf{s}), \tag{26}$$
$$\mu_k=\mu/A.$$

The mean potential induced by this point dipole once again may be regarded as composed of contributions due to each of the running waves, $\exp(i\mathbf{k}\cdot\mathbf{s})$. Consequently, the potentials $\psi_k^{(\mathrm{I})}$, $\psi_k^{(\mathrm{II})}$, and $\psi_k^{(\mathrm{III})}$ associated with each wave vector $\mathbf{k}$ still have forms (8) in the three regions I, II, and III. However, the multiplicative constants are different, and instead of the B's, might be denoted by $C_k^{(\mathrm{I})}$, $C_k^{(\mathrm{II},+)}$, $C_k^{(\mathrm{II},-)}$, $C_k^{(\mathrm{III})}$.

The boundary conditions for determination of the C's now specify that the normal component of the dielectric displacement be continuous across both surfaces $x=0$ and $x=x_c$; also, the mean electrostatic potential, for dipole density $\exp(i\mathbf{k}\cdot\mathbf{s})$, must be continuous across $x=0$, but must experience a discontinuity of $(4\pi/D_e)\exp(i\mathbf{k}\cdot\mathbf{s})$ in crossing $x=x_c$ in the positive x direction.

When the four simultaneous linear equations corresponding to these boundary conditions are solved, it is possible as before to synthesize the actual mean potential corresponding to the point dipole. If this is done, and if the periodicity area A is once again allowed to become infinite to replace $\mathbf{k}$ summations by integrals, the expressions for the mean potential in the three regions is found to be:

$$\psi^{(\mathrm{I})}(\mathbf{r})=-2\mu\kappa^2\int_0^\infty\frac{l(1+l^2)^{\frac{1}{2}}J_0[(\kappa s)l]}{D_e(1+l^2)^{\frac{1}{2}}+D_s l}\cdot\exp[-(\kappa x_c)(1+l^2)^{\frac{1}{2}}+(\kappa x)l]dl;$$

$$\psi^{(\mathrm{II})}(\mathbf{r})=-\frac{\mu\kappa^2}{D_e}\int_0^\infty lJ_0[(\kappa s)l]\left\{\exp[-\kappa(x-x_c)(1+l^2)^{\frac{1}{2}}]+\frac{D_e(1+l^2)^{\frac{1}{2}}-D_s l}{D_e(1+l^2)^{\frac{1}{2}}+D_s l}\exp[-\kappa(x+x_c)(1+l^2)^{\frac{1}{2}}]\right\}dl;$$

$$\psi^{(\mathrm{III})}(\mathbf{r})=\frac{\mu\kappa^2}{D_e}\int_0^\infty lJ_0[(\kappa s)l]\left\{\exp[-\kappa(x-x_c)(1+l^2)^{\frac{1}{2}}]-\frac{D_e(1+l^2)^{\frac{1}{2}}-D_s l}{D_e(1+l^2)^{\frac{1}{2}}+D_s l}\exp[-\kappa(x+x_c)(1+l^2)^{\frac{1}{2}}]\right\}dl. \tag{27}$$

Taking x_c very large amounts to locating the point dipole in the interior of the electrolyte phase. The shielded dipolar potential field in this case is known to be

$$(\mu/D_e l)[\kappa+(1/t)]\exp(-\kappa t)\cos\theta,$$

where θ is the angle to the dipolar axis, and where t has been defined in Eq. (16). Comparing this with results (27) for $\psi^{(\mathrm{II})}$ and $\psi^{(\mathrm{III})}$ in the large x_c limit leads to the dipolar analog of integral identity (16)

$$(\mu/D_e t)(\kappa+t^{-1})\exp(-\kappa t)\,|\cos\theta\,|=\mu\kappa^2/D_e\cdot\int_0^\infty lJ_0[(\kappa s)l]\exp[-\kappa\,|\,x-x_c\,|(1+l^2)^{\frac{1}{2}}]dl,$$
$$\cos\theta=(x-x_c)/t. \tag{28}$$

ACKNOWLEDGMENT

The author wishes to express his thanks to Academician A. N. Frumkin, who pointed out the importance to electrochemists of the discrete adsorbed charge problem during a recent visit to the Bell Telephone Laboratories.

Asymmetry of Cyclotron Resonance Lines in the Reaction Zones of Low-Pressure Acetylene and Cyanogen Flames*

E. M. Bulewicz and P. J. Padley
Department of Physics, Duke University, Durham, North Carolina

(Received March 6, 1961)

A marked asymmetry and shift of line maximum (at 17 000 gauss) by more than 100 gauss is reported for cyclotron resonance lines obtained in or very close to the reaction zones of low-pressure flames containing high concentrations of free electrons. The effect is interpreted in terms of the variation of the real part of the refractive index of the flame plasma, at microwave frequencies, in the neighborhood of the absorption line. The electron concentration gradients in the vicinity of the reaction zone then have the effect of refracting the microwaves traversing the finite thickness of the plasma towards or away from the microwave receiver.

INTRODUCTION AND EXPERIMENTAL

In the course of our work on electron concentrations and electron-molecule collision frequencies in low-pressure flames by the method of cyclotron resonance, we have observed that there is a marked asymmetry of lines obtained for points in the flame in the immediate vicinity of the reaction zone. Until now the effect has only been observed for fuels burning with oxygen in which the maximum electron concentration is large (i.e., about one part in 10^6—10^7 of the total burnt gases). Such fuels include cyanogen and acetylene, and the observations to be described here are restricted to measurements with these two systems.

Detailed experimental conditions are shortly to be described elsewhere.[1] With microwave radiation at about 48 kMc/sec, cyclotron resonance was observed at a magnetic field strength in the region of 17 000 gauss. The flame, of total unburnt volume 800 cc/min at atmospheric pressure, was burnt inside a vertical, cylindrical glass vessel 2 cm in diameter (dimensions limited by the size of the gap between the magnet's poles) above a concentric glass tube 15 mm in diameter; with such an arrangement, acetylene and cyanogen flames at 10–40 mm Hg and 50–200 mm Hg, respectively, could be conveniently studied.

Curves 2, 3, and 4 of Fig. 1 show the shape of cyclotron resonance lines at various points near the reaction zone of a very electron-rich C_2N_2–O_2 flame (C_2N_2:O_2::1:1.4). In the reaction zone itself (curve 2), the line is asymmetric with a "tail" on the low-field side (hereinafter referred to as "positive" asymmetry). Acetylene shows a rather similar, though smaller, effect. Above the reaction zone the lines are usually quite symmetrical (curve 3), particularly when the flame is burning on the low-pressure side of its stability range. However, when either the cyanogen or acetylene flame is burnt at higher pressures (so that the thickness of the reaction zone is reduced to about 2 mm) an intermediate region of "negative" asymmetry (curve 4) is observed for a distance of about 5 mm above the reaction zone. The transition from positive to negative asymmetry is very sharp, whereas that from negative asymmetry to normal (Lorentzian) line shape is much more gradual. A region of negative asymmetry is also observed *beneath* the reaction zone, and in extreme cases this may take the form of curve 1 (obtained 3 mm below the reaction zone for a stoichiometric acetylene flame, burning at 15 mm Hg); in this case an actual *increase* in power is observed over part of the magnetic field range where the normal cyclotron line should appear. This feature has also definitely been observed, though with less reproducibility, on the high field side of curve 2 and on the low field side of curve 4 above the reaction zone. In all cases of asymmetry, the position of the line maximum is shifted—to lower fields when the asymmetry is positive, and vice versa—by at least 100 gauss and often considerably more. A further, important feature is that the linewidth at the half-conductivity points does not depend significantly on the presence or absence of asymmetry.

None of these phenomena appear to depend significantly on flame gas composition though, in general, they diminish in magnitude as the electron concentration decreases (normal working range 5×10^9–5×10^{10} electrons/cc). The magnitude of the effects also seems to be diminished by reducing the pressure at which any particular flame is burning. (This effect does not appear to be simply one of reducing the absolute electron concentration; rather, we are of the opinion that it shows more dependence on the thickness of the reaction zone, i.e., the physical distance through which the gases have to pass in order to reach a given stage in the combustion process.) Again, the effects are not associated with the position of the burner tube in the 2.3-cm gap of the magnet (12-in., 20 000 gauss maximum, Varian Research Series No. 6; homogeneity better than one part in 10^4 over 1-in.^{3} volume at the gap center). Finally, these phenomena are not associated with the "discontinuity" caused by the top of the 15-mm diam glass tube above which the flame burns. This was determined by

* This research was supported by U. S. Air Force Office of Scientific Research of the Air Research and Development Command.

[1] E. M. Bulewicz, J. Chem. Phys. (to be published).

carefully balancing the unburnt gas flow against the flame's burning velocity; in this way the flame could be stabilized, though with some difficulty, at a position well above the top of the central 15-mm tube. The effects remained undiminished in magnitude.

DISCUSSION

Our early observations were made with acetylene only, and we therefore considered the possibility that the effect might be connected with high concentrations of large positive ions similar to those known to exist in the reaction zone, but not in the burnt gases, of such flames.[2,3] The effect of including ordinary electron-ion collisions in the simple theory of cyclotron line shape

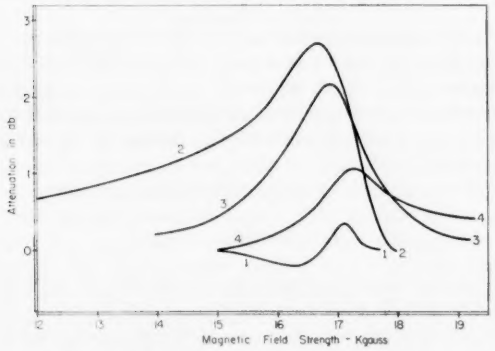

FIG. 1. Shapes of cyclotron resonance lines produced by low-pressure flames. Curve 1, below reaction zone (special case); curve 2, in reaction zone; curve 3, burnt gases (well above reaction zone at high pressures); curve 4, immediately above (at high pressures) and below the reaction zone.

(which only considers electron-neutral molecule collisions)[4] is known not to be one of making the line asymmetric[5]; it effectively results only in a pressure-broadening of the theoretical Lorentzian line shape for electron-neutral molecule collisions. Moreover, to observe even this effect significantly, a concentration of charged particles well in excess of the maximum concentrations that we have found experimentally would be necessary. Our discovery of the asymmetry in cyanogen flame systems also seems to make such a conjecture untenable, because recently Professor Van Tiggelen[6] has kindly informed us that the positive ion spectrum in cyanogen flames is restricted to NO^+.

Equally unlikely as explanations are the effects of Doppler broadening and of space charge. The former effect gives a broadening ΔH_D of about 25 gauss maximum for electrons with flame temperature velocities

[2] S. De Jaegare, J. Deckers, and A. Van Tiggelen, in the *Eighth Symposium on Combustion* (to be published).

[3] P. F. Knewstubb and T. M. Sugden, Proc. Roy. Soc. (London) **A255,** 520 (1960).

[4] J. Schneider and F. W. Hofmann, Phys. Rev. **116,** 244 (1959).

[5] R. C. Hwa, Phys. Rev. **110,** 307 (1958).

[6] A. Van Tiggelen, Universite de Louvain, Belgium (private communication, 1960).

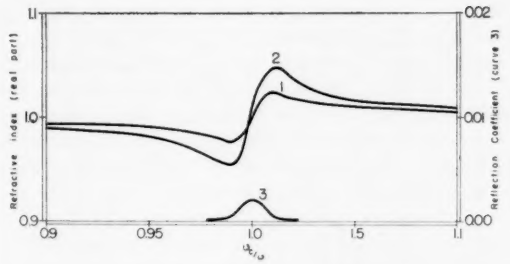

FIG. 2. Variation of refractive index (real part) and reflection coefficient (curve 3) with ω_c/ω in the neighborhood of an absorption line. For each curve $\omega=3\times10^{11}$ sec^{-1}, and $\nu=3\times10^{9}$ sec^{-1}. Curve 1, $N=5\times10^{10}$ cc^{-1}; curve 2, $N=10^{11}$ cc^{-1}; curve 3, $N=10^{11}$ cc^{-1}.

($\bar{v}\sim10^7$ cm/sec; $\Delta H_D/H_0=1.48\bar{v}/c$), and the Doppler shift, as a result of the Hall effect (burnt gas flow rate about 10^4 cm/sec), will also be insignificant. The latter, space charge effect, is only important when ω_p (plasma frequency) $\sim\omega$ (electromagnetic radiation frequency); under our conditions, however, $\omega_p^2 \not> 10^{-3}\omega^2$.

It is now relevant to note that the theory of cyclotron line shape does not, in fact, predict a perfectly symmetrical line; a brief consideration of why this is so, although nonoperative in our case, will lead us, nevertheless, to a highly plausible explanation of the observed asymmetries. For this purpose, it is convenient first to determine the behavior of the refractive index n, the attenuation β (in db), and the reflection coefficient R in the neighborhood of an absorption line. The electric vector of the propagated radiation (frequency ω), its direction of propagation, and the magnetic field are all mutually perpendicular.

The real and imaginary parts of n are given[4] by

$$n' = [\tfrac{1}{2}\{(1+b)^2+a^2\}^{\frac{1}{2}}+1+b]^{\frac{1}{2}}/\sqrt{2}$$

$$n'' = [\tfrac{1}{2}\{(1+b)^2+a^2\}^{\frac{1}{2}}-1-b]^{\frac{1}{2}}/\sqrt{2},$$

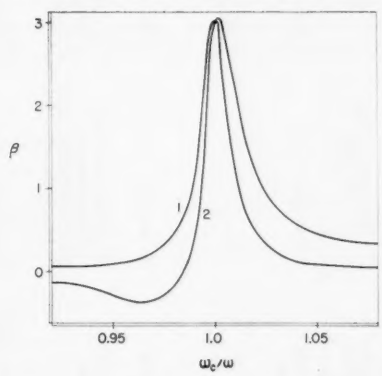

FIG. 3. Curve 1, variation of β with ω_c/ω, using $\nu=3\times10^9$ sec^{-1}, $\omega=3\times10^{11}$ sec^{-1}, and $N=10^{11}$ cc^{-1}. The curve is quite symmetrical. Curve 2, same as for curve 1, but including the effect of variations of n' with ω_c/ω, as depicted in Fig. 2. The curve is highly distorted.

TABLE I.

Waveguide position	System—optical analogy	Low field, $n'<1$		High field, $n'>1$		
		Effect	Apparent absorption	Effect	Apparent absorption	Asymmetry
Immediately below reaction zone	Prism-base up	Refraction away from base	Decreased—some radiation refracted towards detecting horn—if few electrons in direct path, transmission increases over $II=0$ value	Refraction towards base	Increased—less radiation entering detecting horn	−
In reaction zone	Convex lens	Divergence	Increased	Convergence	Decreased	+
Immediately above reaction zone	(a) Prism-base down (high-pressure)	Refraction away from base	Decreased	Refraction towards base	Increased	−
	(b) Parallel-sided block (low-pressure)	None	Normal	None	Normal	0
Well into burnt gases—more than 5 mm from reaction zone	Parallel-sided block	None	Normal	None	Normal	0

respectively, where $a=4\pi\sigma'/\omega$ and $b=4\pi\sigma''/\omega$. σ' and σ'', the real and imaginary parts of the electric conductivity, respectively, are given by the expressions

$$\sigma'=Ne^2[\nu/\{\nu^2+(\omega+\omega_e)^2\}+\nu/\{\nu^2+(\omega-\omega_e^2)\}]/2m$$

$$\sigma''=-Ne^2[(\omega+\omega_e)/\{\nu^2+(\omega+\omega_e)^2\}+(\omega-\omega_e)/\{\nu^2+(\omega-\omega_e)^2\}]/2m,$$

where ω_e is the frequency at which maximum absorption takes place, N is the number of electrons/cc, ν is the electron-neutral molecule collision frequency in the flame, and e and m have their usual significance. R is given by

$$R=\{(n'-1)^2+n''^2\}/\{(n'+1)^2+n''^2\}.$$

n' and R, as a function of ω_e/ω, have the form shown in Fig. 2, using values of ν and N known for acetylene flames under these conditions[1]. ω_e/ω can be simply converted to magnetic field strength H by means of the relationship $\omega_e=eH/mc$. The significance of Fig. 2 will be discussed shortly.

The attenuation β can be expressed in the form

$$\beta=(20\omega n''d/c)\cdot\log_{10}e,$$

when d is the path length, in cm. At low N, β varies symmetrically with ω_e/ω and β_{max} occurs at $\omega=\omega_e$. On the other hand, at high N β_{max} shifts to $\omega_e/\omega<1.0$, and the line becomes slightly asymmetric. The latter conditions, however, are not realized in our systems. With $\nu\sim3\times10^9$ sec^{-1}, $\omega=3\times10^{11}$ sec^{-1}, $N=10^{11}$ electrons/cc (experimental conditions for a typical acetylene flame using the maximum observed value of N), the line has the form of curve 1, Fig. 3, and shows no signs of this theoretical distortion. Even if N were high enough to cause an asymmetry, the shifts $\omega_e/\omega>1.0$ would still remain unaccounted for, and thus this possible explanation can be ruled out.

Radiation passing through the plasma will suffer some reflection, since R (see Fig. 2) is greater than zero in the region of the absorption line. Here, the reflection amounts to hardly 1%, and its effect of giving slightly too small N values and slightly too big ν values is quite negligible. The behavior of n' with ω_e/ω (Fig. 2), however, may be of much greater significance. In outline it has the form of the derivative of n'', and the variation is very similar to that of the refractive index across an optical absorption line—the well known phenomenon of "anomalous" dispersion. The existence of this latter effect is usually fairly simply demonstrated by arranging for the absorbing system to act, formally at least, as a prism in the region of the absorption line. In our case, it is possible for the "anomalous" dispersion to reveal itself because the electron concentration gradients in the flame system act as the equivalent of a system of prism and lenses, depending on the flame position ex-

amined. Radiation crossing the flame will encounter electron concentration gradients (and hence gradients of refractive index) in the vertical direction, i.e., at right angles to its direction of propagation, and will in consequence be deflected in the vertical direction. For a small deflection, the angle θ (rad) turned through will be given by

$$\theta = d \cdot (dn'/dy),$$

where d is the path length and dn'/dy is the mean value of the refractive index gradient over the region through which the radiation passes. At a horizontal distance g from the center of the flame the radiation will have been deflected vertically by an amount Δy, given approximately by

$$\Delta y = gd \cdot (dn'/dy)$$

Experimentally, $g \sim 1.5$ cm, $d \sim 1.5$ cm. The value of (dn'/dy) varies from flame to flame and depends strongly on the position in the flame being examined. We do not yet know its value too accurately, since the spatial resolution in the flame is limited by the finite size (4 mm vertically) of the signal and receiving horns (more details presented later). Our measurements of electron concentrations with time after primary combustion in these systems suggest that (dn'/dy) may have any value between zero and about 0.05, the higher values occurring only in the region of the reaction zone where the gradients are particularly steep. A typical effect of n' variations with ω_c/ω on the theoretical, symmetrical line of Fig. 3, curve 1 is shown in Fig. 3, curve 2; a value of 0.025 was taken for $(dn'/dy)_{max}$, and a position just below the reaction zone was chosen for the calculation. Experimentally, this position corresponds to that at which curves 1 and 4 of Fig. 1 were obtained. All the principal features of these two curves are reproduced by curve 2 of Fig. 3. Exact correspondence will not be given by this particular comparison since (a) the β values of curve 1 of Fig. 3 are much larger than those of curves 1 and 4 of Fig. 1 and (b) curve 2 of Fig. 3 was plotted for the ω/ν conditions obtaining in acetylene flames. On the other hand, curve 4 (also 3 and 2) of Fig. 1 is obtained for cyanogen at a considerably different pressure where a very different ω/ν will be observed. The important point to note is that it is possible to explain (with some precision, when accurate (dn'/dy) values are obtainable) all the important features of Fig. 1 in this way. Table I is a list of all the effects predicted by this explanation; reference to Fig. 1 shows full qualitative agreement with experiment.

For small asymmetries it is important to note that neither the measurements of electron-molecule collision cross sections (dependent on line half-width) nor the values of electron concentration (dependent on the product of half-width and maximum absorption for Lorentzian lines) should be invalidated. We have never detected any significant effect of asymmetry on linewidth; this suggests that the measured asymmetries are not too severe. The maximum and minimum values of n' in Fig. 2 occur at a value of ω_c/ω, corresponding quite closely to the half-power points of the corresponding β plot, and then the largest observable shift in the position of the line maximum should never be greater than one-half the linewidth. The typical shifts depicted in Fig. 1 are never as great as this.

Consideration of the geometrical and theoretical factors suggest that the asymmetry in the reaction zone could be reduced by "stopping-down" the electron lens by using radiation of even higher frequency. The part played by the geometrical factor was tested for by reducing the dimensions of the open waveguides between which the flame burns. Normally, the open ends (4×11 mm) consisted of ordinary I to K waveband transition sections, which acted as convenient horns for transmission of the 48 kMc/sec radiation across the flame gap. With these removed it was noted that the asymmetry in the reaction zone was reduced.

ACKNOWLEDGMENT

We wish to express our gratitude to Dr. Walter Gordy for his continued interest in this work and for making available to us the facilities of his laboratory.

Heat Capacity of $LiCuCl_3 \cdot 2H_2O$*

H. FORSTAT AND D. R. MCNEELY

Department of Physics and Astronomy, Michigan State University, East Lansing, Michigan

(Received April 5, 1961)

The heat capacity of $LiCuCl_3 \cdot 2H_2O$ has been measured in the temperature range 2°–9°K. A λ-type anomaly in the heat capacity curve has been observed at 4.40±0.02°K. This has been identified as the Néel temperature for a paramagnetic-antiferromagnetic transition. The magnetic entropy associated with this transition is 1.35 cal/mole deg which agrees with the theoretical value to within 2% if the spin of the magnetic ion is taken as ½ in $R \log (2S+1)$. The fraction of the magnetic entropy above the Néel temperature is 0.48 which indicates a considerable amount of short-range ordering of the spins of the magnetic ions.

SOME previous work by Vossos, Jennings, and Rundle[1] on the magnetic susceptibility of $LiCuCl_3 \cdot 2H_2O$ indicated a magnetic ordering process above 4.2°K. To continue the study of this magnetic transition, heat capacity and nuclear magnetic resonance experiments have been performed on single crystals of this salt. A subsequent paper will discuss the results of the nuclear magnetic resonance studies.[2] The present paper concerns itself with the heat capacity studies.

By means of heat capacity data it has been possible to determine, unambiguously, the magnetic transition temperature, since the value of the heat capacity increases markedly at this temperature. A measure of the entropy change during this transition can also be obtained, enabling one to determine the ground state spin of the magnetic ions.

EXPERIMENTAL

Single crystals of $LiCuCl_3 \cdot 2H_2O$ were grown at room temperature from an aqueous solution of $CuCl_2 \cdot 2H_2O$ and LiCl. These salts were reagent grade, obtained from J. T. Baker Chemical Company. The crystals were monoclinic and reddish brown in color. Three separate crystals were used in the experiments, each weighing approximately 1.5 g and measuring 1.5×1.0 cm. A chemical analysis[3] was made on one of these crystals which verified its composition.

The heat capacity measurements were made in the temperature range 2°-9°K using a vacuum calorimeter described previously.[4] To each crystal was attached a 56 ohm, Allen-Bradley, $\frac{1}{10}$-w resistor and a winding of manganin wire of approximately 400 ohms. The crystal was mounted in the calorimeter by means of a nylon thread. Helium exchange gas was used for calibration of the resistor against the vapor pressure of liquid helium using the 1958 He^4 temperature scale.[5] Approximately 13 calibration points were taken between 2°-4.2°K. This calibration was first treated on a $\log_{10}R$ vs $1/T$ plot and then checked against the equation $[(\log R)/T]^3 = a + b \log R$ where a and b are arbitrary constants.[6] By choosing a reasonable value of b and then plotting $\log R$ vs a, a smooth curve was obtained. The value of a corresponding to liquid-air temperature also fell on this curve. The temperatures were obtained by reading off the value of a corresponding to the value of $\log R$ and then solving the above equation. It was found that the temperature values obtained in this way were slightly lower than those obtained from a $\log_{10}R$ vs $1/T$ plot. They differed by 0.004°K at 2°K, 0.009°K at 4.4°K, 0.2°K at 6°K, and 0.5°K at 7.2°K. This indicates that there is slightly greater uncertainty in the higher temperature values where an extrapola-

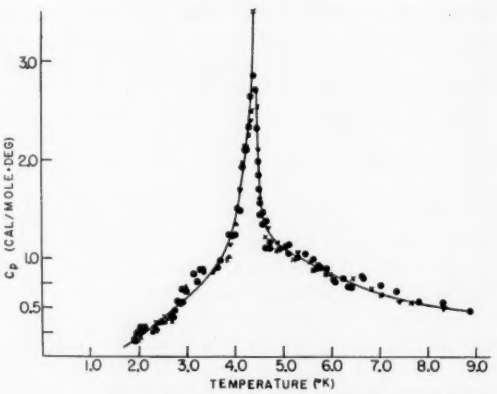

FIG. 1. Molar heat capacity of $LiCuCl_3 \cdot 2H_2O$ as a function of temperature $LiCuCl_3 \cdot 2H_2O$: ×, December 7, 1960; ▲, December 15, 1960; ■, December 19, 1960; ▼, December 27, 1960; ●, January 26, 1961.

* Supported by the Office of Naval Research and an All-University Research Grant from Michigan State University.

[1] P. H. Vossos, L. D. Jennings, and R. E. Rundle, J. Chem. Phys. **32,** 1590 (1960).

[2] R. D. Spence and C. R. K. Murty (to be published).

[3] The chemical analysis was made by Schwarzkopf Microanalytical Laboratory 56-19, 37th Avenue, Woodside, New York.

[4] H. Forstat, G. O. Taylor, and B. King, J. Chem. Phys. **31,** 929 (1959).

[5] F. G. Brickwedde, H. van Dijk, M. Durieux, J. R. Clement, and J. K. Logan, J. Research Natl. Bur. Standards **A64,** 1 (1960).

[6] J. R. Clement, *Temperature* (Reinhold Publishing Corporation, New York, 1955), Vol. II, p. 382.

TABLE I. Heat capacity of $LiCuCl_3 \cdot 2H_2O$. Data on first and second crystals.

December 7, 1960			December 19, 1960		
C_p (cal/mole deg)	ΔT (°K)	T (°K)	C_p (cal/mole deg)	ΔT (°K)	T (°K)
0.15	0.009	1.998	0.21	0.003	2.065
0.19	0.010	2.018	0.27	0.003	2.257
0.25	0.008	2.155	0.22	0.004	2.291
0.25	0.007	2.157	0.23	0.003	2.330
0.24	0.008	2.265	0.36	0.002	2.441
0.34	0.006	2.329	0.38	0.002	2.479
0.34	0.005	2.365	0.35	0.002	2.545
0.39	0.004	2.571	0.32	0.003	2.621
0.37	0.005	2.641	0.88	0.009	3.582
0.34	0.006	2.677	1.97	0.009	4.169
0.93	0.009	3.821			
2.46	0.006	4.387			
3.517	0.004	4.392			
December 15, 1960			December 22, 1960		
0.24	0.005	2.043	0.16	0.005	1.921
0.26	0.005	2.063	0.18	0.004	1.938
0.28	0.005	2.084	0.21	0.004	1.954
0.23	0.005	2.103	0.24	0.003	2.013
0.27	0.004	2.145	0.26	0.006	2.069
0.29	0.004	2.189	0.24	0.003	2.098
0.26	0.004	2.214	0.33	0.003	2.448
0.34	0.003	2.400	0.37	0.021	2.702
0.36	0.004	2.633	0.46	0.013	2.756
0.44	0.004	2.663	0.50	0.011	2.819
0.71	0.012	2.963	1.09	0.015	3.716
0.86	0.008	3.314	2.12	0.007	4.295
0.84	0.009	3.539	0.53	0.180	7.389
0.93	0.008	3.865	0.49	0.204	8.259
1.34	0.016	4.002			

tion was necessary than in the lower, yet well within the accuracy of the experiment in the region of 4.4°K.

Corrections to the heat capacity for the addenda (carbon thermometer, manganin wire heater, glyptal, etc.) amounted to less than 0.5%. The heat capacity data are given in Tables I and II, and Fig. 1.

RESULTS AND DISCUSSION

The heat capacity data were obtained on three separate crystals. The data of 12–7, 12–15, and 12–19–60 were three independent runs on the first crystal; the data of 12–22–60 was obtained on the second crystal, and the third crystal was run on 1–26–61. This latter crystal was also the same crystal on which some nuclear magnetic resonance data was taken.

As is seen from Fig. 1, the heat capacity shows a lambda-type anomaly which is associated with a magnetic ordering process. The nuclear resonance data has helped to identify this transition as a paramagnetic-antiferromagnetic one. From the curve, the Néel temperature is estimated to be 4.40±.02°K.

It is of interest to determine, from the heat capacity data, the magnetic entropy associated with this transition. A method for doing this by considering, separately, the magnetic entropy contribution above and below the Néel temperature has already been described.[7] In this method, it is assumed that above the Néel temperature, the lattice heat capacity is proportional to T^3 and that the magnetic heat capacity is proportional to $1/T^2$, so that the total heat capacity for this region is the sum of those two terms. These entropy contributions amount to 0.70 cal/mole deg for the region below the Néel temperature and 0.65 cal/mole deg above the Néel temperature. The total entropy change is, therefore, 1.35 cal/mole deg. The expected value for this entropy change can be obtained from $R \log(2S+1)$, where R is the universal gas constant and S refers to the ground-state spin of the magnetic ion. The exact composition of the magnetic ion is still in doubt, although Vossos *et al.*[1] have suggested an antiferromagnetic coupling between $Cu_2Cl_6^{2-}$ ions. They indicate, as well, that a good fit to their susceptibility data is obtained if the spin of the magnetic ion is chosen as 1. From the above equation, if one chooses $S=\frac{1}{2}$, the expected value for the entropy change is 1.38 cal/mole deg; if $S=1$, the entropy change to be expected is 2.18 cal/mole deg. From the present data, it would appear that an assignment of $S=\frac{1}{2}$ gives better agreement for the entropy change than $S=1$. If the temperature values above 4.2°K, in the present experiment, were slightly high due to the necessary

[7] S. A. Friedberg, Physica **18,** 714 (1952); D. G. Kapadnis and R. Hartmans, Physica **22,** 181 (1956).

TABLE II. Heat capacity of $LiCuCl_3 \cdot 2H_2O$. This represents the data of January 26 1961.

C_p (cal/mole deg)	ΔT (°K)	T (°K)	C_p (cal/mole deg)	ΔT (°K)	T (°K)
0.17	0.004	1.904	1.51	0.008	4.069
0.15	0.004	1.920	1.48	0.009	4.107
0.23	0.003	1.964	1.93	0.007	4.187
0.25	0.003	1.979	2.10	0.005	4.225
0.24	0.004	2.016	2.09	0.009	4.274
0.29	0.003	2.034	2.64	0.005	4.357
0.20	0.003	2.066	2.86	0.008	4.421
0.26	0.003	2.097	2.71	0.008	4.446
0.29	0.003	2.129	1.98	0.006	4.491
0.26	0.003	2.146	1.44	0.014	4.501
0.26	0.003	2.217	1.47	0.013	4.552
0.25	0.014	2.269	1.32	0.015	4.579
0.29	0.012	2.361	1.38	0.011	4.648
0.35	0.009	2.470	1.11	0.018	4.744
0.38	0.007	2.512	1.17	0.015	4.731
0.36	0.010	2.598	1.14	0.044	4.953
0.40	0.007	2.663	1.17	0.038	5.052
0.41	0.007	2.703	1.16	0.058	5.139
0.47	0.011	2.752	1.02	0.065	5.323
0.56	0.010	2.805	1.09	0.036	5.476
0.57	0.011	2.846	0.99	0.035	5.633
0.45	0.013	2.888	0.91	0.039	5.708
0.70	0.008	2.928	0.93	0.059	5.731
0.67	0.009	2.978	0.90	0.043	5.775
0.67	0.021	3.072	0.89	0.073	5.892
0.84	0.026	3.145	0.76	0.110	6.050
0.88	0.008	3.290	0.81	0.071	6.632
0.88	0.012	3.320	0.80	0.062	6.653
0.90	0.007	3.613	0.73	0.147	6.867
0.90	0.007	3.639	0.72	0.138	7.023
0.96	0.013	3.696	0.67	0.146	7.340
1.23	0.009	3.896	0.58	0.159	7.820
1.20	0.010	3.962	0.56	0.152	8.320
1.22	0.010	4.000	0.47	0.173	8.874

extrapolation, and should be reduced, this would have the effect of reducing the contribution to the magnetic entropy above the Néel temperature. Consequently, this would make the prediction of $S=1$ even more unlikely. A more detailed examination of this point may have to await neutron diffraction experiments.

It is also of interest to note that 48% of the total entropy change occurs above the Néel temperature, an effect which has been observed in varying degree in many other antiferromagnetic substances. This is presumably due to slow diminution of the short-range ordering of the spins of the magnetic ions.

Optically Active Lattice Vibrations as Treated by the GF-Matrix Method

TAKEHIKO SHIMANOUCHI AND MASAMICHI TSUBOI*
Department of Chemistry, Faculty of Science, Tokyo University, Hongo, Tokyo, Japan
AND
TATSUO MIYAZAWA
Institute for Protein Research, Osaka University, Kitaku, Osaka, Japan

(Received March 3, 1961)

A general description has been given of an application of the Wilson's GF-matrix method to the treatment of optically active lattice vibrations. As examples, formulas are derived for the calculation of the frequencies of the lattice vibrations of a one-dimensional, the diamond, and CaF_2 lattices.

THE GF-matrix method originated by E. B. Wilson[1] has been found to be very efficient in the normal coordinate treatments of polyatomic molecules. The method has also been successfully applied to calculations of optically active[2] frequencies of linear high polymers with a translational symmetry.[3–6] The GF-matrix method may also be applied to crystalline lattices with translational symmetries of two and three dimensions. The purpose of this paper is to describe, briefly, the general method of the treating optically active[2] lattice vibrations by the GF-matrix method, and to give a few examples.

GENERAL DESCRIPTION OF THE METHOD

Wilson's method of obtaining the normal frequencies and the normal coordinates of any system (group of atoms) is to obtain eigenvalues and eigenvectors of the matrix **GF**, where **G** is the inverse kinetic energy matrix and **F** the potential energy matrix of the system in question. The secular equation for calculating the normal frequencies is written as

$$|\mathbf{GF}-\mathbf{E}\lambda|=0. \tag{1}$$

In this equation, **E** is the unit matrix with the same order as that of the **G** and **F** matrices, and

$$\lambda=4\pi^2c^2\nu^2, \tag{2}$$

where c is the light velocity and ν is the wave number. When the system is composed of an infinite number of atoms, the order of the **G** or **F** matrix is infinite, since an infinite number of coordinates are to be taken into account. If the system has some translational symmetry, as does any crystal lattice, then the **G** or **F** matrix of infinite order is a mere repetition of submatrices of a finite size. The **G** or **F** matrix of a certain species of vibrations of a crystal can be constructed by summing these submatrices which have been multiplied by a proper set of phase factors.

For lattice vibrations that are active in the infrared absorption and/or Raman effect, the motion of all the Bravais cells[7] take place in phase. For such vibrations, all of the phase factors mentioned above are unity. The **G** or **F** matrix for these optically active vibrations can be obtained by adding the **G** or **F** matrix for a Bravais cell to the sum of all the **G** or **F** matrices representing the interactions between the Bravais cell in question and the neighboring Bravais cells. Let a Bravais cell of a crystal lattice be represented by subscripts i, j, and k and its internal coordinate vector by $\mathbf{R}_{ijk}$. Then, the **G** and **F** matrices for the optically active vibrations of this crystal lattice $\mathbf{G}_{op}$ and $\mathbf{F}_{op}$ are given by

$$\mathbf{G}_{op}=\sum_{i'j'k'}\mathbf{G}_{ijk,i'j'k'} \tag{3}$$

and

$$\mathbf{F}_{op}=\sum_{i'j'k'}\mathbf{F}_{ijk,i'j'k'}, \tag{4}$$

where

$$\begin{aligned} i'&=i, \quad i\pm1, \quad \text{or } i\pm2,\\ j'&=j, \quad j\pm1, \quad \text{or } j\pm2,\\ k'&=k, \quad k\pm1, \quad \text{or } k\pm2, \end{aligned} \tag{5}$$

and $\mathbf{G}_{ijk,i'j'k'}$'s and $\mathbf{F}_{ijk,i'j'k'}$'s are submatrices of the **G** and **F** matrices with respect to the internal coordinates vectors $\mathbf{R}_{ijk}$ and $\mathbf{R}_{i'j'k'}$. The coordinate vector, by which the $\mathbf{G}_{op}$ and $\mathbf{F}_{op}$ matrices are represented, is the "optically active internal coordinate" $\mathbf{R}_{op}$ which is

* Present address: Faculty of Pharmaceutical Sciences, University of Tokyo, Bunkyo-ku, Tokyo, Japan.

[1] E. B. Wilson, J. Chem. Phys. **7**, 1047 (1939); **9**, 76 (1941).

[2] In this paper, "optically active" means "Raman or infrared active."

[3] T. Shimanouchi and S. Mizushima, Sci. Papers Inst. Phys. Chem. Research, Tokyo **40**, 467 (1943); J. Chem. Phys. **17**, 1102 (1949); T. Shimanouchi, *ibid.* **17**, 734 (1949).

[4] T. Shimanouchi and M. Tasumi, Bull. Chem. Soc. Japan **34**, 359 (1961).

[5] T. Miyazawa, Spectrochimica Acta. **16**, 1231, 1233 (1960); J. Chem. Phys. **35**, 693 (1961).

[6] H. Tadokoro, J. Chem. Phys. **33**, 1558 (1960).

[7] Any crystal lattice can be reduced to one of the fourteen Bravais lattices by replacing a certain group of atoms with a point. Such a group of atoms is called here the "Bravais cell" or "Bravais unit cell." In other words, the "Bravais cell" is defined as the smallest unit in which no two groups of atoms become equivalent as a result of a simple translation. See, for example, S. Bhagavantam and T. Venkatarayudu, *Theory of Groups and Its Application to Physical Problems* (Andhra University, Waltair, 1951), 2nd ed., p. 127; M. Hass and G. B. B. M. Sutherland, Proc. Roy. Soc. (London) **A236**, 429 (1956); or M. Tsuboi, Kagaku-no-Ryoiki, Zokan **32**, 37 (1958).

defined by the following equation:

$$\mathbf{R}_{op}=N\sum_{ijk}\mathbf{R}_{ijk}, \tag{6}$$

where N is a normalization factor. With the internal coordinate system the elements of the $\mathbf{G}$ matrix can be obtained in exactly the same way as that in which the elements are obtained of the $\mathbf{G}$ matrices for simple molecules.[1,8] However, the procedure of obtaining the $\mathbf{G}_{op}$ by Eq. (3) is often tedious since a great number of elements must be calculated of the several matrices, $\mathbf{G}_{ijk,i'j'k'}$'s. On the other hand, the $\mathbf{F}_{op}$ matrix elements can be derived easily from the potential function expressed in terms of the internal coordinates.

The coordinate system in the above treatment need not necessarily be that of the internal coordinates, but it may be that of Cartesian or some other coordinates. The inverse kinetic energy matrix $\mathbf{G}^c$ expressed in terms of the Cartesian coordinates $\mathbf{X}$ is diagonal, and the

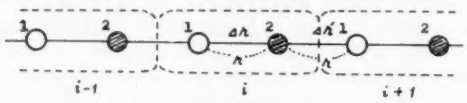

FIG. 1. A one-dimensional lattice.

elements associated with the three Cartesian coordinates of the bth atom of the Bravais cell ijk are equal to the reciprocal mass of the bth atom. The corresponding potential energy matrix $\mathbf{F}^c$ may be obtained from the potential energy matrix $\mathbf{F}^i$ expressed in terms of the internal coordinates $\mathbf{R}$ in the following way. By the use of a transformation matrix $\mathbf{B}$, which is defined by the equation,

$$\mathbf{R}=\mathbf{B}\mathbf{X}, \tag{7}$$

the potential energy V of the crystal is expressed as

$$2V=\mathbf{R}^t\mathbf{F}^i\mathbf{R}=\mathbf{X}^t\mathbf{B}^t\mathbf{F}^i\mathbf{B}\mathbf{X}=\mathbf{X}^t\mathbf{F}^c\mathbf{X}.^9$$

Therefore, $\mathbf{F}^c$ is given as

$$\mathbf{F}^c=\mathbf{B}^t\mathbf{F}^i\mathbf{B}. \tag{8}$$

When the crystal is composed of an infinite number of atoms, the $\mathbf{G}^c$, $\mathbf{F}^c$, and $\mathbf{B}$ matrices, as well as the $\mathbf{G}^i$ and $\mathbf{F}^i$ matrices, are of infinite order. For the optically active vibrations, however, we may define a finite number of the "optically active Cartesian coordinates" $\mathbf{X}_{op}$ which are totally symmetric with respect to the translational symmetries of the crystal in question. Thus,

$$\mathbf{X}_{op}=N\sum_{ijk}\mathbf{X}_{ijk}, \tag{9}$$

where N is the normalization factor and $\mathbf{X}_{ijk}$ is the Cartesian coordinate vector associated with the Bravais cell ijk. The number of the optically active

[8] J. C. Decius, J. Chem. Phys. **16**, 1025 (1948).

[9] The superscript "t" is used to indicate the transpose of a matrix.

FIG. 2. The optically active stretching vibration of the one-dimensional lattice shown in Fig. 1.

Cartesian coordinates obtained here is three times the number of atoms per Bravais cell.

The inverse kinetic energy matrix $\mathbf{G}_{op}{}^c$ expressed in terms of $\mathbf{X}_{op}$ is also diagonal and is derived to be

$$\mathbf{G}_{op}{}^c=\mathbf{G}_{ijk,ijk}{}^c. \tag{10}$$

The elements of the $\mathbf{G}_{op}{}^c$ matrix obtained here are the reciprocal masses of the atoms of the Bravais cell in question. On the other hand, the corresponding potential energy matrix $\mathbf{F}_{op}{}^c$ may be derived to be

$$\mathbf{F}_{op}{}^c=\mathbf{B}_{op}{}^t\mathbf{F}_{op}{}^i\mathbf{B}_{op}, \tag{11}$$

where $\mathbf{F}_{op}{}^i$ is the potential energy matrix expressed in terms of the optically active internal coordinates $\mathbf{R}_{op}$; $\mathbf{B}_{op}$ is defined by the following transformation,

$$\mathbf{R}_{op}=\mathbf{B}_{op}\mathbf{X}_{op}. \tag{12}$$

In order to derive the $\mathbf{B}_{op}$ matrix, the $\mathbf{R}_{op}$ vector will first be expressed as shown below in terms of the Cartesian coordinate vector $\mathbf{X}_{i'j'k'}$ of the Bravais cell $i'j'k'$.

$$\begin{aligned}\mathbf{R}_{op}&=N\sum_{ijk}\mathbf{R}_{ijk}=N\sum_{ijk}\Big(\sum_{i'j'k'}\mathbf{B}_{ijk,i'j'k'}\mathbf{X}_{i'j'k'}\Big)\\&=N\sum_{i'j'k'}\Big(\sum_{ijk}\mathbf{B}_{ijk,i'j'k'}\mathbf{X}_{i'j'k'}\Big),\end{aligned} \tag{13}$$

where $\mathbf{B}_{ijk,i'j'k'}$ is the submatrix associated with the internal coordinate vector $\mathbf{R}_{ijk}$ of the Bravais cell ijk and the Cartesian coordinate vector $\mathbf{X}_{i'j'k'}$ of the cell $i'j'k'$. Since

$$\mathbf{B}_{i,j,k;\,i+a,j+b,k+c}=\mathbf{B}_{i-a,j-b,k-c;\,i,j,k} \tag{14}$$

it follows that

$$\sum_{i'j'k'}\mathbf{B}_{ijk,i'j'k'}=\sum_{i'j'k'}\mathbf{B}_{i'j'k',ijk}=\sum_{ijk}\mathbf{B}_{ijk,i'j'k'} \tag{15}$$

and the sum does not depend upon a particular choice of ijk. Then,

$$\mathbf{R}_{op}=\Big(\sum_{ijk}\mathbf{B}_{ijk,i'j'k'}\Big)\mathbf{X}_{op}, \tag{16}$$

and

$$\mathbf{B}_{op}=\sum_{ijk}\mathbf{B}_{ijk,i'j'k'} \tag{17}$$

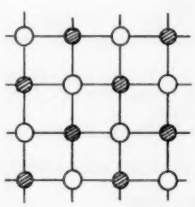

FIG. 3. A two-dimensional lattice.

or

$$\mathbf{B}_{op}=\sum_{i'j'k'}\mathbf{B}_{ijk,i'j'k'}. \tag{18}$$

Thus, the element of the $\mathbf{B}_{op}$ matrix, $(B_{op})_{ab}$, associated with the ath optically active internal coordinate and the bth optically active Cartesian coordinate may be obtained in two different ways. As shown in Eq. (18), $(B_{op})_{ab}$ is equal to the displacement of the ath internal coordinate of a Bravais cell caused by unit displacement of all the bth Cartesian displacements of the crystal. It may also be seen from Eq. (17) that $(B_{op})_{ab}$ is equal to the sum of the displacements of all the ath internal coordinates of the crystal accompanying the unit displacement of the bth Cartesian coordinate of a Bravais cell.

The $\mathbf{B}_{op}$ matrix elements may be calculated only for the internal coordinates in terms of which the potential function is expressed. Usually the bond stretching and angle bending coordinates are used as internal coordinates. However, the repulsive potential between a nonbonded atom pair has been known to be significant. Accordingly, the $\mathbf{B}_{op}$ matrix elements may be derived also for the nonbonded distance and thus the repulsive potential may be taken into account in the normal coordinate analysis by the use of Cartesian coordinates.

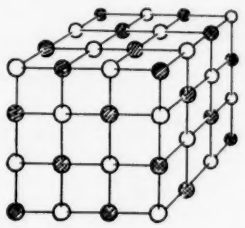

FIG. 4. An NaCl-type lattice.

It may be pointed out here that with the optically active Cartesian coordinates the $\mathbf{G}$ matrix elements are diagonal and the secular determinant may be reduced into a symmetrical one in the following way.[10,11] We first define $\mathbf{G}^{\frac{1}{2}}$ whose diagonal elements are the square roots of the corresponding elements of the $\mathbf{G}$ matrix. Thus,

$$\mathbf{G}^{\frac{1}{2}}\mathbf{G}^{\frac{1}{2}}=\mathbf{G}$$

$$\mathbf{G}^{-\frac{1}{2}}\mathbf{G}^{\frac{1}{2}}=\mathbf{E}.$$

Since

$$\mathbf{GFL}=\mathbf{L\Lambda},$$

($\mathbf{\Lambda}$ is a diagonal matrix whose elements are the eigenvalues of the matrix $\mathbf{GF}$, and $\mathbf{L}$ is the matrix composed of the corresponding eigenvectors),

$$\mathbf{G}^{\frac{1}{2}}\mathbf{FG}^{\frac{1}{2}}\cdot\mathbf{G}^{-\frac{1}{2}}\mathbf{L}=\mathbf{G}^{-\frac{1}{2}}(\mathbf{GFL})=\mathbf{G}^{-\frac{1}{2}}\mathbf{L\Lambda}.$$

The matrix $\mathbf{G}^{\frac{1}{2}}\mathbf{FG}^{\frac{1}{2}}$ is symmetric and its eigenvectors $\mathbf{L}_c$ is given as

$$\mathbf{L}_c=\mathbf{G}^{-\frac{1}{2}}\mathbf{L}.$$

Therefore,

$$\mathbf{L}=\mathbf{G}^{\frac{1}{2}}\mathbf{L}_c.$$

If the crystal lattice in question has any rotational symmetry, the $\mathbf{G}_{op}{}^c$ and $\mathbf{F}_{op}{}^c$ may be factored by a proper choice of optically active Cartesian symmetry coordinates $\mathbf{S}_{op}$, which are given by

$$\mathbf{S}_{op}=\mathbf{UX}_{op}. \tag{19}$$

The inverse kinetic energy matrix $\mathbf{G}_{op}{}^{cs}$ and the potential energy matrix $\mathbf{F}_{op}{}^{cs}$ expressed in terms of the $\mathbf{S}_{op}$ coordinates are derived as shown below.[12]

$$\mathbf{G}_{op}{}^{cs}=\mathbf{UG}_{op}{}^c\mathbf{U}^\dagger, \tag{20}$$

and

$$\mathbf{F}_{op}{}^{cs}=\mathbf{UF}_{op}{}^c\mathbf{U}^\dagger=\mathbf{UB}_{op}{}^t\mathbf{F}_{op}{}^i\mathbf{B}_{op}\mathbf{U}^\dagger$$

$$=\mathbf{B}_{op}{}^{s\,t}\mathbf{F}_{op}{}^i\mathbf{B}_{op}{}^s, \tag{21}$$

where

$$\mathbf{B}_{op}{}^s=\mathbf{B}_{op}\mathbf{U}^\dagger. \tag{22}$$

The unitary matrix $\mathbf{U}$ may be constructed so as to remove the redundant coordinates. The redundant Cartesian symmetry coordinates are

$$[\Delta x^{(1)}+\Delta x^{(2)}+\cdots+\Delta x^{(n)}]/n^{\frac{1}{2}},$$

$$[\Delta y^{(1)}+\Delta y^{(2)}+\cdots+\Delta y^{(n)}]/n^{\frac{1}{2}},$$

and

$$[\Delta z^{(1)}+\Delta z^{(2)}+\cdots+\Delta z^{(n)}]/n^{\frac{1}{2}},$$

where $\Delta x^{(b)}$, $\Delta y^{(b)}$, and $\Delta z^{(b)}$ are the three optically active Cartesian coordinates of the bth atom of the Bravais cell, and n the number of atoms in the Bravais cell. The elements of $\mathbf{B}_{op}{}^s$ associated with the redundant Cartesian symmetry coordinates and the corresponding $\mathbf{F}_{op}{}^{cs}$ matrix elements are all equal to zero. The nonvanishing elements may now be used in calculating the normal frequencies and normal modes.

EXAMPLE I. A ONE-DIMENSIONAL LATTICE

A. Use of the Internal Coordinates

Suppose a one-dimensional lattice of infinite length in which two kinds of atoms (1) and (2) are arranged alternately, with an equilibrium distance, r (see Fig. 1). The Bravais cells of such a lattice are shown by the dotted rectangles in Fig. 1. These cells are indexed by $\cdots, i-1, i, i+1, \cdots$, and the atomic distances at a certain moment are designated as $\cdots; r_{i-1}, r_{i-1}'; r_i, r_i'; r_{i+1}, r_{i+1}'; \cdots$. The $\mathbf{G}$ matrix with repsect to the internal coordinates, $\cdots, \Delta r_i=r_i-r, \Delta r'=r_i'-r\cdots$, is given as

[10] T. Shimanouchi, Jikken Kagaku Koza (compiled by Chem. Soc. Japan) **3**, 231 (1957).

[11] T. Miyazawa, J. Chem. Phys. **29**, 246 (1958).

[12] $\mathbf{U}\dagger$ is the conjugate transpose matrix of $\mathbf{U}$.

$$
\mathbf{G}=\begin{array}{c|cccccc}
 & \cdots\ \Delta r_{i-1} & \Delta r_{i-1}' & \Delta r_i & \Delta r_i' & \Delta r_{i+1} & \Delta r_{i+1}'\ \cdots \\
\hline
\Delta r_{i-1} & \mu_1+\mu_2 & -\mu_2 & 0 & 0 & 0 & 0 \\
\Delta r_{i-1}' & -\mu_2 & \mu_1+\mu_2 & -\mu_1 & 0 & 0 & 0 \\
\Delta r_i & 0 & -\mu_1 & \mu_1+\mu_2 & -\mu_2 & 0 & 0 \\
\Delta r_i' & 0 & 0 & -\mu_2 & \mu_1+\mu_2 & -\mu_1 & 0 \\
\Delta r_{i+1} & 0 & 0 & 0 & -\mu_1 & \mu_1+\mu_2 & -\mu_2 \\
\Delta r_{i+1}' & 0 & 0 & 0 & 0 & -\mu_2 & \mu_1+\mu_2
\end{array}
$$

Here, μ_1 and μ_2 are the reciprocal masses of atoms (1) and (2), respectively. If the potential energy V of this system is assumed to be

$$2V=K[\cdots+(\Delta r_i)^2+(\Delta r_i')^2+\cdots], \tag{23}$$

then, the F matrix becomes

$$
\mathbf{F}=\begin{array}{c|cccccc}
 & \cdots\ \Delta r_{i-1} & \Delta r_{i-1}' & \Delta r_i & \Delta r_i' & \Delta r_{i+1} & \Delta r_{i+1}'\ \cdots \\
\hline
\Delta r_{i-1} & K & 0 & 0 & 0 & 0 & 0 \\
\Delta r_{i-1}' & 0 & K & 0 & 0 & 0 & 0 \\
\Delta r_i & 0 & 0 & K & 0 & 0 & 0 \\
\Delta r_i' & 0 & 0 & 0 & K & 0 & 0 \\
\Delta r_{i+1} & 0 & 0 & 0 & 0 & K & 0 \\
\Delta r_{i+1}' & 0 & 0 & 0 & 0 & 0 & K
\end{array}
$$

As has been mentioned above, the **G** or **F** matrix for the optically active vibrations ($\mathbf{G}_{op}{}^i$ or $\mathbf{F}_{op}{}^i$) can be obtained by adding the submatrix corresponding to a Bravais cell to the sum of the submatrices representing interactions between the Bravais cell in question and the neighboring Bravais cells. These submatrices are indicated by dotted rectangles in the **G** and **F** matrices given above. The $\mathbf{G}_{op}{}^i$ and $\mathbf{F}_{op}{}^i$ are now given as

$$\mathbf{G}_{op}{}^i=\begin{pmatrix}0 & -\mu_1\\ 0 & 0\end{pmatrix}+\begin{pmatrix}\mu_1+\mu_2 & -\mu_2\\ -\mu_2 & \mu_1+\mu_2\end{pmatrix}+\begin{pmatrix}0 & 0\\ -\mu_1 & 0\end{pmatrix}=\begin{pmatrix}\mu_1+\mu_2 & -(\mu_1+\mu_2)\\ -(\mu_1+\mu_2) & \mu_1+\mu_2\end{pmatrix}$$

and

$$\mathbf{F}_{\mathrm{op}}{}^{i}=\begin{pmatrix}0 & 0\\ 0 & 0\end{pmatrix}+\begin{pmatrix}K & 0\\ 0 & K\end{pmatrix}+\begin{pmatrix}0 & 0\\ 0 & 0\end{pmatrix}=\begin{pmatrix}K & 0\\ 0 & K\end{pmatrix},$$

respectively. In the present case, the vector $\mathbf{R}_{ijk}$ in Eqs. (3) and (4) corresponds to

$$\begin{pmatrix}\Delta\boldsymbol{r}_i\\ \Delta\boldsymbol{r}_i'\end{pmatrix}$$

and the vectors $\boldsymbol{R}_{i'j'k'}$'s are

$$\begin{pmatrix}\Delta\boldsymbol{r}_{i-1}\\ \Delta\boldsymbol{r}_{i-1}'\end{pmatrix},\quad \begin{pmatrix}\Delta\boldsymbol{r}_i\\ \Delta\boldsymbol{r}_i'\end{pmatrix},\quad \text{and}\quad \begin{pmatrix}\Delta\boldsymbol{r}_{i+1}\\ \Delta\boldsymbol{r}_{i+1}'\end{pmatrix}.$$

The new coordinates $\mathbf{R}_{\mathrm{op}}$, with respect to which the $\mathbf{G}_{\mathrm{op}}{}^{i}$ and $\Pi{:}\mathbf{r}^{i}$ is given, may be expressed as

$$\Delta\boldsymbol{r}=N\sum_i\Delta\boldsymbol{r}^i,$$

$$\Delta\boldsymbol{r}'=N\sum_i\Delta\boldsymbol{r}_i'.$$

Let us use a set of symmetry coordinates,

$$S_1=(\Delta\boldsymbol{r}+\Delta\boldsymbol{r}')/\sqrt{2}$$

and

$$S_2=(\Delta\boldsymbol{r}-\Delta\boldsymbol{r}')/\sqrt{2}.$$

Then, the transformation matrix is

$$\mathbf{U}=\begin{pmatrix}1/\sqrt{2} & 1/\sqrt{2}\\ 1/\sqrt{2} & -1/\sqrt{2}\end{pmatrix},$$

and we obtain

$$\mathbf{G}_{\mathrm{op}}{}^{ii}=\mathbf{U}\mathbf{G}_{\mathrm{op}}{}^{i}\mathbf{U}^{t}=\begin{pmatrix}0 & 0\\ 0 & 2(\mu_1+\mu_2)\end{pmatrix}$$

and

$$\mathbf{F}_{\mathrm{op}}{}^{ii}=\mathbf{U}\mathbf{F}_{\mathrm{op}}{}^{i}\mathbf{U}^{t}=\begin{pmatrix}K & 0\\ 0 & K\end{pmatrix}.$$

S_1 is now proved to be redundant. For S_2, the secular equation (1) is given as

$$2(\mu_1+\mu_2)K-\lambda=0.$$

Hence,

$$\lambda=2(\mu_1+\mu_2)K. \tag{24}$$

This gives the frequency of the vibration whose mode is shown in Fig. 2.

For the two-dimensional and three-dimensional NaCl-type lattices shown respectively in Figs. 3 and 4, it is shown that the frequencies of the doubly degenerate and triply degenerate infrared-active vibrations are also given by Eq. (24), if only the stretching force constant K between the nearest neighbors is taken into consideration and all other force constants are neglected. Of the NaCl crystal, the absorption is at 164 cm^{-1}, and hence K is calculated to be 0.11 md/A from Eq. (24).

If we assume the angle bending force constants H_1 and H_2, respectively, around the atoms (1) and (2) in the one-dimensional lattice shown in Fig. 1, **G** and **F** matrices for a degenerate vibration with the mode shown in Fig. 5 are

$$\mathbf{G}_{\mathrm{op}}{}^{i}=8(\mu_1+\mu_2)r^{-2}$$

and

$$\mathbf{F}_{\mathrm{op}}{}^{i}=\tfrac{1}{2}(H_1+H_2)r^2,$$

respectively. Then, the frequency of this vibration is given by

$$\lambda=4(H_1+H_2)(\mu_1+\mu_2). \tag{25}$$

B. Use of the Cartesian Coordinates

Let the longitudinal displacements of the atoms in the one-dimensional lattice shown in Fig. 1 be

$$\cdots,\quad \Delta x_{i-1}{}^{(1)},\quad \Delta x_{i-1}{}^{(2)},\quad \Delta x_i{}^{(1)},\quad \Delta x_i{}^{(2)},$$

$$\Delta x_{i+1}{}^{(1)},\quad \Delta x_{i+1}{}^{(2)},\quad \cdots.$$

TABLE I. Some of the $\mathbf{B}_{\mathrm{op}}$ elements of the diamond lattice.

	Δx_α	Δy_α	Δz_α
Δr_1	0	0	1
Δr_2	$-2\sqrt{2}/3$	0	$-1/3$
Δr_3	$\sqrt{2}/3$	$-(6)^{\frac{1}{2}}/3$	$-1/3$
Δr_4	$\sqrt{2}/3$	$(6)^{\frac{1}{2}}/3$	$-1/3$
$\Delta\alpha_{12}$	$4\rho/3$	0	$-2\sqrt{2}\rho/3$
$\Delta\alpha_{13}$	$-2\rho/3$	$(12)^{\frac{1}{2}}\rho/3$	$-2\sqrt{2}\rho/3$
$\Delta\alpha_{14}$	$-2\rho/3$	$-(12)^{\frac{1}{2}}\rho/3$	$-2\sqrt{2}\rho/3$
$\Delta\alpha_{34}$	$-4\rho/3$	0	$2\sqrt{2}\rho/3$
$\Delta\alpha_{42}$	$2\rho/3$	$-(12)^{\frac{1}{2}}\rho/3$	$2\sqrt{2}\rho/3$
$\Delta\alpha_{23}$	$2\rho/3$	$(12)^{\frac{1}{2}}\rho/3$	$2\sqrt{2}\rho/3$

The inverse kinetic energy matrix $\mathbf{G}^c$ associated with these Cartesian coordinates is given as

$$\mathbf{G}^c=\begin{array}{c} \\ \\ \\ \Delta x_{i-1}^{(1)} \\ \Delta x_{i-1}^{(2)} \\ \\ \Delta x_i^{(1)} \\ \Delta x_i^{(2)} \\ \\ \Delta x_{i+1}^{(1)} \\ \Delta x_{i+1}^{(2)} \\ \\ \\ \end{array}\begin{array}{c} \begin{array}{cccccc} \cdots & \Delta x_{i-1}^{(1)} & \Delta x_{i-1}^{(2)} & \Delta x_i^{(1)} & \Delta x_i^{(2)} & \Delta x_{i+1}^{(1)} \end{array} \\ \begin{pmatrix} \ddots & & & & & & \\ & \ddots & & & & & \\ & & \ddots & & & & \\ & & & \mu_1 & 0 & 0 & 0 & 0 & 0 \\ & & & 0 & \mu_2 & 0 & 0 & 0 & 0 \\ & & & 0 & 0 & \mu_1 & 0 & 0 & 0 \\ & & & 0 & 0 & 0 & \mu_2 & 0 & 0 \\ & & & 0 & 0 & 0 & 0 & \mu_1 & 0 \\ & & & 0 & 0 & 0 & 0 & 0 & \mu_2 \\ & & & & & & & & \ddots \\ & & & & & & & & & \ddots \\ & & & & & & & & & & \ddots \end{pmatrix} \end{array}$$

In terms of the optically active Cartesian coordinates

$$\Delta x^{(1)}=N\sum_i \Delta x_i^{(1)}$$

and

$$\Delta x^{(2)}=N\sum_i \Delta x_i^{(2)},$$

the inverse kinetic energy matrix $\mathbf{G}_{\mathrm{op}}{}^c$ is given as

$$\mathbf{G}_{\mathrm{op}}{}^c=\begin{pmatrix} \mu_1 & 0 \\ 0 & \mu_2 \end{pmatrix}.$$

As given by Eq. (23), the potential function is assumed to be expressed in terms of $\Delta \boldsymbol{r}_i$, $\Delta \boldsymbol{r}_i'$, etc., and only the $\mathbf{B}$ matrix elements associated with $\Delta \boldsymbol{r}$ and $\Delta \boldsymbol{r}'$ are necessary. The $\mathbf{B}$ matrix in the present case is written as

$$\mathbf{B}=\begin{array}{c} \\ \\ \\ \Delta r_{i-1} \\ \Delta r_{i-1}' \\ \\ \Delta r_i \\ \Delta r_i' \\ \\ \Delta r_{i+1} \\ \Delta r_{i+1}' \\ \\ \\ \end{array}\begin{array}{c} \begin{array}{cccccc} \cdots & \Delta x_{i-1}^{(1)} & \Delta x_{i-1}^{(2)} & \Delta x_i^{(1)} & \Delta x_i^{(2)} & \Delta x_{i+1}^{(1)} \end{array} \\ \begin{pmatrix} \ddots & & & & & & \\ & \ddots & & & & & \\ & & \ddots & & & & \\ & & & -1 & 1 & 0 & 0 & 0 & 0 \\ & & & 0 & -1 & 1 & 0 & 0 & 0 \\ & & & 0 & 0 & -1 & 1 & 0 & 0 \\ & & & 0 & 0 & 0 & -1 & 1 & 0 \\ & & & 0 & 0 & 0 & 0 & -1 & 1 \\ & & & 0 & 0 & 0 & 0 & 0 & -1 \\ & & & & & & & & \ddots \\ & & & & & & & & & \ddots \\ & & & & & & & & & & \ddots \end{pmatrix} \end{array}$$

By making use of Eq. (18), the B matrix for the optically active vibrations is given by

$$\mathbf{B}_{\mathrm{op}}=\begin{pmatrix} 0 & 0 \\ 0 & 0 \end{pmatrix}+\begin{pmatrix} -1 & 1 \\ 0 & -1 \end{pmatrix}+\begin{pmatrix} 0 & 0 \\ 1 & 0 \end{pmatrix}=\begin{pmatrix} -1 & 1 \\ 1 & -1 \end{pmatrix}.$$

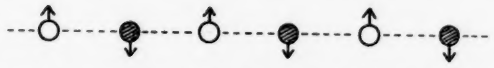

FIG. 5. The optically active deformation vibration of the one-dimensional lattice shown in Fig. 1.

The optically active Cartesian symmetry coordinate may now be derived to be

$$S=(\Delta x^{(1)}-\Delta x^{(2)})/\sqrt{2},$$

which is orthogonal to the redundant coordinate $(\Delta x^{(1)}+\Delta x^{(2)})/\sqrt{2}$. By Eqs. (22) and (21),

$$\mathbf{B}_{op}{}^{s}=\begin{pmatrix}-\sqrt{2}\\+\sqrt{2}\end{pmatrix}$$

and

$$\mathbf{F}_{op}{}^{cs}=\mathbf{B}_{op}{}^{s\dagger}\mathbf{F}_{op}{}^{t}\mathbf{B}_{op}{}^{s}=(-\sqrt{2}\quad+\sqrt{2})\begin{pmatrix}K&0\\0&K\end{pmatrix}\begin{pmatrix}-\sqrt{2}\\+\sqrt{2}\end{pmatrix}=4K.$$

The corresponding inverse kinetic energy matrix $\mathbf{G}_{op}{}^{cs}$ is

$$\mathbf{G}_{op}{}^{cs}=[1/\sqrt{2}\quad-1/\sqrt{2}]\begin{pmatrix}\mu_1&0\\0&\mu_2\end{pmatrix}\begin{pmatrix}1/\sqrt{2}\\-1/\sqrt{2}\end{pmatrix}=\tfrac{1}{2}(\mu_1+\mu_2).$$

Therefore

$$\lambda=2(\mu_1+\mu_2)K.$$

EXAMPLE II. DIAMOND LATTICE

As is well known, in the diamond lattice each carbon atom is surrounded by four carbon atoms which are located at the four corners of a tetrahedron with its center at the first carbon atom. The Bravais cell of this lattice contains two carbon atoms. By the group theoretical consideration, it is seen that the diamond lattice (belonging to $O_h{}^7$) has only one principal normal mode of vibration (class F_{2g}), which is triply degenerate and Raman active. The vibrational frequency and mode of this vibration are derived by the GF-matrix method as shown below.

TABLE II. $\mathbf{B}_{op}$ and $\mathbf{B}_{op}{}^{s}$ elements of the CaF_2 lattice.

	$\mathbf{B}_{op}$			$\mathbf{B}_{op}{}^{s}$	
	Δy_1	Δy_2	Δy_0	$S_1(F_{1u})$	$S_2(F_{2g})$
Δr_{01}	$1/\sqrt{3}$	0	$-1/\sqrt{3}$	$-1/\sqrt{2}$	$1/(6)^{\frac{1}{2}}$
Δr_{02}	0	$1/\sqrt{3}$	$-1/\sqrt{3}$	$-1/\sqrt{2}$	$-1/(6)^{\frac{1}{2}}$
$\Delta r_{01}'$	$-1/\sqrt{3}$	0	$1/\sqrt{3}$	$1/\sqrt{2}$	$-1/(6)^{\frac{1}{2}}$
$\Delta r_{02}'$	0	$-1/\sqrt{3}$	$1/\sqrt{3}$	$1/\sqrt{2}$	$1/(6)^{\frac{1}{2}}$
$\Delta r_{01}''$	$1/\sqrt{3}$	0	$-1/\sqrt{3}$	$-1/\sqrt{2}$	$1/(6)^{\frac{1}{2}}$
$\Delta r_{02}''$	0	$1/\sqrt{3}$	$-1/\sqrt{3}$	$-1/\sqrt{2}$	$-1/(6)^{\frac{1}{2}}$
$\Delta r_{01}'''$	$-1/\sqrt{3}$	0	$1/\sqrt{3}$	$1/\sqrt{2}$	$-1/(6)^{\frac{1}{2}}$
$\Delta r_{02}'''$	0	$-1/\sqrt{3}$	$1/\sqrt{3}$	$1/\sqrt{2}$	$1/(6)$
Δq_{12}	0	0	0	0	0
Δq_{21}	0	0	0	0	0
$\Delta q_{12}'$	1	-1	0	0	$\sqrt{2}$
$\Delta q_{21}'$	-1	1	0	0	$-\sqrt{2}$
$\Delta q_{12}''$	0	0	0	0	0
$\Delta q_{21}''$	0	0	0	0	0

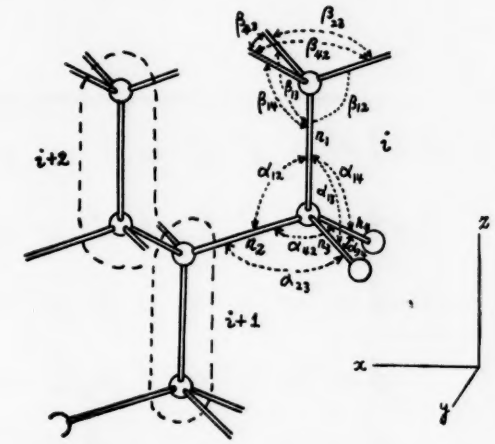

FIG. 6. Three adjoining Bravais cells in a diamond-type lattice.

A. Use of the Internal Coordinates

The Bravais cell of the diamond lattice is shown in Fig. 6. In the figure, one of the six nearest neighboring cells and one of the six next-nearest neighboring cells are also shown by dotted circles indicated as $i+1$ and $i+2$, respectively. The bonds and bond angles are denoted as indicated in Fig. 6. The $\mathbf{G}_{ii}$ is now given by

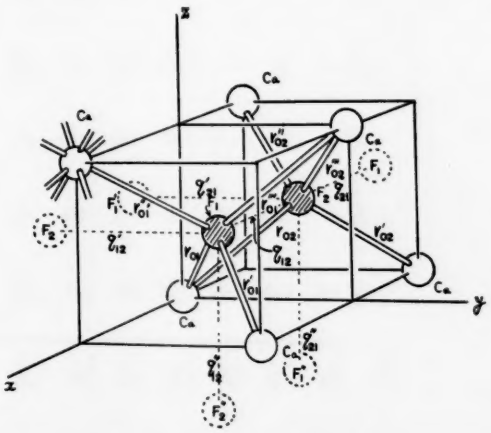

FIG. 7. The Bravais cell in the CaF_2 lattice.

	Δr_1	Δr_2	Δr_3	Δr_4	$\Delta\alpha_{12}$	$\Delta\alpha_{13}$	$\Delta\alpha_{14}$	$\Delta\alpha_{24}$	$\Delta\alpha_{42}$	$\Delta\alpha_{23}$	$\Delta\beta_{12}$	$\Delta\beta_{13}$	$\Delta\beta_{14}$	$\Delta\beta_{34}$	$\Delta\beta_{42}$	$\Delta\beta_{23}$
Δr_1	g_1															
Δr_2	g_5	g_1														
Δr_3	g_5	g_5	g_1													
Δr_4	g_5	g_5	g_5	g_1												
$\Delta\alpha_{12}$	g_6	g_6	g_7	g_7	g_2											
$\Delta\alpha_{13}$	g_6	g_7	g_6	g_7	g_{12}	g_2										
$\Delta\alpha_{14}$	g_6	g_7	g_7	g_6	g_{12}	g_{12}	g_2									
$\Delta\alpha_{34}$	g_7	g_7	g_6	g_6	g_{13}	g_{12}	g_{12}	g_2								
$\Delta\alpha_{42}$	g_7	g_6	g_7	g_6	g_{12}	g_{13}	g_{12}	g_{12}	g_2							
$\Delta\alpha_{23}$	g_7	g_6	g_6	g_7	g_{12}	g_{12}	g_{13}	g_{12}	g_{12}	g_2						
$\Delta\beta_{12}$	g_6	g_8	g_8'	g_8'	g_{11}	g_{11}'	g_{11}'	g_{14}	g_{14}'	g_{14}'	g_2					
$\Delta\beta_{13}$	g_6	g_8'	g_8	g_8'	g_{11}'	g_{11}	g_{11}'	g_{14}'	g_{14}	g_{14}'	g_{12}	g_2				
$\Delta\beta_{14}$	g_6	g_8'	g_8'	g_8	g_{11}'	g_{11}'	g_{11}	g_{14}'	g_{14}'	g_{14}	g_{12}	g_{12}	g_2			
$\Delta\beta_{34}$	g_7	0	0	0	g_{14}	g_{14}'	g_{14}'	0	0	0	g_{13}	g_{12}	g_{12}	g_2		
$\Delta\beta_{42}$	g_7	0	0	0	g_{14}'	g_{14}	g_{14}'	0	0	0	g_{12}	g_{13}	g_{12}	g_{12}	g_2	
$\Delta\beta_{23}$	g_7	0	0	0	g_{14}'	g_{14}'	g_{14}	0	0	0	g_{12}	g_{12}	g_{13}	g_{12}	g_{12}	g_2

Symmetric

,

and one of the six $\mathbf{G}_{i,i+1}$'s is given by

	Δr_1	Δr_2	Δr_3	Δr_4	$\Delta\alpha_{12}$	$\Delta\alpha_{13}$	$\Delta\alpha_{14}$	$\Delta\alpha_{34}$	$\Delta\alpha_{42}$	$\Delta\alpha_{23}$	$\Delta\beta_{12}$	$\Delta\beta_{13}$	$\Delta\beta_{14}$	$\Delta\beta_{34}$	$\Delta\beta_{42}$	$\Delta\beta_{23}$
Δr_1	0	0	0	0	0	0	0	0	0	0	g_8	0	0	0	g_8'	g_8'
Δr_2	g_5	0	0	0	g_8	g_8'	g_8'	0	0	0	g_6	g_7	g_7	g_7	g_6	g_6
Δr_3	0	0	0	0	0	0	0	0	0	0	g_8'	0	0	0	g_8'	g_8
Δr_4	0	0	0	0	0	0	0	0	0	0	g_8'	0	0	0	g_8	g_8'
$\Delta\alpha_{12}$	g_8	0	0	0	g_{15}	g_{15}'	g_{15}'	0	0	0	g_{11}	g_{14}'	g_{14}'	g_{14}	g_{11}'	g_{11}'
$\Delta\alpha_{13}$	0	0	0	0	0	0	0	0	0	0	g_{14}'	0	0	0	g_{14}	g_{14}'
$\Delta\alpha_{14}$	0	0	0	0	0	0	0	0	0	0	g_{14}'	0	0	0	g_{14}'	g_{14}
$\Delta\alpha_{34}$	0	0	0	0	0	0	0	0	0	0	g_{14}	0	0	0	g_{14}'	g_{14}'
$\Delta\alpha_{42}$	g_8'	0	0	0	g_{15}'	g_{15}''	g_{15}'''	0	0	0	g_{11}'	g_{14}	g_{14}'	g_{14}'	g_{11}	g_{11}'
$\Delta\alpha_{23}$	g_8'	0	0	0	g_{15}'	g_{15}'''	g_{15}''	0	0	0	g_{11}'	g_{14}'	g_{14}	g_{14}'	g_{11}'	g_{11}
$\Delta\beta_{12}$	0	0	0	0	0	0	0	0	0	0	g_{15}	0	0	0	g_{15}'	g_{15}'
$\Delta\beta_{13}$	0	0	0	0	0	0	0	0	0	0	g_{15}'	0	0	0	g_{15}''	g_{15}'''
$\Delta\beta_{14}$	0	0	0	0	0	0	0	0	0	0	g_{15}'	0	0	0	g_{15}'''	g_{15}''
$\Delta\beta_{34}$	0	0	0	0	0	0	0	0	0	0	0	0	0	0	0	0
$\Delta\beta_{42}$	0	0	0	0	0	0	0	0	0	0	0	0	0	0	0	0
$\Delta\beta_{23}$	0	0	0	0	0	0	0	0	0	0	0	0	0	0	0	0

The other five $\mathbf{G}_{i,i+1}$'s are obtained by displacements of the elements according to the rule of cyclic changes, 2→3, 3→4, and 4→2, of the suffices of Δr's, $\Delta\alpha$'s, and $\Delta\beta$'s, and by transposing the matrices. One of the six $\mathbf{G}_{i,i+2}$'s is

	Δr_1	Δr_2	Δr_3	Δr_4	$\Delta\alpha_{12}$	$\Delta\alpha_{13}$	$\Delta\alpha_{14}$	$\Delta\alpha_{34}$	$\Delta\alpha_{42}$	$\Delta\alpha_{23}$	$\Delta\beta_{12}$	$\Delta\beta_{13}$	$\Delta\beta_{14}$	$\Delta\beta_{34}$	$\Delta\beta_{42}$	$\Delta\beta_{23}$
Δr_1	0	0	0	0	0	0	0	0	0	0	0	0	0	0	0	0
Δr_2	0	0	g_5	0	0	g_8'	0	g_8'	0	g_8	0	0	0	0	0	0
Δr_3	0	0	0	0	0	0	0	0	0	0	0	0	0	0	0	0
Δr_4	0	0	0	0	0	0	0	0	0	0	0	0	0	0	0	0
$\Delta\alpha_{12}$	0	0	g_8'	0	0	g_{15}'''	0	g_{15}''	0	g_{15}'	0	0	0	0	0	0
$\Delta\alpha_{13}$	0	0	0	0	0	0	0	0	0	0	0	0	0	0	0	0
$\Delta\alpha_{14}$	0	0	0	0	0	0	0	0	0	0	0	0	0	0	0	0
$\Delta\alpha_{34}$	0	0	0	0	0	0	0	0	0	0	0	0	0	0	0	0
$\Delta\alpha_{42}$	0	0	g_8'	0	0	g_{15}''	0	g_{15}'''	0	g_{15}'	0	0	0	0	0	0
$\Delta\alpha_{23}$	0	0	g_8	0	0	g_{15}'	0	g_{15}'	0	g_{15}	0	0	0	0	0	0
$\Delta\beta_{12}$	0	0	0	0	0	0	0	0	0	0	0	0	0	0	0	0
$\Delta\beta_{13}$	0	0	0	0	0	0	0	0	0	0	g_{15}'''	0	0	0	g_{15}''	g_{15}'
$\Delta\beta_{14}$	0	0	0	0	0	0	0	0	0	0	0	0	0	0	0	0
$\Delta\beta_{34}$	0	0	0	0	0	0	0	0	0	0	g_{15}''	0	0	0	g_{15}'''	g_{15}'
$\Delta\beta_{42}$	0	0	0	0	0	0	0	0	0	0	0	0	0	0	0	0
$\Delta\beta_{23}$	0	0	0	0	0	0	0	0	0	0	g_{15}'	0	0	0	g_{15}'	g_{15}

The other five $\mathbf{G}_{i,i+2}$'s are obtained in the same way as that in which the $\mathbf{G}_{i,i+1}$'s are obtained. In these matrices, g_1, g_2, etc., represent the following:

$$g_1=2\mu,\quad g_2=\tfrac{14}{3}\rho^2\mu,\quad g_5=-\tfrac{1}{3}\mu,\quad g_6=-\tfrac{2}{3}\sqrt{2}\rho\mu,\quad g_7=\tfrac{2}{3}\sqrt{2}\rho\mu,\quad g_8=-\tfrac{2}{3}\sqrt{2}\rho\mu,\quad g_8'=\tfrac{1}{3}\sqrt{2}\rho\mu,\quad g_{11}=\tfrac{8}{3}\rho^2\mu,\quad g_{11}'=-\tfrac{4}{3}\rho^2\mu,$$
$$g_{12}=-\tfrac{1}{2}\rho^2\mu,\quad g_{13}=-\tfrac{8}{3}\rho^2\mu,\quad g_{14}=\tfrac{2}{3}\rho^2\mu,\quad g_{14}'=-\tfrac{4}{3}\rho^2\mu,\quad g_{15}=\tfrac{1}{3}\rho^2\mu,\quad g_{15}'=-\tfrac{1}{6}\rho^2\mu,\quad g_{15}''=-\tfrac{2}{3}\rho^2\mu,\quad g_{15}'''=\tfrac{8}{6}\rho^2\mu,$$

where, μ is the reciprocal mass of the carbon atom and ρ is the reciprocal of the C—C bond length r in the diamond lattice. By the addition of all these thirteen matrices,

$$\mathbf{G}_{op}{}^{i}=$$

	Δr_1	Δr_2	Δr_3	Δr_4	$\Delta\alpha_{12}$	$\Delta\alpha_{13}$	$\Delta\alpha_{14}$	$\Delta\alpha_{34}$	$\Delta\alpha_{42}$	$\Delta\alpha_{23}$	$\Delta\beta_{12}$	$\Delta\beta_{13}$	$\Delta\beta_{14}$	$\Delta\beta_{34}$	$\Delta\beta_{42}$	$\Delta\beta_{23}$
Δr_1	A															
Δr_2	C	A														
Δr_3	C	C	A													
Δr_4	C	C	C	A												
$\Delta\alpha_{12}$	K	K	L	L	B											
$\Delta\alpha_{13}$	K	L	K	L	0	B										
$\Delta\alpha_{14}$	K	L	L	K	0	0	B									
$\Delta\alpha_{34}$	L	L	K	K	D	0	0	B								
$\Delta\alpha_{42}$	L	K	L	K	0	D	0	0	B							
$\Delta\alpha_{23}$	L	K	K	L	0	0	D	0	0	B						
$\Delta\beta_{12}$	K	K	L	L	B	0	0	D	0	0	B					
$\Delta\beta_{13}$	K	L	K	L	0	B	0	0	D	0	0	B				
$\Delta\beta_{14}$	K	L	L	K	0	0	B	0	0	D	0	0	B			
$\Delta\beta_{34}$	L	L	K	K	D	0	0	B	0	0	D	0	0	B		
$\Delta\beta_{42}$	L	K	L	K	0	D	0	0	B	0	0	D	0	0	B	
$\Delta\beta_{23}$	L	K	K	L	0	0	D	0	0	B	0	0	D	0	0	B

SYMMETRIC

is obtained, where

$$A=g_1=2\mu \qquad D=g_{13}+4g_{15}''=-\tfrac{16}{3}\mu\rho^2$$
$$B=g_2+2g_{15}=\tfrac{16}{3}\mu\rho^2 \qquad K=g_6+g_8=-\tfrac{4}{3}\sqrt{2}\mu\rho$$
$$C=2g_5=-\tfrac{2}{3}\mu \qquad L=g_7+2g_9'=\tfrac{4}{3}\sqrt{2}\mu\rho$$

By use of the transforming matrix,

$$\mathbf{U}=\begin{array}{c|cccccccc}
 & \Delta r_1 & \Delta r_2 & \Delta r_3 & \Delta r_4 & \Delta\alpha_{12} & \Delta\alpha_{13} & \Delta\alpha_{14} & \Delta\alpha_{34} \\ \hline
 & 3(12^{-\frac{1}{2}}) & -(12^{-\frac{1}{2}}) & -(12^{-\frac{1}{2}}) & -(12^{-\frac{1}{2}}) & 0 & 0 & 0 & 0 \\
 & 0 & 0 & 0 & 0 & 12^{-\frac{1}{2}} & 12^{-\frac{1}{2}} & 12^{-\frac{1}{2}} & -(12^{-\frac{1}{2}}) \\
 & 0 & 2(6^{-\frac{1}{2}}) & -(6^{-\frac{1}{2}}) & -(6^{-\frac{1}{2}}) & 0 & 0 & 0 & 0 \\
 & 0 & 0 & 0 & 0 & 2(24^{-\frac{1}{2}}) & -(24^{-\frac{1}{2}}) & -(24^{-\frac{1}{2}}) & -2(24^{-\frac{1}{2}}) \\
 & 0 & 0 & 2^{-\frac{1}{2}} & -(2^{-\frac{1}{2}}) & 0 & 0 & 0 & 0 \\
 & 0 & 0 & 0 & 0 & 0 & 8^{-\frac{1}{2}} & -(8^{-\frac{1}{2}}) & 0 \\
 & \tfrac{1}{2} & \tfrac{1}{2} & \tfrac{1}{2} & \tfrac{1}{2} & 0 & 0 & 0 & 0 \\
 & 0 & 0 & 0 & 0 & 12^{-\frac{1}{2}} & 12^{-\frac{1}{2}} & 12^{-\frac{1}{2}} & 12^{-\frac{1}{2}} \\
 & 0 & 0 & 0 & 0 & 12^{-\frac{1}{2}} & 12^{-\frac{1}{2}} & 12^{-\frac{1}{2}} & 12^{-\frac{1}{2}} \\
 & 0 & 0 & 0 & 0 & 0 & 8^{-\frac{1}{2}} & -(8^{-\frac{1}{2}}) & 0 \\
 & 0 & 0 & 0 & 0 & 0 & 8^{-\frac{1}{2}} & -(8^{-\frac{1}{2}}) & 0 \\
 & 0 & 0 & 0 & 0 & 2(24^{-\frac{1}{2}}) & -(24^{-\frac{1}{2}}) & -(24^{-\frac{1}{2}}) & 2(24^{-\frac{1}{2}}) \\
 & 0 & 0 & 0 & 0 & 2(24^{-\frac{1}{2}}) & -(24^{-\frac{1}{2}}) & -(24^{-\frac{1}{2}}) & 2(24^{-\frac{1}{2}}) \\
 & 0 & 0 & 0 & 0 & 12^{-\frac{1}{2}} & 12^{-\frac{1}{2}} & 12^{-\frac{1}{2}} & -(12^{-\frac{1}{2}}) \\
 & 0 & 0 & 0 & 0 & 2(24^{-\frac{1}{2}}) & -(24^{-\frac{1}{2}}) & -(24^{-\frac{1}{2}}) & -2(24^{-\frac{1}{2}}) \\
 & 0 & 0 & 0 & 0 & 0 & 8^{-\frac{1}{2}} & -(8^{-\frac{1}{2}}) & 0
\end{array}$$

we are led to

$$G_{\mathrm{op}}{}^{is}=\begin{Vmatrix} A-C & 2(K-L) \\ 2(K-L) & 2(B-D) \end{Vmatrix}=\begin{Vmatrix} \frac{8}{3}\mu & \frac{-16\sqrt{2}}{3}\mu\rho \\ \frac{-16\sqrt{2}}{3}\mu\rho & \frac{64}{3}\mu\rho^2 \end{Vmatrix},$$

which corresponds to two sets of triply degenerate vibrations.

$\Delta\alpha_{42}$	$\Delta\alpha_{23}$	$\Delta\beta_{12}$	$\Delta\beta_{13}$	$\Delta\beta_{14}$	$\Delta\beta_{34}$	$\Delta\beta_{42}$	$\Delta\beta_{23}$	
0	0	0	0	0	0	0	0	S_1' } Triply degenerate vibrations
$-(12^{-\frac{1}{2}})$	$-(12^{-\frac{1}{2}})$	$12^{-\frac{1}{2}}$	$12^{-\frac{1}{2}}$	$12^{-\frac{1}{2}}$	$-(12^{-\frac{1}{2}})$	$-(12^{-\frac{1}{2}})$	$-(12^{-\frac{1}{2}})$	S_2' }
0	0	0	0	0	0	0	0	S_1'' }
$24^{-\frac{1}{2}}$	$24^{-\frac{1}{2}}$	$2(24^{-\frac{1}{2}})$	$-(24^{-\frac{1}{2}})$	$-(24^{-\frac{1}{2}})$	$-2(24^{-\frac{1}{2}})$	$24^{-\frac{1}{2}}$	$24^{-\frac{1}{2}}$	S_2'' }
0	0	0	0	0	0	0	0	S_1''' }
$-(8^{-\frac{1}{2}})$	$8^{-\frac{1}{2}}$	0	$8^{-\frac{1}{2}}$	$-(8^{-\frac{1}{2}})$	0	$-(8^{-\frac{1}{2}})$	$8^{-\frac{1}{2}}$	S_2''' }
0	0	0	0	0	0	0	0	
$12^{-\frac{1}{2}}$	$12^{-\frac{1}{2}}$	$12^{-\frac{1}{2}}$	$12^{-\frac{1}{2}}$	$12^{-\frac{1}{2}}$	$12^{-\frac{1}{2}}$	$12^{-\frac{1}{2}}$	$12^{-\frac{1}{2}}$	
$12^{-\frac{1}{2}}$	$12^{-\frac{1}{2}}$	$-(12^{-\frac{1}{2}})$	$-(12^{-\frac{1}{2}})$	$-(12^{-\frac{1}{2}})$	$-(12^{-\frac{1}{2}})$	$-(12^{-\frac{1}{2}})$	$-(12^{-\frac{1}{2}})$	Redundant coordinates
$8^{-\frac{1}{2}}$	$-(8^{-\frac{1}{2}})$	0	$8^{-\frac{1}{2}}$	$-(8^{-\frac{1}{2}})$	0	$8^{-\frac{1}{2}}$	$-(8^{-\frac{1}{2}})$	
$8^{-\frac{1}{2}}$	$-(8^{-\frac{1}{2}})$	0	$-(8^{-\frac{1}{2}})$	$8^{-\frac{1}{2}}$	0	$-(8^{-\frac{1}{2}})$	$8^{-\frac{1}{2}}$	
$-(24^{-\frac{1}{2}})$	$-(24^{-\frac{1}{2}})$	$2(24^{-\frac{1}{2}})$	$-(24^{-\frac{1}{2}})$	$-(24^{-\frac{1}{2}})$	$2(24^{-\frac{1}{2}})$	$-(24^{-\frac{1}{2}})$	$-(24^{-\frac{1}{2}})$	
$-(24^{-\frac{1}{2}})$	$-(24^{-\frac{1}{2}})$	$-2(24^{-\frac{1}{2}})$	$24^{-\frac{1}{2}}$	$24^{-\frac{1}{2}}$	$-2(24^{-\frac{1}{2}})$	$24^{-\frac{1}{2}}$	$24^{-\frac{1}{2}}$	
$-(12^{-\frac{1}{2}})$	$-(12^{-\frac{1}{2}})$	$-(12^{-\frac{1}{2}})$	$-(12^{-\frac{1}{2}})$	$-(12^{-\frac{1}{2}})$	$12^{-\frac{1}{2}}$	$12^{-\frac{1}{2}}$	$12^{-\frac{1}{2}}$	
$24^{-\frac{1}{2}}$	$24^{-\frac{1}{2}}$	$-2(24^{-\frac{1}{2}})$	$24^{-\frac{1}{2}}$	$24^{-\frac{1}{2}}$	$2(24^{-\frac{1}{2}})$	$-1(24^{-\frac{1}{2}})$	$(-24^{-\frac{1}{2}})$	
$-(8^{-\frac{1}{2}})$	$8^{-\frac{1}{2}}$	0	$-(8^{-\frac{1}{2}})$	$8^{-\frac{1}{2}}$	0	$8^{-\frac{1}{2}}$	$-(8^{-\frac{1}{2}})$	,

If the potential energy of the diamond lattice is expressed[13] by

$$2V=\sum_i K(\Delta r_i)^2+\sum_{i,j} H(r\Delta\alpha_{ij})^2,$$

the **F** matrix corresponding to the above $\mathbf{G}_{\text{op}}{}^{i}$ (namely $\mathbf{F}_{\text{op}}{}^{i}$) is given by

[13] The potential constant of the steric repulsion between the two nearest carbon atoms that are not directly bonded is not concerned with the optically active vibrations, since in these vibrations these carbon atoms should move in phase and hence the distance between these carbon atoms remain constant.

	Δr_1	Δr_2	Δr_3	Δr_4	$\Delta\alpha_{12}$	$\Delta\alpha_{13}$	$\Delta\alpha_{14}$	$\Delta\alpha_{34}$
Δr_1	K							
Δr_2		K						
Δr_3			K					
Δr_4				K				
$\Delta\alpha_{12}$					Hr^2			
$\Delta\alpha_{13}$						Hr^2		
$\Delta\alpha_{14}$							Hr^2	
$\Delta\alpha_{34}$								Hr^2
$\Delta\alpha_{42}$	(off-diagonal elements are all zero)							
$\Delta\alpha_{23}$								
$\Delta\beta_{12}$								
$\Delta\beta_{13}$								
$\Delta\beta_{14}$								
$\Delta\beta_{34}$								
$\Delta\beta_{42}$								
$\Delta\beta_{23}$								

and the $\mathbf{F}$ matrix corresponding to the above $\mathbf{G}_{op}{}^{is}$ is calculated to be

$$\mathbf{F}_{op}{}^{is}=\begin{pmatrix} K & 0 \\ 0 & r^2H \end{pmatrix}.$$

From these $\mathbf{G}_{op}{}^{is}$ and $\mathbf{F}_{op}{}^{is}$, using Eq. (1), we obtain

$$\lambda=0$$

and

$$\lambda=\mu\left[\tfrac{8}{3}K+\tfrac{64}{3}H\right]. \qquad (26)$$

Applying the values in the force constants table given by Shimanouchi[14] to the present case $K=2.8$ md/A and $H=0.24$ md/A. From these values of force constants, the frequency of the lattice vibration corresponding to Eq. (26) is calculated to be $\nu=1334$ cm^{-1}. This is in good accordance with the observed frequency, 1332 cm^{-1}, in the Raman spectrum of diamond.[15]

[14] T. Shimanouchi, J. Chem. Phys **17**, 848 (1949).
[15] Referred by M. Lox and E. Burstein, Phys. Rev. **97**, 39 (1955).

B. Use of the Cartesian Coordinates

As is shown in Fig. 6, the z axis is taken along the r_1 bond, x axis in the r_1r_2 plane along the perpendicular direction to the z axis, and the y axis along the direction perpendicular to both the z and x axes. Let the two carbon atoms in a Bravais cell be called α and β. The optically active Cartesian coordinates M:r are now designated as Δx_α, Δx_β, Δy_α, Δy_β, Δz_α, and Δz_β. With respect to these coordinates, the inverse kinetic energy matrix $\mathbf{G}$:r is given as a sixth-order constant matrix, and each element of it is equal to the reciprocal mass of the carbon atom μ. The optically active Cartesian symmetry coordinates may be chosen as $S^a=(\Delta x_\alpha-\Delta x_\beta)/\sqrt{2}$, $S^b=(\Delta y_\alpha-\Delta y_\beta)/\sqrt{2}$, and $S^c=(\Delta z_\alpha-\Delta z_\beta)/\sqrt{2}$. These are orthogonal to one another and to the redundant coordinates, $(\Delta x_\alpha+\Delta x_\beta)/\sqrt{2}$, $(\Delta y_\alpha+\Delta y_\beta)/\sqrt{2}$, and $(\Delta z_\alpha+\Delta z_\beta)/\sqrt{2}$. The inverse kinetic energy matrix associated with these optically active Cartesian symmetry coordinates becomes

$$\mathbf{G}_{op}{}^{cs}=\begin{pmatrix} \mu & 0 & 0 \\ 0 & \mu & 0 \\ 0 & 0 & \mu \end{pmatrix}.$$

EXAMPLE III. CaF_2 LATTICE

As shown in Fig. 7, there are one calcium atom and two fluorine atoms per Bravais cell of the CaF_2 lattice. The CaF_2 crystal belongs to the space group O_h^5 and has only one F_{1u} type vibration (infrared active) and one F_{2g} type vibration (Raman active). As we have seen in the case of diamond, optically active modes in a cubic crystal are all triply degenerate and the frequencies are the same for the optically active vibrational displacements in the x, y, and z directions. Therefore, in calculating optically active frequencies of the CaF_2 crystal we may take into account only the displacements along any one of the x, y, and z coordinates. In the present case, the $\mathbf{B}_{op}$ elements associated with the optically active y coordinates have been calculated.

The CaF_2 crystal is highly ionic and the potential function may be expressed as the sum of the bond stretching terms associated with the Ca—F distances and the sum of the repulsion terms associated with the F···F nonbonded ion pairs. As long as we are concerned with the optically active frequencies, the repulsion terms associated with the Ca···Ca nonbonded ion pair need not be considered since there is only one calcium ion per Bravais cell and, in optically active

For constructing the corresponding potential energy matrix $\mathbf{F}_{op}{}^{cs}$, it is necessary to obtain

$$\mathbf{B}_{op}{}^{s}=\mathbf{B}_{op}\mathbf{U}^{\dagger},$$

where $\mathbf{B}_{op}$ is given by Eq. (17) or (18). Of the $\mathbf{B}_{op}$ elements, those related to Δx_α, Δy_α, Δz_α; and Δr's and $\Delta\alpha$'s, are shown in Table I. The $\mathbf{B}_{op}$ element related to $\Delta\beta_{ij}$ is equal to the corresponding element related to $\Delta\alpha_{ij}$. The elements related to Δx_β, Δy_β, and Δz_β are equal, respectively, to those related to Δx_α, Δy_α, and Δz_α with opposite signs. The potential energy matrix in terms of the optically-active Cartesian symmetry coordinates is now given as

$$\mathbf{F}_{op}{}^{cs}=\mathbf{U}\mathbf{B}_{op}{}^{t}\mathbf{F}_{op}{}^{i}\mathbf{B}_{op}\mathbf{U}^{\dagger}$$

$$=\begin{pmatrix} \frac{8}{3}K+\frac{64}{3}H & 0 & 0 \\ 0 & \frac{8}{3}K+\frac{64}{3}H & 0 \\ 0 & 0 & \frac{8}{3}K+\frac{64}{3}H \end{pmatrix}.$$

Therefore, for this triply degenerate vibration,

$$\lambda=(\tfrac{8}{3}K+\tfrac{64}{3}H)\mu.$$

vibrations, all the calcium ions in the crystal should move in phase without causing any change in the Ca···Ca distances.

By the group theoretical consideration, the optically active Cartesian symmetry coordinates may be expressed, as shown below, in terms of the optically active y coordinates:

$$S_1(F_{1u}) = [1/(6)^{\frac{1}{2}}](-\Delta y_1 - \Delta y_2 + 2\Delta y_0),$$

$$S_2(F_{2g}) = (1/\sqrt{2})(\Delta y_2 - \Delta y_2),$$

and

$$S_3(\text{redundant}) = 1/\sqrt{3}(\Delta y_1 + \Delta y_2 + \Delta y_0).$$

where Δy_1, Δy_2, and Δy_0 are the optically active coordinates associated with the F_1, F_2, and Ca ions, respectively (see Fig. 7). The $\mathbf{B}_{op}$ and $\mathbf{B}_{op}{}^{\alpha}$ matrix elements derived are presented in Table II (Δq's are the changes in the F···F distances between the nonbonded ion pairs, see Fig. 7).

Making use of Eq. (21), the $\mathbf{F}_{op}{}^{\alpha\beta}$ matrix elements have been derived from the $\mathbf{B}_{op}{}^{\alpha}$ elements and the potential function V,

$$2V = \sum K(\Delta r)^2 + \sum F(\Delta q)^2,$$

where K and F are the force constants for the Ca—F bond stretching and for the F···F repulsion, respectively. The $\mathbf{G}_{op}{}^{\alpha\beta}$ elements for the F_{1u} and F_{2g} vibrations have been obtained by the use of Eq. (20). For the F_{1u} vibration, which is infrared active,

$$\mathbf{G}_{op}{}^{\alpha\beta} = \tfrac{1}{3}\mu_F + \tfrac{2}{3}\mu_{Ca},$$

$$\mathbf{F}_{op}{}^{\alpha\beta} = 4K,$$

$$\lambda = \tfrac{4}{3}K(\mu_F + 2\mu_{Ca}), \tag{27}$$

and for the F_{2g} vibration, which is Raman active,

$$\mathbf{G}_{op}{}^{\alpha\beta} = \mu_F$$

$$\mathbf{F}_{op}{}^{\alpha\beta} = \tfrac{4}{3}K + 4F$$

$$\lambda = \tfrac{4}{3}(K + 3F)\mu_F, \tag{28}$$

where μ_F and μ_{Ca} are the reciprocal masses of the F and Ca ions, respectively.

For the CaF_2 crystal, infrared absorption[16] is observed at about 270 cm^{-1} and Raman effect[17] at 321.5 cm^{-1}. Therefore, from Eqs. (27) and (28), K and F are calculated to be, respectively, 0.31 and 0.18 md/A.

[16] H. Yoshinaga, A. Mitsuishi, and Y. Yamada (private communication).

[17] F. Rasetti, Nature **127**, 626 (1931).

THE JOURNAL OF CHEMICAL PHYSICS VOLUME 35, NUMBER 5 NOVEMBER, 1961

Crystal Spectra of Metal Coordination Compounds. VI. Bis-Salicylaldiminato-Copper (II) and Bis-*N*-Methyl-Salicylaldiminato-Copper (II)

J. FERGUSON

Division of Chemical Physics, C.S.I.R.O. Chemical Research Laboratories, Melbourne, Australia

(Received March 2, 1961)

The polarized crystal absorption spectra of bis-N-methylsalicylaldiminato-copper (II) and bis-salicylaldiminato-copper (II) are reported. In each case measurements have been made with two different crystal faces. An analysis of the spectra shows that the ligand field is rhombic (D_{2h}) and the in-plane symmetry axes do not lie along metal-ligand bonds but between them, as reported previously for the corresponding nickel compounds. The effect of copper-copper interaction in the crystal is briefly discussed.

INTRODUCTION

AN earlier study of the polarized crystal spectrum of bis-*N*-methylsalicylaldiminato-nickel (II)[1] yielded interesting information about the symmetry of the ligand field. It was found that this field is strongly rhombic (D_{2h}) and contrary to expectation it has symmetry axes bisecting ligand-metal bond angles rather than along the bonds. As a result it was suggested that the simple crystal field approach, in which the ligands are replaced by point dipoles, is not a good one and some account should be taken of the geometry of the ligand orbitals. This suggestion is quite general and if valid it should apply to other metal chelates. It was confirmed for bis-acetylacetonato-copper (II)[2] and the present paper extends the study to two other copper compounds: bis-*N*-methylsalicylaldiminato-copper (II) (hereafter called I) and bis-salicyladiminato-copper (II) (hereafter called II).

It is possible to decide the symmetry of the ligand field in two different ways. Firstly, the in-plane dichroism of the absorption bands can be measured and compared with the predictions of the two choices for

[1] J. Ferguson, J. Chem. Phys. **34**, 611 (1961).

[2] J. Ferguson, J. Chem. Phys. **34**, 1609 (1961).

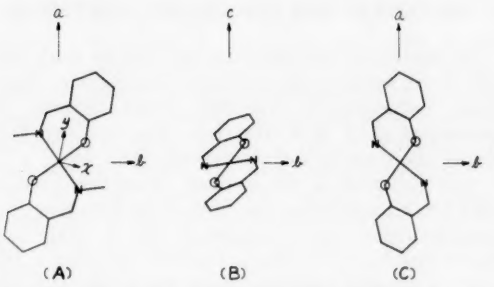

FIG. 1. (A) Projection of the molecule of bis-*N*-methylsalicylaldiminato-copper (II) on the (001) face of the crystal. (B) Projection of the molecule of bis-salicylaldiminato-copper (II) on the (100) face of the crystal. (C) Projection of the molecule of bis-salicylaldiminato-copper (II) on the (001) face of the crystal.

the in-plane symmetry axes. Secondly, for reasons given later, the presence of two bands strongly polarized in the plane of the molecule would indicate that the symmetry axes bisect the metal-ligand bond angles.

The second method depends upon the acceptance of the usual mechanism[3] invoked to explain the appearance of the otherwise forbidden electronic transitions. Granted this, the two methods lead to the same conclusion about the symmetry of the ligand field and a consistent assignment of the bands in the two compounds can be made.

CRYSTAL STRUCTURES

Compound I crystallizes in the orthorhombic system and the orientation of the molecule has been determined by two groups of workers.[4] The needles, which are grown easily from chloroform solution, show

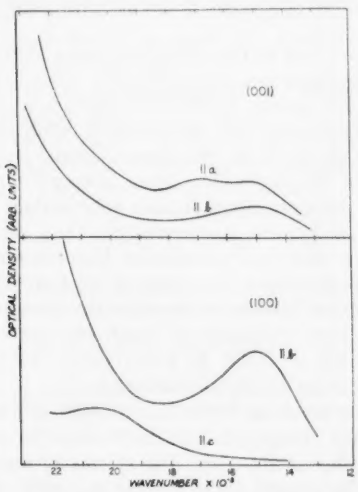

FIG. 2. Crystal spectrum of bis-*N*-metnylsalicylaldiminato-copper (II) for light incident on the (001) and (100) faces.

[3] A. D. Liehr and C. J. Ballhausen, Phys. Rev. **106,** 1161 (1957).

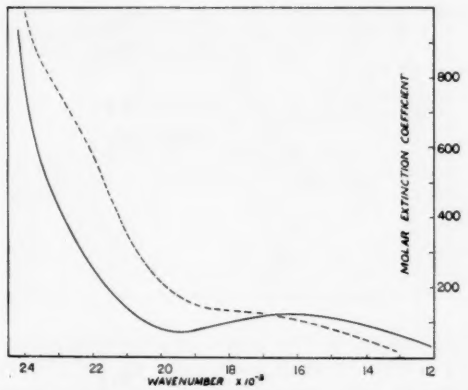

FIG. 3. Solution spectrum of bis-*N*-methylsalicylaldiminato-copper (II) ------ chloroform ——— pyridine.

marked dichroism, appearing red for the electric vector parallel to the needle axis (c) and green perpendicular to it. The well-developed face is the (100); the (001) face was obtained by sectioning the crystals with a hand microtome. The plane of the molecule lies exactly parallel to the (001) face, and the x and y axes each make an angle of 10° with the b and a crystal axes, respectively [Fig. 1(a)]. The projection that the molecule makes on the (100) face can be visualized easily from Fig. 1(a) and it has not been included.

Compound II crystallizes in the monoclinic system and is isomorphous with the corresponding nickel

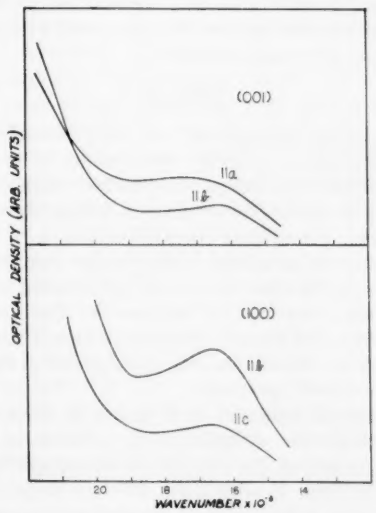

FIG. 4. Crystal spectrum of bis-salicylaldiminato-copper (II) for light incident on the (001) and (100) faces.

[4] B. Meuthen and M. v. Stackelberg, Z. anorg. u. allgem. Chem. **305,** 279 (1960); E. C. Lingafelter, B. Morosin, and G. L. Simmons, Acta Cryst. **13,** 1025 (1960). The author thanks Professor Lingafelter for kindly communicating his results in advance of publication.

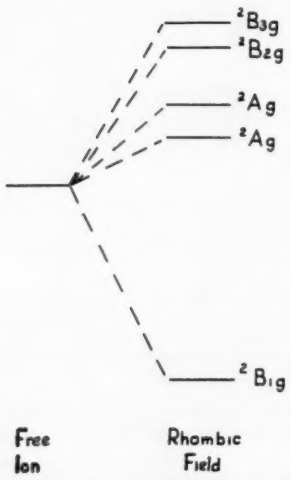

FIG. 5. Energy level diagram showing the removal of the fivefold degeneracy of the free ion by a rhombic field.

compound for which there is a complete structure determination.[5] Again, the well-developed face is the (100) and the (001) face was obtained by sectioning the crystals. The projections which the molecule makes on the two faces are shown in Fig. 1.

EXPERIMENTAL

The method used for recording the crystal spectra has been outlined elsewhere[1] and the compounds were prepared according to the method of Tyson and Adams.[6] Solution spectra were measured with a Beckman DK2 spectrophotometer.

RESULTS

The crystal structure of I is very favorable for a clear determination of the polarization of the bands and, as with the corresponding nickel compound, it is possible to section the crystals to decide the vibronic symmetry. The spectra are given in Fig. 2.

The spectra of square planar copper complexes are sensitive to the effect of an axial perturbation and it is of interest to see whether evidence for this can be obtained from the crystal spectrum. Figure 3 shows the spectrum in chloroform and pyridine for comparison with the crystal spectrum.

The crystal structure of II is not as favorable for clear polarization assignments as I. However, it was possible to section the crystals and obtain spectra from two faces (Fig. 4) with quite different projections of the molecule, and to compare the observed polarization with that predicted on the basis of the assignments made for I.

[5] J. M. Stewart and E. C. Lingafelter, Acta Cryst. **12**, 842 (1959).
[6] G. N. Tyson and S. C. Adams, J. Am. Chem. Soc. **62**, 1228 (1940).

ANALYSIS OF THE SPECTRA AND DISCUSSION

An analysis of the spectrum of I will be made first and it will again be assumed that the electronic transitions, forbidden by symmetry, occur through the perturbing effect of u vibrations. The first step is to decide the symmetry of the vibronic force field.

The dichroism of the in-plane absorption [Fig. 2, (001) face] shows that the field is not tetragonal but must be lower; [the dichroism of Fig. 2, (100) face, shows that it is not higher]. The band at about 17 000 cm^{-1} is strongly polarized along the a axis although there is a weaker b component. This fixes the symmetry axes in the manner shown in Fig. 1(a) for the following reason: A choice of axes along copper-ligand bonds allows a maximum a/b polarization ratio of only 1.9:1, while the observed ratio for the band at about 17 000 cm^{-1} is about 4:1. This is only possible for axes between bonds and is the same choice as that for the corresponding nickel complex.[1]

For reasons similar to those given earlier,[1,2] it will be assumed that the ligand field symmetry is coincident with the vibronic symmetry. A rhombic field then splits the fivefold degeneracy of the $3d$ orbitals into five nondegenerate levels: A_g, A_g, B_{1g}, B_{2g}, and B_{3g} (see Fig. 5). Four absorption bands are therefore expected, but the ligand absorption in the near ultraviolet region overlaps the copper ion absorption bands to some extent and they are not all observed. However, a useful analysis can be made.

The spectrum of the crystal for light incident on the (100) face shows that the two bands of lowest energy (15 000 cm^{-1} and 17 000 cm^{-1}) are polarized completely in the molecular plane. On the other hand, the band at about 20 500 cm^{-1} has a component normal to the molecular plane as well as in the plane [(001) face].

The spectrum of the other face shows that both of the low-energy bands are polarized to different extents. The band at about 15 000 cm^{-1} appears with nearly equal intensity in both polarizations, while the band near 17 000 cm^{-1}, as mentioned above, is stronger parallel to the a axis. The ligand absorption overlaps the next absorption band in both polarizations and the in-plane polarization is obscured but the a component is stronger than the b component. Unfortunately, it is difficult to determine the extent of the b absorption in this band, but it must be less than the a component.

An attempt to analyze the bands can now be made with the aid of Table I, which shows the possible vibronic symmetry representations in D_{2h}.

The two bands at 17 000 and 15 000 cm^{-1} have no out-of-plane component and both must be assigned electronically to $^2B_{1g} \rightarrow {}^2A_g$. The symmetry representation of the ground state is then B_{1g} with the $3d_{xy}$ orbital singly occupied as predicted by crystal field theory. The two lowest excited states have symmetry A_g and correspond to combinations of singly occupied

$3d_{z^2}$ and $3d_{x^2-y^2}$ orbitals, again in agreement with crystal field theory. It should be noted that the observed polarization of these two bands is consistent with the choice of in-plane symmetry axes bisecting angles and not along bonds. In the latter case, the ground state would belong to the A_g representation and the two lowest electronic transitions would be $^2A_g \rightarrow {}^2A_g$ and $^2A_g \rightarrow {}^2B_{1g}$. The former should have a component normal to the molecular plane as well as two in-plane components, contrary to the observed polarization.

The assignment of the next excited state cannot be made with certainty because of the overlapping ligand absorption. However, the absorption band is polarized mainly in the yz plane and is therefore most probably $^2B_{1g} \rightarrow {}^2B_{2g}$ with the $3d_{xz}$ orbital singly occupied in the excited state. The other excited state, $^2B_{3g}$, either lies at higher energy or the transition to it occurs weakly in the same region, in which case it would account for the possibility of absorption in the b component. Its presence at higher energy than the $^2B_{1g} \rightarrow {}^2B_{2g}$ transition is predicted qualitatively by the model outlined earlier[1] to explain the strong rhombic field in the analogous nickel complex. This assumes that a trigonal arrangement of ligand orbitals decides the effective ligand field. The order of increasing stability of the $3d$ orbitals is then xy (b_{1g}), $z^2(a_g)$, $x^2-y^2(a_g)$, $xz(b_{2g})$, and $yz(b_{3g})$, and the polarizations expected for the four bands in increasing energy are xy, xy, yz, and xz. These agree with the experimental polarizations as far as they go.

The absorption bands of II occur at higher energy and the overlap by ligand absorption is greater than with I. Only two bands are resolved, but it will be shown that their polarization is consistent with the assignments made for the two lowest energy bands of I. In doing this it will be assumed that the symmetry of the ligand field is the same, i.e., symmetry axes bisecting ligand-metal bond angles.

Two faces of the crystal, namely (001) and (100), were examined and it is necessary to tabulate the squares of the projections that unit molecular transition moments make on the two extinction directions of each face. These are collected in Table II.

The spectrum of the (100) face appears to have only one band at about 16 500 cm^{-1}, but the spectrum of the other face suggests that there is another band at about 18 500 cm^{-1}, absorbing more strongly in the a direction than in the b direction. The polarization ratio vs wavenumber curve has a maximum a/b ratio around 18 500 cm^{-1} for the (001) face, and a maximum b/c ratio at the same wavenumber for the (100) face. There are then two bands to be compared with the two in I.

If both bands are assigned to $^2B_{1g} \rightarrow {}^2A_g$ there should be no component polarized in the z direction. The spectrum of the (100) face is polarized more strongly in the b direction with a b/c ratio of about 2.3:1. This is somewhat less than for a purely x polarized transition and signifies that the transitions have some y and/or z polarization. The spectrum observed with the (001) face shows that this component is mainly y polarized because the spectrum is polarized more strongly along the a axis (Table II). It is clear then that the two bands are polarized in the plane of the molecule and that any out-of-plane absorption is very small, in agreement with the proposed assignment.

Although the two low-energy bands in each complex have polarizations consistent with the assignment $^2B_{1g} \rightarrow {}^2A_g$, the relative magnitudes of the x and y transition moments are significantly different. The lower energy band has nearly equal absorption intensity along the x and y axes with the former slightly greater in both complexes. However, the x transition moment is about four times larger than the y moment in the other band. This brings out strongly the fact that group theoretical arguments do not give quantitative information about the intensity of a transition, but only whether it is allowed or forbidden. Theoretical investigations of the mechanism of perturbing motions are lengthy and quantitatively approximate, so we must fall back on group theory. Provided that its qualitative nature is fully realized, however, it can be a powerful aid for the assignment of electronic transitions.

A comparison between the crystal spectra of I and II shows that the ligand field is stronger in the latter compound. This deduction is not quite straightforward because of the axial perturbation provided by copper ions from nearest neighbor molecules in I. To a certain extent the copper ion in each molecule is

TABLE I. Vibronic representations in D_{2h} (product of ground electronic state, excited electronic state, and perturbing vibration).

Symmetry representation of perturbing vibration	Symmetry representation of the product of ground and excited electronic wave functions			
	A_g	B_{1g}	B_{2g}	B_{3g}
b_{1u} (z)	B_{1u}	A_u	B_{3u}	B_{2u}
b_{2u} (y)	B_{2u}	B_{3u}	A_u	B_{1u}
b_{3u} (x)	B_{3u}	B_{2u}	B_{1u}	A_u

TABLE II. Squares of the projections which unit transition moments make on the two extinction directions of the (001) and (100) faces of bis-salicylaldiminato-copper (II).

	Extinction direction	Square of the projection of unit transition moment		
		x	y	z
(001)	a	0	0.83	0.15
	b	0.75	0.04	0.20
(100)	c	0.25	0.12	0.65
	b	0.75	0.04	0.20

'solvated' by the copper ion situated about 3.3 Aabove and below the molecule, and the bands are shifted to lower energy as a result of this. The effect of an axial perturbation can be seen with the aid of Fig. 3 which shows the spectrum of I dissolved in chloroform and pyridine. The latter solvent causes a shift of the absorption bands to lower energy and a reduction in the intensity of absorption between 24 000 and 18 000 cm^{-1}. The difference in intensity, not nearly so marked with II, is probably connected with a departure from planarity in chloroform brought about by the bulky methyl groups. Solvation, as in the crystal, then forces planarity of the chelate. The bands of the crystal spectrum show more resemblance to those of the pyridine solution than chloroform. A comparison between Figs. 2 and 3 shows that the maximum of the spectrum in pyridine (16 000 cm^{-1}) lies closer to the estimated unpolarized maximum of the crystal bands (near 16 000 cm^{-1}) than that of the chloroform spectrum (probably between 17 000 and 18 000 cm^{-1}). One concludes therefore that the effect of nearest neighbors in the crystal is similar in magnitude to solvation by pyridine. In the crystal of II the arrangement of molecules is different and there is no appreciable axial perturbation from neighboring molecules. The spectrum of the crystal is similar to that of chloroform solution and not to the pyridine solution.

CONCLUSION

It seems clear from the analysis of the polarization of the crystal absorption bands of I and II that a modification of the usual crystal field model must be made for chelate compounds. Both the assignment and the dichroism of the bands indicate that the field of the ligands is rhombic with in-plane symmetry axes bisecting metal-ligand bond angles. If the orbital geometry of the ligands is taken into account and assuming that the fields provided by nitrogen and oxygen are similar, then the symmetry of the ligand field is coincident with that observed. The observation made at first with bis-*N*-methylsalicylaldiminato-nickel (II) is confirmed by the present analysis, and there seems to be no reason why it should not be general. The agreement between the present work and that from electron spin resonance is very good. Maki and McGarvey[7] have found from an analysis of the electron spin resonance spectrum of bis-salicylaldiminato-copper (II) that the ligand field is rhombic, the in-plane axes lie between the metal-ligand bonds, and the nitrogen and oxygen ligands are approximately equivalent.

---

[7] A. H. Maki and B. R. McGarvey, J. Chem. Phys. **29**, 35 (1958).

Absolute Infrared Intensity Measurements in Thin Films

SHIRO MAEDA* AND P. N. SCHATZ

Department of Chemistry, University of Virginia, Charlottesville, Virginia

(Received April 17, 1961)

A theoretical investigation has been made of the errors which will be incurred if reflection effects (including multiple reflections) are neglected in making absolute (absorption) intensity measurements on thin films of pure liquids and solids. The results are presented in a series of figures for a number of typical experimental situations as a function of two generalized parameters. These figures permit an estimation of the error for any specific case. It is found that the error can be quite appreciable for some experimentally realistic situations. Since a computer program has been written to do the calculations, the authors are willing to run specific cases upon request.

INTRODUCTION

IN making quantitative absorption measurements on pure liquids and solids in the infrared, it is generally necessary to use quite thin samples (less than the wavelength of the radiation) if fundamental vibrations are to be studied. It is well known that under such circumstances the assumption of a simple Beer's law relationship between incident and transmitted intensity may be inadequate because of reflection effects within the sample.[1] Since there has been increasing interest in condensed phase intensities in recent years, and particularly since Dows and Hollenberg have recently developed a method for determining sample thicknesses accurately in thin films,[2] we present here a brief theoretical analysis of the effect of reflection (including multiple reflections and the resulting interference phenomena) on the experimentally measured integrated absorption coefficient. There has been some previous discussion of this problem in the literature,[3,4] but we are not aware of any extensive quantitative treatments which cover a wide range of parameters.

To facilitate the mathematical analysis, it has been assumed that a vibrational transition can be described by a damped harmonic oscillator.[5] Since the number of parameters involved is substantial, our results will be representative rather than exhaustive. They should enable an estimation of the effect for any specific case.[6]

THEORY

The theoretical expressions necessary for our analysis may be obtained by a straightforward application of Maxwell's equations. Since the results are well known and are discussed in detail elsewhere,[1] we shall only summarize here the explicit formulas necessary for our discussion.

Let us assume that an incident beam of radiation impinges at normal incidence on a cell whose front window has refractive index θ, whose rear window has refractive index ϕ, and which contains a sample of a pure substance of thickness d. We discuss in this paper the following two cases: (1) $\theta=\phi=1.5$; (2) $\theta=1.0$ (air), $\phi>1$. The first case corresponds to a typical experiment on a liquid, and the second to an experiment in which a solid is deposited on a halide plate. Let $\alpha(\nu)$ be the true absorption coefficient of the sample, and let $\alpha'(\nu)$

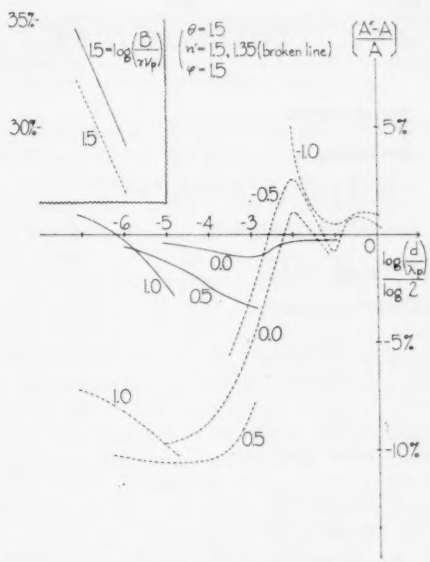

FIG. 1. Percentage error in the integrated absorption intensity which results from the neglect of reflection corrections: some typical liquid cases. The number associated with each line is the value of $\log_{10}(B/\gamma\nu_p)$.

* On leave of absence from the National Defense Academy, Yokosuka, Japan.

[1] O. S. Heavens, *Optical Properties of Thin Solid Films* (Academic Press Inc., New York, 1955).

[2] J. L. Hollenberg and D. A. Dows, J. Chem. Phys. **34**, 1061 (1961).

[3] G. S. Denisov, Optics and Spectroscopy **6**, 301 (1959); M. P. Lisitsa and Iu. P. Tsiashchenko, *ibid.* **6**, 396 (1959).

[4] D. A. Dows and J. L. Hollenberg, J. Chem. Phys. **32**, 1581 (1960).

[5] P. N. Schatz, S. Maeda, J. L. Hollenberg, and D. A. Dows, J. Chem. Phys. **34**, 175 (1961).

[6] Since this treatment has been programmed for a computer, we are prepared to run specific cases (i.e., for given values of the various parameters) upon request.

be the apparent absorption coefficient. That is,

$$I=I_0\exp(-\alpha' d)=I_0\exp[-(\alpha+\Delta\alpha)d]$$
$$=(1/Z)I_0e^{-\alpha d}, \quad (1)$$

where I_0 and I are the observed incident and transmitted intensities respectively, and $\Delta\alpha\equiv\alpha'-\alpha\equiv(1/d)\ln Z$. The true and apparent integrated intensities are then given respectively by,

$$A=\int\alpha d\nu, \quad (2)$$

$$A'=\int\alpha' d\nu=\int(\alpha+\Delta\alpha)d\nu=A+\Delta A, \quad (3)$$

where

$$\Delta A\equiv\int(\Delta\alpha)d\nu=A'-A=(1/d)\int\ln Z d\nu.$$

From reference 1 it follows that

$$1/Z=\frac{I_0e^{-\alpha' d}}{I_0e^{-\alpha d}}=(\phi/\theta)\frac{Pe^{\beta}}{e^{\beta}+Qe^{-\beta}+C\cos\delta+D\sin\delta}, \quad (4)$$

where

$$\beta=\alpha d=4\pi\kappa\nu d,$$
$$\delta=4\pi n\nu d,$$
$$P=[(1+g_1)^2+h_1^2][(1+g_2)^2+h_2^2],$$
$$Q=(g_1^2+h_1^2)(g_2^2+h_2^2),$$
$$C=2(g_1g_2-h_1h_2),$$
$$D=2(g_1h_2+g_2h_1),$$
$$g_1=\frac{\theta^2-(n^2+\kappa^2)}{(n+\theta)^2+\kappa^2},$$
$$h_1=\frac{2\theta\kappa}{(n+\theta)^2+\kappa^2},$$
$$g_2=\frac{(n^2+\kappa^2)-\phi^2}{(n+\phi)^2+\kappa^2},$$
$$h_2=\frac{-2\phi\kappa}{(n+\phi)^2+\kappa^2}.$$

In order to evaluate n and $\kappa(\equiv nk)$, we assume that the vibrational transition can be represented by a damped oscillator model[5]:

$$\epsilon_1=n^2-\kappa^2=(n')^2+\frac{B(\nu_p^2-\nu^2)}{(\nu_p^2-\nu^2)^2+\gamma^2\nu^2}, \quad (5)$$

$$\epsilon_2=2n\kappa=\frac{B\gamma\nu}{(\nu_p^2-\nu^2)^2+\gamma^2\nu^2}, \quad (6)$$

where $B\equiv(1/\pi^2)\tilde{n}A$, A [Eq. (2)] being expressed in units of cm^{-2}. These equations have been discussed in detail previously.[5] Using Eqs. (1) through (6), it is now possible to evaluate $(A'-A)$ for any given choice of the various parameters $(d, \theta, \phi, n', \nu_p, B, \gamma)$.

Fortunately, it is possible to both reduce the number of parameters and put the results in a more general form. A straightforward analysis of Eqs. (1) through (6) indicates that, to a good approximation, the final results will depend on only θ, ϕ, n', $(B/\gamma\nu_p)$, and (d/λ_p) if it is assumed that $\gamma\ll\nu_p$, where $(\nu_p\lambda_p=c)$, and if the integrations in Eqs. (2) and (3) are always performed over a frequency range which is a fixed multiple of γ (the approximate band width at half height). θ and ϕ are defined by the experiment, and n' is in the vicinity of 1.5 for many simple liquids and solids. Consequently, the main variables are (d/λ_p) and $(B/\gamma\nu_p)$.

RESULTS AND CONCLUSIONS

The results of the calculations are shown in Figs. 1–4. It should be noted that the ordinate in these plots is $(A''-A)/A$ rather than $(A'-A)/A$. The reason for this is the following. In general, at frequencies far from resonance, the transmitted intensity I will not coincide with the incident intensity I_0. This is so because of the reflections from the sample and windows. In actually carrying out an absorption experiment, one would handle this problem by matching up the base line (I_0 line) with the distant wings of the absorption band. The equivalent of this is done(approximately) in our calculations by using the limiting value ($\kappa\to0$) of the transmitted intensity as the base line. Consequently, A'' represents the integrated absorption coefficient that would actually be measured experimentally.

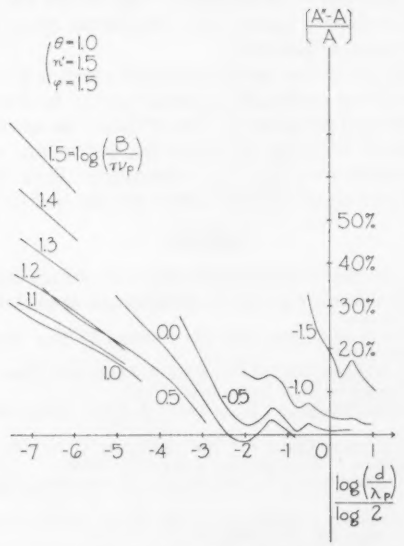

FIG. 2. Percentage error in the integrated absorption intensity which results from the neglect of reflection corrections: some typical cases for a solid deposited on a halide plate. The number associated with each line is the value of $\log_{10}(B/\gamma\nu_p)$.

Since the calculations involved in producing Figs. 1–4 are quite tedious, the problem was programmed for a Burroughs 205 digital computer. In order to restrict the range of parameters investigated, the program rejected all calculations which involved peak absorptions of greater than 90% or less than 10% (approximately). The integrations in Eqs. (2) and (3) were always carried out (Simpson's rule) over a range of 5γ about the band center. It is true that this range corresponds to only about 85%[7] of the total integrated absorption coefficient, but it is found that no appreciable error is introduced thereby since we are interested in the *difference* $(A''-A)$.[7a]

Certain general observations can be made about the results. In the liquid case ($\theta=\phi=1.5$), the error involved in the neglect of reflection effects is generally small (<10%). Only for very large intensities (or a combination of large intensity and very narrow bandwidth) does the effect become quite substantial, and in such cases the required sample thicknesses tend to be experimentally unrealistic ($<\frac{1}{32}\lambda_p$). It is also observed, as might be expected, that reflection effects become more important as n' (the refractive index due to all absorptions except the one under consideration) deviates from the refractive index of the window material.

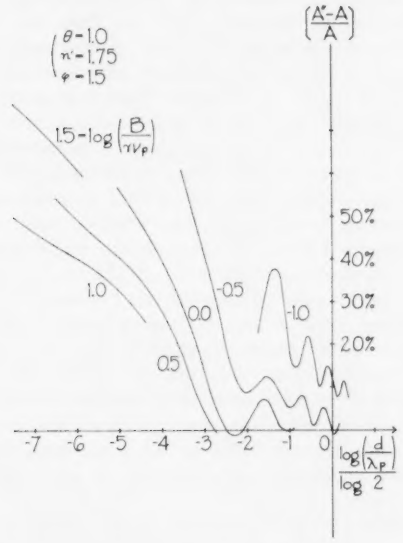

FIG. 3. Percentage error in the integrated absorption intensity which results from the neglect of reflection corrections: some typical cases for a solid deposited on a halide plate. The number associated with each line is the value of $\log_{10}(B/\gamma\nu_p)$.

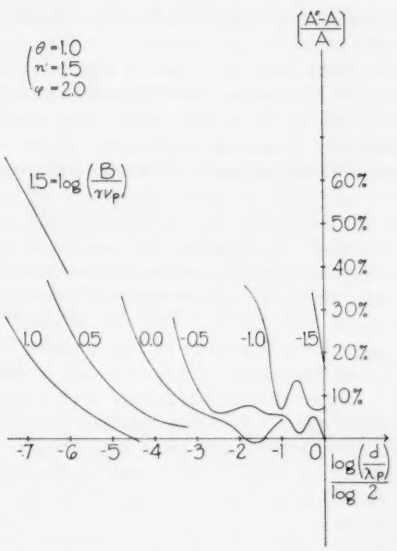

FIG. 4. Percentage error in the integrated absorption intensity which results from the neglect of reflection corrections: some typical cases for a solid deposited on a halide plate. The number associated with each line is the value of $\log_{10}(B/\gamma\nu_p)$.

As an illustration of a practical case, we might consider the 680-cm^{-1} band of liquid benzene ($n'=1.48$) which has been studied in absorption[8] between KBr plates ($\theta=\phi=1.513$). In this case, $\log(B/\gamma\nu_p)\approx 0.5$, and $\log(d/\lambda_p)/\log 2$ varies between about -2 and -4. We see from Fig. 1 that reflection effects are expected to cause only a small error (<5%) in the experimental determination of the absolute intensity of this band. In this connection, it might be noted that a simple correction which takes account of only a single reflection at each liquid-KBr interface will rather badly overestimate the error, particularly for the thinner samples. Thus, considering only a single reflection at each liquid surface and using experimental reflection data, Dows and Hollenberg[4] estimate an error of 11–28% for the 680-cm^{-1} band of benzene, and we get about the same range of errors when we make the equivalent simple correction theoretically. This overestimation results from the neglect of multiple reflection and the consequent interference effects which to a large extent cancel the simple correction, a possibility which was pointed out by Dows and Hollenberg.[4]

Of all the bands of benzene, the 680-cm^{-1} band has the largest value of $(B/\gamma\nu_p)$. Consequently, Fig. 1 predicts that reflection effects will cause even smaller errors in the experimental determinations of the intensities of the other bands.

[7] D. A. Ramsay, J. Am. Chem. Soc. **74,** 72 (1952), Method II.

[7a] *Note added in proof.* Further investigation has revealed that this will not be completely true for very large values of $B/\gamma\nu_p$. In such cases, the position of the true absorption curve shifts with respect to the experimental curve, and furthermore, γ may be appreciably smaller than the half-width. As a result, the range of integration may be somewhat inadequate, and Figs. 1–4 will tend to overestimate the thin film effect for the very large values of $B/\gamma\nu_p$.

[8] I. C. Hisatsune and E. S. Jayadevappa, J. Chem. Phys. **30,** 848 (1959); **32,** 565 (1960).

Experiments involving solid films deposited on halide plates ($\theta=1.0$, $\phi>1$) are illustrated in Figs. 2–4. It is seen that there is a much greater likelihood for substantial error if reflection corrections are ignored. Thus errors as high as 40 or 50% would seem possible for experimentally attainable conditions. Figure 4 is of particular interest because it represents a film deposited on AgCl ($\phi=2.0$), a system for which an accurate method of measuring film thicknesses has recently been presented.[2] To illustrate this case, let us consider the intensity data given in reference 2 for solid benzene deposited on AgCl. We use the bandwidth data reported by Swenson and Person.[9] For the 680-cm^{-1} band, $\log(B/\gamma\nu_p)\approx 0.49$. Reference to Fig. 4 shows that the error due to the neglect of reflection will be less than 10% for sample thicknesses greater than about 0.5μ. The smallest sample thickness reported in reference 2 is 0.70μ. For the 1036-cm^{-1} band, $\log(B/\gamma\nu_p)\approx -0.55$. The thicknesses used in this case corresponded to values of $\log(d/\lambda_p)/\log 2$ between -3.8 and -1.3. Figure 4 shows that the error will be less than 10% down to about -3, but below that (-3 to -3.8) the error increases quite rapidly. Finally, for the 3067-cm^{-1} band, $\log(B/\gamma\nu_p)\approx -1.46$, and the thicknesses used correspond to values of $\log(d/\lambda_p)/\log 2$ between $+0.2$ and -1.0. Although Fig. 4 is rather incomplete for these particular values of the parameters, the indication would be that errors greater than 10% might be expected over a substantial portion of the range of thicknesses used.[9a]

As a closing comment, we might note that absorption measurements made in very thin films ($<\frac{1}{32}\lambda_p$) are almost always going to involve large errors if corrections are not made for reflection effects.

ACKNOWLEDGMENTS

We would like to thank the National Science Foundation for a grant which supported this work. We would also like to thank Dr. Alan Batson, director of the University Computer Center, for his generous assistance in the preparation of the computer program.

[9] C. A. Swenson and W. B. Person, J. Chem. Phys. **33**, 56 (1960).

[9a] *Note added in proof.* In a private communication, Professor David A. Dows has informed us that the bandwidths reported in reference 9 are substantially too large. Using smaller bandwidths increases $\log(B/\gamma\nu_p)$, and reference to Fig. 4 shows that this will cause a decrease in the predicted error in each case.

Mutual Diffusion of the Gas Pairs H_2-Ne, H_2-Ar, and H_2-Xe at Different Temperatures

R. PAUL AND I. B. SRIVASTAVA

Indian Association for the Cultivation of Science, Calcutta 32, India

(Received March 30, 1961)

The mutual diffusion coefficients of H_2 with Ne, Ar, and Xe have been determined by the two-bulb technique of Ney and Armistead in the temperature range $-30°$ to 68°C. Diffusion was allowed to take place through a precision capillary tube connecting the two diffusion bulbs and samples of the gas were analyzed at different times with the help of a previously calibrated thermal-conductivity analyzer.

A least-square method was then followed to calculate the force constants on the Lennard-Jones (12:6) potential model from the experimental values of the diffusion coefficients. Also, using experimental values of the mutual-diffusion coefficient, thermal conductivity, and viscosity of pure components, the thermal conductivity of various mixtures were calculated and a good agreement with the experimental data was obtained.

INTRODUCTION

IT is well known that the accurate determination of the mutual diffusion coefficients of gases over a suitable range of temperature, is necessary for understanding the nature of the unlike molecular interaction. The mutual diffusion coefficient D_{12}, in its first approximation, depends only on the unlike molecular interactions. Hence its accurate determination gives better information about the force laws between the unlike molecules than any other property of gas mixtures, except perhaps the thermal diffusion. Unfortunately the experimental data available in literature is scanty and is limited to a small temperature range. Westenberg[1] has given a summary of the diffusion data up to date.

Klibanov *et al.*[2] measured D_{12} of CO_2-air and H_2O-air by using a modified Loschmidt technique from room temperature to 1500°K, but the precision attained was quite poor. Schafer and Schuhmann[3] measured the mutual diffusion of some noble gases in the temperature range 90° to 473°K by using the two-bulb method. Bunde[4] measured the diffusion in some binary systems by the Loschmidt method over a small temperature range (25° to 85°C) using the same technique. Rumpel[5] has determined the diffusion coefficients of He–H_2 and He–N_2 systems in the same range of temperatures. Diffusion in H_2–Ar has been studied by Strehlow[6] in the temperature range 13° to 150°C but the data do not appear to be of high precision. Boardman and Wild[7] have reported diffusion coefficients of argon with H_2, N_2, and O_2 at a single temperature (20°C). Walker and Westenberg,[8–11] using a point source technique, determined the diffusion coefficients of many binary systems from 300° to 1100°K and arrived at some interesting conclusions regarding the suitability of various potential models.

Several workers[12–14] in this laboratory have measured mutual diffusion coefficients of inert gases in the temperature range of 0° to 45°C, by using the two-bulb diffusion method and have determined the force constants for unlike interactions. It was considered desirable to perform the diffusion experiments with diatomic molecules to see whether the internal energies in the molecules produce any change in the combination rules. In the present work the diffusion of H_2 into Ne, Ar, and Xe has been investigated in the temperature range $-30°$ to 68°C.

DESCRIPTION OF THE APPARATUS

The details of the apparatus and the experimental procedure have been discussed fully by Srivastava and Srivastava.[12] In the present investigation the same apparatus has been used for measuring the diffusion coefficients over a wider range of temperature. The upper and lower limits of temperature were governed by the workability of the greases used. Below $-30°$C the Dow-Corning-Silicone grease became too viscous, thus hindering the smooth operation of the stop-cock. The Apiezon-*T* grease used at high temperature could be used conveniently only up to 70°C. For maintaining the temperature of the thermostatic bath below 0°C, alcohol was used as the bath liquid in the inner chamber

[1] A. A. Westenberg, Combustion and Flame **1,** 346 (1957).
[2] Klibanov, Pomerantsev, and Frank Kamenetsky, J. Tech. Phys. (U.S.S.R.), **12,** 14 (1942).
[3] K. Schafer and K. Schuhmann, Z. Elektrochem **61,** 246 (1957).
[4] R. E. Bunde, University of Wisconsin, CM-850 (August, 1955).
[5] W. F. Rumpel, University of Wisconsin, CM-851 (August, 1955).
[6] R. A. Strehlow, J. Chem. Phys. **21,** 2101 (1953).
[7] L. E. Boardman and N. E. Wild, Proc. Roy. Soc. (London) **A162,** 511 (1937).
[8] R. E. Walker and A A. Westenberg, J. Chem. Phys. **29,** 1139 (1958).
[9] R. E. Walker and A. A. Westenberg, J. Chem. Phys. **29,** 1147 (1958).
[10] R. E. Walker and A. A. Westenberg, J. Chem. Phys. **31,** 519 (1959).
[11] R. E. Walker and A. A. Westenberg, J. Chem. Phys. **32,** 436 (1960).
[12] B. N. Srivastava and K. P. Srivastava, J. Chem. Phys. **30,** 984 (1959).
[13] K. P. Srivastava, Physica **25,** 571 (1959).
[14] K. P. Srivastava and A. K. Barua, Indian J. Phys. **33,** 229 (1959).

TABLE I. Mutual diffusion coefficients in cm²/sec.

Gas mixture	T °K	Pressure in mm Hg	D_p	D_{atm} (exptl)	Previous work (exptl)	D^a	D^b
	242.2	62.50	9.631	0.792		0.790	0.796
	274.2	65.50	11.301	0.974		0.974	0.981
H_2—Ne	303.2	66.19	13.204	1.150		1.157	1.150
	341.2	59.64	17.904	1.405		1.405	1.416
	242.2	66.10	4.714	0.410		0.408	0.414
	274.2	63.52	6.078	0.508		0.509	0.517
H_2—Xe	303.9	67.40	6.901	0.612		0.612	0.619
	341.2	39.80	14.341	0.751		0.749	0.759
	242.2	57.81	7.215	0.562		0.564	0.554
	274.2	65.46	8.104	0.698		0.698	0.687
	287.9	...	...	0.755[c]	0.828[6]	0.759	0.747
	293.2	...	...	0.780[c]	0.77[7]	0.784	0.770
H_2—Ar	303.9	68.00	9.276	0.830		0.825	0.820
	341.2	71.14	10.790	1.010		1.013	1.000
	354.2	...	...	...	1.111[6]	1.055	1.063
	418.0	...	...	...	1.714[6]	1.430	1.402

[a] Calculated from force constants fitted to diffusion data.
[b] Calculated from combination rules and viscosity force constants.
[c] Interpolated values from graph.

of the thermostat, the outer chamber contained alcohol to which liquid oxygen was occasionally added. The temperature was kept constant to within ±0.05°C by the Sunvic-electronic relay of type EA3/T.

THEORY AND FORMULAS

The theory of this method has been considered in detail by Ney and Armistead[15] where it has been shown that the relaxation time $1/\alpha$, of the system as defined by the relation

$$(c_1^\infty - c_1^t)/(c_1^\infty - c_1^0) = \exp(-\alpha t), \qquad (1)$$

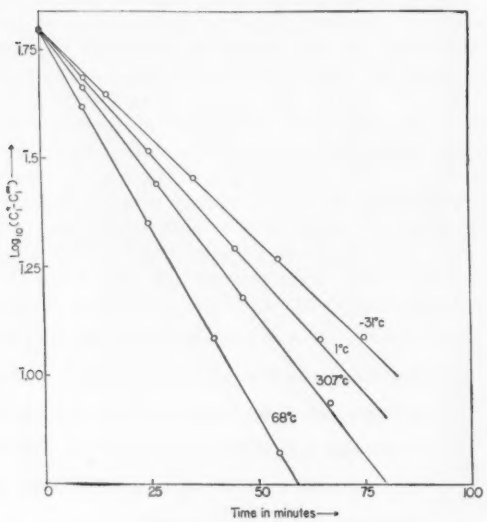

FIG. 1. H_2-Ne mixture.

[15] E. P. Ney and F. C. Armistead, Phys. Rev. **71**, 14 (1947).

is given by

$$\alpha = (D_p A/l) \cdot (V_0/V_1 V_2). \qquad (2)$$

where C_1^0, C_1^t, and C_1^∞ are respectively, the concentrations of the heavier gas initially, at time t sec, and after complete mixing. V_1 and V_2 are the volumes of the bulbs in cc and $V_0 = V_1 + V_2$. D_p is the coefficient of diffusion in cm²/sec at a pressure of p cm of mercury. A and l are the effective cross-sectional area and the effective length of the diffusion path respectively.

From Eq. (1) it is evident that a plot of $\log_e(C_1^\infty - C_1^t)$ against t gives a straight line, its slope being $-\alpha$. Knowing α, D_p can be calculated from Eq. (2). D_{atm}, the diffusion coefficient at atmospheric pressure, is related to D_p by the equation

$$D_{atm} = (D_p \times p)/76 \qquad (3)$$

TABLE II. Potential parameters on the Lennard-Jones (12:6) model from the experimental data.

Gas pair	Present work	Combination rule
H_2—Ne		
ϵ_{12}/k (°K)	39.72	36.84
σ_{12} (A)	2.843	2.852
H_2—Xe		
ϵ_{12}/k (°K)	98.12	93.28
σ_{12} (A)	3.484	3.485
H_2—A		
ϵ_{12}/k (°K)	62.21	64.3
σ_{12} (A)	3.176	3.193

EXPERIMENTAL RESULTS

The gases used were supplied by British Oxygen Company, England and were quoted to be spectroscopically pure, except xenon which contained about 1% krypton.

Constants of the diffusion apparatus

Vol. of bulb I	325 cc
Vol. of bulb II	547 cc
Length of diffusion capillary	9.058 cm
Diam. of diffusion capillary	0.316 cm

$C_1^\infty = 0.373$

C_1^∞ is calculated from the initial concentration in the bulbs, which was further checked for some runs by determining the concentration at an interval of seven times the relaxation time.

Figure 1 gives the plots of $\log_{10}(C_1^t - C_1^\infty)$ versus t for H_2–Ne, at all temperatures. These are straight lines from the slope of which α is determined. Then D_p is calculated from Eq. (2).

The experimental values of diffusion coefficients thus obtained are given in Table I, along with the values available in the literature. The only data already available are those of Boardman and Wild[7] and Strehlow[6] for H_2–Ar. The former are quite consistent with the present investigations but the latter are too high by about 10%. Our results are believed to be accurate to within about ±1%.

DETERMINATION OF POTENTIAL PARAMETERS

The various methods for determining the potential parameters from the measured diffusion coefficients such as; (a) the ratio method, (b) the translation method of Keesom[16] and Lennard-Jones,[17] (c) the intersection method of Buckingham,[18] and (d) the combination method using other transport properties in addition, have been fully discussed by Bunde,[4] and Srivastava and Srivastava,[12] pointing out their advantages and limitations. In the present case the intersection method has been found to be most suitable for the determination of the force constants on the Lennard-Jones (12:6) model. As some scatter was found in the intersection points of the curves, the force constants determined by this method were considered as approximate. These approximate values were used to calculate the parameters more accurately by the method of least-square-fitting (Margenau and Murphy).[19] The method followed here is analogous to that of Whalley and Schneider[20] for determining the potential parameters from the second virial coefficients. The force constants thus determined are tabulated in Table II together with the values obtained from the usual combination rules. It is easily seen that the two sets of force constants agree within the limits of experimental error, though the combination rule value of σ_{12} is always larger as is expected.

TABLE III. Thermal conductivity of H_2—Ne and H_2—Xe mixtures at 30°C in (cal) (cm^{-1}) (sec^{-1}) (deg^{-1}).

Gas pair	H_2—Ne		H_2—Xe	
% of heavier constituent	$K_{exp}\times10^5$	$K_{calc}\times10^5$	$K_{exp}\times10^5$	$K_{calc}\times10^5$
100	11.65[a]	11.65	1.261[a]	1.261
85	14.25	14.31	3.745	3.768
70	17.74	17.63	6.812	6.73
55	21.80	21.54	10.61	10.77
40	26.58	26.16	15.81	15.90
25	32.24	31.66	21.68	23.33
10	38.88	38.06	33.49	33.21
0	43.16	43.16	43.16	43.16

[a] A. K. Barua, Indian J. Phys. **34**, 169 (1960).

TABLE IV. Thermal conductivity of H_2—Ar mixture at 0°C in (cal) (cm^{-1}) (sec^{-1}) (deg^{-1}).

% of heavier constituent	$K_{exp}\times10^5$	$K_{calc}\times10^5$
100	3.90[a]	3.90
91	5.50	5.49
82	7.30	7.25
60	12.60	12.47
40	18.70	18.81
20	27.00	27.62
0	40.40	40.40

[a] T. L. Ibbs and A. A. Hirst, Proc. Roy. Soc. (London) **A123**, 134 (1929).

COMPARISON WITH EXPERIMENTS

(a) Mutual Diffusion Coefficient

By use of the force constants determined here, the mutual diffusion coefficients were calculated for the experimental temperatures and these are recorded in Table I along with those calculated from the combination rule values. Other experimental data where available are recorded in column 5 for the sake of comparison. It will be seen that the force constants derived by us yield values of mutual diffusion coefficient, in good agreement with the experimentally observed values. The reliability of the force constants could be

[16] W. H. Keesom, Leiden Comm. Suppl. No. 25 (1912).
[17] J. E. Lennard-Jones, Proc. Roy. Soc. (London) **A106**, 463 (1924).
[18] R. A. Buckingham, Proc. Roy. Soc. (London) **A168**, 264 (1938).
[19] H. Margenau and G. M. Murphy, *Mathematics of Physics and Chemistry* (D. Van Nostrand Company, Inc., Princeton, New Jersey, 1952).
[20] E. Whalley and W. G. Schneider, J. Chem. Phys. **23**, 1644 (1955).

tested if high temperature data for these substances were available, as has been shown by Walker and Westenberg.[11]

(b) Thermal Conductivity of Mixtures

The experimental values of D_{12} together with other experimentally determined properties such as self-diffusion, thermal conductivity, and viscosity of the pure gases, were used to calculate the thermal conductivity of mixtures, without assuming any particular form of the interaction potential except a central force. This method has been suggested by Weissman *et al.*[21] for testing how well a mixture confirms to the basic assumptions of Chapman-Enskog theory or for determining the consistency of the experimental measurements.

Hirschfelder[22] has obtained the following expression for K_{mix}, the thermal conductivity of gas mixture, consisting of a diatomic gas denoted by subscript 1 and a monatomic gas denoted by subscript 2:

$$K_{mix}=[K_{mix}]_{mon}+\{K_1-(K_1)_{mon}\}\times[1+(x_2/x_1)(D_{11}/D_{12})]^{-1}. \quad (4)$$

The symbols have their usual meanings and expressions given for them on the Chapman Enskog theory by Hirschfelder, Curtiss, and Bird.[23] $(K_1)_{mon}$ and D_{11} were calculated by using the experimental values of η_1, the viscosity of the diatomic gas, with the help of the following expressions:

$$(K_1)_{mon}=\tfrac{15}{4}(R/M)\eta_1 \quad (5)$$

$$D_{11}=98.42(A_1^*\eta_1 T/pM). \quad (6)$$

A^* has been shown by Weissman and Mason[24] to be nearly independent of either temperature or force law and its contribution to the final result is negligible. Therefore a rough estimate of A^* is often adequate. Here we have used the known force constants to find A_1^* from the tables.

$(K_{mix})_{mon}$ involves $(K_1)_{mon}$, K_2, $(K_{12})_{mon}$, A_{12}^*, and B_{12}^*. The value of $(K_{12})_{mon}$ has been calculated from experimental D_{12} values using the relation

$$(K_{12})_{mon}=\tfrac{25}{8}(pD_{12}/A_{12}^*T). \quad (7)$$

A_{12}^* has again been found from tables using our force constants while B_{12}^* has been obtained with the help of experimental values of D_{12} and the following expression given by Weissman *et al.*[21]:

$$B_{12}(\tfrac{1}{12})[2(\partial \ln D_{12}/\partial \ln T)-1][9-2(\partial \ln D_{12}/\partial \ln T)] \quad (8)$$

Thus K_{mix} has been calculated with the help of only experimental quantities and recorded in Tables III and IV, together with the observed values. It can be seen that the agreement between the experimental values of thermal conductivity and the values calculated here from other experimental data is excellent for all the mixtures.

ACKNOWLEDGMENT

The authors are grateful to Professor B. N. Srivastava for his guidance and helpful discussions. One of the authors (R.P.) is thankful to Council of Scientific & Industrial Research, New Delhi, for financial assistance.

[21] S. Weissman, S. C. Saxena and E. A. Mason, Phys. Fluids **3,** 510 (1960).

[22] J. O. Hirschfelder, *Sixth International Symposium of Combustion* (Reinhold Publishing Corporation, New York, 1957), p. 351.

[23] J. O. Hirschfelder, C. F. Curtiss, and R. B. Bird, *Molecular Theory of Gases and Liquid* (John Wiley & Sons, Inc., New York, 1954), Chap. 8.

[24] S. Weissman and E. A. Mason, Physica **26,** 531 (1960).

Observation of Free Radical Kinetics in the Cyclohexane-Oxygen System

R. L. McCarthy and A. MacLachlan
Radiation Physics Laboratory, E. I. du Pont de Nemours & Company, Wilmington, Delaware

(Received March 30, 1961)

Pulsed 6-Mev electrons from a Lineac have been used to initiate free radical reactions in the cyclohexane-oxygen system. The primary radical formed, cyclohexyl, is identified through EPR analysis of the irradiated solid sample at −100°C. In the liquid phase the cyclohexyl-peroxy radical is formed; its decay is observed spectroscopically over a period of 10 msec, and the second-order rate constants calculated. The principal reaction involving the disproportionation of two cyclohexyl-peroxy radicals requires zero (<1 kcal/mole) activation energy. The reaction rate constant is approximately 10^{-4} that for the diffusion-controlled process.

INTRODUCTION

PULSED high-energy electron irradiation has been shown to produce sufficiently high concentrations of free radicals in organic solutions for spectroscopic observation.[1] The present study is concerned with an analysis of the parameters which determine the kinetic behavior of the radicals generated in the cyclohexane-oxygen system.

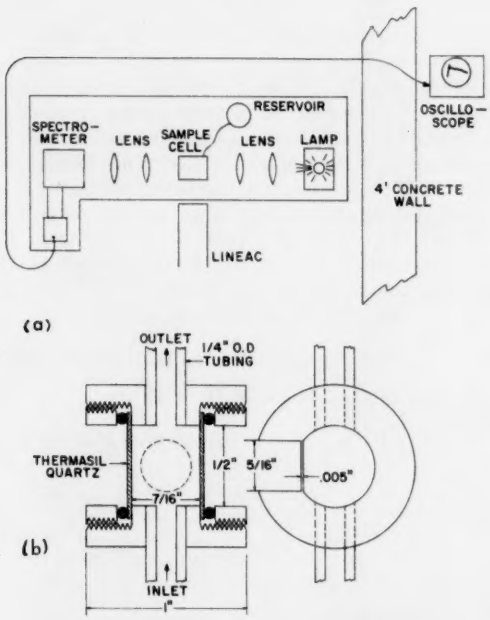

FIG. 1. (a) Equipment arrangement. (b) Sample cell.

EXPERIMENTAL

A pulsed beam of electrons (normally 6 Mev) is produced by a linear accelerator. Normal pulse width is 5 μsec, with a beam cutoff time of 0.1 μsec. A peak current of 240 ma is available; the cross-sectional area of the beam (>90% included) is 0.07 cm² on the atmospheric side of the accelerator window. The diminution in beam intensity in traversing the sample is approximately 30%, and the spread of the beam in the liquid is such that all portions of the sample may be considered to be subjected to a uniform dose rate within 15%. The dose per beam pulse is measured to be 1.4±0.2 joules.

Free radicals formed by the electron pulse are observed by means of the equipment shown in Fig. 1. Analysis light is provided by a 1000-w high-pressure xenon lamp which has a usable continuum down to 2400 A. The spectrometer consists of a grating monochromator ($F=4$), a uv-sensitive photomultiplier, and a dc-coupled cathode follower. The response time constant of the detector including cable is 0.2 μsec. The minimum transient response is 4 μsec due to the signal generated in the structure of the photomultiplier by the x-ray pulse from the Lineac. Recordings of the transient free radical absorption are made from an oscilloscope whose sweep is triggered by the accelerator beam.

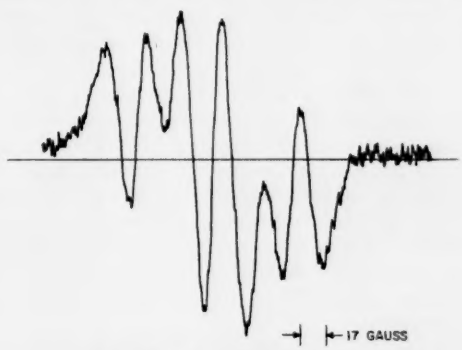

FIG. 2. Cyclohexyl radical.

EPR measurements were made at −100°C after irradiating the frozen sample in liquid nitrogen. A modified[2] Varian spectrometer was used employing 100-kc

[1] R. L. McCarthy and A. MacLachlan, Trans. Faraday Soc. **56**, 1187 (1960).

[2] R. G. Bennett, P. C. Hoell, and R. P. Schwenker, Rev. Sci. Instr. **29**, 659 (1958).

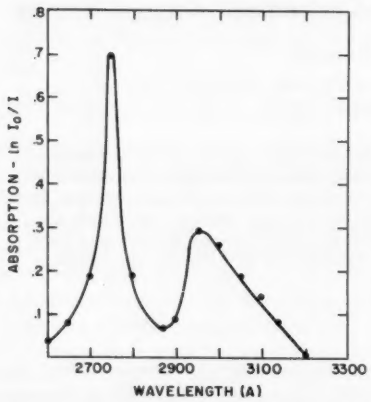

FIG. 3. Spectrum of cyclohexyl peroxy radical.

modulation and a cavity operating in the TE_{011} mode. Samples irradiated in Spectrasil quartz were free from signals generated in the container.

RESULTS

When deoxygenated cyclohexane is irradiated at −190°C with high-energy electrons, the EPR spectrum shown in Fig. 2 is obtained. The intensity ratio of 1, 1, 2, 2, 1, 1 is compatible with the removal of a hydrogen atom from the ring (unequal density distribution for the unpaired electron at the five neighboring protons).[3] Cyclohexane saturated with oxygen yields the same EPR spectrum. On warming up to −60°C this spectrum vanishes irreversibly but no broad asymmetric absorption, which could be attributed to a peroxy radical, is observed. This leads to the hypothesis that at this temperature the rate of diffusion of oxygen through the solid is comparable with the recombination rate for radicals; hence a measurable steady-state concentration of peroxy radicals is not achieved. (By way of comparison, the buildup of the peroxy radical is observed at below −25°C in irradiated solid cyclohexanol plus oxygen.)

No spectroscopically detectable transient above 2400 A is observed in a liquid sample of irradiated deoxygenated cyclohexane. When the sample is saturated with oxygen, the spectrum shown in Fig. 3 is obtained. From the known optical length of the cell, its volume, the calculated number of peroxy radicals based on end-product analysis, and the roughly uniform production of radicals in the sample, an approximate extinction coefficient at 2750 A of 2×10^3 liter/mole-cm has been calculated. The decay of the transient absorption (Figs. 4 and 5) is independent of temperature in the range from 25°C to 71°C. This absorption is attributed to the cyclohexyl-peroxy free radical which, in view of the products measured for the reaction (c.f. Table I), probably takes part in the following reactions:

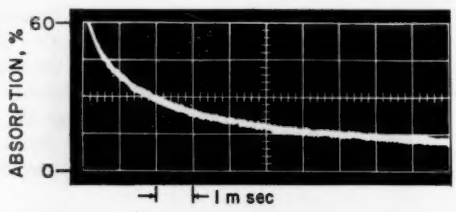

FIG. 4. Cyclohexane+O_2.

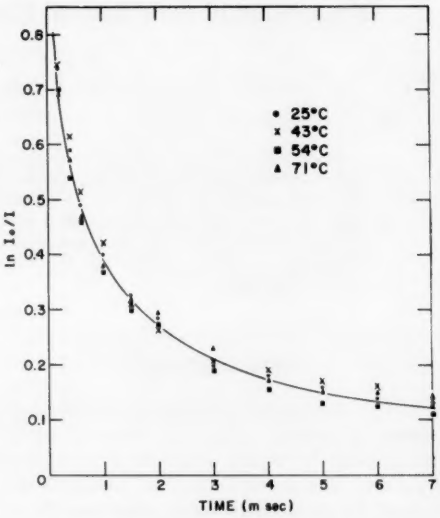

FIG. 5. Transient absorption of $C_6H_{11}O_2$ radical.

$$\text{I}\quad C_6H_{11}O_2\cdot + C_6H_{11}O_2\cdot \rightarrow C_6H_{11}OH + C_6H_{10}O + O_2$$

$$\text{II}\quad C_6H_{11}O_2\cdot + HO_2\cdot \rightarrow C_6H_{11}OOH + O_2.$$

Reaction I describes the major process which con-

TABLE I.

Product[a]	Yield[b]
Cyclohexanol	0.33
Cyclohexanone	0.32
Cyclohexene	0.16
Dicyclohexyl	0.04
Cyclohexyl hydroperoxide	0.15

[a] These products were measured by gas-liquid chromatography using a column filled with polypropylene glycol, UCON LB-500X, operated at 170°C. Ninety-five percent of all liquid products are accounted for and the results are in agreement with other published work [H. A. Dewhurst, J. Chem. Phys. **63**, 813 (1959)].

[b] Cyclohexene and dicyclohexyl are evolved from the excited cyclohexane molecule and the cyclohexyl radical, not the peroxy radical; hence they do not enter into these kinetic studies [A. MacLachlan, J. Am. Chem. Soc. **82**, 1005 (1960)].

[3] The experimental spectrum may be constructed by assigning a 24-gauss splitting to the α-proton, a 40-gauss splitting to the two axial β-protons, and a small (<5-gauss) splitting to the two equatorial β-protons which is not resolvable.

sumes approximately 80% of the peroxy radicals formed.[4] The concurrent reaction, II, consumes about 20% of the cyclohexyl-peroxy radicals, and it is believed essentially all of the HO_2 radicals, since no hydrogen-peroxide product was detected.

Converting absorption into radical concentration by using measured product yields, the curve R^{-1} vs time is obtained (Fig. 6). The initial concentration of cyclohexyl-peroxy radicals is $(3.8)10^{-4}$ mole/liter. The divergence of the reciprocal of the radical concentration from a straight line confirms the fact that more than one reaction is being observed. The rate of disappearance of free radicals is then described by

$$-dR/dt = k_I R^2 + k_{II} RS, \qquad (1)$$

where R=concentration of cyclohexyl-peroxy radicals and S=concentration of HO_2 radicals.

Several approximate methods have been employed to determine the value of both reaction rate constants and all agree within experimental error. The simplest method consists of assuming that reaction I will predominate at long times and calculating k_I from the final slope of the curve. From the initial slope and the known values of R and S at time zero, k_{II} is then calculated. The values thus obtained are

$$k_I = (1.6 \pm 0.6)\,10^6 \text{ liter/mole-sec},$$

$$k_{II} = (3.0 \pm 1)\,10^6 \text{ liter/mole-sec}.$$

Although the absolute values of these rate constants can fall within one another's experimental error, the values based on random errors alone do not overlap. Hence, the two rate constants are believed to be similar but not identical. These values are in good agreement with that obtained for the oxidation of cyclohexane using the rotating sector technique.[5]

DISCUSSION

The diffusion-controlled bimolecular rate constants for reactions I and II have been calculated using the relationship[6]

$$k_D = (4)\,10^3 \pi N_0 r_0 D, \qquad (2)$$

where k_D=diffusion-controlled rate constant, liter/mole-sec, N_0=Avogadro's number, r_0=interaction radius, cm, and D=diffusion constant (sum for both radicals, cm²/sec). The diffusion constant for the cyclohexyl-peroxy radical in cyclohexane was approximated by using the calculated value for a comparable stable molecule, cyclohexanone, yielding a value 2.0×10^{-5} cm²/sec. The values of diffusion-controlled rate constants obtained are

$$k_{D_I} = 2.7\times10^{10} \text{ liter/mole-sec},$$

$$k_{D_{II}} = 2.5\times10^{10} \text{ liter/mole-sec}.$$

[4] G. A. Russell, J. Am. Chem. Soc. **79**, 3871 (1957).
[5] L. Bateman and G. Gee, Proc. Roy. Soc. (London) **A195**, 391 (1948).
[6] T. R. Waite, J. Chem. Phys. **32**, 21 (1960).

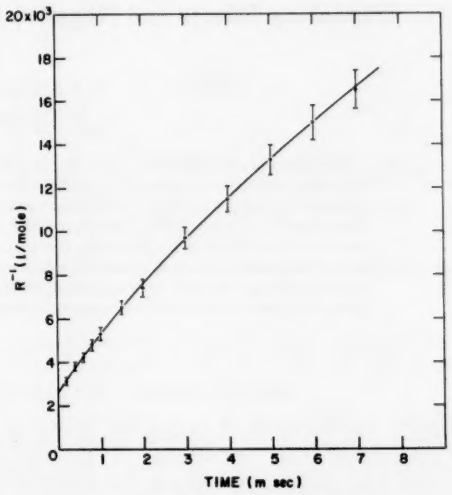

FIG. 6. Cyclohexyl peroxy radical.

For reaction I the measured reaction rate constant is approximately 10^{-4} times the diffusion-controlled rate constant. Using the coventional relation

$$k = Ae^{-E/RT}, \qquad (3)$$

where E is the activation energy (kcal/mole) and A is assumed not to change significantly over the temperature range studied, we calculate that an activation energy of 1 kcal/mole would have produced a measurable change in the rate of the reaction between 25° and 71°C. No systematic variation was observed; hence we conclude that the activation energy for reaction I is less than 1 kcal/mole and have no reason to believe that it is not zero. This appears reasonable since for the reaction of two free radicals no van der Waals repulsion is expected. Therefore, the reduced rate of the reaction must be attributed to steric factors. A steric hinderance to this reaction is understandable, since, for the reaction to occur, one radical must have the peroxy group in the highly unfavorable axial position while the other is in the favored equatorial position.

For reaction II of cyclohexyl-peroxy radicals with HO_2 radicals, any detailed interpretation of the mechanism in terms of activation energy and steric hinderance is unwarranted, since this is a minor reaction to which the measured parameters have a reduced sensitivity.

ACKNOWLEDGMENTS

The authors gratefully acknowledge the aid of V. F. Hanson in the design and construction of the equipment, particularly the sample cell and light source, and of D. C. Reitz for his EPR study of the radical, which will be published shortly.

Quenching Effects and Negative Photoconductivity in Amorphous Selenium

J. DRESNER
RCA Laboratories, Princeton, New Jersey
(Received April 21, 1961)

Negative photoconductivity and long wavelength quenching of photoconductivity have been observed in several evaporated layers of amorphous Se, with both effects showing a maximum for light of energy between 1.9 and 2.1 ev. From the position of the Fermi level, these effects have been identified with transitions from a set of sensitizing centers ranging from less than 0.58 to 0.65 ev above the valence band. Deep traps were investigated by thermally stimulated currents and by the analysis of space charge limited currents. Trapping states at 0.55 ev were detected which probably correspond to the same set of defect levels as the sensitizing centers. Several models which might account for the optical absorption, spectral response, quenching phenomena, and the exponential temperature dependence of the carrier mobilities, are discussed.

INTRODUCTION

SINCE the discovery of photoconductivity in the amorphous form of selenium,[1] the electrical, physical, and optical properties of this material have been studied by many investigators.[2–5] Most of the results obtained during the last decade are summarized in references 3 and 4. Nevertheless, the photoconductive process in amorphous selenium is not well understood. In particular it exhibits an anomalous spectral response, as the onset of photoconductivity occurs for photon energies about 0.6 ev greater than the optical absorption edge. This type of behavior has also been found in 9–10 dichloroanthracene[6] where it has been associated with surface phenomena. In selenium however, it appears to be a bulk property of the material. Moss[3] has suggested an explanation for this effect based on intermolecular barriers (the photoexcited carriers being able to move easily through the selenium chain molecules, but requiring additional energy to overcome the barriers and produce photocurrents).

This paper presents measurements of the optical quenching of photoconductivity and of the negative photoeffect in evaporated layers of amorphous selenium. Neither phenomenon has been previously reported in this form of selenium. These measurements were followed by a study of the distribution of trapping states using thermally-stimulated currents (TSC) and space-charge-limited currents (SCLC). By optical quenching is meant a decrease in photocurrent induced by the application of radiation having a wavelength different from the primary exciting radiation. The study of this well known phenomenon has been especially useful in elucidating the nature of the photoconductive process in CdS and CdSe.[7] The negative photoeffect consists in a decrease of the dark conductivity upon irradiation by light of the proper wavelength. This phenomenon has been reported in several substances,[8] including the gray hexagonal form of selenium. An explanation in terms of the band model has been given by Stockmann,[9] who showed that the effect could be accounted for by a mechanism essentially similar to that of optical quenching, that is, a release of minority carriers from bound states and recombination with majority carriers through fast recombination centers. Since there are restrictive requirements on the energies and cross sections of the bound states participating in the process, negative photoconductivity is seldom observed. The spectral response of these two effects thus gives additional information on the energies of the bound states.

The red amorphous allotrope of selenium can be obtained by rapid cooling from the melt or by evaporation. It is an unstable form which converts slowly to the gray hexagonal selenium at temperatures in excess of 50°C. However, evaporated films kept at room temperature are sufficiently stable so that their electrical properties do not change over a period of several months. Both of these allotropes exhibit intrinsic p-type conductivity.[10] The crystal structure of the hexagonal form consists of parallel spiral chains directed along the c axis of the crystal. Each Se atom is covalently bound to its two nearest neighbors in the chain (2.32 A), and to its four second-nearest neighbors (3.44 A) in adjacent chains. Evidence from x-ray[11] and electron[12] scattering experiments show that the chain structure is preserved in amorphous selenium over domains about 10 A in size, with the second-nearest neighbor distance increased to 3.80 A. While some of the x-ray data can also be interpreted in terms of Se_6 or Se_8 ring molecules

[1] P. K. Weimer, Phys. Rev. **79,** 171 (1950).
[2] T. S. Moss, *Photoconductivity in the Elements* (Academic Press Inc., New York, 1952), pp. 185–203.
[3] T. S. Moss, *Optical Properties of Semiconductors* (Academic Press Inc., New York, 1959), pp. 152–166.
[4] A. F. Ioffe and A. R. Regel, "Non-crystalline, amorphous and liquid electronic semiconductors" in *Progress in Semiconductors,* edited by A. F. Gibson (John Wiley & Sons, Inc., New York, 1960), Vol. 4, p. 237.
[5] R. S. Caldwell and H. Y. Fan, Phys. Rev. **114,** 664 (1959).
[6] E. Bock, J. Ferguson, and W. G. Schneider, Can. J. Chem. **36,** 507 (1958).
[7] R. H. Bube, *Photoconductivity of Solids* (John Wiley & Sons, Inc., New York, 1960), pp. 335–356.
[8] Reference 7, p. 404.
[9] F. Stockmann, Z. Physik **143,** 348 (1955).
[10] A. von Hippel, J. Chem. Phys. **16,** 372 (1948).
[11] H. Richter and F. Herre, Naturwissenschaften **44,** 31 (1957).
[12] H. Friedmann, Z. Naturforsch. **11a,** 373 (1956).

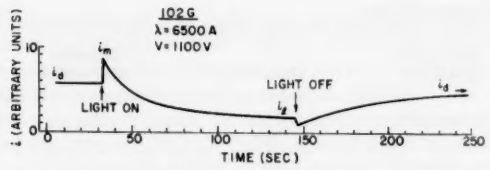

FIG. 1. Negative photoconductivity in a gap cell of amorphous selenium.

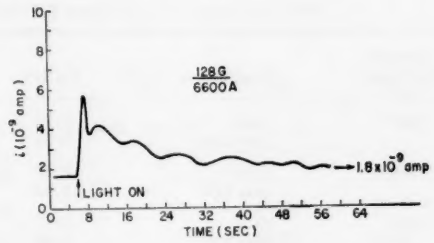

FIG. 3. Oscillations induced upon irradiation by 6600 A light, for which $\Delta i \approx 0$.

viscosity studies on liquid Se indicate that the ring structure is probably a minor constituent of the vitreous phase.[4] Amorphous selenium can then be thought of as composed of randomly oriented chains, where the short range order is preserved over domains containing only a few atoms.

EXPERIMENTAL PROCEDURE

All samples were prepared by vacuum evaporation of spectrographic grade selenium. This material contained traces of Cu, Mg, Pb, and Hg in amounts less than 10 ppm, and less than 1 ppm of As and Te. The thickness of the films was measured by optical means after deposition. All measurements reported are on layers 10μ thick. Evaporated gold films were used for electrodes because the work function of gold, 4.85 ev, is larger than that of Se, 4.62 ev. This situation is favorable for Au to form an ohmic contact for holes on Se, as was verified experimentally. Most measurements were made at room temperature on samples evaporated on a Pyrex substrate. Since the selenium films peel off the glass upon cooling, NaCl crystals were used as substrate for the thermally stimulated current measurements. Films deposited on NaCl were found to withstand several cycles of cooling to -180°C and heating to 40°C without changing their measured electrical properties.

Two types of electrode geometries were used. In sandwich cells, the selenium was evaporated on a thin transparent Au film whose transmission was measured on each sample. The second electrode consisted of an opaque evaporated Au dot of 0.32 cm². This evaporation was done in several steps, at intervals of a few minutes, to insure that the selenium under the dot would not overheat to the point where crystalline nuclei might form. In the second type, the selenium was deposited on opaque Au electrodes having a gap 0.5 mm wide. In these experiments, light always reached the gap through the transparent substrate.

The photocurrents were measured with a fast electrometer coupled to a strip chart recorder having a response time of 0.02 sec. Low temperature measurements were performed in an evacuated cryostat. Except where otherwise specified, the samples were irradiated with light from a B & L monochromator using an incandescent lamp source. For all calculations of the photoconductive gain, the energy falling upon the sample was measured with a thermopile.

Since the evaporation geometry appears to have an effect on the properties of the films, it will be described in detail. The selenium was evaporated from an Al_2O_3-coated boat located 5 cm below the substrate, through a glass column 3.2 cm in diameter. The boat was preloaded with 0.3 gm of Se which was evaporated in 5 min under a pressure of 5×10^{-5} mm Hg. All cells which exhibited either quenching or the negative photoeffect, were obtained with this geometry. These effects were never obtained with a more open geometry; with the diameter of the glass column increased to about 10 cm and the throw distance to 7.5 cm. In both of these geometries, the increase in substrate temperatures during the evaporations ranged from 3 to 6°C above the initial room temperature. It is unlikely therefore, that differences in the substrate heating during evaporation account for this effect. No further investigations of the effect of varying the evaporation geometry were performed. Samples evaporated under identical conditions

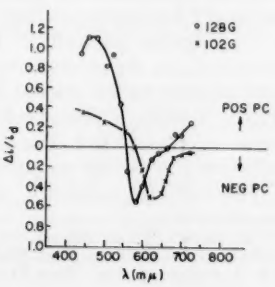

FIG. 2. Spectral dependence of the negative photoeffect.

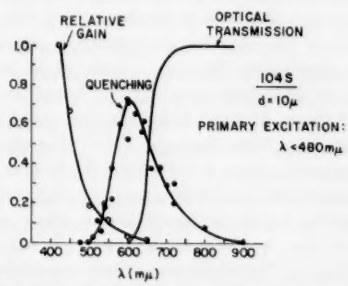

FIG. 4. Spectral dependence of photoconductive gain, long-wavelength quenching and optical transmission of a sandwich cell.

TABLE I. Fermi level and sensitivity data.

Cell no.[a] and type	Illumination	E_{fp} (ev)	Δi (amp)[b] at 4500A	Quenching	Negative photoeffect
104S	dark	0.75	2.9×10^{-8}	...	No
	bias light	0.61	...	Yes	...
100S	dark	0.67	1.8×10^{-7}	..	...[c]
	bias light	0.62	...	Yes	...
105S	dark	0.73	1.8×10^{-9}	...	No
	bias light	0.69	...	No	...
110S	dark	0.78	1.3×10^{-9}	...	No
	bias light	0.71	...	No	...
128S	dark	0.77	2.1×10^{-11}	...	No
	bias light	0.76	...	No	...
101G	dark	0.65	...[c]	...	Yes
102G	dark	0.61	1.9×10^{-10}	...	Yes
128G	dark	0.60	1.1×10^{-9}	...	Yes
122G	dark	0.71	9.1×10^{-11}	...	No
126G	dark	0.74	3.5×10^{-11}	...	No
127G	dark	0.73	3.3×10^{-11}	...	No

$E_{fp}\leq0.65$ ev: quenching or negative photoconductivity

$E_{fp}\geq0.69$ ev: no quenching or negative photoconductivity

[a] S=sandwich cell; G=gap cell.
[b] V=10v for S cells; V=1500 v for G cells.
[c] Not measured.

differed considerably in dark resistivity and photoconductive gain. Two sandwich cells showing long-wavelength-quenching of photoconductivity, and four gap cells showing a negative photoeffect were obtained out of eight evaporations of each type of cell.

EXPERIMENTAL RESULTS

Figure 1 shows the current through a gap cell exhibiting negative photoconductivity. Upon application of 6500 A light, the current rises sharply then decreases to a steady value i_l below the dark current i_d. Although the light initially produces some excitation, the magnitude of the effect is described by $(i_d-i_l)/i_d$ instead of $(i_m-i_l)/i_m$ because an initial current spike is characteristic of the photoconductive response in all amorphous selenium cells, and there is evidence that it is associated in part with polarization due to trapped charge. Upon removing the light, the current rises to its dark value with a time constant $\tau=40$ sec. Values of τ ranging from 5 to 80 sec were observed in other samples. The spectral dependence of the negative photoeffect is shown in Fig. 2 for two gap cells. The two curves show maximum quenching of the dark current for photon energies of 1.95 and 2.15 ev. At shorter wavelengths, the photocurrent becomes positive. Sample 128G also shows positive photoconductivity for $\lambda>6600$ A. In this cell, the current underwent oscillations upon application of light in the negative region of the spectrum. These were most pronounced for $\lambda=6600$ A, where $\Delta i/i_d=0$ and are shown in Fig. 3. The oscillations have a period of about 8 sec and are damped, persisting for about 2 min. They may be of a nature similar to those observed by Liebson[13] in a CdS crystal upon application of infrared light near a rectifying contact.

Figure 4 shows the characteristics of a sandwich cell showing quenching of the photocurrent. The opt cal transmission was computed from the absorption coefficients given by Moss.[3] The spectral response of the cell is shown in terms of photoconductive gain (charge transported across the sample per absorbed quantum). All measured sandwich cells, as well as the gap cells which did not show negative photoconductivity, had essentially the same spectral response. The maximum for positive photoconductivity shown for Se 128G in Fig. 2 is not characteristic of the spectral response since the curve was not corrected for variations of light intensity with wavelength. The quenching curve is that obtained for primary irradiation by an incandescent light passed through a Corning 5-58 filter ($\lambda<4800$ A). The magnitude of the effect is given by $(i_1-i_2)/i_1$, where i_1 is the photocurrent under the primary radiation and i_2 that after the additional application of the quenching light. Maximum quenching occurs for photon energies of 2.1 ev, corresponding closely to the maximum for the negative photoeffect. Upon removal of the quenching light, the photocurrent again rises to i_1 with a time constant on the order of 30 sec.

Figure 4 shows a photoconductive response with a maximum for $\lambda<4200$ A. This is in agreement with the results found by Gilleo[14] on gap cells and those reported by Fotland[15] for sandwich cells. However Moss'

[13] S. H. Liebson, J. Electrochem. Soc. **102,** 529 (1955).
[14] M. M. Gilleo, J. Chem. Phys. **19,** 1291 (1951).
[15] R. A. Fotland, J. Appl. Phys. **31,** 1558 (1960).

measurements on gap cells[2] give a maximum photosensitivity at 4400 A, while those of Weimer and Cope[16] on sandwich cells scanned by an electron beam show that the maximum gain is reached at 4600 A. There is no evident correlation between these various results and the type of cell or the thicknesses of the evaporated layers (ranging from 0.57 to 50μ) used by the different investigators.

The results obtained on all the measured samples are shown in Table I, which lists the illumination conditions, the position of the hole Fermi level E_{fp} above the valence band, the photocurrent at 4500 A, and the presence of quenching or of the negative photoconductivity. The Fermi level is calculated from the relation

$$E_{fp}=kT\ln(e\mu Nv/\sigma),$$

where e is the electronic charge, T the absolute temperature and σ the conductivity. The hole mobility $\mu_p=0.14$ cm^2 sec^{-1} v^{-1} at 20°C,[17,18] while N_v, the density of states at the top of the valence band, was calculated to be 9.3×10^{19} cm^{-3} using the value $m=2.5$ for the hole effective mass.[3] Because of the different geometries and voltages used for the gap and sandwich cells, the values of the photocurrent should be compared only within the same group. Table I shows that all quenching or negative photoeffects were observed when $E_{fp}\leq0.65$ ev above the valence band, whereas all samples where $E_{fp}\geq0.69$ ev did not show either effect. Furthermore, the samples which showed either quenching or negative photoconductivity also were the most sensitive within each group under 4500 A illumination. The negative effect was found only in the gap cells, but in view of the fact that all the measured sandwich cells had $E_{fp}\geq0.65$ ev in the dark, this may not be significant. As discussed further below, the data of Table I indicates the presence of a range of sensitizing centers lying between 0.6 and 0.7 ev above the valence band.

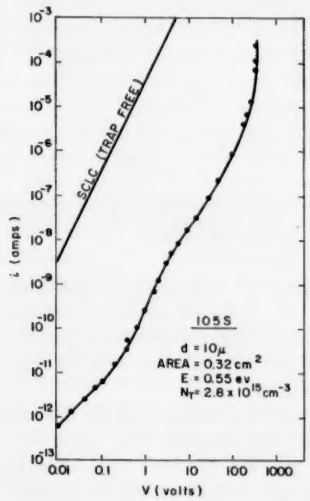

FIG. 5. Current-voltage characteristic for a sandwich cell.

TABLE II. Trap depth data.

Sample	SCLC E_T (ev)	SCLC N_T (cm^{-3})	TSC E_T (ev)	Slope of (I_{dark} versus $1/T$ curve) E (ev)
138S	...	...	...	0.28
139S	...	...	0.52[a]	0.30
140S	...	...	0.56[a]	0.58
	0.58	7×10^{14}	0.56[a,b]	0.26[b]
	...	...	0.52[c,b]	0.26[b]
105S	0.55	2.8×10^{15}	...	...

[a] Heating rate 0.12°K/sec.
[b] After heat treatment (see text).
[c] Heating rate 0.02°K/sec.

The next series of experiments were designed to study the distribution of trapping states in the forbidden gap. Much information about localized defect states in semiconductors can be obtained by sweeping the Fermi level through the forbidden gap by optical or thermal means. In the case of insulators, it is also practicable to vary the position of the steady state Fermi level by the voltage-controlled injection of majority carriers. From the characteristics of this one carrier SCLC,[19,20] the densities of trapping centers and their energies can be obtained, provided the energy distribution is simple, i.e., there are few discrete levels widely separated in energy. This type of analysis has been used to detect the deepest trap levels in CdS crystals.[21]

Figure 5 shows the current-voltage curve obtained with a selenium sandwich cell which had been kept in darkness for 48 hours prior to the measurement. The upper curve shows the SCLC which would be drawn through the sample if it were trap-free. At very low voltages the curve follows a linear relationship, justifying the choice of Au for making ohmic contacts to selenium. As the voltage is increased beyond 0.5 v, the curve approximates a square law through five decades of current. At 400 v the current begins to rise sharply and becomes too unstable to permit further measurements. The experimental points shown in Fig. 5 are

[16] P. K. Weimer and A. D. Cope, RCA Review **12,** 314 (1951).
[17] W. E. Spear, Proc. Phys Soc (London) **B76,** 826 (1960).
[18] In the absence of other mobility data, this value of the drift mobility will be used for the calculations. Spear, on the assumption of a trap controlled mobility, has calculated a value of 60 cm^2 v^{-1} sec^{-1} for the microscopic mobility. Recent measurements performed at this laboratory have given Hall mobilities of the order of 1 cm^2 v^{-1} sec^{-1} for evaporated polycrystalline films of several insulator and semiconductor materials. It is unlikely that the hole mobility would be much greater than this value in an evaporated amorphous Se film.
[19] A. Rose, Phys. Rev. **97,** 1538 (1955).
[20] M. A. Lampert, Phys. Rev. **103,** 1648 (1956).
[21] M. A. Lampert, A. Rose, and R. W. Smith, J. Phys. Chem. Solids **8,** 464 (1959).

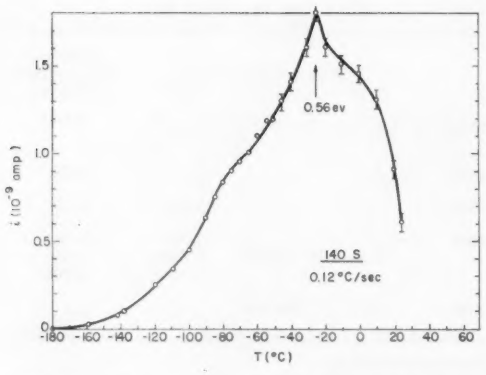

FIG. 6. Thermally stimulated current of a sandwich cell on a NaCl substrate. The arrow indicates the energy of the Fermi level at the peak of the curve.

thermal equilibrium values, the current having been allowed to decay to a steady level after each rise in applied voltage. The shape of the curve is close to that predicted by the theory for one set of trapping levels lying within a narrow energy range. The density of traps N_T can be obtained from the voltage at which the current rises sharply V_f, and is given by the expression $N_T=2V_f\epsilon/ed^2$ (mks), where ϵ is the static dielectric constant, e is the electronic charge, and d the layer thickness. The trap depth is given by

$$E_T=kT\ln(N_v/2\theta N_T),$$

where θ is the ratio of the measured current in the square-law region to that in the trap-free material. The results obtained on two samples by this method are given in the second and third columns of Table II.

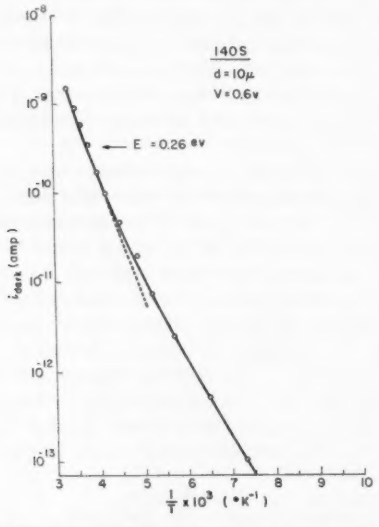

FIG. 7. Dependence of the dark current upon temperature in amorphous selenium.

The distribution of trapping states was also investigated by the method of thermally stimulated currents. Figure 6 shows the results obtained with a film deposited on a NaCl substrate. A broad current peak is observed corresponding to a level 0.56 ev above the valence band, as calculated from the position of the Fermi level at the maximum of the curve. The results of the TSC method are listed in the fourth column of Table II. These results were obtained on freshly evaporated samples, with the exception of two measurements on cell 140S, where the film had been baked for 30 min at 80°C in a vacuum. The trap energies for sample 140S are slightly lower than that calculated from SCLC. The identification of E_{fp} at the peak of the TSC curve with the trap energy, is based on the assumptions of fast retrapping of the released carriers and initial saturation of the traps. If

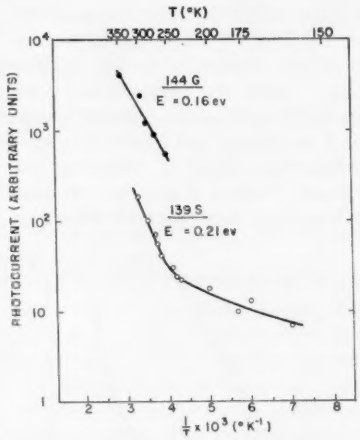

FIG. 8. Temperature dependence of the photocurrent under irradiation by blue light (Corning 4–74 filter). 144G is a gap cell on glass; 139S a sandwich cell on NaCl.

these conditions are only partially satisfied, it can be shown[22] that the calculated trap depth will be lower than the true value. Under the present experimental conditions, it is doubtful that the error in the calculated values is greater than kT.

Figure 7 shows the variation of the dark current with the reciprocal temperature. The slope of the initial straight line portion of the curve corresponds to an activation energy $E=0.26$ ev. All the samples measured showed an initial exponential curve with deviations at low temperatures. The values of E calculated from the initial portion of the curves are given in the last column of Table II. With the exception of one sample, all the values fall within the range 0.26 to 0.30 ev. This data may be interpreted as arising from a curve with slope $E_a/2kT$, characteristic of a level of uncompensated acceptors lying 0.55 ev (average value) above the valence band. It is of interest that the unbaked 140S

[22] R. R. Hearing and E. N. Adams, Phys. Rev. **117**, 451 (1960).

sample showed a value of E twice as high and a resistivity more than 3 orders higher than after baking, suggesting that the heat treatment strongly reduced the degree of compensation. The results of Table II indicate the presence of a defect level with an energy (averaged from SCLC and TSC measurements) 0.55 ev above the valence band.

Figure 8 shows the temperature dependence of the photocurrent on a sandwich cell evaporated on NaCl and on a gap cell on a glass substrate. Both cells were illuminated by broad-band blue light (Corning 4-74 filter). The photocurrent decreases exponentially upon cooling, with initial slopes of 0.16 and 0.21 ev. These are in the range of the slopes given by Spear[23] for the exponential dependence of the hole (0.14 ev) and electron (0.25 ev) mobilities in amorphous selenium. It is thus probable that above 250°K, the variation of the photocurrent with temperature reflects changes in the carrier drift mobility, rather than a change in band gap or in the recombination kinetics.

DISCUSSION

The data of Table II shows the existence of a range of trapping levels centered 0.55 ev above the valence band. Other levels have been reported by Spear,[17,23] whose experiments indicate that the hole- and electron-drift mobilities may be controlled by trapping levels respectively 0.14 ev above the valence band and 0.25 ev below the conduction band. The 0.14 ev level is too shallow to have been detected in the temperature range used in our TSC measurements. Lanyon and Spear[24] have reported a deep trap at 0.79 ev from SCLC measurements. With a correction applied for the lower value of the mobility used in this paper, this level would lie at 0.66 ev. It is of interest that in pure Se monocrystals, the hole mobility and its exponential dependence on temperature are the same as in the amorphous form: 0.14 $cm^2\ v^{-1}\ sec^{-1}$ at 20°C with an activation energy of 0.13 ev.[25] Shallow trapping levels have also been detected in Se monocrystals at 0.10, 0.14, and 0.17 ev by the TSC method.[26] These results suggest that the shallow trapping levels arise from a type of defect common to the vitreous and crystalline states, i.e., a defect associated with the short range structure of the Se chain. The density of these states has been estimated to be of the order of 10^{20} cm^{-3}, which is too high for them to be attributable to impurities.

More information about bound states in the forbidden gap is furnished by the quenching phenomena. These may be interpreted in terms of a phenomenological model with two types of recombination centers, which has been found useful for other photoconductors.[7] The presence of these quenching effects is associated with multiply charged impurity centers which, in a p-type material such as Se, exhibit a small capture cross section for holes when occupied by an electron. The type of effect observed varies with the energy of these states. If they lie below E_{fp}, negative photoconductivity can be observed by a transition from the center to the conduction band, the ejected electron being captured by a fast recombination center. If they lie above E_{fp}, the sample becomes sensitized upon the application of band-gap light as the optically freed electrons collect in these centers. The quenching transition from the centers to the conduction band shifts the electron distribution to the fast recombination centers and desensitizes the material. The data of Table I shows the higher photosensitivity of the samples exhibiting quenching. From the position of the Fermi level, it is seen that some of the sensitizing centers must lie above 0.62 ev and none above 0.69 ev from the valence band. Similarly, the connection between E_{fp} and the occurrence of the negative effect, shows that some of the multiply-charged centers in those samples must lie at least kT below 0.60 ev, while the higher photosensitivity of the same samples under 4500 A illumination indicates that some of these centers must also lie above E_{fp}. The data of Table I can then be interpreted as implying the existence of a distribution of sensitizing centers ranging in energy from below 0.58 ev, to 0.65 ev from the valence band. This range is close to the energies found for the trapping centers listed in Table II.

The possibility also exists that the negative photoconductivity induced by 2.1-ev light is the result of a transition from the level at 0.14 ev to the conduction band, which is compatible with the 2.3-ev optical-band gap. This possibility can be discounted by considering the recovery from the negative effect upon removal of the light. This recovery is effected by the thermal release of a hole from the center to the valence band, which re-establishes the dark carrier concentration. The lifetime τ of the trapped hole is given by

$$1/\tau = S_p v N_v \exp(-E/kT),$$

where S_p is the cross section of the center for hole capture, v is the thermal velocity of holes in the valence band, and E the energy of the center. At 20°C, for $\tau = 10$ sec, $v = 10^7$ cm sec^{-1}, $N_v = 10^{20}$ cm^{-3}, and $E = 0.14$ ev one finds $S_p < 10^{-25}$ cm^2. Although a small value of S_p is required for sensitization and quenching, a value of 10^{-25} cm^2 is unlikely, the smallest cross section indicated by experiments to date being of the order of 10^{-22} cm^2. If the same calculation is performed for a center at $E = 0.55$ ev, a value of $S_p = 10^{-19}$ cm^2 is obtained, which is still several magnitudes smaller than the cross section of the order of 10^{-15} cm^2 to be expected from an uncharged defect center.

These considerations suggest that the sensitizing centers correspond to the same defects as the trapping states of Table II. A similar situation where a set of

[23] W. E. Spear, Proc. Phys. Soc. (London) **B70,** 669 (1957).
[24] W. E. Spear and H. P. L. Lanyon, *Proceedings of the International Conference on Semiconductor Physics, Prague 1960* (Czechoslovak Academy of Sciences, Prague, 1961), p. 987.
[25] K. W. Plessner, Proc. Phys. Soc. (London) **B64,** 671 (1951).
[26] E. N. Arkadeva and S. M. Rivkin, Soviet Phys.—Solid State **1,** 1264 (1960).

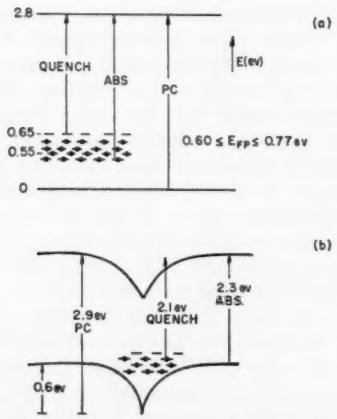

FIG. 9. (a) Band model where strong optical absorption at 2.3 ev is due to transitions from impurity states. (b) Model where anomalous spectral response arises from intermolecular barriers.

centers can perform more than one function has been reported in other photoconductors.[27] Insufficient data is available to determine the nature of these sensitizing centers. It is probable that these are also present in crystalline Se, as evidenced by the occurrence of the negative effect and high photosensitivity. In pure Se crystals, E_{fp} is in the neighborhood of 0.35 ev at 20°C, which would make the high sensitivity of this material consistent with multiply charged centers lying above 0.58 ev. However, in the absence of published data on the spectral dependence of the negative effect in gray Se, no conclusion can be reached about this point.

The absence of negative photoconductivity in samples where $E_{fp} \geqslant 0.69$ ev, cannot be accounted for by the preceding analysis, which considers only the position of the Fermi level. This effect may be associated with variations in the position of the hole demarcation level E_{dp} for the sensitizing center, whose position is given by $E_{dp}=E_{fp}+kT\ln(pS_p/nS_n)$, where n and p are the free-electron and hole-concentrations, and S_n the electron capture cross section. Taking $S_p=10^{-19}$ cm^2 and $S_n=10^{-15}$ cm^2, one finds that as E_{fp} rises from 0.60 to 0.77 ev, E_{dp} decreases from 1.51 to 1.45. If the negative effect is associated with an impurity having multiple levels, a decrease in E_{dp} could change the charging character of the center, since a hole in the upper level is then more likely to capture an electron than to remain in thermal equilibrium with the valence band.

Some of the difficulties in the interpretation of photoconductive phenomena in non-crystalline solids become apparent when an attempt is made to construct a band model for amorphous Se on the basis of the data presented above. Such a model must account for the optical absorption and spectral response of photoconductivity as well as for the quenching phenomena. In the following discussion some of the possible models will be considered. There is disagreement between the values of the photoconductive band gap reported by different investigators and the value 2.8 ev will be used in the discussion, the relative response at this energy being not less than 65% of maximum for any of the data reported.

A simple model might be that of Fig. 9(a), which assumes a band gap of 2.8 ev, with the strong optical absorption at 2.3 ev resulting from transitions from a set of bound states to the conduction band. The holes created by the 2.3 ev light would then not contribute to the conductivity. However it is unlikely that there could exist a density of bound states high enough to account for an absorption coefficient at 2.3 ev of 10^5 cm^{-1}, characteristic of lattice absorption. Furthermore, from the spectral dependence of the absorption coefficient, it can be seen that most of these states should lie between 0.5 and 0.7 ev above the valence band. Since evaporated layers were obtained with dark values of the Fermi level ranging from 0.60 to 0.77 ev, one would expect to find strong differences in absorption in the red portion of the spectrum between samples of different conductivity. No such effects were observed. This last argument can also be applied to models which introduce a split valence band in order to account for the photoconductive response.

Moss[3] has suggested that potential-barriers of about 0.6 ev might impede the transfer of holes between adjacent chains. Such a model is shown in Fig. 9(b), with the sensitizing centers of energy ~0.6 ev located in the barrier region. The 2.3-ev absorption is associated with the chain structure, and holes must be excited from deeper states in order to overcome the barriers and

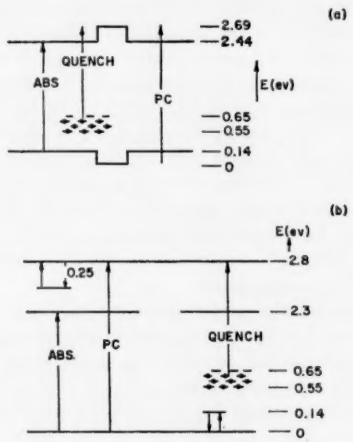

FIG. 10. These two schemes assume that electrons as well as holes must move through the bulk of the sample in order to observe photoconductivity. (a) Model where μ_p and μ_n are controlled by barriers or variations in the band gap. (b) Model where photoconductivity requires a transition to an orbital linking more than one chain molecule.

[27] R. H. Bube, J. Appl. Phys. **31**, 315 (1960).

contribute to conductivity. Although such a model can be made to account for the observed optical absorption, photoresponse, and quenching, it presents several difficulties. Again, the optical absorption in the red part of the spectrum would be due to transitions from states whose occupancy should show strong variations for different samples. Furthermore it cannot readily account for the exponential temperature dependence of the hole and electron mobilities. If, as Spear has suggested, μ_p is controlled by trapping states at 0.14 ev, with a density of the order of 10^{20} cm^{-3}, one would have to assume that these shallow traps are located within the barrier region. The 0.6-ev potential barrier would then itself consist of a domain which contains several chain or ring molecules. A simpler alternative would be to interpret the mobility data as indicating that μ_p and μ_e are controlled by barriers extending respectively 0.14 ev below the valence band and 0.25 ev above the conduction band. This hypothesis gives a photoconductive band gap of 2.69 ev, which agrees with the lowest reported value given by Weimer and Cope.[16] If these potential barriers are associated with the chain terminations, chain lengths of the order of 500 atoms[28] would give the required barrier densities. Such a model, shown in Fig. 10(a), is also able to account for the data of Fig. 2 which shows that the negative effect can be induced by radiation of energy less than 1.7 ev. In this case the electron ejected from a center below the Fermi level need not cross potential barriers but can be captured by a fast recombination center in its own chain.

An alternate model is shown in Fig. 10(b), where the 2.3-ev absorption corresponds to transitions to an excited state of the chain molecule, while photoconductivity is induced by transitions to states linking more than one chain. This model, as well as the previous one, is based on the assumption that the electrons as well as the holes must move through the sample in order for photoconductivity to be observed. However, it is generally unnecessary that the minority carrier be mobile in order to observe high photosensitivity when, as is the case here, the majority carrier can be replenished at the electrodes. This is especially true when the irradiation of the sample is uniform, as for the gap cells described above which showed the same spectral response as the sandwich cells illuminated through one electrode. Furthermore, the results of soft x-ray absorption studies on amorphous selenium[29] show no evidence of any conduction band splitting such as shown in Fig. 10(b). It is evident that none of these models is wholly satisfactory in accounting for the observed photoconductive phenomena in amorphous Se. Furthermore in interpreting the quenching phenomena, one should keep in mind that the maxima in the spectral dependence of quenching and negative photoconductivity are not necessarily indicative of the optical energy involved in the transition. The lowest energy photon which can cause the effects may be the significant quantity. Useful data for the interpretation of the above results might be obtained from an experiment similar to that performed by Kepler[30] on anthracene, where the production of mobile holes and electrons was investigated as a function of wavelength. For the scheme of Fig. 10(b), the onset of the production of free holes would occur at 2.3 ev, while approximately 2.8 ev would be needed to produce free electrons. For the barrier model of Fig. 9(b), these values would be interchanged.

ACKNOWLEDGMENT

The author is indebted to Dr. A. Rose for several helpful discussions.

[28] H. Krebs and F. Schultze-Gebhart, Naturwissenschaften **41**, 474 (1954).

[29] M. P. Givens, C. J. Koester, and W. I. Goffe, Phys. Rev. **100**, 1112 (1955).

[30] R. G. Kepler, Phys. Rev. **119**, 1226 (1960).

Organic Semiconductors: Aromatic Hydrocarbon Positive Ions in Solids

G. E. Blomgren and J. Kommandeur
Parma Research Laboratory, Union Carbide Corporation, Parma 30, Ohio

(Received April 20, 1961)

Mixtures of aromatic hydrocarbons with antimony pentachloride in carbon tetrachloride have been studied by the methods of electron spin resonance and visible spectroscopy. The observation of a Tyndall effect and the spectroscopic properties show that the mixtures are colloidal suspensions. The visible spectra are characteristic of aromatic ions and a comparison of ion concentrations measured by visible spectroscopy and spin concentrations measured by spin resonance indicates that the aromatic ions in the solids are the only paramagnetic species present. The solids were found to exhibit high electronic conductivity.

I. INTRODUCTION

In recent years there has been a growing interest in the reactions of strongly basic aromatic hydrocarbons with Lewis acids. In many of these reactions, good evidence has been found, by the methods of electron spin resonance (ESR)[1] and visible spectroscopy,[2,3] for the occurrence of relatively stable aromatic positive ions as intermediates in these reactions. It is the object of this paper to present evidence that, in the reaction of an aromatic hydrocarbon with antimony pentachloride in carbon tetrachloride, an electronically conducting solid, which contains aromatic positive ions in amounts depending on the particular aromatic chosen, precipitates.

Many years ago Hilpert and Wolf[4] observed the formation of highly colored solids in the reactions of aromatic hydrocarbons with $SbCl_5$. It was not until 1957, however, that Weissman, DeBoer, and Conradi[5] showed that the solid complexes of anthracene, tetracene, and perylene with $SbCl_5$ are paramagnetic and show a single exchange-narrowed line in the ESR spectrum. These authors postulated that the paramagnetism arose, at least in part, from aromatic positive ions and found in support that dissolution of the solid in phosphorous oxychloride resulted in a broad unresolved absorption of about the same width as that of the aromatic positive ions in H_2SO_4 solutions. Unfortunately, $POCl_3$ might be expected to be reactive in this system and this result cannot be regarded as conclusive evidence for the presence of aromatic ions in the solid. Recently Aalbersberg, Hoijtink, Mackor, and Weijland[3] made a spectroscopic study of aromatic-$SbCl_5$ mixtures in nitrobenzene and concluded that electron transfer from the hydrocarbon occurred and that monopositive aromatic ions were formed in solution. The present work, however, shows that this system forms a suspension of small solid particles and that the previously observed results are due to aromatic ions present only in these particles. The experiments leading to these conclusions are discussed below.

[1] A. Carrington, F. Dravnieks, and M. C. R. Symons, J. Chem. Soc. **1959**, 947.
[2] W. Ij. Aalbersberg, G. J. Hoijtink, E. L. Mackor, and W. P. Weijland, J. Chem. Soc. **1959**, 3049.
[3] W. Ij. Aalbersberg, G. J. Hoijtink, E. L. Mackor, and W. P. Weijland, J. Chem. Soc. **1959**, 3055.
[4] S. Hilpert and L. Wolf, Ber. deut. chem. Ges. **46**, 2215 (1913).
[5] S. I. Weissman, E. DeBoer, and J. J. Conradi, J. Chem. Phys. **26**, 963 (1957).

II. EXPERIMENTAL METHODS

A. Solutions

The same solutions were used for the optical and spin resonance determinations. They were prepared by adding a solution of $SbCl_5$ in CCl_4 (0.02 molar) to a solution of hydrocarbon in CCl_4. The hydrocarbons used were reagent grade, and were purified by chromatography over silica gel. The hydrocarbon solutions were dried over CaH_2. It was found that, with hydrocarbon concentrations in the range of 10^{-4}–10^{-5} molar, colloidal solutions of the $SbCl_5$ complexes were obtained. Only after prolonged standing do these solutions show a tendency to precipitate. Under dark field illumination in a microscope, a Tyndall effect could be observed.

B. ESR Measurements

The ESR measurements were performed at 9500 Mc/sec using a magnetic field modulation scheme of the conventional type. To determine spin concentrations, use was made of a technique developed by Singer.[6] This method uses a single crystal of ruby as an internal standard. This crystal is then calibrated by a single crystal of $CuSO_4 \cdot 6H_2O$ of known susceptibility. The method offers the great advantage that the concentration determinations are independent of the conditions under which the calibration is carried out. Signals from sample and ruby are recorded together in one run, whereby only the magnetic field setting is changed.

To obtain a sufficient signal-to-noise ratio, large samples had to be used. Thus, each sample tube was filled to a height which was more than the height of the resonant cavity. This meant that the change of modulation amplitude and microwave field over the

[6] L. S. Singer, J. Appl. Phys. **30**, 1463 (1959).

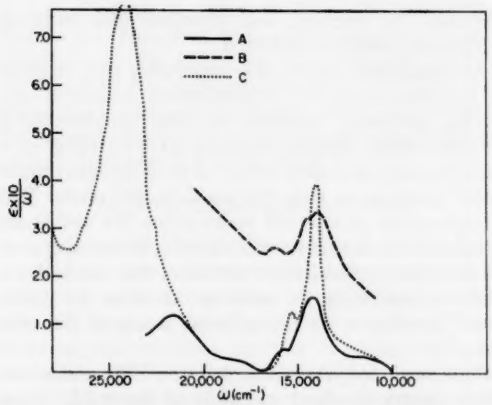

FIG. 1. Spectrum of the anthracene$^+$ ion. A. Anthracene-$SbCl_5$ in colloidal solution (———). B. Solid Anthracene-$SbCl_5$ in KBr pellet (------). C. Anthracene in H_2SO_4 (.....) (anthracene$^+$ and anthracene-H^+).

Note: The spectrum of the solid is on an arbitrary intensity scale.

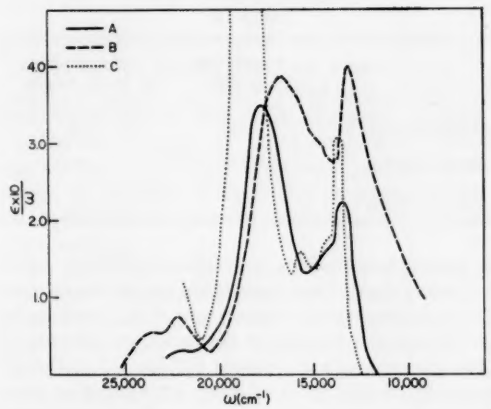

FIG. 3. Spectrum of the perylene$^+$ ion. A. Perylene-$SbCl_5$ in colloidal solution (———). B. Solid Perylene-$SbCl_5$ in KBr pellet (------). C. Perylene in H_2SO_4 (.....).

Note: In (A), the absorption peaks of the neutral perylene show at 22.000 and 23.000 cm^{-1}. In (B), the intensity is an arbitrary scale.

cavity had to be taken into account. The Varian cavity was, therefore, calibrated along its z axis with a very small standard sample. An effective length can then be defined for samples more than 0.5-cm long. This effective length is the length of a sample from which the same signal intensity would have been obtained if the microwave and modulation field had been uniform along the z axis of the cavity. For the cavity used, this effective length was found to be 1.2 cm when the sample tube was filled so as to occupy the whole cavity length of 2.5 cm. The accuracy of a determination of an absolute spin concentration carried out in this way is about 20% at this concentration level.

C. Ultraviolet Spectra

All ultraviolet spectra were recorded on a Carey Model 14 Spectrophotometer. At the concentrations used, cell lengths varied from 1–10 cm. Some dispersion was encountered in the $SbCl_5$ solutions due to the light scattering of the colloids. This, however, contributes mainly to the ultraviolet part of the spectrum, and the accuracy in the visible range is impaired only slightly. Points of no absorption, at long wavelengths, were used as a baseline.

A few experiments were carried out using the well-known infrared technique of dispersing the solid in KBr and pressing transparent disks under exclusion of air. The scattering problem then becomes much more severe but, although quantitative measurements were not attempted, useful spectra on a sloping base line could still be obtained.[7]

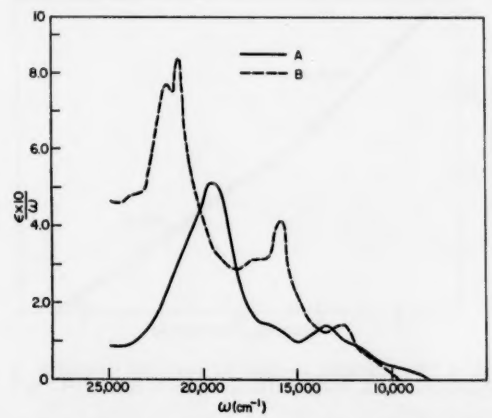

FIG. 2. Spectrum of the pyrene$^+$ ion. A. Pyrene-$SbCl_5$ in colloidal solution (———). B. Pyrene in BF_3-CF_3COOH (------).

III. EXPERIMENTAL RESULTS AND DISCUSSION

As noted by Aalbersberg *et al.*,[3] the spectra of solutions of aromatic hydrocarbons with $SbCl_5$ are very similar to those of the hydrocarbon ions. Figures 1–3 give the spectra of the anthracene, pyrene, and perylene solutions with $SbCl_5$. The spectra of the positive ions in solution are shown for comparison. Those of the anthracene and perylene positive ions were obtained in H_2SO_4 solutions, the spectrum of the pyrene positive

TABLE I.

Hydrocarbon	Derivative linewidth (gauss)
Anthracene-$SbCl_5$	8.7
Pyrene-$SbCl_5$	16
Perylene-$SbCl_5$	4.4

[7] The authors are much indebted to J. Schnell for her cooperation in preparing the KBr disks.

TABLE II.

	Percent ions by ESR	Percent ions by ultraviolet
Anthracene-$SbCl_5$	24	18
Pyrene-$SbCl_5$	73	64
Perylene-$SbCl_5$	10	21

ion was obtained from a (BF_3-CF_3COOH) (22% BF_3) solution. All these spectra are in exact agreement with those obtained by Aalbersberg *et al.*,[3] both as far as position and intensities of the bands are concerned.[8]

Two phenomena are apparent in Figs. 1–3. Although the spectra of the $SbCl_5$ solutions are similar to those of the positive ions, they suffered a red shift and were considerably reduced in intensity. The red shift is especially noticeable in the case of pyrene, while the reduction in intensity is most apparent in the cases of anthracene and perylene. Moreover, the bands are broader.

On increasing the hydrocarbon concentration, black precipitates which were identified as solid $SbCl_5$-hydrocarbon complexes could be isolated from all three solutions. The pyrene complex was extremely unstable and hydrolyzed instantly on contact with air. The anthracene and perylene complexes were quite stable, and could be kept under anhydrous conditions. However, even then the anthracene complex decomposed slowly.[9] Samples of the latter two complexes could be dispersed in KBr and the ultraviolet spectra of the pressed disks were recorded. They are also shown in Figs. 1 and 3. (The intensities are in arbitrary units for these spectra.) It is seen that these spectra are very similar to those of the $SbCl_5$ solutions. Also, in the case of perylene, the bands near 23 000 cm^{-1} correspond to the absorption of neutral perylene.

Electron spin resonance (ESR) measurements were carried out on the same $SbCl_5$ solutions. In every case fairly narrow, slightly asymmetric, almost Lorentz-shaped lines were obtained. The widths of these lines are given in Table I. All of the g values were approximately 2.003. The shapes and widths of these lines were not altered by dilution. This is evidence that the solutions are colloidal in nature. Otherwise, at some point of dilution, the lines should start to broaden and show hyperfine structure due to the coupling of the unpaired electron with the proton spins, and the decrease of the exchange interaction. In a colloid, however, the distance between spins in one particle is not increased by dilution, and therefore the exchange mechanism remains unaffected.

As mentioned before, this conclusion was affirmed by the observation of a Tyndall effect. The most convincing evidence, however, is that perylene-$SbCl_5$ solutions which yield precipitates after standing for a few days may be shaken and then yield the same ultraviolet spectrum as they did when freshly made. This procedure can be repeated many times. No visible absorption of the ions is found in the liquid standing over the precipitate. Also, the observation that the isolated solid has essentially the same spectrum as the "solutions" is evidence for the colloidal nature of the solutions.

It is concluded, therefore, that the ESR and ultraviolet spectra obtained are those of the solid. These solids then are, at least in part, made up of ions. By comparing the extinctions of the $SbCl_5$-complex suspensions with those of the ions in solution, it is possible to arrive at a number indicating the fraction of ionized molecules in the solid. Also, the measurements of the absolute spin concentration by ESR on $SbCl_5$ suspensions of known hydrocarbon content allow calculation of this fraction, since the only paramagnetic species present are the hydrocarbon ions. Table II gives these fractions as determined by ultraviolet spectroscopy and ESR.

The agreement can be called fair in view of the approximations used. It is implicitly assumed that the molar extinctions of the ion spectra do not change in going from the solution to the solid. This is probably not so, since even the energies of the transitions are markedly affected. However, it is gratifying to observe that a high fraction is found for the pyrene complex by both the ESR and the ultraviolet method. It is possible that diamagnetic dipositive ions may also be involved. In the case of perylene, where the agreement is worse, the ultraviolet spectrum of the divalent positive ion[10]

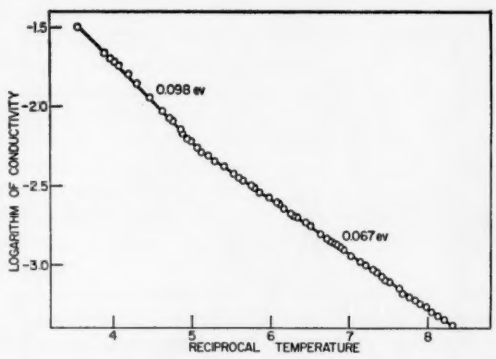

FIG. 4. The activation energies for electronic conduction in solid perlylene-$SbCl_5$. Reciprocal temperature in units of $10^{-3}°K^{-1}$.

[8] To obtain the molar extinction of the anthracene positive ion, Aalbersberg *et al.*'s method and their value for the molar extinction of the protonated ion as measured in anhydrous HF were used. The amount of protonated ion in the H_2SO_4 solution could then be found, and thus the molar extinction of the anthracene positive ion.

[9] Hydrolysis of the complexes yielded chlorinated compounds which were not further identified.

[10] P. J. Zandstra, Ph.D. thesis, Free University of Amsterdam, 1959.

is not significantly different from the monovalent positive ion. Thus both mono- and dipositive ions could contribute to the visible spectrum, whereas only the monopositive ion could contribute to the ESR spectrum. Experiments on tetracene, which has markedly different spectra for mono- and divalent ions, failed due to the occurrence of side reactions.

IV. ELECTRICAL CONDUCTIVITY

It was found that all three complexes were highly conductive. Unfortunately the anthracene and pyrene complexes were too unstable to make measurements over any length of time possible. As mentioned before, however, the perylene complex is quite stable and measurements of its conductivity vs temperature could be carried out. The four-probe apparatus used is described elsewhere.[11] Figure 4 gives a plot of the logarithm of the conductivity vs the reciprocal temperature. It is seen that the conductivity obeys the usual expression:

$$\sigma=\sigma_0 \exp(-E/kT),$$

as found in most other organic semiconductors.[12] In this case, two straight lines are obtained, corresponding to activation energies of 0.067 and 0.098 ev. This is similar to the behavior of the conductivity in the iodine complex of pyrene.[8] There also, impurities may play a role. The present system, however, is so inherently impure, due to the possibility of side reactions, that any more speculation on this point would not be warranted.

[11] J. Kommandeur and F. R. Hall, J. Chem. Phys. **34**, 129 (1961).

[12] C. G. B. Garrett, *Semiconductors*, edited by N. B. Hannay (Reinhold Publishing Corporation, New York, 1959), Chap. 15.

V. CONCLUSIONS

As a result of these experiments, some definite conclusions can be drawn. First, the observed ESR and visible spectra are the properties of finely divided solid particles of hydrocarbon-$SbCl_5$ complexes. Second, a considerable fraction of the hydrocarbon molecules exists in the ionized state in the solid and the KBr disk results for perylene indicate that another fraction of the hydrocarbon molecules exists in a nearly normal unionized state.

The agreement of the intensity of the visible spectra with the ESR spin concentration indicates that the entire resonance signal is due to a single paramagnetic species, the hydrocarbon monopositive ion. In this event, the asymmetry of the ESR line must be caused by anisotropy. The location of the other electron from the hydrocarbon positive ion is a matter for speculation, but, in view of the lack of evidence for another paramagnetic species, it is possible that the electrons pair up, perhaps in a vacant orbital, to form a dinegative $SbCl_5$ ion.

Since these complexes apparently consist of a mixture of molecules and ions, it is not surprising that they exhibit the property of electronic conductivity. The only other requirement is that no great energy change is associated with the "jumping" of a hole or an electron from an ion to a neutral molecule or vice versa. Measurements of the "ionic fraction" may contribute to a better understanding of the conduction processes in organic solids.

ACKNOWLEDGMENT

The authors are indebted to Dr. L. S. Singer for the use of his electron spin resonance equipment, and for several informative discussions.

THE JOURNAL OF CHEMICAL PHYSICS VOLUME 35, NUMBER 5 NOVEMBER, 1961

Metallic Nature of the Starch-Iodine Complex

R. BERSOHN* AND I. ISENBERG†
Marine Biological Laboratory, Woods Hole, Massachusetts

(Received March 23, 1961)

A weak electron resonance has been observed in the amylose-iodine complex. It is shown that if the iodine atoms in each chain are covalently bonded to each other, the band of the $5p\sigma$ states is only partially filled. Hence the row of atoms will have metallic properties including weak paramagnetism and electronic conductivity.

I. INTRODUCTION

THE following pertinent facts are known about the bluish black starch iodine complex. (1) It absorbs light intensely in the 6250 A region. (2) Only amylose, the linear polymer fraction of the starch forms the blue complex. (3) The complexing unit is not I_2 but I_3^-.[1–3] (4) The iodine atoms are arranged linearly[4–7] inside of the amylose helix with an average interatomic spacing of about 3.10 A. (5) There are about 3.9 glucose units per iodine atom. Inasmuch as an amylose molecule consists of anywhere from 200 to 2000 glucose units, the amylose—I_3^- complex contains a row of 50 to 500 iodine atoms. The aim of this paper is to show that the row of atoms behaves as a one dimensional metal.

It was shown by West[5] that the amylose complex is a particular case of a more general type of complex formed by trihalide ions e.g. I_3^-, Br_3^-, or IBr_2^- with polar linear polymers such as polyvinyl borate, nylons, cellulose, and amylose. That the polymer chain serves only as a nonspecific matrix for the linear chain of halogen atoms is shown by the fact that the periodicities in the halogen chains bear no relation to the periodicities of the polymers. Moreover amylose complexes straight chain alcohols and carboxylic acids as well as the trihalide ions.

II. ELECTRON RESONANCE OF AMYLOSE TRIIODIDE COMPLEX

A sample of complex was prepared as follows. One gram of amylose was dissolved in 5 cc of 2*M* KOH, neutralized with HCl and diluted to about 100 ml. A saturated solution of I_2 in aqueous KI was added until in visible excess. The complex was then salted out by addition of KI until the precipitate looked flocculent. It was then filtered off and washed with a saturated solution of I_2 in ethanol. The solid was sucked dry and dried further over silica gel.

The spectrum of the amylose triiodide complex was measured with a Varian 4500 electron spin resonance spectrometer equipped with a Varian 4560, 100-kc field modulation unit. The amylose from which the complex was prepared exhibited no resonance. The complex gave a simple, slightly asymmetric signal with no visible structure. It had a g value of 2.004 ± 0.001 and a linewidth of 3.5 gauss measured between positions of maximum slope. The signal was obtained under conditions where the signal-to-noise ratio on a recorder was approximately 10. By comparing the signal with that obtained from a known quantity of diphenyl picryl hydrazyl it was found that the signal corresponded to 1.2×10^{15} unpaired electrons per gram. A theoretical estimate of this quantity is given in Sec. V.

III. PREVIOUS DESCRIPTIONS OF THE COMPLEX FORMATION

The various explanations proposed for the formation of the amylose complexes depend on assumptions concerning the as yet unknown configuration[8] of the glucose units. We are concerned here with the electronic nature of the halogen atom chain rather than with the energetics of the formation of the complex, so that the previous descriptions will be only briefly summarized. Besides, they are all in need of restatement to allow for the fact that I_3^- and not I_2 is the complexing agent.

Freudenberg *et al.*[9] proposed a boat configuration which placed the nonpolar C—H groups on the inside of the helix and most of the polar CH_2OH and OH groups directed to the outside. The nonpolar I_2 molecules were then supposed to prefer the nonpolar helix interior. While the suggested configuration may well be correct, the reasons may be different. As Rundle[10] observed, affinity of the amylose helix for iodine increases with increasing iodine content. A general adsorption theory would not give this result.

* Department of Chemistry, Columbia University, New York 27, New York.
† Institute for Muscle Research, Marine Biological Laboratory, Woods Hole, Massachusetts.

[1] E. G. Kontos, thesis, Columbia University, 1959 (unpublished).
[2] J. Kuge and S. Ono, Bull. Chem. Soc. Japan **33,** 1269, 1273 (1960).
[3] J. A. Thoma and D. French, J. Am. Chem. Soc. **82,** 4144 (1960).
[4] R. E. Rundle, J. F. Foster, and R. R. Baldwin, J. Am. Chem. Soc. **66,** 2116 (1944).
[5] C. D. West, J. Chem. Phys. **15,** 689 (1947).
[6] R. E. Rundle, J. Chem. Phys. **15,** 880 (1947).
[7] R. E. Rundle and D. French, J. Am. Chem. Soc. **65,** 558, 1707 (1943).
[8] R. J. Ferrier and W. G. Overend, Quart. Rev. (London) **13,** 265 (1959).
[9] K. Freudenberg, E. Schaaf, G. D. Dumpert, and T. Ploetz, Naturwiss. **27,** 850 (1939).
[10] R. S. Stein and R. E. Rundle, J. Chem. Phys. **16,** 195 (1948).

Stein and Rundle[10] proposed an electrostatic theory of the complex in which the fundamental assumption was that each turn of the helix possesses a net dipole moment. A field is then produced inside the helix which polarizes the iodine molecules; the latter then attract each other. While there is a small (3.1 kcal/mole) energy of covalent binding, the major binding energy is electrostatic. One objection to the model is that it segregates the iodine atoms into molecules although the x-ray data show that the iodine atoms are equidistant. Stein and Rundle point out that the 3.10 A interatomic distance is experimentally indistinguishable from alternate stretched bond lengths (say 3.00 A) and compressed intermolecular distances (say 3.20 A). Another objection is that if the amylose helix does possess an appreciable dipole moment per turn, it will possess a large total dipole moment. If the configuration of the amylose molecule in solution was a linear helix, solutions of amylose would be expected to have a large dielectric constant but this is not the case.[11]

Murakami[12] inferred from the rather large interatomic distances in the iodine chain, that the atoms are charged. He proposed a chain configuration in which the oxygen atoms joining neighboring glucose units would form charge transfer complexes with the iodine molecules. The iodine molecules in turn were thought to dimerize to form units approximately $I_4^{=}$. (Murakami rejected the idea of a long chain of mutually interacting iodine atoms for reasons to be discussed below.) Clearly the observation that I_3^- is the complexing agent makes charge transfer from the oxygen atoms much less likely.

IV. MODEL OF THE ONE-DIMENSIONAL METAL

The evidence that iodine atoms tend to be polyvalent with the bonds making roughly 90° or 180° angles with each other has recently been summarized.[13] It is now generally accepted that the wave functions in the polyhalide ions are better represented by delocalized linear combinations of p functions than by localized spd hybrids. Our basic assumption is that the iodine atoms are covalently bonded to each other and that all the bonds are equivalent or nearly so. The stability of the amylose-triiodide complex is ascribed to the dispersion forces between the helix and the iodine atoms and the strength of the covalent bonds between iodine atoms.

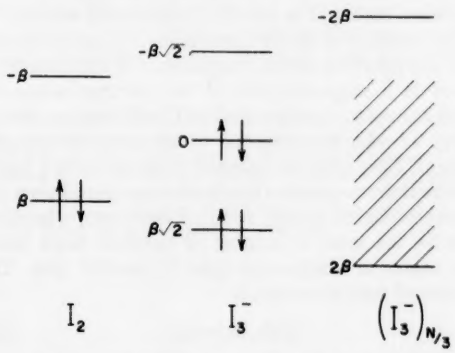

FIG. 1. Energy levels of I_2, I_3^-, and I_3^- chain. β is the I-I resonance integral. Shading shows filled levels of the chain.

TABLE I.

System	Observed Bond distance	Theoretical Bond order	Resonance Energy/atom
I_2	2.67 A[a]	1	β
I_3^-	2.90 A[b]	$1/\sqrt{2}=0.707$	$\frac{2\beta\sqrt{2}}{3}=0.942\beta$
$(I_3^-)_n$	3.10 A[c]	$2/\pi=0.636$	$\frac{2\beta\sqrt{3}}{\pi}=1.10\beta$

[a] G. Herzberg, *Spectra of Diatomic Molecules* (D. Van Nostrand Company, Inc., Princeton, New Jersey, 1950).
[b] R. M. Slater, Acta Cryst. **12,** 187 (1959).
[c] Reference 4.

If we take as our basis for the wave functions the $N5p\sigma$ functions of the N iodine atoms, we will have a band (or bands) of energy levels which will house the $(4N/3)5p\sigma$ electrons of the $(I_3^-)_{N/3}$ chain. If we assume that all the bond distances are equal and use the simplest version of molecular orbital theory, the wave functions of the system will be[14]

$$\Psi_j = A_j^{-\frac{1}{2}}\sum_{r=1}^{N}(-1)^r\left[\sin\pi r\left(\frac{j+1}{N+1}\right)\right]\phi_r, \quad j=0,\cdots,N-1 \tag{1}$$

where

$$A_j=\sum_{r=1}^{N}\sin^2\pi r\left(\frac{j+1}{N+1}\right), \tag{2}$$

and ϕ_r is the $5p\sigma$ function of the rth iodine atom. The corresponding energy levels are given by

$$\epsilon_j=-2\beta\cos\pi(j+1/N+1)+\alpha, \tag{3}$$

where β is the resonance integral connecting adjacent ϕ's and α is the Coulomb integral of the $5p\sigma$ state.

If one substitutes $N=3$ in Eqs. (1)–(3), one obtains the familiar results which apply to I_3^-. Namely, there are three states $\frac{1}{2}(\phi_1\pm\sqrt{2}\phi_2+\phi_3)$, $1/\sqrt{2}(\phi_1-\phi_3)$ with energies $\alpha\pm\beta\sqrt{2}$, α. The resonance energy of an I_3^- which contains four $5p\sigma$ electrons is then $2\beta\sqrt{2}$. Figure 1 shows the energy levels of I_2, I_3^-, and an I_3^- chain assuming identical bond distances.

The total resonance energy of a chain of $N/3$ interacting I_3^- ions is obtained by summing over all the energies of the occupied states and subtracting the coulomb energy of isolated atoms and ions. That is, the

[11] H. R. Kruyt and H. Kunst., Kolloid-Z. **91,** 1 (1940).
[12] H. Murakami, J. Chem. Phys. **22,** 367 (1954); **23,** 1979 (1955).
[13] E. E. Havinga and E. H. Wiebenga, Rec. trav. chim. **78,** 724 (1959).
[14] W. Huckel, Z. Physik **76,** 628 (1932).

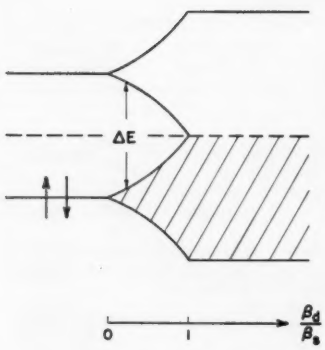

FIG. 2. Energy levels of a chain of I atoms with alternate resonance integrals β_d and β_s. ΔE, the energy gap between the highest filled state and the lowest empty state is shown as a function of β_d/β_s whose maximum value is limited to one.

resonance energy is given by

$$2\sum_{j=N/3}^{N-1}(\epsilon_j-\alpha)=-4\beta\sum_{j=N/3}^{N-1}\cos[\pi(j+1)/(N+1)] \quad (4)$$

$$=N\{2\beta\sqrt{3}/\pi+\Theta(1/N)\}. \quad (5)$$

The factor of two on the left-hand side of Eq. (4) is necessary because each orbital state is occupied by two electrons. The symbol $\Theta(1/N)$ in Eq. (5) stands for all terms which go to zero at least as fast as $1/N$ when $N\to\infty$. The algebra deriving Eq. (5) from Eq. (4) has been omitted.

A set of $N/3$ noninteracting I_3^- ions *with the same internuclear distances* would have a resonance energy of $N/3(2\beta\sqrt{2})$ so that the net gain in resonance energy per I_3^- would be $2\beta(3\sqrt{3}/\pi-\sqrt{2})=0.480\beta$. However the I_3^- internuclear distance is smaller than the internuclear distance in the chain; therefore we must consider more closely the variation in the β integral.

Table I contains the calculated bond orders and resonance energies, and the experimental bond distances in I_2, I_3^-, and the polytriiodide chain. The variation in bond distance with bond order is similar except for scale changes to the corresponding variation with carbon atoms. The resonance energies are quoted in terms of a single integral β which is clearly a function of bond distance. It might be reasonable to estimate its variation by assuming that the resonance integral depends on distance in the same way as the Morse potential for diatomic molecules, i.e.,

$$\beta(r)=\beta_0\{1-\exp[-k(r-r_e)]\}^2, \quad (6)$$

where r_e is the equilibrium bond distance of I_2, i.e., 2.67 A. k is determined by the molecular dissociation energy and force constant, and $\beta_0=\beta(2.67)$. Eq. (6) leads to the values $\beta(2.90)=0.88\beta_0$ and $\beta(3.10)=0.70\beta_0$. Another estimate is obtained by assuming that

$$\beta/S=\int\phi_i H\phi_{i+1}d\tau\Big/\int\phi_i\phi_{i+1}d\tau=\text{const} \quad (7)$$

or

$$\beta(r)=\beta_0[S(r)/S(2.67)]. \quad (8)$$

Equation (8) leads to the values $\beta(2.90)=0.80\beta_0$ and $\beta(3.10)=0.64\beta_0$. The resonance energy stabilization per atom of the polytriiodide chain is

$$2\beta(3.10)3\sqrt{3}/\pi-2\beta(2.90)\sqrt{2}. \quad (9)$$

With either set of values of β, this is negligibly small and even slightly negative; the increase of internuclear distance in effect cancels the superior resonance energy of the chain as compared to the isolated I_3^- units. The reason for the stability of the chain is still obscure and will not be examined in this paper.

V. PROPERTIES OF THE LINEAR POLYTRIIODIDE CHAIN

A. Absorption of Light

The optical absorption properties of the complex are consistent with the metallic model proposed here. The 6250 A absorption may be ascribed to a transition to the σ band shown in Fig. 1 from a π band. The shift of the transition to longer wavelengths is explained by the broadening of the partially occupied highest σ band combined with the fact that the nonbonding π band is relatively less affected by chain formation.[15] The great intensity of the absorption is due to the large polarizability of the chain of atoms.

B. Magnetic Susceptibility and Electron Spin Resonance

When the chain of triiodide ions becomes sufficiently long the energy levels will be quite densely spaced, i.e., the intraband energy level separations will be smaller than kT. The set of σ electrons will then possess a paramagnetic susceptibility which is just the Pauli paramagnetism found in metals. A corresponding electron resonance should be exhibited in spite of the fact that the complex contains no free radical sites in the usual sense. This resonance is analogous to the resonance observed in metallic lithium and sodium.

The intensity of the electron resonance can be inferred from the following familiar argument. If the complex is placed in a magnetic field H the electron states for which the spin is antiparallel to H will have an excess energy of $\gamma\hbar H$ as compared to the states of opposite moment. Here $\gamma\hbar$ is the product of the electron g factor and the Bohr magneton. Inasmuch as at equilibrium the highest occupied energy level of both spin directions must be the same, a number of electrons must move from states of antiparallel spin to parallel spin. The number of such electrons is

$$\tfrac{1}{2}(dn/d\epsilon)\gamma\hbar H, \quad (10)$$

[15] Murakami rejected the linear chain model of the complex because the observed transition probability per atom is essentially constant. This would not be the case for an intraband $\Sigma\to\Sigma$ transition from the highest filled states to the lowest empty state. On the linear chain model, this intraband energy level separation is of the order of β/N which is much too small to explain the observed absorption near 6250 A. The latter is an interband $\Sigma\to II$ transition.

where $dn/d\epsilon$ is the number of states per unit energy interval at the top of the filled band. It follows from Eq. (3) that at the highest occupied level

$$(j=N/3), \qquad dn/d\epsilon=1/\pi\sqrt{3}\beta(3.10).$$

The number of unpaired electrons is then

$$(N/2\pi\sqrt{3})[\gamma\hbar H/\beta(3.10)]. \tag{11}$$

The resonance integral $\beta(3.10)$ may be crudely estimated as follows. On the most naive model $2\beta(2.67)$ is identified with the I_2 dissociation energy which is 34 kcal/mole. $\beta(3.10)$ is about $\frac{2}{3}$ of $\beta(2.67)$ whence $\beta(3.10)\sim 11$ kcal/mole. For a field H of 3200 gauss the number of unpaired electrons would be expected to be $0.8\times10^{-5}N$ independent of temperature. For the complex (assuming 3.9 glucose units per I atom), this would predict 5.6×10^{15} spins per gram as compared to the experimental value of 1.2×10^{15}. Considering the crudeness of the estimate and the difficulty in making accurate intensity measurements, this may be taken as satisfactory agreement.

C. Electrical Conductivity

Besides electron resonance one would expect electrical conductivity in a one-dimensional metal. If one subjected the amylose triiodide complex to microwave radiation at a sufficiently low temperature or a sufficiently high frequency so that dielectric losses were negligible, extensive electric losses should be detectable. A more striking demonstration of this conductivity would be expected to be shown by the oriented chains of triiodide ions which are present in certain stretched polymer triiodide complexes (e.g., polaroid).[16] These oriented materials would be highly absorbing for photons whose electric vector is along the chain and negligibly absorbing when the photons are polarized transverse to the chain. Assuming that one can work under conditions where dielectric loss is negligible, these materials would polarize microwaves as well as light waves.

APPENDIX

Temperature Dependence of the Electron Resonance Intensity

The metallic model as shown schematically in Fig. 1 predicts a temperature independent magnetic susceptibility. Other views[2] of the iodine atom chain are that it is neutral or that it does not contain as much negative charge as is implied by the formula $(I_3^-)_{N/3}$. The exact amount of charge associated with the chain determines the fraction of the band states which are occupied but leave the band only partially filled in any case. The susceptibility remains independent of temperature as long as the atoms are equidistant.

Suppose that one adopts the view that the interatomic distances alternate. The resonance integrals then will take alternate values β_s, β_d along the chain. Figure 2 shows the qualitative behavior of the energy levels as a function of β_s/β_d. The bonding states are occupied and the antibonding states, those above the dotted line in the figure are shown unoccupied. Actually it is the electrons in the antibonding states which give the chain its negative charge. The following conclusions are drawn from Fig. 2. If the atoms are equidistant or if the chain is charged, the observed electron resonance is understandable. If the chain is neutral and the atoms are not equidistant as envisaged by Stein and Rundle, there will be a filled band separated by a gap ΔE from the empty band. The intensity of the electron resonance should vary as $\exp(-\Delta E/kT)$; the observed semiquantitative agreement at room temperature of the theoretical and experimental intensities is confirmation of the view that the chain is charged, the atoms are equidistant, or both. However, observations on the temperature dependence of the resonance would help to check the proposed model.

ACKNOWLEDGMENTS

We appreciate the support of the U.S. Army, Quartermaster Research (Natick) Grant Number I, and the U.S. Atomic Energy Commission. We have benefitted greatly from discussions with Albert Szent-Gyorgyi, C. O. Beckmann, and Y. N. Chiu. Dr. M. Roger of the Rockefeller Institute kindly prepared the sample.

[16] *Note added in proof.* Dr. W. M. Walsh, Jr. of Bell Laboratories has observed an electron resonance signal in a sheet of polaroid which varied with orientation of the sheet with respect to the magnetic field. An oriented polymer is probably more useful for studying the physical properties of a charged row of iodine atoms than is the amorphous amylose-iodine complex. We are grateful to Dr. Walsh for making this measurement.

THE JOURNAL OF CHEMICAL PHYSICS VOLUME 35, NUMBER 5 NOVEMBER, 1961

The Chemical Bond in Molecular Quantum Mechanics*

THOMAS L. ALLEN† AND HARRISON SHULL

Chemistry Department, Indiana University, Bloomington, Indiana

(Received March 30, 1961)

It is postulated that a properly antisymmetrized product function over geminals (electron-pair wave functions) is adequate for discussion of the principal chemical properties of molecules. By application of the virial theorem it is shown that such a wave function has both of the properties essential to the bond-energy concept; namely (a) the energy of a molecule is the sum of the energies of its individual bonds and (b) the bond energies are invariant from one molecule to another. Within the framework of this approximation, bond energies become identified in magnitude with the kinetic energies associated with the respective geminals. The concepts are sufficiently general to include both localized and nonlocalized bonds, unshared electron pairs, odd electrons, and states of various multiplicities.

INTRODUCTION

IT has become evident in recent years that electronic correlation is of fundamental importance in chemical binding, and therefore the one-electron approximation is inherently too inaccurate to provide a suitable basis for the discussion of systems of chemical interest. Electronic correlation is usually introduced by means of a superposition of configurations. Although this method can lead to results of any desired accuracy, for many-electron systems the wave functions are very complicated. It is then extremely difficult to see what factors are significant in stabilizing a particular configuration of electrons and nuclei, and how these factors change in going to a related molecule. This has led to a natural trend toward obtaining results of high numerical accuracy, and an atrophy of the kind of activity traditionally associated with "understanding" chemistry. There appears to be little hope, however, that reasonably accurate wave functions will be calculated in the foreseeable future even for such a relatively simple molecule as, for example, propane.[1] Thus it is still important to utilize accurate calculations on simple molecules to gain an insight into chemical binding which can be applied to more complex molecules. The fundamental problem is to construct molecular wave functions which approximate closely the exact wave functions and which are at the same time of a form sufficiently simple to be comprehensible.

TWO-ELECTRON APPROXIMATION

What kind of wave function will best meet these specifications may be inferred from the molecular model used so successfully in chemistry. The electron pair is the fundamental structural unit, and it is used to form the various chemical bonds, unshared pairs, and inner shells necessary for a complete description of a molecule. For our purposes two properties of the electron pairs in this model should be emphasized. They are localized in nonconjugated systems, and many of them are localized even in conjugated molecules. They are independent of one another to a very high degree, as shown by the remarkable invariance of bond properties in going from one molecule to another.

A wave function appropriate to this model can be constructed from electron-pair functions.[2–12] (To distinguish these two-electron functions from the conventional orbitals, which are one-electron functions, the term *geminal* is useful.[8]) A product is formed from the geminals appropriate to the various chemical bonds and unshared electron pairs (and an orbital if the molecule contains an odd number of electrons). Application of an antisymmetrization operator gives a molecular wave function satisfying the Pauli principle. Further projection operators can be used, if necessary, to construct the desired symmetry properties of the resultant function. As the two electrons in a geminal need not have antiparallel spins, the function may have whatever multiplicity is appropriate to the state being represented.

Simply because the electron-pair concept has been so successful in chemistry, the best wave function of this form will almost certainly be a very satisfactory approximation to the exact wave function. This conjecture is supported by an examination of the correlation properties of an antisymmetrized product of geminals. No

† On leave from the Department of Chemistry, University of California, Davis, California, for 1959–1960.

* Supported in part by grants from the National Science Foundation to each of the authors and in part by a contract with Indiana University by the U.S. Air Force Office of Scientific Research.

[1] G. G. Hall, Repts. Progr. in Phys. **22,** 14 (1959).

[2] L. Pauling, Proc. Roy. Soc. (London) **A196,** 343 (1949).

[3] A. C. Hurley, J. E. Lennard-Jones, and J. A. Pople, Proc. Roy. Soc. (London) **A220,** 446 (1953).

[4] L. A. Schmid, Phys. Rev. **92,** 1373 (1953).

[5] J. C. Slater, Solid-State and Molecular Theory Group, Massachusetts Institute of Technology, Cambridge, Massachusetts, Quart. Progr. Rept. No. 16 (1955), p. 5.

[6] J. M. Parks and R. G. Parr, J. Chem. Phys. **28,** 335 (1958).

[7] E. Kapuy, Acta Phys. Acad. Sci. Hung. **9,** 237 (1958); **10,** 125 (1959); **11,** 409 (1960); **12,** 185 (1960).

[8] H. Shull, J. Chem. Phys. **30,** 1405 (1959).

[9] M. Karplus and D. M. Grant, Proc. Natl. Acad. Sci. U.S. **45,** 1269 (1959).

[10] R. McWeeny and K. A. Ohno, Proc. Roy. Soc. (London) **A255,** 367 (1960).

[11] J. M. Parks and R. G. Parr, J. Chem. Phys. **32,** 1657 (1960).

[12] T. Arai, J. Chem. Phys. **33,** 95 (1960).

limit is placed on the complexity of the individual geminals, and therefore the two electrons in each electron pair may be correlated with one another to any desired degree of accuracy. Thus the principal deficiency in the one-electron approximation is overcome.

For two electrons in different geminals with antiparallel spins we have a case analogous to that of "different orbitals for different electrons" which has been found an effective method of introducing correlation. In addition to this effect, of course, two electrons in different geminals with parallel spins are correlated by the Fermi hole.

One can construct a conceptual process by which an optimum geminal-product wave function could be found for a given molecular system. One might, for example, following the analogy of the familiar self-consistent field process in the orbital scheme, use an energetic criterion for this first optimum term. Such a process has been outlined in detail by Parks and Parr.[6] Or, alternatively, one could imagine the existence of a transformation of the second-order density matrix that would make the first term optimum with respect to overlap with the true function, much as the first natural orbital is in a two-electron system.[13]

We assume that a suitable optimization process exists which leads to a unique optimum geminal product function. From the viewpoint of electron-electron interaction (or correlation), the repulsion effects will be minimized when the optimum geminals are essentially localized in different regions of space. We can expect, therefore, that optimum geminals will be localized, at least in nonconjugated systems. [In conjugated systems the best π geminals will likely have a semi-localized character, corresponding to benzene π equivalent orbitals (see Appendix A).] They should be even more localized than optimum localized orbitals, because in the one-electron approximation, repulsion between electrons in the same orbital hinders localization.

A related argument has been given by Hurley, Lennard-Jones, and Pople to show that the optimum forms of the paired electron functions are of a localized nature.[3] These authors also point out that the transformation properties which make molecular orbitals (delocalized) and equivalent orbitals (localized) mathematically equivalent to each other are not applicable in the two-electron approximation. This observation has interesting consequences regarding the best description of the double bond in ethylene and related molecules. It has been shown that, in the one-electron approximation, the wave function constructed from σ and π orbitals and the wave function constructed from bent-bond (or "banana-bond") orbitals are identical.[14,15] As the equivalence of the two descriptions does not hold in the two-electron approximation, and as the more localized form is expected to be the better function, the optimum electron-pair functions will correspond to a bent-bond description rather than to a σ, π description.

The high degree of invariance of bond properties suggests that geminals will be transferable from one molecule to another to a very good approximation. If essentially the same geminal describes the electron pair of a particular chemical bond in a variety of molecules, the observation that the energy, internuclear distance, force constant, etc., of this bond are essentially the same in each molecule is not an unreasonable consequence. On the other hand, this fact would be very difficult to understand if we were to suppose that the geminal corresponding to the bond varied widely among the different molecules.

Transferability would greatly simplify the construction of good wave functions for complex molecules, as one could then utilize the results obtained with simpler systems. In fact, belief in the existence of this property would seem to be essential to any optimistic view of the application of quantum mechanics to complex molecules. It is rather clear that geminals will be transferable in a qualitative sense, and the question is really one of degree—how large are the differences between the optimum geminals corresponding to a chemical bond in different molecules? This question will be discussed more fully in connection with molecular energies.

BOND ENERGY CONCEPT

While the bond energy method is an approximate one, its relative accuracy is often underestimated. The usual reference state is the enthalpy of the separated atoms in their ground electronic states at 25°C. If excited states (e.g., valence states) are chosen for points of reference, each bond energy is increased by some constant, but the additivity of bond energies is unaffected.[16,17] Therefore one may equally well use the reference state common in quantum-mechanical calculations, the energy of separated electrons and nuclei. This permits a direct comparison of the accuracy of quantum-mechanical calculations and the bond energy method.

The calculation of the energy of propane from the energies of methane and ethane may be taken as a representative example of the accuracy of the bond energy method. Using data for the molecules in the ideal gas state at 0°K with fixed nuclei,[18] and the basic assumption that bond energies are constant, the result is in error by 1.68 kcal/mole. But the energy of propane in this state with respect to separated electrons and nuclei is 74 698 kcal/mole. The relative error of the bond energy method is thus only 0.002%, which is two orders of magnitude better than the accuracy of recent

[13] P. O. Löwdin and H. Shull, Phys. Rev. **101,** 1730 (1956).
[14] G. G. Hall and J. E. Lennard-Jones, Proc. Roy. Soc. (London) **A205,** 357 (1951).
[15] J. E. Lennard-Jones and J. A. Pople, Discussions Faraday Soc. **10,** 9 (1951).
[16] C. T. Zahn, J. Chem. Phys. **2,** 671 (1934).
[17] The relation between bond energies and bond dissociation energies changes, and this is involved in one method of estimating valence state energies [L. Pauling, Proc. Natl. Acad. Sci. U.S. **35,** 229 (1949)].
[18] T. L. Allen, J. Chem. Phys. **31,** 1039 (1959).

quantum-mechanical calculations for much simpler molecules. And even this small error can be almost completely eliminated by including the interactions between next-nearest neighbors.[18]

In attempting to account for the remarkable accuracy of the bond energy method, it is important to note the twofold nature of this concept, according to which (a) the energy of a molecule is the sum of the energies of its individual bonds, and (b) the bond energies are invariant from one molecule to another. Inasmuch as the bond energies are calculated empirically from molecular energies, (a) without (b) is a mere tautology.

Difficulty in explaining additivity of bond energies arises from the complexity of the Hamiltonian operators, which include the Coulomb interaction of every particle with every other particle, and which differ for each molecule. Several authors have investigated the problem of writing expectation values of molecular Hamiltonian operators as the sums of bond energies. It has been shown by Brown,[19] and Dewar and Pettit,[20] that when certain approximations are made in the form of the wave functions and in the integrations, then the total electronic energy is given as a sum of bond energies. But the empirical bond energy concept applies to total molecular energies, and these include the internuclear-repulsion terms. Repulsions between nonbonded nuclei, which are large quantities, cannot be represented by a sum of bond terms (see Appendix B). Therefore the bond energy concept is not valid for electronic energies, and the proposed explanations account for a nonexistent phenomenon.

Hall has shown that in the one-electron approximation the total energy of a saturated molecule (including internuclear repulsions) can be expressed as the sum of suitably defined orbital energies.[21,22] In these quantities potential-energy terms arising from the interactions of distant particles are grouped so that terms of opposite sign tend to cancel. As a consequence of localization, the equivalent orbitals are primarily determined by the atom or atoms around which they are concentrated. It then follows that the orbital energies are approximately invariant. In an investigation of the valence-bond formulation of the two-electron approximation, Slater has given a somewhat similar argument showing that the energy of a molecule can be approximated by a constant part plus a sum of bond energies.[5] The questions of transferability and invariance of bond energies from one molecule to another were not considered.

Bond energies in the two-electron approximation have been studied in greater detail by Parks and Parr.[6] They find that the total molecular energy is rigorously expressible as a sum of bond energies. The bond energies are invariant only when the bonds are essentially homopolar and the "neutral-penetration terms" are negligible. Even in this particular case the bond energies still depend indirectly on one another through the dependence of the A_k coefficients on the other electron pairs. Furthermore, they find that their approximations are badly in error for two bonds which involve the same atom, so that bond energies for such bonds are interdependent. However, different polyatomic molecules (the only kind to which bond energy additivity can apply) necessarily involve a difference in at least one pair of adjacent bonds. If the energies of such bonds are interdependent to a significant extent, bond energies will not be additive, unless the bond energy changes compensate one another. This has not been shown. Also, it is known that additivity of bond energies is not limited to homopolar bonds (for example, it holds extremely well for the chlorinated methanes). Therefore part (b) of the bond energy concept has not been explained, and we have seen that part (a) without (b) is essentially meaningless from an empirical point of view.

[19] R. D. Brown, J. Chem. Soc. **1953,** 2615.
[20] M. J. S. Dewar and R. Pettit, J. Chem. Soc. **1954,** 1625.
[21] G. G. Hall, Proc. Roy. Soc. (London) **A205,** 541 (1951).
[22] G. G. Hall, Proc. Roy. Soc. (London) **A213,** 113 (1952).

APPLICATION OF THE VIRIAL THEOREM

The high relative accuracy of the bond energy concept suggests that it is a direct consequence of some fundamental quantum-mechanical theorem, rather than the result of a somewhat fortuitous cancellation of terms. We demonstrate in the following that application of the very fundamental virial theorem gives a sound theoretical basis to the bond energy concept.

Let L be the class of all functions Λ which are products of geminals, each geminal being normalized and one-electron orthogonal to every other geminal in the same Λ. Using the notation and defining equations introduced by Parks and Parr[6]:

$$\Lambda=[\Lambda_A(1,2)\Lambda_B(3,4)\cdots\Lambda_M(2n-1,2n)], \tag{1}$$

$$\iint |\Lambda_I(1,2)|^2 d\tau_1 d\tau_2=1, \tag{2}$$

$$\int \Lambda_I^*(1,2)\Lambda_J(1,4)d\tau_1=0, \qquad (I\neq J). \tag{3}$$

That trial function of class L which gives the lowest expectation value of the energy for a particular molecule will be termed the best function of class L for that molecule.[23] The Born-Oppenheimer approximation is assumed, and therefore the best wave function of class L describes the molecule with the nuclei fixed at their equilibirum positions.[24]

[23] When each geminal is constructed from only two spin-orbitals, the total wave function consists of a single determinant. The Hartree-Fock or SCF function is the best function of this special type. In general the functions of class L are many-determinant wave functions, and therefore the Hartree-Fock energy is an upper limit to the energy of the best function of class L.

[24] It is known that additivity of bond energies is somewhat improved by replacing conventional bond energies with bond energies calculated from data for the hypothetical state with fixed nuclei. In either case next-nearest neighbor interactions satisfactorily account for the deviations from additivity.[18]

It is also assumed that this wave function is a satisfactory approximation to the exact wave function. Our argument in a preceding section strongly suggests that molecules may be represented to chemical accuracy by a simple antisymmetrized geminal product function. It is not yet clear, however, what auxiliary conditions (for example, orthogonality conditions) can be placed on these geminals and still permit an adequate representation of a chemical system. That one-electron orthogonality [Eq. (3)], which is the orthogonality condition usually placed on electron-pair functions, is not too strong a condition, can perhaps be inferred from some unpublished calculations we have done on the ground state of the beryllium atom. A function of class L has been obtained which has an overlap of 0.99989 with one of the best published wave functions, Watson's 37-configuration function.[25] By contrast, the SCF function has an overlap with the latter of only 0.95758.

The kinetic energy of the molecule in this state then consists solely of electronic kinetic energy and is

$$T=\sum_I T_I, \tag{4}$$

where the summation is taken over all of the geminals in the appropriate Λ, and

$$T_I=2\iint \Lambda_I^*(1,2)\mathbf{T}(1)\Lambda_I(1,2)d\tau_1 d\tau_2. \tag{5}$$

The best wave function is necessarily correctly scaled and obeys the quantum-mechanical virial theorem,[26] which takes a particularly simple form when the nuclei are at their equilibrium positions.[27] In this case the total energy of the molecule (including the internuclear repulsion energy) E, is just the negative of the kinetic energy, so that

$$E=-\sum_I T_I. \tag{6}$$

Thus the total molecular energy is precisely given by a sum of terms, one for each electron pair. This takes care of part (a) of the bond energy concept. If now the geminals are transferable from one molecule to another (and we have already considered one reason for believing that they are at least approximately so), then the geminal energies are invariant. This takes care of part (b). The energy of a chemical bond relative to separated electrons and nuclei is therefore very simply interpreted: It is exactly equal to the negative of the kinetic energy of the geminal or geminals which describe the bond.

It is not suggested, of course, that the kinetic energy is the fundamental cause of chemical binding. But the kinetic energy is directly connected to the potential energy and the total energy through the virial theorem, and therefore it is justifiable and illuminating to analyze the latter quantities, which are very complex, in terms of the much simpler kinetic energy.

The bond energies so defined are identical with empirical bond energies, except that the latter quantities include *pro rata* contributions from inner shells and unshared pairs. There are also the arbitrary differences in reference states previously noted, and the sign conventions are opposite. Empirical bond energies are primarily defined for symmetrical molecules of formula AB_n. Except for the changes in reference states and sign convention necessary to provide a common basis, the empirical bond energy is

$$E(\mathrm{A-B})=E/n. \tag{7}$$

By analogy with equivalent orbitals, the functions for the different bonds differ only in their position in space, and therefore have the same kinetic energy. Let T_{AB} denote the kinetic energy of the geminal(s) describing a bond, and let T_A and T_B denote the kinetic energies of any inner shells or unshared electron pairs on atoms A and B, respectively, T_B being the same for each atom B. Then

$$E=-nT_{AB}-T_A-nT_B, \tag{8}$$

$$E(\mathrm{A-B})=-T_{AB}-T_B-T_A/n. \tag{9}$$

The argument may readily be extended to more complex molecules.

TRANSFERABILITY OF GEMINALS

We shall now obtain a connection between the concept of transferability and the potential energy terms. For this purpose we note that in the class of molecules obeying bond energy additivity, the energy of one molecule may be expressed as a linear combination of other molecular energies. A simple but quite general example is the sequence of molecules BAB, CAC, and BAC, where A, B, and C are atoms and/or radicals. If the molecular energies are E_1, E_2, and E_3, respectively, then

$$E_3=\tfrac{1}{2}(E_1+E_2). \tag{10}$$

Let the best wave functions of class L for these molecules be Λ_1, Λ_2, and Λ_3, respectively, where

$$\Lambda_1=[\beta\beta' abb'], \tag{11}$$

$$\Lambda_2=[\gamma\gamma' acc'], \tag{12}$$

$$\Lambda_3=[\beta\gamma' abc']. \tag{13}$$

The symbols β and γ denote the geminals or products of geminals describing the bonds connecting A and B, and A and C, respectively. Unprimed symbols refer to the left, primed symbols to the right members of each

[25] R. E. Watson, Phys. Rev. **119**, 170 (1960).

[26] The virial theorem is satisfied by the true wave function, but not necessarily by an approximate wave function. If a trial function does not satisfy the virial theorem, application of the scaling procedure leads to a new approximate wave function which is of lower energy than the unscaled function and which also satisfies the virial theorem. This point has been recently emphasized by P. O. Löwdin [J. Mol. Spectroscopy **3**, 46 (1959); Advances in Chem. Phys. **2**, 207 (1959)].

[27] J. C. Slater, J. Chem. Phys. **1**, 687 (1933).

molecule, and a, b, and c are the geminal products describing all inner shells, unshared pairs, and internal bonds in the corresponding radicals A, B, and C. It is assumed that the nuclear frameworks of the BA and CA groupings are the same in each molecule.

The potential energy of a molecule described by a function of class L is

$$V=\sum_I\sum_p U_I(p)+\sum_I S_I+\tfrac{1}{2}\sum_I\sum_{J\neq I}W_{IJ}+\tfrac{1}{2}\sum_p\sum_{q\neq p}(Z_pZ_q/r_{pq}), \quad (14)$$

where we are using atomic units and

$$U_I(p)=-2Z_p\iint\Lambda_I^*(1,2)\,(1/r_{1p})\,\Lambda_I(1,2)\,d\tau_1 d\tau_2, \quad (15)$$

$$S_I=\iint\Lambda_I^*(1,2)\,(1/r_{12})\,\Lambda_I(1,2)\,d\tau_1 d\tau_2, \quad (16)$$

$$W_{IJ}=J_{IJ}-K_{IJ}. \quad (17)$$

The symbols J_{IJ} and K_{IJ}, defined by Eqs. (14) and (15) of Parks and Parr[6] (except for the change to atomic units), involve electron repulsions between different geminals.

Let

$$U_\beta(B)=\sum_{I\epsilon\beta}\sum_{p\epsilon B}U_I(p), \quad (18)$$

that is, the sum of all terms representing the attraction of the electrons in every geminal contained in the bond β to every nucleus contained in the atom or radical B. Also, let

$$S_\beta=\sum_{I\epsilon\beta}S_I, \quad (19)$$

$$W_{\beta\beta'}=\sum_{I\epsilon\beta}\sum_{J\epsilon\beta'}W_{IJ}, \quad (20)$$

and

$$Z_BZ_A/r_{BA}=\sum_{p\epsilon B}\sum_{q\epsilon A}(Z_pZ_q/r_{pq}). \quad (21)$$

Other terms of these same types are defined similarly. The potential energy of molecule BAB is then:

$$\begin{aligned}V_1=&2U_\beta(\mathrm{B})+2U_\beta(\mathrm{A})+2U_\beta(\mathrm{B}')+2U_a(\mathrm{B})+U_a(\mathrm{A})\\&+2U_b(\mathrm{B})+2U_b(\mathrm{A})+2U_b(\mathrm{B}')+2S_\beta+S_a+2S_b\\&+W_{\beta\beta}+W_{bb}+\tfrac{1}{2}W_{aa}+W_{\beta\beta'}+2W_{\beta a}+2W_{\beta b}\\&+2W_{\beta b'}+2W_{ab}+W_{bb'}+2Z_BZ_A/r_{BA}\\&+Z_BZ_{B'}/r_{BB'}. \quad (22)\end{aligned}$$

In deriving this expression we have utilized equations of the type $U_\beta(\mathrm{B})=U_{\beta'}(\mathrm{B}')$, which follow from the supposed equivalence of β to β', and of b to b'.

Analogous equations can be written for V_2 and V_3. From Eq. (10) and the virial theorem, the potential energies are related by

$$V_3=\tfrac{1}{2}[V_1+V_2]. \quad (23)$$

When the detailed expressions for V_1, V_2, and V_3 are substituted into this equation, most of the terms cancel. The terms which remain involve the interactions between the ends of each molecule. To represent these interactions concisely, let $\nu(XYZ)$ be the sum of all potential energy terms arising from the interactions of the electrons and nuclei in X and the bond joining X to Y, with the electrons and nuclei in Z and the bond joining Z to Y. Thus we have

$$\begin{aligned}\nu(\mathrm{BAC})=&U_b(\mathrm{C}')+U_{c'}(\mathrm{B})+\mathrm{U}_\beta(\mathrm{C}')+U_{\gamma'}(\mathrm{B})+W_{bc'}\\&+W_{\beta\gamma'}+W_{\beta c'}+W_{\beta\gamma'}+Z_BZ_{C'}/r_{BC'}, \quad (24)\end{aligned}$$

with similar expressions for the other molecules. The relationship between these interactions, obtained from Eq. (23), is then simply

$$\nu(\mathrm{BAC})=\tfrac{1}{2}\{\nu(\mathrm{BAB})+\nu(\mathrm{CAC})\}. \quad (25)$$

To summarize the argument, if we assume that (a) geminals are transferable, then it follows that (b) bond energies are additive, and (c) the interaction between the ends of molecule BAC is the arithmetic mean of the interactions between the ends of molecules BAB and CAC, as expressed by Eq. (25).

Conversely, (a) is a necessary consequence of (b) and (c). Instead of assuming transferability,[28] let the best wave function of class L for molecule BAC be some function Λ'_3. Let the total energies associated with Λ_3 and Λ'_3 be E_3 and E'_3, respectively, with corresponding designations for the kinetic and potential energies. By the virial theorem and the assumption of (b) and (c),

$$E_3'=\tfrac{1}{2}\{E_1+E_2\}, \quad (26)$$

$$T_3'=\tfrac{1}{2}\{T_1+T_2\}=T_3, \quad (27)$$

$$\begin{aligned}V_3-V_3'=V_3-\tfrac{1}{2}\{V_1+V_2\}=&\nu(\mathrm{BAC})\\&-\tfrac{1}{2}\{\nu(\mathrm{BAB})+\nu(\mathrm{CAC})\}=0. \quad (28)\end{aligned}$$

Therefore $E_3'=E_3$ and $\Lambda_3'=\Lambda_3$.

While it would be of interest to show that transferability of geminals is a necessary consequence of additivity of bond energies *per se*, this has not been possible without some auxiliary assumption such as Eq. (25), or the assumption that Λ_3 is correctly scaled. However, Eq. (25) expresses a plausible relationship. In $\nu(\mathrm{BAC})$, the terms representing attraction between electrons and nuclei will largely cancel the interelectronic and internuclear repulsion terms. Colloquially, the electrons effectively screen the nuclei. The only remaining term is that part of $W_{\beta\gamma'}$ representing the repulsion between the bonding electrons at the central atom or group, and even here the repulsion will be relatively small because of the orthogonality of the bond geminals. Similar considerations apply to $\nu(\mathrm{BAB})$ and $\nu(\mathrm{CAC})$. As A increases in size, and the end groups become further separated, each term in Eq. (25) tends to zero. There

[28] However, it must be noted that it has been necessary to assume that the a function is the same in Λ_1 and Λ_2.

is a corresponding improvement in the accuracy of Eq. (10), in accordance with the general limiting law of Benson and Buss.[29]

Empirical treatments of molecular energies have led to a system of postulates somewhat analogous to (a), (b), and (c) above.[16,18] It is assumed that molecular energies are the sums of bond energies and the energies of interaction between next-nearest neighbors and/or adjacent bonds, designated $\alpha'(\mathrm{BAC})$, etc. In the following set of statements, given (a), then (b) is a necessary and sufficient condition for (c):

(a) these intrinsic bond energies are constant from one molecule to another;

(b) Eq. (10) is valid; that is, conventional bond energies are additive;

$$\text{(c)} \qquad \alpha'(\mathrm{BAC})=\tfrac{1}{2}\{\alpha'(\mathrm{BAB})+\alpha'(\mathrm{CAC})\}. \qquad (29)$$

In concluding this section, we wish to note that transferability of geminals is not to be confused with the usual assumption that matrix elements of the Hamiltonian operator with respect to a particular function are the same throughout a series of molecules. Also, it is not anticipated that geminals will be transferable between molecules of different valence types, or even between different states of the same molecule. For example, the C—H bond geminals in ethane, ethylene, and acetylene will certainly differ significantly from one another. As is well-known, the identity of the C—H bond energies in these molecules is a common, convenient, but completely arbitrary assumption.

DEVIATIONS FROM ADDITIVITY

Although the deviations from strict additivity of bond energies are quite small with respect to total molecular energies, they are still sufficiently large to be of great interest in chemistry. We have seen that transferability of geminals leads to bond energy additivity, and therefore the deviations from additivity necessarily reflect deviations from transferability, or inadequacies in the kind of wave function under consideration, or both.

It is not hard to see why the geminals might vary to some extent. Each is an approximate eigenfunction of an effective Hamiltonian which includes the effective field created by the other electron-pair functions and the nuclei.[30] In going from one molecule to another the change in the effective field is bound to affect the optimum form of a particular geminal. It seems appropriate to call this an inductive effect.[22] The inductive effect should be particularly pronounced when there are changes in nearby nuclei and in geminals localized in the same region of space.

What is perhaps more difficult to understand is why inductive effects do not produce much larger deviations from additivity. There appear to be several factors, however, which restrict inductive changes in molecular energies:

(1) A geminal energy is not affected directly, but only to the extent that the form of the geminal itself responds to changes in nearby geminals and nuclei.

(2) The different bonds of the same valence type are perhaps more alike than is usually supposed. For example, substitution of a chlorine atom for a hydrogen atom in methane may not greatly alter the effective field in which the electrons of the remaining C—H bonds move.

(3) The kinetic energy seems to be relatively insensitive to changes in the wave function. Thus in the reaction $2\mathrm{H}=\mathrm{H}_2$, the wave function undergoes a drastic change. But whereas the electronic potential energy decreases by 1.062 Hartree atomic units, the kinetic energy increases by only 0.174 H. Because of their connection with the kinetic energy terms, the same will be true for the geminal energies.

(4) Considering once again the sequence of molecules BAB, CAC, and BAC, the wave function for molecule BAC obtained by transferring geminals, Λ_3, may be treated as an unperturbed function. The perturbation on β and b, to a first approximation, consists in replacing β' and b' by γ' and c', and the nuclei of the other B by the nuclei of C. For γ' and c' the perturbation consists in replacing γ and c by β and b, and the nuclei of the other C by those of B. As the perturbations are thus equal in magnitude and opposite in sign, the corresponding changes in the geminal energies will largely cancel.

The same conclusion is reached by consideration of the simple picture of hybridization at the central atom or group. Changes in hybridization which strengthen one bond will be accompanied by changes which weaken other bonds.

The deviations from additivity might also be connected with the difference between the best wave functions of class L and the exact wave functions. An improvement in accuracy can be obtained by dropping the requirement of one-electron orthogonality, Eq. (3), while retaining the less restrictive two-electron orthogonality condition,[31]

$$\iint \Lambda_I^*(1,2)\Lambda_J(1,2)\,d\tau_1 d\tau_2=0, \qquad (I\neq J). \qquad (30)$$

The expression for the kinetic energy is now much more complex, including terms such as

$$\iiiint \Lambda_I^*(1,2)\Lambda_J^*(3,4)\mathbf{T}(1)\Lambda_I(3,2)\Lambda_J(1,4) \times d\tau_1 d\tau_2 d\tau_3 d\tau_4,$$

which formerly vanished because of the one-electron orthogonality condition. It is reasonable to class these terms as interactions between the electron-pair func-

[29] S. W. Benson and J. H. Buss, J. Chem. Phys. **29,** 546 (1958).
[30] R. McWeeny, Proc. Roy. Soc. (London) **A253,** 242 (1959); Revs. Modern Phys. **32,** 335 (1960).
[31] See footnote 10 of reference 6.

tions. Besides this complication there will still be inductive effects in going from one molecule to another.

GENERALIZATION OF THE BOND ENERGY CONCEPT

One of the most inviting features of the use of wave functions of class L and the application of the virial theorem outlined above is the possibility of generalizing the concept of bond energies. For any system of chemical interest, a unique energy can be assigned to each electron pair and odd electron, and by Eq. (6) the total energy is precisely given by the sum of these components. Thus energies can be assigned not only to chemical bonds but to unshared pairs, inner shells, and odd electrons. In a multiple bond the several parts will have distinct energies. Furthermore, the generalization broadens the field of systems to include atoms, ions, transition states, excited states, etc.

It will then be possible to obtain detailed descriptions of the differences between related molecules. As comparative studies have proved so fruitful in chemistry, it is to be expected that investigations along these lines will lead to a better understanding of the electronic changes involved in chemical phenomena. A simple example is the question of the extent to which the lithium K shell affects the dissociation energy of the lithium hydride molecule. By comparing the energy of the K shell electron pair in the lithium atom and LiH, it will now be possible to give a definite, quantitative answer to this question.

It should be mentioned that the virial theorem can also yield interesting results when applied to SCF wave functions. Provided that a set of mutually orthogonal orbitals is used, the total energy is then given by a sum of orbital energies, each equal in magnitude and opposite in sign to the expectation value of the kinetic energy operator with respect to the orbital. These orbital energies will differ from the conventional ones, which do not have the property that their sum is equal to the total energy of the system.

Finally, we note that the individual geminals, which are postulated here to be sufficiently accurate to describe most properties of chemical interest, may be subjected to further analysis by the usual natural orbital techniques applicable to such two-electron systems. There is nothing in what has been written above which inherently requires that any given geminal be an eigenfunction of $\mathbf{S}^2$ for example, and we can expect that each one will be a mixture (probably only to a very small extent) of various spin states. But by suitable projection operator techniques and natural orbital transformations, one should be able to find excellent representations of each geminal that would permit discussion of its electron distribution, etc., in ordinary chemical language. We therefore have in principle an orderly scheme solidly based upon the principles of quantum mechanics which will enable us in the future to give a coherent and satisfying description of the nature of the chemical bond.

ACKNOWLEDGMENT

One of the authors (T.L.A.) wishes to express his appreciation to the members of the Chemistry Department at Indiana University for their generous hospitality and for many stimulating discussions.

APPENDIX A. BENZENE π EQUIVALENT ORBITALS

It has been shown by Hall and Lennard-Jones[14] that the three π molecular orbitals of lowest energy in benzene can be transformed into three equivalent orbitals with C_{3v} symmetry. The appropriate transformation is the same as that used in sp^2 hybridization.[32] Expressions for the a_g, e_x, and e_y molecular orbitals as linear combinations of p atomic orbitals are given by Coulson in Eqs. (20), (21a), and (21b), respectively.[33] Substituting a_g for ψ_{2s}, e_x for ψ_{2px}, and e_y for ψ_{2py}, the following expressions are obtained for the equivalent orbitals:

$$\chi_1=\{\psi_1+(1+\sqrt{3})(\psi_2+\psi_3)+\psi_4+(1-\sqrt{3})(\psi_5+\psi_6)\}/3\sqrt{2}, \tag{31}$$

$$\chi_2=\{\psi_5+(1+\sqrt{3})(\psi_6+\psi_1)+\psi_2+(1-\sqrt{3})(\psi_3+\psi_4)\}/3\sqrt{2}, \tag{32}$$

$$\chi_3=\{\psi_3+(1+\sqrt{3})(\psi_4+\psi_5)+\psi_6+(1-\sqrt{3})(\psi_1+\psi_2)\}/3\sqrt{2}. \tag{33}$$

These orbitals fit the description given by Hall and Lennard-Jones.

A simpler set of equivalent orbitals can be derived by interchanging the roles of e_x and e_y in this transformation. Substituting a_g for ψ_{2s}, e_y for ψ_{2px}, and e_x for ψ_{2py}, we obtain:

$$\chi_1'=\{2\psi_6+3\psi_1+2\psi_2-\psi_4\}/3\sqrt{2}, \tag{34}$$

$$\chi_2'=\{2\psi_2+3\psi_3+2\psi_4-\psi_6\}/3\sqrt{2}, \tag{35}$$

$$\chi_3'=\{2\psi_4+3\psi_5+2\psi_6-\psi_2\}/3\sqrt{2}. \tag{36}$$

The charge distributions associated with these orbitals, each doubly occupied, are as follows:

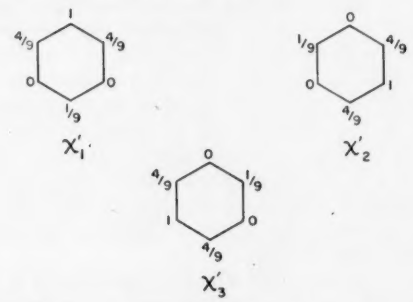

[32] H. Eyring, J. Walter, and G. E. Kimball, *Quantum Chemistry* (John Wiley & Sons, Inc., New York, 1944), p. 224.

[33] C. A. Coulson, *Valence* (Oxford University Press, New York, 1952), p. 240.

It may be seen that the total charge is symmetrically distributed. These four-center orbitals, and the geminals corresponding to them, should be useful in considerations of aromatic substitution reactions, etc.

APPENDIX B. INTERNUCLEAR REPULSIONS

If it were true that internuclear repulsions could be written as a sum of bond terms, then we should have

$$N_3=\tfrac{1}{2}\{N_1+N_2\}, \tag{37}$$

where N_1, N_2, and N_3 are the total internuclear repulsion energies in molecules BAB, CAC, and BAC, respectively. To simplify this discussion let the symbols A, B, and C be restricted to atoms. Substituting the detailed expressions for the internuclear repulsions, terms involving adjacent nuclei cancel, leaving

$$Z_BZ_C/r_{BC}=\tfrac{1}{2}\{Z_B^2/r_{BB}+Z_C^2/r_{CC}\}, \tag{38}$$

or

$$(r_{BC}Z_B/r_{BB}Z_C)+(r_{BC}Z_C/r_{CC}Z_B)=2. \tag{39}$$

It is a fairly good approximation in actual molecules to set

$$r_{BC}=\tfrac{1}{2}\{r_{BB}+r_{CC}\}. \tag{40}$$

Thus in the sequence Cl_2O, HOCl, and H_2O, the nonbonded distance in HOCl calculated from Eq. (40) differs from the experimental result by 4.3%.[34] Equation (40) may also be checked by considering internuclear distances between next-nearest neighbors in more complex molecules. In *n*-butane,[35] $r_{C\cdots H}$ differs from the arithmetic mean of the $r_{H\cdots H}$ and $r_{C\cdots C}$ distances by only 0.5%. The difference between $r_{H\cdots Cl}$ and the arithmetic mean of $r_{H\cdots H}$ and $r_{Cl\cdots Cl}$ in methylene chloride[36] is 0.6%. In every case the arithmetic mean is substantially better than the geometric mean. It may be shown that this is always true when bond distances and bond angles are invariant.

Now let $u=Z_B/Z_C$ and $v=ur_{CC}/r_{BB}$. Then from Eqs. (39) and (40),

$$u+(1/u)+v+(1/v)=4. \tag{41}$$

But as u and v are positive, real numbers $u+(1/u)\geq 2$ and $v+(1/v)\geq 2$. Therefore the only solution to Eq. (41) is $u=1$ and $v=1$, or $Z_B=Z_C$ and $r_{BB}=r_{BC}=r_{CC}$. Thus Eq. (37) cannot be fulfilled when B and C are different atoms, which is of course the only case of interest.

As an illustration of the magnitude of the error in Eq. (37), consider the sequence of molecules CH_4, CH_3Cl and CH_2Cl_2. The total internuclear repulsion energies in these molecules, in Hartree atomic units, are 13.4, 51.1, and 134.7, respectively. (These data were calculated from the experimentally determined structural parameters for methane,[37] methyl chloride,[38] and methylene chloride.[36]) Equation (37) thus leads to a total internuclear repulsion energy in methyl chloride which is in error by 23.0 H, or over 14 000 kcal/mole! If in place of the experimental structural parameters one assumes tetrahedral bond angles and constant bond distances ($r_{CH}=1.091$ A and $r_{CCl}=1.777$ A), the error is slightly reduced to 22.7 H.

Therefore bond energy additivity extends neither to the internuclear repulsion energies nor to the electronic energies taken separately.

---

[34] Structural data: For Cl_2O, J. D. Dunitz and K. Hedberg, J. Am. Chem. Soc. **72,** 3108 (1950); For HOCl, K. Hedberg and R. M. Badger, J. Chem. Phys. **19,** 508 (1951); For H_2O, G. Herzberg, *Infrared and Raman Spectra of Polyatomic Molecules* (D. Van Nostrand Company, Inc., Princeton, New Jersey, 1945), p. 489.

[35] R. A. Bonham and L. S. Bartell, J. Am. Chem. Soc. **81,** 3491 (1959).

[36] R. J. Myers and W. D. Gwinn, J. Chem. Phys. **20,** 1420 (1952).

[37] T. Feldman, J. Romanko, and H. L. Welsh, Can. J. Phys. **33,** 138 (1955).

[38] S. L. Miller, L. C. Aamodt, G. Dousmanis, C. H. Townes, and J. Kraitchman, J. Chem. Phys. **20,** 1112 (1952). See also L. S. Bartell and L. O. Brockway, *ibid.* **23,** 1860 (1955).

Electron Spin Resonance Studies of Radicals Formed in Irradiated Polytetrafluoroethylene

TEIKICHI MATSUGASHITA* AND KENICHI SHINOHARA

Tokyo Laboratories, Japanese Association for Radiation Research on Polymers, Kamifujimae, Bunkyo-ku, Tokyo, Japan

(Received February 17, 1961)

Radicals formed in irradiated PTFE were studied by means of ESR, using reactions with gases. In interpreting the experimental results, it was assumed that the radicals formed in PTFE primarily by irradiation were $-CF_2-\dot{C}F-CF_2-$ and $-CF_2-\dot{C}F_2$. The former were found to be stable, but the latter to be very reactive, at room temperature. A large part of the latter is thought to disappear by recombination, and only a small part to be oxidized by oxygen occluded in the polymer to form less reactive oxide radicals $-CF_2-CF_2-O\cdot$ even in a vacuum vessel. The radicals $-CF_2-\dot{C}F-CF_2-$ give a double quintet and $-CF_2-\dot{C}F_2$, a triplet in the spectrum. When gaseous oxygen was admitted to the irradiated PTFE, oxygenated radicals were formed. They will be $-CF_2-(CF(OO\cdot))-CF_2-$ and $-CF_2-CF_2-OO\cdot$; the former giving asymmetrical signal termed O_I, and the latter a singlet O_{II}. The following reversible reactions were also studied: $-CF_2-\dot{C}F-CF_2-+O_2\rightleftarrows-CF_2-(CF(OO\cdot))-CF_2-$, and $-CF_2-\dot{C}F-CF_2-+NO\rightleftarrows-CF_2-(CF(NO))-CF_2$. Some discussions are given on the reactions between irradiated PTFE and gases.

INTRODUCTION

ELECTRON spin resonance (ESR) spectra of irradiated polytetrafluoroethylene (PTFE) have been studied by several workers.[1-6] Rexroad and Gordy[4] analyzed the spectrum of PTFE irradiated in vacuum, and suggested that the structure of the radical thus obtained would be of the type $-CF_2-\dot{C}F-CF_2-$. They also observed changes of the spectra caused by exposure of the sample to air and other gases. Tsvetkov, Lebedev, and Voevodskiĭ[5,6] studied the reaction of radicals in irradiated PTFE and oxygen $R\cdot+O_2\rightleftarrows RO_2\cdot$ by means of ESR, and made calculations of the rate constants of the forward and reverse reactions. Anderson and his co-workers[7] investigated hyperfine structures of spectra of fluorine-substituted aromatic radicals, and discussed interactions of F nuclei with radical electrons.

The reversible capture-liberation reaction of oxygen with irradiated PTFE studied by ESR has been reported in our previous paper.[8] In the present paper, changes of ESR spectra of irradiated PTFE observed in atmospheres of several kinds of gases are described. The spectra are analyzed and some considerations are given on the structure of radicals formed in irradiated PTFE and their oxygenated ones. Some reactions of PTFE radicals with gases are also discussed.

EXPERIMENTAL

The PTFE samples used were "Teflon," which were in coarse powdered form. About 0.2 g of the sample was evacuated by an oil-diffusion pump for 2 days in a glass tube, sealed, and irradiated. The diameter of the narrow part of the glass tube was made to fit to the sample holder of the cavity resonator of the ESR spectrometer. The inner diameter of the holder was 5 mm (see Fig. 1).

Irradiation was carried out in a 1-kc Co^{60} γ apparatus to a dose of 50 Mrad at room temperature. The tube was then heated with a Bunsen flame keeping the PTFE sample out of the heat. The glass was decolored by this heating. Then a vacuum cock was connected to the tube without exposing the sample to air, using a conventional breakable-seal method.

ESR spectra were observed with a JES-I-type spectrometer[9] at a frequency of 9400 Mc/sec at 25°C. H_2, D_2, CH_4, C_2H_6, CO, CO_2, NO, N_2, and O_2 were used as reactants. They were purchased as purified gases and stored in glass ampoules. Dried air was also used in place of O_2, but no difference was observed in the change of spectrum.

RESULTS

Spectrum of Irradiated PTFE

The spectrum of PTFE irradiated in vacuum and measured also in vacuum without exposing to air was composed of a number of lines as shown in Fig. 2 (a). This did not change for more than one year at room temperature in vacuum, together with the atmosphere of gases liberated from the sample during irradiation.

Changes of Spectrum in Atmosphere of Hydrogen

The spectrum of PTFE changed from (a) to (b) and (b) to (c) in Fig. 2 with admission of 100 mm Hg of H_2 to the sample. It is seen from the figures that the

* On leave from Asahi Chemical Industry Company, Ltd.

[1] E. E. Schneider, J. Chem. Phys. **23,** 978 (1955).

[2] R. J. Abraham and D. H. Whiffen, Trans. Faraday Soc. **54,** 1291 (1958).

[3] S. Ohnishi, Y. Ikeda, N. Kashiwagi, and I. Nitta, Isotopes and Radiation **1,** 210 (1958).

[4] H. N. Rexroad and W. Gordy, J. Chem. Phys. **30,** 399 (1959).

[5] Yu. D. Tsvetkov, Ya. S. Lebedev, and V. V. Voevodskiĭ Vysokomolekulyarnya Soedineniya (High Molecular Weight Compounds) **1,** 1519 (1959).

[6] Yu. D. Tsvetkov, Ya. S. Lebedev, and V. V. Voevodskiĭ Vysokomolekulyarnya Soedineniya (High Molecular Weight Compounds) **1,** 1634 (1959).

[7] D. H. Anderson, P. J. Frank, and H. S. Gutowsky, J. Chem. Phys. **32,** 196 (1960).

[8] T. Matsugashita and K. Shinohara, J. Chem. Phys. **32,** 954 (1960).

[9] Manufactured by Japan Electron Optics Company, Tokyo, Japan.

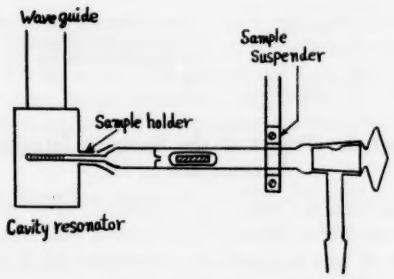

FIG. 1. Sample tube held in cavity resonator.

change of the spectrum takes place in two steps. In the earliest 10 min deformation in the central region of the spectrum occurred [(a) to (b)]. The signal disappearing in this period can be constructed by subtracting spectrum (b) from spectrum (a). It was a triplet as shown in Fig. 3. The intensity ratio was 1:2:1 and the separation of lines was 14 gauss.

Spectrum (b) made a further change to spectrum (c) in the following 24 hr. Subtraction of spectrum (c) from spectrum (b) lead to a complicated pattern as shown in Fig. 4. This was the signal that was analyzed by Rexroad and Gordy[4] and described as a double quintet. The intensity ratio of the quintet lines was roughly 1:4:6:4:1 and the separation of the lines was 33 gauss. The two quintets had the same intensity and the separation of them was 90 gauss.

The residual signal in spectrum (c) made no further change in H_2. It is still not analyzed.

Changes of the Spectrum in Atmospheres of Deuterium, Methane, and Ethane

The spectrum of irradiated PTFE suffered deformation in D_2, and in CH_4 similar to that in H_2. The rates of the disappearance of the triplet and the doublet quintet in gases decreased in the order of H_2, D_2, CH_4, and C_2H_6.

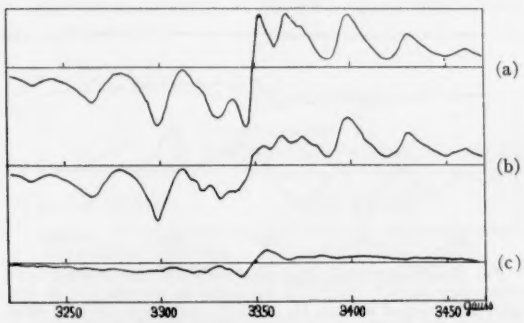

FIG. 2. ESR spectrum of irradiated PTFE and its changes in atmosphere of H_2 (a) PTFE irradiated in vacuum; (b) 10 min after admission of 100 mm Hg of H_2; (c) 24 hr after admission of 100 mm Hg of H_2.

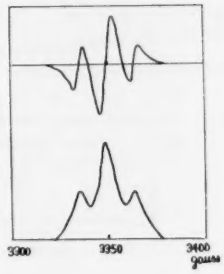

FIG. 3. Triplet signal obtained by subtracting spectrum (b) from spectrum (a) in Fig. 2.

Changes of the Spectrum in Atmosphere of Oxygen

When 100 mm Hg of O_2 was admitted to the PTFE sample irradiated in vacuum, the double quintet and the unanalyzed signal disappeared and the signals of the oxygenated radicals increased [(a) to (b) in Fig. 5]. The change of the triplet was not seen clearly, since the central region of the spectrum was covered by the signals of the oxygenated radicals. The change was completed in less than a few minutes.

By re-evacuation of the oxygenated sample at 150°C for 15 min, the spectrum changed from (b) to (c) in Fig. 5; the signals of the oxygenated radicals partially disappeared and the double quintet was recovered. The signal lost in this change is shown in Fig. 6. It is asymmetric and has an irregular appearance. This signal will be denoted as O_I in this paper. By further evacuation of the same sample at 250°C for 15 min, the spectrum changed from (c) to (d); the signal of the oxygenated radicals disappeared completely. The signal lost within this change is shown in Fig. 7. It was a symmetrical singlet, situated at $g=2.016$. This signal will be denoted as O_{II}.

Change of Spectrum in Atmospheres of Nitric Oxide

The signals disappeared completely in 40 min at room temperature when 100 mm Hg of NO was admitted to the PTFE sample irradiated in vacuum [(a) to (b) in Fig. 8]. The rate of the disappearance was very fast, and was comparable to that in O_2.

As was observed with O_2, signals of the original PTFE radicals could be recovered by re-evacuation of the sample. By evacuation at 50°–80°C, spectrum (c) in Fig. 8 was obtained. This is the same signal as that seen in spectrum (c) in Fig. 2, the signal that survived after exposure to H_2. By evacuation at a temperature higher

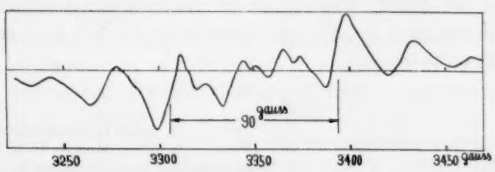

FIG. 4. Double quintet signal obtained by subtracting spectrum (c) from spectrum (b) in Fig. 2.

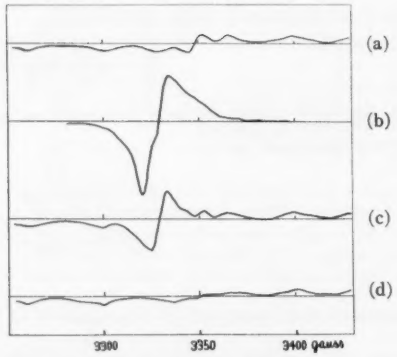

FIG. 5. ESR spectrum of irradiated PTFE and its changes in atmosphere of O_2. Spectrum (a) PTFE irradiated in vacuum; spectrum (b) after admission of 100 mm Hg of O_2 to the sample (a); spectrum (c) after re-evaculation of the sample (b) at 150°C for 15 min; spectrum (d) after evacuation of the sample (c) at 250°C for 15 min. Gain of the amplifier of the spectrometer was 1/10 of that in Fig. 2.

than 100°C, the double quintet was recovered. Complete recovery of this last signal resulted from evacuation at 200°C for 15 min [spectrum (d)]. The triplet could not be recovered by re-evacuation.

Exposure to Nitrogen, Carbon Dioxide, and Carbon Monoxide

No change was observed at room temperature in the spectra of PTFE samples irradiated in vacuum when the samples were exposed to 100 mm Hg of N_2, of CO_2, and of CO.

Changes of the Spectrum of the Oxygenated Samples in Various Gases

When the oxygenated sample was exposed to N_2, CO_2, or H_2 at a temperature higher than room temperature, the signals of the oxygenated radicals disappeared in the same manner as when the sample was evacuated. In N_2 and in CO_2, O_I disappeared and the double quintet was recovered at 50°–150°C, and O_{II} disappeared at 250°C. In H_2, O_I also disappeared at 50°–150°C, but the double quintet was not recovered, since it suffered further change in H_2, as has already been described.

In CO, the change occurred in somewhat different manner. Although O_I disappeared and the double quintet was recovered in the same manner as in other gases, O_{II} also disappeared and the triplet was recovered at 80°–100°C. The signals of the oxygenated radicals disappeared quickly and completely in NO at room temperature.

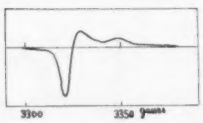

FIG. 6. O_I signal in the spectrum of the oxygenated sample. Gain of the amplifier was the same as in Fig. 5.

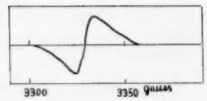

FIG. 7. O_{II} signal in the spectrum of the oxygenated sample. Gain of the amplifier was the same as in Fig. 5.

O_{II} and the Triplet of the Samples Irradiated in Vacuum and in Air

Three samples that were irradiated after different treatment and in different atmospheres were compared. Sample A was prepared by evacuation for 2 days at room temperature followed by further evacuation at 350°C for 3 hrs, irradiation, and admission of air after irradiation (PTFE melts at about 327°C). Sample B was prepared by 2 days evacuation at room temperature, irradiation, and admission of air after irradiation. Sample C was prepared by irradiation in air. It was found that intensity of O_{II} was strongest in sample C, and weakest in sample A. Three samples were then evacuated at 150°C for 15 min. O_I disappears by this treatment. After that, the samples were exposed to CO at 100°C for 15 min. The intensity of the triplet measured after these treatments was found to be strongest in sample C and weakest in sample A (Table I).

When the sample which evacuated at room temperature and irradiated in a vacuum was heated in a vacuum at 100°C for 15 min, intensity of the triplet increased to about 1.5 times the original intensity.[10] With the sample pre-evacuated in the melted state, however, no increase in the intensity of the triplet was observed.

DISCUSSION

Double Quintet

Radical —CF_2—$\dot{C}F$—CF_2— was suggested by Rexroad and Gordy[4] as the origin of the double quintet. The explanation given was as follows. The doublet

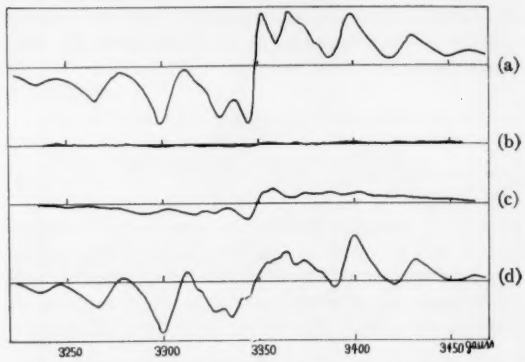

FIG. 8. ESR spectrum of irradiated PTFE and its changes in atmosphere of NO. (a) PTFE irradiated in vacuum; (b) 40 min after admission of 100 mm Hg of NO to the sample (a); (c) after re-evacuation of the sample (b) at 70°C for 15 min; (d) after evacuation of the sample (c) at 200°C for 15 min.

[10] Effects of heat treatment of PTFE irradiated in a vacuum were studied by N. Tamura, J. Phys. Soc. Japan **15**, 943 (1960).

splitting of 90 gauss occurs from hyperfine interaction of the F nucleus that is located at the α position for the radical carbon atom. The quintet splitting of 33 gauss occurs from equal hyperfine interaction of four F nuclei that are located at β position for the radical carbon atom.

O_I and Reaction between $-CF_2-\dot{C}F-CF_2-$ and Oxygen

Disappearance of the double quintet and growth of O_I by admission of O_2 and also the reverse process that occurs by re-evacuation at 150°C for 15 min suggest that O_I is a signal of radicals which are produced when $-CF_2-\dot{C}F-CF_2-$ are oxygenated. The fact that the double quintet is recovered simply by removing O_2 from the atmosphere, e.g., by pumping off O_2 or driving it out of the sample by introducing another gas, suggests that oxygen is probably captured as a molecule by PTFE radical with admission of O_2, and reversibly liberated by re-evacuation. The reaction may therefore be

$$-CF_2-\dot{C}F-CF_2- + O_2 \underset{\text{evacuation}}{\overset{O_2\ \text{admission}}{\rightleftarrows}} -CF_2-\underset{\displaystyle O-\dot{O}}{\underset{|}{CF}}-CF_2-. \quad (1)$$

(double quintet) (O_I)

Reaction between $-CF_2-\dot{C}F-CF_2-$ and Nitric Oxide

As the double quintet disappears and no new signal grows up when NO, which has an unpaired electron, is admitted into the irradiated PTFE sample, $-CF_2-\dot{C}F-CF_2-$ is supposed to react with NO and to form a compound that has no unpaired electron. Since the double quintet is recovered by re-evacuation of the sample, the new compound may be decomposed to the original $-CF_2-\dot{C}F-CF_2-$ and NO. The reaction may be

$$-CF_2-\dot{C}F-CF_2- + NO \underset{\text{evacuation}}{\overset{\text{NO admission}}{\rightleftarrows}} -CF_2-\underset{NO}{\underset{|}{CF}}-CF_2-. \quad (2)$$

[double quintet) (no signal)

Reactions between $-CF_2-\dot{C}F-CF_2-$ and Hydrogen, Deuterium, and Hydrocarbons

The double quintet disappeared in H_2, in D_2, and in CH_4. No growth of new signal in these gases, nor recovery of the double quintet with re-evacuation was observed at any temperature so far tried. Two processes,

TABLE I. Relative intensities of O_I, O_{II}, the double quintet and the triplet of three samples which were irradiated in different atmospheres. Sample B was taken as standard.

Samples	A	B	C
Treatment before irradiation	Evacuation at room temperature followed by evacuation melted state	Evacuation at room temperature	No
Irradiation	In vacuum	In vacuum	In air
Treatment after irradiation	Air admission	Air admission	No
Relative intensities of O_I	1.0	1.00	0.97
Relative intensities of O_{II}	0.85	1.00	5.05
Relative intensities of the double quintet after evacuation at 150°C.	1.0	1.00	1.0
Relative intensities of the triplet after exposure to CO at 100°C.	0.88	1.00	4.55

Eqs. (3) and (3′), may be considered in this case, and it is not clear yet which of them is correct.

$$-CF_2-\dot{C}F-CF_2- + H_2(HR) \rightarrow -CF_2-\underset{H}{\underset{|}{CF}}-CF_2- + H\cdot(R\cdot) \quad (3)$$

and

$$-CF_2-\dot{C}F-CF_2- + H_2(HR) \rightarrow -CF_2-CF{=}CF- + HF + H\cdot(R\cdot). \quad (3')$$

(double quintet) (no signal)

More detailed experiments on reactions between irradiated PTFE and hydrogens and hydrocarbons are now in progress.

Triplet

Assuming that the assignment of the double quintet to $-CF_2-\dot{C}F-CF_2-$ is correct, the triplet must be the spectrum of unpaired electrons interacted equally by two F nuclei.

A splitting of only 14 gauss means a comparatively weak interaction with F nuclei. It is difficult to think of a structure of a radical of a fluorocarbon consistent with the observations. It is therefore assumed that the triplet is the spectrum of oxyfluorocarbon radical $-CF_2-O\cdot$. Equal interaction by two F nuclei and weakness of the interaction can then be explained. Splittings by protons in alkoxy radicals were reported

by Piette and Landgraf[11] to be much smaller than that in hydrocarbon radicals. They were only 3.5 gauss in *n*-butoxy and 2.8 gauss in *sec*-butoxy radicals compared with 20–35 gauss in hydrocarbons.[12]

O_{II} and Relation to the Triplet

When the sample giving the O_{II} signal in the spectrum was reduced by CO, O_{II} disappeared and the triplet grew in size. This fact suggests that O_{II} is the signal of an oxide of the radical giving the triplet. If the triplet is the signal of $—CF_2—O\cdot$, as inferred above, O_{II} may be the signal of $—CF_2—OO\cdot$. Reaction with CO will then be

$$\underset{(O_{II})}{—CF_2—OO\cdot} + CO \rightarrow \underset{(\text{triplet})}{—CF_2—O\cdot} + CO_2. \qquad (4)$$

Occurrence of $—CF_2—O\cdot$ and Possible Existence of Short-Lived $—CF_2$

There were clear differences in the intensity of the triplet between three samples obtained from samples A, B, and C by re-evacuating at 150°C for 15 min and then reducing with CO at 100°C for 15 min. The first one gave the smallest and the last one the largest intensity. This fact seems to support the interpretation that the triplet is the signal of a radical's containing oxygen.

Measurements were made in search of a signal that may be attributed to $—CF_2—CF_2\cdot$ radicals on various samples: The PTFE sample irradiated in a vacuum, the one obtained by evacuation of the oxygenated samples at high temperature, and the one obtained by reduction of the oxygenated samples by NO or H_2. Such a radical would give a triple triplet, since the interaction with two F nuclei at the α position would cause a splitting of nearly 90 gauss and that with two F nuclei at β position would cause a splitting of nearly 33 gauss. Such a signal was not observed in the spectra of any sample. In spite of this, it would be natural to postulate that radicals formed primarily by irradiation would be $—CF_2—\dot{C}F—CF_2—$ and $—CF_2—CF_2\cdot$, since the latter are thought to be forerunners of $—CF_2—O\cdot$. If it is true, the $—CF_2—CF_2\cdot$ that is formed must be assumed to react very quickly. When the irradiation of PTFE was carried out at room temperature, a large part of $—CF_2—CF_2\cdot$ formed might recombine in a very short time, and only a small portion of the radicals which encountered oxygen occluded in the polymer before recombination change to the less reactive $—CF_2—CF_2—O\cdot$, i.e., the radicals giving the triplet. When the samples giving the triplet or O_{II} in the spectra were evacuated at high temperature or reduced by NO or H_2, etc., $—CF_2—CF_2\cdot$ might be formed. But they would not be able to stay in this structure, because they would recombinate or react with NO or H_2. The increase of the triplet with heat treatment of PTFE sample irradiated in vacuum may be attributed to the oxidation of a small quantity of $—CF_2—CF_2\cdot$, which has been left in the polymer, by occluded oxygen.

Reactions of the Triplet Giving Radicals with Gases

The radicals giving the triplet which are now assumed to be $—CF_2—O\cdot$ easily react with H_2, D_2, CH_4, NO, and even with C_2H_6. All these reactions are irreversible. More than two mechanisms can be considered without inconsistency. The data are insufficient to decide which of them are correct.

ACKNOWLEDGMENTS

The authors are grateful to Dr. Z. Kuri and Mr. N. Tamura for helpful discussions throughout the entire course of the work.

[11] L. H. Piette and W. C. Landgraf, J. Chem. Phys. **32**, 1107 (1960).

[12] For example, D. J. E. Ingram, *Free Radicals as Studied by Electron Spin Resonance* (Butterworths Scientific Publications, Ltd., London, 1958), p. 111.

Cuboctahedral Bonding*

JACK R. CANON AND GEORGE H. DUFFEY
Physics Department, South Dakota State College, Brookings, South Dakota

(Received October 3, 1960)

Molecular orbitals belonging to the different irreducible representations of a B_{12} cuboctahedron are set up and parametric expressions for the energy levels obtained. Terms neglected by Lipscomb and Britton are included. Directed orbitals for group O_h coordination of 12 ligands about a central atom are formulated and Pauling strengths calculated.

WE shall consider (a) bonding between 12 atoms arranged at the corners of a cuboctahedron of symmetry O_h and (b) bonding between a central atom and 12 ligands of this symmetry. The former type involves interaction between orbitals which are neither directly opposed nor parallel and is exhibited in certain boron compounds. The latter may be seen in cubic close packed structures.

In UB_{12} and ZrB_{12} boron atoms are bound covalently at corners of empty cuboctahedra.[1] Each boron atom in a given B_{12} polyhedron is also bound to a B atom in another B_{12} group. The metal atoms lie in holes between these polyhedra.

Following Lipscomb and Britton,[1] we arrange the valence orbitals of a given B so that the p_z orbital is directed radially outward, the p_x orbital is directed toward the center of an adjacent triangular face, and the p_y orbital is directed toward the center of a square face. The s orbital is hybridized with the p_z. One of the resulting orbitals is used for the external orbital. The other, directed inward, is combined linearly with similar orbitals on each of the other B's in the cuboctahedron. Likewise, the p_x and p_y orbitals from the different boron atoms in the polyhedron are combined.

Using the group theoretical method described by Eyring *et al.*,[2] we obtain valid molecular orbitals from each set of atomic orbitals. In the work, each valence orbital of a given kind is labeled by the number of the atom on which it is based, following the scheme in Fig. 1.

The internal sp_z hybrids form the basis of the reducible representation

$$A_{1g}+E_g+F_{1u}+F_{2g}+F_{2u}, \tag{1}$$

in which each irreducible representation occurs but once. From a table showing how each atomic orbital transforms under operations of the group, we find that representative functions of each species are

$$\begin{aligned}
&A_{1g}: && (1/\sqrt{12})(r_1+r_2+r_3+r_4+r_5+r_6+r_7+r_8+r_9+r_{10}+r_{11}+r_{12}),\\
&E_g: && (1/\sqrt{24})(2r_1-r_2+2r_3-r_4+2r_5-r_6+2r_7-r_8-r_9-r_{10}-r_{11}-r_{12}),\\
&F_{1u}: && (1/\sqrt{16})(2r_1+r_2+r_4-r_6-2r_7-r_8+r_9+r_{10}-r_{11}-r_{12}),\\
&F_{2g}: && (1/\sqrt{4})(r_1-r_3-r_5+r_7),\\
&F_{2u}: && (1/\sqrt{16})(2r_1-r_2-r_4+r_6-2r_7+r_8-r_9-r_{10}+r_{11}+r_{12})
\end{aligned} \tag{2}$$

where r_i represents the sp_z hybrid directed radially inward from atom i. From these functions we find the same set of levels as Lipscomb and Britton when F_{1u} interaction with p_x and p_y orbitals is neglected.

Likewise the p_x orbitals yield a reducible representation containing only single irreducible ones. Proceeding as before, we find the representative functions

$$\begin{aligned}
&A_{2u}: && (1/\sqrt{12})(t_1+t_2+t_3+t_4+t_5+t_6+t_7+t_8+t_9+t_{10}+t_{11}+t_{12}),\\
&E_u: && (1/\sqrt{24})(2t_1-t_2+2t_3-t_4+2t_5-t_6+2t_7-t_8-t_9-t_{10}-t_{11}-t_{12}),\\
&F_{1g}: && (1/\sqrt{16})(2t_1-t_2-t_4+t_6-2t_7+t_8-t_9-t_{10}+t_{11}+t_{12}),\\
&F_{1u}: && (1/\sqrt{4})(t_1-t_3-t_5+t_7),\\
&F_{2g}: && (1/\sqrt{16})(2t_1+t_2+t_4-t_6-2t_7-t_8+t_9+t_{10}-t_{11}-t_{12}),
\end{aligned} \tag{3}$$

* Supported in part by the National Science Foundation.

[1] W. N. Lipscomb and D. Britton, J. Chem. Phys. **33**, 275 (1960).

[2] H. Eyring, J. Walter, and G. E. Kimball, *Quantum Chemistry* (John Wiley & Sons, Inc., New York, 1944).

where t_i represents the p_z orbital directed toward a triangular face from atom i. From these functions we find the energy levels

$$\begin{aligned}
&A_{2u}: && H_0+4\epsilon-2\zeta-4\eta+\theta,\\
&E_u: && H_0-2\epsilon-2\zeta+2\eta+\theta\\
&F_{1g}: && H_0-2\epsilon-2\eta-\theta,\\
&F_{1u}: && H_0,\\
&F_{2g}: && H_0+2\epsilon+2\eta-\theta,
\end{aligned} \tag{4}$$

where ϵ equals the resonance integral between t_1 and t_2, ζ the one between t_1 and t_3, η the one between t_1 and t_6, and θ the one between t_1 and t_7 and where F_{1u} interaction with the other two sets of orbitals is disregarded.

Finally the p_y orbitals yield the representative functions

$$\begin{aligned}
&A_{2g}: && (1/\sqrt{12})(s_1+s_2+s_3+s_4+s_5+s_6+s_7+s_8+s_9+s_{10}+s_{11}+s_{12}),\\
&E_g: && (1/\sqrt{24})(2s_1-s_2+2s_3-s_4+2s_5-s_6+2s_7-s_8-s_9-s_{10}-s_{11}-s_{12}),\\
&F_{1g}: && (1/\sqrt{4})(s_1-s_3-s_5+s_7),\\
&F_{1u}: && (1/\sqrt{16})(2s_1-s_2-s_4+s_6-2s_7+s_8-s_9-s_{10}+s_{11}+s_{12}),\\
&F_{2u}: && (1/\sqrt{16})(2s_1+s_2+s_4-s_6-2s_7-s_8+s_9+s_{10}-s_{11}-s_{12}),
\end{aligned} \tag{5}$$

where s_i represents the p_y orbital directed from atom i to a square face. From these we obtain the levels, neglecting F_{1u} interaction with the r's and t's,

$$\begin{aligned}
&A_{2g}: && H_0-4\iota+2\kappa-4\lambda-\mu,\\
&E_g: && H_0+2\iota+2\kappa+2\lambda-\mu,\\
&F_{1g}: && H_0-2\kappa-\mu,\\
&F_{1u} && H_0+2\iota-2\lambda+\mu,\\
&F_{2u}: && H_0-2\iota+2\lambda+\mu.
\end{aligned} \tag{6}$$

Parameters ι and κ are the resonance integrals labeled ζ and η by Lipscomb and Britton. And λ equals the resonance integral between s_1 and s_6, μ the one between s_1 and s_7.

The levels that produce bonding, arranged in order of increasing stability after the nonbonding, triply degenerate one are

$$\begin{aligned}
&\Sigma t,\ F_{1u}(3): && H_0\\
&\Sigma r,\ F_{1u}(3): && H_0+2\alpha+0\beta-2\gamma-\delta\\
&\Sigma s,\ F_{1u}(3): && H_0+2\iota+0\kappa-2\lambda+\mu\\
&\Sigma t,\ F_{2g}(3): && H_0+2\epsilon+0\zeta+2\eta-\theta\\
&\Sigma s,\ E_g(2): && H_0+2\iota+2\kappa+2\lambda-\mu\\
&\Sigma t,\ A_{2u}(1): && H_0+4\epsilon-2\zeta-4\eta+\theta\\
&\Sigma r,\ A_{1g}(1): && H_0+4\alpha+2\beta+4\gamma+\delta.
\end{aligned} \tag{7}$$

The additional terms we have introduced do not alter the essential conclusions of Lipscomb and Britton.[1]

Let us now consider bonding between a central atom and ligands possessing the cuboctahedral symmetry. The ligands are numbered as in Fig. 1 and the valence orbital that is directed toward the ith B is labeled ψ_1. This structure is a distortion of the icosahedral one discussed by Macek and Duffey.[3]

Comparing characters of the representation based on σ bonds and characters of the irreducible representations,[4] one finds that the σ representation breaks down into irreducible representations

$$A_{1g}+E_g+F_{1u}+F_{2g}+F_{2u}. \tag{8}$$

Now by Eisenstein's compilation,[5] the s orbital spans the A_{1g} representation, $d_{3z^2-r^2}$ and $d_{x^2-y^2}$ the E_g one, p_x, p_y, p_z, or $f_{\delta 1}$, $f_{\delta 2}$, $f_{\delta 3}$ the F_{1u} one, d_{xz}, d_{yz}, d_{xy} the F_{2g} one, and $f_{\epsilon 1}$, $f_{\epsilon 2}$, $f_{\epsilon 3}$ the F_{2u} one. Employing these symmetry properties, we obtain the normalized orthogonal bond orbitals described in Table I.

The over-all composition of these orbitals is $sp^{3n}d^{5}f^{6-3n}$ where

$$n=\cos^2\alpha. \tag{9}$$

When each orbital has its angular part normalized to 4π, its value S in the direction of the bond varies with n and $\cos\alpha$ as in Table II. Following Pauling,[6] we call S the strength.

When n is 1, S is 3.860, which is considerably less than 3.921, the strength of an icosahedral orbital[3] with the same composition. Thus we expect that overlap of central atom orbitals with ligand orbitals would be

[3] J. H. Macek and G. H. Duffey, J. Chem. Phys. **34**, 288 (1961).
[4] G. Herzberg, *Infrared and Raman Spectra of Polyatomic Molecules* (D. Van Nostrand Company, Inc., Princeton, New Jersey, 1945).
[5] J. C. Eisenstein, J. Chem. Phys. **25**, 142 (1956).
[6] L. Pauling, *The Nature of the Chemical Bond* (Cornell University Press, Ithaca, New York, 1960), 3rd ed.

TABLE I. Coefficients of atomic orbitals in cuboctahedral bond orbital functions.

	s	p_x	p_y	p_z	$d_{3z^2-r^2}$	$d_{x^2-y^2}$	d_{xz}	d_{yz}	d_{xy}	f_{z1}	f_{z2}	f_{z3}	f_{x1}	f_{x3}	f_{x3}
ψ_1	$\frac{1}{\sqrt{12}}$	$\frac{1}{\sqrt{8}}\cos\alpha$	0	$\frac{1}{\sqrt{8}}\cos\alpha$	$\frac{1}{\sqrt{24}}$	$\frac{1}{\sqrt{8}}$	$\frac{1}{2}$	0	0	$\frac{-1}{\sqrt{8}}\sin\alpha$	$\frac{-1}{\sqrt{8}}\sin\alpha$	0	$\frac{1}{\sqrt{8}}$	$\frac{1}{\sqrt{8}}$	0
ψ_2	$\frac{1}{\sqrt{12}}$	0	$\frac{1}{\sqrt{8}}\cos\alpha$	$\frac{1}{\sqrt{8}}\cos\alpha$	$\frac{1}{\sqrt{24}}$	$\frac{-1}{\sqrt{8}}$	0	$\frac{1}{2}$	0	$\frac{-1}{\sqrt{8}}\sin\alpha$	0	$\frac{-1}{\sqrt{8}}\sin\alpha$	$\frac{-1}{\sqrt{8}}$	0	$\frac{1}{\sqrt{8}}$
ψ_3	$\frac{1}{\sqrt{12}}$	$\frac{-1}{\sqrt{8}}\cos\alpha$	0	$\frac{1}{\sqrt{8}}\cos\alpha$	$\frac{1}{\sqrt{24}}$	$\frac{1}{\sqrt{8}}$	$-\frac{1}{2}$	0	0	$\frac{-1}{\sqrt{8}}\sin\alpha$	$\frac{1}{\sqrt{8}}\sin\alpha$	0	$\frac{1}{\sqrt{8}}$	$\frac{-1}{\sqrt{8}}$	0
ψ_4	$\frac{1}{\sqrt{12}}$	0	$\frac{-1}{\sqrt{8}}\cos\alpha$	$\frac{1}{\sqrt{8}}\cos\alpha$	$\frac{1}{\sqrt{24}}$	$\frac{-1}{\sqrt{8}}$	0	$-\frac{1}{2}$	0	$\frac{-1}{\sqrt{8}}\sin\alpha$	0	$\frac{1}{\sqrt{8}}\sin\alpha$	$\frac{-1}{\sqrt{8}}$	0	$\frac{-1}{\sqrt{8}}$
ψ_5	$\frac{1}{\sqrt{12}}$	$\frac{1}{\sqrt{8}}\cos\alpha$	0	$\frac{-1}{\sqrt{8}}\cos\alpha$	$\frac{1}{\sqrt{24}}$	$\frac{1}{\sqrt{8}}$	$-\frac{1}{2}$	0	0	$\frac{1}{\sqrt{8}}\sin\alpha$	$\frac{-1}{\sqrt{8}}\sin\alpha$	0	$\frac{-1}{\sqrt{8}}$	$\frac{1}{\sqrt{8}}$	0
ψ_6	$\frac{1}{\sqrt{12}}$	0	$\frac{1}{\sqrt{8}}\cos\alpha$	$\frac{-1}{\sqrt{8}}\cos\alpha$	$\frac{1}{\sqrt{24}}$	$\frac{-1}{\sqrt{8}}$	0	$-\frac{1}{2}$	0	$\frac{1}{\sqrt{8}}\sin\alpha$	0	$\frac{-1}{\sqrt{8}}\sin\alpha$	$\frac{1}{\sqrt{8}}$	0	$\frac{1}{\sqrt{8}}$
ψ_7	$\frac{1}{\sqrt{12}}$	$\frac{-1}{\sqrt{8}}\cos\alpha$	0	$\frac{-1}{\sqrt{8}}\cos\alpha$	$\frac{1}{\sqrt{24}}$	$\frac{1}{\sqrt{8}}$	$\frac{1}{2}$	0	0	$\frac{1}{\sqrt{8}}\sin\alpha$	$\frac{1}{\sqrt{8}}\sin\alpha$	0	$\frac{-1}{\sqrt{8}}$	$\frac{-1}{\sqrt{8}}$	0
ψ_8	$\frac{1}{\sqrt{12}}$	0	$\frac{-1}{\sqrt{8}}\cos\alpha$	$\frac{-1}{\sqrt{8}}\cos\alpha$	$\frac{1}{\sqrt{24}}$	$\frac{-1}{\sqrt{8}}$	0	$\frac{1}{2}$	0	$\frac{1}{\sqrt{8}}\sin\alpha$	0	$\frac{1}{\sqrt{8}}\sin\alpha$	$\frac{1}{\sqrt{8}}$	0	$\frac{-1}{\sqrt{8}}$
ψ_9	$\frac{1}{\sqrt{12}}$	$\frac{1}{\sqrt{8}}\cos\alpha$	$\frac{-1}{\sqrt{8}}\cos\alpha$	0	$\frac{-1}{\sqrt{6}}$	0	0	0	$-\frac{1}{2}$	0	$\frac{-1}{\sqrt{8}}\sin\alpha$	$\frac{1}{\sqrt{8}}\sin\alpha$	0	$\frac{-1}{\sqrt{8}}$	$\frac{1}{\sqrt{8}}$
ψ_{10}	$\frac{1}{\sqrt{12}}$	$\frac{1}{\sqrt{8}}\cos\alpha$	$\frac{1}{\sqrt{8}}\cos\alpha$	0	$\frac{-1}{\sqrt{6}}$	0	0	0	$\frac{1}{2}$	0	$\frac{-1}{\sqrt{8}}\sin\alpha$	$\frac{-1}{\sqrt{8}}\sin\alpha$	0	$\frac{-1}{\sqrt{8}}$	$\frac{-1}{\sqrt{8}}$
ψ_{11}	$\frac{1}{\sqrt{12}}$	$\frac{-1}{\sqrt{8}}\cos\alpha$	$\frac{1}{\sqrt{8}}\cos\alpha$	0	$\frac{-1}{\sqrt{6}}$	0	0	0	$-\frac{1}{2}$	0	$\frac{1}{\sqrt{8}}\sin\alpha$	$\frac{-1}{\sqrt{8}}\sin\alpha$	0	$\frac{1}{\sqrt{8}}$	$\frac{-1}{\sqrt{8}}$
ψ_{12}	$\frac{1}{\sqrt{12}}$	$\frac{-1}{\sqrt{8}}\cos\alpha$	$\frac{-1}{\sqrt{8}}\cos\alpha$	0	$\frac{-1}{\sqrt{6}}$	0	0	0	$\frac{1}{2}$	0	$\frac{1}{\sqrt{8}}\sin\alpha$	$\frac{1}{\sqrt{8}}\sin\alpha$	0	$\frac{1}{\sqrt{8}}$	$\frac{1}{\sqrt{8}}$

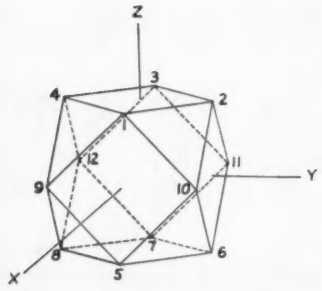

FIG. 1. Orientation of cuboctahedron.

TABLE II. Properties of cuboctahedral bond orbitals.[a]

n	$\cos\alpha$	S
0.0000	0.0000	3.325
0.2000	0.4472	3.677
0.4000	0.6325	3.798
0.6000	0.7746	3.874
0.8000	0.8944	3.917
0.8735	0.9346	3.921
1.0000	1.0000	3.860

[a] The orbitals are of type $sp^{3n}d^5f^{6-3n}$.

greater in the icosahedral structure. Increasing the amount of f to 3.380 increases the S to 3.921,—the maximum for the cuboctahedral structure. Since this is not greater than S for the icosahedron, the cuboctahedron is not favored unless the f orbitals lie low. But if the ligands interact so they attract each other, their closer approach in the cuboctahedron favors it.

When bonding in a complex is essentially ionic, stability is determined by shifts in energy of occupied orbitals caused by electrostatic interaction with the ligands.[7] In the cuboctahedral structure the p orbitals are shifted together since they form the basis[5] of the same representation F_{1u}. The d orbitals are split since $d_{3z^2-r^2}$ and $d_{x^2-y^2}$ belong to E_g while d_{zx}, d_{yz}, and d_{xy} belong to F_{2g}. We expect shifts in these to be upwards because the orbitals are directed towards ligands, and our earlier discussion shows they are used in σ bond formation. The triplets $f_{\delta 1}$, $f_{\delta 2}$, $f_{\delta 3}$ and $f_{\epsilon 1}$, $f_{\epsilon 2}$, $f_{\epsilon 3}$ are shifted upwards different amounts since they belong to F_{1u} and F_{2u}, respectively. The f_{xyz} orbitals belongs to A_{2u}, is not used for σ bond formation, and so is shifted downwards. Note that more splits occur than in an icosahedral field.[3]

Using characters for the representation based on π bonds and the character table for the group, we find that the representation breaks down into irreducible representations

$$A_{2g}+A_{2u}+E_g+E_u+2F_{1g}+2F_{1u}+F_{2g}+F_{2u}. \quad (10)$$

No basis functions for A_{2g}, E_u, or F_{1g} are found among the s, p, d, and f orbitals. Only if higher orbitals are available can these species of π bonds be formed. Since all s, p, d, and f orbitals of E_g, F_{2g}, and F_{2u} are used in σ bonding, these kinds of π bonds are not to be expected. The F_{1u} representation is spanned by either p_x, p_y, p_z or $f_{\delta 1}$, $f_{\delta 2}$, $f_{\delta 3}$, so what is not used in σ bonding is available for π bonding, and three higher orbitals are needed to complete all π bonds of this type. The A_{2u} representation is spanned by f_{xyz}. By Kimball's criterion,[2] the π bond formed from it is strong.

[7] P. George and D. S. McClure in *Progress in Inorganic Chemistry*, edited by F. A. Cotton (Interscience Publishers, Inc., New York, 1959), Vol. 1, p. 381.

Calculations of the Lower Excited Energy Levels of the Cyclic Polyenes, Radicals, and Ions

NICOLAAS BOUMAN

Section of Chemistry, Van der Waals-Lyceum, Amsterdam, Netherlands

(Received December 21, 1960)

The lower excited energy levels of the cyclic polyenes, radicals, and ions with 3 to 8 carbon atoms are calculated with inclusion of all the interelectronic integrals and without empirical data, except the carbon-carbon distance.

INTRODUCTION

THE energy levels of the cyclic polyenes, radicals, and ions will be calculated by the method of antisymmetrized products of molecular orbitals. Details of these calculations will not be given, as these may be found in the papers of Goeppert-Mayer and Sklar,[1] Mulliken,[2] and others.[3-5] All the inter-electronic integrals will be calculated without empirical data, except the carbon-carbon distance.

INTEGRALS ENTERING INTO FORMULAS OF ENERGY LEVELS

Using the notation of the paper of deHeer and Pauncz,[6] we have, for the molecular orbitals of a cyclic polyene with u carbon atoms,

$$\psi_j=(uN_j)^{-\frac{1}{2}}\sum_{\mu=0}^{u-1}\omega^{j\mu}\phi_\mu, \tag{1}$$

with

$$\omega=\exp(2\pi i/u), \tag{2}$$

in which ϕ_μ is the $2p\pi$-Slater atomic orbital on the μth carbon atom and N_j is a normalizing factor.

Referring to the paper of deHeer and Pauncz,[6] we need for the calculation of the energy levels the integrals of Eq. (3) of that paper:

$$(jk\mid lm)=\int\psi_j^*(1)\psi_k(1)(e^2/r_{12})\psi_l^*(2)\psi_m(2)dv_1dv_2. \tag{3}$$

Following Ruedenberg,[7] deHeer, and Pauncz[6] reduce these integrals to simple equations using the special symmetry of these compounds. Applying the approximation of Mulliken,[2] all the interelectronic integrals are included. These authors restrict their formulas to symmetrical cyclic systems with closed-shell structure, i.e., with $2n=4v+2$ atoms. These deductions also hold for a cyclic polyene with any number of carbon atoms.

Hence instead of Eq. (14) of the paper of deHeer and Pauncz we write

$$(jk\mid lm)=u^{-1}N_{jk}N_{lm}f_{j-k}(C) \tag{4}$$

with

$$f_{j-k}(C)=\sum_{\tau=0}^{u-1}\omega^{(j-k)\tau}(00\mid\tau\tau)=\sum_{\tau=0}^{u-1}\omega^{(j-k)\tau}C_\tau \tag{5}$$

in which

$$C_\tau=(00\mid\tau\tau)=\int\phi_0^*(1)\phi_0(1)(e^2/r_{12})\phi_\tau^*(2)\phi_\tau(2)dv_1dv_2, \tag{6}$$

and

$$N_{jk}=\tfrac{1}{2}[(N_j+N_k)/(N_jN_k)^{\frac{1}{2}}]. \tag{7}$$

Equation (4) gives all the relevant integrals, Coulomb integrals $(ii\mid jj)$, exchange integrals $(ij\mid ji)$, and integrals of the type $(jk\mid lm)$ which fulfil the condition $-j+k-l+m=u$. All these equations hold for any cyclic polyene.

All the integrals will be calculated without empirical data except the carbon-carbon distance. We adopt 1.39 A for the carbon-carbon distance in benzene, and following Longuet-Higgins and McEwen[8] we use the same number for the distance of the carbon-carbon atoms in the other cyclic polyenes.

In discussing the Coulomb integrals we write

$$(ii\mid jj)=u^{-1}f_0(C). \tag{8}$$

Clearly these integrals cancel out in the calculation of the energy differences.

For the exchange integrals we have

$$(jk\mid kj)=u^{-1}N_{jk}^2f_{j-k}(C). \tag{9}$$

In calculating these integrals we need the numerical values of the factor N_{jk} of Eq. (7). Hence we have to calculate the normalization constants

$$N_j=\sum_{\tau=0}^{u-1}S_{0\tau}\exp\left(\frac{2\pi j\tau}{u}\right)i, \tag{10}$$

[1] M. Goeppert-Mayer and A. L. Sklar, J. Chem. Phys. **6,** 645 (1938).
[2] R. S. Mulliken, J. chim. phys. **46,** 675 (1938).
[3] D. P. Craig, J. Chem. Phys. **17,** 1358 (1949).
[4] D. P. Craig, Proc. Roy. Soc. (London) **200,** 474 (1950).
[5] R. G. Parr, D. P. Craig, and I. G. Ross, J. Chem. Phys. **18,** 1561 (1950).
[6] J. deHeer and R. Pauncz, J. Mol. Spectroscopy **5,** 326 (1960).
[7] K. Ruedenberg, J. Chem. Phys. **34,** 1878 (1961).
[8] H. C. Longuet-Higgins and K. L. McEwen, J. Chem. Phys. **26,** 719 (1957).

TABLE I. Electronic energy levels of C_5H_5, C_6H_6, and $C_7H_7^+$.

Compound	Symmetry	Observed ev	Calculated as described in this paper	Roothaan and Parr[e]	Parr, Craig, and Ross[f]
C_5H_5	$^2A_2''$	3.68[a]	4.92		
C_6H_6	$^1E_{1u}$	6.74[b]	9.95	9.7	9.9
C_6H_6	$^1B_{1u}$	6.14[b]	7.02	7.2	9.0
C_6H_6	$^1B_{2u}$	4.88[b]	5.69	5.8	4.4
C_6H_6	$^3B_{1u}$	3.66[c]	3.29	3.0	4.1
$C_7H_7^+$	$^1E_3'$	4.51[d]	5.17		

[a] B. A. Trush, Nature **178,** 155 (1956).
[b] H. B. Klevens and J. R. Platt, Technical Report, Laboratory of Molecular Structure and Spectra, University of Chicago, Chicago, Illinois, 1953–1954.
[c] G. N. Lewis and M. Kasha, J. Am. Chem. Soc. **66,** 2100 (1944).
[d] W. E. von Doering and L. H. Know, J. Am. Chem. Soc. **76,** 3203 (1954).
[e] C. C. J. Roothaan and R. G. Parr, J. Chem. Phys. **17,** 1001 (1949).
[f] R. G. Parr, D. P. Craig, and I. G. Ross, J. Chem. Phys. **18,** 1561 (1950).

with the overlap integral

$$S_{ab}=\int \phi_a(1)\phi_b(1)d\tau_1. \tag{11}$$

These overlap integrals can be calculated by means of the formula[9]

$$S_{ab}=[(\rho^3/120)+(\rho^2/10)+(\rho/2)+1]e^{-\rho/2}, \tag{12}$$

in which $\rho=Z(a_z/a_H)$ where Z is the effective charge, a_z is the internal distance, and a_H is the radius of the innermost Bohr orbit.

We must also calculate $C_\tau=(00\mid\tau\tau)$. These integrals are computed with $2p\pi$-Slater atomic orbitals with effective charge 3.18. The rigorously calculated numerical values of these integrals are taken from the tables of the paper of Parr and Crawford.[10] In summary, all the integrals occurring in Eq. (9) are calculated and so the exchange integrals are computed *ab initio.*

The integrals of the type ξ and η, as defined in the appendix of the paper of Parr, Craig, and Ross,[5] are calculated in a similar way.

Finally we need the value of the integral

$$T_j=\int \psi_j^*(1)H_{\text{core}}\psi_j(1)d\tau(1). \tag{13}$$

By use of Eq. (10) given in the paper just quoted, these integrals are expressed in terms of the atomic integrals

TABLE II. Electronic energy levels of ions of cyclic polyenes.

Ion	Symmetry	Excited state wave function	Excitation energy (ev) Singlet [b]	Singlet [c]	Triplet [b]	Triplet [c]
$C_5H_5^+$	$E'(D_{5h})$	$(1/\sqrt{2})\{\chi_0^1\pm\chi_0^{-1}\}$[a]	8.25	10.09	6.09	4.42
$C_6H_4^{++}$	$E_u(D_{6h})$	$(1/\sqrt{2})\{\chi_0^1\pm\chi_0^{-1}\}$	5.86	8.95	3.70	3.57
$C_6H_4^{=}$	$E_u(D_{6h})$	$(1/\sqrt{2})\{\chi_1^2\pm\chi_{-1}^2\}$	5.86	6.77	3.70	1.33
$C_6H_5^-$	$E_1'(D_{5h})$	$(1/\sqrt{2})\{\chi_1^2\pm\chi_{-1}^{-2}\}$	7.22	10.70	4.90	5.22
	$E_2'(D_{5h})$	$(1/\sqrt{2})\{\chi_1^{-2}\pm\chi_{-1}^2\}$	5.79	7.85	4.90	5.22
$C_7H_7^+$	$E_1'(D_{7h})$	$(1/\sqrt{2})\{\chi_1^2\pm\chi_{1-}^{-2}\}$	6.36	8.74	3.77	3.45
	$E_2'(D_{7h})$	$(1/\sqrt{\ })\{\chi_1^{-2}\pm\chi_{-1}^2\}$	4.33	5.17	3.77	3.39
$C_8H_8^{++}$	$E_{1u}(D_{8h})$	$(1/\sqrt{2})\{\chi_1^2\pm\chi_{-1}^{-2}\}$	5.80	7.78	3.09	2.63
	$E_{2u}(D_{8h})$	$(1/\sqrt{2})\{\chi_1^{-2}\pm\chi_{-1}^2\}$	3.67	4.28	3.09	2.63
$C_8H_8^{=}$	$E_{1u}(D_{8h})$	$(1/\sqrt{2})\{\chi_2^3\pm\chi_{-2}^{-3}\}$	5.80	9.20	3.09	4.02
	$E_{3u}(D_{8h})$	$(1/\sqrt{2})\{\chi_2^{-3}\pm\chi_{-2}^3\}$	3.67	5.68	3.09	4.02

[a] For the notation of χ_0^1 see H. C. Longuet-Higgins and K. L. McEwen, reference 8.
[b] Calculated by H. C. Longuet-Higgins and K. L. McEwen, reference 8.
[c] Calculated as described in this paper.

[9] *Handbuch der Physik*, edited by S. Flügge (Springer-Verlag, Berlin, Germany, 1933), Vol. XXIV, p. 643.
[10] R. G. Parr and B. L. Crawford, J. Chem. Phys. **16,** 526, 1049 (1948).

TABLE III. Electronic energy levels of radicals of cyclic polyenes.

Radical	Symmetry	Wave function	Energy (ev) [a]	Energy (ev) [b]
C_3H_3	$^2E''$	$\lvert\psi_0\bar{\psi}_0\psi_1\rvert$	0	0
	$^2E''$	$\lvert\psi_0\bar{\psi}_1\psi_1\rvert$	7.17	7.26
(D_{3h})	$^2A_2''$	$(1/\sqrt{2})\{\lvert\psi_0\psi_1\bar{\psi}_{-1}\rvert-\lvert\psi_0\bar{\psi}_1\psi_{-1}\rvert\}$	7.17	9.89
	$^2A_1''$	$(\sqrt{2}/\sqrt{3})\lvert\bar{\psi}_0\psi_1\psi_{-1}\rvert-(1/\sqrt{6})\lvert\psi_0\psi_1\bar{\psi}_{-1}\rvert$ $-(1/\sqrt{6})\lvert\psi_0\bar{\psi}_1\psi_{-1}\rvert$	7.17	10.30
	$^4A_1''$	$(1/\sqrt{3})\{\lvert\bar{\psi}_0\psi_1\psi_{-1}\rvert+\lvert\psi_0\bar{\psi}_1\psi_{-1}\rvert+\lvert\psi_0\psi_1\bar{\psi}_{-1}\rvert\}$	5.02	1.58
C_5H_5	$^2E_1''$	$\lvert\psi_0\bar{\psi}_0\psi_1\bar{\psi}_1\psi_{-1}\rvert$	0	0
	$^2E_1''$	$\lvert\psi_0\bar{\psi}_0\psi_1\bar{\psi}_1\psi_2\rvert$	5.34	6.54
(D_{5h})	$^2A_2''$	$\lvert\psi_0\bar{\psi}_1\psi_1\bar{\psi}_{-1}\psi_{-1}\rvert$	4.02	4.92
	$^2A_2''$	$(1/\sqrt{2})\{\lvert\psi_0\bar{\psi}_0\psi_1\bar{\psi}_1\psi_{-2}\rvert+\lvert\psi_0\bar{\psi}_0\psi_{-1}\bar{\psi}_{-1}\psi_2\rvert\}$	6.06	8.28
	$^2A_1''$	$(1/\sqrt{2})\{\lvert\psi_0\bar{\psi}_0\psi_1\bar{\psi}_1\psi_{-2}\rvert-\lvert\psi_0\bar{\psi}_0\psi_{-1}\bar{\psi}_{-1}\psi_2\rvert\}$	6.06	8.28
	$^2E_2''$	$(1/\sqrt{2})\{\lvert\psi_0\bar{\psi}_0\bar{\psi}_1\psi_{-1}\psi_2\rvert-\lvert\psi_0\bar{\psi}_0\psi_1\bar{\psi}_{-1}\psi_2\rvert\}$	7.22	10.75
	$^2E_2''$	$(\sqrt{2}/\sqrt{3})\lvert\psi_0\bar{\psi}_0\psi_1\bar{\psi}_{-1}\psi_2\rvert-(1/\sqrt{6})\lvert\psi_0\bar{\psi}_0\bar{\psi}_1\psi_{-1}\psi_2\rvert$ $-(1/\sqrt{6})\lvert\psi_0\bar{\psi}_0\psi_1\bar{\psi}_{-1}\psi_2\rvert$	5.79	8.16
	$^4E_2''$	$(1/\sqrt{3})\{\lvert\psi_0\bar{\psi}_0\bar{\psi}_1\psi_{-1}\psi_2\rvert+\lvert\psi_0\bar{\psi}_0\psi_1\bar{\psi}_{-1}\psi_2\rvert$ $+\lvert\psi_0\bar{\psi}_0\psi_1\psi_{-1}\bar{\psi}_2\rvert\}$	4.45	4.32
C_7H_7	$^2E_2''$	$\lvert\psi_0\bar{\psi}_0\psi_1\bar{\psi}_1\psi_{-1}\bar{\psi}_{-1}\psi_2\rvert$	0	0
	$^2E_2''$	$\lvert\psi_0\bar{\psi}_0\psi_1\bar{\psi}_1\psi_{-1}\bar{\psi}_2\psi_2\rvert$	4.04	4.28
	$^2E_2''$	$\lvert\psi_0\bar{\psi}_0\psi_1\bar{\psi}_1\psi_{-1}\bar{\psi}_{-1}\psi_3\rvert$	4.26	6.86
(D_{7h})	$^2E_2''$	$\lvert\psi_0\bar{\psi}_0\psi_1\bar{\psi}_{-1}\psi_{-1}\bar{\psi}_2\psi_2\rvert$	5.06	6.10
	$^2E_1''$	$(1/\sqrt{2})\{\lvert\psi_0\bar{\psi}_0\psi_1\bar{\psi}_1\bar{\psi}_{-1}\psi\,\psi_{-2}\rvert-\lvert\psi_0\bar{\psi}_0\psi_1\bar{\psi}_1\psi_{-1}\psi_2\bar{\psi}_{-2}\rvert\}$	6.36	8.76
	$^2E_1''$	$(\sqrt{2}/\sqrt{3})\lvert\psi_0\bar{\psi}_0\psi_1\bar{\psi}_1\psi_{-1}\bar{\psi}_2\psi_{-2}\rvert$ $-(1/\sqrt{6})\lvert\psi_0\bar{\psi}_0\psi_1\bar{\psi}_1\bar{\psi}_{-1}\psi\,\psi_{-2}\rvert$ $-(1/\sqrt{6})\lvert\psi_0\bar{\psi}_0\psi_1\bar{\psi}_1\psi_{-1}\psi_2\bar{\psi}_{-2}\rvert$	4.32	5.09
	$^4E_1''$	$(1/\sqrt{3})\{\lvert\psi_0\bar{\psi}_0\psi_1\bar{\psi}_1\bar{\psi}_{-1}\psi_2\psi_{-2}\rvert$ $+\lvert\psi_0\bar{\psi}_0\psi_1\bar{\psi}_1\psi_{-1}\bar{\psi}_2\psi_{-2}\rvert$ $+\lvert\psi_0\bar{\psi}_0\psi_1\bar{\psi}_1\psi_{-1}\psi_2\bar{\psi}_{-2}\rvert\}$	3.48	2.66

[a] Calculated by H. C. Longuet-Higgins and K. L. McEwen, reference 8.
[b] Calculated as described in this paper.

C_r and the penetration integrals $(p: qr)$. The calculations of the integrals C_r have already been given above. The numerical values of the penetration integrals, $(p: qq)$ and $(p: pr)$, are again taken from the tables of the paper of Parr and Crawford,[10] while the penetration integrals of the type $(p: qr)$ are approximated by a formula given by Huzinaga,[11] as follows:

$$(p: qr) = \tfrac{1}{8}S_{qr}\{(p: qq)+(p: ss)+(p: rr)\}, \quad (14)$$

while s lies at the midpoint of q and r.

[11] S. Huzinaga, J. Phys. Soc. Japan **13**, 1189 (1958).

CALCULATION OF ELECTRONIC SPECTRA

First we repeated the calculation of the energy levels of benzene using the method of Goeppert-Mayer and Sklar,[1] with inclusion of all the inter-electronic integrals. Next we calculated the observed values of the spectra of C_5H_5 and $C_7H_7^+$. The results are listed in Table I.

Longuet-Higgins and McEwen[8] calculated the electronic spectra of the cyclic polyenes, radicals, and ions, with 3 to 8 carbon atoms, using the semi-empirical theory of Pariser and Parr.[12]

[12] R. Pariser and R. G. Parr, J. Chem. Phys. **21**, 466, 568, 767 (1953).

TABLE IV. Electronic energy levels of diradicals of cyclic polyenes.

Diradical	Symmetry	Wave function	Energy (ev) Singlet [a]	Singlet [b]	Triplet [a]	Triplet [b]
C_4H_4	$^3A_{2g}$	$(1/\sqrt{2})\{\lvert\psi_0\bar{\psi}_0\psi_1\bar{\psi}_{-1}\rvert - \lvert\psi_0\bar{\psi}_0\psi_{-1}\bar{\psi}_1\rvert\}$			0	0
(D_{4h})	$^1B_{2g}$	$(1/\sqrt{2})\{\lvert\psi_0\bar{\psi}_0\psi_1\bar{\psi}_1\rvert - \lvert\psi_0\bar{\psi}_0\psi_{-1}\bar{\psi}_{-1}\rvert\}$	0	0		
	$^1A_{1g}$	$(1/\sqrt{2})\{\lvert\psi_0\bar{\psi}_0\psi_1\bar{\psi}_{-1}\rvert + \lvert\psi_0\bar{\psi}_0\psi_{-1}\bar{\psi}_1\rvert\}$	1.07	2.74		
	$^1B_{1g}$	$(1/\sqrt{2})\{\lvert\psi_0\bar{\psi}_0\psi_1\bar{\psi}_1\rvert + \lvert\psi_0\bar{\psi}_0\psi_{-1}\bar{\psi}_{-1}\rvert\}$	1.07	2.74		
	$^{1,3}E_u$	$\frac{1}{2}\{\lvert\psi_0\bar{\psi}_0\psi_{-1}\bar{\psi}_2\rvert + \lvert\psi_0\bar{\psi}_{-1}\psi_1\bar{\psi}_1\rvert \pm \lvert\psi_0\bar{\psi}_0\psi_2\bar{\psi}_{-1}\rvert \pm \lvert\psi_{-1}\bar{\psi}_0\psi_1\bar{\psi}_1\rvert\}$	5.86	7.97	5.86	7.96
		$\frac{1}{2}\{\lvert\psi_0\bar{\psi}_0\psi_{-1}\bar{\psi}_2\rvert - \lvert\psi_0\bar{\psi}_{-1}\psi_1\bar{\psi}_1\rvert \pm \lvert\psi_0\bar{\psi}_0\psi_2\bar{\psi}_{-1}\rvert \mp \lvert\psi_{-1}\bar{\psi}_0\psi_1\bar{\psi}_1\rvert\}$	8.03	13.49	3.70	2.45
$C_5H_5^+$	$^3A_2'$	$(1/\sqrt{2})\{\lvert\psi_0\bar{\psi}_0\psi_1\bar{\psi}_{-1}\rvert - \lvert\psi_0\bar{\psi}_0\psi_{-1}\bar{\psi}_1\rvert\}$			0	0
(D_{5h})	$^1E_2'$	$(1/\sqrt{2})\{\lvert\psi_0\bar{\psi}_0\psi_1\bar{\psi}_1\rvert \pm \lvert\psi_0\bar{\psi}_0\psi_{-1}\bar{\psi}_{-1}\rvert\}$	0.45	1.22		
	$^1A_1'$	$(1/\sqrt{2})\{\lvert\psi_0\bar{\psi}_0\psi_1\bar{\psi}_{-1}\rvert + \lvert\psi_0\bar{\psi}_0\psi_{-1}\bar{\psi}_1\rvert\}$	0.90	2.43		
	$^{1,3}E_1'$	$(1/\sqrt{2})\{\lvert\psi_0\bar{\psi}_0\psi_{-1}\bar{\psi}_2\rvert \pm \lvert\psi_0\bar{\psi}_0\psi_2\bar{\psi}_{-1}\rvert\}$	6.96	10.59	6.06	7.96
	$^{1,3}E_1'$	$(1/\sqrt{2})\{\lvert\psi_0\bar{\psi}_{-1}\psi_1\bar{\psi}_1\rvert \pm \lvert\psi_{-1}\bar{\psi}_0\psi_1\bar{\psi}_1\rvert\}$	5.63	8.78	3.30	3.49
	$^{1,3}E_2'$	$(1/\sqrt{2})\{\lvert\psi_0\bar{\psi}_0\psi_1\bar{\psi}_2\rvert \pm \lvert\psi_0\bar{\psi}_0\psi_2\bar{\psi}_1\rvert\}$	7.67	12.02	5.34	6.54
$C_7H_7^-$	$^3A_2'$	$(1/\sqrt{2})\{\lvert\psi_0\bar{\psi}_0\psi_1\bar{\psi}_{-1}\psi_{-1}\bar{\psi}_{-2}\rvert - \lvert\psi_0\bar{\psi}_0\psi_1\bar{\psi}_1\psi_{-1}\bar{\psi}_{-2}\rvert\}$			0	0
(D_{7h})	$^1E_2'$	$(1/\sqrt{2})\{\lvert\psi_0\bar{\psi}_0\psi_1\bar{\psi}_{-1}\psi_{-1}\bar{\psi}_2\rvert \pm \lvert\psi_0\bar{\psi}_0\psi_1\bar{\psi}_1\psi_{-1}\bar{\psi}_{-2}\rvert\}$	0.28	0.79		
	$^1A_1'$	$(1/\sqrt{2})\{\lvert\psi_0\bar{\psi}_0\psi_1\bar{\psi}_{-1}\psi_{-1}\bar{\psi}_2\rvert + \lvert\psi_0\bar{\psi}_0\psi_1\bar{\psi}_1\psi_{-1}\bar{\psi}_{-2}\rvert\}$	0.56	1.58		
	$^{1,3}E_1'$	$(1/\sqrt{2})\{\lvert\psi_0\bar{\psi}_0\psi_1\bar{\psi}_{-1}\psi_{-1}\bar{\psi}_2\rvert \pm \lvert\psi_0\bar{\psi}_0\psi_1\bar{\psi}_1\psi_{-1}\bar{\psi}_2\rvert\}$	5.02	8.93	4.05	6.38
		$(1/\sqrt{2})\{\lvert\psi_0\bar{\psi}_0\psi_1\bar{\psi}_{-2}\psi_{-1}\bar{\psi}_2\rvert \pm \lvert\psi_0\bar{\psi}_0\psi_{-2}\bar{\psi}_1\psi_{-1}\bar{\psi}_2\rvert\}$	5.62	7.75	5.06	6.10
	$^{1,3}E_2'$	$(1/\sqrt{2})\{\lvert\psi_0\bar{\psi}_0\psi_1\bar{\psi}_1\psi_{-1}\bar{\psi}_2\rvert \pm \lvert\psi_0\bar{\psi}_0\psi_1\bar{\psi}_{-1}\psi_2\rvert\}$	5.83	10.27	3.24	5.01
	$^{1,3}E_3'$	$(1/\sqrt{2})\{\lvert\psi_0\bar{\psi}_0\psi_1\bar{\psi}_{-1}\psi_{-2}\bar{\psi}_2\rvert \pm \lvert\psi_0\bar{\psi}_0\psi_1\bar{\psi}_{-1}\psi_2\bar{\psi}_{-2}\rvert\}$	6.64	9.57	4.05	4.28
C_8H_8	$^3A_{2g}$	$(1/\sqrt{2})\{\lvert\psi_0\bar{\psi}_0\psi_1\bar{\psi}_{-1}\psi_{-1}\bar{\psi}_{-2}\rvert - \lvert\psi_0\bar{\psi}_0\psi_1\bar{\psi}_1\psi_{-1}\bar{\psi}_{-2}\rvert\}$			0	0
(D_{8h})	$^1B_{2g}$	$(1/\sqrt{2})\{\lvert\psi_0\bar{\psi}_0\psi_1\bar{\psi}_{-1}\psi_{-1}\bar{\psi}_2\rvert - \lvert\psi_0\bar{\psi}_0\psi_1\bar{\psi}_1\psi_{-1}\bar{\psi}_{-2}\rvert\}$	0	0		
	$^1A_{1g}$	$(1/\sqrt{2})\{\lvert\psi_0\bar{\psi}_0\psi_1\bar{\psi}_{-1}\psi_{-1}\bar{\psi}_2\rvert + \lvert\psi_0\bar{\psi}_0\psi_1\bar{\psi}_1\psi_{-1}\bar{\psi}_{-2}\rvert\}$	0.43	1.23		
	$^1B_{1g}$	$(1/\sqrt{2})\{\lvert\psi_0\bar{\psi}_0\psi_1\bar{\psi}_{-1}\psi_{-1}\bar{\psi}_2\rvert + \lvert\psi_0\bar{\psi}_0\psi_1\bar{\psi}_1\psi_{-1}\bar{\psi}_{-2}\rvert\}$	0.43	1.23		
	$^{1,3}E_{1u}$	$\frac{1}{2}\{\lvert\psi_0\bar{\psi}_0\psi_1\bar{\psi}_{-2}\psi_{-1}\bar{\psi}_2\rvert + \lvert\psi_0\bar{\psi}_0\psi_1\bar{\psi}_{-1}\psi_{-1}\bar{\psi}_{-2}\rvert \pm \lvert\psi_0\bar{\psi}_0\psi_{-2}\bar{\psi}_1\psi_{-1}\bar{\psi}_2\rvert \pm \lvert\psi_0\bar{\psi}_0\psi_1\bar{\psi}_{-1}\psi_1\bar{\psi}_{-2}\rvert\}$	3.67	4.99	5.80	8.48
		$\frac{1}{2}\{\lvert\psi_0\bar{\psi}_0\psi_1\bar{\psi}_{-2}\psi_{-1}\bar{\psi}_2\rvert - \lvert\psi_0\bar{\psi}_0\psi_1\bar{\psi}_{-1}\psi_{-1}\bar{\psi}_{-2}\rvert \pm \lvert\psi_0\bar{\psi}_0\psi_{-2}\bar{\psi}_1\psi_{-1}\bar{\psi}_2\rvert \mp \lvert\psi_0\bar{\psi}_0\psi_1\bar{\psi}_{-1}\psi_1\bar{\psi}_{-2}\rvert\}$	6.37	10.50	3.09	3.33
	$^{1,3}E_{2u}$	$\frac{1}{2}\{\lvert\psi_0\bar{\psi}_0\psi_1\bar{\psi}_{-1}\psi_{-2}\bar{\psi}_2\rvert + \lvert\psi_0\bar{\psi}_0\psi_1\bar{\psi}_1\psi_{-1}\bar{\psi}_{-2}\rvert \pm \lvert\psi_0\bar{\psi}_0\psi_1\bar{\psi}_{-1}\psi_2\bar{\psi}_{-2}\rvert \pm \lvert\psi_0\bar{\psi}_0\psi_1\bar{\psi}_{-1}\psi_{-1}\bar{\psi}_{-2}\rvert\}$	5.80	8.49	3.67	6.74
		$\frac{1}{2}\{\lvert\psi_0\bar{\psi}_0\psi_1\bar{\psi}_{-1}\psi_{-2}\bar{\psi}_2\rvert - \lvert\psi_0\bar{\psi}_0\psi_1\bar{\psi}_1\psi_{-1}\bar{\psi}_{-2}\rvert \pm \lvert\psi_0\bar{\psi}_0\psi_1\bar{\psi}_{-1}\psi_2\bar{\psi}_{-2}\rvert \mp \lvert\psi_0\bar{\psi}_0\psi_1\bar{\psi}_{-1}\psi_{-1}\bar{\psi}_{-2}\rvert\}$	6.37	10.14	3.09	5.09

[a] Calculated by H. C. Longuet-Higgins and K. L. McEwen, reference 8.
[b] Calculated as described in this paper.

We repeated the calculations of the spectra of these compounds, but now with inclusion of all the interelectronic integrals, using the formulas of deHeer and Pauncz[8] as indicated above, no empirical data was used except the carbon-carbon distance.

In Tables II–IV, the results of the calculations of Longuet-Higgins and McEwen[8] and our own are listed. Qualitatively the energy levels calculated with both methods show the same trend. Whether finally the semiempirical theory of Pariser and Parr will also give the best agreement with the observed values, in this case, can only be settled when more experimental data are available.

THE JOURNAL OF CHEMICAL PHYSICS VOLUME 35, NUMBER 5 NOVEMBER, 1961

Low-Temperature Heat Capacities and Thermodynamic Functions of Some Platinum and Palladium Group Chalcogenides. I. Monochalcogenides; PtS, PtTe, and PdTe†

FREDRIK GRØNVOLD AND TORKILD THURMANN-MOE

Chemical Institute A, University of Oslo, Blindern, Norway

AND

EDGAR F. WESTRUM, JR., AND ELFREDA CHANG

Department of Chemistry, University of Michigan, Ann Arbor, Michigan

(Received February 16, 1961)

Heat capacities of platinum monosulfide, platinum monotelluride, and palladium monotelluride were measured in the range 5–350°K. They show the normal sigmoidal temperature dependence with no evidence of transitions or other anomalies. The derived heat-capacity equations were integrated. Values of heat capacities, entropy and enthalpy increments, and of the free-energy function are tabulated for selected temperatures. At 298.15°K, the third-law entropies are 13.16 cal gfw^{-1} $°K^{-1}$ for PtS, 19.41 cal gfw^{-1} $°K^{-1}$ for PtTe, and 21.42 cal gfw^{-1} $°K^{-1}$ for PdTe. The new data on PtS have been correlated with existing decomposition-pressure data to evaluate ΔHf, ΔFf, and ΔSf 298.15°K. Entropies for other platinum-metal monochalcogenides were estimated.

INTRODUCTION

THE present paper is concerned with sulfides, selenides, and tellurides of the platinum and palladium. For these chalcogenides, recently surveyed by Haraldsen,[1] no heat-capacity measurements have been reported. Such data are desirable, however, for evaluation of the entropies of the chalcogenides with a better precision than has been possible in the past, and to get an insight into the causes of variations in heat capacity with the nature of the compounding elements and the properties of the compound.

Excluding the oxides, no monochalcogenides are known with certainty for ruthenium, osmium, and iridium; for the remaining metals of the platinum and palladium groups, the following compounds with exact (or approximate) composition Me*X* have been found: Rh_9S_8 [cu, $a=9.9116$][2]; RhTe [hex B8, $a=3.99$, $c=5.66$][3]; PdS [tetr *B*34, $a=6.4287$, $c=6.6082$][4]; Pd_9Se_8 [cu, $a=10.6060$][2]; PdSe [tetr *B*34, $a=6.73$, $c=6.91$][5]; PdTe [hex *B*8, $a=4.1521$, $c=5.6719$][4]; PtS [tetr *B*, $a=3.4700$, $c=6.1096$][6]; $Pt_{10}Se_8$ [monocl, $a=6.5806$, $b=4.6248$, $c=11.145$, $\beta=78.40°$][6]; PtTe [orthorh, $a=6.6144$, $b=5.6360$, $c=11.865$].[6] The structures and lattice dimensions (*A*) have been included for each substance.

Three of these chalcogenides were chosen for the present investigation, PtS as representative for the tetragonal square-coordinated structures, PtTe for a low-symmetric structure, and PdTe for the NiAs (*B*8)-type structure. Their heat capacities were determined and the thermodynamic functions obtained. On the basis of these and other data, standard entropies of the remaining chalcogenides are estimated.

EXPERIMENTAL

Preparation of the Samples

The samples were prepared from high-purity elements. The platinum, which came from The Mond Nickel Company, Ltd., contained the following impurities (in ppm): Au (1), Fe (<10), (Pb <10), Pd (7), volatile material (90). The palladium, also from the same company, contained: Ag (30), Au (70), Fe (20), Pb (2), Pt (50), Rh (10), insoluble (principally SiO_2) (60), volatile material (120). Before use, both the palladium and platinum were degassed under high vacuum at 600°C for four hours. Sulfur *cryst. puriss.* from Schering-Kahlbaum A.G. was purified before use by techniques similar to those described by v. Wartenberg[7] and Skjerven.[8] The sulfur was first heated by means of a submerged heater with a surface temperature of about 800°C until the carbon deposition ceased; this required about three weeks. Thereafter, it was purified by fractional distillation.

The tellurium was a special product with a stated purity of 99.999% from the American Smelting and Refining Company, in which no impurities had been detected by spectrographic methods.

† This work was supported in part by the Division of Research of the U. S. Atomic Energy Commission.

[1] H. Haraldsen, Plenary Lecture, XVI. Congress of the IUPAC, Paris, 1957, reprinted in Experientia Supple. VII, 165 (1957), and Mémoires présentès à la Section de Chimie Minérale, SEDES, Paris, 1958.

[2] A. Kjekshus, Acta Chem. Scand. **14,** 1623 (1960).

[3] S. Geller, J. Am. Chem. Soc. **77,** 2641 (1955).

[4] F. Grønvold and E. Røst, Acta Chem. Scand. **10,** 1620 (1956).

[5] K. Schubert, H. Breimer, W. Burkhardt, E. Günzel, R. Haufler, H. L. Lukas, H. Vetter, J. Wegst, and M. Wilkens, Naturwissenschaften **44,** 229 (1957).

[6] F. Grønvold, H. Haraldsen, and A. Kjekshus, Acta Chem. Scand. **14,** 1879 (1960).

[7] H. v. Wartenberg, Z. anorg. u. allgem. Chem. **286,** 243 (1956).

[8] O. Skjerven, Z. anorg. u. allgem. Chem. **291,** 325 (1957).

TABLE I. Heat capacities of platinum and palladium monochalcogenides; in calories/(gram formula weight °K).

T, °K	C_p	T, °K	C_p	T, °K	C_p
PtS; gram formula weight = 227.16 g					
Series I		21.32	0.6224	174.93	8.177
54.00	3.074	23.11	0.7472	183.61	8.388
59.79	3.429	24.99	0.8861	192.20	8.645
65.98	3.783	27.16	1.055	201.20	8.849
73.12	4.152	29.67	1.259	210.37	9.033
80.35	4.511	32.54	1.494	219.30	9.220
87.24	4.843	35.75	1.755	228.33	9.384
94.52	5.175	39.16	2.026	237.28	9.550
		42.88	2.308	246.33	9.712
Series II		46.97	2.603	255.30	9.836
6.01	0.014	51.33	2.910	263.94	9.961
6.99	0.025			272.49	10.066
7.77	0.034	Series III		260.99	9.897
8.80	0.052	94.19	5.158	269.64	10.023
10.11	0.084	101.10	5.465	278.25	10.136
11.47	0.1188	108.84	5.805	286.91	10.248
12.74	0.1610	117.40	6.165	295.57	10.343
13.98	0.2091	125.65	6.499	304.40	10.442
15.32	0.2684	132.91	6.791	313.45	10.546
16.74	0.3408	141.06	7.093	322.60	10.610
18.22	0.4236	149.44	7.391	331.86	10.675
19.70	0.5143	157.89	7.676	341.21	10.755
		166.37	7.939	347.63	10.821
PtTe; gram formula weight = 322.70 g					
Series I		Series II		45.52	4.267
67.93	6.799			50.34	4.875
73.71	7.301	4.92	0.019	55.60	5.503
81.17	7.889	5.83	0.031	61.37	6.141
88.74	8.409	6.78	0.049	67.61	6.758
96.25	8.812	7.76	0.077		
103.91	9.173	7.67	0.076	Series III	
111.67	9.508	8.73	0.1178		
119.76	9.791	9.84	0.1751	261.12	11.725
128.22	10.054	10.83	0.2239	270.18	11.783
136.77	10.287	11.95	0.2857	279.15	11.826
142.66	10.433	13.19	0.3727		
151.34	10.599	14.46	0.4735	Series IV	
160.22	10.774	15.76	0.5841		
169.23	10.905	17.12	0.7091	259.71	11.740
178.35	11.034	18.64	0.8600	268.84	11.781
187.73	11.159	20.32	1.033	277.99	11.827
197.16	11.261	22.16	1.235	287.14	11.876
206.61	11.353	24.14	1.463	296.08	11.927
216.02	11.428	26.30	1.728	304.91	11.971
225.33	11.497	28.40	1.991	313.80	11.985
234.50	11.576	30.92	2.319	322.95	12.009
243.63	11.650	34.06	2.737	332.36	12.053
252.67	11.684	37.40	3.183	340.92	12.098
216.61	11.761	41.20	3.695	347.07	12.118
PdTe; gram formula weight = 234.01 g					
5.21	0.026	41.85	4.847	179.39	11.462
6.17	0.040	45.91	5.452	188.52	11.542
7.06	0.061	50.42	6.074	197.80	11.647
7.97	0.090	55.63	6.713	206.63	11.707
8.89	0.1333	57.71	6.962	215.90	11.778
9.82	0.1923	63.61	7.575	225.32	11.844
10.89	0.2492	70.56	8.162	234.65	11.902
12.14	0.3322	78.54	8.741	243.73	11.974
13.41	0.4429	86.71	9.251	252.83	12.019
14.68	0.5675	95.05	9.641	262.19	12.070
15.99	0.7111	103.27	9.963	258.23	12.027
17.42	0.8839	110.97	10.214	267.35	12.070
19.03	1.095	118.60	10.438	276.52	12.124
20.91	1.361	126.80	10.647	285.76	12.182
23.09	1.694	135.61	10.832	295.02	12.235
25.37	2.065	144.51	10.994	304.21	12.263
28.25	2.556	153.32	11.142	313.44	12.296
31.28	3.085	161.82	11.267	322.78	12.338
34.51	3.645	160.22	11.260	332.13	12.367
38.04	4.249	161.29	11.266	340.56	12.387
		170.34	11.374	347.12	12.414

Platinum monosulfide was synthesized in two steps. First, PtS_2 was prepared by heating appropriate amounts of the elements in an evacuated and sealed silica tube at 750°C for one day. The sintered product was crushed and then heated with stoichiometric amounts of finely divided platinum at 900°C for two days. The resulting dark-grey powder with a bluish cast was annealed at 500°C for two days and finally cooled to room temperature over a period of seven days.

Platinum monotelluride was prepared by allowing the elements to react at 1000°C for six hours, and then raising the temperature to 1200°C in order to melt the sample. After about one hour at this temperature, the furnace was shut off and the sample cooled to room temperature overnight. The melt was broken into flaky fragments with lead-grey metallic luster. These fragments were annealed at 500°C for seven days and slowly cooled to room temperature over another seven days.

Palladium monotelluride was prepared from stoichiometric amounts of palladium and tellurium heated in an evacuated and sealed silica tube to 800°C. It was kept in the molten state for about two hours and, after cooling, was broken into fragments of several millimeters in dimension with splendent pale-yellow metallic luster. After annealing for seven days at 500°C, the sample was cooled to room temperature over a period of two days.

X-ray photographs were taken of the samples in powder cameras of 11.46 cm diam utilizing asymmetric film mounting. The lattice constants corresponded, within the limits of experimental error, to those reported earlier for these compounds,[4,6] and no lines from foreign phases could be observed.

Cryostat and Calorimeter

The design and operation of the Mark I cryostat for low-temperature adiabatic calorimetry has been described.[9] A completely gold-plated copper calorimeter, W-7 (similar to W-5 in design except that the volume was only 40.33 cm³ and there were only four vanes) was employed. The same heater, thermometer, amount of indium-tin solder for sealing, and amount of Apiezon-T grease for thermal contact between the heater, thermometer, and calorimeter were used for all measurements. The capsule-type platinum resistance thermometer (laboratory designation A-3) was calibrated by the National Bureau of Standards, and the temperatures are believed to correspond with the thermodynamic scale within 0.03° from 10–90°K, and within 0.04° from 90–350°K. Below 10°K, a provisional scale for temperature was used. Calibrated instruments were used in the determination of all measured quantities.

[9] E. F. Westrum, Jr., and A. F. Beale, Jr. (to be published).

Procedure

The calorimeter was loaded with sample, evacuated, filled with gaseous helium at 8 cm Hg pressure at 26°C (to provide thermal contact between the calorimeter and sample), and sealed. After adjusting the weights of solder and grease used, it was placed in the cryostat. The weights of samples used were 172.448 g of PtS, 196.792 g of PtTe, and 179.866 g of PdTe.

COMPUTATION AND RESULTS

The experimental heat capacity results for the three chalcogenide samples are presented in Table I in chronological order, so that temperature increments for individual determinations may be inferred from adjacent temperatures. The values are expressed in terms of the defined thermochemical calorie, equal to 4.1840 abs j. The ice point is taken as 273.15°K and the gram formula weights of PtS, PtTe, and PdTe as 227.16, 322.70, and 234.01 g, respectively. The densities are found to be 10.09 g cm^{-3} for PtS, 12.01 g cm^{-3} for PtTe (both by pycnometric measurement[6]), and 9.186 g cm^{-3} for PdTe (from x-ray diffraction data).

The heat capacity of the calorimeter, separately determined, represents a maximum at 350°K of 40%, and 34% of the total heat capacities measured when filled with the PtTe and PdTe samples, respectively. The minimum contribution of the empty calorimeter occurs at 10°K, where it represents 14% of the total heat capacity for both compounds. At 6°K, it represents 20% of the total. The contribution for the PtS sample reaches a maximum of 43% at 90°K and a minimum of 23% at 14°K. At 6°K, the value is 30%; and at 350°K, it is 37% of the total heat capacity.

An analytically generated "curvature" correction for the finite temperature increments of the measurements is added to each of the observed values of $\Delta H/\Delta T$. The derivatives (dH/dT) resulting from this correction are equal to C_p (or to C_{sat}) within the limits of experimental error.

The heat capacity vs temperature curve in Fig. 1 is of the usual sigmoid shape with no anomalous departures. Above 30°K, most of the points in Table I deviate from a smooth curve, discussed below, by less than 0.007 cal mole^{-1}. Below 30°K, the deviations become larger due to the smaller absolute heat capacity, the smaller temperature intervals of measurement, and the decreased sensitivity of the thermometer.

The values of C_p, $S°-S_0°$, $H°-H_0°$, and $-(F°-H_0°)/T$ at selected temperatures are given in Table II. The estimated probable error in these functions is less than 0.1% above 100°K. To make the table internally consistent, an additional figure is given over that justified by experimental accuracy. An IBM 704 digital computer was used to generate a least-squares polynomial in temperature from the curvature-corrected heat-capacity data for the region above 25°K and compared with a large-scale plot of the molal heat-capacity vs temperature for the experimental points.

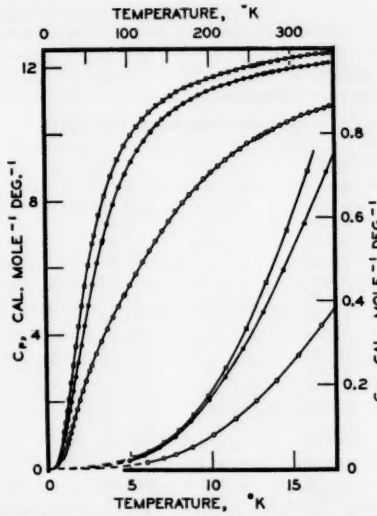

FIG. 1. Heat capacities of the monochalcogenides on a gram formula weight basis: ○ represents PtS, ● represents PtTe, and □ represents PdTe.

The values of the heat capacity presented in Table II are read from the plot below 25°K. Above this temperature, values from both the plot and the smooth polynomial curve are identical. Extrapolation is made with a Debye T^3 function below 6°K. Integration of the experimental C_p data was used to derive the entropy and enthalpy values. The free-energy function is computed from these results.

DISCUSSION

The only compound for which some comparison of thermodynamic data can be made is PtS. On the basis of decomposition-pressure measurements by Biltz and Juza[10] in the PtS/Pt range at the temperatures 1060, 1110, and 1186°C, Kelley[11] calculated the standard value of the entropy of PtS at 298°K to be $S°=12.2$ cal gfw^{-1} °K^{-1}. This was done before heat-capacity data on PtS existed, and the heat-capacity equation assumed by Kelley $C_p=11.14+2.86\times10^{-3}T$ cal gfw^{-1} °K^{-1} (298–1000°K), resulted in an entropy value in fair accord with that determined in this research: $S°=13.16$ cal gfw^{-1} °K^{-1}.

Since it should now be possible to deduce a better high-temperature heat-capacity temperature relationship for PtS, and also because Biltz and Juza appear to have included some questionable values in the low sulfur region (those for $PtS_{0.02}$, $PtS_{0.06}$, and $PtS_{0.07}$) in their average values, a new calculation of the thermodynamic functions was performed.

[10] W. Biltz and R. Juza, Z. anorg. u. allgem. Chem. **190**, 161 (1930).

[11] K. K. Kelley, "Contributions to the data on theoretical metallurgy. VII.," U. S. Bureau of Mines Bulletin 406, Washington, D. C. (1937); cf. K. K. Kelley, "Contributions to the data on theoretical metallurgy. XI.," U. S. Bureau of Mines Bulletin 477, Washington, D. C. (1950).

TABLE II. Thermodynamic properties of platinum and palladium monochalcogenides.

T, °K	C_p cal/gfw °K	$S°-S_0°$ cal/gfw °K	$H°-H_0°$ cal/gfw	$-(F°-H_0°)/T$ cal/gfw °K
PtS; gram formula weight = 227.16 g				
5	0.008	(0.003)	(0.010)	(0.001)
10	0.077	0.024	0.185	0.006
15	0.253	0.085	0.968	0.020
20	0.533	0.194	2.90	0.050
25	0.888	0.350	6.43	0.093
30	1.286	0.547	11.85	0.152
35	1.694	0.776	19.30	0.224
40	2.091	1.028	28.76	0.309
45	2.464	1.296	40.15	0.404
50	2.814	1.574	53.36	0.507
60	3.444	2.144	84.73	0.732
70	3.993	2.717	121.97	0.975
80	4.494	3.284	164.46	1.228
90	4.969	3.841	211.79	1.487
100	5.417	4.387	263.72	1.750
110	5.852	4.924	320.09	2.014
120	6.272	5.452	380.74	2.279
130	6.675	5.970	445.51	2.543
140	7.055	6.479	514.2	2.806
150	7.410	6.978	586.5	3.067
160	7.742	7.467	662.3	3.327
170	8.045	7.945	741.3	3.585
180	8.324	8.413	823.1	3.840
190	8.585	8.870	907.7	4.093
200	8.820	9.316	994.7	4.343
210	9.034	0.752	1083.9	4.590
220	9.231	10.177	1175.3	4.834
230	9.419	10.592	1268.6	5.076
240	0.597	10.996	1363.7	5.314
250	9.761	11.391	1460.5	5.549
260	9.907	11.777	1558.8	5.781
270	10.04	12.153	1658.5	6.011
280	10.16	12.520	1759.5	6.236
290	10.28	12.879	1861.7	6.459
300	10.39	13.230	1965.1	6.679
350	10.81	14.867	2496.4	7.734
273.15	10.07	12.27	1690	6.08
298.15	10.37	13.16	1946	6.64
PtTe; gram formula weight = 322.70 g				
5	(0.020)	(0.007)	(0.025)	(0.002)
10	0.170	0.055	0.416	0.013
15	0.518	0.184	2.07	0.046
20	1.002	0.397	5.82	0.106
25	1.566	0.679	12.20	0.191
30	2.198	1.020	21.60	0.300
35	2.861	1.408	34.24	0.430
40	3.534	1.835	50.24	0.579
45	4.197	2.290	69.58	0.743
50	4.833	2.765	92.17	0.922
60	5.995	3.751	146.43	1.311
70	6.983	4.751	211.45	1.731
80	7.802	5.739	285.52	2.170
90	8.472	6.698	367.00	2.620
100	9.009	7.619	454.69	3.075
110	9.445	8.499	546.8	3.528
120	9.802	9.337	643.2	3.977
130	10.11	10.134	742.8	4.421
140	10.36	10.893	845.1	4.856

T, °K	C_p cal/gfw °K	$S°-S_0°$ cal/gfw °K	$H°-H_0°$ cal/gfw	$-(F°-H_0°)/T$ cal/gfw °K
PtTe; gram formula weight = 322.70 g				
150	10.58	11.615	949.8	5.283
160	10.77	12.304	1056.6	5.700
170	10.92	12.962	1165.1	6.108
180	11.06	13.590	1275.1	6.507
190	11.19	14.192	1386.3	6.895
200	11.29	14.768	1498.7	7.275
210	11.38	15.321	1612.1	7.645
220	11.46	15.853	1726.3	8.006
230	11.54	16.364	1841.3	8.358
240	11.61	16.856	1957.0	8.702
250	11.67	17.331	2073.4	9.038
260	11.73	17.790	2190.4	9.366
270	11.79	18.234	2308.0	9.686
280	11.85	18.664	2426.2	9.999
290	11.90	19.081	2544.9	10.305
300	11.94	19.485	2664.1	10.604
350	12.14	21.338	3265.5	12.008
273.15	11.81	18.37	2345	9.78
298.15	11.93	19.41	2642	10.55
PdTe; gram formula weight = 234.01 g				
5	(0.024)	(0.008)	(0.030)	(0.002)
10	0.184	0.060	0.451	0.015
15	0.602	0.205	2.31	0.051
20	1.230	0.460	6.82	0.119
25	2.004	0.816	14.85	0.221
30	2.862	1.257	27.01	0.356
35	3.728	1.763	43.49	0.520
40	4.559	2.315	64.21	0.710
45	5.321	2.896	88.93	0.920
50	6.019	3.494	117.33	1.148
60	7.209	4.701	183.70	1.639
70	8.120	5.884	260.56	2.162
80	8.841	7.018	345.57	2.698
90	9.410	8.093	436.89	3.239
100	9.842	9.107	533.2	3.775
110	10.19	10.062	633.4	4.304
120	10.48	10.962	736.8	4.822
130	10.72	11.810	842.8	5.327
140	10.92	12.612	951.1	5.819
150	11.09	13.371	1061.1	6.297
160	11.24	14.092	1172.8	6.762
170	11.37	14.777	1285.8	7.214
180	11.47	15.430	1400.0	7.652
190	11.57	16.053	1515.2	8.078
200	11.66	16.648	1631.4	8.492
210	11.73	17.219	1748.3	8.894
220	11.81	17.767	1866.0	9.285
230	11.87	18.293	1984.5	9.665
240	11.94	18.800	2103.5	10.035
250	12.00	19.288	2223.2	10.396
260	12.06	19.760	2343.5	10.747
270	12.11	20.216	2464.4	11.089
280	12.16	20.658	2585.7	11.423
290	12.20	21.085	2707.5	11.749
300	12.24	21.499	2829.7	12.067
350	12.42	23.401	3446.6	13.553
273.15	12.12	20.36	2502	11.20
298.15	12.23	21.42	2807	12.01

In the absence of any high-temperature enthalpy data on PtS, we will assume the same heat capacity at 1000°K as Kelley did ($C_p = 14$ cal gfw^{-1} °K^{-1}) and construct a heat capacity curve which, in addition, goes through our points at 300 and 350°K and obeys the Maier and Kelley[12] relationship $C_p = A + BT + CT^{-2}$. For the reaction considered,

$$2\ \mathrm{PtS(s)} = 2\ \mathrm{Pt(s)} + \mathrm{S_2(g)},$$

[12] C. G. Maier and K. K. Kelley, J. Am. Chem. Soc. **54**, 3243 (1932).

the following heat-capacity equations (in cal gfw^{-1} °K^{-1}) are chosen:

$$\text{PtS(s)},\ C_p=9.97+4.11\times10^{-3}T-0.73\times10^{5}T^{-2},$$

$$\text{Pt(s)},^{13}\ C_p=5.81+1.26\times10^{-3}T+0.06\times10^{5}T^{-2},$$

$$\text{S}_2\text{(g)},^{13}\ C_p=8.72+0.16\times10^{-3}T-0.90\times10^{5}T^{-2}.$$

Thus,

$$\Delta C_p=0.40-5.54\times10^{-3}T+0.68\times10^{5}T^{-2},$$

$$\Delta H_T^\circ=\Delta H_0+0.40T-2.77\times10^{-3}T^2-0.68\times10^{5}T^{-1},$$

$$\Delta F_T^\circ=-RT\ \ln K=\Delta H_0-0.40T\ \ln T+2.77\times10^{-3}T^2-0.34\times10^{5}T^{-1}+IT,$$

and

$$(\Delta H_0/T)+I=-4.57\ \log p_{S_2}+0.92\ \log T-2.77\times10^{-3}T+0.34\times10^{5}T^{-2}.$$

The results of the calculations (and plot of $[\Delta H_0/T]+I$ vs $1/T$) are given in Table III. Using these values, enthalpy, free energy, and entropy data for the decomposition of PtS can be calculated, the latter by the equation

$$\Delta S_T^\circ=(\Delta H_T^\circ-\Delta F_T^\circ)/T=0.40+0.92\ \log T-5.54\times10^{-3}T-0.34\times10^{5}T^{-2}-I.$$

At 298.15°K, the actual values are

$$\Delta H^\circ=70.2\text{ kcal},\ \Delta F^\circ=55.7\text{ kcal},\ \Delta S^\circ=48.3\text{ cal °K}^{-1}.$$

Taking the orthorhombic crystalline phase instead of the diatomic gas for the standard state of sulfur and incorporating the entropies of the elements,[14] the following values for the standard heat of formation, free energy of formation, and entropy of PtS are found at 298.15°K:

$$\text{Pt(s)}+\text{S(rh)}=\text{PtS(s)},$$

$$\Delta Hf^\circ=-19.7\text{ kcal},\quad \Delta Ff^\circ=-18.3\text{ kcal},$$

$$S^\circ=13.1\text{ cal °K}^{-1}.$$

The enthalpy and free energy values are in good agreement with those of Kelley[11] ($\Delta Hf^\circ=-20.18$ kcal, $\Delta Ff^\circ=-18.55$ kcal). The enthalpy is somewhat higher than another estimate[15] ($\Delta Hf^\circ=-20.8$ kcal). Biltz and Juza's own estimate[10] is apparently too high ($\Delta Hf^\circ=-16$ kcal). The entropy is higher than that of Kelley[11] but agrees almost exactly with that from the low-temperature heat-capacity data of this work. On the basis of the solubility product of PtS and other data, Zhuk[16] has reported $\Delta F_{298}^\circ=-17.36$ kcal and $S_{298}^\circ=6.2$ cal gfw^{-1} °K^{-1}. The free energy of formation of PtS from Pt and S_2 gas at high temperatures has been reevaluated from Biltz and Juza's data[10] by Richardson and Jeffes.[17] The equation reported, $\Delta F_T^\circ=-66.100+43.6T$ (1000–1700°K), agrees reasonably well with ours over the common range.

TABLE III. Data for the reaction 2 PtS(s) = 2 Pt(s) + S_2(g).[a]

T, °K	p_{S_2}, atm	$(\Delta H_0/T)+I$	$\Delta H_0/T$
1333	0.047	5.27	52.89
1383	0.124	3.23	50.98
1459	0.409	0.67	48.32

[a] In col. 3, $\Delta H_0=70\,500$; $I_{mean}=47.67$.

For the other monochalcogenides, no published data exist, and standard entropies are estimated for the compounds mentioned in the introduction. Measured values of the entropies of chalcogenides may be well represented by simple additivity of a chalcogen and a metal contribution. Justification will be presented in a forthcoming paper.[18] The values chosen are [in cal (g atom °K)$^{-1}$]: 10.5 for the metal (Me^{2+}), 3.0 for S^{2-}, 7.0 for Se^{2-}, and 9.5 for Te^{2-}. The estimated values are: 1/9 Rh_9S_8, 13.2; RhTe, 20.0; PdS, 13.5; 1/9 Pd_9Se_8, 16.7; PdSe, 17.5; PdTe, 20.0; PtS, 13.5; 1/10 $Pt_{10}Se_8$, 16.1; PtTe, 20.0. These values are probably reliable to better than 0.8 cal (g atom °K)$^{-1}$.

ACKNOWLEDGMENTS

The authors wish to thank The International Nickel Company (Mond), Limited, for the loan of substantial amounts of platinum and palladium to make this study possible. The assistance of Arne Kjekshus in preparing the platinum chalcogenides, and the cooperation of Shu-Sing Chang, Bruce H. Justice, and H. Gary Carlson with the heat-capacity measurements and calculations is thankfully recognized. Fredrik Grønvold expresses his appreciation to Norges Almenvitenskapelige Forskningsråd for assistance. The partial support of the Division of Research of the U. S. Atomic Energy Commission is gratefully acknowledged.

[13] K. K. Kelley, "Contributions to the data on theoretical metallurgy. XIII.," U. S. Bureau of Mines Bulletin 584, Washington, D. C. (1960).

[14] D. R. Stull and G. C. Sinke, "Thermodynamic properties of the elements," Advances in Chem. Ser. No. 18, Washington, D. C. (1956).

[15] "Selected values of chemical thermodynamic properties," Circular 500, National Bureau of Standards, Washington, D. C. 1952.

[16] N. P. Zhuk, Zhur. Fiz. Khim. **28**, 1523 (1954).

[17] F. D. Richardson and J. H. E. Jeffes, J. Iron Steel Inst. (London) **171**, 165 (1952).

[18] F. Gronvold and E. F. Westrum, Jr. (to be published).

Low-Temperature Heat Capacities and Thermodynamic Functions of Some Palladium and Platinum Group Chalcogenides. II. Dichalcogenides; PtS_2, $PtTe_2$, and $PdTe_2$†

EDGAR F. WESTRUM, JR., AND H. GARY CARLSON
Department of Chemistry, University of Michigan, Ann Arbor, Michigan
AND
FREDRIK GRØNVOLD AND ARNE KJEKSHUS
Chemical Institute A, University of Oslo, Blindern, Norway

(Received April 5, 1961)

Heat capacities of platinum disulfide, platinum ditelluride, and palladium ditelluride were measured in the range 5° to 350°K. They show the normal sigmoidal temperature dependence with no evidence of transitions or other anomalies. The derived heat capacity equations were integrated. Values of C_p, $S°-S_0°$, $H°-H_0°$, and $-(F°-H_0°)/T$ are tabulated for selected temperatures. At 298.15°K the entropies are 17.85 cal gfw^{-1} °K^{-1} for PtS_2, 28.92 cal gfw^{-1} °K^{-1} for $PtTe_2$ and 30.25 cal gfw^{-1} °K^{-1} for $PdTe_2$. Thermodynamic values have been estimated for other dichalcogenides and related chalcogenides of the platinum group metals.

INTRODUCTION

As indicated in the first part of this study,[1] no heat-capacity data have been reported on the chalcogenides of the platinum metals, despite the fact that such compounds exist in great number. Dichalcogenides are especially common (except among the oxides), and the majority of them have either pyrite ($C2$)-type structure or cadmium hydroxide ($C6$)-type structure. For a survey of the transition-metal chalcogenides, see Haraldsen.[2] The cubic pyrite-type structure is found for RuS_2(a=5.6090 A),[3] $RuSe_2$(a=5.933),[4] $RuTe_2$(a=6.377),[5] OsS_2(a=5.6192),[3] $OsSe_2$(a=5.945),[4] $OsTe_2$(a=6.3985),[5] and ~$RhSe_2$(a=6.002).[6] In addition, there are pyrite-like structures with more metal deficit than ~$RhSe_2$ (the ~ indicates approximate composition). They are found for ~$RhS_{2.3}$(a=5.58),[7] ~$RhSe_{2.5}$(a=5.985),[6] ~$RhTe_{2.4}$(a=6.439),[7] $IrS_{2.67}$(a=5.589),[8] $IrSe_{3.0}$(a=5.9293),[8] and $IrTe_{2.67}$(a=6.393).[9] The hexagonal cadmium hydroxide-type structure is found for $RhTe_2$(a=3.92, c=5.41),[10] $IrTe_2$(a=3.930, c=6.414),[9] $PdTe_2$(a=4.0365, c=5.1262),[11] PtS_2(a=3.5432, c=5.0388),[12] $PtSe_2$(a=3.7278, c=5.0813),[12] and $PtTe_2$(a=4.0259, c=5.2209).[12] Orthorhombic structures have been found for PdS_2(a=5.460, b=5.541, c=7.531) and $PdSe_2$(a=5.741, b=5.866, c=7.691) that might be considered to be deformed pyrite-like structures, with S_2^{2-} (Se_2^{2-}) groups, but with square instead of octahedral coordination around the metal atoms.[13] Another orthorhombic structure has been found for ~$IrSe_2$(a=20.94, b=5.93, c=3.74),[14] for which only half of the nonmetal atoms are bonded as pairs. Iridium might accordingly be looked upon as trivalent. There are indications that ~IrS_2[8] and Rh_8S_{15}[7] have related structures.

Among this multitude of dichalcogenides three have been chosen for the present study: PtS_2, $PtTe_2$, and $PdTe_2$. These have structures of the cadmium hydroxide-type, and might thus most clearly show the influence of atomic mass on heat-capacity behavior and entropy of the platinum group dichalcogenides. By using the information obtained and other available data, entropy estimates have been made for other dichalcogenides and related chalcogenides of the platinum and palladium groups.

EXPERIMENTAL

Preparation of the Samples

The samples were prepared from the same high-purity elements as the monochalcogenides.[1] Platinum disulfide was synthesized from stoichiometric amounts of the elements in an evacuated and sealed silica tube by heating to 750°C for one day. The sulfide was then in the form of a black powder and was annealed at 500°C for seven days and afterward slowly cooled to room temperature over another seven days.

Platinum ditelluride was prepared by reacting the elements at 1000°C for 5 hr. The grey powder thus obtained was annealed at 500°C for seven days and cooled to room temperature over seven more days.

Palladium ditelluride was prepared by heating a mixture of the elements to 800°C where it was kept

† This work was supported in part by the Division of Research of the U. S. Atomic Energy Commission.

[1] F. Grønvold, T. Thurmann-Moe, E. F. Westrum, Jr., and E. Chang, J. Chem. Phys. **35,** 1665 (1961).

[2] H. Haraldsen, Plenary Lecture, XVI Congress of the IUPAC, Paris, 1957, reprinted in Experientia Supplementum VII (Birkhaüser-Verlag, Basel, Switzerland, 1958), and Mémoires présentés à la Section de Chimie Minérale, SEDES, Paris, 1958.

[3] F. Grønvold and J. Krause (unpublished data).

[4] L. Thomassen, Z. physik. Chem. **B2,** 349 (1929).

[5] W. O. J. Groeneveld Meijer, Am. Mineralogist **40,** 646 (1955).

[6] S. Geller and B. B. Cetlin, Acta Cryst. **8,** 272 (1955).

[7] Ø. Steen, thesis, University of Oslo, Norway, 1955.

[8] L. Søvold, thesis, University of Oslo, Norway, 1954.

[9] E. F. Hockings and J. G. White, J. Phys. Chem. **64,** 1042 (1960).

[10] S. Geller, J. Am. Chem. Soc. **77,** 2641 (1955).

[11] F. Grønvold and E. Røst, Acta Chem. Scand. **10,** 1620 (1956).

[12] F. Grønvold, H. Haraldsen, and A. Kjekshus, Acta Chem. Scand. **14,** 1879 (1960).

[13] F. Grønvold and E. Røst, Acta Cryst. **10,** 329 (1957).

[14] L. B. Barricelli, Acta Cryst. **11,** 75 (1958).

TABLE I. Heat capacities of platinum and palladium dichalcogenides; in calories/(gram formula weight °K).

T, °K	C_p	T, °K	C_p	T, °K	C_p	T, °K	C_p	T, °K	C_p	T, °K	C_p
PtS_2; gram formula weight = 259.22 g											
Series I		193.23	13.108	339.37	16.31	12.38	0.209	11.26	0.165	59.20	3.531
		202.13	13.416	347.31	16.40	13.68	0.269	12.37	0.206	64.36	3.962
78.16	5.139	211.12	13.748			15.06	0.328	13.65	0.267	70.93	4.512
84.65	5.758	220.12	14.028	Series II		16.52	0.394	19.12	0.528	78.52	5.187
91.96	6.418	229.28	14.298			18.11	0.475	20.79	0.625	86.06	5.886
99.50	7.089	238.66	14.547	51.46	2.912	19.89	0.572	22.97	0.766	98.86	6.628
107.27	7.750	247.99	14.783	55.22	3.205	21.90	0.693	25.28	0.920		
115.89	8.474	257.14	15.00	58.99	3.479			27.84	1.102	Series V	
124.78	9.200	266.19	15.15	63.28	3.859	Series IV		30.54	1.301		
133.27	9.838	275.17	15.29	68.26	4.275			33.45	1.522	262.55	15.12
142.09	10.446	284.07	15.50	73.24	4.696	5.42	0.009	36.68	1.769	262.07	14.99
151.26	11.026	292.96	15.66			6.33	0.028	40.14	2.043	271.08	15.17
160.30	11.545	301.95	15.81	Series III		7.53	0.045	44.80	2.401	280.06	15.45
165.57	11.816	311.11	15.96			8.61	0.075	49.56	2.772		
174.98	12.297	320.57	16.06	10.17	0.132	9.42	0.106	54.33	3.144		
184.41	12.730	330.17	16.17	11.21	0.164	10.30	0.140	54.28	3.134		
$PtTe_2$; gram formula weight = 450.31 g											
Series I		143.70	15.82	12.13	0.340	38.92	4.858	167.91	16.49	260.07	17.74
		161.41	16.31	13.50	0.439	42.90	5.701	161.51	16.34	266.80	17.78
64.49	9.744			14.92	0.577	47.14	6.589	170.18	16.52	275.73	17.86
70.99	10.691	Series II		16.36	0.738	51.80	7.512	178.89	16.70	283.06	17.92
77.99	11.569			17.90	0.927	57.10	8.505	187.73	16.86	291.97	18.00
85.00	12.369	5.37	0.024	19.62	1.161	63.45	9.595	196.44	17.00	301.00	18.05
92.84	13.092	6.57	0.047	21.51	1.445	70.39	10.611	205.12	17.11	310.14	18.12
101.23	13.724	7.48	0.071	23.64	1.788			213.88	17.25	319.43	18.17
109.34	14.259	8.22	0.103	26.14	2.228	Series III		222.94	17.36	328.74	18.24
117.58	14.722	9.02	0.137	28.96	2.764			232.31	17.45	337.87	18.28
126.02	15.14	9.89	0.187	32.08	3.396	150.33	16.02	241.69	17.60	346.72	18.32
134.67	15.49	10.89	0.243	35.35	4.079	159.11	16.28	250.92	17.66		
$PdTe_2$; gram formula weight = 361.62 g											
Series I		182.89	17.03	282.61	18.20	7.13	0.059	21.00	1.648	60.26	9.743
		192.27	17.16	291.69	18.28	8.07	0.093	23.06	2.069	65.95	10.616
106.97	14.452	201.40	17.31	300.74	18.34	9.07	0.1403	25.40	2.570	72.16	11.417
115.44	14.922	210.33	17.44	309.84	18.40	10.14	0.2053	28.00	3.155	79.21	12.237
123.62	15.34	210.19	17.44	391.07	18.42	11.32	0.2769	28.64	3.299	86.75	12.997
131.64	15.66	219.26	17.57	328.32	18.52	12.53	0.3757	31.23	3.897	94.35	13.615
139.67	15.95	228.28	17.67	337.48	18.59	13.73	0.5039	34.08	4.555	102.14	14.144
147.95	16.22	237.29	17.77	346.37	18.64	13.59	0.4878	37.24	5.286		
156.84	16.45	247.17	17.88	Series II		14.81	0.6296	40.93	6.102		
166.07	16.69	255.19	17.96			16.13	0.8116	45.18	7.000		
175.21	16.88	264.33	18.02	5.42	0.023	17.55	1.026	49.96	7.949		
173.55	16.82	273.44	18.07	6.30	0.042	19.15	1.306	54.99	8.869		

molten for about 2 hr. After cooling the sample was fragmented to tin-white metallic, molybdenite-like scales. The sample was sealed into a new silica tube, annealed at 500°C for seven days and cooled to room temperature over a period of two days.

X-ray powder photographs were taken of the samples in cameras with 11.46 cm diam and asymmetric film mounting. The lattice constants corresponded within the limits of experimental error to those reported earlier for these compounds,[11,12] and no lines from foreign phases could be observed.

Calorimetric Procedure

The Mark I cryostat and its operation for low-temperature calorimetric measurements[15] and calorimeter of laboratory designation W-9[16] have been described previously. Only $PtTe_2$ was determined in calorimeter W-7.[1]

The platinum resistance thermometer (laboratory designation A-3) used in these measurements was calibrated by the National Bureau of Standards from 10° to above 373°K. Below 10°K a provisional scale for temperature was generated. The thermometer is considered to reproduce the thermodynamic scale within 0.1° from 4° to 10°K, 0.03° from 10° to 90°K, and within 0.04° above 90°K. Sample weights of 155.969 g of PtS_2, 197.380 g of $PtTe_2$, and 253.471 g of $PdTe_2$ were used. Helium gas at 8 cm Hg pressure and 26°C was added in the sample space for thermal

[15] E. F. Westrum, Jr., and A. F. Beale, Jr. (to be published).

[16] E. Greenberg and E. F. Westrum, Jr., J. Am. Chem. Soc. **78**, 4526 (1956).

TABLE II. Thermodynamic properties of platinum and palladium dichalcogenides.

T, °K	C_p (cal/gfw °K)	$S°-S_0°$ (cal/gfw °K)	$H°-H_0°$ (cal/gfw)	$-(F°-H_0°)/T$ (cal/gfw °K)
PtS$_2$; gram formula weight = 259.22 g				
5	0.013	0.004	0.016	0.001
10	0.120	0.038	0.291	0.009
15	0.325	0.124	1.38	0.032
20	0.577	0.250	3.61	0.069
25	0.900	0.413	7.29	0.122
30	1.260	0.608	12.66	0.186
35	1.642	0.831	19.93	0.262
40	2.031	1.076	29.13	0.348
45	2.416	1.338	40.25	0.443
50	2.800	1.612	53.29	0.547
60	3.593	2.192	85.20	0.772
70	4.426	2.808	125.26	1.018
80	5.321	3.457	173.99	1.282
90	6.238	4.136	231.75	1.561
100	7.132	4.840	298.58	1.854
110	7.987	5.561	374.28	2.158
120	8.819	6.292	458.45	2.472
130	9.593	7.029	550.6	2.794
140	10.30	7.766	650.1	3.123
150	10.95	8.499	756.3	3.457
160	11.53	9.224	868.7	3.795
170	12.05	9.940	986.7	4.135
180	12.53	10.642	1109.7	4.477
190	12.97	11.332	1237.2	4.820
200	13.36	12.007	1368.9	5.163
210	13.71	12.668	1504.3	5.504
220	14.03	13.313	1643.0	5.845
230	14.32	13.943	1784.8	6.183
240	14.58	14.558	1929.4	6.519
250	14.82	15.159	2076.4	6.853
260	15.03	15.744	2225.6	7.184
270	15.22	16.315	2376.9	7.511
280	15.42	16.872	2530.2	7.836
290	15.61	17.417	2685.4	8.157
300	15.78	17.949	2842.3	8.474
350	16.43	20.432	3648.2	10.009
273.15	15.29	16.49	2425	7.61
298.15	15.75	17.85	2813	8.42
PtTe$_2$; gram formula weight = 450.31 g				
5	(0.019)	(0.006)	(0.024)	(0.001)
10	0.184	0.057	0.439	0.013
15	0.587	0.199	2.25	0.049
20	1.215	0.449	6.67	0.116
25	2.019	0.804	14.70	0.216
30	2.970	1.254	27.11	0.350
35	4.007	1.789	44.54	0.516
40	5.087	2.395	67.29	0.713
45	6.147	3.055	95.39	0.936
50	7.162	3.756	128.69	1.182
60	9.014	5.230	209.79	1.733
70	10.56	6.739	307.88	2.341
80	11.82	8.234	420.00	2.984
90	12.84	9.687	543.4	3.649
100	13.64	11.082	676.0	4.323
110	14.30	12.415	815.8	4.998
120	14.85	13.684	961.7	5.670
130	15.31	14.891	1112.6	6.333
140	15.69	16.040	1267.6	6.986
150	16.01	17.134	1426.2	7.626
160	16.29	18.176	1587.7	8.253
170	16.52	19.171	1751.8	8.866
180	16.72	20.121	1918.1	9.465
190	16.90	21.030	2086.2	10.050
200	17.05	21.901	2256.0	10.621
210	17.19	22.737	2427.2	11.178
220	17.32	23.539	2599.8	11.722
230	17.44	24.312	2773.6	12.253
240	17.55	25.056	2948.5	12.771
250	17.65	25.775	3124.5	13.277
260	17.74	26.469	3301.5	13.771
270	17.83	27.140	3479.4	14.254
280	17.91	27.790	3658.1	14.726
290	17.98	28.420	3837.5	15.187
300	18.05	29.030	4017.6	15.638
350	18.33	31.835	4927.6	17.76
273.15	17.85	27.35	3536	14.40
298.15	18.03	28.92	3984	15.56
PdTe$_2$; gram formula weight = 361.62 g				
5	(0.017)	(0.006)	(0.022)	(0.002)
10	0.185	0.056	0.432	0.013
15	0.653	0.208	2.38	0.049
20	1.459	0.499	7.54	0.122
25	2.482	0.931	17.32	0.238
30	3.612	1.483	32.54	0.398
35	4.768	2.127	53.50	0.598
40	5.895	2.837	80.17	0.833
45	6.961	3.594	112.35	1.098
50	7.955	4.380	149.69	1.386
60	9.713	5.991	238.32	2.019
70	11.16	7.601	342.91	2.702
80	12.32	9.169	460.51	3.413
90	13.27	10.677	588.6	4.137
100	14.01	12.114	725.1	4.863
110	14.63	13.480	868.5	5.585
120	15.16	14.777	1017.5	6.297
130	15.59	16.008	1171.3	6.997
140	15.96	17.177	1329.1	7.683
150	16.28	18.289	1490.4	8.353
160	16.55	19.349	1654.6	9.008
170	16.77	20.359	1821.2	9.646
180	16.97	21.323	1989.9	10.268
190	17.13	22.245	2160.5	10.874
200	17.29	23.128	2332.6	11.465
210	17.43	23.975	2506.2	12.041
220	17.57	24.789	2681.2	12.602
230	17.70	25.573	2857.5	13.149
240	17.81	26.329	3035.1	13.683
250	17.90	27.058	3213.6	14.203
260	17.99	27.762	3393.2	14.711
270	18.07	28.442	3573.5	15.207
280	18.16	29.101	3754.7	15.692
290	18.24	29.740	3936.6	16.165
300	18.32	30.360	4119.5	16.628
350	18.66	33.211	5044.5	18.798
273.15	18.07	28.65	3630	15.36
298.15	18.31	30.25	4086	16.54

conduction. Since the same quantity of helium gas was used for measurements on the empty calorimeter, no correction was necessary.

RESULTS

The actual experimental heat capacity values for the three dichalcogenide samples are presented in Table I in chronological order after the application of the analytically determined curvature correction. The temperature increments of individual determinations may usually be estimated from adjacent mean temperatures in the table. For most of the points the deviation from a smooth curve was less than 0.009 cal gfw^{-1} $°K^{-1}$ above 25°K. Below 25°K the fractional deviations become larger because of the smaller absolute heat capacity, smaller temperature intervals, and decreased sensitivity of the thermometer.

The data are presented in terms of an ice point of 273.15°K and the thermochemical calorie defined as 4.1840 abs *j*. The gram formula weights of PtS_2, $PtTe_2$, and $PdTe_2$ are taken as 259.22, 450.31, and 361.62, respectively. Experimental densities of the dichalcogenides were found to be 7.80 g cm^{-3} for PtS_2, 10.16 g cm^{-3} for $PtTe_2$ (both by pycnometric measurement), and 8.306 g cm^{-3} for $PdTe_2$ (from x-ray diffraction data).

The contribution of the empty calorimeter to the total heat capacity when filled with the PtS_2 sample reached a maximum of 59% at 68°K and a minimum of 31% at 10°K. At 6°K the value was 42% and at 350°K the value had dropped to 46%. In contrast the contribution of the calorimeter with the $PtTe_2$ sample reached a maximum of 38% at 350°K and a minimum of 17% at 10°K. At 6°K the calorimeter accounted for 24% of the heat capacity measured. The behavior of the calorimeter filled with the $PdTe_2$ sample was similar to this latter case; the maximum of 40% occurred at 350°K and the minimum of 19% at 18°K. At 6°K the value was 27%.

Large-scale plots of heat capacity vs temperature were made over the entire region of investigation. In addition, a least squares polynomial in temperature fit to the data above 25°K with an IBM digital computer gave essentially identical results. The heat capacities at selected temperatures in Table II were taken from the drawn curve below 25°K and calculated by the polynomial representation above 25°K. A Debye T^3 extrapolation was used below 6°K. Values for $H°-H_0°$, $S°-S_0°$, and $(F°-H_0°)/T$ at the selected temperatures listed in Table II were obtained by integration. For internal consistency the values in Tables I and II are given to one more figure than is justified by the estimated experimental precision. In general the thermodynamic functions are believed to have a probable error less than 0.1% above 100°K.

The plots of the experimental heat capacities vs temperature are presented in Fig. 1. No anomalous deviations from the usual sigmoid form are seen.

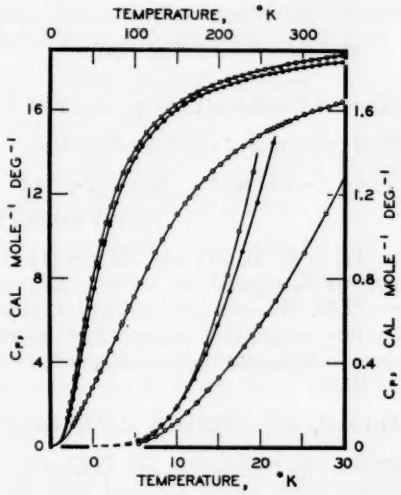

FIG. 1. Heat capacities of the dichalcogenides on a gram formula weight basis: ○ represents PtS_2; ● represents $PtTe_2$, and □ represents $PdTe_2$.

DISCUSSION

The entropy value found here for platinum disulfide, 17.85 cal gfw^{-1} $°K^{-1}$, compares well with that estimated by Kelley,[17] 17.4 cal gfw^{-1} $°K^{-1}$, on the basis of decomposition pressure measurements on PtS_2 by Biltz and Juza[18] and available data on the entropies of the elements. Just as in the PtS/Pt range,[1] Biltz and Juza apparently have included some low-pressure values in the PtS_2/PtS range also (those for $PtS_{1.06}$, $PtS_{1.01}$, and $PtS_{1.06}$), which probably should have been omitted. Furthermore, the estimation of the partial pressure of the diatomic sulfur molecules in the vapor was based upon the work by Preuner and Schupp[19] which has since been shown to be considerably in error,[20,21] and a reevaluation of the thermodynamic functions has therefore been made. It appeared possible to obtain consistent data using the available heat-capacity equations for PtS[1] and S_2 gas[22] and assuming the following heat-capacity equation, which satisfies the present data at 300 and 350°K and reaches the value 20 cal gfw^{-1} $°K^{-1}$ at 1000°K, for PtS_2,

$$C_p = 16.39 + 3.77 \times 10^{-3} T - 1.57 \times 10^{5} T^{-2}.$$

[17] K. K. Kelley, "Contributions to the data on theoretical metallurgy. VII.," U. S. Bureau of Mines Bulletin 406, Washington (1937); cf. K. K. Kelley, "Contributions to the data on theoretical metallurgy. XI.," U. S. Bureau of Mines Bulletin 477, Washington (1950).

[18] W. Biltz and R. Juza, Z. anorg. u. allgem. Chem. **190,** 161 (1930).

[19] G. Preuner and W. Schupp, Z. physik. Chem. **68,** 129 (1909); cf. G. Preuner and I. Brockmöller, *ibid.* **81,** 129 (1912).

[20] W. Klemm and H. Kilian, Z. physik. Chem. **B49,** 279 (1941).

[21] H. Braune, S. Peter, and V. Neveling, Z. Naturforsch. **6a,** 32 (1951).

[22] K. K. Kelley, "Contributions to the data on theoretical metallurgy. XIII.," U. S. Bureau of Mines Bulletin 584, Washington (1960).

The heat-capacity change for the reaction

$$2\,PtS_2(s) = 2\,PtS(s) + S_2(g)$$

is then

$$\Delta C_p = -4.12 + 0.84\times10^{-3}T + 0.78\times10^{5}T^{-2}.$$

A graphical evaluation of the derived function

$$(\Delta H_0/T) + I = -4.57\log P_{S_2} - 9.49\log T + 0.42 \times 10^{-3}T + 0.39\times10^{5}T^{-2}$$

assuming P_{S_2} to be 40, 100, and 250 mm Hg at 889°, 924°, and 964°K, respectively, leads to $\Delta H_0 = 45\,000$ and $I = -72.35$. The constants needed for calculating enthalpy, free energy, and entropy data for the decomposition of PtS_2 are thus available, and the values at 298.15°K are

$$\Delta H^\circ = 44.1 \text{ kcal}, \quad \Delta F^\circ = 30.5 \text{ kcal}, \quad \Delta S^\circ = 44.6 \text{ cal } ^\circ K^{-1}.$$

Incorporating the earlier data for PtS,[1] and taking orthorhombic sulfur as the standard state of sulfur instead of the diatomic gas, the following values for the standard heat of formation, free energy of formation, and entropy of PtS_2 are found at 298.15°K;

$$Pt(s) + 2S(rh) = PtS_2(s)$$

$$\Delta Hf^\circ = -26.3 \text{ kcal}, \qquad \Delta Ff^\circ = -24.0 \text{ kcal},$$

$$S^\circ = 18.1 \text{ cal } ^\circ K^{-1}.$$

There is good agreement with the enthalpy and free energy values of Kelley[17] ($\Delta Hf^\circ = -26.64$ kcal, $\Delta Ff^\circ = -24.28$ kcal), while another enthalpy estimate[23] ($\Delta Hf^\circ = -27.8$ kcal) seems to be somewhat low.

Although high temperature decomposition data are also available for other palladium and platinum group disulfides, heat-capacity data are not. The thermodynamic functions for RuS_2 have already been estimated by Kelley[17] assuming the heat-capacity change to be $\Delta C_p = -5$ cal gfw^{-1} $^\circ K^{-1}$ for the reaction

$$RuS_2(s) = Ru(s) + S_2(g)$$

studied by Juza and Meyer[24] in the temperature range 1396° to 1481°K. A supposedly better estimate can be made by assuming the heat capacity of RuS_2 to have the same values as FeS_2 (pyrite)[25] at 300 and 350°K (14.90 and 15.66 cal gfw^{-1} $^\circ K^{-1}$, respectively) and reaching the value 19 cal gfw^{-1} $^\circ K^{-1}$ at 1000°K according to the equation

$$C_p = 16.38 + 2.83\times10^{-3}T - 2.10\times10^{5}T^{-2}.$$

For Ru, the alleged allotropy[26,27] has not been confirmed by other investigators, and x-ray photographs up to 1600°K showed only the presence of the hexagonal close-packed form.[28] Therefore, the heat-capacity equation derived by Kelley,[22] $C_p = 5.25 + 1.50\times10^{-3}T$ (298–1308°K), has been assumed valid up to 1481°K. The heat-capacity change for the reaction is then

$$\Delta C_p = -2.41 - 1.17\times10^{-3}T + 1.20\times10^{5}T^{-2}.$$

Since the degree of dissociation of the diatomic sulfur gas into sulfur atoms under the experimental conditions of Juza and Meyer does not exceed 2% according to the data giving the highest values,[29] the P_{S_2} values are taken to be 2.8, 5.4, 10.0, and 15.3 mm Hg at 1396°, 1426°, 1457°, and 1481°K, respectively. A graphical evaluation of the derived function

$$(\Delta H_0/T) + I = -4.57\log P_{S_2} - 5.55\log T - 0.59 \times 10^{-3}T + 0.60\times10^{5}T^{-2},$$

leads to $\Delta H_0 = 85\,000$ and $I = -68.08$. The enthalpy, free energy, and entropy values for the decomposition of RuS_2 at 298.15°K are accordingly,

$$\Delta H^\circ = 83.8 \text{ kcal}, \quad \Delta F^\circ = 68.4 \text{ kcal}, \quad \Delta S^\circ = 50.9 \text{ cal } ^\circ K^{-1}.$$

The related enthalpy and free energy values for the reaction

$$Ru(s) + 2S(rh) = RuS_2(s)$$

and the entropy of RuS_2 at 298.15°K are

$$\Delta Hf^\circ = -53.0 \text{ kcal}, \qquad \Delta Ff^\circ = -49.5 \text{ kcal},$$

$$S^\circ = 10.4 \text{ cal } ^\circ K^{-1}.$$

All three values are lower than those of Kelley[17] ($\Delta Hf^\circ = -46.99$ kcal, $\Delta Ff^\circ = -44.11$ kcal, $S^\circ = 12.5$ cal $^\circ K^{-1}$). Another enthalpy estimate[23] based upon the same data is also higher ($\Delta Hf^\circ = -48.1$ kcal). The uncertainty in the entropy value is rather large, since the equilibrium temperatures were high and no heat-capacity data are available for RuS_2. For ruthenium the value $S_{298}^\circ = 6.82$ cal gfw^{-1} $^\circ K^{-1}$ by Clusius and Piesbergen[30] was chosen.

A corresponding calculation for OsS_2 (using the same heat-capacity equation for the compound as for RuS_2 and the available data[22] for the elements) yields a heat-capacity change of $\Delta C_p = -1.97 - 1.79\times10^{-3}T + 1.20\times10^{5}T^{-2}$ for the reaction

$$OsS_2(s) = Os(s) + S_2(g).$$

A graphical evaluation of the derived function

$$(\Delta H_0/T) + I = -4.57\log P_{S_2} - 4.54\log T - 0.90 \times 10^{-3}T + 0.60\times10^{5}T^{-2}$$

[23] *Selected Values of Chemical Thermodynamic Properties*, U. S. National Bureau of Standards Circ. No. 500 (U. S. Government Printing Office, Washington 25, D. C., 1952).

[24] R. Juza and W. Meyer, Z. anorg. u. allgem. Chem. **213**, 273 (1933).

[25] F. Grønvold and E. F. Westrum, Jr., (unpublished data).

[26] F. M. Jaeger and E. Rosenbohm, Proc. Acad. Sci. Amsterdam **34**, 808 (1931); Rec. trav. chim. **51**, 1 (1932).

[27] F. M. Jaeger and E. Rosenbohm, Proc. Acad. Sci. Amsterdam **44**, 144 (1941).

[28] E. O. Hall and J. Crangle, Acta Cryst. **10**, 240 (1957).

[29] W. H. Evans and D. D. Wagman, J. Research Natl. Bur. Standards **49**, 141 (1952).

[30] K. Clusius and U. Piesbergen, Z. Naturforsch. **14a**, 23 (1959).

using the data by Juza,[31] P_{S_2} equal to 27.8, 84.5, 213, and 490 mm Hg at 1217°, 1267°, 1317°, and 1367°K, respectively, leads to $\Delta H_0 = 67\,000$ and $I = -63.61$. The enthalpy, free energy, and entropy values for the decomposition of OsS_2 at 298.15°K are accordingly,

$$\Delta H^\circ = 65.9 \text{ kcal}, \quad \Delta F^\circ = 51.3 \text{ kcal}, \quad \Delta S^\circ = 49.2 \text{ cal } ^\circ K^{-1}.$$

The enthalpy and free energy values for the reaction

$$Os(s) + 2S(rh) = OsS_2(s)$$

and the entropy of OsS_2 at 298.15°K are then

$$\Delta Hf^\circ = -35.1 \text{ kcal}, \qquad \Delta Ff^\circ = -32.1 \text{ kcal},$$

$$S^\circ = 13.1 \text{ cal } ^\circ K^{-1}.$$

The enthalpy value is about 4 kcal lower than Juza's[31] estimate, but agrees completely with a more recent one[23] also based upon his data ($\Delta Hf^\circ = -35$ kcal).

For $\sim IrS_2$ the evaluation is dependent upon assumptions regarding the properties of the lower sulfide Ir_2S_3. Decomposition pressures have been measured for both sulfides by Biltz *et al.*[32] The evaluation is made here on the assumption that the heat capacities of the compounds are equal to those of PtS_2 and $PtS + PtS_2$, respectively. The heat-capacity change for the reaction

$$\tfrac{2}{3}Ir_2S_3(s) = \tfrac{4}{3}Ir(s) + S_2(g)$$

is estimated as

$$\Delta C_p = -1.44 - 3.20 \times 10^{-3} T + 0.63 \times 10^5 T^{-2}.$$

A graphical evaluation of the derived function

$$(\Delta H_0/T) + I = -4.57 \log P_{S_2} - 3.32 \log T - 1.60 \times 10^{-3} T + 0.32 \times 10^5 T^{-2}$$

leads to $\Delta H_0 = 70\,100$ and $I = -61.35$. The enthalpy, free energy, and entropy values for the decomposition or Ir_2S_3 into the elements according to the above equation at 298.15°K are

$$\Delta H^\circ = 69.3 \text{ kcal}, \quad \Delta F^\circ = 54.3 \text{ kcal}, \quad \Delta S^\circ = 50.4 \text{ cal } ^\circ K^{-1}.$$

The corresponding enthalpy and free energy values for the reaction

$$2Ir(s) + 3S(rh) = Ir_2S_3(s)$$

and the entropy of Ir_2S_3 at 298.15°K are

$$\Delta Hf^\circ = -57.7 \text{ kcal}, \qquad \Delta Ff^\circ = -52.7 \text{ kcal},$$

$$S^\circ = 23.2 \text{ cal } ^\circ K^{-1}.$$

Earlier estimates of the enthalpy[23,32] were −51 kcal. In deriving the entropy the value $S_{298}^\circ = 8.50$ cal gfw^{-1} °K^{-1} for iridium determined by Clusius and Losa[33] was used.

Assuming the decomposition of $\sim IrS_2$ to take place according to the simple stoichiometric equation

$$4IrS_2(s) = 2Ir_2S_3(s) + S_2(g)$$

the heat capacity change is

$$\Delta C_p = -4.12 + 0.84 \times 10^{-3} T + 0.78 \times 10^5 T^{-2}.$$

A graphical evaluation of the function

$$(\Delta H_0/T) + I = -4.57 \log P_{S_2} - 9.49 \log T + 0.42 \times 10^{-3} T + 0.39 \times 10^5 T^{-2}$$

gives $\Delta H_0 = 53\,800$ and $I = -69.8$. The corresponding values of the enthalpy, free energy, and entropy of decomposition at 298.15°K are

$$\Delta H^\circ = 52.3 \text{ kcal}, \quad \Delta F^\circ = 39.8 \text{ kcal}, \quad \Delta S^\circ = 42.0 \text{ cal } ^\circ K^{-1},$$

which lead to the following values for the enthalpy, free energy, and entropy of IrS_2 at 298.15°K

$$Ir(s) + 2S(rh) = IrS_2(s)$$

$$\Delta Hf^\circ = -34.2 \text{ kcal}, \qquad \Delta Ff^\circ = -31.5 \text{ kcal},$$

$$S^\circ = 14.7 \text{ cal } ^\circ K^{-1}.$$

An earlier value of the enthalpy of formation[23] is about 4 kcal higher ($\Delta Hf^\circ = -30$ kcal).

For the disulfides of rhodium and palladium only estimates relative to the lower sulfides can be made, but since no heat-capacity data are known for any of the compounds in question, no attempt to evaluate their entropies will be made here.

In estimating entropies for chalcogenides for which no data exist, the additivity principle of a chalcogen and a metal contribution can be used. Justification for this is seen in the data presented here and will be discussed more thoroughly in a forthcoming paper.[25] The values chosen are 10.5 cal g atom^{-1} °K^{-1} for the metal (Me^{2+}, Me^{3+}, Me^{4+}), 3.0 both for S^{2-} and S_2^{2-}, 7.0 for Se^{2-}, 10.0 for Se_2^{2-}, and 9.5 for Te^{2-} and 13.5 for Te_2^{2-}. Estimates in cal gfw^{-1} °K^{-1} are then as follows: $RuSe_2$, $OsSe_2$, 19.5; $RuTe_2$, $OsTe_2$, 24.0; $RhTe_2$, $IrTe_2$, 29.5; $PtSe_2$, 24.5; $\sim IrSe_2$, 22.5; $\frac{1}{8}Rh_8S_{15}$, 15.0. These values are probably reliable to about 0.8 cal g atom^{-1} °K^{-1}. For the deformed pyrite-like structures of PdS_2 and $PdSe_2$, and those of the rhodium and iridium chalcogenides, corresponding estimates would probably give entropy values that would be too low, because the compounds are hyperelectronic with regard to forming pyrite-type structures, just as CoS_2, NiS_2, and $NiSe_2$. An increase in entropy of about 3.0 cal gfw^{-1} °K^{-1} for the rhodium and iridium chalcogenides and about 5 cal gfw^{-1} °K^{-1} for the palladium chalcogenides would seem necessary. For platinum only tetravalent dichalcogenides are known, and the entropy of $PtSe_2$, for example, is thus expected to be lower than that of $PdSe_2$ by 5 cal gfw^{-1} °K^{-1}.

[31] R. Juza, Z. anorg. u. allgem. Chem. **219,** 129 (1934).
[32] W. Biltz, J. Laar, P. Ehrlich, and K. Meisel, Z. anorg. u. allgem. Chem. **233,** 257 (1937).
[33] K. Clusius and C. G. Losa, Z. Naturforsch. **10a,** 545 (1955).

ACKNOWLEDGMENTS

The authors thankfully acknowledge the generosity of The International Nickel Company (Mond) Limited for the loan of platinum and palladium metal. They thank Torkild Thurmann-Moe for assistance with making the tellurides, and Bruce H. Justice, Shu-Sing Chang, and Elfreda Chang for cooperation with the heat-capacity measurements and calculations. One of the authors (F.G.) wishes to thank the Nansen Foundation for financial assistance. The partial support of the Division of Research of the U. S. Atomic Energy Commission is gratefully acknowledged.

THE JOURNAL OF CHEMICAL PHYSICS VOLUME 35, NUMBER 5 NOVEMBER, 1961

Transport Properties of Polar Gases*

L. MONCHICK

Applied Physics Laboratory, The Johns Hopkins University, Silver Spring, Maryland

AND

E. A. MASON

Institute for Molecular Physics, University of Maryland, College Park, Maryland

(Received February 13, 1961)

A model is proposed for the calculation of viscosity, diffusion, thermal diffusion, and the translational part of the heat conductivity of dilute polar gases. It is assumed that the molecular-collision trajectories are negligibly distorted by transfer of internal rotational energy, and that the relative orientation of two colliding dipoles remains fixed throughout the significant portion of the collision trajectory around the distance of closest approach. For this model, the Chapman-Enskog theory retains its usual form, but the collision integrals which appear must be averaged over all possible relative orientations occurring in collisions. Collision integrals have been calculated for the Stockmayer (12–6–3) potential,

$$\varphi(r)=4\epsilon_0[(\sigma_0/r)^{12}-(\sigma_0/r)^6+\delta(\sigma_0/r)^3],$$

for kT/ϵ_0 from zero to 100 and for δ from -2.5 to $+2.5$, and averaged over all orientations (assumed equally probable). Sufficient collision integrals are tabulated that the convergence error of the Chapman-Enskog theoretical expressions is not a problem.

Experimental viscosities and dipole moments of a number of polar gases have been used to determine the potential parameters ϵ_0, σ_0, and δ, which were then used to calculate other properties for comparison with experiment. The over-all agreement between experiment and this model for polar gases is comparable to that of the Lennard-Jones (12–6) model for nonpolar gases.

I. INTRODUCTION

GAS kinetic theory has been most completely worked out for particles interacting with central forces,[1,2] and has proved rather successful for those molecules which can be considered to have spherical symmetry and no internal degrees of freedom.[2] In the important case of polar gases, however, the facts that the molecules have an angle-dependent potential and that rotational-energy transfers are possible on every collision must be taken into account. Although several treatments have been developed for particles with internal degrees of freedom (Taxman[3] for the classical case and Wang Chang and Uhlenbeck[4] for the quantum case), they would tax even the present generation of computing machines if carried out rigorously. In light of this, we are limited to approximate treatments.

The interaction potential which has been used almost exclusively for polar gases (and which will be used here) is the Stockmayer potential,

$$\varphi(r)=4\epsilon_0[(\sigma_0/r)^{12}-(\sigma_0/r)^6]-(\mu_1\mu_2/r^3)\zeta, \quad (1)$$

where

$$\zeta=2\cos\theta_1\cos\theta_2-\sin\theta_1\sin\theta_2\cos\phi, \quad (2)$$

and μ_1 and μ_2 are the dipole moments of the two interacting molecules, θ_1 and θ_2 the angles of inclination of the axes of the two dipoles to the line joining the centers of the molecules, and ϕ is the azimuthal angle between them. In the limit as μ_1 or $\mu_2\to 0$, $\varphi(r)$ is just the Lennard-Jones (12–6) potential with a potential-

* This work was supported in part by the U. S. Navy, and in part by the U. S. Atomic Energy Commission.

[1] S. Chapman and T. G. Cowling, *The Mathematical Theory of Non-Uniform Gases* (Cambridge University Press, New York, 1952), 2nd ed.

[2] J. O. Hirschfelder, C. F. Curtiss, and R. B. Bird, *Molecular Theory of Gases and Liquids* (John Wiley & Sons, Inc., New York, 1954). Hereafter referred to as MTGL.

[3] N. Taxman, Phys. Rev. **110**, 1235 (1958).

[4] C. S. Wang Chang and G. E. Uhlenbeck, University of Michigan Engineering Research Report No. CM-681 (July, 1951). See also MTGL pp. 501–506.

well depth of ϵ_0 and a "diameter" σ_0 such that $\varphi(\sigma_0)=0$. During the actual course of a collision, θ_1, θ_2, and ϕ will be functions of r and of the original rotational velocities at $t=-\infty$.

In the first attempt to handle polar gases, Krieger[5] assigned a fixed value of 2 to ξ. This corresponds to a model where the dipoles maintain a head-to-tail position, corresponding to the maximum attractive orientation, throughout the encounter. This approximation has the advantage that it replaces an angle-dependent force by a central force, and limits consideration to only one relative orientation. The calculations are then no more difficult than those for ordinary central forces except for the introduction of an additional parameter. However, this orientation should also be the position of maximum rotational kinetic energy and, therefore, one may argue that this is the orientation in which the molecules should spend the least amount of time. Furthermore, all repulsive orientations are neglected. Although Krieger's results looked fairly reasonable, Itean, Glueck, and Svehla[6] have detected an error in his calculations. When this was corrected, and the calculations repeated using the same model, the empirical values of σ_0 and ϵ_0 obtained by fitting the available experimental data were physically unrealistic.[6]

Sutton[7] has presented an approximate method for viscosity in the limiting case where rotational-energy transfers may be neglected, and the potential is averaged, quantum mechanically, over all orientations before collision. This model does not lead to the low-temperature behavior expected for polar gases, and is probably most satisfactory as a high-temperature limiting case. In the Appendix, we present an alternative approximation for a similar model.

In the next section, we shall present an alternate model to Krieger's which takes into account all relative orientations but still keeps the advantage of replacing the dipole field by a central field.

II. MODEL AND ASSUMPTION

The two major difficulties in the analysis of the dynamics of binary collisions between polar molecules are the existence of inelastic collisions (rotational-energy transfers) and the very complicated trajectories associated with an angle-dependent potential, even for elastic collisions. In order to reduce the problem to a mathematically tractable form, we are forced to make two important assumptions, which we attempt to justify on more or less physical grounds. Our treatment is entirely classical, and no allowance is made for quantum effects.

The first assumption is that the inelastic collisions, even though they may occur frequently, have little effect on the trajectories. Our justification for this assumption lies in the fact that we would expect most inelastic collisions to involve the transfer of only one quantum of rotational energy. For most molecules at ordinary temperatures, this amount of energy is much less than kT (that is, the molecular rotations are almost classical), but the translational kinetic energy is of the order of kT. On energy grounds, therefore, we expect rotational transfer to have only a small effect on the trajectories, and we neglect it. The reasonableness of this assumption is substantiated by the known results for the transport properties of nonpolar polyatomic gases. Here, rotational energy transfer is also possible, but most transport properties can be described fairly well on the basis of a spherically symmetric potential.[2] Of course, this assumption is inadequate for a property that depends specifically on the transfer of internal energy, and is notoriously bad for the thermal conductivity of polyatomic gases, whether polar or nonpolar. In such cases, the transfer of internal energy is usually handled separately as a diffusion problem, resulting in the well-known Eucken correction or one of its modifications.[1,2,8] The present treatment of polar gases will thus be inadequate for the thermal conductivity, although we may hope it will work for the viscosity and the diffusion properties.

The foregoing argument can be formulated in more mathematical terms through Taxman's[3] classical theory of transport phenomena for molecules with internal degrees of freedom, at least for the case of the viscosity. Taxman's expression for the viscosity η is

$$\eta^{-1}=\frac{8}{5(\pi mkT)^{\frac{1}{2}}}\left[\int \exp(-\epsilon_1)\,d\omega_1\right]^{-1}\left[\int \exp(-\epsilon_2)\,d\omega_2\right]^{-1}$$
$$\times\int[\gamma^4(1-\cos^2\chi)-\tfrac{2}{3}(\gamma'^2+\gamma^2\sin^2\chi)\,\Delta\epsilon]$$
$$\times\exp(-\epsilon_1-\epsilon_2-\gamma^2)\,bdbd\phi\gamma^3d\gamma d\omega_1 d\omega_2, \quad (3)$$

where m is the mass of a molecule, χ is the deflection angle in a binary collision, b is the usual impact parameter, and $\gamma^2\equiv(m/4kT)g^2$, where g is the initial relative speed. The coordinates and momenta of the internal degrees of freedom are represented by ω, and $\epsilon\equiv E_\omega/kT$, where E_ω is the energy associated with the internal degrees of freedom.[9] Quantities after collision are primed, and quantities before collision are unprimed. The subscripts 1 and 2 refer to the two colliding molecules, and $\Delta E\equiv\epsilon_1'+\epsilon_2'-\epsilon_1-\epsilon_2=\gamma^2-\gamma'^2$. By our assumption, we have $\Delta\epsilon\ll\gamma^2$, and the term involving $\Delta\epsilon$

[5] F. J. Krieger, Project Rand Research Memorandum No. RM-646 (July, 1951). See also MTGL pp. 597–599.

[6] E. C. Itean, A. R. Glueck, and R. A. Svehla, NASA Technical Note D-481 (January, 1961). The authors wish to thank Dr. R. S. Brokaw for making these results available to them before publication.

[7] J. R. Sutton, National Engineering Laboratory, East Kilbride, Galsgow, Heat Division Paper No. 167 (August, 1959).

[8] J. O. Hirschfelder, J. Chem. Phys. **26**, 274, 282 (1957); *Sixth Symposium (International) on Combustion* (Reinhold Publishing Corporation, New York, 1957), p. 351; *Proceedings of the Joint Conference on Thermodynamics and Transport Properties of Fluids* (Institution of Mechanical Engineers, London, 1958), p. 133.

[9] This ϵ, which appears only in Eq. (3), should not be confused with the potential parameter ϵ_0 of Eq. (1).

in the integrand can therefore be neglected. Since the initial internal and translational energies are presumably independent, the integrations over $d\omega_1$ and $d\omega_2$ can be carried out to yield

$$\eta^{-1}=\frac{8}{5(\pi mkT)^{\frac{1}{2}}}\int[(1-\cos^2\chi)bdbd\phi]\exp(-\gamma^2)\gamma^7 d\gamma. \quad (4)$$

This is just the usual result[1,2] for no internal degrees of freedom.[10] The same result also follows from Wang Chang and Uhlenbeck's[4] quantum treatment in the limit that the trajectories can be treated classically.

The second assumption concerns the effect of the orientation-dependent potential on the angle of deflection χ in a collision. Although the potential acts along the whole trajectory, the deflection angle is determined primarily by the interaction in the vicinity of the distance of closest approach of the colliding molecules. Thus, the integral which determines χ, given by Eq. (13) for a central potential, has its integrand sharply peaked in the region corresponding to the distance of closest approach. It can be shown that the average time required to complete a collision is of the same order of magnitude as the average rotation time. Over a small range around the distance of closest approach, it seems likely that the relative orientation of two colliding molecules does not change much, so that χ is determined largely by only one relative orientation rather than by all the possible orientations assumed along the entire trajectory from $t=-\infty$ to $t=+\infty$. We therefore assume that in a given collision only one relative orientation is effective, and evaluate χ as if the relative orientation were fixed at one value throughout the entire collision. Different collisions will correspond to different fixed orientations.

A more elaborate justification for this point of view, which we cannot reproduce here, has been given by Hornig and Hirschfelder.[11] In their terminology we are choosing to work in terms of a body-fixed coordinate system.

The assumption of a fixed-relative orientation during a collision changes the emphasis of the problem from the collision dynamics to the kinetic theory. The dynamics of a collision is now a mathematically manageable problem, but the kinetic-theory problem now corresponds to a gas in which collisions follow not one intermolecular potential, but may follow any one of a very large number of potentials, one for each relative orientation. This probelm has fortunately already been solved,[12] and the result is not only accurate to all orders of the usual kinetic-theory approximations but is also very simple: The formal kinetic theory expressions for the transport coefficients are the same as for a single-interaction potential, but the cross sections or collision integrals occurring in these expressions are averages over all possible different potentials. That is, there is a different cross section for each different potential, weighted according to the probability that the collision occurs along this potential. In our averages, we have assigned equal weight to each orientation, and the agreement with available experimental data does not appear to justify anything more elaborate. It is possible that future experimental work will suggest a more sophisticated averaging procedure, however.

The two assumptions which we make seem physically reasonable, although we cannot justify them rigorously. It is our feeling, based on subsequent analysis of experimental data on transport properties and virial coefficients, that nothing more elaborate is justified for the Stockmayer potential, which represents a polar molecule simply as a spherical potential with a point dipole embedded at the center. Unfortunately there is reason to believe that most polar molecules of interest are not very spherical, even if the dipole moment is ignored, and furthermore probably have charge centers near the surface of the molecule, so that their electric fields are not well represented by a point dipole. A familiar example is H_2O, perhaps the most interesting polar molecule of all.

III. GENERAL FORMULAS

We can now write down the expressions for the transport coefficients in the form in which they will be used. The coefficient of viscosity is

$$\eta=\frac{5}{16}\left(\frac{mkT}{\pi}\right)^{\frac{1}{2}}\frac{f_\eta}{\sigma_0^2\langle\Omega^{(2,2)*}\rangle}, \quad (5)$$

where σ_0 is the distance parameter of Eq. (1), $\langle\Omega^{(2,2)*}\rangle$ is a dimensionless collision integral averaged over all relative orientations, and f_η is a correction factor resulting from higher kinetic-theory approximations, which differs from unity by at most a few percent. The numerical calculation of the collision integrals is described in the next section. They are defined so as to be equal to unity for rigid spheres of diameter σ_0. In the present case, they are functions of the reduced temperature $T^*\equiv kT/\epsilon_0$ and of the reduced dipole moment, $\mu^*\equiv\mu/(\epsilon_0\sigma_0^3)^{\frac{1}{2}}$.

The contribution to the coefficient of thermal conductivity from just the translational motion of the molecules λ^0 is

$$\lambda^0=\frac{75k}{64}\left(\frac{kT}{\pi m}\right)^{\frac{1}{2}}\frac{f_\lambda}{\sigma_0^2\langle\Omega^{(2,2)*}\rangle}$$

$$=\frac{15k}{4m}\left(\frac{f_\lambda}{f_\eta}\right)\eta, \quad (6)$$

[10] It should be remarked that a similar treatment of Taxman's expression for the thermal conductivity leads directly to an Eucken correction. The contribution of the internal degrees of freedom to the thermal conductivity will not be further considered in this paper, however.

[11] J. F. Hornig and J. O. Hirschfelder, Phys. Rev. **103,** 908 (1956).

[12] E. A. Mason, J. T. Vanderslice, and J. M. Yos, Phys. Fluids **2,** 688 (1959).

where f_λ is a correction factor similar to f_η. It should be emphasized that λ^0 is *not* the complete thermal conductivity. There is an additional large contribution from the internal degrees of freedom, which we are not considering here.

The coefficient of self-diffusion D_{11} is

$$D_{11}=\frac{3}{8n}\left(\frac{kT}{\pi m}\right)^{\frac{1}{2}}\frac{f_D}{\sigma_0^2\langle\Omega^{(1,1)*}\rangle}, \tag{7}$$

where n is the molecular density and f_D is a correction factor close to unity.

In order to write out the expressions for f_η, f_λ, f_D, and for the isotopic thermal diffusion factor, it is convenient to define the following dimensionless ratios:

$$\begin{aligned}
&\langle A^*\rangle\equiv\langle\Omega^{(2,2)*}\rangle/\langle\Omega^{(1,1)*}\rangle,\\
&\langle B^*\rangle\equiv[5\langle\Omega^{(1,2)*}\rangle-4\langle\Omega^{(1,3)*}\rangle]/\langle\Omega^{(1,1)*}\rangle,\\
&\langle C^*\rangle\equiv\langle\Omega^{(1,2)*}\rangle/\langle\Omega^{(1,1)*}\rangle,\\
&\langle E^*\rangle\equiv\langle\Omega^{(2,3)*}\rangle/\langle\Omega^{(2,2)*}\rangle,\\
&\langle F^*\rangle\equiv\langle\Omega^{(3,3)*}\rangle/\langle\Omega^{(1,1)*}\rangle.
\end{aligned} \tag{8}$$

These ratios also occur in the expressions for the transport coefficients of mixtures (which are not specifically considered in this paper), and are equal to unity for rigid spheres. In terms of these ratios, quite accurate values of the correction factors can be written according to Kihara's second approximation[13] as follows:

$$\begin{aligned}
f_\eta&=1+\tfrac{3}{190}[8\langle E^*\rangle-7]^2,\\
f_\lambda&=1+\tfrac{1}{452}[8\langle E^*\rangle-7]^2,\\
f_D&=1+\tfrac{1}{8}[6\langle C^*\rangle-5]^2[2\langle A^*\rangle+5]^{-1}.
\end{aligned} \tag{9}$$

For a binary mixture of heavy isotopes, the expression for the thermal-diffusion factor α_T can be expanded as a power series in the mass difference of the isotopes,

$$\alpha_T=\alpha_0[(m_1-m_2)/(m_1+m_2)]+\cdots, \tag{10}$$

where α_0 is the so-called reduced thermal-diffusion factor. The expression for α_0 is unfortunately rather complicated,[14] and we will not repeat it here. It can be written with sufficient accuracy according to Kihara's second approximation in terms of the ratios defined in Eq. (8), and we have tabulated numerical values of α_0 directly in order to save the user tedious calculations with this formula.

The averaged $\langle\Omega^{(l,s)*}\rangle$ appearing in the preceding formulas are complicated integrals involving, in the present case, four stages of numerical integration. The collision integrals for a fixed relative orientation are

$$\Omega^{(l,s)*}\equiv[(s+1)!]^{-1}\int_0^\infty \exp(-\gamma^2)(\gamma^2)^{s+1}Q^{(l)*}d(\gamma^2), \tag{11}$$

where

$$Q^{(l)*}\equiv\frac{2}{\sigma_0^2}\left[1-\frac{1}{2}\frac{1+(-1)^l}{1+l}\right]^{-1}\int_0^\infty(1-\cos^l\chi)bdb, \tag{12}$$

$$\chi=\pi-2b\int_{r_c}^\infty\{1-(b^2/r^2)-[\varphi(r)/\tfrac{1}{4}mg^2]\}^{-\frac{1}{2}}(dr/r^2), \tag{13}$$

in which all the symbols appearing have already been defined except for r_c, the distance of closest approach, which is given as a function of b and g by

$$1-(b^2/r_c^2)-[\varphi(r_c)/\tfrac{1}{4}mg^2]=0. \tag{14}$$

If we now assume that all relative orientations are equally probable, the averaged value of $\Omega^{(l,s)*}$ is given by

$$\langle\Omega^{(l,s)*}\rangle=\frac{1}{8\pi}\int_{-1}^1\int_{-1}^1\int_0^{2\pi}\Omega^{(l,s)*}d\phi d(\cos\theta_1)d(\cos\theta_2). \tag{15}$$

In the next section, we shall present the calculations and tabulations of the collision integrals.

IV. CALCULATIONS AND TABULATIONS

The intermolecular potential will now be written as

$$\varphi(r)=4\epsilon_0[(\sigma_0/r)^{12}-(\sigma_0/r)^6+\delta(\sigma_0/r)^3], \tag{16}$$

where

$$\delta=\tfrac{1}{4}\mu^{*2}\zeta(\theta_1,\theta_2,\phi),\qquad \mu^*=\mu/(\epsilon_0\sigma_0^3)^{\frac{1}{2}}, \tag{17}$$

and ζ has been defined in Eq. (2). By our assumptions, the actual trajectory is replaced by one in which the value of ζ (and δ) has a fixed value, reducing the problem to one of calculating angles of deflections of particles interacting with central forces. Since this type of calculation has previously been described several times,[15] we will only outline the main points.

The first step is to calculate χ by numerical integration for a set of values of δ, g, and b. The singularity in the integrand of Eq. (13) at $r=r_c$ can be removed by transforming to the variable

$$\sin\theta=r_c(b)/r. \tag{18}$$

It is convenient to define the parameters

$$\begin{aligned}
&\xi=\sigma_0/r_c(0),\\
&u=r_c(0)/r_c(b), &&0\le u\le 1,\\
&x=\tfrac{1}{8}mg^2/\epsilon_0=\tfrac{1}{4}\gamma^2T^*,\\
&T^*=kT/\epsilon_0,
\end{aligned} \tag{19}$$

where $r_c(0)$ is the distance of closest approach in a head-on collision ($b=0$). The parameter ξ is determined by x,

$$\xi^{12}-\xi^6+\delta\xi^2=x, \tag{20}$$

and from Eqs. (14) and (19), u can be obtained as a

[13] T. Kihara, Revs. Modern Phys. **25**, 831 (1953); E. A. Mason and W. E. Rice, J. Chem. Phys. **22**, 843 (1954).

[14] E. A. Mason, J. Chem. Phys. **27**, 75 (1957).

[15] MTGL, pp. 552–559; E. A. Mason, J. Chem. Phys. **22**, 169 (1954); E. A. Mason and H. W. Schamp, Jr., Ann. Phys. N. Y. **4**, 233 (1958); L. Monchick, Phys. Fluids **2**, 695 (1959).

TABLE I. Asymptotic cross section $A^{(l)}(n)$.

l	$A_+^{(l)}(12)$	$A_-^{(l)}(6)$	$A_+^{(l)}(3)$	$A_-^{(l)}(3)$
1	0.34575	0.4342	0.3116	0.6413
2	0.27869	0.3277	0.3535	0.4642
3	0.39187	0.502	0.4724	0.7711
4	0.35131	0.420	0.5034	0.6361
5	0.41858		0.5811	

function of b or vice versa. The integrand of χ is now a function of the dimensionless quantities δ, x, u, and θ.

The calculation procedure was as follows: For a fixed value of δ, a set of values of x was chosen for which to construct a table of $Q^{(l)*}(\delta, x)$. At these x, tables of χ were calculated at values of u chosen in the manner outlined below.

The integral for χ can be written in terms of the defined dimensionless variables as follows:

$$\chi(\delta, x, u)=\pi-2(b/r_c)$$
$$\times\int_0^{\pi/2}\left\{1+\frac{\sin^2\theta}{x\cos^2\theta}\left[(\xi u)^{12}(1-\sin^{10}\theta)-(\xi u)^6(1-\sin^4\theta)\right.\right.$$
$$\left.\left.+\delta(\xi u)^3(1-\sin\theta)\right]\right\}^{\frac{1}{2}}d\theta, \quad (21)$$

where

$$b/r_c=\left[1-\frac{(\xi u)^{12}-(\xi u)^6+\delta(\xi u)^3}{x}\right]^{\frac{1}{2}}. \quad (22)$$

The range of θ was divided into a number of intervals depending on whether or not orbiting collisions could occur, and a five-point Gaussian integration formula used in each interval. In the nonorbiting region, four intervals were used, and in the orbiting region the number of intervals varied according to the closeness of b to the critical value for orbiting.

A few remarks on orbiting collisions are in order. As is well known, for potentials which are attractive in some region there is a possibility of orbiting.[15] For $\delta>0$, that is an attractive dipole configuration, orbiting will occur for all x less than some critical value $x_{\max}$. For $\delta>0$, there are two repulsive parts to the potential, one at long range and one at short range. In this latter case, it can be shown that no orbiting occurs for $\delta>(\frac{8}{27})^{\frac{1}{2}}\simeq 0.54$; and that for $\delta<0.54$, there will be two critical values, $x_{\max}>x_{\min}>0$, bounding the region within which orbiting occurs.[7] Sutton[7] has shown that there is a logarithmic singularity in χ at the orbiting point. In checking his derivation we found a somewhat different coefficient of the logarithmic term:

$$\lim_{\Delta\to 0_-}\chi=\pi+(2^{\frac{1}{2}}b_0/S_0^{\frac{1}{2}})\ln|\Delta|,$$
$$\lim_{\Delta\to 0_+}\chi=\pi+(2^{\frac{1}{2}}b_0/S_0^{\frac{1}{2}})\ln\Delta, \quad (23)$$

where

$$\Delta\equiv b^2-b_0^2,$$

$$S_0=(\partial^2/\partial y^2)\{1-(b^2/r^2)-[\varphi(r)/\tfrac{1}{4}mg^2]\}_{b=b_0,r=r_c(b_0)},$$

and b_0 is the critical value of b for orbiting, which is the value of b for which Eq. (14) has a double root.

The next step is to calculate $Q^{(l)*}(\delta, x)$ by integration over b (or u), using the values of χ obtained in the

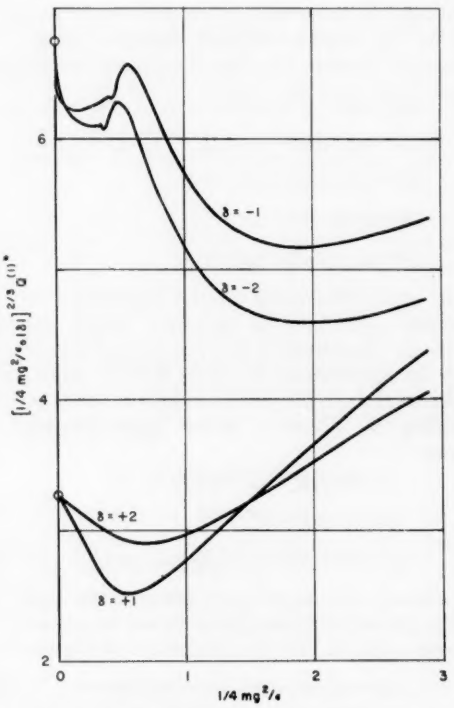

FIG. 1. Reduced cross-sectional function for diffusion $[\frac{1}{4}mg^2/\epsilon_0|\delta|]^{2/3}Q^{(1)*}$ as a function of reduced energy $\frac{1}{4}mg^2/\epsilon$.

TABLE II. True depth and position of the potential minimum: $\varphi(r_m)=-\epsilon$.

δ	ϵ/ϵ_0	r_m/σ_0
0	1.0000	1.1225
−0.25	1.7260	1.0944
−0.50	2.5225	1.0732
−0.75	3.3520	1.0561
−1.0	4.2191	1.0417
−1.5	6.0522	1.0184
−2.0	8.0000	1.0000
−2.5	10.0481	0.9847

first step. For those values of δ and x for which orbiting did not occur, three different integration variables were used: $0 \leq u \leq 0.5$, $0.125 \leq u^3 \leq 0.9$, and $0 \leq b \leq b(u^3=0.9)$. For orbiting x, an additional integration variable $z \propto \ln|\Delta|$ was used on both sides of the orbiting singularity for values of χ between 0 and -2π. The range of integration was subdivided into intervals (usually 14 intervals for nonorbiting and 22 for orbiting), and a five-point Gaussian integration formula used in each interval. The value of χ at each point was evaluated from the table previously set up, using cubic interpolation and b, u^3, or z as the independent variable, the choice depending on which gave the smoothest variation. The contribution of the interval near the orbiting singularity (i.e., $-2\pi > \chi > -\infty$) was calculated by fitting the values of χ near the singularity by the formula,

$$\chi = \pi + A \ln|\Delta|, \tag{24}$$

with A assuming a different value on each side of the singularity. With Eq. (24), an analytic formula is readily obtainable for the contribution to $Q^{(l)*}$ from the orbiting region. $Q^{(l)*}(\delta, x)$ was calculated as a function of x for $\delta = 0$, $+0.25$, ± 0.50, $+0.75$, ± 1.0, ± 1.5, ± 2.0, ± 2.5, and for $l = 1, 2, 3, 4, 5$, and it is felt that for most cases the computational error is about 0.02%, and for all cases is less than 0.1%.

The asymptotic forms of $Q^{(l)*}$ at high and low energies may be established fairly readily. As $x \to \infty$, the repulsive part of the potential becomes increasingly important, and $\varphi(r) \to 4\epsilon_0(\sigma_0/r)^{12}$ as $x \to \infty$. Similarly, as $x \to 0$ the attractive part of the potential becomes dominant, and $\varphi(r) \to 4\epsilon_0\delta(\sigma_0/r)^3$, unless $\delta = 0$, in which case $\varphi(r) \to -4\epsilon_0(\sigma_0/r)^6$. As is well known,[16,17] for inverse-power potentials of the form $\varphi(r) = d(\sigma_0/r)^n$, the reduced cross section takes the form

$$Q^{(l)*} = 2\left[1 - \frac{1}{2}\frac{1+(-1)^l}{1+l}\right]^{-1}\left(\frac{nd}{\frac{1}{4}mg^2}\right)^{2/n} A_{\pm}^{(l)}(n), \tag{25}$$

where $A_{\pm}^{(l)}(n)$ is a pure number whose value depends only on the power n of the potential and on whether the potential is repulsive (subscript $+$) or attractive (subscript $-$). The relevant values of $A_{\pm}^{(l)}(n)$ are summarized in Table I. The values of $A_+^{(l)}(12)$ were obtained by numerical integration of the deflection angles calculated by Bird,[18] and checked by an asymptotic formula given by Mott-Smith.[19] The values of $A_+^{(l)}(3)$ were obtained from Mott-Smith's asymptotic formula.[17,19] The values of $A_-^{(l)}(3)$ were obtained by numerical integration of the deflection angles calculated by Eliason, Stogryn, and Hirschfelder.[17] The values of $A_-^{(l)}(6)$ were taken from the recent summary of Kihara, Taylor, and Hirschfelder.[20] These latter authors also tabulate a number of the other $A^{(l)}(n)$ given in Table I, which had previously been calculated independently by slightly different methods. Their results and ours are in good agreement (better than 0.1%).

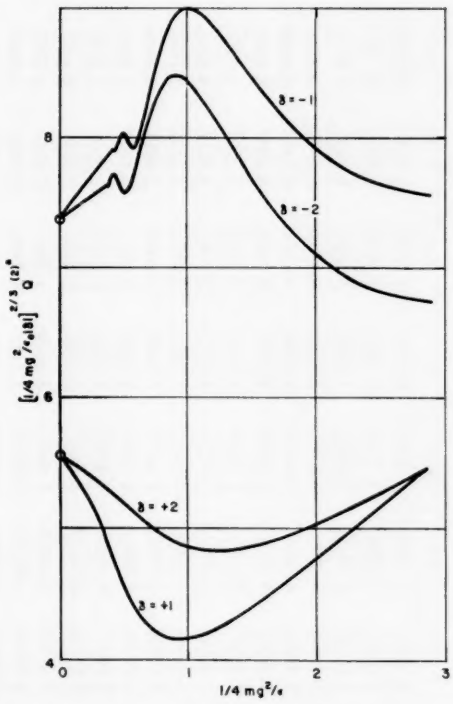

FIG. 2. Reduced cross-sectional function for viscosity $[\frac{1}{4}mg^2/\epsilon_0|\delta|]^{2/3}Q^{(2)*}$ as a function of reduced energy $\frac{1}{4}mg^2/\epsilon$.

We do not tabulate the $Q^{(l)*}$ results here because of their length; but in Figs. 1 and 2 we show graphs of the quantity $[\frac{1}{4}mg^2/\epsilon_0|\delta|]^{\frac{1}{3}}Q^{(l)*}$ as a function of δ and reduced energy for the two most important cases, $l=1$ and 2. This quantity is used rather than $Q^{(l)*}$ itself because it is more slowly varying and is finite at the origin, as Eq. (25) shows. The curves for different values of δ show a clearer family resemblance if the energy is made dimensionless not by ϵ_0, but by the true depth of the potential-energy minimum ϵ. The true depth and position of the minimum are found by numerical solution of the derivative of Eq. (16), and the results are given in Table II for $\delta < 0$ (attractive dipole). The repulsive dipole potential has no minimum for $\delta > (8/27)^{\frac{1}{3}}$, but for consistency we have also used the results of Table II for all $\delta > 0$ in constructing Figs. 1 and 2. The sharp drop from the zero-

[16] MTGL, pp. 546–548.
[17] M. A. Eliason, D. E. Stogryn, and J. O. Hirschfelder, Proc. Natl. Acad. Sci. U. S. **42**, 546 (1956).
[18] MTGL, p. 1155.
[19] H. M. Mott-Smith, MIT Lincoln Laboratory Group Rept. V–2 (December, 1954).
[20] T. Kihara, M. H. Taylor, and J. O. Hirschfelder, Phys. Fluids **3**, 715 (1960).

TABLE III (a). $\Omega^{(1,1)*}$.

T^* \ δ	−2.5	−2.0	−1.5	−1.0	−0.5	0	0.25	0.5	0.75	1.0	1.5	2.0	2.5
0.1	32.491	27.796	22.860	17.337	11.034	4.0079	2.5030	4.8195	7.0752	8.7831	11.683	14.223	16.042
0.2	20.231	17.334	14.250	10.858	7.0967	3.1300	1.8648	2.5558	4.1729	5.3665	7.2732	8.9026	10.378
0.3	15.325	13.141	10.813	8.2836	5.5257	2.6494	1.6049	1.8216	3.0004	3.9671	5.4825	6.7496	7.8875
0.4	12.581	10.796	8.8974	6.8508	4.6309	2.3144	1.4442	1.4953	2.3752	3.1823	4.4702	5.5351	6.4844
0.5	10.796	9.2718	7.6546	5.9160	4.0268	2.0661	1.3343	1.3208	1.9970	2.6795	3.8070	4.7390	5.5655
0.6	9.5286	8.1904	6.7712	5.2434	3.5795	1.8767	1.2556	1.2156	1.7489	2.3320	3.3346	4.1700	4.9086
0.7	8.5753	7.3764	6.1031	4.7278	3.2304	1.7293	1.1966	1.1462	1.5766	2.0795	2.9798	3.7400	4.4118
0.8	7.8277	6.7363	5.5738	4.3143	2.9491	1.6122	1.1509	1.0973	1.4514	1.8890	2.7031	3.4019	4.0205
0.9	7.2226	6.2159	5.1402	3.9730	2.7172	1.5175	1.1144	1.0609	1.3571	1.7411	2.4815	3.1284	3.7032
1.0	6.7201	5.7816	4.7758	3.6850	2.5231	1.4398	1.0845	1.0329	1.2839	1.6235	2.3001	2.9023	3.4399
1.2	5.9263	5.0909	4.1924	3.2244	2.2173	1.3204	1.0382	0.99162	1.1787	1.4496	2.0215	2.5495	3.0269
1.4	5.3195	4.5588	3.7421	2.8717	1.9888	1.2336	1.0038	0.96264	1.1070	1.3283	1.8185	2.2869	2.7165
1.6	4.8352	4.1326	3.3823	2.5938	1.8131	1.1679	0.97690	0.94058	1.0553	1.2394	1.6646	2.0838	2.4742
1.8	4.4363	3.7816	3.0880	2.3694	1.6745	1.1166	0.95503	0.92286	1.0161	1.1719	1.5445	1.9225	2.2797
2.0	4.1006	3.4873	2.8428	2.1852	1.5626	1.0753	0.93686	.90797	0.98537	1.1189	1.4484	1.7912	2.1199
2.5	3.4515	2.9229	2.3808	1.8463	1.3614	1.0006	0.90147	0.87918	0.93080	1.0261	1.2763	1.5509	1.8232
3.0	2.9827	2.5221	2.0594	1.6168	1.2286	0.95003	0.87520	0.85747	0.89424	0.96585	1.1630	1.3887	1.6188
3.5	2.6294	2.2243	1.8258	1.4531	1.1353	0.91311	0.85440	0.83989	0.86740	0.92332	1.0831	1.2724	1.4701
4.0	2.3546	1.9960	1.6495	1.3318	1.0662	0.88453	0.83720	0.82506	0.84643	0.89140	1.0239	1.1852	1.3573
5.0	1.9592	1.6729	1.4042	1.1650	0.97130	0.84277	0.80977	0.80087	0.81486	0.84594	0.94178	1.0637	1.1982
6.0	1.6916	1.4582	1.2435	1.0567	0.90894	0.81287	0.78837	0.78154	0.79143	0.81432	0.88729	0.98319	1.0916
7.0	1.5008	1.3070	1.1318	0.98147	0.86449	0.78976	0.77086	0.76543	0.77282	0.79045	0.84814	0.92586	1.0155
8.0	1.3595	1.1958	1.0494	0.92618	0.83109	0.77111	0.75604	0.75162	0.75737	0.77142	0.81835	0.88283	0.95847
9.0	1.2507	1.1110	0.98706	0.88364	0.80494	0.75553	0.74322	0.73954	0.74416	0.75566	0.79471	0.84923	0.91405
10.0	1.1656	1.0441	0.93815	0.84990	0.78360	0.74220	0.73191	0.72881	0.73262	0.74224	0.77533	0.82214	0.87844
12.0	1.0403	0.94699	0.86604	0.79981	0.75055	0.72022	0.71269	0.71042	0.71316	0.72023	0.74504	0.78084	0.82468
14.0	0.95392	0.87951	0.81546	0.76397	0.72575	0.70254	0.69678	0.69505	0.69714	0.70261	0.72202	0.75047	0.78576
16.0	0.89087	0.82989	0.77819	0.73667	0.70615	0.68776	0.68322	0.68187	0.68354	0.68793	0.70362	0.72688	0.75603
18.0	0.84280	0.79194	0.74929	0.71501	0.69007	0.67510	0.67144	0.67036	0.67174	0.67536	0.68838	0.70782	0.73240
20.0	0.80498	0.76209	0.72605	0.69726	0.67649	0.66405	0.66103	0.66015	0.66133	0.66438	0.67539	0.69194	0.71301
25.0	0.73865	0.70865	0.68355	0.66381	0.64973	0.64136	0.63938	0.63884	0.63970	0.64183	0.64958	0.66134	0.67647
30.0	0.69505	0.67267	0.65416	0.63977	0.62950	0.62350	0.62211	0.62175	0.62244	0.62404	0.62987	0.63875	0.65026
35.0	0.66372	0.64638	0.63216	0.62115	0.61331	0.60882	0.60780	0.60755	0.60814	0.60939	0.61398	0.62099	0.63011
40.0	0.63977	0.62598	0.61475	0.60603	0.59988	0.59640	0.59563	0.59544	0.59597	0.59698	0.60072	0.60642	0.61386
50.0	0.60473	0.59563	0.58819	0.58246	0.57848	0.57626	0.57578	0.57666	0.57612	0.57681	0.57946	0.58347	0.58871
75.0	0.55113	0.54806	0.54560	0.54375	0.54254	0.54146	0.54128	0.54138	0.54158	0.54206	0.54338	0.54532	0.54782
100.0	0.51718	0.51777	0.51829	0.51875	0.51915	0.51803	0.51795	0.51860	0.51820	0.51901	0.51964	0.52049	0.52153

TABLE III (b). $\Omega^{(2,2)*}$.

T^* \ δ	−2.5	−2.0	−1.5	−1.0	−.5	0	0.25	0.5	0.75	1.0	1.5	2.0	2.5
0.1	29.139	25.148	20.830	16.015	10.451	4.1005	3.0142	6.4500	9.4870	11.699	15.508	18.860	21.923
0.2	18.420	15.917	13.211	10.225	6.8596	3.2626	2.1702	3.2515	5.6362	7.1946	9.6786	11.820	13.765
0.3	14.097	12.196	10.146	7.9029	5.4303	2.8399	1.8408	2.2186	4.0126	5.3309	7.3133	8.9737	10.471
0.4	11.668	10.106	8.4275	6.6083	4.6384	2.5310	1.6348	1.7708	3.1216	4.2632	5.9726	7.3682	8.6157
0.5	10.081	8.7414	7.3096	5.7737	4.1155	2.2837	1.4952	1.5375	2.5764	3.5654	5.0888	6.3144	7.4001
0.6	8.9498	7.7708	6.5189	5.1848	3.7272	2.0838	1.3966	1.3997	2.2184	3.0764	4.4541	5.5594	6.5307
0.7	8.0965	7.0416	5.9275	4.7397	3.4170	1.9220	1.3241	1.3105	1.9705	2.7178	3.9732	4.9867	5.8723
0.8	7.4276	6.4722	5.4661	4.3847	3.1588	1.7902	1.2691	1.2487	1.7914	2.4458	3.5951	4.5346	5.3528
0.9	6.8882	6.0142	5.0923	4.0903	2.9388	1.6823	1.2259	1.2034	1.6576	2.2341	3.2899	4.1672	4.9306
1.0	6.4427	5.6362	4.7810	3.8383	2.7488	1.5929	1.1913	1.1688	1.5544	2.0657	3.0384	3.8618	4.5794
1.2	5.7488	5.0427	4.2814	3.4239	2.4382	1.4551	1.1391	1.1192	1.4076	1.8169	2.6495	3.3822	4.0259
1.4	5.2280	4.5900	3.8897	3.0928	2.1967	1.3551	1.1012	1.0846	1.3091	1.6440	2.3638	3.0221	3.6074
1.6	4.8159	4.2254	3.5677	2.8214	2.0057	1.2800	1.0722	1.0587	1.2390	1.5182	2.1464	2.7416	3.2786
1.8	4.4774	3.9202	3.2965	2.5953	1.8522	1.2219	1.0491	1.0382	1.1865	1.4232	1.9762	2.5173	3.0131
2.0	4.1898	3.6589	3.0638	2.4045	1.7270	1.1757	1.0300	1.0212	1.1458	1.3492	1.8399	2.3341	2.7939
2.5	3.6210	3.1378	2.6058	2.0415	1.4993	1.0933	0.99337	0.98859	1.0748	1.2210	1.5960	1.9969	2.3838
3.0	3.1902	2.7466	2.2710	1.7881	1.3486	1.0388	0.96645	0.96415	1.0281	1.1391	1.4361	1.7683	2.0992
3.5	2.8502	2.4433	2.0194	1.6045	1.2430	0.99963	0.94519	0.94453	0.99448	1.0822	1.3240	1.6042	1.8910
4.0	2.5756	2.2032	1.8255	1.4672	1.1655	0.96988	0.92764	0.92808	0.96854	1.0400	1.2414	1.4814	1.7326
5.0	2.1635	1.8526	1.5510	1.2784	1.0605	0.92676	0.89963	0.90136	0.93011	0.98086	1.1281	1.3108	1.5089
6.0	1.8736	1.6134	1.3694	1.1566	0.99273	0.89616	0.87766	0.88005	0.90203	0.94049	1.0539	1.1985	1.3594
7.0	1.6622	1.4429	1.2426	1.0727	0.94537	0.87272	0.85956	0.86230	0.87996	0.91048	1.0012	1.1191	1.2529
8.0	1.5033	1.3169	1.1501	1.0115	0.91013	0.85379	0.84417	0.84709	0.86180	0.88684	0.96160	1.0600	1.1734
9.0	1.3806	1.2208	1.0801	0.96522	0.88269	0.83795	0.83079	0.83379	0.84637	0.86745	0.93046	1.0142	1.1118
10.0	1.2839	1.1456	1.0256	0.92892	0.86055	0.82435	0.81895	0.82198	0.83296	0.85108	0.90517	0.97754	1.0627
12.0	1.1424	1.0364	0.94629	0.87547	0.82661	0.80184	0.79874	0.80172	0.81047	0.82449	0.86609	0.92218	0.98904
14.0	1.0452	0.96153	0.89171	0.83772	0.80132	0.78363	0.78189	0.78478	0.79207	0.80342	0.83680	0.88197	0.93627
16.0	0.97494	0.90740	0.85178	0.80938	0.78137	0.76834	0.76747	0.77024	0.77650	0.78600	0.81365	0.85108	0.89633
18.0	0.92214	0.86654	0.82120	0.78711	0.76498	0.75518	0.75488	0.75753	0.76303	0.77117	0.79464	0.82637	0.86485
20.0	0.88115	0.83457	0.79693	0.76897	0.75112	0.74364	0.74372	0.74626	0.75117	0.75828	0.77859	0.80596	0.83923
25.0	0.81004	0.77827	0.75314	0.73492	0.72377	0.71982	0.72045	0.72270	0.72662	0.73198	0.74700	0.76707	0.79150
30.0	0.76376	0.74088	0.72306	0.71041	0.70302	0.70097	0.70183	0.70381	0.70713	0.71137	0.72317	0.73876	0.75770
35.0	0.73046	0.71348	0.70044	0.69140	0.68638	0.68545	0.68641	0.68813	0.69107	0.69450	0.70412	0.71669	0.73192
40.0	0.70459	0.69195	0.68238	0.67591	0.67256	0.67232	0.67331	0.67480	0.67746	0.68028	0.68832	0.69870	0.71121
50.0	0.66536	0.65902	0.65445	0.65164	0.65061	0.65099	0.65195	0.65314	0.65538	0.65733	0.66314	0.67045	0.67917
75.0	0.60030	0.60470	0.60849	0.61171	0.61438	0.61397	0.61475	0.61624	0.61708	0.61832	0.62067	0.62330	0.62620
100.0	0.55518	0.56801	0.57833	0.58620	0.59170	0.58870	0.58931	0.59240	0.59105	0.59291	0.59278	0.59207	0.59082

TABLE IV. $\langle\Omega^{(1,1)*}\rangle$.

T^* \ δ	0	0.25	0.50	0.75	1.0	1.5	2.0	2.5
0.1	4.0079	4.002	4.655	5.521	6.454	8.214	9.824	11.31
0.2	3.1300	3.164	3.355	3.721	4.198	5.230	6.225	7.160
0.3	2.6494	2.657	2.770	3.002	3.319	4.054	4.785	5.483
0.4	2.3144	2.320	2.402	2.572	2.812	3.386	3.972	4.539
0.5	2.0661	2.073	2.140	2.278	2.472	2.946	3.437	3.918
0.6	1.8767	1.885	1.944	2.060	2.225	2.628	3.054	3.474
0.7	1.7293	1.738	1.791	1.893	2.036	2.388	2.763	3.137
0.8	1.6122	1.622	1.670	1.760	1.886	2.198	2.535	2.872
0.9	1.5175	1.527	1.572	1.653	1.765	2.044	2.349	2.657
1.0	1.4398	1.450	1.490	1.564	1.665	1.917	2.196	2.478
1.2	1.3204	1.330	1.364	1.425	1.509	1.720	1.956	2.199
1.4	1.2336	1.242	1.272	1.324	1.394	1.573	1.777	1.990
1.6	1.1679	1.176	1.202	1.246	1.306	1.461	1.639	1.827
1.8	1.1166	1.124	1.146	1.185	1.237	1.372	1.530	1.698
2.0	1.0753	1.082	1.102	1.135	1.181	1.300	1.441	1.592
2.5	1.0006	1.005	1.020	1.046	1.080	1.170	1.278	1.397
3.0	0.95003	0.9538	0.9656	0.9852	1.012	1.082	1.168	1.265
3.5	0.91311	0.9162	0.9256	0.9413	0.9626	1.019	1.090	1.170
4.0	0.88453	0.8871	0.8948	0.9076	0.9252	0.9721	1.031	1.098
5.0	0.84277	0.8446	0.8501	0.8592	0.8716	0.9053	0.9483	0.9984
6.0	0.81287	0.8142	0.8183	0.8251	0.8344	0.8598	0.8927	0.9316
7.0	0.78976	0.7908	0.7940	0.7993	0.8066	0.8265	0.8526	0.8836
8.0	0.77111	0.7720	0.7745	0.7788	0.7846	0.8007	0.8219	0.8474
9.0	0.75553	0.7562	0.7584	0.7619	0.7667	0.7800	0.7976	0.8189
10.0	0.74220	0.7428	0.7446	0.7475	0.7515	0.7627	0.7776	0.7957
12.0	0.72022	0.7206	0.7220	0.7241	0.7271	0.7354	0.7464	0.7600
14.0	0.70254	0.7029	0.7039	0.7055	0.7078	0.7142	0.7228	0.7334
16.0	0.68776	0.6880	0.6888	0.6901	0.6919	0.6970	0.7040	0.7125
18.0	0.67510	0.6753	0.6760	0.6770	0.6785	0.6827	0.6884	0.6955
20.0	0.66405	0.6642	0.6648	0.6657	0.6669	0.6704	0.6752	0.6811
25.0	0.64136	0.6415	0.6418	0.6425	0.6433	0.6457	0.6490	0.6531
30.0	0.62350	0.6236	0.6239	0.6243	0.6249	0.6267	0.6291	0.6321
35.0	0.60882	0.6089	0.6091	0.6094	0.6099	0.6112	0.6131	0.6154
40.0	0.59640	0.5964	0.5966	0.5969	0.5972	0.5983	0.5998	0.6017
50.0	0.57626	0.5763	0.5764	0.5766	0.5768	0.5775	0.5785	0.5798
75.0	0.54146	0.5415	0.5416	0.5416	0.5418	0.5421	0.5424	0.5429
100.0	0.51803	0.5181	0.5182	0.5184	0.5184	0.5185	0.5186	0.5187

energy intercept for $\delta<0$ in Fig. 1 is a little surprising. It is real, however, and was verified by performing some extra calculations at very low energy.

Once a table of $Q^{(l)*}(\delta, x)$ was available, the third step of calculating $\Omega^{(l,s)*}(\delta, T^*)$ by numerical integration over γ^2 (or x) could be carried out. It was found convenient to transform to the variable

$$\alpha=\exp(-\gamma^2/6)=\exp(-2x/3T^*), \qquad (26)$$

so that Eq. (11) becomes

$$\Omega^{(l,s)*}=6[(s+1)!]^{-1}\int_0^1 \alpha^\delta(-6\ln\alpha)^{s+1}Q^{(l)*}d\alpha. \qquad (27)$$

This new variable α has the advantage that, besides the fact that a finite integration region is obtained, the point where the maximum of the integrand occurs is relatively insensitive to the value of T^* and occurs between $\alpha=0.3$ and 0.7, depending on the value of s.

The $\Omega^{(l,s)*}$ were evaluated by cutting the integration region into eleven intervals and using a seven-point Gaussian integration formula in each interval, the necessary $Q^{(l)*}$ being evaluated at each point by cubic interpolation from the table previously obtained. The $\Omega^{(l,s)*}$ were evaluated for values of l from 1 through 4, and values of s from l through 6. We present here (Table III) only the results for the two most important integrals, $\Omega^{(1,1)*}$ and $\Omega^{(2,2)*}$, because of the length of the tabulations and because a final averaging over orientation must be performed before any transport properties can be calculated. We estimate the accuracy to be generally of the order of 0.05%, except at the extreme ends of the table. This is indicated by the slight deviations of our results from those of Hirschfelder, Bird, and Spotz[21] for $\delta=0$ and of Itean, Glueck, and Svehla[6] for $\delta\leq 0$. For very large values of T^*, our values of $\Omega^{(l,s)*}$ vary with δ in the opposite direction from those of Itean, Glueck, and Svehla. We are not able to offer any explanation for these divergences, which are larger than we would have expected. There is little incentive for tracing down the source of the discrepancies, however, since the discrepancies are small in the first place, and in the second place, at these high temperatures, the model is physically unrealistic because the inverse twelfth-power repulsion term has become almost completely dominant.

The final step is the calculation of the orientation-

[21] J. O. Hirschfelder, R. B. Bird, and E. L. Spotz, J. Chem. Phys. **16**, 968 (1948). See also MTGL, pp. 1126–1127.

TABLE V. $\langle\Omega^{(2,2)*}\rangle$.

T^* \ δ	0	0.25	0.50	0.75	1.0	1.5	2.0	2.5
0.1	4.1005	4.266	4.833	5.742	6.729	8.624	10.34	11.89
0.2	3.2626	3.305	3.516	3.914	4.433	5.570	6.637	7.618
0.3	2.8399	2.836	2.936	3.168	3.511	4.329	5.126	5.874
0.4	2.5310	2.522	2.586	2.749	3.004	3.640	4.282	4.895
0.5	2.2837	2.277	2.329	2.460	2.665	3.187	3.727	4.249
0.6	2.0838	2.081	2.130	2.243	2.417	2.862	3.329	3.786
0.7	1.9220	1.924	1.970	2.072	2.225	2.614	3.028	3.435
0.8	1.7902	1.795	1.840	1.934	2.070	2.417	2.788	3.156
0.9	1.6823	1.689	1.733	1.820	1.944	2.258	2.596	2.933
1.0	1.5929	1.601	1.644	1.725	1.838	2.124	2.435	2.746
1.2	1.4551	1.465	1.504	1.574	1.670	1.913	2.181	2.451
1.4	1.3551	1.365	1.400	1.461	1.544	1.754	1.989	2.228
1.6	1.2800	1.289	1.321	1.374	1.447	1.630	1.838	2.053
1.8	1.2219	1.231	1.259	1.306	1.370	1.532	1.718	1.912
2.0	1.1757	1.184	1.209	1.251	1.307	1.451	1.618	1.795
2.5	1.0933	1.100	1.119	1.150	1.193	1.304	1.435	1.578
3.0	1.0388	1.044	1.059	1.083	1.117	1.204	1.310	1.428
3.5	0.99963	1.004	1.016	1.035	1.062	1.133	1.220	1.319
4.0	0.96988	0.9732	0.9830	0.9991	1.021	1.079	1.153	1.236
5.0	0.92676	0.9291	0.9360	0.9473	0.9628	1.005	1.058	1.121
6.0	0.89616	0.8979	0.9030	0.9114	0.9230	0.9545	0.9955	1.044
7.0	0.87272	0.8741	0.8780	0.8845	0.8935	0.9181	0.9505	0.9893
8.0	0.85379	0.8549	0.8580	0.8632	0.8703	0.8901	0.9164	0.9482
9.0	0.83795	0.8388	0.8414	0.8456	0.8515	0.8678	0.8895	0.9160
10.0	0.82435	0.8251	0.8273	0.8308	0.8356	0.8493	0.8676	0.8901
12.0	0.80184	0.8024	0.8039	0.8065	0.8101	0.8201	0.8337	0.8504
14.0	0.78363	0.7840	0.7852	0.7872	0.7899	0.7976	0.8081	0.8212
16.0	0.76834	0.7687	0.7696	0.7712	0.7733	0.7794	0.7878	0.7983
18.0	0.75518	0.7554	0.7562	0.7575	0.7592	0.7642	0.7711	0.7797
20.0	0.74364	0.7438	0.7445	0.7455	0.7470	0.7512	0.7569	0.7642
25.0	0.71982	0.7200	0.7204	0.7211	0.7221	0.7250	0.7289	0.7339
30.0	0.70097	0.7011	0.7014	0.7019	0.7026	0.7047	0.7076	0.7112
35.0	0.68545	0.6855	0.6858	0.6861	0.6867	0.6883	0.6905	0.6932
40.0	0.67232	0.6724	0.6726	0.6728	0.6733	0.6745	0.6762	0.6784
50.0	0.65099	0.6510	0.6512	0.6513	0.6516	0.6524	0.6534	0.6546
75.0	0.61397	0.6141	0.6143	0.6145	0.6147	0.6148	0.6148	0.6147
100.0	0.58870	0.5889	0.5894	0.5900	0.5903	0.5901	0.5895	0.5885

averaged collision integrals according to Eq. (15). These averaged collision integrals are functions of T^* and of δ_{max}, where $\delta_{max}=\frac{1}{2}\mu^{*2}$ is the maximum value that can be taken by δ as defined in Eq. (17). It was found that a single interval with five-point Gaussian integration in each of the variables, $\cos\theta_1$, $\cos\theta_2$, and ϕ, was sufficient to yield 1–2% accuracy for

$$\langle\Omega^{(l,s)*}(\delta_{max}, T^*)\rangle$$

in extreme cases (large δ_{max} and small T^*), and much better than that in most cases.

The tabulation of the averaged-collision integrals are most conveniently given in terms of the ratios defined in Eq. (8). In Tables IV–XI are tabulated, respectively, the functions $\langle\Omega^{(1,1)*}\rangle$, $\langle\Omega^{(2,2)*}\rangle$, $\langle A^*\rangle$, $\langle B^*\rangle$, $\langle C^*\rangle$, $\langle E^*\rangle$, $\langle F^*\rangle$, and α_0. From these can be calculated all the transport properties of both pure gases and multicomponent mixtures with a convergence error (of the basic kinetic-theory formulas, which are actually infinite series) which is probably less than the usual experimental error.

V. COMPARISON WITH EXPERIMENT

A. Determination of Potential Parameters from Viscosities

The first test of the present model is whether the potential parameters σ_0, ϵ_0, and δ_{max} (or μ^*) can be chosen so as to reproduce the available experimental data on the transport properties of polar gases. Viscosity is unfortunately the only transport property for which suitable data exist. The thermal conductivity cannot be used because of the uncertain Eucken correction, and the data on self-diffusion and thermal diffu-

TABLE VI. $\langle A^* \rangle$.

T^* \ δ	0	0.25	0.50	0.75	1.0	1.5	2.0	2.5
0	1.0065	1.084	1.084	1.084	1.084	1.084	1.084	1.084
0.1	1.0231	1.066	1.038	1.040	1.043	1.050	1.052	1.051
0.2	1.0424	1.045	1.048	1.052	1.056	1.065	1.066	1.064
0.3	1.0719	1.067	1.060	1.055	1.058	1.068	1.071	1.071
0.4	1.0936	1.087	1.077	1.069	1.068	1.075	1.078	1.078
0.5	1.1053	1.098	1.088	1.080	1.078	1.082	1.084	1.084
0.6	1.1104	1.104	1.096	1.089	1.086	1.089	1.090	1.090
0.7	1.1114	1.107	1.100	1.095	1.093	1.095	1.096	1.095
0.8	1.1104	1.107	1.102	1.099	1.098	1.100	1.100	1.099
0.9	1.1086	1.106	1.102	1.101	1.101	1.105	1.105	1.104
1.0	1.1063	1.104	1.103	1.103	1.104	1.108	1.109	1.108
1.2	1.1020	1.102	1.103	1.105	1.107	1.112	1.115	1.115
1.4	1.0985	1.099	1.101	1.104	1.108	1.115	1.119	1.120
1.6	1.0960	1.096	1.099	1.103	1.108	1.116	1.121	1.124
1.8	1.0943	1.095	1.099	1.102	1.108	1.117	1.123	1.126
2.0	1.0934	1.094	1.097	1.102	1.107	1.116	1.123	1.128
2.5	1.0926	1.094	1.097	1.099	1.105	1.115	1.123	1.130
3.0	1.0934	1.095	1.097	1.099	1.104	1.113	1.122	1.129
3.5	1.0948	1.096	1.098	1.100	1.103	1.112	1.119	1.127
4.0	1.0965	1.097	1.099	1.101	1.104	1.110	1.118	1.126
5.0	1.0997	1.100	1.101	1.102	1.105	1.110	1.116	1.123
6.0	1.1025	1.103	1.104	1.105	1.106	1.110	1.115	1.121
7.0	1.1050	1.105	1.106	1.107	1.108	1.111	1.115	1.120
8.0	1.1072	1.107	1.108	1.108	1.109	1.112	1.115	1.119
9.0	1.1091	1.109	1.109	1.110	1.111	1.113	1.115	1.119
10.0	1.1107	1.111	1.111	1.111	1.112	1.114	1.116	1.119
12.0	1.1133	1.114	1.113	1.114	1.114	1.115	1.117	1.119
14.0	1.1154	1.115	1.116	1.116	1.116	1.117	1.118	1.120
16.0	1.1172	1.117	1.117	1.118	1.118	1.118	1.119	1.120
18.0	1.1186	1.119	1.119	1.119	1.119	1.119	1.120	1.121
20.0	1.1199	1.120	1.120	1.120	1.120	1.121	1.121	1.122
25.0	1.1223	1.122	1.122	1.122	1.122	1.123	1.123	1.124
30.0	1.1243	1.124	1.124	1.124	1.124	1.124	1.125	1.125
35.0	1.1259	1.126	1.126	1.126	1.126	1.126	1.126	1.126
40.0	1.1273	1.127	1.127	1.127	1.127	1.127	1.127	1.128
50.0	1.1297	1.130	1.130	1.130	1.130	1.130	1.130	1.129
75.0	1.1339	1.134	1.134	1.135	1.135	1.134	1.134	1.132
100.0	1.1364	1.137	1.137	1.138	1.139	1.138	1.137	1.135
∞	1.14187	1.14187	1.14187	1.14187	1.14187	1.14187	1.14187	1.14187

sion are so meager that they can only be used as checks at the end.

The available viscosity data seldom justify treating all three potential parameters as freely disposable. Furthermore, we wish the parameters to have as much physical significance as possible. We therefore require that the dipole-dipole term of the potential be correct, thereby reducing the number of disposable parameters to two. From a comparison of Eqs. (2) and (16), we see that this imposes the condition

$$4\epsilon_0\sigma_0^3\delta_{\max}=2\mu^2, \tag{28}$$

where μ is the experimentally determined dipole moment of the molecule. To determine ϵ_0 and σ_0 from experimental viscosities and dipole moments, we use a graphical curve translation method. Substituting Eq. (28) into Eq. (5) and converting to practical units, we can write

$$\log[10^7\eta/(M^{\frac{1}{2}}T^{7/6})]=\log[(T^*)^{2/3}\langle\Omega^{(2,2)*}\rangle]^{-1}+0.05377 -\tfrac{4}{3}\log\mu+\tfrac{2}{3}\log\delta_{\max}, \tag{29}$$

$$\log T=\log T^*+\log(\epsilon_0/k), \tag{30}$$

where η is in g/cm-sec, M is the molecular weight in g/mole, T is in °K, and μ is in debyes (1 debye $=10^{-18}$ esu). The value of f_η has been taken as unity, which is consistent with the experimental accuracy of η. From Eqs. (29) and (30), we see that a plot of the experimental quantities $\log[10^7\eta/(M^{1/2}T^{7/6})]$ vs $\log T$ should be superposable by translation of axes on a plot of the theoretical quantities $\log[(T^*)^{2/3}\langle\Omega^{(2,2)*}\rangle]^{-1}$ vs $\log T^*$, if the model is capable of representing the data. The amount of translation along the temperature axis (abscissa) determines ϵ_0/k. The amount of translation along the ordinate is determined by the experimental value of μ and by the choice of $\delta_{\max}$.

The procedure for determining the potential parameters can be summarized as follows: (1) A value of $\delta_{\max}$ is chosen arbitrarily. This value and the known value of μ determine the translation along the ordinate. (2) The experimental plot (on transparent paper) is then moved over the theoretical plot by translation along the abscissa alone until a good fit is obtained with the theoretical curve corresponding to the chosen $\delta_{\max}$. (3) A new value of $\delta_{\max}$ is chosen and the process repeated, until the value of $\delta_{\max}$ is found which gives

TABLE VII. $\langle B^* \rangle$.

T^* \ δ	0	0.25	0.50	0.75	1.0	1.5	2.0	2.5
0	1.1852	1.2963	1.2963	1.2963	1.2963	1.2963	1.2963	1.2963
0.1	1.1960	1.216	1.237	1.269	1.285	1.290	1.297	1.294
0.2	1.2451	1.257	1.340	1.389	1.366	1.327	1.314	1.278
0.3	1.2900	1.294	1.272	1.258	1.262	1.282	1.290	1.299
0.4	1.2986	1.291	1.284	1.278	1.277	1.288	1.294	1.297
0.5	1.2865	1.281	1.276	1.272	1.277	1.286	1.292	1.298
0.6	1.2665	1.264	1.261	1.263	1.269	1.284	1.292	1.298
0.7	1.2455	1.244	1.248	1.255	1.262	1.278	1.289	1.296
0.8	1.2253	1.225	1.234	1.240	1.252	1.271	1.284	1.295
0.9	1.2078	1.210	1.216	1.227	1.242	1.264	1.281	1.292
1.0	1.1919	1.192	1.205	1.216	1.230	1.256	1.273	1.287
1.2	1.1678	1.172	1.181	1.195	1.209	1.237	1.261	1.277
1.4	1.1496	1.155	1.161	1.174	1.189	1.221	1.246	1.266
1.6	1.1366	1.141	1.147	1.159	1.174	1.202	1.231	1.256
1.8	1.1270	1.130	1.138	1.148	1.162	1.191	1.218	1.242
2.0	1.1197	1.122	1.129	1.140	1.149	1.178	1.205	1.231
2.5	1.1080	1.110	1.116	1.122	1.132	1.154	1.180	1.205
3.0	1.1016	1.103	1.107	1.112	1.120	1.138	1.160	1.183
3.5	1.0980	1.099	1.102	1.106	1.112	1.127	1.145	1.165
4.0	1.0958	1.097	1.099	1.102	1.107	1.119	1.135	1.153
5.0	1.0935	1.094	1.095	1.097	1.100	1.109	1.120	1.134
6.0	1.0925	1.092	1.094	1.095	1.098	1.104	1.112	1.122
7.0	1.0922	1.092	1.093	1.094	1.096	1.100	1.106	1.115
8.0	1.0922	1.092	1.093	1.093	1.095	1.098	1.103	1.110
9.0	1.0923	1.092	1.093	1.093	1.094	1.097	1.101	1.106
10.0	1.0923	1.092	1.092	1.093	1.094	1.096	1.099	1.103
12.0	1.0927	1.093	1.093	1.093	1.094	1.095	1.098	1.101
14.0	1.0930	1.093	1.093	1.093	1.094	1.094	1.096	1.099
16.0	1.0933	1.094	1.093	1.094	1.094	1.095	1.096	1.098
18.0	1.0937	1.093	1.094	1.094	1.094	1.094	1.096	1.097
20.0	1.0939	1.094	1.094	1.094	1.094	1.095	1.095	1.097
25.0	1.0943	1.094	1.094	1.094	1.095	1.095	1.096	1.096
30.0	1.0944	1.095	1.094	1.094	1.094	1.095	1.095	1.096
35.0	1.0944	1.094	1.095	1.094	1.094	1.095	1.096	1.096
40.0	1.0943	1.095	1.094	1.094	1.095	1.095	1.095	1.095
50.0	1.0941	1.094	1.094	1.094	1.094	1.094	1.094	1.096
75.0	1.0947	1.095	1.094	1.094	1.093	1.093	1.094	1.095
100.0	1.0957	1.095	1.094	1.093	1.092	1.093	1.093	1.094
∞	1.10185	1.10185	1.10185	1.10185	1.10185	1.10185	1.10185	1.10185

the best fit. The abscissa translation for this best δ_{max} gives the best value of ϵ_0/k. (4) The corresponding best value of σ_0 is then determined by substitution into Eq. (28), which in practical units takes the form

$$\sigma_0^3 = 3622.0\mu^2(\delta_{max})^{-1}(\epsilon_0/k)^{-1}, \qquad (31)$$

where σ_0 is in angstroms, μ is in debyes, and ϵ_0/k is in °K.

One advantage of the graphical curve translation method is that discrepancies and trends in the experimental data are immediately apparent, and allowance for these can be easily made. A disadvantage is that the method is somewhat subjective and is thus probably not suitable for extremely accurate data. In such cases an objective least-squares procedure is probably called for, but the graphical method is still useful for furnishing starting values of parameters. No such cases were encountered in the present work, and indeed some of the discrepancies between different experimental investigations were surprisingly large. It is apparently more difficult to obtain consistent viscosity measurements for polar gases than for nonpolar gases, perhaps because of adsorption and association effects. Steam, for example, is notoriously difficult.

The results are summarized in Table XII, together with the dipole moments used and the references to the experimental data. We have not included the molecules CO and NO, which are so weakly polar that they can reasonably be classed as nonpolar for the present purposes. Dipole moments were taken from the critical compilation of Maryott and Buckley,[22] except for nitrosyl chloride.[23] In some cases the value used is an average of several slightly different experimental values. Many of the gases listed can also be fitted reasonably well by the nonpolar Lennard-Jones (12–6) potential, which corresponds to the present potential with $\delta_{max}=0$. These 12–6 potential parameters are also listed in Table XII for comparison. Many were taken directly from the extensive tabulation in MTGL, but we have redetermined some of them to allow for new

[22] A. A. Maryott and F. Buckley, *Table of Dielectric Constants and Electric Dipole Moments of Substances in the Gaseous State* (National Bureau of Standards, June 25, 1953), Circ. 537.

[23] J. A. A. Ketelaar, Rec. trav. chim. **62,** 289 (1934).

TABLE VIII. $\langle C^* \rangle$.

T^* \ δ	0	0.25	0.50	0.75	1.0	1.5	2.0	2.5
0	0.8889	0.77778	0.77778	0.77778	0.77778	0.77778	0.77778	0.77778
0.1	0.88575	0.8988	0.8378	0.8029	0.7876	0.7805	0.7799	0.7801
0.2	0.87268	0.8692	0.8647	0.8479	0.8237	0.7975	0.7881	0.7784
0.3	0.85182	0.8525	0.8386	0.8198	0.8054	0.7903	0.7839	0.7820
0.4	0.83542	0.8362	0.8306	0.8196	0.8076	0.7918	0.7842	0.7808
0.5	0.82629	0.8278	0.8252	0.8169	0.8074	0.7916	0.7838	0.7802
0.6	0.82299	0.8249	0.8230	0.8165	0.8072	0.7922	0.7839	0.7798
0.7	0.82357	0.8257	0.8241	0.8178	0.8084	0.7927	0.7839	0.7794
0.8	0.82657	0.8280	0.8264	0.8199	0.8107	0.7939	0.7842	0.7796
0.9	0.83110	0.8324	0.8295	0.8228	0.8136	0.7960	0.7854	0.7798
1.0	0.83630	0.8366	0.8342	0.8267	0.8168	0.7986	0.7864	0.7805
1.2	0.84762	0.8474	0.8438	0.8358	0.8250	0.8041	0.7904	0.7822
1.4	0.85846	0.8583	0.8530	0.8444	0.8336	0.8118	0.7957	0.7854
1.6	0.86840	0.8674	0.8619	0.8531	0.8423	0.8186	0.8011	0.7898
1.8	0.87713	0.8755	0.8709	0.8616	0.8504	0.8265	0.8072	0.7939
2.0	0.88479	0.8831	0.8779	0.8695	0.8578	0.8338	0.8133	0.7990
2.5	0.89972	0.8986	0.8936	0.8846	0.8742	0.8504	0.8294	0.8125
3.0	0.91028	0.9089	0.9043	0.8967	0.8869	0.8649	0.8438	0.8253
3.5	0.91793	0.9166	0.9125	0.9058	0.8970	0.8768	0.8557	0.8372
4.0	0.92371	0.9226	0.9189	0.9128	0.9050	0.8861	0.8664	0.8484
5.0	0.93135	0.9304	0.9274	0.9226	0.9164	0.9006	0.8833	0.8662
6.0	0.93607	0.9353	0.9329	0.9291	0.9240	0.9109	0.8958	0.8802
7.0	0.93927	0.9387	0.9366	0.9334	0.9292	0.9182	0.9050	0.8911
8.0	0.94149	0.9409	0.9393	0.9366	0.9331	0.9236	0.9122	0.8997
9.0	0.94306	0.9426	0.9412	0.9388	0.9357	0.9276	0.9175	0.9065
10.0	0.94419	0.9437	0.9425	0.9406	0.9380	0.9308	0.9219	0.9119
12.0	0.94571	0.9455	0.9445	0.9430	0.9409	0.9353	0.9283	0.9201
14.0	0.94662	0.9464	0.9456	0.9444	0.9428	0.9382	0.9325	0.9258
16.0	0.94723	0.9471	0.9464	0.9455	0.9442	0.9405	0.9355	0.9298
18.0	0.94764	0.9474	0.9469	0.9462	0.9450	0.9418	0.9378	9.9328
20.0	0.94790	0.9478	0.9474	0.9465	0.9457	0.9430	0.9394	0.9352
25.0	0.94827	0.9481	0.9480	0.9472	0.9467	0.9447	0.9422	0.9391
30.0	0.94842	0.9484	0.9481	0.9478	0.9472	0.9458	0.9437	0.9415
35.0	0.94852	0.9484	0.9483	0.9480	0.9475	0.9465	0.9449	0.9430
40.0	0.94861	0.9487	0.9484	0.9481	0.9479	0.9468	0.9455	0.9438
50.0	0.94872	0.9486	0.9486	0.9483	0.9482	0.9475	0.9464	0.9452
75.0	0.94881	0.9488	0.9489	0.9490	0.8487	0.9482	0.9476	0.9468
100.0	0.94863	0.9487	0.9489	0.9491	0.9493	0.9491	0.9483	0.9476
∞	0.94444	0.94444	0.94444	0.94444	0.94444	0.94444	0.94444	0.94444

or previously overlooked data. A few strictly nonpolar molecules are also included in the table for comparison or to round out homologous series. Finally, the available results from second virial coefficients[24] for the Stockmayer potential are given in Table XIII for comparison.

Before commenting in detail on Tables XII and XIII, it is helpful to see some of the results of the present model displayed graphically. Figure 3 shows plots of the sort used in determining the potential parameters. The curves for different values of δ_{max} coalesce at high temperatures and have different finite intercepts at zero temperature (except the curve for $\delta_{max}=0$, which has a singularity). The experimental data shown are representative of all the systems studied. For a standard of comparison the typical nonpolar gas N_2 is shown with the $\delta_{max}=0$ curve. The typical feature introduced by the dipole term in these plots is the flattening out of the curve at low temperatures. The results for SO_2 are typical of most gases which are only moderately polar, in that δ_{max} is equal to 0.5 or less. The only atypical thing about the SO_2 results is the rather large temperature range covered. Our only good examples of highly polar gases are NH_3 and H_2O, and the very scattered experimental results for the latter are shown. In a sense this is not a very fair comparison, both because H_2O is so difficult experimentally and also because our model of a point dipole embedded in a spherical 12–6 potential can hardly be expected to represent a molecule which forms hydrogen bonds as readily as H_2O does. Nevertheless, the results at least illustrate the most extreme case encountered. (HCN is probably another highly polar case, but the experimental data are too scanty.) In general, the fits of experimental data are good, and are comparable to those obtained with the 12–6 potential for nonpolar gases.[2]

Returning now to Table XII, we see that the present parameters are generally physically reasonable and show reasonable trends in homologous series. They are not radically different from the parameters obtained by omitting the dipole term (12–6) potential, suggesting that viscosity is not very sensitive to the long-range

[24] J. S. Rowlinson, Trans. Faraday Soc. **45**, 974 (1949); see also MTGL, p. 214.

TABLE IX. $\langle E^* \rangle$.

T^* \ δ	0	0.25	0.50	0.75	1.0	1.5	2.0	2.5
0	0.91667	0.83333	0.83333	0.83333	0.83333	0.83333	0.83333	0.83333
0.1	0.91652	0.8669	0.8258	0.8015	0.7970	0.8081	0.8182	0.8247
0.2	0.91829	0.9129	0.8877	0.8643	0.8511	0.8445	0.8397	0.8409
0.3	0.90774	0.9073	0.8910	0.8715	0.8590	0.8457	0.8426	0.8418
0.4	0.89143	0.8906	0.8859	0.8763	0.8652	0.8500	0.8440	0.8413
0.5	0.87857	0.8810	0.8789	0.8728	0.8649	0.8510	0.8446	0.8416
0.6	0.87081	0.8741	0.8751	0.8725	0.8659	0.8529	0.8456	0.8418
0.7	0.86743	0.8706	0.8731	0.8711	0.8656	0.8535	0.8461	0.8422
0.8	0.86722	0.8702	0.8728	0.8707	0.8662	0.8544	0.8476	0.8435
0.9	0.86899	0.8721	0.8736	0.8714	0.8663	0.8547	0.8475	0.8435
1.0	0.87212	0.8745	0.8753	0.8725	0.8672	0.8555	0.8480	0.8438
1.2	0.88028	0.8812	0.8810	0.8767	0.8707	0.8578	0.8496	0.8450
1.4	0.88909	0.8894	0.8879	0.8830	0.8756	0.8616	0.8517	0.8461
1.6	0.89758	0.8976	0.8940	0.8886	0.8804	0.8650	0.8542	0.8475
1.8	0.90515	0.9041	0.9007	0.8943	0.8861	0.8695	0.8568	0.8494
2.0	0.91188	0.9105	0.9065	0.9001	0.8914	0.8739	0.8609	0.8524
2.5	0.92509	0.9236	0.9205	0.9130	0.9044	0.8857	0.8704	0.8593
3.0	0.93431	0.9329	0.9289	0.9230	0.9141	0.8962	0.8802	0.8669
3.5	0.94095	0.9394	0.9358	0.9305	0.9228	0.9056	0.8893	0.8749
4.0	0.94573	0.9446	0.9414	0.9361	0.9293	0.9139	0.8977	0.8835
5.0	0.95202	0.9511	0.9485	0.9454	0.9388	0.9252	0.9112	0.8974
6.0	0.95577	0.9550	0.9529	0.9496	0.9451	0.9338	0.9210	0.9082
7.0	0.95812	0.9574	0.9558	0.9531	0.9493	0.9399	0.9287	0.9169
8.0	0.95970	0.9592	0.9578	0.9555	0.9524	0.9443	0.9345	0.9240
9.0	0.96077	0.9604	0.9591	0.9572	0.9546	0.9476	0.9391	0.9296
10.0	0.96153	0.9611	0.9602	0.9585	0.9563	0.9502	0.9426	0.9341
12.0	0.96246	0.9621	0.9614	0.9602	0.9584	0.9537	0.9477	0.9409
14.0	0.96297	0.9628	0.9622	0.9611	0.9599	0.9561	0.9511	0.9453
16.0	0.96327	0.9631	0.9626	0.9617	0.9607	0.9577	0.9535	0.9488
18.0	0.96340	0.9633	0.9628	0.9621	0.9613	0.9588	0.9553	0.9513
20.0	0.96348	0.9634	0.9631	0.9626	0.9617	0.9595	0.9567	0.9530
25.0	0.96357	0.9635	0.9632	0.9628	0.9623	0.9607	0.9587	0.9561
30.0	0.96365	0.9635	0.9634	0.9631	0.9627	0.9615	0.9599	0.9580
35.0	0.96373	0.9637	0.9635	0.9633	0.9629	0.9619	0.9606	0.9590
40.0	0.96383	0.9637	0.9636	0.9636	0.9632	0.9623	0.9611	0.9596
50.0	0.96395	0.9641	0.9639	0.9639	0.9636	0.9629	0.9619	0.9606
75.0	0.96373	0.9638	0.9640	0.9645	0.9644	0.9641	0.9631	0.9618
100.0	0.96316	0.9635	0.9642	0.9649	0.9651	0.9649	0.9639	0.9624
∞	0.95833	0.95833	0.95833	0.95833	0.95833	0.95833	0.95833	0.95833

dipole forces in the usual laboratory temperature range. This is all to the good, since it implies that the artificiality of the model is not a severe restriction. Presumably, the 12–6–3 parameters have more physical significance than the 12–6 parameters, although the data are seldom extensive and accurate enough to provide a clear experimental choice between the two. Indeed, most of the data can be fitted about equally well by even less realistic models, such as point centers of repulsion or attracting rigid spheres, although the derived parameters for such models would have little physical significance.

The parameters for many of the polar gases in Table XII are consistent with the parameters for related nonpolar gases. Thus, the values of the "size" parameter σ_0 for the chloromethanes fall comfortably between the values of σ_0 for CCl_4 and CH_4, and the value of σ_0 for C_2H_5Cl is appreciably larger than that for C_2H_6. The value of σ_0 for NH_3 is also appreciably larger than that for Ne, which is the united atom that would result from the collapse of the H atoms into the N atom. This consistency does not hold, however, for the alcohols and ethers. Thus, σ_0 for CH_3OH is less than σ_0 for CH_4, σ_0 for C_2H_5OH and $(CH_3)_2O$ are less than σ_0 for C_2H_6, and σ_0 for C_3H_7OH is less than σ_0 for C_3H_8. Similarly, σ_0 for H_2O is less than σ_0 for Ne. The reason for these discrepancies is probably that the dipole is actually near the surface of these molecules, rather than at the center as assumed in the model.

Turning now to a comparison with the available second virial-coefficient results given in Table XIII, we find great disagreement, much greater than usually found for nonpolar molecules.[25] However, the fault would seem to lie with the second virial results rather than with the viscosity results. The second virial parameters are much more sensitive to the dipole forces, in which case the point-dipole model may be too artificial. For instance, Guggenheim[26] calculates for the least polar molecule, chloroform, the values of $\sigma_0 = 5.02$ A and $\epsilon_0/k = 428$ °K when the polar term is omitted. These values are much different from the ones

[25] MTGL, pp. 1110–1112.

[26] E. A. Guggenheim, Revs. Pure and Appl. Chem. (Australia) **3**, 1 (1953).

TABLE X. $\langle F^* \rangle$.

T^* \ δ	0	0.25	0.50	0.75	1.0	1.5	2.0	2.5
0	0.9417	0.8812	0.8812	0.8812	0.8812	0.8812	0.8812	0.8812
0.1	0.9361	0.9500	0.8928	0.8696	0.8602	0.8594	0.8594	0.8592
0.2	0.9211	0.9134	0.9004	0.8861	0.8761	0.8702	0.8668	0.8645
0.3	0.9063	0.9040	0.8949	0.8831	0.8756	0.8703	0.8679	0.8665
0.4	0.8992	0.8974	0.8909	0.8814	0.8748	0.8698	0.8678	0.8669
0.5	0.8969	0.8953	0.8897	0.8815	0.8754	0.8693	0.8676	0.8668
0.6	0.8972	0.8960	0.8909	0.8840	0.8773	0.8706	0.8677	0.8667
0.7	0.8990	0.8982	0.8939	0.8870	0.8806	0.8719	0.8686	0.8668
0.8	0.9018	0.9007	0.8970	0.8915	0.8844	0.8744	0.8694	0.8673
0.9	0.9053	0.9050	0.9008	0.8953	0.8884	0.8777	0.8714	0.8683
1.0	0.9091	0.9083	0.9054	0.8996	0.8925	0.8811	0.8734	0.8697
1.2	0.9171	0.9165	0.9142	0.9088	0.9019	0.8884	0.8788	0.8731
1.4	0.9250	0.9251	0.9222	0.9169	0.9103	0.8964	0.8852	0.8779
1.6	0.9324	0.9320	0.9293	0.9246	0.9181	0.9035	0.8914	0.8834
1.8	0.9392	0.9386	0.9363	0.9308	0.9248	0.9103	0.8974	0.8881
2.0	0.9454	0.9445	0.9419	0.9374	0.9314	0.9169	0.9035	0.8932
2.5	0.9580	0.9579	0.9554	0.9501	0.9444	0.9299	0.9171	0.9062
3.0	0.9677	0.9671	0.9646	0.9603	0.9545	0.9418	0.9289	0.9170
3.5	0.9751	0.9745	0.9721	0.9682	0.9631	0.9513	0.9385	0.9274
4.0	0.9810	0.9804	0.9783	0.9748	0.9700	0.9586	0.9468	0.9362
5.0	0.9894	0.9889	0.9871	0.9842	0.9803	0.9705	0.9600	0.9496
6.0	0.9951	0.9947	0.9932	0.9908	0.9875	0.9793	0.9700	0.9604
7.0	0.9993	0.9990	0.9977	0.9956	0.9928	0.9857	0.9775	0.9689
8.0	1.0025	1.002	1.001	0.9992	0.9969	0.9908	0.9835	0.9756
9.0	1.0049	1.005	1.004	1.002	1.000	0.9946	0.9881	0.9810
10.0	1.0068	1.007	1.006	1.004	1.003	0.9979	0.9920	0.9855
12.0	1.0097	1.010	1.009	1.008	1.006	1.002	0.9979	0.9925
14.0	1.0117	1.012	1.011	1.010	1.009	1.006	1.002	0.9975
16.0	1.0133	1.013	1.013	1.012	1.011	1.009	1.005	1.001
18.0	1.0145	1.014	1.014	1.013	1.013	1.010	1.008	1.004
20.0	1.0155	1.015	1.015	1.015	1.014	1.012	1.010	1.007
25.0	1.0174	1.017	1.017	1.017	1.016	1.015	1.013	1.011
30.0	1.0188	1.019	1.019	1.018	1.018	1.017	1.015	1.014
35.0	1.0201	1.020	1.020	1.020	1.019	1.018	1.017	1.016
40.0	1.0213	1.021	1.021	1.021	1.021	1.020	1.018	1.017
50.0	1.0231	1.023	1.023	1.023	1.023	1.022	1.021	1.019
75.0	1.0261	1.026	1.027	1.027	1.027	1.026	1.024	1.022
100.0	1.0274	1.028	1.029	1.030	1.031	1.030	1.027	1.023
∞	1.02580	1.02580	1.02580	1.02580	1.02580	1.02580	1.02580	1.02580

in Table XIII. Another indication that the point model may be rather artificial for second virial coefficients comes from calculations estimating the effect of higher multipoles and induction terms on the second virial coefficient.[27–29] These calculations show that the contribution of the higher terms is far from negligible. Another indication of model artificiality is the lack of consistency among the parameters in Table XIII. It is unlikely that σ_0 for $CHCl_3$ and CH_3Cl should be smaller than σ_0 for CH_4, or that σ_0 for NH_3 should be smaller than σ_0 for Ne.

In short, it appears that the model is less satisfactory for second virial coefficients than for viscosities, and that the fault lies in the oversimplification of the point-dipole model. This is another illustration of the well-known fact that the second virial coefficient is much more sensitive to the long-range intermolecular forces than are the transport properties.

Water is a sufficiently interesting substance to be worth some additional discussion, even though we do not expect the present model to be very realistic for water. Since the data scatter so much, as shown in Fig. 3, the best fit is not easy to pick out by the graphical method. Accordingly, a least mean-squares fit was also carried out. The results are somewhat different, as shown in Table XIV. Most of the difference in σ_0 and ϵ_0/k between the graphical method and the least-squares method is only a reflection of the different choice of δ_{max} (which is not well determined by the data for H_2O). A least-squares fit was carried out with δ_{max} set equal to zero, with only a slightly poorer fit (rms deviation of 4%, compared to 3.6%), and the parameters found are also given in Table XIV. Finally, a least-squares "free fit" was carried out in which all three parameters were treated as disposable. As expected, this produced the best fit, but not by much (rms deviation of 2.8%). The "effective" dipole moment corresponding to these parameters is $\mu = 1.985$

[27] H. Margenau and V. W. Myers, Phys. Rev. **66**, 307 (1944); see also reference 40, p. 339.
[28] J. S. Rowlinson, Trans. Faraday Soc. **47**, 120 (1951); see also MTGL, pp. 225–227.
[29] A. D. Buckingham and J. A. Pople, Trans. Faraday Soc. **51**, 1173 (1955).

TABLE XI. $[\alpha_0']_2$.

T^* \ δ	0	0.25	0.50	0.75	1.0	1.5	2.0	2.5
0	0.312	−0.287	−0.287	−0.287	−0.287	−0.287	−0.287	−0.287
0.1	0.291	0.341	0.025	−0.161	−0.243	−0.280	−0.284	−0.283
0.2	0.220	0.200	0.176	0.076	−0.057	−0.193	−0.241	−0.288
0.3	0.103	0.107	0.029	−0.072	−0.148	−0.226	−0.259	−0.270
0.4	0.013	0.016	−0.014	−0.073	−0.136	−0.217	−0.256	−0.274
0.5	−0.036	−0.028	−0.042	−0.086	−0.135	−0.217	−0.256	−0.275
0.6	−0.052	−0.043	−0.053	−0.087	−0.135	−0.212	−0.255	−0.276
0.7	−0.049	−0.039	−0.047	−0.080	−0.128	−0.208	−0.253	−0.277
0.8	−0.034	−0.027	−0.035	−0.068	−0.115	−0.201	−0.250	−0.275
0.9	−0.011	−0.005	−0.019	−0.054	−0.100	−0.189	−0.242	−0.272
1.0	0.015	0.016	0.004	−0.033	−0.083	−0.174	−0.236	−0.267
1.2	0.071	0.070	0.052	0.012	0.041	−0.145	−0.214	−0.256
1.4	0.125	0.124	0.098	0.055	0.001	−0.106	−0.186	−0.238
1.6	0.174	0.169	0.142	0.098	0.044	−0.072	−0.158	−0.214
1.8	0.218	0.210	0.187	0.140	0.084	−0.033	−0.127	−0.193
2.0	0.257	0.248	0.222	0.179	0.120	0.003	−0.097	−0.167
2.5	0.334	0.328	0.302	0.255	0.202	0.083	−0.019	−0.100
3.0	0.389	0.381	0.357	0.316	0.265	0.154	0.051	−0.038
3.5	0.429	0.422	0.399	0.363	0.317	0.213	0.108	0.019
4.0	0.460	0.453	0.433	0.400	0.358	0.260	0.161	0.073
5.0	0.500	0.495	0.478	0.452	0.417	0.333	0.244	0.159
6.0	0.525	0.520	0.507	0.486	0.458	0.386	0.307	0.228
7.0	0.542	0.538	0.527	0.509	0.485	0.425	0.354	0.282
8.0	0.553	0.550	0.540	0.525	0.506	0.453	0.391	0.326
9.0	0.561	0.558	0.550	0.537	0.519	0.474	0.419	0.361
10.0	0.566	0.564	0.557	0.546	0.531	0.491	0.443	0.389
12.0	0.574	0.572	0.567	0.558	0.546	0.515	0.476	0.432
14.0	0.578	0.576	0.572	0.565	0.556	0.530	0.498	0.462
16.0	0.580	0.580	0.576	0.571	0.563	0.542	0.514	0.483
18.0	0.582	0.581	0.578	0.574	0.567	0.549	0.527	0.499
20.0	0.583	0.582	0.580	0.575	0.570	0.555	0.535	0.512
25.0	0.584	0.582	0.582	0.578	0.575	0.564	0.550	0.532
30.0	0.584	0.583	0.582	0.580	0.577	0.569	0.557	0.544
35.0	0.583	0.583	0.582	0.580	0.578	0.572	0.563	0.552
40.0	0.583	0.584	0.582	0.580	0.579	0.573	0.566	0.556
50.0	0.582	0.582	0.582	0.580	0.579	0.576	0.570	0.563
75.0	0.581	0.581	0.581	0.582	0.580	0.577	0.574	0.570
100.0	0.579	0.579	0.579	0.580	0.580	0.580	0.576	0.573
∞	0.554	0.554	0.554	0.554	0.554	0.554	0.554	0.554

debye, only slightly greater than the experimental dipole moment. This can be given a simple physical interpretation. If the dipole of H_2O is really near the surface of the molecule rather than at the center, then the value of the central point dipole assumed in the model should be greater than the true value to compensate.

After the above calculations had been completed, we received from Professor J. Kestin of Brown University a copy of a report ("Progress report on the measurement of the viscosity of steam," November, 1959) giving his new experimental results on the viscosity of steam.[30] These are probably the most accurate measurements yet made. Also, through Professor Kestin's request, we received from Professor J. H. Keenan of MIT an English translation of a Russian article[31] of which we had been unaware, which reported the results of some new, very careful measurements on the viscosity of steam. Because much of our trouble with fitting the H_2O data had arisen from the great scatter of the experimental data, Professor Kestin suggested that we might adopt his and Shifrin's results to the exclusion of previous data. We think Bonilla, Wang, and Weiner's results[32] might also be included in this set of "best data," especially if an empirical correction of 4% for a supposedly systematic error is applied, as suggested by Shifrin.[31] A plot of these "best data" is shown in Fig. 4, to the same scale as used in Fig. 3. Comparing this with the curves of Fig. 3, we see that a very high value of δ_{max} would be required to fit these data (about $\delta_{max}=2.5$). Such a high value of δ_{max} cannot be reconciled with the actual dipole moment of H_2O, unless one is willing to talk about an "effective" dipole, as mentioned in the preceding paragraph. The upshot of this is that we conclude that a point-dipole model is really too artificial to represent the complex force field of H_2O in detail, although it certainly seems to indicate the correct trends.

[30] Subsequently published by J. Kestin and H. E. Wang, Physica **26**, 575 (1960).

[31] A. S. Shifrin, Teploenergetika **6**, 22 (1959).

[32] See reference ff of Table XII.

TABLE XII. Potential parameters derived from viscosity data (graphical method).

Gas	μ (debye)	12–6–3 potential δ_{max}	12–6–3 potential σ_0(A)	12–6–3 potential ϵ_0/k (°K)	12–6 potential σ_0(A)	12–6 potential ϵ_0/k (°K)	Reference for data
H_2O	1.85	1.0	2.52	775			e, i, j, p, y, z, bb, dd, ff
NH_3	1.47	0.7	3.15	358			e, k, o, p, r, aa, cc
HCl	1.08	0.34	3.36	328	3.305[a]	360	g, m, o, u
HBr[c]	0.80	0.14	3.41	417			g
HI	0.42	0.029	4.13	313	4.123[a]	324	g, s, w
SO_2	1.63	0.42	4.04	347	4.026[b]	363	e, l, n, o, q, s, t, cc
H_2S[c]	0.92	0.21	3.49	343	3.591[b]	309	f, o
NOCl[c]	1.83	0.4	3.53	690	3.57[b]	668	x
$CHCl_3$	1.013	0.07	5.31	355	5.430[a]	327	d, e, h, p, v
CH_2Cl_2	1.57	0.2	4.52	483	4.748[b]	398	p
CH_3Cl	1.87	0.5	3.94	414	4.151[b]	355	e, n, p, ee
CH_3Br[c]	1.80	0.4	4.25	382			n
C_2H_5Cl[c]	2.03	0.4	4.45	423			ee
CH_3OH	1.70	0.5	3.69	417	3.666[b]	452	v, ee
C_2H_5OH	1.69	0.3	4.31	431	4.370[b]	415	d, v
n-C_3H_7OH	1.69	0.2	4.71	495			v
i-C_3H_7OH	1.69	0.2	4.64	518			v
$(CH_3)_2O$	1.30	0.19	4.21	432	4.264[b]	412	n, aa
$(C_2H_5)_2O$	1.15	0.08	5.49	362	5.530[b]	351	d, e, h, v, ee
$(CH_3)_2CO$	2.88	0.06	4.50	549	4.669[b]	519	d, v, ee
CH_3COOCH_3	1.72	0.2	5.04	418	5.054[b]	417	d, v
$CH_3COOC_2H_5$	1.78	0.16	5.24	499	5.163[b]	531	d, e, v
Ne					2.858[a]	27.5	
CCl_4					5.881[a]	327	
CH_4					3.796[a]	144	
C_2H_6					4.418[a]	230	
C_3H_8					5.061[a]	254	

[a] MTGL pp. 1110–1113.
[b] Redetermined.
[c] Scanty or uncertain data.
[d] K. Rappanecker, Z. physik. Chem. **72,** 695 (1910).
[e] H. Vogel, Ann. Physik **43,** 1235 (1914).
[f] A. O. Rankine and C. J. Smith, Phil. Mag. **42,** 615 (1921).
[g] H. Harle, Proc. Roy. Soc. (London) **A100** 429 (1922).
[h] R. Suhrmann, Z. Physik **14,** 56 (1923).
[i] H. Speyerer, Z. tech. Physik **4,** 430 (1923).
[j] C. J. Smith, Proc. Roy. Soc. (London) **A106,** 83 (1924).
[k] R. S. Edwards and B. Worswick, Proc. Phys. Soc. (London) **38,** 16 (1925).
[l] M. Trautz and W. Weizel, Ann. Physik **78,** 305 (1925).
[m] M. Trautz and A. Narath, Ann. Physik **79,** 637 (1926).
[n] T. Titani, Bull. Chem. Soc. Japan **5,** 98 (1930).
[o] G. Jung and H. Schmick, Z. physik. Chem. **B7,** 130 (1930).
[p] H. Braune and R. Linke, Z. physik. Chem. **A148,** 195 (1930).
[q] M. Trautz and R. Zink, Ann. Physik **7,** 427 (1930).
[r] M. Trautz and R. Heberling, Ann. Physik **10,** 155 (1931).
[s] M. Trautz and H. Winterkorn, Ann. Physik **10,** 511 (1931).
[t] W. W. Stewart and O. Maass, Can. J. Research **6,** 453 (1932).
[u] J. R. Partington, Physik. Z. **34,** 289 (1933).
[v] T. Titani, Bull. Chem. Soc. Japan **8,** 255 (1933).
[w] M. Trautz and F. Ruf, Ann. Physik **20,** 127 (1934).
[x] M. Trautz and A. Freytag, Ann. Physik **20,** 135 (1934).
[y] W. Schugajew, Physik. Z. Sowjetunion **5,** 659 (1934).
[z] G. A. Hawkins, H. L. Solberg, and A. A. Potter, Trans. Am. Soc. Mech. Engrs. **57,** 395 (1935).
[aa] A. B. van Cleave and O. Maass, Can. J. Research **13B,** 140 (1935).
[bb] D. L. Timroth, J. Phys. (U.S.S.R.) **2,** 419 (1940).
[cc] R. Wobser and F. Müller, Kolloid-Beih. **52,** 165 (1941).
[dd] F. G. Keyes, J. Am. Chem. Soc. **72,** 433 (1950).
[ee] P. M. Craven and J. D. Lambert, Proc. Roy. Soc. (London) **A205,** 439 (1951).
[ff] C. F. Bonilla, S. J. Wang, and H. Weiner, Trans. Am. Soc. Mech. Engrs. **78,** 1285 (1956). This paper gives smoothed data only; the original data are available as ADI 4545 from the Library of Congress.

We have, therefore, not redetermined the potential parameters for the "best data," and all our subsequent calculations have been based on the least-squares determination listed in Table XIV.

B. Calculation of Other Properties

Ideally, one would like to use the parameters of Table XII to calculate a wide variety of polar-gas properties for comparison with experiment. Unfortu-

TABLE XIII. Potential parameters determined from second virial coefficients (Rowlinson; $\delta_{max}=2^{\frac{1}{6}}l^*$).

Gas	μ (debye)	δ_{max}	σ_0 (A)	ϵ_0/k, (°K)
H_2O	1.83	1.70	2.65	380
NH_3	1.47	1.41	2.60	320
$CHCl_3$	1.05	0.14	2.98	1060
CH_3Cl	1.89	0.85	3.43	380
C_2H_5Cl	2.02	0.28	5.41	320
CH_3OH	1.66	1.13	2.40	630
$(CH_3)_2CO$	2.74	0.99	3.76	520

nately, the only other transport data available are a few self-diffusion coefficients and isotopic thermal-diffusion factors. The calculated and experimental self-diffusion coefficients for HCl and HBr are compared in Table XV. Agreement is satisfactory if we recall that the potential parameters for HBr are very uncertain being based on only two viscosity points.

The comparison of calculated and experimental isotopic thermal-diffusion factors is made graphically in Fig. 5 as a plot of α_0 as a function of $T^*=kT/\epsilon_0$. A few measurements for NH_3 and HCl are the only experimental results available for polar gases.[33,34]

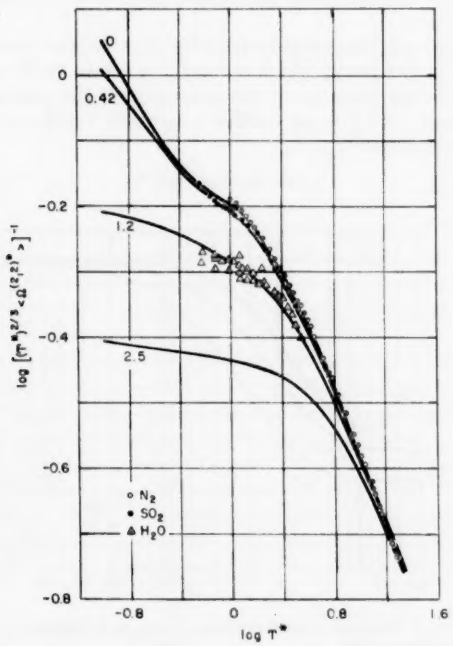

FIG. 3. Reduced viscosity as a function of reduced temperature for $\delta_{max}=0(N_2)$, $0.42(SO_2)$, $1.2(H_2O$ least-squares fit), and 2.5.

TABLE XIV. Potential parameters for H_2O as determined by different methods.

Method	μ(debye)	δ_{max}	σ_0 (A)	ϵ_0/k (°K)
Graphical	1.85	1.0	2.52	775
Least Square[a]	1.83	1.2	2.71	506
Nonpolar	0	0	2.65	800
Free fit	(1.985)	2.5	2.80	260

[a] Recommended value.

Unfortunately, the experimental uncertainty in α_0 is almost as great as the magnitude of α_0 itself, so that not much more can be concluded from Fig. 5 than that the experimental points fall in the general area of the theoretical curves, and that the inversion temperatures are not greatly out of line. It does appear as if the experimental α_0 curves would cross the $\alpha_0=0$ axis with a much greater slope than the theoretical α_0 curves, but it is difficult to be sure because of the experimental uncertainty. More experimental work on the thermal diffusion of polar gases would be very welcome, and the accuracy might now be considerably improved by means of Clusius and Huber's "Trennschaukel."[35,36]

It is interesting to use the present parameters from viscosity data to calculate second virial coefficients, even though we do not expect very good agreement for the reasons discussed in part A of this section. The experimental second virial-coefficient data for the gases listed in Table XIII cover an appreciable temperature range only in the cases of water, ammonia, and methyl chloride, and we therefore limit our comparison to these.

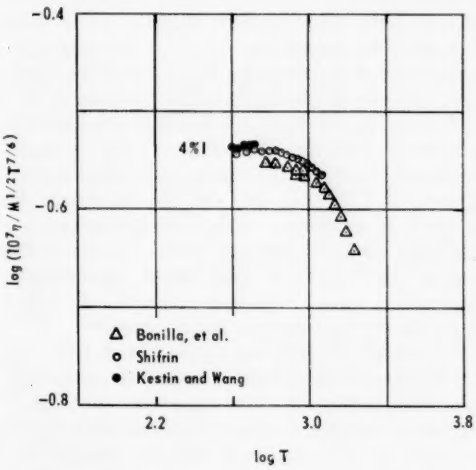

FIG. 4. "Best" viscosity data for steam, to the same scale as Fig. 3.

[33] W. W. Watson and D. Woernley, Phys. Rev. **63,** 181 (1943).
[34] A. Z. Kranz and W. W. Watson, Phys. Rev. **91,** 1469 (1953).
[35] K. Clusius and M. Huber, Z. Naturforsch. **10a,** 230 (1955).
[36] T. I. Moran and W. W. Watson, Phys. Rev. **109,** 1184 (1958).

TABLE XV. Comparison of calculated and experimental self-diffusion coefficients at 1 atm.

Gas	T (°K)	D_{11} (cm²/sec) Calc	Expt[a]
HCl	295.0	0.1269	0.1254
HBr	295.3	0.0739	0.0794

[a] H. Braune and F. Zehle, Z. physik. Chem. **B49,** 247 (1941). We have applied a small correction for the mass of the isotopic tracers used.

The results are shown in Table XVI, the experimental values being those quoted by Rowlinson.[24] The agreement is hardly spectacular, but it is much better than we had anticipated on the basis of the wide discrepancies between the potential parameters in Table XII (viscosity) and in Table XIII (second virial). It is also pertinent to point out that these discrepancies are no worse than those shown by such nonpolar molecules as nitrogen[37] or krypton[38] when second virial coefficients are calculated from 12–6 or exp–6 potential parameters derived by fitting viscosity data.

VI. DISCUSSION

On the whole, we believe it is fair to say that the present 12–6–3 potential model works about as well for polar gases as does the 12–6 potential model for nonpolar gases, so far as we can tell from available experimental data. The data for polar gases are not nearly as extensive as for nonpolar gases, however, and we accordingly feel compelled to seek indirect confirmatory evidence that our derived potential parameters are physically reasonable. Rowlinson[24] has pointed out that two quantities of greater physical interest for polar molecules than the parameters σ_0 and ϵ_0 are the distance of equilibrium separation ($r_{\min}$) of two molecules in the orientation of maximum dipole attraction (head-to-tail), and the dipole-dipole interaction energy in this orientation, $\varphi_{\mu\mu}=-2\mu^2/r_{\min}^3$. For H_2O, the least-square parameters lead to $r_{\min}=2.80$ A and $-\varphi_{\mu\mu}=4.40$ kcal/mole. This value of $r_{\min}$ is fairly close to the 0–0 distance of 2.76 A in ice, and the maximum dipole energy is in agreement with Pauling's estimate of 5 kcal/mole for the energy of the O–H···O hydrogen bond in ice.[39] It is in even better agreement with Rowlinson's more elaborate estimate of 4.30–4.86 kcal/mole for the hydrogen bond energy.[28]

The values for NH_3 are $r_{\min}=3.34$ A and $-\varphi_{\mu\mu}=1.68$ kcal/mole, as calculated from the parameters of Table XII, and are in good agreement with the N–N distance of 3.380 A in the crystal and with Pauling's estimate for 1.3 kcal/mole for the energy of the N—H···N hydrogen bond in ammonia.[39]

As a final theoretical check, we have compared the coefficient of the r^{-6} term in $\varphi(r)$, as found from viscosity, with the theoretical estimates of this coefficient. The experimental viscosity value is simply

$$c_{\text{visc}}=4\epsilon_0\sigma_0^6, \tag{32}$$

and consists, theoretically, of two parts, the London dispersion energy and the induction energy due to the permanent dipole. Each of these can be written as a series,

$$\varphi_{\text{dis}}=-(c_1/r^6)-(c_2/r^8)-(c_3/r^{10})-\cdots, \tag{33}$$

$$\varphi_{\text{ind}}=-(c_1'/r^6)-(c_2'/r^8)-\cdots. \tag{34}$$

Since the experimental result found for c_{visc} must really include some contribution from the higher terms in r^{-8} and r^{-10}, it is considered appropriate[40] to take for the theoretical value of c the following:

$$c_{\text{calc}}=c_1+(c_2/\sigma_0^2)+(c_3/\sigma_0^4)+\cdots+c_1'+\cdots, \tag{35}$$

still higher terms being negligible. Approximate theoretical expressions for the coefficients are[40,41]

$$c_1=\tfrac{3}{4}\alpha^2 h\nu, \qquad c_1'=2\mu^2\alpha,$$

$$c_2=15\alpha^3(h\nu)^2/(4fe^2),$$

$$c_3=315\alpha^4(h\nu)^3/(32f^2e^4), \tag{36}$$

where α is the molecular polarizability, $h\nu$ is an average excitation energy which is usually taken to be the first ionization potential of the molecule, e is the electronic charge, and f is an oscillator strength which can be estimated as[41]

$$f=\alpha m_e(2\pi h\nu/eh)^2, \tag{37}$$

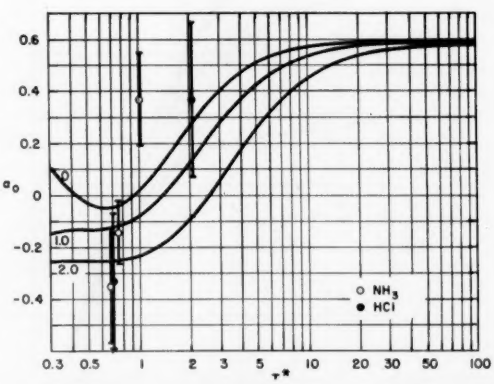

FIG. 5. Isotopic thermal-diffusion factor as a function of reduced temperature.

[37] E. A. Mason and W. E. Rice, J. Chem. Phys. **22,** 843 (1954).
[38] E. A. Mason, J. Chem. Phys. **32,** 1832 (1960).
[39] L. Pauling, *The Nature of the Chemical Bond* (Cornell University Press, Ithaca, New York, 1960), 3rd ed., Chap. 12.
[40] J. A. Beattie and W. H. Stockmayer, *States of Matter* (D. Van Nostrand Company, Inc., Princeton, New Jersey, 1951), H. S. Taylor and S. Glasstone, editors, p. 332; see also MTGL, p. 966.
[41] H. Margenau, Revs. Modern Phys. **11,** 1 (1939).

TABLE XVI. Comparison of calculated and experimental second virial coefficients.

H_2O[a]			NH_3			CH_3Cl		
	$-B$ (cc/mole)			$-B$ (cc/mole)			$-B$ (cc/mole)	
t (°C)	calc	expt	t (°C)	calc	expt	t (°C)	calc	expt
40	1040	976	−30	379	560	−34	782	764
70	690	638	0	284	367	−23	702	668
100	497	450	30	224	261	−18	670	637
150	323	284	60	181	197	10	530	500
200	230	197	100	142	143	38	435	401
300	137	112	150	110	103	65	367	320
400	92	72	200	87	77	93	313	265
			250	71	59	121	271	214
						149	237	184
						177	209	155

[a] Least-square parameters used.

where m_e is the electronic mass and h is Planck's constant. The results of the calculations are summarized in Table XVII, the necessary values of polarizabilities and ionization potentials having been taken from Landolt-Börnstein.[42] Some results for nonpolar gases are also included in the table for comparison.

Several interesting conclusions follow from Table XVII. In the first place, we note that the induction

TABLE XVII. Comparison of theoretical and experimental determinations of the dispersion and induction energy.

Gas	Theoretical					Exptl	Ratio
	$10^{12}c_1$ (erg-A^6)	$10^{12}c_1'$ (erg-A^6)	$10^{12}c_2$ (erg-A^8)	$10^{12}c_3$ (erg-A^{10})	$10^{12}c_{calc}$ (erg-A^6)	$10^{12}c_{visc}$ (erg-A^6)	$\frac{c_{visc}}{c_{calc}}$
H_2O	33.2	10.1	100	160	59.9	110.7	1.85
NH_3	70.6	9.8	234	408	108	193	1.79
HCl	106	6	316	494	144	261	1.81
HI	382	2	1360	2540	472	858	1.82
SO_2	200	20	634	1060	266	801	3.01
$CHCl_3$	936	17	3100	5390	1070	4394	4.11
CH_2Cl_2	555	32	1920	3490	689	2274	3.30
CH_3Cl	280	32	952	1700	380	855	2.25
CH_3OH	135	19	478	887	194	581	2.99
C_2H_5OH	348	30	1240	2310	451	1526	3.38
$(CH_3)_2O$	336	17	1220	2320	430	1328	3.09
$(CH_3)_2CO$	486	105	1830	3630	691	2517	3.64
Ne[a]	4.67	0	6.9	5.3	5.64	9.50	1.68
Ar[a]	55.4	0	120	136	66.7	109.2	1.64
N_2[a]	57.2	0	120	130	66.8	125.6	1.88
O_2[a]	39.8	0	96	120	48.8	102.3	2.10
CCl_4	1460	0	5040	9140	1610	7463	4.64
CH_4[a]	112	0	310	440	135	257.9	1.91

[a] Taken from MTGL p. 966.

[42] Landolt-Börnstein, *Zahlenwerte und Funktionen* (Springer-Verlag, Berlin, Germany, 1950).

energy is usually small compared to the dispersion energy; c_1' is never more than 10% of c_1, except for H_2O, NH_3, CH_3OH, and $(CH_3)_2CO$, and even then it contributes no more to c_{calc} than do the terms in c_2 and c_3. This observation is of importance in connection with the formulation of combination rules for estimating forces between unlike molecules from the forces between like molecules. In the second place, we remark that the approximate theoretical formulas of Eq. (36) are probably a lower limit,[43] so that the ratio in the last column of the table is expected to be always greater than unity, as indeed it is. For the rare gases and small molecules, whether polar or nonpolar, the ratios are about 2 or less; but for large molecules, the ratios are substantially greater. This may be because the repulsive part of the potential falls off faster than r^{-12} for large molecules, if the repulsion is caused by the interaction between the peripheral atoms.[13,40,44–46] The experimental dispersion energy then has to be increased to compensate for the incorrect r^{-12} repulsion. Whatever the explanation may be, it is not the fault of the present 12–6–3 model alone, since the nonpolar 12–6 model behaves similarly. Thus, the ratios for N_2, O_2, and CH_4 are comparable to those for H_2O, NH_3, and HCl. Notice also that the ratios for the three polar chloromethanes fall smoothly between the ratios for the nonpolar CH_4 and CCl_4. The ratios for alcohols, ether, and acetone are also reasonable in that they lie in the same range as the ratios for the chloromethanes.

Our conclusion is thus that all the physical evidence is consistent with the statement that the 12–6–3 model is as successful for the polar gases as the 12–6 model is for comparable nonpolar gases.

ACKNOWLEDGMENTS

The authors wish to thank the APL Bumblebee Computing Center for performing much of the numerical work involved in computing the collision integrals. They also wish to thank Stanley Favin for programming the least mean-squares calculations, and Elaine Shulman, Ronald Chen, Louis Ho, and Philip Shade for their help with many of the hand calculations.

APPENDIX

Quasi-Quantum Formula for the Viscosity of Linear Polar Molecules

Wang Chang and Uhlenbeck[4] have given a general treatment of the transport coefficients of a quantum gas. However, their formulas are extremely complex in that they contain, besides the elastic cross section, the inelastic cross sections involving quantum transitions. A simpler situation arises in the case where all inelastic cross sections are negligibly small. One can then consider the gas to be made up of a mixture of different components i (the various quantum states) whose mole fraction x_i is given by the Boltzmann factor $A\exp(-\epsilon_i/kT)$. The index i contains all the internal degrees of freedom. If one now allows each pair (i, j) to have a separate potential energy of interaction φ_{ij} and calculates the elastic-collision cross section classically, a quasi-quantum approximation is obtained for the transport processes. In this section, we shall only consider the viscosity.

London[47] has considered the case of a set of linear molecules and has derived a formula for the interaction energy of the form

$$\phi_{ij}=\phi_0(r,\mu)\pm[2\mu^2 a_4(i,m;j,m')]/r^3, \qquad \text{(A1)}$$

where a_4 is a function of the rotational quantum numbers of the two molecules under consideration. In general, it is found that a_4 vanishes (treating only the case of molecules of equal moments of inertia and dipole moments) except when

$$i=j\pm 1. \qquad \text{(A2)}$$

φ_0 is the sum of the other contributions such as the repulsive energy, the dispersion energy, and the induced dipole energy.

These results may be obtained from a straightforward perturbation scheme,[41] in which case (A1) with (A2) result at once, or from London's method of "unsharp resonance."[2,41] In the latter case, for sufficiently large r, the dipole term is obtained as the dominant term under the resonance conditions (A2). We shall follow Sutton[7] and adopt this as a convenient model holding for intermediate values of r as well. Sutton presents a formula for the viscosity of such a gas in the quasi-quantum approximation using Buddenberg and Wilke's empirical formula[2]

$$[\eta]_1=\sum_i x_i^2\{x_i^2[\eta_{ii}]_1^{-1}+0.6925\sum_{j\neq i}x_i x_j[\eta_{ij}]_1^{-1}\}^{-1},$$

where $[\eta_{ij}]_1^{-1}$ is understood to be the average over all magnetic quantum numbers m and m'; e.g.,

$$[\eta_{ij}]_1^{-1}=\frac{\sigma_0^2\times 10^7}{266.93(MT)^{\frac{1}{2}}}\sum_{m=-i}\sum_{m'=-j}\frac{\Omega^{(2,2)}[T^*,a_4(i,m;j,m')]}{(2i+1)(2j+1)}.$$

It is implicitly assumed that a_4 remains fixed during the collision. This roughly corresponds to Hornig and Hirschfelder's "body-fixed coordinate" model which treats the rotational degree of freedom classically.[11] Although this model has no quantitative basis, it is the best one available at the present time and leads to a rather simple formula. The formula given by Sutton has the disadvantage that, as $\mu\to 0$ or as $\varphi_{ij}\to\varphi_0$, $[\eta]_1$ does not, in general, approach $[\eta(\varphi_0)]_1$ as it should. We

[43] Reference 40, pp. 300–301.
[44] S. D. Hamann and J. A. Lambert, Australian J. Chem. **7**, (1954).
[45] J. C. McCoubrey and N. M. Singh, Trans. Faraday Soc. **53**, 877 (1957); **55**, 1826 (1959); **56**, 486 (1960).
[46] J. F. Connolly and G. A. Kandalic, Phys. Fluids **3**, 463 (1960).
[47] F. London, Z. Physik **63**, 245 (1930).

shall present an alternative approximation that has the correct behavior as the interaction potentials approach each other.

Treating each quantum state as a different species, the viscosity of the gas of rotating dipoles may be written as

$$[\eta]_1=(kT/2)\sum_j n_j b_{j0} \qquad [7.4\text{–}56] \quad (A3)$$

(The notation of MTGL is used and the numbers in square brackets are derived from the same source.) Here, j is the index of the quantum state and b_{j0} is determined in the first approximation by the (infinite) set of equations

$$\sum_j (Q_{ij}{}^0/R_{i0})b_{j0}=-1, \quad i=1, 2, \cdots. \qquad [7.4\text{–}57] \quad (A4)$$

In terms of the quantities

$$H_{ij}=\frac{x_i x_j}{2[\eta_{ij}]_1}\left[1-\frac{5}{3A_{ij}{}^*}\right], \qquad 8.2\text{–}26$$

$$H_{ii}=\frac{x_1{}^2}{[\eta_{ii}]_1}+\sum_{k\neq i}\frac{x_k}{2[\eta_{ik}]_1}\left[1+\frac{5}{3A_{ij}{}^*}\right], \qquad 8.2\text{–}27$$

this becomes

$$\frac{kT}{2}\sum_j \frac{H_{ij}}{x_i x_j}n_j b_{j0}=1, \quad i=1, \cdots, \qquad (A6)$$

where x_i is the mole fraction of the ith state, n_i is the number of molecules in the ith state and $[\eta_{ij}]_1$ is the first approximation to the viscosity of molecules interacting with the (i, j) interaction.

For most temperatures of interest, $x_i \ll 1$ for all i. In the great majority of interactions, a_4 will vanish and $[\eta_{ij}]_1 \to [\eta_0]_1$, where $[\eta_0]_1$ is the viscosity of a set of molecules interacting with the potential (A1) where $a_4=0$. This suggests a possible perturbation method, in which all terms of order $x_i{}^n (n\geq 2)$ or sums involving only a small number of finite interactions are regarded as second-order effects. Defining

$$h_{ij}=\frac{1}{2[\eta_{ij}]_1}\left[1-\frac{5}{3A_{ij}{}^*}\right]-\frac{1}{2[\eta_0]_1}\left[1-\frac{5}{3A_0{}^*}\right], \quad \text{if} \quad j=i\pm 1,$$

$$h_{ij}=0, \quad j=1\pm 1,$$

$$f=\frac{1}{2[\eta_0]_1}\left[1-\frac{5}{3A_0{}^*}\right], \qquad g=\frac{1}{2[\eta_0]_1}\left[1+\frac{5}{3A_0{}^*}\right],$$

$$g_i'=\frac{1}{2[\eta_0]_1}\left(1-\frac{5}{3A_0{}^*}\right)$$

$$+\sum_{k\neq i\pm 1}\frac{x_k}{2x_i}\left[\frac{1}{[\eta_{ik}]_1}\left(1+\frac{5}{3A_{ik}{}^*}\right)-\frac{1}{[\eta_0]_1}\left(1+\frac{5}{3A_0{}^*}\right)\right], \quad (A6)$$

we may now rewrite (A4) as

$$x_i\frac{kT}{2}\sum_{j\neq i}(f+\lambda h_{ij})n_j b_{j0}+\frac{kT}{2}g n_i b_{i0}+\lambda x_i g_i'\frac{kT}{2}n_i b_{i0}=x_i, \qquad (A7)$$

where λ is a perturbation parameter which will later be set equal to unity.

If we expand b_{j0} in a series in λ,

$$b_{j0}=\sum_{n=0}^{\infty}\lambda^n b_{j0}{}^{(n)}, \qquad (A8)$$

and set coefficients of equal powers of λ equal to zero, we have as the coefficient of λ^0,

$$x_i\frac{kT}{2}+f\sum_j n_j b_{j0}{}^{(0)}+\frac{kT}{2}g n_i b_{i0}{}^{(0)}=x_i+x_i\frac{kT}{2}f n_i b_{i0}{}^{(0)}, \quad i=1, 2, \cdots. \qquad (A9)$$

The solution of (A9), correct through terms of the order $x_i{}^2$ is

$$\frac{kT}{2}n_i b_{i0}{}^{(0)}=\frac{1}{g}\left(1-\frac{kT}{2}f\sum_{j=1}n_j b_{j0}{}^{(0)}\right)[x_i+(f/g)x_1{}^2+\cdots], \qquad (A10)$$

$$[\eta]_1{}^{(0)}=\frac{kT}{2}\sum n_j b_{j0}{}^{(0)},$$

$$=\frac{1}{g+f}+\frac{f\beta}{(g+f)}+\cdots,$$

$$=[\eta_0]_1(1+f[\eta_0]_1\beta+\cdots), \qquad (A11)$$

where

$$\beta=\sum_{i=1}x_i{}^2$$

is by our previous considerations a quantity of second order.

By a similar procedure, it follows from the coefficient of λ^1 that $b_{j0}{}^{(1)}$ is of the order of $x_i{}^2$ and that all higher terms $(b_{j0}{}^{(n)}, n>1)$ will be of higher order.

We find by a simple manipulation that

$$(kT/2)\sum n_j b_{j0}{}^{(1)}=-[\eta_0]_1{}^2(h+g')\beta+\cdots, \qquad (A12)$$

where

$$h\equiv\frac{[\sum x_i{}^2\sum_{k=i\pm 1}(x_k/x_i)h_{ik}]}{\sum x_i{}^2}, \qquad (A13)$$

$$g'=\frac{1}{\sum x_i{}^2}[\sum x_i{}^2 g_i'].$$

If we set λ equal to unity, we then have, through terms of the order $x_i{}^2$,

$$[\eta]_1=[\eta_0]_1\{1+\beta[\eta_0]_1(f-h-g')+\cdots\}. \qquad (A14)$$

Now as all the potentials approach each other, $A_{ij}{}^* \to A_0{}^*$, $[\eta_{ij}]_1 \to [\eta_0]_1$, $g' \to f$, $h \to 0$, and $[\eta]_1 \to [\eta_0]_1$, so that, up through terms of order β, (A14) has the correct asymptotic behavior.

Paramagnetic Resonance of Some Silver (II) Compounds*

J. A. McMillan and B. Smaller
Argonne National Laboratory, Argonne, Illinois

(Received March 15, 1961)

The electron paramagnetic resonance of acidic solutions of silver (II) and several silver (II) solid complex compounds has been investigated. In all cases a strong g anistropy permitted the evaluation of the principal g values. In two cases, the hyperfine splitting could be measured without ambiguity. Parallel measurements of the optical and ultraviolet absorption in the case of silver (II) solutions indicated that the hole is not localized on the paramagnetic ion.

INTRODUCTION

BIVALENT silver has long been known to be paramagnetic. Silver (II) acid solutions have been reported to have 1.98[1] and 1.76[2] effective magnetons per ion from bulk susceptibility measurements. Several solid silver (II) complex compounds have also been found to be paramagnetic.[3–9] The sole exception is the oxide AgO whose diamagnetism indicates a mixed valence state[10] that has been proved by neutron diffraction.[11] In particular, the pyridine complex Ag(II)$pyr_4S_2O_8$ follows Curie's law very closely down to 1.6°K.[12]

We have studied the paramagnetic resonance of liquid and frozen acid solutions as well as the following solid compounds of silver (II): Ag $pyr_4S_2O_8$, Ag(*o*-phn)$_2S_2O_8$, Ag $dipyr_2S_2O_8$, $Ag_2dipyr_5(S_2O_8)_2$, Ag $dipyr_3(NO_3)_2$, Ag $dipyr_3(ClO_3)_2$, Ag $dipyr_3(ClO_4)_2$, and the inner metallic complex of the picolinic acid, Ag(II) α picolinate. Our study of these substances disclosed very strong g anisotropies permitting in all cases a fairly accurate determination of the principal values of the g tensor.[13] In two cases, the hyperfine structure was also resolved and could be measured without ambiguity.

EXPERIMENTAL METHODS AND RESULTS

The electron paramagnetic spectra of the various compounds were measured in a spectrometer operating at 9350 Mc/sec. Using a dual field modulation, the output records very approximately the second derivative of the absorption as a function of the magnetic field.[14]

The Hamiltonian can be represented as

$$\mathcal{H}=\beta_e\bar{S}\cdot\mathbf{g}\cdot\bar{H}+\bar{S}\cdot\mathbf{A}\cdot\bar{I}, \quad (1)$$

where β_e=Bohr magneton, $\bar{S}$= electron spin vector, $\mathbf{g}$=Zeeman coupling tensor, $\bar{H}$=magnetic field intensity vector, $\mathbf{A}$=hyperfine interaction tensor, and $\bar{I}$= nuclear spin vector.

The additional nuclear Zeeman term, $-g_N\beta_N\bar{H}\cdot\bar{I}$, whose contribution is negligible in the cases studied, has been omitted.

The eigenvalues of the Hamiltonian can be easily evaluated as

$$E_\pm=\pm\tfrac{1}{2}g\beta_eH\pm\tfrac{1}{2}[(A_1g_1/g)^2\sin^2\theta\sin^2\psi+(A_2g_2/g)^2\sin^2\theta\cos^2\psi+(A_3g_3/g)^2\cos^2\theta]^{\frac{1}{2}}M_I, \quad (2)$$

where

$$g=(g_1^2\sin^2\theta\sin^2\psi+g_2^2\sin^2\theta\cos^2\psi+g_3^2\cos^2\theta)^{\frac{1}{2}}. \quad (3)$$

In the case of axial symmetry, Eqs. (2) and (3) reduce to

$$E_\pm=\pm\tfrac{1}{2}g\beta_eH\pm\tfrac{1}{2}[(A_{\|}g_{\|}/g)^2\cos^2\theta+(A_\perp g_\perp/g)^2\sin^2\theta]^{\frac{1}{2}}M_I \quad (4)$$

$$g=(g_{\|}^2\cos^2\theta+g_\perp^2\sin^2\theta)^{\frac{1}{2}}. \quad (5)$$

In all cases, the principal values of the hyperfine interaction tensor are expressed in units of 10^{-4} cm^{-1}.

1. Silver (II) in Acid Solutions

The solutions were prepared by oxidizing with $K_2S_2O_8$ solutions of silver (I) nitrate in 1:4 HNO_3 in H_2O (sample I), 1:4 H_2SO_4 in H_2O (sample II), and 1:4 D_2SO_4 in D_2O (sample III). The basic redox reaction is

$$2Ag^+ + S_2O_8^= \rightarrow 2Ag^{2+} + 2SO_4^=.$$

The paramagnetic resonance spectra of the solutions were studied at room temperature and at 77°K. At room temperature, all solutions exhibited the same

* Based on work performed under the auspices of the U.S. Atomic Energy Commission.

[1] A. A. Noyes, K. S. Pitzer, and C. L. Dunn, J. Am. Chem. Soc. **57**, 1229 (1935).
[2] A. B. Neiding and I. A. Kazarnovsky, Doklady Akad. Nauk S.S.S.R. **78**, 713 (1951).
[3] L. Capatos and N. Perakis, Compt. rend. **202**, 1773 (1936).
[4] E. Gruner and W. Klemm, Naturwissenschaften **25**, 59 (1937).
[5] W. Klemm, Z. anorg. Chem. **201**, 32 (1931).
[6] S. Sugden, J. Chem. Soc. **1932**, 161.
[7] G. T. Morgan and F. H. Burstall, J. Chem. Soc. **1930**, 2594.
[8] G. T. Morgan and S. Sugden, Nature **128**, 31 (1931).
[9] B. Banerjee and P. Ray, J. Indian Chem. Soc. **34**, 207 (1957).
[10] J. A. McMillan, J. Inorg. & Nuclear Chem. **13**, 28 (1960).
[11] V. Scatturin, P. Bellon, and A. J. Salkind, Ricerca sci. **30**, 1034 (1960).
[12] H. M. Gijsman, H. J. Gerritsen, and J. van der Handel, Physica **20**, 15 (1954).
[13] F. K. Kneubühl, J. Chem. Phys. **33**, 1074 (1960).
[14] B. Smaller and E. Yasaitis, Rev. Sci. Instr. **24**, 991 (1953).

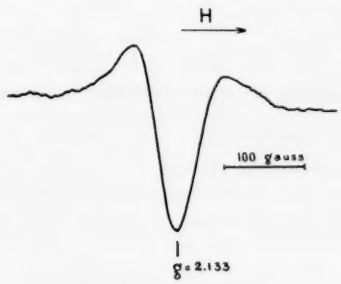

FIG. 1. Spectrum of Ag^{2+} in nitric solution at room temperature.

single broad line spectrum, shown in Fig. 1 for the case of sample I. At 77°K, a doublet at the high-field end was always well resolved, though, at the low-field end, the doublet was only resolved in the case of sample I (see Fig. 2). The anisotropy disclosed in the spectra permitted the evaluation of the principal values of the hyperfine splitting tensor due to magnetic interaction with the nuclei of silver, Ag^{107} and Ag^{109}, both of spin $\frac{1}{2}$ and nuclear magnetic moments differing by less than 20%.

The dotted lines in Fig. 3(a) show the expected absorption of the two doublets with small hyperfine anisotropy and strong g anisotropy, in the absence of broadening processes, taking into account the principal values for both tensors obtained from the experimental results. The full-line curve of Fig. 3(a) represents the expected absorption curve once the broadening processes have been taken into account. Figure 3(b) shows the expected first derivative of curve (a), together with the observed one. This latter was recorded using the conventional single modulation technique. Figure 3(c) shows the theoretically expected and observed second derivatives.

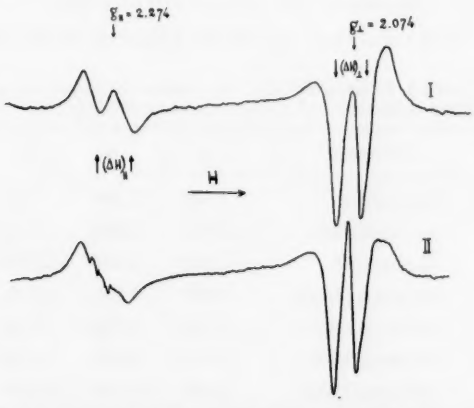

FIG. 2. Spectra of Ag^{2+} in (I) nitric and (II) sulphuric frozen solutions at 77°K.

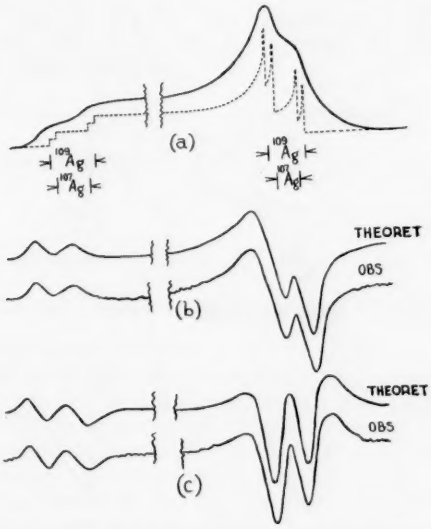

FIG. 3. Comparison between theoretical and observed spectra in the case of frozen acid solutions at 77°K.

The experimental values are

$$g_{\parallel}=2.265\pm0.001 \qquad g_{\perp}=2.065\pm0.001$$

$$|A_{\parallel}/\beta_e g_{\parallel}|=48 \text{ gauss} \qquad |A_{\perp}/\beta_e g_{\perp}|=31.6 \text{ gauss},$$

or, in units of 10^{-4} cm^{-1},

$$(hc)^{-1}|A_{\parallel}|=51\times10^{-4} \text{ cm}^{-1}$$

$$(hc)^{-1}|A_{\perp}|=30.5\times10^{-4} \text{ cm}^{-1},$$

where h is the Planck's constant and c the velocity of light.

Using Polder's relations,[15] $g_{\parallel}=2-8\lambda/\Delta_{\parallel}$ and $g_{\perp}=2-2\lambda/\Delta_{\perp}$, where λ is the spin-orbit coupling coefficient, one can evaluate the values of $\Delta_{\parallel,\perp}$, the splitting of the

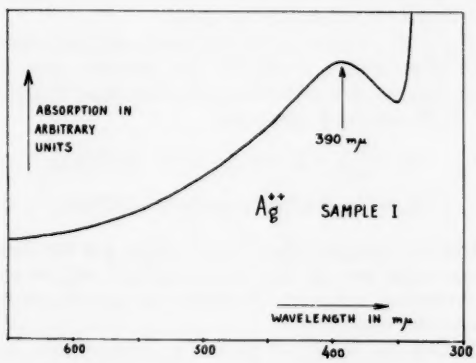

FIG. 4. Optical and ultraviolet absorption curve of Ag^{2+} in nitric solution at room temperature.

[15] D. Polder, Physica 9, 709 (1942).

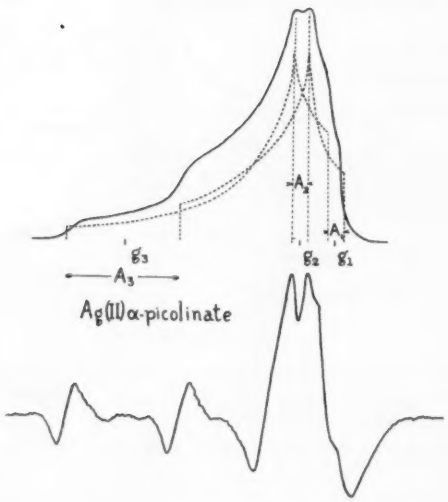

FIG. 5. Spectrum of argentic α picolinate. Top: Absorption curve in the absence of broadening (dotted line) and after broadening has been taken into consideration (full line). Bottom: Observed spectrum at 77°K.

levels of the ^2D term by the crystalline electric field for $\lambda=-1840$ cm^{-1}.[16]

The values

$$\Delta_{||}=-53\,500\text{ cm}^{-1}\text{ and }\Delta_{\perp}=-48\,750\text{ cm}^{-1},$$

when compared with the optical absorption data, are high. Figure 4 shows the optical absorption as a function of the wavelength in the case of concentrated nitric solutions. The brown color of these solutions is accounted for as a tail of the ultraviolet absorption, whose maximum occurs at 25 560 cm^{-1}.

These results indicate that Polder's consideration of an electron hole remaining localized on the paramagnetic ion does not hold in this case, as Bowers[17] pointed out in the case of Ag(II) $pyr_4S_2O_8$.

For a $^2D_{5/2}$ state in a tetragonal field, and the assumption of no s-state promotion, the relations given by Abragam and Pryce[18] between the anisotropic hyperfine tensor $\mathbf{B}$ and the $\mathbf{g}$ tensor are

$$B_{||}=[(g_{||}-2)+3(g_{\perp}-2)/7-4/7]\langle b\rangle, \quad (6)$$

$$B_{\perp}=[(g_{\perp}-2)-3(g_{\perp}-2)/14+2/7]\langle b\rangle, \quad (7)$$

where $\langle b\rangle=g\beta_e g_N\beta_N\langle(3\mu^2-1)/r^3\rangle$, where μ is the cosine of the angle between the electron radius r and the axis of symmetry, and g_N and β_N are the nuclear g factor and magneton, respectively.

Taking the values of $g_{||}$ and $g_{\perp}$ given above, one obtains

$$B_{||}=-0.30\langle b\rangle \qquad B_{\perp}=0.22\langle b\rangle.$$

If the amount of s-state promotion is a, then

$$A_{||}=B_{||}+a, \qquad A_{\perp}=B_{\perp}+a.$$

Since the amount of s-state promotion is certainly small, one might expect the observed values $A_{||}$ and $A_{\perp}$ to have opposite signs. Setting then $a=-\kappa\langle b\rangle$ we finally arrive at

$$A_{||}=-(\kappa+0.30)\langle b\rangle$$
$$A_{\perp}=(0.22-\kappa)\langle b\rangle,$$

from which $\kappa=0.028$.

Verification of the doublet as being due to the hyperfine interaction with the silver nucleus was demonstrated by using isotopically pure silver. The isotopes, available as metal sheets, were dissolved in DNO_3 in D_2O, and oxidized with solid $K_2S_2O_8$. The isotopic effect due to different nuclear magnetic moments (0.1135 nm for ^{107}Ag and 0.1305 nm for ^{109}Ag) was well detected in the doublet at $g_{\perp}=2.065$, the separations being

$$(\Delta H)_{109}=32.6\pm1.0\text{ gauss},$$
$$(\Delta H)_{107}=29.4\pm1.0\text{ gauss}.$$

The ratio of the separations is

$$(\Delta H)_{109}/(\Delta H)_{107}=1.11\pm0.07,$$

in good agreement with the ratio of the nuclear magnetic moments, 1.150 ± 0.001.

The results from solutions observed at room temperature show a single peak with g value equal to 2.124 ± 0.005 which can be accounted for as the average

$$\langle g_{sol}\rangle_{obs}=N\cdot g_{||}+(1-N)\cdot g_{\perp}.$$

The experimental value of $N=0.30$ is in agreement with the theoretical average

$$\langle g_{sol}\rangle_{theoret}=\tfrac{1}{3}(g_{||}+2g_{\perp})=2.131\pm0.001.$$

From the average value of the g factor in liquid solu-

TABLE I. Principal values of the g tensor for several argentic complex compounds. All g values are accurate to ±0.001.

Compound	g_1	g_2	g_3
Ag $pyr_4S_2O_8$	2.049	2.098	2.148
Ag $(o\text{-phn})_2S_2O_8$	2.046[a]	2.046[a]	2.168[a]
Ag $dipyr_2S_2O_8$	2.032[a]	2.032[a]	2.164[a]
Ag_2 $dipyr_5$ $(S_2O_8)_2$	2.040	2.056	2.176
Ag $dipyr_3$ $(NO_3)_2$	2.037[b]	2.047[b]	2.168
Ag $dipyr_3$ $(ClO_4)_2$	2.045[a]	2.045[a]	2.169[a]
Ag $dipyr_3$ $(ClO_3)_2$	2.034	2.065	2.172

[a] Symmetric magnetic complex, $g_1=g_2=g_{\perp}$, $g_3=g_{||}$.
[b] Results from single crystal.

[16] W. P. Gilbert, Phys. Rev. **48**, 338 (1935).
[17] K. D. Bowers, Proc. Phys. Soc. (London) **A66**, 666 (1953).
[18] A. Abragam and M. H. L. Pryce, Proc. Roy. Soc. (London) **A206**, 164 (1951).

tion, the magnetic susceptibility should be due to 1.97 effective magnetons per ion. The value reported by Neiding and Kazarnovsky is low[2]; the value reported by Noyes *et al.*[1] as 1.98 and attributed by these authors to partial orbital contribution is in very good agreement with our results. In order to determine the influence of dipole-dipole interaction on the broadening process, comparison of linewidths was made at 77°K in the cases of samples II and III made with H_2O and D_2O, respectively. It was found that in the case of H_2O the linewidth of the high-field lines was 14 gauss, while for D_2O it was 11 gauss. At 77°K, therefore, dipole-dipole interaction plays some part in this process.

2. Silver (II) Picolinate

The compound was prepared following the technique of Cox *et al.*[19] The spectrum (2nd derivative), together with the estimated absorption curve, is shown in Fig. 5. The experimental results, following the method applied in the foregoing case, are

$$g_1=2.044\pm0.003 \quad g_2=2.072\pm0.003 \quad g_3=2.244\pm0.005$$

$$\left|\frac{A_1}{\beta_e g_1}\right|=\left|\frac{A_2}{\beta_e g_2}\right|=30 \text{ gauss} \qquad \left|\frac{A_3}{\beta_e g_3}\right|=188 \text{ gauss}$$

$$(hc)^{-1}\,|\,A_1\,|=28.0\times10^{-4}\text{ cm}^{-1};$$

$$(hc)^{-1}\,|\,A_2\,|=28.4\times10^{-4}\text{ cm}^{-1};$$

$$(hc)^{-1}\,|\,A_3\,|=201\times10^{-4}\text{ cm}^{-1}.$$

[19] E. G. Cox, W. Wardlowand, and K. C. Webster, J. Chem. Soc. **1936,** 775.

If we assume, as a first approximation, a symmetric complex with $g_{||}=g_3$ and $g_\perp=\frac{1}{2}(g_1+g_2)$, we obtain, from Polder's relations,

$$\Delta_{||}=-60\,500\text{ cm}^{-1} \qquad \Delta_\perp=-66\,000\text{ cm}^{-1},$$

and, from Eqs. (6) and (7),

$$B_{||}=-0.30\langle b\rangle \qquad B_\perp=0.33\langle b\rangle.$$

Consequently, the amount of s promotion is $\kappa=0.24$.

3. Nitrogen Containing Ag(II) Complex Compounds

Seven compounds were prepared and observed for paramagnetic resonance. The results are summarized in Table I. The pyridine compound was prepared according to Palmer[20]; the *o*-phenantroline compound according to Hieber and Mühlbauer.[21] The five dipyridyl compounds were obtained following the techniques of Morgan and Burstall.[22] No hyperfine structure was resolved in any of these cases.

ACKNOWLEDGMENT

We wish to express our thanks to Dr. Joseph Katz and Dr. Henry Crespi for providing us with DNO_3 and D_2SO_4 used in these experiments.

[20] W. G. Palmer, *Experimental Inorganic Chemistry* (Cambridge University Press, Cambridge, England, 1954).
[21] W. Hieber and W. Mühlbauer, Ber. deut. chem. Ges. **61,** 2149 (1928).
[22] G. T. Morgan and F. H. Burstall, J. Chem. Soc. **1937,** 1649.

Ultraviolet Spectra of Carbon Monoxide*

H. LEFEBVRE-BRION AND CARL MOSER

Centre de Mécanique Ondulatoire Appliquée, 155 Rue de Sèvres, Paris 15°, France

AND

R. K. NESBET†

Department of Physics, Boston University, Boston 15, Massachusetts

(Received March 1, 1961)

The vertical excitation energies for many of the known electronic transitions in carbon monoxide have been calculated from LCAO–MO SCF functions built on three different basis sets of functions: (a) 1*s*, 2*s*, 2*s*′, 2*p*, and 2*p*′ atomic functions on each center; (b) 1*s*, 2*s*, 2*p*, 3*s*, and 3*p* atomic functions on each center; (c) 1*s*, 2*s*, 2*s*′, 2*p*, 2*p*′, 3*s*, and 3*p* functions on each center. The excitation energies calculated from the functions built on set (a) are hardly different from those obtained from an earlier calculation where the SCF orbitals were constructed from the simplest possible basis set (1*s*, 2*s* and 2*p* functions on each center). Set (b) gives results which are in quite good agreement with experiment for all the transitions studied. Our calculations support the analysis made many years ago by Mulliken that the presently known electronic transitions in carbon monoxide can be divided into (1) transitions between molecular orbitals both of which are mainly made up of atomic *L* functions; (2) transitions between molecular orbitals the lower of which is mainly made up of atomic *L* functions and the upper is mainly atomic *M* functions. Set (c) gives the best energy for the ground state and moderately good agreement with experiment for both kinds of transitions.

I. INTRODUCTION

IN a previous paper[1] we have calculated the vertical excitation energies of a number of the electronic transitions which have been observed in the ultraviolet spectrum of carbon monoxide. These energies were calculated using occupied and virtual LCAO-MO SCF orbitals which were obtained for the $^1\Sigma^+$ ground state of the molecule. The basis set of functions were 1*s*, 2*s*, and 2*p* atomic functions. The agreement was reasonably good for the states which have been spectroscopically labeled[2] as $a\ ^3\Pi$, $a'\ ^3\Sigma^+$, $e\ ^3\Sigma^-$, and $A\ ^1\Pi$. For the state $B\ ^1\Sigma^+$, $C\ ^1\Sigma^+$, $b\ ^3\Sigma^+$, $d\ ^3\Pi$, and $F\ ^1\Pi$ the difference between calculated and observed energies was so large that it is evident that this basis set is too restricted to account for these states. If the *d* state is assumed to be $^3\Delta$ rather $^3\Pi$,[3] the agreement becomes satisfactory. There are some known higher lying states $E\ ^1\Sigma^+$, $G\ ^1\Pi$, and $c\ ^3\Sigma^+$ which were not discussed at all.

While the characterization of ultraviolet spectra from only vertical excitation energies is necessarily incomplete, most of the calculations reported in the literature give only these results. The exploration for better wave functions to explain the higher states must for practical reasons pass through the stage of considering only the vertical excitations. Better functions will be found by extending the basis set, and each extension results in a considerable increase in computing time.

In this paper we shall compare the vertical excitation energies calculated from LCAO-MO SCF functions obtained from three different augmented sets: (a) 1*s*, 2*s*, 2*s*′, 2*p*, and 2*p*′ atomic functions on each center; (b) 1*s*, 2*s*, 2*p*, 3*s*, and 3*p* functions on each center; (c) 1*s*, 2*s*, 2*s*′, 2*p*, 2*p*′, 3*s*, and 3*p* functions on each center.

II. CALCULATIONS

The LCAO-MO SCF orbitals were calculated for the ground state of CO which has the configuration

$$(1\sigma)^2(2\sigma)^2(3\sigma)^2(4\sigma)^2(1\pi)^4(5\sigma)^2,$$

using the IBM 704 program written by one of us

TABLE I. Exponents used in different calculations.

Calculation	Carbon		Oxygen	
I	1*s*	5.67	1*s*	7.66
	2*s*	1.61	2*s*	2.25
	2*p*	1.57	2*p*	2.23
II	1*s*	5.673	1*s*	7.658
	2*s*	2.4	2*s*	3.37
	2*s*′	1.2	2*s*′	1.685
	2*p*	2.4	2*p*	3.37
	2*p*′	1.2	2*p*′	1.685
III	1*s*	5.7	1*s*	7.7
	2*s*	1.625	2*s*	2.275
	2*p*	1.625	2*p*	2.275
	3*s*	0.4833	3*s*	0.5833
	3*p*	0.4833	3*p*	0.5833
IV	1*s*	5.673	1*s*	7.658
	2*s*	2.4	2*s*	3.37
	2*s*′	1.2	2*s*′	1.685
	2*p*	2.4	2*p*	3.37
	2*p*′	1.2	2*p*′	1.685
	3*s*	0.4833	3*s*	0.5833
	2*p*	0.4833	3*p*	0.5833

* A brief account of some of the results in this paper has been given earlier (J. Chem. Phys. **33**, 931 (1960)).

† On leave of absence 1960–61. U. S. National Cancer Institute Special Fellow at the Institut Pasteur, Paris.

[1] H. Brion and C. Moser, J. Chem. Phys. **32**, 1194 (1960).

[2] See, e.g., G. Herzberg, *Molecular Spectra and Molecular Structure*; *Spectra of Diatomic Molecules* (D. Van Nostrand Company, Inc., Princeton, New Jersey, 1950), 2nd ed.

[3] R. S. Mulliken, Can. J. Chem. **36**, 11 (1958).

(R.K.N.). This program not only calculates the LCAO coefficients of the basis functions but also the matrix elements of the core and SCF operators and all two-electron integrals in the orthogonal basis of the molecular orbitals. Thus we have readily available all that we need to calculate matrix elements of the many-particle Hamiltonian. All calculations were carried out at the observed equilibrium distance 1.1280 A (2.1319 a.u.).[2]

The parameters which were used in each calculation are given in Table I. For purposes of comparison we list the parameters used in the earlier simple calculation (which is called here calculation I).

While the parameters we have chosen are certainly not the "best" in each set, we think that our results are not very sensitive to a particular choice of exponents for two reasons: (1) The exponents in calculation I are those which minimize the energies of the atoms for this set.[4] There is no significant difference in the calculated orbital energies if Slater exponents are used.[5] (2) We see later that some of the states are always computed to have more or less the same energies even with the different basis sets which we present in this paper.

The LCAO coefficients of calculations II, III, and IV are collected in Table II along with the orbital energies.

Excited-state configurations result from single-particle excitations from the ground state to the virtual orbitals. The energies corresponding to the excited configurations have been calculated using the proper Hamiltonian.

Augmenting the basis set introduces flexibility in two different ways in the calculation of excited-state energies. Each orbital is a function of more parameters and there are many more possibilities for single-excited configurations. In calculation I there was only one unoccupied orbital of each symmetry and it was found that the interaction between the two single excitations which were possible for most of the symmetries was very small.

In calculation II the energies corresponding to two different single excitations with the same symmetry were in general far apart and with little interaction between them. Thus, with one exception, we can represent the excited states as particular single excitations. This exception is found for the $^1\Sigma^+$ excited states. There is an accidental near degeneracy between the lowest $\sigma\rightarrow\sigma$ and $\pi\rightarrow\pi$ transitions which has been split by solving the appropriate 2×2 secular equation.

In calculations III and IV, on the contrary, there are a number of single excitations of the same symmetry which are rather close together in energy. For these calculations the state energies are the linear combinations of single-excited functions found from solving a secular equation.

The computed vertical excitations found from the four calculations and the experimental results are collected in Table III. As the experimental data are not always known in sufficient detail, the error in the experimental vertical excitation energies may be at most about 0.1 ev. The calculated energies are given after configuration interaction. In Table IV we give the form of the functions for the various states found in calculation III. The states calculated in calculation IV have been obtained from similar but somewhat larger matrices.

We have, in general, limited ourselves to configurations which result from single excitations from the ground state. Doubly excited configurations in general are higher in energy and interact less. We have in one specific case investigated in considerable detail the effect of larger number of interacting functions. We might think that the lowest excitation, say $^1\Sigma^+\rightarrow{}^1\Sigma^+$, does not correspond to the difference in energy between the ground state and our limited configuration interaction function which represents the first excited state but between the Hartree-Fock energy (in the LCAO approximation, of course) of ground and excited states. The Hartree-Fock energy of the excited state can be approximated by diagonalizing the matrix between the lower excited function and all functions which are different from it only by one orbital. In calculation IV the lowest excitation energy of $^1\Sigma^+$ symmetry corresponds to the excitation $5\sigma\rightarrow6\sigma$. In this calculation one can construct 63 independent wave functions which differ from this function by only one orbital. As the calculation of all matrix elements would have been extremely tedious, we have limited ourselves to calculating the lowering of energy by second-order perturbation theory. Second-order perturbation theory gives a lowering of about 1.0 ev and our choice of configurations gives a lowering of about 0.5 ev. It is likely that second-order perturbation theory slightly exaggerates the lowering. Thus the error introduced in the way we have chosen our configurations does not seem to be very important.

III. DISCUSSION

The results found from calculations I and II are nearly the same. The states which are found to be in satisfactory agreement with experiment are the same in both calculations with only negligible differences in calculated energies. The fact that the states which can be reasonably well described by functions in the L shell are equally well rendered whether the functions are single or double is an indication that the excitation energies are not very sensitive to the choice of parameters.

The total energy of the ground state of carbon monoxide is calculated to be 6.4 ev better by calculation II than by calculation I. This indicates that

[4] C. C. J. Roothaan, Technical Report, Laboratory of Molecular Structure and Spectra, University of Chicago, 1955, p. 24.
[5] B. J. Ransil, Revs. Modern Phys. **32**, 245 (1960).

TABLE II. LCAO coefficients for SCF orbitals of carbon monoxide I. Calculation II.

	$1s_O$	$1s_C$	$2s_O$	$2s'_O$	$2s_C$	$2s'_C$	$2p\sigma_O$	$2p'\sigma_O$	$2p\sigma_C$	$2p'\sigma_C$	ϵ_i (a.u.)
1σ	0.991384	0.000266	0.023151	−0.012071	0.000530	0.005083	0.004426	−0.004727	−0.000929	0.003851	−20.725507
2σ	−0.000765	0.990975	0.000600	−0.001327	0.026059	−0.006633	0.002160	−0.003869	0.005320	−0.001173	−11.424389
3σ	−0.218740	−0.151705	0.262384	0.778685	0.163793	−0.164300	0.081844	0.289090	0.237026	−0.177623	−1.562660
4σ	0.119716	−0.142026	−0.149949	−0.613827	0.217518	0.303667	0.313264	0.390079	0.112520	0.066043	−0.807914
5σ	0.014727	−0.147626	−0.024474	−0.121327	0.212649	0.750918	−0.135707	−0.229788	−0.315153	−0.207930	−0.577427
6σ	0.063401	0.068225	−0.174462	−1.831056	−0.145721	1.784124	0.069914	−0.891237	−0.353808	2.022589	0.482116
7σ	0.000393	0.355798	0.023532	0.071562	−1.218903	0.999251	0.060078	−0.065987	0.968480	−0.918177	1.068530
8σ	0.029394	−0.308087	0.022443	−0.172572	1.121469	−0.540318	−0.359518	−0.396551	1.143669	−0.655276	1.316454
9σ	−0.209595	0.087630	0.648927	−0.453290	−0.592435	0.140048	−1.352854	1.511353	−0.354572	0.269828	2.119748
10σ	0.565176	−0.047467	−1.973381	3.618826	−1.858748	−1.020396	1.861272	0.239536	0.239536	−1.576104	3.626314
	$2p\pi_O$	$2p'\pi_O$	$2p\pi_C$	$2p'\pi_C$							
1π	0.297546	0.558861	0.192314	0.234251							−0.676950
2π	−0.165455	−0.586011	0.177808	0.870621							0.123129
3π	−0.067555	−0.054188	−1.480352	1.316816							1.052217
4π	−1.539170	1.549188	0.266288	−0.600048							2.136733

TABLE II (*continued*) Calculation III.

	$1s_O$	$1s_C$	$2s_O$	$2s_C$	$3s_O$	$3s_C$	$2p\sigma_O$	$2p\sigma_C$	$3p\sigma_O$	$3p\sigma_C$	ϵ_i (a.u.)
1σ	0.996056	0.000237	0.020393	−0.007469	0.004690	−0.004595	0.005574	0.005878	−0.000270	−0.002219	−20.785149
2σ	−0.000234	0.996128	−0.006239	0.021116	−0.012450	0.010088	−0.000959	0.005144	−0.005969	−0.001415	−11.437894
3σ	−0.214320	−0.116587	0.759588	0.251052	0.029459	−0.032440	0.228815	0.171545	−0.051042	−0.059806	−1.550059
4σ	0.126055	−0.145340	−0.650599	0.538841	−0.020254	−0.018970	0.629921	0.076586	−0.013830	−0.058757	−0.775262
5σ	−0.004025	0.136543	−0.036934	−0.702926	−0.204634	0.115848	0.420041	0.547907	−0.058109	−0.004644	−0.522271
6σ	0.013168	0.022838	−0.173496	0.036564	−1.295658	2.151828	0.077502	0.046504	−0.032710	−0.162743	0.029317
7σ	−0.036330	0.002786	0.196589	0.058589	−0.750232	0.465327	−0.076582	−0.043654	−0.035472	−0.798745	0.063090
8σ	0.004772	0.019427	−0.259164	−0.108568	−3.073910	2.544585	0.014547	−0.040237	2.074480	2.570639	0.123800
9σ	−0.004766	0.076359	0.303100	−0.942649	4.182277	−3.667763	0.005015	0.291038	0.639699	−0.867617	0.200899
10σ	0.115525	−0.097255	−1.102651	1.028341	0.034404	−0.083251	−0.961551	1.256176	−0.185358	−0.273548	0.898812
	$2p\pi_O$	$2p\pi_C$	$3p\pi_O$	$3p\pi_C$							
1π	0.762350	0.447165	0.171644	−0.111206							−0.627015
2π	−0.169535	0.096214	−0.083209	1.679864							0.045166
3π	0.062924	0.370466	−2.295193	1.694014							0.136676
4π	−0.684720	0.878996	0.567963	−0.673735							0.227201

(*continued on page 1705*)

TABLE II (*continued*) Calculation IV.

	$1s_O$	$1s_C$	$2s_O$	$2s'_O$	$2s_C$	$2s'_C$
1σ	0.991358	0.000328	0.023228	−0.012418	0.000293	0.005861
2σ	−0.000597	0.990582	0.000169	0.001544	0.027418	−0.012377
3σ	−0.219064	−0.150908	0.262497	0.775458	0.161052	−0.153393
4σ	0.117613	−0.140284	−0.148154	−0.663380	0.205139	0.437285
5σ	0.011434	−0.141139	−0.021829	−0.158866	0.195804	0.864408
6σ	−0.000651	0.026776	−0.014867	−0.226503	0.003995	0.163262
7σ	−0.021981	0.011166	0.027333	0.203257	−0.021413	0.069242
8σ	−0.025147	−0.001497	−0.004274	−0.195321	0.047691	0.055575
9σ	0.019607	0.026666	0.008680	0.352370	−0.105448	−1.171086
10σ	0.062601	0.028871	−0.194668	−1.960083	−0.011502	2.100968
11σ	0.029205	0.020045	−0.004995	−0.172497	−0.024042	0.589753
12σ	0.022493	0.520593	−0.176641	−0.225853	−1.843052	2.280824
13σ	−0.208360	0.123940	0.650842	−0.464920	−0.734904	0.382540
14σ	0.575618	−0.117223	−1.988449	3.895522	−0.138376	−2.515756

	$3s_O$	$3s_C$	$2p\sigma_O$	$2p\sigma'_O$	$2p\sigma_C$	$2p\sigma'_C$	$3p\sigma_O$	$3p\sigma_C$	ϵ_i (a.u.)
1σ	−0.000716	0.000489	0.004390	−0.004765	−0.000913	0.003907	−0.000619	−0.000190	−20.715692
2σ	0.007995	−0.005712	0.001811	−0.002912	0.005325	−0.001839	0.002839	−0.000160	−11.411549
3σ	−0.017128	0.008968	0.081870	0.285648	0.235471	−0.175904	−0.001835	0.002128	−1.552723
4σ	−0.250519	0.189091	0.311726	0.373325	0.108193	0.063592	−0.076437	0.011821	−0.802754
5σ	−0.270924	0.206898	−0.141136	−0.248758	−0.313122	−0.215497	−0.078507	0.032393	−0.572849
6σ	−1.934501	2.698355	0.000258	0.067532	0.051192	−0.042666	0.015749	0.438388	0.022793
7σ	0.153439	−0.288003	0.002765	−0.086602	−0.035060	0.069403	−0.465553	−1.431078	0.060260
8σ	−3.981506	3.240686	−0.052428	0.045904	0.032124	−0.224312	1.826107	2.509825	0.115552
9σ	4.162544	3.523978	0.031454	−0.026366	−0.018849	0.333051	1.289882	−0.404767	0.146021
10σ	−0.649970	0.369051	0.032246	−0.991783	−0.405267	2.170431	−0.439835	−0.463102	0.573040
11σ	−1.260855	1.012201	−0.213830	−0.344002	0.015767	−1.276069	−0.025293	0.563182	1.307843
12σ	−2.368313	1.777850	0.315891	0.033989	−0.005076	−0.159394	−0.588877	0.286016	1.527536
13σ	−0.016903	0.087827	−1.373607	1.574813	−0.296139	0.163352	−0.433482	−0.199634	2.231372
14σ	0.847020	0.609830	−1.064385	1.961154	0.237059	−1.665571	0.273813	0.021227	3.766413

	$2p\pi_O$	$2p'\pi_O$	$2p\pi_C$	$2p'\pi_C$	$3p\pi_O$	$3p\pi_C$	ϵ_i (a.u.)
1π	0.297739	0.560502	0.188410	0.235303	0.014272	−0.022340	−0.668462
2π	−0.061703	−0.167341	0.053855	0.143027	−0.796742	1.621004	0.040943
3π	−0.062775	−0.201308	0.104976	0.680363	−1.854934	1.143573	0.125512
4π	−0.144131	−0.535357	0.141259	0.604344	1.584347	−1.519856	0.157489
5π	−0.023892	−0.086789	−1.555571	1.501572	−0.335187	−0.013167	1.166109
6π	−1.566950	1.602013	0.185705	−0.496695	−0.517767	0.432093	2.223932

although this function is not more suitable than the simplest possible function to describe excited states of the molecule, it should be appreciably better to describe properties of the molecule associated with the ground state, e.g., dipole moment, nuclear quadrupole coupling constant, etc. We shall discuss this point in a future paper.

The results of calculation III are certainly encouraging. In this calculation the states which were adequately described in calculation I and II are here also

TABLE III. Calculated excitation energies for carbon monoxide (ev).

State	Calculation I	Calculation II	Calculation III	Calculation IV	Exptl[a,b]
$X\,^1\Sigma^+$	0	0	0	0	0
$a\,^3\Pi$	6.17	6.34	6.21	6.20	6.22
$a'\,^3\Sigma^+$	7.41	7.82	7.43	7.87	8.25
$e\,^3\Sigma^-$	9.56	9.64	9.55	9.67	8.80
$A\,^1\Pi$	9.23	9.63	9.20	9.37	8.74
$d\,^3\Pi$	24.2		11.53	12.98	
$d\,^3\Delta$	8.48	8.73	8.50	8.77	8.96
$B\,^1\Sigma^+$	23.1	18.0	11.1	12.4	10.8
$C\,^1\Sigma^+$	27.4	24.0	11.8	13.2	11.4
$E\,^1\Sigma^+$	...		13.3	14.8	11.5
$b\,^3\Sigma^+$	23.1	17.9	10.4	11.8	10.4
$c\,^3\Sigma^+$	...		11.7	13.1	11.6
$F\,^1\Pi$	26.0	21.6	11.7	13.1	12.4
$G\,^1\Pi$	...		13.6	14.7	13.1

[a] Data taken from Y. Tanaka, A. S. Jursa, and F. Le Blanc, J. Chem. Phys. **26**, 862 (1957); G. Herzberg, *Molecular Spectra and Molecular Structure; Spectra of Diatomic Molecules* (D. Van Nostrand Company, Inc., Princeton, New Jersey, 1950) 2nd ed.; and *Données Spectroscopiques concernant les Molécules Diatomiques* (Hermann et Cie, Paris, 1951).

[b] These values have been corrected for verticality. As the experimental data is not always sufficient to do this accurately, the error in the observed energies is about 0.1 ev for the higher transitions.

in good agreement with experiment. But, in addition, the higher lying states are also in good agreement.

From these three calculations we can imagine intuitively that certain of the transitions (to the states $a\,^3\Pi$, $a'\,^3\Sigma^+$, $e\,^3\Sigma^-$, $A\,^1\Pi$, and $d\,^3\Delta$) take place between orbitals both of which are made up of atomic L functions (i.e., $n=2$) and certain of the transitions (to the states $B\,^1\Sigma^+$, $C\,^1\Sigma^+$, $E\,^1\Sigma^+$, $b\,^3\Sigma^+$, $C\,^3\Sigma^+$, $F\,^1\Pi$, and $G\,^1\Pi$) take place between orbitals, the lower being made up of atomic L functions, the upper of atomic M functions. This is in agreement with an empirical analysis made by Mulliken[6] nearly 30 years ago but this is, to the best of our knowledge, the first time detailed calculations have brought independent confirmation.

To have some more quantitative information on the separation of states into the two different kinds of transitions we have calculated the gross atomic population[7] for each state and have grouped these together as the number of electrons in the M shell. The results are collected in Table V. The ground state contains 0.2 electron in the M shell from the atomic populations due to the fact that all MO's are linear combinations of functions in the K, L, and M shells. The separation of states into those which correspond to L–L and L–M shells, respectively, is confirmed by this calculation.

Calculation III indicates that there is not likely to be a second $^3\Pi$ state around 9 ev but rather there should be one about 11.5 ev, which has not yet, as far

TABLE IV. Configuration interaction functions (calculation III).

$B\,^1\Sigma^+$	$0.9141\,\psi^{5\sigma,6\sigma}$	$-0.0146\,\psi^{5\sigma,7\sigma}$	$+0.0042\,\psi^{5\sigma,8\sigma}$	$+0.3910\,\psi^{5\sigma,9\sigma}$	$-0.0321\,\psi^{1\pi,2\pi}$	$-0.1008\,\psi^{1\pi,3\pi}$	
$C\,^1\Sigma^+$	-0.0178	$+0.9866$	-0.1421	$+0.0758$	-0.0084	-0.0139	
$E\,^1\Sigma^+$	-0.2957	$+0.0412$	$+0.6854$	$+0.6493$	-0.0787	-0.1155	
$a'\,^3\Sigma^+$	$0.0277\,\psi^{5\sigma,6\sigma}$	$+0.0113\,\psi^{5\sigma,7\sigma}$	$+0.0001\,\psi^{5\sigma,8\sigma}$	$+0.0450\,\psi^{5\sigma,9\sigma}$	$+0.3227\,\psi^{1\pi,2\pi}$	$+0.1287\,\psi^{1\pi,3\pi}$	$+0.9362\,\psi^{1\pi,4\pi}$
$b\,^3\Sigma^+$	0.8363	-0.1152	$+0.0480$	$+0.5260$	-0.0741	$+0.0453$	-0.0293
$c\,^3\Sigma^+$	0.0873	$+0.9772$	-0.1621	$+0.0931$	-0.0042	-0.0487	-0.0107
$A\,^1\Pi$	$0.4346\,\psi^{5\sigma,2\pi}$	$+0.2653\,\psi^{5\sigma,3\pi}$	$+0.8604\,\psi^{5\sigma,4\pi}$	$-0.0047\,\psi^{1\pi,6\sigma}$	$-0.0201\,\psi^{1\pi,7\sigma}$		
$F\,^1\Pi$	0.8539	-0.4224	-0.3007	-0.0392	$+0.0247$		
$G\,^1\Pi$	-0.1381	-0.3099	$+0.1786$	-0.5949	$+0.7064$		
$a\,^3\Pi$	$0.3143\,\psi^{5\sigma,2\pi}$	$+0.2732\,\psi^{5\sigma,3\pi}$	$+0.9091\,\psi^{5\sigma,4\pi}$	$-0.0022\,\psi^{4\sigma,4\pi}$	$+0.0052\,\psi^{1\pi,6\sigma}$	$+0.0017\,\psi^{1\pi,7\sigma}$	
$d\,^3\Pi$	0.8769	-0.4099	-0.1793	$+0.1588$	-0.0610	$+0.0419$	
$e\,^3\Sigma^-$	$0.3648\,\psi^{1\pi,2\pi}$	$+0.1422\,\psi^{1\pi,3\pi}$	$+0.9201\,\psi^{1\pi,4\pi}$				
$d\,^3\Delta$	$0.3420\,\psi^{1\pi,2\pi}$	$+0.1343\,\psi^{1\pi,3\pi}$	$+0.9301\,\psi^{1\pi,4\pi}$				

[6] R. S. Mulliken, Revs. Modern Phys. **4**, 1 (1933).
[7] R. S. Mulliken, J. Chem. Phys. **23**, 1883 (1955).

TABLE V. Number of electrons in the M shell.

State	Principal excitation	Number of electrons in M shell from total atomic population
$X\ ^1\Sigma^+$		0.20
$B\ ^1\Sigma^+$	σ—σ	1.13
$C\ ^1\Sigma^+$	σ—σ	1.14
$E\ ^1\Sigma^+$	σ—σ	1.13
$a'\ ^3\Sigma^+$	π—π	0.20
$b\ ^3\Sigma^+$	σ—σ	1.13
$c\ ^3\Sigma^+$	σ—σ	1.14
$A\ ^1\Pi$	σ—π	0.22
$F\ ^1\Pi$	σ—π	1.10
$d\ ^3\Delta$	π—π	0.21
$a\ ^3\Pi$	σ—π	0.17
$d\ ^3\Pi$	σ—π	1.17
$e\ ^3\Sigma^-$	π—π	0.21

as we know, been observed. This is further evidence in support of the assignment of the d state as $^3\Delta$. By contrast we find evidence for a higher lying $^1\Pi$ state near 12 ev, but it remains to be seen whether or not this state is computed to be bound.

The main drawback to calculation III is that the energy of the ground state (Table VI) obtained from these functions is hardly better than that obtained from calculation I and considerably above calculation II.

The ground-state energy calculated from calculation IV is slightly better than that found from calculation II. The agreement for L shell-L shell transitions is satisfactory. For the L shell-M shell transitions the energies

TABLE VI. Calculated LCAO-MO SCF ground-state energies for carbon monoxide.

Calculation	Energy (a.u.)
I	−112.3276
II	−112.5645
III	−112.3767
IV	−112.5752

are calculated to be about 1.5–2.0 ev higher than in calculation III.

As we have indicated above, this does not seem to be principally due to our choice of configurations. More likely this increase is due to the fact that our representation of L shell functions by two exponents for each atomic orbital is far better than our representation of M shell orbitals with only one exponent each. Each calculation of the type of calculation IV takes about 5 hr on the IBM 704 computer. We estimate that a calculation where each orbital in the M shell was doubled would take about 20 hr and it is possible that it might in fact be necessary to triple the number of exponents.[8]

As there is every reason to believe that calculation IV gives an adequate representation for the ground state and for both types of electronic transitions, we are presently constructing potential curves with this type of function. The results will be reported in due course.

ACKNOWLEDGMENTS

This work has been supported in part by grants from the Martin Company, the Ordnance Corps, U.S. Department of the Army, and the National Science Foundation.

[8] See, e.g., P. O. Löwdin, Phys. Rev. **103,** 1746 (1956).

Modulation Broadening of Unsaturated Lorentzian Lines*

HUGO WAHLQUIST

Jet Propulsion Laboratory, California Institute of Technology, Pasadena, California

(Received April 7, 1961)

Closed, analytic expressions are obtained for the harmonic amplitudes which arise in the modulation of unsaturated Lorentzian absorption lines. Exact formulas relating characteristics of the observed signals (amplitude, width, slope ratios, etc.) to the true half-width for arbitrary modulation amplitude are derived. The results of greatest experimental interest are graphed.

IN the interpretation of magnetic resonance data obtained with phase-detection techniques, it is necessary to allow for the effect of modulation broadening on the absorption lines. Several authors[1] have discussed this problem and supplied useful corrections to observed quantities. These formulas, however, have been either approximate or based on series expansions whose convergence is slow in some regions of experimental interest. The series in fact do not converge at all over certain ranges of modulation amplitude. In connection with an experimental program requiring accurate corrections for large amplitude modulation, the effect of modulation broadening on unsaturated Lorentzian lines was calculated for arbitrary modulation ampltiude. The results are in closed form and are exact for the case of very slow sweep through the line.

Let $H_a(t)$ be the homogeneous applied magnetic field whose time dependence involves only the slow linear sweep across an absorption line. Let H_0 be the field at which resonance occurs, $H_{\frac{1}{2}}$ the half-width (distance between half-intensity points) of the true line, and H_ω the amplitude of the sinusoidal modulation with circular frequency ω. The normalized unsaturated Lorentzian absorption line may be written

$$g(H)=\pi^{-1}\frac{\frac{1}{2}H_{\frac{1}{2}}}{(\frac{1}{2}H_{\frac{1}{2}})^2+(H-H_0)^2}, \tag{1}$$

and under modulation a signal will be generated which is proportional to

$$g[H(t)]=\pi^{-1}\frac{\frac{1}{2}H_{\frac{1}{2}}}{(\frac{1}{2}H_{\frac{1}{2}})^2+[H_a(t)+H_\omega\cos\omega t-H_0]^2}. \tag{2}$$

The sweep rate is assumed to be very small so that $H_a(t)$ remains essentially constant over a time interval $2\pi/\omega$. Writing $H_a-H_0=H_\delta$ and Fourier analyzing $g(t)$,

$$g(t)=\pi^{-1}\frac{\frac{1}{2}H_{\frac{1}{2}}}{(\frac{1}{2}H_{\frac{1}{2}})^2+(H_\delta+H_\omega\cos\omega t)^2}$$

$$=\frac{H_{\frac{1}{2}}}{2\pi}\sum_{n=0}^{\infty}a_n(H_{\frac{1}{2}},H_\omega,H_\delta)\cos n\omega t, \tag{3}$$

where the integrals for the Fourier amplitudes

$$a_n(H_{\frac{1}{2}},H_\omega,H_\delta)$$

$$=(\omega/\pi)\int_{-\pi/\omega}^{\pi/\omega}\frac{\cos n\omega t}{(\frac{1}{2}H_{\frac{1}{2}})^2+(H_\delta+H_\omega\cos\omega t)^2}dt \tag{4}$$

may be performed by a standard technique of contour integration.[2] Using phase detection of the fundamental, the recorded signal will be proportional to the Fourier coefficient a_1. Since the integration may be performed at once for all n, an expression for the amplitude of any harmonic will be displayed. This is then specialized to the case of primary interest here, and the properties of a_1 further investigated.

Define dimensionless parameters α and β where

$$\alpha=(H_\delta/H_\omega)\quad -\infty<\alpha<\infty \qquad \beta=(\tfrac{1}{2}H_{\frac{1}{2}}/H_\omega)\quad 0<\beta<\infty \tag{5}$$

and the auxiliary variables γ, u, r, and ϕ, where

$$\gamma=1+\beta^2+\alpha^2,$$

$$u=\gamma+[\gamma^2-4\alpha^2]^{\frac{1}{2}} \qquad 2<u<\infty,$$

$$r=[u-1-u^{\frac{1}{2}}(u-2)^{\frac{1}{2}}]^{\frac{1}{2}} \qquad 0<r<1,$$

$$\phi=\arccos\{-\sqrt{2}\alpha/u^{\frac{1}{2}}\} \qquad 0<\phi<\pi. \tag{6}$$

* This paper presents the results of one phase of research carried out at the Jet Propulsion Laboratory, California Institute of Technology, sponsored by the National Aeronautics and Space Administration.

[1] M. M. Perlman and M. Bloom, Phys. Rev. **88,** 1290 (1952); E. R. Andrew, *ibid.* **91,** 425 (1953); R. Beringer and J. G. Castle, *ibid.* **81,** 82 (1951); O. E. Myers and E. J. Putzer, J. Appl. Phys. **30,** 1987 (1959).

[2] P. M. Morse and H. Feshbach, *Methods of Theoretical Physics* (McGraw-Hill Book Company, Inc., New York, 1953), Vol. 1, p. 408.

The result of the integration for any n is

$$a_n(H_\frac{1}{2}, H_\omega, H_\delta)=\left(\frac{2}{H_\omega}\right)^2\left\{\frac{[r^{n-1}+r^{-(n-1)}]\sin(n+1)\phi-[r^{n+1}+r^{-(n+1)}]\sin(n-1)\phi}{[r^{-1}-r][r^2+r^{-2}+2\cos 2\phi]\sin\phi}+I_n\right\},$$

where

$$I_0=I_1=0,$$

$$I_2=1,$$

$$I_n=\left\{(d/dx)^{n-2}\left[\frac{1}{(x-z)(x-z^*)[x-(1/z)][x-(1/z^*)]}\right]\right\}_{x=0},\tag{8}$$

$$z=r\exp(i\phi).$$

For the cases $n=0, 1, 2$ the general expression reduces to

$$a_0=\left(\frac{2}{H_\omega}\right)^2\frac{u^\frac{1}{2}}{2(u-2)^\frac{1}{2}(u-\gamma)},\tag{9}$$

$$a_1=\pm\left(\frac{2}{H_\omega}\right)^2\frac{(2\gamma-u)^\frac{1}{2}}{2(u-2)^\frac{1}{2}(u-\gamma)},\tag{10}$$

$$a_2=\left(\frac{2}{H_\omega}\right)^2\left[1+\frac{u^\frac{1}{2}(1+2\gamma-2u)}{2(u-2)^\frac{1}{2}(u-\gamma)}\right].\tag{11}$$

The detected signal, $a_1[H_\frac{1}{2}, H_\omega, H_\delta(t)]$, is obtained by restoring the linear time variation of H_a, or equivalently, H_δ. The pertinent properties of the resulting curve, which is similar in shape to the derivative of the Lorentzian curve, may be obtained by taking the derivative

$$(da_1/dH_\delta)=-(2/H_\omega^3)\frac{u^\frac{1}{2}(u^2-u-2\gamma u+3\gamma)}{(u-2)^\frac{1}{2}(u-\gamma)^3}.\tag{12}$$

Setting the factor $(u^2-u-2\gamma u+3\gamma)$ to zero generates relationships giving the location and amplitude of the two anti-symmetric peaks of a_1 for any modulation amplitude. Letting the symbol for any quantity with a suffix p attached denote that quantity evaluated at the peaks, these relations are

$$(H_\delta)_p=\alpha_p H_\omega=(\alpha_p/2\beta)H_\frac{1}{2},\tag{13}$$

and

$$(a_1)_p=\pm\tfrac{3}{2}(2/H_\frac{1}{2})^2\left[\frac{(u_p-2)}{u_p(2u_p-3)}\right]^\frac{1}{2}\tag{14}$$

$$\alpha_p=\pm\left[1+\tfrac{5}{3}\beta^2-\tfrac{4}{3}\beta(\beta^2+\tfrac{3}{4})^\frac{1}{2}\right]^\frac{1}{2}\tag{15}$$

$$u_p=2+\tfrac{4}{3}\beta^2+\tfrac{4}{3}\beta(\beta^2+\tfrac{3}{4})^\frac{1}{2}.\tag{16}$$

Additional expressions, which often facilitate manipulations, are

$$\gamma_p=\frac{u_p(u_p-1)}{2u_p-3}\qquad 4\alpha_p^2=\frac{u_p^2}{2u_p-3}\qquad 4\beta^2=\frac{3(u_p-2)^2}{2u_p-3}.\tag{17}$$

Figure 1 illustrates the dependence of the location and amplitude of the peaks on the modulation amplitude.

Setting the derivative $(d/dH_\omega)[(a_1)_p]$ to zero, it further results that the maximum possible height of the peaks of a_1 occurs when $\beta=\frac{1}{2}$. On letting the subscript m indicate fulfillment of this condition, the following values are obtained:

$$\alpha_{pm}=\pm\tfrac{1}{2}\sqrt{3}\qquad \gamma_{pm}=2\qquad u_{pm}=3$$

$$(H_\omega)_m=H_\frac{1}{2}\qquad (H_\delta)_{pm}=\pm\sqrt{3}/2(H_\frac{1}{2})$$

$$(a_1)_{pm}=\pm 2(1/H_\frac{1}{2})^2.\tag{18}$$

These results are contained implicitly in Fig. 1. Quantities corresponding to $(H_\delta)_p$ and $(a_1)_p$ for an unbroadened line would be the location $(H_\delta)_{pL}$ and height $(a_1)_{pL}$, of the peaks in the first derivative of a pure Lorentzian curve. Calculation shows that

$$(H_\delta)_{pm}=3(H_\delta)_{pL}\qquad (a_1)_{pm}=(4\pi/3\sqrt{3})(a_1)_{pL}.\tag{19}$$

Another experimentally useful characteristic is the ratio of maximum slopes of a_1. Equating the second derivative

$$d^2a_1/dH_\delta^2=\pm(6/H_\omega^4)\times\frac{(2\gamma-u)^\frac{1}{2}[(\gamma-1)u^3-(\gamma-1)(1+2\gamma)u^2+4\gamma(\gamma-1)u-\gamma^2]}{(u-2)^\frac{1}{2}(u-\gamma)^5}\tag{20}$$

to zero gives the possibilities

$$u=2\gamma,\tag{21}$$

or

$$(\gamma-1)u^3-(\gamma-1)(1+2\gamma)u^2+4\gamma(\gamma-1)u-\gamma^2=0.\tag{22}$$

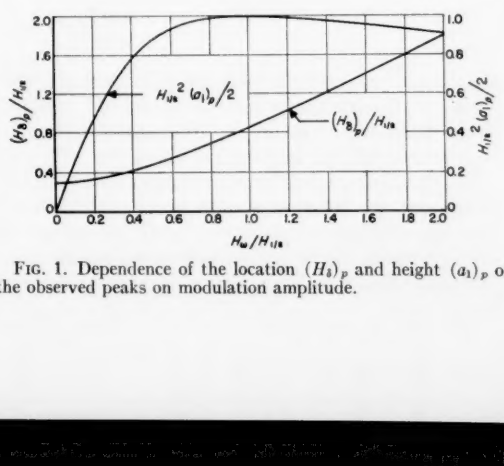

FIG. 1. Dependence of the location $(H_\delta)_p$ and height $(a_1)_p$ of the observed peaks on modulation amplitude.

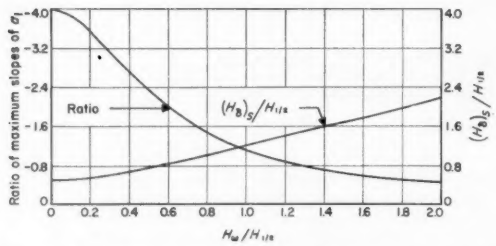

FIG. 2. Dependence of the location of outer maximum slope $(H_\delta)_s$ and the ratio of maximum slopes on modulation amplitude.

The first of these equations implies $H_\delta=0$ from the definition of u. Evaluating Eq. (12), the inner maximum slope of a_1 occurring at $H_\delta=0$ is in general,

$$da_1/dH_\delta\,|_{H_\delta=0}=-2(2/H_{\frac{1}{2}})^3[\beta^2/(1+\beta^2)^{\frac{1}{2}}]. \quad (23)$$

The outer maximum slope is given by one of the roots of the equation

$$(\gamma_s-1)u_s^3-(\gamma_s-1)(1+2\gamma_s)u_s^2+4\gamma_s(\gamma_s-1)u_s-\gamma_s^2=0, \quad (24)$$

where the subscript s indicates the value of a quantity at the place of outer maximum slope. It is quite cumbersome to extract this root straightforwardly, except for the case where $\beta=\frac{1}{2}$ which is discussed below. For the general case, an indirect approach which proceeds as follows seems most feasible. Treating Eq. (24) as a quadratic for γ_s, it is solved to obtain

$$\gamma_s=\frac{u_s}{2(2u_s^2-4u_s+1)}\times\{u_s^2+u_s-4+(u_s-2)(u_s^2-2u_s+5)^{\frac{1}{2}}\}. \quad (25)$$

After selecting a value for u_s, γ_s is fixed by this equation. Then α_s and β are evaluated with the equations

$$\alpha^2=\tfrac{1}{4}u(2\gamma-u) \quad (26)$$

$$\beta^2=\gamma-1-\alpha^2, \quad (27)$$

which follow immediately from the definitions of γ and u. The slope ratio can then be found using Eqs. (12) and (23). Figure 2, showing how the location of outer maximum slope and the slope ratio depend on modulation amplitude, was constructed using this procedure.

Returning to the case when a_1 has maximum amplitude, i.e., $\beta=\frac{1}{2}$, it can be shown that Eq. (24) reduces to

$$u_{sm}^3-5u_{sm}^2+3u_{sm}+5=0, \quad (28)$$

where the subscript m means simply $\beta=\frac{1}{2}$ as before. The only valid root of this equation is expressible as

$$u_{sm}=\tfrac{1}{3}[5+8\cos\{\pi/6+\tfrac{1}{3}\sin^{-1}(5/32)\}]\cong 3.9032, \quad (29)$$

and the other quantities needed are given in terms of u_{sm} by

$$\gamma_{sm}=\frac{u_{sm}^2-5}{2(u_{sm}-2)}\cong 2.6888,$$

$$\alpha_{sm}=\pm\left[\frac{u_{sm}(u_{sm}-\frac{5}{2})}{2(u_{sm}-2)}\right]^{\frac{1}{2}}\cong\pm 1.1995$$

$$(H_\delta)_{sm}=\alpha_{sm}H_{\frac{1}{2}} \quad (30)$$

$$\left(\frac{da_1}{dH_\delta}\right)_{sm}=\left(\frac{2}{H_{\frac{1}{2}}}\right)^3\frac{u_{sm}^{\frac{1}{2}}(u_{sm}-2)^{\frac{1}{2}}(3u_{sm}-5)(u_{sm}-3)}{(u_{sm}^2-4u_{sm}+5)^2}$$

$$\cong 0.31833(2/H_{\frac{1}{2}})^3.$$

Evaluating Eq. (23) for $\beta=\frac{1}{2}$,

$$(da_1/dH_\delta)_{H_\delta=0}=-(4/5(5)^{\frac{1}{2}}](2/H_{\frac{1}{2}})^3\cong -0.35777(2/H_{\frac{1}{2}})^3, \quad (31)$$

and so the slope ratio for $\beta=\frac{1}{2}$ is -1.1239. In comparison, the slope ratio is -4 for the derivative of the Lorentz curve.

ACKNOWLEDGMENTS

The author is indebted to Dr. A. F. Hildebrandt, Dr. C. A. Barth, and Dr. D. D. Elleman for an introduction to this problem and for discussions of its experimental significance.

THE JOURNAL OF CHEMICAL PHYSICS VOLUME 35, NUMBER 5 NOVEMBER, 1961

Reactions of Methyl with Isopropyl Radicals

CARL A. HELLER

Chemistry Division, U. S. Naval Ordnance Test Station, China Lake, California

(Received March 28, 1961)

The photolysis of methyl isopropyl ketone has been used to study the reaction of methyl and isopropyl radicals at 100° in the gas phase. The disproportionation/combination ratio is 0.17±0.03. The ratio, isobutane²/ethane×hexane is 3.5±0.33. Deuterated ketone was used to permit correction for abstraction reactions.

INTRODUCTION

SEVERAL papers have dealt with the reactions of two radicals and these were reviewed recently.[1] There are many systems in which two different radicals are present, and the interradical reaction rates must be known to understand the over-all mechanism. The rate ratios are themselves interesting in clarifying the reaction mechanism involved in disproportionation and combination reactions. The present study was carried out to obtain exact values for the system of methyl and isopropyl radicals. The ketone chosen yields both radicals upon photolysis and the products are explained by well-known reactions.

EXPERIMENTAL AND RESULTS

The ketone was deuterated by exchange with D_2O to 1,1,1,3-tetradeutero, 3-methyl butanone-2. It was analyzed by NMR, gas chromatography, and mass spectrometry. Although better than 99% pure by these instruments, the analysis of the photolysis products show that there was a small ethyl radical producing impurity present (probably diethyl ketone).

The photolyses were carried out in a 326-ml, 10-cm diameter cylindrical quartz vessel in an aluminum block furnace. The full light from two Hanovia S100 lamps was used to produce a high steady-state radical concentration.

The products were separated on a temperature programmed silene-1% anthracene column and collected for mass spectrometer analysis.[2] The peak areas were used for quantitative analysis with an error (from standard blends) of ±4%.

After preliminary runs with undeuterated ketone the data in Table I were obtained with the deuterated ketone. The results of the mass spectrometer analyses of collected peaks are shown in Table II. The column would separate *n*-butane, but none was found.

MECHANISM AND CALCULATIONS

The products and product distribution can be explained by the major reactions:

$$CD_3COCD(CH_3)_2+\text{photon}\rightarrow\cdot CD_3+\cdot COCD(CH_3)_2 \quad \text{(i)}$$

$$CD_3COCD(CH_3)_2+\text{photon}\rightarrow CD_3\dot{C}O+CH_3\dot{C}DCH_3 \quad \text{(ii)}$$

$$\cdot COCD(CH_3)_2\rightarrow CO+CH_3\dot{C}DCH_3 \quad \text{(a)}$$

$$CD_3\dot{C}O\rightarrow\cdot CD_3+CO \quad \text{(b)}$$

$$CD_3+CH_3CDCH_3\rightarrow C_4H_6D_4 \quad (1)$$

$$2CD_3\rightarrow C_2D_6 \quad (2)$$

$$2CH_3CDCH_3\rightarrow C_6H_{12}D_2 \quad (3)$$

$$CD_3+CH_3CDCH_3\rightarrow CD_3H+CH_2=CD-CH_3 \quad (4)$$

$$2CH_3CDCH_3\rightarrow CH_3CDHCH_3+CH_2=CD-CH_3. \quad (5)$$

From the data in Tables I and II, ratios of the above rates were calculated. The disproportionation/combination and cross combination rate ratios are temperature independent within the error. The ratios calculated will be given here, and the calculations with corrections for minor reactions shown below.

$$\text{I}\qquad \frac{(\text{isobutane})^2}{\text{ethane}\times\text{hexane}}=3.5\pm0.33=k_1^2/k_2\cdot k_3$$

(13 runs)

$$\text{II}\qquad 0.16\pm0.04=\frac{\text{methane-}a\,(CD_4)}{\text{isobutane}}=k_4/k_1$$

(7 runs)

$$=\frac{\text{propylene-0.63 hexane}}{\text{isobutane}}$$

(11 runs)

$$=0.17\pm0.03$$

$$\text{III}\qquad \frac{\text{propane-}d_1}{\text{hexane}}=0.67=k_5/k_3.$$

(4 runs)

Mass spectra of two ethane samples show d_6, d_5, and d_3 ethane. The ethane-d_5 presumably arises from CD_2H and indicates that 1.5% of the methyls contain an H atom. The ethane-d_3 is explained by the presence of CH_3CD_2 which indicates diethyl ketone as an impurity. The CH_3CD_2 radical also is revealed by propane-d_5 and pentane-d_3. These, although too small for accurate measurement, are approximately equal. Assuming that the ethane-d_3 would be 5% in all runs and correcting

[1] A. F. Trotman-Dickenson, Ann. Rev. Phys. Chem. **10**, 58 (1959).

[2] C. A. Heller and A. S. Gordon, J. Phys. Chem. **62**, 709 (1958).

TABLE I. Photolysis of methyl isopropyl ketone-d_4. Analyses of products by gas chromatography.

Run	527	508	501	502	503	504	505	506	507
T °C	53	86	93	100.0	99⅓	99½	101	101½	99½
P mm Hg	7.5	10.0	10.0	10.0	20.0	30.0	5.0	10.0	20.0
% decomp.[a]	0.14	0.7	0.21	0.16	0.18	0.17	1.1	0.9	...
Δt sec	100	251	50	50	50	50	250	250	250
				Rates nanomoles l^{-1} sec^{-1}					
Methane (C_1)	0.47	0.83	0.87	1.39	2.87	4.88	0.74	0.98	2.56
CO	5.23	12.3	18.5	13.9	30.6	44.4	9.47	15.7	...
Ethane (C_2)	0.364	1.81	2.63	2.60	6.37	8.42	1.68	3.07	5.06
Ethene[b]	t	...	...	...	...	...	...	...	...
Propane	2.13	2.09	3.62	2.95	5.16	6.89	1.25	2.35	4.38
Isobutane (C_4)	1.97	4.39	5.84	4.92	10.23	15.51	3.04	5.57	9.63
Propene	2.80	3.03	2.14	2.42	5.18	7.94	1.59	2.72	5.28
Isopentane-d_2	0.15	0.01	...		t	0.11	0.017	0.040	0.060
2,3-dimethyl butane-d_2 (C_6)	2.90	2.98	3.19	3.00	5.73	8.84	1.78	3.12	5.52
				Calculated values					
$\Sigma CD_3/\Sigma C_3H_6D$[c]	0.25	0.57	0.67	0.71	0.74	0.78	0.76	0.75	0.74
$\Sigma C_3H_6D/CO$	2.4	1.26	0.97	1.17	1.05	1.08	1.00	1.08	...
$C_4^3/C_2 \cdot C_6$	3.66	3.58	4.14	3.10	2.87	3.23	3.09	3.24	3.32
C_1/C_4	0.24	0.19	0.15	0.28	0.28	0.31	0.24	0.18	0.27
$(C_1\text{-}aCD_4)/C_4$[d]		0.12						0.14	0.21
$\frac{\text{Propene-0.63}C_6}{C_4}$	0.49	0.26	(0.02)	0.11	0.15	0.15	0.15	0.14	0.19
Propane-d_1/C_6					0.70	0.70	0.62	0.67	

Run	520	522	523	524	525	526
T	101½	116	116	116	116	116
P	20.0	10.0	5.0	5.0	10.0	10.0
t sec	250	200	200	200	200	100
% decomp.	0.20	1.1	1.16	1.1	0.95	0.50
				Rates nanomoles l^{-1} sec^{-1}		
Methane	2.83	1.94	1.18	0.94	1.58	1.29
CO	6.88	21.8	11.9	11.5	19.5	20.4
Ethane	0.93	3.64	2.12	2.13	3.62	3.83
Ethene	0.043	t	0	t	...	...
Propane	0.61	2.27	1.34	1.34	2.18	2.47
Isobutane	...	6.46	3.96	3.73	6.33	6.84
Propene	1.02	3.19	1.87	2.05	3.36	3.38
Isopentene-d_2	0.02	0.090	0.054	0.055	0.15	0.073
2,3-dimethyl butane-d_2	0.99	3.17	1.95	1.95	3.22	3.52
				Calculated values		
$\Sigma CD_3/\Sigma C_3H_6D$	...	0.86	0.85	0.81	0.82	0.80
$\Sigma C_3H_6D/CO$	...	0.84	0.93	0.96	0.95	0.97
$C_4^3/C_2 \cdot C_6$	...	3.63	3.80	3.35	3.44	3.47
C_1/C_4	...	0.30	0.30	0.25	0.25	0.19
$(C_1\text{-}aCD_4)/C_4$	...	...	0.21	0.18	0.16	0.12
$\frac{\text{Propene-0.63}C_6}{C_4}$	...	0.18	0.16	0.22	0.21	0.17

[a] Based on CO production.
[b] Ethene peak sometimes hidden by propane peak.
[c] Σ=sum of products from methyl or isopropyl radicals.
[d] CD_4 values from Table II.

the ethane in ratio I gave the value of 3.5 in place of an uncorrected value of 3.4.

Ratio II can be calculated by formulas based upon either the methane or the propylene formed in reaction (4). The "$a(CD_4)$" is a correction to the total methane for methane formed by abstraction reactions from the ketone. The a is calculated from the data for abstraction for diisopropyl ketone-d_2[2] and deuterated acetone.[3] Thus a is the ratio $(CD_4+CD_3H)/CD_4$ expected for CD_3 abstraction from the parent ketone. Most abstraction is from the D in the tertiary position, and a is 1.13, 1.15, and 1.17 at 85°, 100° and 116°C.

The total propylene must be corrected by that formed in reaction (5) and the previously found[2] ratio of k_5/k_3 is used. The values for II found by the two formulas are seen to agree.

If the acetyl and butyryl radicals decomposed sufficiently rapidly the rate of CO production would equal both the sum of methyl and the sum of propyl products. This is not the case, and the ratios of these quantities are temperature dependent. The ratio $\sum C_3H_6D/CO$ is large at low temperature and drops to about 0.95. The ratio $\sum CD_3/\sum C_3H_6D$ is small and rises to 0.85 at 116°C.

Evidently the acetyl concentration is high at the lower temperature and is tied up as biacetyl (which was identified) and acetone. At higher temperatures most of the acetyl decomposes so the methyl and CO production rises relative to isopropyl. But hydrogen abstraction is occurring and some radicals are tied up by combination with ketonyl radicals. The isobutyryl is in low concentration, either because the primary photolysis is reaction ii or because reaction a is rapid.

The acetyl present in the system might be expected to be a source of easily abstracted D atoms for reaction with methyl and isopropyl radicals.[4] Fortunately, not much error is introduced into ratio II if all the CD_4 is due to reaction of CD_3 with CD_3CO since the CD_4 must still be subtracted from the total methane. The factor a becomes 1.00 if all the CD_4 is due to this reaction rather than abstraction from the ketone. Then the largest error would be for run 525 and is 0.17×0.312 or +5% of the value 0.16 which is smaller than the standard deviation. Since some abstraction is undoubtedly occurring, the actual error is smaller.

TABLE II. Deuteration of products.[a]

Methane				Ethane			
Run	% d_4			Run	d_6	d_5	d_3
506	19			522	92.3	3.12	4.6
507	18			524	91.1	2.55	6.4
508	31						
523	25.1			Butanes: All samples analyzed are d_4.			
524	25.0						
525	31.2			Hexanes: all samples analyzed are d_2.			
526	31.3						
527	24.3						
Propane				Pentane			
Run	d_1	d_3	d_5	Run	% d_5		
503	77.8	19.3	3.0	527	100		
504	89.4	7.4	3.2				
505	88.9	7.7	3.3				
506	88.7	7.6	3.7				

[a] Deuteration was obtained for runs 509–521 but the gas chromatograms were inaccurate for these runs.

The acetyl might also react with isopropyl to give acetaldehyde and propylene. If this is true, ratio II calculated from the propylene should rise at lower temperatures. The only two values measured, 0.26 and 0.49 at 85° and 53°, indicate that this reaction does occur.

$$CD_3CO+C_3H_6D\rightarrow CD_3CHO+C_3H_5D.$$

Finally, reaction (5) can be measured by measuring the propane-d_1. The value found for ratio III is close to the more accurate value of 0.63 ± 0.04 found with diisopropyl ketone.[2]

A recent paper[5] gives a value of 0.22 for the disproportionation/combination ratio of methyl-isopropyl radicals. The value 0.17 given in the present paper should be more accurate since the data obtained permitted a more complete picture of the over-all mechanism.

ACKNOWLEDGMENT

The author acknowledges many helpful discussions with Dr. Herman F. Cordes, Dr. Alvin S. Gordon, and Dr. Richard Knipe.

[3] J. R. McNesby and A. S. Gordon, J. Am. Chem. Soc. **76**, 4196 (1954).

[4] M. H. J. Wijnen, J. Chem. Phys. **28**, 271 (1958).

[5] J. A. Kerr and A. F. Trotman-Dickenson, J. Chem. Soc. **1960**, 1609–11.

Chemistry of Positive Ions. I. General Theory Particularly for the Radiation Induced Cross Linkage of Polymers and Polymerization of Saturated Hydrocarbons*

W. F. LIBBY

Department of Chemistry and Institute of Geophysics, University of California, Los Angeles

(Received April 20, 1961)

The chemical properties of positive ions are considered to be analogous to those of the corresponding neutral atom or molecule. However, the charge strengthens bonds and provides the long-ranged attractive polarization force which causes the reaction cross sections to be very large. For organic ions dehydrogenation to form carbonium ions occurs frequently, so in addition to the parent ion radical with its great reactivity as a type of super fluorine atom, the carbonium ions with their extremely acidic (electrophilic) properties cause a wholly different set of reactions. These are analogous to those of carbene and may lead to the radiation-induced polymerization of saturated aliphatic hydrocarbons. Both ion radicals and carbonium ions can play important roles in the radiation induced cross linkage of polyethylene and other polymers. It is predicted that the effect of phase will be very important in radiation chemistry, because the cage effect of the surrounding close-packed molecules in the liquid and solid phase, as contrasted with the gas phase, will cause the fragmentation of the parent ions which is so marked in the gas phase to be reversed to a considerable extent and promote the formation of large molecules, particularly polymers.

I. INTRODUCTION

THE chemical properties of ions produced by the abstraction of an electron from a normal atom or molecule are different from those of ions produced by chemical bonding because the ions produced by ejection of a single electron by ionizing radiation are free radicals, while those produced by normal electron transfer are closed-shell rare-gas types. Therefore, we can understand that A^+ is chemically very active while Cl^- is inert. H_2 and A^+ react[1] avidly to form HA^+, while Cl^- is completely inert to all the systems. This system of reasoning by analogy between properties of the ions and those of the corresponding neutral systems of similar electron structure based, as it is, on the assumption that the electrical charge is a general perturbing force which in no way leads to specific chemical effects, is proposed in this paper as a general theoretical method of attack on the problem of the chemistry of ions. A similar approach has been implied in other studies, particularly by Kaufman and Koski.[2]

Different from either the ion radicals produced by the removal of a single electron by high-energy radiation acting on normal atoms or molecules are the carbonium ions and carbanions of organic chemistry. The carbonium ions have six electrons in the valence shell and although they are neither radicals nor closed-shell structures, they have reactivities intermediate because of the strong acidic (electrophilic) nature given by the missing electron pair. The carbanions on the other hand have a complete octet. Thus, the carbonium ion

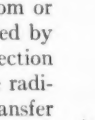

is much more reactive than carbanion

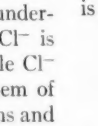

and rivals the free radical

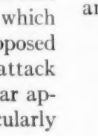

in reactivity because the positive charge imparts a special reactivity due to the attractive long-range polarization force due to the charge as explained and predicted by Eyring, Hirschfelder, and Taylor.[3] According to the present theory, the chemistry of carbonium ions should reflect the strongly electrophilic and acidic nature of this structure. The properties and reactions should be related to the salts which can be formed with bases like alcohols or amines or olefins and, as we shall see, even saturated aliphatic hydrocarbons. These properties of carbonium ions are generally well known and recognized by organic chemists. On the other hand, carbanions have no specific chemical properties; and their

* This research was supported by the U. S. Air Force through the Air Force Office of Scientific Research of the Air Research and Development Command.

[1] G. Gioumousis and D. P. Stevenson, J. Chem. Phys. **29,** 294–299 (1958).

[2] (a) Joyce J. Kaufman and W. S. Koski, J. Am. Chem. Soc. **82,** 3262 (1960). (b) W. S. Koski, Joyce J. Kaufman, and C. F. Pachucki, *ibid.* **81,** 1326 (1959). (c) W. S. Koski, Joyce J. Kaufman, C. F. Pachucki, and F. J. Shipko, *ibid.* **80,** 3202 (1958).

[3] H. Eyring, J. O. Hirschfelder, and H. S. Taylor, J. Chem. Phys. **4,** 479 (1936). These authors showed that the polarization forces cause reactants to be attracted to one another so that large collision cross sections are to be expected. The polarization forces serve to bring the chemical forces into range.

reactions should not be affected by the environment in any way except to stabilize the negative charge. Thus, a lattice or surface presenting electrostatically favorable locations for anions might stabilize carbanions and increase their importance in organic kinetics. An example might be anion exchange resins.

The ion radicals—the third of the general species of organic ions—are probably of great importance in radiation chemistry. They have no analog in organic chemistry. They are charged free radicals with all the great bonding facility characteristic of ordinary free radicals which is still further enhanced kinetically by the long-ranged polarization forces.[3,4]

The recent great interest in ion molecule reactions has followed on the conclusive observation in mass spectrographs[5–7] that reactions occur between the ion radicals produced by the electron beams and the neutral un-ionized molecules in the gas being bombarded and also between the carbonium ions which result from the loss of an H atom by the ion radicals formed in the first instance. These reactions occur in the very short times available in the mass spectrometers. The reaction

$$CH_4^+ + CH_4 = CH_5^+ + CH_3 \qquad (1)$$

was the most remarkable one studied. And this led to the general realization that a new type of reaction was occurring which might explain some of the difficulties in radiation chemistry which had of recent years been concerned more with free radical reactions than with those of ion radicals and carbonium ions. It seems very likely that with further study the proper role of ion molecule reactions in radiation chemistry will be established and the whole problem of the effects of high-energy ionizing radiations on matter may approach a solution.

II. THEORY OF THE CHEMISTRY OF IONS

In order to understand more clearly the chemical reactions occurring between ions and molecules we postulate:

A. The Chemical Properties of an Ion Closely Resemble Those of the Most Similar Uncharged Species except for an Additional Enhancement of Rates of Reaction and Increase of Ionization Potentials Due to the Charge

An ion radical bearing a charge is assumed to be very similar in chemical properties to its isoelectronic homolog which is neutral, except for the extra long-range attraction of the charge polarization forces and the consequent high-reaction cross sections. Thus, we expect that CH_4^+ and atomic F (as well as CH_3, of course) will behave very similarly, except that CH_4^+ will have larger reaction cross sections due to the long-range attractive polarization forces and form somewhat stronger bonds due to the tighter electron binding. So, just as the reaction

$$F\cdot + CH_4 = HF + CH_3\cdot \qquad (1')$$

occurs, so should reaction (1), as written above, occur. This remarkable reaction has been found[5] to occur readily in mass spectrographs with the large collision cross sections predicted by the polarization theory.[5–7] In fact, one knows now that CH_5^+ and its isotopic homologs are very ubiquitous in gaseous discharges in methane. Similarly we speak of $C_nH_{2n+2}^+$ ion with the charge localized on one of the carbon atoms as behaving in respect to that carbon atom as F does. In other words, $R_1R_2R_3R_4C^+$ acts as F. In fact, any closed-shell structure of the first row elements will according to these ideas fit the same analogy, and the second and lower rows will fit the other halogens similarly. These points are set out in Table I.

The carbonium ions $C_nH_{2n+1}^+$ will be strong acids analogous to BF_3, that is, extremely electrophilic, and very rapidly form salts with all bases such as olefines, so we would expect

$$C_nH_{2n+1}^+ + C_mH_{2m} = C_{n+m}H_{2(n+m)+1}^+ \qquad (2)$$

to occur as a general reaction. The straight formation of the salt ion

$$C_{n+m}H_{2(n+m)+1}^+$$

cannot occur with high probability in the gas phase because of momentum conservation requirements and the removal of two H atoms to form H_2 satisfies this requirement. The large heat of formation of the salt ion pays for the difference in C—H and H—H bond energies. In fact, this salt ion

$$C_{n+m}H_{2(n+m)+1}^+$$

is so stable that the reaction

$$C_nH_{2n+1}^+ + C_mH_{2m+2} = C_{n+m}H_{2(n+m)+1}^+ + H_2 \qquad (3)$$

occurs. The extra stabilization of the salt ion pays for the heat of unsaturation. An example is

$$CH_3^+ + CH_4 = C_2H_5^+ + H_2.$$

Carbonium ions are formed by ionizing radiations readily, as we will mention later, because of the strictures of the Franck-Condon principle so these salt ion products of carbonium ion reactions are formed in good yield with only the dehydrogenated form being found in the gas phase.

[4] (a) *The Chemical Effects of Alpha Particles and Electrons* (Chemical Catalog Company, New York, 1928). (b) G. Glockler and S. C. Lind, *The Electro-Chemistry of Gases and Other Dielectrics* (John Wiley & Sons, New York, 1939).

[5] (a) V. L. Tal'roze and A. K. Lyubimova, Doklady Akad. Nauk. S.S.S.R. **86,** 909 (1952). (b) V. L. Tal'roze and E. L. Frankevitch, J. Am. Chem. Soc. **80,** 2344 (1958).

[6] D. P. Stevenson and D. O. Schissler, J. Chem. Phys. **23,** 1353 (1955); **24,** 926 (1956).

[7] (a) F. W. Lampe, J. Am. Chem. Soc. **79,** 1055 (1957). (b) F. H. Field, J. L. Franklin, and F. W. Lampe, *ibid.* **79,** 2419 (1957); (c) **79,** 2665 (1957). (d) F. W. Lampe and F. H. Field, *ibid.* **79,** 4244 (1957); (e) **81,** 3242 (1959).

TABLE I. Chemical analogy table for organic ions.

Part A. Ion radicals and their reactions

I. Species analogous to atomic fluorine with reactions anlogous to

$$F+C_nH_{2n+2}=HF+C_nH_{2n+1}$$

CH_4	13.1 ev	Ion. Pot.	$CH_4^+ + CH_4 = CH_5^+ + CH_3$
C_2H_6	11.7 ev	Ion. Pot.	$C_2H_6^+ + CH_4 = C_2H_7^+ + CH_3$
C_3H_8	11.2 ev	Ion. Pot.	$C_3H_8^+ + CH_4 = C_3H_9^+ + CH_3$
C_5H_{12}	10.24 ev	Ion. Pot.	$C_5H_8^+ + C_5H_{12} = C_5H_8 + C_5H_{12}^+ = C_5H_{10}^+ + C_5H_7$
H_2O	12.67 ev	Ion. Pot.	$H_2O^+ + CH_4 = H_3O^+ + CH_3$; $H_2O^+ + C_2H_6 = H_2O + C_2H_6^+ = HO + C_2H_7^+$
C_2H_5OH	10.6	Ion. Pot.	$C_2H_5OH^+ + CH_4 = C_2H_5OH_2^+ + CH_3$
HF	16.4	Ion. Pot.	$HF^+ + CH_4 = HF + CH_4^+ = F + CH_5^+$

II. Species analogous to atomic chlorine with analogous reactions

HCl	12.78	Ion. Pot.	$HCl^+ + CH_4 = H_2Cl^+ + CH_3$
CCl_4	11.1	Ion. Pot.	$CCl_4^+ + CH_4 = HCCl_4^+ + CH_3$
H_2S	10.5	Ion. Pot.	$H_2S^+ + C_nH_{2n+2} = H_3S^+ + C_nH_{2n+1}$
PH_3	10.0	Ion. Pot.	$PH_3^+ + C_nH_{2n+2} = PH_4^+ + C_nH_{2n+1}$

Part B. Carbonium ions

I. Electrophilic (acidic) behavior as BF_3

$C_nH_{2n+1}^+$ + Nucleophilic agents = salt intermediates = polymers or rearrangement products.

II. Hydride ion transfer and polymerization among saturated hydrocarbons

$$C_nH_{2n+1}^+ + C_mH_{2m+2} = C_nH_{2n+2} + C_mH_{2m+1}^+ \quad (m>n) \quad (1)$$

$$C_nH_{2n+1}^+ + C_mH_{2m+2} = C_{n+m}{}^+H_{2(n+m)+1} + H_2 \quad (1')$$

$$C_{n+m}H_{2(n+m)+1}^+ + C_pH_{2p+2} = C_{n+m+p}H_{2(n+m+p)+1}^+ + H_2 \text{ etc.}$$

The enthalpies of formation ΔH_f of the saturated aliphatic carbonium ions are given approximately by

$$\Delta H_{f(\text{kcal/mole})} = 226 - 7.3n + 116e^{-n} \qquad n=1, 2, 3 \qquad (5)$$

$$\Delta H_{f(\text{kcal/mole})} = 218 - 7.3n \qquad n=4, 5, 6\cdots. \qquad (5')$$

And the ΔH of formation for the saturated hydrocarbons are given by

$$\Delta H_{(\text{kcal/mole})} = -10 - 5n - 8.2e^{-n} \qquad (6)$$

Therefore, the polymerization of saturated hydrocarbons via the carbonium ion is energetically possible if the assumptions and treatment given here are correct. In fact, ΔH for reaction (3) as given above, the formation of the dehydrogenated salt ion from saturated normal straight chain aliphatic carbon with the elimination of hydrogen, will be given by

$$\Delta H_{(\text{kcal/mole})} = 10 - 2.3m + 8.2e^{-m} \qquad (7)$$

which for all cases for $m \geq 4$ and with $n=1, 2, 3$ would be exothermic. On this basis, reaction (3) can continue until neutralization occurs when a free radical or an olefine plus a free radical will be formed, and we thus have a mechanism for the radiation-induced polymerization of saturated aliphatic hydrocarbons. This reaction, as we shall see later, should have the highest yields in condensed phases.

Evidence for radiation-induced polymerization of normal aliphatics is to be found in several papers, but one in particular is the work on *n*-hexane vapor by Futrell,[8] who remarks that 73% of the total hexane decomposed formed products of higher boiling liquids above hexane in molecular weight and apparently of the general empirical formula C_nH_{2n}. He remarks that "drops of liquid were observed to form near the reactor window which could not be removed by flaming during evacuation."

Dewhurst[9,10] studied liquid *n*-hexane and although he did not specifically remark about high molecular weight products, he showed that a decrease in the yield of H_2 from a value of 5.2 molecules per 100 ev of energy absorbed ($G=5.2$) to 3.0 was caused by two entirely different changes: cooling to liquid nitrogen temperature or adding free radical scavengers such as I_2. Thus he showed that about 60% of the H_2 molecules are released by reactions which occur intramolecularly or with next-nearest neighbors, and he went on to show by further analysis that these two possibilities were about equal with the G values for unsaturation (intramolecular H_2 release) and for polymerization, both being about 1.5. The essential point made here—that chain polymerization through carbonium ion intermediates probably is an important effect of radiation—thus seems to be compatible with present information.

Obviously, reaction (3) may also be involved in the radiation-induced cross linkage of polymers and in radiobiological effects.

The mechanism of reaction (3), the polymerization reaction, probably can be represented by the transition complex

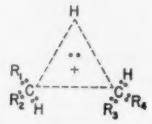

with the three-center electron pair bond holding the two hydrocarbons together as proposed by Winstein.[11]

[8] J. H. Futrell, J. Am. Chem. Soc. **81,** 5921 (1959).
[9] H. A. Dewhurst, J. Phys. Chem. **62,** 15 (1958).
[10] H. A. Dewhurst, J. Am. Chem. Soc. **83,** 1050 (1961).
[11] (a) S. Winstein and H. J. Lucas, J. Am. Chem. Soc. **60,** 836 (1938). (b) S. Winstein and R. Adams, *ibid.* **70,** 838 (1948). (c) S. Winstein and D. S. Trifan, *ibid.* **71,** 2953 (1949); **74,** 1154 1154 (1952). (d) S. Winstein, Experientia Supple. II, 137 (1955). (e) S. Winstein, J. Sonnenberg, and L. de Vries, J. Am. Chem. Soc. **81,** 6523 (1959).

The second characteristic of carbonium ions is that hydride ion transfer will occur between them through the transition complex cited above. The ionization potentials of the saturated aliphatic hydrlcarbon free radicals

$$C_nH_{2n+1}\cdot$$

are given approximately by

$$I_{(ev)}=8.2-(n/10)+5.4e^{-n} \tag{8}$$

so ΔH for the hydride-ion transfer reaction

$$C_n^+H_{2n+1}+C_mH_{2m+2}=C_nH_{2n+2}+C_m^+H_{2m+1} \tag{9}$$

will be given by

$$\Delta H_{(kcal/mole)}=2.3(n-m)-124(e^{-n}-e^{-m}), \tag{10}$$

which is clearly exothermic when m is greater than n.

Therefore, the transition complex pictured above, if it decomposes without reacting to eliminate H_2 and form a polymeric carbonium ion, will leave the charge on the larger of the two fragments resulting in the hydride transfer reaction (9).

The strongly acidic (electrophilic) character of carbonium ions makes them avidly react with all olefins because of their basic or nucleophilic character. These saltlike intermediates so formed can lead to a variety of products. The intermediate can be represented by

where again as with the saturated aliphatics the three-center electron pair bond[11] holds the structure together.

Carbonium ions may have an additional class of reactions in analogy to the properties of methylene radicals as described by Doering[12] and his co-workers.

According to our analogy principle C^+H_3, carbonium ion, and CH_2, methylene radical, should behave very similarly with CH_3^+ being faster and somewhat stronger in its acid electrophilic properties. Doering has shown CH_2 to be able to do three remarkable reactions

$$R_1R_2+CH_2=R_1CH_2R_2 \tag{11}$$

$$\text{—C—H}+CH_2=\text{—C—}CH_3$$

$$\text{—C—X}+CH_2=\text{—C—}CH_2\text{—X}. \tag{13}$$

By the theory outlined here we expect, therefore,

$$R_1R_2+\overset{+}{C}H_3=R_1\overset{+}{C}HR_2 \tag{14}$$

$$\text{—C—H}+CH_3^+=\text{—C—}CH_4^+ \tag{15}$$

$$\text{—C—X}+CH_3^+=\text{—C—}CH_3^+\text{—X}. \tag{16}$$

The products in all of these reactions are saturated molecules of the "H·F" type in the present language and do not react further except when neutralized to release H, H_2, or RH and the corresponding free radical.

The intermediate for the carbene reaction probably is

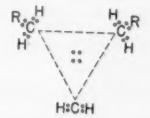

while we would envisage the intermediate for the carbonium insertion reaction to be the analogous structure with the extra H^+ above the shared electron pairs.

B. Charge Will Transfer to Release the Maximum Energy in Reaction

The heat of reaction should be taken into account in considering the identity of the ionic species reacting. Thus, if species M has an ionization potential I_m larger than that of N but the heat evolved in the reaction between M^+ and N is larger than this difference, the reaction can proceed. An example is Ne^+ reacting with H_2 to form NeH^+ and H. The ionization potentials are 21.53 ev and 15.14 ev, respectively; but the bond between "super" F, namely Ne^+, and H should exceed 6.4 ev, thus making the reaction occur. (The normal HF bond is 5.8 ev and, as shown later, the charge enhancement of the H atom affinity for fluorinelike structures is probably about 1.8 ev greater than for the corresponding free radical to give an expected value for HNe^+ bond of 7.2 ev). Thus, the reaction to form HNe^++H atom can occur.

C. Franck-Condon Principle Causes Many Ions to Decompose as Formed

It is generally accepted that the Franck-Condon principle applies to ionization as well as to photon emission and absorption. The ionization act itself, being the collision of a fast-moving electron or proton or gamma ray with an atom or molecule, leaves the ion in the configuration of the original molecule, and subsequent readjustment to the proper normal configuration of the ion frequently causes dissociation to occur in the case of molecules so that the yield of the molecular ion corresponding to the bombarded molecule usually is low.

[12] (a) W. von E. Doering, R. G. Buttery, R. G. Laughlin, and N. Chaudhuri, J. Am. Chem. Soc. **78**, 3224 (1956). (b) W. von E. Doering and P. LaFlamme, J. Am. Chem. Soc. **78**, 5447 (1956).

Therefore, a principal consequence of the Franck-Condon principle is that free radicals and carbonium ions are generated by the ionization of molecules. Thus, for CH_4 the ions formed by 75-ev electrons as in a mass spectrometer working at 10 mm Hg pressure in the ionization chamber are[13]

CH_4^+ 49% CH_2^+ 4.3% CH_3^+ 41% CH^+ 1.8%

(primary in origin)

CH_5^+ 2.2% $C_2H_5^+$ 1.2% (secondary in origin).

The primary ions—those formed as a direct consequence of the act of ionization and thus varying proportionately with the gas pressure in the ion chamber—all must be the result of unimolecular dissociation of the unstable ionized molecule as formed in the ionization act itself, except, of course, for the primary ion of the target molecule. The secondary ions such as CH_5^+ and $C_2H_5^+$ will be formed by ion molecule reactions with the molecules being irradiated.

Since the ionization act can electronically excite the target molecule, the dissociation reactions will correspond to the various nonbonding states which are possible energetically. At the lowest effective energies of the ionizing radiation, only one type of reaction is possible; that is, the formation of the ion of the target molecule. But at higher energies, many different possibilities are realized and the usual conditions of radiation are such that dissociation does occur.

D. Activation Energies Occur

The fourth principle is that ion molecule reactions possess activation energies. Most of the data on the rates of the reactions of ion radicals with ordinary molecules[5–7] have been obtained in mass spectrometers in which the ion necessarily receives a considerable electrical acceleration in order that the ions can be removed from the ion chamber into the evacuated analytical chamber. The significance of the rate data, insofar as the existence of an activation energy is concerned, is difficult to evaluate for this reason. The value of the kinetic energy of an ion reacting in the spectrometer chamber can hardly be known, since the degree of acceleration before reaction occurs cannot be established accurately. The general argument has been advanced, however, that the activation energies must be small because the specific rates found are so high and within a factor of 2 agree with the rates calculated for the formation of the polarization complexes.

It seems probable, however, that ion radicals in general, in reacting with molecules, display an activation energy just as neutral free radicals do, even though the polarization forces pull the reactants together into close contact. The polarization forces probably are not able to establish the exact configuration of atoms of the transition state for certain reactions, and an additional energy of activation will be required.

It is clear also that an activation entropy corresponding to requirements of particular geometrical arrangethose brought about naturally by the polarization forces, also will exist so reactions of the same activation energy requirements will proceed at different rates. The production of stereoisomers from optically active ions or molecules, or both, would be a case in point.

Unfortunately, the evidence about the size of the activation energies is very meager, but it seems likely that further experimentation will reveal the existence of these important quantities for ion molecule reactions and something about their magnitudes.

E. Bond Strengths and Reaction Energies are Like Those of Uncharged Isoelectronic Structures When Corrected for the Electric-Charge Effect Separately

The fifth postulate of the proposed theory of positive ion chemistry is that reaction energies can be calculated on the basis that a charged molecule behaves chemically as does its uncharged isoelectronic analogs, except for a perturbing effect of the charge which can be considered separately and used as a correction.

The concept of chemical bonds is assumed to apply just as well to charged molecules as to neutral ones, and it seems therefore to be likely that the additivity of bond energies which applies so well to molecules—particularly organic molecules—should hold also for their ions. Therefore, we will expect to find a nearly constant H atom affinity for hydrocarbon ion radicals just as is true for the uncharged radicals.

For example, we consider the question as to whether the reaction

$$\begin{matrix} R_1^+ & R_1 & R_1^+ & R_1 \\ HCH + HCH = & HCH + & \cdot CH \\ R_2 & R_2 & R_2H & R_2 \end{matrix}$$

is generally exothermic. As remarked above, the analogous reaction (1) occurs for methane, so we conclude that the H atom affinity of CH_4^+ must exceed the energy of the CH bond in CH_4, 4.44 ev.

In order to estimate the effect of the positive charge on the H atom affinities of the ion radicals and to test the validity of the postulate of constant bond strength, we compare the H atom affinities of the structures: carbonium ions—radicals—ion radicals,

$$\begin{matrix} R_1^+ & R_1 & R_1^+ \\ \vdots & \vdots & \vdots \\ H{:}C & H{:}C\cdot, & H{:}C\cdot H. \\ \vdots & \vdots & \vdots \\ R_2 & R_2 & R_2 \end{matrix}$$

The difference between the mass spectrographic appearance potentials for the ions $R_1R_2CH^+$ and $R_1R_2CH_2^+$

[13] F. H. Field, J. L. Franklin, and F. W. Lampe, J. Am. Chem. Soc. **79**, 2419 (1957).

in various cases is given in Table II, as the carbonium ion H atom affinities. Although the experimental uncertainty is considerably and the Franck-Condon principle means that the $R_1R_2CH_2^+$ ions probably are formed in vibrationally excited states, thus reducing the derived H atom affinities for carbonium ions by perhaps one-half of one electron volt below the true value (this estimate of 0.5 ev is made for the difference between the appearance potential of CH_4^+ and the electron affinity of CH_4^+ by estimating the difference in the ground state average CH distances in CH_4 and CH_4^+ and using the force constants for the stretching and bending vibrations), we see that like those for the free radicals they too are approximately constant at an average value of about 1.8 ev when the Franck-Condon correction of about 0.5 ev is made. The first seven datum are from Lossing and deSousa[14] and the last two from Franklin and Field.[15]

It is enlightening in this connection to compare the H atom affinity of a bare proton, 2.6 ev, with that of an H atom itself, 4.52 ev. In general, we would expect the H atom affinity of a charged molecule with no odd electron, i.e., carbonium ions, to be approximately constant at some value less than a full bond; whereas with a radical, whether charged or neutral, the affinity would be at least that of a full electron pair bond with the bond to the charged radical having extra strength due to the charge. The abstraction of an H atom by a hydrocarbon radical ion from the corresponding uncharged hydrocarbon reaction (9) thus becomes exothermic. Of course, effects of structure will make it easier to abstract from a tertiary than from a secondary or primary carbon atom, and the abstraction reaction between mixed hydrocarbons or between different carbon atoms in a given hydrocarbon will reveal these differences. It seems likely, however, that in general a hydrocarbon ion radical will be able to abstract H atoms from hydrocarbons.

F. Cage Effect

The effects of change of phase should be very marked in ionic radiation chemistry. The effect of surrounding close-packed neighbor molecules in the liquid or solid state in preventing the escape of ion fragmentation products from one another should be large. In the gas-phase fragmentation of the parent ion is the usual result, and the nature of the products can even be predicted[16] with some certainty in the case of hydrocarbons. In the liquid and solid, however, much less fragmentation should occur because radicals and ions would be trapped and probably recombine to form the original ion or one of its isomers. H atoms probably are exceptional and can escape. Thus, we would expect a reduction in the yield of lighter products and an increase in the yield of heavy polymer from the interaction of the carbonium ion of the target hydrocarbon with this hydrocarbon itself.

Relatively few data on this point are available, but Dewhurst[17] gives data for *n*-hexane which show the yield of $C_{12}H_{26}$ to rise fivefold to a G (number of molecules per 100 ev of ionizing energy absorbed) value of 2.0 on condensing the vapor to liquid. Also the yield of CH_4 dropped fourfold to 0.12. All molecules lighter than C_6 decreased several-fold, while those made from the original hexane or its ions rose, with the yield of C_6H_{12} rising from 0.1 to 1.2.

TABLE II. H atom affinities of carbonium ions (ev).

CH_3^+	1.3
$C_2H_5^+$	1.2
$n\ C_3H_7^+$	1.7
$s\ C_3H_7^+$	0.6
$n\ C_4H_9^+$	2.1
$s\ C_4H_9^+$	1.1
$t\ C_4H_9^+$	0.7
$n\ C_5H_{11}^+$	1.2 to 2.8
$n\ C_6H_{13}^+$	0.4 to 0.8
Average	1.3
Franck-Condon correction	0.5
Average H atom affinity	1.8

III. APPLICATION TO THE RADIATION INDUCED CROSS LINKAGE OF POLYMERS

A remarkable general effect of ionizing radiation on hydrocarbon systems is the cross linkage of polyethylene and some of its derivative polymers induced by ionizing radiation. The ions produced by the radiation in this instance are trapped in the solid so fragmentation will be minimized (Sec. II.F). Writing the formula

$$\begin{matrix} R_1 \\ HCH \\ R_2 \end{matrix}$$

for the polymer chain, where R_1 and R_2 are long $(CH_2)_n$ chains, we imagine these chains to be lying in close proximity to other similar chains. Following ionization, the likely reactions are

$$\begin{matrix} R_1^+ & & R_1 \\ HCH & = H\cdot + & HC^+ \\ R_2 & & R_2 \end{matrix} \qquad (18)$$

$$\begin{matrix} R_1 & R_1 \\ HC^+ & + HCH = R_1R_2HC^+CR_1R_2 + H_2 \\ R_2 & R_2 \end{matrix} \qquad (19)$$

$$\begin{matrix} R_1^+ & R_1 & R_1^+ & R_1 \\ HCH & + HCH = & HCH & + \cdot CH. \\ R_2 & R_2 & R_2H & R_2 \end{matrix} \qquad (20)$$

[14] F. P. Lossing and J. B. deSousa, J. Am. Chem. Soc. **81**, 281 (1959).

[15] F. H. Field and J. L. Franklin, *Electron Impact Phenomena* (Academic Press Inc., New York, 1957).

[16] G. R. Lester, "Theoretical aspects of the mass spectra of polyatomic molecules," *Advances in Mass Spectrometry* (Pergamon Press, New York, 1959), p. 287.

[17] H. A. Dewhurst, J. Am. Chem. Soc. **83**, 1050 (1961).

TABLE III. Activation energies for $H+RH=H_2+R$.

CH_4	13.5
C_2H_6	9.0
C_3H_8	8.6
$n\ C_4H_{10}$	8.9
$n\ C_5H_{12}$	8.5
$n\ C_6H_{14}$	9.1
C_6H_6	<7

Considering these reactions as possible cross linkage mechanisms, we take atomic hydrogen first. Atomic hydrogen will be able to abstract hydrogen from some near chain and leave a trapped free radical locked into the chain crystal, and the first critical question is whether this site will be next to the ionization site or not. If it is, there will have been left a free radical near the free radical which will be formed when the carbonium ion of reaction (18) is eventually neutralized, and the obvious junction of these neighboring free radicals could form the cross bond desired. The activation energies for H abstraction by H from various hydrocarbons are given in Table III, as taken from Trotman-Dickenson.[18]

Assuming the activation energy to be 9 kcal/mole and the general temperature in the neighborhood of the ionization site to be 500°K, the Arrhenius factor $\exp\{-9000/RT\}$ will be 10^{-4}. If the temperature were 1000°K, which seems to be a very high figure, it would still be only one percent, so we would certainly seem to be justified in saying that at least one thousand collisions would be required before the abstraction act could occur.

The next question is whether during the thousand or more collisions with surrounding molecules it will have diffused away from the original site so that when it does finally abstract H atom it will form a trapped radical too far away to cause a cross link. Atomic hydrogen being the most pervasive chemical species known would be expected to diffuse most rapidly; and if this is so, therefore, cross linking cannot be explained by the atomic hydrogen formed except by the very inefficient type of process depending on the square of the radiation exposure which eventually results from the chance occurrence of free radicals next to one another. We assume that they cannot migrate except possibly along the chain, as has been suggested by Dole.[19]

The probability of diffusion away from the original site in a hundred collisions or so therefore is very critical and we must examine it as closely as possible. For this purpose, we take experimenal data on the diffusion of helium through polyethylene and assume that the H atom will move at least as rapidly. Barrer[20] and Doty[21] show this diffusion coefficient to be about 2×10^{-7} cm²/sec at room temperature with an effective mean free path of about 11 A and an activation energy for diffusion of 7.7 kcal/mole, which would correspond to an escape probability from any given set of surrounding hydrocarbon groups in one thousand collisions of nearly 100%. It seems likely, therefore, that this is not the cross linkage mechanism.

Carbonium ions seem to have the capability of causing cross linkage as does also the parent ion radical. The carbonium ion would act by reaction (19) with one of the neighboring CH_2 groups when a three-centered pair bond would be formed, and later H_2 would be eliminated to form the cross link directly. This reaction is the same one described earlier, Eq. (3). The new carbonium ion eventually will be neutralized.

The original ion radical

$$\begin{matrix} R_1^+ \\ HCH \\ H_2 \end{matrix}$$

in those cases which do not lose an H atom to form carbonium ions, may afford another fast near neighbor ion molecule mechanism for cross linkage according to reaction (20). From the arguments of Secs. I and II of this paper, we would say that the ionized group temporarily feels as though it had been changed into atomic fluorine, although it still is not free to move out of its position in the solid, and it therefore takes an H atom away from the closest source, one of the neighboring chains or a neighboring CH_2 in its own chain, leaving a free radical. Later when an electron reappears to neutralize the positive charge, the ion

$$\begin{matrix} R_1^+ \\ \quad H \\ HC \\ \quad H \\ R_2 \end{matrix}$$

is reminded that it is not hydrofluoric acid and must return to being a carbon atom group and must give up the extra H atom and the very considerable energy of neutralization. This is very readily accomplished by allowing the departing H to take another H with it combined as H_2 molecule, leaving two near neighbor free radicals to react and from the cross link bond. Specifically,

$$\begin{matrix} R_1^+ & R_1 & R_1 & R_1 \\ \quad H & & & \\ e^- + HC & + \cdot CH = HC \cdot & + \cdot CH + H_2 & \qquad (21) \\ \quad H & & & \\ R_2 & R_2 & R_2 & R_2 \end{matrix}$$

$$\begin{matrix} R_1 & R_1 & R_1 & R_1 \\ HC \cdot & + \cdot CH = HC - CH. & & \qquad (22) \\ R_2 & R_2 & R_2 & R_2 \end{matrix}$$

[18] A. F. Trotman-Dickenson, *Gas Kinetics* (Butterworths Scientific Publications, Ltd., London, 1955).

[19] (a) M. Dole and C. D. Keeling, J. Am. Chem. Soc. **75,** 6082 (1953). (b) M. Dole, C. D. Keeling, and D. G. Rose, *ibid.* **76,** 4304 (1954).

[20] R. M. Barrer, *Diffusion in and through Solids* (Cambridge University Press, New York, 1941).

[21] P. Doty, J. Chem. Phys. **14,** 244 (1946).

Collyns, Fowler, and Weiss[21] have proposed a mechanism different from either of those proposed here which has as its essential step

$$\begin{matrix} R_1 & R_1 & & R_1 & R_1 \\ HCH^+ + HCH = & H_2^+ + & HC - & CH & \end{matrix} \qquad (23)$$
$$\begin{matrix} R_2 & R_2 & & R_2 & R_2 \end{matrix}$$

followed by the neutralization of H_2^+. The present knowledge of bond energies makes it doubtful that this reaction is exothermic. In the case of methane, reaction (23) is endothermic by about 60 kcal/mole.

Weiss[21b] also proposes a second mechanism by which H_2 molecule is eliminated directly, leaving

$$\begin{matrix} R_1 & R_1 \\ H^+C - & CH. \\ R_2 & R_2 \end{matrix}$$

This again, according to the argument of this paper, will be either endothermic or barely exothermic.

The carbonium mechanism proposed here is not completely new in principle, since Collinson, Dainton, and Gillis[22] have found that the gamma ray induced polymerization of liquid isobutene at $-78°$ proceeds solely by a mechanism probably centering on $(CH_3)_3C^+$, and Lampe[23] has pointed out that this ion could be formed in the condensed phase by the reaction

$$i\text{-}C_4H_8^+ + iC_4H_8 = C_4H_9^+ + C_4H_7 \qquad (24)$$

which had been observed in the gas phase in the mass spectrograph.[5a] Lampe points out further that if reaction (24) is faster than the neutralization process by electron recapture, which on the basis of mass spectrographic evidence seems very likely to be true, every ionization results in the formation of one polymerizarion initiator with an energy yield of

$$G = 100/W_{C_4H_8},$$

where $W_{C_4H_8}$ is the energy required to form an ion pair in isobutylene, which he estimates to be 23.6 ev to give a G value of 4.2. This is in good agreement with the observed G of 3.7. Thus it is concluded that reaction (24) is of great importance in the liquid phase polymerization of isobutylene.

The proposed ion radical mechanism would predict a yield of about $100/a \times b \times W$ cross links per 100 ev absorbed energy where the factor $1/a$ is to take account of the reactions of dehydrogenation to form carbonium ions, $1/a$ being the fraction which remains as the ion radical, $1/b$ is the fraction of the time the H is taken from neighboring group in the neighbor chains rather than from groups in the same chain, and W is the average energy of formation of an ion pair in polyethylene. This results in the prediction that G should be close to $4/ab$, since W is about 25 ev. If $1/a$ is estimated to be about $\frac{1}{2}$, and $1/b$ as about $\frac{1}{5}$ according to Dole,[2a,b] we obtain an expected G value of 0.4 for the cross link, which appears to be satisfactory.[24] Charlesby and Davison[25] give G for H_2 as 3.1, and Dole[19] has shown the ratio of cross linkage to total H_2 to be about $\frac{1}{8}$ in polyethylene. Thus, G (cross link) would be about 0.5.

For the carbonium ion mechanism, the analogous calculation is more difficult, since little is known about the relative probability of a carbonium ion forming a three-center bond with an adjacent CH_2 group in the same chain and eliminating H_2 on neutralization.

The evidence on the dependence of the number of cross linkages on total radiation seems to indicate that it is first order, since different investigators using widely different sources of radiations seem to obtain comparable yields per unit energy absorbed. The present mechanisms predict a first-order dependence.

Three other important characteristics of the radiation effects on high polymers that must be compared with the theories are:

(1) Radiation causes unsaturation in the chain in polyethylene about 4 to 5 times as often as cross linkages and the unsaturation produces *trans*-vinylene groups.[19]

(2) Cross linkage occurs under irradiation only if an H atom is located on the C atom alpha to the CH_2 group.[26] Otherwise, degradation of molecular weight predominates.

(3) Irradiation of the polymer in the presence of oxygen, followed subsequently by contact with a monomer, causes copolymerization.[27]

The first point that irradiation causes unsaturation to form a transvinylene group about four or five times as frequently in polyethylene as it causes cross links is to be understood as follows. The ion radical and carbonium ion theories, of course, both say that the neighboring C atoms in the chain are even closer on the average than those from the neighboring chain, so abstraction frequently occurs from one of the neighboring CH_2 groups followed by the same sequence as in the cross linkage mechanism with the final elimination of H_2 and the formation of a double bond in the chain instead of a cross link when neutralization occurs. The geometry of the situation favors a *trans* configuration in the vinylene formed. Consider the original configuration

$$\begin{matrix} & R_1 & \\ & | & \\ H- & C & -H \\ & | & \\ H- & C & -H \\ & | & \\ & R_2 & \end{matrix}$$

[21] (a) B. G. Collyns, J. F. Fowler, and J. Weiss, *Chemistry and Industry* (London) **3,** 74 (1957). (b) J. Weiss, J. Polymer Sci. **29,** 425 (1958).

[22] E. Collinson, F. S. Dainton, and H. A. Gillis, J. Phys. Chem. **63,** 909 (1959).

[23] F. W. Lampe, J. Phys. Chem. **63,** 1986 (1959).

[24] F. S. Dainton, Ann. Rev. Nuclear Sci. **5,** 213 (1955).

[25] A. Charlesby and W. H. T. Davison, Chem. & Ind. (London) **3,** 237 (1957).

[26] A. A. Miller, E. J. Lawton, and J. S. Balwit, J. Polymer Sci. **14,** 503 (1954).

[27] A. Chapiro, Ind. Plastiques Mod. (Paris) **9,** 2–34 (1957).

of the polyethylene chain. The most stretched form of the chain will be with the long chains R_1 and R_2 in the *trans* position, so it would be expected that when the double bond forms intramolecularly it would produce a *trans*-vinylene group. Of course, the theory also says that unsaturation would occur just as well for the *cis* configuration if it were present, so the production of the *trans*-vinylene product is solely because of the stretched and close packed nature of the chains in the polyethylene polymer.

The second feature of radiation induced cross linkage in polymers—that it occurs only if an H atom is located on the alpha carbon to the CH_2 group—has a geometrical explanation similar to that for the *trans*-vinylene unsaturation. Suppose ethylene with a large substitution group X on one of its carbons is polymerized. Then the groups X will be placed as far apart in the polymer lattice as they can be in order to avoid steric strain. The result will be that any two parallel chains will have only HCX and HCH groups neighbor to one another with no pairs of HCH groups neighboring. Consequently, on the basis of the present theories, only those polymers can cross link which have at least one H on the C atom bonded to the X group.

The ability of polymers to react with monomers to form copolymers after irradiation in the presence of oxygen is explained by the electron affinity of oxygen. It captures the ejected electrons and, while still reducing and controlling the buildup of internal space charge through the charge of the negative ion, it gives in the case of the ion radical mechanism both the intermediate

$$\begin{array}{l} R_1{}^+ \\ \quad H \\ HC \\ \quad H \\ R_2 \end{array}$$

and the neighboring free radical a much extended life and, in particular, leaves the neighboring free radical available for subsequent reaction with the added monomer to form the copolymer. In the case of the carbonium ion mechanism the three-center bond complex is given an extended life so the monomer with its more strongly basic (nucleophilic) properties can displace the neighbor chain and on eventual neutralization form a bonded copolymer.

The carbonium ion mechanism probably has a little more trouble with the first point, since the distance to the H atoms on neighboring C atoms in the chain is greater. On the second point it passes just as well as the ion radical mechanism as it does for the third point also. Therefore, we cannot say clearly that the one or other mechanism is the more probable and suggest that both may be important.

IV. CONCLUSION

The chemistry of ions is a subject of potential significance in the understanding of a wide variety of phenomena in addition to those discussed in this paper. Among these are the production of amino acids by ionization of reducing gaseous and liquid solutions as studied by Miller and Urey[28] and others,[29] the chemistry of Geiger counters (the chemical changes in the organic quenching vapors used), the chemistry of electrostatic frictional charges (why various materials differ in the kind and amount of charge developed), the mutations produced in living cells by radiation exposure, and the general chemistry of plasma.

---

[28] (a) S. L. Miller, Science **117,** 528 (1953); J. Am. Chem. Soc. **77,** 2351 (1955); Biochim. et Biophys. Acta **23,** 480 (1957). (b) S. L. Miller and H. C. Urey, Science **130,** 245 (1959).

[29] P. H. Abelson, Carnegie Inst. Wash. Year Book No. **56,** 179 (1957).

Effect of Temperature on the Intensity and Structure of Bands in the Infrared Spectrum of Rhombic Sulfur*†

VERNON D. NEFF‡ AND THOMAS H. WALNUT
Department of Chemistry, Syracuse University, Syracuse 10, New York

(Received April 3, 1961)

The infrared spectrum of rhombic sulfur was obtained in the region between 750 and 2000 cm^{-1}. The relative intensities of the bands at 845, 936, 1298, and 1513 cm^{-1} were measured as a function of temperature and sample orientation from $-190°$ to 85°C.

An expression is given that relates the temperature dependence for an overtone or combination band to the values of the component frequencies. The expression is used in conjunction with the measured temperature dependence to reject some previous assignments and to establish rough values of the component frequencies in the observed overtone and combination bands. A tentative assignment consistent with the rough values found for the component frequencies is made.

In addition, the structure of a band is considered to be the result of combination with acoustic lattice modes, and the temperature dependence of the structure is analyzed from this point of view. The temperature dependence of the intensity of the structure of the band at 845 cm^{-1} far from the peak agrees roughly with the expression obtained, but the dependence close to the peak does not.

INTRODUCTION

THE infrared[1–4] and Raman[5–9] spectra of rhombic sulfur have been observed and analyzed many times before. In the work described in this paper the infrared spectrum was reinvestigated. The aspect of the work that is new is measurement of the relative intensities of bands as functions of temperature. Previous investigations of the temperature dependence of band intensities have been done recently by a number of workers.[10–14] In this paper, temperature dependence is used as an aid in assigning bands.

The functional dependence of the intensities of bands on temperature can be readily developed for the case of electrical anharmonicity. For simplicity it will be assumed that the same temperature dependence obtains for mechanical and mixed anharmonicity. The proof of this assumption will be left for a later publication. For sulfur this assumption is probably not necessary since there is evidence that the dominant cause of the observed overtone and combination bands is electrical anharmonicity.

The temperature dependence is a function of the type of overtone or combination, and of the magnitudes of the component frequencies. Qualitatively it is clear that the anharmonic effects should be larger when the amplitudes of the vibrations become larger, and hence as the temperature is increased the intensity of overtones relative to fundamental bands should increase. Also it should be expected that the higher the order of the combination the more strongly it should depend on the temperature and that combinations involving low-frequency vibrations should show a greater temperature dependence than combinations involving high-frequency vibrations. These expectations are confirmed in the quantitative derivation.

The quantitative derivation follows readily from the expression for the integrated net absorption, $K_{n''n'}$, for a single transition as given by Wilson *et al.*[15] i.e.,

$$K_{n''n'}=(8\pi^3/3ch)(N_{n''}-N_{n'})\nu_{n'n''}\,|\,\mu_{n'n''}\,|^2. \quad (1)$$

Here, $N_{n''}$ and $N_{n'}$ are, respectively, the numbers of systems per unit volume in states n'' and n', $\nu_{n'n''}$ is the frequency of transition, and $\mu_{n'n''}$ is the dipole moment matrix element between the two states. At thermal equilibrium

$$N_{n''}=N\exp(-E_{n''}/kT)/Q \quad (2a)$$

and

$$N_{n'}=N\exp(-E_{n'}/kT)/Q, \quad (2b)$$

where N is the number of systems per unit volume and Q is the vibrational partition function.

---

* Based on a thesis submitted in partial fulfillment of the requirements for the degree of Doctor of Philosophy at Syracuse University.

† Supported by the National Science Foundation.

‡ Present address: Department of Chemistry, Kent State University, Kent, Ohio.

[1] A. M. Taylor and E. Rideal, Proc. Roy. Soc. (London) **A115,** 589 (1927).
[2] R. B. Barnes, Phys. Rev. **39,** 57 (1932).
[3] H. J. Bernstein and J. Powling, J. Chem. Phys. **18,** 1018 (1950).
[4] G. M. Barrow, J. Chem. Phys. **21,** 219 (1953).
[5] P. Krishnamurti, Ind. J. Phys. **5,** 105 (1930).
[6] C. S. Venkateswaran, Proc. Ind. Acad. Sci. **4A,** 345 (1936).
[7] K. Venkateswarlu, Proc. Ind. Acad. Sci. **12A,** 453 (1940).
[8] R. Norris, Proc. Ind. Acad. Sci. **13A,** 291 (1941).
[9] R. Norris, Proc. Ind. Acad. Sci. **16A,** 287 (1942).
[10] V. N. Smirnov and P. A. Bazhulin, Optika i Spektroskopiya **7,** 193 (1959).
[11] N. E. Gaponova, M. P. Lisitsa and Yu. P. Tsyashchenko, Optika i Spektroskopiya **8,** 465 (1960).
[12] M. P. Lisitsa and V. L. Strizhnevsky, Optika i Spektroskopiya **7,** 478 (1959).
[13] M. P. Lisitsa and V. L. Strizhnevsky, Optika i Spektroskopiya **10,** 48 (1961).
[14] M. P. Lisitsa and Yu. P. Tsyashchenko, Optika i Spektroskopiya **10,** 157 (1961).
[15] E. B. Wilson, J. C. Decius, and P. C. Cross, *Molecular Vibrations* (McGraw-Hill Book Company, New York, 1955), pp. 162–166.

If, instead of a single transition, all of the transitions that contribute to a single band are considered, we obtain for the integrated net absorption

$$K=\sum_{n=0}^{\infty}(8\pi^3/3ch)(N_n-N_{n+m})\nu_0\,|\,\mu_{n,n+m}\,|^2, \qquad (3)$$

where ν_0 is the common frequency assumed for all of the contributing transitions. Actually the frequencies $\nu_{n,n+m}$ will be slightly different but the differences are negligible for moderate mechanical anharmonicity.

This equation can be rewritten as

$$K=A\left(\sum_{n=0}^{\infty}N_n\,|\,\mu_{n,n+m}\,|^2-\sum_{n=0}^{\infty}N_{n+m}\,|\,\mu_{n,n+m}\,|^2\right), \qquad (4)$$

where

$$A\equiv(8\pi^3/3ch)\nu_0. \qquad (5)$$

By changing the index in the second sum and noting that $\mu_{n,n+m}=0$ when $n<0$, we obtain

$$K=A\sum_{n=0}^{\infty}N_n(\,|\,\mu_{n,n+m}\,|^2-\,|\,\mu_{n-m,n}\,|^2), \qquad (6)$$

and, hence, since $\mu_{nm}=\mu_{mn}^*$,

$$K=A\sum_{n=0}^{\infty}\{[\exp(-E_n/kT)/Q][\,|\,\mu_{n,n+m}\,|^2-\,|\,\mu_{n,n-m}\,|^2]\}, \qquad (7)$$

where Q is the vibrational partition function.

From this basic expression the temperature dependences for various types of combination bands can readily be determined by inserting the dependence of the quantities $|\,\mu_{n,n+m}\,|^2$ and $|\,\mu_{n,n-m}\,|^2$ on the quantum numbers for the states involved and then evaluating the sum. For example, in a fundamental absorption $\mu_{n,n+1}$ is proportional to the corresponding matrix element $q_{n,n+1}$ where q is the appropriate normal coordinate. These quantities are proportional to $(n+1)^{\frac{1}{2}}$ and, similarly, $\mu_{n,n-1}$ and $q_{n,n-1}$ are proportional to $n^{\frac{1}{2}}$ and have respectively the same proportionality constants as the previous elements. Therefore, from the preceding equation

$$K=B\sum_{n=0}^{\infty}\{\exp(-E_n/kT)[n+1-n]/Q\}=B, \qquad (8)$$

where B is a constant. Consequently the intensity of a fundamental absorption should be independent of temperature.

Similarly, for a binary combination band

$$K=B'(\langle n_1\rangle+\langle n_2\rangle+1), \qquad (9)$$

where B' is a constant and $\langle n_1\rangle$ and $\langle n_2\rangle$ are the thermal average values of the quantum numbers n_1 and n_2; i.e.,

$$\langle n_1\rangle=\sum_{n_1=0}^{\infty}n_1\exp(-n_1h\nu_1/kT)/Q,$$
$$=[\exp(h\nu_1/kT)-1]^{-1}. \qquad (10)$$

Since both $\langle n_1\rangle$ and $\langle n_2\rangle$ increase with increasing temperature, the intensity of a binary combination should increase with temperature.

Other expressions can readily be derived from Eq. (7) for other types of overtones and combinations. From these expressions it is apparent that it should be possible to use the temperature dependence of a band intensity to determine the type of band and the frequency or frequencies of the component fundamental vibrations.

This derivation is similar to that given by Lisitsa and Strizhnevsky.[13]

EXPERIMENTAL SECTION

Large single crystals of rhombic sulfur were obtained from a saturated carbon disulfide solution. The crystals were grown by allowing the stirred saturated solution to evaporate slowly over a period of several days. The solution was held at a constant temperature of 25°C. The normal rate of evaporation through a 6-mm opening was sufficient to produce single crystals with a volume of several cubic centimeters from 1 liter of solution in 4 days.

Commercial sulfur was purified by a single recrystallization from reagent grade carbon disulfide. Small single-crystal seeds were prepared by slow evaporation of saturated solutions in 250-ml beakers covered with aluminum foil.

Samples were prepared by grinding down large crystals to the appropriate thickness and orientation by a method that was essentially identical to that used in the grinding and polishing of rock-salt windows. They ranged in thickness from 0.40 to 2.1 mm. The thickness was measured with a micrometer and each sample was checked for uniformity by measurements at various points on the surface. The variation in the thickness of any sample did not exceed 4%. The samples were clear and transparent and were free from noticeable flaws.

Two different cells were used, one for temperatures above and the other for temperatures below 25°C. The higher temperature cell consisted of two large cylindrical pieces of brass with a hole along the central axis of each for transmitting the radiation. A rock-salt window was cemented to a recessed portion of the inner face of each large piece of brass so that the surfaces of the window and the brass were flush. The two halves of the cell were bolted together and the sample was held between the rock-salt plates. A rubber O-ring was used as a spacer. The cell fit into a suitably designed asbestos covered electric heater. The temperature was measured in both cells with an iron-constantan thermocouple and a standard Leeds and Northrup self-compensating thermocouple potentiometer. In the higher temperature cell the thermocouple was placed in a hole in one of the rock-salt windows next to the sample.

The low-temperature cell was of the type described by Wagner and Hornig.[16] In it the sample was held in place

[16] E. L. Wagner and D. F. Hornig, J. Chem. Phys. **18**, 296 (1950).

by a brass ring, which was attached to the main block with bolts. Aluminum foil was used as a washer between the sample and the ring on one side and the sample and the block on the other. About half of the surface of the sample was covered by the ring and the block. The ring was tightened sufficiently to assure good thermal contact. The thermocouple was attached to the cooling block and its temperature was assumed to be that of the sample.

Cooling was achieved by directing a stream of nitrogen vapor into the cooling well of the cell. The nitrogen vapor was obtained by boiling liquid nitrogen in a 25-l Dewar vessel with an electric heater. This vapor was led to the cell through an insulated tube. The temperature could be held constant to 0.5°C. For the lowest temperature liquid nitrogen itself was used in the cell.

The spectrometer used was a Perkin-Elmer model 112, single-beam double-pass infrared spectrometer. A rock-salt prism was used for bands in the region between 750 and 1350 cm^{-1}, and a fluorite prism for the band at 1513 cm^{-1}.

The principal experimental problem in measuring relative intensities is the determination of the regions of zero absorption of the sample. Regions, close to the observed bands, where there appeared to be no absorption were chosen and the apparent percent absorption for each of the regions was measured for samples of different thickness. For samples of thicknesses 2.0, 1.35, and 0.43 mm, the average apparent percent absorptions were 38, 32, and 28%, respectively. Most of the apparent absorption was due to reflection losses. The rest can be ascribed to internal scattering because the apparent absorption did not vary more than 5% over the whole range of frequency and because it did not change appreciably with temperature.

In plotting the bands, the base line was derived from the points where there was no true absorption. It varied slowly by not more than 3% over the whole region.

The slitwidth was held constant in all of the measurements except that for the wide band at 845 cm^{-1}. In this case a string drive was used. With the string drive the 100% transmission line was held constant to within 1%. The bands were scanned slowly with narrow slits and high amplifier gain.

Plots of optical density vs frequency in wave numbers were made and the areas under the curves were measured to obtain the relative integrated intensities. The integrated intensities of the band at 936 cm^{-1} were checked at different slitwidths (200 and 250 μ) and were found to be the same within 1.2%.

The thickness of the samples used was such that the maximum percent absorption was less than 60% (except for the strong band at 845 cm^{-1} where it reached 80%).

It should be noted that for most of the applications of the temperature dependence technique only the gross features of the intensity vs temperature curves are necessary in deciding between one assignment and another.

DISCUSSION AND ASSIGNMENTS

Structure of Sulfur

A molecule of sulfur in the solid is a puckered ring of eight symmetrically equivalent sulfur atoms. The bond angle made by three neighboring sulfur atoms is 105° and the point group of the ring is D_{4d}.

In the crystal structure[17,18] there are 16 sulfur molecules per unit cell. The planes of the rings of alternate sulfur molecules are perpendicular. The space group is V_h^{24} or F_{ddd}.

Observed Bands

Eight bands were observed in the region between 750 and 2000 cm^{-1}. The frequencies of the bands at 25°C are 845, 876, 903, 936, 986, 1052, 1298, and 1513 cm^{-1}. The band at 845 cm^{-1} is strong, those at 876, 903, 936, 1298, and 1513 cm^{-1} are of medium intensity, and those at 986 and 1052 cm^{-1} are weak. The weak bands will not be discussed further.

Preliminary Observations

A complete assignment is not attempted in this paper because not enough information is available. However, a number of possible assignments are ruled out.

Before the actual assignment is described, there are some general observations on the spectrum that should be noted. The first of these is that there is an absence of observed "hot bands" having frequencies that differ from those of the corresponding bands involving the ground state. Hence, it can be concluded that the frequency corresponding to the transition $0 \rightarrow m$ is close to the frequencies for the transitions $1 \rightarrow m+1$, $2 \rightarrow m+2$, etc.

The cause of frequency differences of corresponding transitions with different initial states is the mechanically anharmonic interaction of the normal modes of vibration. This interaction is also one of the causes of overtone and combination bands. The fact that the anharmonicity is not large enough to shift the high-temperature bands far enough to be observed coupled with the fact that there is no obvious grouping of the overtones close to strong fundamental bands is evidence for the assumption that the observed bands are due to electrical anharmonicity. Small mechanical anharmonicity would mean that the frequencies of overtone and combination bands should closely approximate the sums of the frequencies of the component fundamental vibrations.

A second observation concerns the limiting width of the observed bands at low temperature. In a strongly coupled molecular crystal the overtone and combination bands should have a structure which is related to the frequency distributions of the component optical modes

[17] B. E. Warren and J. T. Burwell, J. Chem. Phys. **3,** 6 (1935).
[18] S. C. Abrahams, Acta Cryst. **8,** 661 (1955).

TABLE I. List of fundamental frequencies in cm^{-1}.

Stretching frequencies this research	Stretching frequencies Bernstein and Powling	Bending frequencies Bernstein and Powling
$\nu_1(a_1)$ 470	$\nu_1(a_1)$ 470	$\nu_2(a_1)$ 216
$\nu_3(b_1)$ 411	$\nu_3(b_1)$ 532	$\nu_4(b_2)$ 267
$\nu_5(e_1)$ 465	$\nu_5(e_1)$ 465	$\nu_6(e_1)$ 190
$\nu_7(e_2)$ 434	$\nu_7(e_2)$ 434	$\nu_8(e_2)$ 152
$\nu_{10}(e_3)$ 434	$\nu_{10}(e_3)$ 520	$\nu_9(e_2)$ 184
		$\nu_{11}(e_3)$ 243

of vibration.[19-21] This structure should be present even at absolute zero.

In the spectrum all of the bands continued to become narrower with decreasing temperature throughout the range of temperature used. Consequently, it was concluded that the intermolecular coupling is small.

This observation and the observation that the frequencies of vibration do not differ by more than a few wave numbers in solution and in the solid suggest that the molecular modes should not be appreciably altered by interaction with neighboring molecules and, hence, that the molecules can be treated as independent entities.

Another noteworthy observation is that only a small fraction of all the allowed overtone and combination bands are present. This is particularly true for the higher combination bands. There does not appear to be any obvious explanation for this fact.

Assignment

The previous assignment by Bernstein and Powling[3] is used as a basis for the assignment in this paper. The fundamental frequencies given by them and used in their assignment are listed in Table I. They can clearly be divided into stretching and bending frequencies. In this paper nearly all of the assignments involve only the stretching frequencies.

There are three fundamental frequencies of rhombic sulfur that can be considered to be unequivocally assigned, $\nu_1(a_1)$ at 470 cm^{-1}, $\nu_2(a_1)$ at 216 cm^{-1}, and $\nu_5(e_1)$ at 465 cm^{-1}. The first two appear as very strong polarized Raman lines and the last is the strongest band in the readily accessible region of the infrared. The rest of the assignments of fundamental frequencies are not certain.

All of the bands observed in this work are either overtones or combinations. The fundamental frequencies are inferred from the frequencies of these bands.

The band at 845 cm^{-1} is a wide band and is the most intense of all the bands observed. It is assigned by Bernstein and Powling as the combination $2\times190(e_1)+465(e_1)$. When the intensity as a function of temperature is calculated for this assignment the result does not agree with the observed intensity dependence as is shown in Fig. 1.

The temperature dependence is consistent only with an assignment as a first overtone or binary combination where the component frequencies are approximately equal. When the orientation dependence of intensity was used as an aid in assignment, the ratio of the absorption coefficient for a sample cut parallel to the 110 plane to that for a sample cut parallel to the 001 plane is 1.43. This is consistent with a symmetry E_1 but not B_2, since the theoretical ratios are, respectively, $\frac{3}{2}$ and $\frac{1}{2}$. This observation is corroborated by the work of Barrow[4] with polarized infrared.

Consequently the band must be either a first overtone or binary combination having nearly equal component frequencies and it must have the symmetry E_1. None of the E_1 combinations of fundamental frequencies given by Bernstein and Powling come within 50 cm^{-1} of 845 cm^{-1}. Therefore some of the fundamental assignments must be incorrect.

Of all of the frequencies possibly involved in the combination the ones which are most likely to be incorrect are $\nu_{10}(e_3)$ at 520 cm^{-1} and $\nu_3(b_1)$ at 532 cm^{-1}. The first of these was assigned because it was in approximate agreement with a normal coordinate calculation based on a simple valence force field adjusted to fit the established frequencies $\nu_1(a_1)$, $\nu_2(a_1)$, and $\nu_3(e_1)$. The actual choice of the frequency 520 cm^{-1} was made because it

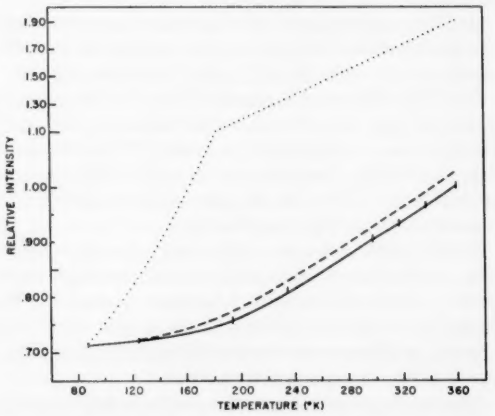

FIG. 1. Relative intensity vs temperature in °K at 845 cm^{-1}. The solid curve is the observed value. The dotted curve is the calculated intensity for the assignment $2\times190(e_1)+465(e_1)$ as given by Bernstein and Powling. The dashed curve is the calculated intensity for the assignment $411(b_1)+434(e_3)$. The experimental relative intensity at the highest temperature is arbitrarily set equal to 1.00 and the experimental and theoretical curves are made to coincide at the lowest temperature. *Note the change in scale of the ordinate at* 1.10.

[19] D. F. Hornig, J. Chem. Phys. **16,** 1063 (1948).
[20] H. Winston and R. S. Halford, J. Chem. Phys. **17,** 607 (1949).
[21] T. H. Walnut, J. Chem. Phys. **20,** 58 (1952).

was a frequency reported by Kohlrausch[22] and Venkateswarlu.[7] Since the work of Norris[8,9] has almost certainly demonstrated that this line is the anti-Stokes line of $\nu_1(a_1)$ from a slightly higher frequency exciting line, there is no basis for the assignment. The other frequency $\nu_3(b_1)$, 532 cm^{-1}, was obtained by difference between an observed band at 1052 cm^{-1} and the assigned frequency at 520 cm^{-1} so that there is also no basis for this assignment.

Since it is possible to reassign both the frequencies $\nu_{10}(e_3)$ and $\nu_3(b_1)$, the most reasonable assignment of the band at 845 *cm*$^{-1}$ is as the combination of these two frequencies. An alternate assignment could be as the combination $\nu_5(e_1)+\nu_7(e_2)$, but the value of $\nu_7(e_2)$ necessary for the assignment is incompatible with the value that satisfactorily explains the band at 876 cm^{-1} as the combination $2\nu_7(e_2)$. Other possible assignments as binary combinations involve combinations of necessarily high frequency stretching modes with low frequency bending modes and, hence, are inconsistent with the data on temperature dependence.

The band at *876 cm*$^{-1}$ was assigned by Bernstein and Powling as the overtone $2\nu_7(e_2)$. The basis of the assignment was the presence of a depolarized line found in the Raman spectrum at 434 cm^{-1} by Venkateswaran.[6] The band is observed by Barrow[4] to have the symmetry species B_2, which is what would be predicted if the band were the overtone. Good temperature dependence data could not be obtained for this band because it was too close to the intense band at 845 cm^{-1}. Nevertheless, the assignment is satisfactory.

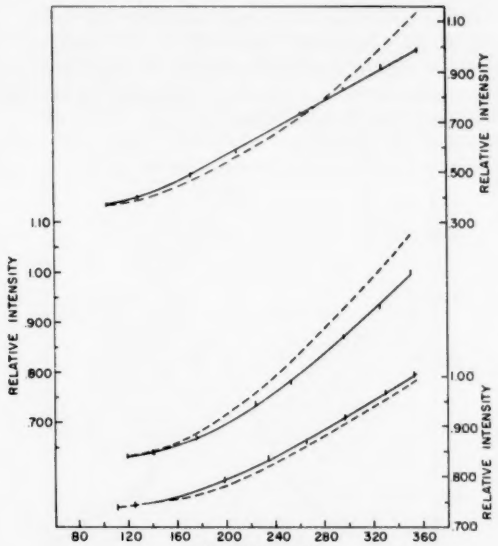

FIG. 2. Relative intensities vs temperature for the bands at 1513 cm^{-1}, 1298 cm^{-1} and 936 cm^{-1}. The solid curves are the observed intensities and the dashed curves are the calculated intensities. The calculated curves are based on the assignments $470(a_1)+465(e_1)$, $3\times434(e_3)$, and $3\times434(e_3)+216(a_1)$, respectively. The experimental relative intensities at the highest temperature are arbitrarily set equal to 1.00 and the experimental and theoretical curves are made to coincide at the lowest temperature. From top to bottom the curves are those for the bands at 1513, 1298, and 936 cm^{-1}.

[22] K. W. F. Kohlrausch, *Ramanspektren* (Edwards Brothers, Inc., Ann Arbor, Michigan, 1945), p. 394.

TABLE II. Assignment of observed bands.

Band	Assignment	Predicted symmetry	Observed symmetry
845 cm^{-1}	$411(b_1)+434(e_3)$	E_1	E_1
876 cm^{-1}	$2\times434(e_2)$	$A_1+B_1+B_2$	B_2
903 cm^{-1}	$465(e_1)+434(e_3)$	B_2	B_2
936 cm^{-1}	$470(a_1)+465(e_1)$	E_1	B_2+E_1
1298 cm^{-1}	$3\times434(e_3)$ $2\times434(e_2)+434(e_3)$	E_1	E_1
1513 cm^{-1}	$\sim200+3\times(\sim430)$	...	E_1

The band at *903 cm*$^{-1}$ was assigned by Bernstein and Powling as the combination $465(e_1)+434(e_2)$. This assignment agrees well as a numerical sum but is in disagreement with the symmetry species as measured by Barrow. The symmetry of the combination as assigned is E_1+E_2, but the observed symmetry species is B_2. This discrepancy means that the assignment of Bernstein and Powling is probably incorrect. The combination $\nu_5(e_1)+\nu_{10}(e_3)$ includes the species B_2 and will yield the correct frequency if $\nu_{10}(e_3)$ is approximately the same as $\nu_7(e_2)$, i.e., 434 cm^{-1}. The band was too close to the peak at 845 cm^{-1} for good temperature dependence data to be obtained, but the data that were obtained indicated that the band was a first overtone or a binary combination where the component frequencies were approximately the same.

The band at *936 cm*$^{-1}$ was assigned by Bernstein and Powling as the combination $470(a_1)+465(e_1)$. This assignment is consistent with the temperature dependence data as shown in Fig. 2, but it does not agree with the orientation effects found in this work and by Barrow. The predicted symmetry species for the band is E_1 whereas that observed is a mixture of E_1 and B_2. No one binary combination can have this symmetry. Consequently, the only way to reconcile the symmetry with the temperature dependence would be to have two binary combinations superimposed.

This requirement is difficult to satisfy so that it is worthwhile to consider whether the observed effect is an artifact of the experimental technique. The reflection anomalies caused by changes in the index of refraction near an absorption band may give an increased transmission on the high frequency side of a band. In the present case the relatively strong band at 845 cm^{-1} has symmetry species E_1 and, hence, the absorption coefficient of a sample cut parallel to the 110 plane is larger than that for a sample cut parallel to the 001 plane. On the other hand, the transmission on the high-frequency

TABLE III. Observed and calculated intensities of the combination $411(b_1)+434(e_3)-\nu_{\text{lattice}}$ relative to the intensity at 298°K.

	Temperature			
ν_{lattice}	86°K	194°K	298°K	360°K
20 obs	0.76	0.89	1	1.27
20 calc	0.21	0.62	1	1.55
30 obs	0.55	0.69	1	1.32
30 calc	0.20	0.57	1	1.49
40 obs	0.285	0.572	1	1.43
40 calc	0.175	0.522	1	1.37
50 obs	0.121	0.455	1	1.46
50 calc	0.161	0.513	1	1.36

side of the band should be greater for the 110 sample than for the 001 sample. The relatively increased transmission for the 110 sample should appear as decreased absorption by the 936 cm^{-1} band and, consequently, should make it appear as if a component of species B_2 were present.

Decreased transmission near the 845 cm^{-1} band was in fact observed at low temperature.

In view of the explanation of the discrepancy in the symmetry observation and the agreement of the temperature dependence data, the assignment is probably correct.

The problem of increased transmission near strong bands and the resulting effect on symmetry determinations should not be important for the other bands. The bands at 845, 1298, and 1513 cm^{-1} are the strongest bands in their neighborhoods and the bands at 876 and 903 cm^{-1} are still in the region of strong absorption by the band at 845 cm^{-1}.

The band at *1298 cm^{-1}* was assigned by Bernstein and Powling as the combination $2\times190(e_1)+2\times465(e_1)$. The infrared active part of this combination would be of symmetry species B_2,[23] but the observed ratio of intensities ($K_{110}/K_{001}=1.54$) demonstrates that the band must have symmetry E_1. The temperature dependence shown in Fig. 2 is consistent only with a second overtone or ternary combination band where all of the component frequencies are approximately equal.

The combinations of the proper symmetry which most nearly agree with the frequency of the observed band are $3\times434(e_3)$ and $2\times434(e_2)+434(e_3)$. There is no other allowed combination which comes within 15 cm^{-1}. Consequently, either one or both of these assignments is probably correct.

The band at 1513 cm^{-1} was assigned by Bernstein and Powling as the combination $2\times190(e_1)+216(a_1)+2\times465(e_1)$. The orientation and temperature dependence data are inconsistent with this assignment. The calculated increase in intensity with temperature is more than twice the observed. The predicted symmetry species is B_2 while the observed ratio of intensities ($K_{110}/K_{001}=1.45$) is consistent only with symmetry E_1.

The temperature dependence curve shown in Fig. 2 indicates that the band is a fourfold combination where one of the frequencies is close to 200 cm^{-1} and the other three are approximately equal to each other. In plotting the theoretical curve the assignment $3\times434(e_3)+216(a_1)$ is used, but there are so many possible consistent assignments and so many of the lower frequencies that are not well established that no definite assignment can reasonably be made.

The assignment described above is summarized in Table II.[24]

Band Structure

In addition to the assignment of bands, some studies were made of the temperature dependence of the widths of bands. The point of view that has been widely used in the study of band structure is that the width of a band can be ascribed to further combinations of the band with acoustic lattice modes. This concept has been expressed most explicitly by Hornig.[19]

It was considered of interest to apply the theory of temperature dependent intensities to the structure of bands on this assumption. So measurements of intensity were made for narrow ranges of frequency on the low-frequency side of the band at 845 cm^{-1}.

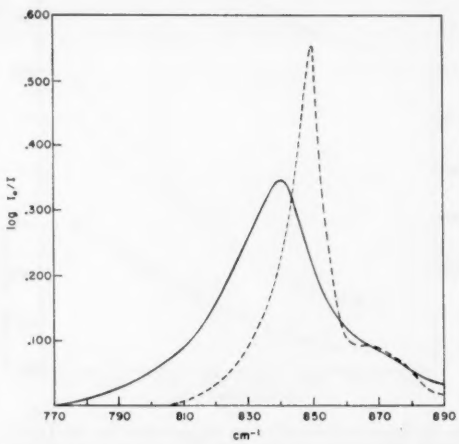

FIG. 3. Optical density vs frequency for the band at 845 cm^{-1}. The solid curve is for the temperature 360°K and the dashed is for 86°K. The sample is cut parallel to the 110 plane and the thickness is 0.432 mm.

[23] There appears to be an error in the symmetry given by Bernstein and Powling for this assignment and for the assignment of the band at 1513 cm^{-1}. The correct symmetry for both is $2A_1+A_2+B_1+B_2+2E_2$ while the symmetry which they give is $B_1+B_2+E_2+E_3+2E_1$.

[24] The assignment is in moderate agreement with the calculations of D. W. Scott and J. P. McCullough, who used a Urey Bradley field. We are indebted to the authors for sending us a preprint of their paper. [D. W. Scott and J. P. McCullough, J. Mol. Spectroscopy **6**, 372 (1961)].

The calculations were made on the assumption that part of the band examined was a combination $411+434-\nu_{\text{lattice}}$. The frequency ν_{lattice} was the difference in frequency between the peak of the band and the part measured. The frequency differences chosen were 20, 30, 40, and 50 cm^{-1}. The total intensity of the lattice combination was considered to be the height of the band at that particular frequency.

The results are recorded in Table III in terms of the intensities relative to the intensity at 298°K. As can be seen, there is rough agreement for the lattice frequencies 40 and 50 cm^{-1} but very poor agreement for the frequencies 20 and 30 cm^{-1}.

From the shape and intensity of the band at 845 cm^{-1} as shown in Fig. 3, it is apparent that the expression used for the prediction of the dependence of intensities on temperature should be invalid for regions sufficiently close to the peak because in this region the intensity increases with decreasing temperature.

A tentative explanation of the discrepancy is that the lattice combinations are caused by mechanical anharmonicity and the usual treatment of mechanical anharmonicity by perturbation theory is no longer valid when the interacting energy levels get sufficiently close. The decrease in intensity of the sides of the band with increasing distance is a strong indication that the structure is caused largely by mechanical anharmonicity since this type of interaction depends inversely on the energy difference between levels whereas electrical anharmonicity does not.

These results tend to support the concept that the structure of bands of this type are simple combinations of the central band with acoustic lattice modes, at least for the part of the band far from the central peak.

General Applicability

At this point it may be worthwhile to discuss some of the limitations on the use of measurements of the temperature dependence of band intensities in making assignments. First of all, the fundamental frequencies should be low or the crystal should be stable at high temperature, otherwise the changes in intensity will not be of sufficient size to be observable. In the present problem, sulfur is satisfactory because even the highest frequency modes have appreciable excited state populations at some of the temperatures of the experiment. On the other hand, solid hydrocarbons of low molecular weight should not be satisfactory because most of the modes are not appreciably excited at temperatures at which the solids are stable.

There is another experimental problem which may limit the applicability of the method. In materials which absorb strongly, reflection changes near absorption bands make even relative intensity measurements difficult. Consequently, for these materials only higher overtones and combinations can be observed easily. In these cases it may be possible to use KBr pellet techniques for measuring intensities (see Ferriso and Hornig[25]).

In spite of these limitations the measurement of the dependence of intensity of absorption on temperature should be a useful additional tool in analyzing infrared spectra.

[25] C. C. Ferriso and D. F. Hornig, J. Chem. Phys. **32**, 1240 (1960).

THE JOURNAL OF CHEMICAL PHYSICS VOLUME 35, NUMBER 5 NOVEMBER, 1961

Neutron Diffraction Study of Solid Deuteroammonia

JOHN W. REED*
Department of Chemistry, Ohio State University, Columbus, Ohio, and Hughes Research Laboratories, Malibu, California
AND
P. M. HARRIS
Department of Chemistry, Ohio State University, Columbus, Ohio

(Received April 13, 1961)

The crystal structure of the stable cubic modification of solid deuteroammonia has been determined by neutron diffraction. The space group is $P2_13-T^4$, and at -196°C the positions of the atoms are 4N at (a) with $u=0.2127\pm0.0021$ and 12D at (b) with $x=0.3740\pm0.0019$, $y=0.2632\pm0.0037$, and $z=0.1094\pm0.0016$. Each nitrogen atom is hydrogen bonded to the six nearest neighbor nitrogen atoms. There is one deuterium atom per site, in contrast to the "half-hydrogen" structure of ice. The N—D bond length of 1.005 ± 0.023 A is indistinguishable from that of the free molecule, while the D—N—D bond angle of $110.4°\pm2.0°$ is appreciably larger than the free molecule value.

INTRODUCTION

AMMONIA is a simple compound whose crystal structure has received relatively little attention until recently. After the early work of deSmedt[1] and Mark and Pohland[2] virtually no structural work appeared until the paper by Olovsson and Templeton.[3] Their approach was to use single crystal methods in order to obtain better data than that of the previous work, which was all done by powder methods. At the time their results were published, the work reported here was nearing completion. Our approach was to make neutron diffraction measurements in order to locate the hydrogen (actually deuterium) positions, the measurements of necessity being made on powder samples. Our work agrees well with that of Olovsson and Templeton and complements it by establishing the hydrogen parameters more firmly and precisely.

EXPERIMENTAL

The diffraction measurements were carried out at liquid-nitrogen temperature. A schematic drawing of the cryostat is given in Fig. 1. Its principal feature is the central sample tube which can be loaded and unloaded without having to break the vacuum in the jacket. The three wells recessed into the top of the nitrogen container hold activated charcoal which, at liquid nitrogen temperature, forms an effective pump. Thus, during the diffraction measurements the cryostat can be disconnected from the external pumping system by closing off the "O"-ring valve. This was essential since it was desired to rotate the cryostat during the measurements. The use of the charcoal proved quite successful; the pressure in the cryostat was kept below 10^{-6} mm for a period of three weeks without additional pumping.

The ND_3 was prepared from 99.5% D_2O and Mg_3N_2 by Dr. Leo Paridon of the Ohio State University Chemistry Department. It was stored in a small stainless-steel cylinder until used. When the sample was prepared for the diffraction measurements, an amount of ND_3 was distilled first into a buret in a gas handling system and then into a stainless-steel tube, maintained at about -110°C, inside a dry box. At this temperature, only the cubic phase should be deposited rather than either of the recently reported metastable phases.[4,5] The tube was then disconnected from the vacuum system and the solid was scraped off in the form of a fine powder with a remaing tool (kept at a temperature well below the melting point of the ND_3). The powder was collected in a thin-walled aluminum cup which could slide freely to the bottom of the sample tube of the cryostat. For this purpose, the upper end of the sample tube was made so that it could be attached to a hole in the bottom of the dry box. A sample of approximately 3.1 g of ND_3 was placed in the cryostat and was kept at liquid nitrogen temperature throughout the measurements.

The diffractometer and associated circuitry, built at Ohio State University, will be described elsewhere. During automatic operation the number of counts (or the number divided by an integral power of 2) received at every $\frac{1}{4}$° interval of 2θ is recorded by a digital printer. A B^{10} enriched BF_3 counter tube is used as the detector. The counting is not done over a fixed time but during the time it takes a monitor counter in the direct beam to reach a preassigned value. The peak wavelength of the neutron beam was found to be 1.113 ± 0.005 A from measurements on a single crystal of sodium chloride. Neither the shape nor the spread of the wavelength distribution was investigated. The amount of contamination by the second-order wavelength was estimated to be less than 0.5% for integrated powder line intensities.

* Present address: Department of Chemistry, Kent State University, Kent, Ohio.
[1] J. deSmedt, Bull. classe sci., Acad. roy. Belg. **11**, 655 (1925).
[2] H. Mark and E. Pohland, Z. Krist. **61**, 532 (1925).
[3] J. Olovsson and D. H. Templeton, Acta Cryst. **12**, 832 (1959).
[4] F. A. Mauer and H. F. McMurdie, June, 1958 Meeting of the American Crystallographic Association, Milwaukee, Wisconsin.
[5] P. A. Staats and H. W. Morgan, J. Chem. Phys. **31**, 553 (1959).

A good indication of the uniformity of the sample was the fact that several runs made in different positions with the cryostat stationary gave results that were not appreciably different from one another. Furthermore, the cryostat was rotated about its axis during the measurements at about 30 rpm. This was done by means of a sprocket wheel mounted at the lower end of the spindle holding the cryostat and run by a chain drive from an electric motor.

The data used in the calculations were the results of six runs, three with the ND_3 sample in the cryostat and three with the cryostat empty. They were all carried out in the same manner. The cryostat was in continuous rotation; the fixed number of monitor counts was set at 2^{19}, requiring approximately four minutes (so that the cryostat underwent over 100 revolutions during one measurement); and the diffraction scaling circuit was set to record every eighth count. The data from each run thus consisted of the number of counts, divided by eight, at $\frac{1}{4}°$ increments of 2θ. The factor $\frac{1}{8}$ will be carried throughout the calculations; however, when the standard deviations of the observed intensities are calculated it must be taken into account.

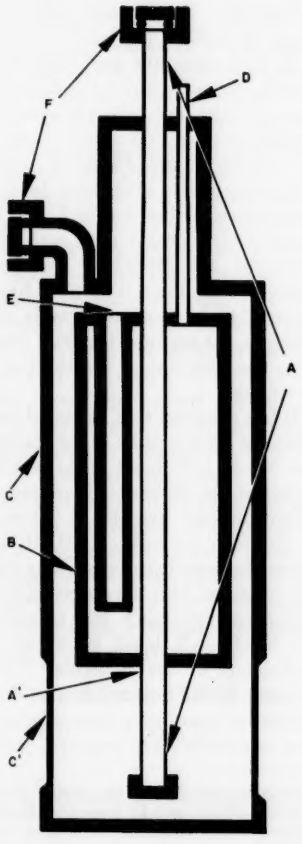

FIG. 1. Nitrogen dewar, schematic. A. Sample tube ($\frac{1}{2}$-in. diam, 0.010-in. wall; material is inconel above A′ and aluminum below A′). B. Inner cylinder. C. Outer cylinder (aluminum; wall is turned down to $\frac{3}{32}$ in. in region C′). D. Nitrogen filling tube (3). E. Activated charcoal well (3). F. "O"-ring valves (shown in closed position with housings removed).

TABLE I. Neutron powder diffraction data for ND_3.

$h^2+k^2+l^2$	$N_N/8(=I_o')$	$\sigma_N/8$	I_o	σ	w
2	503	29.5	11.86	0.724	1.000
3	4575	36.9	160.63	1.294	0.312
4	1643	29.2	76.28	1.355	0.284
5	194	20.4	11.19	1.179	0.326
6	276	21.8	18.99	1.50	0.233
8	319	20.7	28.87	1.88	0.149
9	1360	26.7	137.60	2.70	0.0715
10	759	23.3	84.80	2.59	0.0777
11	160	18.5	19.53	2.27	0.1016
12	174	20.3	23.00	2.68	0.0726
13	118	20.4	16.79	2.90	0.0618
14	343	22.4	52.20	3.41	0.0449
16	0	19.5	0.00	3.35	0.0469
17	125	22.2	22.59	4.01	0.0323
18	539	25.8	102.33	4.89	0.0217
19	106	20.3	21.09	4.04	0.0321
20	0	20.0	0.00	4.15	0.0303
21	848	26.8	183.60	5.81	0.0154
22	222	21.6	49.95	4.87	0.0219

TREATMENT OF DATA

The data were combined into a single set by obtaining for each value of 2θ the sum of the three values from the ND_3 runs n_T and the sum of the three values from the blank runs n_c. The net number of counts n_N at each value of 2θ was then obtained as $n_N=n_T-n_c-n_b$, where n_b represents the straight base line which most closely brings n_N to zero at those values of 2θ for which there are no powder peaks ($h^2+k^2+l^2=7$, 15, 23, 28, 31, 39, and 47). The total background is given by $n_B=n_c+n_b$, so that $n_N=n_T-n_B$. All of these quantities represent $\frac{1}{8}$ times the actual numbers of counts.

The intensity of each peak was obtained by summing n_N over its range of 2θ, $I_o'=\sum n_N$. This is equivalent to trapezoidal integration. In the regions at the bases of the peaks, particularly where the peaks overlapped, some of the data points were replaced by points chosen to bring the curves smoothly to zero. A plot of the data is given in Fig. 2 and the resulting values of I_o' are given in Table I. The Lorentz correction was applied to the intensities I_o' to produce the intensities I_o which will be called the "observed" intensities, $I_o=I_o'\sin^2\theta\cos\theta$. These values are also given in Table I.

No absorption correction was made. It was found from a rough calculation that the resulting error in the relative intensities was, at most, about $\frac{1}{2}\%$. Because of the increasing difficulty of resolving the peaks, no attempt was made to estimate intensities beyond the peak

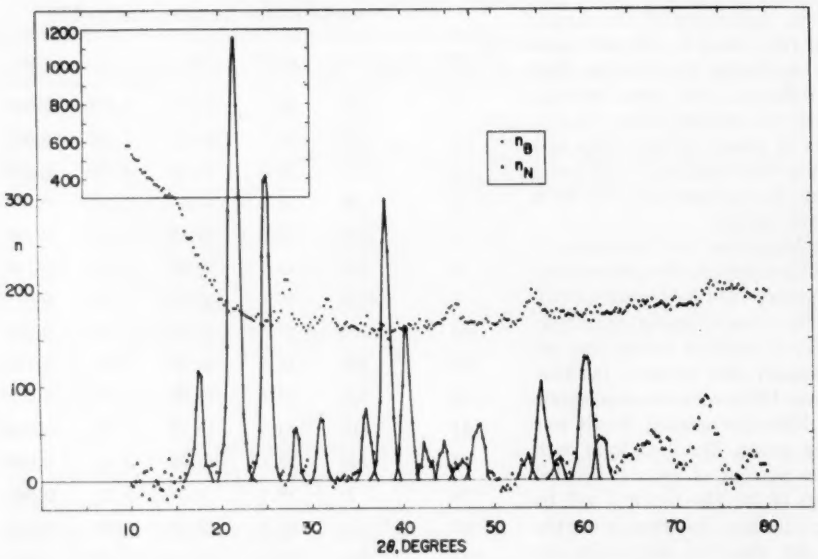

FIG. 2. Neutron powder diffraction pattern of cubic deuteroammonia. The two sets of points represent the ND_3 pattern and the background; the set of observed data points is given by their sum.

for which $h^2+k^2+l^2=22$. Very rough values could have been found for the peaks for which $h^2+k^2+l^2=24$, 25, 26, 27, 29, and 30 (in the range of 2θ from 64° to 76°) by fitting a group of overlapping triangular peaks to the observed data, but this was not done. No correction was made for the second-order wavelength contamination. The two strongest reflections of this wavelength would fall in a blank portion of the primary pattern, but they are not visible above the background.

Estimates of the standard deviations of the intensities were found from the relation[6] $\sigma_N=(\sigma_T^2+\sigma_B^2)^{\frac{1}{2}}=(N_T+N_B)^{\frac{1}{2}}=(N_N+2N_B)^{\frac{1}{2}}$, where the N's represent the actual numbers of counts, $N_N=8\sum n_N=8I_o'$, $N_T=8\sum n_T$, and $N_B=8\sum n_B$, the summations being made over the range of 2θ for which n_N is nonzero. Values of $\sigma_N/8$ are given in Table I, along with the standard deviations of the observed intensities, $\sigma=(\sigma_N/8)\sin^2\theta\cos\theta$. The weights of the observed intensities, which are inversely proportional to the squares of the standard deviations $w_i\propto 1/\sigma_i^2$ are also given in Table I. The (110) reflection was assigned unit weight and the remaining weights were calculated as $w_i=(0.724/\sigma_i)^2$.

DEDUCTION OF TRIAL STRUCTURE AND TRIAL AND ERROR CALCULATIONS

The diffraction pattern is that of a primitive cubic unit cell. The (100) reflection is apparently absent, thus allowing the possibility of a twofold screw axis. It was not possible to obtain reliable estimates of the positions of the peaks, so that a good value of the lattice constant cannot be determined. The best value, based on several of the sharper, better defined peaks, is $a=5.10$ A, so that $Z=4$ molecules per unit cell. In the calculations that follow, Olovsson and Templeton's value of 5.073 A (ND_3 at −196°C) will be used.

A trial structure was deduced by considering the possible ways in which the four ND_3 molecules can be placed in the unit cell. An examination of the site symmetries[7] reveals that only in three space groups, $P23-T^1$, $P2_13-T^4$ and $P\bar{4}3m-T_d^1$, it is possible to place four molecules of symmetry $3m$ in a cubic unit cell. It can be seen further that in T^1 and T_d^1 the four nitrogens would be in contact with each other, while in T^4 the nitrogens are separated by deuteriums. The latter arrangement, since it implies hydrogen bonding, was thought to be more reasonable physically and it was taken as the basis of the trial structure. Furthermore, T^4 is the only one of the three groups with a twofold screw axis.

If it is assumed that the bond length and angle of the molecule are the same as for the free molecule and that the N—D···N bond angle is 180°, then the atomic positions are determined uniquely. The positions obtained this way were 4N at (a) with $u=0.155$ and 12D at (b) with $x=0.315$, $y=0.216$, and $z=0.056$. A few intensities were calculated using this structure but they did not agree with the observed values.

The next approach was to relax the condition that the N—D···N bond be linear, while retaining the dimensions of the molecule. The orientation of the molecule in the unit cell can be described in terms of a cylindrical coordinate system about the threefold axis. Two parameters are required, namely the distance of

[6] H. P. Klug and L. E. Alexander, *X-Ray Diffraction Procedures for Polycrystalline and Amorphous Materials* (John Wiley & Sons, Inc., New York, 1954), pp. 270–274.

[7] *International Tables for X-Ray Crystallography*, edited by N. F. M. Henry and K. Lonsdale (Kynock Press, Birmingham, England, 1952) Vol. I.

the nitrogen from the origin and the angle between one of the deuteriums and a reference direction. Trial and error calculations were carried out in an attempt to find a pair of values which gave agreement with experiment. The calculations were successful and the resulting best set of parameter values, in terms of the Cartesian coordinates, was $u=0.209$, $x=0.362$, $y=0.282$, and $z=0.106$.

In terms of the cylindrical coordinates, the molecule had to be rotated 4.8° and translated 0.47 A from its original position. The values calculated were the intensities of powder peaks $I_c'=\sum m \mid F_c \mid^2$, where the m's are the multiplicities and the summation extends over all reflections with the same value of $h^2+k^2+l^2$. Values of the scale factor k and the temperature factor parameter B were found and used to obtain a scaled set of calculated intensities, $I_c=I_c'[k\exp(-2B\sin^2\theta/\lambda^2)]$. The value of B was 1.37 A^2 but neither it nor the value of k was considered reliable, because of bad scatter. This was presumably the result of the constraint on the dimensions of the molecule. The residual, defined as $R=\sum \mid I_o-I_c \mid /I_o$, had a value of 0.107.

LEAST-SQUARES CALCULATIONS

The approximate structure was refined by the method of least squares.[8,9] A Fortran program was written to carry out the calculations. It consisted of a main program in which the normal equations were assembled and solved and a subroutine in which the structure factors were computed. The input to the subroutine was a set of parameter values consisting of the positional parameters, the scale factor, and a variable number of temperature-factor parameters. Several different interchangeable subroutines were used, so that different forms could be assumed for the temperature factor. Furthermore it was desired at one stage to hold the temperature-factor parameters constant while the other parameters were allowed to seek their optimum values. This was made possible by using two sets of variables p_i and c_i and, in the main program, minimizing with respect to the p_i only. Then, for a given subroutine, those parameters to be held constant were designated c_i and the rest were designated p_i. The output from the subroutine was a set of calculated intensities I_{c_k}.

During one iteration of the calculations, all of the partial derivatives $\partial I_{c_k}/\partial p_j$ were calculated numerically by using the quotient of two increments as an approximation to the derivative. Values were obtained for a set of I_{c_k} using the current values of the p_i. This was repeated substituting 1.001 p_j for p_j for each parameter in turn. The derivatives were then taken to be

$$\partial I_{c_k}/\partial p_j \approx [I_{c_k}(1.001p_j)-I_{c_k}(p_j)]/(1.001p_j-p_j)$$
$$\approx 1000[I_{c_k}(1.001p_j)-I_{c_k}(p_j)]/p_j.$$

Thus, the partial derivatives were never handled analytically. The main program treated all models the same, since it was not concerned with the internal workings of the subroutines but only with the values that the subroutines produced.

After the partial derivatives were found, they were used to obtain the coefficients of the normal equations. All coefficients, including the off-diagonal terms, were evaluated. The system of normal equations was then treated as a matrix equation and solved by the use of matrix inversion and matrix multiplication subroutines.

The calculations were carried out in several steps which differed in the treatment of the temperature factor, as will be outlined below. In the discussion the temperature factor is of the form $e^{-\tau}$, where

$$\tau=\beta_{11}h^2+\beta_{22}k^2+\beta_{33}l^2+\beta_{12}hk+\beta_{23}kl+\beta_{31}lh.$$

For isotropic temperature factors

$$\beta_{11}=\beta_{22}=\beta_{33}=\beta, \qquad \beta_{12}=\beta_{23}=\beta_{31}=0,$$

so that

$$\tau=\beta(h^2+k^2+l^2).$$

(1) In the initial attempt to refine the structure, individual isotropic temperature factor parameters β_D and β_N were used. Convergence failed to occur for all parameter values, particularly the temperature factor parameters.

(2) In the next attempt, the temperature factor parameters were not allowed to vary independently; rather β_D was allowed to vary and β_N was set equal to $\beta_D/7$, as suggested by the Debye-Waller equation. This attempt also failed, for the same reason as before. It later became apparent that this was a very poor assumption, a fact which could have been anticipated from the results of Peterson and Levy[10] who find for D_2O that β_D/β_O is of the order of 1.2 to 1.6 rather than 8. It would have been better, in fact, merely to have used a single parameter $\beta=\beta_D=\beta_N$, but it is doubtful whether convergence would have occurred even then.

(3) In the third attempt, neither temperature-factor parameter was allowed to vary, and the least-squares fit was made with respect to u, x, y, z, and k only. The values of β_D and β_N were chosen arbitrarily and held constant during each set of calculations. The condition $\beta_N=\beta_D/7$ was retained. With this modification, it was found that convergence did occur. The procedure then was to assign various values to β_D and to find for each such value the best values of the other parameters by successive iterations of the least-squares calculations. Values of β_D were chosen by trial and error until a value was found which minimized the residual. This value was $\beta_D=0.027$ (making $\beta_N=0.004$) and the corresponding positional parameters were $u=0.2117$, $x=0.3752$, $y=0.2614$, and $z=0.1097$; the residual was 0.064.

[8] E. T. Whittaker and G. Robinson, *The Calculus of Observations* (Blackie and Son Limited, London, England, 1924), Chap. 9.
[9] D. W. J. Cruickshank, Acta Cryst. **2**, 154 (1949).
[10] S. W. Peterson and H. A. Levy, Acta Cryst. **10**, 70 (1957).

TABLE II. Comparison of parameter values obtained with different models.

	Isotropic			Anisotropic I		Anisotropic II	
	Parameter value	Standard deviation		Parameter value	Standard deviation	Parameter value	Standard deviation
u	0.2127	0.0021	u	0.2148	0.0022	0.2141	0.0021
x	0.3740	0.0019	x	0.3751	0.0022	0.3763	0.0026
y	0.2632	0.0037	y	0.2644	0.0040	0.2648	0.0040
z	0.1094	0.0016	z	0.1079	0.0018	0.1080	0.0019
p_N	0.0099	0.0024	r_N	0.0105	0.0054	0.0124	0.0053
			s_N	0.0066	0.0062	0.0035	0.0063
p_D	0.0235	0.0019	q_D	0.0227	0.0071	0.0218	0.0069
			r_D	0.0192	0.0065	0.0414	0.0124
			s_D	0.0412	0.0120	0.0202	0.0061

(4) The next step was to return to the first model, in which β_D and β_N are allowed to vary independently. The initial parameter values were those resulting from the preceding step. This time convergence did occur. As would be expected, the value of β_D decreased while the value of β_N increased. The results after nine iterations were $u=0.2124$, $x=0.3765$, $y=0.2645$, $z=0.1102$, $\beta_D=0.0240$, and $\beta_N=0.0104$; the value of the residual was 0.0458. The observed values of the intensities were all given unit weight and the weights of the parameters were not determined.

(5) Individual isotropic temperature factors were used in this step also. It differed from the preceding step in that the weights of the observed intensities w from Table I were used and the standard deviations of the derived parameter values were calculated. Also, the notation was changed so that the two temperature factor parameters are called p_D and p_N. The initial values of the parameters were taken from the final iteration of the preceding step. The results after three iterations are given in the second and third columns of Table II. The value of the residual was 0.0489.

(6) In the final step, calculations were carried out to ascertain whether the data were good enough to indicate any anisotropy in the temperature factors. It was clearly out of the question to determine independently all six coefficients of the temperature-factor expression for both deuterium and nitrogen. Instead, models were set up in which the directions of the principal axes of the ellipsoids of vibration were assumed, thereby reducing to three the number of independent coefficients for each type of atom. Furthermore, only two coefficients are required for the nitrogen because of the symmetry about the threefold axis. Thus, the anisotropic model requires the determination of five temperature-factor coefficients, three for the deuterium and two for the nitrogen. Two such models were used.

The nitrogen temperature factor was the same in both cases, namely

$$\tau_N=r_N(h'^2+k'^2)+s_Nl'^2,$$

where h', k', and l' refer to an orthogonal system of coordinates in reciprocal space such that for each nitrogen atom l' lies on the threefold axis through that atom. Because of symmetry, the directions of h' and k' are immaterial.

For the deuterium, the form of the temperature factor was

$$\tau_D=q_Dh'^2+r_Dk'^2+s_Dl'^2$$

for both models. For each deuterium atom in the first model, the l' and k' axes were taken to lie in the plane defined by the deuterium atom and the threefold axis through the corresponding nitrogen atom, with the l' axis parallel to the threefold axis and the k' axis perpendicular to it. In the second model, the l' and k' axes were also in the plane just described, this time with the l' axis parallel to the N—D bond and the k' axis perpendicular to it. The h' axis is the same in both cases, and is parallel to the plane of the three deuterium atoms. It will be noted that l' of one case corresponds more closely to k' of the other case.

In carrying out the calculations, the transformation equations appropriate to each primed coordinate system were derived and substituted into the proper expression for τ, thus giving the temperature factor for each atom in terms of h, k, and l for each reflection. The initial values of the parameters for both models were the same as those of the preceding step: $r_N=s_N=0.0104$ and $q_D=r_D=s_D=0.0240$. The results after three iterations are shown in the last four columns of Table II. The values of the residual were 0.0410 and 0.0403 for cases one and two, respectively.

When the values in Table II are compared, it is immediately apparent that the data do not support a preference of one anisotropic model over the other. The next question is whether the data support an anisotropic model at all. The answer is that with only two exceptions the evidence of anisotropy is of low significance when the standard deviations are considered. These exceptions are s_D of model I and r_D of model II, which are roughly twice the other two corresponding deuterium parameters.

In view of the low degree of significance of the results of the anisotropic models, it would appear better to reserve them for a qualitative discussion and to quote the results of the isotropic model as the best values obtained:

space group: $P2_13$—T^4;

4 N at $u=0.2127\pm0.0021$;

12 D at $x=0.3740\pm0.0019$,

$y=0.2632\pm0.0037$,

$z=0.1094\pm0.0016$.

The values of the more common isotropic temperature factor parameter B, given by $B=4a^2\beta$, are $B_D=2.42A^2$ and $B_N=1.02A^2$. In Table III the observed intensities I_o are compared with the calculated intensities I_c for the isotropic model.

TABLE III. Comparison of observed and calculated intensity values.

$h^2+k^2+l^2$	I_o	I_c
2	11.86	12.29
3	160.63	162.15
4	76.28	72.52
5	11.19	12.04
6	18.99	18.50
8	28.87	31.03
9	137.60	132.78
10	84.80	87.03
11	19.53	18.38
12	23.00	26.23
13	16.79	16.88
14	52.20	53.50
16	0.00	0.06
17	22.59	20.34
18	102.33	106.86
19	21.09	17.87
20	0.00	1.75
21	183.60	178.40
22	49.95	60.85

DISCUSSION

Table IV compares the values of the parameters with those found by Olovsson and Templeton.[3] Because of a different choice of origin, one set of parameters must be transformed to agree with the other. Thus, in the table their y and z parameters have been permuted and all the values have been subtracted from 0.2500. It is seen that the sets of values are in essential agreement. As would be expected, the x-ray data produce a very precise value of the nitrogen parameter and considerably less precise values of the deuterium parameters. The parameters from the neutron diffraction data are all of about the same precision: less than that of the x-ray nitrogen parameter, but greater than that of the x-ray deuterium parameters. The difference between the two nitrogen parameter values is 1.5 times the standard deviation of the neutron diffraction value, so that the agreement is fairly good. The agreement between the deuterium positions is not bad, considering the difficulty of obtaining these values from x-ray data. In addition to random errors, another possible explanation for differences in the results is the fact that the x-ray diffraction data give the positions of maxima in the electron density distribution, while the neutron diffraction data give the average positions of the nuclei.

TABLE IV. Comparison of parameter values from neutron diffraction with those from x-ray diffraction.

	Neutron diffraction	x-ray diffraction[a]
u	0.2127±0.0021	0.2099±0.0006
x	0.3740±0.0019	0.40
y	0.2632±0.0037	0.26
z	0.1094±0.0016	0.11

[a] Transformed coordinates from Olovsson and Templeton's values (see text and reference 3).

The structures described by the two sets of parameters are qualitatively the same, but because of the improved deuterium positions from the neutron diffraction work there are a number of important quantitative differences. For this reason the structure will be discussed in some detail, although there will be some repetition of Olovsson and Templeton's discussion.

The basis of the structure is a cubic close packing of the asymmetric ammonia molecules, distorted so that each molecule has six nearest neighbors and six next nearest neighbors, rather than twelve equidistant neighbors. Each molecule is hydrogen bonded to its six nearest neighbors, three through its own deuteriums and three through deuteriums of its neighbors. The structure is illustrated in Fig. 3, which gives a view along a threefold axis. It is interesting to note that the centers of the equilateral triangles described by the deuteriums lie almost exactly at the close-packed sites (0.249, 0.249, 0.249) compared with $(\frac{1}{4}, \frac{1}{4}, \frac{1}{4})$.

A number of interatomic distances and angles were calculated and are collected in Table V. Specific examples of these quantities occurring in Fig. 3 are given in the third column. The examples given are such that the lines connecting the atoms concerned are nearly parallel to the plane of the drawing. This condition is satisfied exactly or almost exactly for all but the examples given for d_7 and θ_1. The bending of the hydrogen bond is shown almost without distortion.

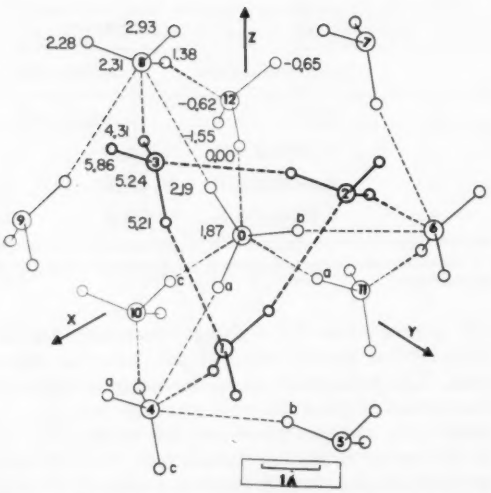

FIG. 3. Structure of cubic ammonia, viewed toward the origin along the line $x=y=z$. Shown are a central molecule (No. 0) with its six nearest neighbors (Nos. 4, 6, 8, 10, 11, and 12) and six next nearest neighbors (Nos. 1, 2, 3, 5, 7, and 9). Numbers 0, 4, 5, 6, 7, 8, and 9 lie roughly in a plane while 1, 2, and 3 lie above and 10, 11, and 12 lie below the plane. The hydrogen bonds are indicated by dashed lines. Distances above and below the plane $x+y+z=0$ are given in angstroms.

TABLE V. Interatomic distances and angles.

Description	Example[a]	Value
N—N distances		
nearest neighbor	N_5—N_4	$d_1=3.352\pm0.011$ A
next nearest neighbor	N_9—N_6	$d_2=3.883\pm0.018$ A
N—D distances		
covalent bond	N_4—D_{4c}	$d_3=1.005\pm0.023$ A
hydrogen bond	D_{5b}—N_4	$d_4=2.374\pm0.028$ A
D—D distances		
within molecule	D_{0a}—D_{0b}	$d_5=1.651\pm0.024$ A
to closest D in molecule to which hydrogen bonded	D_{5b}—D_{4c}	$d_6=2.342\pm0.029$ A
to next closest D in molecule to which hydrogen bonded	D_{0a}—D_{4a}	$d_7=2.772\pm0.009$ A
between D's hydrogen bonded to same nitrogen	D_{10c}—D_{11a}	$d_8=2.545\pm0.040$ A
Angles		
D—N—D bond angle	D_{4a}—N_4—D_{4c}	$\theta_1=110.4°\pm2.0°$
N—D···N bond angle	N_5—D_{5b}—N_4	$\theta_2=164.0°\pm2.4°$
deviation of D from N—N line	N_4—N_5—D_{5b}	$\theta_3=11.3°\pm1.7°$

[a] The numbering of the atoms in the examples refers to Fig. 3.

The length of the N—D bond, 1.005 ± 0.023 A, is equal within experimental error to the free molecule value, 1.008 ± 0.004 A,[11] but disagrees strongly with Olovsson and Templeton's value of 1.13 A. The latter point out that the bond would be expected to lengthen because of the hydrogen bonding. This effect, however, amounts to about 9% in HF (comparing the monomer with the polymer, both gaseous)[12] and about 4% in H_2O (comparing the gas with the solid)[13] and should be even smaller for ND_3, 2 or 3% at most. A 2% increase would produce a bond length which is still within the range of the experimental error of the neutron diffraction value. It is unfortunate that the precision is not high enough to tell whether or not there is a bond lengthening. One can say with certainty that the effect, if it exists, is small. The discussion by Pimentel and McClellan[14] of the A—H length in A—H···B bonds would also predict that in the N—H···N bond of NH_3 the N—H distance would not be much longer than the covalent bond of the free molecule.

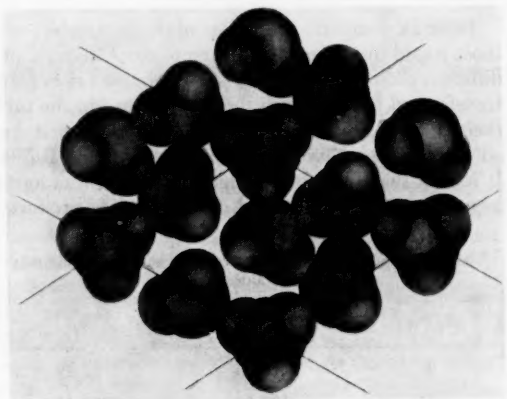

FIG. 4. Structure of one layer of cubic ammonia, illustrating the packing relationships. One hexagonal unit cell with its [0001] axis along the cubic [111] axis is indicated. Successive layers are shifted right or left by one-third of the long diagonal of the hexagonal cell.

The D—N—D bond angle, $110.4°\pm2.0°$, is significantly larger than the free molecule value of $107.4°\pm0.2°$ [11] and Olovsson and Templeton's value of 107°. It is not distinguishable, however, from the tetrahedral angle of 109.5°. The D—O—D angle in ice is quite close to the tetrahedral value,[10] an increase of 5° over the gaseous value, so that an increase of about 2.5° does not appear unreasonable for ND_3.

[11] M. T. Weiss and M. W. P. Strandberg, Phys. Rev. **83**, 567 (1951).

[12] *Tables of Interatomic Distances and Configuration in Molecules and Ions*, edited by L. E. Sutton (Chemical Society, London, 1958), p. M86.

[13] Reference 12, p. M67.

[14] G. C. Pimentel and A. L. McClellan, *The Hydrogen Bond* (W. H. Freeman, San Francisco, California, 1960), Chap. 9.

The distance between nearest neighbor nitrogens, the value usually quoted in discussing the hydrogen bond, is 3.352±0.011 A, in very good agreement with Olovsson and Templeton's 3.349±0.003 A. The distance between a deuterium and a neighboring nitrogen to which it is hydrogen bonded is 2.374±0.028 A. As Olovsson and Templeton observe, the deuteriums do not lie on the lines connecting the nitrogens. The extent of this deviation is indicated by the N—D···N bond angle, which has a value of 164.0°±1.7°. Another useful measure of the deviation is the angle between the N—D bond and the line connecting the two nitrogen atoms, 11.3°±1.7°. This is the angle ϕ defined by Pimentel and McClellan. They quote three other structures in which this angle is significantly different from zero, $Na_2CO_3 \cdot NaHCO_3 \cdot 2H_2O$ in which the deviation is 3.5° (O—H···O), α-resorcinol in which it is 10° (O—H···O), and $CuCl_2 \cdot 2H_2O$ in which it is 15.6° (O—H···Cl). Another example occurs in the structure of diaspore, $AlHO_2$, where it has a value of 12°.[15]

Each nitrogen atom has as close neighbors, i.e., within distances not much greater than the sums of the van der Waals radii (1.5A for nitrogen and 1.2A for hydrogen),[16] only the six deuterium atoms at 1.005A and 2.374A. Each deuterium has, in turn, two nitrogen neighbors at these distances and, of course, the other two deuteriums in the same molecule at 1.651 A. The only other near neighbors are those at the distances d_6, d_7, and d_8 listed in Table V, and of these the 2.772 A separation is decidedly larger than twice the van der Waals radius.

Some of the structural relationships may be seen in Fig. 4 in which the atoms are drawn with their van der Waals radii. Somewhat more than one repeat unit of a close-packed layer is shown. The complete structure is obtained by stacking such layers together. All layers are alike, but each successive layer is shifted, repetition occurring every third layer, just as in the close packing of spheres.

As mentioned above, only qualitative conclusions can be drawn from the results of the calculations using anisotropic temperature factors. There is inconclusive evidence that the motion of the nitrogen atom in directions perpendicular to the threefold axis is greater than that along it. For the deuteriums, on the other hand, the motion parallel to the threefold axis (or perpendicular to the N—D bond, since these motions cannot be distinguished here) can be said with some certainty to be greater than in directions perpendicular to the axis. The resulting picture is that of an oblate spheroid of vibration for the nitrogen and a prolate spheroid of vibration for the deuterium, each with its unique axis parallel to the threefold axis.

ACKNOWLEDGMENTS

The experimental work was done at Ohio State University and at the University's neutron diffraction installation at the Batelle Memorial Institute Research Reactor. Most of the calculations, including all of the IBM 709 computations, were carried out at Hughes Research Laboratories. The work done at Ohio State University was supported in part by the U. S. Air Force Office of Scientific Research. One of the authors (J. W. Reed) wishes to acknowledge support from a grant in aid from Ohio State University. The authors wish to thank Professor R. A. Erickson of the Ohio State University Department of Physics for his assistance in the experimental phase of the work.

[15] W. R. Busing and H. A. Levy, Acta Cryst. **11**, 798 (1958).
[16] L. Pauling, *The Nature of the Chemical Bond* (Cornell University Press, Ithaca, New York, 1960), 3rd ed., p. 260.

Carbon-13 Hyperfine Splitting in the Electron Spin Resonance Spectra of Semiquinones and Cyclooctatetraene*

HERBERT L. STRAUSS† AND GEORGE K. FRAENKEL
Department of Chemistry, Columbia University, New York 27, New York

(Received April 12, 1961)

Measurements have been performed on the carbon-13 hyperfine splitting in the ESR spectra of a series of methyl- and chloro-substituted semiquinones and of the cyclooctatetraene anion radical. The splittings were observed from carbon-13 nuclei present in natural abundance (approx. 1%), and the carbon-13 satellites were distinguished from spurious low-intensity lines arising from side-reaction produced radical impurities by means of careful intensity measurements as well as other techniques. The largest observed carbon-13 splitting had a magnitude of 1.7 gauss, and in most spectra smaller splittings were found. The carbon-13 satellites were overlapped by the major lines in the spectra (arising from proton splitting), but after correcting the measured intensities for this overlap, good agreement was found between the predicted and measured intensities in those spectra in which a detailed analysis was possible. In the *p*-benzosemiquinone ion, a previously observed line of low intensity has been identified as a splitting arising from carbon-13 nuclei, and has been assigned, on the basis of intensity measurements, to the four CH carbon atoms. No splitting was found from the carbon atoms in the CO bonds of this compound, and it was concluded that the splitting is less than 0.6 gauss. Splitting constants tentatively identified with the methyl carbon atoms of the methyl-substituted compounds were in the neighborhood of 1.5 gauss. The splitting in the cyclooctatetraene anion indicates that the three sigma bonds attached to a carbon atom lie in a single plane. The experimental results are in agreement with the theory of carbon-13 hyperfine splittings recently developed by Karplus and Fraenkel. Comparison of theory and experiment indicates that these results provide a very sensitive measure of the pi-electron spin densities in the radicals. The valence-bond theory of the spin-densities in the methyl substituents is shown to be inadequate in its present form, but the molecular-orbital theory appears to give good agreement. This latter agreement is based on certain as yet unjustified assumptions, and therefore both theories require reexamination. The spectrum of the previously observed semiquinone ion formed from 2,5-dihydroxyquinone was interpreted in order to obtain an estimate, in conjunction with other data, of the hyperfine splitting at the carbon-13 nucleus of the carbon atom in a CO bond. The analysis also shows that the two CH carbon atoms in this compound have negative pi-electron spin densities.

I. INTRODUCTION

ALTHOUGH a theoretical description of the mechanism of the isotropic proton hyperfine interaction observed in the electron spin resonance spectra of organic free radicals has been available for several years,[1–4] a theory for the contact interaction arising from carbon-13 nuclei has just recently been formulated.[5] The validity of the theory is difficult to assess, however, because only a small number of carbon-13 splittings have been measured. The present work was initiated to obtain experimental carbon-13 splittings for the semiquinones and the cyclooctatetraene anion radical in order to provide data that would be useful in testing the theoretical predictions.

In the original investigation of the ESR spectrum of the durosemiquinone ion,[6,7] anomalous lines of low intensity were observed which could not be attributed to proton hyperfine splitting. More recently, low-intensity lines were also found in the spectrum of the *p*-benzosemiquinone ion.[8–10] It was suggested that the small lines in the spectra of these two compounds arose from a splitting caused by the presence of carbon-13 nuclei in natural abundance,[8,10,11] but such an interpretation is not readily verified. The fundamental difficulty in interpretation results from the complicated reactions which take place in quinone systems, and under conditions typically employed for obtaining ESR spectra, radicals other than the simple semiquinones are produced.[7,12–14] Analysis of the spectra is then usually ambiguous, for one cannot ascertain whether a small line of low intensity arises from carbon-13 splitting or from a small amount of some spurious radical. The most direct procedure for providing an unambiguous interpretation is, of course, the use of compounds enriched with C^{13}, but the synthesis of a compound with C^{13} in a benzenoid ring is an extremely difficult task. In the absence of C^{13}-enriched samples, it is still possible to obtain reasonable verification of the inter-

* Supported in part by the U. S. Air Force through the Office of Scientific Research.

† National Science Foundation Predoctoral Fellow. Present Address: Department of Chemistry, University of California, Berkeley, California.

[1] H. M. McConnell, J. Chem. Phys. **24,** 632, 764 (1956); H. M. McConnell and D. B. Chesnut, *ibid.* **28,** 107 (1958), and other papers cited therein.

[2] R. Bersohn, J. Chem. Phys. **24,** 1066 (1956).

[3] S. I. Weissman, J. Chem. Phys. **25,** 890 (1956).

[4] H. S. Jarrett, J. Chem. Phys. **25,** 1289 (1956).

[5] A. D. McLachlan, H. H. Dearman, and R. Lefebvre, J. Chem. Phys. **33,** 65 (1960).

[6] B. Venkataraman, thesis, Columbia University (New York, 1955) and unpublished results.

[7] B. Venkataraman and G. K. Fraenkel, J. Am. Chem. Soc. **67,** 2707 (1955).

[8] A. van Roggen, J. Chem. Phys. **33,** 1589 (1960).

[9] J. W. H. Schreurs and G. K. Fraenkel, J. Chem. Phys. **34,** 756 (1961).

[10] D. C. Reitz, F. Dravnieks, and J. E. Wertz, J. Chem. Phys. **33,** 1880 (1960).

[11] B. Venkataraman (unpublished results).

[12] D. H. Anderson, P. J. Frank, and H. S. Gutowsky, J. Chem. Phys. **32,** 196 (1960).

[13] B. Venkataraman, B. G. Segal, and G. K. Fraenkel, J. Chem. Phys. **30,** 1006 (1959).

[14] J. E. Wertz and J. L. Vivo, J. Chem. Phys. **23,** 2441 (1955); J. L. Vivo, thesis, University of Minnesota (Minneapolis, Minnesota, 1955).

pretation if accurate intensity measurements can be made which give results that are in accord with the spectrum predicted for carbon-13 nuclei in natural abundance. Although this latter procedure has been used in several instances,[10,15,16] it requires that the low-intensity lines be well resolved and that the spectra be of high intensity without asymetries or other anomalous or ambiguous features.

In an attempt to surmount these difficulties, we have studied a series of related semiquinone ions to determine if low-intensity lines would be found that could be interpreted in a consistent pattern. Great care was taken to obtain spectra from which reliable intensity measurements of the small lines could be made, since in this way a comparison became possible with the intensity to be expected for lines caused by a natural abundance of carbon-13 nuclei. The spectra were produced under a variety of conditions to sort out lines which were independent of chemical preparation from those which arose from extraneous radicals. In addition to the investigation of the semiquinones, the present study also includes data on carbon-13 splitting in the spectrum of the cyclooctatetraene radical anion.[17]

During the course of these experimental studies it became evident that the theory of McLachlan *et al.*[5] required modification. An account of a revised theory is presented elsewhere,[18] but the results obtained are used in the following for analyzing the experimental data.

II. EXPERIMENTAL METHODS

A new and modified version of the X-band superheterodyne spectrometer described by Hirshon and Fraenkel was employed with a Varian 6-in. magnet.[9,19,20] The experimental techniques employed have been described previously.[9,13] In much of the present work, magnetic-field measurements were made directly from a strip-chart recording of the derivative of the spectrum, using previously measured spacings of the proton hyperfine splittings to calibrate the chart.[13,17] Field modulation at 38 cps was used, and attenuators in the 38-cps twin-tee amplifier and phase-sensitive detector, as well as calibrated attenuators between the detector and the strip-chart recorder, were employed to vary the sensitivity at which a spectrum was recorded. High-sensitivity recordings suitable for studying the lines of low intensity were usually alternated with low-sensitivity recordings appropriate for measurements on the major lines of the spectra. Because of the high sensitivity needed, fairly long time constants had to be employed in the filter on the output of the phase-sensitive detector; and particular care had to be taken, in traversing a line, that the rate of scan was slow enough to avoid distortion in a low-intensity line immediately following a major component. The concentration of some of the radicals decayed during the long times needed to traverse a spectrum, and corrections for the decay had to be made. These corrections were obtained by measurements of the height of the major components interspersed, at recorded time intervals, between measurements on the low-intensity lines. The amplitude linearity of the spectrometer was checked by recording the spectrum of solid diphenylpicrylhydrazyl at two different modulation amplitudes. The amplitudes of the modulation were small compared to the linewidth and one was larger than the other by a factor of almost 100. The height of the spectrum in the large-amplitude recording was too low by only 7%. Corrections for this nonlinearity were not included in processing the data.

The quinones and hydroquinones were the same as those used by Venkataraman, Segal, and Fraenkel,[13] except that durohydroquinone (as well as duroquinone) was employed as a starting material. The durohydroquinone was obtained by reduction of the quinone with $SnCl_2$ in aqueous HCl by the method of Conant and Fieser.[21,22] The methods of preparing the semiquinones,[7,9,13] and the procedure for producing the cyclooctatetraene radical anion,[17,20,23,24] are given elsewhere.

Samples were prepared with different concentrations of starting material and alkali, and were allowed to react for different lengths of time, in order to find the influence of these factors on the low-intensity lines. The detailed procedures are described in the discussion of the results on each individual compound. Spectra were recorded from samples which gave the narrowest possible lines with sufficient intensity to be adequately studied.

A search was always made for additional lines beyond the last major component of a spectrum. This procedure was followed because the satellite from a carbon-13 nucleus with a splitting approximately equal to one of the proton splittings would not be detectable except at the ends of the spectrum. Such a search could not be carried out for the durosemiquinone ion because the last few lines had too low a signal-to-noise ratio.

III. INTERPRETATION OF SPECTRA

The spin of the carbon-13 nucleus is $\frac{1}{2}$, and thus the replacement of a carbon-12 nucleus by a carbon-13

[15] W. D. Phillips, J. C. Rowell, and S. I. Weissman, J. Chem. Phys. **33,** 626 (1960).
[16] N. Hirota and S. I. Weissman, J. Am. Chem. Soc. **82,** 4424 (1960).
[17] T. J. Katz and H. L. Strauss, J. Chem. Phys. **32,** 1873 (1960).
[18] M. Karplus and G. K. Fraenkel, J. Chem. Phys. **35,** 1312 (1961).
[19] J. M. Hirshon and G. K. Fraenkel, Rev. Sci. Instr. **26,** 34 (1955).
[20] H. L. Strauss, thesis, Columbia University (New York, 1960).
[21] J. B. Conant and L. F. Fieser, J. Am. Chem. Soc. **45,** 2194 (1923).
[22] We are indebted to Mr. Philip H. Rieger for preparing this sample.
[23] H. L. Strauss, T. J. Katz, and G. K. Fraenkel (to be published).
[24] T. J. Katz, J. Am. Chem. Soc. **82,** 3784, 3785 (1960).

TABLE I. Carbon atom positions and number of observed carbon-13 splittings.

Radical	C—H carbons	C—CH_3 ring carbons	CH_3 carbons	C—Cl carbons	C—O carbons	Number of carbon positions observed[a]
Derivative of *p*-benzosemiquinone						
unsubstituted	4	0	0	0	2	4
monomethyl	1,1,1[b]	1	1	0	2	5
2,5-dimethyl	2	2	2	0	2	4
2,6-dimethyl	2	2	2	0	2	6
tetramethyl	0	4	4	0	2	8[c] or 10
monochloro	1,1,1[b]	0	0	1	2	4
2,5-dichloro	2	0	0	2	2	4 or 6
2,6-dichloro	2	0	0	2	2	4 or 6
tetrachloro	0	0	0	4	2	0
Cyclooctatetraenyl radical	8	0	0	0	0	8

[a] See Table II and text.
[b] These are inequivalent carbon atoms.
[c] Preferred value.

nucleus causes a doubling of all the lines in the ESR spectrum. The intensity per molecule of each line of the doublet is $\frac{1}{2}$ the intensity of the corresponding line from a molecule not containing a carbon-13 nucleus. If there are k different carbon-atom sites in the molecule, there will be k different sets of doublets with intensities which depend on the number n_k of equivalent carbon atoms in the set k and the abundance of carbon-13 nuclei q. For carbon-13, the natural abundance is 1.108%.[25] The fraction of molecules without any carbon-13 nuclei in the set k is $(1-q)^{n_k}$, and the fraction with one carbon-13 nucleus in set k is $n_k(1-q)^{n_k-1}q$. The fraction with two carbon-13 nuclei in the set k, $(n_k/2)(n_k-1)(1-q)^{n_k-2}q^2$, is negligible for $q \ll 1$. The intensity of each line of a doublet produced by a carbon-13 nucleus is thus $n_kq/2(1-q)$ times the intensity of the corresponding line in the absence of C^{13} nuclei; and for carbon-13 nuclei in natural abundance, this fraction is 0.005602 for a set corresponding to one carbon-atom site, 0.011204 for a set corresponding to two carbon-atom sites, and so on.

In the following, it will be convenient to refer to the lines arising from proton hyperfine interaction as proton lines or major components, and to refer to the lines attributed to carbon-13 splitting as "satellites."

The satellite lines were usually quite close to, and superimposed on, the main proton lines, and corrections had to be made for this overlap. It was assumed that all the components in the ESR spectrum could be adequately described by a Lorentzian shape. There is good evidence of both an experimental and theoretical nature for the validity of this assumption in the central portion of the line,[9,26,27] but since the second moment of the line must be finite, the shape necessarily departs from a Lorentzian function in the wings of the line.[26] The uncertainties about the shape in the wings is fortunately not of concern here because, in this region, the corrections for overlap are undoubtedly small. It is also assumed that all the components of a spectrum have the same width, independent of the value of the nuclear spin quantum numbers, even though it is known that there may be width differences within a spectrum of as much as 20%.[9]

An example of the magnitude of the overlap corrections is given in Fig. 1, which applies to four equivalent carbon-13 nuclei. Two quantities are plotted: the correction to the peak-to-peak height of the derivative of the satellite, which will be called the height correction; and the ratio of the apparent width of the derivative spectrum of the satellite to the width in the absence of overlap, which will be called the width ratio. Both quantities are plotted as a function of the splitting ratio $a_k/2\Delta_0$, where a_k is the hyperfine interaction constant for the carbon-13 splitting and Δ_0 is the half-width of the line at half-maximum intensity. The quantity $a_k/2$ is the displacement of one line of the doublet from the center of the main proton line, and $a_k/2\Delta_0$ is this displacement in units of the linewidth. Figure 1 illustrates the large values of the corrections for small splitting ratios. Thus, for example, at a splitting ratio of 3.4, the apparent height of the satellite would be only 1/8.57 times the height of an unoverlapped satel-

[25] C. H. Townes and A. L. Schawlow, *Microwave Spectroscopy* (McGraw-Hill Book Company, Inc., New York, 1955), App. VII.

[26] R. Kubo and K. Tomita, J. Phys. Soc. Japan **9**, 888 (1954).
[27] J. W. H. Schreurs, G. E. Blomgren, and G. K. Fraenkel, J. Chem. Phys. **32**, 1861 (1960).

lite arising from four equivalent carbon-13 nuclei, so that the height would be only 0.002614 times the height of the main line instead of the value of 0.02241 expected for an unoverlapped satellite. The corrections are larger for spectra arising from a smaller number of equivalent carbon-13 nuclei, and smaller for a larger number.

Large errors are introduced into the correction factors by any uncertainty in the experimentally determined splitting ratio. These errors are particularly serious in the range of splitting ratios in which, as in Fig. 1, the correction to the height is changing rapidly with the ratio. At a splitting ratio of 5, for a satellite aising from four equivalent carbon-13 nuclei, for example, a 10% error in the splitting ratio would cause a 28% error in the height correction.

The location of the center of the derivative spectrum of an overlapped satellite is uncertain. As an estimate of the proper point to choose, the apparent position of the overlapped satellite has been taken to be the mean of the apparent positions of the derivative extrema of the satellite spectrum. Large corrections do not arise for the splitting constants. For example, at a splitting ratio of 3.4, in the case of four equivalent carbon-13 nuclei, the splitting constant is only 2% less than the value for an unoverlapped satellite.

Two or more overlapped satellites occur in some spectra, and a number of specific overlap calculations were necessary for these complicated cases.

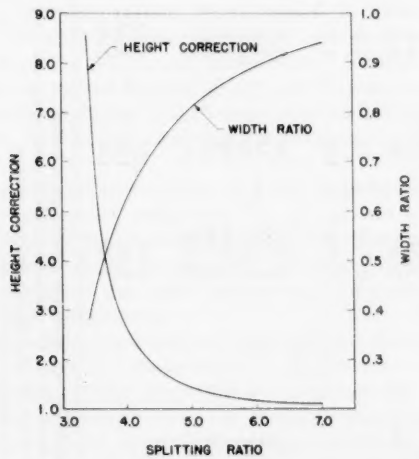

FIG. 1. Plot of the height correction and width ratio vs splitting ratio for an overlapped satellite arising from four equivalent carbon-13 nuclei present in natural abundance. The splitting ratio is $a_k/2\Delta_0$, where a_k is the hyperfine interaction constant for the carbon-13 splitting and Δ_0 is the half-width of the absorption line at half-maximum absorption. The true peak-to-peak height of the derivative of an unoverlapped satellite is obtained by multiplying the observed peak-to-peak height by the height correction. The width ratio is the ratio of the apparent width of the overlapped satellite to the width of an unoverlapped satellite. The width ratio in this figure is Δ/Δ_0; $\Delta=0.866\delta$.

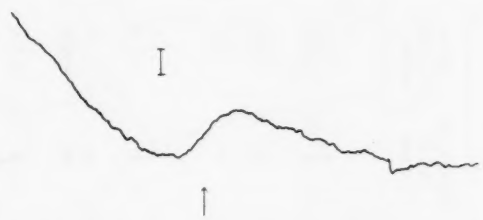

FIG. 2. Derivative of the electron spin resonance spectrum of the high-field side of the central line of the *p*-benzosemiquinone ion. The main line is to the left, off scale. The satellite is 0.296 gauss from the center of the main line. The barred line represents 1% of the height of the main line. The small bump on the right is not a reproducible feature of the spectrum. The magnetic field increases to the right.

IV. RESULTS

General Features of the Spectra

The radicals examined in the present study are listed in Table I. The proton hyperfine splitting has been thoroughly studied in previous investigations.[13,17] In all the spectra observed, except that of the tetrachlorosemiquinone ion, satellites were found which are attributed to carbon-13 splitting. In every spectrum, a satellite found on one major component was also observed on both sides of each proton line in the spectrum except when the nature of the spectrum precluded the possibility of observing the satellite at all the appropriate positions. In the durosemiquinone ion spectrum, for example, the outer proton lines are so weak that no satellites could be observed, while in a number of other spectra there are so many lines that the satellite of one major component occurs at the same position as the main line of another major component.

A number of small lines were seen in many spectra, particularly those of the chlorosemiquinones, that are not attributed to C^{13} splitting. If a line or set of lines was not symmetrically spaced with respect to the major lines in the spectrum, or if the height of a line varied from sample to sample relative to the height of a major component, the line was considered spurious. With the possible exception of two spectra, all of the lines observed could either be interpreted as arising from hyperfine interactions or else were definitely shown to be spurious. The two possible exceptions, which are discussed below, are in the spectra of the durosemiquinone ion and of the 2,6-dichlorosemiquinone ion.

The proton lines differed considerably in width, ranging from 0.06 to 0.15 gauss. The tetrachlorosemiquinone ion spectrum had the largest width and showed no satellites, and in other spectra the lines were sometimes wide enough to obscure one or more satellites.

Details of Individual Spectra

p-Benzosemiquinone Ion

Preliminary experiments showed that one satellite appeared on each side of each major component when

TABLE II. Carbon-13 splittings. Experimental results.

Radical	C^{13} splitting gauss[a]	Width of main lines, milligauss	Splitting ratio[b]	2× height of satellites, %	Width ratio[c]	Predicted width ratio[c]	Height correction	Corrected height, %	Number of carbon atoms	Error in corrected height, %
Derivative of *p*-benzosemiquinone ion										
Unsubstituted										
Center line	0.594	61[d]	4.87[d]	2.74	0.97[d]	0.92[d]	1.57[d]	4.3	4	−4.0
+ 1 line	0.590	61[d]	4.87[d]	3.25	0.97[d]	0.92[d]	1.57[d]	5.1	4	+14.0
Monomethyl										
inside satellite A of line+16	0.728[e]	67[d]	5.4	0.52	0.865	0.85	1.75[f]	0.91	2[e,f]	−59.0
outside satellite B of line+16	1.55[e]	67[d]	11.5	2.92	1.28		1.08	3.2	3[e]	−5.0
line+15	1.54[e]	67[d]	11.5	2.87	1.35		1.12	3.2	3[e]	−5.0
line+14	1.53[e]									
2,5-Dimethyl										
Spectrum I	1.67[d,e]	118	7.1	3.23	1.55		1.56	5.0	4[e]	+12.0
Spectrum II	1.67[d,e]	125	6.8	3.0	1.17		1.24	3.7	4[e]	−17.0
2,6-Dimethyl										
inside satellite A	0.82	76	5.4						2[f]	
outside satellite B	1.38[e]	76	9.0	2.34	2.0		1.42	3.3	4[e]	−26.0
Tetramethyl										
from quinone, inside satellite A	0.742	67	5.5	3.62	1.10	0.99	1.29	4.7	4	+5 0
middle satellite B	1.16	67	8.7	0.6	f		f	f	f	
outside satellite C	1.34	67	10.	3.78			1.15	4.3	4	−4.0
from hydroquinone,										
inside A	0.730	85	4.3	2.68	0.78	0.79	2.0	5.4	4	+21.0
middle B	1.10	85	6.5	f	f		f	f	f	
outside C, low-field side	1.35	85	8.0	3.14	0.94	0.91	1.19	3.7	4	−17.0
high field side	1.35	85	8.0	3.48			1.04	3.8	4	−15.0
Monochloro	0.724[e]	72	5.0	0.81	1.65		f	f	4[e,f]	
2,5-Dichloro	0.984[d,e]	107	4.7	2.12	1.44		f	f	e, f	
2,6-Dichloro										
high-field side, inside A	0.388[d]	53[f]	3.7	1.28	f		4	5.1[f]	f	
middle B	0.770[d]	53[f]	7.3	1.3	f		1.09	1.4[f]	2[f]	−38.0
outside C	1.06[d]	53[f]	10.	1.4	f		1.09	1.5[f]	2[f]	−33.0
low-field side, inside A	0.388[d]	61[f]	3.2	0.64	f		>10.	>6.0[f]	f	
middle B	0.770[d]	61[f]	6.3	0.7	f		1.14	0.8[f]	2[f]	−64.0
outside C	1.06[d]	61[f]	8.7	0.7	f		1.14	0.8[f]	2[f]	−64.0
Cyclooctatetraenyl radical										
Sample 1	1.26	174	3.62	5.6			1.86	10.4	8	+16.
Sample 2	1.31	178	3.68	5.72			1.80	10.2	8	+14.
Average	1.28	176	3.66	...			...	10.3	8	+15.

[a] These values are not corrected for the shift in apparent splitting due to overlap.
[b] The splitting ratio is $a_i/2\Delta_0$ where a_i is the C^{13} splitting and Δ_0 is the width of the main lines.
[c] The width ratio is δ/δ_0 where δ is the distance between derivative extrema.
[d] These are average values for a number of lines and/or spectra.
[e] These satellites arise from more than one kind of carbon atom.
[f] See text.

either NaOH or KOH was used as the base and either 95% ethanol or water as solvent. The spectrum of the satellite on the high-field side of the central proton line is shown in Fig. 2. A flow system was employed to produce a constant concentration of radical in the spectrometer and the same concentrations and conditions were used as in previous studies.[9] In particular, the hydroquinone concentration in the flow-system reservoir was 0.002*M*. When an attempt was made to employ more concentrated hydroquinone solutions, additional small lines of intensity comparable to that of the satellites appeared between the major components. These additional lines were not visible when the 0.002*M* hydroquinone solution was used, yet they would have been observable if their relative intensity had been unchanged as compared to the spectra found for the more concentrated solutions. The additional lines must therefore arise from radicals other than the *p*-benzosemiquinone ion, and presumably are from radicals produced by side reactions involving the various oxidation states of the *p*-benzohydroquinone.

Careful measurements were made on the satellites of the central proton line and on those of the proton line on the high-field side of, and nearest to, the central line (the +1 line). The results for the two satellites are listed separately in Table II as the averages from a number of spectra. The values for the central line are more precise than those for the +1 line.

The single set of satellites observed has an intensity corresponding quite closely to that expected from four equivalent carbon atoms, and is therefore identified as arising from the carbon atoms bonded to hydrogen. Since the splitting from this set of carbon-13 nuclei is 0.59 gauss, the present measurement confirms the suggestion by van Roggen[8] that a satellite observed by him with a splitting of 0.55 gauss was attributable to carbon 13. This satellite was also observed by Reitz *et al.*[10]

A second set of satellites, of $\frac{1}{2}$ the intensity of the above set, should arise from the two carbon atoms bonded to oxygen. A careful search under conditions of high sensitivity did not reveal any additional satellites either between the main components or outside the last major component.

An attempt was made to fit the recorded spectra of the satellite with a computed curve for Lorentz lines of the correct relative intensities and positions. Because of noise and instabilities, the different experimental spectra scattered about these calculated curves to such an extent that a good fit could not be obtained from a single spectrum, but the general characteristics of the observed spectra were reproduced by the computed curves and were concluded to be consistent with them.

p-Tolusemiquinone Ion

The complexity of the proton spectrum made it necessary to confine most of the measurements of the carbon-13 splitting to the outermost proton lines (line number +16 of the work cited in reference 13), although measurements of the two next high-field lines (numbers +15 and +14) are also included for comparison. Two satellites are observed (Fig. 3), an inner one designated by A, and an outer one designated by B.

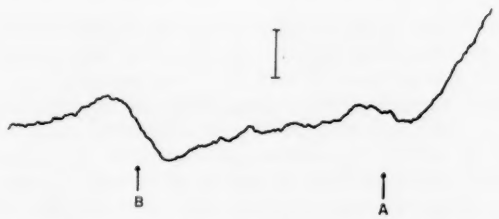

FIG. 3. Derivative of the electron spin resonance spectrum of the high-field side of the high-field main line of the *p*-tolusemiquinone ion. Vertical arrows indicate the apparent centers of the two satellites. The inner satellite is 0.370 gauss and the outer satellite is 0.785 gauss from the center of the main line, which is off scale to the right. The barred vertical line represents 1% of the height of the main line. The magnetic field increases to the left.

The outer satellite B is too wide to be interpretable as a single line, and an approximate calculation indicates that this satellite could arise from three differently situated carbon-13 nuclei with splitting constants that are within a few hundredths of a gauss of each other (see Table II). The analysis was not sufficiently detailed to preclude other possibilities.

The intensity of the inner satellite A could not be fitted by any reasonable assumption, but the width of the satellite is consistent with the assumption that it arises from two differently situated carbon-13 nuclei with splitting constants differing by about 0.03 gauss. This assumption is, however, quite uncertain.

2,5-Dimethylsemiquinone Ion

One satellite was observed, and measurements were made only on the low-field satellite of the low-field proton line. The positions and relative intensities of the inner satellites were examined in detail and found to fit the spectrum predicted on the basis of measurements on the outermost line, but the high degree of overlapping of both proton and satellite lines precluded the use of the inner satellites for the quantitative determination of the splitting constant and intensity of the satellite. The results of two different spectra are given in Table II, and it was found that one spectrum was fitted best if the satellite was assumed to consist of two sets of equivalently situated carbon-13 nuclei with splitting constants differing by 0.09 gauss and the other if the difference in splitting constants was taken to be 0.05 gauss. Thus the splitting constants for the two sets of carbon-13 nuclei probably differ by about 0.05 to 0.1 gauss.

2,6-Dimethylsemiquinone Ion

Two satellites were observed. The spectra were asymmetric and not of particularly good quality, and the

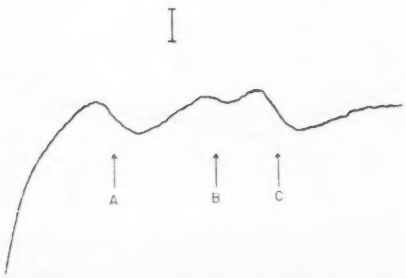

FIG. 4. Derivative of the electron spin resonance spectrum of the low-field side of the +2 line (second line to high-field from the center line) of the durosemiquinone ion derived from durohydroquinone. The center of the main line is of scale to the left. Three satellites are shown. The middle one is considerably smaller on the high-field side of the main line. The inner, middle, and outer satellites are 0.374 gauss, 0.567 gauss, and 0.676 gauss, respectively, from the center of the main line. The barred vertical line represents 1% of the height of the main line. The magnetic field increases to the left.

intensity of only the outer satellite (B) of the high-field proton line was measured. The position of the inner satellite (A) was determined, and its spectrum was consistent with the assignment of satellite A to two carbon-13 nuclei at equivalent sites. Satellite B is too wide to arise from carbon-13 nuclei with a single splitting constant, but calculations for two sets of two equivalent carbon-13 splittings differing by 0.08 gauss indicate that the corrected intensity is more consistent with three carbon-13 nuclei than four. Since, by symmetry, the carbon atoms are equivalent in pairs, it seems appropriate to conclude that satellite B arises from two sets of equivalent pairs of splittings and that the measurements of intensity are in error by 26%.

Durosemiquinone Ion

Satellites in the spectra of this radical have been observed previously,[6] and Venkataraman suggested that they might arise from carbon-13 interactions. Two major satellites are observed, and experiments performed by Goodman showed that they are unaffected if KOH is used in place of NaOH in the preparation of the semiquinone ion, or if pyridine-H_2O or pyridine-D_2O is used as solvent instead of ethanol-water.[28] The spectrum is shown in Fig. 4 and is seen to consist of three satellites. The inner (A) and outer (C) satellites are of about equal intensity, but the middle satellite (B) is considerably smaller than either of the others and its intensity is greater on the low-field side than on the high-field side of a given proton line. Essentially identical spectra, including the asymmetry of satellite B, were obtained from semiquinones produced by both oxidation of the hydroquinone and reduction of the quinone. Satellite B was observed on the five central proton lines, but could not be identified on the other major components because of too low a signal-to-noise ratio. The assumption that the linewidth changes from one side of a proton line to the other cannot account for the asymmetry of satellite B.

Results are listed separately in Table II for the spectra of the radical produced from the duroquinone and the durohydroquinone. The parts of the hydroquinone-derived spectra containing the overlapped satellites B and C were fitted on the low-field side of each proton line by assuming that the middle satellite, B, had half the intensity of the outer satellite, C. The predicted ratio of the height of the larger line, C, to the apparent height of the smaller line B is 2.62; the experimental ratio is 2.6. The corrected intensity of satellite B is 1.9%. On the high-field side, satellite B is of too small an intensity to measure, but its effect on the measured intensity of satellite C was estimated by assuming satellite B to have an intensity of $\frac{1}{4}$ of satellite C, or about 1% of the major component. For simplicity, overlap calculations for satellite C in the quinone-derived spectra were made with a height-correction factor of 1.15, the mean of the values used for the hydroquinone-derived spectra, even though the widths in the two spectra were not exactly the same.

Monochlorosemiquinone Ion

One satellite was observed, and only the satellite on the low-field side of the low-field proton line was measured. Attempts at incomplete overlap calculations were unsuccessful, and although calculations were not made for four satellites of different splitting overlapped with each other and the main line, the spectrum is not inconsistent with such as assignment.

Five extra lines were observed which were unsymmetrically spaced with respect to the monochlorosemiquinone ion proton lines, and their intensity (relative to the main spectrum) could be altered by a factor of ten by changing the amount of base used to prepare the sample. It was concluded that these five lines were spurious.

2,5-Dichlorosemiquinone Ion

One satellite was observed on both sides of each proton line. The high-field satellite of the high-field line was the only satellite measured because the inner satellites were somewhat overlapped by two extra lines. Since these extra lines were unsymmetrically positioned with respect to the main spectrum, they were considered spurious. Four other spurious lines could also be detected under some conditions, but they were not present in the spectra measured. A satisfactory fit to the height and width of the satellite could not be made on the basis of an assumption that it arose from either one or two pairs of equivalent carbon-13 nuclei. Approximate calculations indicate that it is possible that three sets of pairs of equivalent carbon-13 nuclei contribute to the satellite and that the three sets are separated from each other by as much as 0.1 gauss. However, a detailed computation was not made for this case.

[28] S. Goodman (unpublished results).

2,6-Dichlorosemiquinone Ion

Three satellites were observed on each of the three main proton lines. The spectrum was badly asymmetric: the extremum of the derivative of each proton line on the high-field side was about 12% closer to the center of the line than on the low-field side, and the intensity of the satellites on the high-field side of a proton line was considerably greater than on the low-field side. The differences in height of the inner satellite (A) on the low- and high-field sides of a proton line can be accounted for by the asymmetry of the proton lines, but the differences in height of the middle (B) and outer (C) satellites are too large to be explained by this effect. Two different linewidths were used in computing the corrections in Table II, one for the high-field and one for the low-field satellites of a proton line.

It is not possible to exclude the possibility that the observed satellites were at least in part spurious, and the asymmetry was so large that the number of carbon-13 nuclei contributing to the splitting could not be estimated.

Tetrachlorosemiquinone Ion

Only a single line with a width of about 0.150 gauss was observed. Although a careful search for satellites was made, none were found. It would have been possible to detect a satellite arising from four equivalently situated carbon-13 nuclei if the splitting constant were 1.2 gauss (eight times the linewidth) or more, and a satellite from two equivalently situated carbon-13 nuclei would have been detected if the splitting constant were greater than 1.9 gauss. In a more concentrated solution than employed for most of the observations, the linewidth was 0.102 gauss, and therefore exchange narrowing may be taking place. Two lines 0.6 gauss apart (corresponding to a carbon-13 splitting of 1.2 gauss) would be collapsed by exchange if the rate of exchange were fast compared to 2×10^6 sec^{-1}. A collapse of the satellites by exchange seems unlikely, however, because there is no indication from other spectra of semiquinone ions that any exchange phenomena of this high a rate are taking place, and lines have been resolved with separations of much less than 0.6 gauss.[13]

Cyclooctatetraene Anion Radical

Katz and Strauss have studied the ESR spectrum of the radical produced from cyclooctatetraene by treating a solution in tetrahydrofuran with lithium metal. They found a nine-line spectrum with a proton hyperfine splitting of 3.209 ± 0.007 gauss and a spectroscopic splitting factor of 2.0025 ± 0.0001.[17] Spectra have also been obtained from solutions in dimethoxyethane; and sodium and postassium as well as lithium have been used in both solvents.[20,23] Some of the spectra show splitting from interactions with the nucleus of the alkali metal, and others exhibit exchange and line-broadening effects. In a solution of cyclooctatetraene in dimethoxyethane using lithium as the reducing agent, a satellite was observed which was concluded to arise from a carbon-13 splitting (see Table II). The satellite was also found in solutions with lithium in tetrahydrofuran when conditions were adjusted to give narrow lines, and these spectra also exhibited alkali-metal splitting. The other spectra observed did not show satellites attributable to carbon-13 nuclei either because the proton lines were too broad or because the alkali-metal splitting obscured other details of the spectrum.

The results for the carbon-13 splitting for two different samples are given in Table II. A curve computed by assuming Lorentz lines and a 4.48% satellite at the proper position on each side of the proton line was superimposed on an experimental spectrum and found to give excellent agreement.

V. DISCUSSION

The analysis of the carbon-13 splittings will be based on the recently developed theory of Karplus and Fraenkel.[18] This is the only detailed and complete formulation of the problem that gives satisfactory agreement with experiment.[29]

Consider a carbon atom C with sp^2 hybridization that is bonded to three other atoms, X_1, X_2, and X_3. Let ρ^π be the pi-electron spin density on atom C and $\rho_i^\pi (i=1, 2, 3)$ the spin density on atom X_i. The expression obtained by Karplus and Fraenkel for the splitting arising from the carbon-13 nucleus of carbon atom C is

$$a^C=(S^C+\sum_{i=1}^{3}Q_{CX_i}{}^C)\rho^\pi+\sum_{i=1}^{3}Q_{X_iC}{}^C\rho_i{}^\pi. \qquad (5.1)$$

In this equation, S^C and the Q's are the sigma-pi interaction parameters that determine the contribution to the splitting of the carbon atom 1*s* and 2*s* electrons, respectively. The notation $Q_{BC}{}^A$ designates the splitting from the nucleus of atom A that is caused by spin polarization in the bond BC by a pi-electron spin density on atom B. The values of S^C and the Q's in CH and CC bonds estimated from calculations of the sigma-pi interaction in the CHC_2 fragment are (in gauss)[18]: $S^C=-12.7$, $Q_{CH}{}^C=19.5$, $Q_{CC'}{}^C=14.4$, and $Q_{C'C}{}^C=-13.9$. These parameters are for carbon atoms with equivalent sp^2 hybrid bonds and a C—C bond length of 1.38A. An estimate of the Q's can also be made for a CC bond in which the unpaired pi-electron is on an atom with sp^2 hybridization and the other atom has sp^3 hybridization (as in the CH_3CH_2 radical). Taking the bond length to be 1.50A, one finds $Q_{CC'}{}^C=30.0$ gauss and $Q_{CC'}{}^{C'}=-20.9$ gauss.[30] Sigma-pi interaction parameters for other bonding arrangements are also needed

[29] The work of McLachlan *et al.*[5] contains an unfortunate numerical error. Recalculation on the basis of their assumptions gives the value -67.9 gauss for a parameter designated Q_2 instead of -6.9 as quoted. The corrected prediction from their theory for the C^{13} splitting in the β position of the naphthalene negative ion is then -15.8 gauss instead of the experimental value of ±1.2 gauss. Other predictions are in similar disagreement.

[30] M. Karplus and G. K. Fraenkel (unpublished calculations).

for a complete analysis of the experimental data presented in this paper, but values for them are not currently available. A partial estimate of some of these Q's is therefore given in the following discussion.

The analysis of the carbon-13 splitting in the cyclooctatetraene radical appears at first sight to be the most straightforward. The proton splitting of the ESR spectrum shows that all the protons are equivalent, and therefore the pi-electron spin density on each carbon atom is one-eighth. If the cyclooctatetraene radical were a planar regular octagon, the C—C—C bond angle would be 135° and the three carbon-atom sigma bonds would be nonequivalent sp^2 hybrids. This change in hybridization alters the sigma-pi interaction parameters, and calculations based on the CH fragment model[18,23] give $Q_{CH}{}^{C}=-10.0$ gauss for a C—C—C angle of 135° as compared to $Q_{CH}{}^{H}=-23.4$ gauss for a 120° angle. The experimentally determined Q, which is given directly by eight times the splitting constant, is $Q_{CH}{}^{H}=-25.67$ gauss.[17] These considerations, based only on the proton splitting in the ESR spectrum, imply that the cyclooctatetraene radical is not planar, a conclusion that is not in accord with other results.[23] Additional complications in the interpretation may also arise from the Jahn-Teller effect.[18,23,31,32] The uncertainty about these various factors precludes a straightforward interpretation of the carbon-13 splitting as well. For a C—C—C bond angle of 135°, the sigma-pi interaction calculations for the CH fragment give the results $Q_{CH}{}^{C}=8.0$ gauss as compared to the 120° value of $Q_{CH}{}^{C}=19.2$ gauss.[18,30] The predicted carbon-13 splitting based on Eq. (5.1) with parameters calculated for a 120° bond angle is $a^{C}=0.97$ gauss and is to be compared with the experimental result $a^{C}=\pm 1.3$ gauss. With sigma-pi interaction parameters for a 135° angle, the predicted splitting would be negative and have an even smaller magnitude than the result calculated for a 120° angle. Although a detailed discussion of the configuration of the cyclooctatetraene radical is given elsewhere,[23] it is of interest to note here that one simple aspect of its structure is indicated directly by the carbon-13 data: As in the methyl radical, the three sigma bonds about a carbon atom must all lie in the same plane.[18,23,33]

The unsubstituted p-benzosemiquinone ion is the only semiquinone studied in the present work for which the assignment of carbon-13 splittings has been unambiguously determined. We can use Eq. (5.1) and a theoretical calculation of the pi-electron spin densities to predict the carbon-13 splitting or, alternatively, the experimental carbon-13 and proton splittings can be employed to evaluate the pi densities. This second procedure is accomplished by using the relation[1]

$$\rho_i{}^{\pi}=a_i{}^{H}/Q_{CH}{}^{H} \tag{5.2}$$

for proton splittings in conjunction with Eq. (5.1) for the carbon-13 splittings. A molecular-orbital calculation by Vincow and Fraenkel[34] for the $\rho_i{}^{\pi}$ gives $\rho_1{}^{\pi}=0.1071$, $\rho_2{}^{\pi}=0.1072$, and $\rho_7{}^{\pi}=0.1786$ where the oxygen atoms are numbered 7 and 8 and are attached to carbon atoms 1 and 4. These results were obtained by adjusting the molecular-orbital Coulomb and resonance integrals for the carbon-oxygen bond to give agreement with the measured proton splittings in a series of semiquinones. For the p-benzosemiquinone ion, these pi densities correspond to a proton splitting of $a_2{}^{H}=-2.540$ gauss if $Q_{CH}{}^{H}=-23.72$ gauss (the value computed for the CHC_2 fragment[18]) as compared to the experimental result of $a_2{}^{H}=-2.368$ gauss. Using this set of $\rho_i{}^{\pi}$ in Eq. (5.1), one obtains $a_2{}^{C}=0.83$ gauss; the experimental result is $a_2{}^{C}=\pm 0.59$. Alternatively, the experimental proton splitting and Eq. (5.2) with $Q_{CH}{}^{H}=-23.72$ gauss give $\rho_2{}^{\pi}=0.0998$. From Eq. (5.1), together with the experimental carbon-13 splitting (assuming $a_2{}^{C}>0$) and the condition

$$\sum_{\text{all } i}\rho_i{}^{\pi}=1, \tag{5.3}$$

one obtains $\rho_1{}^{\pi}=0.1131$ and $\rho_7{}^{\pi}=0.1872$. Since these densities differ by less than 0.01 units from the molecular-orbital results, the agreement is well within the accuracy of either the molecular-orbital calculations or the theory of carbon-13 splitting. It is to be noted that this change in the $\rho_i{}^{\pi}$ of 7% or less results in a change of the computed carbon-13 splitting by 40%.

Equation (5.1) is also applicable to the splitting of the carbon atoms in the carbon-oxygen bonds, $a_1{}^{C}$. This equation becomes

$$a_1{}^{C}=(S_1{}^{C}+2Q_{C_1C_2}{}^{C_1}+Q_{C_1O}{}^{C_1})\rho_1{}^{\pi}+2Q_{C_2C_1}{}^{C_1}\rho_2{}^{\pi}+Q_{OC_1}{}^{C_1}\rho_7{}^{\pi} \tag{5.4}$$

and contains the two sigma-pi interaction parameters $Q_{CO}{}^{C}$ and $Q_{OC}{}^{C}$ referring to the carbon-oxygen bond. Their values are unknown, but they can be estimated, albeit crudely, from an examination of the spectrum of the semiquinone formed from 2,5-dihydroxyquinone. This spectrum, including the carbon-13 splitting, has been obtained by Reitz *et al.*[10] who found $a_3{}^{H}=\pm 0.79$, $a_1{}^{C}=\pm 2.82$, and $a_3{}^{C}=\pm 6.62$ gauss (where carbon atoms numbered 1, 2, 4, and 5 are bonded to oxygen atoms and carbon atoms 3 and 6 are bonded to hydrogen atoms). We shall now digress to consider the interpretation of this spectrum.

We shall assume that the radical formed from the 2,5-dihydroxyquinone contains 13 pi electrons.[35] A simple Hückel-type molecular-orbital calculation using parameters for the carbon-oxygen bond in the range suggested

[31] H. M. McConnell and A. D. McLachlan, J. Chem. Phys. **34,** 1 (1961).

[32] L. C. Snyder, J. Chem. Phys. **33,** 619 (1960), and private communication.

[33] T. Cole, H. O. Pritchard, N. R. Davidson, and H. M. McConnell, Mol. Phys. **1,** 406 (1958).

[34] G. Vincow and G. K. Fraenkel, J. Chem. Phys. **34,** 1333 (1961).

[35] An 11 pi-electron radical can also, in principle, be made from this compound, but the molecular-orbital calculation for the 11 pi-electron system yields $\rho_7{}^{\pi}\sim 0.3$, which corresponds to a proton splitting of $a_3{}^{H}\cong -8$ gauss. The absolute magnitude of this result is an order of magnitude larger than the observed splitting, whereas the calculations on the 13 pi-electron system are in qualitative accord with the experimental findings.

by the treatment of Vincow and Fraenkel[34] for ortho semiquinones gives a node in the symmetry plane through the two CH bonds perpendicular to the plane of the molecule, i.e., $\rho_3^\pi=0$. This implies that a spin-density calculation including configuration interaction would result in a small negative pi-electron spin density at positions 3 and 6. We shall therefore assume that $\rho_3^\pi<0$, and solve for the pi densities by using Eqs. (5.1)–(5.3) together with the proton and carbon-13 splittings. Taking $a_3^H=+0.79$ gauss and $Q_{CH}^H=-23.72$ gauss gives $\rho_3^\pi=-0.0333$, while from $a_3^C=-6.62$ gauss one obtains $\rho_1^\pi=0.1949$ and $\rho_7^\pi=0.0718$, where atom 7 is an oxygen atom. A negative sign has been selected for a_3^C because rather general assumptions about the pi-electron density distribution require this choice if any degree of consistency is to be obtained. The two positive spin densities can be compared with a molecular-orbital calculation in the Hückel approximation. Taking molecular-orbital parameters for the carbon-oxygen bond as $\delta\alpha=(\alpha_O-\alpha_C)/\beta_{CC}=1.8$ and $\beta_{CO}/\beta_{CC}=1.2$ (where α_O, α_C, are the oxygen and carbon Coulomb integrals, respectively, and β_{CC}, β_{CO}, are the carbon-carbon and carbon-oxygen resonance integrals, respectively) gives $\rho_1^\pi=0.1645$ and $\rho_7^\pi=0.0855$. The empirically determined spin densities are thus roughly consistent with an obviously inadequate theoretical calculation of the odd-electron density. The empirical ρ_i^π can now be used in Eq. (5.4) to estimate the sigma-pi interaction parameters for the carbon-oxygen bond from the measured value of a_1^C. Taking $a_1^C<0$, the choice of sign again being indicated on the basis of rather general assumptions, one obtains

$$0.1949Q_{CO}^C+0.0717_5Q_{OC}^C=1.919. \tag{5.5}$$

From the 2,5-dihydroxysemiquinone-ion data alone it is not possible to proceed further unless an assumption is made about the relation between Q_{CO}^C and Q_{OC}^C. For a carbon-carbon bond, $Q_{CC'}^C\cong-Q_{C'C}^C$, but for a carbon-oxygen bond there may be an appreciable difference between the analogous quantities.[18] Temporarily disregarding the possibility of a large difference, we assume $Q_{CO}^C=-Q_{OC}^C$ and obtain, from Eq. (5.5), the value $Q_{CO}^C=15.6$ gauss, a result that is certainly of a reasonable magnitude.

An estimate of the two quantities Q_{CO}^C and Q_{OC}^C can be made by using data from both the 2,5-dihydroxy compound and the unsubstituted *p*-benzosemiquinone ion. For the latter substance, the experimental data indicates that the splitting of the CO carbon atom must be less than 0.6 gauss, i.e., $|a_1^C|\leqq 0.6$, so that

$$0.6\geqq|-0.9533+0.1131Q_{CO}^C+0.1872Q_{OC}^C|. \tag{5.6}$$

Equations (5.5) and (5.6) have the solutions

$$8.7\leqq Q_{CO}^C\leqq 11.8 \tag{5.7a}$$

and

$$-3.0\leqq -Q_{OC}^C\leqq 5.2, \tag{5.7b}$$

where the upper limits are obtained if it is assumed that a_1^C for the *p*-benzosemiquinone ion is negative and the lower limits if this quantity is assumed to be positive. From the limited experimental and theoretical information available, it is not possible to narrow the uncertainties of these estimates further; but both sets of values are in a range that provides a reasonable and consistent picture of the splitting at the carbon atom of the CO bond.

We next turn to a consideration of the methyl-substituted compounds. Either the CCH_3 fragment or the CH_3CH_2 radical can serve as a prototype for a methyl substituent, and theoretical descriptions of the proton splitting have been given in both the molecular-orbital and valence-bond approximations, the former have been calculated by Bersohn[2] and Chesnut,[36] and the latter by McLachlan.[37] In the molecular-orbital theory, linear combinations of the carbon and hydrogen orbitals in the CH bonds of the CH_3 group are formed in such a way as to include as part of the pi system one orbital from the carbon atom and one from the pseudo-atom set used for the hydrogen atoms. An unpaired spin density then appears at the hydrogen atoms because of the pi density in this H_3 pseudo-atom group. In contrast, the valence-bond approach assumes the pi-electron is localized on the methylene carbon atom of the ethyl radical and accounts for a spin density at the protons through a sigma-pi interaction. The valence-bond structures that give rise to proton splitting are similar to the structures employed in treating the CH fragment. In CH_3CH_2, a CH bond of the CH_3 group is broken and a bond is made between the pi orbital on the CH_2 group and the sp^3 carbon orbital of the broken CH bond. A similar breaking of the C—C bond and a pairing with the pi orbital is also included. Since the hydrogen 1*s* orbital becomes unpaired, this mechanism produces a spin density at the proton. The molecular-orbital theory is thus based on a model which displaces pi-electron charge onto the methyl group, while the model employed in the valence-bond theory shifts spin density without altering the charge distribution.

Although both theories predict a positive spin density at the protons of about the same magnitude, they give a very different value in first approximation for the carbon-13 splitting at the methyl carbon atom. In the valence-bond formulation, both the proton and part of the carbon-13 splittings arise from a spin polarization of the CH bond, and the magnitude of this part of the carbon-13 splitting is determined, to first order, by the proton splitting. The proton splitting can be expressed as $a_{CH_3}^H=507.6\ \Gamma(s_H)$, where $\Gamma(s_H)$ is the atomic-orbital spin polarization for a hydrogen atom averaged over the rotations of the methyl group[18]; it is a measure of the fraction of an unpaired spin which resides in a hydrogen atom 1*s* orbital. Similarly, the contribution of each CH bond to the carbon-13 splitting of the methyl carbon atom can be written as $(\frac{1}{4})(1191)\Gamma(\sigma_{CH})$,

[36] D. B. Chesnut, J. Chem. Phys. **29**, 43 (1958).
[37] A. D. McLachlan, Mol. Phys. **1**, 233 (1958).

TABLE III. Methyl group C^{13} splittings.

Derivative of *p*-benzosemiquinone ion	Exptl. proton splitting[a] $a_{CH_3}^{C}$ (gauss)	Spin density[b] ρ_C^{π}	C^{13} Splitting $a_{CH_3}^{C}$ (gauss) exptl[c]	calc[d]
Monomethyl	2.045	0.0654	±1.51	−1.37
2,5-Dimethyl	2.248	0.0719	±1.60	−1.50
2,6-Dimethyl	2.125	0.0680	±1.46	−1.42
Tetramethyl	1.897	0.0607	±1.35	−1.27

[a] From the work cited in footnote 13.
[b] From Eq. (5.8) and the values of $a_{CH_3}^{H}$ in Col. 2.
[c] These results have been selected from a number of possible alternative assignments (see text); the most favorable of a group of nearly identical splittings was chosen.
[d] From Eq. (5.9).

where the factor $\frac{1}{4}$ is the fraction of a $2s$ orbital in an sp^3 hybrid, and 1191 gauss is the carbon-13 splitting from a $2s$ orbital.[18] To a first approximation, $\Gamma(\sigma_{CH}) = -\Gamma(s_H)$, and thus the contribution of each CH bond to the splitting is $-0.586\ a_{CH_3}^{H}$. As an estimate for $a_{CH_3}^{H}$ we can use the experimental value of 27.2 gauss obtained for the CH_3 protons in the spectrum of the ethyl radical[38] and assume the sign to be positive as predicted by the theory, i.e., we take $a_{CH_3}^{H} = +27.2$ gauss. Each CH bond in a $CC'H_3$ fragment then contributes $Q_{CC'H}^{C'} = -15.9$ gauss to the C^{13} splitting at C′, the CH_3 carbon atom, and the total contribution of the CH bonds is $3Q_{CC'H}^{C'} = -47.8$ gauss. Finally, the polarization of the C—C′ bond must be included. Its value, estimated from the sigma-pi interaction calculation, is $Q_{CC'}^{C'} = -20.9$ gauss. Within the approximations of Eq. (5.1), there is no contribution to the splitting at C′ from $1s$ electrons since the pi-electron density is on C, not C′. Thus the splitting at the methyl carbon atom of the ethyl radical is estimated to be $Q_{CC'H_3}^{C'} = -69$ gauss. Even if the theoretical estimate of $Q_{CC'}^{C'}$ is in error, its sign is well established, and therefore the theory indicates that $|Q_{CC'H_3}^{C'}|$ must be at least as large as 48 gauss. This conclusion is independent of any assumptions about the numerical values of the atomic and molecular exchange integrals; it depends only on the general structure of the valence-bond theory and the measured proton splitting. As will be shown below, this value of $Q_{CC'H_3}^{C'}$ is not in accord with the experimental data.

The molecular-orbital theory is quite different from the valence-bond formulation in that the existence of a proton splitting does not imply a directly related contribution to the carbon-13 splitting at the methyl-group carbon atom. With the hybridization scheme employed, spin polarization of the $2s$ electrons can only be caused by the sp^3 orbital in the bond between the two carbon atoms and by the symmetric linear combination of carbon sp^3 orbitals pointing toward the hydrogen atoms. These functions have the form $\frac{1}{2}[(2s)+\sqrt{3}(2p\sigma)]$ and $\frac{1}{2}\sqrt{3}[(2s)-(1/\sqrt{3})(2p\sigma)]$, respectively, where $(2s)$ is the carbon atom $2s$ orbital and $(2p\sigma)$ is the $2p$ orbital directed from the methyl carbon toward the methylene carbon. Polarization of the first of these hybrid orbitals by the pi electron on the methylene carbon has been given above ($Q_{CC'}^{C'}$). The pi-electron density on the methyl carbon ($\rho_{C'}^{\pi}$) is quite small[36] and its effects can be neglected to a first approximation. The contribution to the carbon-13 splitting of the pi-electron spin density on the pseudo-atom group cannot be estimated without the evaluation of exchange integrals between the pi orbital and the symmetric orbital formed from the pseudo atom, and the integrals formed by these orbitals and the orbital $\frac{1}{2}\sqrt{3}[(2s)-(1/\sqrt{3})(2p\sigma)]$ of the carbon atom. Although this sigma-pi interaction may be large, we shall make the as yet unjustified assumption that it contributes no more than the values found for other carbon-13 Q's, i.e., ~20 gauss. The pi density[36] on H_3 is only 10–15% of ρ_C^{π}, and therefore, if our assumption is valid, the molecular-orbital theory predicts that the carbon-13 splitting at the methyl carbon should be determined primarily by $Q_{CC'}^{C'}$. This quantity, as estimated by the valence-bond sigma-pi interaction calculation, is $Q_{CC'}^{C'} = -20.9$ gauss. The neglected sigma-pi interactions would add an additional negative contribution of unknown magnitude.

The pi-electron spin density ρ_C^{π} on the ring carbon atom to which the methyl group in a semiquinone ion is attached can be estimated from the proton splitting $a_{CH_3}^{H}$. Chesnut's[36] calculation for the ethyl radical gives 27.8 gauss for $a_{CH_3}^{H}$ as compared to the experimental result[37] of 27.2, and the calculated spin density on the methylene carbon is $\rho_C^{\pi} = 0.8677$. An equation analogous to Eq. (5.2) should be approximately obeyed and adjusting the calculations to agree with experiment gives

$$a_{CH_3}^{H} = Q_{CCH_3}^{H}\rho_C^{\pi} = 31.25\rho_C^{\pi}. \qquad (5.8)$$

Chesnut's calculation, as modified by the experimental proton splitting, also indicates that the unpaired pi-electron density on the methyl group (both C and H_3) is 15% of the density ρ_C^{π} on the methylene carbon atom. Our simplified molecular-orbital approach then shows that the carbon-13 splitting at the methyl carbon atom is

$$a_{CH_3}^{C} \leqq -20.9\rho_C^{\pi} = -0.67a_{CH_3}^{H}. \qquad (5.9)$$

The corresponding estimates obtained from the valence-bond theory are $a_{CH_3}^{H} = 27.2\rho_C^{\pi}$ and

$$a_{CH_3}^{C} = -69\rho_C^{\pi} = -2.5a_{CH_3}^{H}. \qquad (5.10)$$

The experimental data available for comparison with Eqs. (5.9) and (5.10) is not entirely satisfactory because it has not been possible to make assignments of splittings to particular carbon atom positions. On the other hand, both the molecular-orbital and valence-bond theories predict that the carbon-13 splitting from the

[38] R. W. Fessenden and R. H. Schuler, J. Chem. Phys. **33,** 935 (1960).

methyl carbon atoms $a_{CH_3}^{C}$ should be proportional to the methyl proton splittings $a_{CH_3}^{H}$ and it is therefore possible to examine the data for such a proportionality. Two carbon-13 satellites which might arise from the methyl carbon atom are found in each of the methyl-substituted compounds studied except the 2,5-dimethylsemiquinone. In this latter radical, only one satellite is observed and the linewidth indicates that the other carbon-13 splittings must be less than 0.9 gauss. Computing the ratio $a_{CH_3}^{C}/a_{CH_3}^{H}$ of the splittings of these carbon-13 satellites to the methyl proton splittings[13] (see Table III) gives the following results: monomethylsemiquinone ion, 0.37 or 0.74; 2,5-dimethylsemiquinone ion, <0.4 or 0.71; 2,6-dimethylsemiquinone ion, 0.39 or 0.69; and tetramethylsemiquinone ion, 0.38 or 0.71. The data can thus be selected to give a constant of proportionality of either 0.38 or 0.71 and the deviations of the ratios for the individual compounds from these mean values is only a few percent. Neither result agrees with the valence-bond prediction of 2.5, [Eq. (5.10)], but the value of 0.71 coincides quite closely with the approximate molecular-orbital result of 0.67 [Eq. (5.9)]. The set of values which agrees most closely with the approximate molecular-orbital theory is listed in Table III. On the average, the experimental results are $(6.5\pm1.9)\%$ larger than these calculated values.

Although the agreement in Table III is excellent, one cannot have complete confidence in the correctness of this approximate molecular-orbital theory calculation until the neglected sigma-pi interaction is evaluated and the assignment of carbon-13 splittings to particular carbon-atom positions is verified. It is clear, however, that the valence-bond predictions for the methyl-group carbon-13 splitting are not in accord with the experimental results. This discrepancy is particularly troublesome because of the rather good agreement found by McLachlan[38] for the methyl proton splittings. A careful re-examination of the values of the exchange integrals employed in the valence-bond calculation, and the inclusion of some neglected terms, appears to be called for. An adequate valence-bond theory might also involve a delocalization of the pi electrons onto the methyl group as in the molecular-orbital calculation.

Further analysis of the data is not fruitful at present since too many sigma-pi interaction parameters (Q's) are unknown and the assignment of the experimental splittings to carbon-atom positions is ambiguous.

VI. CONCLUSIONS

An ESR investigation of a number of related semiquinone ions has indicated that the spectra contain many small lines of low intensity. Some of these lines have been shown to be caused by the splitting of the major proton hyperfine components by carbon-13 nuclei present in nautral abundance. The lines not attributable to carbon-13 splitting arise from small amounts of free-radical impurities formed by side reactions. In many spectra, the identification of the small satellite lines with carbon-13 splittings is based on the close agreement between predicted and measured intensities. The complexity of other spectra has made it impossible to obtain a complete and unambiguous analysis of the satellites by means of intensity measurements alone, but the identification of the small lines with carbon-13 splittings has been possible because of the consistency of the magnitudes of the splitting constants in the entire series of compounds. Further support for the identification of the satellites arises from the overall agreement between the experimental results and the recently developed theory of carbon-13 hyperfine interactions. The small lines attributed to free-radical impurities were identified either by their unsymmetric positions in the spectra or by the dependence of their intensities on chemical preparation. These investigations have shown that when radical-producing side reactions occur, as in the semiquinones, considerable care must be taken to distinguish the carbon-13 satellites from impurity lines.

The largest carbon-13 splitting observed had a magnitude of 1.7 gauss, and the smallest had a magnitude of 0.4 gauss. Since the smallest detectable splitting depends on spectral parameters (e.g., the linewidth) and on the number of equivalent carbon-13 nuclei, it was not always possible to determine the presence of satellites with splitting constants as small as, or smaller than, ±0.4 gauss. As a result, splittings were not observed from all the carbon-atom positions in all the compounds.

The single satellite observed in the *p*-benzosemiquinone ion spectrum has an intensity which corresponds to the carbon-13 splitting expected from four equivalent carbon atoms. This result confirms the previous suggestion of several authors[8–10] that the satellite might be attributable to a carbon-13 interaction. It also serves to identify the carbon atoms with the four CH positions. The experimental value of the splitting constant is within 0.24 gauss of the result predicted from the theory of the carbon-13 hyperfine interactions if the pi-electron spin densities needed in this theory are taken from a molecular-orbital theory calculation. Conversely, if the measured proton and carbon-13 splittings are used to obtain the pi-electron distribution, results are obtained which differ at most by 7% from the molecular-orbital theory values. This small change in pi-electron spin density corresponds to a 40% change in the calculated carbon-13 splitting, thus showing the extreme sensitivity of the splittings to the pi-electron distribution.

Theoretically determined sigma-pi interaction parameters for CO bonds are not available, and none of the splittings observed in the present work can be unambiguously identified with a CO carbon atom. The spectrum of the semiquinone formed from 2,5-dihydroxyquinine[10] does exhibit a splitting identified with the CO carbon atoms, however, and an analysis of this spectrum in conjunction with calculations based on the *p*-benzo-

semiquinone ion spectrum has made it possible to obtain a reasonable limiting range for the values of the CO sigma-pi interaction parameters (Q_{CO}^{C} and Q_{OC}^{C}). The analysis also shows that there is a negative pi-electron spin density on the CH carbon atoms in the radical derived from 2,5-dihydroxyquinone.

The splitting from a carbon-13 nucleus in the methyl position of a methyl-substituted semiquinone is not properly predicted by the currently available valence-bond theory. On the other hand, a molecular-orbital theory calculation does appear to give rather good agreement with experiment. Unfortunately, this latter theory in its present form neglects certain sigma-pi interactions that may make a significant contribution. An interesting difference exists between the models employed in the two theories to transfer spin density to the methyl protons: in the valence-bond theory there is only a spin polarization, while in the molecular-orbital theory there is also a displacement of pi-electron charge. Neither theory is sufficiently complete in its present form.

The carbon-13 splitting found in the spectrum of the cyclooctatetraene anion radical shows that the three sigma bonds of a carbon atom must all lie in a plane. A complete analysis of this spectrum is precluded, however, by uncertainties in the geometrical configuration of the radical.

These experiments show that many interesting structural features can be elucidated by studies of carbon-13 splitting. The full analysis of the results provides a measure of the pi-electron spin densities that serves as a sensitive test of the molecular wave functions. The interpretation of the data, which assumes the validity of the theory of carbon-13 splittings developed by Karplus and Fraenkel, cannot be carried out to its fullest extent in analyzing all of the spectra studied in the present work until some of the sigma-pi interaction parameters (Q's) are evaluated. In particular, the Q's for CO bonds, for a methyl substituent, and for CCl bonds are needed. These might be obtained by calculation, but it will also be necessary to study the spectra of appropriately selected model compounds for which the pi-electron spin densities can be determined from independent information.

Isotropic enrichment in known carbon atom positions would, of course, be extremely helpful in completing the analyses of some of the spectra studied, in determining the sigma-pi interaction parameters, and in evaluating the pi-electron spin densities. In fact, utilization of studies made with the natural abundance of the isotope would become much more fruitful if rough estimates of the Q's and the ρ_i^{π}'s were available for determining the approximate magnitude of the interactions. If such calculations were reliable enough to make tentative identifications of the splittings with carbon atom positions, radicals containing carbon-13 nuclei in natural abundance would often be almost as useful for evaluating the Q's and ρ_i^{π}'s as the enriched samples.

ACKNOWLEDGMENTS

We would like to thank Professor Martin Karplus and Professor Richard Bersohn for many helpful discussions. We are indebted to Professor T. J. Katz for initiating the studies of the cyclooctatetraene radical anion, for the investigations of its chemical properties, and for considerable assistance in both the performance and for considerable assistance in both the performance and the interpreration of many of the experiments carried out on this radical.

Studies of Transient Species Formed During Catalytic Reactions of $CO_2 + D_2$ and of 1-Butene

CHARLES E. MELTON

Chemistry Division, Oak Ridge National Laboratory, Oak Ridge, Tennessee*

(Received April 24, 1961)

Transient species in a catalyzed reaction have been observed in the gas phase by placing the catalyst in a specially designed mass spectrometer ion source.

The reaction,

$$D_2+CO_2 \xrightarrow{Pt} D_2O+CO, \quad (1)$$

was studied over a pressure range 0.1–1 mm Hg and a temperature range 50–1100°C to demonstrate the applicability of the techniques. A free radical, of molecular formula CDO, was shown to be formed by and desorbed from the Pt catalyst during the reaction. In addition, $DCOO^-$ ions were observed suggesting the presence of an intermediate DCOOD on the catalyst.

The production of the products CO and D_2O was not a monotonic function of catalyst temperature, but instead showed a maximum in the temperature range 400–500°C. The rate increased approximately as the first power of P_{CO_2} and was nearly independent of the partial pressure of D_2. The catalytic decomposition of butene-1 was studied in the same way. Free radicals produced by the catalytic decomposition of this compound are compared to those known to occur from thermal decomposition at the same temperature. In the catalytic decomposition, the radicals C_4H_7 and C_3H_5 were found to be most abundant; in contrast, CH_3 and C_3H_5 are most abundant in the thermal decomposition.

INTRODUCTION

THE mass spectrometer offers a direct method for the identification and study of volatile transient species produced by catalytic action. In fields other than catalysis, many investigators have already shown that free radicals produced in the gas phase by thermal decomposition,[1–6] light,[7] flames,[8,9] pyrolysis,[10] charge transfer,[11–13] and ion-molecule reactions[14–16] can be observed in the mass spectrometer. Most of these investigators produced the radicals at high pressure (several mm) in a separate reaction chamber and introduced them into the low-pressure region found in the mass spectrometer by means of a small leak. Ideally, of course, one would like to produce the radicals within the mass spectrometer and therefore reduce both the number of subsequent reactions and the time between production and observation. Since conventional mass spectrometers operate in the pressure range of 10^{-3} to 10^{-8} mm, it was not possible to produce the radicals in sufficient concentrations within the mass spectrometer. Because of these pressure limitations, the mass spectrometer has not been used extensively to study transient species formed during chemical reactions.[17]

Recently, a high-pressure (1 mm) research mass spectrometer[12] was developed at this laboratory, and a series of five consecutive positive and negative ion-molecule polymerization reactions was observed.[18] In view of these observations on consecutive elementary reactions, it was felt that this instrument could also be adapted to the study of radical, atomic, or other species escaping from the surface of a catalyst. Several investigators have reported that free radicals are formed on[19–21] and possibly desorb from [22–24] catalysts during heterogeneous reactions, though these have not heretofore been identified mass spectrometrically.

The free radical products produced by the thermal

* Operated for the U. S. Atomic Energy Commission by the Union Carbide Corporation.

[1] G. C. Eltenton, J. Chem. Phys. **10,** 403 (1942).
[2] G. C. Eltenton, J. Chem. Phys. **15,** 455 (1947).
[3] F. P. Lossing and A. W. Tickner, J. Chem. Phys. **20,** 907 (1952).
[4] J. A. Hipple and D. P. Stevenson, Phys. Rev. **63,** 121 (1943).
[5] A. Langer and J. A. Hipple, Phys. Rev. **69,** 691 (1946).
[6] K. V. Ingold and F. P. Lossing, Can. J. Chem. **31,** 30 (1953).
[7] C. E. Melton, G. A. Ropp, and P. S. Rudolph, J. Chem. Phys. **29,** 968 (1958).
[8] S. N. Foner and R. L. Hudson, J. Chem. Phys. **23,** 1364 (1955).
[9] J. Deckers and A. Van Tiggelen, presented at ASTM Committee E-14 meeting, Los Angeles, California, May 19 (1959).
[10] A. J. B. Robertson, *Mass Spectrometry* (W. S. Cowell, Ltd., Ipswich, 1954), p. 103 ff.
[11] E. Lindholm, Z. Naturforsch. **9A,** 535 (1954).
[12] C. E. Melton, J. Chem. Phys. **33,** 647 (1960).
[13] G. G. Meisels, W. H. Hamill, and R. R. Williams, Jr., J. Phys. Chem. **61,** 1456 (1957).
[14] D. P. Stevenson, J. Phys. Chem. **61,** 1453 (1957).
[15] V. L. Talroze and A. K. Lyubimova, Doklady Akad. Nauk S.S.S.R. **86,** 909 (1952).
[16] C. E. Melton and G. A. Ropp, J. Am. Chem. Soc. **80,** 5573 (1958).
[17] See, for example, J. L. Waldon, *Advances in Mass Spectrometry* (Pergamon Press, New York, 1959).
[18] C. E. Melton and P. S. Rudolph, J. Chem. Phys. **33,** 1594 (1960).
[19] S. Datz and E. H. Taylor, *Recent Research in Molecular Beams* (Academic Press Inc., New York, 1959), p. 157.
[20] R. R. Reeves, G. Manella, and P. Harteck, J. Chem. Phys. **32,** 946 (1960).
[21] L. Belchetz and E. K. Rideal, J. Am. Chem. Soc. **57,** 1168 (1935).
[22] R. P. Eischens and W. A. Pliskin, *Advances in Catalysis* (Academic Press Inc., New York, 1957), Vol. IX, pp. 662 ff.
[23] F. O. Rice, J. Am. Chem. Soc. **61,** 213 (1939).
[24] F. O. Rice and M. D. Dooley, J. Am. Chem. Soc. **56,** 2747 (1934).

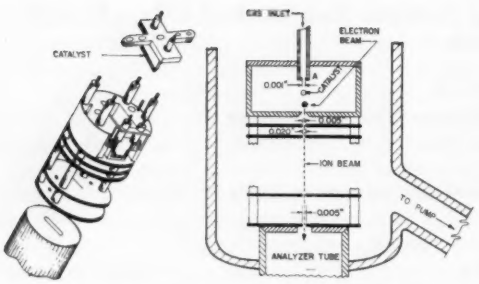

FIG. 1. Mass spectrometer source for catalysis studies.

decomposition of 1-butene are known.[25] Therefore, in the present investigation 1-butene was chosen for initial catalytic study to determine, if possible, the nature of any free radicals evolved from a hot Pt catalyst.

The reaction, which has been studied extensively by other investigators,[26–31]

$$D_2+CO_2 \xrightarrow{Pt} D_2O+CO, \qquad (1)$$

was also selected for investigation to search for possible free radicals and stable intermediate products formed during the heterogeneous reaction. Since the values for the equilibrium constants for this reaction are accurately known[32] in the temperature range 350–1000°C, the concentration of the stable products can be calculated to determine the feasibility of studying this reaction in this temperature range.

EXPERIMENTAL

Heterogeneous reactions were studied by passing reactant gases over the Pt catalyst in the ion source shown in Fig. 1. The catalyst was a spiral of 0.5-mm Pt wire, 3×13 mm with a surface area of ~1 cm². The temperature of the catalyst was directly determined by an optical pyrometer. Products evolved from a heterogeneous reaction on the catalyst passed directly into the electron beam and were ionized. The resultant ions were accelerated into the analyzer tube, separated by the analyzer magnet, and finally detected by the multiplier. Desorbed free radicals were identified by maintaining the energy of the ionizing electrons below that necessary for the appearance of interfering fragment ions from the reactant gases. Products of the heterogeneous reactions were studied as a function of catalyst temperature, pressure, and concentration of each reactant. Interference from products produced by ion-molecule reactions was minimized by maintaining a 10-ev potential, with respect to the exit slit, on the catalyst, thus decreasing the residence time for ions in the ionization chamber. Radicals and intermediates which have a lifetime less than 1 μsec cannot be observed because the transit time from the catalyst to the electron beam is of the order of 1 μsec without collisions for molecules of low mass (<30), for a catalyst temperature of 1000°C, and for a pressure of 1 mm. To be observed by the present method, radicals and intermediates must also be stable either to positive ionization or negative ionization, and the resultant ion must be stable for the order of 1 μsec (ion transit time from the electron beam to the detector).

The research mass spectrometer used in this study has the following features: (1) differential pumping; (2) high sensitivity; (3) a corrosion-resistant electron filament; (4) positive and negative ion detection; (5) precise control of ionizing electron energy. Differential pumping is employed between the reaction chamber (ionization chamber) and the ion collimating and accelerating electrodes, and between the analyzer tube and source region. At the maximum ionization chamber operating pressure of 1 mm (approximately 10^6 times that used in conventional analytical instruments), the analyzer tube pressure is $1=10^{-4}$ mm for noncondensable gases and much less for condensable gases such as CO_2 and C_4H_8. High sensitivity is obtained by combining the 14-stage electron multiplier detector with the counting techniques introduced by White *et al.*[33] The minimum usable signal is approximately 5 ions/sec. Intensities greater than 10^5 ions/sec are measured by the usual electrometer techniques.[34] This sensitivity enables one to detect neutral transient species present in concentrations as low as 10^7 molecules/cc or partial pressures as low as 10^{-12} atms. The energy of ionizing

TABLE I. Radicals[a] detected in the catalytic decomposition of 1-butene over Pt at 1000°C.

M/e	Formula	Relative abundance (Mass 55=100)
15	CH_3	1
39	C_3H_3	29
41	C_3H_5	46
42	C_3H_6	3
43	C_3H_7	3
55	C_4H_7	100

[a] Radicals with a relative abundance less than 1% are not reported.

[25] F. P. Lossing, K. V. Ingold, and T. H. S. Henderson, *Mass Spectrometry* (Institute of Petroleum, London, 1952), p. 102.
[26] C. N. Hinshelwood and C. R. Prichard, J. Chem. Soc. **127,** 1546 (1925).
[27] C. R. Prichard and C. N. Hinshelwood, J. Chem. Soc. **127,** 806 (1925).
[28] G. M. Schwab and K. Z. Naicker, Z. Elektrochem. **42,** 670 (1936).
[29] E. Doehlman, Z. Elektrochem. **44,** 178 (1938).
[30] M. Temkin and E. M. Khailova, Acta Physicochim. U.R.S.S. **2,** 9 (1935).
[31] V. Kondrat'ev and M. Ziskin, Acta Physicochim. U.R.S.S. **18,** 197 (1943).
[32] P. H. Emmett and J. F. Schultz, J. Am. Chem. Soc. **55,** 1390 (1933).
[33] White, Rourke, and Sheffield, Appl. Spectroscopy **12,** No. 2, 46 (1958).
[34] H. M. Rosenstock and C. E. Melton, J. Chem. Phys. **26,** 314 (1957).

electrons obtained from the corrosion resistant thoria-iridium filament previously described[35] is controlled by a Hutchison-type[36] emission regulator. Either positive or negative ions can be detected by suitably adjusting the polarity of the analyzer magnet and 5.1 kev ion accelerating potential. The energy of negative ions impinging upon the electron multiplier is much less than that for positive ions because the first dynode of the electron multiplier is maintained at a potential of −3.8 Kv. However, since the conversion efficiency of the dynode is greater for negative ions,[37] the over-all gain of the multiplier is approximately the same for either positive or negative ions.

The deuterium (Stuart Oxygen Company), carbon dioxide (Matheson, 99.8%), and 1-butene (Phillips, 99.4%) were used in this study without further purification. Labeled formic acid DCOOH was prepared by a method previously described.[38] Labeled $C^{13}O_2$ (67% C^{13}, 33% C^{12}) was synthesized by Dr. G. A. Ropp of this laboratory.

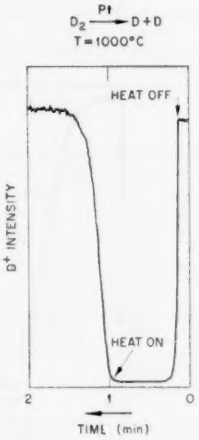

FIG. 2. Typical rise and decay curves for D atom concentration illustrating the effect of the catalyst temperature.

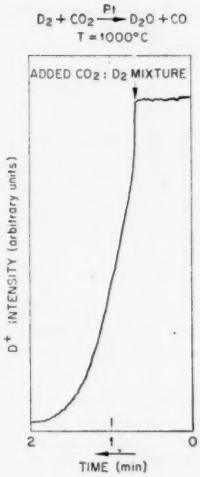

FIG. 3. Decrease in D atom concentration resulting from exposure of the catalyst to CO_2.

RESULTS AND DISCUSSION

1-Butene

A mass spectrometric investigation of the radicals produced in the thermal decomposition of 1-butene at 1000°C shows C—C bond scission to be the predominant process, giving large amounts of methyl and allyl radicals. In sharp contrast, the predominant process in the catalytic decomposition of 1-C_4H_8 over Pt at 1100°C is C—H bond scission giving large amounts of C_4H_7, as shown in Table I. In computing the relative abundances, equal detection sensitivities were assumed for C_3H_5, C_3H_6, C_3H_7, and C_4H_7 with 11 ev ionizing electrons. Results in Table I show that C_1 and C_2 radicals are not very abundant in the catalytic decomposition of 1-C_4H_8.

It is important at this point to consider whether the radicals observed are formed by catalytic action and

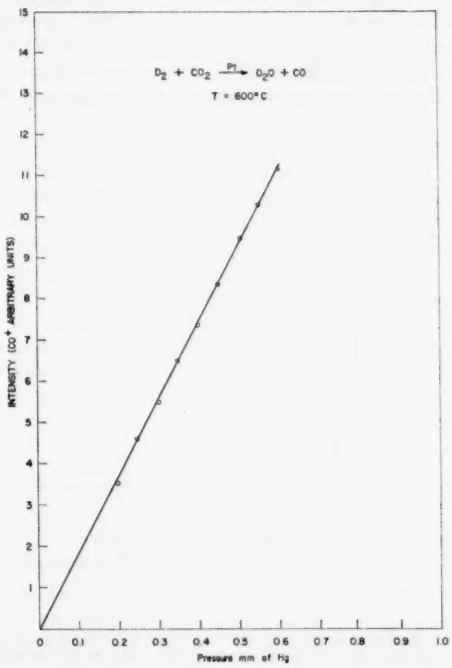

FIG. 4. Variation in CO concentration as a function of total pressure for a constant catalyst temperature and a 1:1 mixture of D_2 and CO_2.

[35] C. E. Melton, Rev. Sci. Instr. **29,** 250 (1958).
[36] D. A. Hutchison and J. R. Wolff, Rev. Sci. Instr. **25,** 1083 (1954).
[37] M. G. Inghram and R. J. Hayden, "A handbook on mass spectroscopy," Nuclear Science Series, Natl. Acad. Sci. Natl. Research Council, Rept. No. 14, p. 44 (1954).
[38] G. A. Ropp and C. E. Melton, J. Am. Chem. Soc. **80,** 3509 (1958).

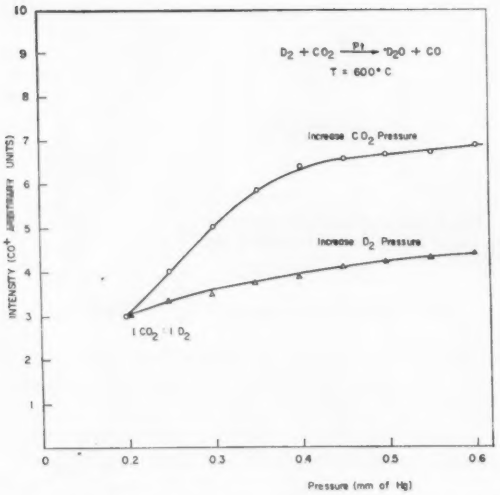
$D_2 + CO_2 \xrightarrow{Pt} D_2O + CO$
T = 600° C
Increase CO_2 Pressure
Increase D_2 Pressure
1 CO_2 : 1 D_2
INTENSITY (CO^+ ARBITRARY UNITS)
Pressure (mm of Hg)

FIG. 5. Variation in CO concentration as a function of the partial pressure for each reactant.

evolve from the catalyst or simply result from thermal decomposition. The striking differences in the composition of the radicals observed in this study as compared to those known to be produced by thermal decomposition are perhaps the strongest experimental evidence supporting catalytic formation. The concentration of each of the radicals closely paralleled the heating and cooling time of the catalyst. Within 10 sec after the heat was turned off the catalyst, the concentration of each of the radicals had decreased to background levels (approximately 1 ion/sec).

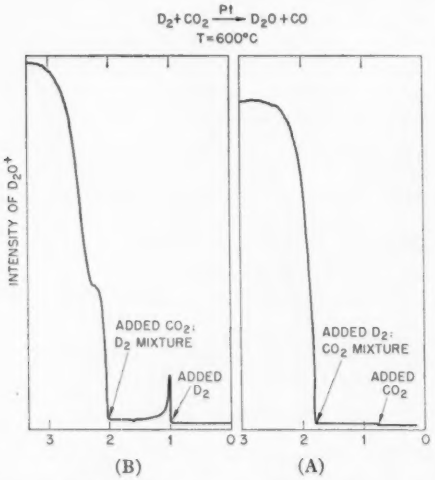

FIG. 6. Variation in D_2O concentration with time. In (A) the catalyst was exposed to the mixture, the mixture was evacuated, then CO_2 was added. No significant increase in D_2O concentration was observed. In (B), the procedure was repeated and the addition of D_2 displaced D_2O from the surface. See Table II for a discussion of these results.

CO_2+D_2

The reaction

$$D_2+CO_2 \xrightarrow{Pt} D_2O+CO \qquad (1)$$

was next selected for investigation. This reaction was selected for several reasons; namely, (a) it is known to be completely heterogeneous at temperatures below 800°C; (b) it involves only simple diatomic and triatomic molecules; (c) calculations based on the known equilibrium constants indicated the yield of products would be high enough to study under our conditions; and (d) the formation of transient species in the reaction has long been suspected. Our approach to the study

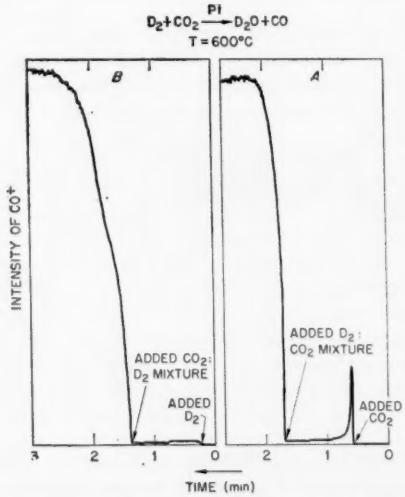

FIG. 7. Variation of CO concentration with time. The experimental procedure was similar to that for Fig. 6. These results are discussed in Table II.

of transient species formed during the course of this reaction included not only the detection of species evolved during the reaction, but also the displacement of adsorbed species by different techniques. For example, we determined the behavior of the catalyst containing the unknown adsorbed species and compared it with the behavior of the catalyst after the latter was exposed to a stable compound having a configuration similar to that of the suspected adsorbed species. Using these combined techniques, we were able to observe directly displaced free radicals and obtain indirect evidence as to the nature and configuration of the adsorbed species.

In order to determine whether D atoms are produced during reaction (1), it was first necessary to investigate the catalytic dissociation of D_2 in the absence of CO_2. The evaluation of the amount of D produced by catalytic dissociation of D_2 is somewhat complicated by the fact that D^+ can also be produced by the dissociative

TABLE II. Experiments exposing the composition of adsorbed species formed during the reaction $D_2+CO_2 \xrightarrow{Pt} CO+D_2O$.

Experiment	Procedure	Observation	Remarks
(a)	The hot (650°C) Pt catalyst was exposed to a 1:1 mixture of D_2 and CO_2. The reaction was allowed to proceed 5 min in order for steady state conditions to prevail and the mixture was quickly pumped out. The catalyst was then exposed to CO_2.	Results from this experiment are shown in Figs. 6(A) and 7(A). The D_2O^+ intensity showed no significant increase, Fig. 6(A), but the CO^+ intensity increased rapidly and decayed exponentially with time, Fig. 7(A). In addition, DCO^+ was observed and its intensity varied with time like that for CO^+.	The rapid increase and exponential decay of the DCO^+ intensity suggests that some D containing species adsorbed on the catalyst reacts with CO_2 to form DCO. If the adsorbed species were the D_2 reactant, D_2O would have been observed.
(b)	After one minute with CO_2 still flowing over the catalyst, a D_2—CO_2 mixture was admitted to the system.	The intensities for both D_2O^+ and CO^+ increased very rapidly, reaching a steady state in about 30 sec as shown in Figs. 6(A) and 7(A).	The transient rate curves for the CO^+ and D_2O^+ are smooth showing no inflection until near steady state conditions prevail.
(c)	The procedure used for experiment (a) was repeated except that after the evacuation of the mixture the catalyst was exposed to D_2.	In Fig. 6(B) when the catalyst was exposed to D_2, the intensity of D_2O^+ increased rapidly and then decayed exponentially with time. The CO^+ intensity showed no significant increase [see Fig. 7(B)].	The rapid rise and exponential decay for the D_2O^+ intensity is evidence that some intermediate containing oxygen adsorbed on the catalyst reacts with D_2 to form D_2O. Since no CO^+ is observed, CO_2 is probably not the adsorbed species.
(d)	After 1 min with D_2 still flowing over the hot catalyst, the D_2—CO_2 mixture was admitted to the system.	The intensities of both CO^+ and D_2O^+ increased very rapidly for about 10 sec [see Fig. 6(B) and 7(B), then showed an inflection after which it went on to reach a steady state. The steady state intensity for both CO^+ and D_2O^+ was higher than that observed in experiment (a)].	Unfortunately, the reason for the inflection and higher steady state intensity has not been satisfactorily explained.
(e)	The procedure for experiment (a) was repeated using $C^{13}O_2$—D_2 to condition the catalyst. The catalyst was then exposed to $C^{12}O_2$.	When the catalyst was exposed to $C^{12}O_2$, $DC^{13}O^+$ was observed. The behavior of this ion was similar to that observed for $DC^{13}O^+$ and CO^+ in experiment (a).	The observation of $DC^{13}O^+$ indicates that some carbon containing intermediate is adsorbed on the catalyst. Combining the results from experiments (a), (c), and (e), the unknown species must contain D, O, and C.

ionization of D_2. To distinguish between these processes, the energy of the ionizing electrons was maintained at 16 ev, well below that required for dissociative ionization of D_2. The behavior of the D^+ ion intensity at 1000°C under these conditions is shown in Fig. 2, in which the catalytic decomposition is readily observable. The observed D^+/D_2^+ ratio was 10^{-1}, although thermal equilibrium at 1000°C requires $D/D_2 \times 10^{-4}$. The difference must arise from a lower detection efficiency for D_2 than for D under the conditions used in this study.

During the monitoring of the D^+ intensity, the CO_2:D_2 mixture was admitted to the system; a rapid decrease in the D^+ intensity was observed (see Fig. 3). The results suggest that the observed D is produced by the catalytic decomposition of D_2, and that the presence of CO_2 inhibits the decomposition. Since reaction (1) has been reported[31] to be both homogeneous and heterogeneous at 1000°C, the reaction was investigated in this study well below 1000°C to avoid interference from the homogeneous contribution.

Typical results showing the variation of concentration of CO with pressure for a 1:1 mixture of CO_2 and D_2 are shown in Fig. 4. This graph suggests that the reaction is first order with respect to total pressure.

The variation of CO concentration with pressure for each of the reactants is shown in Fig. 5. To obtain these results, a mixture of D_2 and CO_2, each having a partial pressure of 0.1 mm was admitted into the reaction chamber. The pressure was then increased in equal increments with either D_2 (lower curve) or with CO_2 (upper curve). These results confirm those shown in Fig. 4, showing that the reaction is first order with respect to the CO_2 pressure until the concentration of $CO_2 = 4(D_2)$ and not greatly affected by the D_2 pressure. These curves suggest that the reaction follows the rate law,

$$V = \frac{k(CO_2)}{1+b(CO_2)} \frac{(D_2)}{1+c(D_2)},$$

where b is between 0.2 and 0.3 and c is between 4 and 5.

In an effort to determine the transient species in reaction (1), a series of experiments was carried out. The results from these experiments are summarized in Table II and in Figs. 6 and 7. The formation and desorption of species containing D, C, and O was deduced from these experiments. To determine the configuration of this intermediate or intermediates, all of the positive

TABLE III. Free radicals and other species[a] detected in the reaction $D_2+CO_2 \xrightarrow{Pt} D_2O+CO$.

M/e	Ion[b]	Probable precursor	Suggested source of precursor
2	D^+, D^-	D	$D_2 \xrightarrow{Pt} D+D$
30	CDO^+	CDO	CDO desorbed
46	$DCOO^-$	DCOOD, DCO_2	$CO_2+D_2 \xrightarrow{Pt} DCOOD$ or DCO_2
60	CO_3^-	D_2CO_3, CO_3	$D_2O+CO_2 \xrightarrow{Pt} D_2CO_3$ or CO_3
62	DCO_3^-	D_2CO_3, DCO_3	$D_2O+CO_2 \xrightarrow{Pt} D_2CO_3$ or DCO_3

[a] Products from ion-molecule reactions are not included.

[b] The intensities of the negative ions given were from two to three orders of magnitude less than those for the positive ions. The intensities of ions from all of these transient species were less than 1% of that of the product ions, CO^+ and D_2O^+.

and negative ions produced from neutral species during the course of the reaction were identified. The results are given in Table III. The positive and negative ions appear to be derived from two structural classes of neutral species namely, a carbonate type giving rise to DCO_3^- and CO_3^- and a formic acid type giving rise to $DCOO^-$ and DCO^+. The behavior of the catalyst containing these species is known from experiments (a) through (e), Table II. It therefore seemed reasonable to test whether we could obtain the same behavior as that for the unknown surface species by exposing the catalyst to a stable compound having either the formic acid or carbonate type configuration. Since D_2CO_3, the suspected carbonate precursor, is not available for such a test, our experimental tests were restricted to formic acid isotopically labeled with deuterium on the carbon atom. In the first trial the procedure for experiment (a) was used, namely, the hot catalyst (650°C) was conditioned by exposing it to DCOOH at a pressure of 0.01 mm, evacuating the excess DCOOH, and exposing the catalyst to D_2. Results from this experiment are shown in Fig. 8. The sharp rise and exponential decay for the D_2O^+ intensity was completely analogous to that observed in experiment (a) for the unknown intermediate. A similar procedure was employed to determine whether DCO was released on adding CO_2. Again the results shown in Fig. 9 are completely analogous to those for the unknown intermediate given in experiment (b).

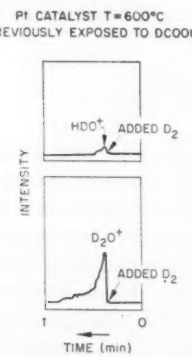

FIG. 8. D_2O and H_2O displaced from the surface of the catalyst by D_2.

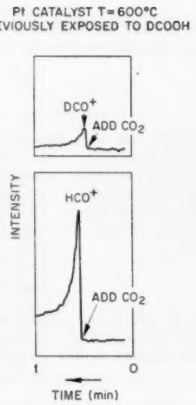

FIG. 9. Radicals displaced from the surface of the catalyst, previously exposed to DCOOH, by CO_2.

It is interesting to note that the amount of D_2O released from the catalyst by D_2 is significantly greater than the amount of HDO (see Fig. 8). Also, as can be seen from Fig. 9, the relative amount of HCO released by CO_2 is considerably greater than that for DCO.

Data for the concentration of CO as a function of temperature for a 1:1 mixture of D_2:CO_2 are given in graphical form in Figs. 10 and 11. The procedure used to obtain the data in Fig. 10 consisted of monitoring the CO^+ intensity, rapidly increasing the temperature

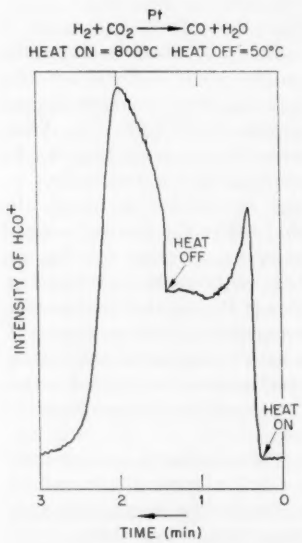

FIG. 10. CO concentration as a function of heating and cooling time for the catalyst.

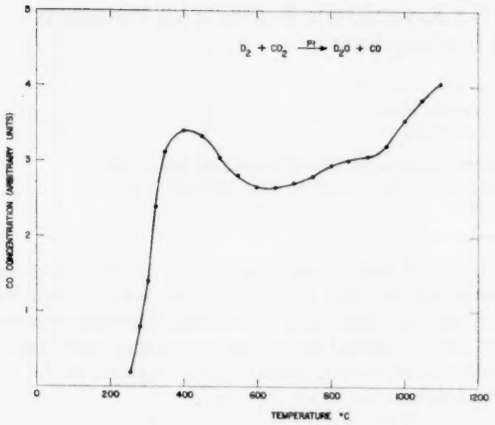

FIG. 11. CO concentration as a function of catalyst temperature.

of the catalyst to 860°C, waiting 1 min for thermal equilibrium, and turning the heat off the catalyst. The CO^+ intensity goes through two maxima, one as the temperature increases and another when the heat is turned off. The dependence of the rate on temperature is seen more clearly in Fig. 11. These data were obtained by increasing the temperature of the catalyst in small increments from 200° to 1270°C. A maximum was found to occur in the temperature range of 300–350°C. The sharp rise in CO concentration in this temperature range may be equilibrium limited. The decrease above 400°C may be explained on the basis of either a decreased residence time for the reactants on the catalyst or thermal decomposition of an intermediate on the surface by another path. The gradual increase starting at about 800°C may be due to a contribution from the homogeneous reaction between D_2 and CO_2 above this temperature.[31]

CONCLUSIONS

Transient species desorbed from a Pt catalyst during the course of heterogeneous reactions were identified by carrying out the reactions within the ion source of a research mass spectrometer. The application of a mass spectrometer to the study of catalytic reactions furnishes information about these reactions in at least four areas outside of the scope of the usual chemical kinetic methods. First, transient species desorbed from the catalyst can be observed directly (in less than 10 μsec); second, these species can be detected by either positive or negative ion techniques; third, reactions are studied primarily in one direction since final products are rapidly evacuated and have little opportunity to back react; and fourth, the existence of suspected intermediates adsorbed on the catalyst can be tested for by independently exposing the catalyst to stable species of similar configuration.

ACKNOWLEDGMENTS

It is a pleasure for the author to acknowledge Professor P. H. Emmett of Johns Hopkins University and Dr. E. H. Taylor to whom he is indebted for valuable suggestions and extensive discussions throughout the course of this investigation.

The assistance of Drs. S. Datz and Russell Baldock in a critical review of the manuscript is deeply appreciated.

Thanks also go to my wife for assistance in the preparation of the manuscript and calculation of the data.

Calculation of Interaction Matrix Elements for Asymmetric Rotors with Resultant Electronic Spin and Nuclear Spin*

R. F. Curl, Jr., and James L. Kinsey†
Department of Chemistry, Rice University, Houston, Texas
(Received December 22, 1960)

The application of Racah or vector recoupling coefficients to the calculation of interaction matrix elements for asymmetric rotors with resultant electronic and nuclear spin is outlined. This approach is compared with Van Vleck's method of reversed angular momenta.

INTRODUCTION

THE system to be considered is an asymmetric rotor molecule with one or more unpaired equivalent electrons and one nuclear spin. Two stable molecules in this category for which extensive spectroscopic data are available are NO_2 and ClO_2. The present work formulates a unified method for calculating the matrix elements needed in fitting the microwave spectra of these molecules.

Such molecules have three angular momenta which can interact: **N** (molecular rotation); **S** (resultant electronic spin); and **I** (nuclear spin).

Because of the interaction between the momenta, they couple, giving a total resultant angular momentum **F**. There are three limiting coupling schemes which result if one considers one interaction much stronger than the others. These schemes are the J scheme, $\mathbf{N}+\mathbf{S}=\mathbf{J}$, $\mathbf{J}+\mathbf{I}=\mathbf{F}$; the G scheme $\mathbf{S}+\mathbf{I}=\mathbf{G}$ $\mathbf{G}+\mathbf{N}=\mathbf{F}$; and the E scheme $\mathbf{N}+\mathbf{I}=\mathbf{E}$, $\mathbf{E}+\mathbf{S}=\mathbf{F}$.

The relationship between these schemes is analogous to that between $j-j$ and $L-S$ coupling in atoms.

The interactions in systems such as this have been discussed by Lin[1] and by Baker.[2] The procedure they follow is first to derive the effective Hamiltonian, then to calculate its matrix elements in a coupled scheme, and finally to diagonalize the Hamiltonian matrix. The portion of this process which is of primary concern here is the calculation of interaction matrix elements in a coupled scheme.

Lin[1] and Baker[2] use Van Vleck's reversed angular momenta[3] for this calculation. The matrix elements may also be found in a quite straightforward manner by use of Racah[4] or vector recoupling coefficients. Under certain circumstances there appears to be an advantage to the latter approach.

RELATIONSHIP BETWEEN MATRIX ELEMENTS IN THE COUPLED AND UNCOUPLED SCHEMES

The calculation of the interaction terms is easiest in the case of complete uncoupling or strong Paschen-Back effect. By the use of vector recoupling coefficients the matrix elements in any coupled scheme may be related to those in the uncoupled scheme. In the next section the calculation of matrix elements in the uncoupled scheme will be discussed.

Each of the interaction terms conceivable for the system (including those with external fields) can be written[5]

$$[\mathbf{T}(k_1)\times\mathbf{U}(k_2)]_{k_{12}}\times\mathbf{V}(k_3)=\mathbf{X}(k). \tag{1}$$

A tensor of rank k_1, $[\mathbf{T}(k_1)]$, couples with a tensor of rank k_2, $[\mathbf{U}(k_2)]$, giving a resultant tensor $\mathbf{W}(k_{12})$; $\mathbf{W}(k_{12})$ then couples with $\mathbf{V}(k_3)$ giving a resultant tensor $\mathbf{X}(k)$ of rank k. $\mathbf{T}(k_1)$ is assumed to act on angular momentum j_1, $\mathbf{U}(k_2)$ on j_2, and $\mathbf{V}(k_3)$ on j_3. j_1, j_2, and j_3 all commute.

It can easily be shown [see reference 6, Eq. (7.1.5.)]

$$\langle\gamma' j_1' j_2' j_{12}' j_3' j' \,||\, \mathbf{X}(k) \,||\, \gamma j_1 j_2 j_{12} j_3 j\rangle=[(2j+1)(2j'+1)(2k+1)(2j_{12}+1)(2j_{12}'+1)(2k_{12}+1)]^{\frac{1}{2}}$$
$$\times\begin{Bmatrix} j_{12}' & j_{12} & k_{12} \\ j_3' & j_3 & k_3 \\ j' & j & k \end{Bmatrix}\begin{Bmatrix} j_1' & j_1 & k_1 \\ j_2' & j_2 & k_2 \\ j_{12}' & j_{12} & k_{12} \end{Bmatrix}\sum_{\gamma''\gamma'''}\langle\gamma' j_1' \,||\, \mathbf{T} \,||\, \gamma'' j_1\rangle\langle\gamma'' j_2' \,||\, \mathbf{U} \,||\, \gamma''' j_2\rangle\langle\gamma''' j_3' \,||\, \mathbf{V} \,||\, \gamma j_3\rangle, \tag{2}$$

where the reduced matrix element is defined by

$$\langle j' \,||\, \mathbf{X} \,||\, j\rangle\begin{pmatrix} j' & k & j \\ -m' & q & m \end{pmatrix}=(-1)^{m'-j'}\langle j'm' \,|\, X(kq) \,|\, jm\rangle \tag{3}$$

* This work was supported by a grant from the Robert A. Welch Foundation.
† Pre-Doctoral Southern Fellow, 1958–59. Present address: Department of Chemistry, University of California, Berkeley 4, California.
[1] C. C. Lin, Phys. Rev. **116**, 903 (1959).
[2] J. G. Baker, thesis, Cambridge University, 1958.
[3] J. H. Van Vleck, Revs. Modern Phys. **23**, 213 (1951).
[4] G. Racah, Phys. Rev. **62**, 438 (1942).
[5] Spherical tensors will be shown in boldface *sans serif* $\mathbf{T}(k)$. Cartesian vectors will be shown in boldface as usual. In Eq. (6) a Cartesian second rank tensor is shown in boldface German capital, $\mathfrak{U}$. The relationship between a spherical tensor and the corresponding Cartesian tensor is indicated by an arrow from the spherical to the Cartesian. ($\mathbf{T}(1)\rightarrow\mathbf{T}$). The direction of the arrow implies the direction of one to one mapping.
[6] A. R. Edmonds, *Angular Momentum in Quantum Mechanics* (Princeton University Press, Princeton, New Jersey, 1957).

TABLE I. Notation for interaction parameters.[a]

Name of interaction	Van Vleck[b]	Lin[c]	Henderson[d]	Baker[e]	This work	Molecule fixed Hamiltonian terms
1. Spin rotation interaction	$-a_0$	$\frac{1}{3}(\epsilon_{xx}+\epsilon_{yy}+\epsilon_{zz})$	$-2(\mu-\frac{1}{3}\lambda)$	$-a_s$	$(O)_s$	$(O)_s\mathbf{N}\cdot\mathbf{S}$
	$-2a$	$\frac{1}{3}(2\epsilon_{zz}-\epsilon_{xx}-\epsilon_{yy})$	$4\lambda/3$	$-2b_s$	$(aa)_s$	$\sum_{ij}^{a,b,c}(ij)_sN_iS_j$
						$(ij)_s$ symmetric and traceless
	$+a+b$	$+\frac{1}{3}(2\epsilon_{yy}-\epsilon_{xx}-\epsilon_{zz})$	$-(2\lambda/3)-(4\eta/b)$	$+c_s+b_s$	$(bb)_s$	
	$+a-b$	$+\frac{1}{3}(2\epsilon_{xx}-\epsilon_{yy}-\epsilon_{zz})$	$-(2\lambda/3)+(4\eta/b)$	$-c_s+b_s$	$(cc)_s$	
	$-e$	$\frac{1}{2}(\epsilon_{yz}+\epsilon_{zy})$			$+(ab)_s$	
	$-d$	$\frac{1}{2}(\epsilon_{xz}+\epsilon_{zx})$			$+(ac)_s$	
	$-c$	$\frac{1}{2}(\epsilon_{xy}+\epsilon_{yx})$	$+A'(1/B+1/A)\delta_+$		$+(bc)_s$	
					$(a)_s$	$\Sigma_{ijk}\epsilon_{ijk}N_iS_j(k)_s$
					$(b)_s$	
					$(c)_s$	$+i\hbar\Sigma_i(i)_sS_i$
2. Fermi interaction		σ		a_I	$(O)_I$	$(O)_I(\mathbf{I}\cdot\mathbf{S})$ $(O)_I=(16\pi/3)g_I\mu_B\mu_N[\psi(O)]^2$ $\mu_B>0$
3. Magnetic dipole dipole interaction		-2λ $\lambda+2\tau$ $\lambda-2\tau$		$2b_I$ $-b_I-c_I$ $-b_I+c_I$	$(aa)_I$ $(bb)_I$ $(cc)_I$	$\Sigma_{ij}(ij)_IS_iI_j$ $(ij)_I$ symmetric and traceless $(ij)_I=-g_ig_I\mu_B\mu_N[(\delta_{ij}-3r_ir_j)/r^3]_{Av}$
					$(ab)_I$	
					$(ac)_I$	
					$(bc)_I$	
4. Nuclear quadrupole interaction		$[eQ/2I(2I-1)]$ $(\partial^2V/\partial a^2)$		$2b_Q$	$(aa)_Q$	$\Sigma(ij)_QI_iI_j$ $(ij)_Q$ symmetric and traceless
		etc.		$-b_Q-c_Q$	$(bb)_Q$	$(ij)_Q=[eQ/2I(2I-1)]/(\partial^2V/\partial x_i\cdot\partial x_j)$
		etc.		$-b_Q+c_Q$	$(cc)_Q$	

[a] Considerable confusion arises from naming of axes. Van Vleck's Hamiltonian has $x\to a$, $y\to b$, $z\to c$. Henderson, Lin, and Baker make the same correspondence, but then in applying the derived equations make a the smallest rotational constant and c the largest. The correspondences in the table above are based on $x\to c$, $y\to b$, $z\to a$ in everyone's formulas.

[b] See reference 3.

[c] See reference 1.

[d] See reference 16.

[e] See reference 2.

TABLE II. Phase factors of $\langle N'\tau' \| D^1 \| N\tau\rangle$ tabulated in the form $i^{\Delta N \Delta K_{-1} \Delta K_{+1}}$ $\Delta N = N' - N$, $\Delta K_{-1} = K_{-1}' - K_{-1}$, $\Delta K_{+1} = K_{+1}' - K_{+1}$.

			$\Delta N = 0$				
${}^aQ_{\pm 2,\mp 1}$	${}^aQ_{0,+1}$	${}^aQ_{0,-1}$	${}^bQ_{+1,-1}$	${}^bQ_{-1,+1}$	${}^cQ_{+1,0}$	${}^cQ_{-1,0}$	${}^cQ_{\mp 1,\pm 2}$
$+1$	$+1$	$+1$	$-i$	$+i$	$+1$	$+1$	$+1$
			$\Delta N = +1$				
${}^aR_{0,+1}$	${}^aR_{+2,-1}$	${}^bR_{+1,+1}$	${}^bR_{-1,+1}$	${}^bR_{+1,-1}$	${}^bR_{-1,+3}$	${}^bR_{+3,-1}$	${}^cR_{+1,0}$	${}^cR_{-1,+2}$
$+1$	-1	$+i$	$+i$	$+i$	$+i$	$+i$	-1	$+1$
			$\Delta N = -1$				
${}^aP_{0,-1}$	${}^aP_{-2,+1}$	${}^bP_{-1,-1}$	${}^bP_{+1,-1}$	${}^bP_{-1,+1}$	${}^bP_{+1,-3}$	${}^bP_{-3,+1}$	${}^cP_{-1,0}$	${}^cP_{+1,-2}$
-1	$+1$	$+i$	$+i$	$+i$	$+i$	$+i$	$+1$	-1

and the symbols in curly brackets are the Wigner $9j$ symbols. The symbol in parentheses in the definition of the reduced matrix element is the Wigner $3j$ symbol. The $9j$ symbol is related to the Fano X coefficient and the $3j$ symbol to the Clebsch-Gordan or vector coupling coefficients. If any one of the five k's $(k_1, k_2, k_3, k_{12}, k)$ is zero, a $9j$ symbol in which it appears reduces to a $6j$ symbol.

In using Eq. (2) several points should be remembered. These are expressed in the equations below.

$$\langle j'\gamma' \| 1 \| j\gamma\rangle = \delta_{jj'}\delta_{\gamma\gamma'}(2j+1)^{\frac{1}{2}} \tag{4}$$

$$[\mathbf{T}(k)\times\mathbf{U}(k)]_0 = (-1)^k(2k+1)^{-\frac{1}{2}}(\mathbf{T}\cdot\mathbf{U}) \tag{5}$$

$$[\mathbf{T}(1)\times\mathbf{U}(2)]_1 \rightarrow -(\tfrac{3}{5})^{\frac{1}{2}}\mathbf{T}\cdot\mathfrak{U} \tag{6}$$

$$[\mathbf{T}(1)\times\mathbf{U}(1)]_1 \rightarrow -i(2)^{-\frac{1}{2}}\mathbf{T}\times\mathbf{U}. \tag{7}$$

To apply this to the problem in hand, j_1, j_2, and j_3 must be identified with N, S, and I. If j_1 corresponds with N, j_2 with S, and j_3 with I (γ is identified with the asymmetric rotor quantum number τ), the matrix elements to be considered are for the J scheme. That is, $j_{12} = J$, $j = F$. What remains is consideration of the particular forms of the interaction and evaluation of the uncoupled scheme matrix elements.

HAMILTONIAN TERMS

The Hamiltonian consists of 6 terms:

$$H = H_0 + H_1 + H_2 + H_3 + H_4 + H_5. \tag{8}$$

The origin of the terms and the calculation of their matrix elements will now be discussed. The subscripts do not refer to the order of the terms as in a perturbation expansion. However, the size of the interaction does decrease with increasing subscript.

The notation of other workers for interaction parameters is compared with the present notation in Table I.

1. Asymmetric Rotor Hamiltonian, H_0

$$H_0 = AN_a^2 + BN_b^2 + CN_c^2. \tag{9}$$

N_a, N_b, and N_c are components of $\mathbf{N}$ along the principal axes of inertia of the molecule. Although the matrix elements of H_0 may be found by use of Eq. (2), this approach is inconvenient as much cancellation occurs. The basis is chosen so that H_0 is diagonal, and may be obtained from the asymmetric rotor tables.[7]

2. Electron Spin-Rotation Interaction,[3] H_1

$$H_1 = \mathbf{T}_{1N}(1)\cdot\mathbf{U}_{1S}(1) + \mathbf{T}'_{1N}(2)\cdot\mathbf{U}'_{1S}(2). \tag{10}$$

Both of these terms arise as the result of a Van Vleck perturbation treatment with inclusion of excited electronic states. If $S = \frac{1}{2}$ all matrix elements of $\mathbf{U}'_{1S}(2)$ are zero. If $S > \frac{1}{2}$ the second term will ordinarily be greater than the first. Equation (2) in J scheme reduces for these interactions to a $6j$ symbol times a simple function of the quantum numbers. In order to apply Eq. (2) to the first term $\langle N'\tau' \| \mathbf{T}_{1N}(1) \| \tau N\rangle$ and $\langle S \| \mathbf{U}_{1S}(1) \| S\rangle$ are required.

$$\mathbf{U}_{1S}(1) = \mathbf{S}$$

$$\langle S' \| \mathbf{S} \| S\rangle = \delta_{SS'}\hbar[S(S+1)(2S+1)]^{\frac{1}{2}}$$

$$\mathbf{T}_{1N}(1) = (0)_S\mathbf{N} + \mathbf{N}\cdot\mathbf{T}_{1N}''(2) - i\sqrt{2}[\mathbf{N}\times\mathbf{T}_{1N}'''(1)]_1 + i\hbar\mathbf{T}_{1N}''' \tag{1}$$

$$\langle N'\tau' \| \mathbf{N}\cdot\mathbf{T}_{1N}''(2) \| N\tau\rangle = \sqrt{5}(-1)^{N'+N} \times \sum_{N''\tau''} \begin{Bmatrix} 1 & 2 & 1 \\ N & N' & N'' \end{Bmatrix} \langle N'\tau' \| \mathbf{N} \| N''\tau''\rangle \times \langle N''\tau'' \| \mathbf{T}_{1N}'' \| N\tau\rangle. \tag{11}$$

$\mathbf{T}''_{1N}(2)$ has constant components in the frame rotating with the molecule.

$$T_{1N}''(2, q) = \sum_{q'} D^2_{qq'}(\alpha, \beta, \gamma)\mathfrak{T}_{1N}(2q') \tag{12}$$

$$\mathfrak{T}_{1N}(2) \Rightarrow (ij)s.$$

$\mathfrak{T}_{1N}(2, q')$ are the constant components of the tensor in the molecular frame. α, β, and γ are the Eulerian angles locating the molecular axes in the space-fixed coordinate system. (D^2qq' is an element of the five-

[7] C. H. Townes and A. L. Schawlow, *Microwave Spectroscopy* (McGraw-Hill Book Company, Inc., New York, 1955), Appendix IV.

dimensional irreducible representation of the rotation group.) Matrix elements of $D^2qq'(\alpha, \beta, \gamma)$ may be evaluated in several ways. For the symmetric top

$$\langle N'K'M' \mid D^2_{qq'} \mid NKM \rangle = (-1)^{K'-M'}[(2N+1)(2N'+1)]^{\frac{1}{2}} \times \begin{pmatrix} N' & 2 & N \\ -M' & q & M \end{pmatrix} \begin{pmatrix} N' & 2 & N \\ -K' & q' & K \end{pmatrix}. \quad (13)$$

The transformation coefficients relating the asymmetric rotor wave functions for given asymmetry parameter κ to the symmetric rotor wave functions were tabulated by Schwendeman and Laurie.[8]

$$\psi_{N\tau}(\kappa) = \sum_{|K|=0}^{N} a_{N\tau}{}^{K}(\kappa)[\psi_{N,K-1} + (-1)^{N+\tau+K}\psi_{N,-K-1}]. \quad (14)$$

Another method for evaluating $\langle N'\tau' \| \mathsf{T}_{1N}''(2) \| N\tau \rangle$ which is usually more convenient is based on the asymmetric rotor line strengths.[9]

$$\langle N'\tau' \| \mathsf{T}_{1N}''(2) \| N\tau \rangle = \sum_{ij}^{a,b,c} (ij)_S \langle N'\tau' \| \mathsf{D}^2{}_{ij} \| N\tau \rangle \quad (15)$$

$$\langle N'\tau' \| \mathsf{D}^2{}_{ij} \| N\tau \rangle = (-1)^{N+N'}(5)^{\frac{1}{2}} \sum_{N''\tau''} \begin{Bmatrix} 1 & 1 & 2 \\ N & N' & N'' \end{Bmatrix} \times \langle N'\tau' \| \mathsf{D}^1{}_i \| N''\tau'' \rangle \langle N''\tau'' \mid \mathsf{D}^1{}_j \| N\tau \rangle$$

$$= (-1)^{N+N'}(5)^{\frac{1}{2}} \sum_{N''\tau''} \begin{Bmatrix} 1 & 1 & 2 \\ N & N' & N'' \end{Bmatrix} {}^{i}P_{N'N'',\tau'\tau''}{}^{j}P_{N''N\tau''\tau} \times [S_{N'\tau'N''\tau''}(i)]^{\frac{1}{2}}[S_{N''\tau''N\tau}(j)]^{\frac{1}{2}}. \quad (16)$$

The ${}^{i}P_{N''N,\tau''\tau}$ are phase factors and are listed in Table II for the types of transitions which contribute significantly. These phases have been made consistent with Edmonds[6] and the choice of axes made in Table I. The $S_{N\tau N''\tau''}(i)$ are the asymmetric rotor line strengths and $(ij)_S$ are components of a traceless symmetric second rank tensor.

Because of molecular symmetry $\mathsf{T}''_{1N}(2)$ may have only a few independent components. For example in the case of ClO_2 with C_{2v} symmetry, $\mathsf{T}''_{1N}(2)$ has only two independent components. The number and type of independent components of these tensor operators for given molecular symmetry may be found by the usual methods of group theory.

The axial vector $\mathsf{T}'''_{1N}(1)$ has constant components in the molecular frame.

$$\langle N'\tau' \| \mathsf{T}_{1N}'''(1) \| N\tau \rangle = \sum_{i}(i)_S \langle N'\tau' \| \mathsf{D}^1{}_i \| N\tau \rangle = \sum_{i}(i)_S {}^{i}P_{N'N,\tau'\tau}[S_{N\tau'N\tau}(i)]^{\frac{1}{2}}. \quad (17)$$

The second term in H_1 has $\mathsf{T}'_{1N}(2)$ a constant in the molecular frame and $\mathsf{U}'_{1S}(2) = (\mathbf{S}\times\mathbf{S})_2$. The same methods may be applied to its evaluation.

3. Electron Spin-Nuclear Spin (Fermi) Interaction

The electron spin and nuclear spin interact through a contact term.[10]

$$H_2 = +(16\pi/3) g_I \mu_N \mu_B \mid \psi(0) \mid^2 (\mathbf{S}\cdot\mathbf{I}) \qquad \mu_N > 0 \qquad \mu_B > 0$$

$$(0)_I = +(16\pi/3) g_I \mu_N \mu_B \mid \psi(0) \mid^2. \quad (18)$$

The calculation of uncoupled matrix elements is very easy. Since k_1 and k are zero, Eq. (2) contains the product of two $6j$ symbols in J scheme.

4. Magnetic Dipole-Magnetic Dipole Interaction

The dipole-dipole interaction between the electronic and nuclear moments takes the form

$$H_3 = \mathsf{T}_{3N}(2)\cdot\mathsf{T}_{3S}(1)\cdot\mathsf{T}_{3I}(1) = -2g_I\mu_N\mu_B\langle[(\mathbf{S}\cdot\mathbf{I})/r^3] - [3(\mathbf{I}\cdot\mathbf{r})(\mathbf{S}\cdot\mathbf{r})/r^5]\rangle_{kl;\tau} \quad (19)$$

$$\mathsf{T}_{3S}(1) = \mathbf{S}, \quad \mathsf{T}_{3I}(1) = \mathbf{I}$$

$$T_{3N}(2, q) = \sum_{q'} D^2_{qq'}(\alpha\beta\gamma)\mathfrak{I}_{3N}(2, q')$$

$$\mathfrak{I}_{3N}(2) \Rightarrow (ij)_I.$$

The matrix elements of $\mathsf{T}_{3N}(2)$ are evaluated in the same way as those of $\mathsf{T}''_{1N}(2)$. Since $k=0$, Eq. (2) reduces, and contains the product of a $9j$ symbol times a $6j$ symbol. If $S=\frac{1}{2}$, the $9j$ symbol may be found as the product of two $6j$ symbols divided by another $6j$ symbol [see reference 6, Eq. (6.4.8.)] or by explicit formulas [see reference 6, Eqs. (6.4.15), (6.3.3), (6.3.4)].

5. Quadrupolar Interaction

The electric quadrupole moment of the nucleus interacts with the molecular electric fields

$$H_4 = -(5^{\frac{1}{2}}/6)\mathsf{T}_{4N}(2)\cdot\mathsf{T}_{4I}(2). \quad (20)$$

$\mathsf{T}_{4I}(2)$ = nuclear quadrupole moment tensor; $\mathsf{T}_{4N}(2)$ = field gradient tensor (constant in the molecular frame); $\langle II \mid \mathsf{T}_{4I}(2) \mid II \rangle = 6^{\frac{1}{2}}/2eQ$; and Q = nuclear quadrupole moment. Matrix elements of $\mathsf{T}_{4N}(2)$ can be evaluated as $\mathsf{T}_{1N}''(2)$, or it can be evaluated as in Townes and

[8] R. H. Schwendeman and V. W. Laurie, available on request from Dr. Schwendeman, Department of Chemistry, Michigan State University, East Lansing, Michigan.

[9] R. H. Schwendeman and V. W. Laurie, *Tables of Line Strengths* (Pergamon Press, New York, 1958).

[10] E. Fermi, Z. Physik. **60**, 320 (1930). See also L. D. Landau and E. M. Lifschitz, *Quantum Mechanics Non-Relativistic Theory*, (Addison-Wesley Publishing Company, Inc., Reading Massachusetts, 1958), p. 486.

TABLE III.

Term	Effect
$[N]_t[N]_{(t)}$	Slight change in the effective moments of inertia.
$[I]_t[I]_{(t)}$	Pseudo-quadrupole term. (2nd rank tensor) additive constant (scalar).
$[S]_t[S]_{(t)}$	Pseudo-quadrupole term $[\mathsf{T}'_{1N}(2)\cdot\mathsf{U}'_{1S}(2)]$ additive constant (scalar).
$[N]_t[I]_{(t)}$ $+[I]_t[N]_{(t)}$	Nuclear spin-rotation interaction (see reference 11). Usually too small to be observed. Same form as electron spin-rotation interaction.
$[N]_t[S]_{(t)}$ $+[S]_t[N]_{(t)}$	Electron spin-rotation interaction. $\mathsf{T}_{1N}(1)\cdot\mathsf{U}_{1S}(1)$.
$[S]_t[I]_{(t)}$ $+[I]_t[S]_{(t)}$	Pseudo-dipole-dipole and pseudo-Fermi interactions. Rotation-electron spin-nuclear spin interaction $(\mathsf{T}_{2N}(1)\times\mathsf{S})_1\cdot\mathsf{I}$.

Schawlow,[7] p. 161.

$$\langle N\tau\,||\,\mathsf{T}_{4N}(2)\,||\,N\tau\rangle=\frac{-6^{\frac{1}{2}}}{2}\left[\frac{2N+1}{(2N-1)(2N+3)N(N+1)}\right]^{\frac{1}{2}}$$
$$\times\left\{\frac{\partial^2V}{\partial a^2}\left[N(N+1)+\epsilon_{N\tau}(\kappa)-(\kappa+1)\frac{\partial\epsilon_{N\tau}(\kappa)}{\partial\kappa}\right]\right.$$
$$+2\frac{\partial^2V}{\partial b^2}\frac{\partial\epsilon_{N\tau}(\kappa)}{\partial\kappa}$$
$$\left.+\frac{\partial^2V}{\partial c^2}\left[N(N+1)-\epsilon_{N\tau}(\kappa)+(\kappa-1)\frac{\partial\epsilon_{N\tau}(\kappa)}{\partial\kappa}\right]\right\}. \quad (21)$$

This formula can be used analogously without the minus sign for expectation values of $\mathsf{T}''_{1N}(2)$ or $\mathsf{T}_{3N}(2)$. Since k_2 and k are zero, Eq. (2) contains the product of two $6j$ symbols.

6. Rotation-Electron Spin-Nuclear Spin Interaction

The perturbation treatment of Van Vleck[3] did not include nuclear spin terms. If these are included[11] it is possible (Appendix II) to get an interaction term of the form

$$H_b=(\mathsf{T}_{bN}(1)\times\mathsf{S})_1\cdot\mathsf{I}, \quad (22)$$

where $\mathsf{T}_{bN}(1)$ is constant in the molecular frame. $\mathsf{T}_{bN}(1)$ will have three components, one along each of the principal axes. The matrix elements of components of $\mathsf{T}_{bN}(1)$ will be proportional to the square root of the asymmetric rotor line strength[9] for the transition corresponding to the matrix element. Equation (2) will contain a $9j$ symbol and a $6j$ symbol.

7. Stark and Zeeman Effect

The Stark interaction is given by $H_x=\boldsymbol{\mu}\cdot\mathbf{X}$ where $\boldsymbol{\mu}$ is the electric dipole moment, and $\mathbf{X}$ is the electric field. $\boldsymbol{\mu}$ is of the form $\mathsf{T}_{6N}(1)$. Matrix elements of $\boldsymbol{\mu}$ are proportional to the square root of the asymmetric rotor line strengths.[9] The field direction is usually chosen along the external z axis so that

$$\langle N'\tau'SJ'IF'M\,|\,\mu_z\,|\,N\tau SJIFM\rangle$$

is required.

The Zeeman interaction is given by $H_Z=-2\mu_B\mathbf{S}\cdot\mathbf{H}$. In both cases Eq. (2) will contain the product of two $6j$ symbols.

NUMERICAL CALCULATION

For some molecules sufficient accuracy can be obtained for most levels by consideration of matrix elements diagonal in N. Explicit formulas have been derived by Baker[2] and Lin[1] for the matrix elements diagonal in N in a symmetric rotor basis. We have rewritten these in the asymmetric rotor basis and listed them in Appendix I. By the use of these formulas, the hyperfine splitting of a rotational level for given interaction parameters can be computed by hand in about thirty minutes.

On the other hand it is often necessary to consider the second order perturbation off-diagonal in N arising from the interactions. Although it is possible in principle to give explicit formulas for the matrix elements, calculation by their use probably will be inconveniently laborious. For hand calculation there exist a number of useful tables of Racah coefficients.[12–15] Programs have been devised for the calculation of these coefficients on electronic computers and the computation may thus be done automatically.

COMPARISON WITH VAN VLECK'S METHOD OF REVERSED ANGULAR MOMENTA

A description of the calculation of matrix elements by the use of reversed angular momenta has been given by Van Vleck,[3] and will not be repeated. It seems likely that Van Vleck's method may be applied to any matrix element of any interaction of this type no matter how complex. For the simpler matrix elements, explicit

[11] See G. R. Gunther-Mohr, C. H. Townes, and J. H. Van Vleck, Phys. Rev. **94**, 1191 (1954).

[12] L. C. Biedenharn, *Tables of the Racah Coefficients* (Oak Ridge National Laboratory, 1952).

[13] Kenneth Smith and John Stevenson, *A Table of Wigner 9j Coefficients for Integral and Half-Integral Values of the Parameters* (Argonne National Laboratory, ANL-5776, 1957); Kenneth Smith, *Supplement to the Table of Wigner 9j Symbols* (Argonne National Laboratory, 1958), ANL-5860 Parts I and II.

[14] M. Rotenberg, R. Bivens, N. Metropolis, and J. K. Wooten, *The 3j and 6j Symbols*, (The Technology Press, Cambridge, Massachusetts, 1959).

[15] K. M. Howell, *Tables of the Wigner 6j Symbols*, University of Southampton Research Rept. U.S. No. 58-1, June 1958.

formulas may be derived more rapidly than by the method outlined in this paper.

On the other hand, in derivations by Van Vleck's method a great deal of reasoning is involved. Almost every step in the derivation requires some thought. This is not the case for the method outlined here. Most of the derivation is algebraic or numerical manipulation. We feel this constitutes the real advantage of this approach. In addition tabulated values of Racah coefficients may be used.

ACKNOWLEDGMENTS

The preparation of this paper was helped considerably by discussions with Professor L. C. Biedenharn. We wish to thank Dr. John Baker for giving us a copy of his thesis. It must be emphasized that the equations in Appendix I are based primarily on Dr. Baker's thesis and are not original with us, although we have introduced the asymmetric rotor basis and checked Dr. Baker's results.

APPENDIX I. EXPLICIT FORMULAS FOR SOME OF THE SIMPLER MATRIX ELEMENTS

1. Spin-rotation interaction

$$\langle N\tau JF \mid H_1 \mid N\tau JF\rangle = -\left[\frac{(0)_s}{2}+\frac{\sum_s}{2(2N+1)}\right]\hbar^2[N(N+1)+S(S+1)-J(J+1)]$$

$$+\frac{(\frac{3}{4}C_J(C_J+1)-S(S+1)N(N+1))}{(2N-1)(2N+3)(2N+1)}\hbar^2\sum_s' \quad \text{for } S>\tfrac{1}{2}$$

$$\sum_s=\sum_{\tau',i}(ii)_S S_{N\tau N\tau'}(i)=[(2N+1)/2N(N+1)]\{(aa)_S[N(N+1)+\epsilon_{N\tau}(\kappa)-(\kappa+1)(\partial\epsilon_{N\tau}/\partial\kappa)]$$

$$+2(bb)_S[\partial\epsilon_{N\tau}(\kappa)/\partial\kappa]+(cc)_S[N(N+1)-\epsilon_{N\tau}(\kappa)+(\kappa-1)(\partial\epsilon_{N\tau}/\partial\kappa)]\}$$

$$\sum_s'=\sum_{\tau',i}(ii)_S' S_{N\tau N\tau'}(i)$$

$$C_J=J(J+1)-S(S+1)-N(N+1).$$

The $(i)_s$ terms have no nonzero resultant terms diagonal in either N or τ.

2. Fermi interaction

$$\langle N\tau JF \mid H_2 \mid N\tau JF\rangle=\frac{\hbar^2(0)_I[F(F+1)-J(J+1)-I(I+1)][J(J+1)+S(S+1)-N(N+1)]}{4J(J+1)}$$

for $S=\frac{1}{2}$

$$\langle N\tau J+1F \mid H_2 \mid N\tau JF\rangle=\frac{+(0)_I[(N+I-F+\frac{1}{2})(N+I+F+\frac{3}{2})(I+F-N+\frac{1}{2})(N-I+F+\frac{1}{2})]^{\frac{1}{2}}\hbar^2}{2(2N+1)}.$$

3. Dipole-dipole for $S=\frac{1}{2}$

$$\langle N\tau JF \mid H_3 \mid N\tau JF\rangle=\frac{\hbar^2[J(J+1)+I(I+1)-F(F+1)][N(N+1)+S(S+1)-J(J+1)]\sum_I}{4J(J+1)(2N+1)}$$

$$\sum_I=\sum_{\tau',i}(ii)_I S_{N\tau N\tau'}(i).$$

$$\langle N\tau J+1F \mid H_3 \mid N\tau JF\rangle=\frac{-\hbar^2[(N+I-F+\frac{1}{2})(N+I+F+\frac{3}{2})(I+F-N+\frac{1}{2})(N-I+F+\frac{1}{2})]^{\frac{1}{2}}\sum_I}{4(2N+1)^2}.$$

4. Quadrupole for $S=\frac{1}{2}$

$$\langle N\tau JF \mid H_4 \mid N\tau JF\rangle=\frac{\hbar^2[3C_F(C_F+1)-4I(I+1)J(J+1)]\sum_Q}{8J(J+1)(2N+1)}$$

$$C_F=F(F+1)-I(I+1)-J(J+1)$$

$$\sum_Q=\sum_{\tau',i}(ii)_Q S_{N\tau N\tau'}(i)$$

$$\langle N\tau J+1F \mid H_4 \mid N\tau JF\rangle=\frac{-3[F(F+1)-I(I+1)-N(N+1)+\frac{3}{4}]\hbar^2\sum_Q}{(2N-1)(2N+3)(2N+1)^2}$$

$$\times[(N+I-F+\tfrac{1}{2})(N+I+F+\tfrac{3}{2})(I+F-N+\tfrac{1}{2})(N-I+F+\tfrac{1}{2})]^{\frac{1}{2}}.$$

5. Rotation-electron spin-nuclear spin interaction. No nonzero matrix elements diagonal in N or τ.

APPENDIX II. DERIVATION OF EFFECTIVE HAMILTONIAN ARISING FROM SECOND-ORDER PERTURBATION

The consideration of the electronic energy levels of a rigid molecule with only Coulombic interactions and in the absence of rotation, neglects certain terms in the Hamiltonian which must be considered for hyperfine structure. These terms[3,11,16] are

$$H_r=-\sum_{\nu}^{a,b,c}A_\nu(L_\nu N_\nu+N_\nu L_\nu)+\sum_j \mathbf{n}_{sj}\cdot\mathbf{s}_j+\mathbf{n}_I\cdot\mathbf{I}, \tag{A.1}$$

where the A_ν are the rotational constants of the molecule

$$\mathbf{L}=m_e\sum_j(\mathbf{r}_j-\mathbf{r}_0)\times(\mathbf{V}_j-\mathbf{V}_0)$$

$$\mathbf{n}_{sj}=(ge\mu_\beta/c)\sum_{K,j}(Z_Ke/|\,\mathbf{r}_j-\mathbf{r}_K\,|^3)(\mathbf{r}_j-\mathbf{r}_K)\times(\tfrac{1}{2}\mathbf{V}_j-\mathbf{V}_K)+(ge\mu_\beta/c)\sum_{k>j}[(-e)/|\,\mathbf{r}_j-\mathbf{r}_k\,|^3](\mathbf{r}_j-\mathbf{r}_k)\times(\tfrac{1}{2}\mathbf{V}_j-\mathbf{V}_k)$$

$$\mathbf{n}_I=(eg_I\mu_N/c)\sum_j|\,\mathbf{r}_j-\mathbf{r}_I\,|^{-3}(\mathbf{r}_j-\mathbf{r}_I)\times\{\mathbf{V}_j-[1+(Z_IM_P/g_IM_I)]\mathbf{V}_I\}.$$

$$\mathbf{r}_0=\sum_k M_k\mathbf{r}_k\qquad \mathbf{V}_0=\sum_k M_k\mathbf{V}_k. \tag{A.2}$$

The first three terms arise because the rotational energy of the molecule is given by $\sum_\nu A_\nu R_\nu^2$, where $\mathbf{R}=\mathbf{N}-\mathbf{L}$ since $\mathbf{N}$ is the total mechanical angular momentum. The last two terms are magnetic dipole interactions.

H_r is nondiagonal in the electronic energy and therefore its effect will be manifested through second order perturbation.

$$\begin{aligned}\langle il_0\,|\,H_{\rm eff}\,|\,i'l_0\rangle&=\sum_{l\neq l_0,i''}(E_{l0}-E_l)^{-1}\langle il_0\,|\,H_r\,|\,i''l\rangle\langle i''l\,|\,H_r\,|\,i'l_0\rangle\\&=\sum_{l\neq l_0,i'',S'}(E_{l0}-E_l)^{-1}[\sum_\nu\langle l_0\,|\,A_\nu L_\nu\,|\,l\rangle\langle i\,|\,N_\nu\,|\,i''\rangle+\sum_{\nu'}\langle l_0\,|\,\eta_{I\nu'}\,|\,l\rangle\langle i\,|\,I_{\nu'}\,|\,i''\rangle\\&\qquad+\sum_{j\nu''}\langle l_0\,|\,\eta_{sj\nu''}\,|\,l\rangle\langle iS\,|\,s_{j\nu''}\,|\,iS'\rangle]\\&\times[\sum_\nu\langle l\,|\,A_\nu L_\nu\,|\,l_0\rangle\langle i''\,|\,N_\nu\,|\,i'\rangle+\sum_{\nu'}\langle l\,|\,\eta_{I\nu'}\,|\,l_0\rangle\langle i''\,|\,I_{\nu'}\,|\,i'\rangle+\sum_{j\nu''}\langle l\,|\,\eta_{sj\nu''}\,|\,l_0\rangle\langle i''S'\,|\,s_{j\nu''}\,|\,i''S\rangle].\end{aligned} \tag{A.3}$$

[Compare with Eq. (A9), reference 11.] The separation of i and l is made possible by restriction to the molecular frame coordinate system. Let us schematically write the equation above as

$$\langle il_0\,|\,H_{\rm eff}\,|\,l_0i'\rangle=\sum_{l,i''}([N]_l+[I]_l+[S]_l)([N]_{\langle l\rangle}+[I]_{\langle l\rangle}+[S]_{\langle l\rangle}),$$

where

$$[N]_l=(E_{l0}-E_l)^{-1}\sum_\nu\langle l_0\,|\,A_\nu L_\nu\,|\,l\rangle\langle i\,|\,N_\nu\,|\,i''\rangle \tag{A.4}$$

there will be six types of terms $[N]_l[N]_{\langle l\rangle}$, $([N]_l[I]_{\langle l\rangle}+[I]_l[N]_{\langle l\rangle})$, etc. Table III lists the various types of terms and their effect.

Let us consider first $([N]_l[S]_{\langle l\rangle}+[S]_l[N]_{\langle l\rangle})$ and then $([S]_l[I]_{\langle l\rangle}+[I]_l[S]_{\langle l\rangle})$ in more detail. We note that $A_\nu L_\nu$ does not connect electronic states with different total spin. Therefore $S'=S$ and

$$\langle i''S\,|\,s_{j\nu''}\,|\,i'S\rangle=k_j\langle i''\,|\,S_{\nu''}\,|\,i'\rangle;$$

then

$$\sum_{l,i''}[N]_l[S]_{\langle l\rangle}+[S]_l[N]_{\langle l\rangle}=\sum_{i'',\nu\nu'}M_{\nu\nu'}\langle i\,|\,N_\nu\,|\,i''\rangle\langle i''\,|\,S_{\nu'}\,|\,i'\rangle+M'_{\nu\nu'}\langle i\,|\,S_{\nu'}\,|\,i''\rangle\langle i''\,|\,N_\nu\,|\,i'\rangle \tag{A.5}$$

where

$$\begin{aligned}M_{\nu\nu'}&=\sum_{l\neq l_0,j}(E_{l0}-E_l)^{-1}[\langle l_0\,|\,A_\nu L_\nu\,|\,l\rangle\langle l\,|\,\eta_{sj\nu'}\,|\,l_0\rangle k_j]\\M'_{\nu\nu'}&=\sum_{l\neq l_0,i}(E_{l0}-E_l)^{-1}[k_j\langle l_0\,|\,\eta_{sj\nu'}\,|\,l\rangle\langle l\,|\,A_\nu L_\nu\,|\,l_0\rangle].\end{aligned} \tag{A.6}$$

If $\nu\neq\nu'$, N_ν does not commute with $S_{\nu'}$ since $\mathbf{N}=\mathbf{J}+\mathbf{S}^r$. It is necessary to go to the space-fixed axis system to commute $\mathbf{N}$ and $\mathbf{S}$. Therefore

$$\begin{aligned}\langle i\,|\,H_{sr}\,|\,i'\rangle&=\sum_{\nu\nu',\mu\mu'}M_{\nu\nu'}(\langle i\,|\,\lambda_\nu^\mu N_\mu\lambda_{\nu'}^{\mu'}S_{\mu'}\,|\,i'\rangle+\langle i\,|\,S_{\mu'}\lambda_{\nu'}^{\mu'}N_\mu\lambda_\nu^\mu\,|\,i'\rangle)\\&=\sum_{\nu\nu',\mu\mu'\mu''}M_{\nu\nu'}(2\langle i\,|\,N_\mu\lambda_\nu^\mu\lambda_{\nu'}^{\mu'}S_{\mu'}\,|\,i'\rangle+\langle i\,|\,i\hbar\epsilon_{\mu'\mu\mu''}\lambda_\nu^\mu\lambda_{\nu'}^{\mu''}S_{\mu'}\,|\,i'\rangle)\end{aligned} \tag{A.7}$$

[16] R. S. Henderson, Phys. Rev. **100**, 723 (1955).

where use has been made of the fact that $A_\nu L_\nu$ and η_ν are pure imaginary operators so that $M'_{\nu\nu'}=M_{\nu\nu'}$ and

$$e_{\mu'\mu\mu''}=0 \text{ unless } \mu\neq\mu',\ \mu\neq\mu'',\ \mu'\neq\mu''$$
$$=(-1)^P, \qquad P=\text{parity of the permutation of } \mu'\mu\mu'' \text{ from } Z,\ X,\ Y$$
$$\sum_{\mu\mu'\mu''} e_{\mu'\mu\mu''}\lambda_{\nu'\mu}\lambda_{\nu\mu''}=\sum_{\nu''}\lambda_{\nu'\nu}{}^{\mu'}e^{\nu''}{}_{\nu\nu'} \tag{A.8}$$

and

$$\sum_{\nu\nu'} M_{\nu\nu'}e^{\nu''}{}_{\nu\nu'}=(\nu'')_S$$
$$\mathsf{T}_{1N}{}'''(1)\Rightarrow(\nu'')_S \tag{A.9}$$

The other terms in $\mathsf{T}_{1N}(1)$ arise from the decomposition of $M_{\nu\nu'}$ into trace, skew tensor (axial vector), and symmetric second rank traceless tensor.

The term $[S]_1[I]_{\langle 1\rangle}+[I]_1[S]_{\langle 1\rangle}$ is treated in the same way, except that **S** and **I** commute. It yields three terms, one is absorbed in the dipole-dipole interaction, another in the Fermi interaction leaving only $[\mathsf{T}_{2N}(1)\times\mathbf{S}]_1\cdot\mathbf{I}$ as a new form.

THE JOURNAL OF CHEMICAL PHYSICS VOLUME 35, NUMBER 5 NOVEMBER, 1961

Thermal Dissociation Rate of Hydrogen

W. C. GARDINER, JR.,* AND G. B. KISTIAKOWSKY
Gibbs Chemical Laboratory, Harvard University, Cambridge 38, Massachusetts

(Received February 3, 1961)

The thermal dissociation rate of hydrogen in xenon-hydrogen mixtures has been studied with shock-wave techniques over the temperature range 3000–4500°K. The observed density profiles were consistent with the rate constant expressions:

$H_2+Xe=Xe+2H$ $\quad k=1.8\times10^{17}T^{-1}\exp(-D/RT)$ cm^3 mole^{-1} sec^{-1}

$H_2+H_2=H_2+2H$ $\quad k=1.8\times10^{20}T^{-1}\exp(-D/RT)$ cm^3 mole^{-1} sec^{-1}

$H_2+H=3H$ $\quad k=1.2\times10^{18}T^{-1}\exp(-D/RT)$ cm^3 mole^{-1} sec^{-1}.

THE dissociation of hydrogen molecules into atoms is of interest as the simplest of all chemical reactions. Extensive studies of the reverse reaction have been carried out at low temperature, but a direct study of the dissociation reaction itself at shock-wave temperatures has not been amenable to the usual shock-wave techniques. On the one hand, it is difficult to heat hydrogen strongly with shock waves due to its high sound speed. On the other hand, the progress of the dissociation reaction is difficult to observe by previously used techniques. The electronic transitions available for absorption measurements are all at very short wavelengths, and an interferometric technique would be insensitive due to the low refractive index. The use of soft x-ray absorption for density measurements in detonation waves has been shown to combine reliability and high time resolution.[1] Its application to the measurement of the hydrogen dissociation rate solved both the sound-speed problem and the analytical problem, since the use of xenon as diluent gas and x-ray absorber decreased the sound speed of the experimental gas to a point where strong incident shocks could be obtained with moderate driver-gas pressures.

We have assumed the dissociation to proceed by three bimolecular mechanisms:

$$H_2+Xe\rightarrow Xe+2\,H, \tag{1}$$

$$H_2+H_2\rightarrow H_2+2\,H, \tag{2}$$

$$H_2+H\rightarrow 3\,H. \tag{3}$$

Recent theoretical studies[2] have shown that such a simple scheme certainly does not represent the correct mechanism for the dissociation of diatomic molecules. It is clear that the rate-determining step is the gradual collisional activation to successive vibrational levels until the dissociation limit is approached, rather than a direct transition from the ground or first vibrational level to the continuum. The details of the collisional activation process, however, are still so uncertain that there is no immediate prospect of making reliable rate

* Present address: Department of Chemistry, The University of Texas, Austin 12, Texas.

[1] G. B. Kistiakowsky and P. H. Kydd, J. Chem. Phys. **25,** 824 (1956); J. P. Chesick and G. B. Kistiakowsky, *ibid.* **28,** 956 (1958).

[2] E. V. Stupochenko and A. T. Osipov, J. Phys. Chem. U.S.S.R. **32,** 1673 (1958); E. M. Montroll and K. E. Shuler, Advances in Chem. Phys. **1,** 361 (1959); E. E. Nikitin and N. D. Sokolov, J. Chem. Phys. **31,** 1371 (1959); and others.

TABLE I. Shock conditions before dissociation.

Run	Mixture	Shock velocity	Shock pressure	Shock temperature
		(m/sec)	(atm)	(deg K)
12	4:1	1346	0.6081	4350
13	4:1	1358	0.5926	4420
14	4:1	1313	0.6197	4155
15	4:1	1438	0.5190	4910
18	4:1	1405	0.5334	4700
19	4:1	1413	0.5485	4750
20	4:1	1510	0.4887	5360
21	1:1	1890	0.3629	4670
22	1:1	1583	0.5286	3430
23	1:1	1735	0.4830	4015
24	1:1	1747	0.4827	4065
25	4:1	1364	0.5945	4455
26	1:1	1518	0.5062	3190

calculations using this model. For the purposes of data analysis there would be no advantage in doing so, since dissociation-rate data are not capable of distinguishing between "one-shot" and ladder climbing models.[3] We shall therefore use the classical collision theory expression for the dissociation-rate constants

$$k = CT^{(\frac{1}{2}-s)} \exp(-D/RT), \qquad (4)$$

where D=dissociation energy, C=a constant, and $s=\frac{1}{2}$ the number of classical degrees of freedom of internal energy which can contribute to the dissociation energy, if it is assumed that relative translational energy only along the line of centers can contribute.

Ideally, an experimental study of the dissociation rate should provide values for both s and C. In practice, however, it is difficult to extend measurements over a sufficiently wide temperature range to obtain an independent measurement of s. In this investigation we have assumed values of s and determined the constants C in (4) for reactions (1)–(3).

Separation of the rate constants for reactions (1) and (2) would be accomplished in an ideal case by observing the initial dissociation rates in mixtures containing almost 100% xenon and almost 100% hydrogen, respectively. With these two rate constants determined, the hydrogen-atom rate constant could be found by observing the later stages of the dissociation reaction. The limitations of our apparatus, however, forced a retreat to considerably less ideal conditions. At high xenon concentrations the density changes due to dissociation become small. At high hydrogen concentrations the sound speed of the gas increases to a point where exceedingly high driver-gas pressures are required to produce shocks strong enough to dissociate appreciable fractions of the hydrogen. Preliminary experiments indicated that the former problem would become serious when the xenon content exceeded 80%, and the latter problem would become serious when the hydrogen content exceeded 50%. The compositions used in the experiments reported here were xenon 82.97%, hydrogen 17.03%, xenon 52.33%, and hydrogen 47.67%.

It should be pointed out that since the increase in hydrogen-atom concentration through the shock is accompanied by a very substantial decrease in temperature, any misassignment of temperature dependence to the rate constants (i.e., any error in s or D) will result in an incorrect assessment of the effect of the growing hydrogen-atom concentration on the over-all rate. This inseparability of temperature and hydrogen-atom effects is the major source of uncertainty in the present experimental method. The rate constant for dissociation upon collision with hydrogen atoms which is derived from the results of these experiments is therefore meaningful only to the extent to which the assumed temperature dependence of the rate constants is correct. This point will be discussed again later.

EXPERIMENTAL

The apparatus described previously[1] was rebuilt to permit shock-wave studies under clean vacuum conditions. The shock tube was made from 3-in. i.d. Rockrite steel tubing and had a 10-ft driver section and an 11-ft expansion section. It could be pumped to a vacuum of less than 10^{-5} mm Hg and had an outgassing rate of 2–3 μ/hr. It was cleaned thoroughly with various solvents before experiments were started. The two sections of the tube were separated by Kodapak cellulose acetate diaphragms. Before each experiment all diaphragm fragments from the previous experiment were carefully removed from the tube.

Shock velocities were measured with a series of five ionization gauges equally spaced upstream and downstream of the x-ray slits. The signals were displayed on a raster sweep oscilloscope. Attenuation of the wave was found to be less than 0.2% in 50 cm.

A Machlett AEG 50-A x-ray tube with a copper anode was operated at 28 kv, 21 ma emission current to supply the x-ray power. Sixty-cycle ripple in the x-ray output intensity, a source of data scatter in the previous apparatus, was reduced to less than 5% by using a dc filament supply to the x-ray tube and strongly filtered high voltage. A redesigned slit system allowed the entire solid angle of radiation emitted by the tube to be utilized for absorption measurements. The x-ray beam was defined by 1.5-mm slits through the wall of the shock tube. The curved 0.010-in. beryllium windows were recessed 0.012 in. back from the inside wall of the shock tube. This indentation was the only irregularity presented to the gas flow.

The intensity of the x-ray beam emerging from the shock tube was measured by a detector consisting of a plastic scintillator block (Plastic Scintillator B, Pilot

[3] E. V. Stupochenko and A. T. Osipov, reference 2.

Chemical Company) machined into a truncated rectangular pyramid and a DuMont 6364 photomultiplier tube. To minimize fluorescence loss the sides and top of the pyramid were coated with a thin layer of aluminum. The photomultiplier tube signal was converted to low impedance by a cathode follower and displayed on a Tektronix 531 oscilloscope. A single sweep of the oscilloscope was triggered by the arrival of the shock at a platinum resistance gauge upstream from the slits and was photographed. A circuit for supplying accurately measured simulated photomultiplier currents to the cathode follower allowed calibration lines to be traced on the same photograph.

The effective extinction coefficient of xenon for the 28-kv x rays was determined by static calibration. Experiments with shock waves in pure xenon confirmed that density measurements correct to about 3–4% could be made in single experiments, and that there were no systematic errors.

A shutter prevented the x-ray beam from passing through the shock tube until about 5 msec before the arrival of the shock wave. Synchronization of the shutter and the shock was accomplished by allowing a signal from the opening shutter to trigger a thyratron driven, solenoid operated, diaphragm slitting device.

Experimental mixtures were prepared in a glass vacuum system of conventional design. Hydrogen was prepared from uranium hydride.[4] Xenon was purified by gettering over titanium at 900°C. Mass spectrometric analysis of the gas mixtures indicated that the impurity level was below 0.005%. The compositions of the mixtures were determined by careful manometric measurements during their preparation.

RESULTS

Thirteen experiments were analyzed in this study. Observations were made in incident shocks only. The conditions in these shock waves before the onset of dissociation are summarized in Table I. Shock densities and temperatures were determined from the measured shock velocities by interpolation on graphs constructed using the Rankine-Hugoniot equations and standard enthalpy tables.[5] It was assumed that the vibrational relaxation of the hydrogen was complete before dissociation was appreciable.[6]

Sample oscilloscope records are shown in Fig. 1. Density values were calculated from photomultiplier currents read from the records at 5- or 10-μsec intervals. Reference point for the density measurements was the final density at dissociation equilibrium.

During the dissociation reaction all the hydrodynamic and thermodynamic parameters change by large amounts. Under these circumstances data reduction becomes a complicated affair. The arguments involved are described in Byron's work on oxygen.[7] The advantages of a digital computer for analyzing the experimental data in a situation like this are obvious. We were fortunate in receiving an offer from the United Aircraft Corporation Research Laboratories to use their computation facilities and a program written by R. W. Patch for integrating the hydrodynamic and kinetic equations describing a shock wave in a mixture of dissociating diatomic gas and inert gas. This program accepts an assumed set of rate constants and the conditions in a shock before dissociation commences as input and computes the reaction profile through the wave until dissociation equilibrium is attained. The data-reduction procedure used in this work was therefore a series of comparisons between computed and experimental density profiles, revising the input-rate constants each time until agreement between computed and experimental density profiles was obtained.

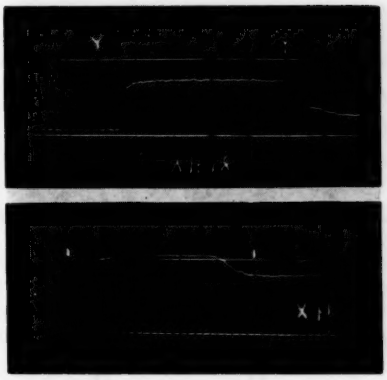

FIG. 1. Sample oscilloscope records. Density increases upwards. Full sweep = 500 μsec.

Experimental values for s in Eq. (4) could not be obtained in this work. The pre-exponential temperature dependence of the rate constants was taken to be the same as that obtained by Byron in his work on the dissociation rate of oxygen.[7] For the atom-molecule reactions, we assume $s=1$ and for the molecule-molecule reaction $s=2$, values which are in accord with the classical collision-theory analysis.[8]

Of the several studies of the gas phase recombination rate of hydrogen atoms the most reliable appears to be that of Farkas and Sachsse.[9] These workers studied the room-temperature recombination rate in the presence of argon as inert gas by a photochemical steady-state method. They found that the rate constants for argon, hydrogen molecules, and hydrogen atoms were the same within the accuracy of their measurements. If it is assumed that the third body efficiency of xenon for recombining hydrogen atoms is

[4] F. H. Spedding *et al.*, Nucleonics **4**, 4 (1949).
[5] *Selected Values of Chemical Thermodynamic Properties* (National Bureau of Standards, Washington, D. C., 1952), Ser. III.
[6] M. Salkoff and E. Bauer, J. Chem. Phys. **29**, 26 (1958).
[7] S. R. Byron, J. Chem. Phys. **30**, 1380 (1959).
[8] R. H. Fowler and E. A. Guggenheim, *Statistical Thermodynamics* (Cambridge University Press, New York, 1952), Chap. 12.
[9] L. Farkas and H. Sachsse, Z. physik. Chem. (Leipzig) **B27**, 111 (1934).

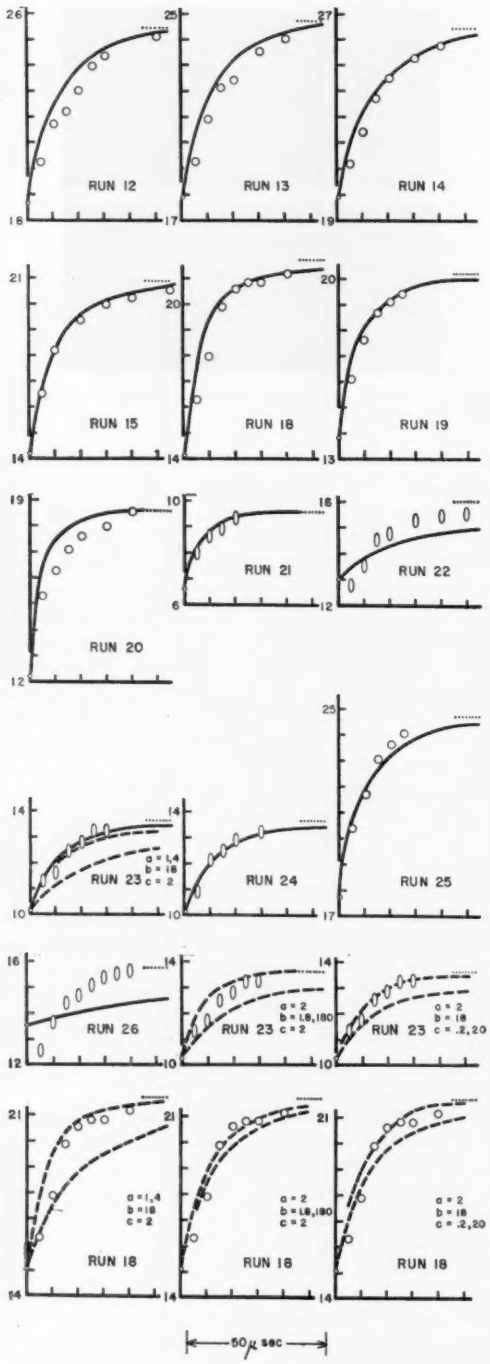
RUN 12
RUN 13
RUN 14
RUN 15
RUN 18
RUN 19
RUN 20
RUN 21
RUN 22
RUN 23 a = 1.4 b = 18 c = 2
RUN 24
RUN 25
RUN 26
RUN 23 a = 2 b = 18,180 c = 2
RUN 23 a = 2 b = 18 c = .2,20
RUN 18 a = 1.4 b = 18 c = 2
RUN 18 a = 2 b = 18,180 c = 2
RUN 18 a = 2 b = 18 c = .2,20
50μ sec

FIG. 2. Comparison of calculated and experimental density profiles. Abscissa = laboratory time, Ordinate = density, g/cc × 10^5. • • • = equilibrium density. ——— = computed using final rate constant expressions. – – – = Computed using the rate-constant expressions $k_{Xe}=a\times10^{17}T^{-\frac{1}{2}}\exp(-D/RT)$, $k_{H_2}=b\times10^{19}\ T^{-\frac{1}{2}}\exp(-D/RT)$, $k_H=c\times10^{17}T^{-\frac{1}{2}}\exp(-D/RT)$.

the same as the third body efficiency of argon, then the recombination-rate constants of Farkas and Sachsse can be converted to the bimolecular dissociation rate constants

$$k_{Xe}=2\times10^{17}T^{-\frac{1}{2}}\exp(-D/RT)\ \text{cm}^3\ \text{mole}^{-1}\ \text{sec}^{-1}$$

$$k_{H_2}=1.8\times10^{20}T^{-\frac{1}{2}}\exp(-D/RT)\ \text{cm}^3\ \text{mole}^{-1}\ \text{sec}^{-1}$$

$$k_H=2\times10^{17}T^{-\frac{1}{2}}\exp(-D/RT)\ \text{cm}^3\ \text{mole}^{-1}\ \text{sec}^{-1}.$$

$$D=4.4769\ \text{ev}.$$

These expressions for the rate constants were taken as a starting point for the first trial integrations. Density profiles were computed for runs 18, 19, 22, and 23. Additional integrations were carried out with increased and decreased values for each of the rate constants separately to determine the magnitude of the effect that such variations would have on the density profile. A check was made to ensure that reducing the size of the integration increment used had no effect on the results.

The density profiles computed for runs 18, 19, and 23 were in reasonable agreement with the experimental results, whereas there was serious disagreement in run 22. The lack of agreement in 22 is discussed below. It appeared that the agreement between calculation and experiment could be improved by reducing the xenon rate constant and increasing the hydrogen-atom rate constant. The former was reduced by a factor of 0.9 and the latter was increased by factors of 6 and 10 for the second set of trial integrations. These were carried out for runs 14, 20, and 21. Comparison of the results indicated that more satisfactory agreement was obtained with the sixfold increase in hydrogen-atom efficiency. The serious disagreement in run 20 is discussed below.

At this point all of the density records were compared with one another and with the computed density profiles. It was decided that no significant improvement in the agreement between computed and experimental density profiles would be obtained by further adjustment of the rate constants. Density profiles were then computed for all 13 experiments using

$$k_{Xe}=1.8\times10^{17}T^{-\frac{1}{2}}\exp(-D/RT)\ \text{cm}^3\ \text{mole}^{-1}\ \text{sec}^{-1}$$

$$k_{H_2}=1.8\times10^{20}T^{-\frac{1}{2}}\exp(-D/RT)\ \text{cm}^3\ \text{mole}^{-1}\ \text{sec}^{-1}$$

$$k_H=1.2\times10^{18}T^{-\frac{1}{2}}\exp(-D/RT)\ \text{cm}^3\ \text{mole}^{-1}\ \text{sec}^{-1}.$$

These profiles and the corresponding experimental data are shown in Fig. 2. The solid lines are computed profiles corresponding to the final rate constants. The other lines correspond to rate constants altered as indicated.

DISCUSSION

The classical collision theory expression for the dissociation rate constant is[8]

$$k=p\sigma^2(8\pi RT/\mu)^{\frac{1}{2}}s!^{-1}(D/RT)^s\exp(-D/RT), \quad (5)$$

where μ=reduced mass of colliding pair, σ=collision diameter, $p=1$ for collisions between unlike molecules and $\frac{1}{2}$ for collisions between like molecules. Equation (5) allows the experimental rate constants to be converted into effective collision diameters for the three collision partners. The collision diameters are thus found to be for xenon 1.2 A, for hydrogen molecules 0.31 A, and for hydrogen atoms 2.6 A. The exceptionally high value for hydrogen atoms is not in agreement with the low-temperature recombination results of Steiner and Wicke.[10]

The form of data reduction used does not lend itself readily to a determination of the error limits within which the rate constants have been measured. An estimate of this can best be made by comparing the agreement between experimental and computed density profiles with the variations in computed density profile effected by altering input-rate constants. The rate constant for xenon is of course the most closely determined and is unlikely to be incorrect by as much as a factor of 2. The rate constants for hydrogen atoms and molecules are probably correct to a factor of 4, if the assumed temperature dependence of the rate constants is correct. To the extent that the classical collision theory is an adequate description of the dissociation process it would seem unreasonable to ascribe such a relatively large collision diameter to the hydrogen atom as follows from the above expressions for the rate constants.

The most uncertain factor in the interpretation of our results lies in the temperature dependence of the rate constants. During the course of the dissociation the temperature changes by as much as 1400°. This means that any misassignment of temperature dependence will lead to a misinterpretation of the relative contribution of the hydrogen atom reaction to the over-all dissociation process, since changing this was the means used to adjust the later portion of the density profiles to agree with the experimental data.

There are two indications that the temperature dependence that we have assigned to the three rate constants may not be correct. First, there is a uniform tendency for the experimental points to lie below the computed density profiles at the start of the dissociation.[11] This means that the rate of dissociation at the higher temperatures prevailing at the start of the dissociation may in fact be lower than it should be compared to the rate later on. Moreover, there is significant disagreement between computed and experimental density profiles for the hottest and coolest shocks (runs 15, 20, 22, and 26). The sense of the disagreement is such as to indicate that the computed rates are too slow at low temperatures and too fast at high temperatures.

The agreement with experiment could be improved by reducing the temperature dependence of the rate constants.[12] For a start it would be quite reasonable to increase the value of s. Camac and Vaughn[13] have recently completed a detailed study of the dissociation of oxygen by argon over the temperature range 3300°–7500°K and find $s=1.5\pm0.2$. We would not feel justified in recomputing all of our results with $s=1.5$ rather than 1.0, since there is no strong analogy between collisions where the masses of the collision partners are about equal and collisions where the mass of one partner is 65 times the mass of the other. Qualitatively, however, we see that such a change would reduce the increase in the xenon rate between 3000° and 5000° by about 30%. This in itself would allow the disagreement at the highest and lowest temperatures to be reduced considerably.

Furthermore, it is by no means impossible that the activation energy for the dissociation might be less than the spectroscopic dissociation energy. The usual requirement that the activation energy of an endothermic reaction must be at least equal to the endothermicity of the reaction presupposes that the reacting molecules are in thermal equilibrium with the heat bath which defines the temperature of the system. This condition, however, is almost certainly not fulfilled in the situation at hand, since it has been shown that the dissociation causes an extensive depopulation of the highest vibrational levels.[2] It does not seem unreasonable to suggest that the process of depopulating the high vibrational levels may be so much faster than the vibrational excitation process, since the former can readily occur by thermal collisions, that all molecules which reach the highest discrete level can just as well be counted as part of the continuum. This is supported

[10] W. Steiner and F. W. Wicke, Z. physik. Chem. Bodenstein Festband, 817 (1931).

[11] In the coolest shocks in the 1:1 mixture (runs 22 and 26) the observed density after 5 μsec is in fact less than the calculated initial density before dissociation starts. If this is a real effect, then it is also an interesting one. An obvious interpretation would be incomplete vibrational equilibration. Theoretical calculations indicate, however, that vibrational relaxation in hydrogen is too fast under these conditions to be observed on the time scale of our experiments.[6] An independent experimental measurement of the hydrogen vibration relaxation time would be required to check this point. A complication due to incomplete rotational equilibration would seem still more unlikely, even though rotational relaxation in hydrogen and translational energy exchange between xenon and hydrogen are inefficient processes. As a result of the extreme difference in mass between hydrogen and xenon the two gases are thermally insulated from one another in passing through the shock front. Immediately behind the wave the xenon temperature is therefore much higher than the hydrogen temperature. Translational relaxation to a common temperature, however, would be expected to be complete in a few hundred collisions at most. Rotational equilibration in hydrogen requires about 300 molecular collisions at room temperature [W. Griffith, J. Appl. Phys. **21,** 1319 (1950)]. Under the conditions of these experiments 1 μsec laboratory time corresponds to about 20 thousand molecular collisions, so that processes on the time scale of hundreds of collisions are not observable. It might be possible to observe a combined translational-rotational relaxation in low-pressure shock waves in xenon-hydrogen mixtures.

[12] In the limited temperature range studied here it would be quite difficult experimentally to determine which temperature-dependent term, i.e., activation energy or s, should be adjusted. These two terms are separable from one another, however, if a wider temperature range is covered.

[13] M. Camac and A. Vaughn, Avco-Everett Research Laboratory Research Rept. 84, AFBMD-TR-60-22 (1959); J. Chem. Phys. **34,** 448, 460 (1961).

by Osipov and Stupochenko's conclusion that transitions from the highest vibrational levels to the continuum are much more probable than transitions between adjacent discrete levels near the dissociation limit.[2] The net result of such a situation would be a slight reduction in the activation energy for the dissociation process as a whole. This, in turn, would easily alter the temperature dependence of the rate constants enough to allow the highest and lowest temperature experiments to be described by the same set of rate constants.

We hesitate, however, to ascribe the disagreement between experimental and computer results to such an effect without further investigation. The strongest argument for this is the excellent agreement with experiment obtained in the oxygen-dissociation study of Camac and Vaughn using an expression of the form of Eq. (4) and the spectroscopic dissociation energy. The upper vibrational levels are more closely spaced in oxygen than in hydrogen, which would mean that any depopulation effect should show itself more strongly in the former. Unless some new evidence becomes available, then, we would be reluctant to propose an activation energy for the hydrogen dissociation reaction other than the spectroscopic dissociation energy.

A large share of the disagreement observed between computed and experimental density profiles for the highest and lowest temperature shocks can be accounted for as indicating that higher values of s in Eq. (1) are more appropriate to the hydrogen-dissociation process. For the present we interpret the remaining disagreement to indicate the presence of an unappreciated experimental difficulty. It does not seem likely that there could be a complication in this temperature range due to incomplete vibrational relaxation of the hydrogen[4] or ionization or electronic excitation of the xenon.[14] It is hoped that an extension of the temperature and composition range studied in the experiments reported here may resolve the difficulty.

ACKNOWLEDGMENTS

We are indebted to R. W. Patch of the United Aircraft Corporation Research Laboratories for his generous assistance with the computations and to P. H. Kydd for helpful discussions.

[14] W. Roth and P. Gloersen, J. Chem. Phys. **29**, 820 (1958).

THE JOURNAL OF CHEMICAL PHYSICS VOLUME 35, NUMBER 5 NOVEMBER, 1961

Proton Magnetic Resonance Study of Ferroelectric Potassium Ferrocyanide Trihydrate

R. Blinc,* M. Brenman,† and J. S. Waugh‡

Department of Chemistry, Laboratory of Chemical and Solid State Physics, and Research Laboratory of Electronics,§ Massachusetts Institute of Technology, Cambridge, Massachusetts

(Received April 13, 1961)

Proton magnetic resonance and vibrational spectra of potassium ferrocyanide trihydrate have been studied between 77° and 300°K. From the observed two sets of O—H stretching frequencies it has been possible to suggest the probable positions of four previously undetermined water molecules in the unit cell. Changes in the vibrational spectra and in the proton resonance second moment in the neighborhood of the Curie point indicate that the onset of ferroelectric behavior is associated with a dynamical orientational ordering of the hydrogen-bonded water molecules. Apparently there is also a contribution to the spontaneous polarization and internal field from displacements and polarizability of the K^+ and $Fe(CN)_6^{-4}$ ions.

INTRODUCTION

FERROELECTRIC phenomena in hydrogen-bonded crystals have been extensively studied in recent years, and every year several new ferroelectrics are discovered. However, our understanding of the basic interactions and the nature of ferroelectricity is not increasing so rapidly, and no comprehensive theory yet exists. In order to improve this situation it seems highly desirable to clarify the role of hydrogen atoms in the ferroelectric transition, i.e., to get precise knowledge of the distribution and dynamics of protons in a number of ferroelectric crystals.

Solid-state proton magnetic resonance studies provide an ideal approach to this problem in many ways, particularly if the interproton distances are of the same order of magnitude as the distances over which important protonic motions occur. In contrast to the situation in ferroelectrics of the KH_2PO_4 type, this condition is obviously fulfilled in the object of the present investigation, potassium ferrocyanide trihydrate, $K_4Fe(CN)_6 \cdot 3H_2O$ (hereinafter abbreviated KFCT), which has recently been found to show ferroelectric behavior below -24.5°C.[1]

* Alfred P. Sloan Postdoctoral Fellow in the School for Advanced Study, on leave from the Institut J. Stefan, Ljubljana, Yugoslavia.

† Buenos Aires University Postdoctoral Fellow, on leave from the National Microbiological Institute, Buenos Aires, Argentina.

‡ Alfred P. Sloan Research Fellow.

§ This work was supported in part by the U. S. Army (Signal Corps), the U. S. Navy (Office of Naval Research), and the U. S. Air Force (Office of Scientific Research, Air Research and Development Command).

[1] S. Waku, H. Hirubayashi, H. Toyoda, and H. Iwusaki, J. Phys. Soc. Japan **14**, 973 (1959).

The dielectric properties of KFCT and deuterated KFCT[2] have been studied in detail and the ferroelectric transitions found to be gradual in nature (presumably of second order). The crystal structure has been studied in both the high- and low-temperature phases.[3,4] It was found that at high temperatures KFCT crystallizes in two modifications: a monoclinic one with space group $C2/c$ having four molecules per unit cell, and a tetragonal one. The tetragonal form suffers an irreversible transition to the monoclinic modification on cooling. The low-temperature ferroelectric phase is also monoclinic but has lost the center of symmetry (the space group is now Cc) and has slightly different unit cell dimensions. The coordinates of the heavier atoms in both high-temperature modifications are known, except that the positions of the hydrogen atoms and of 4 of the 12 water molecules in the unit cell have not been determined. No attempt has been made to find the atomic coordinates in the low-temperature phase and no atomic model for the ferroelectric transition in KFCT has so far been proposed.

The purpose of the present work was to get some information about the distribution and mobility of protons in the low- and high-temperature phases of this substance, and to relate this to possible mechanisms for the ferroelectric transition. Further, it was hoped that some indication might be obtained of the positions of the four, so far undetermined, water molecules by a combined interpretation of NMR and vibrational spectra.

EXPERIMENTAL PROCEDURE AND RESULTS

The broad line magnetic resonance spectrometer and cryostat system used in this study is the lineal descendant of one described previously.[5] An Anderson-type bridge, a permanent magnet, and a fixed frequency (18.3 Mc/sec) oscillator were used. The proton resonance spectra of polycrystalline KFCT were studied over the temperature range 77°–293°K. Because of the large number of interproton vectors in the unit cell and the incomplete knowledge of the x-ray structure, a single crystal study did not seem particularly promising at this stage. All spectra were taken on warming and the temperature was measured with a copper-constantan thermocouple.

The derivatives of the proton absorption lines at 20°, −58°, and −133°C are reproduced in Fig. 1. The room temperature line shape is that expected for highly mobile proton pairs with some intermolecular broadening. The line shape at −58°C exhibits two well-resolved components due to "frozen in" and rapidly reorienting protons, respectively. The width of the narrow component is consistent only with *uncorrelated* molecular reorientation. This suggests a dynamic order-disorder transition with a fair amount of disorder below the Curie point. The amount of "protonic disorder" at −58°C (as calculated from the ratio of the first moments of the absorption derivatives) is approximately the same as the amount of "long-range" dipole disorder calculated from the polarization curves (about 10%).

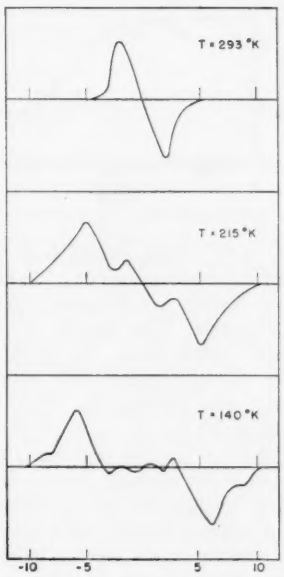

FIG. 1. Proton magnetic resonance absorption derivatives for KFCT powder. The abscissa is in gauss.

The variation of proton resonance linewidth with temperature is shown in Fig. 2, the linewidth being defined as the distance between points of extremal slope. The spectrum below −133°C has only one component, and the linewidth—approximately 12.5 gauss—is of the same order as that observed previously for water molecules in rigid lattices.[6]

The linewidth transition seems to extend over a wide enough temperature range to justify a plot of the correlation frequency vs reciprocal temperature (Fig. 3) as calculated from the BPP formula.[7] From −133° to −30°C we find a nearly straight line showing the validity of the exponential law for the variation of ν_c with temperature, as expected for the case where quantum effects are small. The slope of this line corresponds to an activation energy of 2.5 kcal/mole, which seems reasonable for a motion which should involve the breaking of a weak hydrogen bond and the overcoming of electrostatic interactions. In the vicinity of the Curie point, but still in the ferroelectric range, a break occurs in the $\ln\nu_c$ vs T^{-1} plot, corresponding to a sudden increase in reorientation frequency.

The vibrational spectra of KFCT and the dehydrated

[2] S. Waku, K. Masuno, and T. Tanaka, J. Phys. Soc. Japan **15,** 1698 (1959).
[3] V. A. Posperov and G. S. Zolanov, Zhur. Fiz. Khim. **21,** 405, 521, 879 (1957).
[4] H. Toyoda, N. Niiseki, and S. Waku, J. Phys. Soc. Japan **15,** 1831 (1960).
[5] G. R. Murray, Jr., and J. S. Waugh, J. Chem. Phys. **29,** 207 (1958).
[6] *Tables of Interatomic Distances and Configuration in Molecules and Ions* (Chemical Society, London, 1958), Spec. Publ. No. 11, p. M68.
[7] N. Bloembergen, E. M. Purcell, and R. V. Pound, Phys. Rev. **73,** 679 (1948).

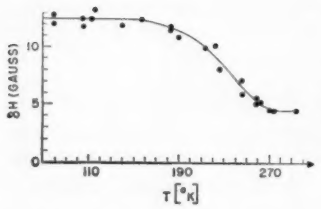

FIG. 2. Linewidth of the proton resonance in KFCT vs temperature.

salt (KFC) were studied both at room and at liquid nitrogen temperatures on a Perkin Elmer 112 and on a Baird-Atomic spectrometer, using LiF, NaCl, and KBr prisms. KBr matrix techniques were used for sample preparation. The room temperature spectra (Fig. 4) agree fairly well with the data of Bonino *et al.*,[8] who studied the vibrational spectrum of the ferrocyanide ion in the nonferroelectric phase. One of the most interesting features is the appearance of two sets of water molecule bands, indicating the existence of two inequivalent sets of hydrogen bonds. The ν_{OH} band centered at 3490 cm^{-1}, showing some smeared out fine structure, and the δ_{OH} band at 1600 cm^{-1} clearly belong to the longer hydrogen bonds. The shoulder at 3270 cm^{-1} and the band at 1630 cm^{-1} represent the stretching and deformation frequencies of the second set of hydrogen bonds, which appear to be of medium length. The intensity ratios of these bands show that the number of longer hydrogen bonds in the unit cell is several times larger than the number of hydrogen bonds of medium length. No librational H_2O bands could be detected at room temperature in the torsion-libration region between 800 and 400 cm^{-1}, showing (in agreement with the NMR data) that the barrier to internal rotation of H_2O molecules must be rather low in the nonferroelectric phase.

The spectra of the low-temperature ferroelectric phase (Fig. 4) exhibit some small but significant changes in the modes involving motions of the protons. However, no drastic frequency shifts have been observed, demonstrating that the phase transition in KFCT is of the order-disorder type as in KH_2PO_4[9] and not a "displacement" type transition.[10]

The frequencies of modes which do not involve proton motions are only slightly changed: The Fe—C stretching frequency at 584 cm^{-1} [Fig. 4(d)], for instance, is shifted by 4 cm^{-1} toward higher frequencies and has some fine structure due to partial lifting of the degeneracy of this mode, showing that the deformation of the $Fe(CN)_6^{-4}$ ion in the ferroelectric phase is very slight.

Furthermore, we may conclude from the vibrational selection rules that in both the high- and low-temperature phases the influence of the crystal field on the $Fe(CN)_6^{-4}$ ion is slight. When the ion can be treated as isolated and of octahedral symmetry only four triply degenerate normal modes of species T_{1u} out of the total of 33 modes (21 "deformations" and 12 "stretchings") are active in absorption. On the other hand, in a monoclinic crystal field with space group

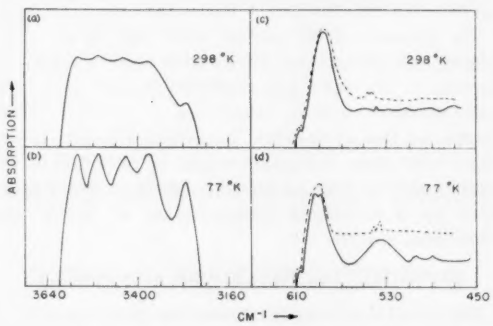

FIG. 4. Infrared spectra of KFCT (solid lines) and KFC (dashed lines) at room and liquid nitrogen temperatures.

$C2/c$ the degeneracy of the bands should be lifted and altogether 16 modes of species A_u should be infrared active. The fact that only three strong $Fe(CN)_6^{-4}$ bands ($\nu_{C\equiv N}=2050$, 2040; $\nu_{Fe-C}=584$ cm^{-1}) occur in the region between 2100 and 500 cm^{-1} supports the above statement. (The fourth T_{1u} mode should be found at lower frequency.)

The ν_{OH} and δ_{OH} bands in the ferroelectric phase occur practically in the same place as in the high-temperature phase, but are now considerably sharper. The fine structure of the ν_{OH} band corresponding to an ordered set of "longer" hydrogen bonds is much more pronounced than at room temperature, and the band is resolved into four components [Fig. 4(b)]. In the torsional region, a completely new band [Fig. 4(d)] appears at 538 cm^{-1}. Since it has no counterpart in the low-temperature spectrum of KFC it must be a water molecule band and can be assigned to one of the librational modes. The fact that this band is found in the ferroelectric phase only (within the wavelength range studied) could perhaps be explained by an in-

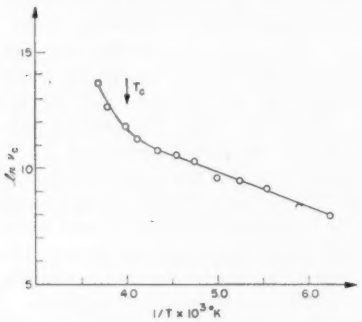

FIG. 3. Logarithm of correlation frequency vs reciprocal temperature.

[8] G. B. Bonino and G. Fabbri, Atti Accad. Nazl. Lincei **19**, 386 (1955).

[9] R. Blinc, J. Phys. Chem. Solids **13**, 204 (1960).

[10] W. Cochran, Phys. Rev. Letters **3**, 412 (1959).

creased barrier to internal rotation of the water molecule—and therefore an increased librational force constant—due possibly to electrostatic dipole-dipole interactions in this phase. The strength of the hydrogen bonds, which also contributes to the restoring force is (as measured by the positions of the ν_{OH} bands) nearly the same in both phases.

DISCUSSION

Two important facts can be adduced from the above data. First, the occurrence of a proton magnetic resonance linewidth transition in the neighborhood of the Curie point suggests that the ferroelectric transition is connected with a rearrangement of the water molecules. Second, the changes in the vibrational spectra, as well as the values of the proton resonance second moments above and below the Curie point (1.9 ± 0.3 and 24 ± 4 gauss^2, respectively) constitute strong evidence for the dynamic order-disorder character of the transition.

In order to relate these experimental results to the molecular mechanism of the ferroelectric transition in more detail, we must first obtain some information about the distribution of the protons in KFCT.

First, the four water molecules per unit cell which have not previously been located by x-ray methods[3] must be found. As was first suggested by Toyoda, Niiseki and Waku,[4] considerations of space group symmetry should place them on the general position 4(e), namely, on the twofold axis. A study of the vibrational spectra confirms this assignment, and furthermore enables us to determine the y coordinates, which are not available from symmetry considerations alone. According to Posperov,[2] 8 of the 12 water molecules in the unit cell lie at the general position 8(f) of $C2/c$, and specifically at the midpoints between centers of symmetry 4(c) or 4(d). Each of these 8(f) H_2O molecules is surrounded by four nitrogen atoms at a relatively large distance of 3.32 A. Thus they cannot be responsible for the OH stretching band at 3270 cm^{-1}, which was assigned to a set of hydrogen bonds of medium length. This band thus clearly belongs to the 4(e) water molecules. Using the relation between ν_{OH} and hydrogen bond length given by Nakamoto, Margoshes and Rundle,[11] and correcting for the nonlinearity of the hydrogen bond, an O—H$\cdots$N bond length of about 2.74 A is obtained. The deviation from linearity was estimated from bonding and potential energy considerations to be 9°. Thus the approximate y coordinate of a 4(e) water molecule is either 0.478 or 0.522; they alternate a bit above and below the $y=0.50$ layer of the 8(f) H_2O molecules in the (010) plane.

The determination of the orientations of the 12 water molecules in the ferroelectric phase represents a problem of quite a different order of magnitude, due to the large number of electronegative nearest neighbors that must be considered. A 4(e) water molecule, for instance, has 7 electronegative near neighbors (two N, four O at a distance of 3.32 A and one N at 2.74 A and

$$\binom{7}{2}=21$$

possible orientations; and an 8(f) water molecule has 4 N and 2 O neighbors at a distance of 3.32 A and therefore 15 possible orientations. Combinations between various orientations of different molecules result in an enormous number of possible models, and clearly there is no straightforward way to determine the proton coordinates from our data. All we can do is to look for models which are consistent with our measurements and with reasonable generalizations about the structure of water molecules in hydrated crystals.

Throughout this procedure we have assumed on the basis of ir evidence that on going from room temperature to the ferroelectric phase the most significant structural change is the rearrangement of protons among possible structural sites. The positions of the heavier atoms—except for K^+ ions, whose absorptions lie outside the region investigated and which have only a minor influence on our results—were explicitly assumed to be the same in both phases. (Small K^+ displacements do apparently occur. See below.) Further, we have assumed that all possible orientations of the water molecules are determined by all possible hydrogen bonds with the closest electronegative atoms. Since it was found in a recent study[12] that H—O—H angles in hydrates are not significantly affected by the atomic environment (they range from 107° to 112°), we have assumed that all H—O—H angles in the unit cell are the same. Our NMR spectra below the linewidth transition, which exhibit only one component, are consistent with this assumption.

In order to reduce the number of unknown parameters we decided to calculate the H_2O interproton distances from line shape data. Thus the intramolecular part of the second moment can be fixed (17.7 gauss^2) and only the intermolecular part, which is very sensitive to the orientations of the water molecules, remains. Using the well-known expression

$$f(h')=(2\pi)^{-\frac{1}{2}}\beta^{-1}\int_{-2\alpha}^{+2\alpha}g(h)\,\exp[-(h'-h)^2(2\beta^2)^{-1}]dh,$$

with $2\alpha=3\mu/r^3$, the observed line shape could be accounted for with $r=1.64\pm0.04$ A and $\beta^2=9$ gauss^2.

The value 1.64 A adopted for the proton-proton distance is slightly larger than the expected value of 1.60 A. However it is within the range 1.53 to 1.65 A quoted by various workers for hydrated compounds. Using 0.98 A for the O—H distance, we get a value of $112°\pm4$ for the H—O—H angles. Comparison of this angle with the angles α formed by the water oxygen and the two electronegative atoms on either side yielded the

[11] K. Nakamoto, M. Margoshes, and R. E. Rundle, J. Am. Chem. Soc. **77**, 6480 (1955).

[12] J. W. McGrath and A. A. Silvidi, J. Chem. Phys. **34**, 322 (1961).

TABLE I. Oxygen and hydrogen coordinates of one asymmetric unit in four models of ferroelectric KFCT.

	A			B			C			D		
Model	x	y	z	x	y	z	x	y	z	x	y	z
O_I	0.000	0.478	0.750	0.000	0.478	0.250	0.000	0.478	0.250	0.000	0.478	0.750
$(H_I)_a$	−0.027	0.532	0.773	−0.027	0.532	0.773	−0.027	0.532	0.773	−0.027	0.532	0.773
$(H_I)_b$	0.058	0.480	0.692	0.058	0.480	0.692	0.058	0.480	0.692	0.058	0.480	0.692
O_{II}	0.250	0.500	1.000	0.250	0.500	1.000	0.250	0.500	1.000	0.250	0.500	1.000
$(H_{II})_a$	0.234	0.550	1.043	0.234	0.550	1.043	0.290	0.451	1.023	0.290	0.451	1.023
$(H_{II})_b$	0.181	0.493	0.933	0.320	0.501	0.933	0.181	0.493	0.933	0.320	0.501	0.933
O_{III}	0.750	0.500	1.000	0.750	0.500	1.000	0.750	0.500	1.000	0.750	0.500	1.000
$(H_{III})_a$	0.820	0.507	1.067	0.679	0.498	1.067	0.820	0.507	1.067	0.820	0.493	0.933
$(H_{III})_b$	0.770	0.450	0.955	0.770	0.450	0.955	0.704	0.553	0.977	0.704	0.553	0.977

amount by which the hydrogen bonds are considered to be bent.

The large number of possible models was reduced by making the following more or less reasonable assumptions:

1. The shortest neighbor distance for the 4(e) water molecules represents a hydrogen bond.
2. There are no hydrogen bonds bent by more than 20°.
3. Each electronegative atom forms at most one hydrogen bond.

Using these assumptions, and remembering that the deviations of the hydrogen bonds from linearity should be as small as possible and that water molecules should, whenever possible, be oriented with their negative poles toward the nearest positive ions, we finally found four possible structural models of low potential energy which all agree with the measured second moment at 77°K within the rather large limits of experimental error.

Table I presents the proton coordinates of the four models. The bonding arrangements, the protonic part of the saturation polarization, and the calculated rigid lattice and room temperature second moments are summarized in Table II. The room temperature second moment was calculated by assuming that the water molecules take on all allowed orientations with equal probability.

In all four models the orientations of the 4(e) H_2O molecules are the same and are chosen to minimize the deviations of both hydrogen bonds from linearity. The differences among the models are due to different orientations of the 8(f) water molecules. In model A, where $\alpha = 104°$ and is thus closest to the gas-phase HOH bond angle of 105°, as well as in model C ($\alpha = 114°$), the 8(f) protons point approximately in the plus

TABLE II. X—O—Y bond angles, protonic polarization, and proton resonance second moments for the four models of Table I. The subscripts on the α's refer to the central oxygen atom of an X—H—O—H—Y hydrogen bond and correspond to Table I. Second moments are in gauss², and polarizations in microcoulomb cm⁻².

α_I	84°	84°	84°	84°
α_{II}	104°	114°	120°	82°
α_{III}	104°	114°	120°	104°
P_∞	1.3	1.3	1.3	4.0
ΔH_2^2 (rigid lattice)	27.1	26.5	25.2	21.6
ΔH_2^2 (″, corrected for libration)	23.3	22.8	21.7	18.7
ΔH_2^2 (room temperature)	1.6	1.6	1.6	1.6

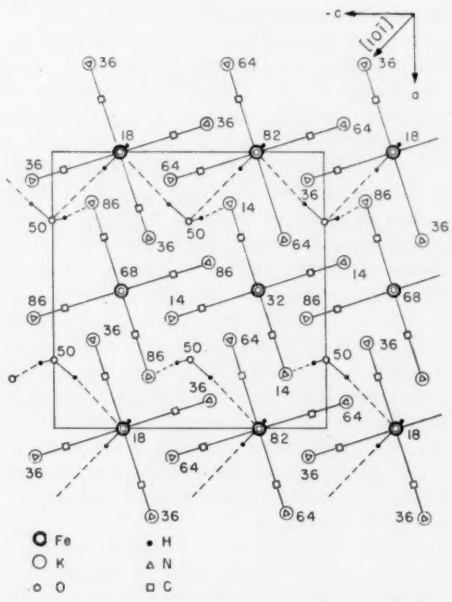

FIG. 5. Projection of the structure of ferroelectric KFCT on the (010) plane according to model A. The figures indicate the height above this plane in units of 0.01 times the b edge. Only the water molecules at level 50 are included.

and minus [101] and [010] directions and their dipole moments cancel in pairs. In model B ($\alpha=120°$), the 8(f) dipole moments again cancel, this time in the [010] and [10$\bar{1}$] directions. In model D ($\alpha=104°$, 82°) the network of hydrogen bonds has the greatest deviations from linearity: On the other hand, this model gives the largest polarization energy. The 8(f) dipole moments cancel in the [010] direction but have a nonvanishing component in the [10$\bar{1}$] direction.

Which of these models represents the true ground state is difficult to decide, though energy considerations as well as polarization data seem to favor model A (Fig. 5). Fortunately it is not essential for our purposes to make this decision.

The point is, that if the 8(f) molecules are left out of the energy considerations entirely, the 4(e) molecules have four equilibrium positions of equal energy, two oriented in the plus and minus [101] and two in the plus and minus [10$\bar{1}$] directions. Introducing the 8(f) molecules according to any of the four models, however, the 4(e) molecules are restricted to only two positions oriented in the [10$\bar{1}$] direction, which is the direction of the ferroelectric axis. The 4(e) molecules thus represent a set of reversible dipoles with two equilibrium positions. The interesting fact is that the direction of the ferroelectric axis is introduced in a natural way from the restrictions put on the 4(e) water molecules resulting from minimization of the crystal energy with respect to the 8(f) water molecules. The ferroelectric state is thus the result of a cooperative ordering of the 4(e) and 8(f) water molecules, though the latter (except in model D) do not contribute to the spontaneous polarization.

According to our NMR data, deviations from the ordered structure show up above −133°C. Evidently the 4(e) water molecules start to reorient about the "short" (2.74 A) hydrogen bond, thus breaking the hydrogen bond which is the weakest because of its deviations from linearity. This lowers the rotational barriers hindering the reorientations of the 8(f) molecules, so that they begin to reorient as well, again providing more "space" for the reorientation of the 4(e) molecules. At −24.5°C the long range order breaks down completely and the spontaneous polarization disappears, though some short range correlations of course remain.

The small value of the room temperature second moment ($\sim$2 gauss^2) shows that the molecules are reorienting in an uncorrelated manner about more than one axis, and the structure is completely disordered, as expected.

While the ferroelectric transition is apparently triggered by the water molecules, preliminary calculations show that the electronic and ionic polarizabilities of K^+ and $Fe(CN)_6^{-4}$ as well as displacements of the K^+ ions contribute significantly to the internal field and spontaneous polarization, thus making the transition possible at such a relatively high temperature.

An argument in favor of the proposed model is offered by the increase of the Curie temperature and saturation polarization on deuteration. As will be shown in a later paper, both these effects can readily be explained in terms of the model proposed if the quantization of the protonic motion is taken into account.

ACKNOWLEDGMENT

The authors wish to thank Professor R. C. Lord for making available the facilities of the M.I.T. Spectroscopy Laboratory and Professor W. M. Whitney for the use of his cryostat.

Meaning of the Tait Coefficients and the Structure of Liquids

ROBERT GINELL*
Department of Chemistry, University of Utah, Salt Lake City, Utah
(Received April 20, 1961)

The coefficient L is in the main concerned with the volume of the large clusters. While this volume is positive for clusters of low molecular weight, it becomes small and finally negative as the clusters increase in size. The clusters can increase in size due to a temperature rise or an increase in molecular weight. Hence the value of L goes through a maximum. It is shown that at the critical temperature $P_c = -L$. Calculations from this relationship give the critical pressure of liquid helium I to be 2.258 atm (experimentally 2.26 atm). This relationship also gives insight into the nature of the critical state. The coefficient J is a function of the change in the fraction of holes with a change in volume at constant temperature. While J appears to be constant with pressure along an isotherm, it is not, however, constant with temperature; it is only a slowly varying function. Various deductions are drawn from the fact that J has almost the same value for groups of related substances. A resume of the structure of liquids in the light of this theory is given.

IN previous papers[1,2] it has been shown that the Tait equation for the isothermal compressibility of liquids can readily be derived from the general equation of state.[3] The Tait equation contains two constants J and L which have been found by several investigators[4–8] to be constant along an isotherm for quite high pressures for a wide variety of liquids. In addition, Gibson and Loeffler have found from their work[4,5] that the constant J is equal to v_0C, where v_0 is the specific volume at 1 atm and C is a constant independent of temperature and that, if a group of related systems are considered, C has the same value in these related substances, all within experimental error. For instance, they found that C for water and concentrated salt solutions in water is the same; also, that benzene, chlorobenzene, brombobenzene, nitrobenzene, and aniline have the same C within experimental error. Carl[7] and Wohl[6] who made calculations on data over a larger range of temperatures, found, however, that C was not a constant with temperature. In view of the fact that the derivation of the Tait equation now ascribes meaning to these constants in terms of the variables in the system, in this paper we shall inquire into the reason for the constancy of these functions and their relation in the nature of the liquid state.

THE CONSTANT L

There has been considerable discussion in the literature as to the exact meaning of L. Wohl[6] and Carl[7] considered it to be some sort of internal pressure. From the thermodynamic definition of internal pressure[9] this is not very probable. Gibson and Loeffler,[5] on the other hand, consider the quantity $(L+P)$ to be equal to the difference between the thermal and attractive pressures or equivalently to the repulsive pressure. While this latter hypothesis is quite attractive, it is rather intuitive in nature.

Similarly, there appear in the literature a number of attempts to represent the variation of L with temperature in a mathematical way. For the range 0–80°C, Wohl[6] considered L to be a linear function of the temperature, namely,

$$L=[b(T_c/T)]-c, \tag{1}$$

where b and c are constants, T_c is the critical temperature, and T is the absolute temperature. Carl, who continued the work of Wohl, used the same relationship. On the other hand, Gibson and Loeffler used an empirical second-order curve of the form

$$L=A+BT+CT^2 \tag{2}$$

to represent their L values in the range from 25° to 85°C. They admit however that this representation is the "weakest part of the whole calculation."

In reality the value of L appears from preliminary calculations from experimental data to be a curve. For water, benzene, and benzene derivatives it has a shape roughly similar to that in Fig. 1. Most of the data and calculations in the literature are too scanty and do not cover a wide enough range to bring out all the features of the curve. But in the helium I[10] liquid, where the range covered is large enough, it can be seen clearly that L is a curve, although experimental uncertainties at this temperature range and propagated calculation errors tend to cloud the exact shape of the curve. The leg of the curve on the high-temperature side appears to be approaching a straight line as we approach the critical temperature.

* Permanent address: Department of Chemistry, Brooklyn College, on leave 1960–61.
[1] R. Ginell, J. Chem. Phys. **34,** 1249 (1961).
[2] R. Ginell, J. Chem. Phys. **34,** 2174 (1961).
[3] R. Ginell, J. Chem. Phys. **23,** 2395 (1955).
[4] R. E. Gibson and O. H. Loeffler, Ann. N. Y. Acad. Sci. **51,** 727 (1949).
[5] R. E. Gibson and O. H. Loeffler, J. Am. Chem. Soc. **61,** 2515 (1939).
[6] A. Wohl, Z. physik. Chem. **99,** 234 (1921).
[7] A. Carl, Z. physik. Chem. **101,** 238 (1922).
[8] P. G. Tait, *Scientific Papers* (Cambridge University Press, New York, 1898), Vols. 1 and 2.
[9] J. O. Hirschfelder, C. F. Curtiss, and R. B. Bird, *Molecular Theory of Gases and Liquids* (John Wiley & Sons, Inc., New York, 1954).
[10] R. Ginell, J. Chem. Phys. **35,** 473 (1961).

The Constant L and the Critical Pressure

This straight line character of the L vs T curve as the critical pressure is approached enables us to make some rather interesting calculations. The Tait equation can be written in the form

$$-J(\partial P/\partial v)_T = L + P. \tag{3}$$

At the critical point $(\partial P/\partial v)_T = 0$, hence,

$$P_c = -L. \tag{4}$$

Since P_c is a positive number, this implies that L must become negative as the temperature increases towards the critical temperature. If one examines the data of Wohl, one sees that in fact he does obtain negative L's under some conditions, but the calculations are nowhere complete enough to verify this relationship. Completely negative values for L are also obtained for glass in some recent calculations.[11] However, it is interesting to see

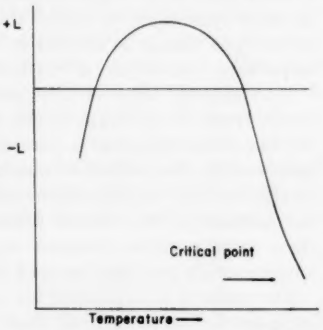

FIG. 1. Schematic sketch of variation of L with temperature.

whether this relationship is real and not some relationship that arises from the inadequacies of the Tait equation. Suitable data for such a calculation is given in a paper [10] on liquid helium I. The values of L from this paper are reproduced in Table I. Since these values define a curve, only the values on the high-temperature leg have been used; quite arbitrarily those from 2.25° to 4.20°K. The points scatter because they include a propagated computational error and an experimental error, although the latter is probably small. A rough graphical extrapolation to 5.20°K $(=T_c)$ showed that indeed L does become negative. A least-square computation on these six points was then performed in three different ways: The temperature was minimized; the temperature and L were minimized; and L was minimized. The results are shown in Table I. Apparently minimization of the temperature gives the lowest average deviation and the closest agreement with the accepted value of P_c, but why minimization of the temperature alone should give the best values is problematic. However, the whole calculation is based on only six values and the extrapolation is quite extensive considering the extent of the temperature range of liquid helium; so on the whole the agreement can be considered good.

TABLE I. Liquid helium I.[a]

T °K	L
1.90	−9.4389
2.00	+6.9831
2.10	9.8629
2.20	8.6281
2.25	8.6675
2.50	7.8792
3.00	6.3891
3.50	4.0128
4.00	2.0364
4.20	1.6239

Extrapolated values of L		P_c[b]	% error	
5.20	−2.258±0.168 (av. deviation)	2.258	0.08	(T minimized)
5.20	−2.284±0.172 (av. deviation)	2.284	1.06	(T and L minimized)
5.20	−2.299±0.173 (av. deviation)	2.299	1.71	(L minimized)

[a] For data, see reference 10.
[b] P_c=2.26 (accepted experimental value).

Most of the values of L as found in the literature are determined over a small range of temperature at or near the crest of the curve of L vs T[4,5] or are very scattered[6] or are in the wrong range, so that the determination of P_c can only be carried out very roughly, if at all. Rough graphical extrapolation using data of Wohl and Carl gives the critical pressure of ethyl ether as 36 atm, whereas the experimental value is 35.5 atm; other data for other substances, although badly scattered, are not inconsistant with the idea that the value of L at the critical temperature is equal to the critical pressure. Careful determination of the variation of L with temperature will probably show that this relationship holds and that it is not an accidental relationship. Proof of this will establish the critical pressure once the compressibility data are known and also will serve as a check

TABLE II. Water.[a] P=1 atm.

°C[b]	$Z_n A_{25}$	$[(v-b)/A_{25}]10^{-5}$ ml/g	L atm	v ml/g
25	0.04169	0.3257	2956.8	1.00294
35	0.04141	0.3389	3015.0	1.00598
45	0.04106	0.3530	3040.7	1.00985
55	0.04064	0.3678	3037.7	1.01448
65	0.04020	0.3831	3012.1	1.01979
75	0.03974	0.3990	2965.7	1.02576

[a] Calculations taken from reference 2 and R. Ginell, J. Chem. Phys. **35**, 1135 (1961).
[b] In going from 25° to 75°C the percentage increase in volume/g=2.30% and the percentage increase in volume of holes/g=22.5%.

[11] S. D. Brown and R. Ginell, "On the partial structure of glass and the reconstructive nature of devitrification processes," presented at American Ceramic Society meeting, Toronto, Canada, April 24–27, 1961.

on the reliability of the compressibility data, if the critical pressure is known.

Meaning of L

According to the concept of Gibson and Loeffler, the function $(L+P)$ represents the repulsive pressure; therefore, according to the above relationship, the repulsive pressure must be zero at the critical point and as the pressure increases (at T constant) beyond the critical pressure, the repulsive pressure increases. This is a reasonable concept and one concludes from this that at the critical temperature and at pressures higher than critical, the only force that keeps the liquid together is the external pressure. The value of $(L+P)$ at other temperatures does not offer a clear-cut picture of what L is. A better concept, which offers some insight into the nature of the liquid state, is given by an equation derived in a previous publication.[1] According to this equation

$$L=RTw/M^0\Sigma i\mathfrak{b}_iN_i, \tag{5}$$

where R and T have their usual meaning, w is the weight of the sample, M^0 is the molecular weight of the 1-mer, N_i is the number of particles of size i in the sample, and $\mathfrak{b}_i$ is the excluded volume of the particle of size i.

If L at higher temperatures and especially near the critical point becomes negative, the only factor in the right-hand side of this equation that can possibly become negative simultaneously is $\mathfrak{b}_i$. The other terms from their very definition are positive. It should be noticed that the quantity $\Sigma i\mathfrak{b}_iN_i$ is so constituted that it is heavily weighted towards the larger particles. For instance, $\mathfrak{b}_iN_i$ represents the total excluded volume of j-mers of size i. Multiplying this factor by i means that we add in the sum, the total volume of the j-mers of size 50, 50 times, while we add the volume of the j-mers of size 2 only twice. That is, the value of the sum depends more on the large particles than on the small particles because of this weighing factor i. This means that if the liquid is conceived as consisting of large particles connected by defects, which are small particles in holes joining the large particles, the value of this expression depends in the greater part on what happens to the large particles.

For L to become negative as the temperature increases the only possible explanation is that the excluded volume of the large particles becomes negative, or, in other words, as the temperature increases, the large particles no longer exclude small particles. Equivalently we may think of this process as follows. At low temperatures the volume of the large particles is positive and is a compact mass resisting the entry of small particles, 1-mers for example, into their occupied space. As the temperature rises they expand in volume. While the average molecular weight of the particles decreases with rise in temperature, as shown by the decrease in the average degree of association Z_n, the remaining ones must also increase in volume. This increase in volume makes them penetrable by very small particles (1-mers) so that $\mathfrak{b}_i$ becomes negative for large values of i. This implies that the clusters are very loose and perhaps hollow in structure. This concept of rather hollow large clusters is consistent with the picture advanced recently by Pauling[12] and others.[13]

CHANGE IN THE VOLUME OF HOLES AND THE CRITICAL STATE

In normal liquids like water, as the temperature increases, the volume of holes increases much more than the volume of the liquid. This is shown in Table II.

We must be careful in defining here what we mean by the volume of holes. Every cluster of size i has a volume $\mathfrak{b}_i$ per mole. This cluster may be loose or relatively tight; that is, it may include in itself (in $\mathfrak{b}_i$) voids of various sizes. The volume of holes we are discussing in this section are given by the relation $(v-\mathfrak{b})$ where $\mathfrak{b}$ is the sum of all the cluster volumes $(\Sigma\mathfrak{b}_iN_i)$. These two kinds of holes must be distinguished from each other. Perhaps the first type could be called cluster voids, while the latter type would be labeled free holes, free volume, or perhaps even better, defect holes.

Undoubtedly some of this increase in free volume comes from the decrease in the degree in association, i.e., due to breakup of large particles and the subsequent release of the cluster-hole volume in these large particles to the free-hole volume. However, the greater part of the increase in free volume probably is because $\mathfrak{b}_i$ in these large particles becomes negative; i.e., they no longer exclude particles but suck them into themselves.

The value of $\mathfrak{b}_i$ is positive for small values of i. As i increases $\mathfrak{b}_i$ increases first, then the rate of increase slows down and later the value of $\mathfrak{b}_i$ starts decreasing and finally becomes negative. This means that as the maximum size of the clusters in the liquid increases, or alternately as the temperature increases (L becomes negative) the value of $\mathfrak{b}$ which is the equal to the $\Sigma\mathfrak{b}_iN_i$ decreases. This means that the value of the free volume $(v-\mathfrak{b})$ increases.

Hence two processes are occuring simultaneously; first the very large particles are breaking up and second, some of the very small particles (probably 1-mers) are being sucked into the remaining large particles. The result is that the free-hole volume or defect space between the large clusters is increased. The very small particles are in a sense the cement which holds the large particles together to form the liquid. As the temperature rises the free volume or space increases. At the critical point, the free volume is so large, that the number of small particles are insufficient to hold the large particles together and the material becomes a gas, unless the particles are pushed together by an external pressure.

One other point concerning L needs to be explained. It will be noticed from plots of L vs T that L tends to also decrease as the temperature decreases. Here the degree of association is increasing and more large par-

[12] L. Pauling, *The Nature of the Chemical Bond* (Cornell University Press, Ithaca, New York, 1960), 3rd ed.
[13] H. S. Frank and A. S. Quist, J. Chem. Phys. **34**, 604 (1961).

ticles are being formed. Apparently these very large particles have a looser structure. In a way this is understandable. These large clusters can readily rearrange and merge the holes included in their structure so as to include more particles. Thus the $\mathfrak{b}_i$ in such cases is also negative.

So now the meaning of L is somewhat clearer than before. L in the main is a measure of the excluded volume of the large particles. The excluded volume may be positive or negative; i.e., it may exclude 1-mers or attract and include them. At very low temperatures, very large clusters exist which are loose in structure and have a negative $\mathfrak{b}_i$. The small particles probably always have a positive $\mathfrak{b}_i$. As the temperature increases, the average molecular weight of the particles decreases meaning that the very large particles with negative $\mathfrak{b}_i$ disappear and L becomes progressively more positive. At the same time due to the increase in temperature, the bonds are loosening and the volume of the particles is slowly increasing. With further increase in the temperature, the process is accelerated and finally the large particles present also acquire a negative $\mathfrak{b}_i$. This again decreases the value of L. Finally the continued breakdown of the larger particles results in so much free volume being present, that the small particles (1-mers) in the defects can no longer hold the large clusters together and we have reached the critical temperature where the large particles are only held together by the external pressure.

MEANING OF J

There has not been as much discussion in the literature [14] as to the nature of the function J as there has been for L. The best way of approaching J is through an examination of the formula for the free volume of holes in the liquid as given in a previous publication,[2] namely

$$(v-\mathfrak{b})=ARTwve^{v/J}/M^0. \tag{6}$$

Dividing both sides by v, and then differentiating the logarithm of this function with respect to v at constant T, we get

$$\{\partial \ln[1-(\mathfrak{b}/v)]/\partial v\}_T=1/J. \tag{7}$$

Thus J is the reciprocal of the change of the logarithm of the fraction of holes with respect to a change in volume at constant temperature. Since the fraction of the volume of holes does not change too greatly[2] over the range in pressure usually experienced, the logarithm of this quantity changes still less. Hence it is not surprising that within experimental error Gibson and Loeffler found over the temperature range that they examined that the constant C in the relation $J=Cv_0$ was constant. However, Wohl and Carl, who did calculations over a much larger range in temperature, expressed J as

$$J=\alpha v_0, \tag{8}$$

where v_0 was the specific volume of the substance at 1 atm and the particular temperature being considered.

They considered α to be a constant for all temperatures for any particular substance although in certain cases where the calculations were carried out over a larger temperature range, they were forced to use different α's over different temperature ranges. In general they found that J was not constant with temperature although it was constant with pressure. From Eq. (7) it can be seen that J is not a constant but rather a term whose value changes slowly. If J is expressed as Cv_0 since v_0 also varies slowly, then C could readily be considered an empirical constant if the experimental data were not too precise. In essence J is a measure of the change in the volume of holes.

From the Gibson and Loeffler data we see that they have found that C for related groups of substances, for example, benzene, and benzene derivatives, or water and concentrated aqueous solutions, is the same, empirically within experimental error. This fact enables us to draw some interesting deductions. While direct comparisons of the volume of holes between these systems is impossible at present owing to the fact that the integration factor A is unknown, the fact that J, the reciprocal of the rate change of the logarithm of the fraction of holes with a change in volume at constant temperature, is almost the same for benzene, chloro- and bromobenzene, nitrobenzene, and aniline, points to one important fact. It must be true that the forces surrounding or in the holes are the same, since the behavior of the hole is alike on compression. This in turn must mean that the groups surrounding the holes are approximately alike. In turn, this forces us to the conclusion that the active group in each of these benzene derivatives is enclosed in the large clusters and not exposed in the defect volume. In the case of water and salt solutions, again $C=J/v_0$ is the same within experimental error. Here, since C is different from that of benzene, the forces are different. Also, this must mean that the salt molecules are enclosed in a sheath or envelope of water, so that the environment of the holes is the same. These conclusions seem seem very reasonable, especially so, if one considers in this connection the structure of clathrates and recent work on the structure of water.[12,13]

STRUCTURE OF LIQUIDS

We can now summarize how this theory depicts the structure of liquids. Liquids apparently consist of two components: large clusters and defects. The large clusters include in themselves a certain amount of space called cluster voids. The clusters are asymmetric as a whole, but locally in the cluster approximate fivefold symmetry, and a coordination number of 12 is exhibited. The defects contain free space and probably very small j-mers. These small j-mers are most likely 1-mers and 2-mers, which serve as bridges between the large clusters

[14] See, for instance, R. E. Gibson and O. H. Loeffler, J. Phys. Chem. **43**, 207 (1939).

and hold the liquid together. The factor L in Tait's equation is to a greater part a function of the volume of the large clusters. This volume when the particles are small, pre-empties the space it occupies. As the particles increase in size, they no longer exclude particles from their structure. That is, as they increase in size, their structure becomes progressively looser and perhaps hollower. Increase in temperature has two effects, first it decreases the average molecular weight of the particle, and second it increases the volume of the remaining particles (b_i). This is the reason why L first increases in value, then decreases in value, finally becoming negative as we come nearer to the critical point. Increase in temperature results in a more rapid increase in the free volume than in the specific volume. As a result, at the critical point the number of small j-mers in the defects is no longer sufficient to hold the liquid together and it becomes a gas.

The coefficient J in the Tait equation is concerned with the change in the fraction of free holes in the liquid. In groups of related substances apparently the differing substituents are held inside the large clusters so that the environment surrounding the defects is the same. This behavior is mirrored in the fact that groups of related substances have the same value of the coefficient $C=J/v_0$. In binary systems in water, apparently the salt molecules are in the clusters surrounded by an envelope of water molecules. Pressure has the effect of decreasing the average molecular weight of clusters and the decrease in the volume is mainly at the expense of the free volume.

ACKNOWLEDGMENT

The courtesy and help of Dr. H. Eyring and the University of Utah in enabling me to complete this paper is acknowledged.

THE JOURNAL OF CHEMICAL PHYSICS VOLUME 35, NUMBER 5 NOVEMBER, 1961

Effect of Pressure on the Optical Properties of Organic Phosphors*

D. W. GREGG AND H. G. DRICKAMER

Department of Chemistry and Chemical Engineering, University of Illinois, Urbana, Illinois

(Received April 26, 1961)

The effect of pressure to 54 kbar has been measured on absorption spectra, emission spectra, and decay rates of four organic phosphors. For fluorescein and dichlorofluorescein the decay rate increases with increasing pressure. The emission spectrum consists of two peaks which approach each other at high pressure. Thus there appears to be an increased mixing of triplet and excited singlet states at high pressure.

For acridine yellow and orange the absorption spectrum shows a dimer and monomer peak. The dimer peak decreases rapidly in intensity with increasing pressure. At high concentrations the component decay rates are largely independent of pressure. At lower concentrations the decay rate becomes slower at higher pressure. Evidently the emission can be associated with the dimer.

THE effect of pressure to 54 kbars has been measured on the absorption spectra, emission spectra, and decay rates of four organic phosphors. These include fluorescein, dichlorofluorescein, acridine orange, and acridine yellow. The formulas are shown in Fig. 1. The fluorescein and dichlorofluorescein were cp from Eastman Organic Chemicals Company. The acridine orange and acridine yellow were Matheson Coleman and Bell pure grade. The compounds were dissolved in boric acid glass.

The apparatus for absorption spectra studies has been previously described[1] as has the equipment for phosphor decay measurements.[2] The emission peaks were measured using a Steinheil Munchen spectrograph model 5063 with Royal X Pan film and the equipment arrangement used for decay studies. A Knorr-Albers microphotometer connected to a Speedomax recorder was used to measure film density.

Since the windows of the bomb subtend only a small solid angle for light emitted in the bomb, the emission spectra took from 30 min to 6 hr to give measurable density at any one pressure.

One point of interest can be noted from all the data. The runs were never quite reversible, indicating a permanent change in the structure of the boric acid matrix. This effect was not large enough to affect the interpretation of results.

Two energy diagrams which have application to many organic phosphors are presented in Fig. 2. The diagram in Fig. 2(a) was presented by Lewis[3,4] for fluoroescein, and the diagram in Fig. 2(b) is a simplified energy vs configurational coordinate diagram of Fig. 2(a). It illustrates one additional necessary condition for phos-

* This work was supported in part by the U. S. Atomic Energy Commission.

[1] R. A. Fitch, T. E. Slykhouse, and H. G. Drickamer, J. Opt. Soc. Am. **47**, 1015 (1957).

[2] D. W. Gregg and H. G. Drickamer, J. Appl. Phys. **31**, 494 (1960).

[3] G. N. Lewis, D. Lipkin, and T. Magel, J. Am. Chem. Soc. **63**, 3005 (1941).

[4] G. N. Lewis and M. Kasha, J. Am. Chem. Soc. **66**, 2100 (1944).

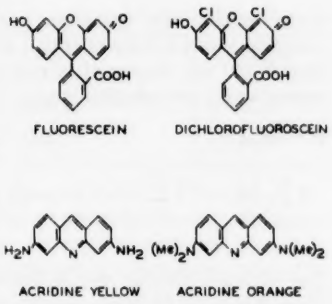

FIG. 1. Structural formulas.

phorescence in many organic phosphors, the crossing or close approach of the energy levels of the S_1 and T_1 states.

S and T represent singlet and triplet states, respectively. Transitions between states of the same multiplicity, $S_n \rightarrow S_m$ or $T_n \rightarrow T_m$, are spin allowed, but transitions between states of different multiplicity, $S \rightarrow T$ or $T \rightarrow S$, are spin forbidden. However, there are conditions under which spin-forbidden transitions can take place, but with considerably less probability than spin-allowed transitions. It is this sort of transition which is responsible for phosphorescence in organic compounds.

The excitation process involves a $S_0 \rightarrow S_1$ step followed by a rapid transition to the T_1 state, where the electron is trapped and released later as phosphorescence. The $S_0 \rightarrow S_1$ transition is spin allowed and appears as a strong peak in the absorption spectrum whereas the transition $S_0 \rightarrow T_1$ is spin forbidden and is usually not detected in the absorption spectrum. Since the transition, $S_1 \rightarrow S_0$, takes place in the order of 10^{-9} sec, it is necessary for the $S_1 \rightarrow T_1$ transition to be highly allowed or all the excited electrons will return to the ground state without being trapped. This transition is spin forbidden, so a possible explanation for its probability is presented with the aid of Fig. 2(b). The transition probability between two electronic states is inversely proportional to the square of the energy difference between them. If the S_1 and T_1 states have an energy crossing or position of close approach as illustrated at y the transition probability would be high at this point even between states with different spins.

After the electron is trapped in the T_1 state it can return to the ground state by several paths, two of which emit phosphorescence. The nonemitting paths, involving quenching of the phosphor, are minimized in glasses. The two emitting paths are: (1) the direct transition

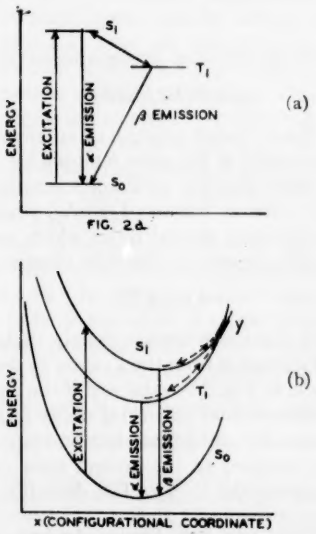

FIG. 2. Energy diagrams for organic phosphors.

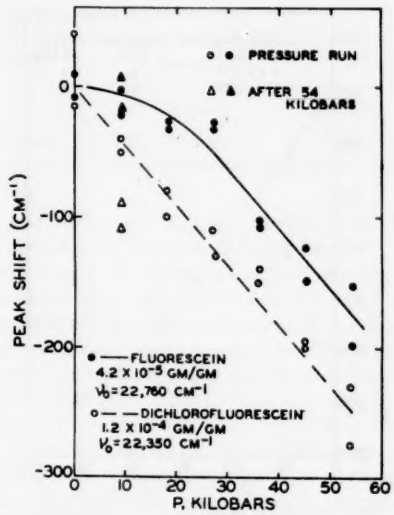

FIG. 3. Shift of absorption peak maxima vs pressure—fluorescein and dichlorofluorescein.

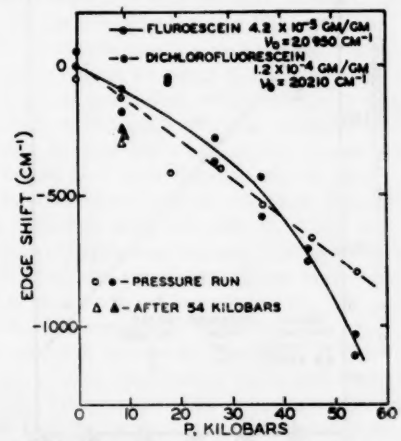

FIG. 4. Shift of low-energy edge of absorption peak vs pressure—fluorescein and dichlorofluorescein.

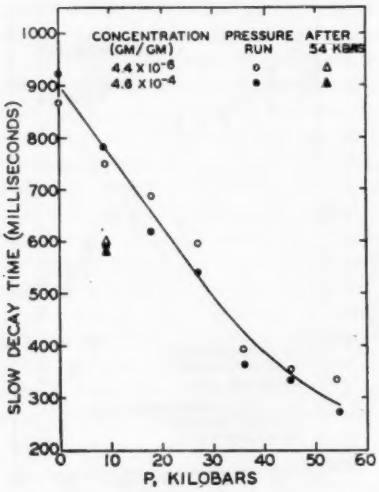

FIG. 5. Slow component decay time vs pressure for two concentrations—fluorescein in boric acid.

from the T_1 state to the S_0 state, called beta emission, and (2) the thermal re-excitation of the electron through point y to the S_1 state from where it then makes the radiative transition to the S_0 state, called alpha emission. The intensity of the alpha emission is quite temperature dependent, whereas that of the beta emission is not as much so. At room temperature, depending on the phosphor, one of these processes may be controlling or they may take place with nearly equal probability.

A spin-forbidden transition is totally forbidden if the spin and orbital momentum of the electron are completely separate. However, under the proper conditions there may be a certain amount of coupling between them making the transition partially allowed. The coupling allows a state of spin a to mix with a state of spin b and the degree of mixing may be found from second-order perturbation theory and is given by[5]

$$\psi^1=\psi_{(s=a)}{}^0 + \sum_j \int \psi_{(s=a)}{}^{0*}\Big[\sum_i \zeta_{nl} l_i s_i\Big]\psi_{j(s=b)}\,d\tau \Big/ (E_a - E_j)\psi_{j(s=b)}. \tag{1}$$

The mixing coefficient may be abbreviated to $K\zeta_{nl}/\Delta E$, where k is in the order of unity. ζ_{nl} is the coupling coefficient. In terms of oscillator strength we have[5]

$$f_{ab}=f^0(K\zeta_{nl}/\Delta E)^2, \tag{2}$$

where f^0 is the oscillator strength of an allowed transition between states of the same multiplicity.

Forster[6] shows that the oscillator strength is related to the decay time as follows: $1/\tau=Kf$, where K is a coefficient containing several terms which are not important for this argument. One then obtains

$$\tau=K'(\Delta E)^2. \tag{3}$$

The above discussion applies mainly to beta decay where the transition is from the T_1 state to the S_0 state.

If the model in Fig. 2 is valid and if the alpha, beta, and any monomolecular quenching decay processes are the only means by which the electron trapped in the triplet state returned to the ground state one would expect an exponential decay. The deviation from an

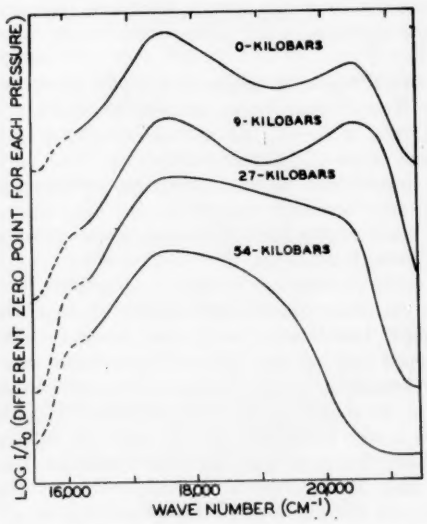

FIG. 7. Emission spectra of fluorescein in boric acid 4.6×10^{-4} g/g.

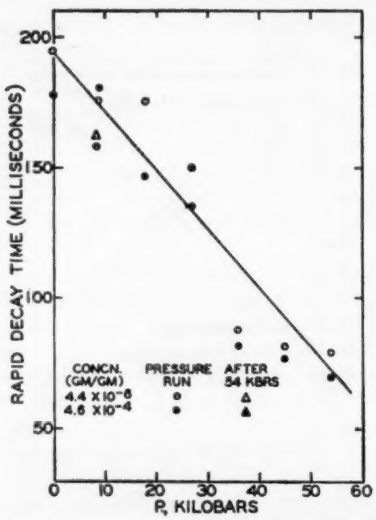

FIG. 6. Rapid component decay time vs pressure for two concentrations—fluorescein in boric acid.

[5] D. S. McClure, *Solid-State Physics* (Academic Press Inc., New York, 1959), Vol. 9, p. 400.

[6] T. Forster, *Fluoreszenz organischer Verleindungen* (Vandenhoek and Ruprecht, Göttingen, 1951).

TABLE I. Comparison of calculated and measured τ.

Pressure	E	τ_1 (measured)	τ_1 (calc)	τ_2 (measured)	τ_2 (calc)
atm	2920 cm^{-1}	900 msec		194 msec	
54 kbar	1600 cm^{-1}	285 msec	(271 msec)	70 msec	(58.3 msec)

exponential decay is most likely due to different molecules having different interactions with the surroundings. This is discussed thoroughly by other authors,[7–13] who propose representing the decay as a summation of exponentials. The reasons for representing the decay as a summation of exponentials are not important for the interpretation of the pressure data and thus will not be considered here. In this work they are represented as such mostly because it is a convenient method of characterizing them.

I. EFFECT OF PRESSURE ON FLUORESCEIN AND DICHLOROFLUORESCEIN PHOSPHORS

Fluorescein and dichlorofluorescein are discussed together because of their similar structural formulas and their similar characteristics under pressure. The results are presented and discussed in three parts: (1) the effect of pressure on the absorption spectra and decay rates of the two compounds, (2) the effect of pressure on the emission spectra of fluorescein, and (3) an interpretation of the results.

Figure 3 shows the shift of the absorption maxima with pressure. These correspond to the $S_0 \rightarrow S_1$ transition in Fig. 2. They both exhibit a single peak which shifts red with pressure, dichlorofluorescein shifting slightly more than fluorescein. However, the most important characteristic that they both exhibit is the large red shift of their low-energy edges. These shifts, presented in Fig. 4, are much larger than the shift of their respective peak maxima. They are important because they represent the shift of the lower edge of the S_1 state from whence the alpha emission takes place. This large shift of the red edge is not completely understood. It can not be explained by a simple broadening of the peak since there is no simililar effect observed on its blue edge. It corresponds to a change of shape of the S_1 state as illustrated in Fig. 2(b).

Atmospheric decays were measured for both fluorescein and dichlorofluorescein each with concentrations ranging from 10^{-3} to 10^{-6} g/g. In both cases the decay was found to be independent of concentration. A filter with a transmission peak at 22 720 cm^{-1} was used on the exciting light so as to excite only the first excited singlet state, and a constant shutter speed of 54.6 rpm was maintained for all the decay measurements.

It was found that the decay of both fluorescein and dichlorofluorescein could be represented by a summa- of two exponentials. The component decay times as a function of pressure are presented in Figs. 5 and 6 for fluorescein. The results for dichlorofluorescein were qualitatively similar although both fast and slow decay rates were 4–5 times faster at each pressure. The effect of pressure on the decay of two concentrations of fluorescein were measured and found to be the same, so pressure effects were measured for only one concentration of dichlorofluorescein.

In all cases both components showed shorter decay times at the higher pressures. At the same time the fraction the initial intensity due to the rapid decay increased with pressure, from 30% at 1 kbar to about 50% at 54 kbar. The question of how each path of decay, alpha and beta, is being affected by pressure will be discussed below. Measurements indicated that the total initial intensity of emission was substantially independent of pressure for both compounds.

The emission spectra of fluorescein at pressures from 0 to 54 kbar is presented in Fig. 7. The dotted portion of the curves in these and similar figures indicate regions where the film sensitivity changes rapidly so that the darkening density could not be established accurately. At atmospheric pressure there are two distinct peaks located at 17 560 and 20 480 cm^{-1}, representing beta and alpha emission, respectively.[3–4] The red peak does not shift measurably with pressure. However, the blue peak shifts red roughly between 1200 and 1400 cm^{-1} in 54 kbar. Both the location and the shift of this peak corresponds closely with that of the low-energy edge of the absorption peak. This evidence helps to justify the assignment of this peak to alpha emission, the $S_1 \rightarrow S_0$ transition, because one would expect the emission peak to be located near the low-energy edge of the absorption peak for transitions between the same two states.[3] It would thus shift with this edge. It is also noted that there does not appear to be a large change in the relative intensities of the two peaks. There may be a slight decrease in the relative intensity of the blue peak, but this is hard to verify with certainty.

The emission spectra of fluorescein in Fig. 7 shows how the relative positions of its S_1 and T_1 states are changing with pressure. This is important because the rate of beta decay depends on the amount of mixing that the T_1 state has with S states near it, or thus the amount of singlet character it assumes. This mixing is a function of the energy difference between the T_1 and

[7] A. Baczynski and M. Czajkowski, Bull. Acad. polon. sci. **VI,** 653 (1958).
[8] R. Bauer and M. Baczynski, Bull. Acad. polon. sci. **VII,** 113 (1958).
[9] A. Jablonski, Acta Phys. Polon. **XVI,** 471 (1957).
[10] A. Jablonski, Bull. Acad. polon. sci. **VI,** 589 (1958).
[11] M. Frackowiak, and J. Held, Acta Phys. Polon. **XVIII,** 93 (1959).
[12] M. Frackowiak and H. Walerys, Acta Phys. Polon. **XIX,** 199 (1960).
[13] H. Walerys, Bull. Acad. polon. sci. **VII, 47 (1959).**

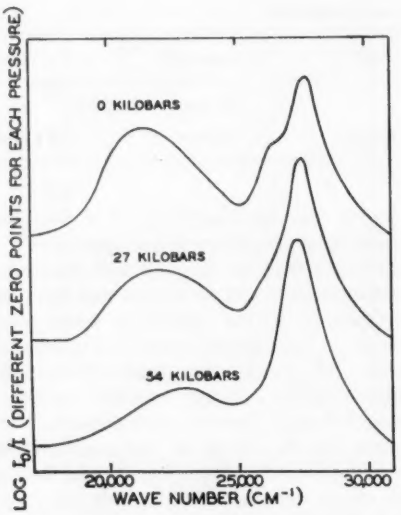

FIG. 8. Absorption spectra of acridine yellow in boric acid—1.8×10^{-4} g/g.

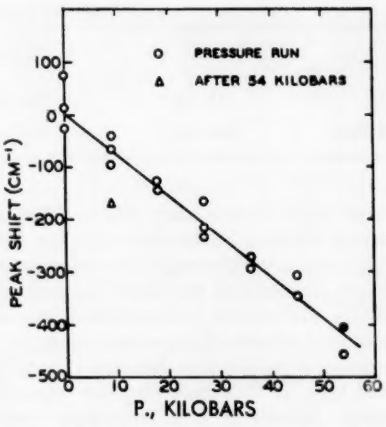

FIG. 10. Shift of monomer absorption peak at 27720 cm^{-1} vs pressure—acridine yellow in boric acid—1.8×10^{-4} g/g.

S states. Since the S_1 state is much closer to the T_1 state than any other S state it probably contributes effectively all of the singlet character present in the T_1 state. As shown in Eq. (5), the part of the decay time associated with this process is proportional to the square of the energy difference between the T_1 and S_1 states. The emission spectrum also shows that there is no large change in peak heights between the alpha and beta emission with pressure, indicating that the alpha emission process is also being enhanced by pressure. This means that the energy crossing, point y, is moving to lower energy along with the S_1 state.

A rough estimate can be made as to how much the change in the energy difference between the S_1 and T_1 states affected the decay rate of the phosphor. Since this energy difference can be related to the beta decay only, the decay will be assumed to be completely of the beta type. From Eq. (3) the following relationship would hold:

$$\frac{\tau(P=0)}{\tau(P=54\text{ kbar})}=\frac{\Delta E(P=0)^2}{\Delta E(P=54\text{ kbar})^2}. \tag{4}$$

Using the ΔE's measured from the emission spectra and the atmospheric τ_n's, the τ_n's at 54 kbar can be calculated and compared with the measured values. As seen in Table I, if the decay were all of the beta type, the change in the energy difference between the S_1 and

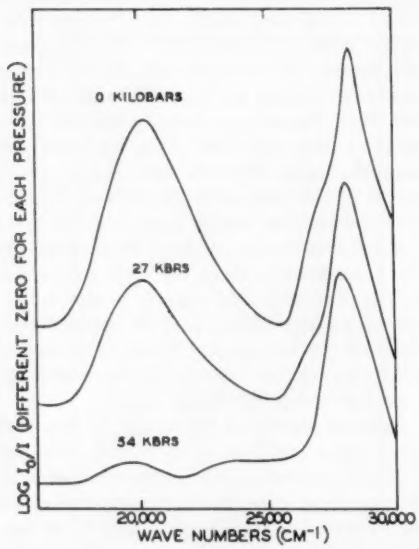

FIG. 9. Absorption spectra of acridine orange in boric acid—5.4×10^{-4} g/g.

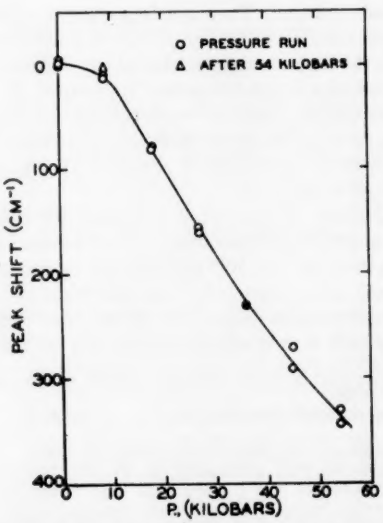

FIG. 11. Shift of monomer absorption peak at 28285 cm^{-1} vs pressure—acridine orange in boric acid—5.4×10^{-4} g/g.

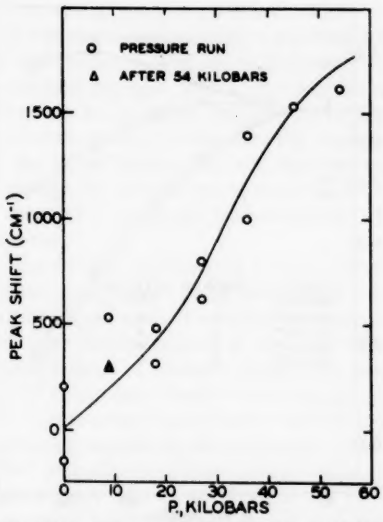

FIG. 12. Shift of dimer absorption peak at 21,700 cm^{-1} vs pressure—acridine yellow in boric acid—1.8×10^{-4} g/g.

T_1 states with pressure would more than account for the decrease in decay times. However, there is a large portion of alpha decay, probably about 30 to 40% (estimated from emission spectra) so the change in the decay time cannot be entirely described in terms of beta decay.

II. EFFECT OF PRESSURE ON ACRIDINE YELLOW AND ACRIDINE ORANGE PHOSPHORS DISSOLVED IN BORIC ACID

Acridine yellow and acridine orange are discussed together because they have similar structural formulas and behave qualitatively the same under pressure.

Typical absorption spectra vs pressure are shown in Figs. 8 and 9. They both show two major peaks with a shoulder on the red side of the blue peak. Other workers have found the red peak to be concentration dependent,[14] the higher the concentration, the larger the red peak relative to the blue peak. This peak has been associated with the formation of a dimer, and the blue peak is associated with the monomer. As pressure is applied the dimer peak decreases in intensity, and so does the shoulder on the monomer peak. One would thus associate the shoulder with absorption in the dimer, perhaps the transition corresponding to the monomer peak, only shifted slightly red.

Figures 10–15 show for both compounds the shift in monomer and dimer peak maxima with pressure, and the change in area of their respective dimer absorption peaks with pressure. For both compounds the monomer absorption peak shifts red with pressure. But, their dimer absorption peak maxima shift in opposite directions. The dimer peak for acridine yellow shows a large blue shift, and that for acridine orange shows a small red shift. However, the red edge of the dimer peak shows

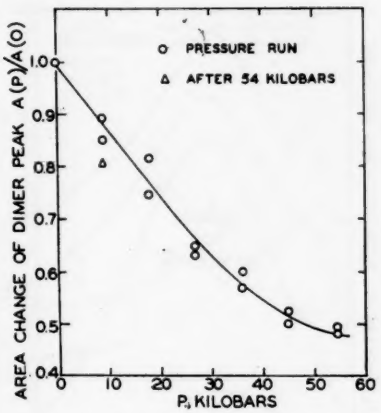

FIG. 14. Area change of dimer absorption peak vs pressure—acridine yellow in boric acid—1.8×10^{-4} g/g.

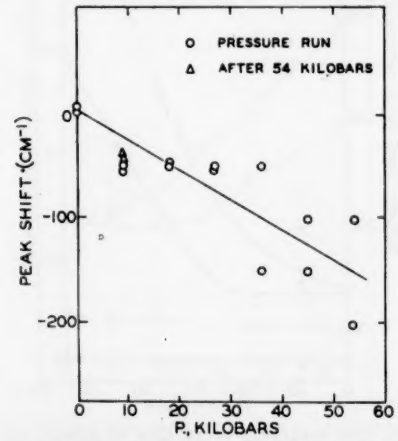

FIG. 13. Shift of dimer absorption peak at 20325 cm^{-1} vs pressure—acridine orange in boric acid—5.4×10^{-4} g/g.

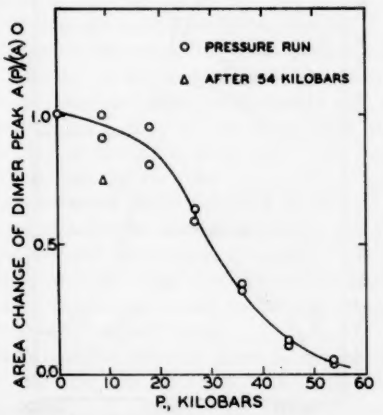

FIG. 15. Area change of dimer absorption peak vs pressure—acridine orange in boric acid—5.4×10^{-4} g/g.

[14] V. Zanker, J. Phys. Chem. **200,** 250 (1952).

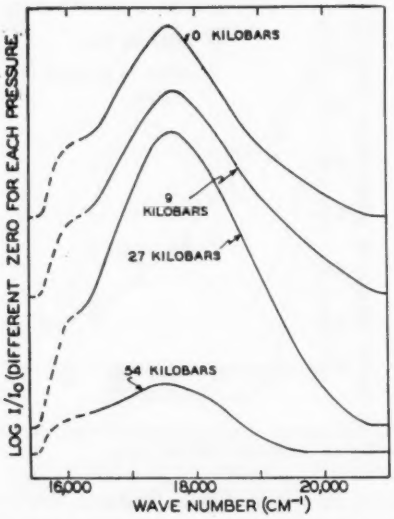

FIG. 16. Emission spectra of acridine orange in boric acid—4.6×10^{-6} g/g.

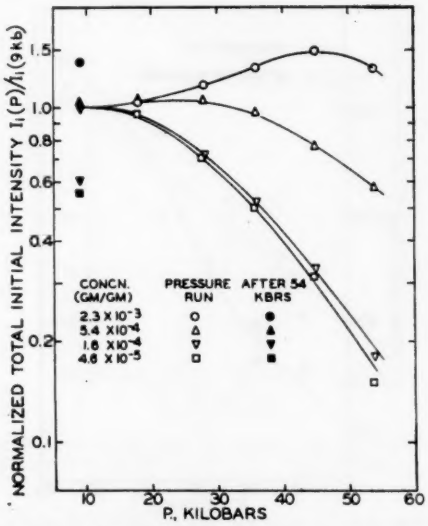

FIG. 18. Total initial emission intensity (normalized to 9 kbar) vs pressure—acridine orange in boric acid.

no shift in either case. The dimer peak of acridine orange shows the larger decrease in area with pressure.

The emission spectra vs pressure for two concentrations of acridine orange are presented in Figs. 16 and 17. The acridine yellow spectra were similar. When making these measurements, no filter was used on the exciting light, so both monomer and dimer peaks were being excited. The shifts of the emission peaks with pressure were small and could not be accurately determined. There appears to be a concentration dependent peak on the red side of the strong peak in acridine orange. These peaks all decrease in intensity with pressure and are located at the red edge of their respective dimer absorption peaks. This would tend to associate the emission with the dimer. The changes in the emission intensity with pressure for several concentrations of acridine orange are shown in Fig. 18. These were measured with a photomultiplier tube. Similar results were obtained for acridine yellow. The pressure effect on the intensity is strongly concentration dependent. This will be discussed in more detail below.

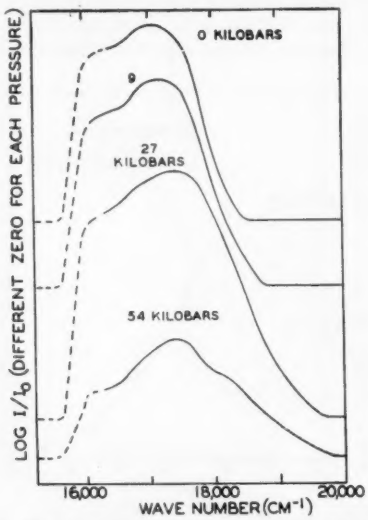

FIG. 17. Emission spectra of acridine orange in boric acid—5.4×10^{-4} g/g.

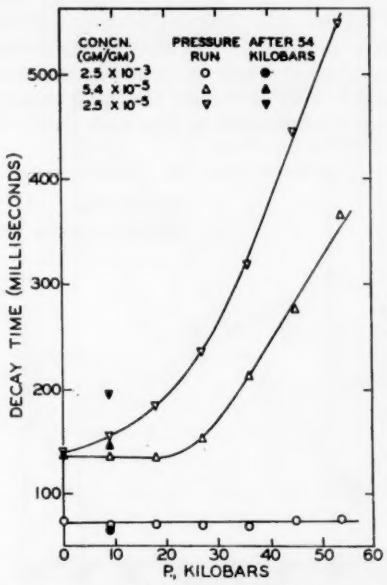

FIG. 19. Slow component decay time vs pressure for three concentrations—acridine yellow in boric acid.

It was found that concentration influenced the decay rate of the compounds and strongly influenced how they changed with pressure. During excitation a filter was used on the exciting light with a transmission peak at 27 800 cm^{-1} so as to excite only the monomer peak. Attempts were made to measure the decays while exciting the dimer peaks, but the emission was not intense enough to obtain measurements. A constant shutter speed of 60 rpm was maintained for all decay measurements.

It was found that the decay of both acridine yellow and acridine orange could be represented by a summation of three exponentials. The effect of pressure on the decay of three concentrations of acridine yellow and four concentrations of acridine orange was measured, and typical component decay times are presented in Figs. 19–21. It is noted that at high concentrations there is little effect of pressure on the component decay times, but at low concentrations they increase with pressure. In all cases there was an increase in the fraction of initial intensity due to the fast decay with increasing pressure (from about 10%–20% of the total in 50 kbar). There was a corresponding decrease in the fractional contribution of the slowest exponential component.

In order to facilitate this discussion the following facts can be listed: (a) The dimer peak for both compounds is concentration dependent and decreases in intensity with pressure. (b) The shoulder on the low-energy side of the monomer peak also decreases with pressure, which associates it with the dimer. (c) The emission peaks were located at the low energy edge of the respective dimer absorption peaks which associates them with the dimer, while the excitation took place in both dimer and monomer peaks. (d) The effect of pressure on the emission intensity is concentration dependent; at the low concentrations there is a large decrease in intensity with pressure. (e) The effect of pressure on the decay times of the component decays is concentration dependent; at the low concentrations there is a large increase in the decay times with pressure. When measuring the decay times a filter with a transmission peak in the region of the monomer absorption peak was used on the exciting light.

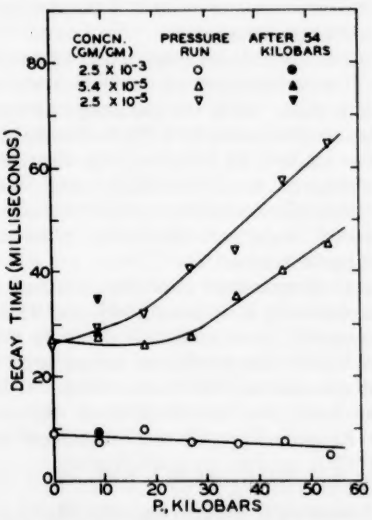

FIG. 20. Medium component decay time vs pressure for three concentrations—acridine yellow in boric acid.

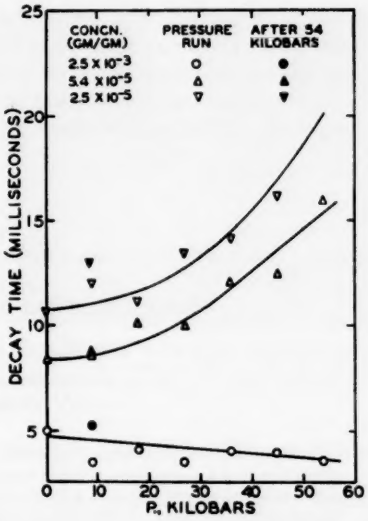

FIG. 21. Rapid component decay time vs pressure for three concentrations—acridine yellow in boric acid.

From a, c, and d one would associate the emission with the dimer peak. When the emission spectra were measured both the monomer and the dimer peaks were excited, but when the decays were measured only the monomer peak was excited. In the case of the decays the excited electron could have been transferred to the dimer in either of two ways. The more likely is that the electron is excited at a monomer site wher it is trapped in a T state associated with the monomer and then is transferred to the T state of the dimer. This transfer may take place in the form of an exciton.[15] The less likely possibility is that the shoulder on the monomer peak which appears to be associated with the dimer site is excited and transfers its excited electron to the T state associated with the dimer peak. This second possibility is less likely because there is no strong line in the Hg exciting light in that region, and the filter on the exciting light is cutting off rapidly there.

The data indicate that the dimer is destroyed with pressure and that the excitation takes place in the

[15] A. N. Terenin and V. L. Ermolaev, Trans. Faraday Soc. 52, 1942 (1956).

monomer and is transferred to a dimer site before emission takes place. The decay data can be explained by assuming there is a critical dimer concentration; above this concentration there is sufficient dimer for the emission process, and below it the dimer concentration becomes the limiting factor in the transfer of an excited electron from the monomer to the dimer site.

ACKNOWLEDGMENT

D. W. Gregg would like to acknowledge a fellowship from the Consolidation Coal Company.

THE JOURNAL OF CHEMICAL PHYSICS VOLUME 35, NUMBER 5 NOVEMBER, 1961

Recombination of Atomic Oxygen on Surfaces*

D. S. HACKER, S. A. MARSHALL, AND M. STEINBERG
Armour Research Foundation, Chicago 16, Illinois

(Received May 26, 1960)

Catalytic surface recombination of atomic oxygen is studied in a flow system by paramagnetic resonance absorption and a comparison is made with platinum wire detectors for the same conditions of flow. Recombination of oxygen atoms on a fuzed quartz surface is found to follow first-order kinetics with a surface recombination efficiency of 4.0×10^{-5} per collision. Recombination on platinum wire detectors held at 200° and at 850°C is also found to be first order in oxygen atoms with surface recombination efficiencies of (0.01 ± 0.002) and (0.1 ± 0.02) per collision, respectively. Efficiencies for platinum are determined from the surface recombination heating and the strength of the oxygen-atom magnetic resonance. The atom-decay rate down the flow tube is found to be first order in oxygen atom with a dependence on the total pressure that suggests the homogeneous formation and subsequent reaction of ozone. The observed rates are consistent with the following scheme:

$$O+O\cdot S \xrightarrow{k_1} O_2+S \qquad (S=\text{surface}).$$

$$O+O_2+M \xrightarrow{k_2} O_3+M \qquad (M=\text{third body}).$$

$$O+O_3 \xrightarrow{k_3} 2\,O_2.$$

The three-body rate constant k_2 is found to have a value of 2.5×10^{14} cc^2 mole^{-2} sec^{-1}.

I. INTRODUCTION

IN recent years considerable attention has been given to problems associated with the exothermic catlytic recombination of atomic species on surfaces. To explain specific mechanisms of such reactions, it is necessary to determine the effectiveness of those atom-surface collisions which lead to recombination and describe the energy partition between the surface and the gaseous-product molecules. To realize these objectives, the atom concentration in the gas near the surface of interest must be determined. In the past, investigators have used hot-wire calorimeters for the study of a variety of atomic reactions.[1–4] However, this technique of monitoring atom concentrations is not applicable when absolute measurements are required. To overcome this limitation, NO titration has been used to standardize calorimetric probe measurements.[5]

The purpose of this investigation is to describe the kinetics of atomic-oxygen recombination on surfaces and in gas phase using the paramagnetic resonance absorption method along with the isothermal hot-wire calorimeter method. In addition, from the recombination heat imparted to a platinum probe and the oxygen-atom concentrations measured by the resonance absorption method, surface-recombination efficiencies on platinum are determined.

Paramagnetic resonance absorption in atomic oxygen was first reported by Rawson and Beringer.[6] This system has subsequently been studied in detail by Abragam and Van Vleck[7] who predict an energy-level scheme and magnetic-spectral distribution, which is in basic agreement with the observations of Rawson and Beringer. Recently Krongelb and Strandberg[8] reported

* This work sponsored by the National Aeronautics and Space Administration.

[1] I. Amdur and A. L. Robinson, J. Chem. Soc. **1933,** 1395.
[2] W. V. Smith, J. Chem. Phys. **11,** 110 (1943).
[3] E. E. Tollefson and D. J. LeRoy, J. Chem. Phys. **16,** 1057 (1948).
[4] J. W. Linnett and D. G. H. Marsden, Proc. Roy. Soc. (London) **A234,** 489 (1956).
[5] L. Elias, E. A. Ogryzlo, and H. I. Schiff, Can. J. Chem. **37,** 1680 (1959).
[6] E. B. Rawson and R. Beringer, Phys. Rev. **88,** 677 (1952).
[7] A. Abragam and J. H. Van Vleck, Phys. Rev. **92,** 1448 (1953).
[8] S. Krongelb and M. W. P. Strandberg, J. Chem. Phys. **31,** 1196 (1959).

a study of the recombination kinetics of atomic oxygen by the use of paramagnetic resonance absorption. They give a detailed account of oxygen-atom magnetic transition probabilities, and justify the use of resonance-absorption signal strengths as a measure of oxygen-atom concentration. Because of this detailed account, such arguments will not be given here.

II. EXPERIMENTAL PROCEDURE

For the recombination study a gas-flow system is employed. At different stations along the flow are located the three components of the system: (1) A 2450-Mc/sec microwave generator for converting molecular oxygen into atomic oxygen, (2) a paramagnetic resonance absorption spectrometer, and (3) an isothermal platinum calorimetric detector. By measuring the concentration of oxygen atoms at various distances along the flow relative to the point of atom generation, the decay scheme and consequently the recombination kinetics can be determined. If oxygen-atom concentration is measured simultaneously by the isothermal calorimetric detector and by paramagnetic resonance absorption, a comparison of output signals can be made. In addition, the calorimeter surface-recombination efficiency can then be determined knowing the heat input to the calorimeter and the intensity of the resonance signal.

Cylinder oxygen (purity >99%) was used in all experiments. The flow rate is determined with a capillary flowmeter whose pressure differential is measured by an oil manometer. Condensible impurities are removed from the system by a liquid nitrogen trap located immediately downstream of the flowmeter. The gas then passes through a fuzed quartz tube having a diameter of 6.75 mm and a length of 150 cm. Downstream from the trap the flow tube passes through the microwave discharge cavity where atomic oxygen is generated. The flow continues downstream carrying the oxygen atoms and enters the resonant cavity of the paramagnetic spectrometer which operates at 9500 Mc/sec. Immediately downstream from the spectrometer cavity is the platinum-wire detector whose diameter and length are 0.0076 and 5 cm, respectively. The detector is wound into a right circular helix with its axis oriented normal to the direction of flow. The flow then passes to a second liquid nitrogen trap, through a throttling valve, and to a high-capacity mechanical vacuum pump. The pressures in the flow tube are measured with a McLeod gauge.

Before generating oxygen atoms, preliminary treatment of the system is carried out with dry activated nitrogen. This operation is continued for 30 to 90 min which seems to be sufficient time to produce a relatively inert and reproducible quartz surface. After the activated nitrogen cleaning, the oxygen atom concentration at any given point along the flow system can be maintained constant for at least 8 hr. In the absence of such pretreatment, the detectable oxygen-atom signal is observed to fade out in times which varied from 10 min to 2 hr.

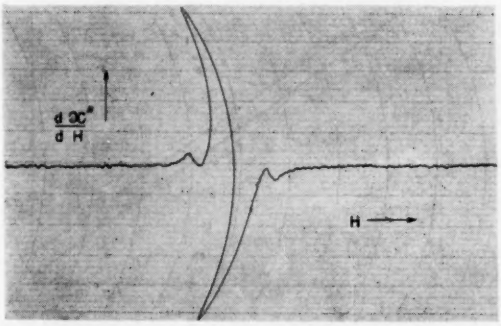

FIG. 1. First harmonic of the oxygen-atom magnetic resonance absorption. The main signal is due to the unresolved four-line spectrum of the $^3P_2$ state while the weaker signals on either side are due to the $^3P_1$ state.

Local oxygen-atom concentration is determined by the paramagnetic resonance spectrometer. The spetrometer uses an X-13 reflex klystron which feeds a rectangular transmission cavity operating in the TE_{012} mode. By low-amplitude frequency modulation, the klystron is locked to the cavity frequency through a converter and correction circuit which is coupled to the klystron repeller. A magnetic field in the neighborhood of 4500 oe is provided by a 4-in. pole diameter electromagnet having a gap spacing of 0.75 in., which provides an acceptable pole-face diameter to gap-spacing ratio. This field is sine-wave modulated at audio frequencies having amplitudes not greater than one fifth the observed absorption-line half-widths. With the use of a phase-sensitive lock-in type detector, the first harmonic of the atom resonance absorption is observed on a recorder tracing. Figure 1 is a reproduction of such a tracing. Assuming the oxygen-atom absorption shape factor to be approximately Lorentzian in character, field modulation at these amplitudes ensures convergence to the total absorption intensity of the doubly integrated first-harmonic output of the phase sensitive lock-in detector.

In this investigation, the four lines of the magnetic spectrum due to the $^3P_2$ state of atomic oxygen are not resolved principally because of atom-molecule and atom-atom collision broadening. It is to be noted, however, that the $^3P_1$ transitions are just resolved (see Fig. 1) which makes it possible to determine the temperature of the gas. At points 10 cm and beyond the point of discharge, all our measurements yield a gas temperature of approximately 300°K.

Atomic oxygen concentration is determined by comparing the integrated paramagnetic-resonance absorption signal with the signal from a secondary standard of 1, 1-diphenyl-2 picryl hydrazyl (dpph). The use of a nonaqueous secondary standard is found to be necessary because of the deletereous effects of water on the quality factor of the cavity resonator. Before being used as a

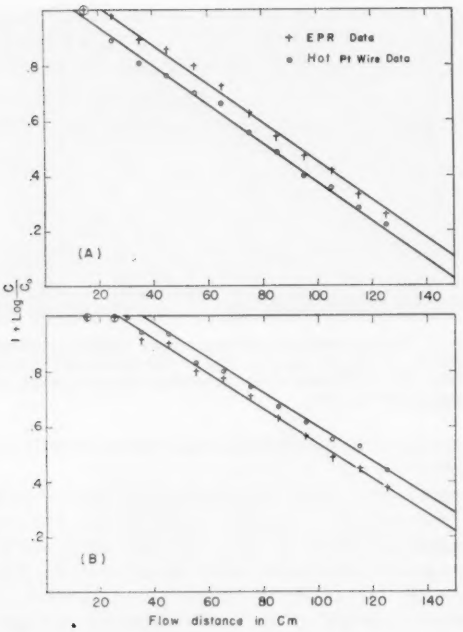

FIG. 2. Experimental relation between $\ln(O)/(O)_0$ and distance from oxygen-atom generator to detector. The open circle points represent data taken by the magnetic resonance spectrometer and the cross points represent data taken by the platinum wire detector at 850°C. (a) Data taken at $P=0.0022$ atm, (b) data taken at $P=0.0015$ atm.

comparison to oxygen atoms, the free radical is compared and standarized against a 0.001 N solution of manganese sulfate. Since the resonance absorption due to dpph and manganese ion are partially coincident, the quantity of dpph used is adjusted to make its absorption fifty times greater than the signal from individual manganese hyperfine components. First-derivative recorder tracings are taken of both resonances, integrated twice, and compared for relative strengths. These strengths are then weighted by accounting for proper transition moments and cavity-resonator field distributions. In this way, the effective spin concentration of dpph is determined.

This procedure is, of course, not without drawbacks. For example, the process of double integration has pitfalls since integration errors tend to compound. Further errors arise in the improper integration of the resonance-absorption wings where area can be lost by the setting of finite integration limits, by drift of the recorder base line, or by excessive instrument noise. It is also possible that some danger exists in comparing gaseous resonance absorptions with those observed in solids, where in the latter case many processes may be operative in establishing line shapes which cannot be characterized, to the degree required for this application, by simple closed form expressions. Although the compounding of these sources of difficulties can lead to serious errors in establishing oxygen atom concentrations, some confidence limits can be established by an internal consistancy experiment. For this purpose the dpph, chemically tested to have less than 1% total impurities, exhibited an absorption intensity having a deviation of less than 10% from prediction when calibrated against the manganese ion.

The rate of recombination of oxygen atoms on the quartz surface is determined by observing the variations in the resonance absorption signal of oxygen atoms as the distance between the discharge and spectrometer cavity is changed. After determining rate constants, the oxygen-atom concentration at the platinum-wire detector can be estimated by keeping the probe sufficiently close to the spectrometer cavity so that no significant atom decay occurs between the two.

During a wire calibration, the oxygen flow is adjusted to some arbitrary value and an electric current is passed through the wire to bring it to a preassigned temperature (200° or 850°C). Preliminary wire temperature measurements are made using a micropyrometer which has been calibrated against a standard tungsten ribbon lamp. The wire current and applied potential are then recorded and the probe resistance calculated. With the discharge on and without altering the flow conditions, the current and potential are then readjusted to yield the predischarge wire resistance which now serves as a thermometer. The difference in electrical power required to maintain wire temperature with and without the discharge is the recombination power. From the energy imparted to the wire and the local atom concentration, the efficiency can be determined. The relation between wire efficiency and local atom concentration is given by

$$\gamma=4P/c\sigma\Delta H(\mathrm{O}),$$

where γ is the recombination efficiency, P is the recombination power delivered to the wire in watts, c is the mean-velocity of oxygen atoms in cm sec^{-1}, σ is the wire area in cm^2, ΔH is the heat of formation of atomic oxygen (2.5×10^5 joules mole^{-1}), and (O) is the oxygen-atom concentration in the gas in moles cm^{-3}.

III. RESULTS

It was found that the disappearance of oxygen atoms down the reactor tube was first order with respect to oxygen atoms as shown in Figs. 2(a) and 2(b). The observed first-order dependence is consistent with the following mechanism for the wall and homogeneous recombination reactions,

$$\mathrm{O}+\mathrm{O}\cdot S\xrightarrow{k_1}\mathrm{O}_2+S \qquad (S=\text{surface}), \tag{1}$$

$$\mathrm{O}+\mathrm{O}_2+M\xrightarrow{k_2}\mathrm{O}_3+M \qquad (M=\text{third body}), \tag{2}$$

$$\mathrm{O}+\mathrm{O}_3\xrightarrow{k_3}2\mathrm{O}_2. \tag{3}$$

At constant temperature and pressure, for low values of oxygen dissociation and under the steady-state ap-

proximation for ozone, the rate of atomic-oxygen disappearance can be given as

$$-d(\mathrm{O})/dz = 1/V_z[k_1+2k_2(\mathrm{O}_2)^2](\mathrm{O}), \qquad (4)$$

where (O) is the oxygen-atom concentration, (O_2) is the oxygen-molecule concentration, V_z is the gas flow velocity, and k_1 and k_2 are the rate constants for the processes given by Eqs. (1) and (2). Equation (4) assumes: (a) one-dimensional flow, (b) the radial oxygen-atom concentration is not diffusion limited, and (c) axial diffusion effects are small compared with the flow velocity.[9] For uniform velocity, the solution to Eq. (4) is

$$\ln(\mathrm{O})/(\mathrm{O})_0 = -1/V_z[k_1+2k_2(\mathrm{O}_2)^2]z, \qquad (5)$$

where $(O)_0$ is the oxygen-atom concentration at the point $z=0$.

Curves similar to those shown in Fig. 2 were obtained for six different pressures. These figures, which represent relative oxygen-atom concentration measured by the magnetic resonance detector and by the platinum-wire detector, demonstrate a direct proportionality between the two detectors. Figure 3 shows a plot of the effective first-order coefficient determined from the slopes of Figs. 2(a) and 2(b) vs the square of the total pressure. For low $(O)/(O_2)$ ratios the O_2 partial pressure is approximated by the total pressure in the gas. From the slope and intercept of the plot in Fig. 3, obtained by a least-squares fit, the two rate constants k_1 and k_2 are obtained. Taking this value of k_1, the recombination efficiency for quartz is determined from the relation

$$\gamma = 2k_1r/c,$$

where r is the radius of the flow tube and c is the mean thermal velocity of the oxygen atoms. Experimental

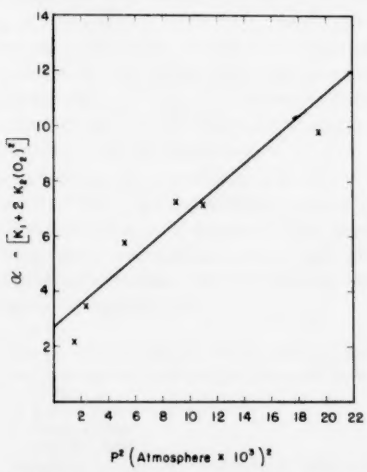

FIG. 3. Plot of $[k_1+2k_2(O_2)^2]$ vs square of total gas pressure.

[9] P. G. Dickens, R. D. Gould, J. W. Linnett, and A. Richmond, Nature (London) **187,** 686 (1960).

TABLE I. Oxygen-recombination rate data.

γ	k_2 (cc^2 mol^{-2} sec^{-1})	Reference
4.0×10^{-5}	2.5×10^{14}	This study
3.2×10^{-4}	...	8
7.7×10^{-5}	1.0×10^{14}	5
1.2×10^{-4}	...	4
2×10^{-5}	2.0×10^{14}	a
...	0.79×10^{14}	b

[a] F. Kaufman, Proc. Roy. Soc. (London) **A247,** 123 (1958).
[b] S. W. Benson and A. E. Axworthy, J. Chem. Phys. **26,** 1718 (1957).

values for γ and k_2 are compared in Table I with measurements of other investigators. The accuracy of the experimental data does not permit an assessment of the contribution of the direct recombination process

$$\mathrm{O}+\mathrm{O}+M \rightarrow \mathrm{O}_2+M \qquad (6)$$

to the observed rate.

In a study similar to that reported here, Krongelb and Strandberg[8] assume Eq. (6) to control the homogeneous disappearance of oxygen atoms down the flow tube. Their experimental results do not appear to be in complete agreement with their analytical model. They approximated the three-body rate constant for Eq. (6) at 5×10^{15} cc^2 mole^{-2} sec^{-1}. If one assumes instead that Eqs. (2) and (3) are the homogeneous atom-decay processes, their data can be shown to be in fair agreement with the first-order expression for oxygen atom given by Eq. (5). Using their value for γ of 3.2×10^{-4}, their data yields values of k_2 from 2 to 4×10^{14} cc^2 mole^{-2} sec^{-1}, which is in agreement with the values listed in Table I.

The recombination efficiency of the platinum-wire detector proved to be strongly temperature dependent. In the presence of atomic oxygen, the wire temperature could be increased to about 300° to 400°C and then it would spontaneously jump to at least 700°C. It was not possible to stabilize the wire at intermediate temperatures in the presence of appreciable atomic oxygen. Such behavior of platinum wires has also been observed by Fryburg and Petrus.[10] For each of the runs, two of which are represented by Fig. 2, an average of 10 data points were taken simultaneously by the platinum-wire detector and the magnetic-resonance spectrometer. Measurements were made at wire temperatures of 200° and 850°C. At 200°C the atomic-oxygen recombination efficiency on bare platinum wire was (0.01 ± 0.002) per collision and at 850°C the efficiency was (0.10 ± 0.02) per collision. At 850°C this average tenfold increase in recombination efficiency on the platinum surface, caused sufficient heating at high oxygen concentrations

[10] G. C. Fryburg and H. M. Petrus, J. Chem. Phys. **32,** 622 (1960).

to maintain the temperature without the application of electrical heating.

IV. DISCUSSION

The observed first-order oxygen-atom recombination with widely differing efficiencies on quartz and platinum is consistent with the model in which the surface is extensively covered with adsorbed atoms. The recombination rate is then controlled by the rate at which gaseous oxygen atoms make successful encounters with adsorbed atoms. Simultaneously, surface sites which have been vacated by the formation of gaseous O_2 are rapidly covered by additional oxygen. The first-order behavior further indicates that the mobility of adsorbed oxygen followed by adsorbed atom recombination is slow compared with the reaction of gaseous atoms with adsorbed atoms at the pressure levels employed here.

The homogeneous recombination of atomic oxygen at low $(O)/(O_2)$ ratios, such as employed in this and similar studies, appears to be described by Eqs. (2) and (3) with no detectable contribution from the direct three body recombination process of Eq. (6).

There appear to be two mechanisms operative in the heterogeneous recombination on platinum, one below and the other above 300° to 400°C. These mechanisms probably relate to the manner in which oxygen is bound to the surface. Reschauer[11] observed that oxygen is adsorbed on platinum by two processes. A low-temperature adsorption occurs at 120° to 350°C with one activation energy, and a high-temperature adsorption is observed with a higher activation energy above 350°C. The magnetic susceptibility of platinum is decreased by oxygen adsorption and the effect increases with temperature.[12] Adsorbed oxygen atoms apparently enter into covalent bonds with the partly filled *d* orbitals of the platinum.

At low temperatures, up to 300°C, in the presence of a few mm Hg of O_2 and O, the adsorbed oxygen probably exists as a monolayer of tightly bound chemisorbed atoms on which some additional oxygen is less tightly held by van der Waals forces. As the temperature is increased, the loosely bound oxygen evaporates, leaving the chemisorbed oxygen. Below 300°C the recombination probably occurs with the loosely held van der Waals layer. Above 400°C the reaction is with the chemisorbed oxygen. Experiments are being continued to obtain oxygen recombination rates as a function of temperature. Activation energies thus obtained may help to describe the nature of the heterogeneous first-order atom recombination on platinum. It should be noted that in all of the foregoing the recombination energy accomodation coefficient on platinum has been taken as unity. This may not be the case, and experiments are in progress to determine the accomodation coefficients.

[11] H. Z. Reschauer, Z. Physik. Chem. **826**, 399 (1934).

[12] T. J. Gray and C. C. McCain, *Proceedings of the Second International Congress on Surface Activity* (Butterworths Scientific Publications, Ltd., London, 1957), Vol. II, p. 260.

Paramagnetic Excitons in Molecular Crystals*

HIMAN STERNLICHT† AND HARDEN M. MCCONNELL‡
Gates and Crellin Laboratories of Chemistry,§ California Institute of Technology, Pasadena, California
(Received April 24, 1961)

The possibility of using electron spin resonance to study paramagnetic excited electronic states of aromatic crystals is explored. Two limiting cases are considered: On the one hand the excitation energy moves from molecule to molecule by a diffusion process; on the other the triplet excitation is described by a Frenkel exciton. In either case intermolecular propagation of the triplet excitation is assumed to proceed through virtual triplet ionization states. The theory of the spin resonance of triplet excitons is developed in some detail. It is shown that there is only a weak dependence of the spectra on the **k** vector of the exciton wave, except when **k** is near regions of band degeneracies. Band degeneracies arise from time-reversal symmetry in benzene, naphthalene, and coronene crystals and occur on boundary planes of the first Brillouin zone. A spin Hamiltonian is calculated for these three aromatic crystals for most **k** vectors which are far removed from regions of band degeneracy. Two-line spectra (with no hyperfine structure), representing an average over the molecular sites in the unit cell, are obtained. Scattering of the exciton wave by lattice vibrations can cause line broadening and also can serve as a mechanism for spin lattice relaxation.

1. INTRODUCTION

WITHIN the past several years a number of successful paramagnetic resonance experiments have been performed on phosphorescent aromatic hydrocarbons. Hutchison and Mangum[1] observed electron spin resonance (ESR) from triplet state naphthalene upon irradiating a single crystal of a solid solution of naphthalene in durene with ultraviolet light. Van der Waals and de Groot[2] obtained ESR spectra from rigid glass solutions of phosphorescing naphthalene, coronene, triphenylene, and 1,3,5-triphenylbenzene. Efforts to obtain resonance spectra from pure phosphorescing aromatic crystals have, to the best of the authors' knowledge, not yet been successful.

The ESR spectra of the pure crystals are of particular interest; it is possible that they may reveal the presence of triplet excitons. Whereas the singlet-exciton concept has been very useful in explaining certain phenomena occurring in molecular crystals (e.g., sensitized fluorescence, Davydov splittings), as yet triplet excitons have not been observed experimentally. The concept of the spin multiplet state exciton has, however, been introduced to explain certain multiplet structures occurring in the optical spectra of ionic crystals.[3]

We discuss below the consequence of triplet exciton motion on the ESR spectra for three organic crystals; naphthalene, coronene, and benzene. The model used suffers from some oversimplifications and numerical uncertainties; nevertheless our conclusions should be useful in guiding experiments.

Aromatic molecules in the triplet state are characterized by a zero-field splitting of the spin states. The removal of the threefold spin degeneracy may be complete or partial, the extent depending upon the symmetry of the molecule and the nature of the triplet state molecular wave function. In aromatic molecules the interaction responsible for this behavior is primarily the (electron spin)−(electron spin) dipolar interaction[4–7]:

$$\mathcal{H}_D = g_e^2 \mid \beta \mid^2 \sum_{i<j} [(\mathbf{s}_i \cdot \mathbf{s}_j) r_{ij}^{-3} - 3(\mathbf{r}_{ij} \cdot \mathbf{s}_i)(\mathbf{r}_{ij} \cdot \mathbf{s}_j) r_{ij}^{-5}]. \tag{1}$$

The sum is over the electrons of the molecule; g_e is the (assumed isotropic) electron g factor; $\mid \beta \mid$ is the electronic Bohr magneton; $\mathbf{s}_i$ is the spin operator of electron i in units of $\hbar$; $\mathbf{r}_{ij}$ is the distance vector directed from i to j. It is possible to put Eq. (1) into the following form, referred to as the spin Hamiltonian:

$$\mathcal{H}_s = D(S_z^2 - \tfrac{1}{3}S^2) + E(S_x^2 - S_y^2). \tag{2}$$

In the case of naphthalene, D and E are found to have the values ± 0.1006 and ∓ 0.0138 cm^{-1}, respectively.[1] The spin-spin interaction in Eq. (2) is often comparable to the Zeeman interaction $\mathcal{H}_z$.

$$\mathcal{H}_z = g_e \mid \beta \mid \sum_i \mathbf{s}_i \cdot \mathbf{H}. \tag{3}$$

As a result the ESR spectrum is highly anisotropic.[1,2] Hutchison and Mangum[1] obtained four ESR lines from their solid solution of naphthalene in durene. One pair of lines could be assigned to each of the two differently oriented sites of naphthalene molecules in durene. (The durene crystal like the naphthalene crystal belongs to the monoclinic system and has two mole-

* Sponsored by the U.S. Public Health Service, by the National Science Foundation, and by the Office of Ordnance Research, U.S. Army.
† Eastman Kodak Predoctoral Fellow.
‡ Alfred P. Sloan Fellow.
§ Contribution No. 2693.
[1] C. A. Hutchison and B. W. Mangum, J. Chem. Phys. **29**, 952 (1958); **34**, 908 (1961).
[2] J. H. van der Waals and M. S. de Groot, Mol. Phys. **2**, 333 (1959); **3**, 190 (1960).
[3] A. W. Overhauser, Phys. Rev. **101**, 1702 (1956).
[4] H. M. McConnell, Proc. Natl. Acad. Sci. U.S. **45**, 172 (1959).
[5] M. Gouterman and W. Moffitt, J. Chem. Phys. **30**, 1107 (1959).
[6] R. Bersohn (unpublished calculations).
[7] H. F. Hameka, J. Chem. Phys. **31**, 315 (1959).

cules per unit cell.) For some special orientations of the external field, the four lines merge to give two lines. This occurs when the external field is along a symmetry element of the crystal.

It is possible that the low-lying triplet excited states of pure aromatic single crystals will give ESR spectra that are qualitatively different from that expected for the isolated molecules that make up the crystal. Differences in the spectra will be most pronounced if (a) there are two or more molecules per unit cell that are not related by a center of symmetry, and if (b) the Davydov splitting[8] of the triplet exciton states is large compared to $|D|$, $|E|$. We believe that condition (b) is almost certain to be the case due to the contribution of charge-transfer interactions to the triplet exciton bandwidths. As we shall see, the paramagnetic resonance of a triplet exciton wave in naphthalene will give rise to essentially only two lines, due to the dipole interaction of Eq. (1), for all orientations of external field. Furthermore, since the triplet exciton is distributed over many molecules, the proton hyperfine structure is washed out in contrast to the proton hyperfine structure that is observed for isolated molecules.[1] Similar results are expected for the triplet exciton states of other aromatic crystals.

A two-line spectrum for an arbitrarily oriented magnetic field does not necessarily prove the existence of coherent exciton waves. For example, if the excitation wave undergoes pronounced scattering by lattice vibrations, the excitation motion may be best regarded as undergoing a "random walk" or diffusion.[9] An average over all sites in the unit cell resulting in a two-line spectrum will occur if

$$\tau^{-1} \gg |D|, \quad |E|. \tag{4}$$

Here τ represents the characteristic time for the random walk between nontranslatory neighbors of the unit cell. In general, we anticipate that (barring any pronounced chemical dimerization of excited molecules in the crystal) the excitation transfer rate τ^{-1} will be at least as large as the triplet exciton Davydov splitting. Therefore, we do expect that the inequality in Eq. (4) will hold for the molecules of interest.

It is clear from the above discussion that the Davydov splitting of the triplet exciton band plays a critical role in the paramagnetic resonance spectra to be expected from aromatic molecular crystals in their paramagnetic excited states. Although the triplet Davydov splittings have not been observed experimentally, it is important to consider the magnitude that these splittings might have. In the first place, Merrifield[10] has pointed out that intermolecular exchange interactions will contribute to the triplet exciton bandwidths. Our order of magnitude estimates indicate that these intermolecular exchange integrals, as calculated with Slater-type functions, are extremely small. However, it is likely that intermolecular charge transfer triplet excited states make significant contributions toward broadening the lowest "neutral" triplet exciton bands. This is discussed later in the present paper. It should be noted, however, that exciton bandwidths in molecular crystals will in general be reduced due to intermolecular and intramolecular self-trapping effects.[11] These self-trapping effects correspond to a nuclear deformation accompanying a propagating exciton wave packet, thus increasing its effective mass. Similar effects have been discussed by Peterson and Simpson,[12] and by Witkowski and Moffitt,[13] in connection with optical absorption spectra of molecular crystals for the "strong and weak coupling cases." In the following discussions in this paper we shall always mean by the exciton bandwidth that bandwidth which includes the self-trapping effects due to nuclear distortions.

2. AN EFFECTIVE HAMILTONIAN FOR TRIPLET EXCITONS

The theory of singlet Frenkel excitons in aromatic molecular crystals has been the subject of extensive theoretical study by Davydov, Fox, and Schnepp; McClure; Simpson; Trlifaj[9]; Craig; and Winston. A comprehensive review and bibliography have been given by McClure.[14] Singlet Frenkel excitons in aromatic crystals are usually treated by elementary degenerate perturbation theory. That is, if $|s\rangle$ represents a state of a crystal in which molecule s is in its first singlet excited state, and all other $N-1$ molecules are in their ground states, then the singlet exciton energies are solutions of the $N \times N$ secular determinant

$$|\langle s|\mathcal{H}_0|s'\rangle - \langle s|s'\rangle \mathcal{E}| = 0, \tag{5}$$

and the singlet exciton functions are the corresponding N linear combinations of the one-molecule excited state functions $|s\rangle$. Here $\mathcal{H}_0$ is the complete exact kinetic and electrostatic Hamiltonian for the problem. The matrix elements $\langle s|\mathcal{H}_0|s'\rangle$ can often be approximated by simple multipole expansions.[14]

The problem of triplet exciton states in molecular crystals appears to be a little less straightforward. This is because, at first sight, one would expect the triplet exciton bandwidths to be extremely narrow. That is, if we now let $|t\rangle$ represent the lowest triplet excited state of molecule t, then, as shown by Merrifield,[10] all matrix elements of the type $\langle t|\mathcal{H}_0|t'\rangle$ in Eq. (5) reduce to two-electron exchange integrals between orbitals on different molecules, and these are indeed expected to be very small. However, recent work by Lyons[15] has pointed out the possible importance of

[8] A. S. Davydov, J. Exptl. Theoret. Phys. (U.S.S.R.) **18,** 210 (1948).
[9] M. Trlifaj, Czechoslov. J. Phys. **8,** 510 (1958).
[10] R. E. Merrifield, J. Chem. Phys. **23,** 402 (1955).
[11] G. Vincow and H. M. McConnell (to be published).
[12] W. T. Simpson and D. L. Peterson, J. Chem. Phys. **26,** 588 (1957).
[13] A. Witkowski and W. Moffitt, J. Chem. Phys. **33,** 872 (1960).
[14] D. S. McClure, *Solid-State Physics* (Academic Press Inc., New York, 1959), Vol. 8, p. 1.
[15] L. E. Lyons, J. Chem. Soc. **1957,** 5001.

intermolecular charge-transfer effects in molecular crystals in connection with photoconductivity. It may well be that triplet exciton intermolecular charge-transfer states make an appreciable ($\sim$1%) contribution to the lowest triplet exciton wave functions, and therefore play an important role in determining the triplet exciton bandwidth. We hesitate to offer any detailed numerical calculations in support of this contention in view of the great uncertainties in molecular electronic wave functions at large distances, and in molecular wave functions of ionized states in crystals. Our main purpose here is to show that the problem of the triplet exciton band can be handled by a secular determinant analogous to that given above in Eq. (5) for singlet excitons by replacing the exact Hamiltonian $\mathcal{H}_0$ by an effective Hamiltonian $\mathcal{H}$ that includes the effects of the charge-transfer states on the triplet exciton bandwidths.

Let $|\mathbf{k}, q\rangle$ represent an intermolecular charge-transfer ionization wave with wave vector $\mathbf{k}$ and band index q. The $|\mathbf{k}, q\rangle$ are to be regarded as variational functions to be used to improve the triplet exciton functions based on the neutral one molecule triplet states $|t\rangle$. Second-order perturbation theory for degenerate systems leads to the following effective Hamiltonian $\mathcal{H}$[16]:

$$\mathcal{H}=\mathcal{H}_0+\sum_{t,t'}R_{tt'}\,|\,t\rangle\langle t'\,|\,, \tag{6}$$

$$R_{tt'}=-\sum_{\mathbf{k},q}(E_{kq}-E^0)^{-1}V_{kqt'}V_{tkq}, \tag{7}$$

$$V_{kqt'}=\langle\mathbf{k}, q\,|\,\mathcal{H}_0\,|\,t'\rangle. \tag{8}$$

That is, to second order the triplet exciton energies derived from the following $N\times N$ secular determinant are the same as those that would be

$$|\,\langle t\,|\,\mathcal{H}\,|\,t'\rangle-\langle t\,|\,t'\rangle\mathcal{E}\,|=0 \tag{9}$$

obtained from the set of N states $|t\rangle$ and all ionization states $|\mathbf{k}, q\rangle$, together with the true Hamiltonian $\mathcal{H}_0$. The assumption that the triplet exciton band is dominated by contributions from the ionization states is then equivalent to the following inequality for neighboring molecular pairs:

$$|\,R_{tt'}\,|>|\,(\mathcal{H}_0)_{tt'}\,|\,. \tag{10}$$

3. EXCITON BAND DEGENERACIES

Let us now consider a crystal of N molecules, where the unit cells are numbered $n=1, 2, 3, \cdots$, and where the molecular sites in the unit cell are specified by θ. Every molecule in the crystal is then completely identified by the pair of numbers n, θ. Let $|n\theta M\rangle$ represent an antisymmetrical crystal wave function in which molecule $n\theta$ is excited to its lowest triplet electronic state, with spin component M, and all other molecules are in their ground states. If one temporarily neglects matrix elements of $\mathcal{H}$ connecting different sites (e.g., $\langle n\theta M\,|\,\mathcal{H}\,|\,n\theta' M\rangle$), then the functions that diagonalize the secular determinant Eq. (9) are the one-site exciton functions $|\,\mathbf{k}\theta M\rangle$.

$$|\,\mathbf{k}\theta M\rangle=\frac{1}{N^{\frac{1}{2}}}\sum_n|\,n\theta M\rangle\,\mathrm{ixp}(\mathbf{k}\cdot\mathbf{R}_{n\theta}) \tag{11}$$

$$\mathrm{ixp}(\mathbf{k}\cdot\mathbf{R}_{n\theta})=\exp 2\pi i\mathbf{k}\cdot\mathbf{R}_{n\theta}.$$

When matrix elements that connect different sites ($\theta\neq\theta'$) are included in the secular determinant Eq. (9), then this determinant is diagonalized by the crystal exciton wave functions,

$$|\,\mathbf{k}_l M\rangle=\sum_\theta C_{l\theta}\,|\,\mathbf{k}\theta M\rangle. \tag{12}$$

Here subscript l is a triplet exciton band index. For convenience of notation the nuclear vibrational functions corresponding to polaron or self-trapping effects are not included explicitly in the above equations. This can be done in a relatively simple way; the net effect is to reduce the exciton bandwidths by a factor depending on the overlap of nuclear vibrational functions. This problem will be discussed elsewhere.[11]

In order to calculate the resonance spectra of the aromatic crystals treated in this paper, it is necessary to determine the regions of band degeneracies. To the extent that we are in a region of the Brillouin zone (BZ) sufficiently far from those values of $\mathbf{k}$ for which there is a degeneracy between the bands (thus ensuring us that the energy separation between the bands is large compared to the spin-spin interaction), it is reasonable to use the following 3×3 determinant to obtain the spin energies of the crystal:

$$|\,\langle\mathbf{k}_l M\,|\,\mathcal{H}_D+\mathcal{H}_Z\,|\,\mathbf{k}_l M'\rangle-E\delta_{MM'}\,|=0; \tag{13}$$

$\mathcal{H}_D$ is given in Eq. (1), and the sum is over all the electrons in the crystal. Since $\mathcal{H}_D+\mathcal{H}_Z$ belongs to the totally symmetric representation of the translation operator, we need only consider elements between states having the same $\mathbf{k}$. In regions of degeneracy or near degeneracy where the separation between the bands is comparable to the spin-spin interactions ($\sim$0.2 cm^{-1}), it is necessary to replace Eq. (13) by

$$|\,\langle\mathbf{k}_l M\,|\,\mathcal{H}_Z+\mathcal{H}_D\,|\,\mathbf{k}_{l'}M'\rangle-E\delta_{MM'}\delta_{ll'}\,|=0, \tag{14}$$

where l now ranges over the degenerate or near degenerate bands. Divide the BZ into two regions, Δ and Γ, whose spin energies are to be calculated by Eqs. (13) and (14), respectively. The Δ region gives triplet resonance spectra that are essentially independent of $\mathbf{k}$ (as will be shown below), while the Γ region gives spectra that are highly dependent on $\mathbf{k}$.

Band degeneracies can be classified as to whether they are required by symmetry or are accidental. The Hamiltonian of the crystal $\mathcal{H}_0$ or $\mathcal{H}$ is invariant to time re-

[16] L. D. Landau and E. M. Lifshitz, *Quantum Mechanics; Non-Relativistic Theory* (Addison-Wesley Publishing Company, Inc., Reading, Massachusetts, 1958), p. 138.

versal and to the space group operations. It is easily shown that in the case of the aromatic crystals treated here there can only be symmetry degeneracies arising from time reversal. Furthermore, one can show that accidental degeneracies can occur for benzene while they do not occur for naphthalene and coronene. The matter of accidental degeneracies will be discussed later.

The effect of time-reversal symmetry on the energy bands of crystals has been treated by Herring,[17] who has shown that, because of time-reversal symmetry, the energy bands of spinless one-particle states stick together in pairs for all reciprocal lattice wave vectors $\mathbf{k}^b$. Here $\mathbf{k}^b$ is any wave vector that terminates on the boundary plane of the BZ that is perpendicular to a twofold screw axis of the reciprocal lattice. The simplest way to verify this conclusion for triplet excitons is to expand the exciton matrix elements $\langle \mathbf{k}^b\theta M \mid 3\mathcal{C} \mid \mathbf{k}^b\theta' M' \rangle$ in terms of molecular matrix elements

$$\langle n\theta M \mid 3\mathcal{C} \mid n'\theta' M' \rangle.$$

If one makes use of the fact that $3\mathcal{C}$ is real, then one can show that when θ and θ' are related by a twofold screw axis, the above exciton matrix element is zero. Since $\langle \mathbf{k}^b\theta M \mid 3\mathcal{C} \mid \mathbf{k}^b\theta M \rangle = \langle \mathbf{k}^b\theta' M \mid 3\mathcal{C} \mid \mathbf{k}^b\theta' M \rangle$ and there is no interaction between the sites, we are led to a degeneracy that is essentially the same as that discussed by Herring.[17] This degeneracy can be removed by the magnetic fine structure interaction, $3\mathcal{C}_Z+3\mathcal{C}_D$, as discussed later.

Benzene belongs to the orthorhombic crystal system[18,19] and the $D_{2h}{}^{15}(Pbca)$ space group that has three mutually perpendicular screw axes. As a result, one encounters degeneracies at all boundary points of the BZ. Naphthalene[20] and coronene[21] belong to the simple monoclinic system and the $C_{2h}{}^5(P2_1/a)$ space group, which has a twofold screw axis. There is a degeneracy for all points on the BZ boundary plane perpendicular to the corresponding screw axis in $\mathbf{k}$ space. In addition, it is possible to show that there are degeneracies in naphthalene and coronene along the lines

$$\mathbf{k}=\pm\tfrac{1}{2}\mathbf{b}_2+K_3\mathbf{b}_3; \qquad \mathbf{k}=\pm\tfrac{1}{2}\mathbf{b}_1\pm\tfrac{1}{2}\mathbf{b}_2+K_3\mathbf{b}_3. \quad (15)$$

The $\mathbf{b}_i$'s are primitive translations in the $\mathbf{k}$ lattice where

$$\mathbf{b}_i\cdot\mathbf{t}_j=\delta_{ij} \quad (16)$$

and

$$\mathbf{k}=K_1\mathbf{b}_1+K_2\mathbf{b}_2+K_3\mathbf{b}_3, \quad (-\tfrac{1}{2}\leq K_1, K_2, K_3\leq\tfrac{1}{2}). \quad (16a)$$

The $\mathbf{t}_j$'s are primitive translations in the monoclinic crystal defined by

$$\mathbf{t}_1=\mathbf{c}=c\sin B\mathbf{e}_1+c\cos B\mathbf{e}_2,$$
$$\mathbf{t}_2=\mathbf{a}=a\mathbf{e}_2,$$
$$\mathbf{t}_3=\mathbf{b}=b\mathbf{e}_3. \quad (17)$$

$\mathbf{e}_1$, $\mathbf{e}_2$, $\mathbf{e}_3$ are three mutually perpendicular unit vectors. The $\mathbf{b}$ axis is the screw axis.

One can show that there are no degeneracies required by the spacial symmetries of these aromatic crystals. To do this it is necessary to introduce the concept of the group of the wave vector $\mathbf{k}'$. This group comprises all those symmetry operations of the space group which leaves $\mathbf{k}'$ invariant. It can be shown[22] that a nonaccidental degeneracy of the band at certain values of $\mathbf{k}(\mathbf{k}=\mathbf{k}')$ can only occur if $\mathbf{k}'$ is left invariant by some symmetry operation. $\mathbf{k}'$ must therefore be either parallel to a rotation (or screw) axis or in the plane of a reflection (or glide) plane. $\mid \mathbf{k}_l'M \rangle$ will denote a crystal exciton function where $\mathbf{k}'$ is along a symmetry element.

A member of the group of the wave vector $\mathbf{k}'$ can be denoted by $\{\mathbf{B} \mid \mathbf{t}\}$, $\mathbf{B}$ being a rotation, proper or improper, $\mathbf{t}$ any combination of lattice translations and translations between sites. The various $\mathbf{B}$'s of this group are isomorphous with *a* point group. The irreducible representation of *this* point group determines the transformation behavior of $\mid \mathbf{k}_l'M \rangle$. If there is a two-dimensional irreducible representation of this point group, there must be two wave functions $\mid \mathbf{k}_1'M \rangle$ and $\mid \mathbf{k}_2'M \rangle$ of the same energy and $\mathbf{k}$ value.[23]

$$\{\mathbf{B} \mid \mathbf{t}\}\begin{pmatrix} \mid \mathbf{k}_1'M \rangle \\ \mid \mathbf{k}_2'M \rangle \end{pmatrix} = \exp(\mathbf{k}'\cdot\mathbf{t})\mathbf{R}(B)\begin{pmatrix} \mid \mathbf{k}_1'M \rangle \\ \mid \mathbf{k}_2'M \rangle \end{pmatrix}. \quad (18)$$

Here $\mathbf{R}(B)$ is a two-dimensional irreducible matrix of the group of k'. If the point group has an n-dimensional representation, then there must be n functions of the same $\mathbf{k}'$ (but from n different bands) that have the same energy, and which form a basis for the n-dimensional irreducible representation.

The crystal systems treated in this paper are either monoclinic or orthorhombic. For these systems all irreducible representations of the group of the wave vector $\mathbf{k}'$ are unidimensional. This follows most quickly by noting that the point groups underlying the *crystal* space groups all have unidimensional representations. The orthorhombic lattice shows D_{2h} symmetry, while the monoclinic lattice shows C_{2h} symmetry. The point groups associated with the group of the wave vector for the orthorhombic and monoclinic systems must be subgroups of D_{2h} and C_{2h}, respectively; hence they too are unidimensional. Overlap of the bands is, of course, permissible.

[17] C. Herring, Phys. Rev. **52**, 361 (1937).
[18] E. G. Cox, Proc. Roy. Soc. (London) **A135**, 491 (1932).
[19] E. G. Cox and J. A. S. Smith, Nature **173**, 75 (1954)
[20] J. M. Robertson and J. G. White, Acta Cryst. **2**, 233 (1949).
[21] J. M. Robertson and J. G. White, J. Chem. Soc. **1945**, 607.
[22] L. P. Bouckaert, R. Smoluchowski, and E. Wigner, Phys. Rev. **50**, 58 (1936).
[23] G. F. Koster, *Solid-State Physics* (Academic Press Inc., New York, 1957), Vol. 5, p. 211.

As pointed out by several authors[24,25] it is possible to determine the coefficients $C_{l\theta}$ when $\mathbf{k}=0$ and determine relationships among the coefficients when $\mathbf{k}$ is along a symmetry element of the crystal by applying group theoretical arguments. When $\mathbf{k}=0$ the crystal wave functions $|\,\mathbf{k}_l M\rangle$ serve as a basis for an irreducible representation of the factor group. We have for naphthalene (or coronene)

$$|\,\mathbf{k}_l M\rangle=[\,|\,\mathbf{k}\mathrm{I}M\rangle+(-1)^l\,|\,\mathbf{k}\mathrm{II}M\rangle]/\sqrt{2} \qquad (l=1,2) \tag{19}$$

and for benzene

$$|\,\mathbf{k}_l M\rangle=\sqrt{2}^{-1}\sum_{\theta=\mathrm{I}(1)}^{\mathrm{IV}(4)}\sin(\pi l\theta/2+\pi/4)\,|\,\mathbf{k}\theta M\rangle \qquad (l=1,2,3,4). \tag{20}$$

When $\mathbf{k}$ is not zero but is along a symmetry element, say parallel to the screw axis in the direction of $\mathbf{b}$, we again find simple relationships. For naphthalene (or coronene) we have

$$C_{\mathrm{II}}=\pm C_{\mathrm{III}}, \tag{21}$$

and for benzene

$$C_{\mathrm{II}}=\pm C_{\mathrm{III}};\qquad C_{\mathrm{III}}=\pm C_{\mathrm{IIV}}. \tag{22}$$

(The sites have been labeled so that site I is transformed into site III and site II into site IV by the screw axis operation.) Symmetry arguments cannot be used as a means to determine the coefficients of a general $\mathbf{k}$. Any linear combination of the one-site functions will have the same transformation properties as any other combination. It is then necessary to solve a secular determinant for the coefficients.

We shall assume in the present work that *only nearest-neighbor terms* are important in the effective Hamiltonian [Eq. (6)]. This approximation appears to be reasonable although a detailed study of the *ionization states* would be required to establish the validity of the approximation. On the basis of this assumption, the coefficients, $C_{l\theta}$, are the same as for the $\mathbf{k}=0$ states. With naphthalene as an example, Eq. (6) leads to the following secular determinant:

$$\begin{vmatrix} H_{\mathrm{I,I}}(\mathbf{k})-\mathcal{E} & H_{\mathrm{I,II}}(\mathbf{k}) \\ H_{\mathrm{II,I}}(\mathbf{k}) & H_{\mathrm{II,II}}(\mathbf{k})-\mathcal{E}\end{vmatrix}=0, \tag{23}$$

where

$$H_{\mathrm{I,I}}(\mathbf{k})=H_{\mathrm{II,II}}(\mathbf{k})=2A\cos 2\pi\mathbf{k}\cdot\mathbf{a}+2B\cos 2\pi\mathbf{k}\cdot\mathbf{b}+2C\cos 2\pi\mathbf{k}\cdot\mathbf{c},$$

$$H_{\mathrm{I,II}}(\mathbf{k})=4P\cos(\pi\mathbf{k}\cdot\mathbf{a})\cos(\pi\mathbf{k}\cdot\mathbf{b}). \tag{24}$$

The above expression [Eq. (24)] suggests that the two bands stick together on the planes $K_2=\pm\frac{1}{2}$, $K_3=\pm\frac{1}{2}$. Time reversal only required a degeneracy on the planes $K_3=\pm\frac{1}{2}$ and along the lines defined by Eq. (15). Taking into account nonnearest neighbor interactions, we find that the bands separate for all points except those dictated by time-reversal symmetry.

In the case of naphthalene (or coronene one easily sees that there can be no accidental degeneracies. In the case of benzene it is possible to establish that accidental degeneracies can occur within the BZ. Taking into account nonnearest neighbor contributions to the band energies, and noting that time-reversal requires pairwise degeneracy on the surfaces of the BZ, we find that there can be (1) curves of degeneracies in the $K_1=0$ or $K_2=0$ or $K_3=0$ planes and (2) points of degeneracy on the symmetry axes. The ordering of the band energies and the symmetry of the corresponding wave functions at $\mathbf{k}=0$ determine in which of the above three planes the degeneracy curves will lie. If, however, one omits nonnearest neighbor interactions, one finds surfaces of "accidental" degeneracies. These surfaces extend throughout the BZ and intersect the boundary planes along the boundary edges. If the nonnearest neighbor interactions exceed the spin-spin dipolar interactions, the regions of "accidental" degeneracies are confined only to the neighborhoods of the aforementioned curves and points. Clearly, the total region of the BZ occupied by those values of $\mathbf{k}$ that are sufficiently close to the curves or points of degeneracies [so that Eq. (14) is required to calculate the spin energies] is quite small. It is small in fact in comparison to the region occupied by those $\mathbf{k}$'s that are sufficiently near the boundaries of the *BZ* where time-reversal degeneracies occur.

4. RESONANCE SPECTRA

In using Eq. (13) to calculate the spin energies in the Δ region of the BZ, we encounter matrix elements of the form

$$\langle\mathbf{k}_l M\,|\,\mathcal{H}_D\,|\,\mathbf{k}_l M'\rangle=\sum_\theta|\,C_{l\theta}\,|^2\langle n\theta M\,|\,\mathcal{H}_D\,|\,n\theta M'\rangle+\sum_\theta F(k_l\theta MM')+\sum_{\theta<\theta'}G(k_l\theta\theta' MM'), \tag{25}$$

where

$$F(k_l\theta MM')=\sum_{t(\neq n)}|\,C_{l\theta}\,|^2\langle n\theta M\,|\,\mathcal{H}_D\,|\,t\theta M'\rangle\,\mathrm{ixp}\mathbf{k}\cdot(\mathbf{R}_{t\theta}-\mathbf{R}_{n\theta}),$$

$$G(k_l\theta\theta' MM')=\sum_t[C_{l\theta}{}^*C_{l\theta'}\langle n\theta M\,|\,\mathcal{H}_D\,|\,t\theta' M'\rangle\times\mathrm{ixp}\mathbf{k}\cdot(\mathbf{R}_{t\theta'}-\mathbf{R}_{n\theta})+C_{l\theta}C_{l\theta'}{}^*\langle t\theta' M\,|\,\mathcal{H}_D\,|\,n\theta M'\rangle\times\mathrm{ixp}\mathbf{k}\cdot(\mathbf{R}_{n\theta}-\mathbf{R}_{t\theta'})]. \tag{26}$$

If one ignores the small terms $F(k_l\theta MM')$ and $G(k_l\theta\theta' MM')$, it becomes a simple matter to calculate the matrix elements $\langle\mathbf{k}_l M\,|\,\mathcal{H}_D\,|\,\mathbf{k}_l M'\rangle$. (An estimate of the F and G terms will be made later on.) With naphthalene as a representative example, we integrate

[24] H. Winston, J. Chem. Phys. **19**, 156 (1951).
[25] D. Fox and O. Schnepp, J. Chem. Phys. **23**, 767 (1955).

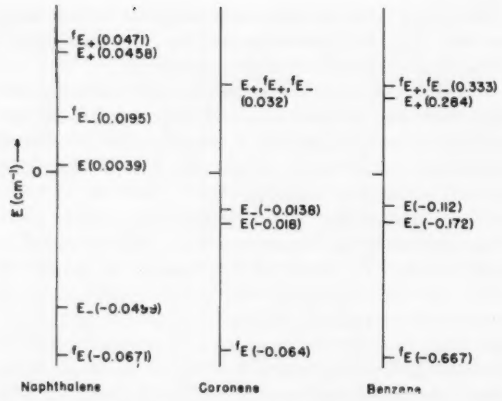

FIG. 1. Zero-field energies of the triplet exciton states of crystalline naphthalene, coronene and benzene. ^1E, $^1E_\pm$ denote zero-field energies of the isolated molecules; E, $E_\pm$ denote the triplet exciton spin energies. ^1E, E refer to the energies of the $M=0$ states. Energies are in cm^{-1} except for benzene where the units are D (see text).

over the space coordinates and obtain a matrix element involving only *spin functions* and *spin operators*.

$$\langle \mathbf{k}_l M \mid \mathcal{H}_D \mid \mathbf{k}_l M' \rangle$$
$$\sim \tfrac{1}{2}\{\langle M \mid [D(S_z^2-\tfrac{1}{3}S^2)+E(S_x^2-S_y^2)]_{\mathrm{I}} \mid M' \rangle$$
$$+\langle M \mid [D(S_z^2-\tfrac{1}{3}S^2)+E(S_x^2-S_y^2)]_{\mathrm{II}} \mid M' \rangle\}. \quad (27)$$

Here $D=\pm 0.1006$ cm^{-1}; $E=\mp 0.0138$ cm^{-1}.

The x axis corresponds to the long axis of the molecule; the y axis corresponds to the short axis of the molecule. The subscripts I and II indicate that the x, y, z axes coincide with the molecular axes at sites I and II, respectively. To facilitate the computation the spin functions were taken as quantized along the **b** axis (screw axis) with unit vectors $\mathbf{e}_z$, $\mathbf{e}_y$, $\mathbf{e}_x$ in the direction of **b**, **a**, and **c**′ (**c**′ being perpendicular to **a** and **b**).[20] It is a simple matter to transform the spin operators from their respective molecular axis systems $(x, y, z)_{\mathrm{I}}$ or $(x, y, z)_{\mathrm{II}}$ to the $\mathbf{e}_z$, $\mathbf{e}_y$, $\mathbf{e}_x$ Cartesian system and calculate the matrix elements.

The following spin Hamiltonian was found to reproduce the energies from the secular determinant Eq. (13) ($\mathcal{H}$ expressed in cm^{-1}):

$$\mathcal{H}_s=-0.00588(S_z^2-\tfrac{1}{3}S^2)-0.0345(S_x^2-S_y^2)$$
$$+0.0332(S_xS_y+S_yS_x).$$
$$(\mathbf{e}_z, \mathbf{e}_y, \mathbf{e}_x \text{ Cartesian system}) \quad (28)$$

This spin Hamiltonian can be further simplified by rotating through an angle $\theta=68°$, counterclockwise about the **b** axis, thus transforming the Cartesian system from $\mathbf{e}_z$, $\mathbf{e}_x$, $\mathbf{e}_y$ to $\mathbf{e}_z$, $\mathbf{e}_{x'}$, $\mathbf{e}_{y'}$. $\mathcal{H}_s$ becomes

$$\mathcal{H}_s=-0.00588(S_z^2-\tfrac{1}{3}S^2)+0.0478(S_{x'}^2-S_{y'}^2). \quad (29)$$

For coronene we have

$$\mathcal{H}_s=0.0273(S_z^2-\tfrac{1}{3}S^2)-0.0229(S_x^2-S_y^2), \quad (30)$$

where the x, y, z axes are taken as coinciding with **c**′, **a**, **b**, respectively.[21] For benzene the following spin Hamiltonian[26] is obtained:

$$\mathcal{H}_s=D[0.168(S_z^2-\tfrac{1}{3}S^2)-0.228(S_x^2-S_y^2)]. \quad (31)$$

Here x, y, z axes coincide with **b**, **a**, **c**, respectively.[18,19] Figure 1 indicates the exciton spin energies relative to those of the free molecules and summarizes the above results.

We now estimate the F and G terms [Eq. (25)] for naphthalene, the results being qualitatively the same for the other systems. $F(k_l\theta M M')$ involves terms of the type $\langle n\theta M \mid \mathcal{H}_D \mid t\theta M' \rangle$, which can, after slight manipulation, be approximated by the following equation, when $M=M'=1$.

$$\langle n\theta 1 \mid \mathcal{H}_D \mid t\theta 1 \rangle \quad (t\neq n)$$
$$\sim \tfrac{1}{2}g_e^2 \mid \beta \mid^2 \langle u_{n\theta}'(1)u_{t\theta}(2) \mid r_{12}^{-3} \mid u_{n\theta}(1)u_{t\theta}'(2) \rangle$$
$$-3g_e^2 \mid \beta \mid^2 \langle u_{n\theta}'(1)u_{t\theta}(2)\alpha(1)\beta(2) \mid$$
$$\times(\mathbf{s}_1\cdot\mathbf{r}_{12})(\mathbf{s}_2\cdot r_{12})r_{12}^{-5} \mid u_{n\theta}(1)u_{t\theta}'(2)\beta(1)\alpha(2) \rangle. \quad (32)$$

$u_{n\theta}'$ denotes the "excited" orbital of molecule $n\theta$ (the lowest unfilled molecular orbital of the unexcited molecule); $u_{n\theta}$, the highest filled orbital of the unexcited molecule. An estimate can be made of the value of the terms in Eq. (32) by replacing $(r_{12})^{-3}$ by $(R_{nt}^2 r_{12})^{-1}$ and $(\mathbf{s}_1\cdot\mathbf{r}_{12})(\mathbf{s}_2\cdot\mathbf{r}_{12})r_{12}^{-5}$ by $(\mathbf{s}_1\cdot\mathbf{e}_{nt})(\mathbf{s}_2\cdot\mathbf{e}_{nt})R_{nt}^{-2}r_{12}^{-1}$ and then using the Davydov-type dipole approximation. $\mathbf{e}_{nt}$ is a unit vector connecting the centers of molecules $n\theta$ and $t\theta$; $R_{nt}=\mid \mathbf{R}_{n\theta}-\mathbf{R}_{t\theta} \mid$.

This approximation is good when the distance between centers of molecules is several times larger (say 8 to 10 times larger) than the dimensions of the molecule. Unfortunately this is not true for nearest neighbors, and only roughly true for next-nearest neighbors. It is expected, however, that the above substitution will be within an order of magnitude of the correct value. (This technique cannot be used in the case of benzene because the dipole transition matrix vanishes and an octapole matrix is necessary.[25] The conclusions based on the naphthalene crystal should be qualitatively applicable to the benzene crystal.) The six nearest naphthalene neighbors need only be considered, and the dipole transition matrix element can be obtained from the experimental oscillator strength for the transition, $^1A_{1x}^- \rightarrow {}^1B_{2u}^+$.[27] (The lowest triplet of naphthalene is the $^3B_{2u}^+$ state.) We obtain the maximum value of 4.8×10^{-4} cm^{-1} for

$$\mid \sum_\theta F(k_l\theta 11) \mid$$

[26] The spin Hamiltonian of benzene molecule is $D(S_z^2-\frac{1}{3}S^2)$, z being normal to the molecular plane. Hameka[2] calculated D to be 0.15 cm^{-1} for a $^3B_{1u}^+$ state.

[27] R. Pariser, J. Chem. Phys. **24**, 250 (1956).

when $k=0$. The other matrix elements, $F(k_l\theta MM')$, are of the same order of magnitude. The term

$$|\sum_{\theta<\theta'} G(k_l\theta\theta' 11)|$$

can be evaluated in a similar manner as above and gives a maximum value of about 5×10^{-6} cm^{-1} for $\mathbf{k}=0$.

One therefore obtains about 0 to 4.8×10^{-4} cm^{-1} as the range of values for

$$|\sum_{\theta} F(k_l\theta MM')+\sum_{\theta<\theta'} G(k_l\theta\theta' MM')|.$$

It is most probable that the approximations used underestimate the actual range. It may well be that the true maximum value is a factor 5 to 10 times larger than 4.8×10^{-4} cm^{-1}.

It is interesting to note that when $k=\mathbf{k}^b$, a vector terminating on the boundary of the BZ, where time-reversal symmetry requires that the bands stick together in pairs in the absence of an external magnetic field, the spin-Hamiltonian [Eq. (2)] significantly different from that of the Δ region. One expects in the cases of naphthalene and coronene that the spectra obtained from the $\mathbf{k}^b$ states to be *very nearly the same* as those from an "oriented gas" of isolated molecules (see Introduction). In the case of benzene, however, the spectra from the $\mathbf{k}^b$ states are not approximately the same as those from an "oriented gas" of isolated benzene molecules. The spectra from the "oriented gas" would show no averaging over sites. Its ESR spectra would show hyperfine structure and would consist of (a) eight lines for an arbitrary $\mathfrak{H}$ and (b) two lines when $\mathfrak{H}$ is along **a**, **b**, or **c**. The spectra from the $\mathbf{k}^b$ states on the other hand should consist of four lines for an arbitrary $\mathfrak{H}$, except when $\mathfrak{H}$ is along **a**, **b**, or **c**, whereupon two line spectra should be obtained. In general, the ESR spectra are highly dependent on **k** in the Γ region.

All the crystals so far treated have had at least two differently oriented molecules per unit cell. Crystals that do not have at least two sets of differently oriented molecules will give essentially the same resonance spectra as the isolated molecules except for the absence of nuclear hyperfine structure. It is assumed, of course, that the lowest triplet state of the crystal is not strongly perturbed by low-lying ionization states.

5. CONCLUSION

We have calculated the ESR spectra to be expected for triplet exciton states of benzene, naphthalene, and coronene. Except for small regions of time reversal and accidental degeneracies and certain small terms (F, G), the spectra are independent of the exciton wave vector **k**. Two-line spectra (with no hyperfine structure), representing an average over the molecular sites in the unit cell, are obtained. The extent of the coupling of the excitation waves to the phonon field is not known. It is possible that at sufficiently low temperature (say helium temperatures) the lattice perturbations of the exciton wave will be small enough so that the exciton wave picture used need not be replaced by an excitation diffusion model. Even so, one must consider two time-dependent exciton-phonon interactions that can lead to line broadening and spin lattice relaxation. First, an exciton can be scattered so that its **k** vector moves from the Δ region of the BZ to the Γ region, and back to the Δ region. Since the stationary spin states in the two regions are in general different, this exciton scattering is clearly a relaxation mechanism. It is interesting to note that in certain special cases this relaxation mechanism ceases to be effective. If, for example, in the case of naphthalene, the steady applied field is along the twofold screw axis (or perpendicular to it), and if the applied field is so strong that the Zeeman energy is large relative to the zero-field splittings, then the stationary spin states in the Δ and Γ regions are essentially the same, and the Δ to Γ scattering does not lead to relaxation.

A second type of relaxation mechanism arises when the electronic excitation density on the various molecules of the unit cell varies with time. This may be achieved by mixing exciton states with the same **k** vector. This mixing clearly can be brought about by intermolecular and intramolecular lattice vibrations that make various molecules in the unit cell nonequivalent to one another. Certain degenerate intermolecular vibrations may be particularly effective in this respect. But here again this relaxation mechanism can be made relatively ineffective in certain cases by the application of a strong, steady external field in special crystal directions.

In the case that an exciton diffusion model is more appropriate, it is again the jumping of excitation between the various molecules of the unit cell that is doubtless the most important source of spin-lattice relaxation and line broadening. It is comparatively easy to make order-of-magnitude estimates of resonance linewidths $\Delta\nu$ due to this effect

$$\Delta\nu\sim Z^2\tau. \tag{33}$$

Here Z is of the order of the zero-field splitting and τ is the characteristic time for random walk between nontranslatory neighbors in the unit cell. If the triplet exciton Davydov splittings are of the order of 1–10 cm^{-1}, then we may reasonably expect that the diffusion rate (τ^{-1}) will be at least as large as this. Thus, tolerable resonance linewidths are expected from Eq. (33) when Z is in the range 0.01–0.1 cm^{-1}. Again, for strong external fields and special crystal orientations, the present relaxation mechanism can be almost completely eliminated for some crystal systems.

Note added in proof. (a) The above discussion has neglected interactions between excitons. At high exciton concentrations one of course expects an exchange

narrowed spin resonance line shape centered near $g=2$. In our opinion it is quite likely that many crystalline free radicals that show strong exchange narrowed spin resonance line shapes at room temperature will show triplet exciton resonances at low temperatures, rather than resonances characteristic of ferromagnetic or antiferromagnetic states. This expectation is based in part on the fact that aromatic molecules tend to pack in crystals so that the strongest interactions are along one-dimensional chains, and such chains are notoriously unstable with respect to displacements that produce an alternation in internuclear distances. Recent work by D. B. Chesnut and W. D. Phillips (private communication) suggests the presence of this type of triplet exciton state in the crystalline TCNQ charge transfer complexes.

(b) The vanishing of nuclear hyperfine structure in paramagnetic exciton and polaron states has already been pointed out by M. F. Deigen and S. I. Pekar, Soviet Physics—JETP **34**, 471 (1958).

THE JOURNAL OF CHEMICAL PHYSICS VOLUME 35, NUMBER 5 NOVEMBER, 1961

Vibrational Spectra of Inorganic Molecules. III. Infrared Reflection Spectra of Molten Lithium, Sodium, and Potassium Hydroxides

J. K. WILMSHURST

Parma Research Laboratory, Union Carbide Corporation, Parma 30, Ohio

(Received March 24, 1961)

The infrared reflection spectra of molten lithium, sodium, and potassium hydroxides have been obtained from 4200–200 cm^{-1} and the optical constants derived by the method of Robinson and Price. The absorption spectra are consistent with some latticelike structure in the liquid state, with the degree of order in the three melts being virtually identical. The hydroxide ion is most probably unassociated and freely rotating in all melts.

A PREVIOUS study of the infrared reflection spectra of the fused alkali nitrates[1] suggested some degree of lattice-like structure in these melts with the rotation of the nitrate ion being restricted in certain cases. In an endeavor to further improve our knowledge of the liquid ionic state and determine if such lattice aggregates and also restricted rotation of the polyatomic ions are general, it appeared desirable to investigate other ionic liquids. In the present investigation, the simplest dipolar ion, OH^- was chosen and the infrared reflection spectra of liquid lithium, sodium, and potassium hydroxides have been obtained and analyzed using the method of Robinson and Price.[2a] In every case, the spectra consisted of only two regions of absorption: a very weak region around 3500 cm^{-1}, consisting principally of two absorption maxima associated with the unresolved P and R rotational branches of the OH^- stretching vibration band, indicating that in these melts the hydroxide ion is rotating freely, and a very intense region below 600 cm^{-1} due to the latticelike vibrations.

EXPERIMENTAL

With the experimental arrangement described elsewhere,[1] the infrared reflection spectra were obtained using a Perkin-Elmer model 12C spectrometer equipped with LiF, NaCl, KBr, and CsI prisms. Either "Fisher's" anhydrous lithium or sodium hydroxide or "Baker's Analyzed" anhydrous potassium hydroxide was contained in a nickel crucible and a flowing atmosphere of argon maintained throughout the entire system. The reflection spectra were analyzed by the method of Robinson and Price,[2a] as discussed previously,[1] using a Royal McBee LGP-30 computer.[2b]

The experimental reflection spectra, together with the derived absorption spectra and refractive index curves for lithium, sodium, and potassium hydroxides are shown in Figs. 1–3, respectively, and the observed frequencies and their assignments are given in Table I.

ASSIGNMENT

The hydroxide ion, having point group symmetry $C_{\infty v}$, should give rise to only one vibrational frequency, active in both the infrared and Raman spectrum around 3500 cm^{-1}. The observed spectrum for each of the hydroxides in this region, however, shows two relatively prominent, though weak, broad bands, together with one or two other weaker bands. The assignment of these bands is not immediately obvious and it is necessary to consider the possible configurations of the hydroxide ion in the melt.

Although the hydroxide ion is conceivably capable of forming a polymeric hydroxide lattice by hydrogen bonding, the long O—O distance of ~3.35 Å in the low-

[1] J. K. Wilmshurst and S. Senderoff, J. Chem. Phys. **35**, 1078 (1961).

[2] (a) T. S. Robinson and W. C. Price, *Molecular Spectroscopy*, edited by G. Sell (The Institute of Petroleum, London, 1955), p. 211. (b) I am indebted to Dr. H. J. Bowlden of these Laboratories for programming the electronic computer.

temperature form of crystalline sodium and potassium hydroxide[3a] and the even longer O—O distance of ~4 A in the high-temperature form of the latter,[3b] make it doubtful that these hydrogen bonds would be strong enough to allow such a lattice to exist in the liquid at 360–500°C ($RT \sim 1.4$ kcal mole^{-1}). However, smaller polymeric entities, especially the cyclic dimer $(OH)_2^=$, may exist. Such a dimeric ion should give rise to two infrared active bands in the 3000 cm^{-1} region, related to each other (ignoring potential function cross terms) as

$$\nu_1/\nu_2 = \tan\theta,$$

where 2θ is the dimer ring angle, together with one lower frequency band due to the ring buckling vibration. Thus the pair of prominent bands observed around 3500 cm^{-1} in all the hydroxides could be assigned to the stretching modes of such a ring dimer with $2\theta \simeq 84°$. However, the absence of any band in the lower frequency region that could be assigned to the ring buckling mode does not

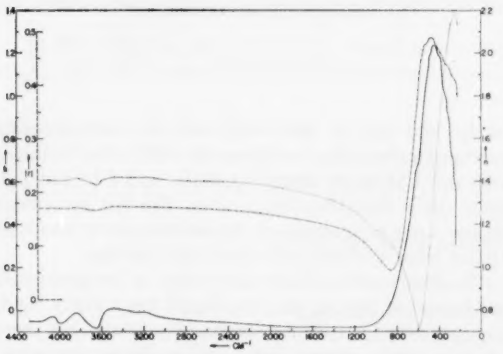

FIG. 1. – – – The infrared reflection spectrum of molten lithium hydroxide at 490°C. —— The derived absorption spectrum. • • • The derived refractive index dispersion curve.

support this hypothesis, although this band may, of course, be very weak and therefore not observed. Further, the greater of the two frequencies around 3500 cm^{-1}, assigned to the dimer stretchings, is not much less than in the solid and, in fact, in lithium hydroxide this frequency is even higher than the value in the solid. This is most surprising, for if our assumption of dimers is correct, it would be expected that the OH force constant in the dimer should be considerably less than in the monomer (e.g., in diborane[4] the inner ring *BH* force constant is only 1.43×10^5 dynes cm^{-1} compared to the outer *BH* force constant of 3.42×10^5 dynes cm^{-1}) and consequently the dimer frequencies should also be considerably lower (~20%). Therefore, while the hypothesis of dimeric $(OH)_2^=$ ions might explain the pair of

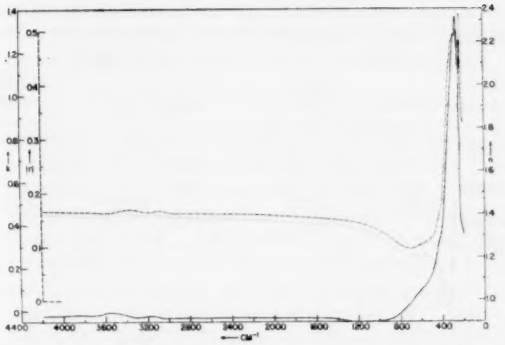

FIG. 2. – – – The infrared reflection spectrum of molten sodium hydroxide at 350°C. —— The derived absorption spectrum. • • • The derived refractive index dispersion curve.

prominent bands around 3500 cm^{-1} it appears unlikely that this is the true explanation.

The remaining possible explanation is to assume the hydroxide ion to be sitting in a cavity surrounded by cations and either fixed in direction, undergoing a torsional motion, or alternatively, freely rotating. While the former possibility would give rise to two bands due to $(+\leftrightarrow-)$ transitions from the sublevels of the upper and lower vibration levels, it is unlikely that the splitting experienced by these sublevels would occur to the extent necessary (~350 cm^{-1}) to explain the observed spectrum. Further, the degree of splitting of these sublevels depends on the barrier hindering rotation of the hydroxide ion, and it is certain that this potential barrier will be considerably less for potassium hydroxide than for lithium hydroxide.[5] Thus, the splitting of the hydroxyl frequency should also be much less in potassium hydroxide than in lithium hydroxide contrary to the observation. On the other hand, if the hydroxide ion was freely rotating it would give rise to a parallel type vibration-rotation band with *P* and *R* branches. If the

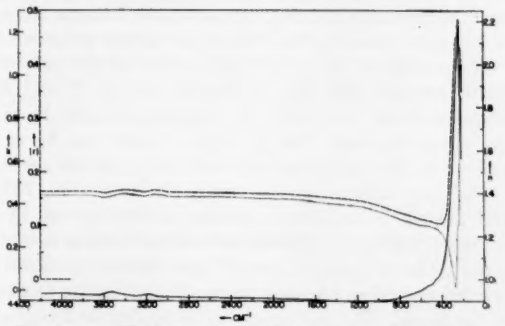

FIG. 3. – – – The infrared reflection spectrum of molten potassium hydroxide at 430°C. —— The derived absorption spectrum. • • • The derived refractive index dispersion curve.

[3] (a) T. Ernst and R. Schober, Nachr. Akad. Wiss. Göttingen, Math.-physik Kl. **76** (1946); **49** (1947). (b) W. Teichert and W. Klemm, Z. anorg. u. allgem. Chem. **243,** 138 (1939).

[4] R. P. Bell and H. C. Longuet-Higgins, Proc. Roy. Soc. (London) **A183,** 357 (1944).

[5] In the liquid nitrates (reference 1) the potential barrier was found to decrease drastically from the lithium salt to the potassium salt.

TABLE I. The infrared spectra of lithium, sodium, and potassium hydroxides.

LiOH		NaOH		KOH		
Liquid (490°C)	Solid[a] ~20°	Liquid (360°C)	Solid[b] ~20°	Liquid (440°C)	Solid[c] ~23°	Assignment
~4060						3652+441=4093
		~3845				3295+570=3865
~3840		~3545		~3536		
(3652)[d]	3678	(3295)[d]	3637	(3300)[d]	3600	OH stretching mode
~3495		~3155		~3180		
~3195						3652−441=3211
					643	OH liberation[e]
				~515		
		~570		~450		
~610		~425		~310		
~478		~319		~253		
		~285				
441		265		233	<270	lattice vibration
~385		238		218		
~360		~210				
~335						
~308						
~290						
~267						
~242						

[a] K. A. Wickersheim, J. Chem. Phys. **31,** 863 (1959).
[b] W. R. Busing, J. Chem. Phys. **23,** 933 (1955).
[c] R. G. Snyder, J. Kumamoto, and J. A. Ibers, J. Chem. Phys. **33,** 1171 (1960).
[d] Approximate band center.

OH^- bond length is assumed to be ~0.97 A, the *PR* separation expected in lithium, sodium, and potassium hydroxides is calculated to be 267, 243, and 258 cm^{-1}, respectively, which can be compared with the observed separations 345, 390, and 356 cm^{-1}, respectively. The agreement between the calculated and observed *PR* spacings does not, at first sight, appear to be good, but it should be remembered that the presence of the cation field removes the m degeneracy of the energy levels of the diatomic rotator and this could produce a drastic change in the *PR* separation. A similar change in *PR* separation has been noted, for instance, for HCl gas in nitrogen at 396 amagats[6] and for HCl in stannic chloride liquid[7] where the *PR* separations are ~185 and ~195 cm^{-1}, respectively, much greater than the *PR* separation of 124 cm^{-1} observed for HCl vapor at low pressures.[8]

If we assume this latter explanation of the pair of bands around 3500 cm^{-1} as being just the *P* and *R* branches of the hydroxide ion vibration-rotation band, the remaining weak bands in this region can be explained as sum and difference tones with a lattice mode.

The very intense low-frequency bands at 440, 265, and 233 cm^{-1}, in lithium, sodium, and potassium hydroxides, respectively, possess a structure similar to that expected for a "sums of states" type band of a crystalline lattice and can be assigned to the latticelike modes in the liquid. The frequency ratios ν_{Li}/ν_{Na} and ν_{Na}/ν_{K} for this band are observed to be 1.66 and 1.14, respectively, and can be compared with the corresponding averaged values obtained from the solid alkali halides,[9] 1.25 and 1.18 using eigenfrequencies and 2.11 and 1.20 using the reststrahlan frequencies. The fair agreement supports our assignment of the low-frequency bands as arising from a cation-anion latticelike motion.

The observation of latticelike modes in the liquid does not imply, of course, that the liquid has a fairly rigid, highly ordered, latticelike structure but only that there are reasonably strong anion-cation forces operative. The relative sharpness of the band, however, does imply that the interatomic distances from any particular ion to its first and second nearest neighbors cannot have too wide a possible range of values, for, if they did, a wide range of energy levels would exist and the band would be badly broadened out. This conclusion is in agreement with the results of x-ray investigations on ionic melts.[10]

Some idea of the general change in the degree of order in the melt as the cation is varied may be obtained from a consideration of the band intensity of this lattice mode. If we assume a cybotactic model of the melt in which all the crystallites are cubes of edge l then the number of linear ion chains running down through the cube from any face is $(l/R)^2$, where R is the cation-anion internuclear distance.[11] If now the change of dipole moment of one of these chains upon vibration is taken as Λ, the total change of dipole moment for the

[6] R. Coulon, L. Galatry, B. Oksengorn, S. Robin, and B. Vodar, J. phys. radium **15,** 641 (1954).
[7] W. J. Jones and N. Sheppard, Trans. Faraday Soc. **56,** 625 (1960).
[8] W. Burmeister, Ber. deutsch. physik. Ges. **15,** 595 (1913).
[9] R. B. Barnes, Z. Physik. **75,** 723 (1932).
[10] H. A. Levy, P. A. Argon, M. A. Bredig, and M. D. Danford, Ann. N.Y. Acad. Sci. **79,** 762 (1960).
[11] R is computed using Pauling's ionic radii [*Nature of the Chemical Bond* (Oxford University Press, New York, 1950)], assuming the ionic radius of the hydroxide ion to be 1.53 A.

cube will be $\Lambda(l/R)^2$ and hence the intensity I of the lattice mode will be proportional to $\Lambda^2(l/R)^4$.

If the low-frequency wing of the latticelike band is extrapolated down to the base line, the relative integrated intensity of this band in the different hydroxides is observed to be $I_{LiOH}/I_{NaOH}=1.85$ and $I_{LiOH}/I_{KOH}=3.21$ and, hence, if we assume Λ to be the same in each of the hydroxides, the relative values of l in the three melts are computed to be $l_{LiOH}/l_{NaOH}=1.00$ and $l_{LiOH}/l_{KOH}=0.99_7$. Thus, to the extent that the above treatment for the lattice mode intensity is valid and also remembering the possible error that could be inherent in the estimation of the relative intensities of the latticelike bands due to the necessary extrapolation, we can say that the crystallite size, in the cybotactic model, is identical in each of the hydroxide melts investigated. We might further expect, that on any other model for the ionic liquid state, the degree of order in lithium, sodium, and potassium hydroxides would also be virtually identical.

REFRACTIVE INDICES

If the refractive index dispersion curves for each of the hydroxides studied are treated as if they contained only the one dispersion region arising from the latticelike vibrations, the high-frequency tail of this dispersion curve can be fitted to the two-parameter expression

$$n(\nu)=n(\infty)+A/(\nu_l^2-\nu^2),$$

where ν_l is the frequency of the latticelike mode. On extrapolation of this expression, the refractive index corresponding to the frequency of the sodium D line can be determined for lithium, sodium, and potassium hydroxide to be 1.420 (490°C), 1.407 (350°C) and 1.394 (430°C), respectively, in reasonably good agreement, considering the long extrapolation involved and simplifications assumed, with the values 1.427 (350°C) and 1.414 (430°C) observed by Meyer and Heck[12] for sodium and potassium hydroxides, respectively.

Note added in proof. Since this article was submitted for publication, J. Greenberg and L. J. Hallgren [J. Chem. Phys. **35,** 180 (1961)] have reported the infrared absorption spectrum of liquid NaOH in the 10 000–3330 cm^{-1} region and observed a broad band at 3547 cm^{-1} coincident with the higher frequency component of the doublet observed by us.

[12] G. Meyer and A. Heck, Z. physik. Chem. **100,** 316 (1922).

THE JOURNAL OF CHEMICAL PHYSICS VOLUME 35, NUMBER 5 NOVEMBER, 1961

Effect of Interstitial Li on the Density of Si*

J. S. PRENER AND F. E. WILLIAMS†
General Electric Research Laboratory, Schenectady, New York

(Received April 17, 1961)

The densities of silicon and of silicon containing interstitial Li^+ were determined. There is a volume expansion of 4.7×10^{-24} cm^3 per Li^+ dissolved in silicon. This expansion is interpreted as arising from the Coulombic repulsion between the Li^+ and the partially shielded Si^{4+} cores. Calculations based on a simple model of the charge distribution in silicon are in accord with this interpretation. The density change accompanying the room temperature deionization and aggregation of the lithium was also measured. During the initial stages of this process, the volume increases linearly by 6.0×10^{-24} cm^3 per lithium transferred from the ionized to the deionized state. This expansion is interpreted as arising from overlap repulsive forces between the Si and aggregates of neutral lithium in neighboring interstitial sites. Considerations based on the size of Li^0 in these aggregates and the free energy change for the deionization and aggregation process support this interpretation. A final nonlinear region in the observed volume expansion is interpreted as being due to the precipitation of lithium metal so as to leave itself and the silicon strain free.

I. INTRODUCTION

LITHIUM is soluble in silicon and its donor properties and fast diffusion have been generally accepted as evidence for its presence as an interstitial impurity.[1,2] At 800°C the saturation solubility of Li in equilibrium with an external phase of Li_2Si is about $2\times10^{19}/cm^3$. By rapidly quenching a sample to room temperature after equilibrium has been attained, this high-temperature solubility can be determined from conductivity and Hall measurements.[3]

After an induction period which depends upon the oxygen content of the sample, deionization and aggregation of the dissolved lithium occurs; the kinetics of

* This work was in part supported by the Cambridge Air Force Research Center.

† Present address: Physics Department, University of Delaware, Newark, Delaware.

[1] E. M. Pell, J. Phys. Chem. Solids **3,** 74 (1957).

[2] H. Reiss and C. S. Fuller, J. Phys. Chem. Solids **4,** 58 (1958).

[3] E. M. Pell, *Symposium on Solid State Physics and Telecommunications* (Academic Press Inc., New York, 1961), Vol. 1, p. 26.

TABLE I. Density of silicon at 25.0°C.

Density	Method	Reference
2.32913[a]	Density gradient column	This paper
2.32902	Hydrostatic weighing	A. Smakula and V. Sils, Phys. Rev. **99**, 1744 (1955).
2.32912	x-ray density[b]	A. Smakula, J. Kalnajs, and V. Sils, Phys. Rev. **99**, 1747 (1955).
2.33068	Density gradient column	F. H. Horn, Phys. Rev. **96**, 1521 (1955).

[a] Corrected to 25.0°C.
[b] Using atomic weight computed from masses and abundances of isotopes and Birge's value for Avogadro's number 6.022338×10^{23} mole^{-1}.

this aggregation process have been extensively studied by Pell.[3] In this paper we present the results and interpretation of measurements of the density of silicon containing dissolved lithium and of the changes in density accompanying the room temperature aggregation and deionization of the lithium.

II. EXPERIMENTAL

The densities of the various samples in the form of about 3-mm cubes (etched in 3:1 HNO_3–HF) were determined using a density gradient column.[4] The flotation liquid was a slightly acidified (with formic acid) aqueous solution of thallium (I) formate containing a small quantity of Igepal 630 as a surface active agent. Columns prepared with this liquid, thermostatted to ±0.001°C, were stable for many months even with continuous usage and did not chemically attack the samples. The density columns were maintained in a thermostatted water bath, the temperature of which was checked regularly with a National Bureau of Standards calibrated thermometer having 0.1°C markings and monitored for constancy with a Beckman thermometer having 0.01°C markings. The column used in the measurements described in this paper had a density gradient of about 10^{-4} g cm^{-4} and was calibrated with four hollow glass spheres. The densities of these spheres were determined by adjusting solutions of thallium (I) formate so as just to float the spheres.[5] The densities of the solutions were finally determined using a bicapillary pycnometer calibrated with freshly boiled distilled water. The floating positions of the centers of the calibrating spheres and samples were determined with a cathetometer readable to 0.1 mm. Since the variation of density with distance along the column was extremely close to linear, interpolation between the calibrating spheres was accomplished by graphical means. The precision in the density of the calibration spheres was $\pm2\times10^{-5}$ g cm^{-3}, and with a gradient of 10^{-4} g cm^{-4}, density differences of 10^{-6} g cm^{-3} with a precision of $\pm0.4\times10^{-6}$ g cm^{-3} could be detected between different samples or within the same sample during deionization of the Li^+. The total error in the absolute density of any one sample arising from the uncertainty of ±0.05°C of the temperature of the thermostat, was $\pm3\times10^{-5}$ g cm^{-3} but for our purposes only density differences were of importance.

The initial Li^+ concentration of the silicon samples and the change in Li^+ concentration during deionization at 27.4°C were determined by simultaneous conductivity measurements carried out on a section of the same bar of silicon from which samples for the density measurements were cut. The diffusion of Li into silicon at 800°C and the conversion of conductivity data to concentration are described in a previous paper by Pell.[3] Assuming that Stokes' law for moving spheres in a fluid may be applied approximately to the cubes of silicon used, it can be shown that for the density gradient columns used, the rate of change of position of the sample and of density are proportional during the deionization of the Li^+.

(1) The density of Merck vacuum grown floating zone silicon was found to be 2.32906 g/cm^3 at 27.40°C. Densities of silicon crystals as grown and those quenched from 800°C were the same. Using the value of 4.15×10^{-6}/C° for the coefficient of linear expansion[6] we obtain a value of 2.32913 for the density of silicon at 25.0°C. Recent values of the density of silicon together with our result are shown in Table I.

(2) The densities of Merck vacuum grown floating zone silicon containing 1.8×10^{19} Li per cm^3 and of silicon containing 4×10^{17} oxygen per cm^3 and 1.6×10^{19} Li per cm^3 were both found to be 2.32907 g cm^{-3} at 27.4°C.

If we define v as the macroscopic volume expansion of silicon per dissolved lithium ion, then in terms of the measured density change $\Delta\rho$, the density of silicon ρ_0, the concentration of lithium, c, and the atomic weight of Li M we have $v=\rho_0^{-1}(M/N_0-\Delta\rho/c)$. Using $\rho_0=2.33$, $M=6.94$ and $N_0=6.02\times10^{23}$, we calculate for both samples $v=4.7\times10^{-24}$ cm^3 per Li^+.

(3) After about 10 days at 27.4°C the density of the floating zone silicon containing 1.8×10^{19} Li per cm^3 began to decrease slowly. The density after 40 days had decreased to a value of 2.32878 g cm^{-3}.

For silicon containing oxygen, the deionization of lithium at 27.4°C has an induction period of only several hours,[3] and also proceeds at a sufficiently rapid rate so that the density can be followed over a fairly large change in the concentration of Li^+.

Defining v_i as the macroscopic volume increment per Li transferred from the ionized to the deionized state, one finds that v_i can be determined from the slope

[4] A. Weissberger, *Physical Methods of Organic Chemistry* (Interscience Publishers, Inc., New York, 1959), Vol. I, Part I, pp. 168–170.
[5] F. H. Horn, Phys. Rev. **97**, 1521 (1955).
[6] A. Smakula and J. Kalnajs, Phys. Rev. **99**, 1737 (1955).

of the plot of the density versus the concentration of Li^+.

$$v_i = \rho^{-1}(d\rho/dc).$$

The changes in density with time are shown in Fig. 1 for two different samples of silicon, and the corresponding curves for the changes in concentration of Li^+ are given in Fig. 2. In Fig. 3 is shown the plot of density against concentration of Li^+. There is a linear decrease in density until about 60% of the lithium has deionized after which the density decreases more rapidly. From the slope of the linear region $v_i = 6.0 \times 10^{-24}$ cm^3/Li. The slope near the end of the nonlinear region yields a value of v_i of approximately 19×10^{-24} cm^3/Li.

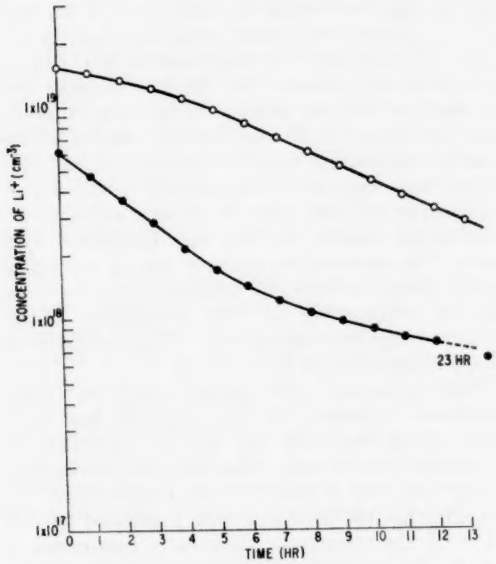

FIG. 1. Time dependence of Li^+ concentration in silicon during deionization and aggregation at 27.4°C. ● Initial Li^+ concentration 1.5×10^{19} cm^{-3}, oxygen content 5×10^{17} cm^{-3}. ○ Initial Li^+ concentration 1.6×10^{19} cm^{-3}, oxygen content 4×10^{17} cm^{-3}. The time from quenching until start of measurements was different for the two samples.

III. INTERPRETATION

A. The macroscopic volume expansion v was found to be 4.5×10^{-24} cm^3 per Li^+ dissolved in silicon. Several possible contributions to this expansion have been considered.

(1) The overlap repulsion force between the interstitial Li^+ and the surrounding Si shown in Fig. 4 resulting from the nonorthogonality of the $1s^2$ electrons of Li^+ with the bonding electrons of the Si appears to be quite small. The ionic radius of Li^+ is only 0.6 A and the Li^+–Si distance is 2.35 A. Consideration of the spatial relation between the interstitial Li^+ and the neighboring Si shows that bonding electrons have a small density near the interstitial site. This is discussed more fully in the later section on interstitial Li^0 where the overlap repulsion forces are important.

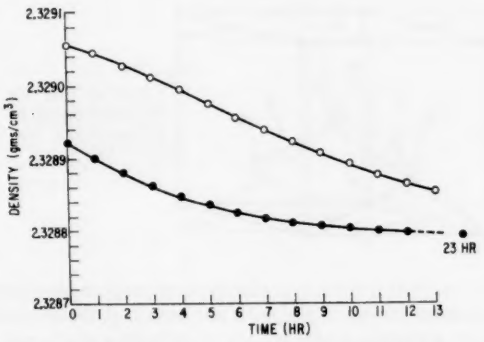

FIG. 2. Time dependence of density of silicon: Li during deionization and aggregation at 27.4°C. Samples as in Fig. 1.

(2) The addition of the conduction electrons with the Li^+ might be expected to cause some volume expansion.[7] The conduction electrons can be treated as a Fermi gas which exerts a pressure which is an explicit function of electron concentration, temperature and effective mass.[8] We find that this pressure produces a volume expansion which is a factor of 30 smaller than observed.

(3) We propose that the principal repulsive force responsible for the volume expansion v observed on dissolving Li^+ arises from the Coulombic repulsion between the interstitial Li^+ and the partially screened Si^{+4} cores. In order to evaluate this proposal we compute a Coulomb potential at the interstitial site which

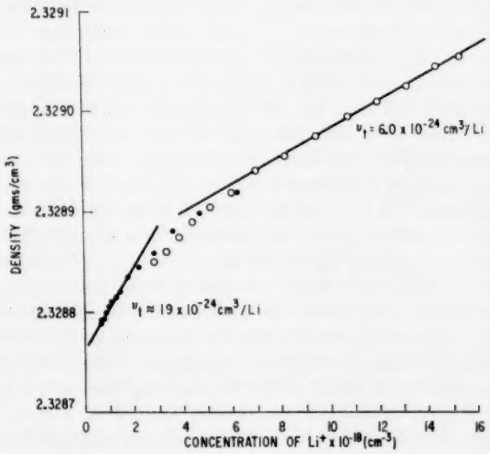

FIG. 3. Density of silicon: Li vs concentration of Li^+ during deionization and aggregation at 27.4°C. Samples as in Fig. 1.

[7] We are indebted to K. Weiser for bringing this possibility to our attention.

[8] J. C. Slater, *Introduction to Chemical Physics* (McGraw-Hill Book Company, Inc., New York, 1939), p. 82.

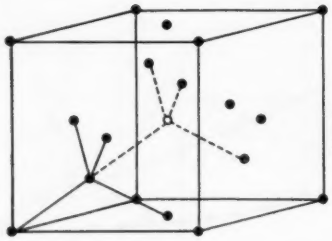

FIG. 4. Unit cell of silicon containing Li^+ at an interstitial site. ● Si, ○ Li^+.

is consistent with the observed expansion and then compare this potential with one obtained theoretically from a simple model for the distribution of charge in silicon.

To calculate a Coulomb potential at the interstitial site from the observed expansion v we assume that silicon can be treated as an elastic medium characterized by shear and bulk moduli μ and K and that the potential arises from the surface charges on a spherical cavity of arbitrary size. The detailed model for silicon will be shown later to be consistent with this general model. From the theory of Eshelby[9] and electrostatics, we calculate the potential ϕ

$$\phi=\frac{4\mu v}{[1+(4\mu/3K)]q}$$

where q is the charge on the Li^+. We obtain μ and K from the elastic constants[10] and find that $\phi=4.8$ volts.

We next consider a simple model for the distribution of charge in silicon in order to determine whether such a distribution does in fact give rise to a potential at the interstitial site of the same magnitude as calculated above from the measured volume expansion. The model consists of spherical Si^{4+} cores, nonoverlapping with the Li^+ and tetrahedrally surrounded by four bonding electrons, each with a spherical charge distribution centered between the Si^{4+} cores and nonoverlapping with the Li^+. The potential at the interstitial site calculated for this charge distribution arising from the four nearest neighbors is 4.9 v, and for the ten near neighbors is 6.4 v. Further shells of Si do not make any large contribution to the potential. For example, five shells containing 42 silicon atoms yield a potential of 6.0 v. Thus two shells containing 10 atoms give approximately the correct potential at the interstitial site and compare favorably with the potential of 4.8 v determined from the measured expansion. The validity of the calculation based on the 10 near neighbors which lie to a good approximation on the surface of a sphere supports the assumption of surface charge on a spherical cavity used in the derivation of the equation for ϕ.

Polarization by the Li^+ has not been included. This would increase the shielding of the Si^{4+} and thereby reduce the potential. Shielding of Li^+ by conduction electrons is negligible at these concentrations. Since the overlap repulsion between Li^+ and the surrounding Si is small, the stable Li^+ position may not be the center of the interstitial cavity. However, since the Coulombic potential in the cavity is quite flat for some distance from the center, one may approximate the actual potential by the potential at the center.

B. We now consider the interpretation of the decrease in density accompanying deionization of interstitial Li^+. The initial linear region, shown in Fig. 3, corresponds to a value of v_i of 6.0×10^{-24} cm³. This is a factor of 2.8 too small for the precipitation of a separate phase of lithium metal so as to leave itself and the silicon strain free. If the lithium is assumed to precipitate as a metal in a cavity and the silicon is elastically strained, then the observed volume increase would be too small by even a larger factor unless we assume that the precipitated lithium metal is compressed to less than one half its normal volume.[9] We therefore propose that the observed volume increase in this region results from the formation of aggregates of neutral lithium atoms at neighboring interstitial sites within the silicon lattice; these aggregates corresponding to Li_2^0, $Li_3^0\cdots Li_{M'}^0$ where the last refers to lithium metal with a coordination number of four and tetrahedral symmetry. The observed expansion is due to overlap repulsive forces between the relatively large Li atoms and the surrounding Si. The deionization of Li^+ accompanying this aggregation is facilitated by the energy of formation of $Li_2^0\cdots Li_{M'}^0$.

These aggregates have approximately the correct interatomic distances for incorporation into interstitial silicon sites. For the free Li_2 molecules, the equilibrium interatomic distance and dissociation energy are 2.67 A and 1.12 ev, respectively.[11] We estimate that the binding energy is reduced by only 0.1 ev if the interatomic distance is constrained to 2.35 A, the nearest-neighbor interstitial site distance in Si. Lithium metal is body centered cubic with an interatomic distance of 3.04 A. The structure of silicon allows, however, only the four nearest-neighbor sites which tetrahedrally surround an interstitial Li to be occupied by other interstitial Li. Using the bond length rule of Pauling,[12] the nearest-neighbor distance for lithium metal with tetrahedral coordination is 2.82 A. The aggregation to form $Li_2\cdots Li_{M'}$ is expected, therefore, to expand the silicon lattice.

In order that aggregation of the type described occurs concurrently with deionization, it is necessary that the Gibbs free energy change be negative for the reaction

$$Li^+ + e \rightarrow 1/n\ Li_n^0$$

in which the Li are at interstitial sites. This change in free energy, neglecting the small entropy and strain

[9] J. D. Eshelby, *Solid-State Physics* (Academic Press Inc., New York, 1956), Vol. 3, pp. 79–144.
[10] H. J. McSkimmin, J. Appl. Phys. **24**, 988 (1953).
[11] G. Herzberg, *Spectra of Diatomic Molecules* (D. Van Nostrand Company, Princeton, New Jersey, 1950), p. 147.
[12] C. A. Coulson, *Valence* (Clarendon Press, Oxford, 1952), p 291.

energy changes and the small pressure volume work, can be written

$$\Delta G_n = -I + F + U_p + \Delta E_R^n - E_D^n.$$

The ionization potential of Li I is 5.4 ev; the electron affinity for the lowest conduction band state of silicon F is 3.5 ev,[13] and the polarization energy U_p calculated from the continuous dielectric model of Si is 2.7 ev. E_D^n is the dissociation energy of the Li aggregate per Li. E_D^1 is zero, and for E_D^2 we can use one-half the dissociation energy of Li_2. Finally, E_D^n for large n will be less than the energy of vaporization of lithium metal which is 1.4 ev. The quantity ΔE_R, which is the difference in repulsion energy for the Li in the two states is the most difficult quantity to estimate. Since deionization of isolated lithium ions, which has been considered by others,[14] does not occur, $\Delta G_1 > 0$. This sets the lower limit, $\Delta E_R^1 > -0.8$ ev. If we assume that large aggregates are stable, then $\Delta G_n < 0$, and using the value of E_D^n for large n given previously, we get an upper limit on $\Delta E_R^n < 0.6$ ev. In other words, on the basis of our assumption regarding the aggregation of Li into neighboring interstitial sites concurrently with deionization, ΔE_R^n for all n must be approximately zero. We shall now show that ΔE_R^n is not too far from zero.

First we consider the difference in repulsion energy between interstitial isolated lithium atoms and the silicon and between lithium aggregated into Li_2, Li_3, $Li_{M'}$, and the silicon. In a tight binding treatment, the repulsion energy E_R originates from the nonorthogonality of the atomic wave functions and from exchange effects. An empirical analysis of the results on alkali halides[15] indicates that E_R varies approximately as the sum over all electron pairs of the squares of the overlap integrals. The overlap integral S_{ij} is given by

$$S_{ij} = \int \psi_i \psi_j dv$$

and ψ_i and ψ_j are one-electron functions centered on the different atoms.

We have considered in detail the change in overlap repulsion between an interstitial Li and the nearest-neighbor Si arising from the formation of a molecular bond between two interstitial Li as shown in Fig. 5. The two electron molecular wave function is described in the Heitler-London approximation in terms of Hartree-Fock $2s$ functions[16] of Li, and the overlap S_{ac} is reduced by the factor 0.84 and $S_{ac'}$ is increased by 1.05 as a consequence of molecular bond formation. This leads to the repulsion energies for $2Li^0$ and Li_2 with the silicon being very nearly equal. Similarly, for higher aggregates $\Delta E_R^n \approx \Delta E_R^1$. Because $S_{ac} < S_{ac'}$, the

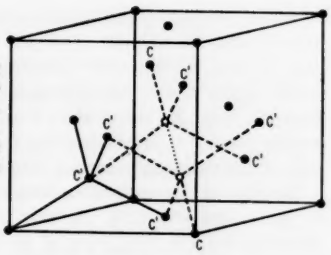

FIG. 5. Unit cell of silicon containing Li_2^0 occupying two neighboring interstitial sites. Nearest neighbor silicon atoms are marked c and c'. See text for details.

equilibrium interatomic distance for Li_2 in silicon will be slightly larger than the distance between interstitial sites.

The repulsive energy E_R, for interstitial Li^0 interacting with the four surrounding Si was estimated by evaluating the necessary overlap integrals using atomic wave functions, and from the empirical relation between the repulsive energy and the overlap integrals for alkali halides. For the valence electrons, Slater atomic functions[17] were used for the radial functions in constructing $3s$, $3p\sigma$, and $3p\pi$ orbitals for the $3s3p^3$ configuration of silicon. These, combined with the $2s$ electron wave function of Li were used to compute the overlap integrals using the published tables.[18] Because of the diffuseness of the wave function for the $2s$ electron of Li, the overlap integrals with the Si cores are appreciable. Atomic wave functions were used for the Si cores.[19]

The overlap integrals arising from the $2s$ electron of the Li and the $2s$ and $2p\sigma$ core electrons of a nearest-neighbor silicon were 0.076 and 0.02, and 0.031 and 0.01 for a next-nearest-neighbor silicon; the other core interactions are negligible. From these we estimated that E_R arising from the interaction of Li^0 with the nearest and next-nearest silicon cores is 0.75 ev.

The overlap integrals arising from the $2s$ electron of the Li and the silicon bond wave function directed away from the interstitial site was 0.03 and, neglecting spin, 0.15 for the other three tetrahedral wave functions of each of the four nearest neighbors. The other half of these bonds represented in terms of tetrahedral $3s3p^3$ atomic wave functions of the six next-nearest neighbors gave overlap integrals of 0.33 neglecting spin. The overlap between the valence bond orbitals of the silicon and the Li is reduced, however, by a factor of two because the single $2s$ electron of the Li and each of the $3s3p^3$ bond electrons have, in the approximation of unperturbed atomic functions, equal probabilities of the same and opposite spins. In this approximation E_R arising from the interaction of Li with the bond electrons is 9.8 ev. This is reduced by the bond orbitals being perturbed as follows: the valence electrons which overlap most with the Li will have a greater probability

[13] F. G. Allen, J. Phys. Chem. Solids **8,** 119 (1959).
[14] H. Reiss, J. Chem. Phys. **35,** 681 (1956); P Kaus, Phys. Rev. **109,** 1944 (1948); K. Weiser, J. Phys. Chem. Solids **17,** 149 (1960).
[15] P. O. Löwdin, thesis, University of Uppsala (1948).
[16] R. K. Nesbet and R. E. Watson, Ann. Phys. **9,** 260 (1960).
[17] T. Woodruff, Phys. Rev. **103,** 1159 (1956).
[18] R. S. Mulliken, C. A. Rieke, D. Orloff and H. Orloff, J. Chem. Phys. **17,** 1248 (1949).
[19] H. Donley, Phys. Rev. **50,** 1012 (1936).

of having opposite spin to the spin of the $2s$ electron of the Li, and the valence electrons will be further localized in the Si—Si bonds because of bond formation itself. From these considerations we have estimated that the total E_R is less than 7 ev. Since the repulsion energy for Li^+ is approximately 6 ev, we conclude that ΔE_R is approximately zero.

Because of the approximations involved, particularly in the estimate of ΔE_R, the coincidence of aggregation with the lithium remaining at interstitial sites and deionization has not been proved but rather shown to be plausible. A quantitative theory of the accompanying density change has not been achieved; however, a density decrease less than for precipitation of a separate metallic phase is consistent with the model.

The nonlinear portion of Fig. 3 can be explained on the basis of precipitation of a separate phase of lithium metal. We visualize that aggregates of lithium in interstitial sites attain sufficient size so that the strain field becomes great enough for precipitation to occur. This may occur by fracture or by a dislocation mechanism. The asymptotic v_i of Fig. 3 is 19×10^{-24} cm^3/Li, which is in satisfactory agreement with the value of 17×10^{-24} cm^3/Li expected for strain-free precipitates of lithium metal.

IV. CONCLUSIONS

Silicon is found to expand when Li^+ is introduced into interstitial sites. This expansion can be accounted for by the Coulomb repulsion with the Si^{4+} cores screened by the unperturbed Si-Si bond orbitals. A further expansion is observed as the Li^+ become deionized with time following an initial induction period. This expansion is consistent with aggregation and deionization of Li^+ to form Li_2, Li_3, $\cdots Li_M$, with each Li remaining at interstitial silicon sites. Li_M, refers to lithium metal with tetrahedral coordination. The final nonlinear expansion with Li^+ deionization is the correct magnitude for precipitation of a separate phase of lithium metal.

ACKNOWLEDGMENTS

We are indebted to Mrs. D. J. Weil for assistance with the density measurements, to D. J. Locke for the resistivity measurements, to D. S. Story for numerical analyses, and to J. D. Kingsley, J. Mitchell, and E. M. Pell for helpful discussions.

Polarized Visible Spectra of Crystalline Trisoxalatometallates

T. S. PIPER AND RICHARD L. CARLIN*
William Albert Noyes Laboratory of Chemistry, University of Illinois, Urbana, Illinois
(Received April 17, 1961)

The absorption of polarized light by single crystals of $NaMgAl(C_2O_4)_3 \cdot 9H_2O$ with part of the aluminum isomorphously replaced by the trivalent ions of Ti, V, Cr, Mn, Fe, and Co is reported. Assignments of the observed transitions are made. The polarizations prove that both the spin-allowed and spin-forbidden transitions are electric dipolar. They are made allowed by the static asymmetric ligand field and not by coupling to vibrations. The trigonal field strength is evaluated in terms of the parameter K which is found to range from -350 to $+500$ cm^{-1}.

INTRODUCTION

THE theory of the electronic spectra of the first-row transition-metal ions now has a firm foundation. The basic phenomenon involved in a splitting of the degenerate electronic eigenstates of the free metal ion by the surrounding ligand field when the ion is in a chemical compound. Transitions among these levels are responsible for the colors of these compounds. The theoretical and experimental background for this work has been reviewed recently by McClure[1] and by Dunn.[2]

Our interest in this area arises from the question as to what will be the effect on the electronic eigenstates of fields of symmetry lower than cubic. We have attacked this problem by a study of the visible spectra of some trisoxalatometallate ions in which the ligand field is essentially octahedral but possesses a smaller trigonal (axial) component. Our purpose in this work has been to make assignments, estimate the field parameters and identify the source of the intensity.

A complex with three bidentate ligands belongs to the point group D_3. The irreducible representations of this group are A_1, A_2, and E. Since a center of inversion is lacking, the $3d$ orbitals will be mixed with odd atomic and molecular orbitals. Thus the transitions will not be forbidden by the Laporte rule. This symmetry affords the selection rules

$$A_{1,2} \overset{\perp}{\longleftrightarrow} E;$$

$$A_1 \overset{\parallel}{\longleftrightarrow} A_2;$$

$$A_{1,2} \leftrightarrow A_{1,2};$$

and

$$E \overset{\parallel,\perp}{\longleftrightarrow} E.$$

Here $\parallel$ and $\perp$ refer to the polarization of the electric vector of the light with respect to the trigonal axis.

The only previous work on the spectra of complex ions with D_3 symmetry is that of Yamada and Tsuchida.[3] These workers studied the (room temperature) polarized spectra of $Cr(en)_3^{3+}$ and $Co(en)_3^{3+}$ ions. These species are nearly octahedral with only a weak trigonal field. The spectra, however, show a marked dichroism with light polarized with respect to the trigonal axis. The polarizations agreed with the above selection rules and confirmed the assignments which had been previously made on energy grounds alone. We have recently published[4] some preliminary observations on the spectra of trisoxalatometallates which led to similar conclusions.

EXPERIMENTAL

As a colorless diluent crystal we have chosen $NaMgAl(C_2O_4)_3 \cdot 9H_2O$ which belongs to the hexagonal system; it readily admits trivalent transition metal ions. Only the analogous chromium compound has been previously prepared.[5] The aluminum compound is obtained from the reaction in water of stoichiometric amounts of $Al_2(SO_4)_3$, $Ba(OH)_2$, NaOH, MgO, and $H_2C_2O_4$. Large single crystals were readily grown by evaporation or by seeding a supersaturated solution. Impurity ions may be added to the solution in growing mixed crystals for optical examination.

Titanium ion was introduced as $Ti_2(C_2O_4)_3 \cdot 10H_2O$; this compound precipitates upon adding ethanol to a cold solution of titanium trichloride and an excess of oxalic acid.

Vanadium pentoxide was reduced to the vanadyl ion by treatment with oxalic acid in a sulfuric acid solution. The resulting solution was reduced electrolytically at a mercury pool cathode under nitrogen to form the bright green solution of aquated vanadium ion. The requisite amounts of oxalic acid, soldium hydroxide, and magnesium oxide were added. The ion $V(C_2O_4)_3^{3-}$ is reasonably stable to air oxidation.

The ferric compound was prepared by adding stoichiometric amounts of $H_2C_2O_4$, NaOH, and MgO to hy-

* Present Address: Department of Chemistry, Brown University, Providence 12, Rhode Island.

[1] D. S. McClure in *Solid-State Physics*, edited by F. Seitz and D. Turnbull (Academic Press Inc., New York, 1959), Vol. 9.

[2] T. M. Dunn in *Modern Coordination Chemistry*, edited by J. Lewis and R. G. Wilkins (Interscience Press Inc., New York, 1960).

[3] S. Yamada and R. Tsuchida, Bull. Chem. Soc. Japan **33,** 98 (1960).

[4] T. S. Piper and R. L. Carlin, J. Chem. Phys. **33,** 608 (1960).

[5] L. Frossard, Schweiz. mineral. petrog. Mitt. **36,** 1 (1956).

TABLE I. Positions.

Number of positions	Point symmetry
6	2
6	$\bar{1}$
4	3
4	3
2	32
2	32
2	$\bar{3}$
2	32

drous ferric oxide. The sources of the ions $Mn(C_2O_4)_3^{3-}$ and $Co(C_2O_4)_3^{3-}$ were the potassium salts.[6,7]

The growth of mixed crystals containing Mn^{3+} presented special difficulties because of the instability of the $Mn(C_2O_4)_3^{3-}$ ion. Use was made of the fact that the rate of deposition is largest on the $(10\bar{1}1)$ face. A slightly less than saturated solution of $NaMgAl(C_2O_4)_3$ was prepared. To this solution was added a small amount of $K_3Mn(C_2O_4)_3$ and a large seed crystal of

$$NaMgAl(C_2O_4)_3 \cdot 9H_2O$$

with the $(10\bar{1}1)$ face exposed. The solution was set aside in the dark in a cold room at 4°C to allow deposition of the mixed crystal on the seed.

The oxalate crystals grow as large hexagonal prisms. The perfect cleavage plane normal to the sixfold axis was useful in obtaining crystals of the necessary size. Furthermore, crystals could be ground to the appropriate size on sandpaper or with a wet cloth. The crystals examined optically were usually about $1 \times 0.5 \times 0.1$ cm^3.

All spectra were obtained with a Cary model 14 spectrophotometer. A standard double-walled silvered glass Dewar served for obtaining the spectra at liquid nitrogen temperature (77°K). A Nicol prism was used to polarize the light.

CRYSTAL STRUCTURE

The preparation and characterization of

$$NaMgCr(C_2O_4)_3 \cdot 8H_2O$$

was reported by Frossard[5] along with some crystallographic studies. He established the space group as $P\bar{3}1c$ by single crystal x-ray diffraction; there are two formula units per unit cell. In this space group[8] the general position is twelve-fold; the special positions are listed in Table I.

The ion $[Cr(C_2O_4)_3]^{3-}$ must occupy a position with symmetry 32 (D_3); the ions Na^+ and $[Mg(OH_2)_6]^{2+}$ may occupy the other twofold positions. This leaves four molecules of water per unit cell unaccounted for, but they may not occupy the available fourfold positions. This analysis led us to suspect that the empirical formula of Frossard is in error with respect to the water of hydration. We have analyzed the aluminum compound and obtained in two separate determinations; the results are given in Table II.

These analyses are sufficiently accurate to give us confidence that the compound is a nonahydrate. Furthermore the noncoordinated water molecules now number six per unit cell and may occupy the sixfold sites of symmetry 2.

While we have no further structural data available on the crystal under discussion, it will be of value to discuss briefly some related structures. Evidence for trigonal distortion in oxalato complexes is found in the analysis of the crystal structure[9] of $K_3Cr(C_2O_4)_3 \cdot 3H_2O$. The three bond angles about the chromium ion within the chelate ring were reported as 81° (twice) and 74°. These values cannot be accurate since the improper space group was chosen in order to make the analysis simpler. They do indicate, however, that the O–Cr–O angle is appreciably less than 90°. A more careful analysis of *trans*-$K[Cr(C_2O_4)_2(OH_2)_2] \cdot 3H_2O$ has been reported by van Niekerk and Schoening.[10] Although the total field about the metal ion is not the same in this case, the metal-oxalate system is expected to be similar. Here, the O–Cr–O angle is reported as 83°. Again, in triclinic $(NH_4)_3Cr(C_2O_4)_3 \cdot 2H_2O$,[11] the O–Cr–O angle is about 85°. Similar results have been found in the analysis of $K_3Fe(C_2O_4)_3 \cdot 3H_2O$.[12]

It is thus apparent that the desired geometry has been obtained with the crystalline trisoxalate. We can also argue in the reverse manner; the experimental spectra we will discuss can be explained only in terms of a trigonal splitting of the energy levels of the central transition metal ion.

MAGNETIC DATA

We list in Table III effective magnetic moments of several trisoxalates which have been investigated. These data are important in establishing the ground states. All of the first row metal ions form high-spin complexes

TABLE II. Results of analysis.

	% Found	% calc. $8H_2O$	% calc. $9H_2O$
Hydrogen	3.66, 3.64	3.34	3.63
Carbon	14.45, 14.52	14.94	14.40

[6] G. H. Cartledge and W. P. Ericks, J. Am. Chem. Soc. **58**, 2061 (1936).
[7] J. C. Bailar, Jr. and E. M. Jones, Inorg. Syntheses **1**, 37 (1939).
[8] *International Tables for X-Ray Crystallography* (Kynoch Press, Birmingham, 1952).
[9] J. N. van Niekerk and F. R. L. Schoening, Acta Cryst. **5**, 196 (1952).
[10] J. N. van Niekerk and F. R. L. Schoening, Acta Cryst. **4**, 35 (1951).
[11] J. N. van Niekerk and F. R. L. Schoening, Acta Cryst. **5**, 499 (1952).
[12] P. Herpin, Bull. soc. franç. minéral. et crist. **81**, 245 (1958).

with the exception of Co^{3+}; the cobalt compound is diamagnetic.

RESULTS

Three different spectra may be obtained—the axial, σ, and π spectra. In the axial spectrum the light is parallel to the trigonal axis. The crystal may also be oriented so that the light is incident normal to the trigonal axis; we will define such spectra as orthoaxial. In the orthoaxial spectra, polarized light may be used; for the σ spectrum the electric vector is perpendicular to the trigonal axis and for the π spectrum parallel.

Some of the polarized orthoaxial spectra obtained are illustrated in Fig. 1. The data are collected in Table IV and discussed for each ion separately in the sections following. Although we usually restrict the discussion to the σ and π spectra, in all cases we have measured the axial spectrum as well and found it the same in regard to band shape and position as the σ spectrum. In a few cases the extinction coefficients have been compared but we usually report simply the ratio $\epsilon_{\parallel}/\epsilon_{\perp}$ obtained from orthoaxial spectrum.

TITANIUM

Trivalent titanium does not appear to form a trisoxalato complex in solution. Pecsok[13] found no evidence for $Ti(CO_2O_4)_3^{3-}$ in a continuous variations study. He found that a solution of titanium (III) in excess oxalic acid has an absorption bond at 25 600 cm^{-1} with $\epsilon_{max}=350$ and half-width of about 7500 cm^{-1}.

We have succeeded in growing several axial crystals of $NaMgAl(C_2O_4)_3\cdot 9H_2O$ which contain small amounts of Ti^{3+} and exhibited a single band at 24 000 cm^{-1}. Great difficulty was encountered in growing the crystals because of air oxidation of Ti^{3+} and because it was not possible to increase the free oxalate concentration without precipitating MgC_2O_4. Unfortunately we have not been able to grow an orthoaxial crystal large enough to examine spectrophotometrically. However, a smaller crystal was examined under a microscope and was found to become colorless with light polarized parallel to the trigonal axis. This is good evidence (1) that the Ti^{3+} is present as a trisoxalato complex, (2) that the transition is $^2E_b \leftarrow {}^2A_1$, where b refers to the higher of the two ^2E levels, and (3) that K is positive. We have searched in the near infrared down to 7000 cm^{-1} for $^2E_a(^2T_2)$ without success. The transition to ^2E_b in hydrated $Ti(C_2O_4)_2^-$ occurs at 1600 cm^{-1} higher in energy presumably because of the larger axial splitting of the $^2T_2$ ground level.

Further information was obtained by examining crystals of $(CH_3NH_3)_2NaAl(C_2O_4)_3\cdot H_2O$ containing Ti^{3+}. These crystals are monoclinic and may be grown from solutions containing a large excess of oxalate ion; it was therefore easy to obtain appreciable amounts of Ti^{3+} in the crystals. We have good evidence from spectra of Cr^{3+} in this same crystal that the field is nearly trigonal and the threefold axes of all the trisoxalate complex ions are nearly parallel to one another. These conclusions are based on the fact that the transition $^4T_1 \leftarrow {}^4A_2$ of the chromium ion in the monoclinic crystal is just as completely polarized as in the hexagonal crystal. The spectra of Ti^{3+} in the monoclinic crystal [Fig. 1(a)] show the expected polarization behavior of the band at 24 000 cm^{-1} but weak absorptions are also found at about 17 000 cm^{-1}. We doubt that these absorptions belong to ^2E_a. This would require a K of +5700 cm^{-1} and in a strong trigonal field the off-diagonal matrix elements connecting the ^2E orbitals would prohibit the two levels from approaching as close as 7000 cm^{-1}. It seems more likely that these absorptions are due to basic oxalate complexes which may fit more readily into the monoclinic crystal.

Further confirmation of the assignment of the ground state to $^2A_1$ and not ^2E_a is found in a comparison with trisacetylacetonatotitanium. Magnetic data[14] indicate strongly a $^2A_1$ ground state. We have observed the transition $^2E_a \leftarrow {}^2A_1$ at 15 300 cm^{-1}; we doubt that the trigonal field can be larger in the oxalate.

TABLE III. Magnetic properties of $K_3M(C_2O_4)_3\cdot 3H_2O$.

Ion	μ_{eff} B. M.	Ground state O_h
V^{3+}	2.80[a]	$^3T_1$
Cr^{3+}	3.8[b]	$^4A_2$
Mn^{3+}	4.88[c]	^5E
Fe^{3+}	5.94[d]	^6S

[a] B. N. Figgis, J. Lewis, and F. Mabbs, J. Chem. Soc. **1960**, 2480.
[b] S. Berkman and H. Zocker, Z. physik. Chem. (Leipzig) **124**, 318 (1926).
[c] N. Goldenberg, Trans. Faraday Soc. **36**, 847 (1940).
[d] L. C. Jackson, Proc. Roy. Soc. (London) **A140**, 695 (1933).

VANADIUM

Magnetic data prove that the ground state must be the $^3A_2$ component of the $^3T_1$ level. Hartmann[15,16] and co-workers have done some calculations on the trisoxalatovanadate (III) ion and measured the solution spectrum. Bands were found at 16 450 ($\epsilon=16$), 23 500 (shoulder, $\epsilon=120$), and 29 200 cm^{-1} ($\epsilon=500$). The first band was assigned to $^3T_2$ and the shoulder at 23 500 to $^3A_2$. Trigonal splittings were not observed in the solution spectrum and it was concluded that the ligand field is essentially octahedral.

Our spectra suggest that there is a trigonal splitting of the level $^3T_2$. At 77°K the data are quite similar to those in Table IV except that the π component occurs at 16 880 cm^{-1} and the intensities have increased by

[13] R. L. Pecsok, J. Am. Chem. Soc. **73**, 1304 (1951).

[14] H. S. Jarrett, J. Chem. Phys. **27**, 1298 (1957).
[15] H. Hartmann and H. L. Schlaefer, Angew. Chem. **66**, 768 (1954).
[16] H. Hartmann, C. Furlani, and A. Buerger, Z. physik. Chem. (Frankfurt) **9**, 62 (1956).

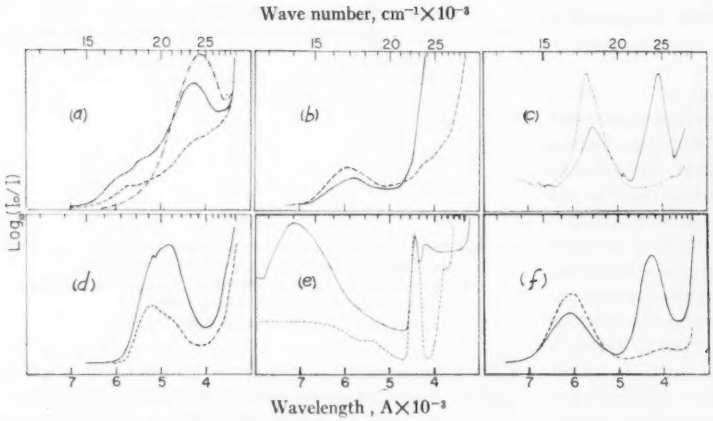

FIG. 1. Orthoaxial spectra of M^{3+} in $NaMgAl(C_2O_4)_3 \cdot 9H_2O$. The solid line is the σ polarization and the dashed line the π polarization. (a) Ti^{3+} at 25°C. In this spectrum only, the host crystal is $(CH_3NH_3)_2NaAl(C_2O_4)_3 \cdot H_2O$. The dash-dotted line is an axial spectrum in $NaMgAl(C_2O_4)_3 \cdot 9H_2O$ at 77°K. (b) V^{3+} at 77°K. (c) Cr^{3+} at 77°K. (d) Mn^{3+} at 77°K, calculated from the spectrum with light incident on the $(10\bar{1}1)$ face, (e) Fe^{3+} at 77°K in the pure crystal $NaMgFe(C_2O_4)_3 \cdot 9H_2O$. (f) Co^{3+} at 25°C.

about 20%. We take the trigonal splitting as 350 cm^{-1} from the 77°K spectrum.

Our previous report[4] of a band at 24 390 cm^{-1} is in error. In the σ polarization there is an intense tail merging into the charge transfer region without any definite maxima below 30 000 cm^{-1}. In the π polarization there are two weak diffuse bands centered at 23 500 cm^{-1} and 26 300 cm^{-1}. The ratio $\epsilon_{\parallel}/\epsilon_{\perp}$ is certainly less than 10^{-2} or 10^{-3} if $\epsilon_{\perp}$ is about 500 as in the solution spectra. We disagree with Hartmann's assignment which was based on energy considerations alone and prefer to assign the σ absorption to $^3E \leftarrow {}^3A_2$. The transition $^3A_2 \leftarrow {}^3A_2$ is forbidden by symmetry. This selection rule may be broken down by simultaneous excitation of vibrations. However a comparison to the polarization ratio (0.06) of $^4T_1 \leftarrow {}^4A_2$ for Cr^{3+} makes it doubtful that an $A_2 \leftrightarrow A_2$ transition could have an extinction coefficient much greater than about 10. The weak absorptions in the π polarization may be due to transitions to $^3A_2$ or possibly to $^1T_1$ and $^1T_2$.

Vanadium has three spin singlets in a trigonal field in the vicinity of 10 000 cm^{-1}. In corundum[17] two of these have been observed at 8770 and 9660 cm^{-1}. We have observed only a single, asymmetric band at 9615 cm^{-1} which appears only in the axial and σ spectra. The transition $^1A_1 \leftarrow {}^3A_2$ at 20 480 cm^{-1} also appears only in the axial and σ spectra. These observations prove that the spin-forbidden transitions are electric dipolar.

CHROMIUM

The solution spectrum of trisoxalatochromate (III) shows electronic transitions at 17 600 and 24 000 cm^{-1}. The first excited doublet state ^2E appears even in room temperature spectra at about 14 500 cm^{-1}. The spin-allowed transitions in the crystal, as listed in Table IV, show splittings of the levels in a trigonal field at room temperature. At 77°K the bands shift to $18\,020\sigma$, $17\,620\pi$ and $23\,950\sigma$ cm^{-1}. The extinction coefficients in the crystal were measured for this ion. The results of several measurements in Table V are not too precise but they indicate (1) that the σ and axial spectra are the same and (2) that the solution spectra are definitely more intense.

The excited doublet states of Cr^{3+} in ruby have been extensively studied by Sugano[1,18,19] and Low.[20] We have found sharp lines in the pure chromium oxalate crystal at 77°K (Table IV) which are quite analogous to those in ruby. The transitions to ^2E are the most sharp and of highest extinction coefficient ($\epsilon = 2.6$). The transitions to $^2T_1$ are incompletely polarized but stronger in the σ spectrum. The transitions to $^2T_2$ are completely σ polarized except for the lowest energy component which appears with equal intensity, $\epsilon = 0.3$, in both polarizations.

Many weaker, more diffuse lines were observed which we ascribe to vibrations; they were not strongly polarized. Especially interesting are the lines at 14 771 and 14 792 cm^{-1}. They are one-tenth as intense as the components of ^2E, are also split by 21 cm^{-1}, and are each 316 cm^{-1} above the respective ^2E line. It appears quite reasonable that these lines are simultaneous electronic (^2E) and vibrational transitions. Metal-oxygen stretches are in the vicinity of these energies and therefore we assign one of the chromium-oxygen stretching frequencies as 316 cm^{-1}. Other weak absorptions in this region at higher energies are also probably due to vibrations but there are no obvious assignments or 1:1 correspondences to the known infrared spectrum in the region 400–900 cm^{-1}. We will publish separately a more complete study of these lines.

MANGANESE

Spectra were obtained at 0°C in a dilute aqueous solution saturated with potassium oxalate-oxalic acid; the spectrum agrees with that published by Furlani.[21]

[17] M. H. L. Pyrce and W. A. Runciman, Discussions Faraday Soc. **26,** 34 (1958).

[18] S. Sugano and Y. Tanabe, J. Phys. Soc. Japan **13,** 880 (1958).

[19] S. Sugano and I. Tsujikawa, J. Phys. Soc. Japan **13,** 899 (1958).

[20] W. Low, J. Chem. Phys. **33,** 1162 (1960).

[21] C. Furlani and A. Ciana, Ann. chim. (Rome) **48,** 286 (1958).

A dilute crystal spectrum was obtained with light incident on the $(10\bar{1}1)$ face. The σ and π spectra in Fig 1 were then calculated using the known inclination of this face to the trigonal axis.

For d^4 the ground state is ${}^5E_a$. The selection rules allow transitions to the excited ${}^5E_b$ level in both polarizations and therefore there is no clean resolution into the split components of the ${}^5T_2$ excited state. However, the transition ${}^5A_1 \leftarrow {}^5E_a$ should appear only in the σ polarization and since the σ component of the band is at higher energy we conclude ${}^5A_1$ is at higher energy than ${}^5E_b$. The total splitting is estimated to be about 1500 cm^{-1}. This seems unusually large when compared to the other metals and may well be due in part to distortion from trigonal symmetry caused by the Jahn-Teller splitting.

TABLE IV. Spectra of M^{3+} in $NaMgAl(C_2O_4)_3 \cdot 9H_2O$[a]

Ion and ground state	Band max. cm^{-1}	$\Delta\nu$ cm^{-1}	$\Gamma(D_3)$	$\Gamma(O_h)$	Remarks
Ti^{3+}	24 000	5600	${}^2E_b$	${}^2E$	77°K, axial
$3d^1({}^2A_1)$					
V^{3+}	9615 σ	250		${}^1E, {}^1T_2$	77°K
$3d^2({}^3A_2)$	16 670 σ	2500	${}^3A_1$	${}^3T_2$	25°C
	17 230 π	2500	${}^3E_b$		$\epsilon_{\|}/\epsilon_{\perp}=1.3$
	20 480 σ	30	${}^1A_1$		77°K, $f=1.2\times10^{-7}$
Cr^{3+}	14 455	10			$f=1.2\times10^{-7}$, axial
$3d^3({}^4A_2)$	14 476	10		${}^2E$	$f=1.3\times10^{-7}$, axial
	15 216	30			all doublets
	15 284	50		${}^2T_1$	at 77°K
	15 323	40			
	17 316 π	2800	${}^4A_1$	${}^4T_2$	$\epsilon_{\|}/\epsilon_{\perp}=1.3$
	17 620 σ	2700	${}^4E_a$		25°C
	20 555	30			
	20 704	90		${}^2T_2$	axial
	21 119	60			
	23 670 σ	3200	${}^4E_b$	${}^4T_1$	$\epsilon_{\|}/\epsilon_{\perp}\leq0.06$
	...		${}^4A_{2b}$		at 25°C
Mn^{3+}	9700	1500		${}^3T_1$	Solution at
$3d^4({}^5E_a)$	20 100	5000		${}^5T_2$	0°C
Fe^{3+}	10 000 σ	1700		${}^4T_1$	$\epsilon=0.8$, 77°K
$3d^5({}^6A_1)$	14 120 σ	2100		${}^4T_2$	$\epsilon=1.0$
	22 497	1000		${}^4A_1, {}^4E$	$\epsilon=2.0$
	22 990				
	23 810 σ			${}^4T_2$	$\epsilon=1.6$
Co^{3+}	16 350 σ	2700	${}^1E_a$	${}^1T_1$	$\epsilon_{\|}/\epsilon_{\perp}=1.6$, 25°C
$3d^6({}^1A_1)$	16 500 π	2600	${}^1A_2$		
	23 400 σ	3400	${}^1E_b$	${}^1T_2$	$\epsilon_{\|}/\epsilon_{\perp}=0.05$
	...		${}^1A_{1b}$		

[a] We define ϵ by $I=I_0\,10^{-\epsilon c l}$. The concentration is in moles/liter of crystal or solution and the path length l in cm. The oscillator strengths are approximated by $f=4.6\times10^{-9}\epsilon\Delta\nu$, where ϵ is the ϵ_{max} for the band and $\Delta\nu$ its width in cm^{-1} at half-height.

TABLE V. Extinction coefficients of $NaMgCr(C_2O_4)_3 \cdot 9H_2O$ at 25°C.

Sample	Band maximum, in cm^{-1}	ϵ	Average ϵ
Orthoaxial crystal	17 620 σ	34	34
	17 316 π	45	45
	23 670 σ	67, 56	61
Axial crystal	17 620	25, 30, 35	30
	23 670	57, 66, 61	58
Solution	17 544		70
	23 800		88

These spectra indicate Dq to be of the order of 2000 cm^{-1}, neglecting distortions from octahedral symmetry. For the hexaquomanganese (III) ion, Dq has been reported[1] as 2100 cm^{-1}. These values are certainly too high in view of the expected Jahn-Teller splitting of the ${}^5E$ ground state. Furthermore, placing ${}^5T_2$ on the Tanabe-Sugano diagram at 20 000 cm^{-1} places ${}^3T_1$ at 6500 cm^{-1}. The experimental value for the oxalate complex would then require an unusual raising of atomic terms. If ${}^5E_a$ were split by, say, 6000 cm^{-1} and a value of Dq chosen at 1700 cm^{-1}, then ${}^5T_2$ would still occur at 20 000 cm^{-1}, while ${}^3T_1$ would be placed at 13 000 cm^{-1}. This seems to be a more reasonable fit of the data.

IRON

No reliable assignment of the bands of Fe^{3+} has previously been made. All the transitions are spin-forbidden and the simple orbital selection rules presented earlier do not apply. Ferric ion is isoelectronic with manganous ion. Indeed our spectra are markedly similar to those of Mn^{3+} both as to band position and half-width.

The components of ${}^4G$ are readily assigned as indicated in Table IV. The ${}^4T_1$ and ${}^4T_2$ transitions are σ polarized. It can be seen in Fig. 1 that the transition to ${}^4A_1$, ${}^4E$ is more intense in the π polarization. The weak shoulder at 22 990 cm^{-1} may be due to splitting of ${}^4A_1$, ${}^4E$ which are degenerate in an octahedral field. There is little change on going to 77°K.

To estimate Dq we have fitted the three components of ${}^4G$ to the parameters Dq, B, and C assuming an octahedral field. This yields $Dq=1522$, $B=609$, and $C=3283$ cm^{-1}. The next highest state is then ${}^4D$ at 26 800 cm^{-1}; its ${}^4T_2$ component is calculated to occur at about 25 000 cm^{-1}. We therefore assign the band at 23 810 cm^{-1} in the σ spectrum to ${}^4T_2({}^4D)$.

The axial spectrum is the same as the σ spectrum. Therefore these spin-forbidden transitions are electric dipolar, unlike those of $Mn(OH_2)_6^{2+}$ which are probably magnetically allowed.[22]

[22] S. Sugano, Progr. Theoret. Phys., Suppl. No. 14, 66 (1960).

TABLE VI. Crystal field parameters.

Ion	Dq, H_2O cm^{-1}	Dq, oxalate cm^{-1}	K cm^{-1}
Ti^{3+}	2030	<2400	>0
V^{3+}	1800	1750	−230
Cr^{3+}	1760	1770	+270
Mn^{3+}	2100	~1700	+500
Fe^{3+}	1400	1500	...
Co^{3+}	1910	~2000	−100

COBALT

Trigonal splittings do not appear in the solution spectrum[23] of trisoxalatocobalate (III) ion, where bands at 16 610 and 23 700 cm^{-1} are found. The extinction coefficients and band half-widths determined in our work are, respectively, $\epsilon=138$, $\Delta\nu=2700$ cm^{-1}, and $\epsilon=182$, $\Delta\nu=3600$ cm^{-1}. The first ultraviolet band was found at 41 700 cm^{-1} with $\epsilon=20\,000$. Crystal data at 25°C are given in Table IV. The spectra at 77°K are essentially the same except that the bands shift about 150 cm^{-1} to higher energy and increase in ϵ by about 20M. An approximate fit of the first band may be obtained from the Tanabe and Sugando diagram with $Dq=2000$ cm^{-1}. But this value of Dq is quite unreliable.

CRYSTAL FIELD PARAMETERS

We list in Table VI the crystal field parameters estimated in this work. For comparison Dq values for the hexaquo ions are included.[1]

In estimating the trigonal splitting parameter K[18] only the diagonal matrix elements have been retained. These are listed in Table VII for the first few states of the ions for which they are needed. Details of the calculations for d^2 and d^3 may be found in the literature.[17,18] We have calculated the matrix elements for the remaining configurations.

Our values of K are quite uncertain. Several assumptions are involved. First, for cases in which both components of a T level are allowed by the D_3 selection rules we have assumed that the selection rules are rigorously obeyed. This assumption seems well founded in view of the marked polarizations observed when one component of the T level is forbidden. The second assumption is that the vibrational and spin-orbit broadening of the bands is similar for both components of a T level. This assumption may not be justified. Since the bands are 2000 to 4000 cm^{-1} broad we cannot expect to determine accurately trigonal splittings which total 100 to 500 cm^{-1}. However, this method of determining K derives some justification from the fact that values of K calculated from the broad bands of Cr^{3+} in ruby [1] are in fair agreement with those derived from an analysis of the spin-forbidden transitions.[18] We believe that the sign of K is reliably determined in this work by the cumulative evidence of trigonal splittings, polarizations, and magnetic data.

One value of K, that of vanadium, seems out of line. If the trigonal field depends on the angle O–M–O as predicted by the ionic model, then the value of K for all the ions Ti^{3+} through Mn^{3+} ought to have the same sign since this angle is certainly less than 90°; the reversal at Co^{3+} is understandable in that this ion is considerably smaller and the angle may well be close to or larger than 90°. Furthermore, the reversal of sign of K on going from V^{3+} to Cr^{3+} seems unusual when a comparison is made to values of K for these ions in Al_2O_3; for vanadium,[17] K is -400 cm^{-1} and for chromium,[18] K is -350 cm^{-1}. However, in this case, K probably depends more on the lattice and less on the particular metal ion. The fact remains that the negative value for K for V^{3+} in the oxalate crystal is required to explain the ground state $^3A_2$ and the splitting of the $^3T_2$ level. Furthermore, the polarization behavior of the transitions to $^1A_1$ and $^3T_2$ levels confirm the ground state assignment and the sign of K as well.

CONCLUSION

The observed polarizations prove that the transitions occur by the electric dipole mechanism and that both the spin-forbidden lines ($\epsilon\sim3$) and the spin-allowed bands ($\epsilon\sim100$) are electronically allowed as opposed to vibronically allowed. Simultaneous vibrational transitions are observed for the spin-forbidden lines but their intensities are a tenth of those of the 0–0 lines. In view of the widths of the spin-allowed bands the vibrations are certainly strongly excited but it is likely that the symmetric modes are excited as is commonly the case with electronically allowed transitions. Any vibronic intensity of otherwise forbidden transitions leads to extinction coefficients less than about 5. The mechanism by which the d–d transitions become allowed electronically is probably by admixture of odd molecular orbitals in the asymmetric trigonal field. Thus the transitions acquire some charge transfer character.

TABLE VII. Diagonal matrix elements of the trigonal field, V_3.

Configuration	$\Gamma(O_h)$	$\langle A_i \mid V_3 \mid A_i\rangle$	$\langle E \mid V_3 \mid E\rangle$
$d^1\ t_2^1$	$^2T_2$	$-2K$	$+K$
$d^2\ t_2^2$	$^3T_{1a}$	$+2K$	$-K$
$t_2^1e^1$	$^3T_2$, $^3T_{1b}$	$+K$	$-\frac{1}{2}K$
$d^3\ t_2^2e^1$	$^4T_2$, $^4T_1$	$-K$	$+\frac{1}{2}K$
$d^4\ t_2^3e^1$	$^5T_2$	$+2K$	$-K$
$d^6\ t_2^5e^1$	$^1T_1$, $^1T_2$	$-K$	$+\frac{1}{2}K$

[23] A. Kiss, J. Csaszar, and L. Lehotai, Acta Chim. Acad. Sci. Hung. **12**, 73 (1957).

Turning to the trigonal field parameter K, the fact that the negative value is found for vanadium in contrast to positive values for titanium and chromium proves that K is not a simple function of the O—M—O bond angle in the chelate ring; this angle is certainly less than 90° in these cases. It will be necessary to allow for variation in the radial parameters as well to explain this observation.

ACKNOWLEDGMENT

We thank the National Science Foundation for a grant and a fellowship (RLC).

THE JOURNAL OF CHEMICAL PHYSICS VOLUME 35, NUMBER 5 NOVEMBER, 1961

Kinetics of the Photolysis of Sodium Azide

JACK G. DODD*

Department of Physics, Drury College, Springfield, Missouri

(Received April 14, 1961)

The evolution of N_2 from solid NaN_3 during photolysis is shown to result from active sites located as deep as a few hundred lattice constants within the crystallites. These active sites diffuse to the free surface to produce N_2, exhibiting a diffusion constant $\sim 10^{-15}$ cm²/sec. The absorption constant of NaN_3 for 2537-A radiation is measured to be about 1.8×10^5/cm, and quantum efficiencies for photolysis are determined to be 0.040 for photolysis of the surface layer and 0.12 for equilibrium nitrogen evolution from a partially decomposed mass. The reaction is shown to be first order with respect to light intensity. A mechanism for photolysis is suggested based upon Thomas and Tompkins' exciton decomposition scheme.

I. INTRODUCTION

THE photolysis of the azides has been the subject of several investigations. An early study of Gurney and Mott suggested that the mechanism involved was probably the same as in the silver halides; however, subsequent work by Thomas and Tompkins failed to detect the photoconductivity required by Mott's theory of free hole formation.[1,2] Through a study of the reaction order and thermal activation energy of the photodecomposition of barium azide, Thomas and Thompkins arrived at a mechanism involving double decomposition of trapped excitons by tunnelling of electrons to adjacent anion vacancies, forming F centers and holes. This hypothesis was supported by an exhaustive study of potassium azide.[3]

In the work cited above, radiation intensities employed were generally high, so that appreciable decomposition occurred during a single determination. This tended to obscure the early features of decomposition when the sample was still relatively "pure." Also, quantum efficiencies for photolysis were calculated assuming total absorption of the incident radiation, which was generally unfiltered.

The study reported upon here was designed to establish the kinetics of decomposition in the early stages, and to determine accurate quantum yields calculated from absorbed intensities of reasonably monochromatic radiation.

II. EXPERIMENTAL DESIGN

To enable direct measurement of the nitrogen evolution rate during photolysis, a continuously pumped water-jacketed decomposition cell was employed, its pressure being measured by a calibrated ion gauge. [Fig. 1(a)]. The pumping system used was a two-stage silicone oil Pyrex diffusion pump backed by a Welch Duo-Seal mechanical pump. The ion gauge employed automatic emission stabilization, and its output, after one stage of current amplification, was recorded on the Y axis of a Mandrel model ER-90 XY recorder. The X axis was actuated by the output of a motor-driven potentiometer, enabling sweep rates of from $\frac{1}{60}$ to $\frac{1}{3}$ in./sec to be employed.

Calibration of the decomposition cell was accomplished by introducing dry nitrogen through leaks of known conductance attached to the cell in place of the sample holder.[4] The system sensitivity was 6.7×10^{11} molecules of N_2/sec/in. of recorder deflection. Least count of the system was one-tenth of this rate.

The sample holder [Figure 1(b)] consisted of two Chromel Constantan thermojunctions supporting ½-mil aluminum disks of 1 cm² area each, so arranged that irradiation of one shadowed the other, which served as the reference junction. The inside of the cell was blackened to reduce scattered radiation. The difference potential between the junctions was measured by a

* Present address: Department of Physics, University of Arkansas, Fayetteville, Arkansas.

[1] N. F. Mott, Proc. Roy. Soc. (London) **A172,** 325 (1939).

[2] J. G. N. Thomas and F. C. Tompkins, Proc. Roy. Soc. (London) **A209,** 550 (1951).

[3] P. W. M. Jacobs and F. C. Tompkins, Proc. Roy. Soc. (London) **A215,** 254 (1952).

[4] To be published elsewhere.

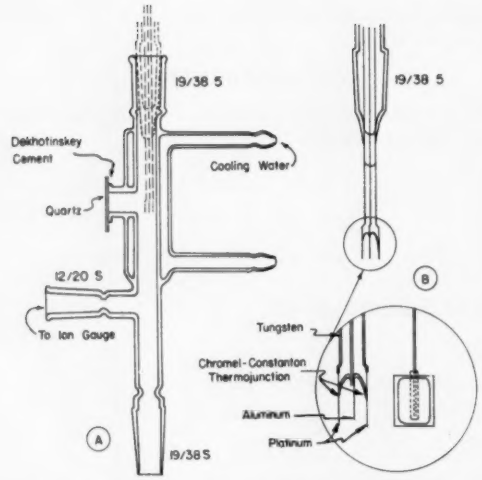

FIG. 1. Photolysis cell and radiometer sample holder.

Leeds-Northrup type P wall galvanometer with a sensitivity of about 1 μv/mm/m. The sample holder was calibrated after blackening, mounting in the cell, and pumping down to the working pressure of 5×10^{-6} mm. A 38.2-cp standard lamp at a distance of 40 cm was used as the standard source. The thermojunction sensitivity was measured as 101 ergs/sec/mm which corresponded to a photon flux sensitivity of 1.3×10^{13} photons/sec/mm for 2537-A radiation.

The light source employed for irradiation was a small G.E. ozone generating bulb. Absorbed intensities of actinic radiation were determined from the difference between galvanometer reading for unfiltered radiation from the bulb and for radiation filtered through $\frac{1}{8}$ in. of soft glass, which effectively eliminated actinic wavelengths as evidenced by complete cessation of photolysis upon filter interposition. It was therefore not possible to monitor the absorbed intensity of actinic radiation except at the beginning and end of each run. The bulb was operated at a current of 0.8 amp. More than 90% of the actinic radiation was of the 2537-A line.

Sample Preparation

The sodium azide used in this study was prepared from Fisher purified sodium azide by three successive fractional precipitations from saturated aqueous solutions by the addition of reagent grade acetone. This procedure was used to reduce hydrolysis and subsequent carbonate formation by CO_2 takeup from the atmosphere. The final product was microcrystalline, of unknown habit, and analyzed better than 99.9% of theoretical in azide concentration. No cationic impurities were detectable by standard qualitative analysis techniques. Preparations were carried out in yellow light to prevent pre-exposure.

III. MEASUREMENT PROCEDURE

Irradiation runs of from 6 min to $2\frac{1}{2}$ hr were made, graphical representation of the decomposition rates being automatically obtained by the instrumentation described under Sec. II. A log of total irradiation time was kept for each sample. Absorbed actinic radiation was determined by a 90-sec interposition of the soft glass filter at the end of each run, as described under Sec. II. The pressure in the decomposition cell was allowed to return to the "background" level after each run, before the next was started.

IV. RESULTS

The general characteristics of photolysis are typified by Figs. 2 and 3. Figure 2 typifies the initial rise of the nitrogen evolution rate within the first few minutes of irradiation of a fresh sample at a rather high rate (7×10^{13} photons/sec). Within the time constant of the equipment ($\sim$3 sec), response to irradiation was instantaneous. This initial rise will be called *fast photolysis*. Figure 3 is a composite taken from successive graphs obtained during a single $2\frac{1}{2}$-hr exposure (at a lower intensity than Fig. 2) and illustrates the gradual increase in rate after the initial rise. This gradual rise will be termed *slow photolysis*. Upon cessation of irradiation, the decomposition rate relapsed toward zero in a manner occurately reciprocal to the rise.

Quantum efficiencies for fast photolysis calculated after 500 sec from the decomposition rates in terms of molecules of NaN_3 decomposed per absorbed quantum, ranged from 0.040 for a fresh sample (Fig. 2) to 0.019 for a sample which had absorbed a total of 5.7×10^{17} quanta.

For slow photolysis, the quantum efficiency wascalculated from Fig. 3 to be 0.12 molecules/photon using the rate attained after $2\frac{1}{2}$ hr continuous irradiation at a level of 3.3×10^{13} photons/sec. It may be seen that this probably approximated the decomposition rate at infinite time. The low irradiation rate was employed to reduce sample decomposition during the long exposure time necessary to approach equilibrium. In spite of this precaution it is certain that considerable decomposition had taken place by the end of the run;

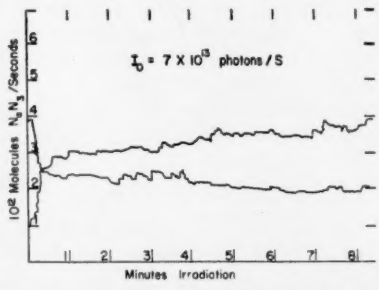

FIG. 2. Rate vs time (fast photolysis) rise ξ decay.

the value of 0.12 must therefore be taken as a lower limit.

The reaction order with respect to absorbed photon concentration was determined for fast photolysis by plotting the logarithm of the rate of nitrogen evolution against the logarithm of the absorbed radiation rate (Fig. 4). The slope of the straight line so obtained was 1.05, which determined the fast photolysis reaction to be of the first order. The results of Müller and Brous in which exposure times of hours were employed, establish slow photolysis also as a first-order reaction.[5]

V. DISCUSSION

The absorption constant k for actinic radiation may be estimated as follows:

The rate of photolysis dN/dt of azide molecules is assumed to be proportional to the number of photons absorbed in unit time. The constant of proportionality P is defined as the apparent quantum efficiency. Then in a layer of thickness Δx located a distance x from the surface, the rate of photolysis may be written

$$dN/dt = -P\Delta x[I_0 k \exp(-kx)], \tag{1}$$

where I_0 is the total photon absorption rate of the sample, and k is the absorption constant for the wavelength involved.

Now for an undecomposed sample containing N_0 molecules/cm² in each lattice plane, there will exist some maximum quantum yield P_0. After some decomposition has occurred, we may write

$$P = P_0(N/N_0), \tag{2}$$

where N is the number of undecomposed molecules still present in a layer. Substituting (2) into (1) and evaluating the result at the surface of the sample ($X=0$)

$$dN/dt = -P_0 I_0 k N \Delta x/N_0, \tag{3}$$

and integrating,

$$\ln(N/N_0) = -P_0 I_0 k \Delta x(t-t_0)/N_0. \tag{4}$$

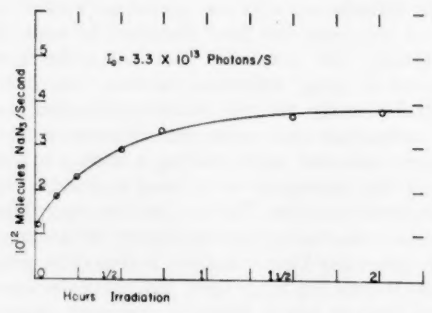

FIG. 3. Rate vs time (slow photolysis).

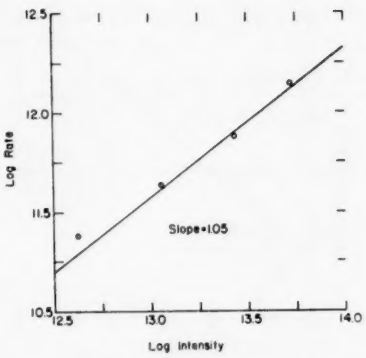

FIG. 4. Log rate vs log intensity.

Now from (3) it is clear that since dN/dt is proportional to N, we may replace N/N_0 in (4) by

$$\frac{dN}{dt} \Big/ \frac{dN}{dt}\Big|_{t=0},$$

the ratio of the photolysis rates at the two times t and t_0. But in the above we have assumed that we are observing a surface layer only, hence if we assume that fast photolysis is a surface phenomena, we are clearly talking about the ratio of fast photolysis rates at the times t and t_0. Since this ratio is just the ratio of the apparent fast photolysis quantum efficiencies at t and t_0, we may finally write

$$\ln(q/q_0) = -P_0 I_0 k \Delta x(t-t_0)/N_0 \tag{5}$$

or

$$k = \frac{N_0 \ln(q_0/q)}{P_0 I_0 \Delta x(t-t_0)}, \tag{6a}$$

where q and q_0 are the fast photolysis quantum efficiencies at t and t_0. We now recall that for $I_0(t-t_0) = 5.7\times10^{17}$ quanta, $q_0=0.040$ and $q=0.019$ molecules/photon. Assuming the observed slow photolysis quantum efficiency of 0.12 molecules/photon to be P_0 and choosing $\Delta x = 4\times10^{-8}$ cm and $N_0 = 6\times10^{14}$/cm² for a fresh sample of NaN_3, we obtain from (6a)

$$K = 1.8\times10^5/\text{cm}. \tag{6b}$$

Since the calculation of P_0 was necessarily made on a partially decomposed sample, (6b) gives an upper bound on k.

A model for the photolysis of sodium azide, based upon the exciton mechanism suggested by Thomas and Tompkins for barium azide, is described below.

Let an incident photon generate a mobile exciton in the interior of a crystallite. This exciton, having a probable lifetime of $<10^{-8}$ sec, may return to the ground state by emission of a quantum[6,7] or by lattice

[5] R. H. Müller and G. C. Brous, J. Chem. Phys. **1**, 482 (1933).

[6] M. G. Evans, H. Eyring, and J. F. Kincaid, J. Chem. Phys. **6**, 349 (1938).

[7] R. Audubert, Trans. Faraday Soc. **35**, 197 (1939).

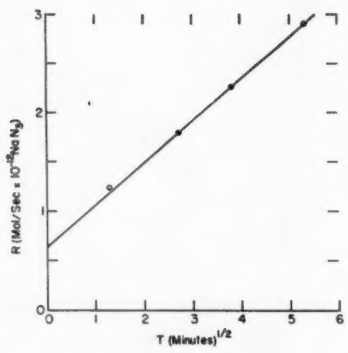

FIG. 5. Rate vs (time)$^{\frac{1}{2}}$.

interaction (phonon generation), or it may be trapped (for example, by an anion vacancy, perhaps generating a hole and an F center by tunneling.[8] Only a trapping process will lead to eventual decomposition. Formation of molecular nitrogen probably cannot take place within the lattice because of steric hinderance, but may occur at a free surface, or major lattice defect. For barium azide, the observed second-order kinetics suggests random hole-hole reactions at such a generalized surface. For sodium azide, at least in the early stages of decomposition, first-order kinetics seems dominant (Sec. IV), suggesting the presence of deep traps at the decomposition surface. Suitable trapping sites might be cation vacancies,[9] or surface impurities such as NaOH and Na_2CO_3 and in fact both compounds have been detected in sodium azide crystallized by evaporation from an aqueous solution.[10]

At any rate, since hole decomposition may take place some distance from the *free* surface of a crystallite, the nitrogen reaction product will generally have to diffuse to escape.

We may symbolize this by the following steps: Let n active centers of unspecified nature be formed in the interior of the crystal, diffuse to the free surface with diffusion constant D, and upon arrival instantly become free nitrogen molecules. Assume that these centers are generated by a first-order reaction at a rate given by

$$r = PkI_0 \exp(-kx). \tag{7}$$

We may immediately write the kinetic equation for the entire reaction in the form

$$\partial n/\partial t = PkI_0 \exp(-kx) + D(\partial^2 n/\partial x^2). \tag{8}$$

The boundary conditions for (8) are

$$n(0, x) = 0 \tag{8a}$$

$$\lim_{x\to\infty} n(x, t) = 0 \tag{8b}$$

$$R = -D(\partial n/\partial x)\,|_{x=0} \tag{8c}$$

$$n(t, 0) = 0. \tag{8d}$$

The first three conditions are self-evident. Condition (8d) is a reflection of the assumption that active centers reaching the surface instantly become nitrogen molecules.

Equation (8) may be conveniently solved by means of Laplace transforms (see mathematical Appendix). The final solution is

$$R = PI_0\{1 - \exp(k^2 Dt)\ \mathrm{erfc}[k(Dt)^{\frac{1}{2}}]\}, \tag{9}$$

where erfc refers to "error cofunction."

Equation (9), while exact, is inconvenient. Limiting cases for t large and t small are:
For t large:

$$R \doteq PI_0; \tag{9a}$$

for t small:

$$R \doteq 2I_0 Pk(Dt/\pi)^{\frac{1}{2}} \tag{9b}$$

(see Mathematical Appendix).

Equation (9b) provides a direct test of the model, since it predicts that a plot of the observed nitrogen evolution rate against $t^{\frac{1}{2}}$ should be linear. Such a plot, using the first four points in Fig. 3, is shown in Fig. 5. It is evident that the points fall on an excellent straight line. From the slope of this line and Eq. (9b) D may be estimated, since I_0, P, and k are all measurable or calculable quantities. The value obtained for D is 10^{-15} cm^2/sec.

The fact that the line in Fig. 5 fails to intersect the rate origin at $t=0$ reflects the tacit assumption in the mathematical model that the surface of the crystal is passive, i.e., does not photolyze. This is obviously inappropriate. However, in other respects, the model seems adequate.

The diffusion equation as applied to physical situation of this type has been discussed in some detail by Waite.[11] He concludes that first-order kinetics indicates a large difference between the diffusion activation energy and the reaction activation energy. The assumption that active centers instantly become nitrogen molecules upon reaching a surface is equivalent to the assumption of a small activation energy of the surface reaction. The fact that first-order kinetics are in fact observed appears to support this assumption.

The preceding kinetic analysis is thus quite general, in that it does not hinge upon any particular internal crystal process, but is simply a statement about the

[8] P. W. M. Jacobs and F. C. Tompkins, Proc. Roy. Soc. (London) **A209**, 271 (1952).
[9] Reference 8, p. 272.
[10] Mary Farmer, Drury College (private communication, 1958).
[11] P. R. Waite, Phys. Rev. **107**, 463–70 (1957).

rate-determining mechanisms involved. The value obtained for D, however, is too small for either excitons or holes, and seems to suggest that molecular or atomic diffusion underlies the long time constants observed here. This is supported by observation of occasional "bursts" of gas from the irradiated sample.

Finally, that the primary photon absorption process in sodium azide involves exciton rather than free hole formation seems supported by the absence of photoconductivity in single crystals of sodium azide.[12]

ACKNOWLEDGMENT

The author would like to express his gratitude to Dr. Z. V. Harvalik, Director, Basic Research Group of the Engineer Research and Development Laboratories, Fort Belvoir, Virginia, for his encouragement throughout this investigation, and for his many helpful comments and suggestions.

Thanks are also due the Engineer Research and Development Laboratories for the financial support which made this study possible.

MATHEMATICAL APPENDIX

Equation (8) with associated boundary conditions (8a), (8b), (8c), and (8d) is solved by Laplace transforms in the following manner:

Let the transform of n with respect to t be $f(s)$. Then the transform of (8) becomes

$$sf=(kI_0P/s)\exp(-kx)+D(\partial^2 f/\partial x^2). \tag{10}$$

Note that condition (8a) has been applied. Letting the transform of $f(s)$ with respect to x be $g(z)$, and transforming (10), we obtain

$$D\left(z^2g-zf_0-\frac{\partial f}{\partial x}\bigg|_{x=0}\right)-sg+\frac{kI_0P}{s(s+k)}. \tag{11}$$

[12] R. B. Kay, Drury College (private communication, 1958).

Using the method of partial fractions, the inverse of (11) may be written as

$$f=f_0\cosh[x(s/D)^{\frac{1}{2}}]+\frac{\partial f}{\partial x}\bigg|_{x=0}\frac{\sinh[x(s/D)^{\frac{1}{2}}]}{(s/D)^{\frac{1}{2}}}$$
$$-\frac{kPI_0}{sD(k^2-s/D)}\left\{\exp(-kx)-\cosh[x(s/D)^{\frac{1}{2}}]\right.$$
$$\left.+\frac{k\sinh[x(s/D)^{\frac{1}{2}}]}{(s/D)^{\frac{1}{2}}}\right\}. \tag{12}$$

Applying (8b) we obtain

$$0=f_0+\frac{\partial f}{\partial x}\bigg|_{x=0}\left\{(s/D)^{-\frac{1}{2}}-\frac{kPI_0[k/(s/D)^{\frac{1}{2}}-1]}{Ds(k^2-s/D)}\right\}^{-1} \tag{13}$$

by setting equal to zero all terms of (12) which do not vanish as $x\to\infty$.

From (8c) and (8d) applied to (13) we obtain

$$L_x(R)=kI_0PD^{\frac{1}{2}}/s(s^{\frac{1}{2}}+kD^{\frac{1}{2}}). \tag{14}$$

The inverse of (14) yields Eq. (9).

For t large, expansion of the erfc in an asymptotic series yields

$$\operatorname{erfc}[k(Dt)^{\frac{1}{2}}]\doteq\frac{\exp(-k^2Dt)}{k(Dt\pi)^{\frac{1}{2}}}(1-\cdots). \tag{15}$$

The rest of the terms in the last parenthesis become small for large t. Substituting (15) into (14) yields (9a).

For small t, erfc $[k(Dt)^{\frac{1}{2}}]$ may be expanded in the series

$$\operatorname{erfc}[k(Dt)^{\frac{1}{2}}]=1-(2/\pi^{\frac{1}{2}})[k(Dt)^{\frac{1}{2}}](1-k^2Dt\cdots). \tag{16}$$

Assuming the last parentheses $\sim$unity, and substituting in (9) with the further approximation in (9) that $\exp(k^2Dt)\sim$unity, we obtain (9b).

Salt Effect in Metal-Ammonia Solutions: Sodium Chloride in Sodium-Ammonia Solution at −33°C.

DONALD S. BERNS, GERARD LEPOUTRE, ELIZABETH A. BOCKELMAN, AND ANDREW PATTERSON, JR.

Sterling Chemistry Laboratory, Yale University, New Haven, Connecticut

(Received April 10, 1961)

Using the model of Becker, Lindquist, and Alder for the equilibria in a solution of sodium in liquid ammonia, the authors have assumed an additional equilibrium between sodium and chloride ions and dissociated sodium chloride to compute the concentrations of ionic species, atoms and dimers when the common-ion electrolyte sodium chloride is added. Estimates of the ionic activity coefficients are included in the calculation. The calculated concentrations of conducting species are employed in the Onsager-Kim theory for the conductance at low fields of a mixture of ions. Values of $[Na]_{total}$ ranging from 5×10^{-4} to 6×10^{-2} and of the ratio of sodium chloride to $[Na]_{total}$ ranging from zero to 28.5 are included in the calculations. All data are for −33°. The computed conductances are compared with some newly-reported experimental measurements. The calculations are described and the results analyzed and criticized in light of values of the equilibrium constants for the sodium-ammonia system available from a variety of measurements.

SEVERAL different theories have been proposed to account for the physical properties of the solutions of metals in liquid ammonia and amine-type solvents.[1–3] Of the theories which pertain to dilute solutions, those proposed by Becker *et al.*[5] and by Diegen and Tsvirko[6] have been the most successful in accounting for many of the physical properties of metal-amine solutions. In order to account for the dilute solution properties the above authors suggest the presence of "solvated electrons" or "polarons" which interact with metal ions to form ion pairs (monomers) or *F* centers. The ion pairs or *F* centers interact to form diamagnetic quadrupoles called either dimers or F_2 centers. The dynamic equilibria between these species may be written as

$$M^+ + e^- \rightleftharpoons M$$

$$M \rightleftharpoons 1/2 M_2$$

where M^+ is the metal ion; e^- is the solvated electron or polaron; M is the ion pair, monomer, or *F* center; and M_2 is the dimer or F_2 center.

Recent direct support for the Becker *et al.* model may be found in the sodium-ammonia nuclear magnetic resonance studies of McConnell and Holm[9] in conjunction with the theoretical interpretation of their results by Blumberg and Das.[10] Evers[11] and Frank, using the mass action concept of Becker *et al.*,[5] have derived a conductance function which successfully reproduced the sodium-ammonia date of Kraus[12] (the most precise data for metal-amine solutions in the dilute range). Berns *et al.*[13] have applied the same conductance function to precise dilute solution measurements of lithium in methylamine at −78° and have successfully reproduced the experimental data. This is certainly strong support for the Becker-type model and for the applicability of electrolyte theory to dilute metal solutions.

The present authors have undertaken to compute theoretically, using a set of equilibria such as that just noted, plus an ionization equilibrium for an added salt, the concentrations of all postulated species in solution when sodium chloride is added to a sodium-ammonia solution. Then, using the theory of Onsager and Kim for the low-field conductance of an assembly of ions, the authors have computed the conductance of solutions having concentrations of ions given by the just-mentioned equilibrium calculations. This final result is compared with some experimental data of Lepoutre with gratifying results.

In the sections which follow, the calculations (which have been programmed for the IBM 650 data processing machine) are described, and the results analyzed and criticized in comparison with available experimental data.

Mixed-Electrolyte Concentration Calculations

We assume that the following six species are in equilibrium in solutions of sodium and sodium chloride in liquid ammonia at −33°: e^-, Na^+, Cl^-, M (or Na atoms), M_2 (dimers), and NaCl. We further assume

[1] C. A. Kraus, J. Franklin Inst. **212,** 537 (1931).
[2] S. Freed and N. Sugarman, J. Chem. Phys. **11,** 354 (1943).
[3] W. N. Lipscomb, J. Chem. Phys. **21,** 52 (1953).
[4] J. Kaplan and C. Kittel, J. Chem. Phys. **21,** 1429 (1953).
[5] E. Becker, R. Lindquist, and B. J. Alder, J. Chem. Phys. **25,** 871 (1956).
[6] M. F. Deigen and Yu A. Tsvirko, Ukrain. Fiz. Chem. **1,** 245 (1956).
[7] J. F. Dewald and G. Lepoutre, J. Am. Chem. Soc. **76,** 3369 (1954).
[8] J. Jortner, J. Chem. Phys. **30,** 839 (1959).
[9] H. M. McConnell and C. Holm, J. Chem. Phys. **26,** 1517 (1957).
[10] W. Blumberg and T. Das, J. Chem. Phys. **30,** 251 (1959).
[11] E. C. Evers and P. W. Frank, Jr., J. Chem. Phys. **30,** 61 (1959).
[12] C. A. Kraus, J. Am. Chem. Soc. **43,** 749 (1921).
[13] D. S. Berns, E. C. Evers, and P. W. Frank, J. Am. Chem. Soc. **89,** 310 (1960).

the three following equilibria:

$$Na^+ + e^- \rightleftharpoons M,$$

$$M \rightleftharpoons 1/2M_2,$$

$$Na^+ + Cl^- \rightleftharpoons NaCl,$$

and define these three equilibrium constants

$$K_1 = \frac{[e^-][Na^+]f^2}{[M]}, \quad (1)$$

$$K_2 = [M_2]^{\frac{1}{2}}/[M], \quad (2)$$

$$K_3 = \frac{[Na^+][Cl^-]f^2}{[NaCl]}. \quad (3)$$

In Eqs. (1) and (3), f is the ionic activity coefficient, given by

$$\ln f = -\delta_f\{[e^-]+[Na^+]+[Cl^-]\}^{\frac{1}{2}}. \quad (4)$$

The coefficient δ_f is evaluated by means of the Debye-Hückel theory. Next we define

$$x = [NaCl]/[Na]_{total}, \quad (5)$$

where

$$[NaCl]_{total} = [Cl^-]+[NaCl], \quad (6)$$

and

$$[Na]_{total} = [e^-]+[M]+2[M_2]. \quad (7)$$

We express conservation of charges as

$$[Na^+] = [e^-]+[Cl^-]. \quad (8)$$

The values of K_1, K_2, and K_3 in Eqs. (1)–(3) are taken as[11,14] $K_1 = 7.23\times10^{-3}$; $K_2 = 27.03$; and $K_3 = 1.45\times10^{-3}$. We have also used the value $K_2 = 99$, derived for potassium by Deigen[6] from a statistical analysis. See the discussion for further consideration of this point. The value of δ_f is computed as 7.73, using $D = 22$ for the dielectric constant of ammonia.

Using these eight equations, we could, for each set of values of $[Na]_{total}$ and x, compute all the concentrations of the six species in equilibrium, but a complete algebraic solution would certainly be difficult. We have preferred, for each set of values for $[Na]_{total}$ and x, to make a first guess on the value of the concentration of one species, i.e., $[M]$. We can compute the other unknowns through Eqs. (1)–(8). It is then possible to calculate a new value of $[M]$, and to start again with this new value. Practically, since the $[M]$ values oscillate, we make the process rapidly converging by using each time, instead of the preceding output value of $[M]$, the average between the preceding input and output values. We obtain a stable value after two or three iterations. The values of the concentrations of the other species are those found in the last iteration. We do not keep the results which correspond to total ionic strength greater than $0.1M$, since the Debye activity coefficients would become meaningless beyond such a value.

The first guess for a value of $[M]$ is taken from a least-square fit to $[M]$ calculated from Evers' data.[11] Thereafter as x is increased the first guess for $[M]$ is the previous value calculated. The entire calculation was programmed for and run on an IBM 650 computing machine. For ease in computation $[Na]_{total}$ was held constant while x varied over the range zero to 28.5.

Quantities were computed as follows:

$$[NaCl]_{total} = [Na]_{total}(x) \quad \text{from Eq. (5)},$$

$$[M_2] = \{K_2[M]\}^2 \quad \text{from Eq. (2)},$$

$$[e^-] = [Na]_{total} - [M] - 2[M_2] \quad \text{from Eq. (7)},$$

$$[Na^+] = [e^-]+[Cl^-] \quad \text{from Eq. (8)},$$

$$[Cl^-] = ([e^-][NaCl]_{total}) \Big/ \left(\frac{K_1}{K_3}[Na]+[e^-]\right)$$

from Eq. (6) and Eqs. (1)–(3),

$$f^2 = 1/[\exp(21.87)[Na]^{\frac{1}{2}}] \quad \text{from Eqs. (4) and (8)},$$

$$[M]_{new\ value} = [Na^+][e^-]f^2/K_1 \quad \text{from Eq. (1)}.$$

As mentioned before, the whole process is repeated using as a new guess for $[M]$ the average of the two values of $[M]$. Once $[M]$ changes by less than 0.01%, the computer exits from the loop.

The results are given for the species $[e^-]$, $[Na^+]$, $[M]$, and $[M_2]$ in Tables I–IV, and in Figs. 1–4. The results for $[Cl^-]$ are very similar to those obtained for $[Na^+]$.

Discussion of Equilibrium Calculation Results

It is clear for this system that the concentrations of ionic species are always much greater than the concentrations of atoms (monomer) and molecules (dimer), as reflected in the choice of scales for Figs. 1 and 2 compared to 3 and 4. In the dilute solution range there is the normal and expected common-ion effect when salt is added. At higher concentrations there are other interesting effects. Both monomer and dimer exhibit concentration maxima, which may be interpreted as reversals of equilibria. Beyond these maxima there are probably new dissociations. We postulate that the maxima are due to interionic forces which yield low values of the activity coefficients.

[14] C. A. Kraus and W. Bray, J. Am. Chem. Soc. **35**, 1315 (1913).

TABLE I. Electrons.

$[Na]_{total}$	$x=0$	$x=0.1$	$x=0.2$	$x=0.4$	$x=0.8$	$x=1.6$	$x=3.2$	$x=6.4$	$x=28.5$
	$[e^-]$								
5×10^{-4}	0.000480	0.000478	0.000477	0.000475	0.000471	0.000465	0.000456	0.000445	0.000427
7.924×10^{-4}	0.000747	0.000745	0.000743	0.000738	0.000731	0.000720	0.000704	0.000687	0.000679
1.256×10^{-3}	0.001157	0.001152	0.001148	0.001140	0.001127	0.001107	0.001082	0.001059	0.001109
1.991×10^{-3}	0.001774	0.001765	0.001758	0.001744	0.001721	0.001689	0.001655	0.001638	0.001863
3.155×10^{-3}	0.002684	0.002669	0.002657	0.002634	0.002599	0.002557	0.002530	0.002579	
5.000×10^{-3}	0.003997	0.003976	0.003957	0.003927	0.003887	0.003862	0.003924	0.004228	
7.924×10^{-3}	0.005870	0.005848	0.005832	0.005813	0.005815	0.005925	0.006360	0.007257	
1.256×10^{-2}	0.008581	0.008591	0.008612	0.008682	0.008907	0.009569	0.01101		
1.991×10^{-2}	0.01273	0.01289	0.01308	0.01353	0.01460	0.01681			
3.155×10^{-2}	0.01989	0.02067	0.02152	0.02330	0.02651				
5.000×10^{-2}	0.03546	0.03827	0.04068						
6.000×10^{-2}	0.04691								

TABLE II. Sodium ions.

$[Na]_{total}$	$x=0$	$x=0.1$	$x=0.2$	$x=0.4$	$x=0.8$	$x=1.6$	$x=3.2$	$x=6.4$	$x=28.5$
	$[Na^+]$								
5×10^{-4}	0.0004797	0.0005195	0.0005586	0.0006348	0.0007808	0.001054	0.001557	0.002476	0.008430
7.924×10^{-4}	0.0007473	0.0008059	0.008633	0.009751	0.001189	0.001589	0.002331	0.003714	0.01373
1.256×10^{-3}	0.001157	0.001242	0.001326	0.001489	0.001801	0.002391	0.003501	0.005645	0.02409
1.991×10^{-3}	0.001774	0.001898	0.002019	0.002257	0.002717	0.003598	0.005307	0.008795	0.04571
3.155×10^{-3}	0.002684	0.002865	0.003044	0.003397	0.004087	0.005445	0.008200	0.01431	
5.000×10^{-3}	0.003997	0.004269	0.004540	0.005078	0.006156	0.008355	0.01313	0.02496	
7.924×10^{-3}	0.005870	0.006297	0.006726	0.007595	0.009380	0.01322	0.02235	0.04672	
1.256×10^{-2}	0.008581	0.009297	0.01003	0.01154	0.01477	0.02222	0.04108		
1.991×10^{-2}	0.01273	0.01404	0.01542	0.01834	0.02491	0.04054			
3.155×10^{-2}	0.01989	0.02266	0.02563	0.03206	0.04607				
5.000×10^{-2}	0.03546	0.04203	0.04855						
6.000×10^{-2}	0.04691								

TABLE III. Sodium atoms.

$[Na]_{total}$	$x=0$	$x=0.1$	$x=0.2$	$x=0.4$	$x=0.8$	$x=1.6$	$x=3.2$	$x=6.4$	$x=28.5$
	[Na]								
5.000×10^{-4}	0.00001972	0.00002089	0.00002199	0.00002404	0.00002762	0.00003334	0.00004144	0.00005131	0.00006679
7.924×10^{-4}	0.00004248	0.00004463	0.00004664	0.00005031	0.00005656	0.00006617	0.00007899	0.00009304	0.00009936
1.256×10^{-3}	0.00008796	0.00009158	0.00009493	0.0001010	0.0001110	0.0001257	0.0001437	0.0001599	0.0001241
1.991×10^{-3}	0.0001732	0.0001787	0.0001837	0.0001926	0.0002069	0.0002264	0.0002469	0.0002563	0.0001098
3.155×10^{-3}	0.0003208	0.0003281	0.0003347	0.0003459	0.0003630	0.0003834	0.0003960	0.0003730	
5.000×10^{-3}	0.0005544	0.0005624	0.0005693	0.0005805	0.0005951	0.0006045	0.0005815	0.0004610	
7.924×10^{-3}	0.0008921	0.0008981	0.0009025	0.0009078	0.0009072	0.0008764	0.0007476	0.0004151	
1.256×10^{-2}	0.001343	0.001341	0.001337	0.001322	0.001275	0.001129	0.0007434		
1.991×10^{-2}	0.001900	0.001875	0.001846	0.001775	0.001594	0.001153			
3.155×10^{-2}	0.002504	0.002408	0.002300	0.002058	0.001546				
5.000×10^{-2}	0.002830	0.002512	0.002206						
6.000×10^{-2}	0.00267								

TABLE IV. Sodium molecules.

$[Na]_{total}$	$x=0$	$x=0.1$	$x=0.2$	$x=0.4$	$x=0.8$	$x=1.6$	$x=3.2$	$x=6.4$	$x=28.5$
	$[Na_2]$								
5.000×10^{-4}	0.0000002840	0.0000003187	0.0000003533	0.0000004223	0.0000005574	0.0000008119	0.000001254	0.000001924	0.000003259
7.924×10^{-4}	0.000001319	0.000001455	0.000001589	0.000001849	0.000002337	0.000003199	0.000004559	0.000006324	0.000007212
1.256×10^{-3}	0.000005654	0.000006126	0.000006583	0.000007447	0.000008997	0.00001154	0.00001508	0.00001867	0.00001125
1.991×10^{-3}	0.00002192	0.00002333	0.00002466	0.00002710	0.00003126	0.00003745	0.00004453	0.00004799	0.000008802
3.155×10^{-3}	0.00007520	0.00007865	0.00008182	0.00008743	0.00009628	0.0001074	0.0001146	0.0001017	
5.000×10^{-3}	0.0002245	0.0002310	0.0002367	0.0002462	0.0002587	0.0002670	0.0002471	0.0001553	
7.924×10^{-3}	0.0005814	0.0005892	0.0005951	0.0006021	0.0006014	0.0005613	0.0004084	0.0001259	
1.256×10^{-2}	0.001318	0.001314	0.001306	0.001278	0.001189	0.0009311	0.0004038		
1.991×10^{-2}	0.002639	0.002570	0.002489	0.002302	0.001857	0.0009718			
3.155×10^{-2}	0.004580	0.004236	0.003866	0.003096	0.001746				
5.000×10^{-2}	0.005852	0.004610	0.003556						
6.000×10^{-2}	0.005209								

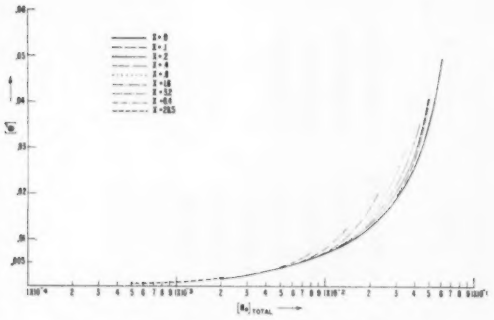

FIG. 1. $[e^-]$ vs $[Na]_{total}$ for various values of x.

When there is no salt ($x=0$), both maxima occur at $[Na]_{total}=0.045$, which is the concentration at which the equivalent conductance has a minimum. The increasing conductance which ensues at higher concentration could then be related to the proposed new dissociations. When salt is added, both maxima occur at the same value of $[Na]_{total}$ for each value of x. Whatever the value of x, all maxima occur at the same total ionic strength, 0.065. This is interpreted as an indication that the maxima are due to interionic forces, and it implies that the maxima shift toward lower values of $[Na]_{total}$ when salt is added.

Some measurements of equivalent conductances of sodium-ammonia solutions have been made, for varying ratios of added sodium chloride.[15] The equivalent conductances decrease with increasing concentration of sodium, have a minimum, and increase again. These data will be compared with computed equivalent conductances in the following sections. In Table V, however, we have computed for various values of x the sodium concentrations for which we have computed a maximum of association (Fig. 3 and Table III) and the sodium concentration for which we have found experimentally a minimum of conductance. We cannot claim high precision for the experimental results, and the number of experimental points which can be compared with the calculated values is small, but qualitatively it is striking that one observes [M] maxima always occurring at very closely the same $[Na]_{total}$ at which the minima in Λ occur.

The conductance minimum may well be regarded as an inversion of equilibrium. We show elsewhere[16] that this inversion is not simple.

Figure 5, which is an enlargement of Fig. 3, reveals additional features of the salt effect. In the very dilute range, the effect is normal; ionization is decreased and [Na] is increased by addition of salt. However, all the curves cross in a complicated manner, and the salt effect is reversed at higher concentrations. This effect happens sooner for higher salt/metal ratios, so that at intermediate values of $[Na]_{total}$ (e.g., 3×10^{-3}), a small addition of salt increases [Na] and a large addition decreases it. This means that plots of [Na] against [NaCl] for various values of $[Na]_{total}$ would also present maximum values. At high concentrations, beyond 10^{-2}, the salt effect is completely reversed. This progressive reversal is interpreted as being due to increasing interionic forces. Indeed, all these peculiar properties are presumably due to strong variations of the activity coefficients with concentration. The slope of such variations depends on the dielectric constant of the solvent and on the temperature, both quantities being much lower for liquid ammonia than for aqueous solutions. As a result, these strange features are observed in a rather small range of concentration.

We shall comment on the choice of equilibrium constants after the presentation of the computed conductances.

Conductance Calculations

The computed ionic concentrations are next used to predict the equivalent conductances of such mixed ion solutions. The conductance theory used is that of Onsager and Kim[17] for solutions of electrolytes containing s ions.

Equations (9) and (10),

$$2B=(1-T_{Na^+}{}^0)\omega_{Na^+}{}^2+(1-T_{e^-}{}^0)\omega_{e^-}{}^2 + (1-T_{Cl^-}{}^0)\omega_{Cl^-}{}^2, \quad (9)$$

$$C=\omega_{Na^+}{}^2\cdot\omega_{e^-}{}^2\cdot\omega_{Cl^-}{}^2\left(\frac{T_{Na^+}{}^0}{\omega^2_{Na^+}}+\frac{T_{e^-}{}^0}{\omega_{e^-}{}^2}+\frac{T_{Cl^-}{}^0}{\omega_{Cl^-}{}^2}\right), \quad (10)$$

are solved for B and C, where ω_i are ionic mobilities, and $T_i{}^0$ are transference numbers at infinite dilution.

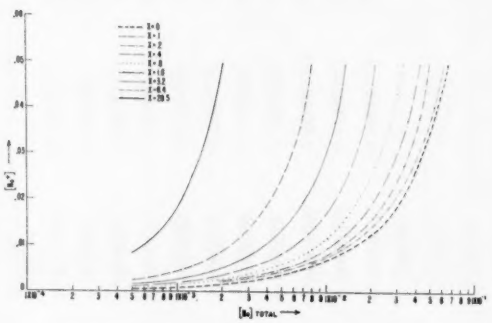

FIG. 2. $[Na^+]$ vs $[Na]_{total}$ for various values of x.

[15] G. Lepoutre, doctoral dissertation, Yale University, 1953.
[16] G. Lepoutre and A. Patterson, Bull. Soc. Chim. France **1961**, 989.
[17] L. Onsager and S. K. Kim, J. Phys. Chem. **61**, 215 (1957).

The values of B and C are used to compute α_2^2 and α_3^2 from Eqs. (11) and (12)

$$\alpha_2^2 = B - (B^2 - C)^{\frac{1}{2}} \tag{11}$$

$$\alpha_3^2 = B + (B^2 - C)^{\frac{1}{2}}. \tag{12}$$

In solving Eqs. (11) and (12) the values of limiting conductances of Na^+, Cl^-, and e^- are needed. Using limiting conductance of $\Lambda_{Na}{}^0 = 1022$ from Evers[11] and $\Lambda_{NaCl}{}^0 = 309$ from Kraus[14] and the fact that the ratio of mobilities of e^- to Na^+ near infinite dilution is approximately 7 to 1,[18] we arrive at $\lambda_{e^-}{}^0 = 892$, $\lambda_{Na}{}^0 = 130$, and $\lambda_{Cl^-}{}^0 = 179$. In Eqs. (9) and (10) the mobilities are taken as $\omega_{Na^+} = 130K$; $\omega_{e^-} = 892K$; and $\omega_{Cl^-} = 179K$, where K is a constant which will cancel out in every equation involving ω's. Next we define the transference numbers of these species at infinite dilution as

$$T_{Na^+}{}^0 = \frac{\lambda_{Na^+}{}^0(1+x)}{\lambda_{Na^+}{}^0(1+x) + \lambda_{e^-}{}^0 + \lambda_{Cl^-}{}^0 x}, \tag{13}$$

$$T_{e^-}{}^0 = \frac{\lambda_{e^-}{}^0}{\lambda_{Na^+}{}^0(1+x) + \lambda_{e^-}{}^0 + \lambda_{Cl^-}{}^0 x}, \tag{14}$$

$$T_{Cl^-}{}^0 = \frac{\lambda_{Cl^-}{}^0 x}{\lambda_{Na^+}{}^0(1+x) + \lambda_{e^-}{}^0 + \lambda_{Cl^-}{}^0 x}. \tag{15}$$

Here, x is $[NaCl]_{total}/[Na]_{total}$.

Knowing α_2 and α_3, one solves for N_2 and N_3, using

$$N_p^{-2} = \sum_{i=1}^{s} \frac{T_i{}^0 \omega_i^2}{(\omega_i^2 - \alpha_p^2)}. \tag{16}$$

Thereafter

$$\psi_i{}^p = N_p \frac{\omega_i}{(\omega_i^2 - \alpha_p^2)},$$

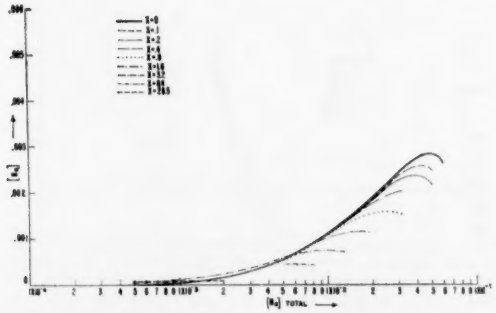

FIG. 3. $[Na]$ vs $[Na]_{total}$ for various values of x.

[18] C. A. Kraus, J. Am. Chem. Soc. **36**, 864 (1914).

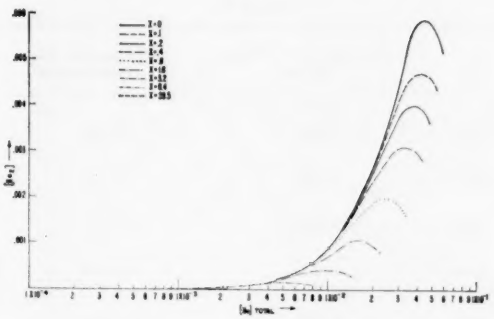

FIG. 4. $[Na_2]$ vs $[Na]_{total}$ for various values of x.

where there are six values of ψ. The equation

$$q_p = \bar{\omega} \sum_{i=1}^{s} \frac{T_i{}^0 \omega_i}{(\omega_i^2 - \alpha_p^2)}, \tag{17}$$

where

$$\bar{\omega} = \frac{\sum_{i=1}^{s} n_i e_i^2 \omega_i}{\sum_{i=1}^{s} n_i e_i^2} \tag{18}$$

is solved first for $\bar{\omega}$, remembering that $n_i = [Na^+]$, etc. Knowing $\bar{\omega}$ one can solve for q_2 and q_3.

The conductance Λ_i is next calculated, using

$$\lambda_j = \lambda_j{}^0 - \left\{ \frac{FN\epsilon^2 \mid z_j \mid}{6c \times 10^{-8}(250\pi R)^{\frac{1}{2}}\eta(DT)^{\frac{1}{2}}} + \lambda_j{}^0 \left(\frac{\pi}{250R}\right)^{\frac{1}{2}} \cdot \frac{N^2\epsilon^2}{3R} \cdot \frac{z_j}{(DT)^{\frac{1}{2}}} \cdot \sum_{p=2}^{s} (1 + (q_p))^{\frac{1}{2}} (T_\sigma{}^0 \psi_\sigma{}^p z_\sigma) \right\} \Gamma^{\frac{1}{2}}. \tag{19}$$

The parameters used in Eq. (19) are defined as follows:

$$T_\sigma{}^0 \psi_\sigma{}^p z_\sigma = T_1{}^0 \psi_1{}^p z_1 + T_2{}^0 \psi_2{}^p z_2 + T_3{}^0 \psi_3{}^p z_3,$$

$$\Gamma^{\frac{1}{2}} = ([Na^+] + [e^-] + [Cl^-])^{\frac{1}{2}},$$

$$\frac{FN\epsilon^2}{6c \times 10^{-8}(250\pi R)^{\frac{1}{2}}\eta(DT)^{\frac{1}{2}}} = \frac{29.16}{\eta(DT)^{\frac{1}{2}}},$$

$$\left(\frac{\pi}{250R}\right)^{\frac{1}{2}} \cdot \frac{N^2\epsilon^3}{3R(DT)^{\frac{1}{2}}} = \frac{1.981 \times 10^6}{(DT)^{\frac{1}{2}}}.$$

Equation (19) is used to solve for λ_{Na^+}, λ_{e^-}, and λ_{Cl^-}. Then,

$$\lambda_{Na} = \lambda_{Na^+} + \lambda_{e^-} \tag{20}$$

$$\lambda_{NaCl} = \lambda_{Na^+} + \lambda_{Cl^-}$$

and finally,

$$\lambda_{total} = \frac{[e^-]}{[Na]_{total}} \cdot \lambda_{Na} + \frac{[Cl^-]}{[Na]_{total}} \cdot \lambda_{NaCl}$$

TABLE V.

x	$[Na]_{total}$ for $[Na]_{max}$ (theory)	$[Na]_{total}$ for Λ_{min} (experimental)
0.0	0.046	0.045
0.2	0.038	...
0.4	0.031	...
0.44	...	0.032
1.6	0.016	...
2.6	...	0.016
3.2	0.0097	...

The calculated values of total λ are plotted in Fig. 6, together with the available experimental data.[15]

Discussion of Conductance Results

There is good agreement between experimental and calculated results at all λ values except those where the ratio of salt to total sodium is 28.5. Even in this extreme case, the calculated values predict the correct direction of change of conductance with increasing concentration. At the very high ratio of salt to total sodium a number of explanations can be invoked to account for the disparity, each one of which probably plays a part: The mobility of the electrons goes up; the computed values of f are imprecise, owing to the use of the Debye-Hückel theory where it should not be applicable; and there is decomposition of the solutions under these extreme circumstances, so that one has not employed the correct concentrations in the computation or measured the conductances which should be observed.

The good agreement between the computations and the experimental results lends further support to the employment of electrolyte theory[11,13] and (1)–(3) in the interpretation of the behavior of alkali metal solutions in liquid ammonia. The conductance calculations presented are also a significant test of the Onsager-Kim theory[17] for solutions of mixed electrolytes. This initial success indicates a need for further experimental work on the effect of an added common ion on the physical properties of metal-amine solutions. It is not to be expected that such an approach will explain adequately the properties of solutions in the concentrated range, when electronic conduction becomes significant, but it is in fact surprising that the electrochemical approach functions as well as it does near the intermediate range of concentration between dilute and concentrated solutions.

It should be mentioned that in the process of carrying out these calculations the equilibrium constant value for the monomer-dimer reaction evaluated by Deigen[6] was also used to calculate concentrations and conductances. The results are shown in Fig. 7 on an expanded scale. The Deigen value of K_2 is 99; it was evaluated for potassium, not sodium. The computed results do not fit the experimental data satisfactorily. The ionic concentrations calculated indicate a substantial increase in dimer species, as would be expected, which is in agreement with magnetic observations on both sodium and potassium solutions at concentrations above 10^{-2}, but is incompatible with the precise dilute solution conductance data for which $K_2=27.03$ is the best value.[11] The reasons for undertaking this last calculation are to be found in the paucity of equilibrium constant data for the sodium-ammonia system, and in some unresolved inconsistencies in data taken in the intermediate range of concentration by electrochemical and by magnetic measurement techniques.

Discussion of Equilibrium Constant Data

Except for Dye's recent work (see below), at −33°, the temperature considered in this work, the only available data are: for $K_1\times10^3$, Deigen gives 7.9 for potassium[6]; Alder gives 30 for potassium[5]; and only Evers' conductance value, 8.0 is available for sodium. Conductance data in the common range of concentration covered experimentally with both sodium and potassium show potassium to be slightly more conducting than sodium, while the shapes of their conductance-concentration curves are almost identical. Magnetic data show that the paramagnetic susceptibilities of sodium and potassium solutions are identical; they are higher for sodium at higher temperature, and probably lower at lower temperature. Because the equilibrium involving K_2 governs the magnetic behavior directly, values of K_2 obtained from magnetic data should be preferred, while K_1 should best be derived

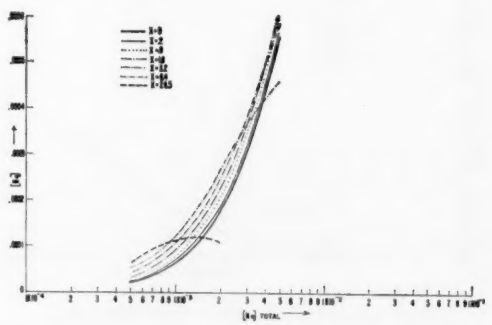

FIG. 5. Tenfold enlargement of lower section of Fig. 3, showing details of variation of [Na] vs $[Na]_{total}$ for various values of x.

from conductance data since it involves the conducting species. One would thus choose Deigen and Alder's values of K_2 and Evers' value of K_1. Alder's K_1 value may be ignored since it did not result from considerations of activity, while Evers' value includes corrections for both activities and mobilities. Deigen's K_1 is checked fairly well by conductance data, but Evers' K_2 is too low if magnetic data are to be accounted for. It is apparent from Fig. 7 that 99 is not a suitable choice for K_2. According to conductance and ionic size data, sodium should be less dissociated than potassium, but if it has a lower K_2 it should have fewer molecules, more atoms and ions, and should be more conducting. This is in disagreement with the conductance result quoted above. Moreover, since the magnetic properties of sodium and potassium are identical at $-33°$, their K_2's should be identical if their K_1's are identical. Everything would be more consistent if both Deigen's K_1 and Evers' K_2 could be slightly increased. It is possible that this might be done without much harm, since each is computed as a second-order effect. If this cannot be done, especially after the accumulation of much more precise data from magnetic measurements, then this might be taken as a strong indication that the second choice of equilibrium

$$M \rightleftharpoons 1/2M_2$$

was unwarranted, and that another choice, involving conducting species, should be preferred, for example,

$$M^0 + e^- \rightleftharpoons M^-,$$

or

$$2e^- \rightleftharpoons (e^-)_2.$$

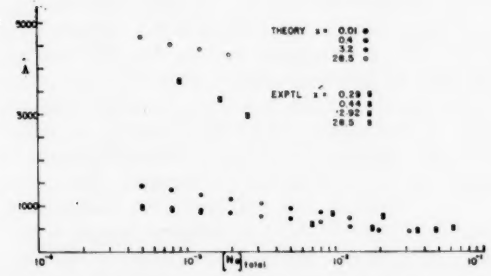

FIG. 6. A plot of the experimental measurements of Lepoutre, reference 15, of the conductance of sodium in liquid ammonia with added sodium chloride as a function of various values of x, compared with theoretical calculations of these conductances, using concentration data displayed in Figs. 1–5, and the Onsager-Kim theory for the conductance of solutions of mixed electrolytes, vs $[Na]_{total}$. In the lowest curve, a number of theoretical points are omitted between $[Na]_{total}=2\times10^{-3}$ to 10^{-2} for $x=0.01$, since they cannot be distinguished on this scale from the points for $x=0.4$.

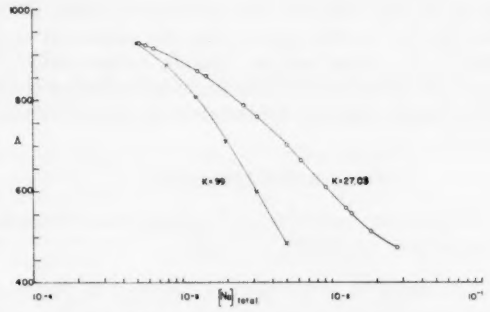

FIG. 7. Plots made to test the correspondence of theoretical calculations with experimental conductance results for varying values of K_2; the ordinate is expanded, but otherwise the plot is similar to Fig. 6. In the upper curve, labeled $K=27.03$, this value of K_2 has been employed to duplicate some experimental data of Kraus, reference 12. Karus' concentrations were taken as input data, the concentrations of the several ionic species computed as described in the first half of this paper, and the Onsager-Kim theory used to compute the conductances which are plotted as circles. The smooth curve drawn with the circles delineated Karus' original conductance data. The theory and the experimental values agree well. For the lower curve, labeled $K=99$, this value of K_2 has been used for a similar calculation. As would be expected, the results, shown as crosses with a smooth curve drawn through them, do not agree with the experimental data. Nevertheless, there are some ambiguities between experimental results obtained by conductance and by magnetic measurements which must be resolved. See Discussion of Equilibrium Constant Data.

Additional evidence is to be found in recently reported measurements of Dye[19–21] concerning absorption spectra for both sodium and potassium, and of transference numbers and activity coefficients of sodium in liquid ammonia solution. His spectral measurements on potassium indicate negative deviations from Beer's law and thus more extensive dimer formation in such solutions, which is consistent with the choice for sodium of a value of K_2 lower than the value of 99 obtained by Deigen for potassium. His measurements of transference numbers led to a choice of $K_1=9.2\times10^{-3}$ and $K_2=18.5$, based on an assumption of the same equilibria as we have utilized. From his activity coefficient and electrochemical data Dye obtained $K_1=9.6\times10^{-3}$ and $K_2=23$.

The close agreement of the constants obtained from transference numbers and emf's of cells with transference with the constants obtained from conductance data, coupled with our own results for the conductances of solutions of mixed electrolytes, lead us, with Dye and

[19] R. C. Douthit and J. L. Dye, J. Am. Chem. Soc. **82,** 4472 (1960).

[20] J. L. Dye, R. F. Sankauer, and G. E. Smith, J. Am. Chem. Soc. **82,** 4797 (1960).

[21] J. L. Dye, R. F. Sankauer, and G. E. Smith, J. Am. Chem. Soc. **82,** 4803 (1960).

Evers, to feel that the two equilibria specified in the introduction to this paper, plus the ionization equilibrium for added sodium chloride, satisfactorily explain the behavior of sodium-ammonia solutions in the dilute range, and into the transitional range of concentration.

ACKNOWLEDGMENT

We are most grateful to the National Science Foundation for their support of this work.

Note added in proof. We are indebted to Professor Dye who has called our attention to a possible misinterpretation of the inversions shown at high concentrations in Figs. 3 and 4. We have stated that these may be interpreted as reversals of equilibria. Perhaps a better way of interpreting this result is to expect a phase separation; phase separation does not occur at the concentrations shown in our calculations, but does occur not far above these concentrations, e.g., D. D. Cubicciotti, J. Phys. Chem. 53, 1302 (1949). As we have pointed out, in this range there are serious limitations on the use of the Debye-Huckel theory, so that only qualitative predictions of trends would be expected. We expect to elaborate on this point in a later paper.

THE JOURNAL OF CHEMICAL PHYSICS VOLUME 35, NUMBER 5 NOVEMBER, 1961

Double-ζ SCF MO Calculation of the Ground and Some Excited States of N_2†*

JAMES W. RICHARDSON‡

Laboratory of Molecular Structure and Spectra, Department of Physics, The University of Chicago, Chicago 37, Illinois

(Received April 25, 1961)

Self-consistent field wave functions for the ground and certain ionized and excited states of the nitrogen molecule, evaluated at the ground state internuclear distance, 1.094 A, are obtained in the molecular orbital (MO) form. The MO's are represented in the usual linear combination of atomic orbitals (LCAO-MO) form, but an expanded basis set is used which contains two each of $2s$, $2p\sigma$, $2p\pi$, and $2p\bar{\pi}$ Slater-type atomic orbitals of differing nuclear charges. All electronic interactions are properly included and calculated without approximation. The computed total energy of the ground state is -108.785 a.u., which is 21.8 ev above the experimental value but 5.8 ev better than a previous result in which strictly atomic (Slater) orbitals were used in the conventional LCAO form. Excitation and ionization energies obtained by direct calculation of the respective states involved are in reasonably good agreement with experiment, though no better than those same quantities calculated from ground-state orbitals in the usual manner. The wave functions for the various states are analyzed and implications drawn regarding the changes wrought in atomic orbitals by bond formation; relevance to the semiempirical interpretation of quadrupole coupling constants is emphasized. Some conjecture about the correlation energy suggests that the ground-state energy obtained may be only a few electron volts above the true molecular Hartree-Fock energy.

I. INTRODUCTION

IT has become abundantly clear that utilization of large-scale digital computers now greatly facilitates the long-awaited systematic investigation of the various approaches to the theoretical computation of molecular properties. These developments are quite adequately documented, for example, in the recent compilation of papers presented at the Conference on Molcular Quantum Mechanics at Boulder, Colorado, in 1959.[1] Briefly, it may be said that two general types of study are being made in this connection: (a) abandonment of the orbital approach with specific inclusion of electronic correlation and (b) refinement of the orbital approximation in the direction of obtaining molecular Hartree-Fock wave functions. The present work is of the latter type.

Even the earliest calculations on H_2 demonstrated that using the minimum set of strictly atomic-orbital functions from which to construct molecular wave functions can give only a qualitatively correct result. Varying the "effective nuclear charges" (or orbital exponents, ζ's) of atomic orbitals used and/or expanding the set of orbital functions in either molecular orbital (MO) or valence bond (VB) calculations is clearly necessary for improvement. With respect to larger molecules, only fragmentary indications of the precise changes have been available until recently.

In a general program of LCAO-MO-SCF computations on a variety of first-row diatomic molecules including hydrides, Ransil[2] has reported wave functions ("best-limited" LCAO-MO's) obtained by minimizing the energy with respect to the orbital exponents characterizing the minimum set of $1s$, $2s$, and $2p$ Slater-type orbitals (STO's). Improvements up to several electron volts in total molecular energy were noted.

For a given molecule these calculations reveal the best ζ's simultaneously for all the MO's in a given electronic configuration. Remaining, however, is the question of the extent to which the energy and wave function may be improved by allowing an independent variation of orbital exponents within *each* molecular orbital. Some evidence regarding this generalization has been obtained by Huzinaga[3] and by Phillipson and Mulliken,[4] who have found the best orbital exponents in $1\sigma_g$ and $1\sigma_u$ in the $^1\Sigma_u^+$ and $^3\Sigma_\pi^+$ states of H_2 are very different. [At R_e for the $^1\Sigma_u^+$ state, $\zeta(1\sigma_g)=1.450$ and $\zeta(1\sigma_u)=0.275$, representing the extreme values reported.] By such adjustment not only are the computed total energies much improved but also are the singlet-triplet splittings desirably decreased.

Extension of this specific idea to larger molecules is greatly complicated by the larger number of nonlinear parameters introduced and by the grave problems of retaining orthogonality and of manipulating properly the energy integrals during the course of, say, an SCF calculation.

A much better approach is to employ an expanded basis set and return to the linear variation technique already well developed. In the specific case here, the atomic inner shell $1s$ AO's were retained,[1] but each second-quantum AO was replaced by a pair of STO's with appropriately chosen ζ's as discussed below. In a recent note, Lefebvre-Brion *et al.*[5] have reported some

* This work was assisted by a grant from the National Science Foundation.

† Presented in part at the Symposium for Molecular Structure and Spectra at Ohio State University, June 13–17, 1960.

‡ Present address: Department of Chemistry, Purdue University, Lafayette, Indiana.

[1] Revs. Modern Phys. **32**, 169–476 (1960); see especially the paper by L. C. Allen and A. M. Karo, p. 275.

[2] B. J. Ransil, Revs. Modern Phys. **32**, 239, 245 (1960).

[3] S. Huzinaga, Progr. Theoret. Phys. (Kyoto) **18**, 139 (1957); **19**, 125 (1957); **20**, 15 (1958).

[4] P. Phillipson and R. S. Mulliken, J. Chem. Phys. **28**, 1248 (1958).

[5] H. Lefebvre-Brion, C. M. Moser, and R. K. Nesbet, J. Chem. Phys. **33**, 931 (1960).

TABLE I. Overlap integrals between orbitals used in the double-ζ N_2 calculation.

$\chi_i\chi_j$	One-center	Two-center
$1s\ 1s$	1.000000	0.000081
$1s\ 2s$	0.140928	0.069010
$2s\ 2s$	1.000000	0.633826
$1s\ 2s'$	0.322665	0.035545
$2s\ 2s'$	0.849540	0.432658
$2s'\ 2s'$	1.000000	0.296476
$1s\ 2p\sigma$	0	0.116870
$2s\ 2p\sigma$	0	0.508387
$2s'\ 2p\sigma$	0	0.536419
$2p\sigma\ 2p\sigma$	1.000000	0.164264
$1s\ 2p\sigma'$	0	0.060041
$2s\ 2p\sigma'$	0	0.280814
$2s'\ 2p\sigma'$	0	0.328780
$2p\sigma\ 2p\sigma'$	0.849540	0.253262
$2p\sigma'\ 2p\sigma'$	1.000000	0.316757
$2p\pi\ 2p\pi$	1.000000	0.464128
$2p\pi\ 2p\pi'$	0.849540	0.262701
$2p\pi'\ 2p\pi'$	1.000000	0.159687

preliminary results of such an extended basis set calculation on the CO molecule, also with significantly improved results. Upon performing the SCF calculations the wave functions obtained may be analyzed in such a way as to indicate that would be the best minimum set of STO's to represent each MO.

The N_2 molecule was selected for this calculation because of the variety of bonding interactions present and because of its history of theoretical and experimental interest. Previous calculations, exact in the sense that no approximations are employed beyond those inherent in the LCAO MO SCF theory, have been done by Scherr[6] using Slater AO's and by Ransil[2] as previously mentioned.

It was possible to examine independently, by this method, not only the ground state but also a limited selection of excited states (all at the same internuclear distance with the same basis set and integrals). It is of considerable interest to compare excitation energies by direct calculation of the states involved to those estimated from properties of the ground state calculation only.

II. COMPUTATIONAL DETAILS

A. Basis Set and Parameters

The basis set chosen for all the calculations reported here consists of seven normalized (but not orthogonalized) STO's on each of the two centers. The z axes of center a and center b are directed toward each other. The σ-type MO's are thereby represented in the form

$$\phi_i = c_{i1}(1s_a \pm 1s_b) + c_{i2}(2s_a \pm 2s_b) + c_{i3}(2s_a' \pm 2s_b') + c_{i4}(2p\sigma_a \pm 2p\sigma_b) + c_{i5}(2p\sigma_a' \pm 2p\sigma_b') \quad (1)$$

and the π-type MO's in the form

$$\phi_i = e_{i6}(2p\pi_a \pm 2\pi_b) + c_{i7}(2p\pi_a' \pm 2p\pi_b'), \quad (2)$$

with the complex conjugate of Eq. (2) representing the other of the degenerate pair of π-type MO's. The + and − signs, of course, apply to the σ_g and π_u MO's and to the σ_u and π_g MO's, respectively.

The STO's in Eqs. (1) and (2) were assigned the following ζ values:

$$\zeta(1s) = 6.6645$$
$$\zeta(2s) = \zeta(2p\sigma) = \zeta(2p\pi) = 1.46$$
$$\zeta(2s') = \zeta(2p\sigma') = \zeta(2p\pi') = 2.44. \quad (3)$$

The ζ for the $1s$ function was obtained as a weighted average of the $1s$ ζ's for various states of the N atom calculated by Roothaan[7]; the weighting coefficients used are the same as those which relate the energies of the various atomic states to the energy of the valence state V_3 corresponding to 26% $s-p$ promotion.

The ζ values for the second-quantum AO's were fixed as ±25% of the Slater exponent 1.95. These choices are based upon a preliminary study of the representation of AO's by double-ζ functions, which is reported in the Appendix. As established there, within that ±25% limit, the energy calculated ought to be at least as good as from any corresponding single-ζ wave function inpendently minimized with respect to each ζ in each MO. Furthermore, after the double-ζ wave function is obtained there may be estimated what the best alternate set of single-ζ STO functions would be.

Clearly the ζ values selected above are not necessarily optimum values for N_2; indeed results subsequently reported here suggest this. Variation with respect to ζ's would be desirable, though perhaps not as rewarding as a further expansion of the basis set. At the outset of the calculation the direction and extent of change in atomic ζ's was not certain. The present choice represents a decision to "play it safe."

The older Raman value for the equilibrium internuclear distance $R = 1.094$ A$^8 = 2.0675$ a.u.[9] was retained in the present computations, since the prior theoretical results are for this value and since the small

[6] C. W. Scherr, J. Chem. Phys. **23**, 569 (1955).

[7] C. C. J. Roothaan, Technical Report of the Laboratory of Molecular Structure and Spectra, Department of Physics, University of Chicago, Chicago, Illinois (1955).

[8] G. Herzberg, *Spectra of Diatomic Molecules* (D. Van Nostrand Company, Inc., Princeton, New Jersey, 1950), p. 552.

[9] The following conversion factors are used here: the atomic unit of distance = 0.52915 A and the atomic unit of energy = 27.210 ev.

TABLE II. Molecular orbitals for N_2 ground state.[a]

MO	c_1	c_2	c_3	c_4	c_5	c_6	c_7	ϵ (in a.u.)
$1\sigma_g$	0.70218	−0.00726	0.01813	−0.00335	0.00370			−15.70512
$1\sigma_u$	0.70154	−0.02375	0.02251	−0.01030	0.00729			−15.70192
$2\sigma_g$	−0.19172	0.13935	0.38096	0.00299	0.25903			−1.49301
$2\sigma_u$	−0.14904	0.74825	0.29428	0.09066	−0.24080			−0.76287
$3\sigma_g$	−0.05089	0.34026	0.06358	−0.16861	−0.41891			−0.62225
$3\sigma_u$[b]	−0.08710	0.20103	0.59336	0.22701	−0.52866			+0.86354
$1\pi_u$						0.32235	0.31976	−0.61378
$1\pi_g$[b]						0.72566	0.21158	+0.19606

[a] Calculated for the exact minimum by Nesbet's program.
[b] Unoccupied orbital.

energy correction to the correct experimental distance 1.0976[10] may be easily made.

All the necessary one- and two-electron integrals among the orbitals of the basis set were evaluated using the digital computer programs written for the Univac Scientic 1103 computer by Roothaan, Yoshimine, McLean, and Weiss. All integrals are considered accurate to seven decimal places. Because of the vast number of such integrals, only the most subsequently useful—the overlap integrals—are given here in Table I.

B. SCF Procedure

At the time these computations were begun, the available SCF routines were of insufficient capacity to handle a basis set of the size taken. A combination of automatic SCF and numerical minimization schemes was adopted, which, incidentally, easily allowed a generalization to the excited and ionized states which are also computed here.

For the closed shell ground state configuration[10] $1\sigma_g^2 1\sigma_u^2 2\sigma_g^2 2\sigma_u^2 1\pi_u^4 3\sigma_g^2$ ($^1\Sigma_g^+$), the total electronic energy of the molecule may be written in the following form:

$$E=\sum_{\sigma} H_\sigma+\sum_{\sigma,\sigma'}(2J_{\sigma,\sigma'}-K_{\sigma,\sigma'})+\sum_{\sigma,\pi}(2J_{\sigma,\pi}-K_{\sigma,\pi}) +\sum_{\pi} H_\pi+\sum_{\pi,\pi'}(2J_{\pi,\pi'}-K_{\pi,\pi'}), \quad (4)$$

where the σ, σ' indices label the σ-type MO's and the π, π' indices label the π-type MO's. H, J, and K are the kinetic+nuclear potential, Coulomb, and exchange energies, respectively, according to the usual definitions.[11]

What was done was to assume a fixed π-electron distribution by at first fixing the coefficients c_6 and c_7 in Eq. (2). This completely determines the last two terms of Eq. (4) and reduces the third term to a quadratic function of the coefficients in the σ MO's—just as is the case with the H_σ terms. Therefore, the $\sigma-\pi$ interaction matrix may be evaluated once the π MO coefficients are given and then added to the H matrix for the σ MO's. The usual SCF procedure[11] may then be employed to determine coefficients in the σ MO's and, after the proper terms are added, the total electronic energy. Subsequently, alternative choices of π MO coefficients are chosen and the process repeated. The minimum total energy is finally found numerically by interpolation.

The two-electron integrals involving only σ-type STO's were computed and arranged in proper supermatrix order entirely by machine operations. Proper arrangement and combination of the remaining integrals were done by hand. This phase of the calculation has been checked and found correct by comparison with a fully automatic computation on the N_2 ground state using a program subsequently written by R. K. Nesbet for the IBM 704. It should be noted that the energy obtained is the minimum with respect to variation of the orbital coefficients, and therefore the result is in every sense an LCAO MO SCF result.

In actual practice the calculation was performed as a function of the ratio of the two $1\pi_u$ MO coefficients

$$\lambda_u=c_6/c_7 \quad (5)$$

Initially, several broadly separated values of λ_u were chosen to give the approximate minimum, then three others selected in that vicinity in order to secure a better interpolated minimum.

For the ionized state $1\pi_u^3$ ($^2\Pi_u$) and excited states of the configuration $1\pi_u^3 1\pi_g^1$ ($^1\Sigma_u^+$, $^3\Sigma_u^+$, $^{1,3}\Sigma_u^-$, $^1\Delta_u$, $^3\Delta_u$) the exact total energy expression will differ from Eq. (4) by the elimination of various terms from H_π and from $\sigma-\pi$ and $\pi-\pi$ electron interactions and the addition of certain others, depending upon the particular state of the configuration. It is observed that the problem now can be treated in exactly the same way as before, except

[10] A critical survey through 1956 of spectroscopic constants and proposed electronic configurations for the established states of the nitrogen molecule and ions is given by R. S. Mulliken, *The Threshold of Space* (Pergamon Press, New York, 1957), p. 169.

[11] C. C. J. Roothaan, Revs. Modern Phys. **23**, 69 (1951).

TABLE III. Atomic orbitals for the N atom.[a]

AO	c_1	c_2	c_3	c_6	c_7	ϵ (in a.u.)
$2s^22p^3$; V_3						
$1s$	0.99359	−0.01140	0.02451			−15.63754
$2s$	−0.25516	0.55839	0.51181			−0.92128
$2p$				0.56056	0.47906	−0.52308
$2s^22p^3$; ^4S						
$1s$	0.99355	−0.01148	0.02468			−15.62338
$2s$	−0.25457	0.56158	0.50844			−0.91601
$2p$				0.54857	0.49118	−0.55800

[a] In this table the $1s$ and $2s$ AO's are expressed as $c_1(1s)+c_2(2s)+c_3(2s')$ and the $2p$ AO is $c_6(2p)+c_7(2p')$, with the same set of ζ's as used in the molecular calculation.

that for the N_2 excited states the forms of both the $1\pi_u$ and $1\pi_g$ MO's must be specified, in terms now of two parameters λ_u and λ_g. Unfortunately, the $^3\Sigma_u^+$ and $^2\Sigma_g^+$ states of N_2^+ could not be calculated by this procedure. These states involve open σ shells which the machine program then available could not handle.

Eleven different combinations of λ_u and λ_g were assumed and the energy minima found individually for all states of the $^1\pi_u^3 1\pi_g^1$ configuration.

Because of the slight additional effort involved, a rough minimization was also done upon the $1\pi_u^4\, 3\sigma_g^0$ $^1\Sigma_g^+$ state of N_2^{++}. This system is also of interest since it is isoelectronic with C_2.

Finally, energies and wave functions for the ^4S and V_3 ground state configurations of the N atom were computed using the same set of basis STO's.

III. WAVE FUNCTIONS AND ENERGIES

A. N_2 Ground State

Total energies for N_2 were computed for $\lambda_u=0.95$, 1.00, and 1.05, giving the values (in a.u.) −108.78489, −108.78531, and −108.78512, respectively. By quadratic interpolation, the calculated minimum total energy is −108.78532 a.u. occurring at $\lambda_u=1.009$. The exact minimum calculated by Nesbet's program occurs at $\lambda_u=1.008_1$ with at most a difference of ±0.00002 between exact and interpolated coefficients. Orbital energies and coefficients for the important MO's of the N_2 ground state are listed in Table II.

Orbital energies and coefficients for the ^4S ground state and the valence state V_3 of the N atom are presented in Table III. The calculated total energy for $N(^4S)$ is −54.32855; for the V_3 state the energy is −54.27155 which upon adding the proper exchange integrals yield an approximate energy of the ^4S state of −54.32836.

B. N_2^+ ($^2\Pi_u$) and N_2^{++} ($^1\Sigma_g^+$)

For N_2^+, total energies evaluated at the points $\lambda_u=$ 0.65, 0.75, and 0.85 are −108.20616, −108.20660, and −108.20405, respectively. The interpolated minimum total energy of −108.20665 (with an estimated error of perhaps ±0.00005) occurs at $\lambda_u=0.715$. For N_2^{++}, total energies evaluated at $\lambda_u=0.30$, 0.55, 0.65, and 0.80 are −107.08682, −107.10178, −107.09236, and −107.07042, respectively. Using the first three points for quadratic minimization, the total energy is −107.1019 a.u. (with an error of perhaps ±0.005) at $\lambda_u=0.539$.

MO coefficients and orbital energies for N_2^+ and N_2^{++} are listed in Tables IV and V.

It will be observed that the method of calculation employed does not yield directly the ϵ's for the π MO's.

TABLE IV. Molecular orbitals for $N_2^+(3\sigma_g^2 1\pi_u^3;\ ^2\Pi_u)$.[a]

MO	c_1	c_2	c_3	c_4	c_5	c_6	c_7	ϵ (in a.u.)
$1\sigma_g$	0.7022	−0.0073	0.0181	−0.0041	0.0047			−16.2063
$1\sigma_u$	0.7015	−0.0255	0.0228	−0.0119	0.0086			−16.2032
$2\sigma_g$	−0.1939	0.1009	0.4070	−0.0049	0.2882			−1.9836
$2\sigma_u$	−0.1573	0.7669	0.3442	0.1742	−0.2792			−1.1895
$3\sigma_g$	−0.0676	0.3072	0.1167	−0.1104	−0.4590			−1.0531
$1\pi_u$						0.2703	0.3781	−0.8157[b]

[a] Interpolated for minimum at $\lambda_u=0.715$ from calculations at $\lambda_u=0.65$, 0.75, and 0.85.
[b] Calculated as discussed in text.

TABLE V. Molecular orbitals for $N_2^{++}(3\sigma_g^0 1\pi_u^4; {}^1\Sigma_g^+)$.[a]

MO	c_1	c_2	c_3	c_4	c_5	c_6	c_7	ϵ (in a.u.)
$1\sigma_g$	0.7026	−0.0069	0.0168	−0.0016	0.0016			−16.7881
$1\sigma_u$	0.7020	−0.0193	0.0204	−0.0067	0.0049			−16.7858
$2\sigma_g$	−0.2020	0.0869	0.4469	0.0103	0.2598			−2.4204
$2\sigma_u$	−0.1702	0.7312	0.4124	0.2070	−0.4795			−1.5664
$1\pi_u$						0.2284	0.4238	−1.5174

[a] Interpolated for minimum at $\lambda_u=0.539$ from calculations at $\lambda_u=0.30$, 0.55, and 0.65.

These quantities may be resurrected, however, in the following way:

For the N_2 and N_2^{++} calculations, the total electronic energy may be written

$$E_{el}=\sum_\sigma \epsilon_\sigma+\sum_\sigma H_\sigma+2\epsilon_\pi+2H_\pi, \tag{6a}$$

while for the $^2\Pi_u$ N_2^+ calculation, ϵ_π may be defined in such a way that

$$E_{el}=\sum_\sigma \epsilon_\sigma+\sum_\sigma H_\sigma+(\tfrac{3}{2})\epsilon_\pi+(\tfrac{3}{2})H_\pi, \tag{6b}$$

where the summations extend over the MO's. The first, second, and fourth terms on the right-hand sides of these equations may be readily evaluated (the second was done automatically within the computer). E_{el}, of course, has already been computed by an alternate route; thus the respective ϵ_π may be obtained.

C. N_2 $1\pi_u^3 1\pi_g^1$ Excited States

In this case separate contributions from the $1\pi_u$ and $1\pi_g$ electrons to the $\sigma-\pi$ interaction terms of Eq. (4) were computed and added to the H_σ matrix for all combinations between the set $\lambda_u=1.00$, 0.85, and 0.70, and the set $\lambda_g=1.3$, 2.0, 3.0, and 5.6, except for the $\lambda_u=0.70$, $\lambda_g=5.6$ pair. A grid of 11 energy calculations was thus obtained for each of the five energetically distinct states of the $1\pi_u^3\,1\pi_g^1$ configuration, upon adding the particular $\pi_u-\pi_g$ electron interaction integrals appropriate to each state as indicated by Scherr.[6]

The two-parameter quadratic minimization procedure described by Ransil[2] was then used to obtain the energy minima. For the states $^3\Sigma_u^+$, $^{1,3}\Sigma_u^-$, $^1\Delta_u$, and $^3\Delta_u$, energies calculated for the points $(\lambda_u, \lambda_g)=(1.00, 2.0)$, (1.00, 1.3), (0.85, 3.0), (0.85, 2.0), (0.85, 1.3), and (0.70, 2.0) were employed. The minimum for the very high $^1\Sigma_u^+$ state lies outside the range of parameters chosen; its minimum is obtained rather unreliably by extrapolation.

For all but the $^1\Sigma_u^+$ state, the λ_u and λ_g values at the minima are very close to each other and for most practical purposes, the λ values for the remaining wave functions may be taken the same. The coefficients and orbital energies for these averaged MO's at $\lambda_u=0.92$ and $\lambda_g=1.73$ are listed in Table VI. Each value was obtained by interpolation by fitting a function of the type

$$c_i=c_0+c_1\lambda_u+c_2\lambda_g+c_1c_2\,\lambda_u\lambda_g, \tag{7}$$

to the four nearest calculated points.

The energies obtained at their respective minima have been converted to energies in electron volts above the $^1\Sigma_g^+$ ground state and are listed in the second column of Table VII. The energies of these same states have been computed also in the conventional manner by taking the difference between $\epsilon(1\pi_u)$ and $\epsilon(1\pi_g)$ obtained from the ground-state calculation and adding the proper

TABLE VI. Averaged molecular orbitals for N_2 $3\sigma_g^2 1\pi_u^3 1\pi_g$ excited states.[a,b]

MO	c_1	c_2	c_3	c_4	c_5	c_6	c_7	ϵ (in a.u.)
$1\sigma_g$	0.7021	−0.0074	0.0185	−0.0037	0.0041			−15.6711
$1\sigma_u$	0.7014	−0.0244	0.0232	−0.0108	0.0079			−15.6684
$2\sigma_g$	−0.1914	0.1343	0.3820	0.0009	0.2674			−1.4845
$2\sigma_u$	−0.1480	0.7949	0.2895	0.1170	−0.2380			−0.7551
$3\sigma_g$	−0.0512	0.3511	0.0578	−0.1711	−0.4122			−0.6029
$1\pi_u$						0.3085	0.3354	...
$1\pi_g$						0.5783	0.3343	...

[a] The very high $^1\Sigma_u^+$ state is not included. See text.
[b] Interpolated for average minimum at $\lambda_u=0.92$, $\lambda_g=1.73$, from calculations at the following sets of λ_u, λ_g values: 1.00, 2.00; 1.00, 1.30; 0.85, 2.00; and 0.85, 1.30.

TABLE VII. Comparisons of vertical excitation energies for N_2 (in ev).

State	Double-ζ			Experimental	
	Direct calculation[a]	Ground state ε's	Scherr from ε's[b,c]	Corrected to $R=1.094$ A[d]	Uncorrected
N_2 $A\ ^3\Sigma_u^+$	6.33	6.69	6.58	7.9	6.17[e]
$^3\Delta_u$	7.50	7.82	7.83	...	...
$a'\ ^1\Sigma_u^-$ / $Y\ ^3\Sigma_u^-$	8.67	8.94	9.07	9.7 / 9.5	8.40[f] / 8.16[g]
$w\ ^1\Delta_u$	9.48	9.65	9.89	10.1	8.89[f]
$b'\ ^1\Sigma_u^+$	22.6	22.93	24.90	~15.6	12.85[e]
N_2^+ $A\ ^2\Pi_u$	15.75	16.69	15.77	17.0	16.69[e]
$X\ ^2\Sigma_g^+$	...	16.91	14.82	15.6	15.58[e]
$B\ ^2\Sigma_u^+$	...	20.76	19.86	18.7	18.76[e]

[a] Computed by subtracting the energy of the ground state from the energies calculated for the various excited states.
[b] Computed from $\epsilon(1\pi_u)$, $\epsilon(1\pi_g)$ and electron interaction integrals from the ground state calculation.
[c] Reference 6.
[d] The magnitudes of the verticality corrections (estimated by fitting a Morse curve) for N_2 states are taken from Lofthus and Mulliken, J. Chem. Phys. **26**, 1010 (1957).
[e] Reference 10.
[f] P. G. Wilkinson and R. S. Mulliken, J. Chem. Phys. **31**, 674 (1959).
[g] P. G. Wilkinson, J. Chem. Phys. **32**, 1061 (1960).

electron-repulsion integrals evaluated in terms of the $1\pi_u$ and $1\pi_g$ MO coefficients also obtained in the ground-state calculation.

IV. DISCUSSION OF RESULTS

A. Ground-State Total Energy

In Table VIII a comparison between the total energies of N_2 and of two N atoms in the ^4S ground state is indicated for several "equivalent" SCF calculations. Each pair of values is "equivalent" in the sense that the same reasoning was used in arriving at the orbitals taken in both calculations. For example, the best-limited row of results pertains to both an atomic and a molecular calculation in which simple AO's were used in STO form and then minimized with respect to the orbital exponents.

The difference between these pairs of energies represents a calculated dissociation energy, the interpretation of which is, of course, subject to considerable controversy. As is commonly understood, even if the exact molecular and atomic Hartree-Fock energies were at hand, different correlation energies would be found for N_2 and 2N, leading to an inaccurate (and, in fact, too low; see Sec. D below) prediction of D_e. It should be recalled that in the double-ζ calculations on the N atom, the same value of $\zeta(1s)$ was used as was selected for the molecular calculation, and not the value previously established for the N ^4S ground state by Roothaan.[7] If that value had been used, a somewhat smaller double-ζ dissociation energy would have been obtained. Nevertheless, inspection of Table VIII still indicates that variation and/or expansion of the basis set is more important for the molecule than for the atom. Thereby the error in the calculated total electronic energy of N_2 is reduced from 27.6 ev in Scherr's calculation to 21.8 ev in the present, an improvement comparable to that obtained by Lefebvre-Brion *et al.* in CO.[5]

With respect to the virial theorem, the ratio of potential and kinetic energies is -2.0046 here, compared to -1.9964 obtained by Scherr. If varying the linear coefficients in the double-ζ AO's is equivalent to varying the orbital exponent of a single-ζ AO, then, one might expect the energy obtained here to be more nearly a minimum with respect to scaling all basis functions (except the $1s$). Thus, at first sight, the slightly poorer agreement with the virial theorem is surprising. How-

TABLE VIII. Comparison of equivalent SCF ground state total energies for N_2 and N.

	N_2 (in a.u.)	2N (in a.u.)	D_e (in ev)
Slater-ζ simple orbitals	−108.574[a]	−108.530[a]	1.20
Best limited simple orbitals	−108.634[b]	−108.538[c]	2.61
Double-ζ (this calculation)	−108.785	−108.657	3.48
Hartree-Fock	...	−108.797[d]	...
Experimental	−109.586	−109.224:	9.90[f]

[a] Reference 6.
[b] Reference 2.
[c] Reference 11.
[d] C. C. J. Roothaan (personal communication).
[e] C. E. Moore, *Atomic Energy Levels* (National Bureau of Standards Circular 467, 1949), Vol. I.
[f] See reference 8.

TABLE IX. Comparisons among various calculated orbital energies (in a.u.).

	$\epsilon(1\sigma_g)$	$\epsilon(1\sigma_u)$	$\epsilon(2\sigma_g)$	$\epsilon(2\sigma_u)$	$\epsilon(3\sigma_g)$	$\epsilon(1\pi_u)$	$\epsilon(3\sigma_u)$	$\epsilon(1\pi_g)$
Slater-ζ simple orbitals	−15.72176	−15.71965	−1.45241	−0.73066	−0.54451	−0.57951	+1.10087	+0.27290
Best limited simple orbitals	−15.80452	−15.80219	−1.47922	−0.75409	−0.56759	−0.60486	1.04956	0.24041
Best atomic simple orbitals	−15.64705	−15.64423	−1.42106	−0.71370	−0.55548	−0.54540	1.22618	0.30021
Double-ζ	−15.70512	−15.70192	−1.49301	−0.76287	−0.62225	−0.61378	0.86345	0.19606
Experimental	...	...	...	−0.69	−0.57	−0.62	...	...

ever, the energy is not necessarily minimized with respect to the internuclear distance, either. Assume for the moment that only this latter factor is yet to be considered. At any internuclear distance

$$-R(dE/dR)=2\langle T\rangle+\langle V\rangle; \qquad (8)$$

$2\langle T\rangle+\langle V\rangle$ is negative (in fact equal to −0.49592 a.u.) and dE/dR is therefore positive. Thus, according to the present calculation, the assumed internuclear distance, 1.094 A, would lie on the ascending part of the theoretical potential curve. Its energy minimum would therefore lie at a rather smaller distance. Actually the probable distance is, if anything, greater.

A second extreme possibility is that all the disagreement with the virial theorem is due *only* to an incorrect choice of $\zeta(1s)$. One may then estimate the change in $\zeta(1s)$ which would produce agreement by holding constant all MO coefficients and all energy terms except those involving only $1s$ AO's on the same center in $1\sigma_g$ and $1\sigma_u$. Calculation then reveals that increasing $\zeta(1s)$ by 0.0185 to 6.6830 would make $2\langle T\rangle+\langle V\rangle=0$ (and incidentally would lower the total molecular energy by only 0.013 ev). This estimated $\zeta(1s)$ compares to the lower value 6.6677 obtained by Ransil in the best-limited LCAO-MO's and the higher Slater value 6.70 used by Scherr.

Actually, however, there is no reason to suppose that the final double-ζ wave function is properly scaled, even with respect to the $2s$ and $2p$ AO's. One can as a third alternative simply scale all distances and bring the energies into exact agreement with the virial theorem. This will, in fact, occur if distances are scaled by the factor $s=1.0023$, which lowers the total molecular energy by 0.016 ev. Thus, in any event, only a slight change in wave function and energies is indicated.

B. Excited State Energies

Except for the elusive $^3\Delta_u$ and the very high $^1\Sigma_u^+$ states, the excited states of N_2 corresponding to the configuration $1\pi_u^3\,3\sigma_g^2\,1\pi_g^1$ appear finally to have been accurately located and characterized. Thus some fairly reliable comparisons between the several calculated and the experimental vertical excitation energies become possible. See again Table VII and the footnotes therein.

As is to be expected, the excitation energies obtained by direct calculation of energy differences are all smaller than those estimated from ground-state orbital energies and except for $^1\Sigma_u^+$ these in turn are all smaller than the experimental values. Furthermore, agreement with experimental value is in general slightly worse than Scherr obtained. Allowing different ζ values for $1\pi_u$ and $1\pi_g$ has therefore not produced the improvement noted in calculations on excited states of H_2.[3,4]

Theoretical ionization potentials, as estimated from orbital energies according to Koopmans' theorem,[12] are compared for various calculations on N_2 in Table IX. For occupied orbitals, various ϵ's are not greatly different, and actually the average deviation where experimental values are known is worst for the double-ζ calculation. And, just like the calculation using best atomic ζ's, $\epsilon(3\sigma_g)$ is calculated higher than $\epsilon(1\pi_u)$, in disagreement with experiment.

Again these comparisons demonstrate the informal theorem of quantum chemistry that the first "improvement" of a previous good result may yield a poorer result, at least in some respects. What is shown here, however, is the approximate character of Koopmans' theorem in this application.

Even if good Hartree-Fock energies have been obtained for the ground and excited states of N_2, a consideration of correlation energies indicates that these excitation energies *should be* too low. In an excited state there is one less *intra*-orbital correlation term (i.e., between two electrons in the *same* orbital) of perhaps 1.2 ev or more in magnitude, and for singlet (but not triplet) states roughly one more *inter*-orbital term (i.e., between two electrons in different orbitals) perhaps 25% as large. Thus discrepancies in the direct calculation of excitation energies are of reasonable magnitude and sign. This explanation can be only partially correct, however. The error (1.6 ev) in the $A\ ^3\Sigma_u^+$ state is greater than the error (1.2 ev) in the $A\ ^2\Pi_u$ state of N_2^+ (where the excited electron has been completely removed) whereas the reverse should be

[12] Details of the development more directly related to atoms and molecules and discussion of the validity of the approximation involved in those cases are given by (a) G. G. Hall and J. E. Lennard-Jones, Proc. Roy. Soc. (London) **A202,** 155 (1950); (b) C. C. J. Roothaan, reference 11; and (c) R. S. Mulliken, J. chim. phys. **46,** 497 (1949).

TABLE X. MO $\bar{\zeta}$ values.[a]

		N_2 $(3\sigma_g^2\,1\pi_u^4)$	N_2[b] $(3\sigma_g^2\,1\pi_u^3\,1\pi_g^1)$	N_2^+ $(3\sigma_g^2\,1\pi_u^3)$	N_2^{++} $3\sigma_g^0\,1\pi_u^4$
$2\sigma_g$	$2s$	2.13	2.13	2.20	2.24
	$2p\sigma$	2.43	2.44	2.46	2.50
$2\sigma_u$	$2s$	1.69	1.68	1.72	1.76
	$2p\sigma$	3.38	(4.30)[c]	(6.77)[c]	(...)[c]
$3\sigma_g$	$2s$	1.59	1.57	1.69	...
	$2p\sigma$	2.10	2.10	2.21	...
$1\pi_u$	$2p\pi$	1.89	1.910±0.005	1.96	2.03
$1\pi_g$	$2p\pi$	...	1.755±0.015	...	...

[a] Obtained from ratios of coefficients in the respective MO's.
[b] Excluding $^1\Sigma_u^+$; by extrapolation $\zeta(2p\pi)=1.86$ in $1\pi_u$ and 1.59 in $1\pi_g$.
[c] In $2\sigma_u$ the coefficients of $2p\sigma$ and $2p\sigma'$ occur with opposite sign (Tables II, IV, V, and VI) and these particular combinations are not very well represented by a single-ζ AO function.

true. Actually, the error in the ionization to the $A\ ^2\Pi_u$ state is unexpectedly small.

The $b'\ ^1\Sigma_u^+$ state has dropped considerably from Scherr's calculation, but remains much higher than where Mulliken[10] has placed it. Both below and above this state at $R=1.094$ A, however, there lie some Rydberg states of the same symmetry. Configuration interaction may therefore be especially important, or, for somewhat overlapping reasons, use of a still further expanded basis set for $1\pi_g$ may be necessary. As pointed out below, the (extrapolated) minimum for this state lies at a value of λ_g corresponding to a rather diffuse $1\pi_g$ MO. Inclusion of $3p\pi$, $3d\pi$ AO's or even some Rydberg-type orbitals into the $1\pi_g$ variation function may be necessary to lower significantly the calculated energy of this state.[13]

C. Wave Functions

Analyzing the more general ground-state wave function obtained here along the lines of Mulliken's population analysis[14] has led to some difficulties in interpretation. A detailed study of the computed charge distribution and its relation to bonding in N_2 is thus reserved to a later paper. The discussion here will be limited to comments upon the observed expansion and contraction of atomic orbitals, and to the sensitivity of the wave functions (and energies) to the λ_u and λ_g values taken.

As mentioned in Sec. II, each (double-ζ) pair of STO's on a given center with the same n, 1, m values may be replaced by a resemblant (single-ζ) STO whose $\bar{\zeta}$ value is determined by the ratio of the coefficients of the double-ζ pair. Valence shell wave functions for all N_2 states calculated have been analyzed in this way, and the results listed in Table X.

In H_2 and Li_2, where orbital exponents have been varied to minimize the single bond energies, a contraction of AO's has been found.[2] A similar result has been found here for the $2\sigma_g$ MO, which carries the burden of the σ bonding. Interestingly, though, the $1\pi_u$ MO's which give the strong multiple bonding character, are if anything, somewhat more diffuse than in the atom. The pronounced contraction of the $2p\sigma$ AO's in the molecule persists in the $2\sigma_u$ and $3\sigma_g$ MO's as well.

One consequence of this calculated result with respect to quadrupole coupling effects has already been noted.[15] According to the usual recipe for interpreting quadrupole coupling constants in terms of the imbalance of p electron density (U_p) from $s-p\sigma$ hybridization and partial ionic character,[16] if U_p is 0 (equal density in $2p\sigma$, $2p\pi$, and $2p\bar{\pi}$ AO's) the coupling constant should be zero. The exact cancellation of the $2p\sigma$ contribution by those from $2p\pi$ and $2p\bar{\pi}$ does not result if the radial functions of $2p\sigma$ and $2p\pi$ are different. In fact, a rather large coupling constant is produced when the difference is as great as calculated here for N_2. Similar effects may well be important at any quadrupolar nucleus in a region of strong bonding.

In passing to the singly and doubly ionized molecules

TABLE XI. Variation of N_2^+ MO coefficients and energies (in a.u.) as a function of $\bar{\zeta}$ assumed for $1\pi_u$.[a]

		$\bar{\zeta}=1.99$	$\bar{\zeta}=1.96$	$\bar{\zeta}=1.93$
$2\sigma_g$	c_1	0.194	0.194	0.194
	c_2	−0.102	−0.100	−0.099
	c_3	−0.406	−0.407	−0.409
	c_4	0.004	0.005	0.006
	c_5	−0.287	−0.289	−0.291
	ϵ	−1.976	−1.987	−1.998
$2\sigma_u$	c_1	−0.157	−0.157	0.158
	c_2	0.769	0.766	0.763
	c_3	0.342	0.345	0.348
	c_4	0.173	0.175	0.177
	c_5	−0.278	−0.280	−0.282
	ϵ	−1.184	−1.192	−1.200
$3\sigma_g$	c_1	0.067	0.068	0.069
	c_2	−0.309	−0.306	−0.305
	c_3	−0.115	−0.117	−0.120
	c_4	0.113	0.109	0.105
	c_5	0.457	0.460	0.463
	ϵ	−1.047	−1.056	−1.065
$1\pi_u$	c_6	0.256	0.278	0.297
	c_7	0.394	0.370	0.349
	ϵ	−0.813	−0.817	−0.820
Total energy		−108.20616	−108.20660	−108.20405

[a] Coefficients defined in accordance with Eqs. (1) and (2).

[13] A third possibility, suggested by Professor Mulliken (private communication) who doubts the importance of configuration interaction with Rydberg states in this case, is that the b' state results from a strong mixing of $1\pi_u^4\ 3\sigma_g\ 3\sigma_u$, $^1\Sigma_u^+$, with $1\pi_u^3\ 3\sigma_g^2\ 1\pi_g$, $^1\Sigma_u^+$. Both states should be high and perhaps reasonably similar in energy and internuclear distance. Under these conditions, strong configuration interaction may be expected between these two valence-shell states.

[14] R. S. Mulliken, J. Chem. Phys. **23,** 1833, 1841 (1955).

[15] J. W. Richardson, Revs. Modern Phys. **32,** 461 (1960).

[16] See, for example, the discussion by T. P. Das and E. L. Hahn, *Nuclear Quadrupole Resonance Spectroscopy, Suppl. 1 of Solid-State Physics, Advances in Research and Applications* (Academic Press Inc., New York, 1958), Part III.

there is the expected rather uniform contraction though on the average not quite to the extent to be anticipated from the use of Slater's screening constants for atoms. In $2\sigma_u$, the $2p\sigma$ and $2p\sigma'$ STO's occur with coefficients of opposite sign. Hence their combination is only roughly approximated by a resemblant $2p\sigma$ STO in the ground state and not at all well in the ions. This is only one of the points in which a conventional interpretation of this generalized and more flexible LC–STO wave function runs into difficulty.

Since the excited state σ MO's are not much different from those of the ground state (except for $^1\Sigma_u^+$), $\bar{\zeta}$ values for resemblant σ STO's are not much different. (The apparent exception, $2p\sigma$ in $2\sigma_u$ is a result of the very sensitive relationship of $\bar{\zeta}$ to the coefficient ratio when that ratio is negative.) In $1\pi_u$ there is a slight contraction amounting to 0.02 in $\bar{\zeta}$ whereas $1\pi_g$ is relatively much more expanded. The *much* greater diffuseness of $1\pi_g$ in the $^1\Sigma_u^+$ state mentioned earlier is noted; by extrapolation $\bar{\zeta}$ in $1\pi_g$ is 1.59 while $\bar{\zeta}$ in $1\pi_u$ is 1.86.

It is interesting to note the considerable difference between coefficients in the $1\pi_g$ virtual orbital from the ground state calculation ($\lambda_g=3.44$) and those from the direct calculation of excited states ($\lambda_g=1.73$). Despite this difference, excitation energies computed the two different ways are remarkably close.

By virtue of the way in which the calculations were performed, it is possible to draw some conclusions about the sensitivity of the wave functions and energies to the variation of $\bar{\zeta}$ in the $1\pi_u$ and $1\pi_g$ MO's. One example is cited, drawn from the calculations on N_2^+. In Table XI are tabulated for comparison valence shell MO coefficients, ϵ's, and total energies for the λ_u choices, 0.65, 0.75, and 0.85, corresponding to $\bar{\zeta}$ values of 1.99, 1.96, and 1.93 in $1\pi_u$. Very clearly revealed is the relative insensitivity of the MO coefficients and the total energy to this variation. However, a greater sensitivity in the orbital energies is revealed.

D. Correlation Energies

The low calculated dissociation energy of N_2 is due, of course, to the fact that there is less electronic correlation energy in the separated atoms than in the molecule. Account of this difference has been made by Hurley,[17] for example, who has added configuration interaction to Scherr's wave function and applied the intra-atomic correlation correction. The dissociation energy thus obtained is somewhat greater than 9.18 ± 0.5 ev. Such corrections have not been applied to the double-ζ functions here.

One of the aims of seeking the best Hartree-Fock energies for atoms and molecules is to discover if "rules of thumb" exist for estimating correlation energies. A basis for some hope in this direction is provided by the early observations of Mulliken[120] that correlation energies (CE) in H_2 and He are both about the same, 1 ev. There is the possibility that these corrections are roughly additive and have values characteristic of the pairs of electrons involved.

With this assumption in mind, Hartree-Fock energies for ground states of N^{5+}, N^{4+}, N^{3+}, and N^0 can be used to estimate the various contributions to CE. (Note, however, relevant comments by Linderberg and Shull.[18]) The total CE's in these systems are 1.79, 1.90, 4.23, and 5.48 ev, respectively. Thus, the total $1s-1s$ CE is 1.79 ev. Subtracting that amount from 1.90 gives 0.11 ev for the CE of *each* $1s-2s$ pair of opposite spin. Subtracting $1.79+2(0.11)$ from 4.23 leaves 2.22 ev for the $2s-2s$ CE in N^{3+}. Finally, subtracting $1.79+2(0.11)+2.22$ from 5.48 ev leaves 1.25 ev left for the three $1s-2p$ and the three $2s-2p$ correlation terms in N^0. (The three $2p$ electrons have the same spins and hence are already presumably adequately correlated.) Making the further assumption that the $1s-2p$ and the $1s-2s$ CE's are equal, then the $2s-2p$ CE becomes 0.31 ev for each $2s-2p$ electron pair or 0.62 ev for each $2s-2p$ orbital pair. Finally, it may be assumed that the intra-orbital CE's for $2s$ and $2p$ are equal.

Generalizing these observations and recalling the equality of H_2 and He CE's one might estimate that in the molecule the inner-shell (i.e., $1\sigma_g$ or $1\sigma_u$) intra-orbital CE is 1.79 ev, per MO, that all inner-shell-valence-shell interorbital CE's are 0.22 ev per pair of MO's, and that all valence-shell intra-orbital CE's are 2.22 ev and interorbital CE's 0.62 ev. The total CE for N_2 estimated in this way equals 22.5 ev. Actually, as the subsequent analysis of the MO charge distributions has revealed, $2\sigma_g$ and $2\sigma_u$ are almost nonpenetrating, and the total estimated CE may, therefore, reasonably be reduced by 0.62 to 21.9 ev. That this is almost exactly the total error of the double-ζ energy is surely fortuitous but does suggest that the true Hartree-Fock energy for N_2 may not be too much lower.

An alternate assessment of the accuracy of these assumptions may be found by analyzing errors in predicting ionization and excitation energies by the exact calculations. For example, the errors in $a'\,^1\Sigma_u^+$ and $^1\Delta_u$ average at 0.75 ev compared to the "rules of thumb" above which would predict $2.22-0.62/2=1.91$ ev., off by a factor of nearly 3. The error in $A\,^3\Sigma_u^+$ of 1.6 ev compares to the estimated 2.22 ev, which is closer. But the error in N_2^+ $A\,^2\Pi_u$ of only 1.2 ev is very small (as noted earlier) conpared to the estimated $2.22\text{ ev}+2(0.22)/2+4(0.62)/2=3.68$ ev. Assuming the additivity of CE's, there is no way to explain how this ionization potential error is smaller than the error in calculating $A\,^3\Sigma_u^+$. To this extent, there is here perhaps some substantiation for Linderberg and Shull's contention that the amount of CE in an atom (or molecule) is not strictly additive, but depends to a significant extent upon the electronic configuration and state. More

[17] A. C. Hurley, Proc. Phys. Soc. (London) **A69**, 767 (1956).

[18] J. Linderberg and H. Shull, J. Mol. Spectroscopy **5**, 1 (1960).

TABLE XII.[a] Comparative properties of double ζ 2p AO's in Li $1s^2 2p$ configuration.

α_i \ α_j	$\alpha_j=\alpha_i$	0.18	0.20	0.22	0.24	0.26	0.30	0.34	0.40
0.10	0.0984 03	0.1273 27	0.1277 77	0.1272 40	0.1258 25	0.1237 11	0.1183 31	0.1129 74	0.1071 08
	1	−0.097	0.065	0.229	0.404	0.603	1.110	1.838	3.478
	0.76146	0.99883	0.99974	0.99687	0.99073	0.98146	0.95356	0.91616	0.86110
	0.136	0.843	1.039	1.247	1.455	1.643	1.880	1.879	1.628
	0.514	0.974	1.074	1.215	1.399	1.626	2.172	2.715	3.272
0.12	0.1096 11	0.1274 31	0.1277 92	0.1275 83	0.1268 93	0.1258 39	0.1231 38	0.1203 48	0.1169 43
	1	−0.145	0.087	0.321	0.567	0.835	1.473	2.276	3.963
	0.86501	0.99934	0.99981	0.99807	0.99438	0.98893	0.97361	0.95484	0.92768
	0.234	0.873	1.023	1.173	1.313	1.434	1.590	1.629	1.555
	0.618	0.970	1.061	1.174	1.307	1.453	1.753	2.018	2.293
0.14	0.1180 88	0.1275 30	0.1277 91	0.1277 76	0.1275 37	0.1271 30	0.1260 26	0.1248 13	0.1231 86
	1	−0.224	0.119	0.459	0.810	1.181	2.016	3.013	4.879
	0.93454	0.99968	0.99989	0.99900	0.99719	0.99458	0.98762	0.97952	0.96782
	0.362	0.904	1.011	1.112	1.203	1.281	1.392	1.446	1.458
	0.721	0.974	1.043	1.122	1.205	1.290	1.450	1.581	1.720
0.16	0.1238 85	0.1276 19	0.1277 79	0.1278 42	0.1278 25	0.1277 52	0.1274 85	0.1271 46	0.1266 28
	1	−0.388	0.179	0.730	1.284	1.850	3.060	4.409	6.745
	0.97623	0.99988	0.99996	0.99964	0.99900	0.99812	0.99585	0.99327	0.98952
	0.550	0.937	1.004	1.066	1.121	1.171	1.249	1.304	1.355
	0.824	0.983	1.0255	1.070	1.114	1.156	1.232	1.292	1.357
0.18		0.1270 55	0.1277 59	0.1278 11	0.1278 53	0.1278 85	0.1279 27	0.1279 46	0.1279 46
		1	0.387	1.658	2.858	4.013	6.260	8.490	11.899
		0.99615	0.99999	0.99995	0.99987	0.99975	0.99946	0.99913	0.99863
		0.792	1.001	1.032	1.062	1.090	1.142	1.190	1.255
		0.926	1.009	1.023	1.036	1.049	1.072	1.091	1.113
0.20			0.1276 54	0.1277 14	0.1276 94	0.1276 78	0.1276 57	0.1276 54	0.1276 76
			1	−5.715	−12.509	−23.388	−94.30	+286.	+75.0
			0.99955	0.99997	0.99992	0.99985	0.99968	0.99943	0.99930
			1.086	1.009	1.018	1.025	1.059	1.096	1.160
			1.029	0.983	0.972	0.964	0.953	0.946	0.940
$\alpha_i=\alpha_j$				0.1257 31	0.1213 38	0.1145 20	0.0937 70	0.0637 60	0.0018 16
				1	1	1	1	1	1
				0.99073	0.97308	0.94925	0.89057	0.82552	0.72819
				1.445	1.878	2.383	3.680	5.33	8.68
				1.132	1.235	1.338	1.542	1.750	2.058

[a] For each pair of α_i, α_j parameters there are tabulated five numbers. From top to bottom these numbers are: (1) that part of the total energy of Li which depends upon the 2p electron, the 1s electrons being held constant, (2) λ_{ij}, (3) overlap with Roothaan's best single-ζ AO (4) ratio of $\langle 1/r^2 \rangle$ to the single-ζ value, and (5) ratio of $\langle r^2 \rangle$ to the single-ζ value.

definitive conclusions, however, must await a more accurate assessment of the total CE for N_2.

ACKNOWLEDGMENTS

The inestimable contribution made by Mr. Tracy Kinyon in assisting with the extensive numerical work involved is gratefully acknowledged and deeply appreciated. The considerable assistance of Dr. Andrew Weiss in modifying his SCF programs to accommodate the present calculations and in other programming aids is also acknowledged with gratitude. Thanks are also due to Professor R. S. Mulliken for many helpful discussions and for comments upon the manuscript, and to Professor R. K. Nesbet for his cooperation in checking the N_2 result with his program.

APPENDIX. SOME PROPERTIES OF DOUBLE-ζ AO's

The choice of basis functions for the N_2 calculation was guided by some preliminary atomic calculations on Li. These results are included here to reveal the extent to which single-ζ and double-ζ representations are the same.

This work was done some time ago by hand. So as to keep the computational labor to a reasonable minimum, the $1s^22p$ configuration of Li was selected. The best single-ζ $1s$ and $2p$ STO's, determined by Roothaan,[11] are characterized by $\zeta(1s)=2.6858$ and $\zeta(2p)=0.52295=0.19471\zeta(1s)$. The calculated total energy is -7.35036 a.u. For the present work, the $\zeta(1s)$ was held fixed at Roothaan's value, and the $2p$ orbital represented by the function

$$2p(\zeta_1,\zeta_2)\sim 2p(\zeta_1)+\lambda_{12}2p(\zeta_2). \tag{A1}$$

In this equation ζ_1 and ζ_2 range over a selected array of points, and for each point λ_{12} is varied to minimize the total energy.

Following Roothaan's scheme of calculation in order to utilize some of his integrals, the parameter α is introduced and defined by the equation

$$\alpha_i=\zeta_i/\zeta(1s). \tag{A2}$$

The points (α_i,α_j) corresponding to (ζ_i,ζ_j) are defined by taking all possible α_i from the set $\alpha_i=0.10$, 0.12, 0.14, 0.16, 0.18, 0.20, and pairing successively with each α_j from the set $\alpha_j=0.18$, 0.20, 0.22, 0.24, 0.26, 0.30, 0.34, 0.40.

For each of the points (α_i,α_j) the following quantities were evaluated: (a) λ_{ij} and E_{ij}, (b) the overlap of this function with Roothaan's single-ζ orbital and (c) the ratios of $\langle r^2\rangle$, $\langle r\rangle$, $\langle 1/r\rangle$, and $\langle 1/r^2\rangle$ to the respective quantities calculated from the single-ζ AO. Numerical results are collected in Table XII.

First it is observed that the quite modest improvement in the energy (0.003 a.u. lower) occurs at the approximate values $\alpha_1=0.186$ and $\alpha_2=0.36$ corresponding to $\zeta_1=0.500$ and $\zeta_2=0.967$. It would seem that what little improvement does occur happens in the region of the nucleus. Evidently, a single-ζ AO is relatively satisfactory in this system. This situation is not likely to persist, however, in systems with more electrons in the second-quantum shell. Witness, for example, the much greater corresponding improvement in the N atom calculation (Table VIII).

Most striking, however, is the flatness of the energy surface over a wide range of parameters. Generally speaking, it is found that if ζ_1 is anywhere up to 25% less than the best single-value and ζ_2 anywhere up to 25% more, the double-ζ energy is equal to or lower than the single-ζ energy. Furthermore, anywhere within this range, the overlap between the double-ζ and the single-ζ $2p$ functions exceeds 0.995. It may be noted also that even when ζ_1 and ζ_2 are *both* somewhat either less or more than the single-ζ value, still a reasonably good orbital was obtained.

Except in these latter cases, it is found that all averages of the various powers of r are greater than the single-ζ values. Clearly this indicates that the double-ζ function has greater density both near to and far from the nucleus but less in the region of the maximum. These differences are certainly in the direction expected for the Hartree-Fock $2p$ orbital. Although these differences are not large, it is well worth noting their size compared to the magnitude of the overlap integral. Obviously there can remain quite significant differences in two functions even though their overlap may be almost unity. There are clear implications, for example, to the problem of curve-fitting numerical wave functions with analytic functions.

If a minimized double-ζ function has been obtained, there remains the converse question of determining what would be the best single-ζ function to use in its stead. If the pair of ζ's lies approximately within the $\pm 25\%$ limit mentioned above, then it is found that single-ζ function which has maximum overlap with the double-ζ function is indeed the one desired.

Primary Processes in Hg($^3P_1$) Photosensitized Reaction of Cyclopropanes*

D. W. SETSER,† B. S. RABINOVITCH, AND E. G. SPITTLER‡
Department of Chemistry, University of Washington, Seattle, Washington

(Received April 24, 1961)

Cyclopropane-d_2 and 1,2-dimethylcyclopropane have been studied at 25°C and above. *Cis-trans* isomerization is apparently of general occurrence in Hg($^3P_1$) photosensitization of substituted cyclopropanes. The most important primary process in the quenching of Hg atoms by cyclopropane-d_2 seems to be the formation of triplet cyclopropane diradicals through which isomerization proceeds. Some exchange occurs at higher temperature. The Hg($^3P_1$) photosensitized polymerization and exchange of D_2 mixtures with cyclopropane also proceeds readily at elevated temperature (135°C).

THE Hg($^3P_1$) photosensitized reaction[1a] of cyclopropane is abnormal compared to other hydrocarbons, as brought out mainly by Gunning and coworkers.[1(b)–(d)] This is manifested by an unusually long induction period which varies with the purity of the cyclopropane and the pressure, by the comparative unreactivity of cyclopropane-hydrogen mixtures, and by the intricacy of the processes leading to the end product, principally polymer.

The cross section for the quenching of Hg($^3P_1$) atoms by cyclopropane is 1.1 A^2, while those for propane and propene are 1.3 and 31 A^2, respectively.[2] The characteristically different magnitudes of the paraffin and olefin reflect different quenching processes[3,4]: The high-quenching cross sections and reactions of olefins have been interpreted as indicating the formation of electronically excited triplet molecules. For alkanes, however, the quenching mechanism involves C–H rupture (with conservation of spin angular momentum at each step) to give a radical and a hydrogen atom. The latter mechanism has also been proposed[5] for some cycloalkanes—cyclobutane, cyclopentane, and cyclohexane.

The close similarity of cross sections of propane and cyclopropane is not necessarily evidence that their quenching mechanisms are the same, due to the unknown relative position of the triplet potential surface of cyclopropane and of the transmission coefficient for quenching with excitation. An excited molecule (or diradical) intermediate was proposed by Gunning and Steacie[1(a),(c)] in their earlier papers on cyclopropane, and more recently also by Ivin,[1(d)] but in a later interpretation the quenching process of importance was suggested as being H split-off.[1b] The photosensitization products are in contrast to those produced from both thermally activated cyclopropane[6] and from chemically activated cyclopropane formed by addition of methylene radicals to ethylene.[7] The latter techniques give structural isomerization to propylene; more recently, it has been shown that 1,2 disubstituted cyclopropanes also undergo concomitant *cis-trans* isomerization.[8,9] The geometric isomerization reaction provides a new means of testing for excited molecule formation in the Hg($^3P_1$) quenching process.

In the present work, the Hg($^3P_1$) photosensitized *cis-trans* isomerization of *trans*-cyclopropane-d_2 has been studied, together with a few experiments on 1,2-dimethylcyclopropane. Attention was focused upon qualitative and semiquantitative features of the primary process; *cis-trans* isomerization is interpreted in terms of an excited triplet molecule mechanism.

EXPERIMENTAL

Trans and *cis*-cyclopropane-d_2 were described previously.[8] There was 6% *cis* contaminant in the *trans* sample. All runs were made with *trans* isomer; its isotopic composition, determined by low-voltage parent-peak mass-spectrographic analysis, was 12.4%-d_1, 84.3%-d_2, and 3.3%-d_3. Extreme purification techniques were not attempted; GLPC placed the maximum chemical impurity at 0.05%.

Cis- and *trans*-dimethylcyclopropane were A.P.I. standards with 0.13% impurities. The *cis-* compound was used as reactant without further purification. Oil

* Work supported by the National Science Foundation and in part by the Office of Naval Research. Abstracted in part from the Ph.D. thesis of D.W.S., University of Washington, 1961.

† National Science Foundation Predoctoral Fellow.

‡ Summer visitor. Permanent address, West Baden College, West Baden Springs, Indiana.

[1] (a) L. Harris, A. A. Ashdown, and R. T. Armstrong, J. Am. Chem. Soc. **58,** 682 (1936); H. E. Gunning and E. W. R. Steacie, J. Chem. Phys. **17,** 351 (1949). (b) H. W. Ford, P. J. Kozak, and H. E. Gunning, American Chemical Society National Meeting, spring, 1960; H. W. Ford, Ph.D. thesis, Illinois Institute of Technology, 1953. (c) R. J. Scott and H. E. Gunning, J. Phys. Chem. **56,** 156 (1952). (d) K. J. Ivin, J. Chem. Soc. **1956,** 2241.

[2] B. de B. Darwent and M. K. Phibbs, J. Chem. Phys. **22,** 110 (1954); B. de B. Darwent, M. K. Phibbs, and F. G. Hurtubise, *ibid.* **22,** 859 (1954).

[3] K. J. Laidler, J. Chem. Phys. **10,** 43 (1942); **15,** 712 (1947).

[4] E. W. R. Steacie, *Atomic and Free Radical Reactions* (Reinhold Publishing Corporation, New York, 1954).

[5] D. L. Kantro and H. E. Gunning, J. Chem. Phys. **21,** 1797 (1953); G. A. Allen, D. L. Kantro, and H. E. Gunning, J. Am. Chem. Soc. **72,** 3588 (1950).

[6] (a) T. S. Chambers and G. B. Kistiakowsky, J. Am. Chem. Soc. **56,** 399 (1934); (b) A. F. Trotman-Dickenson, *Gas Kinetics* (Butterworths Scientific Publications, Ltd., London, 1955).

[7] H. M. Frey and G. B. Kistiakowsky, J. Am. Chem. Soc. **79,** 6373 (1957).

[8] B. S. Rabinovitch, E. W. Schlag, and K. B. Wiberg, J. Chem. Phys. **28,** 504 (1958); E. W. Schlag and B. S. Rabinovitch, J. Am. Chem. Soc. **82,** 5996 (1960).

[9] B. S. Rabinovitch, E. Tschuikow-Roux, and E. W. Schlag, J. Am. Chem. Soc. **81,** 1081 (1959).

TABLE I.

Temp. °C	Reactant pressure cyclopropane	(atm) N_2	Irradiation time (hr)[a]	Product analysis % *cis*[b]	% (C_6+polymer)[c]	Cyclopropane-d_2[d] $\%d_1$	$\%d_1$	$\%d_3$
25	0.20	0.7	1.3	8.2	33			
	0.20	5.0	2.0	11	...			
	0.18	5.0	1.3	8.3	6			
	0.11	18.9	2.0	10	2	13.4[e]	83.5	3.1
	0.20	21	4.0	14	5	13.8[e]	83.4	2.8
	0.18	21	8.0	24	19	12.3	84.4	3.3
	0.013		0.17	0.7	33			
	0.21		1.3	6.5	64			
	0.53		3.0	8.0	40			
	1.3		4.0	6.5	12			
	2.6		10.0	10	7			
	5.0		10.0	22	11	12.6	84.2	3.2
	5.8		0.8	4.0	3			
	5.8		15	12	5	12.4	84.0	3.6
	5.8		33	23	4	12.7	84.0	3.3
	5.8		53	27	13	12.2	84.5	3.3
65	25		40	23	6	12.7	84.0	3.3
135	5.9		20	45	58	11.5[f]	84.2	4.3
	5.9		40	50	72	11.9[f]	80.5	7.6
	29		48	40	25	17.0[g]	71.0	12.0
	70		12	19	7	14.0	81.3	4.7
	70		25	32	6	16.6	75.6	7.8
	70		41	50	26	19.9[g]	65.9	14.2

[a] It should be remembered that at higher pressures the reactor volumes became progressively smaller and hence the solid angle subtended and dosage per unit time became less.

[b] % *cis* formation in the recovered cyclopropane; equilibration corresponds to 50%.

[c] % (C_6+polymer) = (original volume of reactant − volume fraction II)/original volume.

[d] Average for composition of starting material d_1:d_2:d_3 = 12.4:84.3:3.3.

[e] Slight increase believed to be analytical error since there is no increase in $-d_3$, as expected for exchange, and the result is not borne out by other data.

[f] Depletion of d_1 and d_3 compounds by isotopic fractionation relative to d_2 is evident at these large amounts of polymerization (reaction).

[g] Increase of d_1 is not equal to d_3 probably because of preferential removal of lighter material, during the extensive total reaction, by kinetic isotopic fractionation.[8] Compare footnote f.

pumped N_2 was passed through a hot copper column and through silica gel at −195°C. No oxygen impurity could be detected by mass-spectrographic analysis.

The light source was a tubular General Electric germicidal lamp (G 15T8) stated to emit >86% at 2537 A, and with no output at 1850 A. Reactants were saturated with mercury at 25°C and were contained in quartz tubes of various diameters and lengths in accordance with the desired total pressure (e.g., at pressures of 0.01, 5.8, and 70 atm, the internal dimensions were 1.34×27, 0.34×2.8, and 0.16×3.4 cm, respectively). The vessels were placed 1 cm from the lamp. Simple geometric estimates placed the intensity at 1.6×10^{-8} einsteins/cm²sec. After irradiation, the material was separated into three fractions by distillation: I. Gases not condensable at −196°C (hydrogen and methane).[1] II. A fraction distillable at −78°C within 3 min, which was largely cyclopropane, C_2, and C_3 compounds. III. Residue (C_6 and up). Fraction I was minute and was not investigated. Fraction II was used directly for *cis-trans* cyclopropane-d_2 analysis, since there was no interference from impurities; following removal of traces of propane, ethane and propene by GLPC, mass-spectral data were obtained. Fraction III was usually small since most of the material that counted as "C_6+polymer" remained in the reactor as a deficit in the carbon balance; a small proportion of cyclopropane failed to come over in fraction II, but was not of a magnitude

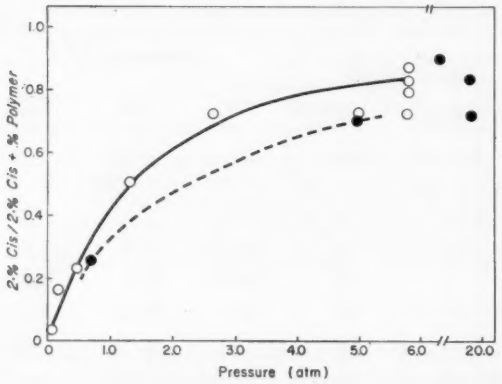

FIG. 1. A representation of the relative importance of geometric isomerization and polymerization as a function of pressure. ○, cyclopropane-d_2 alone ●, 15 cm cyclopropane-d_2+added nitrogen. The percentages referred to on the ordinate are defined in Table I. This figure is a rough representation, inasmuch as consideration of the differing advancement of the two reactions toward completion was not included, in the interest of simplicity; such consideration would in no way alter the characteristic trend revealed by the figure.

such as to sensibly disturb the analysis. Whenever desired, mass-spectral data were obtained from fraction III without further treatment.

Cis-trans analysis of the cyclopropane-d_2 was done by ir analysis as described.[8] Analysis for the *trans* and *cis* isomers of dimethylcyclopropane, propene, and propane, etc., was done by conventional GPLC. A Consolidated 21-103 mass spectrograph was used.

RESULTS

Since quantum yields and complete chemical analysis of high-boiling products were not obtained, these data are largely qualitative, with only semiquantitative trends and qualitative tests being reliable.

The data for photosensitization of *trans*-cyclopropane-d_2 are shown in Table I. Pressures were corrected for molecular volume and shielding factors,[9] and the recorded values are the equivalent ideal gas pressure. Propane product, and especially propene, were always small in amount and diminished with increasing pressure. For example, a low-pressure run at 0.21 atm gave 3.5% propane, 0.4% propene, and traces of ethane and and ethylene; at 5.8 atm, the runs show a maximum of 0.3% propane and no propene. Allene was not detected. H–D exchange only occurred at the highest temperature (135°C), and was enhanced at higher pressures.

Several experiments were done with light cyclopropane and deuterium. A 10:1 mixture of D_2:C_3H_6 at a pressure of 55 cm was photosensitized for 20 hr at 135°C. 30% polymerization occurred with <1% of total propane, ethane, and propene products. The ratios of cyclopropane-d_1:-d_2:-d_3:-d_4 were determined to be 82:100:52:15. Identical experiments at room temperature yielded no deuterated cyclopropanes, small quantities of propane, and no polymer.

A run under the same conditions as those for the 0.53 atm run in Table I, but with the vessel filled with crushed quartz, showed no significant deviation in yields or product proportions from the normal. Another run at 0.53-atm cyclopropane with 0.08 mm D_2 added showed no effects of an induction period[1(b)] relative to the 0.53-atm run in Table I.

The relative variation of *cis* isomer and polymer products with pressure are depicted in Fig. 1. The percent *cis* has been multiplied by two in order to represent the true number of reaction events. With provision for inefficient collisional deactivation by N_2 relative to cyclopropane[6(b)] (~0.25), both curves show the same trend. The results (Table I) at higher temperature show that, as the temperature was raised, somewhat higher pressures were required to reduce polymerization.

Two runs of 5.5- and 17-hr duration, respectively, with *cis*-1,2 dimethylcyclopropane, at corrected pressures of 31 atm of N_2 plus 1.3 atm of cyclopropane, were made at 110°C. *Cis-trans* isomerization and extensive polymerization occurred, as well as formation of a variety of volatile products in much larger yield (4% of the total products) than for cyclopropane-d_2 under similar conditions. No detailed analyses were made. The percent polymerization and the *trans*/*cis* ratio of the recovered cyclopropane for the 5.5- and 15-hr runs were 30% and 1.1, and 65% and 2.3, respectively. The greater variety of products suggests the occurrence of other important primary processes such as C-H rupture on methyl.

DISCUSSION

Primary Process Leading to Cis-Trans Isomerization

Possible mechanisms for the *cis-trans* isomerization of cyclopropane-d_2 are: 1. Reactions of (planar or inverted)[10] cyclopropyl-d_2 (or -d_1 radicals, either involving recombination with H and D atoms or abstraction reactions

$$\nabla\text{-}d_2 \text{ (or -}d_1\text{)} + \text{H (or D)} \rightarrow \textit{cis}\text{- (or } \textit{trans}\text{-)}\nabla\text{-}d_2 \qquad \text{(1a)}$$

$$+\text{RH (or RD)} \rightarrow \textit{cis}\text{- (or } \textit{trans}\text{-)}\nabla\text{-}d_2 + \text{R}\cdot \qquad \text{(1b)}$$

with some hydrocarbons. 2. Collisional stabilization

$$\nabla\text{-}d_2^* + \text{M} \rightarrow \textit{cis}\text{- (or } \textit{trans}\text{-)}\nabla\text{-}d_2 + \text{M} \qquad (2)$$

of excited cyclopropane molecules in which inversion of configuration has taken place.

[10] D. E. Applequist and A. H. Peterson, J. Am. Chem. Soc. **82,** 2372 (1960). Cyclopropyl radicals are known to be reasonably stable with respect to isomerization to allyl at these temperatures; see J. D. Roberts and P. H. Dirstine, J. Am. Chem. Soc. **67,** 1281 (1945); D. E. Applequist, G. F. Fanta, and B. W. Henrikson, *ibid.* **82,** 2369 (1960).

Reaction (2) is predominant, as is clear from the high-pressure runs at 25° and 65°C, and from the runs at 5.9 atm and 135°C, which showed extensive *cis-trans* isomerization with little or no exchange. For any reasonable ratio of H/D isotopic rate values,[8] the occurrence of a large degree of exchange would be evident in the runs cited if geometric isomerization had proceeded through (1). The very large amount of geometric isomerization (Table I) shows that reaction (3), rather than (4), must

$$\nabla + \mathrm{Hg}(^3P_1) \rightarrow \nabla^* + \mathrm{Hg}(^1S_0) \quad (3)$$

$$\nabla + \mathrm{Hg}(^3P_1) \rightarrow \nabla\cdot + \mathrm{H} + \mathrm{Hg}(^1S_0) \quad (4)$$

predominant as the primary quenching process. The Hg($^3P_1$) photosensitization of the isoelectronic ring molecule ethylene oxide also appears to proceed by an excited molecule mechanism.[11]

H—D Exchange of Cyclopropane-d_2

Exchange occurs only at elevated temperatures (135°C). Slow steps could be the production of a cyclopropyl radical by abstraction of H or D from cyclopropane, or H or D abstraction by cyclopropyl radicals following their production by reaction (4). Mercury photosensitization of hydrogen- or deuterium-cyclopropane mixtures (10:1) has been shown previously,[1(a)] and confirmed under our conditions, to give little reaction at room temperature,[1(b),(c)] and no exchange; at 135°C, Hg($^3P_1$) photosensitization of deuterium-cyclopropane mixtures leads here to both exchange and polymerization. This proceeds undoubtedly via H abstraction from cyclopropane by D atoms, with ~13.1 kcal activation energy,[12] and production of cyclopropyl radicals.

The nature of the exchange process seems clear enough to support the conclusion that it has little relevance to the main geometric isomerization.

Nature of ∇^*

Depending upon whether or not spin angular momentum is conserved, quenching could result in either an excited triplet state or in a vibrationally excited ground singlet state.[13]

It is possible that the small quenching cross section of cyclopropane, relative to olefins, indicates a forbidden process of formation of vibrationally excited ground singlet state molecules. However, a much smaller cross section would then be expected; such a process is further ruled against as follows: The triplet state cyclopropane molecule may be regarded as a triplet trimethylene diradical; internal rotation with inversion would yield equilibrium proportions of *cis-* and *trans*-cyclopropane after collisional deactivation, at all pressures used.[8] By contrast, the extent of *cis-trans* isomerization (with rate constant k_ϵ) of a vibrationally excited ground state singlet molecule would be an inverse function of the pressure.[9] Rough estimates of the total irradiation dosage from the geometry and irradiation times, for the data in Table I, show that the production of *cis*-cyclopropane-d_2 for equivalent dosages certainly did not decline, although the pressure rose by a factor of 300, and may even have increased at higher pressures. This is evidence against the vibrationally excited singlet state.

The use of sufficiently high pressure offers a crucial qualitative test for distinguishing which electronic state is formed; virtually complete inhibition of *cis-trans* isomerization should occur in the singlet case. The data and calculations of Rabinovitch, Roux, and Schlag,[9] for vibrationally excited *trans*-cyclopropane-d_2 singlet molecules, show however, that at ~112 kcal/mole^{-1} the required pressure would be much higher than the highest pressure (70 atm) used here. Dimethyl cyclopropane is more useful because of its increased molecular complexity and reduced value of k_ϵ; various assumptions (Appendix) give a range of k_ϵ between 10^9 and 10^8 sec^{-1}. At the pressure used here, the specific rate of collisional interaction was $\sim 4\times 10^{11}$ sec^{-1}. Hence *cis-trans* isomerization through a vibrationally excited ground state should be almost completely inhibited. Extrapolation to higher pressures of Frey's,[14] and our own,[15] data for vibrationally excited ground singlet dimethylcyclopropane at $\geqslant$100 kcal/mole^{-1} supports this view, and our estimates of k_ϵ. Actually, the experimental data at 110°C show that the *cis-trans* isomerization and concomitant polymerization reactions proceeded even faster than was observed for cyclopropane-d_2. Thus all the experimental data indicate that spin angular momentum is conserved in this mode of quenching of Hg(6^3P_1) by cyclopropane. Although less efficient, cyclopropane in this respect again resembles olefins. A study to determine whether Hg photosensitized *cis-trans* isomerization occurs with substituted cyclobutanes, where marked chemical similarity to olefins is lacking, would be of interest.

Primary Process for Polymerization

Figure 1 suggests the concept of an excited species which can be collisionally deactivated at higher pres-

[11] M. K. Phibbs, B. de B. Darwent and E. W. R. Steacie, J. Chem. Phys. **16,** 39 (1948).

[12] J. R. McNesby and A. S. Gordon, J. Am. Chem. Soc. **78,** 825 (1957). This high E value agrees with the known high strength of cyclopropyl bonds, comparable to vinyl.

[13] An electronically excited singlet state presumably is not involved since the energy required would be higher than 112 kcal mole^{-1} [P. Wagner and A. B. F. Duncan, J. Chem. Phys. **21,** 516 (1953)], and spin angular momentum also would not be conserved.

[14] H. M. Frey, Proc. Roy. Soc. (London) **A251,** 575 (1959).

[15] B. S. Rabinovitch and D. W. Setser, J. Am. Chem. Soc. **83,** 750 (1961).

sures before leading to polymerization. Possible polymerization mechanisms of triplet cyclopropane are discussed elsewhere.[16] We have no explanation for the possible discrepancy between the implications of Fig. 1 and the findings of Harris *et al.*[1(a)] that the rate of pressure change is independent of pressure up to 5 atm. Inhibition of polymerization by wall effects, due to the progressively smaller ampoules used here at higher pressures, seems eliminated by the lack of an effect in packed vessel experiments at 40 cm.

Our interpretation of polymerization can be made to accord with that of Gunning and coworkers, which stresses reaction (4) in the polymerization process, by a composite mechanism of (3) and (4); reaction (3) would then lead mainly to *cis-trans* isomerization. As a consequence of known magnitudes of $Hg(^3P_1)$ quenching cross sections of alkanes leading to C–H rupture, reaction (4) must occur simultaneously with (3) to some extent.

ACKNOWLEDGMENTS

We are grateful to Dr. Hadley W. Ford for lending us his Ph.D. thesis and thank him and Dr. H. E. Gunning for their comment on the manuscript.

[16] D. W. Setser, Ph.D. thesis, University of Washington, 1961.

APPENDIX

The specific rate constant k_ϵ for dimethylcyclopropane was calculated from an expression

$$k_\epsilon = A[(E-E_0+a'E_z')(E+aE_z)]^{s-1}$$

given by Rabinovitch and Diesen[17], and is similar to the equation for cyclopropane-d_2 used previously.[9] The quantities a and a' are empirical correction factors (0.93 and 0.85, respectively) which bring the equation into approximate agreement with a more accurate value which would be obtained from an exact count of vibrational energy levels.[18] E_z was taken as 83 and E_z' as 81 kcal mole^{-1}. A was taken as $10^{15.25}$ and E_0 as 60 kcal mole^{-1} from the work of Flowers and Frey.[19]

The range of k_ϵ values given in the text was obtained by various combinations of assumptions: $E=107[Hg(^3P_0)]-112[Hg(^3P_1)]$ kcal mole^{-1}, $s=33$–39.

Molecular diameters used in the calculation of collision rates were: cyclopropane, 4.92×10^{-8} cm; nitrogen, 3.85×10^{-8} cm; dimethylcyclopropane, 8.0×10^{-8} cm.

[17] B. S. Rabinovitch and R. W. Diesen, J. Chem. Phys. **30,** 735 (1959).

[18] R. E. Harrington, B. S. Rabinovitch, and R. W. Diesen, J. Chem. Phys. **32,** 1245 (1960). B. S. Rabinovitch, and J. H. Current, *ibid.* (to be published).

[19] M. C. Flowers and H. M. Frey, Proc. Roy. Soc. (London) **A257,** 122 (1960).

THE JOURNAL OF CHEMICAL PHYSICS VOLUME 35, NUMBER 5 NOVEMBER, 1961

Measurement of Electrodiffusion. Effect of Electrosmosis on Diffusion*

P. C. SCHOLTEN AND KAROL J. MYSELS

Department of Chemistry, University of Southern California, Los Angeles 7, California

(Received April 13, 1961)

If a tube containing an electrolyte is subjected to an axial alternating electric field, an oscillating electrosmotic flow will generally occur. The resulting increase in diffusional transport is calculated and compared with the increase in transport due to a simultaneously occurring reaction, i.e., with electrodiffusion. It is shown that for tubes a few millimeters wide electrodiffusion is generally overshadowed by ordinary diffusion and the increase of the latter by electrosmosis. Therefore such systems are not suitable for the determination of reaction rate constants through the measurement of electrodiffusion.

1. INTRODUCTION

WHEN a system in dynamic chemical equilibrium, such as

$$A \underset{k_2}{\overset{k_1}{\rightleftarrows}} B, \tag{1.1}$$

where the electrophoretic mobilities of A and B are different, is placed in an electric field, there must occur an increase in diffusion along the direction of the field because of the randomness in the lifetimes of particles in the two states. This increase, called electrodiffusion, has been the subject of several theoretical discussions[1–6] and is now known[4–6] to be given for an alternating electric field by

$$D_e = \frac{(u_1-u_2)^2 E_0^2 k_1 k_2}{2(k_1+k_2)[\omega^2+(k_1+k_2)^2]}. \tag{1.2}$$

In principle, electrodiffusion could be used for the measurement of reaction rates in an equilibrium system by experiments lasting a long time compared to the half-life of the reaction. This would be especially useful in the determination of rate constants for quite rapid reactions.

There seem to be two basic experimental approaches to the measurement of electrodiffusion. The first is essentially based on the Tiselius electrophoresis technique. Here a stabilizing density gradient in a vertical tube is used to reduce mixing by thermal convection currents and electrosmosis. It is in this connection that electrodiffusion was originally envisaged by Ogston[7] and later by Lamm.[2] Cann, Kirkwood, and Brown[8] considered for the same system the effects of reactions whose half-lives are of the same order as the duration of the experiment. The need for swamping electrolytes to maintain electrical and chemical homogeneity of the system complicates this approach. Nevertheless, as will be shown later, it appears to be more promising than the following.

A second approach is based on the use of a horizontal tube containing a system of uniform density. A tracer technique is used to observe self-diffusion. This was the approach we selected. With proper precautions convection due to mechanical disturbances and Joule heating of 1 w/cm³ was found to be negligible in a horizontal diffusion cell 2 mm in diameter. However, calculation of the effect of electrosmosis upon diffusion, as given below, showed that this approach is rather hopeless except under exceptional combinations of circumstances.

In an ideal open system, electrosmosis gives rise to a plug flow which should not cause an increase in diffusional transport if the net displacement of the liquid is taken into account, or, better, if the displacement is annulled by inversion of the current. In principle, the "open system" condition might be imitated by closing one end with a piston moving back and forth at the same rate as the liquid. In the presence of any back pressure, however, and especially in the more easily realizable closed system, a Poiseuille-type return flow will take place. Even if this flow is exactly reversed after some time, the temporary deformation of the system will cause an increase in diffusion in the axial direction. This is illustrated in Fig. 1 which shows how two originally plane-parallel surfaces perpendicular to the axis are deformed during flow, increasing their area considerably, and at the same time decreasing their separation, except in the center of the tube. Clearly, both of these effects cause a more rapid diffusion between the two surfaces.

The magnitude of the increase in diffusion thus produced is estimated in Sec. 2 below. As expected, it decreases rapidly as the frequency of the applied field increases. However, as shown by Eq. (1.2), electrodiffusion also decreases at higher frequencies. Section 3

* This work was supported by the National Science Foundation.

[1] K. J. Mysels, J. Chem. Phys. **24**, 371 (1956).

[2] O. Lamm, Acta Chem. Scand. **10**, 1132 (1956).

[3] T. A. Bak and W. G. Kauman, Trans. Faraday Soc. **55**, 1109 (1959).

[4] S. Ljunggren, Trans. Roy. Inst. Technol. Stockholm **142** (1959).

[5] P. C. Scholten and K. J. Mysels, Trans. Faraday Soc. **56**, 994 (1960); **57**, 764 (1961).

[6] T. Thedeen, Trans. Roy. Inst. Technol. Stockholm **165** (1960).

[7] A. G. Ogston, Nature **157**, 193 (1946).

[8] J. R. Cann, J. G. Kirkwood, and R. A. Brown, Arch. Biochem. Biophys. **72**, 37 (1957). Cf. P. C. Scholten, *ibid.* **93**, 568 (1961); J. R. Cann and H. R. Bailey, *ibid.* **93**, 576 (1961).

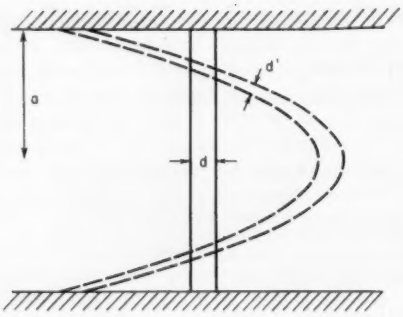

FIG. 1. Increase of diffusional transport by temporary deformation of the liquid.

deals with the accuracy of the determination of reaction-rate constants. The accuracy is maximal at some intermediate frequency since at high frequencies electrodiffusion becomes negligible compared to ordinary diffusion, and at low frequencies compared to the electrosmotic increase of diffusion. However, even at the optimal frequencies the system is not promising for the measurement of reaction-rate constants.

List of Symbols

a	radius of tube
c	concentration
D_0	diffusion coefficient
D_e	electrodiffusion coefficient
D_{obs}	experimentally observed diffusion coefficient
E	electric field strength
k_i	reaction constant
r	distance to axis
t	time
u_i	electrophoretic mobility
v	linear velocity
z	distance in axial direction, stationary coordinates
η	viscosity
ϵ	dielectric constant
ζ	zeta potential
ξ	distance in axial direction, moving coordinates
ω	angular frequency.

2. INCREASE OF DIFFUSION BY ELECTROSMOSIS

The electrosmotic flow in a closed cylindrical tube due to an axial electric field of the form $E=E_0\cos\omega t$ has at radius r a velocity

$$v_r=\frac{\epsilon\zeta E_0}{2\pi\eta}\left(\frac{r^2}{a^2}-\frac{1}{2}\right)\cos\omega t. \tag{2.1}$$

Let us consider an experiment of the relaxation type: A boundary is established between two solutions of different concentrations in a long tube, and after some time the amount of material transported through the boundary plane is determined. (In steady-state experiments additional difficulties would arise from electrosmotic flow through the boundaries.)

The changes in concentrations due to diffusion and electrosmotic flow can be described by the differential equation

$$\frac{\partial c}{\partial t}=D_0\frac{\partial^2 c}{\partial z^2}+\frac{D_0}{r}\frac{\partial}{\partial r}\left(r\frac{\partial c}{\partial r}\right)-\left(\frac{r^2}{a^2}-\frac{1}{2}\right)U\omega\cos\omega t\frac{\partial c}{\partial z}, \tag{2.2}$$

where $U=\epsilon\zeta E_0/2\pi\eta\omega$.

Introduction of $\xi=z-(r^2/a^2-\frac{1}{2})U\sin\omega t$, which attaches the coordinate system to the moving liquid, changes Eq. (2.2) to

$$\frac{\partial c}{\partial t}=\frac{\partial^2 c}{\partial\xi^2}D_0\left(1+\frac{4r^2U^2}{a^4}\sin^2\omega t\right)+\frac{D_0}{r}\frac{\partial}{\partial r}\left(r\frac{\partial c}{\partial r}\right)$$
$$-4\frac{UD_0}{a^2}\sin\omega t\frac{\partial}{\partial\xi}\left(c+r\frac{\partial c}{\partial r}\right), \tag{2.3}$$

where the differentiations vs r are along the curved ξ planes.

Although this equation is more complicated than Eq. (2.2), it has a simpler physical meaning: The transport terms on the right-hand side are now due only to the diffusion of solute with respect to solvent and not to the flow of the solvent itself. The oscillating flow still affects the rate of diffusion as shown by the $\sin\omega t$ factors. However, if the conditions are such that the changes of concentrations (and of their gradients) during one cycle are very small, and that many cycles are involved in an experiment, it is permissible to average the above oscillating factors over each full cycle. This makes the last term nil and replaces $\sin^2\omega t$ by $\frac{1}{2}$, giving

$$\partial c/\partial t=(\partial^2 c/\partial\xi^2)D_0[1+(2r^2U^2/a^4)], \tag{2.4}$$

which is valid if $a^2/D_0\gg 1/\omega$; i.e., the time for diffusion across the tube is very long compared to the length of a cycle.

Equation (2.4) describes diffusion in an anisotropic cylinder, in which the coefficient of axial diffusion increases with the radius.

This problem can be attacked with the aid of the simplifying assumption that the duration t of the experiment is long compared to the time of diffusion across the tube

$$t\gg a^2/D_0\gg 1/\omega.$$

In this case differences in concentrations over one cross section will remain small, and we can average Eq. (2.4) over a cross section, giving

$$\partial c/\partial t=(\partial^2 c/\partial\xi^2)D_0[1+(U^2/a^2)]. \tag{2.5}$$

The diffusion coefficient observed in this case is

$$D_{obs}=D_0[1+(U^2/a^2)]. \tag{2.6}$$

The deviation from (2.6) in cases where cross diffusion

is not sufficiently fast can be estimated by calculating the transport in case of negligible cross diffusion, i.e., for

$$a^2/D_0 \gg t \gg 1/\omega.$$

Here the tube can be divided into concentric cylindrical shells, and the contribution of each shell to the transport calculated separately. Since in a relaxing system this transport is proportional to the square root of the local axial diffusion coefficient, the total transport M due to an initial concentration difference C_0 is

$$M = C_0 \int_0^r \frac{2r}{a^2}\left[D_0\left(1+\frac{2r^2U^2}{a^2}\right)t\right]^{\frac{1}{2}} dr = C_0(D_{obs}t)^{\frac{1}{2}}, \quad (2.7)$$

which gives

$$D_{obs} = D_0 \frac{a^4}{9U^4}\left[\left(1+2\frac{U^2}{a^2}\right)^{3/2}-1\right]^2. \quad (2.8)$$

While this expression differs greatly in form from Eq. (2.6), numerical computation shows that the resulting D_{obs} deviates by at most 11.3%. Since the deviation must be even less in intermediate cases, one is justified to use the simple Eq. (2.6) as a reasonable approximation for all conditions.

The effect of the wave form is rather small. For the case of a square wave field we found (through Fourier expansion of the field strength) a D_{obs} which was $\pi^2/12 \sim 0.8$ times the D_{obs} of Eq. (2.8).

For small capillaries or low frequencies the effect of electrosmosis will be less than expected from Eq. (2.6)

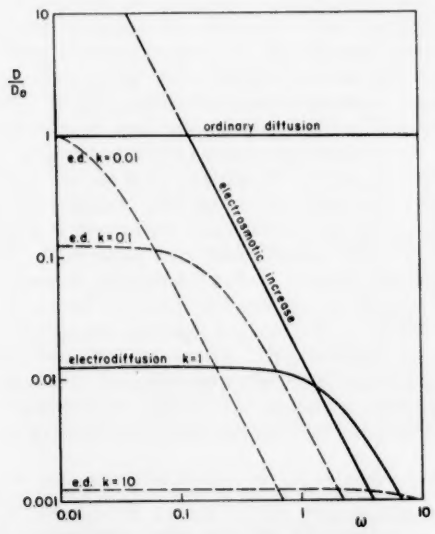

FIG. 2. Comparison of the effects of diffusion, electrosmosis, and electrodiffusion assuming $\zeta = 80$ mv, $\epsilon = 78.5$, $\eta = 78.94\times10^{-3}$ poise, $E_0 = 10$ v cm^{-1}, $a = 0.1$ cm, $u_1 - u_2 = 2\times10^{-4}$ cm^2 sec^{-1} v^{-1}, $D_0 = 2\times10^{-5}$ cm^2 sec^{-1}.

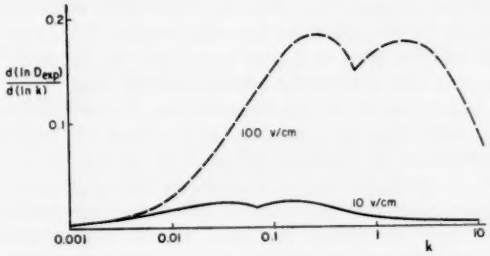

FIG. 3. Maximum sensitivity for different values of the reaction constants.

because of cross diffusion during one cycle. Finally, if $a^2/D \ll 1/\omega$, the effect will disappear completely.

3. ACCURACY

The diffusion coefficient observed for a substance undergoing electrodiffusion in a closed cylindrical tube with an ac field is the sum of the coefficients of ordinary diffusion, of its increase by electrosmosis and of electrodiffusion.

$$D_{obs} = D_0 + D_0\frac{\epsilon^2\zeta^2E_0^2}{4\pi^2300^4a^2\eta^2\omega^2} + \frac{(u_1-u_2)^2E_0^2k_1k_2}{2[\omega^2+(k_1+k_2)^2](k_1+k_2)}. \quad (3.1)$$

(ζ in volts, E_0 in v/cm). In Fig. 2 the values of the three terms of Eq. (3.1) are plotted versus frequency for an arbitrary but realistic example. We considered an aqueous solution in a field of 10 v/cm in a 2-mm wide Teflon tube ($\zeta = 80$ mv) and a mobility difference (2×10^{-4} cm^2 sec^{-1} v^{-1}) which, for small ions, is rather large. It appears that a perceptible electrodiffusion contribution can be expected only for a narrow range of k values. For fast reactions, normal diffusion predominates, whereas for slow reactions a low frequency has to be used and the electromosis contribution becomes high. Below $\omega = 0.1$, the latter will be somewhat less than indicated as a result of cross diffusion, but not enough to change the situation radically.

The usefulness of the method in the measurement of reaction-rate constants can be characterized by the sensitivity γ, defined as the ratio of a relative change in the experimentally observed quantity D_{obs} to the corresponding relative change in k. It is given by

$$\gamma = \frac{d\ln D_{obs}}{d\ln k} = \beta\left(\frac{\omega^2}{4k^2}-1\right)\left(\frac{\omega^2}{4k^2}+1\right)^{-1} \times\left[\left(\frac{\omega^2}{4k}+k\right)\left(1+\frac{\alpha}{\omega^2}\right)+\beta\right]^{-1}, \quad (3.2)$$

with

$$\alpha = \epsilon^2\zeta^2E_0^2/4\pi^2300^4\eta^2a^2, \qquad \beta = (u_1-u_2)^2E_0^2/16D_0,$$

and can be used to find the optimal frequency and sensitivity for a given k. A plot of the sensitivities at the

optimal frequency for different values of k is given in Fig. 3. Even in the most favorable range of 0.1–10 sec^{-1} the relative error in k, due to an error in D_{obs} only, is already 5 to 10 times the relative error in D_{obs}.

Improvement of the situation can be obtained by increasing the field strength. This reduces the relative importance of ordinary diffusion, cf. dotted curve in Fig. 3. Joule heating puts a limit on this approach. In wider tubes the electrosmosis effect becomes smaller, but here convection problems become rapidly more serious. Reduction of the zeta potential would also decrease the elèctrosmosis, but this is generally not possible.

As stated in Sec. 2, the electrosmotic effect disappears for fine capillaries. Therefore it seems possible to measure electrodiffusion in a porous material, e.g., sintered glass with a pore size around one micron. For the same reason paper electrophoresis seems a promising approach. However, the large surface introduced by such methods may tend to complicate the reaction.

4. CONCLUSION

If diffusion is measured in an alternating electric field, a large increase due to deformation of the liquid by electromosis can be expected. For the measurement of electrodiffusion it is advisable to minimize this effect by the use of an artificial density gradient or by imitating the open-cell condition with the aid of a moving piston or by drastically reducing the cross section of channels used.

Negative Ion Formation in Ozone*

R. K. CURRAN
Westinghouse Research Laboratories, Pittsburgh, Pennsylvania
(Received April 13, 1961)

Negative ion formation in ozone was studied in a mass spectrometer. Negative ions of O, O_2, and O_3 were observed. The appearance potentials of O^- and O_2^- are 0 ev and 0.42±0.03 ev, respectively. The data on O^- formation yield $D(O_3-O) \leq 1.02\pm0.15$ ev and the data on O_2^- formation lead to a limiting value for the electron affinity of O_2 of $EA(O_2) \geq 0.58$ ev.

I. INTRODUCTION

THERE has been no previous study of the ozone molecule for negative ion formation on electron impact. The positive ions of ozone have been observed by Herron and Schiff[1] and Grundland.[2] Herron and Schiff reported O^+, O_2^+, and O_3^+. Grundland observed O_3^+ and O_4^+.

II. APPARATUS

The mass spectrometer used has been described previously.[3] The negative ion current was detected with a vibrating reed electrometer and a Faraday cage. The kinetic energy of formation of the ions was measured by operating with the analyzer at high voltage and the collector and source at ground potential. The retarding curve for the negative ion kinetic energy determination could be traced out by varying the potential of the ion source with respect to ground. The SF_6^- ion from SF_6 was used to calibrate the zero of the ion kinetic energy scale. The zero point of the electron energy scale for the processes leading to O^- and O_2^- formation in ozone was determined by the point of vanishing electron current on the electron retarding curve. The source was equipped to use the RPD[4] method. To gain sensitivity in ion detection, a constant pusher voltage was used in the source. This led to some broadening of the electron distribution.

Ozone was made by passing dry oxygen through an all glass ozonizer. The ozone was liquified at liquid nitrogen temperatures and purified by pumping off oxygen. The ozone was then distilled into the mass spectrometer and again liquified. Gaseous ozone from the surface of the liquid ozone at liquid nitrogen temperatures passed through a glass tube of about 1 m length into the ion source. This resulted in some differential in the pressures at the liquid ozone and the mass spectrometer source. The maximum source pressure is estimated as being between 10^{-4} and 10^{-3} mm Hg. The filament used in the source was made from thoriated iridium ribbon.

III. RESULTS

The positive ion spectrum of O_3 was scanned and the ions O^+, O_2^+, O_3^+, and O_4^+ were observed. The appearance potential of O_3^+ was measured as 12.89±0.10 ev in agreement with the value 12.80±0.5 ev found by Herron and Schiff.[1] The O_3^+ signal was observed to have no breaks indicative of excited states of O_3^+ for about 2 ev above threshold. The O_4^+ signal was not intense enough for a reliable appearance potential measurement to be made.

Using the total electron beam with an energy spread of about 1 ev with the lowest energy electrons at 0 ev the pressure in the source was raised to a somewhat higher value than normal and a very weak O_3^- ion was seen. The pressure dependence and electron energy dependence of this peak could not be determined. O^- was found with an appearance potential in the range 0 to 0.05 ev. The appearance potential of O_2^- was found to be[5] 0.42±.0.03 ev. Figure 1 shows the O^- current observed as a function of electron energy. Figure 2 is the O_2^- current as a function of electron energy. Also shown in the figures is the electron retarding curve used to calibrate the electron energy scale. The electron distributions had a width at half maximum of about 0.2 ev.

The kinetic energy of O_2^- was measured as being in the range of 0 to 0.05 ev. The O^- ion was observed to have a maximum kinetic energy of 0.3±0.1 ev. Because of the reduction in sensitivity of detection with decreasing cross section of the O^- forming process, the kinetic energy measurement could only be made to within 0.2 ev of threshold. The 0.3±0.1 ev value for the maximum kinetic energy of the O^- ion was observed for an electron energy range of about 1 ev starting at 0.2 ev above threshold.

* This work supported in part by the Advanced Research Projects Agency and the Office of Naval Research.
[1] J. T. Herron and H. I. Schiff, J. Chem. Phys. **24**, 1266 (1956).
[2] M. I. Grundland, Compt. rend. **236**, 476 (1953).
[3] R. E. Fox, *Advances in Mass Spectrometry* (Pergamon Press, London, 1959), p. 397.
[4] R. E. Fox, W. M. Hickam, D. J. Grove, and T. Kjeldaas, Jr., Rev. Sci. Instr. **26**, 1101 (1955).
[5] The error quoted here is arrived at by attaching an experimental uncertainty to each appearance potential measurement of 0.1 ev, and then taking the average appearance potential and considering the error to be random. Checks were made to detect systematic errors in the appearance potential measurements, such as determining the appearance potentials to be independent of electron beam current, pusher field, and electron d stribution width and by verifying that the ion peaks are directly proportional to electron beam current.

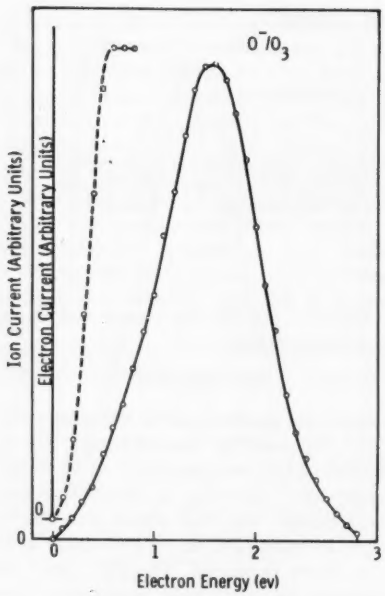

FIG. 1. O^- ion current as a function of electron energy. The electron energy scale is determined by taking the point of vanishing current on the electron retarding curve as the point of zero electron energy.

The pressure dependence of the O^- and O_2^- ion currents is shown in Fig. 3. The negative ion current for O^- and O_2^- has been plotted against the O_2^+ ion current. The O_2^+ current was chosen as a measure of the O_3 pressure in the source since it is the dominant fragment ion from O_3. Since it is inconvenient to switch from positive to negative ions for each O_3 pressure, the reading of an ion gauge was used as a parameter to relate the negative and positive ion currents for corresponding pressures. The linearity of the pressure dependence of the O^- and O_2^- ion peaks rules out the possibility of their formation by a three-body process.

Nothing definite can be said of the absolute cross sections for negative ion production. The relative cross sections for O^- to O_2^- formation at their peaks is 11/7. A very crude estimate of the absolute cross sections is that they lie in the region of 10^{-17} to 10^{-18} cm^2.

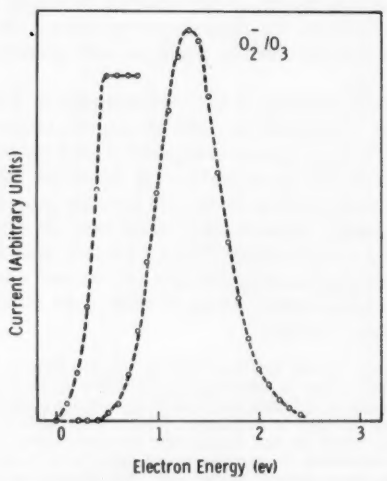

FIG. 2. Electron energy dependence of the O_2^- ion current. The energy scale is again determined from the electron retarding curve.

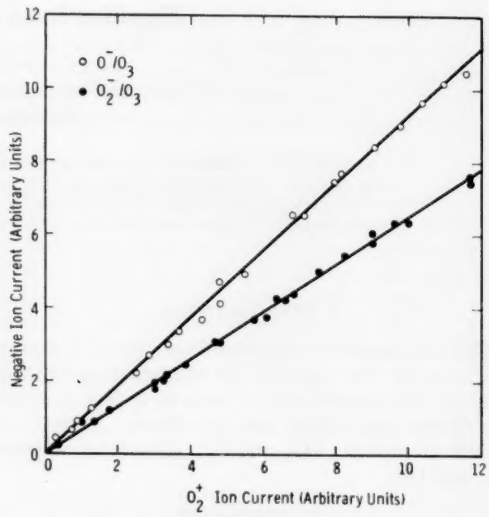

FIG. 3. Pressure dependence of the O^- and O_2^- ion currents. The O_2^+ ion current is used as a measure of the O_3 pressure since O_2^+ is the dominant ion in the O_3 positive ion spectrum.

IV. DISCUSSION

From the measured appearance potential and kinetic energy of the O^- a lower limit for the dissociation

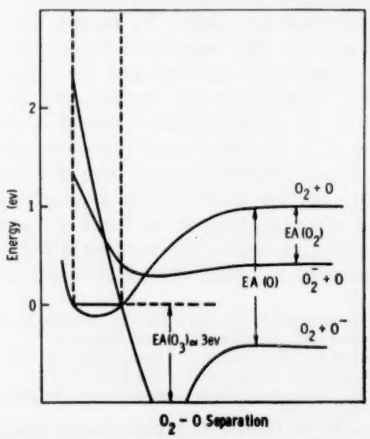

FIG. 4. Hypothetical potential curves for O_3^-. The construction of these curves is described in the text.

energy of the O_2 and O bond in O_3 can be evaluated. The appearance potential of the O^- ions is in the range 0 to 0.05 ev. The kinetic energy of O^- is taken as 0.3 ± 0.1 ev at threshold which implies a total kinetic energy, KE, of $(3/2)\times(0.3\pm0.1$ ev) for the process. Thus one has from

$$KE+D(O_2-O)\leq AP(O^-)+EA(O)$$

that $D(O_2-O)\leq 1.02\pm0.15$ ev. The inequality holds since nothing is known of the vibrational state of the O_2 fragment. The electron affinity of oxygen, EA(O), is taken as[6] 1.465 ± 0.005 ev. This value for $D(O_2—O)$ is in good agreement with the thermochemical value of 1.0 ev derived from the atomic heat of formation[7] for O_3 of 140.6 kcal/mole or 6.1 ev using the dissociation energy[8] of 5.115 ± 0.002 ev for oxygen.

A lower bound on the electron affinity of O_2 may be obtained from the measured appearance potential and kinetic energy of the O_2^- ion. Taking the appearance potential of the O_2^- ion to be 0.42 ± 0.03 ev and the total kinetic energy, KE, to be 0 ev

$$KE+D(O_2-O)\leq AP(O_2^-)+EA(O_2)$$

one has that $EA(O_2)\geq 0.58$ ev. The inequality is again used since the vibrational state of the O_2^- fragment is not known. The thermochemical value of 1.0 ev obtained above has been used for $D(O_2-O)$.

From the energy dependence of the O^- and O_2^- ion currents a set of hypothetical potential curves for the O_3^- ion can be constructed as shown in Fig. 4. The curves are constructed by determining the region of overlap of the Franck-Condon region with a potential curve as the width in electron energy of the negative ion current less the width of the electron energy distribution. The width of the electron energy distribution is subtracted from the total width observed for the ion current since the electron energy scale is determined by the fastest electrons in the distribution and the ion current will therefore continue to be measured for one distribution width after the energy at which the cross section for the process vanishes. The dissociation limits are determined from the known value of the electron affinity of atomic oxygen and the value of the electron affinity of molecular oxygen derived here. These dissociation limits are only limiting values since, as pointed out above, the vibrational states of the O_2 and O_2^- are not known in this experiment.

The value obtained above for the electron affinity of O_2 does not agree with the value obtained from lattice energies[9] of 0.95 ± 0.07 ev. The best value for the electron affinity of O_2 from a swarm experiment is in the recent work of Phelps and Pack[10] who obtained a value of 0.46 ev. Since the degree of excitation of the O_2^- ion is not determined it is possible that the discrepancy between their result and the present result arises from their O_2^- ions being excited by one vibrational quantum above the O_2^- ions observed in the present experiment.

ACKNOWLEDGMENTS

The author is indebted to Dr. A. V. Phelps and Dr. G. J. Schulz for their valuable comments.

[6] L. M. Branscomb, J. Chem. Phys. **29,** 452 (1958).
[7] A. G. Gaydon, *Dissociation Energies* (Chapman and Hall, London, 1953).
[8] P. Brix and G. Herzberg, J. Chem. Phys. **21,** 2240 (1953).
[9] H. O. Pritchard, Chem. Revs. **52,** 529 (1953).
[10] A. V. Phelps and J. Pack, Phys. Rev. Letters **6,** 111 (1961).

Potential Energy Curves for the $X\ ^1\Sigma_g^+$ and $B\ ^1\Sigma_u^+$ States of Hydrogen*

IRWIN TOBIAS† AND JOSEPH T. VANDERSLICE
Institute for Molecular Physics, University of Maryland, College Park, Maryland

(Received April 26, 1961)

The recently reported accurate data of Herzberg and Howe have been used to calculate the potential energy curves for the $X\ ^1\Sigma_g^+$ and $B\ ^1\Sigma_u^+$ states of hydrogen by the Rydberg-Klein-Rees (RKR) method. The results are compared with the results of the quantum calculations of Kolos and Roothaan and Dalgarno and Lynn. The agreement is good; in fact, the interaction energy obtained by Dalgarno and Lynn for the ground state agrees with the RKR values to within 2% in the region where the two curves overlap. The rotational predissociation observed in the $v''=14$ level of the $X\ ^1\Sigma_g^+$ state is discussed. It appears as if there may exist here an unusual case of a sharp spectral line associated with a state which is very close in energy to the maximum of a potential barrier.

INTRODUCTION

IT is particularly important to have an accurate, complete, experimental internuclear potential energy curve for the ground state ($X\ ^1\Sigma_g^+$) of the hydrogen molecule. Such a curve would, of course, be invaluable in any consideration of the phenomena requiring a knowledge of the energy of interaction between two hydrogen atoms. For example, Herzberg and Howe[1] comment on the need for a reliable curve at large values of r in order to interpret fully their results on rotational predissociation in the $X\ ^1\Sigma_g^+$ state. Also, since hydrogen is one of the simplest of molecules, new theoretical techniques for calculating molecular energies are likely to be applied here first. The experimental curve would serve then as a standard of comparison for the theoretical results, thereby helping to evaluate the worth of the new method.

Some time ago, the Rydberg-Klein-Rees quasi-classical method[2–4] for determining experimental potential energy curves from spectroscopic data was described and applied to the ground state of the hydrogen molecule.[5] The quantity of data then available was insufficient to allow the curve to be extended beyond the eleventh vibrational level, approximately 5000 cm^{-1} below the dissociation limit. A comparison between the RKR results and the results of a Dunham calculation[6] in the region of the minimum, where the latter is known to be accurate, showed the two to be in excellent agreement. Subsequently, Jarmain[7] showed that the two methods should be equivalent at the lower vibrational levels. It was not possible to make a direct comparison with Dalgarno and Lynn's theoretical results,[8] which are accurate at large internuclear distances, but it did appear that the two would merge smoothly. There was some question, in fact, about the accuracy of the RKR method for energies close to the dissociation energy.[9] It appeared that in this region any errors in the experimental data or inaccuracies in the equations used to fit the data would cause large errors in the potential curve.

For these reasons, we thought it worthwhile to redo the calculation of the ground-state curve for hydrogen using the recent precise data of Herzberg and Howe[1] who have obtained rotational and vibrational data for all vibrational levels of the $X\ ^1\Sigma_g^+$ state. The data enabled us to extend the experimental potential curve for the ground state to distances great enough so that it overlapped the reported curve of Dalgarno and Lynn sufficiently to enable a careful comparison to be made between the two. The results of our calculation also helped us better to assess the accuracy of the method at large internuclear distances as well as to focus attention on the extremely interesting problem of line broadening and tunneling through a barrier at energies near the maximum, for which Herzberg and Howe have acquired the necessary data.

In addition to recalculating the potential curve for the $X\ ^1\Sigma_g^+$ state, we have also calculated the curve for the $B\ ^1\Sigma_u^+$ state from the accurate data of Herzberg and Howe.[1]

Both the $X\ ^1\Sigma_g^+$ and the $B\ ^1\Sigma_u^+$ states of hydrogen are treated by Kolos and Roothaan[10] in a recent paper. Also of interest, therefore, is a comparison of their predictions for these two states with the experimental curves.

RESULTS AND DISCUSSION

The results of the RKR calculations on the ground state and the first excited state of hydrogen are con-

* This research has been supported in part by the Office of Naval Research.

† Present address: Department of Chemistry, Rutgers, The State University, New Brunswick, New Jersey.

[1] G. Herzberg and L. L. Howe, Can. J. Phys. **37**, 636 (1959).
[2] R. Rydberg, Z. Physik **73**, 376 (1931); **80**, 514 (1933).
[3] O. Klein, Z. Physik **76**, 226 (1932).
[4] A. L. G. Rees, Proc. Phys. Soc. (London) **59**, 998 (1947).
[5] Vanderslice, Mason, Maisch, and Lippincott, J. Mol. Spectroscopy **3**, 17 (1959); Errata **5**, 83 (1960).
[6] J. L. Dunham, Phys. Rev. **41**, 713, 721 (1932).
[7] W. R. Jarmain, Can. J. Phys. **38**, 217 (1960).
[8] A. Dalgarno and N. Lynn, Proc. Phys. Soc. (London) **A69**, 821 (1956).
[9] J. T. Vanderslice, E. A. Mason, and W. G. Maisch, J. Chem. Phys. **32**, 515 (1960).
[10] W. Kolos and C. C. J. Roothaan, Revs. Modern Phys. **32**, 219 (1960).

tained in Tables I and II, respectively. Figure 1 shows the energies for the two states plotted as a function of r, the internuclear distance. The two dissociation limits, one at 38 283.1 cm^{-1} [11] and the other at 120 584.4 cm^{-1} are indicated by the dotted lines.

It is not necessary to repeat here the details of the RKR method since they may be found elsewhere.[2-5] One remark should be made, however, concerning the calculation of the turning points at the energy of the highest vibrational level of the ground electronic state ($v''=14$). Recall that for computational purposes in the RKR method, the energy scale is divided into a number of regions arranged such that within each region i,

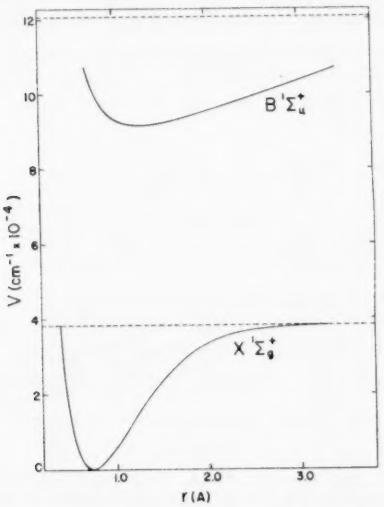

FIG. 1. Potential energy curves for the $X\ ^1\Sigma_g^+$ and $B\ ^1\Sigma_u^+$ states of hydrogen. The dashed lines are the dissociation limits.

the energy levels of the nuclear motion E_{vJ} are given by an expression of the form[2-5,12]

$$E_{vJ}=A_i+B_iJ(J+1)+[\omega_i-\alpha_iJ(J+1)](v+\tfrac{1}{2})-(\omega x)_i(v+\tfrac{1}{2})^2, \quad (1)$$

where A_i, ω_i, $(\omega x)_i$, α_i, and B_i are constants determined from the spectroscopic data. To obtain the constants ω_i and $(\omega x)_i$ for the region including $v''=14$ it was necessary, in this case, to extrapolate the experimental ΔG vs v curve from $v''=13$ to $v''=14$ where ΔG is the difference between two successive rotationless vibrational states, i.e., $E_{v+1,0}-E_{v,0}$. It is believed that the uncertainty in the value of the turning points introduced by the extrapolation does not exceed that introduced by the method itself in this region.

[11] G. Herzberg and A. Monfils, J. Mol. Spectroscopy **5**, 482 (1960).

[12] J. T. Vanderslice, E. A. Mason, W. G. Maisch, and E. R. Lippincott, J. Chem. Phys. **33**, 614 (1960).

TABLE I. Potential energy curve of the $X\ ^1\Sigma_g^+$ state of hydrogen.

v	V (cm^{-1})	r_{min} (A)	r_{max} (A)
0	2170	0.634	0.883
1	6331	0.571	1.013
2	10 257	0.535	1.119
3	13 952	0.509	1.219
4	17 420	0.489	1.316
5	20 662	0.473	1.414
6	23 676	0.460	1.515
7	26 458	0.449	1.621
8	29 001	0.439	1.731
9	31 294	0.432	1.852
10	33 320	0.425	1.996
11	35 057	0.419	2.164
12	36 472	0.416	2.375
13	37 521	0.413	2.682
14	38 143	0.411	3.284

The RKR results for the ground state overlap the Dalgarno and Lynn results from 2.12 to 3.28 A and the two agree throughout this range to within 2%. In absolute terms, this means the agreement is within 5 cm^{-1} at 3.28 A and within 50 cm^{-1} at 2.12A. The perturbation procedure used by Dalgarno and Lynn in their calculation should yield the most reliable results for large values of r. The fact that the Dalgarno-Lynn curve agrees so well with the RKR results at the smaller

TABLE II. Potential energy curve of the $B\ ^1\Sigma_u^+$ state of hydrogen.

v	V (cm^{-1})	r_{min} (A)	r_{max} (A)	$V+T_e$[a] (cm^{-1})
0	674.2	1.105	1.552	92 373
1	1993	0.993	1.777	93 692
2	3274	0.931	1.954	94 973
3	4521	0.888	2.113	96 220
4	5734	0.854	2.258	97 433
5	6914	0.826	2.397	98 613
6	8061	0.803	2.530	99 761
7	9177	0.783	2.661	100 876
8	10 261	0.766	2.789	101 960
9	11 314	0.750	2.915	103 013
10	12 336	0.736	3.038	104 035
11	13 328	0.723	3.163	105 027
12	14 290	0.711	3.286	105 989
13	15 224	0.700	3.412	106 923

[a] T_e is the energy difference between the bottoms of the two potential curves.

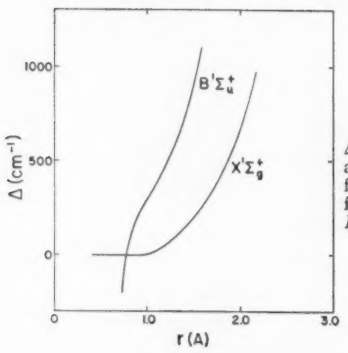

FIG. 2. The deviation, Δ, of the Kolos-Roothaan potential curves from the RKR results for both the $X\,^1\Sigma_g^+$ and $B\,^1\Sigma_u^+$ states.

r values, where one might expect the former to be most in error, is a good indication that the curve is indeed reliable for $r > 2.12$ A.

In Fig. 2 we have plotted, as a function of r, the deviation Δ of Kolos and Roothaan's results from the experimental curves. For the ground state the agreement is is excellent until approximately 1.0 A after which the deviation rapidly increases. This is not surprising since the Kolos and Roothaan wave function is of a polynomial type which requires more and more terms for increasing r to approach the correct asymptotic form.[10] Since they included only 40 terms one would expect the deviation to increase rapidly with increasing r. The deviations for the $B\,^1\Sigma_u^+$ state are greater than for the ground state but here only a 34-term wave function was used. Actually the agreement is "astonishingly good" since such agreement should occur after corrections have been made for finite nuclear masses.[10] The favorable comparison between these experimental and theoretical curves may be taken as a sign that quantitative potential energy curve results can now be achieved for simple systems from quantum mechanical calculations.

It is worth mentioning at this point that no peculiar behavior appeared in the RKR curve for the $X\,^1\Sigma_g^+$ state as it did in the case of the curve for the $B\,^3\Sigma_u^-$ state of oxygen which developed a hook near the dissociation limit.[9]

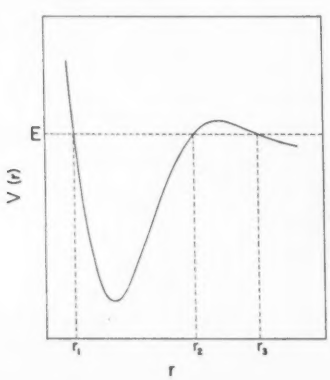

FIG. 3. A typical effective potential energy curve.

TRANSMISSION THROUGH ROTATIONAL POTENTIAL BARRIERS

When the rotational angular momentum of the nuclei is taken into account, the curves $V(r)$ in Fig. 1 are replaced by effective potential energies $V_J(r)$ which are related to $V(r)$ by

$$V_J(r) = V(r) + (\hbar^2/2\mu r^2)\,J(J+1) \qquad (2)$$

where μ is the reduced mass of the nuclei.[13] The rotational quantum number J, in the case of sigma states, can assume positive integral values including zero. Let us consider the case in which the dissociation limit of the electronic state corresponds to two neutral atoms. Then, at large r, $V(r) \sim r^{-6}$ and $V_J(r)\,(J \neq 0)$ is repulsive at such distances. Hence, there will exist in this case at

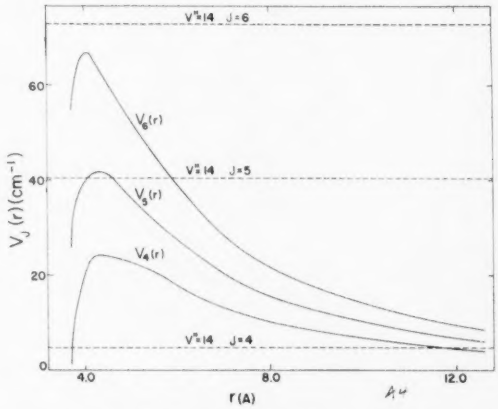

FIG. 4. The observed $v''=14$, $J=4$ and 5 rotational levels and the hypothetical $v''=14$, $J=6$ rotational level of the ground state together with the appropriate V_J curves.

some $r > r_3$ a maximum in the function $V_J(r)$. Figure 3 depicts a typical $V_J(r)$. It is possible for one or more of the upper vibrational levels associated with $V_J(r)$ to have an energy greater than that of the dissociation limit. From general considerations, it can be shown that the energy of levels in this range is continuous[14] and indeed, experimental observation of such levels has shown them to be broadened.[15]

From a quasiclassical point of view, the broadening of a discrete level of energy, E, for a particle localized between r_1 and r_2 (Fig. 3) may be thought to arise because of the possibility for the particle to tunnel through the barrier and escape in to the region $r > r_3$. We may then assign a mean lifetime τ to the level which will be broadened by an amount $\Delta E \sim \hbar/\tau$.

Experimentally, it is found that the $v''=14$, $J=4$ and 5 levels of the ground state of hydrogen lie 4.8 and

[13] G. Herzberg, *Spectra of Diatomic Molecules* (D. Van Nostrand Company, Inc., Princeton, N. J., 1950), pp. 425–427.

[14] L. D. Landau and E. M. Lifshitz, *Quantum Mechanics—Nonrelativistic Theory* (Addison-Wesley Publishing Company, Inc., Reading, Massachusetts, 1958), p. 58.

[15] L. Farkas and S. Levy, Z. Physik **84**, 195 (1933).

40.5 cm^{-1}, respectively, above the dissociation limit.[1,11] In addition, neither exhibit any broadening effects.[1,16] The $v''=14$, $J=6$ level is not observed. Figure 4 shows the relative position of each of these levels and also the corresponding $V_J(r)$ in the region of the maximum. The position of the hypothetical $J=6$ level was obtained from an extrapolation of the energies of the first five rotational levels of the $v''=14$ vibrational level. To obtain the effective potential energies for the various J values, we have chosen for $V(r)$ the experimental RKR curve coupled with the results of Dalgarno and Lynn which extend to 6.5 A. The $V_J(r)$ curves were then obtained from Eq. (2).

We see from Fig. 4 that the $J=6$ level lies above the maximum in the $V_6(r)$ curve in agreement with the fact that this level is not observed. The $J=4$ and 5 levels lie below their corresponding maxima by amounts of 19.3 cm^{-1} and 1–2 cm^{-1}, respectively. We have used the following expression for the transmission coefficient[17,18]

$$D=\left\{1+\exp\left[(2/\hbar)\int_{r_2}^{r_3}p_r dr\right]\right\}^{-1}, \tag{3}$$

where

$$p_r^2=2\mu(E-V(r)-\hbar^2(J+\tfrac{1}{2})^2/2\mu r^2), \tag{4}$$

and have obtained for these two levels $D(J=4)=9.7\times10^{-4}$ and $D(J=5)=0.46$.

To calculate the magnitude of the broadening ΔE of the $J=4$ level due to tunneling, we may use the expression[19,20]

$$\Delta E(\text{cm}^{-1})=(\omega/4\pi)\exp\left[(-2/\hbar)\int_{r_2}^{r_3}p_r dr\right] \tag{5}$$

which is valid at energies E such that ΔE is small compared to the distance between successive levels. Here ω is the classical frequency in cm^{-1}. Numerical calculation yields $\Delta E\sim0.6$ cm^{-1} which is about the measured half-width.[16]

The observed sharp $v''=14$, $J=5$ level presents quite a problem. This level is so close to the top of the barrier that, according to the usual ideas of tunneling,[13,15,17] one might expect it to be too broad to be observed. According to Eq. (5), the lines should become broader as the level gets closer to the top of the barrier if the frequency does not change too rapidly with energy. Such behavior has been found in the case of AlH,[15] for example. Since r_2 is close to r_3 (Fig. 3) near the maximum, one does not expect the derivation of Eq. (5) to be valid in this region,[21,22] and hence it should not be used to discuss the broadening of the $v''=14$, $J=5$ level. Curiously, it does predict, however, that ΔE approaches zero as E approaches extremely close to the energy of the maximum, since the frequency approaches zero in this region.

All of the above remarks are based on the assumption that the $V(r)$ curve is reliable. This appears to be the case. The $V(r)$ curve cannot be lowered by more than a few wave numbers in the region around 4.2 A without causing the $v''=14/J=5$ level to be unbound and the $v''=14$, $J=4$ level to be measurably broadened, In order to have the $J=5$ level sufficiently far below the maximum for Eq. (5) to predict a sharp line, the $V(r)$ curve would have to be raised by approximately 20 cm^{-1} in the region of the maximum, 4.3 A. This would require $V(r)$ itself to have a maximum. There does not seem to be any theoretical reason why such a maximum should exist. Furthermore, under these conditions the $v''=14$, $J=6$ level would then be bound and no such bound level has been observed. Finally, the agreement between the experimental RKR potential curve and the Dalgarno-Lynn curve (which appears to be the most reliable theoretical curve at large r) makes it seem likely that neither one can be greatly in error. It appears, therefore, that some unexpected effect occurring near the maximum of the potential hump is causing the $v''=14$, $J=5$ level to remain sharp. We are at present investigating the spread of spectral lines for levels which lie quite close to the barrier maximum.

SUMMARY AND CONCLUSIONS

The RKR method in conjunction with the recent experimental work of Herzberg and Howe has been used to calculate the potential energy curves for the $X\,^1\Sigma_g^+$ and $B\,^1\Sigma_u^+$ states of molecular hydrogen. These curves have been compared with the calculated results of Kolos and Roothaan and Dalgarno and Lynn. The agreement is very good indeed. In the region of the overlap, from 2.12 A to 3.28 A, the RKR ground state curve agrees with the results of Dalgarno and Lynn to within 2%. The agreement between these two curves which were obtained by such widely different methods speaks well for the accuracy of both.

The rotational predissociation observed by Herzberg and Howe in the $X\,^1\Sigma_g^+$ state is considered. It appears that there may be rather unusual case here of having a sharp spectral line only a few wave numbers below a barrier maximum.

ACKNOWLEDGMENT

The authors are grateful to Professor Herzberg for informing them of his interest in this problem. They also wish to thank him for sending them his results on the dissociation energy of hydrogen before they appeared in print and for helpful correspondence on the observed widths of some spectral lines.

[16] G. Herzberg (private communication).
[17] E. C. Kemble, *The Fundamental Principles of Quantum Mechanics* (McGraw-Hill Book Company, Inc., New York, N.Y., 1937), pp. 109–112.
[18] R. E. Langer, Phys. Rev. **51,** 669 (1937).
[19] O. K. Rice, Phys. Rev. **35,** 1538, 1551 (1930).
[20] Reference 17, p. 186.
[21] S. Goldstein, Proc. London Math. Soc. (2) **33,** 246 (1932).
[22] R. E. Langer, Bull. Am. Math. Soc. **40,** 574 (1934); Trans. Am. Math. Soc. **36,** 90 (1934).

Paramagnetic Relaxation in Metal-Ammonia Solutions*

D. E. O'REILLY
Argonne National Laboratory, Argonne, Illinois

(Received October 21, 1960)

Relaxation processes for electrons in alkali metal-ammonia solutions are calculated to proceed via hyperfine interaction with nitrogen 14 nuclei in dilute solutions ($<0.15M$) and via spin-orbit interactions in concentrated solutions. Dipolar and exchange interactions are estimated to make only a small contribution to the observed relaxation times. Comparison of the mean square width due to the hyperfine interaction as obtained from relaxation time data and the observed N^{14} Knight shift allows a construction of an effective wave function for the electron in dilute solutions. In more concentrated solutions ($0.60M$) relaxation results from fluctuations in the electric potential at an unpaired electron with a correlation time of the order of 10^{-14} sec. Effects due to the substitution of D for H and Na for K are examined.

1. INTRODUCTION

MAGNETIC resonance measurements[1,2] of alkali metal-ammonia solutions have served to clarify the nature of these much investigated and unique solutions. In particular, measurements of transverse and spin-lattice relaxation times[1,2] of potassium-ammonia and -deutero-ammonia solutions have yielded data which, when considered with other available information on the solutions, may allow a rather detailed specification of a microscopic model for these systems. Previous considerations of paramagnetic relaxation of electrons in metal-ammonia solutions have been given by Kaplan and Kittel[3] using the cavity model[3] for the solutions. These authors considered the width of the electron paramagnetic resonance line to be caused by motional narrowing[4] of the hyperfine interaction of an electron spin with protons of ammonia molecules.

The more recent experimental data[1b,2] show that (a) N nuclei[1,4] in Na-NH_3 solutions exhibit a considerable Knight shift, which was not observed for protons[1b]; (b) at equal extents of molecular motion, the transverse relaxation times T_2 of electrons in K-NH_3 and K-ND_3 solutions are equal within 10%[2]; and T_2 is equal to T_1 in concentrated K-NH_3 and K-ND_3 solutions.[1f,2]

Kubo and Tomita[5a] have developed a general quantum mechanical formalism for the computation of relaxation times. This formalism has been applied to a number of situations by Kivelson,[5b] and for details of the method of calculation of relaxation times the reader may consult references 5.

II. HYPERFINE INTERACTION

For the present, a single electron spin interacting with a "lattice" of nuclear spins of a single kind is considered. The unperturbed Hamiltonian is

$$\mathcal{H}_0 = -\hbar\omega_z{}^e S_z - \hbar\omega_z{}^n \sum_j I_{jz} + \mathcal{H}_2, \tag{1}$$

where $\omega_z{}^e$ and $\omega_z{}^n$ are the Larmor precession frequencies of the electron and nuclear spins in the applied magnetic field, S_z is the z component of the electron spin operator, I_{jz} is the z component of the spin of nucleus j and $\mathcal{H}_2$ is the Hamiltonian of the "lattice" or liquid ammonia solvent and metal ions. The perturbation Hamiltonian is the "contact" hyperfine interaction,[6] that is,

$$\mathcal{H}' = \sum_j A_j \mathbf{S}\cdot\mathbf{I}_j \tag{2}$$

where the sum extends over all nuclei in the liquid.

One may proceed to evaluate the correlation function $G(t)$ of the transverse electron spin magnetizations to various orders of perturbation theory developed in reference 5a. In zero order one obtains the imaginary part of the susceptibility for the electron as follows.

$$\chi_e''(\omega) = \frac{\pi\omega\hbar^2\gamma_e{}^2 S(S+1)\delta(\omega\pm\omega_z{}^e)}{6kT}, \tag{3}$$

where γ_e is the electron gyromagnetic ratio. The first order component of $G(t)$ is zero and the second-order component yields the secular (T_2') and nonsecular (T_1') transverse electron relaxation times.

$$1/T_2' = \sigma^2\tau, \qquad 1/T_1' = \sigma^2\tau', \tag{4}$$

where τ and τ' are relaxation times characteristic of

* Based on work performed under the auspices of the U.S. Atomic Energy Commission.

[1] (a) C. A. Hutchison and R. C. Pastor, Phys. Rev. **81,** 282 (1951); J. Chem. Phys. **21,** 1959 (1953); (b) H. M. McConnell and C. H. Holm, *ibid.* **26,** 1517 (1957): (c) R. T. Carver and C. P. Slichter, Phys. Rev. **102,** 975 (1956); (d) R. J. Blume, *ibid.* **109,** 1867 (1958); (e) V. L. Pollak and R. E. Norberg, Bull. Am. Phys. Soc. **1,** 397 (1956); (f) V. L. Pollak, J. Chem. Phys. **34,** 864 (1961).

[2] (a) C. A. Hutchison, Jr., and D. E. O'Reilly, J. Chem. Phys. **34,** 1279 (1961); (b) D. E. O'Reilly, Ph.D. thesis, University of Chicago (1955).

[3] J. Kaplan and C. Kittel, J. Chem. Phys. **21,** 1429 (1953).

[4] (a) N. Bloembergen, E. M. Purcell and R. V. Pound, Phys. Rev. **73,** 679 (1948); (b) P. W. Anderson and P. R. Weiss, Revs. Modern Phys. **25,** 269 (1953); (c) D. Pines and C. P. Slichter, Phys. Rev. **100,** 1014 (1955).

[5] (a) R. Kubo and K. Tomita, J. Phys. Soc. Japan **9,** 888 (1954); (b) D. Kivelson, J. Chem. Phys. **27,** 1087 (1957); **33,** 1094 (1960).

[6] E. Fermi and E. Segre, Z. Physik **82,** 729 (1933).

the "lattice" which are derived from the time correlation function of the hyperfine interaction $f(\tau)$.

$$\tau = Re\int_0^\infty f(\tau)d\tau = a(0),$$

$$\tau' = Re\int_0^\infty \exp[-i(\omega_z^e-\omega_z^n)\tau]f(\tau)d\tau = a(\omega_z^e-\omega_z^n), \quad (5)$$

where $a(\omega)$ is the frequency Fourier transformation amplitude of $f(\tau)$ and

$$f(\tau) = \sum_j A_j(\tau)A_j(0)/\sum_j A_j^2, \quad (6)$$

$$\sigma^2 = [I(I+1)/3\hbar^2]\sum_j A_j^2. \quad (7)$$

The quantity σ^2 is equal to $\frac{1}{2}$ of the mean-square width of the electron absorption spectrum in the "rigid lattice" limit. This may be readily seen by evaluation of the mean-square width by means of the procedure of Waller and Van Vleck.[7]

The Hamiltonian of interest is

$$\mathcal{H} = g\beta\mathbf{H}\cdot\mathbf{S} + \sum_j A_j\mathbf{I}_j\cdot\mathbf{S}.$$

As shown by Van Vleck, the mean-square absorption frequency $\langle\omega^2\rangle_{Av}$ is

$$\langle\omega^2\rangle_{Av} = Tr\,|\,[\mathcal{H}, S_x]\,|^2/\hbar^2 Tr(S_x)^2. \quad (8)$$

Similarly the mean absorption frequency is given by

$$\langle\omega\rangle_{Av} = Tr([\mathcal{H}, S^+]S^-)/\hbar Tr(S^+S^-). \quad (9)$$

Evaluation of Eqs. (8) and (9) yields

$$\langle\omega^2\rangle_{Av} = (1/\hbar^2)(G^2+\tfrac{2}{3}I(I+1)\sum_j A_j^2),$$

where $G = g\beta H$.
Similarly

$$\langle\omega\rangle_{Av} = G/\hbar,$$

and thus

$$\langle(\Delta\omega)^2\rangle_{Av} = \langle(\omega-G/\hbar)^2\rangle_{Av} = (2/3\hbar^2)I(I+1)\sum_j A_j^2. \quad (10)$$

Equation (10) is valid for all values of the relative strength of the Zeeman and hyperfine interactions. This expression is larger by a factor of two than the mean-square width quoted previously by Kip *et al.*[8] In the derivation given in reference 8, first-order perturbation theory was used along with selection rule $\Delta m_I = 0$, $\Delta m_S = \pm 1$, and hence the contribution of the nuclear absorption line at ω_z^n produced by S_x to the mean-square width is not included in the expression for $\langle(\Delta\omega)^2\rangle_{Av}$ given in reference 8.

[7] (a) I. Waller, Z. Physik **79,** 380 (1932); (b) J. H. Van Vleck, Phys. Rev. **74,** 1168 (1948).
[8] A. F. Kip, C. Kittel, R. A. Levy, and A. M. Portis, Phys. Rev. **91,** 1066 (1953).

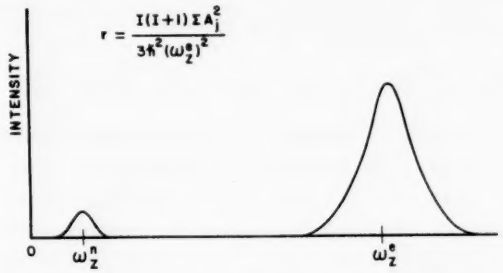

FIG. 1. Radio-frequency transitions produced by S_x in the presence of electron-nuclear hyperfine interaction. The intensity ratio of the absorptions shown is given by r in the rigid lattice and for $[(\Delta\omega)^2]_{Av}^{\frac{1}{2}} \ll \omega_z^e$.

This situation is schematically illustrated in Fig. 1, wherein an absorption line at ω_z^n is produced by S_x in a rf field applied perpendicularly to the static magnetic field. This effect is due to mixing of states $|\,m_S m_I\,\rangle$ with states $|\,m_S\pm 1, m_I\pm 1\,\rangle$, so that by first-order radiation theory, transitions occur with $m_S = 0$, $m_I = \pm 1$ and the intensity ratio r to the main line is as shown in Fig. 1. This resonance increases the second moment by a factor of two over that calculated by retaining only the I_zS_z terms in the hyperfine interaction. Also, a shift of the unperturbed resonance line at ω_z^e to higher frequency occurs due to the appearance of the absorption at ω_z^n, since $\langle\omega\rangle_{Av} = \omega_z^e$ with and without hyperfine interaction. The total transverse electron relaxation is

$$1/T_2 = 1/T_2' + 1/T_1' = \sigma^2(\tau+\tau'). \quad (11)$$

The electron spin-lattice relaxation time is readily evaluated from the formalism of reference 5(a) to be

$$1/T_1 = \sigma^2(\tau_+' + \tau_-'), \quad (12)$$

where

$$\tau_\pm' = \int \exp[\pm i(\omega_z^e-\omega_z^n)\tau]f(\tau)d\tau.$$

It is of interest to note that in the case of extreme narrowing, i.e., when the average frequency ω_c of the fluctuations of the hyperfine interaction Hamiltonian caused by molecular motion greatly exceeds the resonance frequency ($\omega_c \gg \omega_0$) then

$$1/T_2 = 2\sigma^2\tau_c$$

and

$$T_1 = T_2,$$

since $\tau = \tau' = \tau_c$; therefore, the linewidth is twice the linewidth due to the secular part of T_2.[9] This result for the hyperfine interaction differs from the corresponding relationship[5] for the dipolar interaction between

[9] This same result has been arrived at independently by G. E. Pake, Bull. Am. Phys. Soc. **5,** 252 (1960).

TABLE I. Comparison of computed T_2 values due to dipolar interaction and observed T_2 values (K—NH_3).

$T=240°K$ M, mole liter^{-1}	μ (cm^2 volt^{-1} sec^{-1})[a]	N_e (cm^{-3})[b]	$(T_2)_d$, μ sec	$(T_2)_{obs}$ μ sec[b]
0.02	4.4×10^{-3}	3.7×10^{18}	12.9	1.07
0.50	1.1×10^{-2}	1.5×10^{19}	8.0	1.06
0.80	2.1×10^{-2}	2.1×10^{19}	10.9	0.3[c]

[a] See reference 12(a).
[b] See reference 2.
[c] Extrapolated value, reference 2.

like spins, in which case the linewidth is $\frac{1}{3}$ the linewidth due to the secular interaction.

Another property of $f(\tau)$ is that $a(0)\geq a(\omega)$ since $T_1\geq T_2$.

A frequently used[4a,10] expression for $f(\tau)$ to represent the motion of particles under the influence of Brownian forces is the exponential relaxation function

$$f(\tau)=\exp(-|\tau|/\tau_c).$$

This function is the correlation function for the decay of a quantity which has constant probability per unit time of changing value from unity to zero. With the exponential relaxation function[5]

$$1/T_1=2\sigma^2\tau_c/(1+\omega_0^2\tau_c^2),$$
$$1/T_2=\sigma^2\tau_c+\sigma^2\tau_c/(1+\omega_0^2\tau_c^2). \quad (13)$$

III. DIPOLAR AND EXCHANGE INTERACTIONS

Relaxation times resulting from the dipolar interaction between electron spins may be evaluated by way of the Kubo-Tomita theory as illustrated in reference 5. Kaplan and Kittel[3] consider the dipolar interaction between rapidly diffusing electron spins to be the source of the electron resonance linewidth in relatively concentrated ($0.5M$) metal-ammonia solutions. Quantitative expressions for relaxation times resulting from this mechanism have been derived[4a,11] and are as follows:

$$(1/T_1)_d=0.88(1/T_2)_d=3\pi\gamma_e^4\hbar^2N_e/20aD, \quad (14)$$

where $(a^2/D)^2\omega_0^2\ll1$, N_e is the number of unpaired electrons per unit volume, $2a$ is the distance of closest approach of spins, and D is the translational diffusion coefficient of spins. From the measured conductivity[12] of the solutions, D may be estimated by the Einstein relation

$$D=\mu kT/e, \quad (15)$$

where μ is the mobility of the electrons. For both the cavity[3] and monomer[13] models for the unpaired electrons of alkali metal-ammonia solutions, the effective radius of the species is about 3A. For distances of approach of two unpaired electron species less than 6A, therefore, the electronic exchange interaction will dominate resulting in pairing of electrons or a strong repulsion, depending on whether the electron spins are antiparallel or parallel, respectively. Relaxation times computed from Eq. (19) with $2a=6$A are given in Table I and compared with observed values for several different concentrations. It appears rather unlikely that the dipolar interaction can account for linewidths in dilute solutions or the considerably shorter values of T_2 observed for more concentrated solutions. In addition, this mechanism cannot account for the temperature dependence of relaxation times[2a] in concentrated alkali metal-ammonia solutions.

Relaxation via dipolar interaction with protons is not considered in view of the experimental results of reference 2(a).

For the electron exchange interaction, $\mathcal{H}'$ is of the following form

$$\mathcal{H}'=\sum_{i<j}J_{ij}\mathbf{S}_i\cdot\mathbf{S}_j. \quad (16)$$

J_{ij} is the (isotropic) exchange coupling constant between spins i and j. An interaction of the form of Eq. (16) cannot cause spin-lattice relaxation since it commutes with the Zeeman energy and hence cannot alter the expectation value of this energy. As was shown by Van Vleck,[7b] the exchange interaction does not alter the second moment of dipolar-broadened resonance. A somewhat analogous result is valid for the present considerations: $\mathcal{H}'$ given by Eq. (16) commutes with S^+ and S^- and up to and including second order in the perturbation theory of reference 5 does not contribute to $G(t)$, where the perturbing Hamiltonian is the sum of Eqs. (2) and (16). In addition, the exchange interaction does not appear to cause an observable effect on the linewidth of metal-ammonia solutions for the following reasons: (a) Over the concentration range of interest the "unpaired spin volume" is greater than 4×10^3A^3 and hence the "rigid lattice" width would not be expected to be appreciably affected by exchange. Thus one would not expect appreciable exchange *narrowing* of the solution resonance to occur; (b) Since $T_1=T_2$ in concentrated solutions,[2] there is negligible *broadening* of the resonance in these solutions due to "collisions" of unpaired spins resulting in an interruption of the Larmor frequency due to mutual spin precession. Hence, it is unlikely that there is appreciable broadening due to the influence of the exchange interaction during collisions at lower concentrations, since collisions of unpaired spins are less frequent at lower spin concentration.

[10] (a) S. Chandrasekar, Revs. Modern Phys. **15,** 1 (1943); (b) M. C. Wang and G. E. Uhlenbeck, Revs. Modern Phys. **17,** 323 (1945).
[11] D. F. Holcomb and R. E. Norberg, Phys. Rev. **98,** 1074 (1955).
[12] (a) C. A. Kraus, J. Am. Chem. Soc. **36,** 864 (1914); *ibid.* **43,** 749 (1921); C. A. Kraus and W. W. Lucasse, *ibid.* **43,** 2529 (1921); **45,** 2551 (1923); (c) G. E. Gibson and T. E. Phipps, *ibid.* **48,** 312 (1926); (d) C. A. Kraus and W. W. Lucasse, *ibid.* **44,** 1941 (1922).
[13] E. Becker, R. H. Lindquist, and B. J. Alder, J. Chem. Phys. **25,** 971 (1956).

IV. DILUTE SOLUTIONS

There are several mechanisms to be considered for electronic relaxation in dilute alkali metal-ammonia solutions. These are listed as follows: (a) spin-orbit coupling to solvent molecules and metal ions (Sec. V); (b) hyperfine coupling with protons[3] (Sec. II); (c) hyperfine coupling with N^{14} nuclei (Sec. II); (d) anisotropy of g-factor[14]; (e) dipolar interaction with protons.

As shown in references 2, T_2 in dilute solutions increases with temperature as $T\eta^{-1}$. This fact, in addition to those listed in Sec. I, allows one to eliminate from consideration mechanisms involving interactions (*a*) (*b*), and (*e*). Interaction (*a*) would lead to a decrease of T_2 with increase in temperature while mechanisms (*b*) and (*e*) are inconsistent with data for K-ND_3 solutions. Interaction (*d*) simply cannot account for the observed relaxation times assuming upper limits for the anisotropy of g based on observed resonance spectra of frozen metal-ammonia solutions.[15] From considerations of this kind, interaction (*c*) appears to be quite favorable to explain the relaxation behavior of dilute solutions, especially in view of the large N^{14} Knight shift observed for Na-NH_3 solutions.[1b] Pursuing this conjecture further, the quantities A_j of Eq. (6) will decay in time as $\exp(-\tau/\tau_0)$ as inferred from the electrical conductivity of dilute solutions discussed in Sec. VI. The quantity τ_0 is approximately equal to the Debye rotational relaxation time

$$\tau_D=\eta V_0/kTN_{Av}, \tag{17}$$

where V_0 is the molar volume and N_{Av} is the Avogadro number. Using Eqs. (13) one finds

$$T_1^{-1}=T_2^{-1}\approx 2\sigma_S^2\tau_D \tag{18}$$

for $\omega_0\ll\tau_D^{-1}$. τ_D decreases and hence T_2 and T_1 increase with temperature as $T\eta^{-1}$ in agreement with experiment. Calculating τ_D from Eq. (17) using density[16] and viscosity data[17] previously obtained, and inserting this value into Eq. (18) yields from T_2 data[2] at $0.02M$

$$\sigma_S^2\approx 1.3\times 10^{17}\ \text{rad}^2\ \text{sec}^{-2}.$$

The value of σ_S^2 is related to the unpaired electron density at N^{14} since A_j of Eq. (5) is as follows[6]:

$$A_j=-\tfrac{1}{3}(16\pi)(\beta\mu_N/I_N)\,|\Psi(j)|^2, \tag{19}$$

where β is the Bohr magneton, μ_N and I_N are the magnetic moment and spin of N^{14}, and $|\Psi(j)|^2$ is the value of the unpaired electron density at nucleus j.

From Eqs. (19) and (10) one obtains

$$\sigma^2=\frac{256\pi^2}{27\hbar^2}\left(\frac{I_N+1}{I_N}\right)\beta^2\mu_N^2\sum_j|\Psi(j)|^4. \tag{20}$$

With $I_N=1$, $\mu_N=2.038\times10^{-24}$ erg gauss^{-1}, one obtains

$$\sum_j|\Psi(j)|^4=2.2\times10^{48}\ \text{cm}^{-6}.$$

The N^{14} density at an unpaired electron has been obtained by McConnell and Holm[1b] from the observed Knight shift of N^{14}. These authors find the total N^{14} spin density at an unpaired electron to be

$$\sum_j|\Psi(j)|^2=4.5\times10^{24}\ \text{cm}^{-3},$$

independent of metal concentration. It is possible to relate the value of $\sum_j|\Psi(j)|^2$ to the value of $\sum_j|\Psi(j)|^4$ derived above if the spatial dependence of the unpaired electron is known.

For this purpose it is assumed that the unpaired electrons are bound to some sort of attractive center, such as a cavity or positive ion in the solvent. The exact form of the potential of this center is not important for the present considerations, and a spherically symmetric square well potential is employed. Outside of such a potential well the electron wave function has the following form[18]:

$$\Psi=Ce^{-\beta r}, \tag{21}$$

where

$$\beta=(2m|E|/\hbar^2)^{\frac{1}{2}}.$$

E is the energy of the electron relative to the top of the well and C is a constant. The ratio R of the square of the total of the electron density at N^{14} nuclei to the total of the squares of the electron density at N^{14} nuclei, i.e.,

$$R=\frac{(\sum|\Psi(j)|^2)^2}{\sum|\Psi(j)|^4}\approx\frac{(\int\Psi^2d\tau)^2}{V_0\int\Psi^4d\tau} \tag{22}$$

may be well approximated as shown in Eq. (22) where V_0 is the molecular volume for liquid ammonia.

If $\beta^{-1}\gg a$, the effective radius of the square well potential, evaluation of Eq. (22) yields

$$R=8\pi/V_0\beta^3.$$

From the values of $\sum|\Psi(j)|^2$ and $\sum|\Psi(j)|^4$ given above, $R=9.2$ and hence $\beta=3.9\times10^7$, $E=0.61$ ev, and $\langle r\rangle_{Av}=3.9$ A using $V_0^{-1}=2.3\times10^{22}$ cm^{-3} as obtained from density data.[18] Exact evaluation of the integrals of Eq. (22) with $a=3$A yields $\beta=6.2\times10^7$ cm^{-1}, $|E|=1.5$ ev, and $\langle r\rangle_{Av}=2.4$ A. These values of β, $|E|$, and $\langle r\rangle_{Av}$ are quite reasonable when considered

[14] H. M. McConnell, J. Chem. Phys. **25,** 709 (1956).
[15] H. C. Clark, A. Horsfield, and M. C. R. Symons, J. Chem. Soc. **1959,** 2478.
[16] C. A. Hutchison, Jr., and D. E. O'Reilly, J. Chem. Phys. **34,** 163 (1961).
[17] C. A. Hutchison, Jr., and D. E. O'Reilly (to be published).
[18] L. I. Schiff, *Quantum Mechanics* (McGraw-Hill Book Company, Inc., New York, 1949).

for the cavity[3] or monomer[12] model for the solutions. For the cavity model, the radius $a=3$A corresponds to a volume which can be filled by 2–3 NH_3 molecules. Such a cavity would have 10–20 ammonia molecules on the periphery. If N^{14} nuclei of these molecules are equally coupled to the unpaired electron and there is negligible electron density at N^{14} nuclei in the second coordination shell of molecules, then

$$R=N_1=9,$$

where N_1 is the number of molecules in the first coordination shell in fair agreement with the above estimate from the cavity model. The value of $|E|$ derived above is comparable to the energy of the observed peak at 1.5 micron ($0.8\frac{1}{2}$ev) in the infrared spectrum of dilute solutions.[19]

Since only a relatively small electron density is present at protons, the wave function cannot be of the exact form of Eq. (21) but must rather be somewhat as follows:

$$\Psi\sim c'e^{-\beta r}\sin\langle k\rangle(r-a'), \tag{23}$$

for $r>a$, where $\langle k\rangle\simeq\pi/2r_0$, r_0 is the average molecular radius of the ammonia molecule in the liquid phase and a' is a constant chosen so that Eq. (23) has a node in the vicinity of protons which may be considered to result from an orthogonalization procedure. The form of this wave function is also justified if the unpaired electron wave function is considered to be a linear combination of wave functions of the type suggested by Pitzer.[20]

In more concentrated, but still quite dilute, solutions of K in NH_3 and ND_3 cw measurements[2] of T_1 at 7 Mc indicate T_1 to be as large as $2T_2$. However, more recent spin-echo measurements of Pollak[1f] at 31 Mc indicate $T_1=T_2$ at all concentrations. In view of this difference, a discussion of the significance of the $T_1\neq T_2$ results will not be in order until further experimental results on T_1 are available. It will suffice to say, such a difference in T_1 and T_2 may possibly be accounted for in terms of interactions of the unpaired electron with the metal ions.

V. CONCENTRATED SOLUTIONS

There are several mechanisms to be considered for electron paramagnetic relaxation in concentrated metal-ammonia solutions. These are as follows: (a) dipolar interaction between electron spins (Sec. III); (b) exchange interaction (Sec. III); (c) spin-orbit coupling.

For the reasons given in Sec. III, mechanisms via interactions (a) and (b) are not considered to be important. In the mechanism via interaction (c), the electric perturbation is considered to arise from the interaction of a bound, unpaired electron with positive ions and other negative species in solution.

Kronig[21] proposed a mechanism for spin-lattice relaxation of electrons by way of spin-orbit coupling to the "lattice." Spin flips are produced by molecular motions which cause excitation of the electron in a bound state to excited orbital states. In metal-ammonia solutions these states may consist of a discrete set of bound orbital states or a continuous set of quasi-bound or virtual states, which have nonzero angular momentum and a relatively large probability density in the spatial vicinity of the electron in the ground state. Under the action of an electric perturbation, such as the collision of an unpaired electron with a positive ion, there is a finite probability of a spin flip due to mixing of excited orbital states with definite spin orientation into the orbital ground state of opposite spin orientation through the $\lambda\mathbf{L}\cdot\mathbf{S}$ interaction. The extent of this mixing is of the order of λ/Δ, where Δ is the energy difference between the excited state and ground state. Lloyd and Pake[22] have given the following expression for T_1 produced by this mechanism through a single orbital excited state:

$$T_1=T_2\simeq(\Delta^4/\lambda^2\bar{\delta}^2)\tau_c. \tag{24}$$

where τ_c is the correlation time of the perturbation which is considered to be a random variable and

$$\bar{\delta}^2=\langle\,|\int\Psi f(\mathbf{r})\Psi d\tau-\int\phi f(\mathbf{r})\phi d\tau\,|^2\rangle_{Av}; \tag{25}$$

$f(\mathbf{r})$ is the operator representing the electric perturbation, Ψ and ϕ are the ground and excited orbital state wave functions, respectively. $\bar{\delta}^2$ is the mean square of the deviation of Δ produced by $f(\mathbf{r})$. Also, it follows from the above model, that $\Delta g=\lambda/\Delta$ where Δg is the deviation of the electron g factor from the free electron value.

As discussed in Sec. VI, the mobility μ of electrons in concentrated ($>0.3M$) solutions is given by the following expression:

$$\mu=\Lambda/F=n\langle r^2\rangle_{Av}e/6kT, \tag{26}$$

where n is the mean number of displacements or jumps of the electron per unit time, $\langle r^2\rangle_{Av}$ is the mean displacement per jump, Λ is equivalent conductivity, and F is the Faraday. So as to account for the mobility of the electron at infinite dilution, $\langle r^2\rangle_{Av}\simeq V_0^{\frac{2}{3}}=1\times10^{-15}$ cm^2, as shown in Sec. VI. Consideration of the conduction process in concentrated solutions indicates that the equivalent conductivity of an unpaired electron is approximately equal to Λ/α where Λ is the observed equivalent conductivity and α is the fraction of the electrons that are unpaired. The large conductivity is considered to be due to excitation of the unpaired

[19] W. L. Jolly, Progr. in Inorg. Chem. **1**, 235 (1960).
[20] K. S. Pitzer, J. Chem. Phys. **29**, 453 (1958).
[21] R. de L. Kronig, Physica **6**, 33 (1939).
[22] J. P. Lloyd and G. E. Pake, Phys. Rev. **94**, 579 (1954).

electron by the diffusive motions of other species in solution. Hence, a correlation time is obtained by rearrangement of Eq. (26), i.e.,

$$n^{-1}=\tau_c=eF\langle r^2\rangle_{Av}/6kT(\Lambda/\alpha), \tag{27}$$

where Λ/α has been substituted for Λ in Eq. (26). τ_c is the correlation time of the fluctuating electric fields at an unpaired electron. At 0.6M and 298°K for K-NH_3, $\tau_c=1.7\times10^{-14}$ sec.

According to the modified Debye-Hückel theory[23] of ionic solutions, the mean potential V at an ion due to the "ionic atmosphere" made up of other ions in solution is as follows:

$$V=(e\kappa/\mathfrak{D})(1+\kappa a)^{-1}, \tag{28}$$

where κ^{-1} is the mean radius of the ionic atmosphere and is defined by the relation

$$\kappa^2=(4\pi e^2/\mathfrak{D}kT)\sum m_i z_i^2;$$

a is a parameter to represent the distance of closest approach of ions, $\mathfrak{D}$ is the dielectric constant of the solvent, m_i is the concentration of ions of kind i, and z_i is the charge (in units of e) of ions of kind i. Although association of electrons and ions undoubtedly occurs in metal-ammonia solutions, there are several reasons to expect the Debye-Hückel theory to approximate the effect of electrostatic interactions in these solutions. The most important of these is as follows: if the solutions are considered to contain e^- and $e_2^{=}$ centers, these species have effective radii[18] of 3 and 4A, respectively; the Debye-Hückel theory is known to best represent solutions of large ions with high polarizability.[24] With this in mind, $\bar{\delta}$ is taken to be equal to eV [Eq. (46)] with κ given by

$$\kappa^2=4\pi(3-\alpha)ML,$$

where L is the "Debye length," $e^2/\mathfrak{D}kT$. At 0.6M and 240°K, $\bar{\delta}$ is computed to be 0.10 ev.

Placing $\lambda/\Delta=\Delta g$, and τ_c and σ as given by Eqs. (27) and (28) in Eq. (24), one obtains

$$T_1=\frac{F\Delta^2\langle r^2\rangle_{Av}\mathfrak{D}^2(1+\kappa a)^2}{6kT(\Delta g)^2(\Lambda/\alpha)e^3\kappa^2}. \tag{29}$$

The quantity Δ is equal to 0.8 ev as estimated from the infrared absorption of the solutions.[19] At $M=0.60$ mole liter^{-1} and −33.7°C, $\Lambda=1230$[12e] ohm^{-1} mole^{-1} cm^2, $\Delta g=10^{-3}$, $\alpha=0.045$, $a=5.0$Å and $\mathfrak{D}=23$. The quantity T_1 as calculated from Eq. (29) is 1.2×10^{-6} sec, the observed value[2] of T_1 is 0.88×10^{-6} sec. Although this agreement is probably somewhat fortuitous it is indicative of the nature of the relaxation process in concentrated solutions.

From Eq. (29) the temperature dependence of T_1 at constant M is as follows:

$$T_1\propto T^{-3}(\alpha/\Lambda), \tag{30}$$

since $\mathfrak{D}\propto T^{-1}$ between −33° and 25°C[25] and a, Δ, Δg, and $\langle r^2\rangle_{Av}$ are assumed to be independent of T. In addition, the variation of κ with temperature at constant M is neglected. At constant temperature, the dependence of T_1 on concentration is

$$T_1\propto M^{-1}[(1+\kappa a)^2/(3-\alpha)(\Lambda/\alpha)]. \tag{31}$$

The correspondence of the observed[2a] relaxation times to the relations given by Eqs. (30) and (31) is shown in Table II. Values of equivalent conductivity at 274° and 298°K have been calculated from the measured temperature coefficients[12b] assuming the temperature coefficient to be independent of temperature.[12e] The agreement between observed and calculated temperature and concentration dependence of T_1 values is considered good in view of the limitations of the model.

It must be noted that Eq. (29) would not be expected to apply at sufficiently low concentration so that Λ/α is not a good approximation to the equivalent conductivity of unpaired electrons. Furthermore, if associated

TABLE II. Comparison of temperature and concentration dependence of observed and calculated spin-lattice relaxation times in concentrated K—NH_3 solutions.

		$M=0.60$ mole liter^{-1}		
T, °K	α[a]	Λ[b]	$[T_1/T_1(240)]_{obs}$	$[T_1/T_1(240)]_{calc}$
240	0.045	1230	1.00	1.00
274	0.099	2870	0.55	0.63
298	0.143	5240	0.40	0.39
		$T=298$°K		
M mole liter^{-1}	α[a]	Λ[b]	$[T_1/T_1(0.60)]_{obs}$	$[T_1/T_1(0.60)]_{calc}$
0.60	0.143	5240	1.00	1.00
0.50	0.147	3500	1.34	1.61
0.40	0.151	2380	2.11	2.58
0.30	0.174	1940	3.54	3.98

[a] See reference 18.
[b] See references 12a, b, c; ohm^{-1}mole^{-1}cm^2.

[23] H. H. Harned and B. B. Owen, *Physical Chemistry of Electrolytic Solutions* (Reinhold Publishing Corporation, New York, 1958).

[24] The theory of Kaplan and Kittel (reference 3) may be improved by inclusion of the contributions of electrostatic interactions and entropy of charging to the expression for free energy given in reference 3. These quantities are conveniently expressed by the Debye-Hückel and Born theories respectively. The resulting expression for the equilibrium constant of the reaction $2e^- \rightleftharpoons e_2^{=}$ fits rf susceptibility of K-NH_3 solutions quite well (reference 2b) and yields a reasonable quantity for the number of "holes" in the solvent.

[25] H. M. Grubb, J. F. Chittum, and H. Hunt, J. Am. Chem. Soc. **58**, 776 (1935).

species are presumed to occur, such as the monomer, the above procedure must be modified to include the contribution of these species to Λ in concentrated solutions. At lower temperature (240°K) the influence of the hyperfine interaction on the observed relaxation times persists to considerably higher concentration than 298°K.

The relaxation times of concentrated K-ND_3 solutions are longer than those of K-NH_3 solutions of equal concentration and temperature.[2a] From Q-factor measurements, it was found[2b] that the conductivity of K-ND_3 solutions is about 20% less than that of K-NH_3 solutions of equal concentration ($>0.15M$) at 298°K. The electric dipole moment of ND_3 is reported[26] to be 2% greater than that of NH_3 and hence the dielectric constant of liquid ND_3 is expected to be somewhat larger than that of liquid NH_3 at equal temperature, consistent with the larger viscosity[17] and slightly larger molecular density[16] of liquid ND_3. It is reasonable to assume that Δ, $\langle r^2\rangle_{Av}$, a,[2b] and Δg are very nearly equal for NH_3 and ND_3 and hence one would expect from Eq. (29) that the relaxation times of concentrated K-ND_3 solutions would be longer than the corresponding K-NH_3 solutions in agreement with the data of reference 2a.

Comparison of the measured relaxation times of concentrated Na-NH_3 solutions[1d] with those of K-NH_3[2a] shows that at equal concentration and temperature K-NH_3 solutions have shorter relaxation times than Na-NH_3 solutions. This result is also consistent with Eq. (29) if the quantity (Λ/α) for K-NH_3 solutions is greater than that for the corresponding Na-NH_3 solutions.

At intermediate concentrations ($0.10<M<0.30$ at 298°K) relaxation is considered to take place via both hyperfine interaction with N^{14} nuclei and the spin-orbit interaction.

VI. MOTIONAL EFFECTS AND ELECTRICAL CONDUCTIVITY

Information on electronic motions in metal-ammonia solutions can be inferred from consideration of the electrical conduction properties of the solutions. For very dilute solutions ($<0.001M$) of alkali metals in liquid ammonia, the equivalent conductivity Λ of the "anion"[12a] is 900 ohm^{-1} $mole^{-1}$ cm^2 at 240°K. Equating the expression for the diffusion coefficient of a particle undergoing random flights[10] and that given by Eq. (15) one obtains

$$\mu(kT/e)=\tfrac{1}{6}(n\langle r^2\rangle_{Av}), \tag{32}$$

where n is the mean number of displacements or jumps of the particle per second and $\langle r^2\rangle_{Av}$ is the mean square displacement per jump. Placing

$$\mu=\Lambda/F,$$

where F is the Faraday, from Eq. (26) one obtains

$$n\langle r^2\rangle_{Av}=1.2\times10^{-3}\ cm^2\ sec^{-1}.$$

Taking $\langle r^2\rangle_{Av}=V_0^{\frac{2}{3}}$, then $n=1\times10^{12}\ sec^{-1}$.

According to the hole theory of liquids, the jump frequency n_1, associated with viscous flow is as follows:

$$n_1=kT/h\exp(-\Delta F_{vis}/RT)=\tau_D^{-1}.$$

At 240°K for liquid NH_3, $\Delta F_{vis}=1.320$ kcal $mole^{-1}$ [17] and $n_1=3\times10^{11}\ sec^{-1}$. This jump frequency is of the order of that found to be greater than necessary to account for the equivalent conductivity of the electron in very dilute solutions. Substituting n_1 in Eq. (26) for n, one obtains

$$\Lambda=[eF(V_0)^{\frac{1}{3}}/6h]\exp(-\Delta F_{vis}/RT)$$

so that

$$\frac{d\Lambda}{\Lambda dT}=\frac{\Delta F_{vis}}{RT^2}-\frac{2}{3}\frac{d\rho}{\rho dT}=1.3\times10^{-2}/°K \tag{33}$$

at 240°K, Kraus[12] finds a temperature coefficient of conductivity equal to 1.9×10^{-2}°K^{-1}, approximately independent of temperature, for very dilute solutions. For more concentrated solutions[12b] ($0.1M$), the coefficient is 1.4×10^{-2}°K^{-1} independent of concentration up to about $0.3M$ at 240°K. For these reasons τ_e was chosen to be qual to τ_D in the discussion of paramagnetic relaxation in Sec. IV.

At 240°K, Kraus[12] found that the equivalent conductivity first decreases with increase in concentration to about $0.05M$, then increases with further increase in concentration to considerably larger values than in the infinitely dilute solution. It is possible[27] to interpret the decrease in equivalent conductivity as predominantly due to pairing of electrons, the paired species having an equivalent conductivity much less than that of the unpaired electron. In more concentrated solutions ($>0.3M$) the equivalent conductivity increases with temperature in proportion to the number of unpaired electrons as shown by data given in Table II. Since the paired electron species is energetically more stable than the unpaired electron species, the high equivalent conductivity would appear to be due almost exclusively to the unpaired electron. The equivalent conductivity of an unpaired electron is hence given by Λ/α as assumed in Sec. V. The high equivalent conductivity is evidently due to fluctuating, coulombic perturbations by other ions in the solution rather than by the solvent as for more dilute solutions. The correlation time of these perturbations may thus be computed from Eq. (32) with $\langle r^2\rangle_{Av}$ equal approximately to $V_0^{\frac{2}{3}}$. τ_e computed in this way is of the same order of magnitude as the theoretical ionic collision frequency calculated according to formulae given by Debye[28a] and Montroll[28b].

[26] J. M. A. de Bruyne and C. P. Smythe, J. Am. Chem. Soc. **57,** 1203 (1934).

[27] (a) G. Candela, thesis, Boston University, Massachusetts (1952); (b) J. L. Dye, R. F. Sankuer, and G. E. Smith, J. Am. Chem. Soc. **82,** 4797 (1960).

[28] (a) P. Debye, Trans. Electrochem. Soc. **82,** 265 (1942); (b) E. Montroll, J. Chem. Phys. **14,** 202 (1946).

THE JOURNAL OF CHEMICAL PHYSICS VOLUME 35, NUMBER 5 NOVEMBER, 1961

The Polyhedral Clathrate Hydrates, Part 2. Structure of the Hydrate of Tetra *Iso*-Amyl Ammonium Fluoride*

D. FEIL† AND G. A. JEFFREY

The Crystallography Laboratory, The University of Pittsburgh, Pittsburgh 13, Pennsylvania

(Received April 13, 1961)

The hydrate $[i-C_5H_{11}]_4N^+ \cdot F^- \cdot 38H_2O$ belongs to a type of polyhedral clathrate structure in which the water molecules and the anions form the "host" structure and the cations are the "guests". The structural unit of the hydrogen-bonded clathrate cage is the $H_{40}O_{20}$ pentagonal dodecahedron. These dodecahedra are regularly associated in the crystal lattice by sharing faces, giving rise, therefore, to other polyhedra. In this hydrate, the other polyhedra are the tetrakaidecahedron and pentakaidecahedron, which form the cages enclosing the cations. A detailed three-dimensional single crystal structure analysis has been completed.

INTRODUCTION

THE pentagonal dodecahedron of water structure, $H_{40}O_{20}$, is known to exist in the crystalline gas hydrates from the work of Claussen,[1] von Stackelberg and Muller,[2] and Pauling and Marsh.[3] It has also been proposed as a structural unit in liquid water by Pauling.[4]

The x-ray stoichiometric investigation by McMullan and Jeffrey[5] of some alkyl ammonium salt hydrates, some of which were originally prepared by Fowler, Loebenstein, Pall and Kraus,[6] showed that these compounds have characteristics similar to those of the gas hydrates and might be structurally related to them. The work described in this paper is concerned with one of these compounds, $[i-C_5H_{11}]_4N^+F^- \cdot 38H_2O$, which has been found, in fact, to have a crystal structure based on an arrangement of pentagonal dodecahedra.

THE CRYSTAL DATA

The tetra *iso*-amyl ammonium fluoride hydrate crystals were prepared as described in the first paper.[5] They were deposited from aqueous solutions at room temperature as well-formed orthorhombic prisms, mp 31°C. The unit cell dimensions at room temperature are $a=12.08\pm0.01$ A, $b=21.61\pm0.02$ A, $c=12.82\pm0.01$ A; the space group, from the extinctions (Okl) absent for k odd, is $Pb2_1m$, $Pbm2$, or $Pbmm$; the subsequent analysis established $Pbmm$ (No. 51). With two formula units in the cell, the calculated densities in gm/cc are 0.99 for $38H_2O$, 1.01 for $39H_2O$, and 1.03 for $40H_2O$. Although the density measured by flotation was 1.02 gm/cc, the subsequent analysis established the hydration number as 38. For the isomorphous chloride and bromide, the measured and calculated densities agreed within 1% for the 38 hydrate. Reproducible chemical analyses and density measurements were difficult to obtain on this class of compounds, particularly for the fluorides.

EXPERIMENTAL MEASUREMENTS

The unit cell dimensions were measured from equi-inclination Weissenberg photographs. The crystal densities were determined by flotation. The intensity measurements were made visually from CuK_α equi-inclination Weissenberg photographs with multiple Ilford Industrial G. films at room temperature. Three layers about $[a]$, thirteen about $[b]$, and five about $[c]$ were recorded. With exposures up to twenty hours, 1050 independent reflections were observed and 350 were unobserved within a reflecting sphere radius of $\sin\theta=0.75$ with CuK radiation. The intensities were corrected by an IBM 650 data reduction program and the amplitudes were correlated by scale factors deduced from reflections common to various layers. No corrections were made for absorption errors. From the dimensions of the crystal these were estimated to be less than 5% in the intensities.

SOLUTION OF THE STRUCTURE

The key to the solution of the phase problem and at the same time the determination of the space group was provided by the three-dimensional Patterson synthesis, computed on an IBM 650.[7] The two most striking features of this synthesis was a peak at $(\frac{1}{2}, \frac{1}{2}, 0)$ three-quarters the height of the origin peak, and the tenfold axial symmetry in the a axis direction of the vector peaks close to the origin, shown in Figs. 1 and 2. The former indicated a pseudo C face-centered structure and the latter suggested the fivefold axial symmetry of the pentagonal dodecahedron as the basic unit of

* Part 1 of this series is a paper by R. McMullan and G. A. Jeffrey, J. Chem. Phys. **31,** 1231 (1959).

† Present address, Laboratory of Crystal Chemistry, University of Utrecht, Netherlands.

[1] W. F. Claussen, J. Chem. Phys. **19,** 259, 662, 1425 (1951).

[2] M. von Stackelberg and H. R. Muller, J. Chem. Phys. **19,** 1319 (1951).

[3] L. Pauling and R. E. Marsh, Proc. Natl. Acad. Sci. U. S. **38,** 112 (1952).

[4] L. Pauling, Trans. Internatl. Conf. on the Hydrogen Bond, Ljubljane (1957).

[5] R. C. McMullan and G. A. Jeffrey, J. Chem. Phys. **31,** 1231 (1959).

[6] Fowler, Loebenstein, Pall, and Kraus, J. Am. Chem. Soc. **62,** 1140 (1940).

[7] R. Shiono, University of Pittsburgh Computation and Data Processing Center, Tech. Rept. No. 2 (1957).

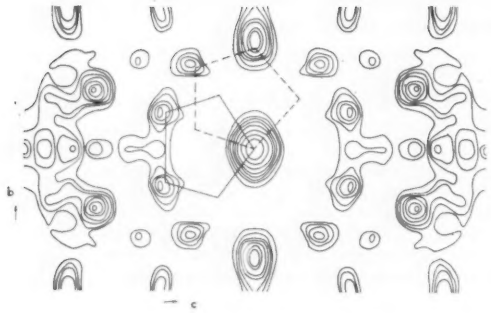

FIG. 1. Tetra *iso* amyl ammonium fluoride hydrate; Patterson synthesis at $x=\frac{1}{2}$, showing large peak at $(\frac{1}{2}, 0)$ in center and ten-fold symmetrical distribution of vector peaks.

structure. The pseudo C centering was, of course, apparent from the observation that the $(h+k)$ odd reflections were systematically much weaker than the even reflections. Placing pentagonal dodecahedra with edge lengths of 2.8 A in a C-centered array across the (001) face of the unit cell gave a periodicity consistent with the observed a and b axes and led to a trial model shown in Fig. 3. In this model the dodecahedra share faces to form columns in the [a] and [110] directions. Small deformations of the dodecahedra from the dimensions of the regular solid are necessary to achieve this type of packing. This model accounts for 60 of the 76 water oxygen atoms in the unit cell and adds a mirror plane perpendicular to the a axis to the space group *Pbmm* to give the centered symmetry *Cmmm*. Structure factor calculations based on this model gave an agreement index of 0.55 for the reflections with $(h+k)$ even and, of course, zero values for the $(h+k)$ odd reflections. Despite this rather discouraging start, successive three-dimensional Fourier synthesis, difference synthesis, and structure factor calculations with the 650 $(h+k)$ even reflections enabled atomic positions to be allocated for 20 more atoms. As shown later these included the nitrogen and fluorine atoms (which were indistinguishable from oxygen atoms at this stage). The agreement index was then 0.35 and the Fourier maps also began to show peaks which could be associated with the carbon atoms of the alkyl chains. Because of the omission of the $(h+k)$ odd terms, the number of carbon atom peaks was doubled, and the problem was to select the correct ones. At this stage it was necessary to determine the space group. Owing to the pseudo-symmetry, whereby three-quarters of the diffraction pattern was due to a C-centered arrangement of the water structure, this determination of the space group from the Patterson synthesis followed a procedure which, although similar in principle, was somewhat different in practice from the usual.

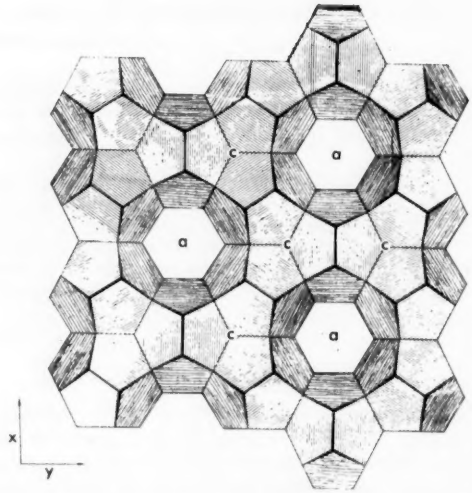

FIG. 3. Tetra *iso* amyl ammonium fluoride hydrate; Arrangement of pentagonal dodecahedra sharing faces 'two-dimensionally' on the (001) face.

In the $(h+k)$ even Patterson and Fourier syntheses there are mirror planes perpendicular to the principal axes, corresponding to the space group *Cmmm*. In the complete Fourier synthesis, one or two of these mirror planes must be removed, according to the space group, by the addition of the $(h+k)$ odd terms with their correct, but unknown, phases. A $(h+k)$ odd Fourier

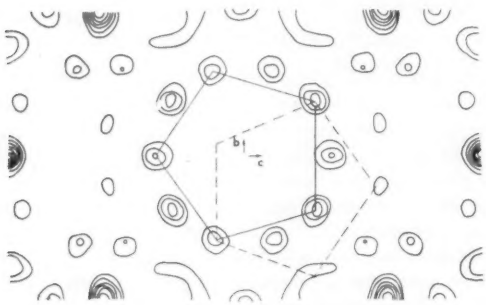

FIG. 2. Tetra *iso* amyl ammonium fluoride hydrate; Patterson synthesis at $x=0$, showing the ten-fold symmetrical distribution of atomic vector peaks around the origin, at center, with origin peak removed.

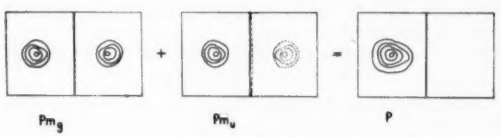

FIG. 4. The production of a Fourier peak, (P) by the combination of the 'even' mirror related peaks, (Pm_g), from the $(h+k)$ even terms with the 'odd' mirror related peaks, (Pm_u), from the $(h+k)$ odd terms; (full contours+*ve*, dotted contours−*ve*).

synthesis will therefore have either one or two "odd" mirror planes, m_u in Fig. 4, at (100), (100), and (010) or (100) and (001) according to whether the true space group is *Pbmm*, $Pb2_1m$, or $Pbm2_1$. The location and distinction of the "odd" and "even" mirror planes, m_u and m_g, in the $(h+k)$ odd Fourier syntheses can be made by examining the $(h+k)$ odd Patterson synthesis. A m_u plane in Fourier space results in a lower than average density along the axis perpendicular to m_u in Patterson space, while a m_g plane gives a higher than average density.

It was found that the average $(h+k)$ odd Patterson density along the a axis was negative while along the b and c axes it was positive, indicating the absence of a true mirror plane perpendicular to a and the presence of mirror planes perpendicular to b and c, and hence the space group *Pbmm*.

Four of the oxygen atoms were disordered by the pseudo mirror symmetry of the *Cmmm* structure and all the carbon atoms in the alkyl group were disordered by the true mirror planes perpendicular the b and c axes (see Fig. 5). It was not too difficult to distinguish the atoms belonging to the two mirror related hydrocarbon chains and to select one. Having made this arbitrary choice, the correct choice between the pairs of pseudo mirror related oxygen atoms had to be made. This was made somewhat difficult by the overlapping between real atoms and the mirror related images of real atoms. By examining carefully a $(h+k)$ odd Fourier synthesis for which the signs were calculated from the hydrocarbon chain atoms alone, it was possible to identify progressively the true oxygen positions, and reduce the R factor for this group of reflections from 0.5 to 0.3. The $(h+k)$ odd Fourier terms also distinguished between the N^+ and the F^-, by diminishing the former (from O to N) and augmenting the latter (from O to F). Thereafter three-dimensional Fourier difference syntheses with all terms were used for further adjustment of the atomic positions to give an overall R factor of 0.25. All the independent atoms, i.e., 38 oxygens, 1 nitrogen, 1 fluorine, and 20 carbon atoms were located, and with the exception of a few weak reflections the phase problem was solved.

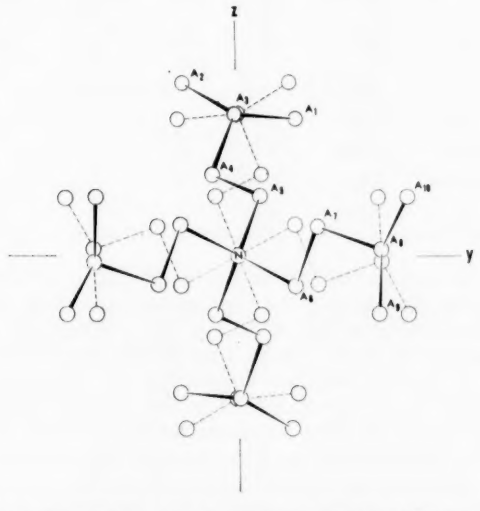

FIG. 5. Tetra *iso* amyl ammonium fluoride hydrate. The mirror plane related disorder of the *iso* amyl groups of the cations.

TABLE I. The effect of variation of weighting in the least-squares refinement on the parameters of the oxygen atoms in general positions.

Procedure (see text)		I	II	III	IV	V
Oxygen (1)	x	0562	0559	0570	0561	0563
	y	1400	1411	1402	1390	1396
	z	1737	1717	1724	1713	1725
	B	3.66	4.30	4.60	4.21	3.78
(2)	x	4433	4411	4410	4424	4412
	y	3572	3557	3566	3577	3572
	z	1778	1793	1795	1786	1794
	B	3.76	3.09	3.55	2.46	2.80
(3)	x	0627	0615	0624	0626	0624
	y	9448	9453	9446	9447	9445
	z	2995	2985	2989	2977	2982
	B	3.40	4.59	4.15	5.32	3.65
(4)	x	4423	4417	4424	4419	4425
	y	9429	9437	9430	9427	9431
	z	3027	3026	3030	3041	3028
	B	3.85	3.68	3.55	3.71	3.09
(5)	x	2532	2516	2520	2513	2517
	y	0838	0847	0841	0839	0841
	z	1099	1082	1083	1080	1086
	B	3.82	3.73	3.67	2.67	3.32
(6)	x	2539	2538	2543	2547	2543
	y	9647	9637	9648	9636	9636
	z	1780	1767	1778	1784	1782
	B	4.01	4.08	4.02	3.93	3.50

REFINEMENT OF THE STRUCTURE

The 76 oxygen atoms in the unit cell are at the following positions of the space group *Pbmm*

48 in the 8-fold (l); x, y, z, etc.,

12 in the 4-fold (i); $x, y, 0$, etc.,

8 in the 4-fold (k); $x, \frac{1}{4}, z$, etc.,

8 in the 4-fold (j); $x, y, \frac{1}{2}$, etc.

The two N^+ and two F^- are at the 2-fold (f), $x, \frac{1}{4}, \frac{1}{2}$, positions, and the 40 carbon atoms of the alkyl group are twofold disordered across the mirror planes and occupy 10 eightfold general positions. The number of variable positional parameters is therefore 64 and together with the 25 individual isotropic temperature factors, there are 89 variable parameters for an isotropic refinement, excluding scale factors.

These parameters were refined by the Busing and

TABLE II. Fractional atomic coordinates and isotropic temperature factors (key to atomic positions in Fig. 9).

Atom No.	O(1)	O(2)	O(3)	O(4)	O(5)	O(6)	O(7)	O(8)
x	0.0563	0.4412	0.0624	0.4425	0.2517	0.2543	0.0642	0.4514
y	0.1396	0.3571	0.9445	0.9431	0.0841	0.9636	0.8162	0.8147
z	0.1725	0.1794	0.2982	0.3028	0.1086	0.1782	0.0000	0.0000
B	3.78	2.80	3.65	3.09	3.32	3.50	3.41	3.60
	O(9)	O(10)	O(11)	O(12)	O(13)	N^+	F^-	
x	0.2588	0.1681	0.3901	0.1507	0.3894	0.0135	0.5128	
y	0.8900	0.2500	0.2500	0.9204	0.8885	0.2500	0.2500	
z	0.0000	0.2158	0.2926	0.5000	0.5000	0.5000	0.5000	
B	2.80	3.55	3.84	3.96	4.34	1.58	1.29	
	C_1^P	C_2^P	C_3^P	C_4^P	C_5^P			
x	0.0853	0.1642	0.1998	0.2626	0.2840			
y	0.1895	0.1744	0.1079	0.0744	0.1072			
z	0.4576	0.5408	0.5068	0.5949	0.4032			
B	1.12	2.46	5.83	6.22	6.03			
	C_1^T	C_2^T	C_3^T	C_4^T	C_5^T			
x	0.9396	0.8559	0.8014	0.7263	0.7203			
y	0.2739	0.2262	0.2606	0.1987	0.3095			
z	0.4063	0.3715	0.2681	0.2142	0.2757			
B	1.11	1.99	3.06	5.34	3.57			

Some typical standard deviations of these parameters

Atom	O(1)	O(7)	O(10)	N^+	F^-	C_1^P
s.d. x	0.0006	0.0009	0.0010	0.0014	0.0010	0.0017
s.d. y	0.0004	0.0005				0.0010
s.d. z	0.0007		0.0010			0.0015
s.d. B	0.25	0.34	0.35	0.41	0.31	0.52
	C_2^P	C_3^P	C_5^P	C_1^T	C_3^T	C_4^T
s.d. x	0.0020	0.0017	0.0035	0.0016	0.0014	0.0026
s.d. y	0.0012	0.0011	0.0024	0.0009	0.0015	0.0018
s.d. z	0.0019	0.0089	0.0035	0.0015	0.0015	0.0028
s.d. B	0.74	0.90	1.64	0.53	0.64	0.93

Levy full matrix least squares IBM 704 program.[8] By using a Hughes weighting scheme,[9] the refinement converged to negligible shifts after 4 cycles. A subsequent anisotropic cycle failed due to one of the temperature matrices not being positive-definite. It was concluded that the experimental data were insufficient to justify the anisotropic parameter computation and no further attempts were made.

[8] W. R. Busing and H. A. Levy, Oak Ridge National Laboratory, Central Files, Number 59-4-37.

[9] E. W. Hughes, J. Am. Chem. Soc. **63,** 1737 (1941).

In addition to the Hughes weighting, four other means of weighting the experimental data were explored. A comparison of the five sets of parameters so obtained is shown in Table I for the six oxygen atoms in the general positions. Column I is for the Hughes weighting. For Column II, an experimental error weighting was obtained by estimating the relative errors for each diffraction spot on a film from the reproducibility in estimating the same film many times. These errors were then used in averaging the intensities from multiple films and from different layer lines. Column

III parameters were obtained by using the intensities from the 13 *b* axis layers only and correlating the layers by using the scale factors as variables in the least squares computation. The weighting was as for II. Column IV parameters were obtained using the same procedure on the five *c* axis layer intensities.

For Column V, the reflexions used in III and IV were treated as independent observations, even if they had the same indices (as indeed they were). This required 18 variable scale factors, one for each Weissenberg layer. These varied from 0.33 to 0.39 and introduced corrections to the experimental interlayer scaling of up to 10%. The corresponding increase in the observational date (to 1295 reflections) more than compensated for this increase in variables and the standard deviations from the least-squares calculations were the lowest for this procedure. It appeared, as might be expected, that the errors in correlating the layers by means of common reflections as used in the procedures I and II, exceeded the errors in the intensity estimations of the individual reflexions. We believe therefore that this procedure gave the best parameters which could be obtained from these particular experimental data. The weighting was as in procedure II. All the observed reflexions were included and the unobserved reflexions were omitted throughout the refinements.

TABLE III. Bond distances in A. (see Fig. 9 for key to atomic positions).[a]

O—O in lic. oxygen polyhedra.

1–3	2.82 A	3–3	2.83 A	6–5	2.75 A
1–5	2.77	3–6	2.81	6–9	2.78
1–7	2.81	3–12	2.85	7–7	2.86
1–10	2.80	4–4	2.82	7–9	2.84
2–4	2.81	4–6	2.81	8–8	2.80
2–5	2.77	4–13	2.86	8–9	2.84
2–8	2.80	5–5	2.78	10–11	2.86
2–11	2.80	5–6	2.75	12–13	2.97

Mean value = 2.810; spread 2.75–2.86 (excluding 12–13).

N^+—O and F^- to O

N–10	4.09 A.
N–12	4.18
F–11	3.04
F–13	3.21

N—C and C—C in tetra alkyl cations.

Chain fitting in the tetrakaidecahedron		Chain fitting in the pentakaidecahedron	
$N—C_1$	1.58 A	$N—C_1$	1.66 A
$C_1—C_2$	1.51	$C_1—C_2$	1.47
$C_2—C_3$	1.66	$C_2—C_3$	1.56
$C_3—C_4$	1.76	$C_3—C_4$	1.54
$C_3—C_5$	1.44	$C_3—C_5$	1.67

Mean value for C—C = 1.57

[a] The standard deviations of the O—O, O—N^+ and O—F^- lie between 0.01 and 0.02 A. The s.d. of the C—C distances is 0.05 A in the chain, and 0.08 A involving the terminal CH_3 groups.

TABLE IV. Bond angles (see Fig. 9 for key to atomic positions).

O—O—O in Polyhedra,

5– 1–10	91°	6– 4–13	113°	7– 7– 1	110°
3– 1– 5	109	6– 4– 2	101	9– 7– 1	104
7– 1– 5	111	4– 4– 4	105	1– 7– 1	104
10– 1– 3	133	13– 4– 2	110	9– 8– 2	101
10– 1– 7	97	13– 4– 4	118	2– 8– 2	93
3– 1– 7	114	2– 4– 4	109	8– 8– 9	125
5– 2–11	111	1– 5– 2	114	8– 8– 2	109
5– 2– 4	107	1– 5– 6	109	6– 9– 6	110
5– 2– 8	105	1– 5– 5	107	6– 9– 7	108
11– 2– 4	111	2– 5– 6	108	6– 9– 8	110
11– 2– 8	105	2– 5– 5	109	7– 9– 8	111
4– 2– 8	117	5– 5– 6	109	1–10–11	121
6– 3–12	102	3– 6– 4	109	1–10– 1	117
6– 3– 1	102	3– 6– 5	118	2–11– 2	112
6– 3– 3	108	3– 6– 9	112	2–11–10	92
12– 3– 1	126	4– 6– 5	110	3–12– 3	131
12– 3– 3	111	4– 6– 9	111	3–12–13	114
1– 3– 3	106	5– 6– 9	106	4–13– 4	124
		7– 7– 9	124	4–13–12	97

Mean value = 110.0°, spread 91°–133°.

Angles involving N^+ or F^-

1–10–N	88°	2–11–F	110°
11–10–N	97	10–11–F	139
3–12–N	89	4–13–F	108
13–12–N	105	12–13–F	125
10–14–N	126	11–15–F	122
10–14–N	102	11–15–F	100
12–14–N	123	13–15–F	137

Valence angles in alkyl chains

Chain in tetrakaidecahedron		Chain in pentakaidecahedron	
C_1–N–C_1	111°	C_1–N–C_1	117°
N–C_1–C_2	112	N–C_1–C_2	105
C_1–C_2–C_3	101	C_1–C_2–C_3	100
C_2–C_3–C_4	100	C_2–C_3–C_4	111
C_2–C_3–C_5	123	C_2–C_3–C_5	113
C_4–C_3–C_5	103	C_4–C_3–C_5	106

C_1^T–N–C_1^P = 108°, 107°

Mean value 108.4°

Standard deviations in the angles:

O—O—O 0.5–1.0°; C—C—C 2°; C—C—CH_3 4°.

The variation in the parameters shown in Table I is of the same order as the standard deviations.

The final coordinates for all the atoms obtained by the procedure V, are given in Table II, together with some typical examples of the standard deviations. The final structure factor agreement was $R = \Sigma \mid \Delta F \mid / \Sigma \mid F_0 \mid = 0.135$, with the weighted structure factors $R' = \Sigma\omega \mid \Delta F \mid / \Sigma\omega \mid F_0 \mid = 0.126$. There were no trends in the agreement between the low- and high-order reflexions. No extinction effects were observed. The hydrogen atom scattering was omitted from the structure factors since the experimental data, in relation to the complexity of the structure, obviously did not permit any deductions to be made concerning the positions of the hydrogens. The observed and calculated structure factors are available from the authors, on request.

TABLE V. Interatomic distances less than 4.0 A between alkyl carbon atoms and oxygen atoms of tetra- and pentakaidecahedra.

In tetrakaidecahedron			In pentakaidecahedron		
C_1	O(1)	3.80 A	C_1	O(1)	3.83 A
	O(3)	3.94		O(3)	3.97
	O(10)	3.72		O(10)	3.51
	O(12)	3.56		O(12)	3.75
C_2	O(1)	3.98	C_2	O(1)	3.97
	O(3)	3.93		O(10)	3.52
	O(12)	3.57		O(11)	3.83
C_3	O(1)	3.95	C_3	none less than 4.0 A	
	O(7)	3.99			
C_4	O(2)	3.68	C_4	O(2)	3.90
	O(4)	3.85		O(3)	3.95
	O(6)	3.54		O(4)	3.81
	O(7)	3.75		O(4)	3.81
	O(8)	3.50		O(5)	3.81
	O(9)	3.35		O(6)	3.77
				O(12)	3.79
C_5	O(2)	3.74	C_5	O(2)	3.52
	O(3)	3.94		O(4)	3.71
	O(4)	3.51		O(5)	3.83
	O(6)	3.57		O(11)	3.63
	O(9)	3.95		O(13)	3.60
Mean of 20 distances, 3.74 A.			Mean of 19 distances, 3.76 A.		

The isotropic temperature factors for the oxygen atoms of the polyhedral structure are fairly uniform, ranging from 2.8 to 4.3 A^2. Those of the N^+ and F^-, which lie on the special positions at the intersection of the two mirror planes are significantly lower, 1.4 A^2. The first two carbon atoms, C_1^p, C_1^t of the alkyl chains have temperature factors similar to those of the N^+, and the thermal motion increases progressively along the chain to values of close to $B=6$ A^2 for the terminal atoms, (with the exception of C_5^t which appears to be anomalous in this respect).

The interatomic distances and valence angles are given in Tables III, IV, and V, with the standard deviations. The key to the location of the atoms is shown in Fig. 9.

DESCRIPTION OF THE STRUCTURE

The structure is of the clathrate type in which the "host molecule" is a three-dimensional hydrogen bonded water structure, which also includes the fluorine anion, and the "guest molecules" are the tetra alkyl ammonium cations The water structure contains three types of cages: the pentagonal dodecahedron, volume ≈ 170 A^3; the tetrakaidecahedron, volume ≈ 220 A^3; and the pentakaidecahedron, volume ≈ 240 A^3; the last 2 polyhedra having 12 pentagonal faces and, respectively, 2 and 3 hexagonal faces (see Fig. 6). Since, in this structure, only the larger voids are occupied by the alkyl groups of the cations, it is quite appropriate to describe the structure in terms of the $H_{40}O_{20}$ pentagonal dodecahedron unit.

If these units are placed face to face so as to form a two-dimensionally repeating array, a pattern such as shown in Fig. 3 is obtained. The regular polyhedra have to be distorted by about 3° in interedge angles in order to pack in this manner. This is the arrangement on the (001) face of the structure. As shown in Fig. 6, the dodecahedra share faces to form columns in the [100] and [110] directions. There is no way in which dodecahedra can be packed so as to completely fill the (001) face and in this particular arrangement hexagons are left open. These constitute one of the two opposite hexagonal faces of the tetrakaidecahedra which lie above and below this layer of dodecahedra.

Figure 7 shows the layer of polyhedra between those of the dodecahedra shown in Fig. 3. This layer consists of tetrakaidecahedra (*a* and *b*) and pentakaidecahedra (*c*), with the three hexagonal faces of the latter end on in this view. Face *a* of the tetrakaidecahedra is the bottom face which is formed by the packing of the dodecahedra and is shown in Figure 3. Face *b* is rotated through 90° with respect to face *a* and is the top face of the tetrakaidecahedron. This whole pattern is then repeated in the [001] direction by the mirror planes which contain the *a* and *b* hexagonal faces, i.e., at $z=0$ and $\frac{1}{2}$.

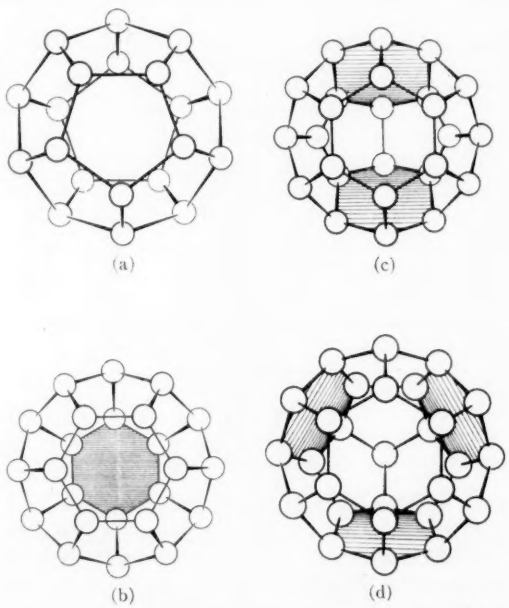

FIG. 6. The polyhdera found in the clathrate hydrates: (a) the pentagonal dodecahedron with 12 congruent regular pentagonal faces; (b) the tetrakaidecahedron with 12 regular pentagonal and 2 regular hexagonal faces, (the back face is shown smaller for clarity in diagram); (c) the pentakaidecahedron with 12 regular pentagonal and 3 regular hexagonal faces, (two of which are shaded); (d) the hexakaidecahedron with 12 regular pentagonal and 4 regular hexagonal faces, (three of which are shaded).

An alternate way of describing this structure is that it consists of a *C*-centered arrangement of columns of tetrakaidecahedra sharing hexagonal faces. In alternate layers in the *c* axis direction these columns are connected by dodecahedra and pentakaidecahedra. Both the tetrakai- and pentakaidecahedra share their hexagonal faces with congruent polyhedra, but their pentagonal faces are shared between different polyhedra.

In this description, the polyhedra are as regular as is compatible with the face-shared packing of the dodecahedra and the clathrate cage has the symmetry *Cmmm*. The true structure deviates from this because 4 out of the 80 vertices, which constitute the unit cell polyhedral structure, are actually N^+ and F^- atoms. These atoms occupy the opposite vertices of the hexagonal faces of the tetrakaidecahedra, as shown in Fig. 8. These positions are common vertices of four large polyhedra, two tetrakai- and two pentakaidecahedra. It is into these voids that the alkyl legs of the cation extend, since the centers of the voids, are tetrahedrically disposed with respect to the N^+ site.

The effect of introducing these hetero atoms into the polyhedral structure is to strain it further from regularity. Whereas most of the oxygen to oxygen first neighbor distances are close to 2.80 A, the N^+ to oxygen distances are 4.1 and 4.2 A, and the F^- to oxygen distances are 3.0 and 3.2 A. The interatomic distances and angles of the clathrate cage are given in Tables III and IV and Fig. 9. All the oxygen to oxygen hydrogen bond distances lie between 2.75 and 2.86 A, except O_{12}–O_{13} which is 2.97 A. It is interesting to note that this distance is the O–O edge of the distorted hexagon which contains the N^+ and F^- atoms (see Fig. 9).

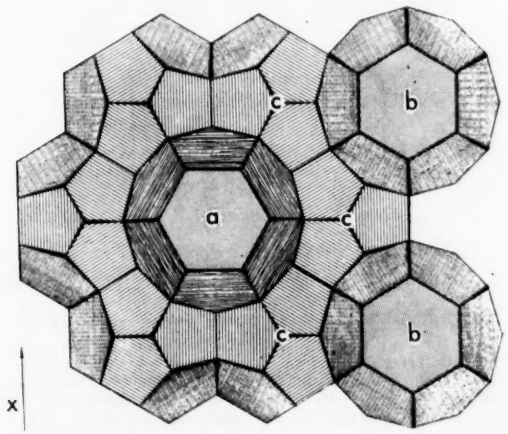

FIG. 7. Tetra *iso* amyl ammonium fluoride hydrate. Layer of tetrakaidecahedra (a and b) and pentakaidecahedra (c). These polyhedra interleave the successive layers of pentagonal dodecahedra shown in Fig. 3 in the *c* axis direction.

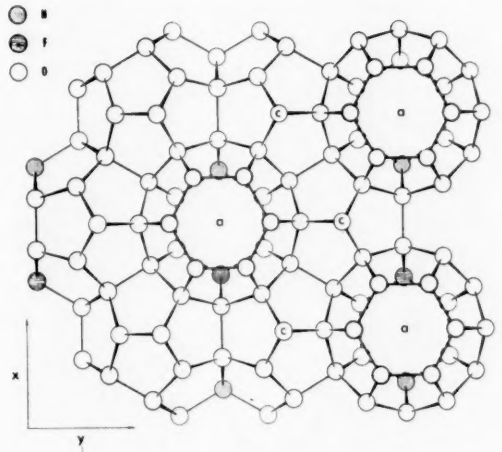

FIG. 8. Tetra *iso* amyl ammonium fluoride hydrate. Ball and stick diagram of Fig. 7, showing sites of N^+ and F^- atoms.

The arrangement of the alkyl groups in the large polyhedra is illustrated in Fig. 10. Two of the *iso*-amyl chains lie in the tetrakaidecahedra and two in the pentakaidecahedra. Due to the steric repulsions between the alkyl groups and the cage, the carbon atoms are displaced from the mirror planes and the *mm* symmetry of the crystal structure is obtained statistically. Since an individual cation may be twisted about its twofold axis parallel to *a*, either left- or right-handedly, the crystal is a racemate of *d* and *l* oriented cations in the *mm* symmetry clathrate cage. There is also an interesting and apparently significant correlation between the volume of the polyhedra and the temperature factors of the carbon atoms therein. The thermal motion of the C_1 atoms adjacent to the N^+ is the same in both, as would be expected. Thereafter the motion of the alkyl "legs" is significantly greater in the pentakaidecahedron, which is the larger of the two occupied polyhedra, (cf. Table II).

Within the rather large errors in the carbon atomic positions, there is no evidence of distortion in the stereochemistry of the cations. All the interatomic distances between the alkyl carbon atoms and the surrounding oxygen are greater than 3.5 A, with the exception of C_4^T–O(9) of 3.35 A. Although the van der Waals separations are a little larger on average for the alkyl groups in the larger void, the effect is not nearly so obvious as in the thermal motion (cf. Tables III and V). It is apparent from the large number of distances in the range 3.4–3.9 A for the terminal groups of the alkyl chains that both the tetra- and the pentakaidecahedra have about the optimum dimensions for occupancy by the *iso*-amyl residues. This must be a significant factor in the exceptionally good crystallization behavior of this hydrate, the melting point of

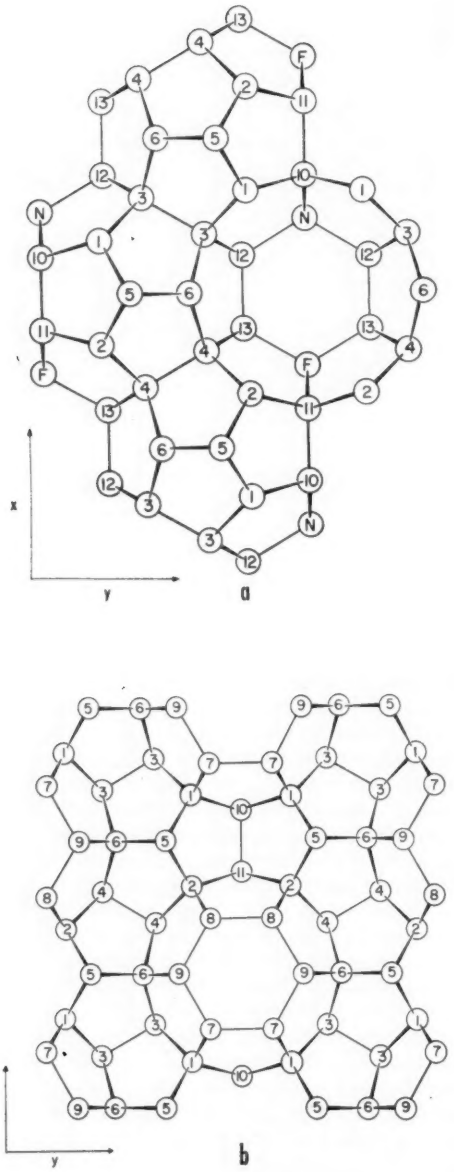

FIG. 9. (a) Key to interatomic dimensions in tetra and pentakaidecahedra. (b) Key to interatomic dimensions in pentagonal dodecahedra, see Tables III and IV.

which is the highest we have yet encountered in this series of compounds.

RELATIONSHIP TO THE GAS HYDRATES

There is a close relationship between this structure and those of the gas hydrates and for this reason we have maintained our description of the structure as a clathrate. If, however, the strict definition of a clathrate compound requires no chemical reactivity between the "host" and "guest" molecules, (e.g., Mandelcorn[10]), it might be a question of semantics whether these compounds fall in this class. Since the "host" molecule, in this structure, is certainly the water structure plus the anions and the "guest" is the cations, the interaction between them cannot be wholly van der Waals, although the interatomic distances are consistent with this type of weak-bonding interaction.

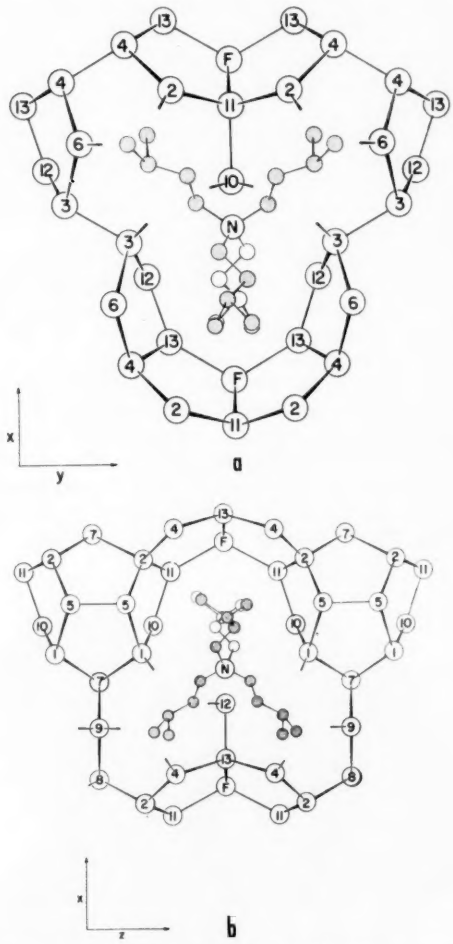

FIG. 10. Tetra *iso* amyl ammonium fluoride hydrate. Location of alkyl chains in polyhedral voids, showing the distortion of the polyhedra, cf. Fig. 9. (a) x, y view, showing sections of two pentakaidecahedron and one tetrakaidecahedron. (b) x, z view, showing sections of two tetrakaidecahedra, one pentakaidecahedron, and two distorted pentagonal dodecahedra.

[10] L. Mandelcorn, Chem. Revs. **59,** 827 (1959).

It would be interesting to explore the hydration of a compound such as $Na^+ \cdot [(n-C_4H_9)_4B^-]$ to discover whether the role of the cations and anions can be reversed in this type of compound formation.

The gas hydrates have been known for nearly 150 years, being first discovered by Davey in 1811.[11] As far as is known at present, they all form one or other of two types of crystal structure, the 12 A cubic structure with a hydration number of $7\frac{2}{3}$ and the 17 A cubic structure with a hydration number of 17. The crystal data and range of formation, which has been reported for these compounds, is summarized in Table VI. The 12 A cubic structure consists of pentagonal dodecahedra and tetrakaidecahedra, the 17 A cubic structure of pentagonal dodecahedra and hexakaidecahedra (see Figure 6d). It is believed that the "gas" molecules occupy the larger polyhedra. The evidence that the dodecahedra can also be occupied, e.g. by Argon or H_2S, is, in our opinion, somewhat inconclusive.

Only the Cl_2 7·67 H_2O structure has been subjected to a detailed crystal structure analysis, based on powder diffraction measurements which can, under some circumstances, fail to reveal the true crystal symmetry. However there is no reason, *per se*, to suspect this particular analysis.

The chlorine hydrate appears to be the simplest type of clathrate hydrate structure. The pentagonal dodecahedra form a pseudo body-centered arrangement by linking, through hydrogen bonds, at 8 of the 20 vertices forming a 40 H_2O unit cell of water structure. An additional 6 water molecules at the sixfold (c) positions of the space group $Pm3n$, i.e., $\frac{1}{4}$, $\frac{1}{2}$, 0, etc., then complete the tetrakaidecahedra and forms the 6 larger voids in the unit cell, in which the chlorine molecules lie (see Fig. 11). The hydrate of tri-*n*-butyl sulfonium fluoride, $(n-C_4H_9)_3S^+ \cdot F^- \cdot 20H_2O$, has been found to be *iso* structural with this gas hydrate.[10]

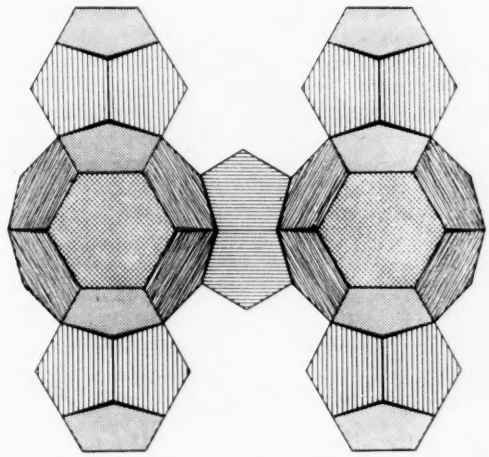

FIG. 11. Arrangement of dodecahedra and tetrakaidecahedra in the chlorine gas hydrate.

Another possible type of gas hydrate structure is one in which the pentagonal dodecahedra share faces two-dimensionally, with the small distortion from regularity which is necessary to obtain this packing of the polyhedra. This is the arrangement we have found in the structure of the tetra *iso* amyl ammonium fluoride hydrate, which contains 76 H_2O, $2N^+$ and $2F^-$ in the polyhedral framework. As discussed above it gives rise to the formation of both tetrakai- and pentakaidecahedra as the larger voids. Quite obviously the N^+ and F^- sites in this structure could be occupied by water molecules to form a much more regular polyhedral structure with 80 water molecules in the unit cell. If the larger voids were then filled with gas molecules, the structure would correspond to a $X \cdot 10H_2O$ gas hydrate. There is no evidence of the existence of this hydrate, unless the $Cl_2 10H_2O$ originally reported by Faraday,[13] in 1823, is different from that examined by x rays by Pauling and Marsh.[3]

The analogy between the geometry of the gas hydrates and that of the intermetallic compounds containing the dual polyhedron, the icosohedron, has been pointed out by Frank and Kasper.[14] The 12 A and 17 A, cubic gas hydrates have their counterparts in known alloy structures, $A15$ and $C15$. This hypothetical decahydrate corresponds to a basic, but hypothetical, A_4B_3 alloy structure[15] described in Frank

TABLE VI. Crystal data for gas hydrate structures.

Type X·7.67 H_2O[a,b,d]
6 Cl_2·46 H_2O; cubic, $a_0=11.88$ A.; space group, $P\cdot m3n$; $D_x=1.26$ g/cc.,
Also with X = Br_2; SO_2; H_2S; Xe; CH_4; C_2H_6; CH_3SH; CH_3Cl; CH_3Br; C_2H_4O; CH_2Cl_2; C_2H_5Cl; $CHCl_3$—H_2S; CCl_4—H_2S; CH_2Cl_2—H_2S; C_2H_5Cl—H_2S; C_2H_5Br—H_2S; with $a_0=11.9$–12.3 A.
Type Y·17 H_2O[a,b,e]
8 $CHCl_3$·136 H_2O; cubic, $a_0=17.2$ A.; space group, $F\cdot d3m$;
Also with Y = $CHCl_3$; CH_2Cl_2; C_2H_5Cl; $CHCl_3$·2 H_2S; C_3H_8; CH_3I; C_2H_5Cl: CF_2BrCl[e]: C_4H_8O; $(CH_3)_2O$, 2A.

[a] M. V. Stackelberg, *et al.*, Z. Electrochemi. **58,** 25, 40, 99, 104, 162 (1954).
[b] M. V. Stackelberg and B. Meuthen, Z. Electrochemi. **62,** 130 (1958).
[c] D. N. Glew, Can. J. Chem. **38,** 208 (1960).
[d] K. W. Allen, J. Chem. Soc. **1959,** 4131.

[11] H. Davey, Phil. Trans. Roy. Soc. (London) **101,** 155 (1811).

[12] G. A. Jeffrey, D. Feil and R. McMullan, Acta Cryst. **13,** 1029 (1960).
[13] M. Faraday, Quart. J. Sci. **15,** 71, 1823.
[14] F. C. Frank and J. S. Kasper, Acta Cryst. **12,** 483 (1959).
[15] We are grateful to a referee for recognizing this.

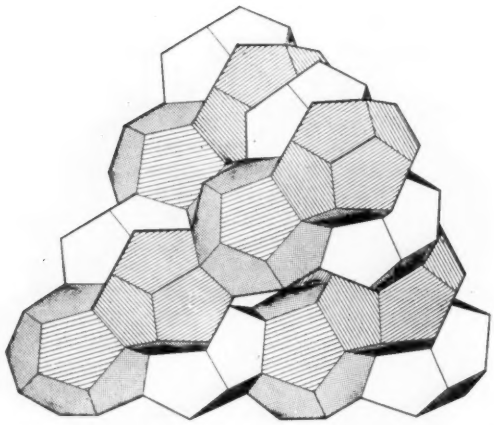

FIG. 12. The polyhedral structure of the 17 A cubic gas hydrate cage, showing the pentagonal dodecahedra sharing faces "three dimensionally."

and Kasper's general treatment[14,16] of the topology and geometry of the polyhedra formed by sphere packing.

The third type of structure is that in which the pentagonal dodecahedra share faces three-dimensionally, again with small distortions from regularity. This is the structure of the 17 A cubic gas hydrate with 136 water molecules in the unit cell (see Fig. 12). The large polyhedra, in this case are hexakaidecahedra, see Figure 6(d). So far we have obtained no 17 A cubic tetraalkly ammonium or phosphonium salt hydrate. On the basis of our present incomplete knowledge of these structures, we believe that we may not find such a compound, because in this arrangement of the dodecahedra there is no vertex in the polyhedra which would provide a suitable site for the central atom of the cation by being a common point for four tetrahedrally disposed large voids.

There remain, however, the large structural group of the tetragonal tetra *n*-butyl ammonium salts, reported in the earlier paper,[15] to be explored, as well as several isolated structures and polymorphs, and we suspect that the continued chemical preparation will reveal more structures of this general type.

THE HYDROGEN BONDING

In both the 12 and 17 A cubic gas hydrates, each edge of the polyhedral clathrate frame is a hydrogen bond and there are as many edges as there are water hydrogen atoms in the structure. Each water oxygen atom is hydrogen bonded to four others in a distorted tetrahedral coordination, two of the bonds being donor and two acceptor. In the tetra *iso*-amyl ammonium fluoride hydrate some of the oxygen sites are occupied by formally ionized atoms which contribute no protons to the hydrogen bond system. In the 76 $H_2O \cdot 2N^+2F^-$ polyhedral frame there are eight hydrogen atoms less than in the corresponding fully hydrogen bonded (hypothetical) gas hydrate structure. It is reasonable to conclude that each N^+ forms no hydrogen bonds with its four nearest neighbor oxygen atoms and that each F^- forms four hydrogen bonds. There will then be 152 hydrogen bonds in the unit cell, corresponding with the number of water hydrogen atoms.

The distribution of interatomic distances in the vicinity of the anion and cation is shown in Fig. 13. The 4.1 and 4.2 A N^+ to O distances are consistent with the complete absence of bonding to the central atom of the cation. The F^- to oxygen distances of 3.0 and 3.2 A are inconclusive but presumably they also are associated with hydrogen bonding. The distances, however, are considerably longer than would be ex-

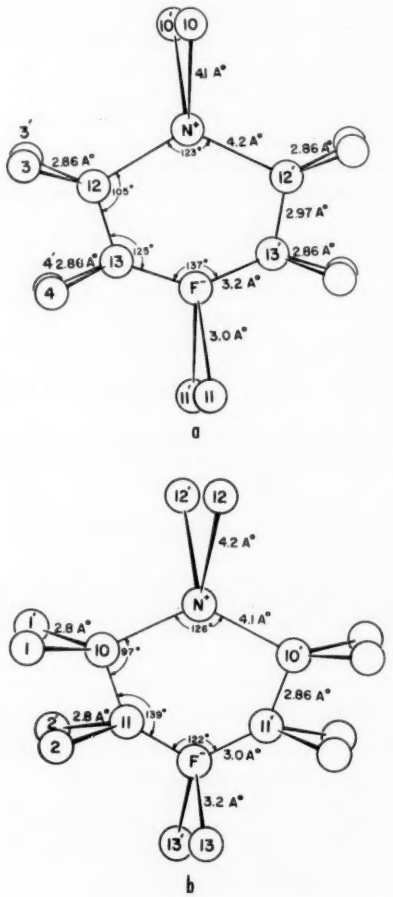

FIG. 13. Distribution of hydrogen bond distances and angles in the hexagonal faces of (a) the tetrakaidecahedra; and (b) the pentakaidecahedra.

[16] F. C. Frank and J. S. Kasper, Acta Cryst. **11**, 184 (1958).

pected for a water to fluorine ion hydrogen bond separation and at present we have no explanation for this. Surprisingly, we were unable to find any structure determinations that reported a comparable $H_2O\cdots F^-$ hydrogen bond distance. The $H_2O\cdots Cl^-$ separations in *iso* leucine, HCl. H_2O, for example, were 3.04 and 3.23 A.[17]

The differences of 0.1 A and greater between the corresponding edges of the hexagonal faces of the tetrakai and the pentakaidecahedra, shown in Fig. 13, are also highly significant in terms of the standard deviations. In the absence of direct evidence concerning the location of the hydrogen atoms, there is no obvious interpretation of these differences, other than to remark on the distortion of the hydrogen bond system from regularity due to the presence of the peralkyl cations and on the possible sensitivity of the hydrogen bond distances to the environment of the oxygen atom in a clathrate cage structure of this type. Both O(10) and O(12) have only three hydrogen bonded neighbors in a nearly trigonal planar arrangement (see Fig. 10). Only O(12), however, has one of these distances longer than the average value.

[17] J. Trommel and J. M. Bijvoet, Acta Cryst. **7**, 703 (1954).

ACKNOWLEDGMENTS

The research was supported by the Air Force Office of Scientific Research. The computing associated with the research was carried out through the University of Pittsburgh Computation and Data Processing Laboratory using programs developed with the support of the National Science Foundation, with the exception of the 704 least-squares program that was kindly supplied by Dr. Busing.

THE JOURNAL OF CHEMICAL PHYSICS VOLUME 35, NUMBER 5 NOVEMBER, 1961

Theory of the Spin and Charge Distribution in Aromatic Ion Radicals; Application to the Naphthalene Negative Ion

JOHN C. SCHUG*

Gulf Research and Development Company, Pittsburgh, Pennsylvania

THOMAS H. BROWN

Union Carbide Research Institute, Tarrytown, New York

AND

MARTIN KARPLUS†

Department of Chemistry and Watson Scientific Computing Laboratory, Columbia University, New York 27, New York

(Received April 7, 1961)

The valence-bond method is extended to positive- and negative-ion radicals. General formulas for the required energy, overlap, spin-density, and charge-density matrices are developed and specialized to pi-electron systems. An application of the method to the pi electrons of the naphthalene negative ion is given. Included in the calculation are all unexcited structures with the negative charge in each of the ten possible positions. When approximate exchange and transfer integrals are used to determine the coefficients of valence-bond structures, the α to β position spin-density ratio is found to be equal to 2.60, in good agreement with the "experimental" value of 2.65. The magnitudes of the calculated spin densities are such that a Q of -26.3 gauss is required to obtain the measured hyperfine splittings.

To test the validity of these valence-bond results, their sensitivity to the molecular integral values is examined. Also, comparisons with a variety of molecular-orbital calculations are given. It is of considerable interest that the *charge distributions* obtained from the valence-bond theory and the molecular-orbital theory are very different in spite of the similarity of the *spin distributions* calculated by the two methods.

I. INTRODUCTION

THE hyperfine interactions observed in the spin-resonance spectra of organic radicals are an important tool for the study of the electronic structure of these molecules. Since the hyperfine splittings depend on the unpaired electron spin density at the magnetic nuclei, an analysis of the spectra can give detailed information about the wave function. That is particularly true for aromatic or conjugated molecules, in which the unpaired spin tends to be delocalized over the entire pi-electron system and can interact with a number of nuclei. For the in-plane protons in such molecules, the observed coupling with the pi-electron spins is related to the sigma-pi exchange interactions between pairs of electrons. By a perturbation theory treatment

* Part of the work included in this paper was submitted in a doctoral dissertation to the Department of Chemistry of the University of Illinois. Acknowledgment is made to the donors of The Petroleum Research Fund, administered by the American Chemical Society, for partial support of the research done at the University of Illinois.

† Alfred P. Sloan Foundation Fellow. Reprint requests should be sent to this author.

of these sigma-pi interactions, it has been shown[1] that the proton hyperfine constant for a localized C—H bond is approximately proportional to the unpaired spin density in the pi orbital of the bonded carbon. Since the constant of proportionality appears to be relatively independent of the detailed structure of the molecule, this result implies that the theory of pi-electron systems can be utilized directly for the interpretation of hyperfine splittings.

Both the molecular-orbital and the valence-bond approximations have been used for the calculation of unpaired pi-electron spin densities in a variety of systems. Because of the simplicity of the single-configuration Hückel theory, most of the studies have been based on this technique.[2] However, the valence-bond approach has sometimes yielded additional insight into the unpaired spin distribution. This is particularly true for odd-alternant radicals in which the valence-bond method in its simplest form predicts positive and negative spin densities in qualitative agreement with experiment.[3–5]

One important restriction on the valence-bond method has been its limitation to neutral radicals. Since ionic species (e.g., even-alternant radicals) are also of considerable interest, an extension of the method seems desirable. Further, the quantitative problems that have arisen in calculations for neutral systems[4] indicate the need for a more refined treatment that provides for the inclusion of ionic terms.

In this paper we employ a more general valence-bond method for the calculation of pi-electron spin densities. Polar structures and charge delocalization are included in the theory. The required energy, overlap, charge-density, and spin-density matrices are formulated in terms of molecular integrals, and consideration is given to their evaluation. Exploratory calculations are made for the naphthalene negative ion and the results compared with those obtained from experimental data and molecular orbital theory. Both the charge and the spin distributions are examined, since the two are not simply related in valence-bond theory.

II. THEORETICAL DEVELOPMENT

Although the original valence-bond theory was formulated in terms of nonpolar structures, a few attempts to include polar terms have been made. Both Sklar[6] and Craig[7] used structures with charges on adjacent atoms. Simonetta and Schomaker[8] provided a more general treatment and applied it to certain heterocyclic compounds.[9] More recently McWeeney[10] has introduced polar structures into a valence-bond method based on orthogonalized atomic orbitals. In this section we outline a procedure for the inclusion of polar structures in a valence-bond theory for neutral and ionic systems. The development is applied to energy and overlap matrix elements along lines similar to those followed by Simonetta and Schomaker. Also a method is derived for the calculation of spin and charge densities from the generalized valence-bond functions.

Energy and Overlap Matrices

Since we are concerned here with the wave functions and energies of free radicals, we have to consider systems with an odd number $(2n-1)$ of electrons. As it is most convenient to treat an even number of electrons, we introduce a phantom electron and a phantom orbital in such a way that the $2n$-electron function corresponds to a singlet state.[11] A complete set of valence-bond structures for such a system is obtained by distributing the electrons in all possible ways (singly or in pairs) among the m available atomic orbitals, and then forming all canonical structures for each of the electron distributions. The distribution u contains

$$(2n-2\rho_u)!/[(n-\rho_u)!(n-\rho_u+1)!]$$

canonical structures, where ρ_u is the number of doubly occupied orbitals. The total number of canonical structures U, which is obtained by summing over all distributions, is given by the expression

$$U=\sum_u \frac{(2n-2\rho_u)!}{(n-\rho_u)!(n-\rho_u+1)!}. \tag{1}$$

Since U rapidly becomes large with increasing n and m, it is often convenient to use an incomplete set containing only the most important structures.

The valence-bond wave function Ψ has the form

$$\Psi=\sum_{l,u} c_l{}^u \psi_l{}^u, \tag{2}$$

where the $c_l{}^u$ are coefficients determined by the variational method and the $\psi_l{}^u$ can be written

$$\psi_l{}^u=\left[\frac{(2^{\rho_u})}{(2n)!2^n}\right]^{\frac{1}{2}} \sum_R (-1)^R R \sum_P (-1)^P P\bar{a}(1)b(2)\cdots; \tag{3}$$

the superscript u indicates the electron distribution to which the function belongs, and the subscript l, the

[1] H. M. McConnell and D. B. Chesnut, J. Chem. Phys. **28,** 107 (1958); S. Aono, Progr. Theoret. Phys. (Kyoto) **21,** 779 (1959); A. D. McLachlan, H. H. Dearman, and R. Lefebvre, J. Chem. Phys. **33,** 65 (1960).

[2] See for example, E. de Boer and S. I. Weissman, J. Am. Chem. Soc. **80,** 4549 (1958).

[3] P. Brovetto and S. Ferroni, Nuovo cimento **5,** 142 (1957).

[4] H. M. McConnell and H. H. Dearman, J. Chem. Phys. **28,** 51 (1958).

[5] A. D. McLachlan, J. Chem. Phys. **32,** 1488 (1960).

[6] A. L. Sklar, J. Chem. Phys. **5,** 669 (1937).

[7] D. P. Craig, Proc. Roy. Soc. (London) **A200,** 390 (1950).

[8] M. Simonetta and V. Schomaker, J. Chem. Phys. **19,** 649 (1951).

[9] M. Simonetta, J. chim. phys. **49,** 68 (1952).

[10] R. McWeeney, Proc. Roy. Soc. (London) **A223,** 306 (1954).

[11] L. Pauling, J. Chem. Phys. **1,** 280 (1933). See also H. Eyring, J. Walter, and G. E. Kimball, *Quantum Chemistry* (John Wiley & Sons, Inc., New York, 1944), for a useful discussion.

number of the canonical function in that distribution. The letters a, b, etc., refer to the atomic orbitals that are occupied in distribution u. A bar over an atomic orbital implies that the spin function β is associated with it and conversely, the absence of a bar refers to the spin function α. Any of the m available atomic orbitals may appear once, twice, or not at all, depending on the disposition of the electrons in the given distribution. If it appears twice, an orbital must be associated with both spin β and spin α. The operators P and R have their usual significance. The former produces all permutations of orbitals among the electrons, and the latter interchanges the spins of bonded pairs. The symbol $(-1)^P$ equals ± 1, depending on whether the permutation is even or odd, and $(-1)^R$ equals ± 1 for an even or an odd number of spin interchanges respectively. For doubly occupied orbitals, the spin functions are interchanged by R in the same fashion as for pairs of bonded orbitals, but the permutations that involve the same orbital with different spins are omitted.[8]

A convenient representation of the valence-bond structures is afforded by the Rumer-Pauling diagrams.[11,12] The canonical set of structures for a given electron distribution is obtained by placing the orbitals appearing in Eq. (3) at the corners of a $2n$-sided polygon. Bonded pairs of orbitals and doubly occupied orbitals are connected by arrows, with the tail of each arrow indicating spin β and the head, α. The desired set is found by forming all possible bonding schemes that have no crossing arrows, with each doubly occupied orbital always bonded to itself.

The matrix $\mathbf{M}$, which may be either the Hamiltonian matrix or the overlap matrix required for the secular equation, can be written in the block form,

$$\mathbf{M}=\begin{pmatrix} (u,u) & (u,v) & \cdots \\ (v,u) & (v,v) & \cdots \\ \cdots & \cdots & \cdots \end{pmatrix} \tag{4}$$

where the diagonal blocks, (u, u), (v, v), etc., contain matrix elements between structures having the same electron distribution, and the others, (u, v) etc., contain those between structures having different distributions. Each diagonal block is itself a square matrix, whose order is given by the appropriate term in Eq. (1).

To describe the individual elements of the Hamiltonian matrix $\mathbf{H}$ and the overlap matrix $\mathbf{S}$, we use the notation

$$H_{lm}{}^{uv}=\langle \psi_l{}^u \mid \mathcal{H} \mid \psi_m{}^v \rangle; \qquad S_{lm}{}^{uv}=\langle \psi_l{}^u \mid \psi_m{}^v \rangle, \tag{5}$$

where $\mathcal{H}$ is the Hamiltonian operator for the system.

The elements $H_{lm}{}^{uu}$ and $S_{lm}{}^{uu}$ which appear in the diagonal blocks are given directly by the well-known Pauling rules,[11]

$$S_{lm}{}^{uu}=2^{i-n}; \qquad H_{lm}{}^{uu}=2^{i-n}\{C^u+\sum_k f_k \epsilon_k{}^u\}. \tag{6}$$

In Eq. (6), i is the number of islands (closed polygons) that appears in the superposition diagram for the structures $\psi_l{}^u$ and $\psi_m{}^u$ (such a superposition diagram will be referred to by the symbol, $[\psi_l{}^u \mid \psi_m{}^u]$). The quantity C^u is the Coulomb integral for distribution u, and the summation includes all the exchange integrals $\epsilon_k{}^u$ that are considered in the formulation. For calculations restricted to single exchange integrals, the f_k have the values $+1$, -2, or $-\frac{1}{2}$, depending on the form of the superposition diagram.[11] The exchange integrals involving the phantom orbital do not have to be listed, since they are set equal to zero.

The doubly occupied orbitals in a diagonal block, which were not considered in Pauling's original theory, are automatically accounted for by the present method. They each add one island to the diagram, which just cancels the increase in n due to the presence of two more electrons. As a result of the exclusion in Eq. (3) of the transposition of the electron pairs in doubly occupied orbitals, no exchange integral involving only one such orbital can occur. However, exchanges with other orbitals are included and appear twice because of the two electrons.

It is to be noted that in Eq. (6) the Coulomb and exchange integrals have been differentiated by the superscript u which refers to the electron distribution. This has to be done in general because the molecular Hamiltonian $\mathcal{H}$ includes interactions involving the entire molecule. If two electron distributions are sufficiently different, the values of the exchange integrals for interchanges between the same orbitals cannot be assumed to be equal.

In all off-diagonal blocks $(u \neq v)$, the elements of the overlap matrix are zero,

$$S_{lm}{}^{uv}=0, \qquad (u \neq v) \tag{7}$$

within the usual approximation of orthogonal orbitals. Correspondingly, no Coulomb integrals occur in the Hamiltonian matrix elements of the off-diagonal blocks. The integrals that do appear in the $H_{lm}{}^{uv}$ correspond to atom-atom jumps by one or more electrons, and are referred to as transfer integrals. From Eqs. (3) and (5) the general form of these Hamiltonian matrix elements is given by the expression

$$H_{lm}{}^{uv}=\frac{2^{(\rho_u+\rho_v)/2}}{(2n)!2^n}\langle \sum_{R'}(-1)^{R'}R' \sum_{P'}\{(-1)^{P'}P'\bar{a}(1)b(2) \cdots \mid \mathcal{H} \mid \sum_R (-1)^R R \sum_P (-1)^P P \bar{c}(1)d(2)\cdots\rangle. \tag{8}$$

The first permutation operator P' under the integral produces $(2n)!/2^{\rho_u}$ identical terms (because permutations of electrons in the same orbital are not included),

[12] G. Rumer, Göttinger Nachr. 377 (1932).

and Eq. (8) reduces to

$$H_{lm}{}^{uv}=\frac{2^{\Delta\rho/2}}{2^n}\langle\sum_{R'}(-1)^{R'}R'\bar{a}(1)b(2)\cdots|\mathcal{H}|\sum_{R}(-1)^{R}R\sum_{P}(-1)^{P}P\bar{c}(1)d(2)\cdots\rangle, \quad (9)$$

where $\Delta\rho=\rho_v-\rho_u$ and v, u are chosen such that $\Delta\rho>0$. This is always possible since $\mathbf{H}$ is a symmetric matrix.

Because $u\neq v$ in Eq. (9), the functions $\psi_l{}^u$ and $\psi_m{}^v$ differ by at least one orbital. If they differ by more than two orbitals, $H_{lm}{}^{uv}$ is equal to zero for orthogonal atomic orbitals or with the neglect of orbital overlap. For functions that differ by only one or two orbitals, Eq. (9) becomes

$$H_{lm}{}^{uv}=\sum_k\sum_{P_k}(-1)^{r_k}(-1)^{P_k}2^{(\Delta\rho+2i_k'-2n)/2}\tau_k{}^{uv} \qquad (u\neq v), \quad (10)$$

where $\tau_k{}^{uv}$ is a transfer integral, P_k are the permutations giving rise to the integral, i_k' is the number of islands in the diagram $[\psi_l{}^u \mid P_k\psi_m{}^v]$, and r_k is the number of arrow reversals required for a satisfactory spin orientation. The exact form of $\tau_k{}^{uv}$ depends on the functions involved, although each nonzero transfer integral must have all the orbitals except for one or two in $\psi_l{}^u$ matched with those of $\psi_m{}^v$. In contrast to elements of the diagonal blocks, those belonging to the off-diagonal blocks have only relatively few permutations that lead to nonzero contributions.

To show how Eq. (10) is applied to negative-ion radicals, we consider the cyclobutadiene negative ion. Neglecting additional charge separation in the molecule, we have structures of the form

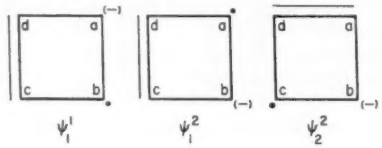

These three structures correspond to the Rumer-Pauling diagrams

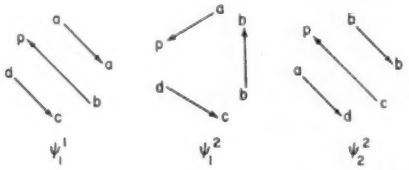

where p is the phantom orbital. The atomic orbitals in structures $\psi_1{}^2$ and $\psi_2{}^2$ have been written in different orders for the purpose of illustrating the procedures that are involved. In most calculations, structures belonging to the same electron distribution would have identically ordered atomic orbitals. The diagram $[\psi_1{}^1 \mid \psi_1{}^2]$ can be formed directly since all identical orbitals are matched. We have

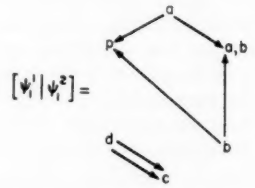

For this case Eq. (10) becomes

$$H_{11}{}^{12}=\sum_k\sum_{P_k}(-1)^{r_k+P_k}2^{i_k'-n}\tau_k{}^{12}. \quad (11a)$$

If P_k corresponds to the identity or simple transpositions, Eq. (11a) reduces to the Pauling formula [Eq. (6)] and we have the nonzero contributions

$$\langle aabcd \mid \mathcal{H} \mid abbcd\rangle,$$
$$-\tfrac{1}{4}\langle aabcd \mid \mathcal{H} \mid acbbd\rangle,$$
$$-\tfrac{1}{4}\langle aabcd \mid \mathcal{H} \mid adbcb\rangle.$$

In addition there are the terms $-\frac{1}{4}\langle aabcd \mid \mathcal{H} \mid acbbd\rangle$ arising from the permutations (a, b) followed by (b, c), and $-\frac{1}{4}\langle aabcd \mid \mathcal{H} \mid adbcd\rangle$ from (a, b) followed by (b, d).

The resulting matrix element is

$$H_{11}{}^{12}=\langle aabcd \mid \mathcal{H} \mid abbcd\rangle-\tfrac{1}{2}\langle aabcd \mid \mathcal{H} \mid acbbd\rangle-\tfrac{1}{2}\langle aabcd \mid \mathcal{H} \mid adbcd\rangle. \quad (11b)$$

Because of the mismatch of identical orbitals in the diagram $[\psi_1{}^1 \mid \psi_2{}^2]$ a permutation must first be applied to $\psi_2{}^2$ in the calculation of $H_{12}{}^{12}$. Diagramming the permutation P, we have

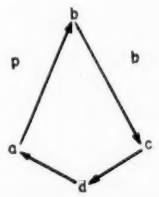

where each arrow points from an orbital in the unpermuted function to the position that the orbital occupies in the permuted function. For $P\psi_2{}^2$, $[\psi_1{}^1 \mid P\psi_2{}^2]$ and and $[\psi_1{}^1 \mid RP\psi_2{}^2]$, where R matches the spins, the diagrams are

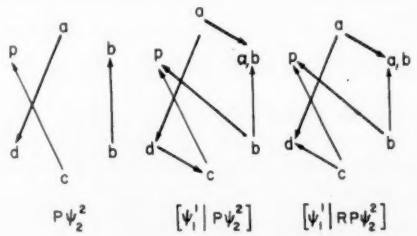

Since P is an odd permutation and $R=1$, Eq. (10) becomes

$$H_{12}^{12}=\sum_k \sum_{Pk'}(-1)^{\tau_{k'}+Pk'}2^{i_k''-n}\tau_k^{12}, \qquad (12a)$$

where $P_k', \tau_{k'}$ refers to the permutations that are applied to $RP\psi_2^2$, and i_k'' is the number of islands in $[\psi_1^1 \mid P_k' RP\psi_1^2]$. The same procedure that was used for H_{11}^{12} is again applicable and we find

$$H_{12}^{12}=\tfrac{1}{2}[\langle aabcd \mid \mathcal{H} \mid abbcd\rangle-\tfrac{1}{2}\langle aabcd \mid \mathcal{H} \mid acbbd\rangle -\tfrac{1}{2}\langle aabcd \mid \mathcal{H} \mid adbcb\rangle] \qquad (12b)$$

that is, $H_{12}^{12}=\frac{1}{2}H_{11}^{12}$.

Equation (10) is a general expression for evaluating Hamiltonian matrix elements between structures with different electronic arrangements. For ions and systems with polar structures, manipulations corresponding to those illustrated above lead from Eq. (10) to the desired off-diagonal matrix elements. No general simplification of the equation can be given since the arbitrary ordering of the orbitals in the diagrams determines the initial R and P values required for matching of identical orbitals. However, the order leading to the minimum permutations for orbital matching (e.g., structures of type ψ_1^1 and ψ_1^2) is not always the most desirable. Its use may complicate the ulitization of spatial symmetry for the simplification of the calculation by group theoreical techniques. Convenient ordering schemes must be determined to fit each situation.

Spin and Charge Density Evaluation

Having determined the linear combination of structures [Eq. (3)] that lead to the ground-state function Ψ[Eq. (2)], we can evaluate the spin and charge densities in the molecule. For neutral radicals with no polar structures [corresponding to a set of functions associated with a single block u of Eq. (4)], a number of authors[3,4] have given formulas for the calculation of spin densities. Since no proof for these formulas seems to be available, we derive an expression for the spin densities for the general valence-bond function and apply it to the "single block" function as a special case. Corresponding formulas are obtained for the charge densities.

The spin density ρ_N in atomic orbital ϕ_N is given by the expectation value of the spin density operator, ϱ_N. That is,

$$\rho_N=\langle\Psi \mid \varrho_N \mid \Psi\rangle, \qquad (13)$$

where ϱ_N has the form

$$\varrho_N\sum_k \mathbf{S}_{kz}=\sum_k \mathbf{S}_{kz}\Delta_N(k). \qquad (14)$$

Here the summation is over all electrons k in the system. S_{kz} is the z-component spin operator (in units of $\hbar$) for electrons k, and $\Delta_N(k)$ is an "orbital δ function" [1] with the property

$$\langle\phi_{N'}(k) \mid \Delta_N(k) \mid \phi_{N''}(k)\rangle=\delta_{NN'}\delta_{NN''}. \qquad (15)$$

That is, $\langle\phi_{N'}(k) \mid \Delta_N(k) \mid \phi_{N''}(k)\rangle$ is unity if electron k is in orbital ϕ_N, and is zero otherwise. From Eqs. (14) and (15) it is evident that, when we refer to spin density in an atomic orbital, we mean the integrated density in the entire orbital and not just the density at the nucleus.

For the function Ψ in Eq. (2), we have

$$\rho_N=\sum_{u,v}\sum_{lm} c_l^u c_m^v (\varrho_N)_{lm}^{uv}, \qquad (16)$$

where

$$(\varrho_N)_{lm}^{uv}=\langle\psi_l^u \mid \varrho_N \mid \psi_m^v\rangle. \qquad (17)$$

Inserting Eq. (14) into Eq. (17) and making use of Eq. (3), we obtain

$$(\varrho_N)_{lm}^{uv}=\frac{2^{\Delta\rho/2}}{2^n}\langle\sum_{R'}(-1)^{R'}R'\bar{a}(1)b(2) \cdots \mid \{\sum_k \mathbf{S}_{kz}\Delta_N(k)/\langle S_z\rangle\} \mid \times\sum_R(-1)^R R\sum_P(-1)^P P\bar{c}(1)d(2)\cdots\rangle, \qquad (18)$$

where the permutations P' have been eliminated by multiplying by $[(2^n)!/2^{\rho_u}]$ as in Eq. (9). Here $\langle S_z\rangle$ is the z component of spin angular momentum for the entire radical ($\pm\frac{1}{2}$). From the form of operator in Eq. (18), it is evident that all $(\varrho_N)_{lm}^{uv}(u\neq v)$ vanish identically for orthogonal atomic orbitals. Thus Eq. (16) can be simplified to

$$\rho_N=\sum_u\sum_{lm} c_l^u c_m^u (\varrho_N)_{lm}^u, \qquad (19)$$

with

$$(\varrho_N)_{lm}^u=\langle\psi_l^u \mid \rho_N \mid \psi_m^u\rangle =1/2^n\langle\sum_{R'}(-1)^{R'}R'\bar{a}(1)b(2) \cdots \mid \{\sum_k \mathbf{S}_{kz}\Delta_N(k)/\langle S_z\rangle\} \mid \times\sum_R(-1)^R R\sum_P(-1)^P P\bar{a}(1)b(2)\cdots\rangle. \qquad (20)$$

Furthermore, of the $[(2n)!/2^{\rho_u}]$ permutations produced by the operator P, only the identity yields a nonzero contribution. We have

$$(\varrho_N)_{lm}^u=1/2^n\langle\sum_{R'}(-1)^{R'}R'\bar{a}(1)b(2) \cdots \mid \{\sum_k \mathbf{S}_{kz}\Delta_N(k)/\langle S_z\rangle\} \mid \sum_R(-1)^R R\bar{a}(1)b(2)\cdots\rangle. \qquad (21)$$

By means of the property of the $\Delta_N(k)$ operator [Eq. (15)], Eq. (21) reduces to the expression

$$(\varrho_N)_{lm}^u=1/2^n\langle\sum_{R'}(-1)^{R'}R'\bar{a}(1)\cdots\phi_N(k) \cdots \mid \mathbf{S}_{kz}/\langle S_z\rangle \mid \sum_R(-1)^R R\bar{a}(1)\cdots\phi_N(k)\cdots\rangle. \qquad (22)$$

where all integrations over the space coordinates have

been performed and only those of the spins remain [the symbol $\bar{\alpha}(1)$ now represents only the spin function β associated with electron 1, etc.].

Each operator R in Eq. (21) produces a sum of (2^n) terms, (2^i) of which also appear in the other summation. The (2^i) terms that appear in both sums are the only ones that are not equal to zero. We refer to them as "satisfactory spin functions." To obtain the signs of these terms, we consider an orbital ϕ_N that is in the same island as the phantom orbital in the superposition diagram $[\psi_l{}^u \mid \psi_m{}^u]$. If ϕ_N is an odd number of bonds away from the phantom in each of the satisfactory spin functions, electron k has the opposite spin function from the phantom electron. Since the phantom electron has the opposite spin from the radical as a whole, this implies that electron k has the same spin as the radical. Correspondingly, if electron k is an even number of bonds away from the phantom, electron k has a spin function that is different from the net spin function for the radical. For the two possibilities, we have

$$(\mathbf{S}_{kz}/\langle S_z\rangle \mid \sum_R (-1)^R R\bar{\alpha}(1)\cdots\phi_N(k)\cdots\rangle = \pm \mid \sum_R (-1)^R R\bar{\alpha}(1)\cdots\phi_N(k)\cdots\rangle, \quad (23)$$

where the upper sign holds for the former and the lower sign for the latter case. Inserting Eq. (23) into Eq. (22) and integrating over the spin coordinates, we have the result

$$(\varrho_N)_{lm}{}^u = \pm S_{lm}{}^{uu} = \pm 2^{i-n}, \qquad \begin{matrix}(+)\text{ for odd}\\(-)\text{ for even.}\end{matrix} \quad (24)$$

If orbital ϕ_N is in an island which does not contain the phantom orbital, half of the (2^i) satisfactory spin functions will have $S_{kz}/\langle S_z\rangle = +1$, and half, $S_{kz}/\langle S_z\rangle = -1$. The two contributions cancel one another, giving

$$(\varrho_N)_{lm}{}^u = 0; \quad (25)$$

Eqs. (24) and (25) provide the general rules for calculating spin densities by the valence-bond theory.

To determine the net charge q_N contributed to atom N by the electrons in orbital ϕ_N, we write the charge density operator $\mathbf{q}_N$ in the form

$$\mathbf{q}_N = (\sum_k \Delta_N(k)) - 1. \quad (26)$$

For the function Ψ of Eq. (2), we have

$$q_N = \sum_{u,v}\sum_{lm} c_l{}^u c_m{}^v (\mathbf{q}_N)_{lm}{}^{uv} \quad (27)$$

Because of the orthogonality of the atomic orbitals and the form of the charge-density operator, the quantity $(\mathbf{q}_N)_{lm}{}^{uv}$ is zero unless the charge in the distributions u and v is in the position N. Writing this as $u=v=N$, we obtain

$$q_N = \sum_{l,m} c_l{}^N c_m{}^N S_{lm}{}^N \quad (28)$$

for the atomic charge density q_N.

A convenient check that is often used in spin density calculations is that the total density for all orbitals must be unity, i.e., $\sum_N \rho_N = 1$. This statement can be proved by considering

$$\sum_N \rho_N = \sum_N \sum_u \sum_{l,m} c_l{}^u c_m{}^u (\varrho_N)_{lm}{}^u = \sum_u \sum_{l,m} c_l{}^u c_m{}^u \sum_N (\varrho_N)_{lm}{}^u, \quad (29)$$

where $(\varrho_N)_{lm}{}^u$ is given by Eqs. (24) and (25). The orbitals for which $(\varrho_N)_{lm}{}^u \neq 0$ can be divided into two classes, those for which the quantity $(\varrho_N)_{lm}{}^u$ is positive, and those for which it is negative. Because the island with the phantom orbital contains an odd number of orbitals, the former class has one more orbital than does the latter. Hence,

$$\sum_N (\varrho_N)_{lm}{}^u = 2^{i-n}, \quad (30)$$

and

$$\sum_N \rho_N = \sum_u \sum_{l,m} c_l{}^u c_m{}^u 2^{i-n} = 1, \quad (31)$$

since the expression on the right of Eq. (31) corresponds to the condition for normalization of the ground-state wave function.

III. NAPHTHALENE NEGATIVE ION

The valence-bond theory of the previous section is here applied to a pi-electron calculation of the naphthalene negative ion. This ion radical is of particular interest because it is a simple, unsubstituted aromatic hydrocarbon, with nonequivalent carbon and hydrogen positions present in the molecule. Since only carbon-carbon interactions appear, it is possible to determine the relative importance of Coulomb, exchange, and transfer integrals. Also the availability of electron-spin resonance data and molecular orbital calculations for the molecule permits a comparison of the various approaches to the pi-electron spin and charge distributions.

For notational purposes, we label the naphthalene framework according to the diagram

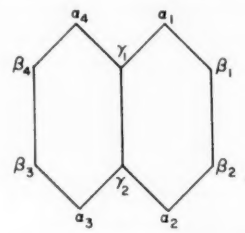

In the negative ion, the electron pair can appear in any of the ten orbitals, that is, in the four equivalent ones of type α, the four equivalent ones of type β, or the two equivalent ones of type γ. Upon addition of the phantom orbital and electron, the pi-electron system constitutes a twelve-electron, eleven-orbital problem. The large number of distributions and structures [Eq. (1)] forming a complete set is such that some

simplifications are necessary. All polar structures with charge separation in addition to the negative charge on the ion should make a relatively small contribution and are neglected. This reduces the number of distributions to ten, each with one doubly occupied and ten singly occupied orbitals (including the phantom orbital). Since these ten distributions correspond to 420 canonical structures, and use of the molecular symmetry does not reduce this number to a reasonable size, the additional assumption is made that only unexcited structures [structures without long bonds] contribute appreciably to the ground-state wave function. For the electron pair in the α_1 position, there are seven unexcited structures, for the β_1 position there are six, and for the γ_1 position, five. Typical canonical structures for the three types of distributions are:

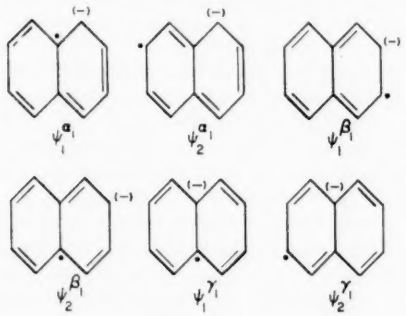

The symmetry operations of group C_{2v} convert the eighteen structures for the α_1, β_1, and γ_1 positions into a complete set of 62 unexcited structures. For the ground state, the resulting secular determinant is of order sixteen, with each of the basis functions corresponding to the completely symmetric linear combination of appropriate structures. For example, one such basis function is

$$\psi_1^{\alpha}=\psi_1^{\alpha_1}+\psi_1^{\alpha_2}+\psi_1^{\alpha_3}+\psi_1^{\alpha_4}, \tag{32}$$

where $\psi_1^{\alpha_1}$ is the structure shown in the diagram and the remaining $\psi_1^{\alpha_i}$ are the structures obtained by applying the operators of C_{2v} to $\psi_1^{\alpha_1}$.

The matrices **H** and **S** making up the secular equation have the block form

$$\begin{pmatrix} (\alpha,\alpha) & (\alpha,\beta) & (\alpha,\gamma) \\ (\beta,\alpha) & (\beta,\beta) & (\beta,\gamma) \\ (\gamma,\alpha) & (\gamma,\beta) & (\gamma,\gamma) \end{pmatrix}$$

in which (α,α), (β,β), and (γ,γ) are square matrices of order seven, six, and three, formed from the basis functions with the electron pair in the α, β, and γ positions, respectively. Since the basis functions are linear combinations of structures corresponding to different distributions (e.g., α includes α_1, α_2, α_3, α_4), transfer integrals, as well as Coulomb and exchange integrals, appear in the diagonal blocks. For the off-diagonal blocks, only transfer integrals are required. The coefficients of all of the integrals in the matrix elements can be obtained by forming superposition diagrams and applying the results of the previous section [Eqs. (6), (7), and appropriate forms of Eq. (10)]. Since the Hamiltonian matrix is symmetric and of order sixteen, there are 105 distinct elements to be evaluated when the $(\alpha\gamma)$ block is neglected (see below). Each of the basis functions [Eq. (32)] must be decomposed into the appropriate linear combination of canonical structures. In many cases this means that several superposition diagrams must be considered for a single matrix element. Furthermore, permutations of the type illustrated by the example in Sec. II arise in some instances. Although relatively straightforward, the set of manipulations required for the construction of the matrix is very lengthy. However, we do not reproduce the work here since it depends on the specific canonical structures that are employed.

A variety of integrals occur in the elements of the energy matrix. There are the standard Coulomb integrals and exchange integrals for the three different types of distributions. In the first approximation we assume that all of the Coulomb integrals are equal, that all but the nearest-neighbor exchange integrals are zero and that all of the nonzero exchange integrals are equal. The transfer integrals are of two types, both of which were mentioned in the previous section. There are those of the form $\langle aabc\cdots \mid \mathcal{H} \mid abbc\cdots\rangle$, which correspond to an orbital-orbital jump $(a\rightarrow b)$ by one electron, and those of the form $\langle aabcd\cdots \mid \mathcal{H} \mid adbcb\cdots\rangle$, which correspond to a rearrangement involving more than two orbitals. We neglect all of the transfer integrals of the latter type and in the former include only those with electron jumps between adjacent atoms. These are all taken to have the same value. With such simplifying assumptions, the form of the ground-state wave function is independent of the Coulomb integral and depends only on the ratio of the transfer integral (τ) to the exchange integral (ϵ). To estimate the ratio (τ/ϵ) we use a two-center approximation and shielded carbon core (see Appendix). With the component integrals listed in the Appendix, we obtain $\epsilon=-2.32$ ev and $\tau=-5.68$ ev with $\tau/\epsilon=2.44$ for an internuclear distance $R=1.41$ A. The value of ϵ is in good agreement with the more complete exchange integral calculation made by Altmann[13] ($\epsilon=-2.27$ ev for $R=1.39$ A), and with an empirical estimate of Coulson and Altmann[14] ($\epsilon=-2.46$ ev for $R=1.39$ A). No comparable attempts to evaluate transfer integrals have been made, although Simonetta[9] suggests that the transfer integral arising in his calculation should be less than ϵ, in contrast to the τ value obtained here.

[13] S. L. Altmann, Proc. Roy. Soc. (London) **A210**, 327, 343 (1951).

[14] C. A. Coulson and S. L. Altmann, Trans. Faraday Soc. **48**, 293 (1952).

TABLE I. Pi-electron spin densities in the naphthalene negative ion.

	ρ_α	ρ_β	ρ_γ
Valence-bond theory			
Calculated coefficients	0.187	0.072	−0.018
Equal coefficients	0.121	0.093	0.072
Molecular-orbital theory			
Hückel theory (single config.)[a]	0.181	0.069	0.000
Hückel theory (config. inter.)[b]	0.221	0.054	−0.050
Approx. SCF (extended)[c]	0.211	0.055	−0.032

[a] E. DeBoer and S. Weissman, J. Am. Chem. Soc. **80,** 4549 (1958).
[b] G. J. Hoijtink, Mol. Phys. **1,** 157 (1958).
[c] A. D. McLachlan, Mol. Phys. **3,** 233 (1960).

Spin Distribution

Solution of the naphthalene negative ion secular equation for $(\tau/\epsilon)=2.44$ makes possible a determination of the ground-state wave function Ψ[Eq. (2)]. From Ψ, the spin distribution in the pi-electron system is calculated by means of Eqs. (19), (24), and (25). The resulting spin densities on the three types of carbon atoms are found to have the values given in Table I. For comparison the results of a number of other calculations are also listed in the table. The second valence-bond treatment was made with the assumption that every unexcited structure contributes equally to the ground-state wave function.[15] Of the three molecular-orbital calculations, the first[16] is based on single-configuration Hückel theory, the second[17] includes configuration interaction with the excited states of the ion, and the third[18] uses a perturbation approach to obtain an LCAO approximation to the unrestricted Hartree-Fock function.

It is seen that all of the theoretical results (except for the equal-coefficient approximation) are in qualitative agreement; that is, the spin density ρ_α is large and positive (on the order of 0.2), while ρ_β and ρ_γ are both considerably smaller with ρ_β positive, and ρ_γ negative or zero. Quantitatively, however, considerable differences are found among the calculations. To evaluate these differences, as well as to test the qualitative conclusions, it would be helpful to have accurate experimental values for the spin densities at all three positions. Although these are not available, an estimate of the ratio (ρ_α/ρ_β) can be made by means of the proton hyperfine splittings measured for the α and β position. Using the simple proportionality suggested by McConnell,[1] we write

$$a_H=Q\rho_c, \tag{33}$$

where a_H is the experimental hyperfine splitting constant for the proton H, ρ_c is the unpaired spin density in the pi orbital of the attached carbon atom, and Q is a "constant," which is assumed to be approximately independent of ρ_c and the other structural features of the molecule.[1,19] With Q the same for the α and β positions, the most recent experimental work of Atherton and Weissman[20] on the naphthalene negative ion yields

$$\left|\frac{a_H(\alpha)}{a_H(\beta)}\right|=\frac{4.95}{1.87}=\frac{\rho_\alpha}{\rho_\beta}=2.65. \tag{34}$$

In Table II, we list the value for (ρ_α/ρ_β) obtained by the various theoretical approaches to the pi-electron spin density. It is seen that the valence-bond theory based on the calculated coefficients and the *simplest* Hückel theory are in very good agreement with the experimental ratio. The more refined molecular-orbital approaches, as well as the oversimplified valence-bond model, are considerably in error.

In comparing the theoretical spin density ratio with the hyperfine measurements, it is possible to argue that Q is not exactly constant. One might expect that Q would depend on the net charge of the carbon to which the proton is bonded. Both theory and experiment[21] indicate that Q decreases with increasing negative charge on the atoms. Writing $Q=Q_0(1+kq)$ for the first terms of a power series expansion of Q as a function of the charge q on the carbon atom, we find that the work of Carrington *et al.*[21] suggest that k is on the order of $+0.01$ ($q<0$ for a negative charge). Correction of the refined molecular-orbital calculations[17,18] by a Q variation of this magnitude would leave the (ρ_α/ρ_β) ratio still far from agreement with experiment.

TABLE II. Hyperfine splitting results for the naphthalene negative ion.

	ρ_α/ρ_β	Q[e] (gauss)	$a_H(\alpha)$ (gauss)	$a_H(\beta)$ (gauss)
Valence-bond theory				
Calculated coefficients	2.60	−26.3	−4.93	−1.89
Equal coefficients	1.30	−31.9	−3.86	−2.96
Molecular orbital theory				
Hückel (single config.)[a]	2.62	−27.2	−4.91	−1.87
Hückel (config. inter.)[b]	4.09	−24.7	−5.46	−1.33
Approx. S. C. F. (extended)[c]	3.83	−25.6	−5.39	−1.41
Experiment[d]	2.65	—	±4.95	±1.87

[a–c] See footnotes of Table I.
[d] N. M. Atherton and S. I. Weissman, J. Am. Chem. Soc. **83,** 1330 (1961).
[e] Q is chosen so as to fit the experimental width of the electron resonance spectrum, which is equal to 27.3 gauss[d].

[15] Approximate valence-bond calculations of this type have frequently been used, e.g., L. Pauling, *Nature of the Chemical Bond* (Cornell University Press, Ithaca, New York, 1960).
[16] E. de Boer and S. Weissman, J. Am. Chem. Soc. **80,** 4549 (1958).
[17] G. J. Hoijtink, Mol. Phys. **1,** 157 (1958).
[18] A. D. McLachlan, Mol. Phys. **3,** 233 (1960).
[19] H. M. McConnell, J. Chem. Phys. **24,** 764 (1956).
[20] N. M. Atherton and S. I. Weissman, J. Am. Chem. Soc. **83,** 1330 (1961).
[21] A. Carrington, F. Dravnieks, and M. C. R. Symons, J. Chem. Soc. **1959,** 947.

To obtain theoretical values for the hyperfine splitting constants $a_H(\alpha)$ and $a_H(\beta)$, a knowledge of Q is required. Detailed calculations on simple model systems[22] indicate that Q is on the order of -25 gauss. Attempts to fit a variety of experimental measurements have yielded Q values between -20 and -28 gauss.[18] The uncertainty in these estimates makes difficult a direct comparison of theory and experiment in the naphthalene negative ion. As an alternative,[18] we select a Q value for each calculation by requiring agreement between predicted and measured widths of the entire electron-spin resonance spectrum. From Table II, we see that only the complete valence-bond theory and the simple Hückel theory give good results, although the Q values are somewhat higher than those required for the more detailed molecular-orbital calculations.

Charge Distribution

The charge distributions of molecules and ions are of considerable interest, particularly because of their probable relationship to reactivities. Although there are no measurements of the charge distribution for the naphthalene negative ion, a comparison of the theoretical results is possible. For a valence-bond wave function [Eq. (2)], the atomic charges q_N can be calculated by means of Eq. (28). Using the coefficients c_l^u determined by solution of the appropriate secular equation with $\tau/\epsilon=2.44$, we find the values $q_\alpha=0.104$, $q_\beta=0.143$, and $q_\gamma=0.008$ for the charge densities in the three positions. As was true for the spin density (Table I), almost all of the charge is in the α and β positions. However, the distribution of charge between the two positions is very different from the spin densities. We see that the ratio (q_α/q_β) is equal to 0.73, while (ρ_α/ρ_β) equals 2.60. To find the origin of this difference we examine the contribution to the spin densities made by structures with the chage in each type of position (Table III). Here the symmetric basis functions [e.g., Eq. (32)] are used and ρ_α, for example, is the average spin density for the four α positions resulting from the charge on any one position. We see that there is no simple relationship between atomic charges and spins. In particular, the charge in the α positions contributes significantly to both ρ_α and ρ_β, while for the charge in the β positions a large ρ_α contribution results, with only a negligible (actually negative) ρ_β term. Since q_γ is very small, its spin density terms have little effect. Additional insight can be obtained by looking at the simplified valence-bond treatment (equal-coefficient approximation). Here one finds that the charges and spin densities are nearly identical with $(q_\alpha/q_\beta)\cong(\rho_\alpha/\rho_\beta)\cong1.3$. In going from this result to the calculation with variationally-determined coefficients, charge is shifted from the α to the β positions and the ratio (q_α/q_β) decreases. Concomitantly, the ratio (ρ_α/ρ_β) is increased, since the spin and charge are complementary in valence-bond theory (e.g., for a neutral AB system with a pure covalent bond [one electron on A and one on B], the negative ion formed by adding an electron to A has the unpaired spin on B).

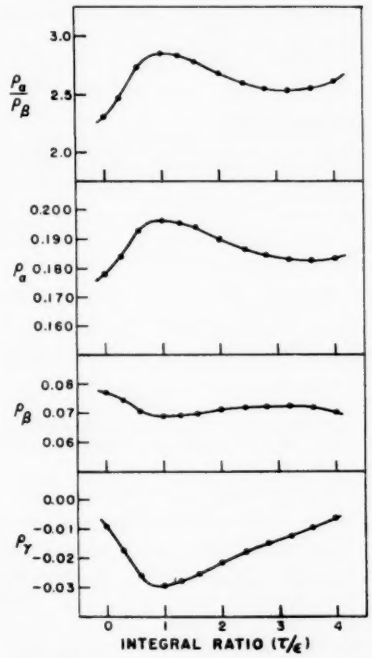

FIG. 1. Naphthalene negative ion pi-electron spin densities as a function of the transfer integral to exchange integral ratio (τ/ϵ). It should be noted that the scales are drawn so as to *exaggerate* the small changes that occur when (τ/ϵ) is varied.

Comparison of the valence-bond results with molecular orbital theory shows a striking contrast. For the simple Hückel theory, whose spin densities agree closely with the valence-bond values, the charges are very different. Since the alternant character of the naphthalene molecule requires that all atoms be neutral in the Hückel theory with equal atomic integrals,[23] the charge distribution is exactly equal to the spin distribution. From Table I, we have $q_\alpha=0.181$, $q_\beta=0.69$, and $q_\gamma=0$ with $(q_\alpha/q_\beta)=2.62$, in contrast to the valence-

TABLE III. Charge distribution contributions to spin densities.

	ρ_α	ρ_β	ρ_γ
Charge			
$q_\alpha=0.104$	0.033	0.073	−0.003
$q_\beta=0.143$	0.155	−0.002	−0.009
$q_\gamma=0.008$	−0.003	0.003	0.006

[22] H. S. Jarrett, J. Chem. Phys. **25**, 1289 (1956); M. Karplus, *ibid.* **30**, 15 (1959).

[23] C. A. Coulson and G. S. Rushbrooke, Proc. Cambridge Phil. Soc. **36**, 193 (1940).

TABLE IV. Variation of pi-electron spin densities with integral parameters.

	ρ_α	ρ_β	ρ_γ
1. ΔC variation $(\tau/\epsilon=2.44)$[a]			
(a) $\Delta C/\epsilon=0$	0.1869	0.0721	−0.0180
(b) $\Delta C/\epsilon=0.35$	0.1858	0.0727	−0.0170
(c) $\Delta C/\epsilon=0.70$	0.1843	0.0736	−0.0160
2. Bond-length variation $(\tau/\epsilon=2.44)$[b]			
(a) $\epsilon'/\epsilon=1, \tau'/\epsilon=2.44, \Delta C/\epsilon=0$	0.1869	0.0721	−0.0180
(b) $\epsilon'/\epsilon=1.4, \tau'/\epsilon=2.68, \Delta C/\epsilon=0$	0.1698	0.0788	0.0028
(c) $\epsilon'/\epsilon=1.4, \tau'/\epsilon=2.68, \Delta C/\epsilon=0.35$	0.1688	0.0792	0.0039

[a] See text for the definition of ΔC.
[b] ϵ' and τ' are, respectively, the exchange and transfer integral for the α—β bond, while τ and ϵ are the corresponding integrals for all other bonds.

bond value of 0.73 for this ratio. If the approximate self-consistent field calculation of McLachlan[18] is used instead of the simple theory, the charge distribution is negligibly altered (± 0.02 electrons) in spite of the fact that the spin densities change so as to increase the (ρ_α/ρ_β) ratio to 4.7.

The difference between the molecular orbital and valence-bond charge distributions cannot be resolved at present because of the lack of pertinent experimental data, as well as of more detailed calculations. Both the molecular orbital and valence-bond treatments used here are limited, since the approximations are such that the neutral naphthalene molecule would have a uniform charge distribution. Removal of this restriction in the valence-bond method would require the introduction of ionic structures for the neutral system; no such calculations have been made as yet. In the molecular-orbital approach, refinements beyond the approximate self-consistent field theory of Pople[24] are required. Variation in the atomic integrals, as well as the resonance integrals, would have to be included. Such a calculation has been made for naphthalene by Pritchard and Skinner,[25] who examined the effect on the bond orders and charges resulting from an adjustment of the atomic integral of the γ carbon atoms. No corresponding study has been made on the naphthalene negative ion. Qualitatively, one might expect from the results of the molecular orbital calculations that a reduction in the (q_α/q_β) ratio would be required to obtain the experimental (ρ_α/ρ_β) ratio in the self-consistent theory.[25a] Such a charge shift would bring the molecular-orbital results somewhat closer to the valence-bond treatment. However the main point of this discussion is *not* to argue that the valence-bond charge distribution is more likely to be correct than that obtained from molecular orbital theory, but rather to point out that additional calculations are required to obtain a reliable charge distribution for the naphthalene negative ion, as well as for naphthalene itself.

[24] J. A. Pople, Trans. Faraday Soc. **49,** 1375 (1953). See also C. A. Coulson and J. Jacobs, Proc. Roy. Soc. (London) **A206,** 287 (1956), R. Pariser, J. Chem. Phys. **24,** 250 (1956), and A. Brickstock and J. A. Pople, Trans. Faraday Soc. **50,** 901 (1954).
[25] H. O. Pritchard and F. H. Skinner, Trans. Faraday Soc. **51,** 457 (1955).
[25a] *Note added in proof.* A calculation of this type has been done by J. Colpa (private communication); see also the recent publication of J. R. Hoyland and L. Goodman, J. Chem. Phys. **34,** 1446 (1961).

Parameter Variation

Since the valence-bond calculation is in good agreement with the experimental (ρ_α/ρ_β) ratio, it is of some interest to determine the sensitivity of the results to the values of the integral parameters. This is particularly true because few valence-bond treatments have been done for ionic systems. With the assumptions given at the beginning of this section, the only parameter affecting the spin densities is the ratio (τ/ϵ). For τ/ϵ between 0 and 3, Fig. 1 gives the values found for the spin densities and the (ρ_α/ρ_β) ratio. It is seen that the results are relatively insensitive to the (τ/ϵ) parameter in the reasonable range of values (0.5 to 3). For agreement with the "experimental" (ρ_α/ρ_β) ratio, τ would have to be equal to about 2.2ϵ, which is close to the value calculated from the molecular integrals. From the figure, it is evident that $(\tau/\epsilon)\cong 0.5$ would also yield the correct result. As τ/ϵ becomes small however, (ρ_α/ρ_β) changes more rapidly and actually becomes less than unity for negative (τ/ϵ) values.

In the treatment of the naphthalene negative ion, the assumption was made that the Coulomb integrals for the three different arrangements are equal. This is certainly not exactly correct. By considering the effect of an atom-to-atom jump in the two-center approximation, one finds that the Coulomb integral with the negative charge in the γ position should be somewhat smaller than it would be for the charge in the α or β position. Crude estimates indicate that ΔC, the difference be-

TABLE V. Integral and energy values.

R (A)	1.32	1.41	1.50
$(ZR/2a_0)$	4.00	4.25	4.50
$W(2p)$ (ev)	−9.0	−9.0	−9.0
$\langle a \mid b \rangle$	0.2869	0.2510	0.2186
$\langle a \mid e^2/r_a \mid b \rangle$ (ev)	4.094	3.478	2.944
$\langle a \mid e^2/r_b \mid a \rangle$ (ev)	9.820	9.345	8.908
$\langle ab \mid e^2/r_{12} \mid ba \rangle$ (ev)	1.144	0.8609	0.6426
$\langle ab \mid e^2/r_{12} \mid aa \rangle$ (ev)	3.720	3.179	2.744
$\langle ab \mid e^2/r_{12} \mid ab \rangle$ (ev)	9.341	8.924	8.536
ϵ (ev)	−3.13	−2.32	−1.71
τ (ev)	−6.57	−5.68	−4.81
τ/ϵ	2.10	2.44	2.81

tween the Coulomb integrals, should be of the order of a few tenths of an electron volt. Calculations for $\Delta C/\epsilon$ equal to 0.35 and 0.70 are given in Table IV. It is seen that the unpaired spin densities are only negligibly affected by this refinement.

Another possible concern in the valence-bond treatment is the dependence of the integrals on differences among the bond lengths. If we assume that naphthalene and the naphthalene negative ion have the same structure,[26] the α—β bond ($R_{\alpha\beta}=1.36$ A) is somewhat shorter than the other bonds ($R_{\beta\beta}=1.40$ A, $R_{\alpha\gamma}=1.42$ A, $R_{\gamma\gamma}=1.40$ A). On the basis of these bond lengths, a trial calculation was made with

$$R_{\alpha\beta}=1.32\text{ A}(ZR/2a_0=4.00)$$

and

$$R_{\beta\beta}=R_{\alpha\gamma}=R_{\gamma\gamma}=1.41\text{ A}(ZR/2a_0=4.25).$$

Both $\Delta C/\epsilon=0$ and $\Delta C/\epsilon=0.35$ were considered; the resulting spin densities are given in Table IV. Again the changes from the basic treatment are relatively small, although somewhat larger than for $(\Delta C/\epsilon)\neq 0$ alone. The ratio (ρ_α/ρ_β) shows that the introduction of the bond-length variation actually gives worse agreement with experiment (on the basis of a constant Q) than the basic treatment. Of course, the wrong choice of $R_{\alpha\beta}$, which was made for convenience in the integral evaluation, overemphasizes the bond-length effect.

The relative lack of sensitivity of the spin densities to the exact values of the various valence-bond parameters can be regarded from two points of view. It suggests that the valence-bond result is more reliable than might have been expected, since one of the most uncertain aspects of the calculation is the integral parameter evaluation. However, it does make difficult the use of hyperfine measurements for the determination of empirical integral parameters, which could be employed for the estimation of other properties of naphthalene or related molecules.

ACKNOWLEDGMENT

This work was begun while the authors were in the Department of Chemistry of the University of Illinois. They wish to thank Dr. H. S. Gutowsky for some stimulating conversations concerned with the subject of this paper. Also, they thank Dr. G. K. Fraenkel for helpful comments. Grateful acknowledgment is made for the support provided by a General Electric predoctoral fellowship (J.S.C.) and a National Institute of Health post-doctoral fellowship (T.H.B.). Also, we thank the Digital Computer Laboratory of the University of Illinois and the Computational Analysis Section of the Gulf Research and Development Company for assistance with the calculations.

APPENDIX

The integrals ϵ and τ were estimated by expressing them in terms of a two-center approximation of the form

$$\epsilon=\langle a(1)b(2)\mid \mathcal{H}\mid b(1)a(2)\rangle \qquad \text{(A1)}$$

$$\tau=\langle a(1)b(2)b(3)\mid \mathcal{H}\mid a(1)a(2)b(3)\rangle, \qquad \text{(A2)}$$

where a and b are pi orbitals on adjacent carbon nuclei and $\mathcal{H}$ is an effective two-center Hamiltonian. From Eqs. (A1) and (A2), we have

$$\epsilon=e^2\{2W(2p)\langle a\mid b\rangle^2+(\langle a\mid b\rangle^2/R)+\langle ab\mid 1/r_{12}\mid ba\rangle -2Z_e\langle a\mid b\rangle\langle a\mid 1/r_a\mid b\rangle\}, \qquad \text{(A3)}$$

and

$$\tau=e^2\{3W(2p)\langle a\mid b\rangle+(\langle a\mid b\rangle/R)+\langle ab\mid 1/r_{12}\mid ab\rangle \times\langle a\mid b\rangle-2\langle a\mid 1/r_b\mid a\rangle\langle a\mid b\rangle+2\langle ab\mid 1/r_{12}\mid aa\rangle -Z_e\langle a\mid 1/r_a\mid b\rangle\} \qquad \text{(A4)}$$

For a carbon core-potential[27] with $Z_e=1.542$ and Slater functions with $Z=3.18$, the required integral values were obtained for the three internuclear distances $R=1.32$, 1.41, and 1.50 A by the use of appropriate tables and formulas.[28] The $W(2p)$ value was determined from the experimental ionization potential of the methyl radial,[29] which should be closer to the desired quantity than the valence-state ionization potential of an isolated carbon atom.

A list of values is given in Table V.

As a crude test of the approximations, estimates were made for ϵ and τ with the inclusion of four-center interactions (i.e., the orbitals a and b and their next-neighbor carbon orbitals). The extra terms yielded small corrections ($\sim$5 to 10%), which were positive for both ϵ and τ. Since only the ratio τ/ϵ is of interest here, these corrections were neglected.

[26] F. Ahmed and D. Cruickshank, Acta Cryst. **5,** 852 (1952). D. W. J. Cruickshank and R. A. Sparks, Proc. Roy. Soc. (London) **A258,** 270 (1960).

[27] M. Karplus, J. Chem. Phys. **30,** 11 (1959).

[28] J. Miller, J. M. Gerhauser, and F. A. Matsen, *Quantum Chemistry Integrals and Tables* (University of Texas Press, Austin, Texas, 1959). M. Kotani, A. Amemiya, E. Ishiguro, and T. Kimura, *Tables of Molecular Integrals* (Maruzen Co. Ltd., Tokyo, Japan, 1955).

[29] G. Herzberg and J. Shoosmith, Can. J. Phys. **34,** 523 (1956).

Markoff Chain Model for Growth of Polymer Single Crystals

FRASER P. PRICE

General Electric Research Laboratory, Schenectady, New York

(Received March 24, 1961)

A theory is presented wherein the development of a polymer single crystal is envisioned as the successive coherent addition of layers of segments of polymer molecules, each layer acting as the substrate for the succeeding layer. The substrate is assumed smooth and the distribution of segment lengths in the next layer is assumed to be controlled by equilibrium considerations. The theory predicts that as the supercooling is increased the energy gained due to the bulk energy of crystallization tends to overwhelm the energy lost due to formation of new surfaces. This has the result of making the average segment length of the adding layer closer and closer to the substrate length. In some cases it even exceeds the substrate length. The net result is that the temperature dependence of ultimate crystal thickness is not as great as was implied by the $(\Delta T)^{-1}$ laws of previous theories.

The theory has been satisfactorily fitted to the experimentally observed dependence on temperature of single crystals of linear polyethylene grown from dilute xylene solution. The parameters used to fit theory to experiment are a lateral surface energy of 13.3 ergs/cm², an end (fold surface) energy of 110 ergs/cm², and a solution temperature of 113°C. The theory also indicates that the surface of the polyethylene crystals is remarkably smooth with an average roughness of only one to two angstroms. Predictions are also made concerning the profile of a single crystal in the region of its primary nucleus (central region). It is shown that hollows, sharp spikes, or flat topped mesas of considerable extent may be observed depending on the supercooling.

EVER since the first description of single crystals of polymers precipitated from dilute solution was presented,[1–3] there has been considerable interest in obtaining explanations for this intriguing phenomenon. Recently, two types of theories have been proposed. One by Fischer and Peterlin[4] explains the phenomenon in terms of an equilibrium situation where the extreme anisotropy of the polymer crystal due to the covalent bonds along the chain direction causes the energy of the crystal to increase as the thickness in the chain direction increases. This increase in energy is offset by a decrease in surface energy and the net result is a temperature dependent preferred thickness in the chain direction. The other type of theory, proposed independently and essentially simultaneously by the author,[5] and by Hoffman and Lauritzen,[6] considers the phenomenon of chain folding to be controlled by kinetic considerations. In the latter theory, the growth of the crystal is controlled by the formation of coherent folded nucleii on the existing crystal substrate. The fold length and hence the thickness of the adding layer is determined by the appropriate interfacial energies and by the bulk free energy of transformation (the supercooling). Once a nucleus of critical size or larger was formed, it is envisioned that the new layer expands by the folding of additional segments of the chain, each fold length being identical to that of nucleus. This process continues in a direction parallel to the fold plane until a crystal edge is reached. Thus the fold surfaces of the adding layer are mathematically smooth. This paper, in part, considers the situation in which these surfaces are not required to be smooth but rather neighboring fold lengths are allowed to differ thus giving a distribution of fold lengths within the adding layer.

Further, the nucleation type theories examine only very cursorily the problem of the addition of many layers, one upon the other. This paper examines this problem in considerable detail. It is important to do so, because the actual experimental observation of morphology (average crystal thickness as well as deviation from that average) depends not on a single layer but upon many such layers.

Frank and Tosi[7] have recently published a treatment of this problem from the point of view of a flux determined situation. The present paper approaches the problem from the point of view of a restricted equilibrium.

THE MODEL

Consider a layer of folded polymer molecules laid down coherently on a smooth substrate of height B, as is shown schematically in Fig. 1. We will do this by first breaking the dissolved polymer molecule into a large number N of segments of various lengths $b_k+\Delta$. The length Δ is the contour length of a fold. For purposes of convenience we will measure b_k in terms of B. Let

$$b_k = x_k B, \tag{1}$$

where x_k has the range $x_{k\,\min}$ to infinity. We will identify $x_{k\,\min}$ with the critical nucleus length in the b direction as defined in previous papers.[5,6] This critical nucleus length can be shown to be that length for which the bulk free energy of transformation is just balanced by the energy of the end surfaces ($h-\Delta a$ surfaces).

[1] P. H. Till, J. Polymer Sci. **24**, 301 (1957).
[2] A. Keller and A. O'Connor, Discussions Faraday Soc. **25**, 114 (1958).
[3] A. Keller, Phil. Mag. **2**, 1171 (1957).
[4] A. Peterlin and E. W. Fischer, Z. Physik **159**, 272 (1960).
[5] F. P. Price, J. Polymer Sci. **42**, 49 (1960).
[6] J. I. Lauritzen, Jr. and J. D. Hoffman, J. Research Natl. Bur. Standards **A64**, 73 (1960).
[7] F. C. Frank and M. P. Tosi, Proc. Roy. Soc. (London) (to be published).

Lengths shorter than this will have a positive free energy of deposition and hence will be neglected.

Next we lay the segments down on the substrate so that they are coherent with the substrate but do not touch each other. We will consider only the length b_k of each segment to be coherent with the substrate. For each length b_k there will be a certain amount of energy V_{x_k} involved in this step.

We then bring the segments into contact along their lateral surface. This destroys some surface between neighboring segments. The destruction of this surface gives back an amount of energy $V_{x_k,x_{k+1}}$ for each pair.

We then make folds between each pair of segments using the contour length Δ and reconnect the segments. An amount of energy δ is required to make the fold. The energy of recombination is just canceled by the energy of the original scission of the chain and thus may be neglected.

We will describe the chain of segments constructed in this manner by the conditional probability functions

$$p_{k,k+1}(x, x') = \text{probability that } x_{k+1} = x' \text{ given that } x_k = x. \quad (2)$$

We will assume the chain to be Markoffian—that is, that $p_{k,k+1}$ is independent of the position "k" in the chain. Thus

$$p_{k,k+1}(x, x') = p(x, x') \quad (3)$$

for all possible N values of "k."

The following joint distribution functions may then be introduced:

$$q^{(1)}(x) = \text{probability of finding any } x_k = x \text{ in chain},$$

$$q^{(2)}(x, x') = \text{probability of finding } x_k = x,\ x_{k+1} = x',$$

$$q^{(3)}(x, x', x'') = \text{probability of finding } x_k = x,\ x_{k+1} = x',\ x_{k+2} = x'', \quad (4)$$

etc.; and from (3) and (4) the following may be obtained:

$$q^{(2)}(x, x') = q^{(1)}(x)\,p(x, x'),$$

$$q^{(3)}(x, x', x'') = q^{(1)}(x)\,p(x, x')\,p(x', x''), \text{ etc.} \quad (5)$$

The following restrictions apply:

$$\sum_x p(x, x') = 1 \text{ for all } x',$$

$$\sum_x q^{(1)}(x) = 1,$$

$$\sum_x \sum_{x'} q^{(2)}(x, x') = 1,$$

$$q^{(1)}(x) = \sum_{x'} q^{(2)}(x, x') = \sum_{x'} \sum_{x''} q^{(3)}(x, x', x''). \quad (6)$$

Now, there are many such chains of N segments as are described by the q's or p's. We wish to find the most probable chain. This we will assume to be that for which the average free energy per segment in the completed chain is at a minimum (the equilibrium chain). To do this we follow Mullins.[8] His derivation shows that the distribution $q^{(1)}(x)$ that we seek is defined by

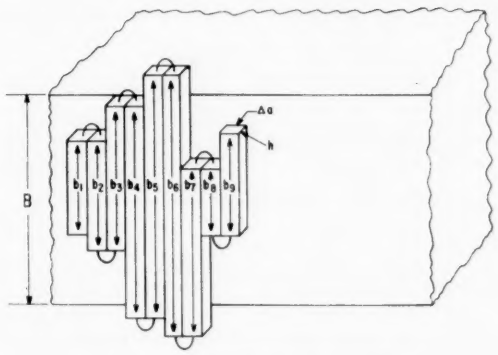

FIG. 1. Schematic diagram of model.

$$q^{(1)}(x) = C^2(x), \quad (7)$$

where $C^2(x)$ is defined by

$$C(x) = \lambda \sum_{x'} C(x') \exp[-u(x, x')] \quad (8)$$

when λ the smallest possible positive eigenvalue with the eigenvector normalized to unit length and

$$u(x, x') = E(x, x')/kT, \quad (9)$$

where $E(x, x')$ = the average energy of laying down the pair, (x, x') including the folds plus the interaction energy of the pair (x, x').

Further, we will be interested in the binary probability

$$q^{(2)}(x, x') \quad (10)$$

which can be shown to be

$$q^{(2)}(x, x') = \lambda C(x) C(x') \exp[-u(x, x')]. \quad (11)$$

We will be particularly interested in the average value of

$$\bar{x} = \sum x C^2(x) / \sum C^2(x) \quad (12)$$

and the average value of the absolute difference between x and x',

$$\langle | x - x' | \rangle_{Av} = \sum_x \sum_{x'} | x - x' | q^{(2)}(x, x'). \quad (13)$$

ENERGETICS

Here we will be concerned with the form of the expression $u(x, x')$. First, we note that the conditions expressed in Eqs. (2) and (3) make b_k, V_{x_k}, and $V_{x_k,x_{k+1}}$ independent of "k" and we may write

$$b_k = b = xB,$$

$$V_{x_k} = V_x,$$

$$V_{x_k,x_{k+1}} = V_{x,x'}. \quad (14)$$

[8] W. W. Mullins, Phys. Rev. **114**, 389 (1959).

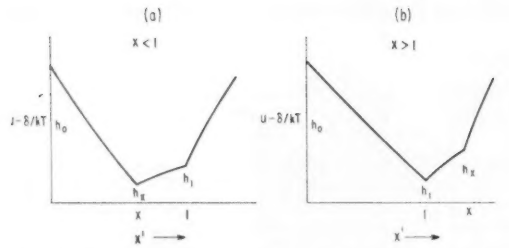

FIG. 2. Plots of reduced length of adding segment (x') vs energy of addition ($u-\delta/kT$).

The energy required to lay down a length $b=xB$ including the fold is

$$V_x=-h\Delta a\Delta G_V Bx+2hB\sigma_2 x+\delta \quad \text{when } x<1,$$
$$=-h\Delta a\Delta G_V Bx+2hB\sigma_2 x+2\Delta aB\sigma_2(x-1)+\delta \quad \text{when } x>1, \quad (15)$$

and similarly for $V_{x'}$.

The pair interaction energy is

$$V_{xx'}=-2hB\sigma_2 Y, \quad (16)$$

where $Y=x$ or x' whichever is smaller. In the above expressions, h and Δa have the significance indicated in Fig. 1, σ_2=interfacial energy of lateral, $(b-h)$ surfaces, δ=energy required to make fold, ΔG_V=bulk free energy of transformation per unit volume under the particular thermodynamic conditions under consideration. We will approximate ΔG_V by

$$\Delta G_V=\Delta H_V(\Delta T/T_m), \quad (17)$$

where ΔH_V=bulk enthalpy of transformation, ΔT=supercooling, T_m=melting point or solution temperature of the macroscopic single crystal.

Then

$$E(x,x')=\tfrac{1}{2}(V_x+V_{x'})+V_{xx'}. \quad (18)$$

If Eqs. (9) and (15)–(18) are combined, the result is

$$u(x,x')=-\alpha(x+x')+\beta\,|\,x-x'\,|+\gamma\beta Z+\delta/(kT), \quad (19)$$

where

$$Z=\begin{cases} x+x'-2 & \text{when } x>1,\ x'>1 \\ x-1 & x>1,\ x'<1 \\ x'-1 & x<1,\ x'>1 \\ 0 & x<1,\ x'<1 \end{cases}$$

and

$$\alpha=\frac{h\Delta aB\Delta H_V\Delta T}{2kTT_m}, \qquad \beta=\frac{\sigma_2 hB}{kT}, \qquad \gamma=\frac{\Delta a}{h}.$$

In the present treatment the free energy of transition has been used while in Mullins'[8] treatment the enthalpy of transition is employed. This procedure is justifiable, since Mullins is concerned essentially only with the identification of the entropy of the chain due to the order of the various chain elements (no other entropy changes are considered), while in the present case an entropy of melting (or solution) obviously is involved. The only proper way to take this into account is to use the free energy of melting rather than only the enthalpy of melting.

It should be mentioned that in this treatment we neglect those segments with $x<1$ which, by virtue of their position on the substrate, still project above one edge of the substrate. It is felt that this omission does not seriously affect the conclusions of the paper inasmuch as (a) the solutions are still rather crude and (b) the available experimental data with which to test the conclusion are also imprecise.

PROPERTIES OF THE MODEL

The desired solution of Eq. (8) is obtained by finding the smallest eigenvalue λ of the matrix A whose elements are

$$A_{xx'}=\exp[-u(x,x')].$$

This may be achieved by finding the largest root $1/\lambda$ of the secular equation of order m

$$|\,A-(1/\lambda)I\,|=0, \quad (20)$$

where m is the order of the square matrix A, and I is the identity matrix. This has been done for a range of values of α, β, and δ for several fixed values of γ by successive iterations of the matrix A with $m=11$. However, before proceeding with a description of the results, it is desirable to examine in more detail the properties of the matrix A. First, it should be noted that in Eq. (19) the term δ/kT is a constant which, when incorporated into the elements $A_{xx'}$ of the matrix, merely multiplies each element by a constant. Since all the functions with which we will be concerned [$C(x)$, $q^{(2)}(x,x')$ etc.] are normalized, this constant can be taken outside the matrix and neglected. Secondly, examination of Eq. (19) shows that it is symmetric in x and x'. Thus the matrix A is symmetric.

TABLE I.

$x<1$		$x>1$	
Intersections			
$h_0=(\beta-\alpha)x$		$h_0=\beta[x(1+\gamma)-1]-\alpha x$	
$h_x=-2\alpha x$		$h_1=\beta(1+\gamma)(x-1)$ $-\alpha(x+1)$	
$h_1\beta(1-x)-\alpha(x+1)$		$h_x=2\gamma\beta(x-1)-2\alpha x$	
Region	Slope	Region	Slope
$x>x'$	$-(\alpha+\beta)$	$x'<1$	$-(\alpha+\beta)$
$x<x'<1$	$\beta-\alpha$	$1<x'<x$	$\beta(\gamma-1)-\alpha$
$1<x'$	$\beta(1+\gamma)-\alpha$	$x<x'$	$\beta(1+\gamma)-\alpha$

This is consistent with the idea that the distribution defined by $C^2(x)$ should be independent of whether the sequence of segments is read from right to left or from left to right. If a matrix had been constructed such that $A_{ij} \neq A_{1i}$, a situation which can be justified on the basis that adding a long segment to a short one involves creation of more surface than adding a short to a long, then this reversibility of sequence is not obtained.

Equation (8) was cast in integral form and Fredholm's method for solution of integral equations was applied. Whereas a solution sufficiently precise to be useful was not obtained by this method, it was possible to show that with no upper limit to the range of x' solutions cannot exist if $\alpha/\beta > \gamma/2$.

Since the function $u(x, x')$ controls the behavior of the system, it is instructive to examine it in more detail. In Fig. 2 are plotted $u - \delta/kT$ versus x' for the cases where $x<1$ and $x>1$.

The heights of the various intersections and the slopes of the lines in the various regions are summarized in Table I.

If the form of Eq. (11) is considered, the plots in Fig. 2 indicate the probability, neglecting considerations of order entropy, of forming a pair xx' given that one member of the pair is x. It can be seen that, with the plots as drawn, if $x<1$, then x' tends to lie close to x; while if $x>1$, x' tends to lie toward unity. Since negative values of x and x' are not permissible, it is conceivable that the slopes of the lines on the right of the plots in Fig. 2 might be small enough to make insufficient the tendency of x' to stay within finite limits. Therefore, it is of interest to examine the behavior of the various slopes. First we note that, since α and β are defined definite positive, the slopes of the left-hand lines in the plots of Fig. 2 are always negative, i.e.,

$$-(\alpha+\beta)<0.$$

Next we inquire when the slope of the left hand is smaller in absolute magnitude than the slope of the extreme right-hand line. Then

$$\alpha+\beta<\beta(1+\gamma)-\alpha$$

or

$$\alpha/\beta<\gamma/2. \tag{21}$$

Since Fredholm's method for the solution of integral equations showed that no solution existed when $\alpha/\beta>\gamma/2$, this is obviously the limiting maximum interesting value of α/β and expresses the condition of equal steepness of extreme slopes.

We will next inquire whether any of the other lines can have negative slopes. In Fig. 2(a), when $x<x'<1$ the slope is negative when

$$0>\beta-\alpha$$

or

$$\alpha/\beta>1. \tag{22}$$

In Fig. 2(b), when $1<x'<x$, the slope is negative when

$$0>\beta(\gamma-1)-\alpha$$

or

$$\alpha/\beta>\gamma-1. \tag{23}$$

In both plots the slope of the line on the extreme right is negative when

$$0>\beta(1+\gamma)-\alpha$$

or

$$\alpha/\beta>1+\gamma. \tag{24}$$

Now, since solutions of Eq. (8) cannot exist for $\alpha/\beta>\gamma/2$ and since, as is shown below, γ is less than 2; the conditions expressed in Eqs. (22) and (24) are not fulfilled. Thus, we infer from Eq. (22) that when $x<1$ and $x<x'<1$, $du/dx'>0$; and from Eq. (24) we infer that the slopes of the extreme right-hand lines in both Figs. 2(a) and 2(b) are positive. In Fig. 2(b) ($x>0$), we can see from Eq. (23) that when $1<x'<x$, only if $\gamma=2$ does $du/dx'=0$. For values of $\gamma<2$, $du/dx'>0$ in this region and the plots are as shown.

We wish now to inquire if there is any limit other than $\alpha/\beta<\gamma/2$ which will restrict our range of interest in solutions of Eq. (8). One such limit obviously is where $\alpha/\beta=0$ for, at this point, $\Delta T=0$ and negative values of ΔT are uninteresting. Another such limit would be that at which the average free energy change per chain segment becomes positive. This is calculable according to Mullins[8] from the smallest eigenvalue of Eq. (8). This average free energy is given by $kT \ln\lambda$. However, we have investigated the behavior of λ as a function of the order of the matrix A and have found it quite sensitive to the order up to order 11. On the other hand, we have found the distributions defined by $C^2(x)$ quite insensitive to the order of the matrix. Therefore, we prefer to define another average free energy change per chain segment by

$$\bar{d}=kT[-2\alpha\bar{x}+\beta\langle|x-x'|\rangle_{Av}]+\delta \tag{25}$$

and to define the range of interest of α and β to that where

$$\bar{d}<0. \tag{26}$$

Thus far we have considered only the addition of one layer of folded molecules to a smooth substrate of height B. A real crystal is built of many such layers each of which acts as a substrate for the next. While it is recognized that the layer serving as substrate probably is not smooth (i.e., all the segment lengths are not equal); if we wish to build up a three dimensional crystal using this model, there is no obvious method other than to make the assumption of smoothness. It will be shown below that in real crystals of polyethylene this assumption is probably quite good, the average roughness being of the order of 1–2 A. Accordingly, we will envision the crystal as being built up by first laying down a layer of average segment length $\bar{x}_1 B$ on the substrate. The length $\bar{x}_1 B$ serves as a smooth

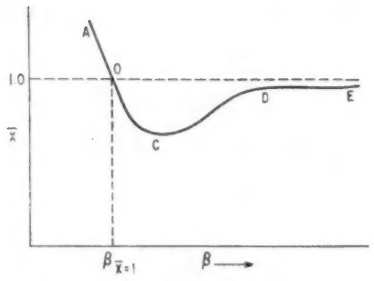

FIG. 3. Generalized plot of $\bar{x}$ vs β.

substrate for the next layer whose average length is $\bar{x}_2\bar{x}_1B$ and so on to the nth layer, the average segment length of which is

$$\bar{b}_n=\bar{x}_n\cdot\bar{x}_{n-1}\cdots\bar{x}_2\cdot\bar{x}_1B. \tag{27}$$

Now if a value of $\bar{x}_n=1$ is ever reached then all subsequent layers will have the same average segment length, and that length will be the final crystal thickness. To actually accomplish this calculation using the model we first return to the definition of α and β [Eq. (19)]. It can be seen that the ratio α/β has (for a given polymer system) ΔT as its only variable. Thus, calculations made at a constant value of α/β are equivalent to crystal formation at a fixed temperature. Further, the form of Eq. (19), aside from the normalizing term involving δ/kT, is such that at fixed ratio of α/β all the terms are proportional to β. Further, β, for a given polymer system, is a function only of the substrate length, B. Thus, various substrate lengths at the same supercooling can be considered by solving Eq. (20) with the matrix elements $(A_{xx'})^r$ with varying values r that are proportional to B and hence to β. Then, if a plot is made of $\bar{x}$ versus β for the fixed α/β, the value of β when $\bar{x}=1$ is proportional to the stable segment length of the crystal and each succeeding layer will have the same average segment length. This stable segment length is thus equal to the constant thickness to which the crystal will ultimately grow. In this manner it is possible to construct theoretical curves of $\beta_{\bar{x}=1}$ versus α/β which have the same shape as crystal thickness versus supercooling curves. The theoretical curves can then be fitted to experimental ones to obtain the pertinent parameters.

We now turn to a more detailed consideration of the morphology of the crystal in the region of its approach to constant thickness. In what follows, we will assume that the growth takes place at constant ΔT ($\alpha/\beta=$ const.). It should be noted that, in order to have a constant thickness of the final crystal, first there must be some value of β for which $\bar{x}=1$, and second, when $\bar{x}=1$, $d\bar{x}/d\beta<0$. The first condition is necessary in order that some two successive layers have the same thickness. The second criterion is necessary in order to have all subsequent layers fluctuate about some identical average thickness. If the second condition is not met, i.e., if $d\bar{x}/d\beta>0$ at $\bar{x}=1$, then any fluctuation which leads to $\bar{x}>1$ will produce a runaway condition and successive layers will have longer and longer fold lengths. Now let us consider the variation of crystal thickness $\bar{b}$ with the number of layers n. First we note that the slope of a plot of thickness $\bar{b}$ versus n is

$$\Delta\bar{b}/\Delta n=\bar{b}_{n+1}-\bar{b}_n, \tag{28}$$

but

$$\bar{b}_{n+1}/\bar{b}_n=\bar{x}_n.$$

Hence,

$$\Delta\bar{b}/\Delta n=(\bar{x}_n-1)\bar{b}_n. \tag{29}$$

Now $\bar{x}_n$ is related to $\bar{b}_n$ through the $\bar{x}$ versus β plot. Therefore, we can let $\bar{x}_n=x(\bar{b}_n)$ and taking limits of $\Delta\bar{b}\to0$ and $\Delta n\to0$ and dropping subscripts we can write

$$d\bar{b}/dn=(x(\bar{b})-1)\bar{b}. \tag{30}$$

A generalized plot of $\bar{x}$ versus β is shown in Fig. 3. We will first consider the situation where the initial substrate length B makes β lie between 0 and C. If we approximate $x(\bar{b})$ by the average value of $\bar{x}$ in the region $0C$, $\langle\bar{x}\rangle$, then we get

$$n=(1-\langle\bar{x}\rangle)^{-1}\ln(B/\bar{b}), \tag{31}$$

which is identical with the solution of Eq. (27) under the same conditions. Thus, to the approximation that we can consider $\bar{x}=\langle\bar{x}\rangle$ when $\beta>\beta_{\bar{x}=1}$, and $\beta=\beta_{\bar{x}=1}$ for all other values of x, the plot of $\bar{b}$ versus n is a logarithmically decaying one until $\bar{b}$ is that determined by $\beta_{\bar{x}=1}$, and thereafter $\bar{b}$ is independent of n. This is shown in curve A of Fig. 4. If we take into account the variation of $\bar{x}$ with β in the region $0C$, the decay will not be so rapid and might appear as in curve B of Fig. 4. If the initial substrate length B makes β lie in the region $A0$ of Fig. 3, then the $\bar{b}-n$ plot will have the shape shown by curve C of Fig. 4. If the initial substrate length B makes β lie in the region DE of Fig. 3 and the value of $\bar{x}$ in this region was extremely close to unity, the $\bar{b}-n$ plot will have the shape shown by curve D in Fig. 4. Now the $\bar{b}-n$ curves actually are profiles through the crystal in the region of the primary nucleus. Thus we can get three types of profile: (a) a monotonically decreasing thickness which will pro-

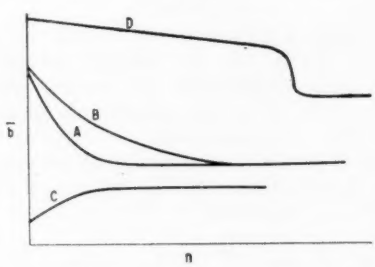

FIG. 4. Theoretical profiles of single crystals in region of primary nucleus. See text for description of curves.

duce a bump in the center of the crystal, (b) an essentially constant thickness with an abrupt decrease to the final thickness which will produce a sort of mesa in the center, and (c) a monotonically increasing thickness which will produce a hole in the center of the crystal. All the above considerations of profile have been made on the assumption of constant growth temperature. It is obvious that these ideas can also be invoked to examine the change in crystal thickness following an abrupt change in growth temperature.

Before proceeding to a description of the actual calculations and the results, there only remains the question of expressing the lower limit of x, $x_{\min}$. It can be shown that the definition of $x_{\min}$ (that value of xB which is equal to the critical nucleus length) leads to

$$x_{\min}=1/2\alpha\cdot\delta/kT. \tag{32}$$

The definition of $x_{\min}$ is somewhat arbitrary; however, it is clear that $\bar{x}$ cannot fall below this value, and it is probable that the exclusion of segments shorter than the critical nucleus length does not introduce serious error into the calculation.

Solutions of Eq. (8) were made by successive iterations of the matrix A on an IBM 650 computer. The range of x and x' was 0–2 with $\Delta x=\Delta x'=0.2$. The master matrix was thus of the eleventh order. Calculations were made with a number of values of α/β and β with $\delta/kT=1$, 2, 3, and 4, and with $\gamma=1.0$, 1.2, and 1.5. In order to take into account the criterion of Eq. (32), values of $x_{\min}$ were thereby calculated using the specific values of α and δ/kT. Those matrix elements for which x or $x'\leq x_{\min}$ were equated to zero before the iteration of the matrix. Thus, in some cases the matrix was of lower than eleventh order.

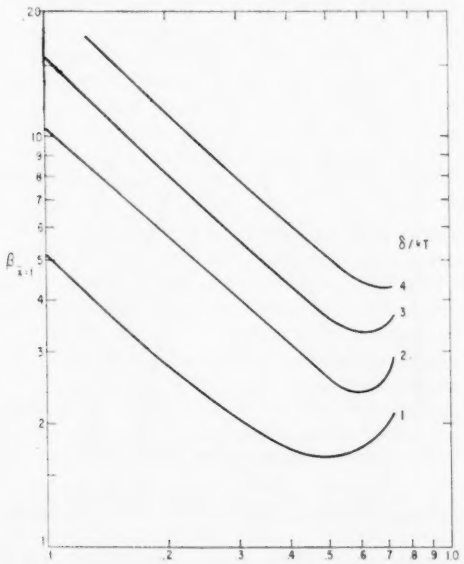

FIG. 5. Theoretical plots for $\beta_{\bar{x}=1}$ vs α/β with $\gamma=1.5$ and $\delta/kT=1$, 2, 3, 4.

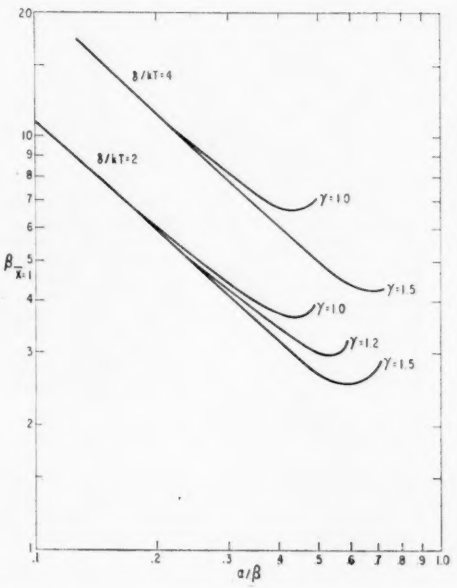

FIG. 6. Theoretical plots of $\beta_{\bar{x}=1}$ vs α/β with $\delta/kT=2$, 4 and $\gamma=1.0$, 1.2, 1.5.

RESULTS

General Considerations

Before proceeding to a discussion of the results, it should be emphasized that this theory is not an equilibrium theory in the sense of that of Fischer and Peterlin[4] but is much more akin to the kinetic theories of Frank and Tosi,[7] and Lauritzen and Hoffman.[6] In the present theory, the equilibrium is restricted in that an equilibrium distribution of segment lengths is permitted within each layer subject to the influence of the substrate, but a nonequilibrium situation prevails from layer to layer.

In Fig. 5 are displayed calculated curves of β versus α/β for $\gamma=1.5$ for several values of the fold energy δ/kT. These curves are essentially plots of crystal thickness (expressed in the dimensionless variable $\beta_{\bar{x}=1}$) versus supercooling (expressed by the dimensionless variable α/β). The effect of the maximum allowable value of $\alpha/\beta=\gamma/2=0.75$ is evidenced by the upswing of the curves as α/β approaches this value. Qualitatively, this upswing is due to the supercooling becoming so large that the segment lengthening effect of the bulk free energy terms overwhelm the restricting effects of the surface energy terms. It is clear that as the fold energy δ is increased, this upswing in $\beta_{\bar{x}=1}$ is moved to greater supercoolings. This is reasonable, for the greater is the energy required to make the fold the

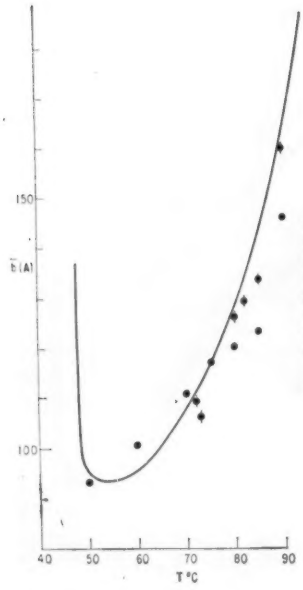

FIG. 7. Effect of precipitation temperature (T) on thickness ($\bar{b}$) of polyethylene single crystals precipitated from dilute xylene solution. Solid line is theoretical curve calculated with $\delta/kT=4$, $T_m=113°$, $\gamma=1.0$. Points are experimental (● this laboratory, ● Keller and Bassett).

greater will be the bulk free energy required to become overwhelming.

If it is assumed that, as in the previous simplified theories,[5,6] the crystal thickness is essentially the critical nucleus length, then it can be shown that this length expressed in dimensionless terms is

$$\beta_g^* = \delta/2kT \cdot \beta/\alpha. \tag{33}$$

This expression, when plotted on a log–log plot such as Fig. 5 would give lines of unit negative slopes having values of β_g^* of 5, 10, 15, and 20 at $\alpha/\beta=0.1$ for δ/kT values of 1, 2, 3, and 4, respectively. Inspection of Fig. 5 shows that, at the lower values of α/β, the plots are approaching such lines of unit slope but that $\beta_{\bar{x}=1}$ is always somewhat larger than β_g^* at a given value of α/β. The difference between $\beta_{\bar{x}=1}$ and β_g^* increases as α/β increases (supercooling increases).

In Fig. 6, $\beta_{\bar{x}=1}$ versus α/β is plotted for several values of γ and two values of δ/kT. It is seen that at fixed δ/kT, decreasing γ decreases the supercooling at which the bulk free energy terms start to overwhelm the surface energy ones. This is to be expected as decreasing γ corresponds to decreasing the energy required for a segment to project beyond the substrate.

Application to Polyethylene

We will now consider the application of the model to the growth of single crystals of polyethylene. We will consider the growth temperature to be 400°K which makes $kT=5.6\times10^{-14}$ ergs and we will let $\Delta G_V=0.66\times10^7\ \Delta T$ ergs/cm³. Inspection of the unit cell of polyethylene where $a_0=7.4$ A and $b_0=4.9$ A shows that if growth proceeds with production of 110 crystal faces $h=4.05$ A, $\Delta a=4.45$ A; while if growth proceeds with production of 100 faces $h=4.9$ A, $\Delta a=7.4$ A. Thus, for 110 crystal faces, $\gamma=1.1$; while for the 100 faces, $\gamma=0.81$. If the above figures are inserted into the equations defining α and β along with the assumptions that $\sigma_2=10$ ergs/cm², $B=100$ A, and ΔT is some tens of degrees, the results indicate that the interesting values of β should be in the range five to fifteen while the values of α/β should be between zero and 0.75.

It is immediately apparent that, in order to get values of β in range of interest, δ/kT must be in the neighborhood of 4. This value is considerably higher than those previously estimated by the author[5] and by Hoffman and Lauritzen,[6] but is close to that estimated by Frank and Tosi[7]. To fit the curves of Figs. 5 and 6 to actual data, the crystal thicknesses determined experimentally by both Keller and Bassett[9] and by the author[10] were plotted on a log–log plot against the supercooling (assuming various values of T_m between 100° and 120°). The experimental plot was superimposed upon the best fitting theoretical plot by vertical and horizontal translations. The sliding factors then gave the following relationships

$$\bar{b}=13.4\times10^{-8}\beta_{\bar{x}=1},$$
$$\Delta T=130(\alpha/\beta), \tag{34}$$

when $T_m=113°$C and $\delta/kT=4$, $\gamma=1.0$. A plot of the

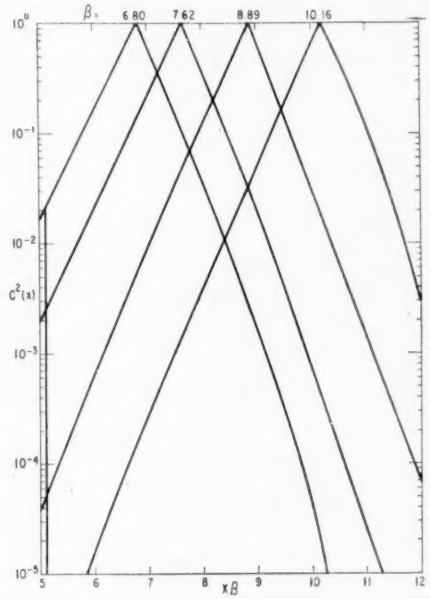

FIG. 8. Distribution curves for lengths of segments deposited on substrates of various lengths. $\delta/kT=4$, $\gamma=1.0$, $\alpha/\beta=0.393$.

[9] A. Keller and D. C. Bassett (unpublished work cited in reference 7).

[10] F. P. Price (unpublished work).

experimental points and the theoretical curve derived in this manner is shown in Fig. 7. The agreement is reasonably good; and in view of the uncertainty of the experimental data and the approximations in the theory, it is accepted as satisfactory.

The numerical constants in Eq. (34) permit calculation of $\sigma_2=13.3$ ergs/cm^2 and $\Delta a=h=3.2$ A. The magnitude of σ_2 is somewhat larger than that usually accepted, but it must be remembered that these experimental points were obtained from crystals grown from dilute xylene solution and not from the bulk polymer where a lower value might be expected. The small value of h and Δa is somewhat disturbing although perhaps the imprecision of both experiment and theory can encompass the discrepancy. In any event, these dimensions are about 30% smaller than the corresponding lattice dimensions.

If the value of $\delta/kT=4$ is combined with the calculated values of h and Δa, an end surface energy of $\sigma_1=110$ ergs/cm^2 is calculated. As mentioned above, this corresponds much more closely to that calculated by Frank and Tosi[7] than to that previously calculated by Hoffman and Lauritzen[6] and the author.[5] Frank and Tosi have discussed at length possible reasons for the large magnitude of σ_1. However, there seems to be no escape from the conclusion that the end surface free energy is considerably larger than previously estimated.

We now will consider briefly the roughness of the adding layer of polymer. In Fig. 8 are plotted the normalized distribution functions $C^2(x)$ against the length $x\beta$ for several values of β with δ/kT, α/β, and γ fixed at 4, 0.393, and 1.0, respectively. For these values of δ/kT, α/β, and γ it was found that $\beta_{\bar{x}=1}=6.70$. From this semilogarithmic plot it is obvious that the distribution of segments in the adding layer is very strongly peaked at the substrate length. There is, in general, a very slight bias toward shorter segment lengths but this bias is ultimately overwhelmed by the restriction of a minimum finite length of $\beta=5.08$. If the information presented in Fig. 8 is combined with Eq. (34), it can be shown that for the above values of δ/kT, α/β, and γ a segment equal in length to the substrate occurs ten times more often than one 13 A shorter or longer than the substrate and one hundred times more often than one 20 A shorter or longer than the substrate. Thus, the adding layer is quite smooth having an average fluctuation up or down of only one to two angstroms. With such small fluctuations, the contributions of the $\beta(1\langle|x-x'|\rangle_{Av}1)$ term to Eq. (25) are quite negligible and therefore the condition expressed in Eq. (26) was found always to be met in the interesting range of α/β. Thus, although it is conceivable that some very small supercooling might produce a condition where $\bar{d}>0$, this supercooling apparently is too low to be studied experimentally with polyethylene single crystals. This means that, contrary to the predictions of the theory of Frank and Tosi,[7] the theory presented here predicts no practical lower limit in supercooling at which the crystals cease growing.

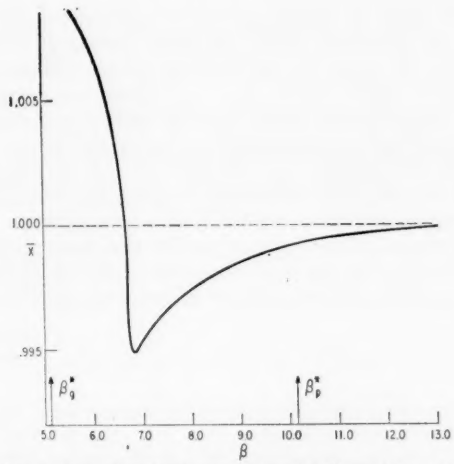

FIG. 9. Plot of reduced average length $\langle\bar{x}\rangle$ vs β for $\delta/kT=4$, $\gamma=1.0$, $\alpha/\beta=0.393$. β_p^* is value of β for substrate length equal to that of primary homogeneous nucleus. β_g^* is value of β for substrate length equal to that of minimum growth nucleus.

Finally, we come to the question of the morphology of the central region of a real polyethylene crystal. In Fig. 9 is plotted $\bar{x}$ vs β for $\alpha/\beta=0.393$, $\gamma=1.0$, and $\delta/kT=4$. Also indicated on the plot are the values of β_g^* [Eq. (33)] and β_p^*, the value of β when the substrate has the same length as a critical primary homogeneous nucleus,

$$\beta_p^*=\delta/kT\cdot\beta/\alpha. \tag{35}$$

It can be seen that if the crystal starts with a thickness characteristic of β_p^* it will at first slowly decrease in thickness and then abruptly decrease and then level off at $\beta_{\bar{x}=1}=6.70$. If we apply Eq. (31), with its approximations, to this case, $B/\bar{b}=\beta_p^*/\beta_{\bar{x}=1}^*=10.14/6.70$ and $\langle\bar{x}\rangle=0.9975$, we calculate that $n=33$ layers. If each layer adds 4 A, the bump in the center will be about 130 A in radius. The height of the bump calculated using Eqs. (34) and the difference between β_p^* and $\beta_{\bar{x}=1}^*$ is 60 A. Comparison of the curve in Fig. 6 with $\delta/kT=4$, $\gamma=1$, with the theoretical curve in Fig. 7 shows that a value of $\alpha/\beta=0.393$ represents a relatively high degree of supercooling. Only in the case where the stable crystal thickness is larger than the primary nucleus length will there be a hollow in the center of the crystal as discussed above. In practical situations with polyethylene it may be that a requisite supercooling is unattainable.

CONCLUSIONS

It has been shown that this model which is essentially an equilibrium type one is capable of giving reasonable predictions about the morphology of polymer single crystals.

The theory predicts essentially no lower limit to the

supercooling at which growth can occur. It predicts that at high supercoolings the bulk free energy overwhelms the surface energy and the crystals increase in thickness without limit. It is reasonable that at such high supercoolings other growth mechanisms, particularly dendrite producing ones, may intervene.

The predictions of the theory have been correlated with the observed morphology of polyethylene single crystals. The thickness dependence on temperature of polyethylene single crystals precipitated from dilute xylene solution has been correlated with the theory by assuming an energy of the lateral surfaces of 13.3 ergs/cm^2, an energy of the folded surfaces of 110 ergs/cm^2 and a solution temperature of the macroscopic crystal of 113°C.

ACKNOWLEDGMENTS

The author wishes to express his gratitude to Mr. Wilson Barnes for carrying out some of the experimental work described herein and to Miss Ann Warner for many of the computations. Thanks are also due Dr. B. H. Zimm, Dr. G. M. Roe, and particularly to Dr. P. L. Auer for stimulating and helpful discussions during the course of this work.

THE JOURNAL OF CHEMICAL PHYSICS VOLUME 35, NUMBER 5 NOVEMBER, 1961

Strength of the N—F Bonds in NF_3 and of N—F and N—N Bonds in N_2F_4

AL KENNEDY AND CHARLES B. COLBURN

Rohm and Haas Company, Redstone Arsenal Research Division, Huntsville, Alabama

(Received April 26, 1961)

The heat of formation of the difluoroamino free radical is found to be 8.9±2.5 kcal/mole. The NF_2—F bond in NF_2 is the weakest bond in NF_3 in contrast to ammonia where the NH_2—H bond is the strongest bond. The strength of the NF_2—F bond is 57.1±2.5 kcal/mole while the average NF bond strength in NF_2 and N_2F_4 is 71 kcal/mole. The strength of the N—N bond in tetrafluorohydrazine, as determined from appearance potential data, is 20.7 kcal in excellent agreement with the value 19.8 kcal found by thermal measurements.

THE heat of formation of tetrafluorohydrazine (N_2F_4) has recently been reported to be

$$\Delta H_{f_{25}}{}^0[N_2F_4(g)] = -2.0 \pm 2.5 \text{ kcal/mole.}^1$$

Johnson and Colburn have measured the heat of dissociation of tetrafluorohydrazine $N_2F_4 \rightleftarrows 2NF_2$ by three methods: (a) measurement of the pressure-temperature relationships of the system at constant volume,[2] (b) a spectrophotometric method based on the temperature dependence of the ultraviolet absorption of the difluoramino radical,[2] and (c) by a study of the temperature dependence of the EPR signal of the difluoramino free radical.[3] These three methods yield a heat of dissociation for tetrafluorohydrazine of 19.8±0.8 kcal/mole.[3]

The heat of formation of tetrafluorohydrazine,[1] together with the heat of dissociation of tetrafluorohydrazine,[3] leads to a value for the heat of formation of the difluoramino free radical of 8.9±2.5 kcal/mole.

The heat of formation of NF_3 has been determined by Armstrong and co-workers[4] to be −29.7±1.8 kcal/mole. This information combined with the heat of formation of NF_2 and F[5] yields the heat of the reaction

$$NF_2 - F \rightarrow NF_2 + F$$

$$\Delta H = D(NF_2 - F) = 57.1 \pm 2.5 \text{ kcal/mole.}$$

Since the mean bond energy E(N—F) in NF_3 is 66.4±0.8 kcal/mole[4] the above value of $D(NF_2-F)$ means that the mean dissociation energy of the last two N—F bonds in NF_3, i.e., D(NF—F) and D(N—F) is 71 kcal/mole.

The distribution of bond energies in NF_3 has been made earlier by Reese and Dibeler[6] who distributed the bonds in NF_3 in a manner similar to that found by Altshuller[7] for NH_3. These values together with those found in this work are given in Table I.

Mass spectrometric evidence is in agreement with the values arrived at in this work. Reese and Dibeler[6] pointed out that the mass spectrum of NF_3 is similar to the spectra of other pyramidal, Group V halogen compounds[8] but unlike that of ammonia[9] and other

[1] G. T. Armstrong, S. Marantz, and C. F. Coyle, National Bureau of Standards Rept. No. 6584, October, 1959.
[2] F. A. Johnson and C. B. Colburn, J. Am. Chem. Soc. **83,** 3043 (1961).
[3] L. H. Piette, F. A. Johnson, K. A. Booman, and C. B. Colburn, J. Chem. Phys. **35,** 1481 (1961).
[4] G. T. Armstrong, S. Marantz, and C. F. Coyle, J. Am. Chem. Soc. **81,** 3798 (1959).
[5] Values for the heats of formation of the gaseous atoms used herein were obtained from T. L. Cottrell, *The Strengths of Chemical Bonds* (Butterworth's Scientific Publications, Ltd., London, 1958), 2nd ed., p. 153.
[6] R. M. Reese and V. H. Dibeler, J. Chem. Phys. **24,** 1175 (1956).
[7] A. P. Altshuller, J. Chem. Phys. **22,** 1947 (1954).
[8] P. Kusch, A. Hustrulid, and J. T. Tate, Phys. Rev. **52,** 840 (1937).
[9] M. M. Mann, A. Hustrulid, and J. T. Tate, Phys. Rev. **58,** 340 (1940).

Group V hydrides.[10] This difference (the large size of the NF_2^+ peak compared with the NF_3^+ peak and the relatively low appearance potential of NF_2^+ compared with AP of NF_3^+) must be due to the fact that either the binding energy of F in NF_3 is much smaller than the binding energy of the remaining fluorine atoms or else the ionization potential of NF_2 is much smaller than that of NF_3. It would appear from this study that both of these factors play a part.

The strength of the N—N bond in tetrafluorohydrazine has recently been reported to be 19.8±0.8 kcal.[3] This value was arrived at by three different thermal measurements[2,3] of the bond strength and is in disagreement with the value of the N—N bond in tetrafluorohydrazine reported from appearance potential measurements (i.e., 30 kcal[11] and 52 kcal[12]).

This value of the dissociation energy of the N—N bond in tetrafluorohydrazine (19.8±0.8 kcal/mole) not only permits the derivation of the new bond energy distribution in NF_3 and a rationalization of the difference in mass cracking patterns between NF_3 and NH_3 and other Group V hydrides but also necessitates re-evaluation of the interpretation of the mass spectral data of Loughran and Mader [as has been done by Colburn and Johnson[13]) and of Herron and Dibeler.

Loughran and Mader (in a note by Colburn and Johnson[13]) have re-evaluated their earlier work[11] on N_2F_4. Their data can now be best interpreted by the following reactions:

$$N_2F_4 + e \rightarrow NF_2^+ + NF_2 + 2\,e, \qquad A_1 = 12.5 \text{ ev}, \quad (1)$$

and

$$NF_2 + e \rightarrow NF_2^+ + 2\,e, \qquad A_2 = 11.8 \text{ ev}. \quad (2)$$

The appearance potential of reaction (2) is the ionization potential of the difluoramino radical.

For reaction (1) $A_1 = \Delta H_f(NF_2^+) + \Delta H_f(NF_2) - \Delta H_f(N_2F_4)$ and for reaction (2) $A_2 = \Delta H_f(NF_2^+) - \Delta H_f(NF_2)$. Then, $A_1 - A_2 = 2\Delta H_f(NF_2) - \Delta H_f(N_2F_4)$. Hence,

$$\Delta H_f(NF_2) = 0.4 \text{ ev or } 9 \text{ kcal/mole},$$

$$\Delta H_f(NF_2^+) = 12.2 \text{ ev or } 281 \text{ kcal/mole}$$

since

$$\Delta H_f(N_2F_4) = -0.1 \text{ ev or } -2 \text{ kcal}.$$

This value of $\Delta H_f(NF_2) = 9$ kcal/mole is in excellent agreement with the value derived by purely thermal considerations (8.9±2.5 kcal/mole).

The dissociation energy of the NF_2—F bond can be derived from mass spectral evidence as follows:

Reese and Dibeler[6] obtained the appearance potential for the following process:

$$NF_3 + e \rightarrow NF_2^+ + F + 2\,e, \qquad A = 14.2 \text{ ev},$$

$$A(NF_2^+) = D(NF_2\text{—}F) + I(NF_2).$$

$I(NF)$ can be obtained from the combined data of Herron and Dibeler[13] and Colburn *et al.*[3] as follows:

$$N_2F_4 + e \rightarrow NF_2^+ + NF_2 + 2\,e \qquad A = 12.7 \text{ ev}$$

$$I(NF_2) = A(NF_2^+) - D(F_2N\text{—}NF_2)$$

$$= 12.7 \text{ ev} - 0.9 \text{ ev} = 11.8 \text{ ev}.$$

This value is identical to that obtained by Colburn and Johnson[13] in their re-interpretation of the work of Loughran and Mader.[11]

This value of $I(NF_2)$ then leads to a value for $D(F_2N\text{—}F)$ of 2.4 ev or 55.2 kcal in good agreement with the thermal value of 57.1 kcal.

TABLE I. Distribution of bond energies of NF_3 and NH_3.

NH_3[a]		NF_3[b]		NF_3[c]	
$D(NH_2\text{—}H)$	104 kcal	$D(NF_2\text{—}F)$	73 kcal	$D(NF_2\text{—}F)$	57 kcal
$D(NH\text{—}H)$	88 kcal	$D(NF\text{—}F)$	62 kcal	$D(NF\text{—}F)$	71 kcal
$D(N\text{—}H)$	88 kcal	$D(N\text{—}F)$	62 kcal	$D(N\text{—}F)$	71 kcal

[a] See reference 7.
[b] See reference 6.
[c] This work.

ACKNOWLEDGMENTS

The authors wish to express their appreciation to Dr. Robert W. Walker for several helpful discussions during the course of this work and to the referee of the paper for several valuable suggestions for the improvement of this paper. The work was conducted under Army Ordnance.

[10] H. Neuert and H. Classen, Z. Naturforsch. **7a,** 410 (1952).
[11] E. D. Loughran and C. Mader, J. Chem. Phys. **32,** 1578 (1960).
[12] J. T. Herron and V. H. Dibeler, J. Chem. Phys. **33,** 1595 (1960).
[13] C. B. Colburn and F. A. Johnson, J. Chem. Phys. **33,** 1869 (1960).

Letters to the Editor

THE Letters to the Editor section is subdivided into three parts entitled Communications, Comments and Errata, and Notes. These three sections are all subject to the same limitations on length. The textual material of each Letter is limited to a number of words equal to 950 minus the following: (a) 200 words for each average-sized figure; (b) 50 words for each displayed equation; (c) 7 words for each line of table including headings and horizontal rulings. No proof will be sent to the authors of "Communications" and "Comments and Errata." Proof will be sent to the authors of "Notes." The publication charge for Letters is $30 per page, with a minimum of $30 per Letter. If honored, the Institution will be entitled to 100 reprints without covers. See issues of May–September, 1957, for descriptions of categories.

Communications

Low-Field Nuclear Magnetic Resonance of Coupled Spin—One-Half Particles

DON D. THOMPSON AND ROBERT J. S. BROWN

California Research Corporation, La Habra, California

(Received August 25, 1961)

PROTON free-precession signals at low fields have been previously shown[1,2] to exhibit structure in their spectra. We wish now to consider the low-field free-precession signal obtained from two nuclei of spin one-half coupled isotropically. The sample was $HPO(OH)_2$. The hydrogen atom bonded directly to the phosphorus atom has a coupling constant $J_{HP}=695$ cps.[3] The other two hydrogen atoms exchange rapidly with the solvent water.

The energy levels for the H-P fragment as functions of applied field are given by the Breit-Rabi[4] formula,

$$E_{11}=\tfrac{1}{2}\nu_H+\tfrac{1}{2}\nu_P+\tfrac{1}{4}J_{HP}$$

$$E_{1-1}=-\tfrac{1}{2}\nu_H-\tfrac{1}{2}\nu_P+\tfrac{1}{4}J_{HP}$$

$$E_{10}=-\tfrac{1}{4}J_{HP}+\tfrac{1}{2}[(\nu_H-\nu_P)^2+J_{HP}{}^2]^{\frac{1}{2}}$$

$$E_{00}=-\tfrac{1}{4}J_{HP}-\tfrac{1}{2}[(\nu_H-\nu_P)^2+J_{HP}{}^2]^{\frac{1}{2}},$$

with the energies expressed as frequencies. ν_H and ν_P are the uncoupled hydrogen and phosphorus precession frequencies. The allowed perpendicular transitions in the low-field limit are $\psi_{11}\rightarrow\psi_{00}$ and $\psi_{1-1}\rightarrow\psi_{00}$, and the allowed parallel transition is $\psi_{10}\rightarrow\psi_{00}$. At zero field, E_{00} corresponds to the pure singlet state and the others to the triplet.

The signals were observed by producing population differences in the various states by applying a strong dc polarizing field and then suddenly removing it, receiving signals by appropriate coils. At fields of 0.5 and 1.5 gauss, where ν_H is still substantially larger than J_{HP}, we previously observed the transitions $\psi_{11}\rightarrow\psi_{00}$ and $\psi_{10}\rightarrow\psi_{1-1}$ while observing signals at low fields from various coupled nuclear systems such as the ammonium ion.[1] These transitions were observed independently at the higher of these two fields by Erbeia,[5] using a steady-state technique.

The use of this system as a very low-field magnetometer has some merit, as the technique is simple and straightforward and the measurement absolute. The use of a sample containing strongly coupled spin systems extends the range of the conventional free-precession magnetometer using water, glycerine, or hexane to approximately 10^{-4} gauss. A nearly transverse field of about 8×10^{-3} gauss in our apparatus was measured with an accuracy of 5×10^{-5} gauss, and better accuracy is believed possible. The signal is, furthermore, observable even in exactly zero field. One can also measure spin coupling constants directly and accurately.

With residual fields of a few milligauss we have now observed transitions between the E_{00} level and the other three. With a receiving coil parallel to the residual field the $\psi_{10}\rightarrow\psi_{00}(\Delta m=0)$ transition is observed. With the receiving coil perpendicular to the residual field the other two transitions are observed ($\Delta m=\pm1$). At intermediate angles all three can be observed, the effect being, in the limit of low fields, that of a carrier at frequency J_{HP} modulated at a frequency $\omega/2\pi=\frac{1}{2}(\nu_H+\nu_Q)$. If β is the angle between the initial polarization and the residual field, the signal is of the form $(\cos^2\beta+\sin^2\beta\cos\omega t)\cos Jt$.

The frequency difference between the $\Delta m=+1$ and $\Delta m=-1$ lines is exactly $(\nu_H+\nu_P)$ at any field strength, and it is thus directly proportional to the field. The frequency of the $\Delta m=0$ line is $[(\nu_H-\nu_P)^2+J^2]^{\frac{1}{2}}$ and is therefore not a sensitive indication of field strength for very weak fields. A requirement for a modulated signal (to sensitively indicate field strength) is that the initial polarization be not parallel to the residual field. One can reorient the initial polarization by adiabatically reducing the polarizing field (of the order of a kilogauss) to an intermediate value, greater than J/ν_H and in a different direction.

There are probably better materials to use than $HPO(OH)_2$. We hope to obtain a pure sample of $FPO(OH)_2$, which has a higher concentration of coupled spins and has $J=954$ cps. There are more complex systems which should also be suitable magnetometer samples.

It is planned to publish a more detailed account of this work in the near future.

[1] R. J. S. Brown and D. D. Thompson, J. Chem. Phys. **34,** 1580 (1961).
[2] D. F. Elliot and R. J. Schumaker, J. Chem. Phys. **26,** 1350 (1957).
[3] H. S. Gutowsky, D. W. McCall, and C. P. Slichter, J. Chem. Phys. **21,** 279 (1953).
[4] N. F. Ramsey, *Molecular Beams* (Oxford University Press, New York, 1956), p. 80.
[5] A. Erbeia, Compt. rend. **251,** 1493 (1960).

Formation, Lifetime, and Decay of OH Radicals in Discharge-Flow Systems

F. KAUFMAN AND F. P. DEL GRECO

Ballistic Research Laboratories, Aberdeen Proving Ground, Maryland

(Received September 14, 1961)

MANY studies have been reported of OH radicals using ultraviolet,[1,2] microwave,[3,4] electron paramagnetic resonance,[5] or mass spectrometric[6] techniques. In most of these studies OH was obtained from electrical discharges in water vapor. Yet, the identity, concentrations, and reactions of atoms and radicals produced in such discharges are still imperfectly understood.

We have built an apparatus for the study of OH reactions whose characteristics are as follows: Atoms and radicals are produced in a microwave discharge (Raytheon PGM-100, generating up to 800 w at 2450 Mc); then the gas mixture is pumped through a quartz tube 3.0 cm i.d. and 150 cm long by a two-stage Roots pump (Consolidated VP-R-152A, manufactured by W. C. Heraeus G.m.b.H., pumping speed 50 liters/sec) backed by an oil pump (Cenco Hypervac 25); the local OH concentration is measured by a uv absorption system, movable along the quartz tube, consisting of a H_2O-Ar microwave discharge emitting OH radiation; a set of mirrors and quartz lenses permitting three light traversals across the tube within a total width of 1.3 cm; and a grating monochromator (Jarrell-Ash, model 82-000, 0.5 m Ebert, photoelectric, recording) serving to isolate particular rotational lines. The light source is so adjusted (large Ar:H_2O ratio, $p=18$ mm Hg, low microwave power from Raytheon Microtherm) that the low members of all branches of the (0, 0) band of the OH transition $A\,^2\Sigma^+ - X\,^2\Pi$ exhibit a rotational temperature of about 100°C. This is important in decreasing the Doppler width of the emission lines and thereby increasing the absorption of OH molecules whose kinetic and rotational temperature was found to be about 25°C. Normally, OH was measured by absorption of the Q_1-4 line of the (0, 0) band.

Experiments with water discharges gave the following results: Such discharges are very poor sources of OH, but efficient sources of H. Rough estimates based on the light absorption gave 0.1 to 0.3% OH. Neither adding He, Ar, H_2, or N_2, changing to H_2-O_2 mixtures, nor decreasing the microwave discharge power improved the OH yield, but adding O_2, particularly downstream of the discharge, did somewhat. Similar findings have been reported.[5,6] Moreover, the variation of (OH) down the tube was abnormal, often S-shaped or showing an increase of (OH) along the tube followed by a slow decrease. It is clear from these experiments and from those described below that the OH observed in water discharge products is not all produced in the discharge, but is continuously generated throughout flow system by the reactions

$$H+O_2+M\rightarrow HO_2+M,\quad H+HO_2\rightarrow H_2O_2{}^*\rightarrow 2OH.$$

Therefore, the lifetimes of 0.1 to 0.3 sec reported by Oldenberg[1] and Townes *et al.*[4] are probably in error.

To clarify this point, OH was produced chemically from discharged H_2-He mixtures by the downstream addition of NO_2, $H+NO_2\rightarrow OH+NO$. Two results were immediately apparent: Much larger (OH) could be obtained; and the decay of OH was now extremely rapid. To minimize temperature increases resulting from the rapid, exothermic reaction, most experiments are run in 50- to 200-fold dilution with He or Ar. NO_2 is added through a 3-mm glass tube which traverses the quartz tube and has 10 holes of 0.1-mm diameter so arranged to produce a sheet of added gas for fast mixing. The NO_2 concentration is monitored by light absorption at 4358 A along the full length of the quartz tube. Thus, an independent estimate of (OH) and of the original (H) is obtained by measurement of the maximum amount of NO_2 instantly destroyed when the discharge is started. In agreement with recent work by Rosser and Wise,[7] all our data indicate that the $H+NO_2$ reaction is extremely fast.

Typical experimental conditions are as follows: total pressure = 3.90 mm Hg of which 99% is He and 1% H_2. With the discharge on, 0.032 mm of NO_2 are destroyed corresponding to 41% dissociation of H_2. Average gas velocity = 38 m/sec. On the assumption that Beer's law is approximately obeyed, we find the decay of OH to be second order and the half-life 1.4 msec at a concentration estimated at 0.012 mm Hg. This is two orders of magnitude shorter than has previously been reported and it implies that most of the OH observed in water discharge products is formed outside the discharge region.

Why discharges produce so much H and so little OH is not yet clear. It can be argued that in the discharge OH may be more rapidly dissociated than H_2O, and that the rapid reaction $O+OH\rightarrow O_2+H$ will remove O atoms and greatly decrease (OH). The absence of sizable O concentrations in discharge products is indicated by the weak air afterglow when NO is added downstream.

The rapid, second-order decay of OH produced from $H+NO_2$ was found to be unaffected by added NO, and its rate constant independent of initial (OH), total pressure, and the diluent (He or Ar). The decay cannot be ascribed to a heterogeneous process and its principal reaction may be $2OH\rightarrow H_2O+O$ with a rate constant near 10^{-12} cm^3 molecule sec^{-1}.

[1] O. Oldenberg, J. Chem. Phys. **3,** 266 (1935).
[2] O. Oldenberg and F. F. Rieke, J. Chem. Phys. **6,** 439, 779 (1938); **7,** 485 (1939).
[3] T. M. Sanders, A. L. Schawlow, G. C. Dousmanis, and C. H. Townes, J. Chem. Phys. **22,** 245 (1954).
[4] G. C. Dousmanis, T. M. Sanders, and C. H. Townes, Phys. Rev. **100,** 1735 (1955).
[5] H. E. Radford, Phys. Rev. **122,** 114 (1961).
[6] S. N. Foner and R. L. Hudson, J. Chem. Phys. **25,** 602 (1956); **23,** 1974 (1955).
[7] W. A. Rosser, Jr. and H. Wise, J. Phys. Chem. **65,** 532 (1961).

Rates of Electron Removal by Recombination, Attachment, and Ambipolar Diffusion in Nitric Oxide Plasmas

ROBERT C. GUNTON AND EDWARD C. Y. INN

Lockheed Missiles and Space Company, Sunnyvale, California

(Received July 27, 1961)

ONE important aspect in the study of plasmas is a knowledge of the rate coefficients of the basic reactions which control the disposition of the charged particles. Thus, the rates of electron-ion recombination, electron attachment to neutral molecules, and ambipolar diffusion in nitric oxide plasmas are of considerable interest in studies of reactions in the ionosphere and other air plasmas since the NO^+ ion is an important constituent.

Nitric oxide plasmas have been successfully produced by photoionization of NO gas for use in a diagnostic study of the decaying plasma by microwave techniques.[1] It has been shown that absorption of radiation by NO in the region of the Lyman-α line of hydrogen resulted only in the production of NO^+ ions and electrons.[2] Thus, plasmas produced by this method should consist only of NO, NO^+, and electrons.

Briefly, the experimental arrangement was as follows. The NO gas was contained in a quartz cell fitted with a thin lithium fluoride window and the cell inserted in a cylindrical X-band microwave cavity. The NO gas was irradiated through the LiF window with an external light source by means of a small aperture in one wall of the microwave cavity. The light source was a conventional capillary-type hydrogen discharge tube with a LiF window. A narrow gap of air (about 1–2 mm) between the light source and cell and the LiF window provided sufficient filtering of most of the undesired vacuum ultraviolet radiation, except for the region of the Lyman-α line of hydrogen. The light source was pulsed, with a duration of 5 μsec and repetition rate adjustable from a few to several hundred flashes per second. By measuring the change in resonance frequency of the cavity the electron density was determined as a function of time in the decaying plasma.[3] The range of electron densities observed was about 10^8-10^{10} cm^{-3}.

It was found that for NO pressures between 4–16 mm Hg and low initial electron densities the dominant electron loss mechanism was attachment. In fact, over this pressure range the electron density decay rate was found to be proportional to the square of the NO pressure, indicative, therefore, of a three-body attachment process. In view of the predicted existence of $(NO)_2$ dimers[4] in the gas phase in equilibrium with NO molecules, the over-all reactions leading to the formation of negative ions may be tentatively described as follows:

$$NO+NO \rightleftarrows (NO)_2, \qquad (NO)_2+e^- \rightarrow NO^-+NO,$$

where the stable existence of NO^- has been assumed. A rough estimate of the $(NO)_2$ concentration based on data calculated in reference 4 yielded values of the same order of magnitude as the electron densities observed, namely 10^8-10^{10} cm^{-3}, which could account for the observed decay rates. The average value of the attachment rate coefficient obtained from these measurements was $K=4\times10^{-31}$ cm^6 sec^{-1}.

At NO pressures of a few tenths of a millimeter and low initial electron densities ambipolar diffusion was the dominant electron loss mechanism. The decay appeared to proceed in the lowest order diffusion mode, at a rate described by an ambipolar diffusion coefficient, $D_a p=80$ cm^2 sec^{-1} mm Hg.

At NO pressures of several tenths of a millimeter and high initial electron densities electron-ion recombination appeared to be emphasized relative to diffusion and attachment losses. From the analysis of the observations, taking necessary account of higher order diffusion mode losses, it was possible to calculate the loss due to recombination and therefore the rate coefficient for the latter. The average value obtained was $\alpha=1.3\times10^{-6}$ cm^3 sec^{-1}. This large value immediately suggested the following dissociative recombination

$$NO^+ + e^- \rightarrow N^* + O^*,$$

where the asterisks indicate excited products.

It should be pointed out that in the photoionization process the liberated photoelectrons have an energy of about 1 ev since the ionization potential of NO is 9.25 ev and the photon energy 10.2 ev. However, it can be shown that these electrons thermalize within a few microseconds; hence all the above measurements refer to an electron temperature of about 0.04 ev.

[1] R. C. Gunton and E. C. Y. Inn, Bull. Am. Phys. Soc. **6**, 387 (1961).
[2] K. Watanabe, J. Chem. Phys. **22**, 1564 (1954).
[3] M. A. Biondi and S. C. Brown, Phys. Rev. **76**, 1697 (1949).
[4] O. K. Rice, J. Chem. Phys. **4**, 367 (1936).

Comments and Errata

Comments on a Communication by El-Sayed and Robinson*

MOSTAFA EL-SAYED AND G. WILSE ROBINSON

Gates and Crellin Laboratories of Chemistry, California Institute of Technology, Pasadena, California

(Received August 7, 1961)

A RECENT communication of ours[1] was concerned with the splitting of the symmetric and antisymmetric components $(\Psi_A\Psi_B' \pm \Psi_A'\Psi_B)$ of the lowest n, π^* singlet and triplet states of the diazines.

We attempted to show that the splittings could be computed by assuming that the excited π^* orbital is

localized near the nitrogen because of the Coulomb attraction of the excited electron with the localized "nonbonding positive hole." The problem then is like that of a two-center exciton[2] or the interaction between two helium atoms, one in its ground and one in its excited state.[3] Neglecting two-center overlap and letting the prime refer to electronic excitation, the excitation transfer splitting $\Delta E = E_+ - E_-$ between the symmetric and antisymmetric components becomes

$$\Delta E(\text{triplet}) = -2S_{n',n}{}^2K$$

$$\Delta E(\text{singlet}) = 2S_{n',n}{}^2(2J-K),$$

where

$$J = e^2\langle n_A(1)n_B(2) \mid r_{12}{}^{-1} \mid \pi_A{}^*(1)\pi_B{}^*(2)\rangle$$

and

$$K = e^2\langle n_A(1)n_B(1) \mid r_{12}{}^{-1} \mid \pi_A{}^*(2)\pi_B{}^*(2)\rangle.$$

$S_{n',n}$ is a one-center overlap integral between the nonbonding orbitals n and n' in the ground and excited states. The expressions have been corrected from I by: (1) insertion of a factor of 2; (2) a correction to the K integral; and (3) the inclusion of $S_{n',n}$. In the one-electron approximation, the nonbonding orbitals appearing in J and K are for the ground state and are presumably close to sp^2 hybrids. Assuming sp^2 hybridization for the excited states and using the same effective Z as in I, calculated ΔE(singlet) values are +860, +1590, and +12 400 cm^{-1}, and ΔE(triplet) values are −24, −275, and −5500 cm^{-1} for para-, meta-, and ortho-diazine, respectively. These calculated values for the singlets are larger by a factor of about 2 than the observed values.[1] A change in hybridization upon excitation can account for much of the discrepancy since $S_{n',n}{}^2 = 0.67$ in the limit $n' = 2p$. This kind of hybridization in the excited state is required to explain the (n, π^*) singlet-triplet interval in the azines.[4]

Neglect of K and expansion of J in a two-center expansion gives the familiar expression for the singlet splitting in terms of virtual transition dipoles **M** on the individual centers R_{AB} apart.

Using 0.01 for the oscillator strength[5] of the $n \rightarrow \pi^*$ transition of pyrazine (para-diazone), dividing this by 2 to obtain the value for the individual transitions at each end of the molecule, and taking $R_{AB} = 2.74$ A,[6] the value of ΔE is +165 cm^{-1}. Such a representation of the J integral is only a fair approximation in this case where n is a hybrid orbital, since the transition moment is nonvanishing only for the $2s$ part of n. However, the addition of the $2p$ term will cause the agreement to be even worse, since this contribution appears with a negative sign. If the experimental oscillator strength is correct, these kinds of calculations, while suggestive, must apparently be modified to include some π^*-delocalization and other more subtle aspects of the diazine eigenfunctions.

It was stated in I that "the forbidden component in pyrazine gains most of its intensity through mixing with a (π, π^*) state." This statement was based upon the work of Innes and his co-workers which suggested[7] that a band, 385 cm^{-1} from the origin of the allowed transition and which we believe to belong to the forbidden system, was in-plane polarized; and upon a suggestion by Ito *et al.*[8] that this band had a shape different from that of the main bands. The polarization of this band is now in doubt because of overlapping bands.[9] If the band turns out to be polarized out of plane, in all probability it corresponds to an in-plane vibration ν_{12} (820 cm^{-1}) in the excited state of the forbidden system. Thus, contrary to our statement in I, vibronic coupling between the symmetric and antisymmetric (n, π^*) components would then account for most (but not quite all) of the intensity of the transition to the antisymmetric component in pyrazine. An unambiguous polarization assignment is needed, but, in either case, the arguments for two (n, π^*) states with measurable excitation transfer splitting remain intact.

We wish to thank Dr. J. H. Scott for correcting our original calculation.

* Contribution No. 2724.

[1] M. A. El-Sayed and G. W. Robinson, J. Chem. Phys. **34,** 1840 (1961).

[2] For a brief discussion of the general exciton problem inclusive of electron exchange, see R. E. Merrifield, J. Chem. Phys. **23,** 402 (1955).

R. A. Buckingham and A. Dalgarno, Proc. Roy. Soc. (London) **A213,** 327 (1952).

[4] L. Goodman, J. Mol. Spectroscopy **6,** 109 (1961).

[5] S. F. Mason, J. Chem. Soc. **1959,** 1240.

[6] V. Schomaker and L. Pauling, J. Am. Chem. Soc. **61,** 1769 (1939). The excited state value should actually be used.

[7] K. Innes, J. Merritt, W. Tincher, and S. Tilford, Nature **187,** 500 (1960). These authors associated this band with an out-of-plane vibration in the symmetric (n, π^*) state. We therefore concluded that they had examined the rotational fine structure pattern and found the vibronic polarization to be in plane.

[8] M. Ito, R. Shimada, T. Kuraishi, and M. Mizushima, J. Chem. Phys. **26,** 1508 (1957).

[9] K. Innes (private communication).

Erratum: Tunneling through High Periodic Barriers. II. Application to Nuclear Magnetic Resonance on Solids

T. P. Das

Department of Physics, University of California, Riverside, California

[J. Chem. Phys. **27,** 763 (1957)]

On page 781, the paragraph "In Urea . . . whole molecule" should be replaced by

In urea, a similar calculation, using $H_{OO} = H_{CO} = \beta$ gave the energy of the II electrons as 6.88β. The energy of the II electrons when one of the C—N resonance integrals is set equal to zero (corresponding to 90° rotation of one NH_2 group about the C—N axis) is 6.20β. The difference between the two energies, 0.68β

is the height of the potential barrier hindering the motion of an NH_2 group about the CN bond. This value 12.24 kcal is in very good agreement with the experimental $V_0=12.7$ kcal obtained from Kromhout and Moulton's data (Table VIII).

The author is very grateful to R. Bersohn and R. Widman for pointing out this error to him.

Perturbation Theory Calculations

A. DALGARNO*

Geophysics Corporation of America, Bedford, Massachusetts

(Received June 28, 1961)

IN a recent paper, Snyder and Parr[1] have discussed the problem of evaluating the perturbation theory expressions for such quantities as the magnetic susceptibilities and nuclear magnetic shielding constants of atoms and molecules. They show that the use of an average excitation energy may be seriously misleading and they stress the desirability of finding a reliable alternative procedure. The purpose of this letter is to draw attention to the fact that such a procedure already exists and indeed has been used in several investigations, though not any concerning magnetic shielding and diamagnetic susceptibility problems.

The basic problem is the evaluation of an infinite summation, which includes an integration over the continuum, of the form

$$S=\mathbf{S}_n{}'(\psi_0, f_1\psi_n)(\psi_n, f_2\psi_0)/(E_n-E_0), \tag{1}$$

where ψ_n and E_n are the eigenfunction and eigenvalue, respectively, of the nth excited state of the system and f_1 and f_2 are selected functions or operators. If H is the Hamiltonian of the system, it may be shown[2] that

$$S=-(\psi_0, f_2\chi_1), \tag{2}$$

where

$$(H-E_0)\chi_1+f_1\psi_0=(\psi_0, f_1\psi_0)\psi_0 \tag{3}$$

such that $(\psi_0, \chi_1)=0$ and alternatively that

$$S=-(\psi_0, f_1\chi_2), \tag{4}$$

where

$$(H-E_0)\chi_2+f_2\psi_0=(\psi_0, f_2\psi_0)\psi_0 \tag{5}$$

such that $(\psi_0\chi_2)=0$. The identity of (1), (2), and (4) becomes transparent on solving (3) and (5) formally by expanding the solutions in terms of the complete set of eigenfunctions of H according to $\mathbf{S}Q_n\psi_n$.

Equations (3) or (5) may always be solved variationally by minimizing the functional

$$J=[\chi, (H-E_0)\chi]+2\{\chi, [f-(\psi_0, f\psi_0)]\psi_0\} \tag{6}$$

for some trial form of χ. In the case where $f_1\equiv f_2$, the summation S is equal in magnitude to the functional J.

It is of interest to consider the simple trial function

$$\chi=\lambda\{f-(\psi_0, f\psi_0)\}\psi_0, \tag{7}$$

where λ is a variational parameter. The procedure is then equivalent to using an average excitation energy $\bar{E}$ in place of E_n-E_0 with the important advantage over the usual method that $\bar{E}$ is now specified by

$$\bar{E}=-1/[f\psi_0, (H-E_0)f\psi_0]. \tag{8}$$

In the examples considered by Snyder and Parr, it is unnecessary to use the variational procedure since the solution to (3) can be written down immediately. If $\mathbf{r}\equiv(x, y, z)$ is the position vector of the electron of a hydrogen atom referred to the nucleus as origin, their f_1 has the form

$$f_1=-i[(\partial/\partial\phi)-x_0(\partial/\partial y)+y_0(\partial/\partial x)], \tag{9}$$

where ϕ is the azimuthal angle and x_0 and y_0 are the Cartesian coordinates of an arbitrary fixed point. It is obvious that the solution of (3) is

$$\chi_1=(-m/\hbar^2)(-x_0y+y_0x)\psi_0. \tag{10}$$

* On leave from the Department of Applied Mathematics, The Queen's University of Belfast, North Ireland.

[1] L. C. Snyder and R. G. Parr, J. Chem. Phys. **34,** 837 (1961).

[2] A. Dalgarno and J. T. Lewis, Proc. Roy. Soc. (London) **A233,** 70 (1955); **A69,** 628 (1956); A. Dalgarno, *Quantum Theory*, edited by D. R. Bates (Academic Press Inc., New York, 1961), Vol. A.

Perturbation Theory Calculations

ROBERT G. PARR

Department of Chemistry, Carnegie Institute of Technology Pittsburgh, Pennsylvania

AND

LAWRENCE C. SNYDER

Bell Telephone Laboratories, Inc., Murray Hill, New Jersey

(Received July 11, 1961)

IN our paper discussing perturbation theory calculation of diamagnetic susceptibility and nuclear magnetic shielding of molecules,[1] our purpose was to illustrate, in an especially contrived simple context, the difficulties inherent in *conventional perturbation theory* of magnetic properties, not to comparatively discuss various alternative methods. The solution Dalgarno obtains for our particular problem by another method[2,3] is of no interest for our purposes. His Eq. (10) in fact is the solution one can obtain by inspection upon shifting the origin of the vector potential back to the proton.

We are in agreement with Dalgarno that conventional perturbation theory is of little value for calculating magnetic properties of molecules. In papers now in preparation, various variational methods will be dis-

cussed,[4] and a new method[5] will be described which takes as its initial point of departure a recent paper by Rebane.[6] In this work we have found it useful to refer to Dalgarno's several basic papers on perturbation theory. Among other results, we have shown that the gradient of the function $f(r)$ of Dalgarno and Lewis[3] may be interpreted as a gauge factor for the vector potential for a problem; selection of f to simplify the evaluation of the perturbation sum in the magnetic susceptibility represents a particular choice of this gauge factor.

[1] L. C. Snyder and R. G. Parr, J. Chem. Phys. **34,** 837 (1961).
[2] A. Dalgarno, J. Chem. Phys. **35,** 000 (1961) (preceding comment).
[3] A. Dalgarno and J. T. Lewis, Proc. Roy. Soc. (London) **A233,** 70 (1955); **A69,** 628 (1956), and later papers; for example, A. Dalgarno and A. L. Stewart, Proc. Roy. Soc. (London) **A238,** 269 (1956); **A247,** 245 (1958); A. Dalgarno and N. Lynn, *ibid.* **A70,** 223 (1957). See also C. Schwartz, Ann. Phys. **6,** 156, 170 (1959).
[4] T. Arai, A. G. Turner, and R. G. Parr (to be published).
[5] R. G. Parr, A. G. Turner, and K. Ruedenberg (to be published).
[6] T. K. Rebane, J. Exptl. Theoret. Phys. (U.S.S.R.) **38,** 963 (1960) [Translation: Soviet Phys.—JETP **11,** 694 (1960)]. See also C. W. Kern and W. N. Lipscomb, Phys. Rev. Letters **7,** 119 (1961).

Remark on the Radiolysis of Aqueous Nitrate Solution

K. SHINOHARA, T. SHIDA, AND N. SAITO

Institute of the Physical and Chemical Research, University of Tokyo, Bunkyo-Ku, Tokyo, Japan

(Received July 17, 1961)

MAHLMAN and Boyle[1] and Mahlman,[2] among other authors, studied the radiolysis of aqueous nitrate solution. It was shown that the hydrogen yield decreases approximately with the cube root of the solute concentration. They noted the departure from the cube root relationship at solute concentrations

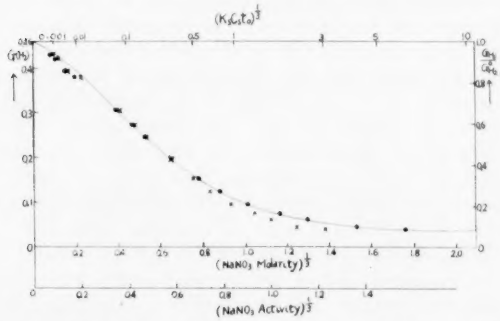

FIG. 1. Sworski-type plot [M. Burton and K. C. Kurien, J. Phys. Chem. **63,** 901 (1959)] of the hydrogen yield vs the cube root of solute concentration. The curve is theoretical[4] and the plots are taken from reference 3. Open circles are plotted against (molarity)$^{1/3}$, crosses against (activity)$^{1/3}$.

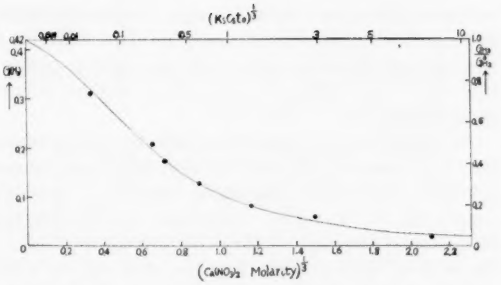

FIG. 2. Sworski-type plot of the hydrogen yield vs the cube root of solute concentration. The curve is theoretical[4] and the plots are taken from reference 5.

greater than 0.30 M, while $G(H_2)$ vs the cube root of the activity, instead of the molarity, is linear to a concentration of 1.0 M $NaNO_3$. They suggested that the suppression of molecular product formation should be discussed in terms of the scavenging solute activity rather than the solute molarity.

Mahlman[3] continued to study concentrated solutions up to 9.1 molal of $NaNO_3$ and found that when $G(H_2)$ is plotted against the cube root of the solute activity it exhibits a sharp break at 1.30 molal. From this result he concluded that the molecular hydrogen is produced from two mechanisms.

We wish to remark that the application of the expanding spur theory of Ganguly-Magee[4] can explain their results without the concept of the solute activity and the two different mechanisms of molecular hydrogen formation. The theory is surely approximate and should not be pushed too far. But the agreement between experimental and the theoretical results is surprisingly good.

Because only the hydrogen atom is scavenged by the nitrate ion,[5] we regard H as R in the discussion of Ganguly-Magee. The curves in Figs. 1 and 2 are reproduced from Ganguly-Magee's calculation for the 0.5-Mev β-particle track (see Fig. 2 in reference 4).

In Fig. 1, $G_{H_2}/G_{H_2}{}^0$ vs the cube root of a dimensionless quantity is proportional to the reactivity of solute,[4] and the observed $G(H_2)$ vs the cube root of the molarity and the activity of $NaNO_3$ are shown.[2,3]

Circles are the observed $G(H_2)$ plotted as (molarity)$^{\frac{1}{3}}$ and crosses as (activity)$^{\frac{1}{3}}$. The best fit to the theoretical curve is obtained if we take Ks as 9.2×10^9 liter mole^{-1} sec^{-1}. The value thus obtained is the rate constant of the scavenging reaction.

$$H+NO_3^-\rightarrow NO_2+OH^-. \qquad (1)$$

Sowden[5] also observed that $G(H_2)$ can be expressed with two functions of the type of

$$G(H_2)=A-B(NO_3^-)^{\frac{1}{3}}.$$

He did not give any explanation for the sharp break of $G(H_2)$ at a concentration of 1.0 molal of NO_3^-. He irradiated the aqueous calcium nitrate solution with a

mixture of fast neutrons and γ rays. Despite this difference in experimental conditions, his data will also fit the theoretical curve well if we take Ks as 6.9×10^9 liter mole^{-1} sec^{-1} (Fig. 2). Both Ks values are in fairly good agreement.

Although the concept of the activity of electrolyte may have some significance in the radiolysis of aqueous solution, the radical scavenging reaction is generally considered to be rather insensitive to the electrical field around the radical. We wish to mention that the decrease of $G(H_2)$ with the cube root of the solute activity at high concentrations is not predicted by any theory at present.

[1] H. A. Mahlman and J. W. Boyle, J. Chem. Phys. **27,** 1434 (1957).
[2] H. A. Mahlman, J. Chem. Phys. **31,** 993 (1959).
[3] H. A. Mahlman, J. Chem. Phys. **32,** 601 (1960).
[4] A. K. Ganguly and J. L. Magee, J. Chem. Phys. **25,** 129 (1956).
[5] R. G. Sowden, Trans. Faraday Soc. **55,** 2084 (1959).

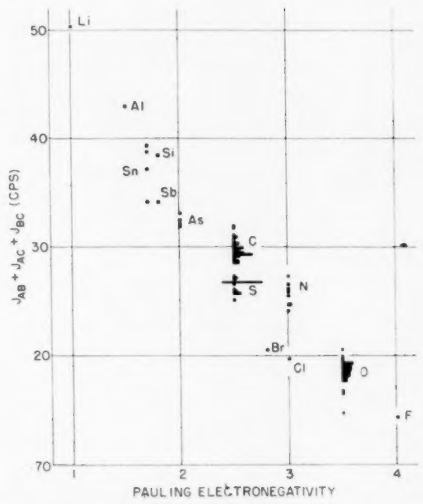

FIG. 1. Relationship between the sum of the three spin-spin coupling constants in the vinyl group and the electronegativity of the element immediately attached to it. Points are plotted at intervals of 0.2 cps and accumulated toward the right when duplications occur. The results are from many sources but mainly from reference 2.

Erratum and Further Comments: Exact Analysis of Three-Spin NMR Spectra

J. S. WAUGH*

Department of Chemistry, Research Laboratory of Electronics,† and Laboratory of Chemical and Solid State Physics, Massachusetts Institute of Technology, Cambridge, Massachusetts

AND

S. CASTELLANO

Istituto di Chimica Industriale, Politecnico di Milano, Milano, Italy

[J. Chem. Phys. **34,** 295 (1961)]

IN Table I of our paper, the signs of the last terms of H_{nn} in lines 5, 6, and 7 should be changed in order for the consequences later deduced to make sense.

We should have said on p. 299 that Eq. (16′) (Appendix A) as well as Eq. (16) are needed to determine unambiguously the quadrant in which Θ lies.

It has been pointed out to us that our use of the solidus in the definitions of $\alpha\pm$ and K (p. 300) is confusing. The last two terms in the former are $\mathcal{E}W\mp/2$ and $-9\mathcal{E}^3/2$. The square bracket in the latter should be $[7\mathcal{E}^2/6+(T_+ + T_-)/16]$.

When the spin system of interest comprises the three protons of a vinyl group, as in the examples we considered, a good deal of labor can be saved by making use of the remarkably good correlation between each of the spin-spin coupling constants J and the electronegativity of the atom immediately attached to the vinyl group, first noticed by Banwell and Sheppard.[1] Figure 1 shows this correlation for the *sum* of the three coupling constants, using results on over 100 vinyl compounds, mostly taken from the compendious paper of Brügell *et al.*[2] and extending over a very wide range of electronegativity.

The utility of this relationship in the present context arises from the fact that the *sum* of the coupling constants is immediately deducible from the repeated spacings in the raw NMR spectrum, but with some ambiguity arising from the 15 possible ways (groupings) of dividing the spectrum into three quartets and three combination lines and the four possible arrangements of each grouping. We have already pointed out that this ambiguity, and the consequent necessity of carrying out repeated rather lengthy calculations, can in practice be very greatly reduced by making use of certain sum rules for the intensities. The relationship of Fig. 1 reduces it still further. As an example, the spectrum of tetravinyl silicon (kindly run by Dr. R. Arndt on a Varian *A*-60 spectrometer) was examined. Generating the 15 groupings by the use of a pair of dividers, it was quickly found that the absolute sum of the coupling constants (equal to the sum of the repeated spacings with the various possible sign permutations) must have one of the 10 values 9.5, 10.7, 18.3, 20.1, 25.7, 38.5, 45.9, 47.9, 55.3, 84.3 cps. Each occurs six times in different groupings among the 60 arrangements. Clearly only $\sum J = 38.5$ cps is at all consistent with Fig. 1. The number of choices was quickly further reduced to two by application of the intensity sums. From this point the analysis could be completed, if desired, either by the methods of our paper or by using the spacings found as starting values for an iterative calculation.

Figure 1 also permits a rapid check of the correctness of previous spectral analyses for vinyl compounds. In

particular, the absolute values of the sums of the coupling constants given by Brügel *et al.*[2] for tetravinyl silicon (5.6) methyl (3.7)—and ethyl (2.5)—vinyl ketones, acrylyl fluoride (5.2) and 1-vinylcyclohexene-1 (9.6) fall completely outside the plot in Fig. 1.

The correlation with electronegativity is difficult to reconcile with theories of spin-spin coupling which ascribe variation in J to changes in bond angles,[3] without explicit allowance for transfer of charge into and out of the vinyl system.[4] This seems particularly to be the case when it is considered that all three coupling constants in the vinyl group vary with electronegativity *with the same slope*.[1]

The recent suggestion of Reddy and Goldstein[5] that the sum of the coupling constants always falls into one or the other of two (or possibly three) well-defined ranges (~20 cps, ~30 cps) may be seen from Fig. 1 to amount to the statement that most easily available organic substituents begin with either an oxygen or a carbon atom.

* Alfred P. Sloan Research Fellow.
† This work was supported in part by the U. S. Army Signal Corps, the Air Force Office of Scientific Research, and the Office of Naval Research, and in part by a grant from the National Institute of Health.

[1] C. N. Banwell and N. Sheppard, Mol. Phys. **3,** 351 (1960).
[2] W. Brügel, Th. Ankel, and F. Krückeberg, Z. Electrochem. **64,** 1121 (1960).
[3] H. S. Gutowsky, M. Karplus, and D. M. Grant, J. Chem. Phys. **31,** 1278 (1959).
[4] C. S. Johnson, Jr., M. A. Weiner, J. S. Waugh, and D. Seyferth, J. Am. Chem. Soc. **83,** 1306 (1961).
[5] G. S. Reddy and J. H. Goldstein, J. Chem. Phys. **35,** 380 (1961).

Erratum: Potential Energy Functions for Diatomic Molecules

HUGH M. HULBURT AND JOSEPH O. HIRSCHFELDER

Department of Chemistry, University of Wisconsin, Madison, Wisconsin

[J. Chem. Phys. **9,** 61 (1941)]

THERE is a typographical error in Eq. (17) of this paper which should read

$$b=2-[(\tfrac{7}{12})-(Da_2/a_0)]/c. \qquad (17)$$

The sign following the 2 in this equation was written as plus rather than minus. Unfortunately this error has been perpetuated in more recent articles and texts[1,2] and has led a number of experts to conclude that the Hulburt-Hirschfelder potential gives an extremely poor fit to experiment.

[1] Tawde and Gokalkrishnan, Ind. J. Phys. **28,** 469 (1944).
[2] G. Herzberg, *Spectra of Diatomic Molecules* (D. Van Nostrand Company, Inc., Princeton, New Jersey, 1950), 2nd ed. Eq. (III, 102) should read $b=2-(1/c)[\cdots]$.

Notes

Group Theory and Aromatic Molecules

J. S. GRIFFITH*

Department of Chemistry, University of Pennsylvania, Philadelphia 4, Pennsylvania

(Received May 12, 1961)

PARR[1] has recently proposed that calculations on molecules isoelectronic with benzene should be performed in a scheme using the molecular orbitals appropriate to D_{6h} symmetry. All operators for the molecule are to be classified by their group-theoretic behavior and the calculation of their matrix elements simplified by group-theoretic means. He then further suggested that larger π-electron systems might often be treated in a similar way, using a model considered by Moffitt[2] (see also Petruska[3]) in which the basic molecular orbitals are those suitable for a periphery passing through each conjugated carbon nucleus. For example, the π systems of both naphthalene and azulene are related to the 10-carbon periphery, with pseudo-symmetry D_{10h}, and the internal bond is a one-electron operator whose matrix is to be determined in this scheme. Parr emphasizes the desirability of suitably powerful group-theoretic methods.

I have been led to an almost identical point of view from the opposite direction, having been interested in the development of group-theoretic techniques for finite symmetry groups analogous to, and as powerful as, those of Racah[4] and Wigner[5] for the full rotation group. The V, W, and X coefficients which I have discussed elsewhere[6,7] for the octahedral group may be used equally well for the dihedral groups. They need only be tabulated for the pure rotation groups because any other is isomorphic with a rotation group or is a direct product. The coefficients for a direct product may be taken as the products of the coefficients for the two separate groups.[8] Finally for a dihedral group D_n, with $n>2$, the power $(-1)^a$ of a representation symbol[6] should be defined as $+1$ except for $a=A_2$ when it is -1. Combining this apparatus with the concept of irreducible tensor operator[4,5,7,9] then gives an apparatus which, I suggest, satisfies Parr's requirements.

I have written a book on V, W, X and the irreducible tensor method for point symmetry groups which explains some of the things mentioned in the last paragraph in more detail.[8] However, I would like to point out here that, because the group D_{6h} is the triple direct product $D_3\times C_2\times\sigma_h$, where each of C_2 and σ_h contain just two elements, V, W, and X for D_{6h} are trivially implicit in my tables already given[6] for the octahedral group O. For if we restrict the latter group to its dihedral group about the (111) axis of the octahedron, we see that the irreducible representations A_1, A_2 and E of O become A_1, A_2 and E of D_3. Therefore, the coefficients for D_3 are just those parts of the tables for O

which do not contain either T_1 or T_2. Finally, writing A and B for the irreducible representations of C_2, those of D_6 in their conventional notation correspond to those of $D_3 \times C_2$ according to the scheme

$$A_1A \rightarrow A_1 \qquad A_2A \rightarrow A_2 \qquad EA \rightarrow E_2$$

$$A_1B \rightarrow B_1 \qquad A_2B \rightarrow B_2 \qquad EB \rightarrow E_1.$$

* Present address: King's College, Cambridge, England.

[1] R. G. Parr, J. Chem. Phys. **33,** 1184 (1960).
[2] W. Moffitt, J. Chem. Phys. **22,** 320 (1954).
[3] J. Petruska, J. Chem. Phys. **34,** 1111 (1961).
[4] U. Fano and G. Racah, *Irreducible Tensorial Sets* (Academic Press Inc., New York, 1959).
[5] E. P. Wigner, *Group Theory and Its Application to the Quantum Mechanics of Atomic Spectra* (Academic Press Inc., New York, 1959).
[6] J. S. Griffith, Mol. Phys. **3,** 285 (1960).
[7] J. S. Griffith, Mol. Phys. **3,** 457 (1960).
[8] J. S. Griffith, *The Irreducible Tensor Method for Molecular Symmetry Groups* (Prentice-Hall, Inc., Englewood Cliffs, New Jersey, to be published).
[9] Y. Tanabe and H. Kamimura, J. Phys. Soc. Japan **13,** 394 (1958).

Franck-Condon Factors and the Shape of Ionization Efficiency Curves

MORTON E. WACKS AND MORRIS KRAUSS
Physical Chemistry Division, National Bureau of Standards, Washington, D. C.

(Received July 7, 1961)

ANY discussion of the finer details of electron or photon ionization of molecules necessitates having the Franck-Condon probabilities for transitions between vibronic states. In the Born-Oppenheimer approximation the probability of a transition is given by

$$P_{ev,e'v'} \sim \left| \int G_{e,e'}(R, r) \Psi_{e,v}(R) \Psi_{e',v'}(R) d\tau_R \right|^2,$$

where $\Psi_{e,v}(R)$ and $\Psi_{e',v'}(R)$ are the vibrational wave functions for the neutral molecule and ion, respectively.[1] For electron impact ionization near threshold $|G_{e,e'}|^2$ varies linearly with the excess energy above threshold.[2] For photo-ionization it is assumed that the probability near threshold can be approximated by a step function. If the variation of the perturbation integral $G_{e,e'}$ with R is small, then we have

$$P_{ev,e'v'} \sim |G_{e,e'}(R_e r)|^2 \cdot \left| \int \Psi_{e,v}(R) \Psi_{e',v'}(R) d\tau_R \right|^2.$$

Those features of the ionization efficiency curves that are due to transitions to the various vibrational levels of the ion can be described to a good approximation by the vibrational overlap integral. Considerable discussion of the problems concerning the computation of these integrals has been given by Nicholls and coworkers.[3] Under Nicholls' direction a program has been prepared for the 704 electronic digital computer at NBS which will evaluate these integrals for Morse vibrational functions.[4] We have utilized this program to compute values for the transitions $O_2(X\,^3\Sigma_g - v' = 0, 1)$ to $O_2^+(X, a, A, b)$, $NO(X\,^2\Pi v' = 0)$ to $NO^+(X, A)$, and CO $(X\,^1\Sigma^+ v' = 0)$ to $CO^+(X, A, B)$. The results for the oxygen transitions $O_2(X, v' = 0) \rightarrow O_2^+(X, a, A, b; v'' = 0 \rightarrow 10)$ and those of NO to the ground state of NO^+ are tabulated in Table I.

TABLE I. Transition probabilities $M(X_{v'=0}) \rightarrow M^+(v'' = 0 \rightarrow 10)$.

v''	$O_2^+(^2\Pi_g)$	$O_2^+(^4\Pi_u)$	$O_2^+(^2\Pi_u)$	$O_2^+(\Sigma_g^-)$	$NO^+(^1\Sigma^+)$
0	0.23545	0.00988	0.00281	0.40574	0.15500
1	0.39021	0.03667	0.01226	0.33613	0.32417
2	0.26277	0.07411	0.02920	0.16424	0.29725
3	0.09197	0.10839	0.05038	0.06294	0.15702
4	0.01771	0.12872	0.07068	0.02123	0.05281
5	0.00182	0.13202	0.08583	0.00671	0.01180
6	0.00009	0.12152	0.09375	0.00277	0.00178
7	0.00000	0.10301	0.09455	0.00064	0.00018
8	0.00000	0.08192	0.08970	0.00020	0.00001
9	0.00000	0.06197	0.08116	0.00006	0.00000
10	0.00000	0.04506	0.07078	0.00002	0.00000

These values permit a closer look at three ionization experiments: the photo-ionization of NO by Watanabe *et al.*[5,6] the electron-impact spectrum of NO^+ obtained by Morrison,[7] and the electron-impact ionization of O_2 by Frost and McDowell.[8] In the latter work the resulting ionization efficiency curves are considered to be equivalent to curves obtained by mono-energetic electrons.

The interpretation of the NO photoionization curve becomes simple with the assumption that the photoionization probability in the neighborhood of threshold is a step function. The relative ratios of the first four vibrational levels (Table II) are seen to be in reasonable agreement with the calculated values.

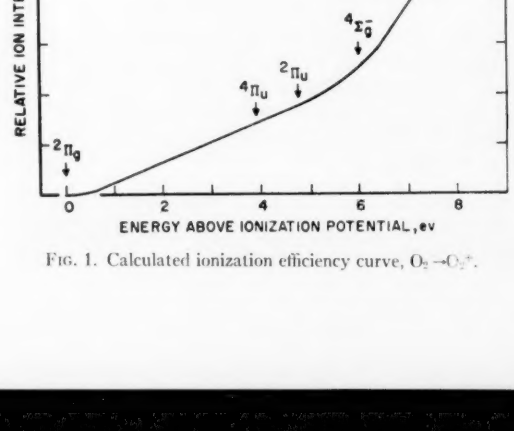

FIG. 1. Calculated ionization efficiency curve, $O_2 \rightarrow O_2^+$.

TABLE II. Ratio of transition probability $NO[X^2\Pi] \rightarrow NO^+[X^1\Sigma^+ v_n'']$ to $NO^+[X^1\Sigma^+ v''=1]$.

v''	Calc.	Exp.[6]
0	0.48	0.7_9
1	1.00	1.0_0
2	0.92	1.0_5
3	0.49	0.6_7

Morrison[7] has shown that the interpretation of the second derivative of the electron impact ionization efficiency curve for NO is in agreement with the photoionization results. Evidently the assumption of a linear law for electron ionization is valid at least for this region above threshold. In both experiments at about 1.5 ev above the ground state there is a sudden increase in intensity which can not be explained by the vibrational factors.

The trend in the transition moment with internuclear distance can be found by a method of Fraser's.[9] For continuous absorption

$$I_{v'v''}/I_{v'n} = |(v'v'')|^2/|(v'n)|^2 \cdot |R_{e'}(\bar{r}v'v'')|^2/|R_{e'}(\bar{r}v'n)|^2,$$

these quantities are defined in reference 9. We obtain the relative values of the square of the transition moment as a function of the r-centroid value for the particular vibrational transition. These values appear to be too rapidly varying and more data on the progressions would be required to settle the question.

The use of the Franck-Condon approximation for the interpretation of electron-impact data is far more uncertain. We have attempted to reproduce the shapes of the O_2 curves of Frost and McDowell under the same assumptions that are normally made for their interpretation; i.e., the energy dependence of the electronic transition is linear in the excess energy of the ejected electron for the range of energies under observation. The ionization efficiency curves for O_2 are computed so that the relative limiting slopes for the electronic transitions are matched, where possible, to those observed by Frost and McDowell. Figure 1 shows that the vibrational transitions obscure the electronic transition thresholds. It is necessary to introduce an additional unknown factor to explain the observation of certain thresholds by the intersection of linear sections of the curve. The simple assumptions implicit in the interpretation of these experiments may require re-examination.

[1] A. S. Coolidge, H. M. James, and R. D. Present, J. Chem. Phys. **4,** 193 (1936).
[2] D. R. Bates, A. Fundaminsky, J. W. Leech, and H. S. W. Massey, Trans. Roy. Soc. (London) **A243,** 93 (1950); S. Geltman, Phys. Rev. **102,** 171 (1956); R. E. Fox and W. M. Hickam, J. Chem. Phys. **22,** 2059 (1954); G. H. Wannier, Phys. Rev. **100,** 1180 (1956).
[3] W. R. Jarmain and R. W. Nicholls, Can. J. Phys. **32,** 201 (1954).
[4] The development of this computer program by Miss Irene Stegun and Miss Ruth Zucher of the Computation Section of the Applied Mathematics Division at NBS under Dr. Nicholl's direction was supported by ONR. The program was checked against the results of hand computations published in reference 3. R. W. Nicholls, J. Research Natl. Bur. Standards (to be published).
[5] K. Watanabe, F. F. Marmo, and E. C. Y. Inn, Phys. Rev. **91,** 1155 (1953).
[6] "Final report on ionization potential of molecules by a photoionization method", K. Watanabe, T. Nakayama, and J. Mottl, Department of Physics, University of Hawaii, December, 1959.
[7] J. D. Morrison, Rev. Pure Appl. Chem. **1955,** 22.
[8] D. C. Frost and C. A. McDowell, J. Am. Chem. Soc. **80,** 6183 (1958).
[9] P. A. Fraser, Can. J. Phys. **32,** 515 (1954).

Study of Hydrogen Bonding. The Microwave Rotation Spectrum of CF_3COOH—HCOOH

C. C. COSTAIN AND G. P. SRIVASTAVA*
Division of Pure Physics, National Research Council, Ottawa, Canada
(Received July 17, 1961)

A MICROWAVE investigation of the gas-phase rotation spectra of hydrogen-bonded molecules has been started in the hope of providing new information on hydrogen bonds. In the first experiments, a series of broad absorption lines has been measured for the bimolecule CF_3COOH-HCOOH. The variation of intensity with temperature and pressure follows that expected from the association constants[1] of the carboxylic acid dimers; e.g., at 50-μ pressure, the absorption is very strong at $-40°C$, but difficult to detect at 0°C.

Under suitable conditions of temperature and pressure, two vibrational satellites were seen, forming shoulders on the main line. The strongest, on the low-frequency side, has a Boltzmann factor corresponding to a frequency of approximately 180 cm^{-1}. If this vibration, with a small positive α, is assumed to be the symmetric stretching vibration of the hydrogen bond, the H-bond force constant is found to be $k=0.31\times 10^5$ d/cm.

TABLE I. CF_3COOH—HCOOH rotation lines.

J	Freq. in Mc/sec	(B+C) in Mc/sec
3←2	3462.2	1154.1
7←6	8079.1	1154.2
8←7	9235.2	1154.4
9←8	10 388.5	1154.3
16←15	18 473.0	1154.6
17←16	19 621.8	1154.2
18←17	20 779.2	1154.4
19←18	21 938.5	1154.7

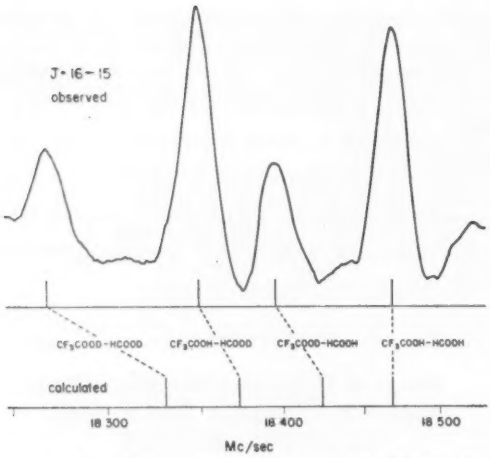

FIG. 1. $J=16\leftarrow15$ transition for normal CF_3COOH-HCOOH and three deuterated species. The difference between the calculated and observed spectrum results from the lengthening of the hydrogen bond on deuteration.

If it is assumed that the bi-molecule is planar, except for the F_3 group, a large asymmetry results, with $\kappa=-0.95$. For the $J=16\leftarrow15$ transition, the lines with K=4 to K=15 are predicted to be spread over 60 Mc/sec. Contrary to this prediction, the observed line has a total width at half-intensity of only 13 Mc/sec. The lines with K=0, 1, 2 and 3 are predicted to be spread over 1000 Mc/sec. A very careful search was made in the neighborhood of the $J=16\leftarrow15$, $J=7\leftarrow6$ and $J=3\leftarrow2$ lines, but only the strong central component could be found.

Both of these results could be explained if the formic acid is rotated by a considerable amount with respect to the carboxyl group of the trifluoroacetic acid, making the bi-molecule more nearly a symmetric top. However, a rotation of over 80° from the plane is necessary to bring the K=1 lines into the central line. It is more likely that for the high J, low K lines the Stark voltage of 3500 v/cm was insufficient to separate the Stark lobes from the lines.

The frequencies of the measured lines are given in Table I.[2] These frequencies can be fitted reasonably well by the equation $\nu=(B+C)(J+1)$. The value of $B+C$ gives an O-H···O distance of 2.69 A for the planar model.

When HCOOD is mixed with CF_3COOH four isotopic species of the bi-molecule are produced by: (a) the rapid exchange by tunneling of H and D in the bi-molecule, and (b) the exchange of the constituent molecules effected as the bi-molecules break and reform. Figure 1 is a tracing of the $J=16\leftarrow15$ line for the four species. Two very interesting results are obtained from this figure. First, there is the difference in intensity of the lines of the two singly deuterated species. Instead of being nearly equal in energy, the relative intensities show a Boltzmann dependence, with the ground state of the species with D on the formic acid about 110 cm^{-1} lower in energy. This is a surprisingly large zero-point isotope effect.

Second, the observed frequencies of the deuterated species differ markedly from the frequencies calculated from the assumed geometry. To fit the observed frequencies, the O···O distance in the O—D···O bond must be 0.011 A longer than in the O—H···O bond. This figure fits closely on the curve given by Gallagher[3] for the Ubbelohde effect in crystals. The present measurement in the comparatively free environment of the gas phase is certainly the most important result of this work.

A linear extrapolation of the 0.011 A isotope effect predicts a shortening of 0.073 A in the O···O distance when the OH vibration is excited from the $v=0$ to $v=1$ state. Such a shortening has been postulated by Sheppard[4] to explain the very broad OH bands so characteristic of dimers.

Further efforts are being made to locate the low K lines in order to determine the configuration, and more isotopic species are being studied to obtain other structural details.

* N.R.C. Postdoctorate Fellow 1960–61.

[1] G. C. Pimentel and A. L. McClellan, *The Hydrogen Bond* (W. H. Freeman and Company, San Francisco, California, 1960).

[2] The authors have been informed in a private communication that some of these lines have also been observed by R. Keller and W. D. Gwinn, University of California.

[3] K. J. Gallagher, *Hydrogen Bonding*, Ljubljana Conference, edited by D. Hadgi (Pergamon Press, New York, 1959), p. 48.

[4] N. Sheppard, *Hydrogen Bonding*, Ljubljana Conference, edited by D. Hadgi (Pergamon Press, New York, 1959), p. 92.

Antiferromagnetic-Ferromagnetic Transformation in FeRh

L. MULDAWER
Temple University, Philadelphia, Pennsylvania
AND
F. DEBERGEVIN
Institute Fourier, Grenoble, France

(Received July 27, 1961)

IN 1938, Fallot[1] observed a sharp increase in the magnetization of iron-rhodium with increasing temperature, the transition temperature rising as the rhodium content increased. Fallot and Hocart[2] explained the effect in terms of a crystal structure change similar to the alpha-gamma transformation in pure iron. We have shown that such is not the case; x-ray diffraction studies[3] show that the alloy has the cesium chloride structure above and below the magnetic transition, even down to 80°K. Where the α (CsCl) phase exists, it is ordered up to at least 800°C. The α phase is stable up to a temperature which is a function of composition; above this temperature it transforms to γ (disordered face-centered cubic). For the 50% alloy this limit is

near 1300°C; for the 60% alloy it is near room temperature. In the region of the magnetic transformation, the lattice constant a shows an abrupt variation of about 0.3%. This indicates a first order transformation. Qualitatively this transformation resembles that of chromium modified manganese antimonide.[4]

A 1400°C anneal of an alloy with a T_c near 50°C (56% rhodium) gave an interesting but unexplained result. Upon cooling, the lattice constant a was found to be about 0.3% below that of the antiferromagnetic phase and 0.6% below that of the ferromagnetic phase. Furthermore, it remained ferromagnetic in liquid nitrogen as shown by holding the specimen at the end of a magnet in liquid nitrogen. Prior to the 1400°C anneal, it would fall off when so placed. After successive 1-hr 1000°C anneals, the lattice constant and magnetic properties were gradually recovered. In the process, it was noted that the lines from the normal phase and the magnetically unknown phase coexisted; the anneals gradually diminishing one and increasing the other. As far as we could tell, this unknown phase was as well ordered as the normal phase; perhaps the high-temperature anneal produced excess vacancies[5].

Neutron-diffraction studies[6] have been carried out on alloy powders prepared chemically. Runs were taken above and below T_c for a 56% rhodium sample. As expected, evidence was found for an antiferromagnetic ordering with a pattern of the type expected from a Heusler alloy, space group $Fm3m$. The unit cell lattice constant is doubled and presumably there are two kinds of iron differentiated by spin direction. Thus far we have assumed no contributions (magnetically speaking) from the rhodium atoms. There seem to be some inconsistencies in the neutron diffraction intensities and it has been suggested that the rhodium moment may be as large as one-third that of the iron moment.

The recent theory of Kittel[7] would seem to be an ideal one for this system. The basic assumption is that the exchange coupling between the two magnetic sublattices changes sign at a critical value of the lattice constant. There are some difficulties in applying this theory to the iron-rhodium case. Since the lattice constant of pure iron is 2.86 A and that of FeRh around 2.98 A, we would expect that the lattice constant in the alpha iron-rhodium alloys would increase with increasing rhodium content. This increase occurs for γ iron-rhodium from 50 to 60%; this does not necessarily also hold for the α phase. Fallot and Hocart found no variation in lattice constant for α phase in this composition region. The temperature at which the critical value of the lattice constant is reached determines T_c. T_c should decrease as the rhodium content increases if rhodium expands the alpha iron-rhodium lattice; just the opposite is observed. Secondly, the ferromagnetic phase of abnormally low a cannot be explained on the basis of a single critical lattice constant. Thus, while a critical value of the lattice constant exists, it is probably an explicit function of the composition and there may exist a second lower valued a_c giving a bounded range of lattice constant for the existence of the antiferromagnetic phase.

[1] M. Fallot, Ann. phys. **10,** 291 (1938).
[2] M. Fallot and R. Hocart, Rev. sci. No. 8, **498** (1939).
[3] F. deBergevin and L. Muldawer, Compt. rend. **252,** 1347 (1961).
[4] T. J. Swoboda, W. H. Cloud, T. A. Bither, M. S. Sadler, and H. S. Jarrett, Phys. Rev. Letters **4,** 509 (1960).
[5] An explanation in terms of changes in surface composition and subsequent diffusion is untenable.
[6] F. deBergevin, E. F. Bertaut, and G. Roult, Compt. rend. (to be published).
[7] C. Kittel, Phys. Rev. Letters **120,** 335 (1960).

Symmetry-Adapted LCAO MO's for Long-Chain Polyenes

MARVIN C. TOBIN
Chemical Research Department, Central Research Division, American Cyanamid Company, Stamford, Connecticut
(Received May 22, 1961)

THE problem of the electronic structure of long-chain conjugated molecules has attracted the attention of numerous workers.[1,2] These workers solved their secular equations by direct reduction of the secular determinants of cyclic or noncyclic molecules, generally by expansion into minors.

Longuet-Higgins and Salem[3] attacked the problem by setting up symmetrical LCAO MO's for a cyclic polyene and obtaining the energy levels from these. Koutecký and Zahradník[4] treated a number of conjugated systems using Bloch functions. Their calculation, unlike many of the previous ones, included overlap.

We should like to propose another approach in which the Born-von Karman cyclic boundary conditions are assumed to hold for a finite, linear chain. This model will not give a good approximation to the energy levels for short linear chains, but becomes asymptotically correct for infinite chains. Use of the model makes it possible to use LCAO MO symmetry orbitals which are adapted to the line group (one-dimensional space group)[5] of the system. Use of cyclic boundary conditions, upon which the line group irreducible representations are based, requires inclusion of resonance integrals across the end atoms. With this stipulation, integrals such as

$$\int \Gamma_i^* H \Gamma_j d\tau$$

will vanish if symmetry orbitals Γ_i^* and Γ_j belong to different irreducible representations. The secular equation will thus factor into diagonal blocks. The method is, of course, perfectly general, and not restricted to polyenes.

As an example, a long-chain polyene with alternating bond lengths (factor-group symmetry C_{2h}) will be treated including next-nearest neighbor interaction. The appropriate irreducible representation matrices for this group may easily be selected from those of Table II, reference 5, using coset representatives T, σ_h, C_2, and i. The pi symmetry orbitals are found to belong to A_u and B_g (factor group) and $(\mathbf{k}, A_2)$ (interior). The secular equation, for a chain of N repeat units ($2N$ chain atoms), splits into two 1×1 factor-group blocks, $(N\text{-}2)/2$ 4×4 interior blocks, and two 1×1 Brillouin-zone-boundary blocks.

An appropriate set of orthonormal symmetry orbitals (assuming an orthonormal atomic orbital basis) is

$$\Gamma(\mathbf{k})^{\pm}=(2N)^{-\frac{1}{2}}[\phi_1\pm\phi_2+\exp(-2\pi i\mathbf{k}\cdot\mathbf{t}_1)\phi_3$$
$$\pm\exp(-2\pi i\mathbf{k}\cdot\mathbf{t}_1)\phi_4\cdots\pm\exp(-2\pi i\mathbf{k}\cdot\mathbf{t}_{N-1})\phi_{2N}] \quad (1)$$

Here $\mathbf{k}$ ranges from $\mathbf{k}=0$ for the factor group orbitals to $\mathbf{k}=\mathbf{b}/2$ for the Brillouin-zone-boundary orbitals[5] for the correct total of $2N$ symmetry orbitals.

Evaluation and suitable transformation of the interior blocks of the secular equation gives, finally, the expression

$$\epsilon=\pm[\beta_1^2+\beta_2^2+2\beta_1\beta_2\cos(2\pi l/N)]^{\frac{1}{2}},\ 0\leq l<N \quad (2)$$

where β_1 and β_2 are resonance integrals over the long and short bonds. The quantity $\epsilon=\lambda-\alpha-\eta$, where λ is the energy, α the Coulomb integral, and $\eta=2\gamma\cdot\cos(2\pi l/N)$, $0\leq l<N$. Here γ is the next-nearest-neighbor resonance integral. Equation (2) is similar to the expression obtained by Longuet-Higgins and Salem[3] for a cyclic chain, if γ is set equal to zero. It is apparent that in the present approximation inclusion of next-nearest neighbor interaction will change the band shapes, but not the energy gap.

Longuet-Higgins and Salem[3] give for β as a function of r an expression equivalent to

$$\beta=2317\exp(-r/0.3106)\ \text{kcal/mole}. \quad (3)$$

Use of their bond lengths in Eq. (3) and the resulting values of β_1 and β_2 in Eq. (2) gives an estimate of about 4 kcal/mole or 0.15 ev for the energy gap in polyenes. The case of infinite polyenes with all bonds of equal length may be treated in a similar fashion. Now the line group symmetry is V_h, and the symmetry orbital symmetries B_{2g} and B_{1g} (factor group), and $(\mathbf{k}, B_2)$ and $(\mathbf{k}, A_2)$ (interior). The symmetry orbitals are

$$\Gamma\begin{pmatrix}B_2\\ \mathbf{k},\\ A_2\end{pmatrix}:\ (2N)^{-\frac{1}{2}}\{\phi_1\pm\exp(-2\pi i\mathbf{k}\cdot\mathbf{o})\phi_2$$
$$+\exp(-2\pi i\mathbf{k}\cdot\mathbf{t}_1)\phi_3\pm\cdots$$
$$\pm\exp[-2\pi i\mathbf{k}\cdot(\mathbf{o}+\mathbf{t}_{N-1})]\phi_{2N}\}, \quad (4)$$

where $\mathbf{o}$ is the glide reflection vector. Including nearest neighbor interactions only, this leads to energy levels

$$\lambda=\alpha\pm2\beta\cos(\pi l/N)\quad 0\leq l<N. \quad (5)$$

Equation (5) may be obtained directly from Eq. (2) by setting $\beta_1=\beta_2$ and $\gamma=0$.

The interior energy levels in (2) and (5) are seen to be doubly degenerate; this is a consequence of the $(\mathbf{k}, -\mathbf{k})$ degeneracy in the line group representations.

The present method has the advantage of avoiding lengthy expansions of determinants. It properly sorts the energy levels into symmetry-classified bands. Inclusion of overlap or next-nearest-neighbor interactions add little complication. On the other hand, it must be emphasized that the results are correct only in the limit of an infinitely long chain. The method thus cannot be used to investigate short chains or boundary effects.

[1] C. A. Coulson, Proc. Roy. Soc. (London) **A164,** 383 (1938); **A169,** 413 (1939); C. A. Coulson and H. C. Longuet-Higgins, *ibid.* **A191,** 39 (1947); C. A. Coulson and G. S. Rushbrooke, Proc. Cambridge Phil. Soc. **44,** 272 (1948); F. G. Fumi, Nuovo cimento **8,** 1 (1951).

[2] T. A. Hoffman, Acta. Phys. Acad. Sci. Hung. **1,** 5, 175 (1951); **2,** 195 (1952) for related work on chains of metal atoms.

[3] H. C. Longuet-Higgins and L. Salem, Proc. Roy. Soc. (London) **A251,** 172 (1959).

[4] J. Koutecký and R. Zahradník, Collection Czechoslov. Chem. Communs. **25,** 811 (1960).

[5] M. C. Tobin, J. Mol. Spectroscopy **4,** 349 (1960).

Infrared Spectra of Synthetic Diamond

J. J. Charette

Department of Physics, University Lovanium of Leopoldville, Congo

(Received June 19, 1961)

We have been able to measure the infrared absorption of eight synthetic diamonds made at the Adamant Research Laboratory of Johannesburg. They were more or less cubic stones, yellow with black inclusions, of size 0.2 to 0.3 mm. They have been made at a pressure of 75 000 bar and a temperature 2400°C. The starting material is not revealed.

The spectra were obtained with the Perkin-Elmer prism-grating 112 G spectrometer with the microscope attachment, model 85. The absorption bands appeared only weakly—except for the two at 1126 and 1343 cm^{-1}—over a background of pseudo-abosrption produced by the inhomogeneity of the synthetic stones and their small and irregular shape giving rise to internal reflec-

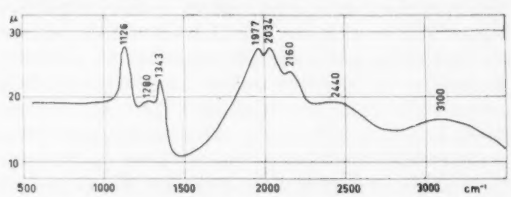

FIG. 1. Absorption spectra of a synthetic diamond.

tions. The resulting loss of light is estimated by comparing the absorption coefficient of the synthetic and natural diamonds for the vibration bands at 2034, 2440, and 3200 cm^{-1}: 27, 19, 16 cm^{-1} for the synthetic vs 14, 6, and 3 for the natural.[1] The absorption coefficients were calculated with the uncorrected transmission $T=I/I_0$ by the Fan's formula[2]

$$T=(1-r)^2/(e^{\mu t}-r^2e^{-\mu t}),$$

where t is the thickness in centimeters and μ the absorption coefficient in cm^{-1}; the reflectivity r was given by

$$r=(n-1)^2/(n+1)^2$$

with $n=1.39$. Figure 1 gives the curve μ vs the wave number for one of the specimens. The other spectra are similar. The contrast is greatly enhanced here as compared to the curve obtained with T in ordinate.

Three things of interest appear in these spectra. First, all the synthetic stones exhibit the bands common to all natural diamonds and attributed to two phonon processes in the 2000–2500 cm^{-1} region and to three phonon processes in the region 3100 to 3300 cm^{-1}. There is even a very good agreement in the wave numbers of the peaks measured at 1977, 2034, 2160, and 2400 cm^{-1}.

Secondly, are these diamonds of type I or type II? Of the characteristic bands of the type I in the 8-μ region, the 1280 cm^{-1}, which is usually the strongest, appears in our spectra, though only weakly. Kaiser and Bond[3] have demonstrated that these bands correlate to those with nitrogen impurity. No nitrogen was introduced deliberately in the synthetic diamonds, but it is possible that nitrogen from air entrapped in the pressure cavity enters the diamond during the synthesis process. Dr. F. A. Raal of the Diamond Research Laboratory measured the absorption of six synthetic diamonds in the ultraviolet: Three were whitish and transmitted down to 2250 A; three were yellow and transmitted only to 3000 A. No ultraviolet measurements were made on our stones but their yellow color relates them to the last group. This, with the presence of the 1280 cm^{-1} band seems enough to consider them as nitrogen-containing type I.

Third, the best-defined bands in the whole spectra are two fairly intense and narrow bands near 1126 and 1343 cm^{-1}. The wave numbers for the eight specimens are (within 2 cm^{-1}), *SD*1: 1126, 1343; *SD*2: 1126, 1343; *SD*3: 1127, 1344; *SD*4: 1124, 1343; *SD*5: 1122, 1343; *SD*6: 1121, 1330, 1343; *SD*7: 1331; *SD*8: 1119, 1343.

Those bands do not appear in natural diamonds. Their wave numbers correspond to the symmetric and antisymmetric vibrations of $=SO_2$ groups. We do not know if this is a mere coïncidence. It must be noted that Smith and Hardy[4] have found a peak at 1122 cm^{-1} in neutron-irradiated diamonds. The Raman frequency is at 1333 cm^{-1}.[5] An infrared band has been reported at the same wavenumber in some diamonds[1,6] but never as high as 1343 cm^{-1}.

We wish to thank Dr. F. A. Raal for providing the ultraviolet results, Dr. P. Kemmey for many helpful comments, and Dr. J. F. H. Custers for providing the specimens and showing a constant interest in our work.

[1] J. J. Charette, Physica (to be published).
[2] H. Y. Fan, Repts. on Progr. in Phys. **19,** 107 (1956).
[3] W. Kaiser and W. L. Bond, Phys. Rev. **115,** 857 (1959).
[4] S. D. Smith and J. R. Hardy, Phil. Mag. **5,** 1311 (1960).
[5] R. Robertson, J. J. Fox and A. E. Martin, Phil. Trans. Roy Soc. London **A232,** 463 (1934).
[6] G. B. B. M. Sutherland, D. E. Blackwell, and W. G. Simeral, Nature **174,** 901 (1954).

Attempts to Find Photoconductivity in Dilute Sodium-Ammonia Solutions

R. L. Potter, R. G. Shores, and J. L. Dye
Kedzie Chemical Laboratory, Michigan State University, East Lansing, Michigan

(Received July 28, 1961)

OGG has reported[1,2] that very dilute solutions of sodium in liquid ammonia are photoconductive. There appears to be no verification of this photoconductivity (or "inner photoelectric effect"). In view of recent models of the solvated electron in very dilute solutions,[3,4] the presence or absence of such an effect is important since it would imply excitation of bound electrons to a conduction band located about 0.8 ev above the trapped electron level,[1] and the dilute solutions would be classed as semiconductors. It is to be noted that Ogg also reports a photoconductive effect in solutions of sodium amide in ammonia.[5]

The studies by Ogg involved the measurement of current through a "moderately sensitive" galvanometer, using a dc source and visible light from a projection lamp, together with various filters. His cell utilized platinum wire electrodes and the cell was made one arm of a Faraday tube so that the concentration could be varied. Ogg reports,[1] "Extremely dilute sodium solutions (some 10^{-5} molar) observed in the temperature range $-35°$ to $-75°$ displayed a marked increase in electrical conductivity upon irradiation with visible light." He further noted the quantum efficiency of this photoconductivity to be an inverse function of concentration, which necessitated the use of 10^{-5} to 10^{-4} molar solutions.

The present note is an account of our failure to observe photoconductivity using either ac or dc methods.

Great care was taken to prepare pure solutions of sodium in ammonia. The conductance cell was made one arm of a Faraday tube so that it could be rinsed out prior to use, and so that various concentrations could be obtained with a single preparation. The purification of sodium and ammonia, and the manipulation of the cell were similar to the techniques reported by Douthit and Dye[6] for obtaining absorption spectra. The elec-

trodes were platinum balls about two millimeters in diameter which were fused to tungsten wires sealed through Pyrex. The cell constant (1.93) was determined by comparison with a Leeds and Northrup type A cell using an aqueous KI-I_2 mixture as recommended by Kraus.[7] Cell resistance were measured at frequencies of 400, 600, 1000, 2000, and 4000 cps using a bridge described elsewhere,[8] and also with a dc Wheatstone bridge. In addition, measurements of current through the cell under an applied dc potential were made, using a Scalamp galvanometer, model 7904/S. For illumination, a 500-w projection lamp and a 9-w mercury ultraviolet lamp were used, together with suitable lens systems to allow illumination of the entire cell, or a desired portion of the cell. It should be noted that, due to absorbance by the Pyrex cell the lower wavelength limit penetrating the solution is about 300 mμ. Acetone containing dry ice was used as a bath liquid.

After preparing a $\sim 10^{-2}$ molar solution in one arm of the Faraday tube, the cell was repeatedly rinsed with the solution, and ammonia was distilled into the cell until the cell was filled with a dilute sodium solution. The concentration of the solution was calculated from its resistance using the data of Fristrom.[9] The rate of decomposition of the solution could be determined from the variation of resistance with time. The concentration of the solution in the cell was varied by the addition of solution or ammonia from the other arm.

A number of runs were made at concentrations from 1.5×10^{-5} to 2×10^{-4} molar. Decomposition was quite slow considering the dilute nature of the solutions. For example, at 1.5×10^{-5} molar the initial decomposition rate was 1.3%/hr. Polarization effects were appreciable at the bright platinum electrodes. An increase of 27% in the resistance reading at 600 cps compared to the 4000-cps resistance was observed for a concentration of 1.5×10^{-5} molar. The corresponding increase for a 1.3×10^{-4} molar solution was 1.4%. These effects were even more pronounced when the resistances were measured with a dc Wheatstone bridge.

Illumination of the whole cell, or a part of the cell in no case gave a change in resistance which could be attributed to photoconductivity. A *slow* decrease in resistance amounting to a 2 to 3% change occurred, and was attributed to heating by the lamp. After the light was turned off, the resistance returned slowly to its initial value.

Besides checking the resistance at balance, the current during electrolysis of the solution under a dc potential was observed in the presence and absence of illumination with no effect observed due to light. After the solution had been permitted to decompose until colorless the resistance of the dilute sodium amide solution formed was examined. No photoconductive effect was observed.

Although we attempted to reproduce the conditions reported by Ogg, all of our results were negative. In contrast to his reports of a "marked increase" in conductivity upon illumination, we found no change, even though a sudden change as small as ±0.1% could easily have been detected. Thus we have been unable to verify the existence of photoconductivity in dilute sodium-ammonia solutions.

This work was performed as a special research project in Chemistry 113H at Michigan State University by R.L.P. and R.G.S. The advice and assistance of Professor R. N. Hammer, G. E. Smith, and G. Jacobs is gratefully acknowledged.

[1] R. A. Ogg, Jr., J. Am. Chem. Soc. **68,** 155 (1946).
[2] R. A. Ogg, Jr., Vortex **9,** 62 (1948).
[3] J. Jortner, J. Chem. Phys. **27,** 823 (1957); **30,** 839 (1959).
[4] M. C. R. Symons, Quart. Revs. (London) **13,** 99 (1959).
[5] R. A. Ogg, Jr., J. Chem. Phys. **14,** 295 (1946).
[6] R. C. Douthit and J. L. Dye, J. Am. Chem. Soc. **82,** 4472 (1960).
[7] C. A. Kraus, J. Am. Chem. Soc. **36,** 864 (1914).
[8] J. L. Dye, M. P. Faber, and D. J. Karl, J. Am. Chem. Soc. **82,** 314 (1960).
[9] R. M. Fristrom, Ph.D. thesis, Stanford University, 1949; Doctoral Dissertations No. **16,** 32 (1948–49).

Substitution of Fe^{3+} Ion in Sc_2O_3 and In_2O_3

S. Geller, H. J. Williams, and R. C. Sherwood
Bell Telephone Laboratories, Murray Hill, New Jersey

(Received June 9, 1961)

THE brief study reported here has resulted from a study of scandium substituted gadolinium iron garnet now being completed.[1] In certain cases an extraneous phase with the Sc_2O_3 structure occurs. This phase contains various amounts of Fe^{3+} ion substituted for the Sc^{3+} ion. In order to learn more about the extent of this substitution several specimens were prepared by direct solid state reaction at high temperatures. On finding that considerable amounts of Fe^{3+} would replace the Sc^{3+}, it was felt that magnetic measurements on at least one specimen would prove of some interest. We have found (Fig. 1) that $(ScFe)O_3$ with the Sc_2O_3 structure (better known as the Mn_2O_3 or Tl_2O_3

TABLE I. Lattice constants of specimens in $(Sc_{2-x}Fe_x)O_3$ system.

x	a, A
0.00	9.845[a]
0.75	9.684±0.003
1.00	9.627
1.25[b]	9.573

[a] From H. E. Swanson and R. K. Fuyat, Natl. Bur. Standards Circ. No. 539, Vol. III, 17 (1954).
[b] Specimen contained trace of α-Fe_2O_3 type phase probably containing dissolved Sc_2O_3.

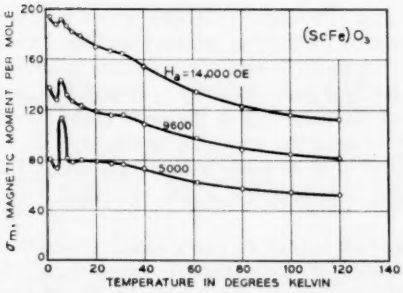

FIG. 1. Magnetic moment vs temperature for $(ScFe)O_3$ at three different applied magnetic fields.

structure type[2] $D5_3$) shows rather strange magnetic behavior (not presently understood) with a magnetic transition of some sort at 7±1°K and possibly one at about 35°K. It is of interest to note that recently Meisenheimer and Cook have found[3] that pure Mn_2O_3 is antiferromagnetic with a Néel temperature of 80°K.

Specimens in the $(Sc_{2-x}Fe_x)O_3$ and $(In_{2-x}Fe_x)O_3$ systems were prepared by grinding appropriate mixtures of the sesquioxides in an agate mortar, compacting the mixtures into pellets and firing at 1400° to 1465°C in air. Although no detailed study was made, it was apparent that solubility of Fe_2O_3 in either Sc_2O_3 or In_2O_3 was increased with increasing temperature as was reported for the $(Mn_{2-x}Fe_x)O_3$ system. The lattice constants of specimens $(Sc_{2-x}Fe_x)O_3$ are listed in Table I and plotted in Fig. 2.

The lattice constant vs composition behaves linearly and extrapolates to 9.410 A for $x = 2$. No Fe_2O_3 with this structure has ever been reported, but there is no reason to preclude its existence other than perhaps extreme sensitivity to ionic size in the range of small ions. It should be mentioned that the lattice constant of Mn_2O_3 has been reported[4] to be 9.419 A and the effective CN(6) radii of the Fe^{3+} and Mn^{3+} ions are very nearly the same (see, e.g., reference 5).

In the $(In_{2-x}Fe_x)O_3$ system, a specimen with $x=1$ fired at 1400°C was not single phase. The same specimen fired at 1465°C was also not single phase, gave a poorer x-ray diffraction pattern, but indicated increased solution of Fe_2O_3. The lattice constants of the $(In_{2-x}Fe_x)O_3$ phases in the two cases were 9.874 and 9.838 (±0.005)A, respectively. If a linear relation exists between lattice constant and composition as in the $(Sc_{2-x}Fe_x)O_3$ system and we assume 9.41 A to be the hypothetical Fe_2O_3 lattice constant, the lattice constants obtained above would imply $x=0.69$ and 0.87, respectively, the latter value probably being near the maximum in this system.

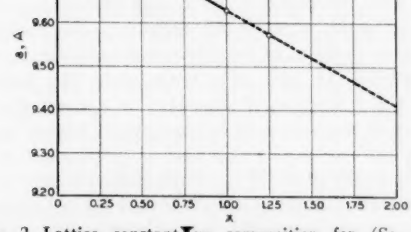

FIG. 2. Lattice constant vs composition for $(Sc_{2-x}Fe_x)O_3$ system.

We have also noticed that there appears to be some solubility of Sc_2O_3 and In_2O_3 in α-Fe_2O_3.

We do not intend to study these systems any further.

[1] S. Geller, H. J. Williams, and R. C. Sherwood (to be published).
[2] C. Hermann, O. Lohrmann, and H. Philipp, *Strukturbericht* (Akademische Verlagsgesellschaft, Leipzig, 1937), Vol. II, p. 38.
[3] R. G. Meisenheimer and D. L. Cook, J. Chem. Phys. **30,** 605 (1959).
[4] B. Mason, Geol. Fören. i Stockholm Förh. **65,** 95 (1943). [See A. J. C. Wilson, N. C. Baenziger, J. M. Bijvoet, and J. M. Robertson, Structure Repts. (N.V.A. Oosthoek's Uitgevers MIJ, Utrecht, 1955), Vol. 9, p. 272.]
[5] S. Geller, Acta Cryst. **10,** 243 (1957).

Simultaneous Infrared Absorption Involving Rotational Transitions of H_2

J. A. A. KETELAAR* AND R. P. H. RETTSCHNICK
Laboratory for Physical Chemistry of the University of Amsterdam, The Netherlands

(Received June 23, 1961)

A SIMULTANEOUS absorption band in mixtures of CO and H_2 was observed by Colpa and Ketelaar.[1] This band is due to the vibrational transition in CO and the $J=1\rightarrow J=3$ rotational transition in H_2. Welsh and co-workers[2] observed simultaneous vibrational-rotational transitions in solid H_2. We have found two absorption bands at 2936 and 3162 cm^{-1} and a weak one at about 2700 cm^{-1} in compressed mixtures of CO_2 and H_2 that can be interpreted as simultaneous transitions of the ν_3 vibration of CO_2 and three different rotational transitions of H_2. Since the intensities of these bands are proportional to the products of the densities of CO_2 and H_2 they must arise from transitions in collision pairs of the molecules, giving rise to the sum frequencies. During these collisions the variable dipole field of the antisymmetric stretching vibration of CO_2 ($\nu_3=2349$ cm^{-1}) induces a dipole moment in the anisotropic polarizable H_2 molecule. The rotational transitions $J=0\rightarrow J=2$ ($\nu=354$ cm^{-1}), $J=1\rightarrow J=3$ ($\nu=587$ cm^{-1}), and $J=2\rightarrow J=4$ ($\nu=814$ cm^{-1}) take part in the three simultaneous transitions, respectively. The major part of the absorption intensities can be explained by the dipole interaction mentioned above. The contribution of overlap interaction is probably of minor importance.

TABLE I. Frequencies of simultaneous transitions.

Mixture	Rotational transition of H_2	Calculated frequency (cm^{-1})	Observed frequency (cm^{-1})
CF_4+H_2	$\Delta J=0$	1267+4155=5422	5429
CF_4+H_2	$J=0\rightarrow2$	1267+4498=5765	5764
CF_4+H_2	$J=1\rightarrow3$	1267+4713=5980	5979
CF_4+H_2	$J=2\rightarrow4$	1267+4917=6184	6182
CF_4+H_2	$J=3\rightarrow5$	1267+5109=6376	(6360)
SF_6+H_2	$\Delta J=0$	947+4155=5102	5096
SF_6+H_2	$J=0\rightarrow2$	947+4498=5445	(5440)
SF_6+H_2	$J=1\rightarrow3$	947+4713=5660	5656
SF_6+H_2	$J=2\rightarrow4$	947+4917=5864	5862
SF_6+H_2	$J=3\rightarrow5$	947+5109=6056	(6055)

The quadrupole fields of CO_2 and H_2 give no contribution to these intensities as can be seen from a consideration of the symmetry of the molecules. A calculation of the intensities, based on an electrostatic model of the interaction, is forthcoming.

In mixtures of H_2 with other gases several simultaneous vibrational-vibrational transitions have been measured.[3–6] One might expect in consequence of the wide separation of the rotational levels of H_2 that some rotational structure of these simultaneous vibrational bands will be observable.[7]

Simultaneous vibrational-vibrational bands have been measured by Rinehart[5] for H_2 and CF_4 at 5429 cm^{-1} and by Schachtschneider[6] for H_2 and SF_6 at 5096 cm^{-1}, respectively. We have repeated these experiments and in both cases we observed four satellite bands due to rotational transitions of H_2 with $J=+2$ in accordance with the selection rules for simultaneous vibrational transitions derived by Colpa and Ketelaar.[7] From these rules it follows that the rotational quantum number of H_2 may change its value by $\Delta J=0, \pm2$.

The frequencies corresponding with the transitions of H_2 as given in Table I, have been calculated with rotational and vibrational constants given by Stoicheff.[8] The relative intensities of the satellite bands (see Fig. 1) correspond with the populations of the rotational levels of para and ortho hydrogen. For the calculation of the frequency of the simultaneous band with $\Delta J=0$ we used the frequency of the $Q(1)$ line of H_2 (4155 cm^{-1}) as at room temperature about $\frac{2}{3}$ of the hydrogen molecules are in the rotational state with $J=1$.

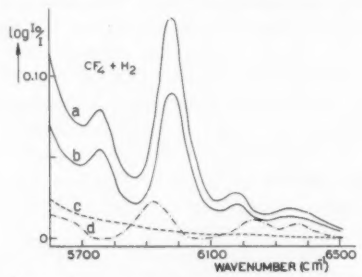

FIG. 1. Absorption spectra of mixtures of CF_4 and H_2. Path length=100 cm, temperature=298°K, densities in amagat units (Am). The spectra of the mixtures (a and b) have been corrected for the absorption of CF_4. a, mixture of H_2 (91 Am) and CF_4 (47.6 Am); b, mixture of H_2 (69 Am) and CF_4 (45.8 Am); c, H_2 (92.5 Am); d, CF_4 (48.1 Am).

This work is part of the research program of the Foundation for Fundamental Research of Matter (F.O.M.) and was made possible by financial support from the Netherlands Organization for Pure Research (Z.W.O.).

* Present address: Laboratory for Electrochemistry of the University of Amsterdam.

[1] J. P. Colpa and J. A. A. Ketelaar, Mol. Phys. **1,** 14, 343 (1958).
[2] H. P. Gush, W. F. J. Hare, E. J. Allin, and H. L. Welsh, Phys. Rev. **106,** 1101 (1957).
[3] J. Fahrenfort, thesis, Amsterdam, 1955; J. Fahrenfort and J. A. A. Ketelaar, J. Chem. Phys. **22,** 1631 (1954).
[4] R. Coulon, J. research C.N.R.S. **9,** 305 (1958); B. Vodar, Spectrochim. Acta **14,** 213 (1959).
[5] R. W. Rinehart, thesis, Minnesota, 1959.
[6] J. H. Schachtschneider, thesis, Minnesota, 1959.
[7] J. P. Colpa and J. A. A. Ketelaar, Physica **24,** 1035 (1958).
[8] B. P. Stoicheff, Can. J. Phys. **35,** 730 (1957).

$CH_2(COOH)$ in Malonic Acid*

HARDEN M. MCCONNELL† AND CONCETTO R. GIULIANO
Gates and Crellin Laboratories of Chemistry,‡ California Institute of Technology, Pasadena, California

(Received June 26, 1961)

THE paramagnetic resonance of the radical $CH(COOH)_2$ (I) that is produced in malonic acid by x-ray damage has been the subject of numerous theoretical and experimental studies.[1–5] Our early work on malonic acid indicated that in addition to I, x irradiation produced other less stable paramagnetic radicals that could be removed by aging or heat treatment.[1,2] From analyses of proton hyperfine structure, both Horsfield, Morton, and Whiffen (HMW)[6,7] and independently the present authors,[8] concluded that these less stable radicals have the formula CH_2COOH. In addition to I, our proton hyperfine structure from x-irradiated malonic acid could be interpreted in terms of roughly equal concentrations of two radicals II and III, both with the formula CH_2COOH.[8] Radical II (or III) is derived from a molecule of malonic acid in the crystal lattice by removing the carboxyl group that is perpendicular (or parallel) to the plane of the three carbon atoms of the undamaged molecule. Radicals II and III are assumed to have orientations in the crystal lattice such that the remaining carboxyl group retains the orientation it had

FIG. C^{13}–D hyperfine splittings in x-irradiated perdeuteromalonic acid. The outer multiplets arise from combined C^{13} (natural abundance) and *D* hyperfine splittings of the radica CD_2COOD (III).

in the undamaged parent molecule, and the CH_2 group is coplanar with the remaining carboxyl group, with an H–C–H angle equal to 120°. II and III are assumed to be π radicals, with unit spin density on the CH_2 group. A detailed analysis of the proton hyperfine structure will be published by HMW.[7] We note, however, that our analysis of this hyperfine structure was made difficult by the fact that all three radicals, I, II, and III give overlapping proton hyperfine spectra.[8] Therefore, we report here additional evidence for the presence of radical III in which there is no uncertainty due to overlapping multiplets. Thus, Fig. 1 exhibits a spectrum of x-irradiated perdeuteromalonic acid when the external field lies in the molecular *yz* plane and makes an angle of 30° with the *z* axis. (This *xyz* axis system is defined in reference 2.) In this case the external field is nearly parallel to the odd electron π orbital of radical III, and one easily observes the expected C^{13} hyperfine splitting of 190 Mc (corresponding to the 212 Mc C^{13} splitting in I)[4,5] as well as the five hyperfine lines due to the two deuterium atoms in the CD_2 group of III. The deuterium hyperfine splitting ($\sim$9 Mc) is equal to that predicted for this orientation on the basis of previous work on I and the general theory of σ-proton hyperfine structure.[2] The C^{13} hyperfine splittings of the perdeuterated radical III showed the expected behavior at other crystal orientations. Unfortunately, a comparably certain identification of radical II was not possible since the C^{13} hyperfine splittings of I and II are so similar that overlapping spectra are observed at all orientations.

Spectra of aged x-irradiated malonic crystals containing 50% deuterium isotopic substitution (in all positions) showed that in radical I there is no isotope effect on the hyperfine structure. For example, when the applied field was parallel to the *c* axis of the crystal, the proton/deuteron splitting ratio was observed to be 6.6±0.2, while the ratio of the nuclear *g* factors is 6.52. This is in agreement with the observation of Venkataraman and Fraenkel[9] that there is no isotope effect on the σ-nuclear isotropic hyperfine structure in π-electron radicals. Our results further indicate no significant isotope effect on the anisotropic hyperfine interaction.

* Sponsored by the U. S. Public Health Service, by the National Science Foundation and by the Office of Ordnance Research, U. S. Army.

† Alfred P. Sloan Fellow.

‡ Contribution No. 2723.

[1] T. Cole, C. Heller, and H. M. McConnell, Proc. Natl. Acad. Sci. U.S. **45,** 525 (1959).
[2] H. M. McConnell, C. Heller, T. Cole, and R. W. Fessenden, J. Am. Chem. Soc. **82,** 766 (1960).
[3] H. M. McConnell, D. D. Thompson, and R. W. Fessenden, Proc. Natl. Acad. Sci. U.S. **45,** 1600 (1959).
[4] H. M. McConnell and R. W. Fessenden, J. Chem. Phys. **31,** 1688 (1959).
[5] T. Cole and C. Heller, J. Chem. Phys. **34,** 1085 (1961).
[6] A. Horsfield, J. R. Morton, and D. H. Whiffen, Nature **189,** 481 (1961).
[7] D. H. Whiffen (private communication).
[8] C. R. Giuliano, thesis, California Institute of Technology, 1961.
[9] B. Venkataraman and G. K. Fraenkel, J. Chem. Phys. **24,** 737 (1956).

Self-Association Constant of Chloroform from NMR Chemical Shifts*

CHARLES F. JUMPER,† MERLE T. EMERSON, AND BENTZ B. HOWARD
Department of Chemistry, The Florida State University, Tallahassee, Florida

(Received July 17, 1961)

IN the process of studying the hydrogen bonding of chloroform to bases,[1] it became necessary to consider the behavior of chloroform itself in cyclohexane and carbon tetrachloride. A number of recent investigators, using both NMR[2–4] and infrared[5–7] techniques, have interpreted concentration shifts of chloroform as due to self-association. The same interpretation has been given for the temperature variation of infrared intensities[5] and NMR shift[2] of chloroform. There has been no published estimate of the self-association constant, however.

Assuming chloroform associates to form only dimers, the proton chemical shift is given by $\delta=\delta_0+(n_d/n_1)\Delta\delta'$, where δ_0 is the free chloroform shift, n_d and n_1 the number of moles of dimer and total chloroform, respectively, and $\Delta\delta'$ is the association shift. The expression for the self-association equilibrium constant K' yields

$$2(n_d/n_1)=1+(4K'+1)^{-1}(n_s/n_1)-\{[1+(4K'+1)^{-1}(n_s/n_1)]^2-4K'/(4K'+1)\}^{\frac{1}{2}},$$

where n_s is the number of moles of solvent. For an assumed value of K', n_d/n_1 values can be calculated from the experimental concentrations. The best least-squares fit to a straight line of experimental shifts vs n_d/n_1 yields the best K'; the slope gives $\Delta\delta'$.

The chemical shifts were measured by a 40-Mc high-resolution Varian NMR spectrometer at 25±1°C using the side-band technique. All shifts were measured with respect to 1% cyclohexane internal reference with an average deviation of less than ±0.002 ppm. The observed shifts were semiempirically corrected for the difference in solvent shift between chloroform and

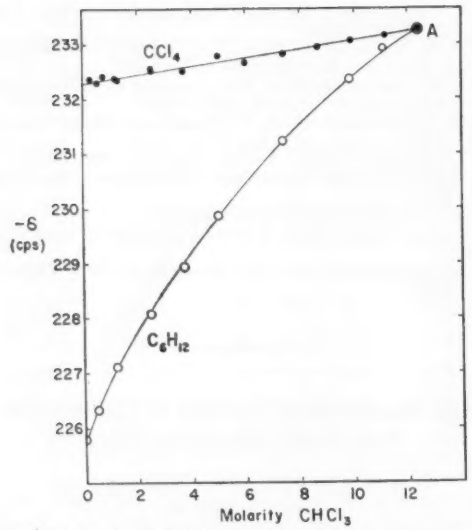

FIG. 1. The chemical shift of chloroform in cps, measured at 40 Mc with respect to a 1% cyclohexane internal reference, is plotted against concentration of $CHCl_3$ in cyclohexane (circles) and CCl_4 (dots). Point A represents pure $CHCl_3$.

cyclohexane by a method suggested by Glick *et al.*[8,9] This correction was never greater than 0.02 ppm.

The change in uncorrected chemical shift with the change of chloroform concentration in cyclohexane is shown in Fig. 1. The data exhibit a distinct curvature, of the form expected when association is present, and a total dilution shift of 0.19 ppm. These results give $K'=0.16\pm0.006$ (m.f.)$^{-1}$ and $\Delta\delta'=-1.55\pm0.5$ ppm. This value of K' is roughly an order of magnitude smaller than the association constants found for the association of chloroform to bases such as triethylamine and acetone.[1,4,10] However, the value of $\Delta^{R'}$ is comparable in magnitude to those found for chloroform association to these stronger bases.

The shift for chloroform in carbon tetrachloride, also shown in Fig. 1, is linear with concentration and has a total dilution shift of only 0.022 ppm. This result can be explained if we assume that chloroform associates with carbon tetrachloride with an association constant of approximately 0.1 (m.f.)$^{-1}$ and that the association shift is about the same as for dimerization.

It should be pointed out that other solvent effects,[9] in particular the effect of the polar reaction field[11] of chloroform, might account for part of the observed shift and curvature in cyclohexane, and also the differences between the two solvents. A rough calculation, however, indicates that nonspecific solvent effects can account for at most about half the observed dilution shift. The association shift, and possibly also K', might well be somewhat smaller than the values given above, but are probably correct to an order of magnitude. At present the theory of solvent effects is not well enough developed to allow more precise corrections to be made.

* Supported in part by the Air Force Office of Scientific Research.

† National Science Foundation Predoctoral Fellow, 1959–1960; present address: Bell Telephone Laboratories, Murray Hill, New Jersey.

[1] C. F. Jumper, B. B. Howard, and M. Emerson (to be published).
[2] L. W. Reeves and W. G. Schneider, Can. J. Chem. **35,** 251 (1957).
[3] G. Korinek and W. G. Schneider, Can. J. Chem. **35,** 1157 (1957).
[4] C. M. Huggins and D. R. Carpenter, J. Phys. Chem. **63,** 238 (1959).
[5] R. B. Bernstein and M. Tamres, J. Chem. Phys. **23,** 2201 (1955).
[6] U. Liddel and E. D. Becker, J. Chem. Phys. **25,** 173 (1956).
[7] E. D. Becker, Spectrochim. Acta **15,** 743 (1959).
[8] R. E. Glick, D. F. Kates, and S. J. Ehrenson, J. Chem. Phys. **31,** 567 (1959).
[9] B. B. Howard, B. Linder, and M. T. Emerson, J. Chem. Phys. (to be published).
[10] G. C. Pimentel and A. L. McClellan, *The Hydrogen Bond* (W. H. Freeman and Company, San Francisco, California, 1960), pp. 384, 385.
[11] A. D. Buckingham, Can. J. Chem. **38,** 300 (1960).

Magnetization and Proton Relaxation Time in Antiferromagnetic $LiCuCl_3\cdot2H_2O$*

R. D. SPENCE AND C. R. K. MURTY
Department of Physics, Michigan State University, East Lansing, Michigan

(Received July 31, 1961)

THE studies of Hardeman, Poulis, Van der Lugt, and Hass[1–3] of the sublattice magnetization and proton spin lattice relaxation time in $CuCl_2\cdot2H_2O$ reveal discrepancies between the observed temperature dependence of these quantities and the theoretical predictions of spin-wave theory. Hardeman *et al.* find that the magnetization difference $M(O)-M(T)$ varies as T^4 at low temperatures while the theoretical results of Kubo[4] give a T^2 dependence. Hardeman *et al.* also show that the proton spin lattice relaxation time varies as T^{-n}, where n lies between 7 and 8. The theoretical calculation of Van Kranendonk and Bloom[5] indicates a T^3 dependence for the proton spin-lattice relaxation time.

The compound $LiCuCl_3\cdot2H_2O$, which has been shown to be antiferromagnetic at low temperatures by Vosso, Jennings, and Rundle,[6] offers an opportunity to study the temperature dependence in a crystal with the same magnetic ion, essentially the same Néel temperature (4.3°K in $CuCl_2\cdot2H_2O$; 4.5°K in $LiCuCl_3\cdot2H_2O$) but quite different crystal structure. The space group of $CuCl_2\cdot2H_2O$ is $Pbnm$ and $P2_1/c$ for $LiCuCl_3\cdot2H_2O$. We find that the proton resonance spectrum[7] of $LiCuCl_3\cdot2H_2O$ consists of 16 lines each exhibiting a doublet structure arising from the interaction between hydrogens on the same water molecule. The 16 different local fields at the proton sites have four different magnitudes which at 4.1°K have the values $H_1=320$,

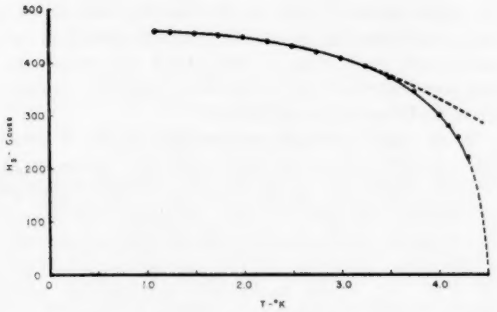

FIG. 1. Temperature dependence of the local field H_3. Upper dashed line $H_3=461.5-2.00T^3$ gauss.

$H_2=306$, $H_3=280$, $H_4=113$ gauss. The temperature dependence of H_3 in zero applied field is shown in Fig. 1. Other local fields exhibit the same temperature dependence to within 1%. Assuming that the sublattice magnetization has the same temperature dependence as the local field we have attempted to fit the low-temperature portion of Fig. 1 with an expression of the form $H_L(0)-H_L(T)=aT^m$. We find that over a considerable temperature our data can be fitted with $a=2.00$ gauss deg^{-3} and $m=3$. This is to be compared with the T^4 temperature dependence found by Hardeman *et al.* for the same type of experiment.

The proton spin-lattice relaxation time was measured for a line arising from the local field H_2 with an external field of 2536 gauss parallel to the b axis. This line was chosen because of its favorable intensity and negligible proton-proton splitting. In this orientation the applied field is 33° from the direction of the internal field.

Our results are shown in Fig. 2. The temperature dependence is approximately as T^{-4}. Thus it appears that as far as the sublattice magnetization and proton relaxation time are concerned the discrepancies between the predictions of spin-wave theory and experiment are much less serious in $LiCuCl_3\cdot 2H_2O$ than in $CuCl_2\cdot 2H_2O$. Our results also suggest that the temperature dependence of these quantities is extremely structure sensitive. Unfortunately the temperature range in which the conventional spin-wave theory of antiferromagnetism can be expected to be valid is not well known. From these experiments one can state that if such a region exists it is less than one-fourth the Néel temperature. However, in the case of the spin-lattice relaxation time the experimental temperature dependence appears to depart from the theoretical one n a way that leaves little possibility for improved agreement at lower temperatures.

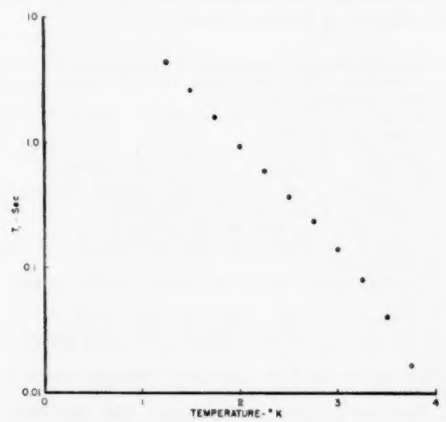

FIG. 2. Temperature dependence of the spin-lattice relaxation for protons.

* Supported by the Air Force Office of Scientific Research.

[1] G. E. G. Hardeman, N. J. Poulis, and W. Van der Lugt, Physica **22,** 48 (1956).
[2] G. E. G. Hardeman, N. J. Poulis, W. Van der Lugt, and W. P. A. Hass, Physica **23,** 907 (1957).
[3] N. J. Poulis, G. E. G. Hardeman, W. Van der Lugt, and W. P. A. Hass, Physica **24,** 280 (1958).
[4] R. Kubo, Phys. Rev. **87,** 568 (1952).
[5] J. Van Kranendonk and M. Bloom, Physica **22,** 545 (1956).
[6] P. H. Vossos, L. D. Jennings, and R. E. Rundle, J. Chem. Phys. **32,** 1590 (1960).
[7] R. D. Spence and C. R. K. Murty, Physica (to be published).

Ion-Molecule Reactions Studied with Mass Analysis of Primary Ion Beam*

CLAYTON F. GIESE AND WILLIAM B. MAIER, II
Department of Physics, University of Chicago, Chicago 37, Illinois
(Received July 26, 1961)

IN the studies of ion-molecule reactions to date, it has been conventional to mass analyze only the ions emerging from the reaction chamber, this being in most cases a standard mass spectrometer ionization chamber. Identification of the primary ion is done typically by studies of the ion intensities as functions of ionizing electron energy. Recently, some doubt has been expressed in the literature as to the reliability of this technique in certain cases.[1]

Lindholm[2] has used an apparatus in which the ion beam from one mass spectrometer crosses *transversely* the ionization chamber of a second mass spectrometer. The apparatus thus discriminates strongly against reactions in which momentum is transferred, as in typical ion-molecule reactions, and selects those interactions which are initiated by charge-transfer in which there is little or no momentum transfer. To avoid this discrimination, we use a primary ion beam which passes through *longitudinally*. Experiments of this type had only been done at energies in the kilovolt range.[3]

The apparatus used, which will be more fully described in a later report, is a conventional 60° sector field mass spectrometer with 12-in. magnetic radius and with, however, an unconventional ion lens.[4] This lens focuses the ions, primary and secondary, emerging from a field

TABLE I. Ion-molecule reactions.

	Presumed reactions	Cross section in units of 10^{-16} cm^2
(1)	$H_2^+ + H_2 \rightarrow H_3^+ + H$	13
(2)	$\rightarrow H^+ + H_2 + H$	1
(3)	$H_2^+ + He \rightarrow HeH^+ + H$	5
(4)	$H_2^+ + He \rightarrow H^+ + He + H$	0.4
(5)	$H^+ + He \rightarrow HeH^+$	<0.07
(6)	$\rightarrow He^+ + H$	<0.07
(7)	$He^+ + H_2 \rightarrow HeH^+ + H$	<0.1
(8)	$\rightarrow H^+ + He + H$	<0.05
(9)	$H_2^+ + Ar \rightarrow ArH^+ + H$	44
(10)	$\rightarrow Ar^+ + H_2$	12
(11)	$\rightarrow H^+ + Ar + H$	1
(12)	$Ar^+ + H_2 \rightarrow ArH^+ + H$	160
(13)	$\rightarrow H^+ + H + Ar$	0.4
(14)	$Ar^+ + Ar \rightarrow Ar_2^+$	<0.2
(15)	$N_2^+ + N_2 \rightarrow N_3^+ + N$	0.2
(16)	$\rightarrow N_4^+$	<0.003

free reaction chamber. The primary ions entering the chamber are selected by a small mass spectrometer with 1-in. magnetic radius built within the ion source housing. This mass spectrometer has a resolution of about 40 (full width at half-maximum) and produces, with 30 v of accelerating potential, about 10^{-13} amp of primary ion current in favorable cases. The reaction path length is 1.15 cm. With the partial pressure of 2×10^{-5} mm typically used, a detected secondary ion current of 10^{-19} amp corresponds to a reaction cross section of order 10^{-18} cm^2.

Some provisional results which were obtained using this equipment are given in Table I. The primary ions have been retarded to about 4 ev, and have an energy bandwidth of 0.6 ev. Primary ionizing energy was 50 ev. Pressures were determined from corrected ion gauge readings, and total pressures were typically 4×10^{-5} mm. No quantitative comparison with other work has been made because the experimental conditions here are quite different from those typically used and, further, the possible systematic errors in the cross sections have not been studied carefully yet.

Study of the hydrogen system reveals the familiar reaction (1) and the somewhat less familiar reaction (2),[5] interesting in that it is necessarily endothermic, unless the neutral species H_3 is bound.

The hydrogen-helium system is of particular interest at present. Hertzberg *et al.*[1] have reached the conclusion from appearance potential studies that one cannot neglect reaction (3) in comparison with reaction (7), as in earlier treatments, and quote a ratio of ion currents from (3) as compared with (7) of 0.5. Under our conditions at least, reaction (3) dominates over reaction (7) by at least a factor of 50. For the ratio of cross sections of reaction (3) and (1), we obtain 0.4, as compared with their value of 0.07 ± 0.03. The other reaction seen, reaction (4), is one which must be endothermic if HeH neutral is not bound.

In the argon-hydrogen system, both modes of formation of ArH^+, reactions (12) and (9), occur in the ratio of about four to one. Recent articles[6–8] mention no evidence for reaction (9). Schaeffer and Thompson,[9] however, have postulated the existence of reactions of this type. Reaction (11) is analogous to reactions (2) and (4), again necessarily endothermic unless ArH is bound. The failure to detect reaction (14) is consistent with the evidence that Ar_2^+ is formed from Ar^*.[10]

In the nitrogen system, reaction (15), leading to N_3^+ formation, is detected. The appearance potential curve for N_3^+, however, parallels that for N_2^+, contrary to the findings of other workers.[10,11] No N_4^+ ions were seen, in agreement with Kaul and Fuchs.[10] With the small mass spectrometer tuned to $m/e=14$, an $m/e=56$ secondary peak appeared. This had an appearance potential corresponding to $N_2^{+\,+}$,[12] so we attribute the apparent $m/e=56$ peak to the reaction, after acceleration, $N_2^{+\,+}+N_2\rightarrow N_2^+ + N_2^+$, analogous to a reaction seen with oxygen.[13] Quantitative comparison with Saporoschenko's[11] reported N_4^+ is difficult because his experimental conditions were vastly different from ours.

The results given here prove that low-energy studies of ion-molecule reactions with a mass-analyzed primary ion beam are feasible, permitting positive identifications of the primary reacting ion. Also, it should be possible to study the energy dependences of cross sections. Before this can be done, and before more accurate cross sections can be measured, it is necessary to study the efficiency of detection of primary and secondary ions under varying conditions, and to improve the measurement of pressure. These matters will be the subjects of further reports.

* This research has been supported by grants from the National Science Foundation, the Louis Block Fund for Basic Research, and the Esso Education Foundation.

[1] M. Hertzberg, D. Rapp, I. B. Ortenburger, and D. D. Briglia, J. Chem. Phys. **34,** 343 (1961).
[2] E. Lindholm, Naturwissenschaften **9A,** 535 (1954); E. Gustafsson and E. Lindholm, Arkiv Fysik **18,** 219 (1960).
[3] See, for example, F. M. Rourke, J. C. Sheffield, W. D. Davis, and F. A. White, J. Chem. Phys. **31,** 193 (1959).
[4] C. F. Giese, Rev. Sci. Inst. **30,** 260 (1959).
[5] H. Eyring, J. O. Hirschfelder, and H. S. Taylor, J. Chem. Phys. **4,** 479 (1936).
[6] A. Giardini-Guidoni and G. G. Volpi, Nuovo cimento **17,** 3127 (1960).
[7] D. P. Stevenson, J. Phys. Chem. **61,** 1453 (1957).
[8] D. P. Stevenson and D. O. Schissler, J. Chem. Phys. **23,** 1353 (1955).
[9] O. A. Schaeffer and S. O. Thompson, Radiation Research **10,** 671 (1959).
[10] W. Kaul and R. Fuchs, Z. Naturforsch. **15a,** 326 (1960).
[11] M. Saporoschenko, Phys. Rev. **111,** 1550 (1958).
[12] H. D. Hagstrum and J. T. Tate, Phys. Rev. **59,** 354 (1941).
[13] W. McGowan and L. Kerwin, Can. J. Phys. **38,** 642 (1960).

A Kinetic Method for Measuring Solubilities of Gases in Liquids

KEDMA BAR-ELI AND FRITZ S. KLEIN
Isotope Department, Weizmann Institute of Science, Rehovoth, Israel
(Received June 22, 1961)

SEVERAL standard methods are known for the measurement of the solubility of gases in liquids.[1,2] Not one of these methods can be used, when the dissolving gas reacts with the solvent, since during the time required for estimating the amount of dissolved gas, appreciable changes in the gas concentration can occur. No reliable solubility measurements are therefore possible, when the gas reacts with the solvent.

This note describes a new method, where the rate of reaction between a gas and its solvent is utilized to estimate the amount of gas dissolved. This makes it possible to obtain solubility coefficients of at least medium accuracy. The principle of this method is to measure the apparent rate of reaction, while shaking the reaction mixture intermittently for varying time intervals.

Experimental procedure: Solvent and gaseous reactant are put into the reaction vessel, which is connected to a shaking apparatus.[3] The partial pressure P_0 of the reacting gas in the gas phase is measured. Practically no material exchange of the gas occurs between the two phases, when the reaction mixture is at rest. Vigorous shaking is then started. The partition equilibrium of the gas between the gaseous and liquid phases is at once established. The partial pressure of the reactant gas consequently falls to a value of P_0', for which the following equation holds, assuming the chemical reaction to be irreversible:

$$P_0(V-u)/RT = P_0'[hu+(V-u)/RT], \quad (1)$$

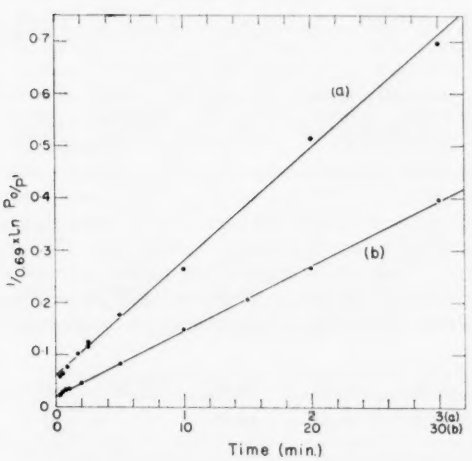

FIG. 1. Experimental isotope exchange as a function of the time interval between samples. (a) at −41.6°C. (b) at −64.0°C.

where V and u are the volumes of the reaction vessel and the liquid, respectively, R the gas constant, T the absolute temperature, and h is the absorption coefficient of the gas, defined as the volume (STP) of the gas dissolved in a unit volume of solvent at unit partial pressure of the gas. After a time t the shaking is stopped and a second measurement P' of the partial pressure of the gas is taken.

The true reaction rate assuming a first-order rate is given by

$$kt = \ln P_0'/P', \quad (2)$$

while the observed rate is

$$k_{obs}t = \ln P_0/P' = kt + \ln P_0/P_0'. \quad (3)$$

Performing a number of analogous experiments for different times t, the value of $\ln P_0/P_0'$ can be found from the intercept of the linear plot (k_{obs}) vs t [see Eq. (3)]. The absorption coefficient h of the gas can then be found from Eq. (1).

In order to check this method, the solubility of deuterium gas in a dilute solution of potassium amide in liquid ammonia[3] was measured. Deuterium reacts rapidly, exchanging the isotope with the solvent.

Two such experiments are given in Fig. 1, graphs (a) and (b), from which the following solubilities: $h_{-41.6}° = 0.025 \pm 0.0013$ ml STP/ml·atm and $h_{-64.0}° = 0.0117 \pm 0.0005$ ml STP/ml·atm were calculated by the least-mean-square method.

The experimental heat of solution of deuterium in liquid ammonia is found to be +3.3 kcal/mole.

Extrapolating the solubility data for hydrogen in liquid ammonia given by Larson and Black,[4] one finds the absorption coefficients $h_{-41}° = 0.018$ and $h_{-61}° = 0.010$ STP/ml·atm. Considering the rather high temperatures and pressures at which the solubilities were measured, the extrapolated values compare well with our measured solubilities. A correction for the difference in the solubilities of hydrogen and deuterium would be much smaller, than the error in the extrapolated values of h.[3,5]

This kinetic method is applicable to the measurement of solubilities of a wide range of reacting gases. The change of the partial pressure of the reactant can be followed by any convenient method. In each case the chemical reaction has to be slow enough to be easily measurable and the mixing should be efficient, so that the partition equilibrium is established fast, compared with the chemical reaction.

[1] W. J. Nader, R. D. Vold, and M. J. Vold, *Physical Methods of Organic Chemistry* (Interscience Publishers, Inc., New York, 1959), 3rd ed., part 1, Vol. 1, p. 677.
[2] H. Kienitz, "Physikalische methoden," *Methoden der organische Chemie* (Georg Thieme Verlag, Stuttgart, 1955), Vol. 3, part 1, p. 239.
[3] K. Bar-Eli and F. S. Klein (to be published).
[4] A. T. Larson and C. A. Black, Ind. Eng. Chem. **17**, 715 (1925).
[5] M. W. Cook, D. N. Hansen, and B. J. Adler, J. Chem. Phys. **26**, 748 (1957).

Diamagnetic Susceptibility in Thomas-Fermi Model for Latter's and Byatt's Effective Charge Distribution

T. TIETZ

University Łódź, Department of Theoretical Physics, Łódź, Poland

(Received March 28, 1961)

IT is known that the original Thomas-Fermi model[1] is inadequate to explain the molar diamagnetic susceptibilities χ_{dia} for free neutral atoms because of the overspreading of the electron cloud within the model. For this reason it was corrected in different ways.[2] We obtain the best values for χ_{dia} in the case of free neutral atoms if we use the Fermi-Amaldi modified Thomas-Fermi model or the Thomas-Fermi-Dirac model. The purpose of this note is to calculate χ_{dia} for the Latter's[3] potential and Byatt's[4] fits for the Hartree field. We start from the known formula for χ_{dia}.

$$\chi_{dia}=-(7.9227\times10^{-7})a_0^{-2}(0\mid\sum_j\mid r_j\mid^2\mid 0), \quad (1)$$

where r_j is the distance of the jth electron from the nucleus, a_0 is the Bohr radius, and 0 denotes the ground state of the atom. For a spherical symmetric atom we have

$$(0\mid\sum_j\mid r_j\mid^2\mid 0)=6\int_0^\infty Z_p(r)r\,dr, \quad (2)$$

where $Z_p(r)$ is the effective charge. In the Thomas-Fermi model for free neutral atom $Z_p(r)$ is related to Thomas-Fermi function for free neutral atoms $\phi_0(x)$ as follows: $Z_p=Z\phi_0(x)$. In the last formula Z is the atomic number and x is related to r as $x=r/\mu$ where $\mu=0.88534a_0Z^{-\frac{1}{3}}$. For the Latters's potential $Z_p(r)$ is defined as follows: $Z_p=Z\phi_0(x)$ if $Z\phi_0(x_0)\geq1$ and $Z_p=Z\phi_0(x)=0$ if $Z\phi_0(x)<1$. Equation (2) for the Latter's expression of Z_p is

$$(0\mid\sum_j\mid r_j\mid^2\mid 0)=6\int_0^{r_0} Z\phi_0(x)r\,dr. \quad (3)$$

The upper limit r_0 in the last integral is given by $Z\phi_0(x_0)=Z\phi_0(r_0/\mu)=1$. Using Eqs. (1)–(3) we obtain for the gram-atomic susceptibility χ_{dia} in case of Latter's potential the following formula:

$$-10^6\chi_{dia}=3.7260Z^{\frac{1}{3}}\int_0^{x_0} x\phi_0(x)\,dx. \quad (4)$$

Using the table of Kobyashi and Taima[5] for $\phi_0(x)$ function we have calculated numerically the x_0 values and the integral in Eq. (4). The results are given in

TABLE I. The numerical values of the constants c_i and b_i appearing in Eqs. (5) and (6) according to Byatt.

Element	c_1	c_2	c_3	b_1	b_2	b_3
He	1.25	−0.25	0.0	1.75	3.845	0.0
Ne	1.0	0.0	0.0	0.978	0.0	0.0
Ar	0.659	0.341	0.0	0.574	2.77	0.0
Kr	0.415	0.51	0.075	0.378	1.48	7.0
C	1.25	−0.44	0.19	0.828	1.41	4.29
O	1.25	−0.35	0.1	0.991	1.63	18.3
Fe	0.25	0.56	0.19	0.335	0.828	3.76
As	0.295	0.705	0.0	0.387	1.295	0.0
Hg	0.19	0.56	0.25	0.257	0.779	3.16

TABLE II. A comparison of our results for $-\chi_{dia}\times10^6$ of Eqs. (4) and (6) with the corresponding numerical values calculated by another method and experimental values.

		Our values								
Element[a]	Z	x_0	$\int_0^{x_0} x\phi_0(x)\,dx$	Eq. (4) for Latter's potential	Eq. (6) for Byatt's fits	Uncorrected Thomas-Fermi-model	Fermi Amaldi Kobyashi	Thomas Fermi-Dirac Kobyashi	Hartree Fock	Experimental values
He	2	...	...	...	1.73	...	...	...	...	1.88
C	6	2.85	1.149	7.78	8.38	...	...	...	...	...
O	8	3.59	1.498	11.16	6.55	...	...	...	...	...
Ne	10	4.24	1.758	14.11	8.39	67.0	12.62	14.33	8.06	6.8
Ar	18	6.26	2.495	24.36	19.97	81.0	21.67	22.15	...	19.5
As	33	8.88	3.354	40.74	28.57	...	...	...	...	...
Kr	36	9.31	3.461	42.58	38.61	10.20	37.34	35.51	31.10	28.0
Xe	54	11.51	3.957	55.73	...	117.0	49.53	45.96	...	42.4
Hg	80	14.00	4.439	80.00	61.40	...	...	...	...	...

[a] A. J. Freeman [Phys. Rev. **91**, 1410 (1953)] shows that O and C contain and As does not contain the effect of exchange on Z_p. For the remained elements see D. R. Hartree, Repts. Progr. in Phys. **71**, 113 (1946).

Table II. Ruark[6] suggested for $Z_p(r)$ the following form:

$$Z_p = Z\{c_1 \exp[-(b_1/\mu)r] + c_2 \exp[-(b_2/\mu)r] + c_3 \exp[-(b_3/\mu)r]\} \quad (5)$$

In Table I we have the Byatt's[6] numerical values of the constants c_i and b_i for several Z.

Substituting Eq. (5) into Eq. (1) we obtain

$$-10^6\chi_{\text{dia}} = 3.7260Z^{\frac{1}{3}}[(c_1/b_1^2)+(c_2/b_2^2)+(c_3/b_3^2)]. \quad (6)$$

In Table II we have made a comparison between our values for χ_{dia} according to Eqs. (4) and (6) and the numerical values of the unmodified Thomas-Fermi model,[7] the Fermi-Amaldi model,[7] the Thomas-Fermi-Dirac model,[7] and experimental values.[7]

From Table II we see that the χ_{dia}'s given by Eqs. (4) and (6) are better than the corresponding results for the unmodified Thomas-Fermi model. Equation (4) gives a little poorer results and Eq. (6) a little better results than the numerical Kobyashi's values.

[1] P. Gombas, *Die statistische Theorie des Atoms und ihre Anwendungen* (Springer-Verlag, Vienna, 1949).
[2] See reference 1; also T. Tietz, J. Chem. Phys. **26**, 490 (1957). S. Kobayashi, J. Phys. Soc. Japan **14**, 1039 (1959).
[3] R. Latter, Phys. Rev. **99**, 510 (1955).
[4] W. J. Byatt, Phys. Rev. **104**, 1298 (1956).
[5] S. Kobyashi and T. Taima, "Table of exact values of the T-F function," Memoirs of the Faculty of Liberat Arts and Education, Kagawa University, Kagawa-Japan, 1956.
[6] See reference 4.
[7] See references 1 and 2.

Negative Hydrogen Ion

T. TIETZ
Department of Theoretical Physics, University Lódź, Lódź, Poland
(Received March 22, 1961)

MOST of the previous authors, Hylleraas and Midtdal,[1] and also Hart and Hertzberg,[2] obtained the ground-state wave function for H^- by help of the Ritz variational principle, of mainimum energy using wave functions with various modifications, and as many as 24 adjustable parameters to calculate the electron binding energy of H^-. These calculations have satisfactorily converged on 0.754 ev. Pekeris,[3] taking into consideration a new method for solving the wave equation of H^-, has slightly improved the value 0.754 ev of the electron affinity of hydrogen atom given by Hart and Herzberg. The purpose of this note is to construct a simple ground wave function for H^- using a modified Hulten s^4 potential. Our obtained ground wave function for H^- gives the correct value 0.754 ev. For a two-electron atomic system the discrete and continuum wave functions are the solutions of the following Schrödinger equation:

$$\{\nabla_1^2+\nabla_2^2+2(E+r_1^{-1}+r_2^{-1}-r_{12}^{-1})\}\Psi(r_1, r_2)=0. \quad (1)$$

In Eq. (1) we have adopted as the atomic units for length the first Bohr radius of hydrogen atom, and for energy, two Rydberg units. The indices in Eq. (1) refer to the first and second electron. For the discrete wave function Ψ_d and the continuum function Ψ_c we adopt the function of the form

$$\phi_0(r_1)\phi_0(r_2)$$

and

$$(1/\sqrt{2})\{\phi_0(r_1)\phi_k(r_2)+\phi_0(r_2)\phi_k(r_1)\}, \quad (2)$$

where the continuum radial wave function ϕ_k and the discrete radial wave function ϕ_0 fulfill the following equation:

$$\{\nabla^2-2V(r)+2E\}\phi=0. \quad (3)$$

The spherical potential $V(r)$ is chosen so that it will yield the required electron affinity of the hydrogen atom. We solve Eq. (3) for the following potential:

$$V(r) = -b[e^{-ar}/(1-e^{-ar})], \quad (4)$$

where a and b are constants. In Table I we have a comparison of the potential Eq. (4) with the Hartree field. Table I shows that the potential Eq. (4) agrees quite well with the Hartree field. For the potential, Eq. (4), one can solve Eq. (4). The 1-s eigenvalue and the corresponding normalized wave function are given by

$$k_0^2 = 2|E_0| = [(2b-a^2)/2a] \quad (5)$$

and

$$\phi_0 = \frac{[2k_0(k_0+a)(2k_0+a)]^{\frac{1}{2}}}{2a(\pi)^{\frac{1}{2}}} \times \frac{\exp(-k_0r)-\exp[-(k_0+a)r]}{r}. \quad (6)$$

Adopting for the constant b the unchanged value 2.5 and changing a little the value for the constant a from $a=2.3$ to $a=2.013088$ we obtain for E_0 the value 0.754 ev. For this value of E_0 the value of k_0^2 is $k_0^2=0.05538$. In Table II we have compared our function with the corresponding constructed Geltman's[5] function. For the comparison of our results with the corre-

TABLE I. A comparison of our potential $-V(r)$, Eq. (4), for $a=2, 3$ and $b=2, 5$ with the Hartree field $-V_H(r)=e^{-2r}(1+1/r)$.

r	0	0.1	0.3	0.5	0.8	1.0	1.2	1.5	1.8	2.0	2.5	3.0
$-V_H(r)$	$+\infty$	9.006	2.378	1.104	0.454	0.271	0.166	0.0830	0.0425	0.0275	0.00943	0.00330
$-V(r)$	$+\infty$	12.354	2.511	1.157	0.472	0.279	0.169	0.0862	0.0405	0.0254	0.00798	0.00252

TABLE II. A comparison of our values for $\phi_0(r)$, Eq. (6) with the corresponding Geltman's numerical values for his $\phi_0(r)$.

r	0	0.5	1.0	1.5	2.0	3.0	4.0
Geltman's results for $\phi_0(r)$	0.428	0.266	0.171	0.108	0.0689	0.0364	0.0216
Our results	0.456	0.255	0.155	0.101	0.0696	0.0372	0.0222
r	6.0	8.0	10.0	12.0	14.0	16.0	20.0
Geltman's results for $\phi_0(r)$	0.00903	0.00425	0.00210	0.00109	0.000584	0.000321	0.000100
Our results	0.00926	0.00435	0.00234	0.00114	0.000614	0.000334	0.000105

sponding results of Geltman we have adopted in Table I, according to Geltman, the value of Henrich[6] for the electron affinity of the hydrogen atom, $E_0=0.747$ ev. The best value for the electron affinity of the hydrogen atom given by Pekeris or Hart and Herzberg will negligibly change our values in Table II. Table II shows a good agreement between Geltman's and our values, so that we can adopt for the ground state function of H^- the following function: $\Psi_d=\phi_0(r_1)\phi_0(r_2)$, where ϕ_0 is given by Eq. (6). Our ground wave function of H^- is very simple in comparison with the corresponding results obtained by Henrich,[6] Chandrasekhar,[7] Geltman,[5] Hylleraas and Midtdal[1] and also by Hart and Herzberg.[2]

[1] E. A. Hylleraas and J. Midtdal, Phys. Rev. **109,** 1013 (1958).
[2] J. F. Hart and G. Herzberg, Phys. Rev. **108,** 79 (1957).
[3] C. L. Pekeris, Phys. Rev. **112,** 1649 (1958).
[4] For reference, see T. Tietz, J. Chem. Phys. **29,** 684 (1958).
[5] S. Geltman, Phys. Rev. **104,** 346 (1956).
[6] L. R. Henrich, Phys. Rev. **104,** 346 (1956).
[7] S. Chandrasekhar, Astrophys. J. **102,** 395 (1945).

Increase in Publication Charge

Starting with the January, 1962 issue, the publication charge for this journal and other AIP-owned journals will be increased to $40 per page. With the great increase in the quantity of material being published and the gradual rise of printing costs, it is necessary to increase publication charges or to raise subscription rates, or both. Our basic justification of the publication charge is that a research investigation is not completed until the results are made generally available through publication. It is therefore proper for the agency which supports the research to include the small amount, estimated at less than 1%, required to support publication. We believe that physicists should have their own copies of many journals and that subscription prices should therefore be kept as low as possible. The "ideal" arrangement toward which we are striving would have the publication charges cover the costs of editorial work and composition so that the individual subscriber would have to pay only for the printing and handling of his own copy. Since our ability to finance publication of the journal would not depend on the number of subscribers, there would be no danger that a loss of subscriptions because of the growing use of photocopying would jeopardize continued publication.

HUGH C. WOLFE, *Director of Publications*
American Institute of Physics